
# Modelling Guide for Timber Structures

**2022 - First Edition**

*Edited by*
Zhiyong Chen
Dorian Tung
Erol Karacabeyli

Special Publication SP-544

FPInnovations

Modelling Guide for

# Timber Structures

Special Publication SP-544


Edited by

**Zhiyong Chen**

**Dorian Tung**

**Erol Karacabeyli**



2022

Pointe-Claire, Que.

Modelling Guide for Timber Structures

Special Publication SP-544
ISBN 978-0-86488-613-2 (print)
ISBN 978-0-86488-612-5 (electronic)

Please submit inquiries about this document to:

FPInnovations
570 Saint-Jean Blvd
Pointe-Claire, QC
Canada H9R 3J9
info@fpinnovations.ca

Follow us:

*Front cover: Artistic rendering of 2150 Keith Drive building, Vancouver, Canada courtesy of images provided by DIALOG and CadMakers.*
*Back cover: Image of building courtesy of CadMakers.*

# ACKNOWLEDGEMENTS

The *Modelling Guide for Timber Structures* was financially supported by Natural Resources Canada through the Expanding Wood Use Towards 2025 project and the Green Construction through Wood (GCWood) program. We also acknowledge the financial contribution from Ministère des Forêts de la Faune et des Parcs du Québec.

The contributors to this guide include researchers who are well versed in computer modelling of timber structural engineering, progressive collapse, wind engineering, and earthquake engineering; practising engineers who have applied computer modelling to timber structures; manufacturers of timber products and connections; and structural analysis software developers with an interest in structural analysis of timber-based structural systems. The time and effort that the contributors invested in the development of the guide are greatly appreciated.

A special acknowledgement goes to our copyeditors, Anne Godlewski, Blazej Szpakowicz, and Joanna Odrowaz, as well as to FPInnovations' Communications team for its contributions to this guide.

Finally, the advice received from the advisory group for the development of this guide, comprising Mohammad Mohammad, Robert Jonkman, Philip Line, Conroy Lum, and Marjan Popovski, was invaluable and is gratefully acknowledged.

# CONTRIBUTORS

## Government Entities and Associations

| | | |
|---|---|---|
| APA – The Engineered Wood Association | Borjen Yeh | USA |
| American Wood Council (AWC) | Philip Line | USA |
| Canadian Construction Materials Centre (CCMC) | Jasmine McFadden | Canada |
| Canadian Wood Council (CWC) | Ali Mikael | Canada |
| | Robert Jonkman | Canada |
| Forestry Innovations Investment (FII) | Antje Wahl | Canada |
| | Sonya Zeitler Fletcher | Canada |
| National Lumber Grades Authority (NLGA) | Richard Desjardins | Canada |
| Natural Resources Canada (NRCan) | Mohammad Mohammad | Canada |
| WoodWorks | Scott Breneman | USA |

## Research Institutes

| | | |
|---|---|---|
| Chalmers University of Technology | Robert Jockwer | Sweden |
| Clemson University | Weichiang Pang | USA |
| Colorado School of Mines | Shiling Pei | USA |
| Colorado State University | John van de Lindt | USA |
| Czech Technical University in Prague | Petr Kabele | Czech Republic |
| FPInnovations | Christian Dagenais | Canada |
| | Chun Ni | Canada |
| | Conroy Lum | Canada |
| | Dorian Tung | Canada |
| | Erol Karacabeyli | Canada |
| | Jieying Wang | Canada |
| | Lin Hu | Canada |
| | Marjan Popovski | Canada |
| | Rod Stirling | Canada |
| | Samuel Cuerrier Auclair | Canada |
| | Sylvain Gagnon | Canada |
| | Zhiyong Chen | Canada |
| Griffith University | Benoit Gilbert | Australia |
| KTH Royal Institute of Technology | Roberto Crocetti | Sweden |
| Kyoto University | Hiroshi Isoda | Japan |
| Laval University | Alexander Salenikovich | Canada |
| Linnaeus University | Thomas Bader | Sweden |
| McMaster University | Lydell Andree Wiebe | Canada |
| TNO | Jan Niederwestberg | Netherlands |
| TU Wien | Markus Lukacevic | Austria |

| | | |
|---|---|---|
| University of Alberta | Lei Zhang | Canada |
| | Ying Hei Chui | Canada |
| University of Auckland | Ashkan Hashemi | New Zealand |
| | Nicholas Chan | New Zealand |
| | Pierre Quenneville | New Zealand |
| University of Bologna | Luca Pozza | Italy |
| University of British Columbia | Chunping Dai | Canada |
| | Kate Semple | Canada |
| | Meiling Chen | Canada |
| University of Canterbury | Minghao Li | New Zealand |
| University of Illinois | Md Abdul Hamid Mirdad | USA |
| University of Liverpool | Zhongwei Guan | United Kingdom |
| University of Nevada | Keri Ryan | USA |
| University of Northern British Columbia | Asif Iqbal | Canada |
| | Thomas Tannert | Canada |
| University of Ottawa | Ghasan Doudak | Canada |
| University of Technology Sydney | Keith Crews | Australia |
| University of Toronto | Frank Vecchio | Canada |
| Washington State University | Daniel Dolan | USA |
| Western University | Girma Bitsuamlak | Canada |
| | Matiyas Bezabeh | Canada |

**Consultants**

| | | |
|---|---|---|
| Arup | Maja Belic | Australia |
| | Sebastian Kaminski | United Kingdom |
| | Vincenzo Reale | United Kingdom |
| CadMakers | Kai Yang | Canada |
| | Nicolas Cantin | Canada |
| | Vasco Chan | Canada |
| dedaLEGNO | Maurizio Follesa | Italy |
| DIALOG | Cameron Ritchie | Canada |
| Douglas Consultants Inc. | Kevin Below | Canada |
| Elema | Jake Estok | Canada |
| Fast + Epp | Carla Dickof | Canada |
| | Robert Jackson | Canada |
| KPFF Consulting Engineers | Reid Zimmerman | USA |
| L2C Experts | Jean-Philippe Carrier | Canada |
| Moelven | Rune Abrahamsen | Norway |
| Moses Structural Engineers | David Moses | Canada |
| Mott MacDonald | Seifu Bekele | Australia |
| MTC Solutions | Jean-Philippe Letarte | Canada |

| | | |
|---|---|---|
| PTL | Andy Buchanan | New Zealand |
| | Daniel Moroder | New Zealand |
| | Francesco Sarti | New Zealand |
| RWD Conseils | Richard Desjardins | Canada |
| Stonewood Structural Engineers | Scott Nyseth | USA |
| StructureCraft Builders | Brandon Sullivan | Canada |
| | Gerald Epp | Canada |
| | Justin Brown | Canada |
| | Lucas Epp | Canada |
| | Pietro Vinco da Sesso | Canada |
| | Shasan Chokshi | Canada |
| SWECO | Magne Aanstad Bjertnæs | Norway |
| Timber Engineering | Hercend Mpidi Bita | Canada |
| | Robert Malczyk | Canada |
| Time for Timber | Richard Harris | United Kingdom |
| TWW | Alex Zecevic | Australia |
| Vistek Structural Engineers | Jeremy Church | Australia |
| | Nathan Benbow | Australia |

## Companies - Timber Products and Connections

| | | |
|---|---|---|
| Australian Sustainable Hardwoods | Nathan Benbow | Australia |
| Henkel | William Nguegang Nkeuwa | USA |
| Nordic Structures | Keven Durand | Canada |
| Structurlam | Nicholas Sills | Canada |
| Tectonus | Ashkan Hashemi | New Zealand |
| Timberlab | Hans-Eric Blomgren | USA |
| Timberlink | Jeremy Church | Australia |
| West Fraser | William Nguegang Nkeuwa | Canada |

## Companies - Software

| | | |
|---|---|---|
| Altair | Marinos Stylianou | USA |
| Dlubal Software | Amy Heilig | USA |
| | Bastian Kuhn | Germany |
| | Gerhard Rehm | Germany |
| WoodWorks® Software | Yang Du | Canada |

## EXECUTIVE SUMMARY

Due to the awareness of the importance of reducing environmental footprint and the rising costs of construction, timber structures have been increasingly attracting attention and, subsequently, adoption for being built taller and larger. Computer modelling plays a crucial role in the analysis and design of large and tall timber structures, and in the development of wood-based products, connections, and systems. A survey by FPInnovations showed that practising engineers are typically unfamiliar with timber structure modelling, and researchers generally lack resources for advanced modelling of timber systems. Therefore, in 2020, FPInnovations initiated a project to develop a guide that would support the application of numerical modelling on the analysis and design of timber structures, and the development and optimisation of wood-based products and systems. The *Modelling Guide for Timber Structures* is the result of a global effort involving over 100 collaborators, including experts from research institutes, consulting firms, manufacturers, software companies, government entities, and associations.

This guide brings together the experience gained from recently built timber projects, and the latest research development in the modelling of timber structures. It includes a wide range of practical and advanced modelling topics, such as key modelling principles, methods, and techniques specific to timber structures; modelling approaches and considerations for wood-based components, connections, and assemblies; and analytical approaches and considerations for timber structures during progressive collapse, wind, and earthquake events. It also presents the differences in the modelling approaches to timber, steel, and concrete structures.

The information presented in this guide is intended to assist practising engineers to apply computer modelling to timber structures, enrich researchers' resources for advanced computer modelling of timber systems, and assist software companies in identifying knowledge gaps so that they may upgrade programs accordingly to accommodate the advanced computer modelling of timber structures.

# CONTENTS

## Chapter 7: Load-Resisting Systems

# CHAPTER 1

## Introduction


**Authors**
Zhiyong Chen
Dorian Tung
Erol Karacabeyli
Conroy Lum
Marjan Popovski

**Reviewers**
Mohammad Mohammad
Robert Jonkman
Philip Line

# TABLE OF CONTENTS

## 1.1 BACKGROUND AND OBJECTIVES

Computer modelling is essential for analysing and designing mid- and high-rise buildings and long-span structures where traditional engineering hand calculations or spreadsheets typically adopted by designers for low-rise timber buildings are not adequate. It is also a valuable tool for optimising wood-based products, connections, and systems that improve structural performance. A survey by FPInnovations (Chen, Karacabeyli, & Lum, 2017) showed that practising engineers are relatively unfamiliar with modelling of timber structures, and that researchers generally lack resources for advanced modelling of timber systems. Further, wood design features currently available in some structural analysis software packages are usually not suitable for modelling complex or hybrid timber structures. This will hinder the application and development of timber construction given that timber structures increasingly require demonstration of performance or equivalency through computer modelling, regardless of whether prescriptive or performance-based design procedures are used.

This guide focuses on the modelling and analysis of timber structures. The objectives of the guide are to help engineers apply computer modelling concepts to the design of timber constructions, enrich researchers' resources for advanced computer modelling of timber systems, and assist software companies in identifying the gaps and upgrading programs accordingly to accommodate advanced computer modelling of timber structures.

## 1.2 SCOPE

This modelling guide has been developed to:

- Establish the basic principles for applying computer modelling in timber structure analysis, including modelling assumptions and validating the assumptions and results; and
- Guide the selection of efficient modelling methodologies, appropriate analysis methods, and robust evaluation criteria for timber structures.

This is a free downloadable and printable publication developed by more than 40 experts from countries around the world. The author team is composed of:

- Researchers who are well versed in computer modelling of timber structural engineering, progressive collapse, wind engineering, and seismic engineering;
- Practising engineers who have applied computer modelling to timber structures;
- Manufacturers of timber products and connections; and
- Software companies with an interest in the analysis of timber-based structural systems.

This modelling guide complements the overview of the analysis and design of tall wood buildings in FPInnovations' *Technical Guide for the Design and Construction of Tall Wood Buildings in Canada* (Karacabeyli & Lum, 2022) and the fundamental information and knowledge related to timber system modelling in the Canadian Wood Council's *Advanced Wood Design Manual* (in press).

## 1.3 CONTENT AND ORGANISATION

This modelling guide has been written with practising engineers and researchers in mind. It has been developed with the understanding that computer modelling of timber structures is a specialty to which many engineers and researchers have limited exposure in either education or practice. The guide consists of three parts: Part A – Introduction (appears in green in Figure 1), Part B – Modelling (in red), and Part C – Analyses (in blue).

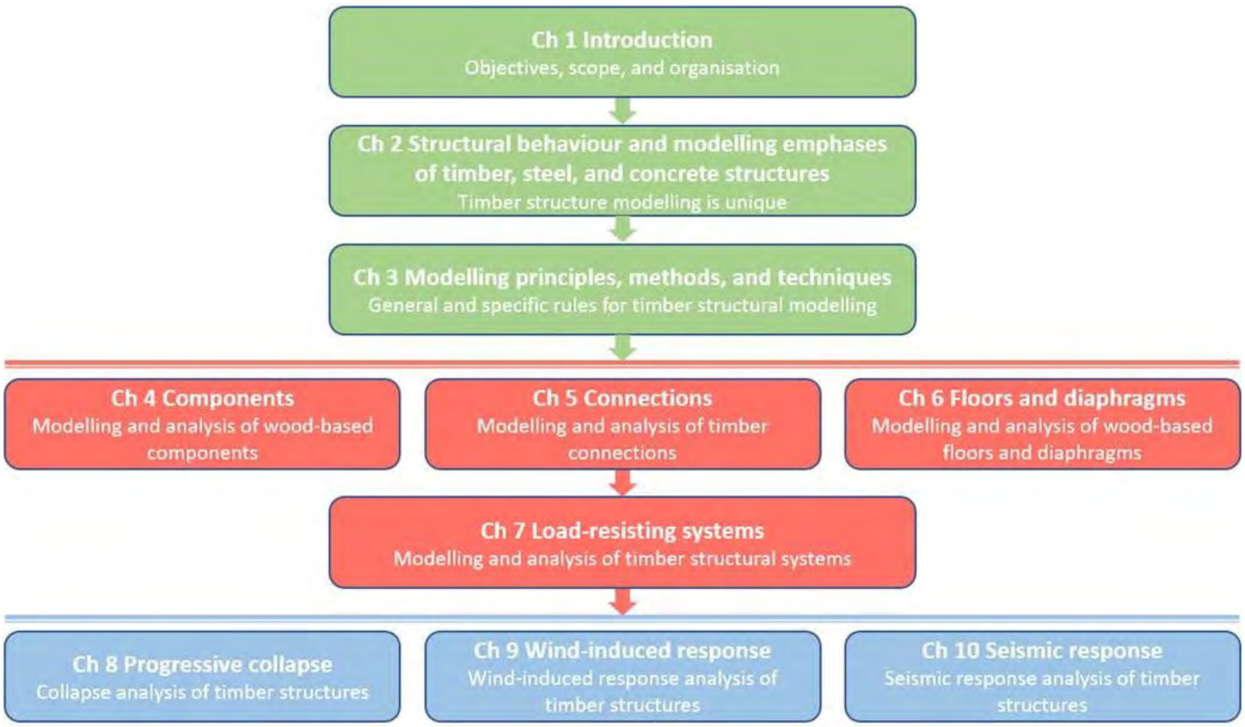


**Figure 1. Organisation of this modelling guide**

The subjects covered in Part A are as follows:

Chapter 1 introduces the background, objectives, scope, content, and organisation of the guide.

Chapter 2 compares timber structures with other structures in terms of structural behaviour and the approaches to modelling, including assumptions. This chapter helps those unfamiliar with modelling of timber structures learn more about the major differences and similarities between timber and other commonly used construction materials.

Chapter 3 introduces modelling principles, methods, and techniques. It also provides general rules for structural modelling and specific rules for timber-based systems.

The subjects covered in Part B are as follows:

Chapter 4 highlights the key mechanical characteristics of wood for modelling. It introduces advanced and practical modelling solutions for the analysis and design of wood-based products. Moreover, this chapter provides modelling solutions for optimising wood-based products and experimental test plans.

Chapter 5 highlights the key roles and influencing factors of connections in timber systems. It presents advanced and practical modelling solutions for analysing and designing timber connections. It also discusses modelling solutions for optimising connections.

Chapter 6 introduces modelling methods for the analysis and design of different types of floor and roof assemblies, such as light wood-frame, mass timber, and composite floor systems. It also discusses the modelling of floor and roof assemblies under gravity loads in out-of-plane directions, in terms of strengths, deflections, and vibration, along with modelling under lateral (in-plane) loads for properties such as strength and deflection.

Chapter 7 discusses the advanced and practical modelling solutions for light wood-frame, mass timber, hybrid timber, advanced timber, and long-span timber structures. This chapter also introduces general modelling considerations for gravity systems.

The subjects covered in Part C are as follows:

Chapter 8 introduces the approaches to collapse analysis for timber structures and advanced and practical modelling solutions for shear wall and post-and-beam structures. This chapter also introduces key modelling considerations for progressive collapse analysis of hybrid systems, long-span structures, and prefabricated modular structures.

Chapter 9 introduces the behaviour and mechanism of timber buildings under wind loads and the application of computational fluid dynamics for modelling wind environments and determining cladding wind loads. It also presents advanced and practical modelling solutions for estimating the wind-induced response of timber structures.

Chapter 10 introduces the behaviour and mechanism of timber buildings under earthquake loads, selection and scaling methods of ground motions, and advanced and practical modelling solutions for estimating the seismic response of timber structures.

## 1.4 REFERENCES

Canadian Wood Council. (in press). *Advanced wood design manual*.

Chen, Z., Karacabeyli, E., & Lum, C. (2017). *A survey on modelling of mass timber.* FPInnovations.

Karacabeyli, E., & Lum, C. (2022). *Technical guide for the design and construction of tall wood buildings in Canada (2nd ed.)*. FPInnovations.

# CHAPTER 2

## Structural behaviour and modelling emphases of timber, steel, and concrete structures

**Authors**
Zhiyong Chen
Lydell Wiebe
Frank Vecchio

**Reviewers**
Sebastian Kaminski
Kevin Below

# TABLE OF CONTENTS

## 2.1 INTRODUCTION

Every structural material has unique mechanical characteristics. Correspondingly, different design strategies have been adopted for structural systems using different materials to optimise the material use. The structural behaviour and modelling emphases of structural systems with different materials vary accordingly. Currently, most practising engineers and researchers are more familiar with steel and concrete structures than with timber structures, especially mass timber structures. As such, to help these practitioners become acquainted with timber structures, this chapter compares timber structural systems with analogous ones from steel and concrete, in terms of their structural behaviour and modelling emphases.

## 2.2 GENERAL COMPARISONS

### 2.2.1 Material Behaviour

Steel (Figure 1[a]) is an iron alloy with a controlled level of carbon. It is generally considered to be a homogeneous, isotropic, elastoplastic material with equal strength in tension and compression. It is also a ductile material, which behaves elastically until it reaches yield, at which point it becomes plastic, and fails in a ductile manner with large strains before fracture.

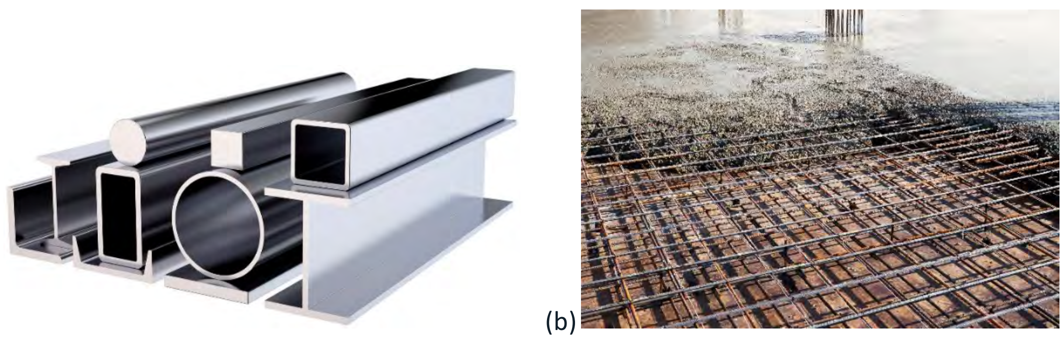

(a) (b)

**Figure 1. Typical (a) steel elements and (b) reinforced concrete**

Concrete is a mixture of water, cement, and aggregates. The proportion of these components is important to create a concrete mix of a desired compressive strength. When reinforcing steel bars are added into concrete in bending, such as the panels shown in Figure 1(b), the two materials work together, with concrete providing the compressive strength, and steel providing the tensile strength primarily. Conventional (plain, unreinforced) concrete is a nonlinear, nonelastic, and generally brittle material. It is strong in compression and weak in tension. Due to its weakness in tension capacity, concrete fails suddenly and in a brittle manner under flexural (bending) or tensile force unless adequately reinforced with steel (Maekawa et al., 2008). Reinforced concrete (RC) is concrete into which steel reinforcement bars, plates, or fibres have been incorporated to strengthen a material that would otherwise be brittle.

Wood (Figure 2) has characteristic anisotropy due to its fibrous structure, which can be considered as producing three-dimensional orthotropy (Hirai, 2005). Its stiffness and strength properties vary as a function of grain orientation among the longitudinal, radial, and tangential directions (Chen et al., 2020; Chen et al., 2011; Sandhaas et al., 2012). The failure modes and the stress-strain relationships of wood depend on the direction of the load relative to the grain and on the type of load (tension, compression, or shear). For wood in tension and shear, the stress-strain relationship is typically linear, and the failure is brittle, while for wood in compression, the stress-strain relationship is typically nonlinear, and the failure is ductile (Forest Products Laboratory, 2010). When loaded in tension and shear, wood elements behave in a brittle manner. On the other hand, in compression parallel and perpendicular to the grain, wood elements show a degree of inelastic behaviour and ductility, except under buckling, when wood is very brittle. When loaded in bending, the ductility in wood elements is generally related to plasticisation in the compression zone, as the tension zone tends to fail in a brittle manner. Therefore, ductility in bending is difficult to achieve in practice, and it is recorded in tests only when the strength of the tension area is considerably higher than that of the compression area. Similarly, shear failure of wood elements, which can happen in short, tapered beams, in beams with end splits, or where there is stress concentration (e.g., close to notches or around holes), is brittle, characterised by a sliding of the fibres and thus cracking parallel to the grain.

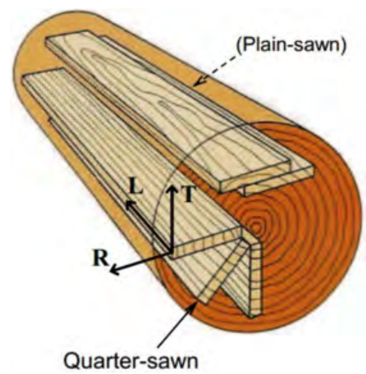


**Figure 2. Three main axes of wood with respect to grain direction: longitudinal (L), radial (R), and tangential (T) (Mokdad & Missoum, 2013)**

### 2.2.2 Structural Behaviour

Due to their high strength-to-weight ratio, steel elements are, in general, relatively slender (Figure 1[a]). Under tension, steel elements can provide excellent stiffness, strength, and ductility. However, two main areas that require attention in the design of steel structures are buckling and connections. In compression and bending, stability (global or local buckling) is often a concern, so the design should account for the buckling resistance of slender steel compression and bending elements. Connections can also be a point of relative weakness in steel structures. As such, care is needed to ensure that connections do not unduly influence the overall response of a steel structure, especially for seismic design, where ductility is of primary importance. In other words, connections that are not intended to yield should be capacity-protected, while connections that are intended to yield should be designed to ensure that yielding does not progress to failure under repeated cycles of seismic loading.

Detailing of reinforcement, particularly for seismic conditions, is a key design aspect for RC structures. As a composite material, RC (Figure 1[b]) resists not only compression but also bending and other direct tensile actions. The reinforcement in an RC structure, such as a steel bar, must be able to undergo the same strain or deformation as the surrounding concrete to prevent discontinuity, slip, or separation of the two materials under load. Maintaining composite action requires the transfer of load between the concrete and steel. The direct stress is transferred from the concrete to the bar at the interface to change the tensile stress in the reinforcing bar along its length. This load transfer is achieved by means of bond (anchorage) and is idealised as a continuous stress field that develops in the vicinity of the steel-concrete interface. The RC element acts like a rigid element.

Because of their anisotropic mechanical properties, timber elements (Figure 2) possess much higher stiffness and strength in the parallel-to-grain direction than in the perpendicular directions. Due to the presence of growth characteristics (e.g., knots), which significantly impair the tension and shear strength of wood, timber elements are most suitable for use in resisting compression parallel to the grain, followed by bending. Tension strength parallel-to-grain is as good or better than compression strength parallel-to-grain; however, the tension connections are prone to brittle failure. Tension perpendicular to the grain should be avoided or minimised in timber elements whenever possible because the capacity of wood in this direction is limited, and any splits effectively remove this capacity altogether. The main area that requires attention in the design of timber structures is connections. Timber connections typically govern the strength of timber structures, either light wood-frame structures or mass timber structures, and can contribute significantly to the stiffness of the structures. In mass timber structures, the timber elements are typically designed with higher capacity than the connections due to the complex mechanical properties and limited ductility in timber elements.

### 2.2.3 Modelling Emphases

To model steel elements and connections, material models must simulate the homogeneous, isotropic, and elastoplastic behaviour of steel. Depending on the level of complexity required of the model, an elastic model may be adequate. More sophisticated models may include yielding and strain hardening under uniaxial loading, or even full hysteretic loops that capture various phenomena observed under cyclic loading, such as the Bauschinger effect, kinematic and isotropic strain hardening, and cyclic strength and stiffness degradation. Fatigue can also be considered for elements subjected to many loading cycles.

For simple or equivalent models, RC elements can be simulated using elastic material models with effective stiffness, while an inelastic mechanism can be simulated using plastic hinges. With respect to complex or detailed models, typically, the constitutive response of the concrete and reinforcement comprising the RC are modelled separately. The material model for uncracked or confined concrete typically consists of an isotropically hardening yield surface that is active when the stress is dominantly compressive; an independent 'crack detection surface' may be used in tandem to determine whether a point fails by cracking. For cracked concrete, orthotropic damage-based models are commonly used in which the effects of cracking are 'smeared' (Maekawa et al., 2008). Reinforcing bars can be modelled discretely using one-dimensional strain theory elements (i.e., truss elements) or, where appropriate, as a unidirectional smeared field of reinforcement; an elastoplastic-with-strain-hardening constitutive response is typically assumed. With this modelling approach, the behaviour of the concrete is considered largely independent of the behaviour of the reinforcement. However, the interaction effects associated with the reinforcement-concrete interface, such as tension stiffening, bond slip, and dowel action, can have a significant influence on the composite behaviour; these can be accounted for either by modifying the element constitutive models or by including specialized elements in the structural model (e.g., bond link elements). Defining the reinforcement and associated interaction effects can be tedious in complex problems; however, it is important that this be done accurately, since not doing so may cause an analysis to determine key failure mechanisms improperly.

Timber elements generally can be simulated using orthotropic elastic material models. In some cases, such as balloon-type mass timber walls, elastoplastic behaviour of timber elements must be included in the material models at the wall bottom that connects to the foundation. Compared to other connections, timber connections are much more complex due to the highly variable anisotropic mechanical properties of wood, existing growth characteristics such as splits and knots, and other effects, such as moisture content and temperature. Various types of failure modes can occur in timber connections, and they should have ductile failure modes, such as yielding, rather than brittle modes, such as splitting. Where possible, the yielding should happen in the parts of a connection that are made from a material other than wood, such as steel. Reale et al. (2020) recommend that (a) connections with steel fasteners yielding in Johansen plastic hinge mode that are very ductile be essential for seismic design; (b) connections with timber crushing locally that possess limited ductility not be permitted in seismic design; and (c) connections with brittle failure, such as splitting, not be acceptable in any cases, since the connections have effectively failed, and the load-carrying capacity has lost once the brittle failure occurs. When properly designed, timber connections can be simulated using models that represent the connection stiffness and strength. For analysing timber systems under cyclic loading, suitable hysteretic models are required to accurately reflect the structural response of timber connections and assemblies, as these may possess highly pinched hysteresis and degradation of strength and stiffness.

In summary, the design and modelling of timber structural elements, connections, assemblies, and systems differ from that of steel and concrete in ways that are important and usually more complex.

## 2.3 COMPARISONS OF SELECTED LATERAL LOAD-RESISTING SYSTEMS

### 2.3.1 Shear Walls

Shear walls of cross-laminated timber (CLT) (Karacabeyli & Gagnon, 2019) are the latest lateral load-resisting system of timber structures accepted by codes and standards around the world, such as the *Engineering design in wood* standard (CSA, 2019) and the *National Design Specification for Wood Construction* standards (American Wood Council, 2018), while RC shear walls are a system made of other materials that is most similar to CLT shear walls. Both types of shear walls may take the form of isolated planar walls, flanged walls, and larger three-dimensional assemblies such as building cores.

The structural behaviour of RC shear walls is often categorised as slender (flexure-governed) or squat (shear-governed), according to the governing mode of damage and failure (Figure 3). Slender RC shear walls detailed to current seismic design requirements, having low axial stress and designed with sufficient shear strength to avoid shear failure, perform similarly to RC beam-columns. Ductile flexural behaviour with stable hysteresis can develop up to hinge rotation limits that are a function of axial load and shear in the hinge region. Simple slender walls (including coupled walls) can be modelled with reasonable accuracy and computational efficiency as vertical beam-column elements with lumped flexural plastic hinges at the ends. The modelling parameters and plastic rotation limits of the *Seismic Evaluation and Retrofit of Existing Buildings* standard (American Society of Civil Engineers [ASCE], 2017) may be used for guidance. Fibre-type models are commonly used to model slender walls, in which the wall cross-section is discretised into a number of concrete and steel fibres. With appropriate material nonlinear axial stress-strain characteristics, the fibre wall models can capture with reasonable accuracy the variation of axial and flexural stiffness due to concrete cracking and steel yielding under varying axial and bending loads. Advanced modelling of RC, using detailed two-dimensional membrane, three-dimensional shell, or solid elements with smeared or explicit representation of reinforcement and concrete cracking, is useful for assessing walls where there is a strong interaction between shear and flexure, such as in flexural hinge regions where the shear force demand is close to the shear capacity. It is also useful in situations where nonlinear stress and strain fields violate the assumptions of idealised hinge or fibre models. Squat shear walls fail in shear rather than flexure and present significant modelling challenges. Monotonic tests show greater displacement ductility than can be relied on in cyclic loading, where degradation of stiffness and strength is observed. These behaviours are not easily captured using beam-column or fibre-type elements. Some analysis platforms contain suitable formulations comprising in-series nonlinear shear and flexure springs. In addition, detailed nonlinear finite element (FE) formulations for RC are available in some platforms and can reproduce most observed features of behaviour (Cortés-Puentes & Palermo, 2020; Palermo & Vecchio, 2007).

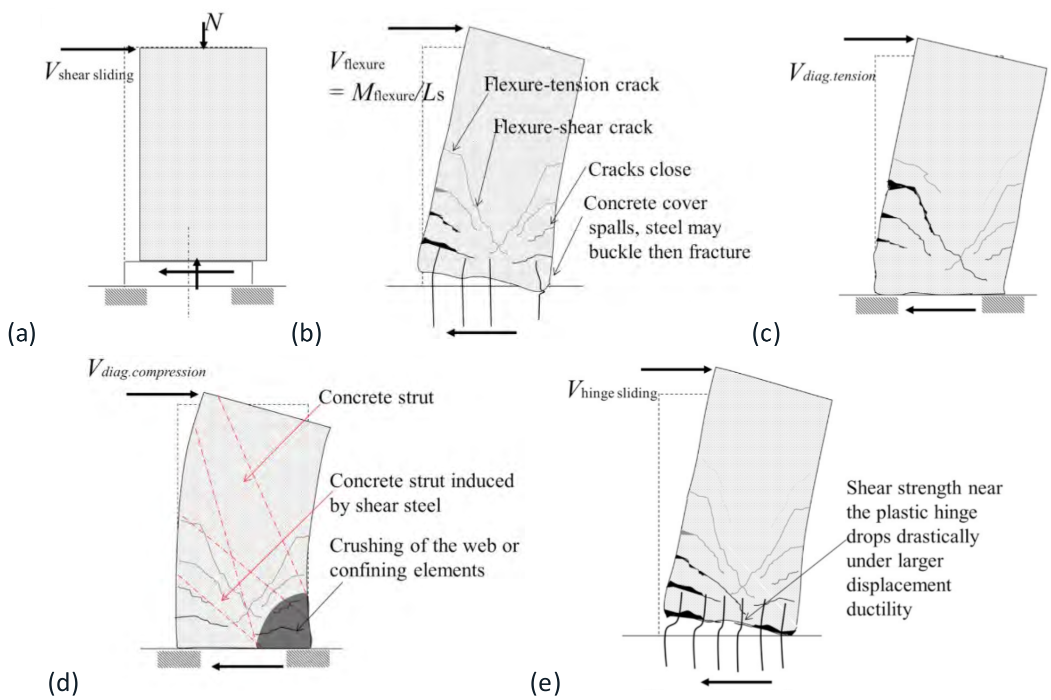


**Figure 3. Typical failure mechanisms of RC walls (Tang & Su, 2014): (a) shear sliding failure, (b) flexure failure, (c) diagonal tension failure, (d) diagonal compression failure (crushing of web or boundary elements), and (e) hinge sliding failure**

Unlike RC shear walls, CLT shear walls are typically made of CLT panels connected to the foundation or floors using hold-downs to resist vertical uplift forces, and shear connectors, shear keys, or both to resist the shear forces. For coupled walls, vertical joints are used to connect the adjacent panels. According to existing studies (Chen & Popovski, 2020a; Gavric et al., 2015), the stiffness and lateral load-carrying capacity of CLT shear walls is governed by (a) the rocking of the panel due to crushing of the timber in compression and stretching of the hold-down in tension, (b) the slip of the wall relative to the foundation due to the shear flexibility of the hold-down and shear connectors, (c) the shear deformation of the panel, and (d) the bending deformation of the panel (Figure 4).

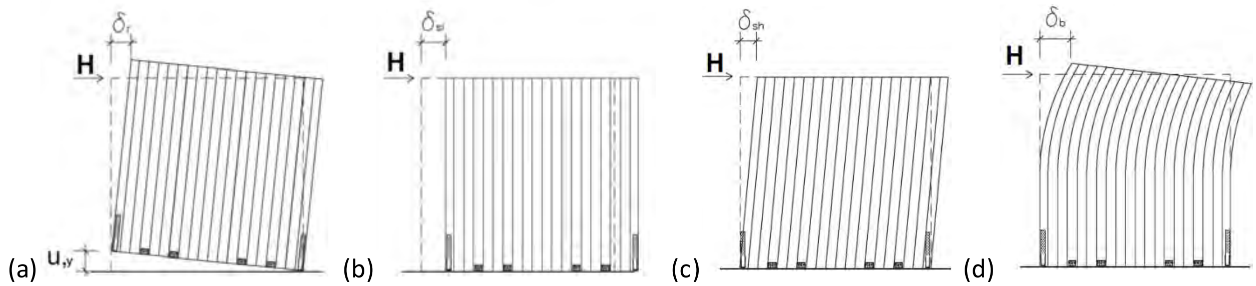


**Figure 4. Deflection components of a single CLT wall panel (Gavric et al., 2015): (a) rocking, (b) sliding, (c) shear, and (d) bending**

Generally, CLT shear walls under in-plane lateral loading conditions present a complex stress state and many possible failure modes, such as bending failure and shear failure (gross shear, net shear, rolling shear, and torsion), that must be considered during design (Chen & Popovski, 2021a; Danielsson & Serrano, 2018). Typically, it is recommended that shear walls be designed following a capacity design methodology for all types of lateral loads (i.e., seismic and wind loads), such that the capacity of the wall system is governed by the connections only (Chen & Popovski, 2020a). The CLT panels exhibit in-plane elastic deformation, while the connections provide all the ductility and energy dissipation. Thus, the strength of the CLT shear walls is governed by the shear connectors, hold-downs, and vertical joints if present. This is a major difference between CLT shear walls and RC shear walls. Typically, CLT panels are simulated using shell elements with orthotropic elastic or elastoplastic material models, while the vertical joints, shear connectors, and hold-downs are simulated using springs. Depending on the type of analysis, the connections adopt an elastic or elastoplastic backbone curve or hysteretic springs. For multistorey, platform-type buildings, the influence of the floor panels between two vertical walls should also be considered in the wall models (e.g., using elastoplastic springs or other equivalent methods). For balloon-type walls with high vertical loads or a large aspect ratio, the compressive strength of the CLT panels must be considered in the material model, especially at the wall bottom, so that the pivot point, the moment arm of overturning resistance, and hence, the lateral resistance and deflection of the walls can be calculated accurately. See Sections 7.2.3.1 and 7.2.3.2 for more information.

## 2.3.2 Braced Frames

A braced frame is essentially a planar vertically cantilevered truss (Bruneau et al., 2011). The beams and columns that form the frame carry vertical loads, and the bracing system carries the lateral loads. Various configurations of concentrically braced frames (Sabelli et al., 2013) are shown in Figure 5. Configurations (f) to (j) are not generally permitted for seismic design of concentrically braced steel frames, while configurations (d) to (g) and (j) are not generally permitted for seismic design of timber frames (Chen & Popovski, 2021b).

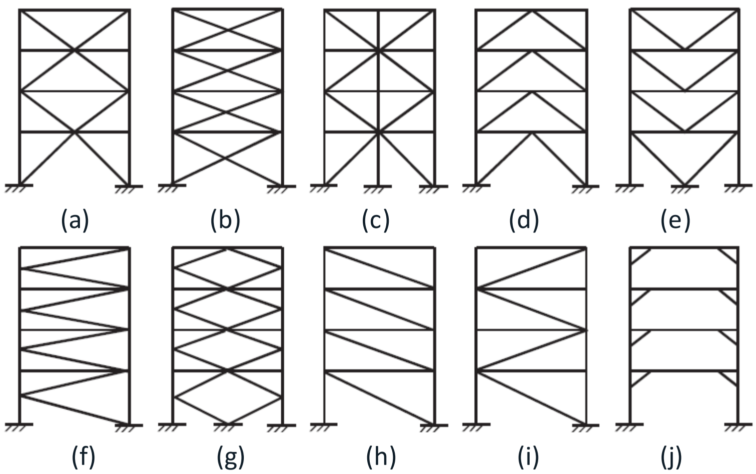


**Figure 5. Concentrically braced frame configurations: (a, b, c) X-braced frames; (d, e) inverted V-braced and V-braced frames, also known as inverted chevron-braced and chevron-braced frames, respectively; (f, g) K-braced and double K-braced frames; (h, i) single diagonal braced frames; and (j) knee-braced frame**

Under seismic loads, steel concentrically braced frames are expected to yield and dissipate energy through post-buckling hysteretic behaviour of the bracing elements in compression followed by yielding of the braces in tension (Figure 6), potentially with some contribution from the brace connections. The design strategy is to ensure that plastic deformation occurs only in the braces and their connections, capacity-protecting the columns and beams to enable the structure to survive strong earthquakes without losing its gravity-load resistance. Modelling inelastic brace behaviour is complicated by the interactive effects of yielding, overall element buckling, local buckling, and fracture. Several alternatives exist for modelling this nonlinear buckling response of braces. A commonly used approach is modelling the brace with fibre beam-column elements, which capture yielding, overall buckling, and concentration of plastic rotation in the buckled hinge, provided the number of elements along the length of the brace is adequate. Local buckling and fracture can be inferred from the plastic rotation and strains in the hinges (Uriz & Mahin, 2008). In an alternative modelling approach, the brace can be represented by a uniaxial phenomenological spring to capture brace yielding and overall buckling (Tang & Goel, 1989; Uriz & Mahin, 2008). While this type of element is simple to use, it can be more challenging to define and is limited by the tests available to calibrate it. In a more fundamental (though computationally expensive) analysis approach, the brace can be modelled with continuum FEs to directly simulate yielding, overall buckling, and local buckling (Schachter & Reinhorn, 2007). With appropriate material formulation, FE models can also simulate fracture initiation (Fell et al., 2010). In all cases, although the brace and its connections are the primary location of expected inelastic response, the surrounding beams and columns are also often modelled in a way that can capture some nonlinear behaviour.

(a)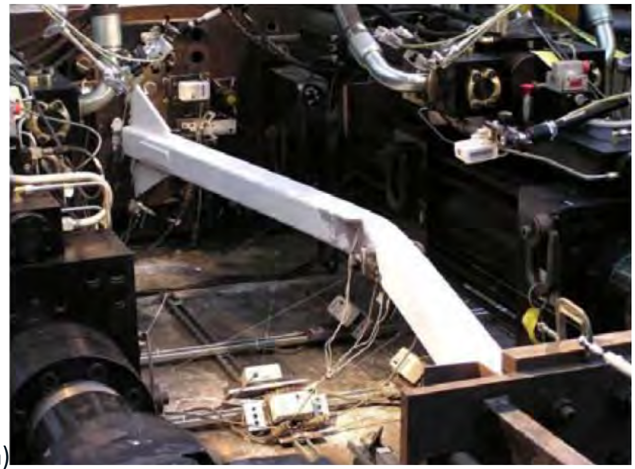(b)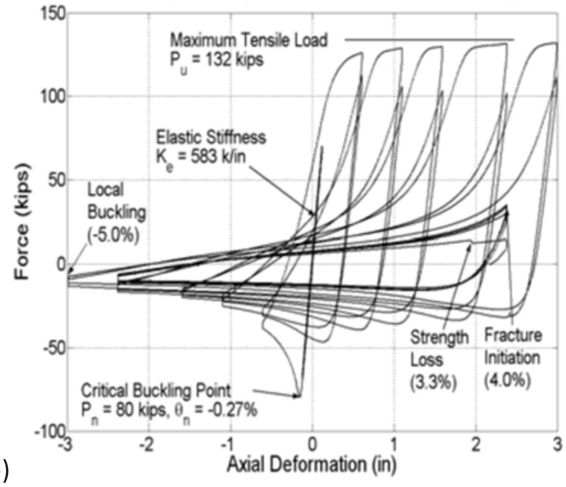


**Figure 6. Cyclic testing of a steel brace (Fell et al., 2010): (a) experimental set-up, and (b) measured axial force-deformation response**

Unlike braced steel frames, braced timber frames are expected to yield and dissipate energy primarily through energy-dissipative connections at the ends of the diagonal braces (Chen & Popovski, 2020b, 2021b). Therefore, for braced timber frames with energy-dissipative connections, the end connections of diagonal braces must be specially designed to sustain plastic deformation and dissipate hysteretic energy in a stable manner through successive cycles. The design strategy is to ensure that plastic deformation occurs only in the energy-dissipative connections, leaving the columns, braces, and beams undamaged, thus allowing the structure to survive earthquakes without losing its gravity-load resistance. To model the behaviour of the diagonal brace assemblies, each including a diagonal brace with two end connections (Figure 7[a]), an equivalent nonlinear connector (spring) element can be used to simulate the total performance of the whole diagonal brace assembly (Figure 7[b]). A continuous-column model, in which the columns are modelled using beam elements continuously from the top to the bottom, should be ensured through design and adopted for modelling braced timber frames (Chen et al., 2019). This can prevent underestimating the stiffness, frequency, strength, and ductility of braced frame buildings (Bruneau et al., 2011; MacRae, 2010; MacRae et al., 2004; Wada et al., 2009), which would occur in a pinned connection model, where the columns are modelled using truss elements. The horizontal beams can be modelled using truss elements and pinned to the columns, which are also connected to the ground using pin connections. See Section 7.2.3.3 for more information.

(a)  (b) 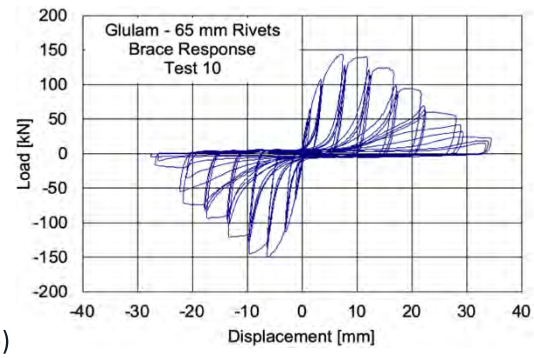


**Figure 7. Testing of a glued laminated (glulam) brace with riveted connections (Popovski, 2004): (a) experimental set-up, and (b) measured axial force-deformation**

## 2.3.3 Moment-Resisting Frames

Moment-resisting frames, which can be constructed using timber, steel, and concrete, are rectilinear assemblages of beams and columns, with the beams rigidly connected to the columns. The lateral load resistance is provided primarily by rigid frame action—that is, by the development of bending moment and shear force in the frame elements and joints. By virtue of the rigid beam-column connections, a moment frame cannot displace laterally without bending the beams or columns. The bending rigidity and strength of the frame elements is therefore the primary source of lateral stiffness and strength for the entire frame.

For non-timber systems that use capacity design principles, such as special concrete and steel moment frames (Hamburger et al., 2016; Moehle & Hooper, 2016), the inelastic deformation should occur primarily in flexural hinges in the beams and the column bases. In frames that do not meet special moment-frame requirements, inelastic effects may occur in other locations, including element shear yielding, connection failure, and element instability due to local or lateral-torsional buckling. Beam-columns are commonly modelled using either concentrated hinges, fibre-type elements, or layered elements (Guner & Vecchio, 2010a, 2010b, 2011, 2012). Whatever the model type, the analysis should be capable of reproducing (under cyclic loading) the element cyclic envelope curves that are similar to those from tests or other published criteria, such as in the *Seismic Evaluation and Retrofit of Existing Buildings* standard (ASCE, 2017) and *Modelling and Acceptance Criteria for Seismic Design and Analysis of Tall Buildings* (Applied Technology Council, 2010). The inelastic response of flexural beams and columns is often linked to the response of the connections and the joint panels between them. The inelastic behaviour in the beams, columns, connections, and panel zone (Figure 8[a]) can be modelled through idealised springs, as shown in Figure 8(b). Alternatively, it can be modelled through properly defined continuum behaviour (in equivalent fibre/layer models), along with appropriate consideration of a finite-size panel and how its deformation affects the connected elements. In steel structures, the yielding regions (i.e., beams, panel zones, and possibly columns and connections) tend to deform independently, except insofar as the strength of one element may limit the maximum forces in an adjacent element. On the other hand, in concrete frames, the inelastic deformation in the beams and columns can be coupled with the panel zone behaviour, due to the bond slip of longitudinal beam and column bars in the joint region. Thus, for concrete frames, the flexural hinge parameters should consider how the deformation due to bond slip is accounted for—either in the beam and column hinges or in the joint panel spring. Depending on the specific software implementation, the finite-size joint panel may be modelled using kinematic constraint equations, equivalent bar-spring assemblies, or approximate rigid end offsets (ASCE, 2017; Charney & Marshall, 2006).

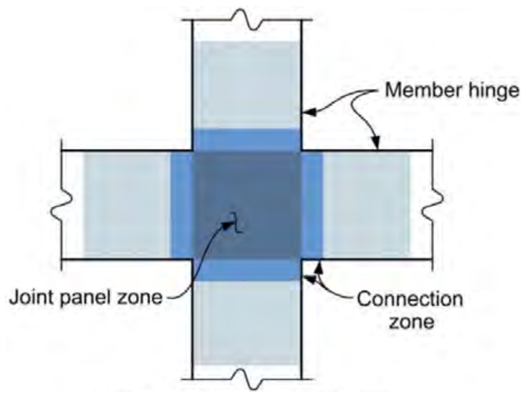


(a)

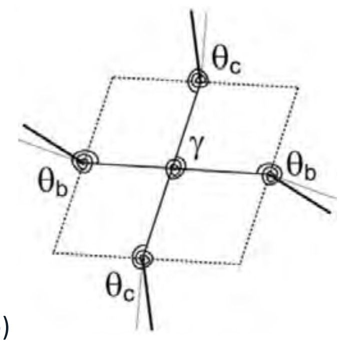


(b)

**Figure 8. Beam-to-column connection (Deierlein et al., 2010): (a) hinging region of beams and columns and deformable panel zone, and (b) idealised analysis model**

Timber moment-resisting frames consist of beams and columns that are connected using moment connections with (Figure 9) or without (Figure 10) inserted steel plates. The fasteners (e.g., bolts) can be arranged in a circular pattern (Blaß & Schädle, 2011; Branco & Neves, 2011; Negrão et al., 2016). The stiffness and strength of the connections can be adjusted by varying the radius of the fastener pattern, the number of fasteners, the thickness of the side and middle timber, the quality of the timber (embedment strength), the diameter of the fastener, and the quality of the fastener. According to the European yield model (European Committee for Standardization, 2004), there are three failure modes for the three-element connections: embedment of the side or middle timber, one plastic hinge in the fastener, or two plastic hinges in the fastener. Moment connections with the third failure mode should be applied in seismic areas because this results in the highest energy dissipation. According to Rinaldin et al. (2013), it is known that in a timber structure, most of the dissipative capacity takes place in the steel fasteners as timber behaves mostly elastically with only little plasticization in compression, parallel and perpendicular to the grain (for connections that are not reinforced). Timber connections with slender or semirigid fasteners have a higher equivalent energy ratio than those with nonslender or rigid fasteners. In slender-fastener timber connections, the steel fastener must deform plastically before the timber element fails. One of the brittle failure mechanisms (Van der Put, 1975) that can occur when using the moment connection is splitting of the timber near the connection.

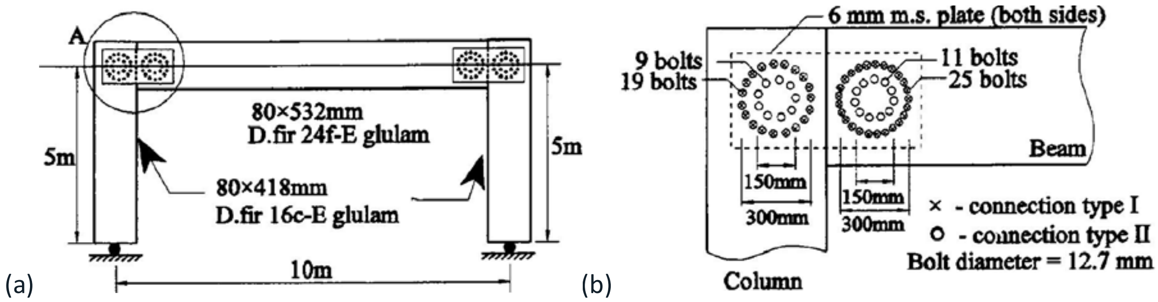


**Figure 9. A timber moment-resisting frame (Chui & Ni, 1995): (a) elevation, and (b) detail A**

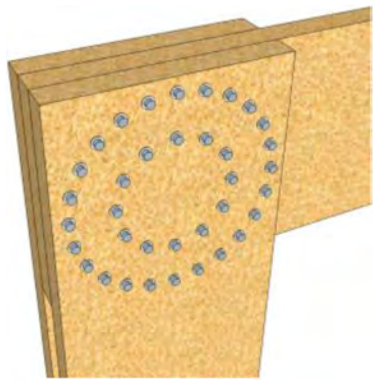

**Figure 10. A moment-transmitting connection (Fokkens, 2017)**

Unlike in steel and concrete moment-resisting frames, there is no deformable panel zone in timber moment-resisting frames, but the nonlinearity and failure of the moment-resisting connections are concentrated in the connection area. Typically, linear or nonlinear springs are used to simulate the connections, while elastic beam elements are used for the beam-columns. For detailed FE models, a specific material model of wood that can represent the anisotropic behaviour and also predict various failure modes, such as Wood$^{ST}$ (Chen et al., 2020), should be adopted. For more information, refer to Chapter 5 and Section 7.2.3.4.

## 2.4 SUMMARY

In this chapter, different structural systems using timber, steel, and concrete are compared in terms of structural behaviour and modelling emphases. The following are some of the most important points of comparison:

- As construction materials, wood is anisotropic, steel is isotropic, and RC is composite. Depending on the level of complexity that is required in a structural model, these behaviours may be adequately approximated through elastic material models in certain cases, whereas more sophisticated models may include factors such as yielding, brittle failure, and hysteretic behaviour. In this regard, this chapter presents key considerations for various structural configurations.
- Unlike RC shear walls, CLT panels are typically capacity-designed, and the connections govern the capacity of the CLT shear walls. CLT panels can be modelled as orthotropic plates, and the connections must be simulated using specific models to represent their stiffness, strength, plastic deformation, and even the hysteretic behaviour.

- Unlike braced steel frames, braced timber frames yield and dissipate energy primarily through energy-dissipative connections. The diagonal brace assemblies, each including a diagonal brace and two end connections, must be modelled with equivalent spring elements that can represent their stiffness, strength, plastic deformation, and hysteretic behaviour, while other timber elements can be modelled as elastic truss or beam elements.
- Unlike in moment-resisting frames using steel or concrete, the inelasticity of timber moment-resisting frames is typically concentrated in the beam-to-column connection area due to the nonlinear response of the connections. The beams and columns can be simulated using elastic beam elements, while the connections are modelled using linear or nonlinear spring elements.

The comparisons presented in this chapter are intended to help practising engineers become more acquainted with modelling timber structures. More specific and detailed methods are provided in other chapters.

## 2.5 REFERENCES

American Society of Civil Engineers. (2017). *Seismic evaluation and retrofit of existing buildings (ASCE/SEI, 41-17).*

Applied Technology Council. (2010). *Modeling and acceptance criteria for seismic design and analysis of tall buildings* (PEER/ATC-72-1).

American Wood Council. (2018). *National design specification for wood construction*.

Blaß, H. J., & Schädle, P. (2011). Ductility aspects of reinforced and non-reinforced timber joints. *Engineering Structures, 33*(11), 3018-3026. https://doi.org/10.1016/j.engstruct.2011.02.001

Branco, J. M., & Neves, L. A. C. (2011). Robustness of timber structures in seismic areas. *Engineering Structures, 33*(11), 3099-3105.

Bruneau, M., Uang, C.-M., & Sabelli, R. (2011). *Ductile design of steel structures* (2nd ed.). McGraw-Hill.

Charney, F., & Marshall, J. (2006). A comparison of the Krawinkler and Scissors models for including beam column joint deformations in the analysis of moment resisting steel frames. *Engineering Journal, 43*, 31-48.

Chen, Z., Ni, C., Dagenais, C., & Kuan, S. (2020). Wood$^{ST}$: A temperature-dependent plastic-damage constitutive model used for numerical simulation of wood-based materials and connections. *Journal of Structural Engineering, 146*(3), 4019225. https://doi.org/10.1061/(ASCE)ST.1943-541X.0002524

Chen, Z., & Popovski, M. (2020a). Mechanics-based analytical models for balloon-type cross-laminated timber (CLT) shear walls under lateral loads. *Engineering Structures, 208*, 109916. https://doi.org/10.1016/j.engstruct.2019.109916

Chen, Z., & Popovski, M. (2020b). Connection and system ductility relationship for braced timber frames. *Journal of Structural Engineering, 146*(12), 4020257. https://doi.org/10.1061/(ASCE)ST.1943-541X.0002839

Chen, Z., & Popovski, M. (2021a). *Seismic performance of CLT balloon walls made of* Larch *in mid-rise and high-rise construction in Korea – Year 1*. FPInnovations.

Chen, Z., & Popovski, M. (2021b). *Expanding wood use towards 2025: Performance and draft design guidelines for braced timber frames under lateral loads*. FPInnovations.

Chen, Z., Popovski, M., & Symons, P. (2019). *Solutions for upper mid-rise and high-rise mass timber construction: Seismic performance of braced mass timber frames – Year 1*. FPInnovations.

Chen, Z., Zhu, E., & Pan, J. (2011). Numerical simulation of wood mechanical properties under complex state of stress. *Chinese Journal of Computational Mechanics, 28*(4), 629-634, 640.

Chui, Y. H., & Ni, C. (1995, June 5–7). *Dynamic response of timber frames with semi-rigid moment connections* [Conference presentation]. Canadian Conference on Earthquake Engineering, Montreal, Canada.

Cortés-Puentes, W. L., & Palermo, D. (2020). Modeling of concrete shear walls retrofitted with SMA tension braces. *Journal of Earthquake Engineering, 24*(4), 555-578. https://doi.org/10.1080/13632469.2018.1452804

CSA Group. (2019). *Engineering design in wood* (CSA O86:19).

Danielsson, H., & Serrano, E. (2018). Cross laminated timber at in-plane beam loading – Prediction of shear stresses in crossing areas. *Engineering Structures, 171*, 921-927. https://doi.org/10.1016/j.engstruct.2018.03.018

Deierlein, G. G., Reinhorn, A. M., & Willford, M. R. (2010). *NEHRP Seismic Design Technical Brief No. 4 – Nonlinear structural analysis for seismic design: A guide for practicing engineers* (NIST GCR 10-917-5). National Institute of Standards and Technology.

European Committee for Standardization. (2004). *Eurocode 5: Design of timber structures - Part 1-1: General - Common rules and rules for buildings* (EN 1995-1-1:2004).

Fell, B., Kanvinde, A. M., & Deierlein, G. G. (2010). *Large-scale testing and simulation of earthquake induced ultra low cycle fatigue in bracing members subjected to cyclic inelastic buckling* (Technical Report No. 172). http://purl.stanford.edu/ry357sg5506

Fokkens, T. J. H. (2017). *Behaviour timber moment connections with dowel-type fasteners reinforced with self-tapping screws in seismic areas* (Document No. A-2017.188). [Master's thesis, Eindhoven University of Technology].

Forest Products Laboratory. (2010). *Wood handbook: Wood as an engineering material* (General Technical Report FPL-GTR-190). U.S. Department of Agriculture.

Gavric, I., Fragiacomo, M., & Ceccotti, A. (2015). Cyclic behavior of CLT wall systems: Experimental tests and analytical prediction models. *Journal of Structural Engineering, 141*(11), 4015034. https://doi.org/10.1061/(ASCE)ST.1943-541X.0001246

Guner, S., & Vecchio, F. J. (2010a). Pushover analysis of shear-critical frames: Formulation. *ACI Structural Journal, 107*(1), 63-71. https://doi.org/10.14359/51663389

Guner, S., & Vecchio, F. J. (2010b). Pushover analysis of shear-critical frames: Verification and application. *ACI Structural Journal, 107*(1), 72-81. https://doi.org/10.14359/51663390

Guner, S., & Vecchio, F. J. (2011). Analysis of shear-critical reinforced concrete plane frame elements under cyclic Loading. *Journal of Structural Engineering, 137*(8), 834-843. https://doi.org/10.1061/(ASCE)ST.1943-541X.0000346

Guner, S., & Vecchio, F. J. (2012). Simplified method for nonlinear dynamic analysis of shear-critical frames. *ACI Structural Journal, 109*(5), 727-738. https://doi.org/10.14359/51684050

Hamburger, R. O., Krawinkler, H., Malley, J. O., & Adan, S. M. (2016). *NEHRP Seismic Design Technical Brief No. 2 – Seismic design of steel special moment frames: A guide for practicing engineers* (NIST GCR 16-917-41) (2nd ed.). National Institute of Standards and Technology. https://doi.org/10.6028/NIST.GCR.16-917-41

Hirai, T. (2005). Anisotropy of wood and wood-based materials and rational structural design of timber constructions. *Proceedings of Design & Systems Conference, 15*, 19-22. https://doi.org/10.1299/jsmedsd.2005.15.19

Karacabeyli, E., & Gagnon, S. (Eds.). (2019). *Canadian CLT Handbook* (2nd ed.) FPInnovations.

MacRae, G. A. (2010, March 3–5). *The development and use of the continuous column concept* [Conference presentation]. Joint Proceeding of the 7th International Conference on Urban Earthquake Engineering and the 5th International Conference on Earthquake Engineering, Tokyo, Japan.

MacRae, G. A., Kimura, Y., & Roeder, C. (2004). Effect of column stiffness on braced frame seismic behavior. *Journal of Structural Engineering, 130*(3), 381-391. https://doi.org/10.1061/(ASCE)0733-9445(2004)130:3(381)

Maekawa, K., Vecchio, F., & Foster, S. (2008). *Practitioners' guide to finite element modelling of reinforced concrete structures* (Bulletin No. 45). FIB International.

Moehle, J. P., & Hooper, J. D. (2016). *NEHRP Seismic Design Technical Brief No. 1 – Seismic design of reinforced concrete special moment frames: A guide for practicing engineers* (NIST GCR 16-917-40) (2nd ed.). National Institute of Standards and Technology. https://doi.org/10.6028/NIST.GCR.16-917-40

Mokdad, F., & Missoum, S. (2013, August 4–7). *A fully parameterized finite element model of a grand piano soundboard for sensitivity analysis of the dynamic behavior* [Conference presentation]. ASME 2013 International Design Engineering Technical Conferences and Computers and Information in Engineering Conference, Portland, USA.

Negrão, J. H., Brito, L. D., Dias, A. G., Júnior, C. C., & Lahr, F. R. (2016). Numerical and experimental study of small-scale moment-resistant reinforced concrete joints for timber frames. *Construction and Building Materials, 118*, 89-103.

Palermo, D., & Vecchio, F. J. (2007). Simulation of cyclically loaded concrete structures based on the finite-element method. *Journal of Structural Engineering, 133*(5), 728-738. https://doi.org/10.1061/(ASCE)0733-9445(2007)133:5(728)

Popovski, M. (2004). *Structural systems with riveted connections for non-residential buildings*. FPInnovations.

Reale, V., Kaminski, S., Lawrence, A., Grant, D., Fragiacomo, M., Follesa, M., & Casagrande, D. (2020). *A review of the state-of-the-art international guidelines for seismic design of timber structures* [Conference presentation]. World Conference on Earthquake Engineering, Sendai, Japan.

Rinaldin, G., Amadio, C., & Fragiacomo, M. (2013). A component approach for the hysteretic behaviour of connections in cross-laminated wooden structures. *Earthquake Engineering & Structural Dynamics, 42*(13), 2023-2042. https://doi.org/10.1002/eqe.2310

Sabelli, R., Roeder, C. W., & Hajjar, J. F. (2013). *NEHRP Seismic Design Technical Brief No. 8 – Seismic design of steel special concentrically braced frame systems: A guide for practicing engineers* (NIST GCR 13-917-24). National Institute of Standards and Technology.

Sandhaas, C., Van de Kuilen, J.-W., & Blass, H. J. (2012, July 15–19). *Constitutive model for wood based on continuum damage mechanics* [Conference presentation]. World Conference on Timber Engineering, Auckland, New Zealand. http://resolver.tudelft.nl/uuid:55c1c5e5-9902-43ad-a724-62bb063c3c80

Schachter, M., & Reinhorn, A. M. (2007). *Three-dimensional modeling of inelastic buckling in frame structures* (Technical Report MCEER-07-0016). Multidisciplinary Center for Earthquake Engineering Research.

Tang, T. O., & Su, R. K. L. (2014). Shear and flexural stiffnesses of reinforced concrete shear walls subjected to cyclic loading. *The Open Construction and Building Technology Journal, 8*, 104-121.

Tang, X., & Goel, S. C. (1989). Brace fractures and analysis of phase I structure. *Journal of Structural Engineering, 115*(8), 1960-1976. https://doi.org/10.1061/(ASCE)0733-9445(1989)115:8(1960)

Uriz, P., & Mahin, S. (2008*). Towards earthquake-resistant design of concentrically braced steel-frame structures*. Pacific Earthquake Engineering Research Center.

Van der Put, T. V. d. (1975). *Proeven op stiftverbindingen hout op hout en staal op hout horizontaal gelamineerd hout en in constructiehout*.

Wada, A., Qu, Z., Ito, H., Motoyui, S., Sakata, H., & Kasai, K. (2009). Seismic retrofit using rocking walls and steel dampers. In B. Goodno (Ed.), *Improving the seismic performance of existing buildings and other structures* (pp. 1010-1021). American Society of Civil Engineers. https://doi.org/10.1061/41084(364)92

Image courtesy of Kai Yang, CadMakers

# CHAPTER 3

## Modelling principles, methods, and techniques

**Authors**
Zhiyong Chen
Vincenzo Reale
Sebastian Kaminski
Lucas Epp
Marinos Stylianou

**Reviewers**
Conroy Lum
Scott Nyseth
Nicolas Cantin
Kai Yang
Vasco Chan

## TABLE OF CONTENTS

## 3.1 INTRODUCTION

Structural analysis models are precise but inherently inaccurate. The very word *model* makes this clear: as engineers, we create these models *to approximate reality*. While analysis models cannot reflect reality perfectly, creating models (by hand or computer) that are sufficiently accurate to reflect our best understanding of the materials with which we build, and the loads to which they are subjected, is fundamental to the art of structural engineering. This statement may sound surprising, but as structural engineers, we are employed to model structures we do not fully understand, with techniques that have not yet been perfected.

The emphasis of early structural modelling was on how to achieve the mathematical solution, and the model development process was a minor issue (MacLeod, 2010). Currently, access to software packages capable of carrying out complex analysis is ubiquitous. However, developing appropriate models, using the tools available properly, and understanding the results and the limits of the analyses carried out by software have all become essential skills for structural engineers. Modelling techniques, assumptions, and analysis algorithms for steel and concrete structures are well established. Steel and concrete structures have the ability to mobilise different load paths due to the ability of steel rebar and shapes to yield and redistribute stresses to different parts of the structure. This tends to make modelling of steel and concrete structures more forgiving of small modelling mistakes. However, this is less true for timber structures, in which an intrinsically brittle and anisotropic material is used and where connections with discreet elements and complex local interactions play a very important role in the stability of the structure.

This chapter introduces principles that underpin the modelling of timber structures, available methods, and techniques that are suitable to properly set up analyses for timber structures.

## 3.2 PRINCIPLES

To obtain the best possible analysis results, it is important that engineers follow a formal modelling process that is based on sound engineering and finite element (FE) analysis principles such as the ones that follow.

### 3.2.1 Modelling Process

To reduce risk in structural analysis, a formal modelling process based on sound engineering and FE analysis principles should always be adopted. What is meant by formal is that a written record of the process activities should be produced. A formal modelling process is one that has been thought through before sitting in front of a computer to model a structure. It is one that is maintained and updated with lessons learned by engineers with years of practising structural analysis and design. Such a process can minimise some of the risks inherent in building a model for structural analysis and design, and avoid omission of important activities and aspects.

As for other types of structures, the process of modelling a timber structure depends on multiple factors, including:

- Project stage (e.g., conceptual, preliminary, schematic, detail; these stages are generally defined in detail by appropriate national or international standards or regulatory bodies);

- Project location (e.g., projects in a seismic area will require additional checks);
- Project use (depending on the scale and function of the structure, specific analysis tasks will be required; e.g., robustness analysis, fire safety analysis, vibration analysis); and
- Constraints (which, for example, can be included in the project's brief or may emerge from discussion with the client or any other disciplines involved in the design).

Making the process formal provides evidence of the use of good practices. A typical modelling process includes the following key elements:

- Understanding the structure and planning the modelling process;
- Selecting the software;
- Developing the analysis model;
- Verifying the results;
- Performing a sensitivity analysis; and
- Deciding on the accepted model and results.

It is important to understand that the process, although presented here linearly, may involve a significant amount of looping, as during the process, the assumptions and project specifications may change in light of the results from the analyses.

During structure design, a general calculation plan should always be laid out first, and the specific analyses to be carried out, the tools required, and the formal review process should all be preliminarily defined and agreed on. As always, the specifics of a project may greatly influence the choices of a designer.

## 3.2.2 Model Development

### *3.2.2.1 Understanding the Structure and Planning the Modelling Process*

Certain preliminary steps should be carried out when modelling a structural design, the first of which are correctly understanding the design brief and carefully planning the overall modelling process.

Multiple factors influence the design of a structural timber project. Among them are:

- Availability of material. Sourcing timber and timber composites may not be as simple as for other traditionally used materials. For example, the lack of availability of a specific type of timber composite, such as cross-laminated timber (CLT), and the high cost of importing it to a specific country may mean that the project will have to be developed without that material, focusing on others, such as a light wood-frame structure made of solid timber elements.
- Climate and exposure. Because timber is a natural material, it is susceptible to rot and insect attack. Depending on the project location, the use of timber in a building may require specific measures, such as protection from rain or separation from the ground, which would inevitably influence the choices for the project and the final structure that is developed.

- Level of craftsmanship of site contractors. Timber is a material that can be easily formed using traditional methods, but it can also be engineered and formed to high degrees of accuracy using computer numerical control (CNC) machines. Depending on the project location, budget, and experience of the local contractors, some details may not be economically achievable. The limitations due to manufacturing techniques and local contractors should then be considered early on in the project: just because one type of connection can be modelled and designed, it does not mean that it will be possible to fabricate it satisfactorily.

Once the process has been determined, designers should define the structural options that are feasible within the project's constraints. The outcome of this phase is generally choosing one or more systems that can be successively modelled and analysed. The choice of one system over another will have implications on the overall modelling, as different systems have different behaviours that may require a different analysis approach. Some of the most common timber systems include:

- Light wood-frame buildings
- Mass timber buildings (CLT, mass plywood panels, nail-laminated timber, etc.)
- Braced timber buildings
- Moment-framed timber buildings

Different options would also behave differently in different contexts. For example, in highly seismic areas, where a certain degree of ductility is required of a structure, some options will not be acceptable by national and international codes, or would be greatly penalised in terms of structural capacity. Designers should be aware of the possible modelling implications of each option and evaluate the one that is most suitable for the design's brief.

Other considerations include the required performance of the building and the required accuracy of the results. Other such considerations depend on the context and, especially, the degree of risk involved, both with respect to the consequences of failure and to the degree of innovation involved.

Once the options have been defined for each structural system considered, an analysis should be carried out to understand how the loads (vertical and horizontal) are applied to the structure, distributed within the structure, and transferred to the foundations. This modelling step is usually referred to as load path analysis. Understanding the correct path of the structure will inform every further modelling assumption; it is therefore critical that this process is thoroughly carried out and reviewed. The load path analysis should start from the point of application of the loads (e.g., external surfaces for wind, as shown in Figure 1, or centre of mass for seismic forces) and follow the transfer of these forces from one element to another. As always in timber buildings, the analysis of the transfer of the forces from one member to another through connections is vital to understanding the behaviour and capacity of a building. It is usually advised that these connections be sketched or drawn to scale, even at preliminary stages, as the geometry of the different members and their connectors, with their 3D properties and eccentricities (Figure 2), will influence the forces and moments each element is subjected to.

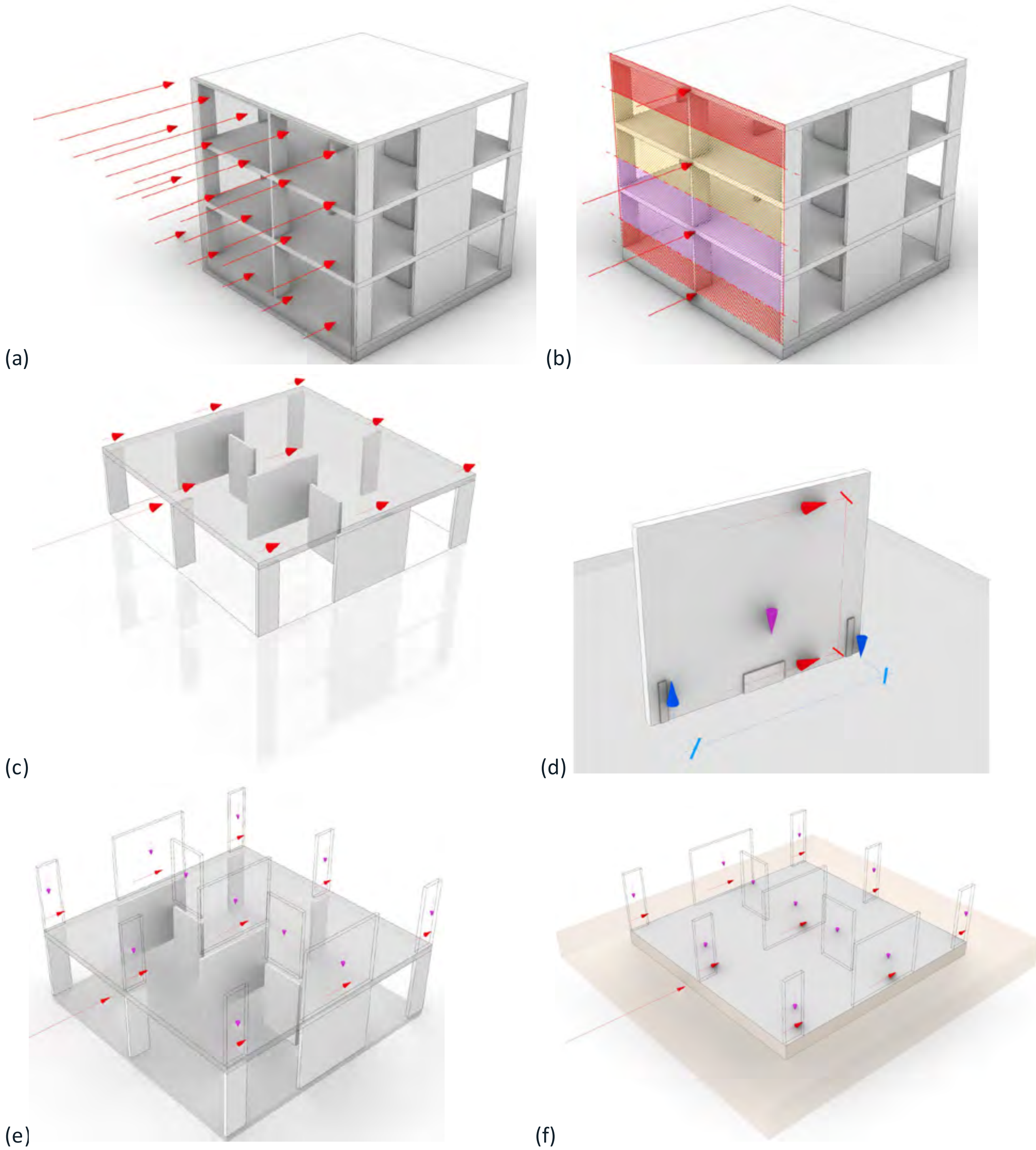
(a) (b) (c) (d) (e) (f)

**Figure 1. Example of the wind load path for a CLT building: (a) wind load is applied to the facade; (b) the load is distributed from the facade by tributary areas to the diaphragms; (c) the rigid diaphragms distribute the loads to the vertical resisting system (walls) based on their relative stiffness where all eccentricities of the loads or the resisting system are resolved; (d) each wall transfers the horizontal and vertical loads from the diaphragms to the floor below through shear and force couple; (e) the walls transfer the loads to the floor below together with the tributary loads from the facade associated with the floor; and (f) the loads finally continue to be transferred to the levels below until they reach the foundation level, where they are ultimately transferred to the ground**

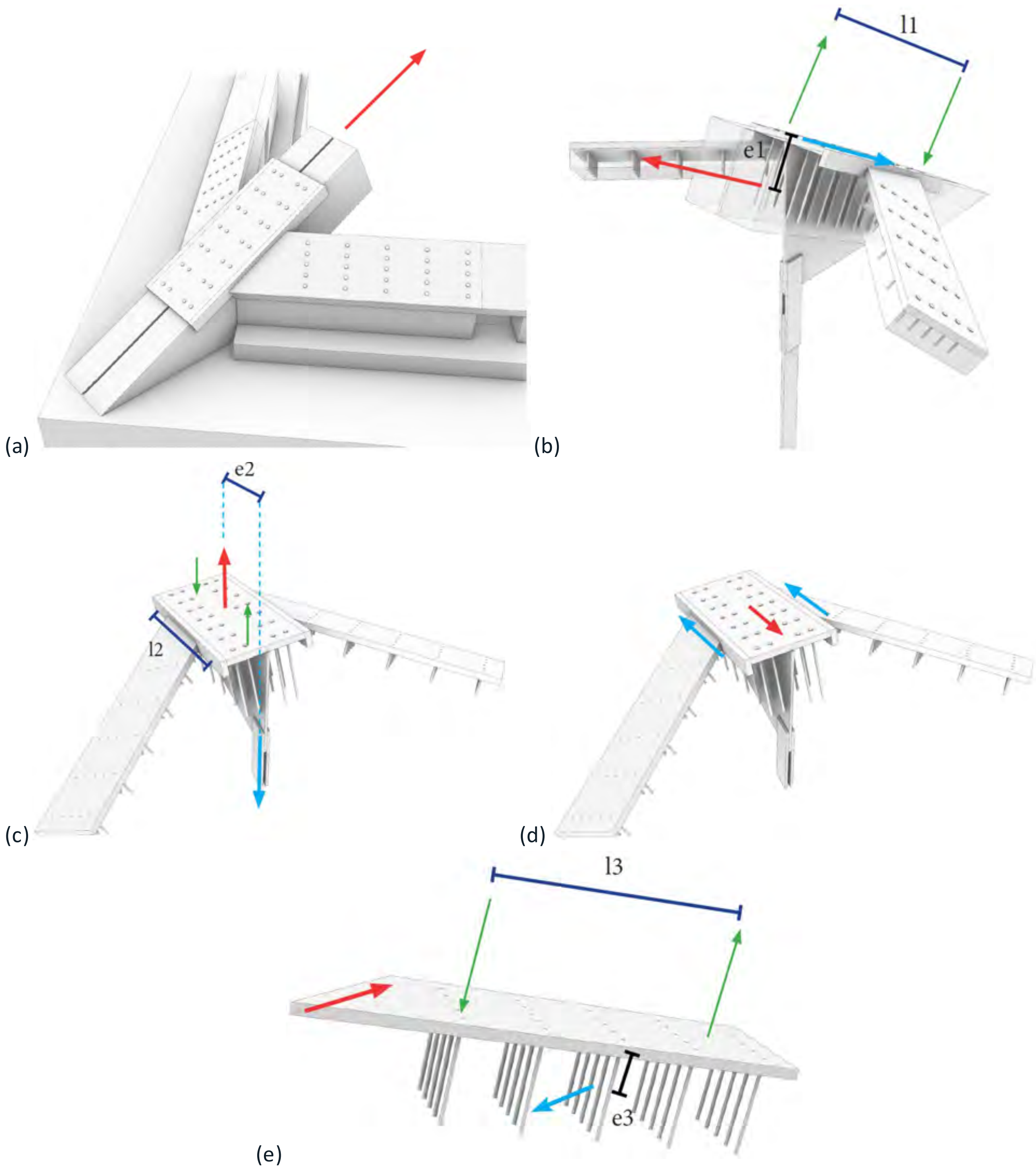


**Figure 2. Example of the load path into a timber connection and influence of eccentricities: (a) the corner rafter of a timber roof is in net tension under some load combinations; (b) the tension load from the rafter is transferred through steel connectors to a steel plate, where the eccentricity between the centreline of the rafter and that of the plate generate a moment that has to be taken in push-pull by the screws of the plate; (c) the vertical component of the force applied to the plate is resisted by a tie offset due to the wall below, which generates a further moment that is resisted in push-pull by the screws of the plate; (d) the horizontal component of the force applied to the plate is resisted by the side plates; and (e) the in-plane force of the side plates is resisted by the screws fixed into the side timber beams where the eccentricity of the resisting forces generates a moment that has to be taken in push-pull by the screws of the plate**

Based on the load path, along with simple calculations and rules of thumb, the structural elements of the structure can be assigned a preliminary size. In timber structure design, it is always important to carry out the preliminary sizing of the structural elements together with the preliminary design of their connections, which may generally govern and inform the overall required dimensions of the different members. After this step, the structural designer can not only communicate and discuss material quantities and geometric constraints with the other parties involved, but will also have a starting model capturing the overall weight distribution, stiffness, and mass of the building, which will be the base for further and more refined structural checks.

Once the designer has achieved a general understanding of the building behaviour and has sized all the main elements, more sophisticated or specialistic analysis can be carried out. Taking care to follow best practices and recommendations, the designer should consider whether a specific part of the building or the overall structure requires digital modelling. Before starting to develop these models, the designer should be clear on the model's assumptions, limits, and expected outputs. Examples of such models could include a general model of the structure to carry out a spectrum analysis or a simple isolated model of a floor plate and its supports to run a footfall analysis and understand vibration performance.

It is worth stressing again that when digital models are required, the parameters informing them may change depending on the objectives each try to fulfil. For example, connections may be modelled differently if the analysis deals with vibration versus long-term loads. In fact, while in the former the connection between a floor plate and its supporting structure can be considered fully fixed, in the latter it should be modelled as pinned. This is because for the purposes of the limited displacements accounted for in a serviceability state vibration check, the connections do not experience the significant movements and rotations to be accounted for under longer-term and higher ultimate state loading.

Moreover, because of the many uncertainties in modelling timber buildings (due to the aforementioned specifics of the material and construction technology), the model developed may require several runs with different properties (e.g., connection stiffness) for different elements within the system. These sensitivity analyses are required to capture the possible bounds of behaviour that a loaded structure can exhibit.

#### *3.2.2.2 Software Selection*

During this stage, should general or specific digital analyses be required, the designer must choose software that is suitable for the different tasks. Numerous commercial software packages are available that can help engineers develop linear and nonlinear FE numerical models of buildings (Chen et al., 2017). Examples include Abaqus, ADINA, Ansys, DRAIN-3DX, Dlubal, ETABS, midas Gen, NONLIN, NONLIN-Pro, OpenSees, P-FRAME, PERFORM-3D, RAM, RISA, S-FRAME, S-TIMBER, SAFI, SAP2000, SeismoStruct, SOFiSTiK, ST STRUDEL, STAAD, and many others. The key to choosing a suitable analysis program in design practice or research is to look for the characteristics of the specific engineering problems related to the structure to be modelled, and whether the program can provide a suitable model to replicate the structure and its performance according to its use.

All software packages used in design practice and research can be divided into two main categories: general-purpose programs and design-oriented programs. General-purpose programs such as Abaqus and Ansys are suitable for more advanced analyses. For special engineering problems, such as seismic, blast, and fire, general-purpose programs are the right option as they have extensive material modes, elements, and different solvers (e.g., explicit or implicit solvers). With Abaqus, many researchers have developed user subroutines that can model the unique structural behaviour of wood-based components, connections, assemblies, and even entire building structures, which are unavailable in most software packages. This has resulted in many consultant companies using this type of software in their design practice in recent years. For a conventional structural analysis, design-oriented software packages such as SAP2000, ETABS, S-FRAME, and Dlubal are the best options. However, they usually have limited capacity to model certain types of structures and have limited types of FEs compared to general-purpose programs. Their advantage is their capacity to more easily model structures commonly found in the architecture, engineering, and construction industry and to carry out design checks based on any codes and standards that have been preprogrammed. They can therefore quickly post-process the analysis results and design the structure according to codes of practice. Currently, more and more structural design programs have preliminary added wood modules, such as Dlubal, S-FRAME, SAFI, and RISA, and some have been specifically developed for modelling, analysis, and design of wood structures, such as S-TIMBER. These software programs provide a more user-friendly function for practising engineers to design timber structures.

#### *3.2.2.3 Principles of Model Development*

A useful strategy in the early part of modelling is to draw up an issue or feature list to help in making decisions about the model. The features are the factors that may need to be considered in relation to the model, in terms of material behaviour, loading, boundary conditions, etc. The next step is to develop a computational model incorporating the means of achieving a solution, such as the type of FE scheme to be used and the degree of mesh refinement. In some cases where new structures are to be analysed, it may be best not to develop just one model but to investigate a few options, evaluate them, and choose the one to be used. The general rules for structural model development of timber structures are listed below. Specific principles and considerations for timber structures are indicated by **[√]**.

- **Start with a simple model and refine it step by step.** If you decide to move into an area of analysis that is unfamiliar, build experience by starting with simple (smaller) elastic models and load cases for which solutions are known, if practical. If using nonlinear analysis, start with an elastic model, then move into separate nonlinear material and nonlinear geometry models, and then combine them. At each stage, review the results to assess whether they are acceptable.
- **Keep the model at a level as simple as practical.** More precise and complicated modelling should focus on key structural components and connections, while simplifications can be made on parts of the structure that are of secondary importance.
- **Ensure that the model is sufficiently detailed and realistic, but not overly complicated.**
- **Select a suitable type of model (1D, 2D versus 3D)** based on the analysis problem and the characteristics of the structure.
- **Use symmetry to reduce computation/analysis resource demand**. If a structure has an axis of symmetry, then the order of solution can be reduced. While the need to reduce the size of models is now less important due to the high level of computing power available, there may be circumstances in which the use of a symmetric model is disadvantageous, such as in frequency analysis (any unsymmetric modes that actually exist in the full model cannot be represented). For mirror symmetry to be satisfied, all geometric and material properties and all loading must be the same at

corresponding points on either side of the axis of symmetry. The cross-sectional properties of the member on the axis of symmetry of the symmetrical (antisymmetric ally) equivalent model are half of those for the complete frame.

- [√] **Remember that the structural and material behaviour of timber structures is different from that of other types of structures, such as steel or concrete, and the modelling is correspondingly different.** See Chapter 2 for more information.

- **Choose appropriate elements for the structural components.** Usually, there are many types of elements to choose from. The choice is often obvious, but consider the following guidelines and pick the ones most suitable based on the conventional rules and the output requirements.

  - Line elements (these are for members with length-to-width ratios that are sufficiently high):

    - ❖ Bar/truss elements: Straight, with only one axial degree of freedom at each end. Such elements are typically used to model pin-connected struts.
    - ❖ Beam elements: Include (a) a plane frame (2D beam) element incorporating a single plane of bending plus axial effects with three degrees of freedom per node; (b) a grillage element incorporating a single plane of bending and torsional effects; and (c) 3D beam element incorporating bending in two planes, axial and torsional actions, with six degrees of freedom at each node. In all cases, the bending component may include shear deformation (thick beam) or neglect shear deformation (thin beam).

  - Surface elements:

    - ❖ Plane stress (membrane) elements: No stress and no restraint to movement in the out-of-plane direction.
    - ❖ Plane strain elements: No strain, but there is stress in the out-of-plane direction.
    - ❖ Plane bending elements (basic components of traditional flat shell elements): To model flat plates that are subjected only to out-of-plane bending actions. The boundary between thin and thick plate bending theories is a span-to-depth ratio of 10:1. A small deflection assumption is validated when the maximum deflection is less than the plate depth for thin plates.
    - ❖ Shell elements: To model curved surfaces and flat plates for which in-plane and out-of-plane actions need to be factored in. Shell elements tend to have six degrees of freedom at each node, taking into account in-plane (membrane) and out-of-plane (bending) actions. They can be flat or curved.

  - Volume elements (3D elements, or brick elements): Tend to be used more in advanced structural analysis and mass structures of nonlinear and elastic soils.

- **Conduct convergence analysis to assess the meshing strategies for FE models.** Convergence for mesh refinement implies that as mesh density is increased, the results will converge towards the exact solutions. The rate of convergence depends on the type of element, the number of elements in the mesh, and the loading type. Meshing principles are listed below.

  - FE meshing is more of an art than a science. The more we experiment with it, the better we become.

- Mesh density: A basic principle is to choose a mesh density at which the convergence curve starts to flatten off. The challenge, of course, is that there is rarely a convergence curve.

- Quadrilateral versus triangular: Quadrilateral elements are more accurate and should always be preferred over triangular ones. Modern meshing algorithms primarily use quadrilateral elements and triangular ones only when absolutely necessary due to geometric constraints.

- Element shape: The ideal shape for a quadrilateral element is a square and for a triangular element an equilateral triangle. As the shapes of these elements deviate from the ideal shapes, so does their accuracy. Many structural analysis programs issue a warning when the element shape is distorted to the point where its accuracy is questionable. An accurate mesh usually looks good to the eye. If a mesh looks ugly to you, you should probably replace it with another mesh. Automatic meshing is available in many structural analysis programs and should be used to improve the quality of meshes.

- Curved boundaries: Typically, a larger number of elements is needed to accurately represent a curved boundary (circular, elliptic, etc.) than a straight boundary. As a rule of thumb, some element boundaries can be curved. Accuracy for these elements decreases as the sides' offset from straight increases.

- Stress gradients: A good strategy is to have a finer mesh in areas of a high stress gradient and a coarser mesh where the stress gradient is low. However, for models with a large number of elements it may be best to investigate stress concentrations in separate detailed models (e.g., using sub-modelling to study the detailed stress distribution in the area of an important connection).

- **[√] Choose appropriate material models for structural components.** In structural analysis the constitutive relationships tend to have the following two assumptions: (1) a definition of material behaviour (e.g., linear elastic behaviour or plasticity); and (2) assumptions with regard to the stress distribution within the differential element types. For example, for the plane stress condition, stresses are defined in a plane with zero stress at right angles to the plane; for bending elements (such as beams and shells), the stresses are assumed to vary linearly within the depth of the element. Wood is an anisotropic material with a different stress-strain response in different directions or under different loading conditions in the same directions (Chen et al., 2011, 2020). Such complex response induces various types of failure modes in the wood components and connections. Therefore, the material constitutive model should be chosen to meet the model requirements. Correct material models can help predict specific yield and failure modes of wood components and connections. See Chapter 4 for more information.

- **[√] Choose appropriate elements for connections**. Select pinned, rigid, or semirigid types according to the structure you are investigating. Joint elements, which are used for modelling plastic hinges and semirigid connections, normally consist of a set of springs that connect two nodes or two freedoms (e.g., linear elastic spring and elastoplastic spring). The depths of beams or columns and eccentricities need to be modelled properly. For timber structures, the connections typically play a key role in the structural response (e.g., deformation and resistance). Therefore, it is crucial to model the timber connections using an appropriate method (Chen & Chui, 2017; Chen et al., 2013; Reale et al., 2020). For capacity-based design timber structures, the timber components can be simulated as elastic material, while the energy-dissipative connections should be simulated with elastoplastic behaviour. Also note that timber connections have high variability in stiffness and strength (Jockwer & Jorissen, 2018). See Chapter 5 for more information.

One very important part of the detailed analyses is the design of connections. As it is extremely complex to model the anisotropy of timber given the imperfections of the material, these analyses should involve careful calculation that factors in all of the different failure modes (e.g., splitting and block shearing) as defined and codified by the most up-to-date standards and guidance, such as Eurocode 5 (European Committee for Standardization, 2004).

- **[√] Choose appropriate force-deformation models for assemblies if macroelements are used**. Timber assemblies, such as shear walls, respond differently from steel and concrete assemblies (e.g., pinching effect); the force-deformation models should be chosen to meet the model requirements. See Chapters 6 and 7 for more information.
- **Adopt appropriate model input.** The required model input varies according to the modelling situation: (a) analysis objectives: design values are needed for practising design while test results are preferred for research; and (b) analysis types: less input for elastic or static analyses and more for nonlinear or dynamic analyses. The necessary parameters for the models and how they can be derived are discussed in Chapters 4 to 10.
- **Choose appropriate types of constraints on the structural components and assemblies.** Constraints are conditions imposed on the deformation of a structure—effectively a compatibility condition. Constraints can be incorporated into the model using constraint equations, a rigid link, and a beam element.
- **Choose appropriate types of loads applied to the structural components and assemblies.** A point load usually induces a stress concentration issue. Such an issue, however, can be avoided by applying the load on a certain area. Judge whether the effect of finite widths of members at the connections can be neglected.
- **Choose appropriate types of support applied to the structural components and assemblies**. An analysis model of a structure must be defined in relation to a frame of reference. It must be fixed in space; it must be supported. A reaction force corresponds to each restrained freedom of the structure. These reaction forces must at least form a set that is statically determinate. Conventional restraints include a horizontal roller, pin, fixed restraint, vertical roller (nonrotation, at axis of symmetry), and translational and rotational springs. Neglecting fixity where there is a degree of restraint tends to be conservative for estimates of deformation and internal forces. The assumption that a column is fully restrained at its base may result in an overestimate of stiffness and an underestimate of the maximum frame moments. Issues to be considered when validating a fixed column support include (a) whether the stiffness of the frame is a critical issue; and (b) the detailing at the support (i.e., is the foundation sufficiently massive that the rotational stiffness at the support will be negligible?).

- **Choose an appropriate type of foundation model for the structure**. In this context the structure includes the superstructure and the foundation, and the ground that is below the foundation, including soil and rock. The model of a structure is more likely to be realistic if the deformation of a rock support is included than if the effect of a soil support is neglected. Four basic ways of defining the supports for a structure (Figure 3) are:
  - Support fixity model: Deformations of the ground are ignored and the nodes for the structure at the contact with the ground are given fixed restraints.
  - Winkler model: The ground is modelled by linear elastic springs at the structure-soil interface. The springs are not coupled (i.e., when one spring deforms, the other springs are unaffected by shear transfer in the ground).
  - Half-space model: The ground is modelled by coupled springs at the structure-soil interface (i.e., shear transfer in the ground is factored in).
  - Element model for the ground: The ground is modelled using FEs that have fixities adequately far away from the superstructure.

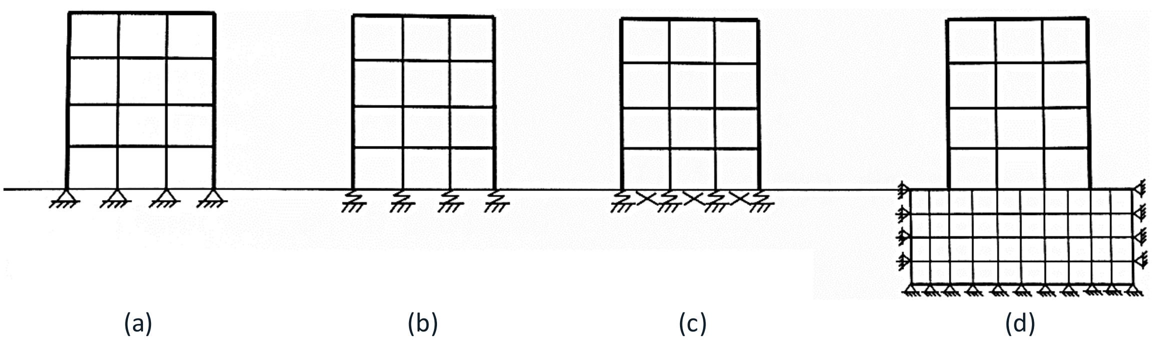


**Figure 3. Models for structure support (MacLeod, 2010): (a) support fixity model, (b) Winkler spring model, (c) half-space model, and (d) element model of ground**

Soil tends to be nonhomogeneous, with mechanical properties that may be time-dependent, functions of water content, and nonlinear in relation to stress and strain. Addressing these features requires advanced analysis that is outside the scope of this guide. Taking account of the structure and the ground in a single analysis is known as soil-structure interaction. This is very difficult to model accurately. While ‘garbage in, garbage out’ needs to be avoided, using approximate models (such as the Winkler model) is better than completely ignoring the impact foundations can have on the behaviour of a superstructure. See Chapters 7 to 10 for more information.

- **[√] Develop appropriate load paths in the structure**. Ensure that proper load paths have been designed into the structure and that the models can reflect the corresponding load paths (Reale et al., 2020). Understanding how vertical and lateral load is distributed in a structure is an essential feature in modelling. It depends on the continuity (simply-supported versus continuous) and stiffness (flexible versus rigid) of the member directly resisting the loads, and the stiffness (flexible versus rigid) of the members supporting the former. The load paths are especially important for structures with load-resisting elements/assemblies with significant stiffness (e.g., hybrid timber structures). See Chapters 8 to 10 for more information.

- **Consider nonstructural elements and non–lateral load-resisting elements according to engineering judgment**. Also carefully consider the actual stiffness and strength of all possible lateral load-resisting structures in all directions. Secondary, facade, or nonstructural walls or structures may all carry significant loads, and beams may provide unintended coupling action between shear walls. See Chapters 7 to 10 for more information.

- **Consider nonlinear geometry in the models, if necessary**. When a structure is loaded, the geometry changes. The change in geometry causes the relationship between loads and displacements to be nonlinear, and hence this is described as geometric nonlinearity.

  Criterion for neglecting nonlinear geometry effects: The critical load ratio ($\lambda$), the ratio between the axial load and the elastic critical load, is the main parameter for assessing the potential effects of nonlinear geometry. If $\lambda$ is less than 0.1, then the nonlinear geometry effects can be ignored; otherwise, they should be accounted for in the models. Apart from the level of the applied load, the main factor affecting the nonlinear geometry effect is the stiffness of the structure. This depends on several parameters, including the material properties, such as Young's and shear moduli, connection types, support conditions, restraints, and cross-sectional properties. During the sizing of members, the minimum slender ratio should be considered as specified in the design standards. In some cases, elastic limits may be exceeded before a critical condition is reached, and nonlinear material behaviour must be factored in. See Chapters 8 to 10 for more information.

- **Consider appropriate loading conditions in the models**. The term loading can imply the general concept of external action on the structure. In this context it implies dead load, live load, snow loads, wind loads, and seismic loads. In bridge design in particular, it is important to manipulate loads whose position on the structure is not fixed (e.g., moving loads). The influence line is the main technique used to identify critical positions of moving loads. The best pattern of loading must be considered for bridges, floors, and roofs. See Chapters 6 and 8 to 10 for more information.

- **[√] Consider both local and resultant stresses in modelling of timber structures, if necessary**. For example, for a simply-supported beam under two-point loading, the horizontal direct stress (i.e., compression and tension) is the resultant stress due to the bending moment, while the local effect is compression perpendicular to the grain in the vicinity of the point loads and supports. Unlike with steel and concrete, the compression strength perpendicular to the grain of wood-based materials is an order of magnitude lower than the strength parallel to the grain. Therefore, whereas the local effect can be ignored in a steel structure, it must be accounted for when modelling timber structures.

- **[√] Develop a good model based on the knowledge of the investigated members, connections, and structures.** The observance of physical behaviour is one of the most important strategies for developing a good understanding of a structure's behaviour, which can help in developing more accurate models. This is especially important for timber structures.

## 3.2.3 Model Validation and Result Verification

### *3.2.3.1 Model Validation*

Model validation may not be critical for common structural designs, but it is essential for new and innovative structural designs in which a plethora of experience may be lacking or where the risk of consequences is high. To validate a model, it is necessary to understand the assumptions made in creating it and to relate these to the behaviour of the structure being modelled. The process involves listing the assumptions, performing an analysis, and comparing the results and behaviour with those of the real structure. Is the model capable of representing the real behaviour? The validation process can identify the need for modelling adjustments. Information about the validity of the models may be gained from studying:

- Existing records of material testing;
- Existing records of testing and performance (including failures) of similar structures;
- Latest research publications and experimental work; and
- Sensitivity analysis.

Typically, a range of acceptance criteria must be used. Typical outcomes that may result from a validation of an analysis model include:

- Criterion satisfied: A check against a stated criterion is positive; for example, the span-to-depth ratio, $L/d$, of a beam is greater than the minimum ($L/d$ > 10 for using bending theory, while $L/d$ < 10 for including shear deformation).
- Conventional assumption: The assumption is standard practice for the type of structure being modelled; for example, the finite depths of members are neglected in a timber frame analysis.
- Later stage requirement: The modelling issue will be satisfied by later actions (e.g., by designing the structure to a code of practice); it is important that such requirements are implemented at the later stages.
- Sensitivity analysis: Acceptance is based on information in a sensitivity analysis.
- To be resolved: The final validation decision must await further research or use of the model.

A risk-based validation method is recommended since it provides an efficient approach to distinguish the important criteria or outcomes using different degrees of uncertainty. Risk is normally defined as the combination of the likelihood and the consequences of an event that can cause failure and harm. Here, risk is defined as the combination of the degree of uncertainty of an assumption and its importance. The levels of uncertainty and the importance are given values (normally qualitatively assessed) ranging from 1 to 5, where 5 means high uncertainty or high importance (Table 1). The objective is to ensure that no assumption falls within the shaded areas of the table.

**Table 1. Risk matrix for model validation**

| | | Degree of uncertainty (1 = low, 5 = high) | | | | |
|---|---|---|---|---|---|---|
| | | 1 | 2 | 3 | 4 | 5 |
| Importance of assumption (1 = low, 5 = high) | 5 | | | | | |
| | 4 | | | | | |
| | 3 | | | | | |
| | 2 | | | | | |
| | 1 | | | | | |

#### *3.2.3.2 Result Verification*

In verification, error tends to be the main consideration, and in validation, uncertainty tends to dominate. It is important to appreciate the difference between error and uncertainty because the tolerance in acceptability is likely to be much greater for uncertainty than for error.

- In defining stiffness for lumber, a deviation (uncertainty) of 15% could be satisfactory.
- In the solutions of the equations in an FE model, an error check for equilibrium or symmetry is of the order of $10^{-12}$.

As for the risk-based validation method, the acceptance criteria for results can be based on risk principles (i.e., on considering the combination of likelihood of modelling errors and the consequence of a resulting structural failure). The questions that should be asked in a result verification are: Do the results correspond to what is expected from the model? Or have any errors been made in performing the analysis (hand calculations, ad hoc spreadsheets)? General items for the result verification of the timber structure model are listed as follows:

- Check and address all warnings and errors issued by the software.
- Check input data (dimensions, sectional properties, material properties, supports, constraints, loads).
- Check that the units used in dimensions, loads, and material properties are correctly assigned.
- Verify the numerical models for the components, connections, and assemblies against the available test result data. This is paramount to ensure that equivalent properties and model assumptions are used in the static and dynamic analyses and that produced results are trustworthy.
- Carry out a qualitative analysis of the results by looking at the deflected shape and the distribution of element forces (load path) and stresses. Do these conform with what is expected?
  - Are the reactions equal to the total applied loads? (Overall equilibrium check.)
  - Is the meshing too large or too small?
  - Are the chosen meshing elements excessively long or short in some locations?
  - Are there too many or not enough restraints applied?
  - Is there over- or under-release in bending moment of structural components?

- Are there any inappropriate offsets?
- Are all loads present or are some missing (e.g., torsion)? Are they applied correctly?
- If the structure is symmetric, then it is worth applying a symmetric loading case and checking the corresponding deformation (or force actions) in relation to a pair of symmetric degrees of freedom.

- Check the results from the developed numerical models against:
  - Simplified methods of calculation or test results. For example, the fundamental periods of the tall wood buildings computed by modal analysis should be compared with available empirical formulas (Karacabeyli & Lum, 2022) and any available similar test data to ensure the results are not biased.
  - Analysis results of a checking model that is a simplified version of the main model but has adequate accuracy for checking purposes.
  - If a static analysis is being performed, a free vibration analysis should also be run, and vice versa. Do the results make sense?
- Check the specific timber structural models, including:
  - Components: elasticity, yielding, and local failure.
  - Connections: energy-dissipative and non-dissipative connections.

#### *3.2.3.3 Sensitivity Check*

A sensitivity analysis investigates the effects of different values for features or parameters. The need for a sensitivity analysis depends on the degree of uncertainty of key model parameters (dimensions, material properties, section properties, loads [e.g., combinations and patterns], among others). When working on an unusual structural design, a sensitivity analysis may be essential to gain a better understanding of the general behaviour of the model and to increase confidence in the model. The following issues are relevant to sensitivity analysis:

- Work from a reference model, changing one variable at a time and reverting to the reference model after each change. As the designer gains understanding, it may be better to change the reference model, but if the changes are compounded it becomes difficult to make sensible comparisons. This can lead to an overwhelmingly large number of permutations, and formal procedures may be required to properly interpret the results. This topic is dealt with in the study of robust design, design of experiments, and optimisation. Some structural analysis programs are beginning to offer rudimentary tools to assist the designer (e.g., the multiple scenarios feature in S-FRAME, which allows the designer to evaluate multiple modelling instances of the same structure in a single run).
- Make comparisons with indicative parameters (i.e., parameters that tend to exemplify the behaviour). Typical indicative parameters include:
  - Maximum deflection in the direction of the main loading;
  - Deflection in the line of a single-point load used as a checking load case;

  - o Maximum bending moment, shear force, axial force, or torque in the structure; and
  - o Value of the fundamental natural frequency.

- Make the results nondimensional (i.e., comparing percentage changes to those obtained from the reference models). Whenever possible, make the independent variables nondimensional.

A sensitivity analysis can lead to deeper understanding of the model behaviour and thus to a better interpretation of analysis results. The sensitivity analysis can show if some characteristics can be ignored or simplified. Conduct a rigorous sensitivity analysis, varying the different connection and element stiffness within their realistic bounds. Combinations of upper and lower bound values should be checked; however, use engineering judgment to reduce the number of permutations. Brittle elements should be designed with appropriate overstrength factors for the envelope of the load paths based on all the different sensitivity analyses that have been carried out.

### 3.2.4 Model Interpretation

Reflective consideration of analysis results is a more effective source of understanding than numerical processing (MacLeod, 2010). A qualitative study of the analysis results in animation (even for static results) should be part of every verification process. Engineers can often spot irregularities more quickly when observing the structural behaviour in animation than from studying numerical values. Based on the model validation and result verification, the designer can understand the models better.

When assumptions are made for the analysis model, they should be incorporated into the member sizing processes. For example, for a triangulated frame, if bending of the members is considered in the analysis model, then it must also be considered in the member sizing process. All the internal forces from an analysis model should be considered in the member sizing process. If any are ignored, then the internal forces used for the design will not be in equilibrium with the applied load. The structure after sizing would not behave as expected.

When comparing models, it is crucial not to judge prematurely. Some models may coincidentally yield a good correlation in a certain condition as a result of compensating assumptions and may not be more reasonable than other models. An example of compensating assumptions for the lateral stiffness of a timber frame could be when the column bases are assumed to be pinned, which is less stiff than in the real situation, and the connections connecting the beam to the column are assumed to be fully fixed, which is stiffer than in the real situation.

The designer should be able to predict if the computed results would be higher or lower than the test results based on the assumptions adopted. If the models would potentially underestimate or overestimate the response of the structures, the sensitivity analysis can lead to deeper understanding of how the structure behaves and can thus help to better interpret the analysis results.

### 3.2.5 Competence of Modellers

Modelling is a powerful tool for helping designers and researchers understand and predict the response of components, connections, assemblies, and structures under various actions; this would otherwise be difficult to achieve using hand calculations or experimental methods. No matter how sophisticated the model is, it requires exercising engineering judgment. In fact, the more advanced the modelling is, the more judgment is required. Therefore, the intent of modelling is not to replace or rely less on engineering judgment but to have a reliable numerical measure or relative performance given the conditions assumed.

The effective use of modelling requires competency in the following areas:

- Understanding the basic principles of structural mechanics, including equilibrium, compatibility, and force-deformation relationships;
- Using the modelling process (e.g., Section 3.2.1);
- Understanding conceptually the behaviour of the structure being modelled; and
- Understanding the solutions process.

Furthermore, construction details should be specified to ensure that the structures behave as designed and modelled.

## 3.3 METHODS

Various numerical modelling methods are available for simulating the behaviour of structures under different loading conditions. This section introduces four types of modelling approaches.

### 3.3.1 Mechanics-based Modelling

Mechanics-based modelling, also called analytical modelling, is used to calculate the forces and deformation in a structure induced by various actions through applying engineering principles and fundamental mechanics. It usually involves establishing and solving equilibrium, compatibility, and constitutive equations. Hand calculation or any engineering calculation software can be adopted depending on the complexity of the equations.

Mechanics-based models provide simple methods that help understand and predict the performance of structures. Such models are suitable for conceptual designs and for verifying the results obtained from complex FE models. Several analytical models have been developed to predict the deflection and resistance of platform (Gavric et al., 2015; Nolet et al., 2019; Reynolds et al., 2017; Sandoli et al., 2016; Sustersic & Dujic, 2012; Tamagnone et al., 2018) and balloon-type (Chen & Popovski, 2020a) mass timber buildings with CLT. Figure 4 shows two mechanics-based models developed for balloon-type CLT walls by Chen and Popovski (2020a). Once such models are developed, the analysis of corresponding structures with various key parameters (e.g., sensitivity analysis) is straightforward. These types of models are more suitable for analysing relatively simple problems (e.g., static performance) of uncomplicated structures (e.g., elastic material behaviour and/or boundary conditions). With respect to structures for which mechanics-based models do not exist or their development outweighs the benefit, FE modelling is a more efficient approach.

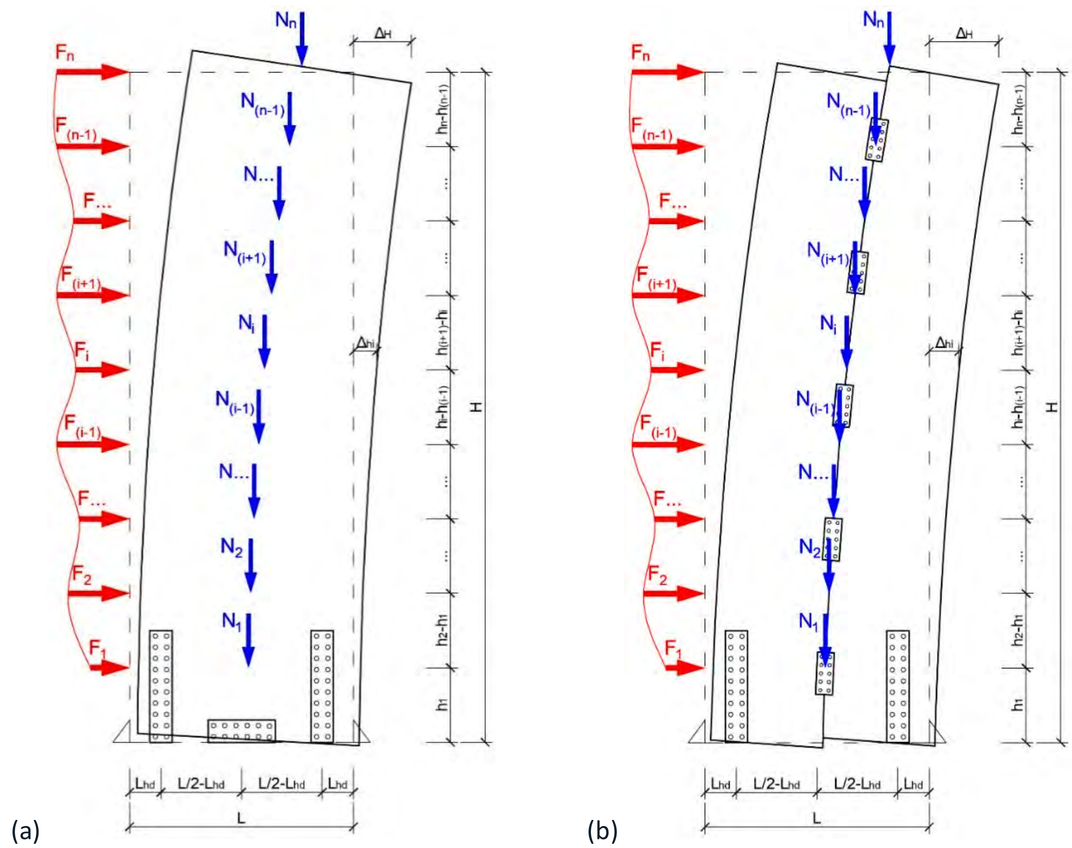


**Figure 4. Mechanics-based models for (a) single- and (b) coupled-panel balloon-type CLT shear walls**

### 3.3.2 FE Modelling

In this modelling approach, the major structural components and connections are developed using any FE-type software previously mentioned. The software develops and solves equilibrium equations, compatibility equations, and constitutive equations. Problems ranging from simple to complex (e.g., time-history analysis) and models with different levels of complexity (e.g., nonlinear material behaviour and boundary conditions) can be analysed by FE modelling, which is usually limited by software capacity (e.g., material models) (Chen et al., 2017).

In terms of model scale, two types of models are available: microscale and macroscale. Microscale models form a broad class of computational models that simulate fine-scale details. In contrast, macroscale models amalgamate the details into selected coarse-scale categories. The goals and complexities of the models determine which modelling scale is used for a specific work. In the area of structural engineering, microscale models are commonly used in analyses of structural components (Chen et al., 2011; Martínez-Martínez et al., 2018) and connections (Chen et al., 2020), with testing results of materials as model input. These models focus on how the behaviour of the modelled object is influenced by its geometric and material properties. In contrast, macroscale models are widely used in the analyses of structural assemblies (Christovasilis & Filiatrault, 2010; Di Gangi et al., 2018; Pozza et al., 2017; Rinaldin & Fragiacomo, 2016; Xu & Dolan, 2009a; E. Zhu et al., 2010) and entire buildings (Chen & Ni, 2020; Filiatrault et al., 2003; Xu & Dolan, 2009b). Figure 5 shows a 6-storey light wood-frame building with portal frames using macro-wall elements (Chen, Chui, Ni, &

Xu, 2014) and a 19-storey mass timber building on a concrete podium using macro-connection elements (Chen, Chui, & Popovski, 2015; Chen, Li et al., 2015).

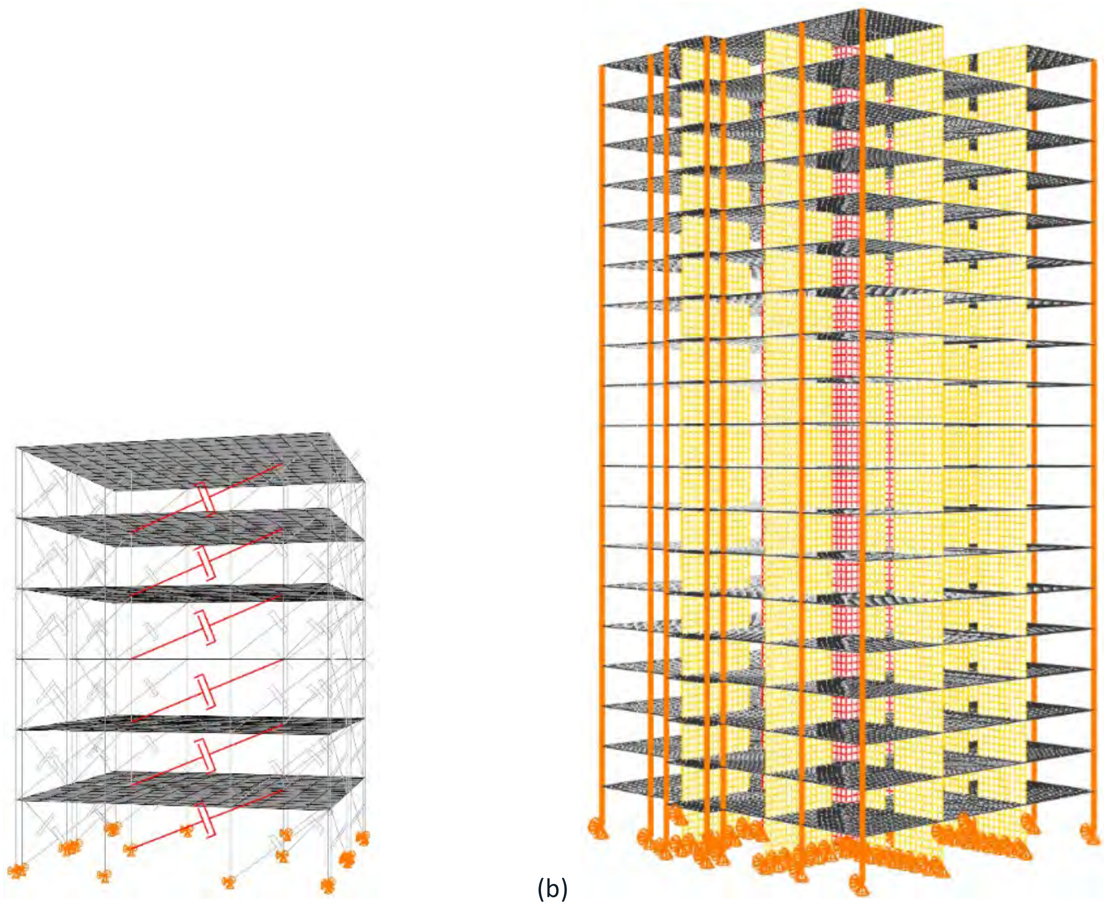

(a) (b)

**Figure 5. FE models for timber structures: (a) 6-storey light wood-frame building and (b) 19-storey mass timber building (Checker building) on a concrete podium (not shown)**

In the FE modelling approach, the major structural components and connections should be developed using any type of software (Chen et al., 2017). Typically, beam elements should be used to model structural components in bending or under a combination of bending and axial loads (e.g., columns and beams). Truss or bar elements should be used to model axial structural components in situations when it is deemed that bending can be ignored (e.g., webs in a truss structure). Shell elements should be adopted to model structural components with a thickness that is significantly smaller than the other two dimensions, such as floors and walls. Because of the anisotropic material characteristics of wood (Chen et al., 2011), orthotropic material properties are required for the 2D or 3D model input for wood-based products. When the capacity design is used, the timber structural components that are capacity-protected can be modelled as orthotropic elastic members.

Connections play a critical role in any timber structural model in terms of stiffness, ductility, and energy dissipation of the entire system. Connections that experience semirigid behaviour can be modelled using spring or connection elements. In cases of conducting nonlinear analyses (pushover or nonlinear dynamic analysis), suitable backbone curve models that can represent the yielding and post-yield behaviour of the connections, as well as hysteretic models that can represent the energy dissipation and the pinching effect of timber connections, must be used. As timber connections have high variability in stiffness and strength, the ranges of these parameters have to be established during modelling, and the lower and upper bounds of the connection mechanical properties should be considered. Specific key connections should be considered as semirigid joints when calculating the deformation or stiffness and the natural period of vibration of the building. Upper bound limits should also be used when analysing the natural period of vibration of the buildings because simplified numerical models can easily produce unrealistically high and therefore nonconservative natural vibration periods.

Floor and roof diaphragms as horizontal assemblies distribute the gravity and lateral loads to load-resisting assemblies underneath. Diaphragm flexibility is a key factor affecting the lateral load distribution to the walls and other elements below (Chen, Chui, Mohammad et al., 2014; Chen, Chui, Ni et al., 2014; Chen & Ni, 2021). It is suggested that diaphragms be modelled in the structural models according to their stiffness and deformability characteristics. Nonstructural components, such as gypsum wallboard, provide considerable additional stiffness to lateral load-resisting systems (Chen, Chui, Doudak, & Nott, 2016; Lafontaine et al., 2017). Engineers must exercise judgment about whether the contribution of nonstructural components should be considered in the model.

For structures where the storey shear deformation is the major component induced by lateral loads, such as low-rise light wood-frame buildings, mass-spring-damper models can be used to simulate the entire building or the main lateral load-resisting assemblies at each storey (Chen & Ni, 2020; Xu & Dolan, 2009b). When bending deformation cannot be ignored under lateral loads (e.g., balloon-type mass timber shear wall structures), mass-spring-damper models are no longer suitable, and the lateral load-resisting assemblies must be modelled in a relatively more detailed approach. The connections in these assemblies, however, can be simulated using suitable nonlinear hysteretic springs (Xu & Dolan, 2009a; E. Zhu et al., 2010).

### 3.3.3 Hybrid Simulation

Evaluation of structure performance has traditionally been explored using either experimental or modelling methods. Full-scale testing is generally viewed as the most realistic method for evaluating structural components, assemblies, or even entire structures. The testing methods, however, require a full-scale testing set-up (e.g., strong floor and strong wall testing facilities, or a shaking table), which is available only at some universities and institutes, and is mostly out of reach for most design practitioners. Furthermore, issues of size, equipment capacity, and availability of research funding continue to limit the use of full-scale testing of structures. Numerical modelling, on the other hand, is limited to solving specific types of problems and in some cases fails to capture complex behaviours or failure modes of structures or some components. Combining experimental and modelling tools in a single simulation while taking advantage of what each tool has to offer is referred to as hybrid simulation (Kwon, 2017; Schellenberg et al., 2009; Yang et al., 2017). Figure 6 schematically shows the hybrid simulation for a braced timber frame structure.

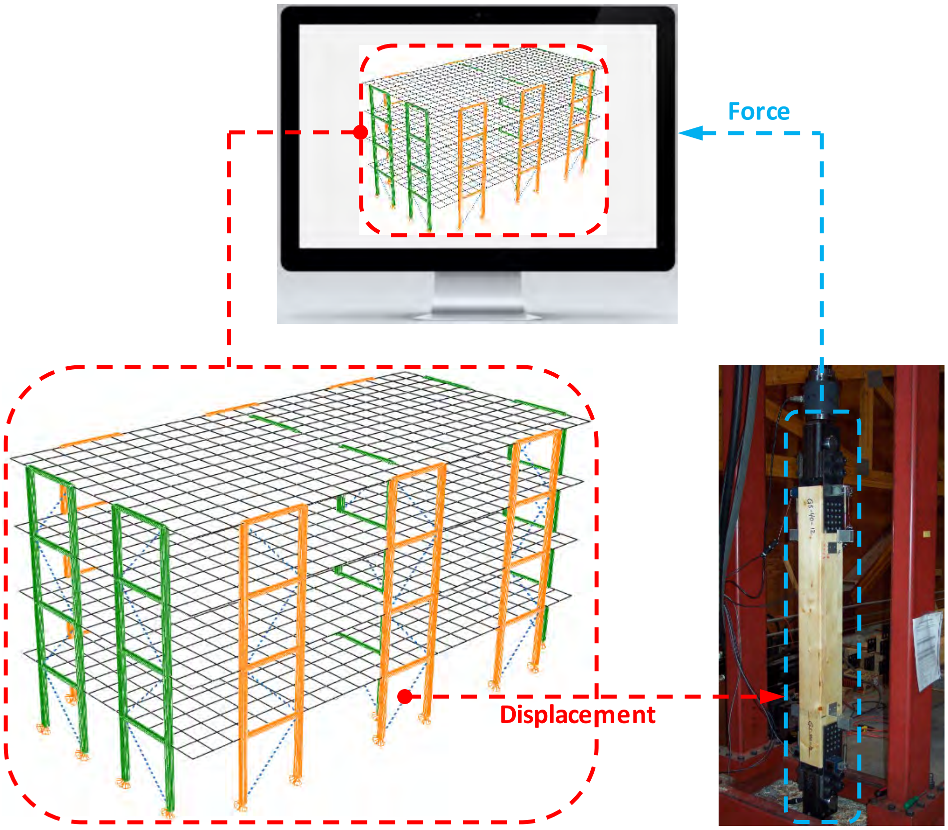


**Figure 6. Schematic diagram of hybrid simulation for braced timber frames**

In hybrid simulation of timber buildings, the entire structure is simulated and analysed by structural analysis software or general-purpose FE software, while key structural components, connections, or assemblies are tested in a laboratory. At each time step of the numerical integration of the equations of motion, the trial displacement calculated by the software is applied to the specimen. The force feedback of the specimen is then used by the software to check equilibrium before proceeding to the next time step. This way, the dynamic response of the entire building can be obtained with the real input from the tested components, connections, or assemblies. Hybrid simulation can provide many significant advantages, including:

- Experimental costs can be reduced because only a portion of the structure is tested in a laboratory;
- Specimens can be tested on a large scale because most of the structural components are modelled numerically;
- Testing configurations can be complex because most of the loads are simulated; and
- Large and/or complex structures can be tested using geographically distributed laboratories, which means that resources such as lab space, testing equipment, and research personnel from different laboratories can be shared.

Hybrid simulation is suitable for complex timber buildings, particularly resilient buildings with structural fuses, because nonlinearity is typically concentrated at connections that are complex and can be tested in a laboratory without significant effort. The remaining structure, which is capacity-designed and therefore considered to behave linearly, can be easily modelled with accuracy. Hybrid simulation frameworks, such as UI-SimCor (Kwon, 2008) and OpenFresco (Schellenberg et al., 2008), provide an interface between a numerical integration scheme and a few analysis packages, such as Abaqus, OpenSees, VecTor Suite, S-FRAME, etc. (Huang & Kwon, 2020).

### 3.3.4 Material-based Modelling

Over the past several decades, digital progress has transformed the entire construction industry, ushering in a technological era now known as the fourth industrial revolution. New digital technologies, including building information modelling (BIM) and artificial intelligence (e.g., machine learning), have begun to enter the industry, gradually changing how infrastructure, residential, and nonresidential buildings are designed, constructed, operated, and maintained. More refined models, which are capable of exchanging construction details among different areas such as architecture, fabrication, and construction, and reducing or even eliminating the need for large-scale tests and calibrations, are desired for design and analysis of structural assemblies or entire structures. Rapid development of high-performance computing (e.g., cloud computing), more comprehensive constitutive models for the material behaviour (Chen et al., 2011; Sandhaas et al., 2012), and more accurate contact models provide a solid foundation for using more refined structure models. To fulfil the new demand of the construction industry, a material-based modelling method was developed (Chen & Popovski, 2020b) that simulates the seismic response of post-tensioned shear walls. The material-based models possess necessary details and parameters to support the design information exchange between BIM and structural modelling while providing strategic simplifications to reduce the computation cost. If there are sufficient details on the material and geometric properties, and boundary conditions have been considered, the developed model can accurately predict the behaviour of the modelled structures without calibration. Only the material (physical and mechanical) and geometric properties of the components and connections are required as input for the material-based models. Key points of the material-based modelling method are listed below.

- Structural components:
    - Structural components should be categorised as main or secondary, based on the structural contribution and influence. The main components are modelled with as much detail as possible, while the secondary components are modelled with more strategic simplifications to reduce the unnecessary details.
    - Geometric models of the structural components should be developed with the necessary design information.
    - Constitutive models that are capable of fully describing the key material behaviour should be selected.
    - Structural components should be meshed using elements that are compatible with the geometric and constitutive models. The mesh should be dense in the key spots and can be looser in other locations.

- Connections:
  - Connections can be simple or more complex components. Some can be treated like a structural component, while others must be modelled using microscale models.
  - Developing geometric and constitutive models and the element mesh for the connections should follow the same rules as those for the structural components mentioned above.
- Contact zones (constraints and interactions):
  - Constraints can be grouped as rigid, semirigid, and of pinned type. It is straightforward to model the first and the last types. Attention should be paid, however, to make sure that no unrealistic stress concentration is developed in the components due to the constraints. In the case of semirigid constraints, specific elements and modelling techniques should be adopted to properly simulate the stiffness and strength of such constraints.
  - Interactions between two components can be classified as having either 'hard' or 'softened' contact in the normal direction of the contact area, and with or without friction in the tangential direction. Appropriate interaction models should be selected for each case.

The material-based modelling method was adopted in the modelling of post-tensioned CLT walls (Figure 7). With this modelling method, the parametric structural design can be done more easily, and the gap between BIM and other areas of modelling can be bridged, while expending the virtual design and construction.

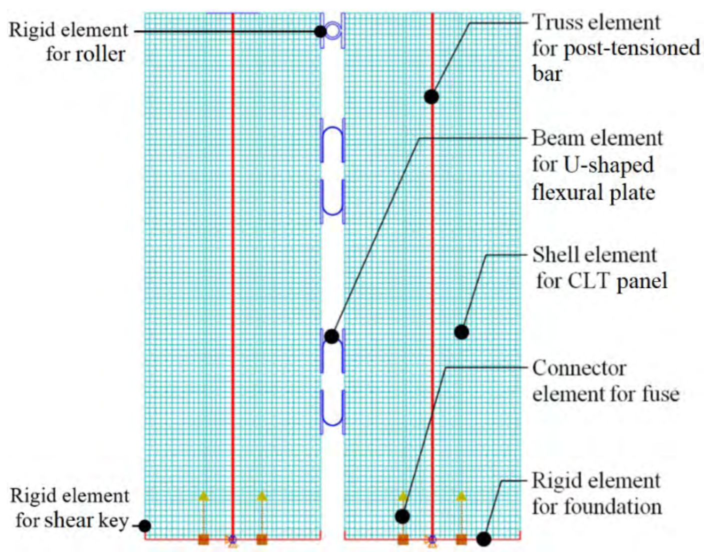


**Figure 7. Material-based model for post-tensioned coupled CLT**

This modelling guide provides mechanics-based modelling and FE modelling solutions to wood-based components, connections, assemblies, and structures. See Chapters 4 to 10 for more information.

## 3.4 TECHNIQUES

Various numerical modelling techniques are available for simulation problems. This section introduces the stochastic finite element method (SFEM), computational structural design and optimisation, and BIM.

### 3.4.1 SFEM

From a structural point of view, wood and timber can be considered a natural unidirectional fibre composite with highly anisotropic properties. For specific species, geographical location, and local growth conditions, the material properties depend on factors such as age, presence of potential strength-reducing growth characteristics, and the location of timber within the tree; these factors contribute to the high variability in strength and stiffness. One of the consequences of this variability is a phenomenon known as the size effect, a regressive course of strength with increasing volume (Brandner & Schickhofer, 2014). The Weibull size effect law (Weibull, 1939) is the most common model used for describing size effects on the strength of timber in its brittle failure modes. According to this model, a structural member fails when the stress level reaches the strength at a single material point. In current practice using the Weibull size effect law, a Weibull distribution is fitted to data obtained from experiments on specimens with standardised dimensions. The Weibull size effect law is then used to predict the strength of pieces of timber either with higher volumes (Madsen, 1990; Madsen & Tomoi, 1991), such as timber beams, or lower volumes (Clouston & Lam, 2002; Tannert et al., 2012), which are usually small elements considered in FE analyses of timber structures. However, experimental data from the literature (Tannert et al., 2012; Zhu et al., 2001) shows that this procedure can result in relative errors in predicting the size effect on timber strength as high as 400%. This is attributed to the fact that the spatial correlation in the strength field is neglected in the Weibull size effect law. The finite element method (FEM) with consideration of variable wood properties is desired (Kandler et al., 2015; Kandler et al., 2018; Moshtaghin et al., 2016).

The FEM is deterministic by nature and is therefore limited to describing the general characteristics of a structure. It cannot directly study a structure's reliability or failure probabilities. To compensate for uncertainty with a deterministic approach, a common practice in engineering is to use safety factors. Safety factors cannot quantify or predict the influence and sources of randomness in a structure (Moens & Vandepitte, 2006). Timber structures require the engineer to have a deeper understanding of the physical phenomena to comprehend and assess reliability. To represent the stochastic nature of a structure, random fields are introduced to the classic FEM to capture and create different stochastic scenarios. The influence of the random fluctuations is evaluated by calculating the statistical information of the response variables and evaluating the probability of an outcome of the structure, such as failure. Civil engineering has started to adopt the SFEM as a tool to assess the reliability of foundations and structures.

The SFEM is an extension of FEM that accounts for the uncertainty of a structure that occurs as a result of variations in geometry, materials, or loading condition (Arregui-Mena et al., 2016) (Figure 8). Different sources of uncertainty arise in the study of complex phenomena. These include human error (Hughes & Hase, 2010), dynamic loading (Schuëller, 2006), inherent randomness of the material (Hurtado & Barbat, 1998), and lack of data (Moens & Vandepitte, 2006). In practice, a researcher who uses the deterministic FEM is typically restricted to the average values of loads and material properties applied to a model with an idealised geometry, thus reducing the physical significance of the model. For significant variations and randomness, the average values of the properties of a physical structure are only a rough representation of the structure.

For timber structures, the wood-based products and the connections possess high variability in mechanical properties. It is important to consider the influence of the variation of material properties and connection properties on the structural behaviour of timber structures.

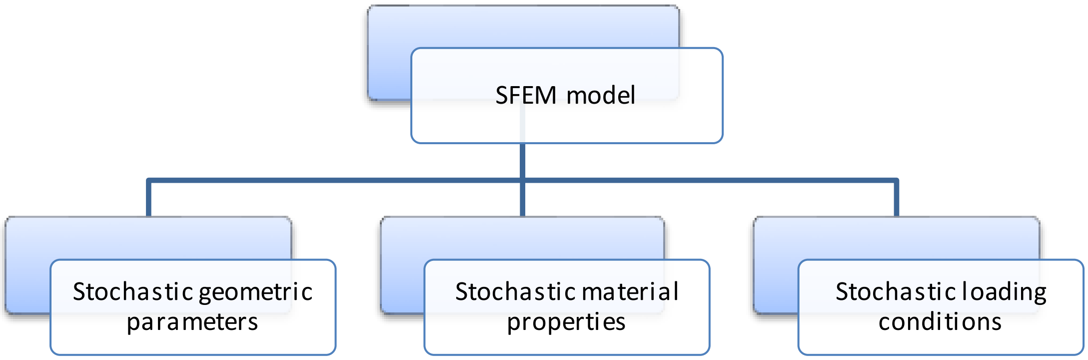


**Figure 8. Stochastic variables considered in the SFEM**

To study the uncertainty and inherent randomness of a structure, the SFEM adopts different approaches. Each uses the mean, variance, and correlation coefficients of the response variables to assess a quantity of interest, such as the probability of failure of a structure. Several variants of the SFEM have been developed. The following three are the most commonly used and accepted: Monte Carlo simulation (Astill et al., 1972), perturbation method (Liu et al., 1986), and the spectral SFEM (Ghanem & Spanos, 1991). Each method adopts a different approach to represent, solve, and study the randomness of a structure. The following sections discuss the main methodology of each variant and the general structure of each method. For a concise evaluation of the advantages and disadvantages of each method, refer to the report by Sudret and Der Kiureghian (2000).

Monte Carlo simulation is the most general and direct approach for the SFEM (Hurtado & Barbat, 1998; Schuëller & Pradlwarter, 2009). The Monte Carlo FEM merges the Monte Carlo simulation technique with the deterministic FEM. It proceeds as follows:

- Determine the set of random and deterministic variables;
- Characterise the density function and correlation parameters of the random variables;
- Use a random field generator to produce a set of random fields;
- Calculate the solution of each realisation with the deterministic FEM;
- Gather and analyse the information of the simulations; and
- Verify the accuracy of the procedure (Figure 9) (Haldar & Mahadevan, 2000).

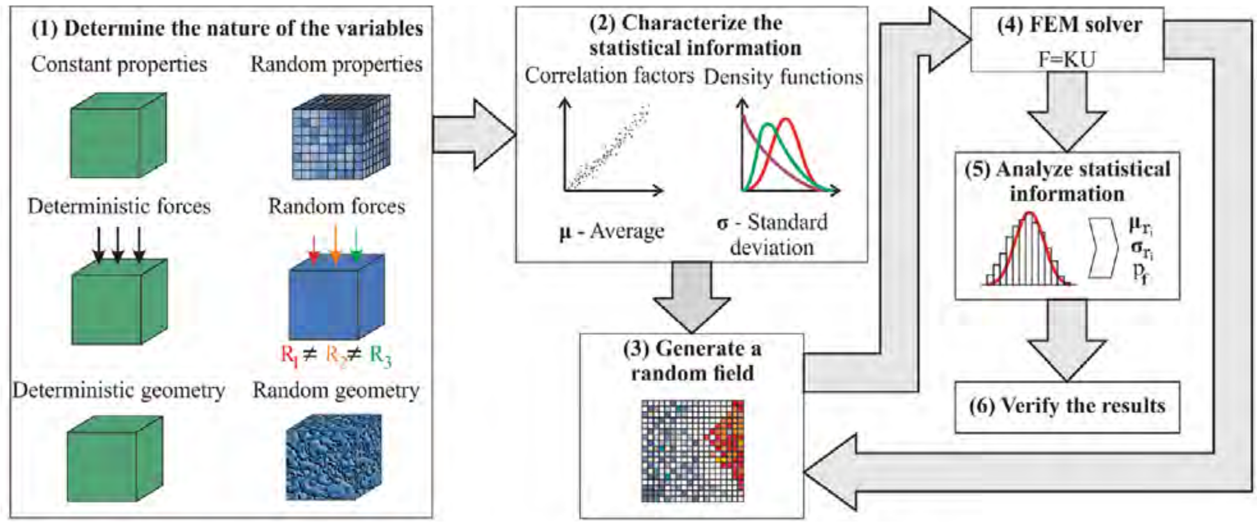


**Figure 9. General procedure of Monte Carlo simulation (Arregui-Mena et al., 2016)**

Monte Carlo simulation is the most simple and direct approach. In general, of all the methods, this one requires the most computational power, especially with structures that have great variability and involve complex models that include several random variables. Even with this disadvantage, Monte Carlo simulation is widely accepted and is often used to validate the perturbation method and the spectral SFEM. In several cases, the latter two approaches are complemented or merged with the Monte Carlo simulation. Furthermore, alternative procedures have been proposed to reduce the computational effort to calculate the response variables and the probability of failure of a structure by reducing the population of the required samples (Hurtado & Barbat, 1998).

The perturbation method is another popular branch of the SFEM (Ariaratnam et al., 1988; Elishakoff & Ren, 2003; Kleiber & Tran Duong, 1992). This method uses Taylor series expansions to introduce randomness into the structure. In general, the perturbation method is limited to values of random variables that are not large compared to their mean values. The coefficient of variation is usually set at 10 to 15% of the mean value of the variable of interest. However, studies using higher coefficients of variation do exist (Elishakoff & Ren, 2003). The perturbation method is a popular and simple approach that can be useful to generate reasonable estimates of the statistical moments of the response variables. This method offers a balance between complexity and computational effort to estimate the influence of the mean, standard deviation, and covariance of response variables on the behaviour of a structure.

The spectral SFEM (Ghanem & Spanos, 1991) is mainly concerned with representing the random material properties of a structure. To introduce the random parameters, the method uses the Karhunen-Loève expansion. The representation of the random parameters in this form seeks to reduce the computational power used in other methodologies, such as the Monte Carlo simulation. To increase the efficiency of the spectral SFEM, the solution space is mapped with Fourier-type series. The spectral SFEM and the spectral representation of random variables have received more attention recently, because the purpose of the methodology is to reduce the computational power required to analyse a stochastic process compared to the Monte Carlo simulation. Since its inception, further developments in efficient algorithms have improved the capabilities and performance of the original spectral SFEM.

The three variants of the SFEM share a common component that describes the inherent randomness of a structure, namely, random fields. An ideal random field should capture the main attributes of the random structure by taking into account the minimum number of meaningful and measurable parameters of a structure. A random field can be described as a set of indexed random variables that depict the random nature of a structure. The index represents the position of the random variable in space or time or both (Vanmarcke, 1983). Random fields are characterised by the main statistical information of the variable of interest, such as the mean, variance, probability distribution, and autocorrelation function, among other statistical parameters. Several random field representation methods that determine the properties of a material can be found in literature, namely, the local average method (Vanmarcke & Grigoriu, 1983), turning-bands method (Matheron, 1973), Fourier transform method (Yaglom, 1962), and the local average subdivision method (Fenton & Vanmarcke, 1990).

Several software developers have incorporated SFEM algorithms or created specialised SFEM solvers and reliability tools to study structures with random variations (Pellissetti & Schuëller, 2006), such as COSSAN (Pradlwarter et al., 2005) and NESSUS (Southwest Research Institute, 2020). They are general-purpose software packages capable of handling a wide range of applications and have additional tools for studying the reliability of a structure. They offer various procedures to calculate the reliability of a structure, such as the Monte Carlo simulation, advanced Monte Carlo simulation (Pradlwarter & Schuëller, 1997), response surface method (Schuëller et al., 1991), first-order reliability method, and second-order reliability method (Haldar & Mahadevan, 2000; Melchers & Beck, 2017).

## 3.4.2 Computational Structural Design and Optimisation

### *3.4.2.1 Introduction to Computational Design*

Computational design, depending on the how it is defined, arguably started even before the first computer-aided design (CAD) software—Ivan Sutherland's Sketchpad (1963). In the architecture, engineering, and construction industry today, the term computational design typically implies using computing to influence or enable the exploration of design space (Epp, 2018). Throughout the past decade, the field of computational design has gained significant practical application in the construction industry, especially in complex structures but now even in the design of more standard structures. The fairly brilliant ascent of this new worldview among designers can be largely attributed to the development of new user-friendly software tools, which empower the creation of parametric scripts without requiring computer programming skills. Applying computational design has become expected in leading architectural and engineering practices around the world, especially in geometrically complex or free-form structures.

Early visual programming tools for parametric CAD (e.g., Bentley Systems' GenerativeComponents) initially began acquiring prominence in the early 2000s, especially in the architectural community in London, England. With David Rutten's 2007 release of Grasshopper, which is a plug-in to the Rhinoceros 3D modelling software, it immediately turned into the standard for parametric modelling and computational design in architecture, engineering, and construction. Other software tools, such as Ian Keough's Dynamo for Autodesk Revit, have developed on the achievement of Grasshopper. These tools utilise a straightforward node-based interface called visual programming. Each node on the canvas (Figure 10) is called a component and is the container for a small algorithm. Each component conducts an operation, obtaining inputs on the left, running the algorithm internal to the component, and exporting outputs on the right. For instance, a Line node would take two points as inputs, or a Structural Beam node would take a collection of Lines, a Cross Section, and a Material as inputs. Each component can be connected by means of 'wires', and the topology of the wires linking the components characterise the data flow and algorithm logic, creating a script.

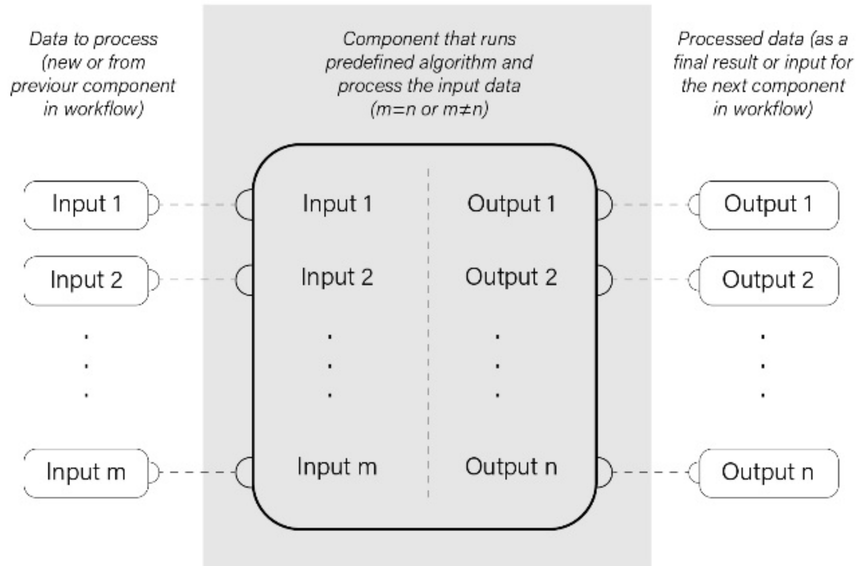


**Figure 10. Typical layout of a component**

Modelling and analysing a structure in a parametric environment first requires breaking down the end goal into a series of typically linear operations. The required process to achieve the desired outcome can be schematised and divided into smaller operations which either exist as predefined components in the computational design program or can be sourced from external libraries. For example, a task to model and analyse a simply-supported beam in a parametric environment could be divided into three steps: creation of 1D geometry, structural property definition and FE analysis, and result visualisation (Figure 11). Each step can be further divided into smaller operations until a preexisting component is found that performs the desired operation.

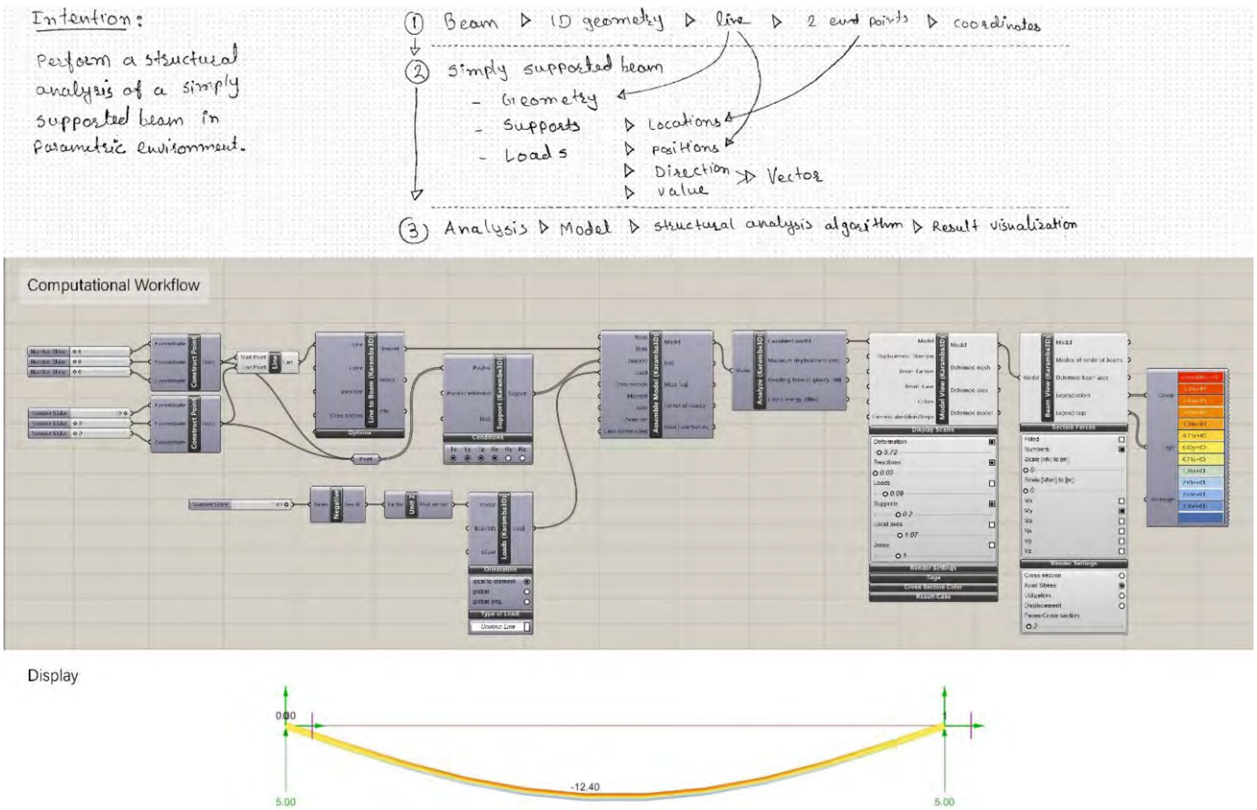


**Figure 11. Example of a typical process of structural analysis in a parametric environment: structural analysis of a simply-supported beam using Grasshopper and Karamba3D**

Computational design tools (e.g., Grasshopper) support a design approach that specifies the geometry of structures parametrically; the guiding geometric principles of a design are revealed as parameters, which can be changed anytime during the design. This allows rapid examination of variations on a certain design or geometry. Critical advances in software design enable real-time analysis to be conducted as the geometric parameters are altered. For instance, this implies that while altering the geometry of a truss, a designer can watch in real time as the structural forces change. Engineers can apply many different variables and constraints in creating the geometry and analysis model, and using optimisation techniques, they can find the solution that best meets the design objectives. Figure 12 illustrates a more complex task: to determine the optimal geometry for a hybrid timber-steel truss that meets architectural, structural, fabrication, and shipping requirements while minimising material use. The parametric workflow leaves the position of truss joints and cross-sections as variable parameters. Exploring the solution space with optimisation algorithms enable the most suitable geometry to be found. This is a step change from traditional analysis methods, which involve transferring geometry to separate analysis software and then running the analyses, often taking minutes or hours. The design-performance feedback loop has thus been reduced significantly.

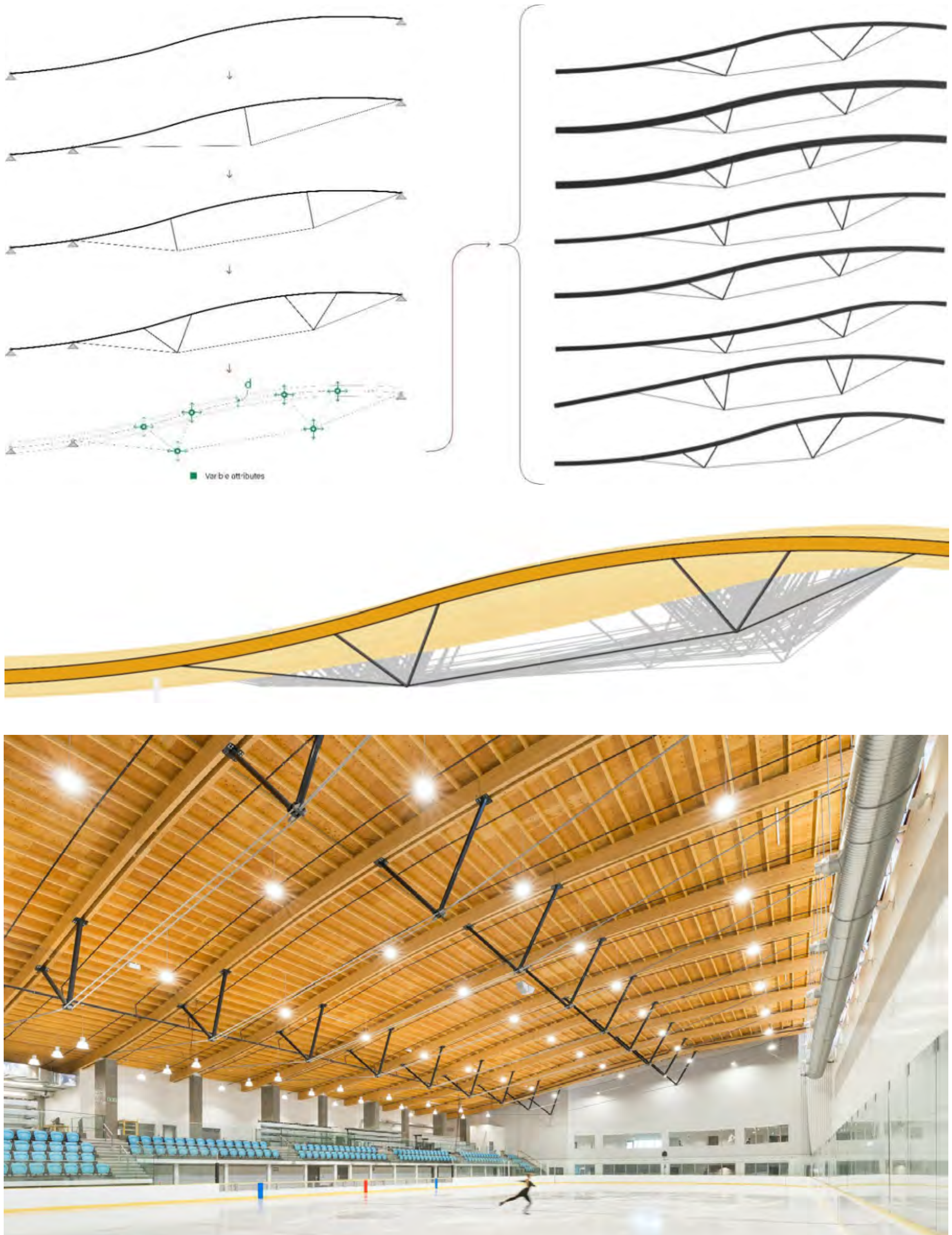


**Figure 12. Structural and cost optimisation of a timber-steel hybrid truss spanning 130 ft. over an ice arena: (a) possible geometric configurations and required section sizes; (b) optimal solution overlaid with all geometries studied; and (c) completed structure (North Surrey Sports & Ice Complex)**

In the advancement of computational software tools (e.g., Grasshopper and Dynamo), vigorous user communities have contributed custom plug-ins facilitating various kinds of computation and analyses, varying from geometric to mathematical to machine learning. The performance attributes of structures that can be assessed are broad. They include daylighting and building energy modelling, people movement, structural FE analysis, CNC robotic modelling and toolpath generation, geometric analysis, optimisation (such as for free-form facade panel planarity), form-finding (such as Gaudi's hanging chains), and physics simulation, including computational fluid dynamics.

The potential uses of computational design in structures are practically boundless; they are not restricted to parametric geometric and structural investigation of form and can be applied to real generative design, where an algorithm creates the forms by observing specific guidelines. Nevertheless, computational design in architecture and engineering has essentially been centred around the parametric definition of geometric form, and the performative assessment of such forms. The capability to rapidly evaluate the performance attributes of designs while changing design parameters can significantly benefit design selection.

Computational design has experienced early implementation in complex projects, but the principles of computation are not restricted to those that are complex. Utilising node-based visual programming, computational design approaches can be applied easily to a wide range of issues. Interest in incorporating timber in structures both complex and simple is expanding. An emphasis on off-site and modular techniques in timber construction makes computational design appropriate to this field, and its utilisation will keep expanding substantially in North America and abroad.

#### *3.4.2.2 Parametric Analysis*

Parametric design refers to a process in which the designer develops a general algorithmic rule that generates different design outputs by varying the inputs (parameters); in conventional design, a fixed geometry is defined, analysed, and subsequently amended. It is often used for investigating and optimising the geometry or topology of a structure, often to help achieve architecturally interesting forms with a goal of attaining the most structurally efficient or lowest-cost structure. This parametric process generating different options based on input parameters can often be linked simultaneously to calculation spreadsheets and structural analysis software. For example, after having set up a structural grid that can be altered parametrically (with inputs such as bay dimension, number of bays, loading, etc.), the designer can generate an algorithm that allows for the members to be automatically sized and connections drawn, outputting not only the required dimensions but also the calculations. Similarly, when looking at a specific connection, by altering input forces and geometric constraints, a different arrangement of connectors could be produced by the process. After the structural analysis has been run, the resulting structural forces can be used downstream to automatically size the elements and calculate material usage or cost. This gives the designer immediate feedback on important attributes of the structural configuration.

While generally these parametric workflows could be developed for any type of structure with any type of material, it is the emphasis on geometric constraints in timber design that makes them powerful for the analysis of timber structures. The geometric and dimensional constraints play an important role in the design of a timber building. This is due to several factors. First, the sizing of timber elements is often governed by the size of their connections, where steel connectors have to be placed in a specific number and at specific distances. Second, the limitation on sizes of the timber elements, which—unlike concrete—are formed off site, require transportation, and generally come in specific dimensions (particularly solid timber elements). Furthermore, even composite products, such as glued laminated timber (glulam) and CLT, have limitations that are linked to the geometry of the constituting elements (e.g., the thickness of the laminates influences the geometric shapes achievable for glulam elements). Because of the influence of these geometric considerations, the use of widely available parametric tools, such as the Grasshopper plug-in for Rhinoceros 3D, for generating and analysing different viable options becomes useful to the designer. Parametric design and analysis can be used for anything, from helping to determine optimal column grids or structural configurations to automating the creation of 4D models (construction of a structure through time), simulating CNC machine toolpaths, or simply parsing and displaying data about the geometry or structure of a building in a graphic and interactive manner. Figure 13 shows the results of a parametric analysis of bay size on floor vibration response.

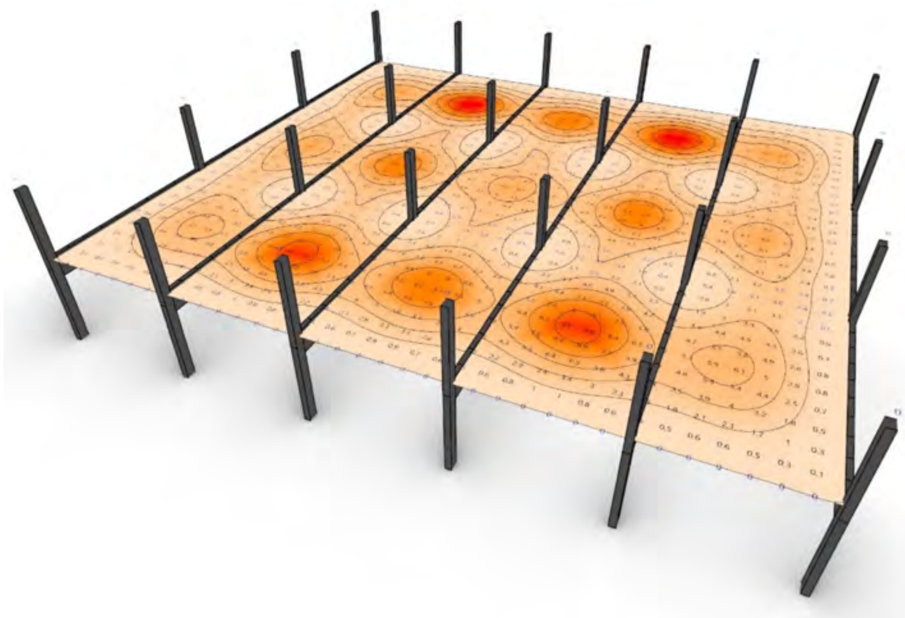

**Figure 13. Parametric analysis of bay size on floor vibration response factors, using custom C# modal analysis components in Grasshopper**

The geometry of a structure can be imported from a CAD format (e.g., .dwg or .3dm) or from a structural analysis model (e.g., Dlubal RFEM or Oasys GSA) and stored within specific components (hexagonal-shaped components). Alternatively, the structural geometry can be generated through a parametric set-up: constraints, 1D and 2D members, and loads can be defined through coordinates and values. These values can be adjusted easily, allowing for the model to be updated in real time. The adjustable input can be specified via other panels, through number sliders, or be retrieved from external spreadsheets. The different components designers use in the project can also be customised using scripting languages such as Python, C#, or Visual Basic.

Once the model has been set up, its geometry and properties can be streamed directly into a structural analysis package. The structural calculations can be performed completely within the Grasshopper environment (e.g., with plug-ins such as Karamba3D), or the content of the model can be imported to other software packages and then eventually the structural results retrieved (e.g., through plug-ins such as Oasys GSA-Grasshopper or GeometryGym). Figure 14 shows an example of a structural workflow in Oasys GSA-Grasshopper for the analysis of a floor structure.

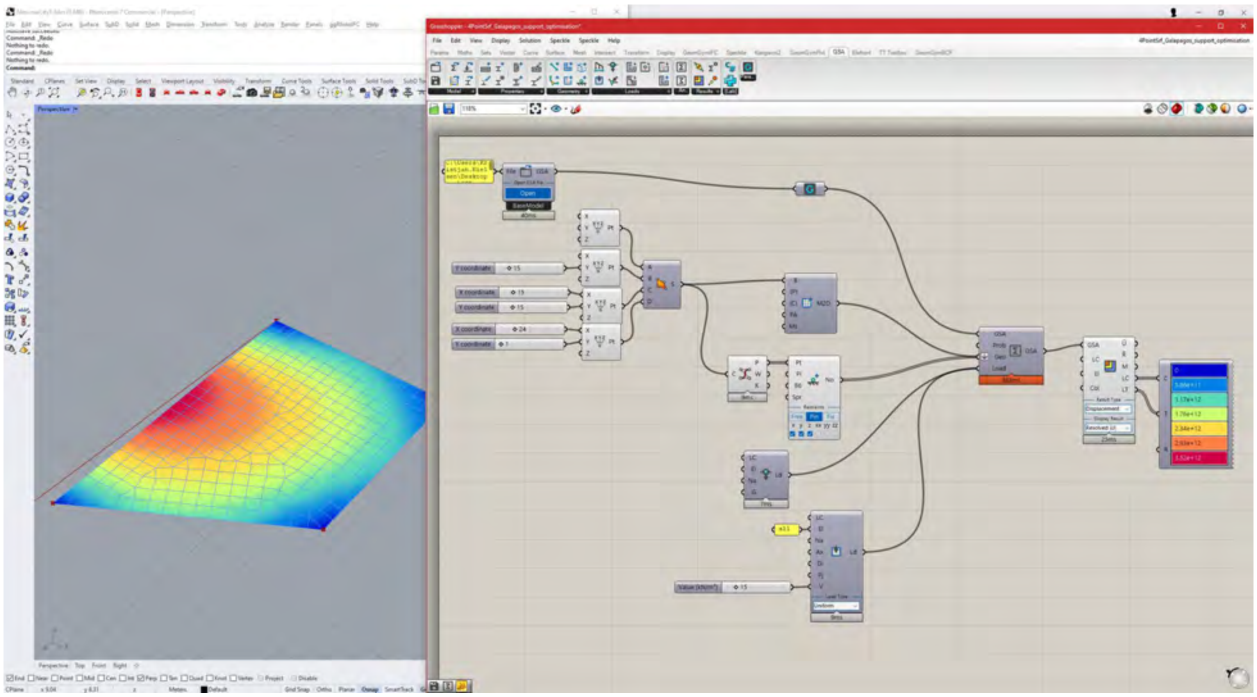

**Figure 14. Grasshopper definition with Oasys GSA-Grasshopper, modelling, and analysis of a floor plate structure. (Courtesy of Kristjan Nielsen, Arup)**

As mentioned, the possibility for high customisation of the shape of timber structural members, thanks to numerical control machining and timber composites, has led to an increased use of parametric software for designing timber structures. Initially, parametric tools were used mostly to define structural geometries of complex timber buildings; for example, the model in Figure 15 was developed using Rhinoceros 3D combined with scripting to extrapolate the complex geometry of the Centre Pompidou-Metz, France. However, the iterative and interactive process between modelling and analysing is increasingly becoming more seamless.

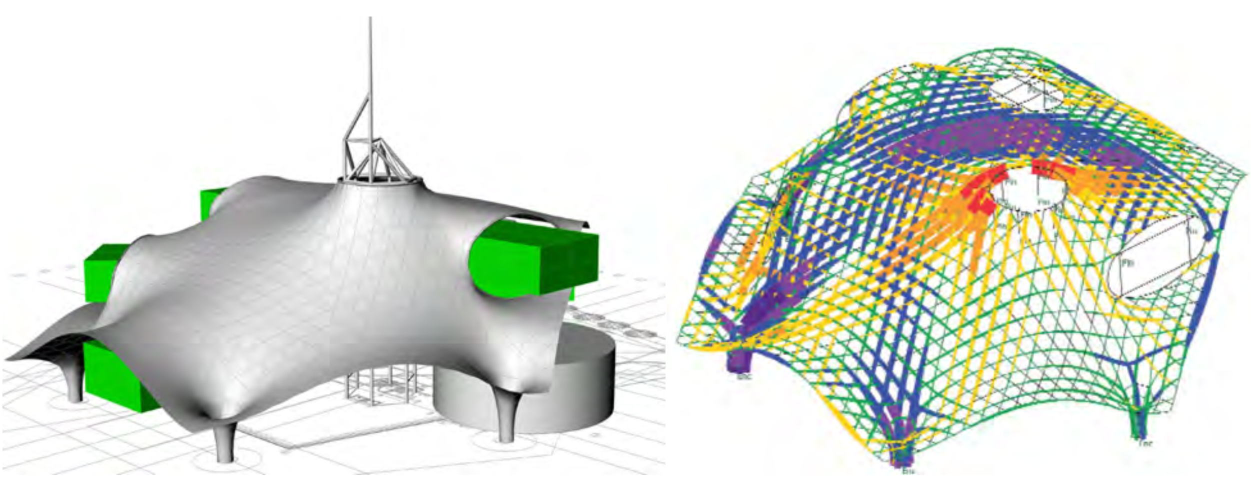

**Figure 15. Defining the structure of the Rhinoceros 3D model of the Centre Pompidou-Metz, France, and the resulting structural model derived with parametric techniques**

As a relatively recent example, Arup structural engineers were involved in developing a schematic diagram of a building whose outer perimeter would be supported by curved glulam columns (Figure 16). Because the maximum curvature that is allowed for a glulam element depends on the thickness of its laminate layers, the overall geometry had to be constrained by the input properties of the columns. A parametric definition was defined in Grasshopper to allow the maximum curvature of the elements, for a given laminate thickness, to define the options available, while other parameters, such as the spacing of columns and interstorey height, could be controlled.

(a) 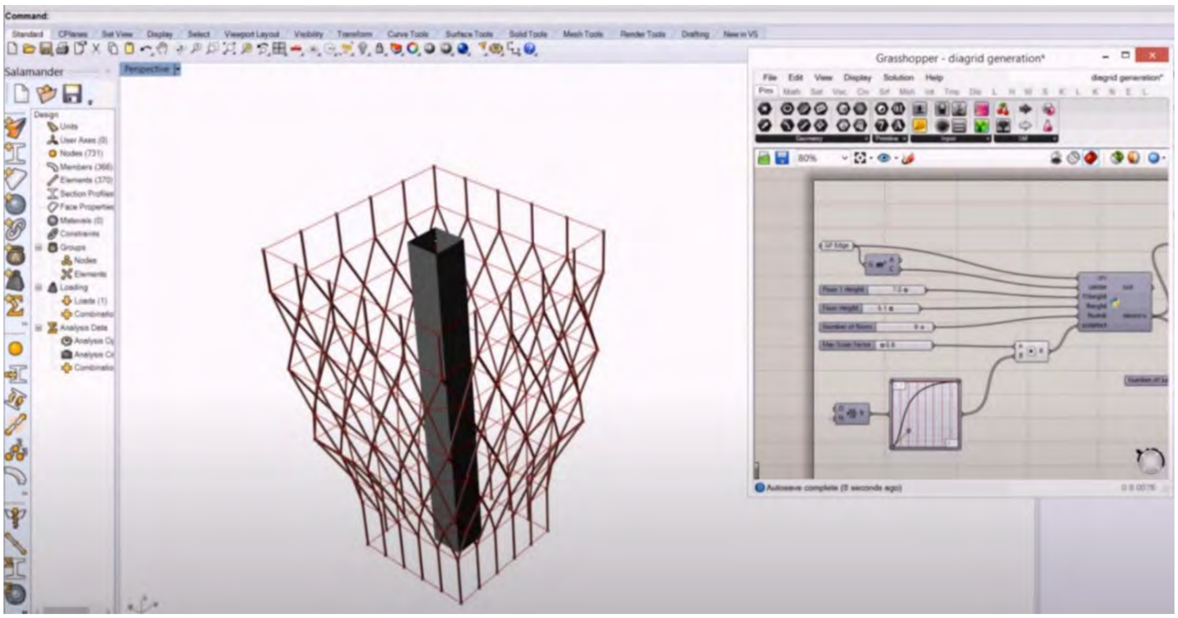


(b) 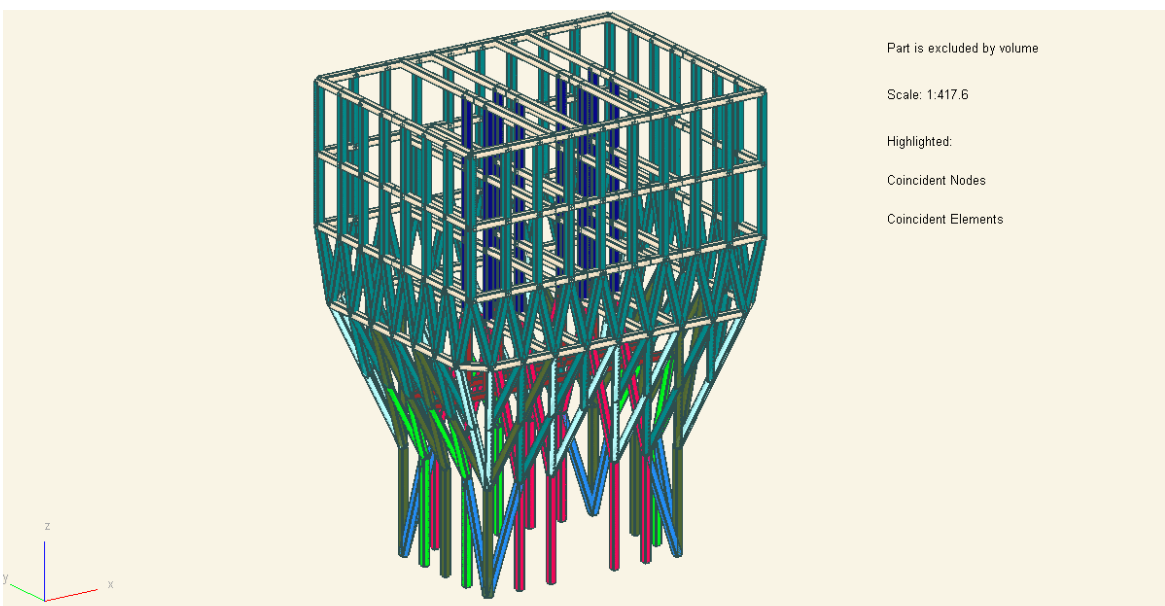


**Figure 16. Timber structure with curved glulam columns: (a) parametric model and (b) structural model**

While the parametric definition developed would allow for generating geometries compliant with the timber element properties, it would also output a GSA model that could be analysed by structural software for understanding the building performance. The process was quite efficient as any architectural changes to the initial shape could be checked easily just by altering the parameters of the definition, allowing for a geometric and structural check without having to remodel the building completely. Also, the analysis results could flag any excessive stress and in turn inform the modification of the original parameters.

Parametric definition of geometry of the timber gridshell domes on the recently completed Taiyuan Botanical Garden, China, was central to achieving an efficient structure (Figure 17). Geometry generation, structural analysis, element design, level of development (LOD) 400 model creation, CNC file generation, and piece drawings were all performed and created in a custom Rhinoceros 3D/Grasshopper workflow using Branch, a software platform for engineering, designing, and manufacturing timber structures.

(a) 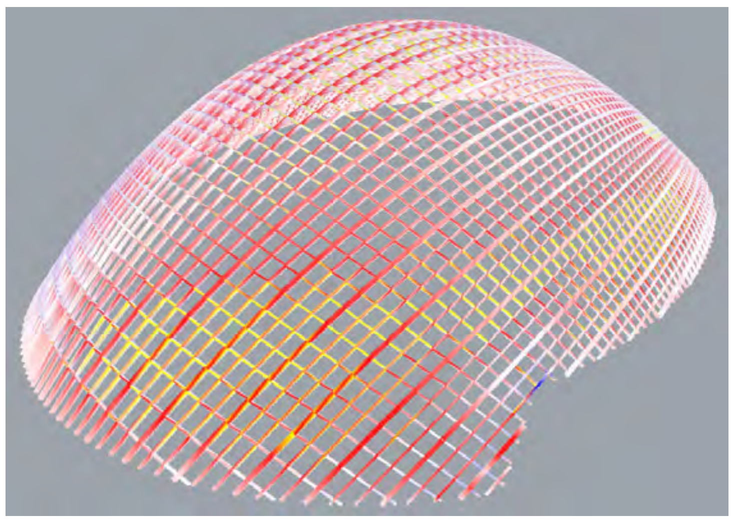

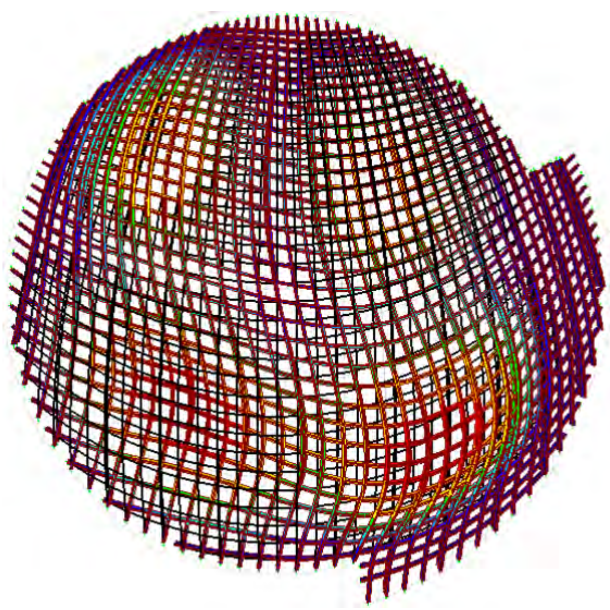
(b)

**Figure 17. Taiyuan Botanical Garden, China: (a) element design and ultilisation and (b) buckling analysis**

Computational design was critical in enabling the 3D geometry creation, structural analysis, CNC milling, and fabrication drawings for developing a free-form soffit for a new public library in Calgary, Canada (Figure 18). Custom algorithms were written to randomise the position of batten joints across the soffit while respecting fabrication constraints, such as the maximum overlap between panels. A parametric 3D modelling approach allowed rule sets for the prefabricated panels and battens to be established and then 3D models and fabrication information for all 170 panels automatically produced. Computational design on this project enabled a vertically integrated approach, linking design, engineering, and fabrication information. As the overall geometry of the surface changed throughout the design, structural analysis and generation of fabrication information was automatically updated.

(a)

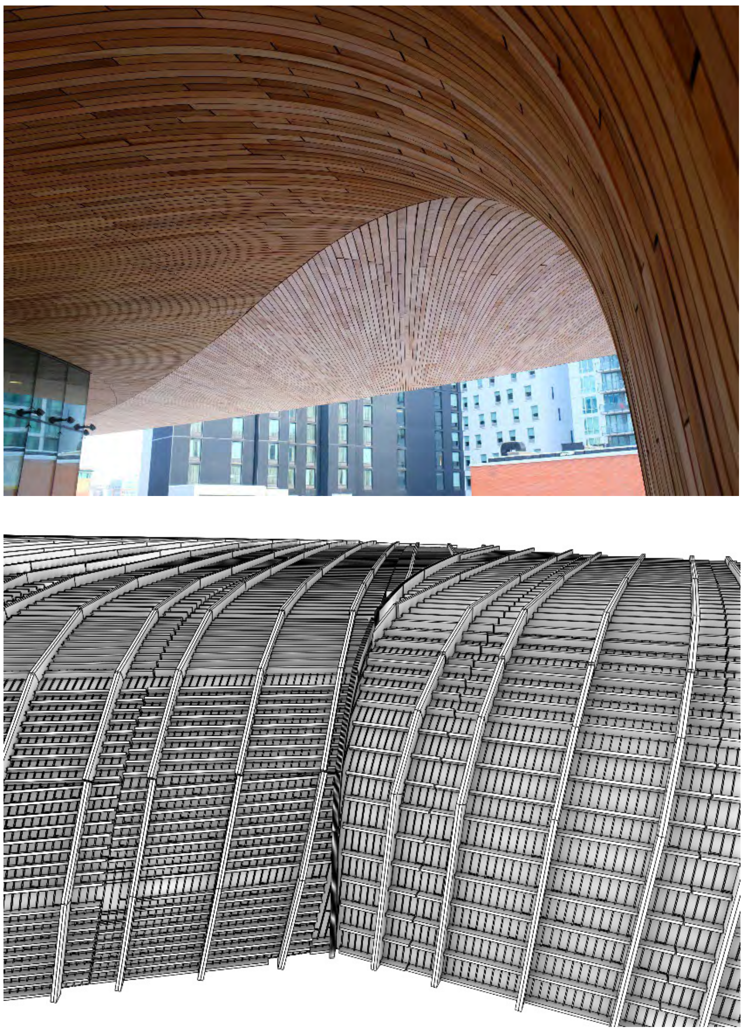

(b)

**Figure 18. Wooden soffit of Calgary Central Library, Canada: (a) entrance and (b) 3D model**

### *3.4.2.3 Structural Optimisation*

Structural optimisation entails using numerical techniques to investigate and optimise the performance of a structure within given boundary conditions and constraints. In contemporary design practice, structural optimisation is predominantly used to find the balance between various aspects, such as structural performance, constructability, material usage, durability, environmental impact, cost, and desired spatial experience.

#### 3.4.2.3.1 Optimisation

Beyond structural engineering, optimisation is used in disciplines such as climate design, facade design, architectural design, urban design, project management, sustainability design, etc., to optimise various aspects. So, in a current multidisciplinary environment, the complexity of engineering a structure has grown due to the diversity of objectives (sometimes conflicting) from different disciplines for a particular design. This is where the optimisation process comes into the picture. Historically, it was a prolonged task to find a design that would meet various objectives, but with modern computational power, this has become swift and versatile, and can be much more intricate.

To understand optimisation, you must understand the following key definitions:

- **Parameters:** The variables that can be changed during the optimisation process;
- **Objective:** The value, or result, that must be minimised or maximised by changing the parameters;
- **Constraint:** The minimum or maximum range within which the objective value is expected;
- **Fitness criteria:** The criteria defined to establish the performance, or fitness, of each solution;
- **Fitness function or value(s):** A single value, often defined by a formula combining multiple fitness criteria with different weighting factors. In true multi-objective optimisation, all defined fitness criteria can be optimised for simultaneously, with different weightings on each;
- **Fitness landscape:** The fitness values plotted across the range of possible solutions and parameters. This is also known as the solution space;
- **Solution:** The result of an objective for a particular set of parameter values; and
- **Pareto optimal (nondominated) solutions:** In the case of more than one objective, it is possible that there is more than an optimal solution which is not dominated by others. This means that no objective value can be improved without losing the other objective.

The optimisation process in general can be divided into two types: single-objective optimisation and multi-objective optimisation. Single-objective optimisation optimises the design for one objective. Similarly, multi-objective optimisation optimises the design for more than one objective. Usually, single-objective optimisation provides one result which is best for that objective, but it is not necessarily true in multi-objective optimisation. With more than one objective, there is a possibility that objectives can conflict with each other (while one objective is improved, another worsens for the same parameter values), and thus, multi-objective optimisation does not provide a single optimal solution. However, it often helps to find the solutions that are close to the optimal result. Some tools offer the possibility of applying weight on the objectives to indicate their importance. This usually improves the chance of finding an optimal solution based on the requirements.

#### 3.4.2.3.2 Types of structural optimisation

There are multiple ways to optimise the geometry of a structure (Figure 19), three of which follow and focus on material optimisation:

1. Size optimisation: This changes the cross-section size or length of an individual element or a group of elements to improve structural performance and reduce material.
2. Shape optimisation: This changes the shape of the overall structure or a smaller section of it to improve performance and reduce material.
3. Topology optimisation: This changes the surface geometry of structural elements and removes non-useful regions from the geometry to improve structural performance.

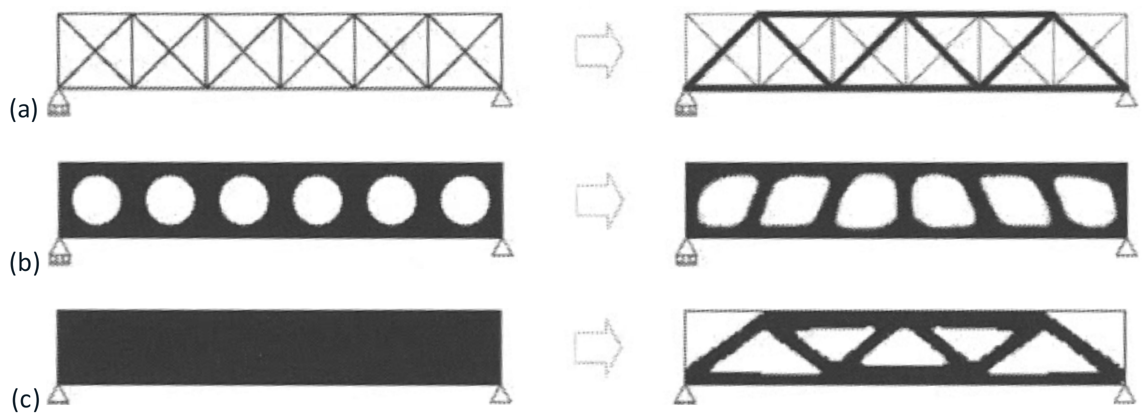


**Figure 19. Types of structural optimisation: (a) size optimisation, (b) shape optimisation, and (c) topology optimisation**

A designer can choose the type of optimisation as necessary for the design requirements. However, size optimisation is usually performed for structural details with 1D geometry and variation in cross-section size, while shape and topology optimisation techniques are useful for optimising details with 2D or 3D geometry.

The following principles are recommended for structural optimisation:

- Set up the problem properly. Check boundary conditions and assumptions, and thoroughly check the possible structural arrangements that will be generated during optimisation.
- Define the parameter ranges and limit them strongly to ranges that are realistic or viable, as this will help with the speed of the optimisation convergence and with the next principle.
- Ensure the analysis runs and gives expected results in the edge cases (i.e., at the edges of the parameter ranges that have been defined).
- Check the fitness values and fitness function by manually changing and investigating input parameters, ensuring that the fitness function is behaving as desired.

Many optimisation techniques can be used to investigate the effects of changing parameters on the fitness value. Three common types of optimisation algorithms are summarised as follows:

1. Analytical optimisation techniques (function minimisation or gradient descent algorithms): These algorithms use approximations of the first derivative (gradient descent) or second derivative (Newton-Raphson) of the fitness function to determine local optima in the fitness function. These algorithms optimise towards a solution by changing parameters in the direction of the 'steepest' improvement relative to the current solution; they rely on the fitness function being differentiable (continuous). These optimisation techniques are poor at addressing problems with a noisy or discontinuous solution space and complex multidimensional optimisation problems.
2. Heuristic optimisation techniques (simplex or probabilistic algorithms): These algorithms include binary search, simulated annealing, Nelder-Mead, and others. They iterate towards optimal solutions using various methods, including constructive methods and local search methods. These algorithms can solve some problems more efficiently than analytical optimisation techniques by adjusting optimality, accuracy, or precision to increase speed.
3. Genetic algorithms: These heuristic algorithms use evolutionary principles to investigate the broad solution space by mating 'fit' solutions with each other and using the process of mutation and survival of the fittest to arrive at optimal solutions. These algorithms are very forgiving but often have long run times; they are great at finding optimal solutions to complex or poorly defined optimisation problems.

The solution space for any given optimisation can be quite complex: there may be multiple local optima, areas where the fitness function is undefined, or areas of very jagged peaks and valleys, like the one shown in Figure 20. Choosing an appropriate optimisation algorithm is key to achieving good optimisation results.

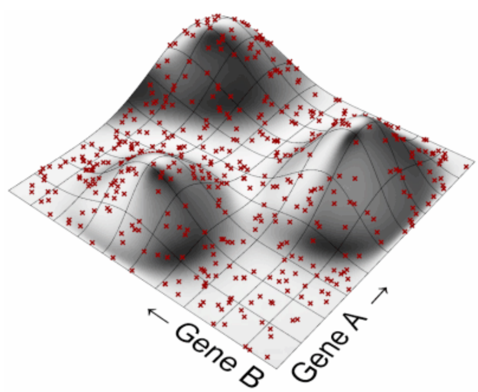


**Figure 20. Fitness landscape illustrated for an optimisation problem with two variables (Rutten, 2011)**

As a simple example of structural optimisation, consider a simply-supported Vierendeel truss (Figure 21) with densely spaced webs, each of which can be turned on or off.

- Parameters: density of the webs, controlled by the active state of each web element
- Fitness criteria: $M$, mass of the system; $\delta$, deflection of the system

- Fitness function:

$$f(\delta, M) = \begin{cases} M^2, & \delta > 1.25 * \delta_{initial} \\ M, & otherwise \end{cases}$$

In other words, this fitness function will minimise the mass in the system by removing webs while not increasing the deformation by more than 25% from the initial solution with all webs active.

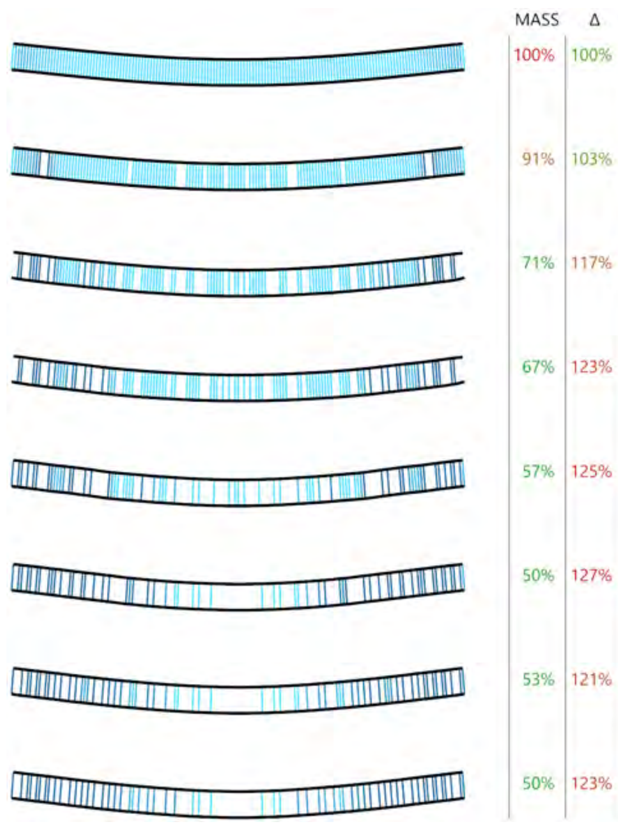


**Figure 21. Optimisation of a simply-supported Vierendeel truss**

The optimisation problem would naturally start with all webs active and then proceed to actively remove webs, measuring the mass and deflection of the structural system in each solution or configuration of webs investigated. To illustrate the performance of a direct search optimisation technique, a Nelder-Mead optimisation algorithm was used in Figure 21. This technique works by extrapolating the behaviour of the fitness function at a measured point and taking steps in the direction of minimising the function. In optimisation problems which have an obvious fitness goal with few trade-offs, direct search techniques provide a quick and efficient means to determine an optimal solution. In this example, using a genetic algorithm to achieve the same result would have taken approximately 10 to 15 times longer.

Figure 22 shows an example of a structural workflow implementing a genetic algorithm to iteratively changing the structure and minimising the amount of structural material using Grasshopper. There are several ways to run geometry and section optimisation; one solver that can be used that is native to the Grasshopper environment is Galapagos. With a set goal objective (e.g., minimum structural material) and parameters that can be altered (e.g., shape of the building, spans), Galapagos allows optimisation of these parameters to minimise the objective function. This is carried out using a genetic optimisation algorithm, which means that Galapagos will not run all the possible combinations of the input parameters but will rather build different families (genomes), evaluate them, and then try to learn from these values the right direction to reach the goal objective. This process is significantly faster than running all possible combinations, but the designer should always carry out a sanity check to avoid a local minimum of the optimisation solution.

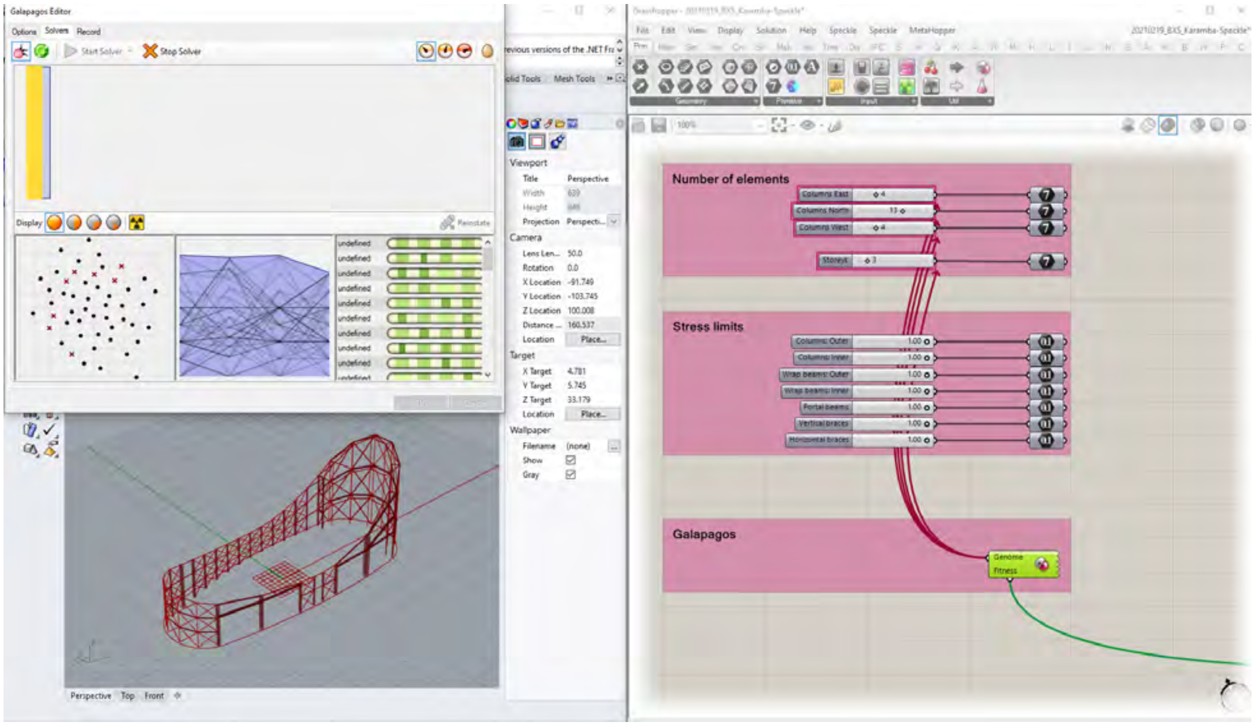


**Figure 22. Grasshopper definition with a Karamba3D analysis linked to a Galapagos component, allowing for material optimisation. (Courtesy of Jim Yip, Arup)**

## 3.4.3 BIM

### *3.4.3.1 Introduction to BIM*

BIM is a technology-driven integrated digital process that uses intelligent geometric and data models to provide coordinated, reliable information about a project throughout its entire life cycle (Abanda et al., 2015) (Figure 23). BIM implementation represents a major change in the tools and processes used to design, construct, and manage buildings and infrastructure. When properly implemented, it delivers major performance improvements in designer efficiency, design quality, constructability, waste reduction, environmental performance, and capital and operational cost management (Eastman et al., 2008; Lu et al., 2017; Porwal & Hewage, 2013).

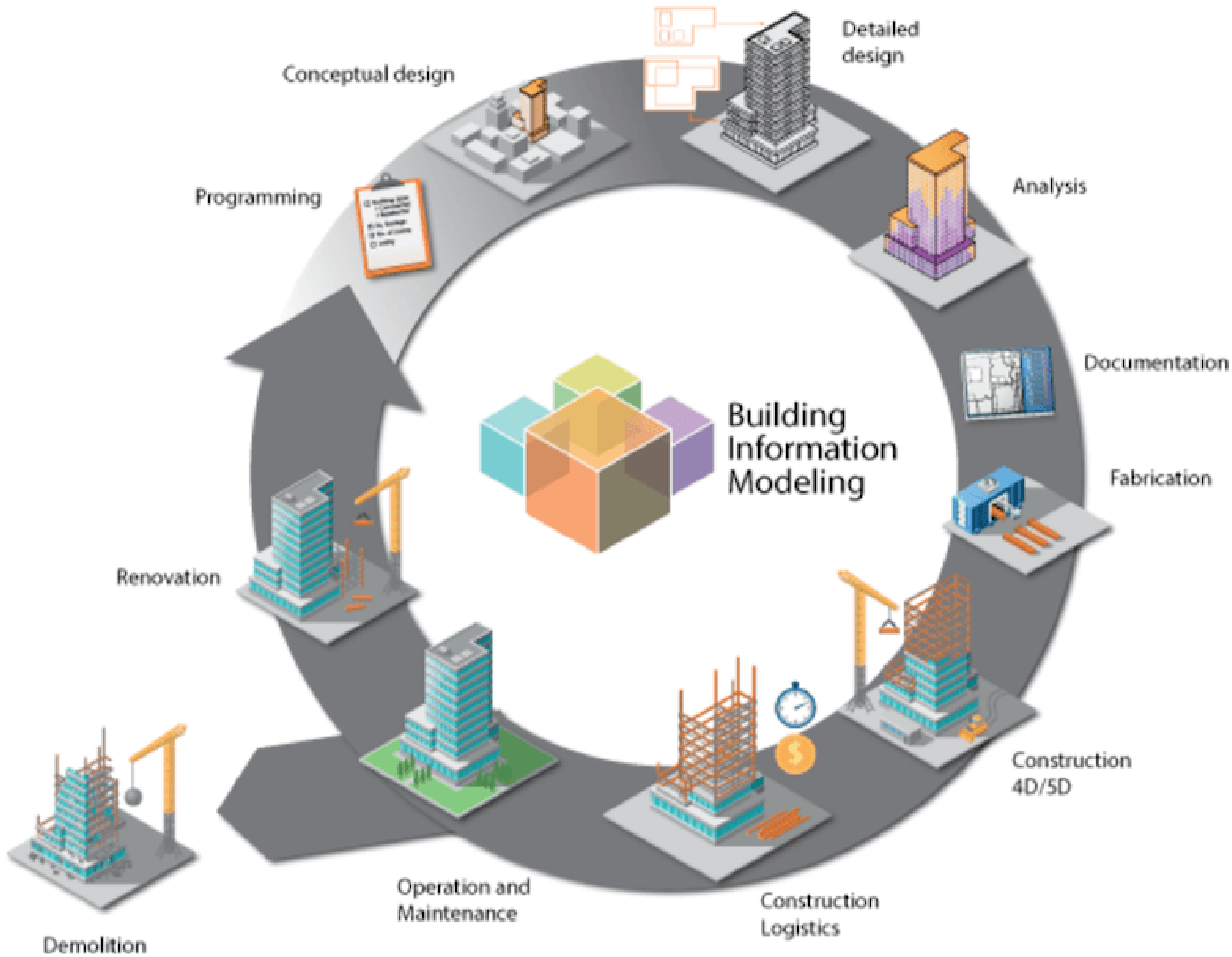


**Figure 23. The interrelationship of BIM with various aspects of a building. (Source: BIMMDA)**

The main benefits of using BIM in construction projects are as follows:

- Providing 3D model–aided visualisation: BIM generates 3D images and simulations, which can significantly aid in client design reviews, including approving the design intent, analysing the logistic and environmental impacts, identifying the cost implications, and making upfront decisions, minimising design changes during the construction stage.
- Accelerating design clash detection: All modelled building systems can be monitored according to a predefined matrix of building systems (architectural, structural, HVAC, gas, drain, fire suspension, water supply, fire alarm, lighting, power, low voltage, lightning protection, and telecommunication). BIM software (e.g., Autodesk Navisworks) can be used to run independent clash detection and track specific clash sets.
- Supporting validation of the bill of quantity and tender analysis: The main purpose of validating the bill of quantity is to determine the consultants' major quantities by identifying major discrepancies between those quantities and the quantity take-offs of the elements modelled in BIM. In the tender phase, the BIM environment provides a transparent and efficient method for quantity and cost analysis for the contractors, quantity surveyors, and the client to ensure consistency across the

proposals. The suppliers can use the model developed by the design team to undertake their cost assessment, typically assisting to reduce the tendering period.

- Providing 4D-enabled constructability analysis and planning: 4D-enabled constructability analysis can help the project team resolve constructability issues earlier in the process, the results of which allow the progression of the construction model (floor-by-floor) and help accelerate the production of effective and efficient delivery schedules. 4D modelling (Figure 24) is used to clarify the week-by-week and day-by-day scope of work, the on-time involvement of the subcontractors as they are required, and the 'just-in-time' material submittals and delivery.
- Providing an as-built model for facility management: This final model (i.e., LOD 500) should have captured as-built information and can thus assist the client in its facility management operations after integration with the organisation's existing asset management practice.

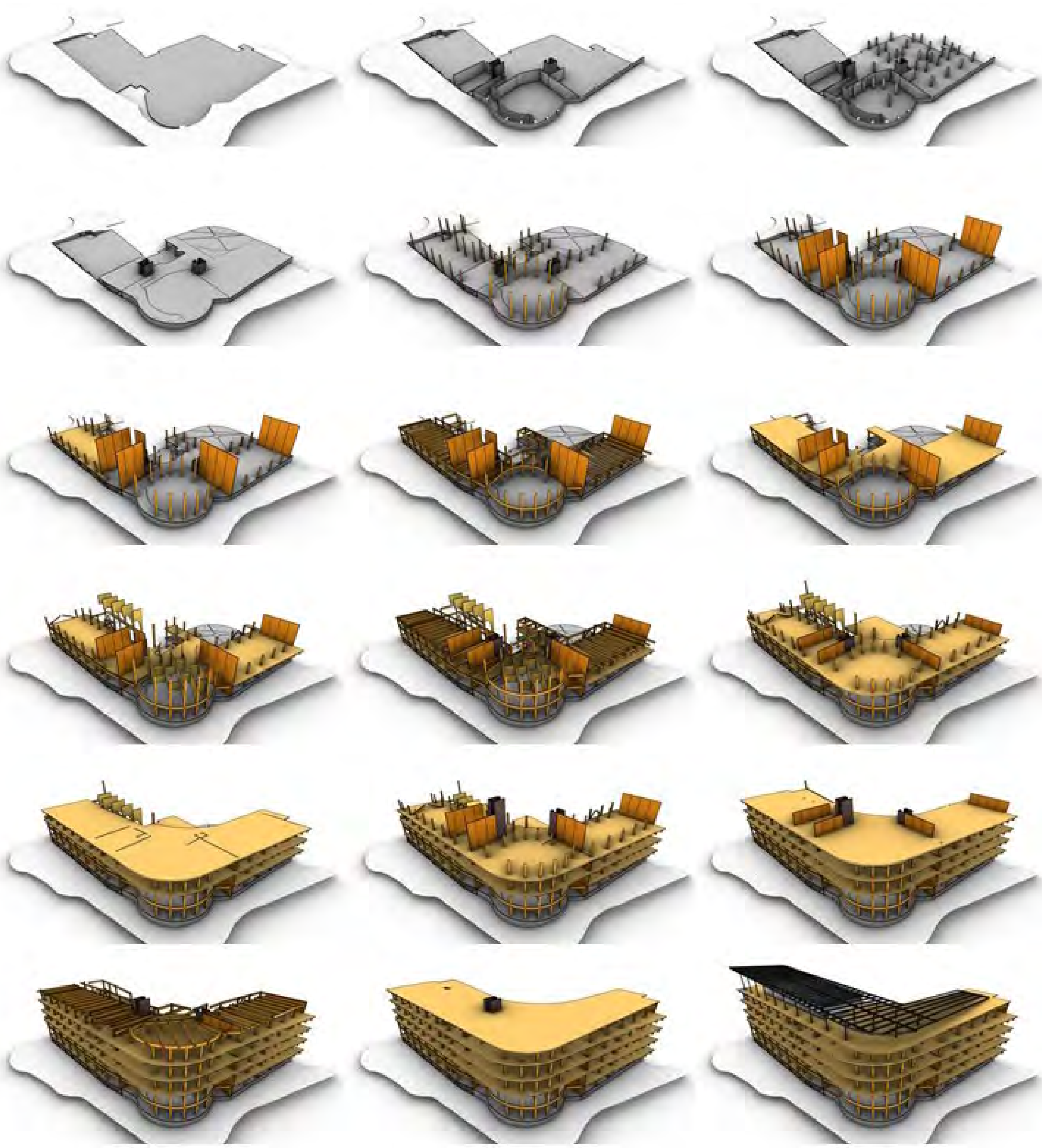

**Figure 24. 4D sequencing model for a mass timber structure**

Owing to the acclaimed benefits of BIM, public client organisations and private clients have mandated the use of BIM to improve the performance of construction projects. For example, the UK government has set up a BIM Task Group and agreed on a BIM strategy that requires using collaborative 3D BIM to reduce the capital expenditure on all public sector projects by 20% starting in 2016 (British Standards Institution, 2013). Also, a government-driven BIM mandate has already been enforced in several other countries, such as the US, Norway, Finland, South Korea, Singapore, and Australia (Chartered Institute of Building, 2014; Wong et al., 2011).

The effectiveness of working with BIM depends on the degree of sophistication involved in developing the model contents and the way it is coordinated and managed across the life cycle of a project, a concept called BIM maturity levels (Bew & Richards, 2008. BIM implementation can be divided into several tiers of maturity, namely, levels 0, 1, 2, and 3 (Figure 25).

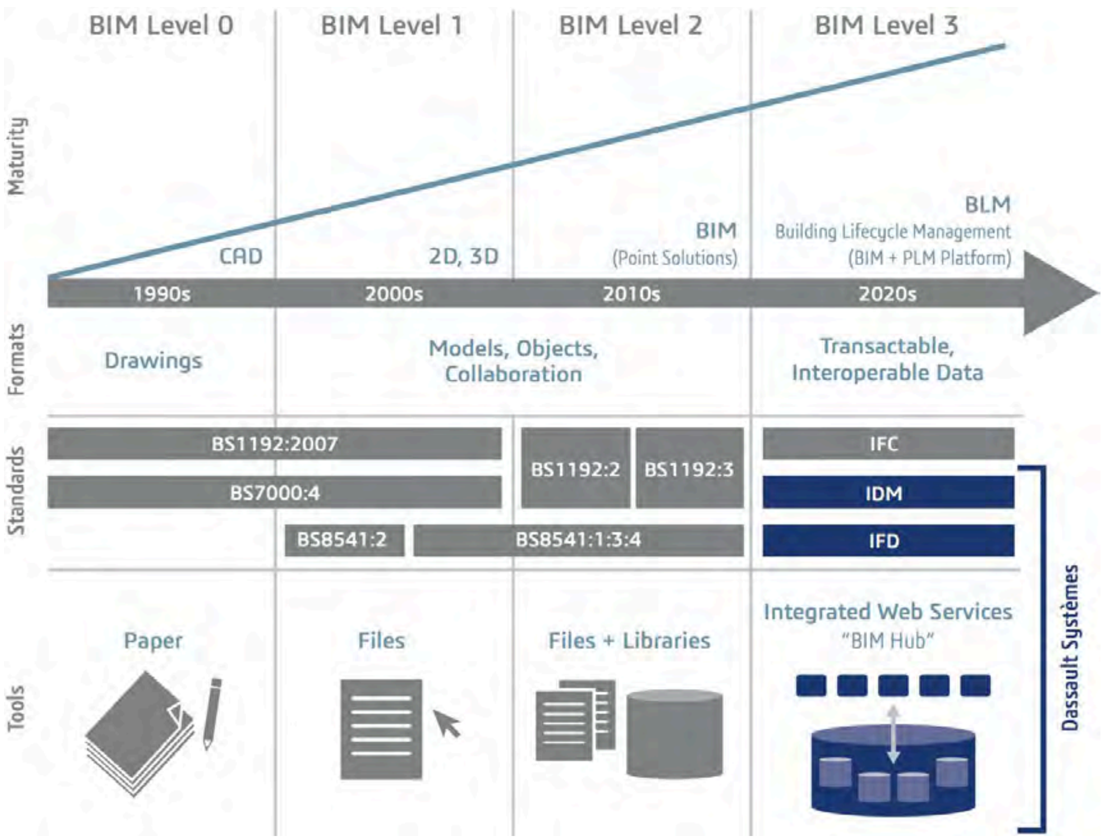


**Figure 25. An updated BIM maturity model from CAD to building life cycle management. (Courtesy of Marty Rozmanith, AECCafé Blogs)**

A BIM maturity level refers to the technology-enabled processes and collaborative BIM applications in a project. Level 0 BIM maturity reflects unmanaged CAD in two dimensions, which is represented and exchanged in paper documents (including electronic documents). The collaboration at level 0 is minimal, as information is exchanged using ad hoc methods that offer little or no chance of information integration to support collaborative working. Level 1 denotes a managed CAD environment that uses 2D and 3D representations of building information. The information content at level 1 is created using standardised approaches to data structures (CAD standards), and is stored in standard formats that can be exchanged between different CAD applications. Also, level 1 replaces the ad hoc information exchange mechanisms with the introduction of a common data environment (CDE), which is used to share and exchange CAD files between various project participants. However, traditional CAD information still consists of drawings and documents without any embedded intelligence, which can offer opportunities for information integration by unlocking the potential of collaborative working. Level 2 denotes a managed BIM environment that contains intelligent BIM models held in separate disciplines (discipline models), shared and coordinated using a structured approach in a CDE, and integrated using proprietary or customised middleware for design (e.g., architectural, structural), analysis (e.g., energy analysis, clash detection), project management (e.g., 4D, 5D), and maintenance purposes (e.g., construction operations building information exchange). Level 2 BIM is most desired by client organisations, as it can be achieved without fundamental changes to business practices and can provide significant improvements in project delivery. Level 3 BIM denotes fully integrated and collaborative BIM, which is enabled by web services to facilitate collaborative building information using open standards (e.g., industry foundation class [IFC]) without interoperability issues. It also extends the use of BIM applications towards the life cycle management of building projects.

To achieve high-performing, low-cost built environments, BIM adoption requires a higher level of collaborative work among construction disciplines beyond the traditional work boundaries and restricted contractual relationships. Also, early project stages are critical for establishing comprehensive BIM development and implementation strategies that can facilitate integration and collaboration among team members through the entire project (Porwal & Hewage, 2013).

Various BIM software packages are provided by different companies (e.g., Autodesk, Bentley, ArchiCAD). Using these software packages, designers from different disciplines working on a project can generate detailed digital representations of a building or infrastructure and allow for coordination from the early design stages. At the same time, because the objects modelled are not solely geometric but also embed different properties, several evaluations (e.g., material quantities, energy characteristics, schedules of elements) can be extracted from the model. In addition, BIM software packages generally allow detailed construction drawings to be extracted directly from the model and remain up-to-date throughout the process and capture all the changes, with limited interaction required from the drawing technicians. Figure 26 presents a typical framework of a CDE, developed by Shafiq (2019) using Bentley's ProjectWise, which coordinated with the BIM (architecture, structure, mechanical, electrical, and plumbing) developed using Autodesk Revit Suite. ProjectWise is a model collaboration platform that supports native Revit model exchanges, providing document management services with model-based project management support. The BIM models were developed using the Autodesk Revit platform (i.e., Revit architecture; Revit mechanical, electrical, and plumbing; and Revit structure), which used inputs from 2D documents and drawings. All the models were exchanged using the CDE through ProjectWise. Moreover, Navisworks was used to create 4D models (taking a feed from a Primavera P6 schedule and LOD 300 Revit model), and Autodesk BIM 360 Glue was used for document management and cloud-enabled information for synchronisation and collaboration. The interoperability issues were resolved using the IFC format and the xBIM IFC viewer and analyser.

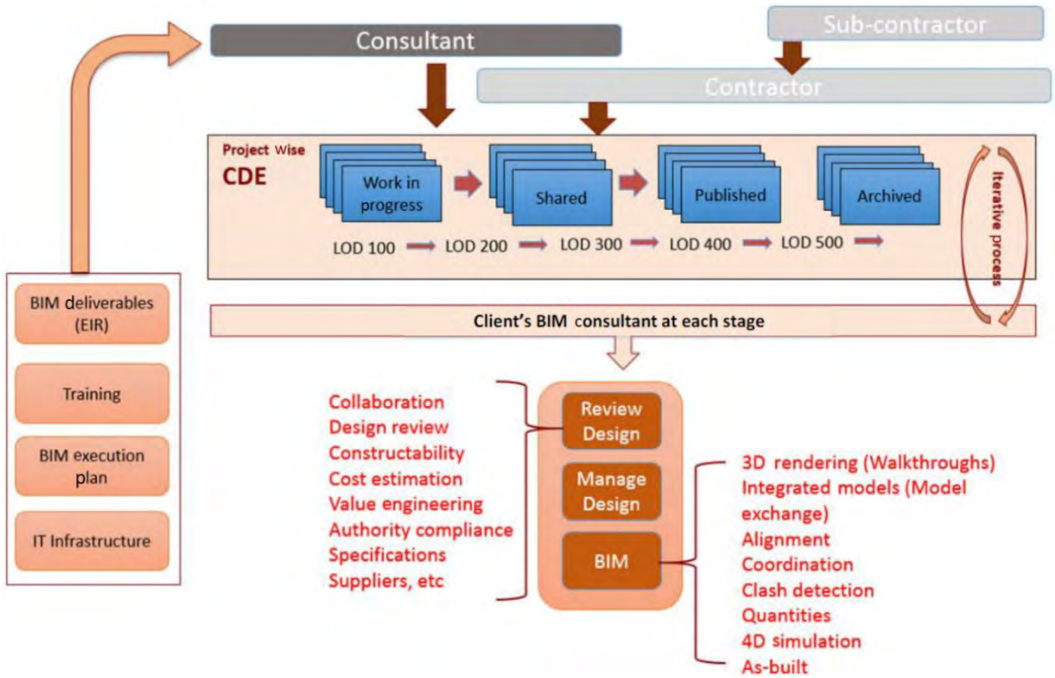


**Figure 26. The structure of a project CDE (Shafiq, 2019)**

All the project participants should agree to follow the implementation of the LOD as defined by a specific protocol (e.g., the LOD specification by BIMForum [2020]). The model will be progressively developed from LOD 100 to LOD 300 at the design stage (Table 2), which is used to generate collaborative design reviews and clash detection, and constructability reviews. The methodology and nomenclature of the BIMForum's LOD specification are used to control the information sharing and collaboration tasks (i.e., work in progress, shared, published, and archived). Further, the fully coordinated clash-free BIM model (LOD 300) is handed over to the successful bidder at the tender stage to further develop the LOD 400 model. The LOD 400 model is used to perform construction clash detection (e.g., clearances) and 4D simulations to support the planning process. It is the contractor's responsibility to update the LOD 400 model with the as-built information (floor by floor) and submit it to the client with the required information for the facility management tasks, thus delivering an as-built model (LOD 500) at the project handover.

**Table 2. Example of graphical part representation of information about the specific element processed in BIM by using the LOD specification by BIMForum (adapted from BIMForum, 2020)**

| 100[a] | 200 | 300 | 350 | 400 | 500[b] |
|---|---|---|---|---|---|
| | 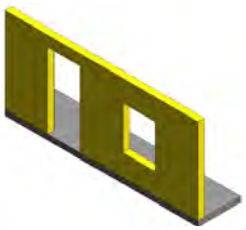 | 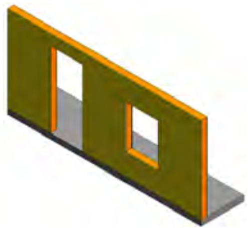 | 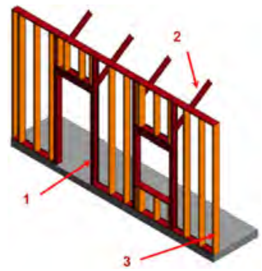 | 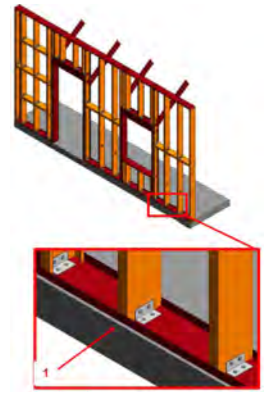 | |

Note:

[a] Assumptions for foundations are included in other modelled elements such as an architectural floor element or volumetric mass that contains layer for assumed structural framing depth. Or, schematic elements that are not distinguishable by type or material. Assembly depth/thickness and locations still flexible (BIMForum, 2020, p. 18)

[b] The Model Element is a field verified representation in terms of size, shape, location, quantity, and orientation. Non-graphic information may also be attached to the Model Elements (BIMForum, 2020, p. 246)

There are clear benefits of adapting the BIM process for timber design. The rapid construction techniques using timber and the efficient workflows of the BIM environment complement each other in that BIM enables interdisciplinary coordination and 4D planning of the site, and the model can be adopted by the fabricator to reduce lead-in time. Moreover, coordination between structure, architecture, and mechanical systems is carried out from an early stage, allowing a smooth process and avoiding issues on site.

#### *3.4.3.2 Beyond BIM: A Perspective – Digital Twin and DfMA*

BIM has become ubiquitous in the architecture, engineering, and construction industry; however, despite the move from 2D to 3D, countless studies on construction efficiency have shown that current processes for constructing buildings are fundamentally flawed. Modern methods of construction provide techniques purported to address this issue of construction efficiency. Modular construction in its current form provides answers for certain building types (Figure 27) but leaves a large proportion of buildings unaddressed. Manufacturers' systems often limit creativity and provide only region-specific solutions. What is needed is an industry-wide change in the design and procurement process—a reconnection of design to both manufacturing and construction.

**Figure 27. Prefabrication of mass timber lends to high LOD BIM models**

With the BIM revolution, the focus has been on the *M*—modelling: creating accurate and highly detailed models and drawings which represent the design, effectively creating digital twins. Figure 28 and Figure 29 show examples of digital twins for two buildings. However, the building industry does not merely need increasingly more detailed 3D models; it needs a design for manufacture and assembly (DfMA) process to increase design and on-site efficiency while systematically reducing construction change orders.


**Figure 28. Digital twins: (a) fabrication of LOD 400 BIM model of mass timber structure, (b) construction, and (c) finished building (The Soto, San Antonio, US)**

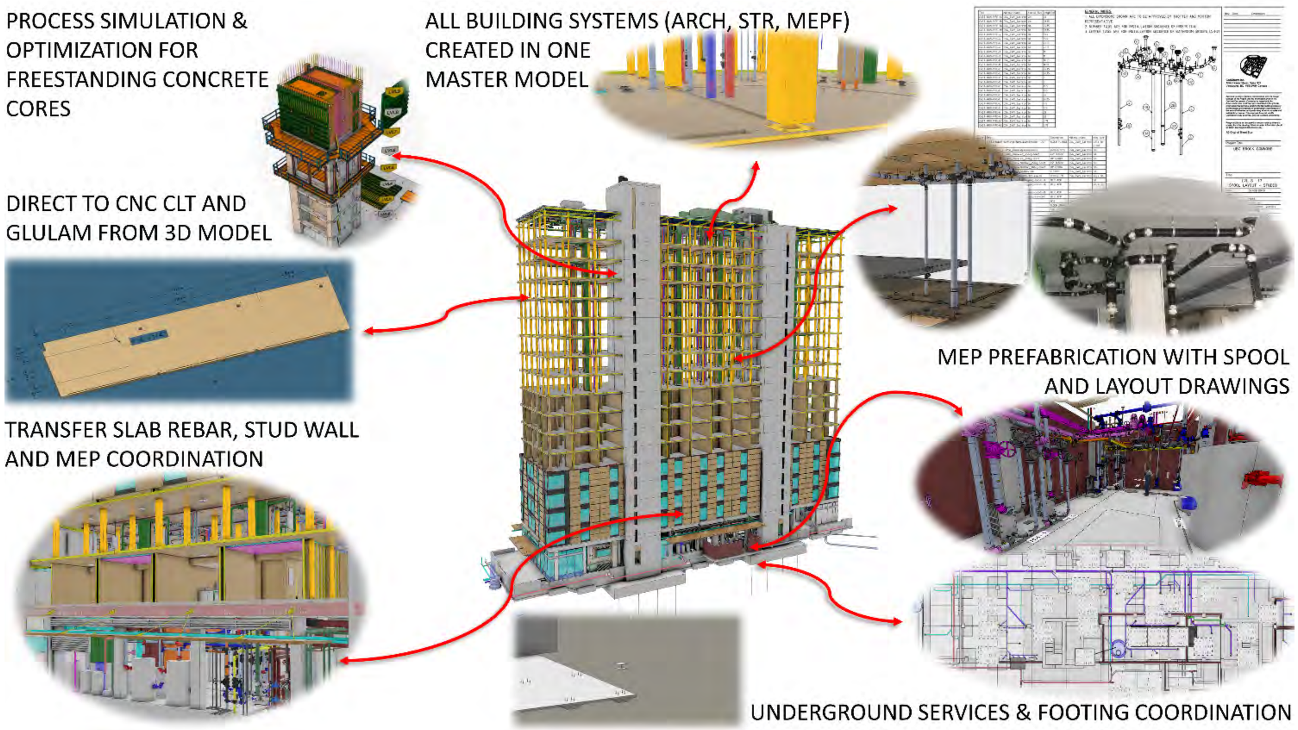


**Figure 29. Digital twin model of Brock Commons Tallwood House, Vancouver, Canada, with an overview of some studies and outputs developed (Yang, 2019)**

As a new construction material, mass timber has become a catalyst for design and construction firms to question the somewhat disjointed design-bid-manufacture-construct process that is prevalent in the construction industry (Epp, 2021). Vertically integrated companies are disrupting the traditional procurement model by bringing the control of manufacturing and assembly processes directly into designers' hands. Mass timber uniquely encourages this—allowing designers to integrate DfMA into their design processes (Figure 30). As a result, designers embed the manufacturing and assembly process into their designs. Material availability, milling processes, shipping, and prefabrication techniques then become design mandates, not peripheral considerations talked about briefly and then left for post-tender. With DfMA constraints embedded into design software, more rapid customisation and design exploration can be performed without significant cost and schedule implications to projects.

**Figure 30. Coordination of mechanical, electrical, and plumbing servicing with a mass timber model (T3 West Midtown building, Atlanta, US)**

This new paradigm will be enabled by the advent of design software, which takes this thinking out of the realm of specific companies and brings it to the wider design community. The software platform Branch provides real-time structural analysis and manufacturing and assembly feedback to designers, connecting the entirety of the design-manufacture-assemble process. Analysis, design, connection detailing, CNC file generation, logistics, and assembly are incorporated into a single Rhinoceros 3D-based platform, enabling direct integration with the site and building performance analysis tools readily available within the Rhinoceros 3D ecosystem.

Mass timber as the newest (and perhaps oldest) building material is central to this revolution in the building design process. Its ability to enable mass customisation is driving a new kind of design software, design processes, and delivery models across the industry. Design—not manufacturing processes, robots, or drones—is the key to creating efficiency in the architecture, engineering, and construction industry. The next challenge is creating design software and tools which are both manufacturing- and construction-aware, led by vertically integrated companies that are focused on enabling real-time data flow between all stakeholders, whether designers, machinists, or foremen. Perhaps the industry will move back to the master-builder paradigm from where it originated, back to a place where architects and engineers are also builders.

## 3.5 SUMMARY

This chapter introduces modelling principles, methods, and techniques, and provides general rules for structural modelling and specific rules for timber-based systems. The following are some of the most important points:

- General and specific principles, in terms of the modelling process, model development, model validation, result verification, model interpretation, and competence are introduced. Following these principles, the best possible analysis results of timber structures can be achieved.
- Four types of modelling methods, namely, mechanics-based modelling, FE modelling, hybrid simulation, and material-based modelling, are introduced for simulating the behaviour of timber structures under different loading conditions. This modelling guide, however, focuses on the first two modelling methods for timber structures.
- The SFEM is introduced to quantify or predict the influence and sources of randomness in timber structures which are complex due to the highly variable anisotropic mechanical properties of wood.
- Computational structural design, including parametric analysis, structural optimisation, and form-finding, is introduced. Its application will dramatically improve the efficiency of identifying the best solutions for the structural design of geometrically complex or free-form timber structures.
- BIM, which uses intelligent geometric and data models that can provide coordinated, reliable information about a project throughout its entire life cycle, is introduced, along with the concept of digital twin and DfMA.

The information presented in this chapter is intended to help practising engineers and researchers become more familiar with the modelling principles, methods, and techniques for timber structures.

## 3.6 ACKNOWLEDGEMENTS

The authors would like to acknowledge Ms. Maja Belic for her contributions to Section 3.4.3.

## 3.7 REFERENCES

Abanda, F. H., Vidalakis, C., Oti, A. H., & Tah, J. H. M. (2015). A critical analysis of building information modelling systems used in construction projects. *Advances in Engineering Software, 90*, 183-201. https://doi.org/10.1016/j.advengsoft.2015.08.009

Ariaratnam, S. T., Schuëller, G. I., & Elishakoff, I. (Eds.). (1988). *Stochastic structural dynamics: Progress in theory and applications*. Elsevier Applied Science.

Arregui-Mena, J. D., Margetts, L., & Mummery, P. M. (2016). Practical application of the stochastic finite element method. *Archives of Computational Methods in Engineering, 23*(1), 171-190. https://doi.org/10.1007/s11831-014-9139-3

Astill, C. J., Imosseir, S. B., & Shinozuka, M. (1972). Impact loading on structures with random properties. *Journal of Structural Mechanics, 1*(1), 63-77. https://doi.org/10.1080/03601217208905333

Bew, M., & Richards, M. (2008). *BIM maturity model* [Paper presentation]. Construct IT Autumn 2008 Members' Meeting, Brighton, UK.

BIMForum. (2020). *Level of development (LOD) specification: Part I & commentary for building information models and data*.

Brandner, R., & Schickhofer, G. (2014). Length effects on tensile strength in timber members with and without joints. In S. Aicher, H. W. Reinhardt, & Garrecht (Eds.), *Materials and Joints in Timber Structures* (pp. 751-760). RILEM Bookseries, Vol. 9. Springer, Dordrecht. https://doi.org/10.1007/978-94-007-7811-5_67

British Standards Institution. (2013). *Specification for information management for the capital/delivery phase of construction projects using building information modelling* (PAS 1192-2:2013).

Chen, Z., & Chui, Y.-H. (2017). Lateral load-resisting system using mass timber panel for high-rise buildings. *Frontiers in Built Environment, 3*(40). https://doi.org/10.3389/fbuil.2017.00040

Chen, Z., Chui, Y.-H., Doudak, G., & Nott, A. (2016). Contribution of type-x gypsum wall board to the racking performance of light-frame wood shear walls. *Journal of Structural Engineering, 142*(5), 4016008. https://doi.org/10.1061/(ASCE)ST.1943-541X.0001468

Chen, Z., Chui, Y. H., Mohammad, M., Doudak, G., & Ni, C. (2014, August 10–14). *Load distribution in lateral load resisting elements of timber structures* [Conference presentation]. World Conference on Timber Engineering, Quebec City, Canada.

Chen, Z., Chui, Y. H., Ni, C., Doudak, G., & Mohammad, M. (2014). Load distribution in timber structures consisting of multiple lateral load resisting elements with different stiffness. *Journal of Performance of Constructed Facilities, 28*(6). https://doi.org/10.1061

Chen, Z., Chui, Y. H., Ni, C., & Xu, J. (2014). Seismic response of midrise light wood-frame buildings with portal frames. *Journal of Structural Engineering, 140*(8), A4013003. https://doi.org/10.1061/(ASCE)ST.1943-541X.0000882

Chen, Z., Chui, Y. H., & Popovski, M. (2015). Development of lateral load resisting system. In Y. H. Chui (Ed.), *Application of analysis tools from NEWBuildS research network in design of a high-rise wood building* (pp. 15-36).

Chen, Z., Karacabeyli, E., & Lum, C. (2017). *A survey on modelling of mass timber buildings*. FPInnovations.

Chen, Z., Li, M., Chui, Y. H., & Popovski, M. (2015). Analysis and design of gravity load resisting system. In Y. H. Chui (Ed.), *Application of analysis tools from NEWBuildS research network in design of a high-rise wood building* (pp. 37-47).

Chen, Z., & Ni, C. (2020). Criterion for applying two-step analysis procedure to seismic design of wood-frame buildings on concrete podium. *Journal of Structural Engineering, 146*(1), 4019178. https://doi.org/10.1061/(ASCE)ST.1943-541X.0002405

Chen, Z., & Ni, C. (2021). Seismic force-modification factors for mid-rise wood-frame buildings with shearwalls using wood screws. *Bulletin of Earthquake Engineering, 19*, 1337-1364. https://doi.org/10.1007/s10518-020-01031-7

Chen, Z., Ni, C., Dagenais, C., & Kuan, S. (2020). Wood$^{ST}$: A temperature-dependent plastic-damage constitutive model used for numerical simulation of wood-based materials and connections. *Journal of Structural Engineering, 146*(3), 4019225. https://doi.org/10.1061/(ASCE)ST.1943-541X.0002524

Chen, Z., & Popovski, M. (2020a). Mechanics-based analytical models for balloon-type cross-laminated timber (CLT) shear walls under lateral loads. *Engineering Structures, 208*, 109916. https://doi.org/10.1016/j.engstruct.2019.109916

Chen, Z., & Popovski, M. (2020b). Material-based models for post-tensioned shear wall system with energy dissipators. *Engineering Structures, 213*, 110543. https://doi.org/10.1016/j.engstruct.2020.110543

Chen, Z., Zhu, E., & Pan, J. (2011). Numerical simulation of wood mechanical properties under complex state of stress. *Chinese Journal of Computational Mechanics, 28*(4), 629-634, 640.

Chen, Z., Zhu, E., & Pan, J. (2013). Lateral structural performance of Yingxian wood pagoda based on refined FE models. *Journal of Building Structures, 34*(9), 150-158.

Christovasilis, I., & Filiatrault, A. (2010). A two-dimensional numerical model for the seismic collapse assessment of light-frame wood structures In S. Senapathi, K. Casey, & M. Hoit (Eds.), *Proceedings of the 2010 Structures Congress* (pp. 832-843). American Society of Civil Engineers. https://doi.org/10.1061/41130(369)76

Clouston, P. L., & Lam, F. (2002). A stochastic plasticity approach to strength modeling of strand-based wood composites. *Composites Science and Technology, 62*(10-11), 1381-1395. https://doi.org/10.1016/S0266-3538(02)00086-6

Construction Manager. (2014, January 19). EU votes 'yes' to BIM-friendly procurement shake-up. Chartered Institute of Building. https://constructionmanagermagazine.com/eu-votes-embed-bim-europe-wide-procurement-rules/

Di Gangi, G., Demartino, C., Quaranta, G., Vailati, M., Monti, G., & Liotta, M. A. (2018). *Timber shear walls: Numerical assessment of the equivalent viscous damping*.

Eastman, C., Teicholz, P., Sacks, R., & Liston, K. (2008). *BIM handbook: A guide to building information modeling for owners, managers, designers, engineers and contractors*. Wiley.

Elishakoff, I., & Ren, Y. (2003). *Finite element methods for structures with large stochastic variations*. Oxford University Press.

Epp, L. (2018). Computational design with timber. *Wood Design & Building*, *78*, 39-43.

Epp, L. (2021). Is parametric design the answer? It depends on the question. *Wood Design & Building, 88*, 10-13.

European Committee for Standardization. (2004). *Eurocode 5: Design of timber structures - Part 1-1: General - Common rules and rules for buildings* (EN 1995-1-1:2004).

Fenton, G. A., & Vanmarcke, E. H. (1990). Simulation of random fields via local average subdivision. *Journal of Engineering Mechanics, 116*(8), 1733-1749. https://doi.org/10.1061/(ASCE)0733-9399(1990)116:8(1733)

Filiatrault, A., Isoda, H., & Folz, B. (2003). Hysteretic damping of wood framed buildings. *Engineering Structures, 25*(4), 461-471. https://doi.org/10.1016/S0141-0296(02)00187-6

Gavric, I., Fragiacomo, M., & Ceccotti, A. (2015). Cyclic behavior of CLT wall systems: Experimental tests and analytical prediction models. *Journal of Structural Engineering, 141*(11), 4015034. https://doi.org/10.1061/(ASCE)ST.1943-541X.0001246

Ghanem, R. G., & Spanos, P. D. (1991). *Stochastic finite elements: A spectral approach*. Springer-Verlag.

Haldar, A., & Mahadevan, S. (2000). *Reliability assessment using stochastic finite element analysis.* Wiley.

Huang, X., & Kwon, O.-S. (2020). A generalized numerical/experimental distributed simulation framework. *Journal of Earthquake Engineering, 24*(4), 682-703. https://doi.org/10.1080/13632469.2018.1423585

Hughes, I., & Hase, T. (2010). *Measurements and their uncertainties: A practical guide to modern error analysis*. Oxford University Press.

Hurtado, J. E., & Barbat, A. H. (1998). Monte Carlo techniques in computational stochastic mechanics. *Archives of Computational Methods in Engineering, 5*(1), 3. https://doi.org/10.1007/BF02736747

Jockwer, R., & Jorissen, A. (2018). *Load-deformation behaviour and stiffness of lateral connections with multiple dowel type fasteners*. In R. Gorlacher (Ed.), *Proceedings of the International Network on Timber Engineering Research* (pp. 141-158). Timber Scientific Publishing.

Kandler, G., Füssl, J., & Eberhardsteiner, J. (2015). Stochastic finite element approaches for wood-based products: Theoretical framework and review of methods. *Wood Science and Technology, 49*(5), 1055-1097. https://doi.org/10.1007/s00226-015-0737-5

Kandler, G., Lukacevic, M., Zechmeister, C., Wolff, S., & Füssl, J. (2018). Stochastic engineering framework for timber structural elements and its application to glued laminated timber beams. *Construction and Building Materials, 190*, 573-592. https://doi.org/10.1016/j.conbuildmat.2018.09.129

Karacabeyli, E., & Lum, C. (2022). *Technical guide for the design and construction of tall wood buildings in Canada* (2nd ed.). FPInnovations.

Kleiber, M., & Tran Duong, H. (1992). *The stochastic finite element method: Basic perturbation technique and computer implementation*. Wiley.

Koo, K. (2013). *A study on historical tall-wood buildings in Toronto and Vancouver.* FPInnovations.

Kwon, O.-S. (2008). A framework for distributed analytical and hybrid simulations. *Structural Engineering and Mechanics, 30*(3), 331-350. https://doi.org/10.12989/SEM.2008.30.3.331

Kwon, O.-S. (2017). Multi-platform hybrid (experiment-analysis) simulations. In A. G. Sextos & G. D. Manolis (Eds.), *Dynamic response of infrastructure to environmentally induced loads: Analysis, measurements, testing, and design* (pp. 37-63). Springer International Publishing.

Lafontaine, A., Chen, Z., Doudak, G., & Chui, Y. H. (2017). Lateral behavior of light wood-frame shear walls with gypsum wall board. *Journal of Structural Engineering, 143*(8), 4017069. https://doi.org/10.1061/(ASCE)ST.1943-541X.0001798

Liu, W. K., Belytschko, T., & Mani, A. (1986). Random field finite elements. *International Journal for Numerical Methods in Engineering, 23*(10), 1831-1845. https://doi.org/10.1002/nme.1620231004

Lu, W., Webster, C., Chen, K., Zhang, X., & Chen, X. (2017). Computational building information modelling for construction waste management: Moving from rhetoric to reality. *Renewable and Sustainable Energy Reviews, 68*, 587-595. https://doi.org/10.1016/j.rser.2016.10.029

MacLeod, I. A. (2010). *Modern structural analysis: Modelling process and guidance.* Thomas Telford.

Madsen, B. (1990). Size effects in defect-free Douglas fir. *Canadian Journal of Civil Engineering, 17*(2), 238-242. https://doi.org/10.1139/l90-029

Madsen, B., & Tomoi, M. (1991). Size effects occurring in defect-free spruce – pine – fir bending specimens. *Canadian Journal of Civil Engineering, 18*(4), 637-643. https://doi.org/10.1139/l91-078

Martínez-Martínez, J. E., Alonso-Martínez, M., Álvarez Rabanal, F. P., & del Coz Díaz, J. J. (2018). Finite element analysis of composite laminated timber (CLT). *Proceedings of the 2nd International Research Conference on Sustainable Energy, Engineering, Materials and Environment, 2*(23), 1454. https://doi.org/10.3390/proceedings2231454

Matheron, G. (1973). The intrinsic random functions and their applications. *Advances in Applied Probability, 5*(3), 439-468. https://doi.org/10.2307/1425829

Melchers, R. E., & Beck, A. T. (2017). *Structural reliability: Analysis and prediction*. Wiley.

Moens, D., & Vandepitte, D. (2006). Recent advances in non-probabilistic approaches for non-deterministic dynamic finite element analysis. *Archives of Computational Methods in Engineering, 13*(3), 389-464. https://doi.org/10.1007/BF02736398

Moshtaghin, A. F., Franke, S., Keller, T., & Vassilopoulos, A. P. (2016). Random field-based modeling of size effect on the longitudinal tensile strength of clear timber. *Structural Safety, 58*, 60-68. https://doi.org/10.1016/j.strusafe.2015.09.002

Nolet, V., Casagrande, D., & Doudak, G. (2019). Multipanel CLT shearwalls: An analytical methodology to predict the elastic-plastic behaviour. *Engineering Structures, 179*, 640-654. https://doi.org/10.1016/j.engstruct.2018.11.017

Pellissetti, M. F., & Schuëller, G. I. (2006). On general purpose software in structural reliability – An overview. *Structural Safety, 28*(1), 3-16. https://doi.org/10.1016/j.strusafe.2005.03.004

Porwal, A., & Hewage, K. N. (2013). Building information modeling (BIM) partnering framework for public construction projects. *Automation in Construction, 31*, 204-214. https://doi.org/10.1016/j.autcon.2012.12.004

Pozza, L., Savoia, M., Franco, L., Saetta, A., & Talledo, D. (2017). Effect of different modelling approaches on the prediction of the seismic response of multi-storey CLT buildings. *The International Journal of Computational Methods and Experimental Measurements, 5*(6), 953-965. https://doi.org/10.2495/cmem-v5-n6-953-965

Pradlwarter, H. J., Pellissetti, M. F., Schenk, C. A., Schuëller, G. I., Kreis, A., Fransen, S., Calvi, D., & Klein, M. (2005). Realistic and efficient reliability estimation for aerospace structures. *Computer Methods in Applied Mechanics and Engineering, 194*(12), 1597-1617. https://doi.org/10.1016/j.cma.2004.05.029

Pradlwarter, H. J., & Schuëller, G. I. (1997). On advanced Monte Carlo simulation procedures in stochastic structural dynamics. *International Journal of Non-Linear Mechanics, 32*(4), 735-744. https://doi.org/10.1016/S0020-7462(96)00091-1

Reale, V., Kaminski, S., Lawrence, A., Grant, D., Fragiacomo, M., Follesa, M., & Casagrande, D. (2020, September 13–18). *A review of the state-of-the-art international guidelines for seismic design of timber structures* [Conference presentation]. 17th World Conference on Earthquake Engineering, Sendai, Japan.

Reynolds, T., Foster, R., Bregulla, J., Chang, W.-S., Harris, R., & Ramage, M. (2017). Lateral-load resistance of cross-laminated timber shear walls. *Journal of Structural Engineering, 143*(12), 06017006. https://doi.org/10.1061/(ASCE)ST.1943-541X.0001912

Rinaldin, G., & Fragiacomo, M. (2016). Non-linear simulation of shaking-table tests on 3- and 7-storey X-Lam timber buildings. *Engineering Structures, 113*, 133-148. https://doi.org/10.1016/j.engstruct.2016.01.055

Rutten, D. (2011, March 4). *Evolutionary principles applied to problem solving*. I eat bugs for breakfast. https://ieatbugsforbreakfast.wordpress.com/2011/03/04/epatps01/

Sandhaas, C., Van de Kuilen, J.-W., & Blass, H. J. (2012, July 15–19). *Constitutive model for wood based on continuum damage mechanics* [Conference presentation]. World Conference on Timber Engineering, Auckland, New Zealand. http://resolver.tudelft.nl/uuid:55c1c5e5-9902-43ad-a724-62bb063c3c80

Sandoli, A., Moroder, D., Pampanin, S., & Calderoni, B. (2016, August 22–25). *Simplified analytical models for coupled CLT walls* [Conference presentation]. World Conference on Timber Engineering, Vienna, Austria.

Schellenberg, A., Huang, Y., & Mahin, S. A. (2008, October 12–17). *Structural FE-software coupling through the experimental software framework, OpenFresco* [Conference presentation]. World Conference on Earthquake Engineering, Beijing, China.

Schellenberg, A. H., Mahin, S. A., & Fenves, G. L. (2009). *Advanced implementation of hybrid simulation* (2009/104). Pacific Earthquake Engineering Research Center.

Schuëller, G. I. (2006). Developments in stochastic structural mechanics. *Archive of Applied Mechanics, 75*(10), 755-773. https://doi.org/10.1007/s00419-006-0067-z

Schuëller, G. I., & Pradlwarter, H. J. (2009). Uncertain linear systems in dynamics: Retrospective and recent developments by stochastic approaches. *Engineering Structures, 31*(11), 2507-2517. https://doi.org/10.1016/j.engstruct.2009.07.005

Schuëller, G. I., Pradlwarter, H. J., & Bucher, C. G. (1991). Efficient computational procedures for reliability estimates of MDOF-systems. *International Journal of Non-Linear Mechanics, 26*(6), 961-974. https://doi.org/10.1016/0020-7462(91)90044-T

Shafiq, M. T. (2019, June 12–15). *A case study of client-driven early BIM collaboration* [Conference presentation]. Canadian Society for Civil Engineering Annual Conference, Laval, Canada.

Southwest Research Institute. (2020). *NESSUS User's manual, version 9.9*.

Sudret, B., & Der Kiureghian, A. (2000). *Stochastic finite element methods and reliability: A state-of-the-art report* (Report No. UCB/SEMM-200/08). University of California, Berkeley.

Sustersic, I., & Dujic, B. (2012). *Simplified cross-laminated timber wall modelling for linear-elastic seismic analysis* [Paper presentation]. Working Commission W18 under the International Council for Building Research and Innovation, Växjö, Sweden.

Sutherland, I. E. (1963). *Sketchpad: A man-machine graphical communication system* (pp. 329-346). In *Proceedings of the May 21–23, 1963, Spring Joint Computer Conference*. https://doi.org/10.1145/1461551.1461591

Tamagnone, G., Rinaldin, G., & Fragiacomo, M. (2018). A novel method for non-linear design of CLT wall systems. *Engineering Structures, 167*, 760-771. https://doi.org/10.1016/j.engstruct.2017.09.010

Tannert, T., Vallée, T., & Hehl, S. (2012). Probabilistic strength prediction of adhesively bonded timber joints. *Wood Science and Technology, 46*(1), 503-513. https://doi.org/10.1007/s00226-011-0424-0

Vanmarcke, E. (1983). *Random fields: Analysis and synthesis*. MIT Press.

Vanmarcke, E., & Grigoriu, M. (1983). Stochastic finite element analysis of simple beams. *Journal of Engineering Mechanics, 109*(5), 1203-1214. https://doi.org/10.1061/(ASCE)0733-9399(1983)109:5(1203)

Weibull, W. (1939). *A statistical theory of the strength of materials*. Royal Swedish Institute of Engineering Research, Stockholm, Sweden.

Wong, A. K. D., Wong, F. K. D., Nadeem, A. (2011). Government roles in implementing building information modelling systems: Comparison between Hong Kong and the United States. *Construction Innovation, 11*(1), 61-76. https://doi.org/10.1108/14714171111104637

Xu, J., & Dolan, J. D. (2009a). Development of nailed wood joint element in ABAQUS. *Journal of Structural Engineering, 135*(8). https://doi.org/10.1061/(ASCE)ST.1943-541X.0000030

Xu, J., & Dolan, J. D. (2009b). Development of a wood-frame shear wall model in ABAQUS. *Journal of Structural Engineering, 135*(8). https://doi.org/10.1061/(ASCE)ST.1943-541X.0000031

Yaglom, A. M. (1962). *An introduction to the theory of stationary random functions* (R. A. Silverman, Ed. & Trans.). Dover Publications, Inc. (Original work published in 1962)

Yang, K. (2019, October 28–November 2). *Building tall with mass timber – The digital twin approach* [Conference presentation]. Council on Tall Buildings and Urban Habitat 10th World Congress, Chicago, USA.

Yang, T. Y., Tung, D. P., Li, Y., Lin, J. Y., Li, K., & Guo, W. (2017). Theory and implementation of switch-based hybrid simulation technology for earthquake engineering applications. *Earthquake Engineering & Structural Dynamics, 46*(14), 2603-2617. https://doi.org/10.1002/eqe.2920

Zhu, E., Chen, Z., Chen, Y., & Yan, X. (2010). Testing and FE modelling of lateral resistance of shearwalls in light wood frame structures. *Journal of Harbin Institute of Technology, 42*(10), 1548-1554.

Zhu, J., Kudo, A., Takeda, T., & Tokumoto, M. (2001). Methods to estimate the length effect on tensile strength parallel to the grain in Japanese larch. *Journal of Wood Science, 47*(4), 269-274. https://doi.org/10.1007/BF00766712

# CHAPTER 4

Components

# TABLE OF CONTENTS

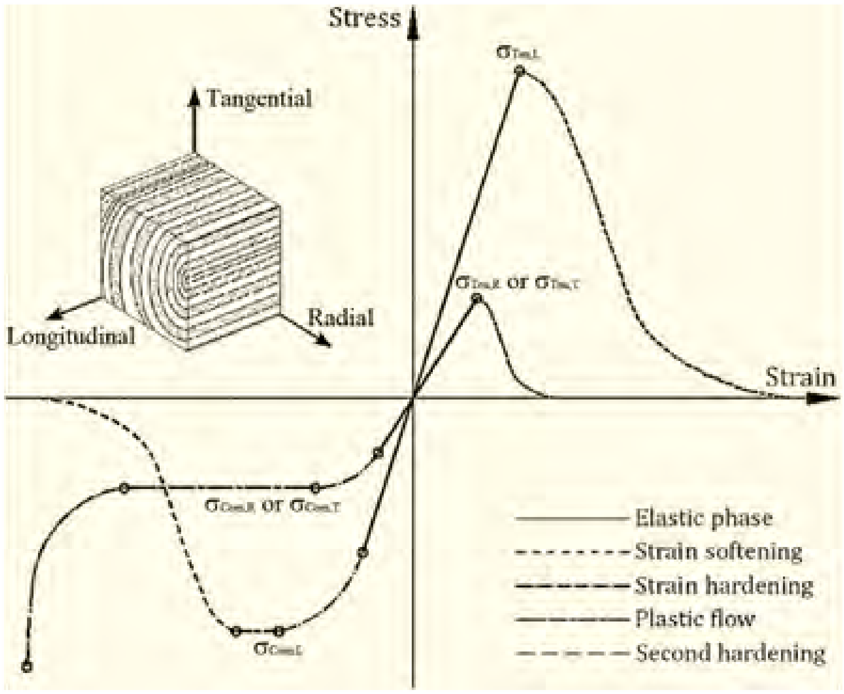


# CHAPTER 4.1

## Constitutive models and key influencing factors

**Authors**
Zhiyong Chen
Chun Ni
Christian Dagenais
Jieying Wang

**Reviewers**
Thomas Bader
Petr Kabele

# TABLE OF CONTENTS

## 4.1.1 Introduction

Wood is an anisotropic material. Because of its inherent characteristics, the mechanical behaviour of wood depends on the direction of the grain and the load type (Chen et al., 2011; Chen et al., 2020). The mechanical properties of wood change as temperature, moisture, and loading time change (Mackerle, 2005). Moreover, growth characteristics such as slope of grain and knots significantly affect the mechanical behaviour of wood-based products.

These aspects may pose significant challenges for modelling of wood-based products. This chapter introduces constitutive models suitable for simulating the structural behaviour of wood-based products under various loads along with specific modelling considerations for key influencing factors.

## 4.1.2 Material (Stress-Strain) Models

The anisotropic characteristics of wood are a result of its fibrous structure and its 3D orthotropic nature (Figure 1) (Hirai, 2005). The stiffness and strength of wood vary as a function of the three main grain orientations: longitudinal (L), radial (R), and tangential (T).

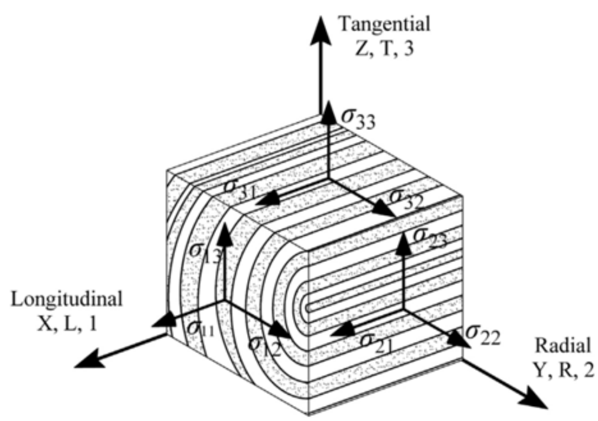


**Figure 1. 3D stress components and orthogonal material directions for a timber element (Gharib et al., 2017)**

The failure modes and the stress-strain relationships of wood depend on the direction of the load relative to the grain and the type of load (tension, compression, or shear). As illustrated in Figure 2, for wood subjected to tension or shear, the stress-strain relationship is typically linear elastic and the failure is quasi-brittle; for wood in compression, the stress-strain relationship is typically nonlinear and the failure is ductile (Chen et al., 2011; Chen et al., 2020).

To model the mechanical behaviour of wood-based products under various forces, the constitutive model should include the following components: (a) elastic properties; (b) strength criterion; (c) post-peak softening for quasi-brittle failure modes; (d) plastic flow and hardening rule for yielding failure modes; and (e) second hardening (densification) perpendicular to grain. Depending on the modelling complexities, scenarios, and demands, different constitutive models with various combinations of these components can be adopted. For example, a constitutive model consisting of elastic properties is usually sufficient to determine the deflection and stress distribution of a wood-based element when the load is small; however, strength criterion needs to be included in the constitutive model when the load-carrying capacity, failure mode, or both are required. If the post-strength behaviour is of interest, the post-peak softening, hardening, and yielding—or all—are required in the constitutive model.

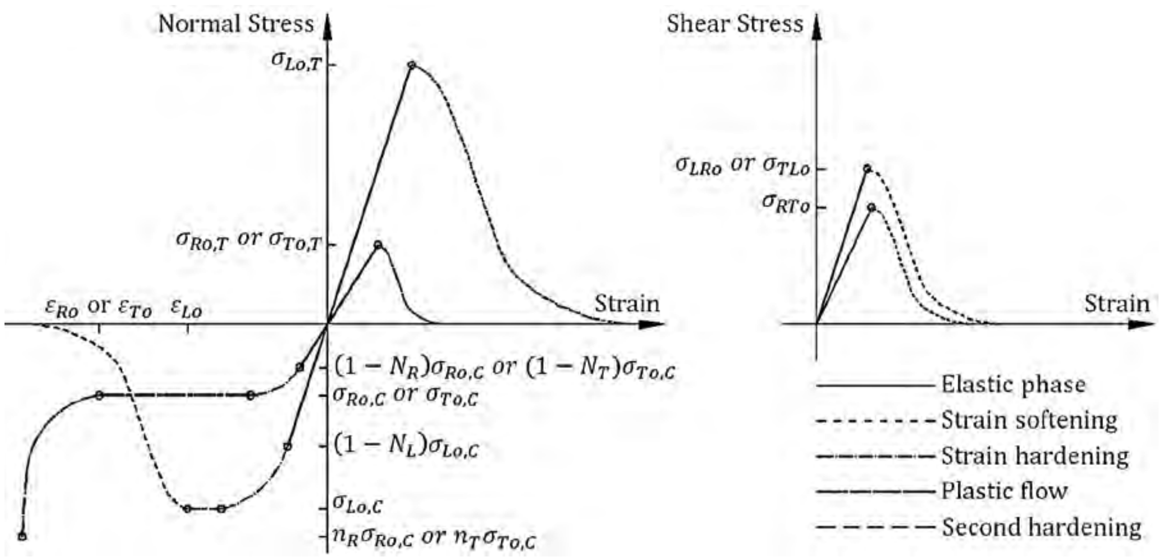


**Figure 2. Typical stress-strain behaviour of wood**

*Note: $\sigma_{io}$ is the axial strength in the i direction [MPa]; $\sigma_{io,T}$ and $\sigma_{io,C}$ are the tensile strength and the compressive strength in the i direction [MPa]; $\sigma_{ijo}$ is the shear strength in the $i-j$ plane [MPa]; $N_i$ and $n_i$ are parameters to determine the initial and final ultimate yield surface, respectively; $\varepsilon_{Lo}$ is the initial damage strain for compression parallel to grain; $\varepsilon_{Ro}$ and $\varepsilon_{To}$ are the initial second-hardening strain for compression perpendicular to grain.*

### 4.1.2.1 Elastic Behaviour

The elasticity of a material defines its strain, $\varepsilon_{ij}$, response to applied stresses, $\sigma_{ij}$. Commonly, wood is simplified into orthotropic material, so nine independent material parameters are needed to replicate its orthotropy: three moduli of elasticity ($E_L$, $E_R$, and $E_T$), three shear moduli ($G_{LR}$, $G_{LT}$, and $G_{RT}$), and three Poisson's ratios ($\nu_{LR}$, $\nu_{LT}$, and $\nu_{RT}$). For common species of wood, these parameters have been measured and are recorded in handbooks, for example, *Wood Handbook – Wood as an Engineering Material* (FPL, 2010). The nine material parameters together define a constitutive relation for wood in the form of a 3D generalised Hooke's law.

$$\begin{bmatrix}\sigma_L\\ \sigma_R\\ \sigma_T\\ \sigma_{LR}\\ \sigma_{RT}\\ \sigma_{TL}\end{bmatrix}=\begin{bmatrix}\frac{E_L(1-\nu_{RT}\nu_{TR})}{\Upsilon} & \frac{E_L(\nu_{RL}+\nu_{TL}\nu_{RT})}{\Upsilon} & \frac{E_L(\nu_{TL}+\nu_{RL}\nu_{TR})}{\Upsilon} & 0 & 0 & 0\\ \frac{E_L(\nu_{RL}+\nu_{TL}\nu_{RT})}{\Upsilon} & \frac{E_R(1-\nu_{LT}\nu_{TL})}{\Upsilon} & \frac{E_R(\nu_{TR}+\nu_{LR}\nu_{TL})}{\Upsilon} & 0 & 0 & 0\\ \frac{E_L(\nu_{TL}+\nu_{RL}\nu_{TR})}{\Upsilon} & \frac{E_R(\nu_{TR}+\nu_{LR}\nu_{TL})}{\Upsilon} & \frac{E_T(1-\nu_{LR}\nu_{RL})}{\Upsilon} & 0 & 0 & 0\\ 0 & 0 & 0 & 2G_{LR} & 0 & 0\\ 0 & 0 & 0 & 0 & 2G_{RT} & 0\\ 0 & 0 & 0 & 0 & 0 & 2G_{LT}\end{bmatrix}\begin{bmatrix}\varepsilon_L\\ \varepsilon_R\\ \varepsilon_T\\ \varepsilon_{LR}\\ \varepsilon_{RT}\\ \varepsilon_{TL}\end{bmatrix} \quad [1]$$

$$\Upsilon = 1-\nu_{LR}\nu_{RL}-\nu_{RT}\nu_{TR}-\nu_{TL}\nu_{LT}-2\nu_{RL}\nu_{TR}\nu_{LT} \quad [2]$$

$$\nu_{RL} = \nu_{LR}(E_R/E_L) \quad [3]$$

$$\nu_{TL} = \nu_{LT}(E_T/E_L) \quad [4]$$

$$\nu_{TR} = \nu_{RT}(E_T/E_R) \quad [5]$$

If the difference in the mechanical properties between the radial and tangential direction are not significant, transverse isotropy can also be adopted. Thus, the number of independent parameters can be reduced to five by assuming:

$$E_R = E_T \quad [6]$$

$$G_{LR} = G_{LT} \quad [7]$$

$$G_{RT} = \frac{E_T}{2(1+\nu_{RT})} \quad [8]$$

$$\nu_{LT} = \nu_{LR} \quad [9]$$

As a result, any specific elastic property perpendicular to grain can be taken as the average of the corresponding property in the radial and tangential direction. However, this assumption leads to gross overestimation of the rolling shear modulus (Akter et al., 2021), and this simplification may not be suitable where rolling shear is one of the main modelling parameters.

### *4.1.2.2 Failure Modes and Strength Criteria*

Wood behaves elastically under tensions or shear, and fails quasi-brittlely once the stresses reach the failure strengths. It performs nonlinearly under compression and yields in a ductile manner once the stresses reach the yield strengths. Typical failure modes of clear wood in tension or compression parallel or perpendicular to grain are illustrated in Figures 3 to 6. The idealised stress-strain behaviour of wood under tension, compression, or shear is illustrated in Figure 2.

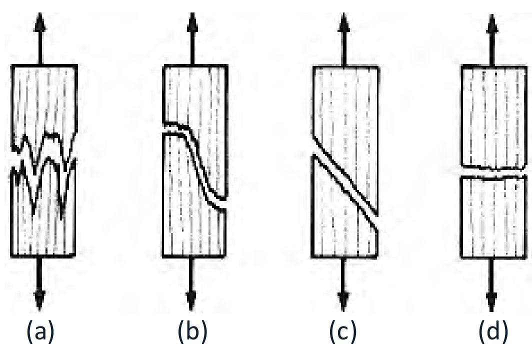


**Figure 3. Failure types of clear wood in tension parallel to grain (Bodig & Jayne, 1982): (a) splintering tension; (b) combined tension and shear; (c) diagonal shear; and (d) brittle tension**

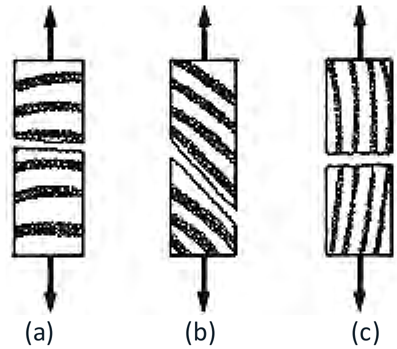


**Figure 4. Failure types of clear wood in tension perpendicular to grain (Bodig & Jayne, 1982): (a) tension failure of earlywood; (b) shearing along a growth ring; and (c) tension failure of wood rays**

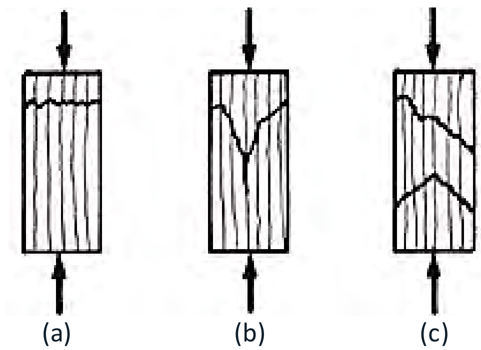


**Figure 5. Failure types of non-buckling clear wood in compression parallel to grain (Bodig & Jayne, 1982): (a) crushing; (b) wedge splitting; and (c) shearing**

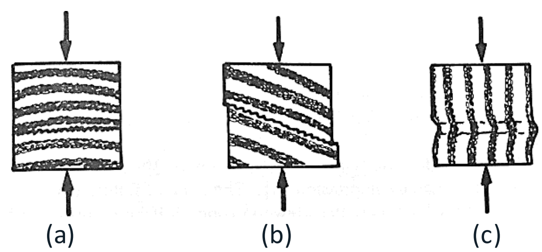


**Figure 6. Failure types of clear wood in compression perpendicular to grain (Bodig & Jayne, 1982): (a) crushing of an earlywood zone; (b) shearing along a growth ring; and (c) buckling of the growth rings**

Unlike steel, which is an isotropic material, wood has significantly different strengths in the longitudinal, radial, and tangential directions. The strength in the longitudinal direction is greater than that in the radial and tangential directions. In other words, the compression strength parallel to grain is about 10 times the compression strength perpendicular to grain. Radial and tangential strengths are generally similar, and wood is usually referred to as transversely isotropic. Longitudinal strength is popularly known as the parallel-to-grain strength, whereas radial and tangential strengths are generally categorised as perpendicular-to-grain strength (CSA Group, 2019; Winandy, 1994). Moreover, the strengths of wood under tension differ from the strengths under either parallel-to-grain or perpendicular-to-grain compression.

Various strength criteria (Cabrero et al., 2021) have been developed for predicting localised material failure due to stress caused by static load (Nahas, 1986). A brief summary of typical strength criteria is given below and a comparison of these criteria is in Table 1.

**Maximum stress**:

$$|\boldsymbol{\sigma_{ij}}| = \boldsymbol{\sigma_{ijo}} \tag{10}$$

This is one of the most commonly applied limit theories. Failure occurs when any component of stress exceeds its corresponding strength.

**Coulomb-Mohr** (Coulomb, 1773; Mohr, 1900):

$$\pm\frac{\boldsymbol{\sigma_i - \sigma_j}}{\mathbf{2}} = \frac{\boldsymbol{\sigma_i - \sigma_j}}{\mathbf{2}}\boldsymbol{sin}(\emptyset) + \boldsymbol{c} \cdot \boldsymbol{cos}(\emptyset) \tag{11}$$

where $\sigma_i$ and $\sigma_j$ are principal stresses; $c$ is the intercept of the failure envelope with the $\tau$ axis, also called the cohesion; and $\emptyset$ is the angle of internal friction. This is the most common strength criterion used in geotechnical engineering. It is used to determine the failure load as well as the angle of fracture in geomaterials (rock and soil), concrete and other similar materials with internal friction. Coulomb's friction hypothesis is used to determine the combination of shear and normal stress that will cause a fracture of the material. Mohr's circle is used to determine which principal stresses that will produce this combination of shear and normal stress, and the angle of the plane in which it will occur. According to the principle of normality the stress introduced at failure will be perpendicular to the line describing the fracture condition. Generally, the theory applies to materials for which the compressive strength far exceeds the tensile strength.

**Von Mises** (1913), **maximum distortion strain energy**:

$$\sqrt{\frac{\mathbf{1}}{\mathbf{2}}\left[\left(\boldsymbol{\sigma_k - \sigma_j}\right)^2 + \left(\boldsymbol{\sigma_j - \sigma_k}\right)^2 + (\boldsymbol{\sigma_k - \sigma_i})^2 + \mathbf{6}\left(\boldsymbol{\sigma_{ij}^2 + \sigma_{jk}^2 + \sigma_{kl}^2}\right)\right]} = \boldsymbol{\sigma_o} \tag{12}$$

where $\sigma_o$ is the yield strength of material. In this theory, a ductile material under a general stress state yields when its shear distortional energy reaches the criteria shear distortional energy under simple tension. Von Mises criterion is usually used as the initial yield criterion for metals.

**Tresca** (1864), **maximum shear stress**:

$$\boldsymbol{Max}\left(|\boldsymbol{\sigma_i - \sigma_j}|, |\boldsymbol{\sigma_j - \sigma_k}|, |\boldsymbol{\sigma_k - \sigma_i}|\right) = \boldsymbol{\sigma_o} \tag{13}$$

The material remains elastic when all three principal stresses are roughly equivalent (a hydrostatic pressure), no matter how much it is compressed or stretched. If one of the principal stresses becomes smaller or larger than the others, the material is subject to shearing. In such situations, if the shear stress reaches the yield limit, then the material enters the plastic domain. This is a special case for Coulomb-Mohr criterion with the coefficient of internal friction equal to zero.

**Hill** (1950):

$$\boldsymbol{A}(\boldsymbol{\sigma_L - \sigma_R})^2 + \boldsymbol{B}(\boldsymbol{\sigma_R - \sigma_T})^2 + \boldsymbol{C}(\boldsymbol{\sigma_T - \sigma_L})^2 + \boldsymbol{D\sigma_{LR}^2} + \boldsymbol{E\sigma_{RT}^2} + \boldsymbol{F\sigma_{LT}^2} = \mathbf{1} \tag{14}$$

where $A$ to $F$ are coefficients determined from uniaxial and pure shear tests. This theory is a generalisation of von Mises theory for orthotropic materials. It considers 'interaction' between the failure strengths as forming a smooth failure envelope.

**Tsai-Wu** (Tsai & Wu, 1971), originally developed for anisotropic material:

$$\boldsymbol{F_1\sigma_L + F_2(\sigma_R + \sigma_T) + F_{11}\sigma_L^2 + F_{22}(\sigma_R^2 + \sigma_T^2 + 2\sigma_{RT}^2) + F_{66}(\sigma_{LR}^2 + \sigma_{LT}^2) + 2F_{12}(\sigma_L\sigma_R + \sigma_L\sigma_T)}$$
$$\boldsymbol{+2F_{23}(\sigma_{RT}^2 - \sigma_R\sigma_T)} = 1 \qquad [15]$$

where $F_i$ and $F_{ij}$ are coefficients determined from uniaxial, biaxial, and shear tests. Seven coefficients must be defined for transversely isotropic applications. The non-interaction coefficients that contain one component of stress are determined from measured uniaxial and pure shear strengths. The interaction coefficients that have two or more components of stress multiplied together are determined from measured biaxial strengths.

**Hoffman** (1967):

$$\boldsymbol{A(\sigma_L - \sigma_R)^2 + B(\sigma_R - \sigma_T)^2 + C(\sigma_T - \sigma_L)^2 + D\sigma_{LR}^2 + E\sigma_{RT}^2 + F\sigma_{LT}^2 + G\sigma_L + H\sigma_R + I\sigma_T = 1} \qquad [16]$$

where $A$ to $I$ are coefficients determined from uniaxial and pure shear tests. Hoffman extended Hill's criterion for orthotropic materials to account for different strengths in tension and compression. Six coefficients are determined from uniaxial stress and pure shear tests. Biaxial strengths are not needed.

**Norris** (1962):

$$\boldsymbol{\frac{\sigma_i^2}{\sigma_{io}^2} - \frac{\sigma_i\sigma_j}{\sigma_{io}\sigma_{jo}} + \frac{\sigma_j^2}{\sigma_{jo}^2} + \frac{\sigma_{ij}^2}{\sigma_{ijo}^2} = 1} \qquad [17]$$

Norris developed one failure criterion consisting of three equations for mutually orthogonal *i*–*j* planes. Each equation contains quadratic stress terms (no linear terms). Nine coefficients are determined from uniaxial and pure shear tests. Tensile strengths are used when the corresponding stresses are tensile. Compressive strengths are used when the corresponding stresses are compressive.

**Modified Hashin** (1980):

$$\boldsymbol{\frac{\sigma_L^2}{\sigma_{\parallel o}^2} + \frac{(\sigma_{LR}^2 + \sigma_{LT}^2)}{S_{\parallel o}^2} = 1} \qquad [18a]$$

$$\boldsymbol{\frac{(\sigma_R + \sigma_T)^2}{\sigma_{\perp o}^2} + \frac{(\sigma_{RL}^2 - \sigma_R\sigma_T)}{S_{\perp o}^2} + \frac{(\sigma_{LR}^2 + \sigma_{LT}^2)}{S_{\perp o}^2} = 1} \qquad [18b]$$

where $S_{\parallel o}$ and $S_{\perp o}$ are the shear strength parallel to grain and perpendicular to grain, respectively. Hashin (1980) formulated a quadratic stress polynomial in terms of the invariants of a transversely isotropic material. Separate formulations are identified for longitudinal, radial, and tangential modes by assuming that failure is produced by the normal and shear stresses acting on the failure plane. In addition, the longitudinal, radial, and tangential modes are subdivided into tensile and compressive modes. The assumptions are that (1) biaxial compressive strength perpendicular to the grain is much greater than the uniaxial compressive strength, and (2) shear stress does not contribute to compressive failure parallel to the grain. All coefficients are determined from six uniaxial and shear strengths.

**Extended Yamada-Sun** (Yamada & Sun, 1978):

$$\frac{\sigma_i^2}{\sigma_{io}^2}+\frac{\sigma_{ij}^2}{\sigma_{ijo}^2}+\frac{\sigma_{ik}^2}{\sigma_{iko}^2}=\mathbf{1} \qquad [19]$$

Three yield equations are reported for mutually orthogonal planes. Each criterion predicts that the normal and shear stresses are mutually weakened. Nine strengths are determined from uniaxial and pure shear tests.

**Table 1. Comparison of various strength criteria**

| Criterion | Ductile or brittle material | Interaction between the strengths? | Indicate brittle or ductile failure? | Account for different strengths in tension and compression? |
|---|---|---|---|---|
| Maximum stress | Both | No | Yes | Yes |
| Coulomb-Mohr | Brittle | No | No | Yes |
| Von Mises | Ductile | No | No | No |
| Tresca | Ductile | No | No | No |
| Hill | Ductile | Yes | No | No |
| Tsai-Wu | Both | Yes | No | Yes |
| Hoffman | Both | Yes | No | Yes |
| Norris | Both | Yes | Yes | Yes |
| Hashin | Both | Yes | Yes | Yes |
| Extended Yamada-Sun | Both | Yes | Yes | Yes |

Based on the descriptions provided above:

- The von Mises and Tresca strength (yield) criteria apply to very ductile isotropic materials, but function poorly for all other materials.
- The Coulomb-Mohr criterion is suitable for brittle materials.
- The Hill strength (yield) criterion can be used for orthotropic materials; however, it is not directly applicable to wood-based materials because it does not model different strengths in tension and compression.
- The maximum stress criteria consider different strengths in tension and compression, but do not include the interaction between the strengths.
- The Tsai-Wu and Hoffman interactive strength criteria predict when a given set of stresses will produce failure, but they do not predict the mode of failure.
- The Norris approach can predict the failure in orthogonal planes rather than orthogonal axes.

- Both Hashin and extended Yamada-Sun criteria are capable of predicting the failure modes caused by tension or compression in different axes.

Compared to these criteria, the Tsai-Wu, Hoffman, Norris, Hashin, and extended Yamada-sum criteria are more suitable for wood-based material. Although the maximum stress, Coulomb-Mohr, von Mises, Tresca, and Hill criteria were originally developed for materials which behave very differently to wood-based material, these criteria could be the only options in some programs. If that is the case, they can still be utilised for wood-based material if using engineering judgments and necessary assumptions.

#### *4.1.2.3 Post-strength Behaviour of Quasi-Brittle Failure*

Tension and shear stresses beyond the elastic limit (Figures 3, 4, and 6[b]) generate voids and microcracks in the wood matrix which gradually degrade its mechanical properties, including its stiffness (Sirumbal-Zapata et al., 2018). When further loads are applied, the microcracks grow and coalesce, producing macrocrack zones and irreversible damage which eventually leads to failure (Khelifa et al., 2016). As the damage and deformation increase, the material resistance to stress gradually decreases, that is, it softens (Figure 2). This is called quasi-brittle failure.

Continuum damage mechanics (Matzenmiller et al., 1995), based on the thermodynamics of irreversible processes theory, have been widely used for modelling the nonlinear behaviour of brittle materials such as concrete, rock, and more recently, timber (Chen et al., 2011; Sandhaas et al., 2012). Strain-based damage models of continuum damage mechanics rely on the concept of effective stress and the hypothesis of strain equivalence. Effective stress is defined as the stress acting in the reduced undamaged net surface area of the material, with no consideration given to the portion of area of the microcracks and voids. Taking into account that the total force acting in the material body is constant, the magnitude of the effective stress acting in the reduced undamaged area is higher than the magnitude of the Cauchy (true) stress acting over the total nominal surface area. On the other hand, the hypothesis of strain equivalence states that the strain associated with the Cauchy stress in the damaged state is equivalent to the strain associated with the effective stress in the undamaged state (Simo & Ju, 1987).

Using continuum damage mechanics to model the degradation of properties, a scalar damage parameter, $d_i$ (where $0 \leq d_i \leq 1$), transforms the stress tensor associated with the undamaged state, $\bar{\sigma}_{ij}$, into the stress tensor associated with the damaged state, $\sigma_{ij}$:

$$\boldsymbol{\sigma_{ij}} = (\boldsymbol{1} - \boldsymbol{d_i})\boldsymbol{\bar{\sigma}_{ij}} = \boldsymbol{D_d}\boldsymbol{\varepsilon_{ij}} \qquad [20]$$

where $\boldsymbol{D_d}$ is a reduced stiffness matrix with damage parameters. The damage parameter ranges from zero for no damage to approaching unity for maximum damage. Thus, '$1 - d_i$' is a reduction factor associated with the amount of damage. Two advantages can be obtained by using this formulation: (1) stiffness is degraded in conjunction with strength; and (2) progressive softening depends on subsequent loading.

Figure 7 shows how the damage parameter affects the stress-strain curve.

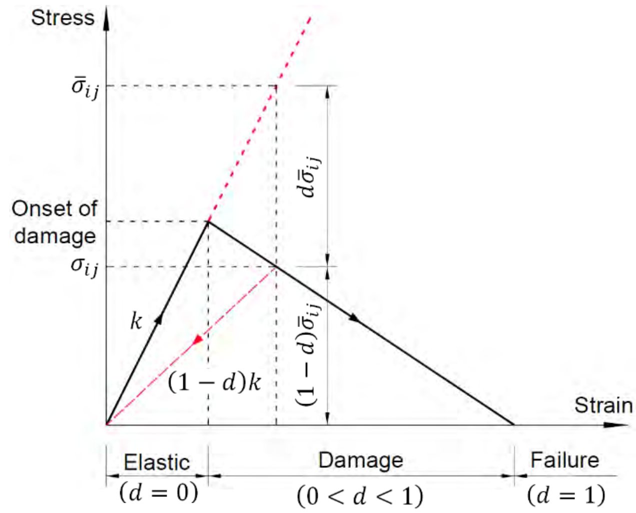


**Figure 7. Schematic of continuum damage mechanics**

Damage formulations are typically based on strain, stress, or energy. Chen (2011) proposed an exponential damage evolution based on the accumulating effect of strains:

$$\boldsymbol{d_i = 1 - exp\left[\frac{-(\tau_i - \tau_{i,o})}{\tau_{i,o}}\right]} \qquad [21]$$

where $\tau_{i,o}$ and $\tau_i$ are the undamaged elastic strain-energy norms at the time when stresses meet the strength criterion in the $i$ direction and beyond, respectively. The strain-based theory (Simo & Ju, 1987) can be used to calculate the undamaged elastic strain energy based on the total strains and the undamaged moduli of elasticity. Assuming that the damage parameters in the three major directions are independent of each other, the undamaged elastic strain-energy norms, $\tau_i$, can be calculated using Equation 22:

$$\boldsymbol{\tau_i = \sqrt{\sigma_i^*\varepsilon_i + 2\left(\sigma_{ij}^*\varepsilon_{ij} + \sigma_{ki}^*\varepsilon_{ki}\right)}} \qquad [22]$$

where $\sigma_{ij}^*$ is undamaged stress.

Another issue is strength coupling, in which degradation in one direction affects degradation in another. If failure occurs in the longitudinal modes, all six stress components degrade uniformly. This is because longitudinal failure is catastrophic and renders the wood useless. The wood is not expected to carry load in either the longitudinal or transverse (radial and tangential) direction once the wood fibres are broken. If either the radial or tangential mode fail, only the transverse stress components degrade. This is because neither radial nor tangential failure are catastrophic, and the wood is likely to be able to continue to carry the load in the longitudinal direction.

Based on these assumptions, the reduced stiffness matrix, $\boldsymbol{D_d}$, can be expressed as follows:

$$\boldsymbol{D_d} = \begin{bmatrix} \alpha\frac{E_L(1-\nu_{RT}\nu_{TR})}{\Upsilon} & \beta\frac{E_L(\nu_{RL}+\nu_{TL}\nu_{RT})}{\Upsilon} & \gamma\frac{E_L(\nu_{TL}+\nu_{RL}\nu_{TR})}{\Upsilon} & 0 & 0 & 0 \\ \beta\frac{E_L(\nu_{RL}+\nu_{TL}\nu_{RT})}{\Upsilon} & \beta\frac{E_R(1-\nu_{LT}\nu_{TL})}{\Upsilon} & \eta\frac{E_R(\nu_{TR}+\nu_{LR}\nu_{TL})}{\Upsilon} & 0 & 0 & 0 \\ \gamma\frac{E_L(\nu_{TL}+\nu_{RL}\nu_{TR})}{\Upsilon} & \eta\frac{E_R(\nu_{TR}+\nu_{LR}\nu_{TL})}{\Upsilon} & \gamma\frac{E_T(1-\nu_{LR}\nu_{RL})}{\Upsilon} & 0 & 0 & 0 \\ 0 & 0 & 0 & 2\beta G_{LR} & 0 & 0 \\ 0 & 0 & 0 & 0 & 2\eta G_{RT} & 0 \\ 0 & 0 & 0 & 0 & 0 & 2\gamma G_{LT} \end{bmatrix} \quad [23]$$

where $\alpha = 1 - d_L$, $\beta = 1 - d_R$, $\gamma = 1 - d_T$, $\eta = 1 - max(d_R, d_T)$, $d_L = d(\tau_L)$, $d_R = max[d(\tau_L), d(\tau_R)]$, and $d_T = max[d(\tau_L), d(\tau_T)]$. These factors take into account the coupling effect of damage. Once the scalar damage parameter, $d_i$, reaches its maximum value, the corresponding element can be removed using the element deletion techniques available in advanced modelling tools or software.

#### *4.1.2.4 Post-strength Behaviour of Ductile Failure*

Ductile yielding of wood under either parallel-to-grain or perpendicular-to-grain compression (Figures 5, 6[a] and 6[c]) occurs once the strength criterion is satisfied, based on the plastic flow and hardening evolution rule (Sirumbal-Zapata et al., 2018). From a physical point of view, plasticity in compression occurs in the material matrix, between voids and cracks, leading to local hardening behaviour (de Borst, 2001). Softening, similar to that described in Section 4.1.2.3, is triggered when the compression strain parallel to grain reaches a specific criterion, $\varepsilon_{Lo}$. A second hardening happens once the compression strain perpendicular to grain reaches a specific criterion, $\varepsilon_{Ro}$ or $\varepsilon_{To}$ (see Figure 2).

##### 4.1.2.4.1 Plastic Flow

The plasticity algorithms limit the stress components once the strength criterion is satisfied. This is achieved by bringing the stress state back to the yield surface. A typical approach for modelling plasticity is to partition the stress and strain tensors into elastic and plastic parts:

$$\boldsymbol{\Delta\varepsilon_{ij} = \Delta\varepsilon_{ij}^{e} + \Delta\varepsilon_{ij}^{p} = \Delta\varepsilon_{ij}^{e} + \Delta\lambda\frac{\partial g}{\partial\sigma_{ij}}} \quad [24]$$

where $\Delta\varepsilon_{ij}$, $\Delta\varepsilon_{ij}^{e}$, and $\Delta\varepsilon_{ij}^{p}$ are total, elastic, and plastic strain increments, respectively; $\Delta\lambda$ is the plastic flow parameter increment; and $g$ is a plastic potential function. Partitioning is conducted with return mapping algorithms that enforce the plastic consistency conditions. Such algorithms allow for the control of plastic strain generation. In addition, return mapping algorithms with associated flow satisfy the second law of thermodynamics. Radial-return algorithm (Lubliner, 2008) is typically used, and the plastic potential function, $g$, can be simplified to yield or strength function. The plastic flow parameter increment, which depends on the yield function, can be derived by solving the plastic consistency condition. Where extended Yamada-Sun criteria (Equation 19) are adopted as the yield function (Chen et al., 2011), the yield function and the corresponding increment of the plastic flow parameter $\Delta\lambda$ can be expressed as follows:

$$\boldsymbol{f_i(\sigma_i, \sigma_{ij}, \sigma_{ki}) = \frac{\sigma_i^2}{\sigma_{io,C}^2} + \frac{\sigma_{ij}^2}{\sigma_{ijo}^2} + \frac{\sigma_{ki}^2}{\sigma_{kio}^2} - 1} \quad [25]$$

$$\Delta\lambda_i = \frac{f_i^*/4}{\frac{E_i(1-\nu_{jk}\nu_{kj})}{\Upsilon}\frac{\sigma_i^2}{\sigma_{io,C}^4}+4G_{ij}\frac{\sigma_{ij}^2}{\sigma_{ijo}^4}+4G_{ik}\frac{\sigma_{ij}^2}{\sigma_{kio}^4}} \quad [26]$$

where $f_i^*$ is the value of the failure criterion calculated from the trail elastic stresses (Lubliner, 2008).

4.1.2.4.2 Hardening Rule

Wood exhibits pre-peak nonlinearity in parallel-to-grain and perpendicular-to-grain compression. A translating yield-surface approach that simulates a gradual change in modulus of elasticity is typically adopted to describe the post-yield portion of the stress-strain curve. The approach is to define initial yield surfaces that harden (translate) until they coincide with the ultimate yield surfaces, as demonstrated in Figure 8 for the longitudinal hardening. The location of the initial yield surface determines the onset of plasticity. The rate of translation determines the extent of nonlinearity.

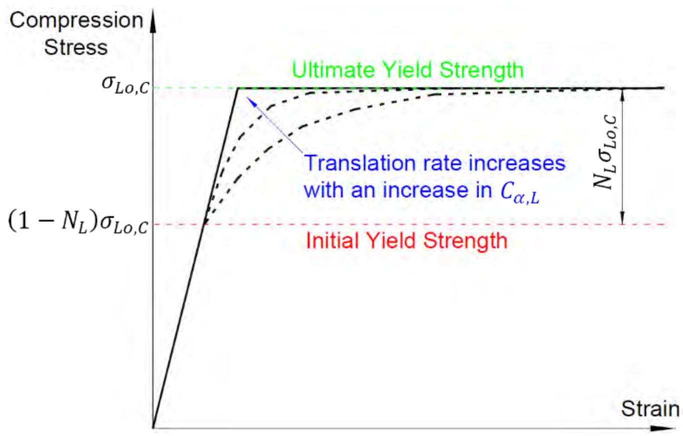


**Figure 8. Hardening in longitudinal direction**

The state variable that defines the translation of the yield surface is known as the backstress. The value of the backstress is zero upon initial yield and is the total translation of the yield surface in stress space at ultimate yield (in uniaxial compression). Either isotropic or kinematic hardening rule (Lubliner 2008) can be adopted to define the growth of the backstress based on the stress and plastic strain. This is accomplished by defining the incremental backstress.

When extended Yamada-Sun criteria (Equation 19) are adopted as the strength function (Chen et al., 2011), the ultimate yield surface is described in Equation 25 and the initial yield surface is described in Equation 27:

$$f_i(\sigma_i,\sigma_{ij},\sigma_{ki}) = \frac{\sigma_i^2}{\sigma_{io,C}^2(1-N_i)^2}+\frac{\sigma_{ij}^2}{\sigma_{ijo}^2}+\frac{\sigma_{ki}^2}{\sigma_{kio}^2}-1 \quad [27]$$

where $N_i$ is a parameter to determine the initial yield surface. The corresponding incremental backstress, $\Delta\alpha_i$, can be expressed as follows:

$$\Delta\alpha_i = C_{\alpha,i}G_{\alpha,i}(\sigma_i-\alpha_i)\Delta\varepsilon_i^{eff} \quad [28]$$

where $\Delta\alpha_i$ and $\Delta\varepsilon_i^{eff}$ are the increment of backstress and effective strain, respectively, in the $i$ direction, and $C_{\alpha,i}$ and $G_{\alpha,i}$ are hardening parameters in the $i$ direction. The parameter $C_{\alpha,i}$ determines the rate of hardening and must be calibrated from test data. The parameter $G_{\alpha,i}$ restricts the motion of the yield surface so that It cannot translate outside the ultimate surface (Sandler et al., 1984).

#### 4.1.2.5 Densification Perpendicular to Grain

Unlike for parallel-to-grain compression, where the stress drops (strain softening), as illustrated in Figure 2, the stress increases sharply with strain in wood under perpendicular-to-grain compression beyond the plastic region (Bodig, 1965; Easterling et al., 1982; Tabarsa & Chui, 2000, 2001). This rapid increase in stress is due to the elimination of air voids and compression of the solid wood structure; hence, this region is termed the densification region. Accordingly, when the perpendicular-to-grain compression strain reaches the criterion $\varepsilon_{Ro}$ or $\varepsilon_{To}$, a second hardening occurs, as shown in Figure 9. Like the hardening (Section 4.1.2.4.2), the translating yield-surface approach can also be used for second hardening, in which the ultimate yield surface will harden (translate) to the final ultimate yield surface.

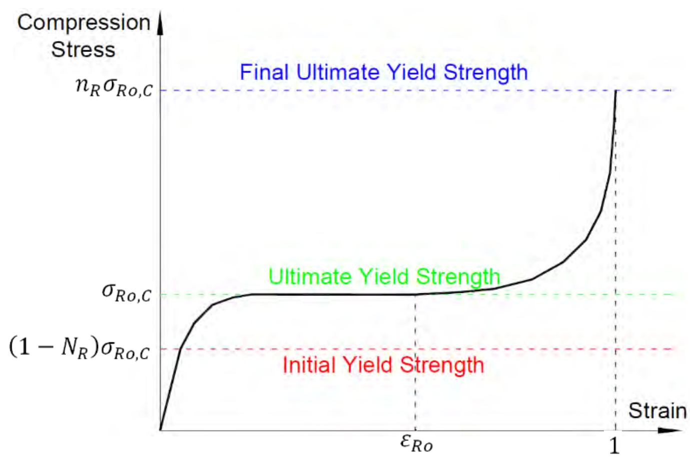


**Figure 9. Hardening in perpendicular direction**

For example, when Chen et al. (2011) adopted extended Yamada-Sun criteria as the strength function, the ultimate yield surface (Equation 25) hardens (translates) to final ultimate yield surface, as described by Equation 29:

$$\boldsymbol{f_{i,fn}(\sigma_i,\sigma_{ij},\sigma_{ki}) = \frac{\sigma_i^2}{n_i^2\sigma_{io,C}^2} + \frac{\sigma_{ij}^2}{\sigma_{ijo}^2} + \frac{\sigma_{ki}^2}{\sigma_{kio}^2} - 1} \quad [29]$$

where $n_i$ is a parameter to determine the final ultimate yield surface. A strain-based hardening evolution is developed to define the second backstress, $\beta_i$:

$$\boldsymbol{\beta_i = -(n_i-1)\sigma_{io,C}\sqrt{1-\left(\frac{\sigma_{ij}^2}{\sigma_{ijo}^2}+\frac{\sigma_{ki}^2}{\sigma_{kio}^2}\right)}\left(\frac{\varepsilon_i^{eff}+\varepsilon_{io}}{1+\varepsilon_{io}}\right)^2} \quad [30]$$

#### 4.1.2.6 Typical Constitutive Modes

The constitutive models incorporated in existing finite element (FE) software packages are often limited, making the general FE software unsuitable for accurately predicting the mechanical behaviour and failure modes of wood-based materials. Some researchers have developed specific constitutive models for wood-based members (e.g., Chen et al., 2011; Danielsson & Gustafsson, 2013; Khennane et al., 2014; Schmidt &

Kaliske, 2007, 2009; Zhu et al., 2005) and connections (e.g., Chen et al., 2020; Franke & Quenneville, 2011; Kharouf et al., 2005; Khelifa et al., 2016; Oudjene & Khelifa, 2009; Resch & Kaliske, 2010; Sandhaas et al., 2012; Sirumbal-Zapata et al., 2018; Xu et al., 2014; Zhu et al., 2010).

Wood$^S$ model, developed by Chen et al. (2011), is a structural orthotropic elastoplastic-damage constitutive model for wood. The model incorporates the effects of orthotropic elasticity and linear softening (damage), anisotropic plasticity with kinematic hardening, large plastic deformations, and densification. The constitutive model takes into account eight types of brittle and ductile failure modes, each of which is associated with a different failure criterion. Wood$^S$ is one of the first constitutive models capable of simulating the complete stress-strain behaviour and various failure modes of wood-based members (Figure 10) under different loading conditions, thus providing an important approach for the numerical modelling of wood. A similar constitutive model was developed by Sandhaas et al. (2012).

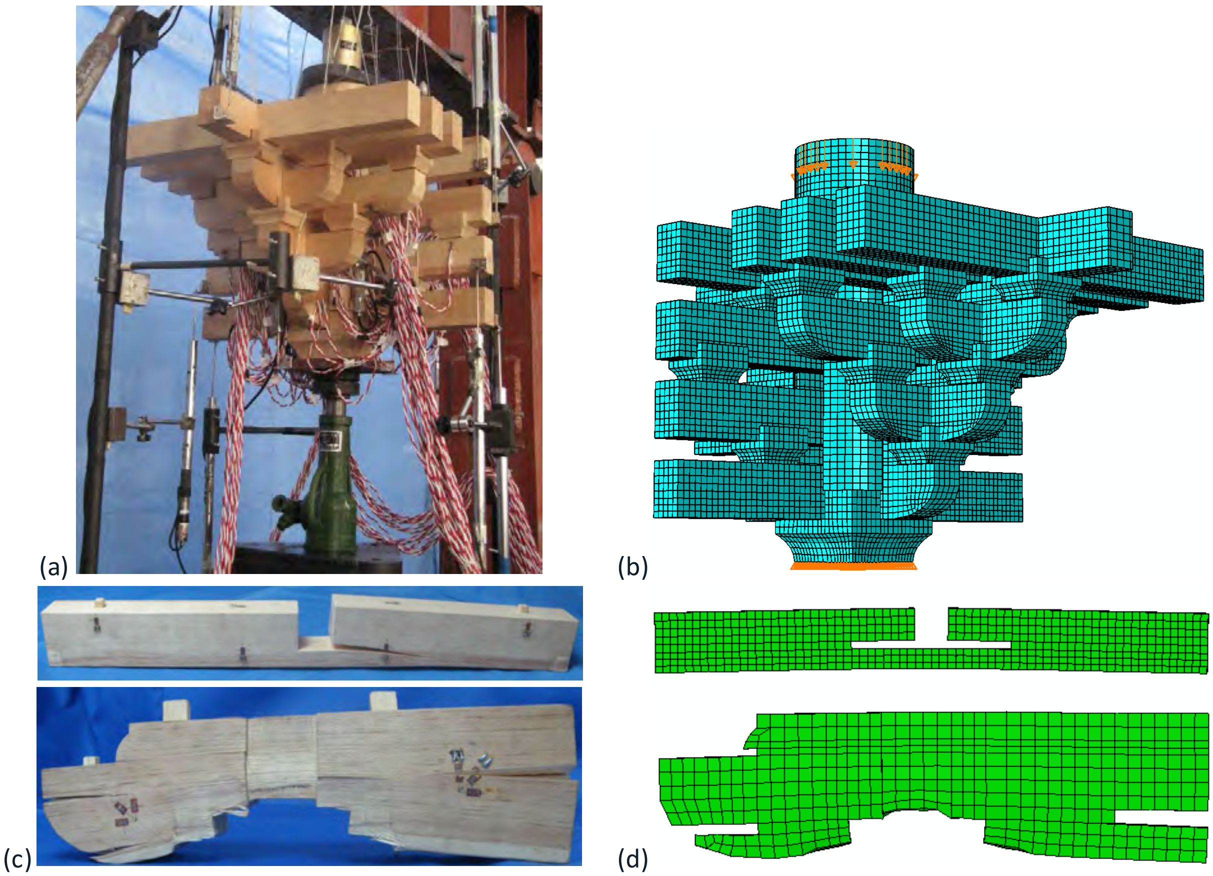

**Figure 10. Dou-Gong brackets under vertical load (Chen, 2011): (a) Specimen installed in testing setup; (b) FE modelling using Wood$^S$; (c) typical failure modes; and (d) failure modes obtained from modelling**

The Wood$^S$ model has been recently upgraded to Wood$^{ST}$ (Chen et al., 2020) for simulating the structural response of wood-based members (Figure 11) and connections subjected to the thermal effects of fire.

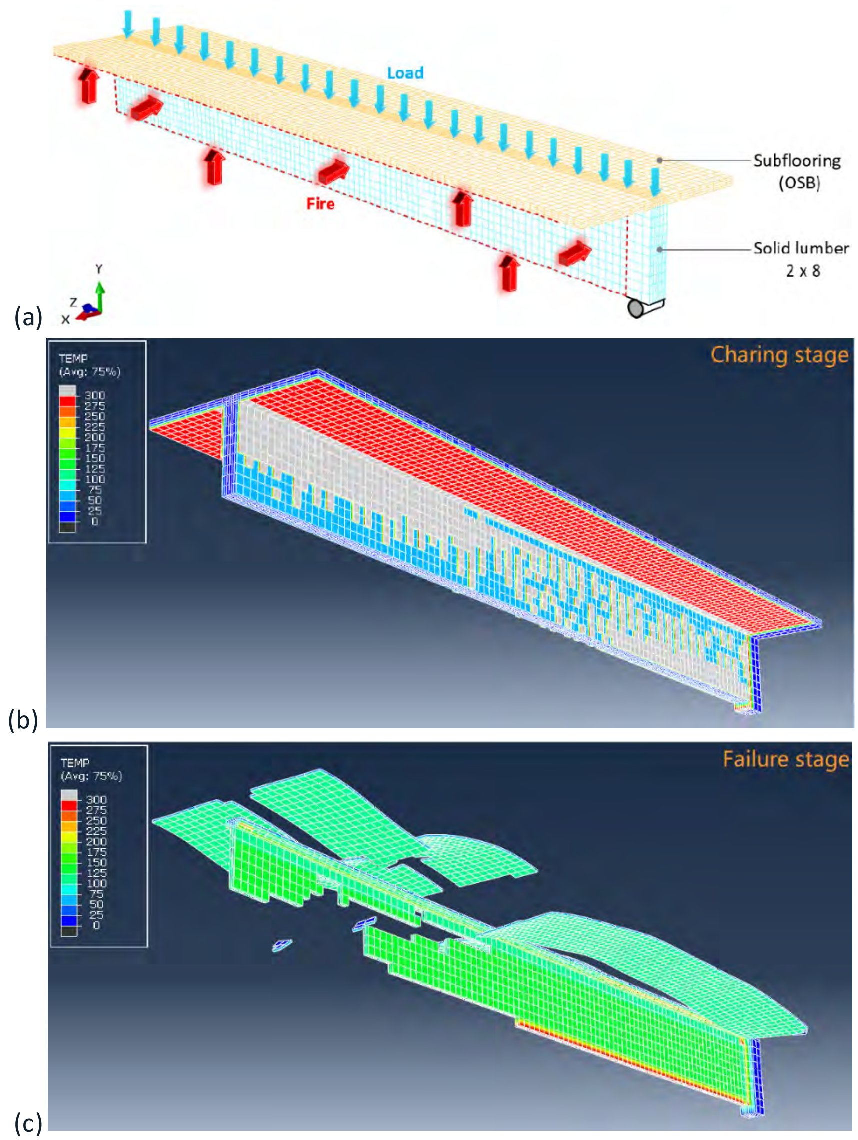


**Figure 11. Modelling of wood-frame floor exposed to fire using Wood$^{ST}$ (Chen & Dagenais, in press): (a) one-half FE model; (b) charring stage (grey elements represent the charred wood); and (c) failure stage**

As tall or large timber structures are becoming a viable option in the construction industry, the structural elements and connections are becoming more complex, and the corresponding design is beyond the compatibility of general design software packages. Designers can still carry out the design using any tools by making more assumptions. The design as well as the assumptions must be verified by testing, numerical simulation, or both. In such a scenario, general purpose FE software with a comprehensive constitutive model of wood-based material is the first choice for the simulation. A comprehensive constitutive model can predict potential failure modes, including those that may be overlooked in design, providing more reliable analysis results to support the design. When the chosen software does not have comprehensive constitutive models, engineers can select available constitutive models, whichever model is most suitable for the specific design case based on suitable assumptions. Selecting constitutive models depends on the modelling scope and objectives. With the appropriate constitutive model, the strength, stability, and deflection problems of wood-based members can be investigated and evaluated. The outputs, however, need to be interpreted more carefully using engineering judgment.

### 4.1.2.7 Model Input

The input fed into the constitutive models usually includes the elastic properties (e.g., $E$, $G$, and $v$; see Section 4.1.2.1, Equations 1 to 9), strengths (e.g., tensile, compressive, and shear strength), key strain values, parameters governing the curve shape (e.g., the hardening parameters), and others. Two types of mechanical properties can be used to derive input for the timber structural modelling depending on the analysis purpose. Test results (mean values) are often used to investigate the actual response of timber structures. With respect to structural design, design values (also called characteristic values or lower bound properties) may be used for the modelling. For limit states design (LSD), the specified strength design values of wood-based products are found in *CSA O86:19 Engineering Design in Wood* (CSA Group, 2019). The strength values used in analysis in allowable stress design (ASD) methodology, may be found in the *National Design Specification for Wood Construction* (AWC, 2018). Whether the analysis is made per LSD or ASD, the strength and modification factors based on the applicable wood design standard should be used.

Moreover, *Strength and Related Properties of Woods Grown in Canada* (Jessome, 2000) identifies some tested mechanical properties of Canadian species of commercial importance and *Wood Handbook – Wood as an Engineering Material* (FPL, 2010) does the same for some American species. The data were derived from tests performed on small, clear specimens of lumber, free of growth characteristics such as knots, cross grain, decay, checks, shakes, wane, or reaction wood. While these data could be used as input for the modelling of wood-based components and connections, the effects of growth characteristics and other parameters should be taken into account (Section 4.1.3).

Specified strength and allowable design stress can be converted to mean value using the schemes (Figure 12) suggested by Chen et al. (2018).

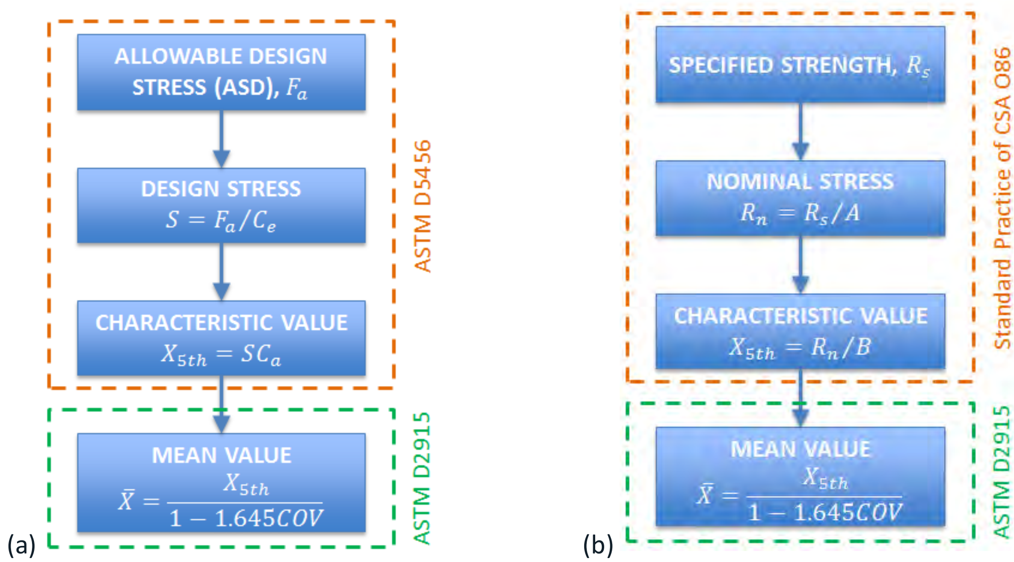


**Figure 12. Schemes for converting (a) allowable design stress and (b) specified strength to mean value**

Examples showing the derivation of the mean values of the tensile and compressive strength of laminated veneer lumber (LVL) and glulam used in the variation are given in Example 1 and Example 2.

**Example 1**: To determine the mean values of the tensile and compressive strength of LVL based on allowable design stress.

(a) Tensile strength

| | | |
|---|---|---|
| a) | $F_a$ = 14.8 MPa | (3100Fb-2.0E Versa-Lam LVL) |
| b) | $S$ = 14.8 / (1/1.6) / (1/0.86) = 20.4 MPa | (1.6 and 0.86 are factors for duration of load [DOL] and size effect) |
| c) | $X_{5th}$ = 20.4 × 2.1 = 42.8 MPa | (2.1 is adjustment factor) |
| d) | $\bar{X}$ = 42.8 / (1 - 1.645 × 10%) = 51.2 MPa | (10% is assumed coefficient of variation (COV) for LVL) |

(b) Compressive strength

| | | |
|---|---|---|
| a) | $F_a$ = 20.7 MPa | (3100Fb-2.0E Versa-Lam LVL) |
| b) | $S$ = 20.7 / (1/1.6) / (1/1.0) = 33.1 MPa | (1.6 and 1.0 are factors for DOL and size effect) |
| c) | $X_{5th}$ = 33.1 × 1.9 = 62.9 MPa | (1.9 is adjustment factor) |
| d) | $\bar{X}$ = 62.9 / (1 - 1.645 × 10%) = 75.3 MPa | (10% is assumed COV for LVL) |

This ASD conversion method is essentially the background on which the strength adjustment factor for fire resistance ($K$) is based in National Design Specification (NDS). Following NDS, the average LVL tensile strength is estimated as 58.1 MPa ($S \times K$ = 20.4 × 2.85), which is greater than the value of 51.2 MPa shown above. The difference relies on the assumed COV. NDS assumes a COV of 16% for all wood products, whereas the example shown above assumes a COV of 10% for LVL.

**Example 2**: To determine the mean values of the tensile and compressive strength of glulam based on specified strength.

(a) Tensile strength

| | | |
|---|---|---|
| a) | $R_s$ = 17.0 MPa | (20f-EX S-P glulam) |
| b) | $R_n$ = 17.0 / 0.8 = 21.3 MPa | (0.8 is to convert to short-term DOL) |
| c) | $X_{5th}$ = 21.3 / 1.05 = 20.2 MPa | (1.05 is a reliability normalisation factor) |
| d) | $\bar{X}$ = 20.2 / (1 - 1.645 × 15%) = 26.9 MPa | (15% is assumed COV for glulam) |

(b) Compressive strength

| | | |
|---|---|---|
| a) | $R_s$ = 25.2 MPa | (20f-EX S-P glulam) |
| b) | $R_n$ = 25.2 / 0.8 = 31.5 MPa | (0.8 is to convert to short-term DOL) |
| c) | $X_{5th}$ = 31.5 / 0.98 = 32.2 MPa | (0.98 is a reliability normalisation factor) |
| d) | $\bar{X}$ = 32.2 / (1 - 1.645 × 15%) = 42.7 MPa | (15% is assumed COV for glulam) |

This LSD conversion method is essentially the background on which the strength adjustment factor for fire resistance ($K_{fi}$) is based in CSA O86. If following CSA O86, the average glulam tensile strength is estimated as

22.9 MPa ($R_s \times K_{fi}$ = 17.0 × 1.35), which would then be adjusted for DOL ($K_D$ = 1.15) to 26.4 MPa. In contrast to the NDS approach, the adjustment factor $K_{fi}$ in CSA O86 implicitly considers various COV for wood products, in which a COV of 15% is assumed for glulam (Dagenais & Osborne, 2013).

## 4.1.3 Key Influencing Factors

### *4.1.3.1 Growth Characteristics*

Wood is a non-homogeneous material, containing oblique fibres (slope of grain), knots, etc. These growth characteristics, which serve the needs of the tree, usually significantly reduce the strength of cut timber, and it is used for other purposes (Thelandersson & Honfi, 2009). The slope of grain can be simulated by adjusting the local coordinate system of material to follow the wood grain. Usually, a rectangular Cartesian axis system is sufficient. A cylindrical axis system can be adopted to consider the location of pith. Two typical approaches take into account the effect of knots and other local growth characteristics: an efficient approach is to use test results as material input; these can be either be the results of full-scale tests conducted using representative materials or the results of converting the design values, as discussed in Section 4.1.2.7. A more sophisticated approach is to build the growth characteristics into the models using a stochastic simulation method, as discussed in Section 3.4.1 and Chapter 4.3.

### *4.1.3.2 Temperature and Fire*

In general, the moduli of elasticity, shear moduli, and strengths of wood decrease when heated or increase when cooled (FPL, 2010). The change in properties that occurs when wood is quickly heated or cooled is termed an 'immediate' effect. At temperatures below 100 °C, the immediate effect is essentially reversible, meaning the property will return to the state at the original temperature if the temperature change is rapid.

At elevated temperatures, the effect is irreversible. This permanent effect is caused by degradation of the wood, resulting in loss of weight and strength. The effects in most fire events are irreversible. Above 300 °C, wood is fully converted into char and has no strength or stiffness.

Deriving realistic temperature-dependent mechanical properties requires taking into account complicated algorithms, such as thermal transport by mass flow (e.g., moisture/air movement), the constantly changing geometry, and the formation of cracks in charcoal by thermal stresses. The complexity of these problems leads to a huge input effort, coupled simulations, and lengthy calculations. Simplified relationships between the mechanical properties and the temperature are conventionally adopted to implicitly account for the complex physical and chemical phenomena (European Committee for Standardization, 2004; Laplanche et al., 2006). The local values of mechanical properties for wood-based members should be multiplied by a temperature-dependent reduction factor, $k_{MP}$. A multilinear reduction model, Equation 31, is usually used to describe the effect of temperature on the modulus of elasticity, shear modulus, and strength of wood (see Figure 13):

$$\boldsymbol{k_{MP}} = \begin{cases} \boldsymbol{k_{MP,1}} & \boldsymbol{T \le T_1} \\ \boldsymbol{k_{MP,1} + \frac{T - T_1}{T_2 - T_1}\left(k_{MP,2} - k_{MP,1}\right)} & \boldsymbol{T_1 < T \le T_2} \\ \boldsymbol{k_{MP,2} + \frac{T - T_2}{T_3 - T_2}\left(k_{MP,3} - k_{MP,2}\right)} & \boldsymbol{T_2 < T \le T_3} \\ \boldsymbol{k_{MP,3}} & \boldsymbol{T_3 < T} \end{cases} \qquad [31]$$

where $k_{MP}$ is the temperature reduction factor for mechanical properties, and $k_{MP,i}$ is the temperature reduction factor for mechanical properties at different temperature, $T_i$.

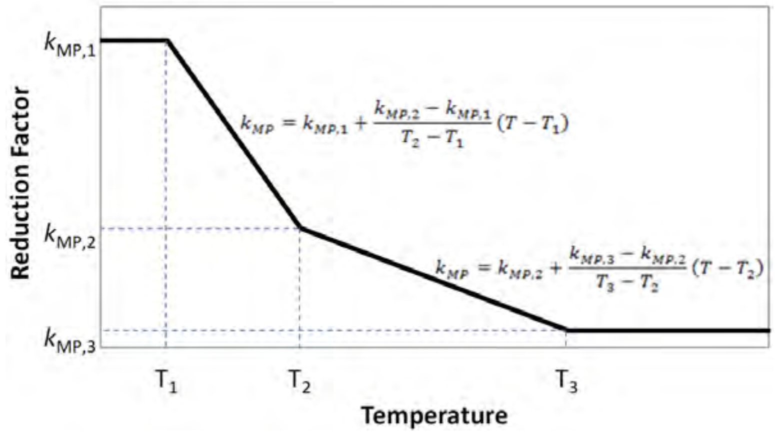


**Figure 13. Reduction factor for mechanical properties versus temperature**

The critical temperatures and corresponding reduction factors for wood-based products are given in Table 2 (Chen et al., 2020). The reduction factors for the tension, compression, and shear strength, and the modulus of elasticity parallel to grain of softwood in EN1995-1-2 (European Committee for Standardization, 2004) are adopted for wood-based members exposed to a standard fire in CAN/ULC S101 (SCC, 2014), ASTM E119 (ASTM, 2016), and ISO 834-1 (ISO, 2012), as shown in Figure 14. According to EN1995-1-2, the same reduction of strength as for compression parallel to grain may be applied to compression perpendicular to grain; for shear with both stress components perpendicular to grain (rolling shear), the same reduction of strength may be applied as for compression parallel to grain. Based on the Gerhards (1982) test results, it is reasonable to apply the same reduction of modulus of elasticity parallel to grain to the modulus of elasticity perpendicular to grain, and shear modulus parallel and perpendicular to grain, and the same reduction of compressive strength parallel to grain to tensile and shear strength perpendicular to grain. Due to lack of research data, the influence of temperature on other parameters for the constitutive model, for example, Position's ratios, hardening, and softening, can be neglected.

**Table 2. Critical temperatures and corresponding reduction factors for wood-based products**

| $i$ | $T_i$ [°C] | $k_{MP,i}$ | | | |
|---|---|---|---|---|---|
| | | $E_L$, $E_R$, $E_T$, $G_L$, $G_R$, and $G_T$ | $\sigma_{Lo,T}$ | $\sigma_{Lo,C}$, $\sigma_{Ro,C}$, $\sigma_{To,C}$, $\sigma_{Ro,T}$, $\sigma_{To,T}$, and $\sigma_{RTo}$ | $\sigma_{LRo}$ and $\sigma_{TLo}$ |
| 1 | 20 | 1.00 | 1.00 | 1.00 | 1.00 |
| 2 | 100 | 0.425 | 0.65 | 0.25 | 0.40 |
| 3 | 300 | 0.01* | 0.01* | 0.01* | 0.01* |

*Note: * 0.01 is suggested to avoid convergence problems in the analysis.*

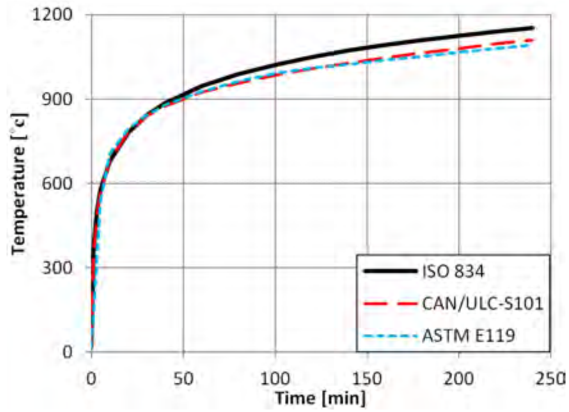


**Figure 14. Standard time-temperature curves**

Consequently, a simple conductive heat transfer analysis and thermal-mechanical analysis can be carried out without needing to specifically model many of the physical complexities of timber combustion and charring. Effects like moisture migration, transient thermal creep, formation of char, shrinking, and cracking of charcoal are represented by adjusted 'effective values' rather than using measured material properties. The literature contains many different proposals for the temperature-dependent mechanical properties of timber (e.g., Buchanan, 2002; Cachim & Franssen, 2009; Frangi, 2001; Hopkin et al., 2011; König, 2006; König & Walleij, 1999). A 'k-ρ-c model' (European Committee for Standardization, 2004), which implicitly takes into account a moisture content of 12% in the density function and heat of vaporisation in the specific heat function, is usually adopted to determine the thermophysical properties of timber under standard fire exposure (Figure 14). Table 3 gives the thermal conductivity, specific heat, and ratio of density to dry density of softwood with temperature (European Committee for Standardization, 2004). The thermal conductivity perpendicular to grain listed in Table 3 is derived by scaling down the conductivity parallel to grain using an average factor of 1.8 (FPL, 2010). Given that wood is converted into char at 300 °C, the properties beyond that threshold are 'effective values', as explained by König and Walleij (1999). Average values for the thermal expansion coefficient of oven-dry wood are 0.0038%/°C in the longitudinal direction and between 0.019%/°C and 0.038%/°C in the transverse direction for most species of wood (FPL, 2010).

The modelling approach described in this section has been implemented in Wood$^{ST}$ (Chen et al., 2020). Figure 11 shows an application of Wood$^{ST}$ on the modelling of a wood-frame floor exposed to fire.

#### *4.1.3.3 Moisture Content*

Wood can be characterised as a natural, cellular, polymer-based, hygrothermal viscoelastic material (Mackerle, 2005). The effect of moisture content (mostly ambient humidity) on the mechanical behaviour of timber structures is seen as swelling and shrinkage. Swelling and shrinkage create internal stresses that can lead to shape distortion. The moisture content also affects the mechanical and rheological properties in which the influence of moisture prevails. With increasing moisture content, the stiffness and strength properties first increase slightly and then decrease until fibre saturation is reached, as shown in Figure 15. Note that moisture affects perpendicular-to-grain properties more than it does parallel-to-grain properties.

Fibre saturation refers to saturation of the cell walls with water, but no liquid exists in the cell cavities. The fibre saturation point of wood averages about 30% moisture content, but it can vary by several percentage points in different species and even pieces of wood (FPL, 2010). It is generally assumed that the mechanical properties do not change above the saturation point.

**Table 3. Thermal properties for standard fire exposure**

| Temperature [°C] | Thermal conductivity [W/(m·K)] | | Specific heat [kJ/(kg·K)] | Ratio of density to dry density[(a)] |
|---|---|---|---|---|
| | Parallel | Perpendicular | | |
| 20 | 0.12 | 0.07 | 1.53 | 1+ω |
| 99 | | | 1.77 | 1+ω |
| 100[b] | | | 13.60[b] | 1+ω |
| 120 | | | 13.50 | 1.00 |
| 121[b] | | | 2.12[b] | 1.00 |
| 200 | 0.15 | 0.08 | 2.00 | 1.00 |
| 250 | | | 1.62 | 0.93 |
| 300 | | | 0.71 | 0.76 |
| 350 | 0.07 | 0.04 | 0.85 | 0.52 |
| 400 | | | 1.00 | 0.38 |
| 500 | 0.09 | 0.05 | | |
| 600 | | | 1.40 | 0.28 |
| 800 | 0.35 | 0.19 | 1.65 | 0.26 |
| 1200 | 1.50 | 0.83 | 1.65 | 0.01[(b)] |

*Note: Data can be derived using linear interpolation for empty cells. (a) ω is the moisture content; and (b) data is added or modified on purpose to avoid convergence problem during the modelling.*

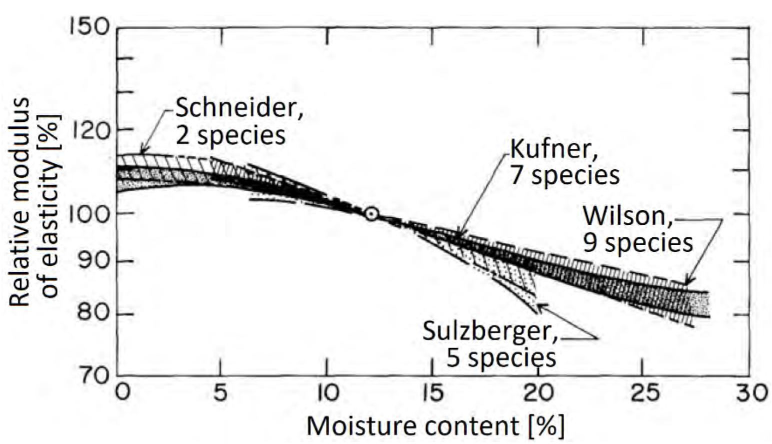


**Figure 15. Effect of moisture content at about 20 °C on modulus of elasticity parallel to grain (Gerhards, 1982): 100% at 12% moisture content**

In normal service environments (e.g., temperature below 50 °C), the effect of humidity on the mechanical properties of timber structures is much more significant than temperature. Like the effect of temperature, the influence of moisture content, for example, reduction factors, can be represented using a quadratic curve or a multi-segment straight line derived by fitting the test results. The mechanical properties are often considered to be constant above the fibre saturation point, equalling the values at the fibre saturation point.

The timber structures under changing moisture content conditions may be simply simulated by conducting thermal-moisture analogy analysis. The moisture content [%] and the shrinkage coefficient [% length/% moisture content] can be analogised as temperature [°C] and thermal expansion coefficient [% length/°C]. Average shrinkage values from green to oven-dry are 0.15% longitudinally and 6.0% transversely for most species (FPL, 2010). Since wood becomes dimensionally stable beyond the fibre saturation point, that is, 30%, the converted thermal expansion coefficient can be taken as 0.005%/°C in the longitudinal direction and 0.2%/°C in the perpendicular direction (Chen, 2019). In addition, the reduction factors representing the influence of moisture content should be converted accordingly.

### 4.1.3.4 Creep

Wood is a rheological material and deforms depending upon the loading history and the elapsed time. The creep of wood is a highly nonlinear and occurs in three phrases (Figure 16): primary, secondary, and tertiary. Primary creep is a linear viscoelastic phase during which the rate of deformation accumulation decreases with elapsed time. Secondary creep is a nonlinear viscoelastic phase during which the rate of deformation accumulation is constant. Tertiary creep is a nonlinear viscoelastic phase during which the rate of deformation accumulation increases with elapsed time. Wood is assumed to be linear viscoelastic, and therefore, reversible up to a certain stress level (the ratio of applied load to the short-term strength), called the 'limit of linearity' (Reichel & Kaliske, 2015). Beyond the limit of linearity, a disproportional increase of irreversible deformation occurs that can lead to creep failure at high stress levels, as illustrated in Figure 16. The terms 'creep rupture' and 'static fatigue' are synonymous and refer to a situation where tertiary deformation has progressed to the point of failure. In addition to the stress level, types and directions of loading significantly influence creep (Konopka et al., 2017). Deformations due to shear and torsional loading are typically larger than those due to compressive loading, which in turn are larger than those of tensile loading at the same stress level. Creep resulting from loading perpendicular to the grain is much more noticeable than creep from loading parallel to the grain.

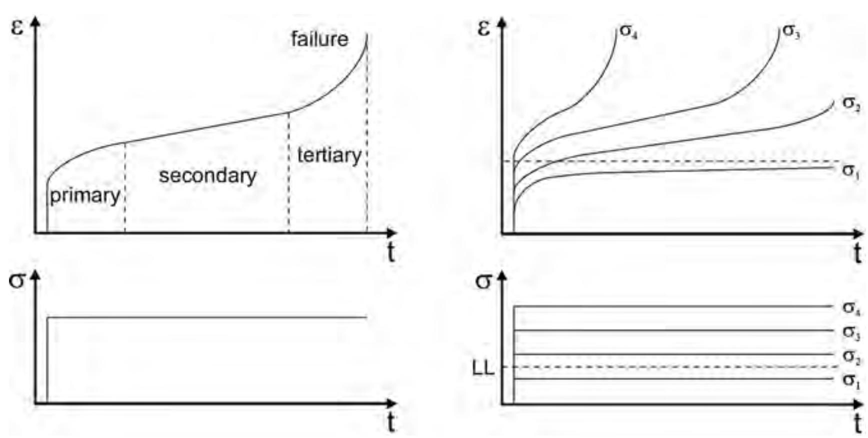


**Figure 16. Creep phases with dependency on loading (Reichel & Kaliske, 2015): LL indicates the limit of linearity**

In broad terms, the rheological behaviour is also a function of the thermal and moisture histories and of their interaction with the loading history (Smith, Landis, & Gong, 2003). The dependency of viscoelastic creep behaviour on temperature is often considered by applying a time-temperature-equivalence hypothesis (Dlouhá et al., 2009). A change in Young's modulus with respect to temperature is equivalent to a shift in time on the logarithmic timescale. However, the largest impact on the process of creep is caused by changing moisture content, the so-called mechanosorptive effect (Toratti, 1992). This effect is often assumed to be time-independent since the influence of time is much smaller.

Models developed to describe the creep process can be categorised into three groups: structural models, mechanical (rheological) models, and purely mathematical models. Structural models are based on molecular features of the material (i.e., microscopic, submicroscopic) and aim to directly describe the material behaviour. Combining the theory of hydrogen bond breaking and rebonding and a lenticular trellis model is most suitable for simulating a creep process of wood (Hanhijärvi, 1995). What numerous phenomenological approaches have in common is that their macroscopic parameters are calibrated to the results of specific experiments. Mechanical and mathematical models are phenomenological approaches. Mathematical approaches may be described as pure approximation functions with a potentially lower number of required inputs and a good adaptability to experimental measurements. Utilising rheological models is a compromise in complexity, number of input parameters, and representation of physical processes. Rheological models provide a simpler physical interpretation, which is the most challenging for a mathematical approach. Rheological models composed of the basic 'spring' (elastic behaviour) and 'dashpot' (viscous behaviour) elements can describe linear viscoelastic behaviour. Within the Maxwell element, spring and dashpot are connected serially; the parallel arrangement is called the Kelvin element. Both Maxwell and Kelvin elements are frequently used to describe the mechanosorptive responses of wood (Bažant, 1985).

At a higher level, a standard-solid body model consists of a spring connected in series to a Kelvin element whereas a Burgers model combines one Kelvin element and one Maxwell element. The standard-solid body model sufficiently captures primary creep, whereas a Burgers model produces a constant creep velocity and thus adequately describes the secondary creep phase. These characterising models simply describe the phenomena to a certain degree, but the extended standard-solid body model is more general and comprehensive and captures all phases of the creep process, including mechanosorption and creep failure. The extended standard-solid body model includes a serially connected Bingham element to describe the secondary phase, that is, the viscoplastic deformation (Figure 17). Whereas the sum of strains due to mechanical load, hygroexpansion and mechanosorption is captured in one equation with respect to the origin of loads, the total strain ($\varepsilon$) corresponding to Figure 17, expressed as the structural response, is given as the sum of elastic ($\varepsilon^{el}$), viscoelastic ($\varepsilon^{ve}$) and viscoplastic strain ($\varepsilon^{vp}$):

$$\boldsymbol{\varepsilon} = \boldsymbol{\varepsilon}^{el} + \boldsymbol{\varepsilon}^{ve} + \boldsymbol{\varepsilon}^{vp} \qquad [32]$$

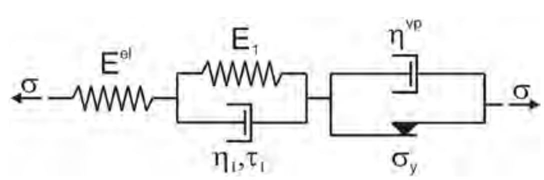


**Figure 17. Extended standard-solid body model (one-dimensional) (Reichel & Kaliske, 2015)**

The tertiary creep and creep failure can be modelled using a strain-energy density approach. Depending on the stress level, different time-strain functions might lead to creep failure at a high stress level (Figure 18).

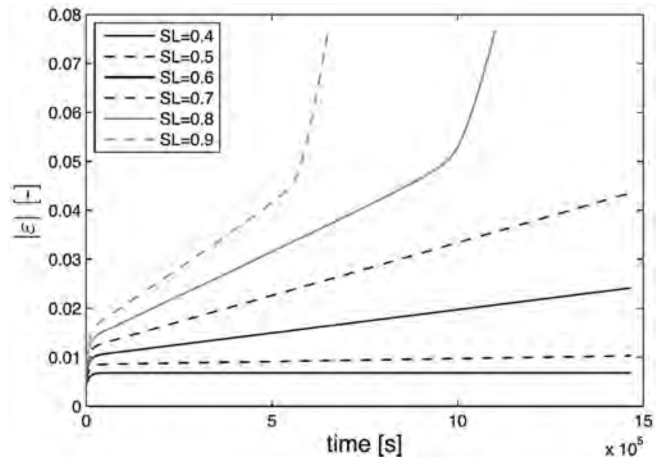


**Figure 18. Time-dependent deformation of spruce wood in tangential compression depending on stress level (Reichel & Kaliske, 2015)**

#### 4.1.3.5 Duration of Load

Strength of wood under constant loading decreases with time, as illustrated in Figure 19. This phenomenon is known as duration of load (DOL). The DOL feature distinguishes timber engineering from the structural engineering of other commonly used materials (e.g., steel), whose strength is little affected by the load history. DOL also depends on the current climate and climate history. The combined action of load and change in moisture content further reduce load-carrying capacity (Svensson, 2009).

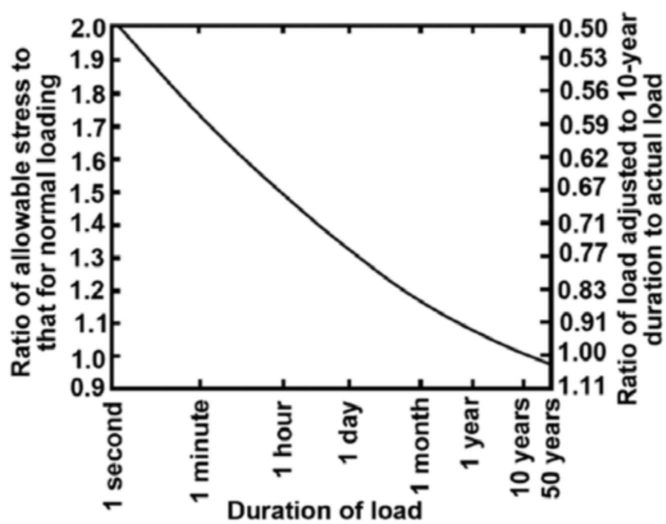


**Figure 19. Relation of strength to duration of load (FPL, 2010)**

Six types of models have been developed to predict the DOL effect of an arbitrary load on the strength of a structural wood member. The first models for the stress level versus time to failure were linear and nonlinear regression curves based on the FPL-Madison test results, called Madison curves. The hyperbolic Madison curves (Pearson, 1972; Wood, 1947; Wood, 1951) were determined based on long-term constant load tests, short-term ramp load tests, and impact tests.

In Arrhenius type models, the natural logarithm of rate is proportional to the activation energy, under isothermal conditions, or to the ratio of applied load and short-term capacity (Gerhards, 1977, 1979; Gerhards & Link, 1987). Phenomenological type models (Foschi & Barrett, 1982; Foschi & Yao, 1986; Wood, 1951) are damage accumulation models which state that damage accumulation (rate) is a function of load, capacity, and load duration.

Fracture mechanics type models (Hilleborg, 1977; Nielsen, 1979) are based on the hypothesis that the material contains ultracracks and that damage accumulates when the cracks grow. Failure starts when ultracracks in a material region connect and form propagating microcracks. Strain energy-type models (Bach, 1973; Fotheringham & Cherry, 1978; Fridley et al., 1992; Liu & Schaffer, 1997) postulate that there is a limit for the energy input or a defined fraction of the energy input, where energy input on or above this limit leads a failure state. Deformation kinetics type models (Caulfield, 1985; Fish, 1983; van der Put, 1989) describe the breaking and rebonding of bonds between molecules in wood cells under long-term effects. Failure as a result of long-term loading is determined by a localised strain deformation, that is, strain limit.

These models can be incorporated into the material constitutive models. Alternatively, the strengths are scaled up or down using one of the above-mentioned models before inputting them into the material models.

## 4.1.4 Summary

Appropriate material models are the fundamental basis of reliable simulations, especially for timber structures. In this chapter, sub-models for describing the elastic properties, strength criterion, post-peak softening for quasi-brittle failure modes, plastic flow and hardening rule for yielding failure modes, and densification perpendicular to grain are discussed. Depending on the modelling complexities, scenarios, and demands, however, different constitutive models with various combinations of the sub-models can be adopted. Typical constitutive models developed for wood-based materials and the derivation of model input are introduced. The key influencing factors, including growth characteristics, temperature and fire, moisture content, creep, and DOL are discussed along with corresponding modelling recommendations. The information presented in this chapter is intended to help practising engineers and researchers become more acquainted with the constitutive models of timber structures.

## 4.1.5 References

Akter, S., Serrano, E, & Bader, T. (2021). Numerical modelling of wood under combined loading of compression perpendicular to the grian and rolling shear. *Engineering Structures, 244,* 112800. https://doi.org/10.1016/j.engstruct.2021.112800

ASTM. (2016). ASTM E119: Standard test methods for fire tests of building construction and materials. West Conshohocken: ASTM International.

AWC. (2018). National design specification for wood construction. American Wood Council.

Bach, L. (1973). Reiner–Weisenberg's theory applied to time-dependent fracture of wood subjected to various modes of mechanical loading. *Wood Science, 5*(3), 161-171.

Bažant, Z. P. (1985). Constitutive equation of wood at variable humidity and temperature. *Wood Science and Technology, 19*(2), 159-177. https://doi.org/10.1007/BF00353077

Bodig, J. (1965). The effect of anatomy on the initial stress-strain relationship in transverse compression. *Forest Products Journal, 15*, 197-202.

Bodig, J., & Jayne, B. A. (1982). *Mechanics of Wood and Wood Composites*. New York: Van Nostrand Reinhold.

Buchanan, A. (2002). *Structural Design for Fire Safety*. John Wiley & Sons Ltd.

Cabrero, J., Blanco, C., Gebremedhin, K., & Martín-Meizoso, A. (2021). Assessment of phenomenological failure criteria for wood. *European Journal of Wood and Wood Products*, *70*, 871-882.

Cachim, P., & Franssen, J. (2009). Comparison between the charring rate model and the conductive model of Eurocode 5. *Fire and Materials, 33*, 129-143. https://doi.org/10.1002/fam.985

Caulfield, D. F. (1985). A chemical kinetics approach to the duration-of-load problem in wood. *Wood and Fiber Science,* (17), 504–521.

Chen, Z. (2011). *Behaviour of typical joints and the structure of Yingxian Wood Pagoda.* [Doctoral dissertation, Harbin Institute of Technology].

Chen, Z. (2019). *Effects of spray polyurethane foam on the structural behaviour of metal plate connected roof trusses: Phase I - Preliminary study*. Pointe-Claire, QC: FPInnovations.

Chen, Z., & Dagenais, C. (in press). Fire-resistance design of timber structures using coupled thermal-mechanical model Wood$^{ST}$. *Journal of Performance of Constructed Facilities*.

Chen, Z., Ni, C., & Dagenais, C. (2018). *Advanced wood-based solutions for mid-rise and high-rise construction: Modelling of timber connections under force and fire*. Pointe-Claire, QC: FPInnovations.

Chen, Z., Ni, C., Dagenais, C., & Kuan, S. (2020). Wood$^{ST}$: A temperature-dependent plastic-damage constitutive model used for numerical simulation of wood-based materials and connections. *Journal of Structural Engineering, 146*(3), 04019225. https://doi.org/10.1061/(ASCE)ST.1943-541X.0002524

Chen, Z., Zhu, E., & Pan, J. (2011). Numerical simulation of wood mechanical properties under complex state of stress. *Chinese Journal of Computational Mechanics, 28*(4), 629-634, 640.

Coulomb, C. A. (1773). Mémoires de mathématique et de physique. *L'Imprimerie Royale, 7*, 343–382.

CSA Group. (2019). *CSA O86:19 – Engineering design in wood*. CSA Group.

Dagenais, C., & Osborne, L. (2013). *Development of a Canadian fire-resistance design method for massive wood members*. Pointe-Claire, QC: FPInnovations.

Danielsson, H., & Gustafsson, P. J. (2013). A three dimensional plasticity model for perpendicular to grain cohesive fracture in wood. *Engineering Fracture Mechanics, 98*, 137-152. https://doi.org/10.1016/j.engfracmech.2012.12.008

De Borst, R. (2001). Some recent issues in computational failure mechanics. *International Journal for Numerical Methods in Engineering, 52*(1 - 2), 63-95. https://doi.org/10.1002/nme.272

Dlouhá, J., Clair, B., Arnould, O., Horáček, P., & Gril, J. (2009). On the time-temperature equivalency in green wood: Characterisation of viscoelastic properties in longitudinal direction. *Holzforschung, 63*(3), 327-333. https://doi.org/10.1515/HF.2009.059

Easterling, K. E., Harryson, R., Gibson, L. J., & Ashby, M. F. (1982). On the mechanics of balsa and other woods. *Proceedings of the Royal Society of London. Series A, Mathematical and Physical Sciences,* (383), 31-41.

European Committee for Standardization. (2004). Eurocode 5: Design of timber structures – Part 1-2: General - structural fire design.

Fish, A. M. (1983). *Thermodynamic model of creep at constant stresses and constant strain rates* (US Army Corps of Engineers, CRREL Rep. 83–33). https://erdc-library.erdc.dren.mil/jspui/bitstream/11681/9285/1/CR-83-33.pdf

Foschi, R. O., & Barrett, J. D. (1982). Load-duration effects in Western Hemlock Lumber. *Journal of the Structural Division, 108*(7), 1494-1510. https://doi.org/10.1061/JSDEAG.0005984

Foschi, R. O., & Yao, F. J. (1986, September). *Another look at three duration of load models* [Conference presentation]. Council for Research and Innovation in Building and Construction CIB-W18/19-9-1, Florence, Italy.

Fotheringham, D. G., & Cherry, B. W. (1978). Strain rate effects on the ratio of recoverable to nonrecoverable strain in linear polyethylene. *Journal of Material Science*, *13*(2), 231–238. https://doi.org/10.1007/BF00647765

FPL. (2010). *Wood Handbook – Wood as an Engineering Material*. Madison, WI: Forest Products Laboratory (FPL).

Frangi, A. (2001). *Brandverhalten von Holz-Beton-Verbunddecken.* [Doctoral dissertation, Eidgenössische Technische Hochschule Zürich]. https://doi.org/10.3929/ethz-a-004228944

Franke, B., & Quenneville, P. (2011). Numerical modeling of the failure behavior of dowel connections in wood. *Journal of Engineering Mechanics, 137*(3), 186-195. https://doi.org/10.1061/(ASCE)EM.1943-7889.0000217

Fridley, K. J., Tang, R. C., & Soltis, L. A. (1992). Load-duration effects in structural lumber: strain energy approach. *Journal of Structural Engineering, 118*(9), 2351-2369. https://doi.org/10.1061/(ASCE)0733-9445(1992)118:9(2351)

Gerhards, C. (1977, October 10–12). *Time-related effects of loads of strength of wood* [Conference presentation]. Conference on Environmental Degradation of Engineering Materials College of Engineering, Blacksburg, VA, USA.

Gerhards, C. C. (1979). Time-related effects of loads of wood strength: A linear cumulative damage theory. *Wood science*, *11*(3), 139-144.

Gerhards, C. (1982). Effect of moisture content and temperature on the mechanical properties of wood: An analysis of immediate effects. *Wood and Fiber Science, 14*, 4-36.

Gerhards, C., & Link, C. L. (1987). A cumulative damage model to predict load duration characteristics in lumber. *Wood and Fiber Science*, *19*(2), 147-164.

Gharib, M., Hassanieh, A., Valipour, H., & Bradford, M. A. (2017). Three-dimensional constitutive modelling of arbitrarily orientated timber based on continuum damage mechanics. *Finite Elements in Analysis and Design, 135*, 79-90. https://doi.org/10.1016/j.finel.2017.07.008

Hanhijärvi, A. (1995). *Modelling of creep deformation mechanisms in wood.* [Doctoral dissertation, Helsinki University of Technology].

Hashin, Z. (1980). Failure criteria for unidirectional fiber composites. *Journal of Applied Mechanics, 47*(2), 329-334. https://doi.org/10.1115/1.3153664

Hill, R. (1950). *The mathematical theory of plasticity*. Oxford, UK: Oxford University Press.

Hilleborg, A. (1977). *Materialbrott [Material failure]* (Rep. TVMB-3004). Lund, Sweden.

Hirai, T. (2005). Anisotropy of wood and wood-based materials and rational structural design of timber constructions. *The Proceedings of Design & Systems Conference, 2005.15*, 19-22. https://doi.org/10.1299/jsmedsd.2005.15.19

Hoffman, O. (1967). The brittle strength of orthotropic materials. *Journal of Composite Materials, 1*(2), 200-206.

Hopkin, D. J., El-Rimawi, J., Silberschmidt, V., & Lennon, T. (2011). An effective thermal property framework for softwood in parametric design fires: Comparison of the Eurocode 5 parametric charring approach and advanced calculation models. *Construction and Building Materials, 25*(5), 2584-2595. https://doi.org/10.1016/j.conbuildmat.2010.12.002

ISO. (2012). Fire-resistance tests: Elements of building construction. Part 1: General requirements. Geneva: ISO.

Jessome, A. (2000). *Strength and related properties of woods grown in Canada* (Publication SP-514E). Vancouver: Forintek Canada Corporation.

Kharouf, N., McClure, G., & Smith, I. (2005). Postelastic behavior of single- and double-bolt timber connections. *Journal of Structural Engineering, 131*(1), 188-196. https://doi.org/10.1061/(ASCE)0733-9445(2005)131:1(188)

Khelifa, M., Khennane, A., El Ganaoui, M., & Celzard, A. (2016). Numerical damage prediction in dowel connections of wooden structures. *Materials and Structures, 49*(5), 1829-1840. https://doi.org/10.1617/s11527-015-0615-5

Khennane, A., Khelifa, M., Bleron, L., & Viguier, J. (2014). Numerical modelling of ductile damage evolution in tensile and bending tests of timber structures. *Mechanics of Materials, 68*, 228-236. https://doi.org/10.1016/j.mechmat.2013.09.004

König, J. (2006). Effective thermal actions and thermal properties of timber members in natural fires. *Fire and Materials, 30*(1), 51-63. https://doi.org/10.1002/fam.898

König, J., & Walleij, L. (1999). *One-dimensional charring of timber exposed to standard and parametric fires in initially unprotected and post-protection situations* (Report I 9908029). Stockholm: Trätek.

Konopka, D., Gebhardt, C., & Kaliske, M. (2017). Numerical modelling of wooden structures. *Journal of Cultural Heritage, 27*, S93-102. https://doi.org/ 10.1016/j.culher.2015.09.008

Laplanche, K., Dhima, D., & Rachet, P. (2006, August 6–10). *Thermo-mechanical analysis of the timber connection under fire using a finite element model* [Conference presentation]. World Conference on Timber Engineering, Portland, USA.

Liu, J. Y., & Schaffer, E. L. (1997). Duration of constant and ramp loading on strength of wood. *Journal of Engineering Mechanics, 123*(5), 489-494. https://doi.org/10.1061/(ASCE)0733-9399(1997)123:5(489)

Lubliner, J. (2008). *Plasticity theory*. New York: Dover Publications.

Mackerle, J. (2005). Finite element analyses in wood research: a bibliography. *Wood Science and Technology, 39*(7), 579-600. https://doi.org/10.1007/s00226-005-0026-9

Matzenmiller, A., Lubliner, J., & Taylor, R. L. (1995). A constitutive model for anisotropic damage in fiber-composites. *Mechanics of Materials, 20*(2), 125-152. https://doi.org/10.1016/0167-6636(94)00053-0

Mohr, O. (1900). Welche Umstände bedingen die Elastizitätsgrenze und den Bruch eines Materials. *Zeitschrift des Vereines deutscher Ingenieure, 46*, 1524-1530.

Nahas, M. (1986). Survey of failure and post-failure theories of laminated fiber-reinforced composites. *Journal of Composites, Technology and Research, 8*(4), 138-153. https://doi.org/10.1520/CTR10335J

Nielsen, L. F. (1979, August 14–16). *Crack failure of dead-, ramp- and combined loaded viscoelastic materials* [Conference presentation]. The 1st International Conference on Wood Fracture.

Norris, C. B. (1962). *Strength of orthotropic materials subjected to combined stresses*. (U.S. Department of Agriculture, Misc. Pub FPL-1816).

Oudjene, M., & Khelifa, M. (2009). Elasto-plastic constitutive law for wood behaviour under compressive loadings. *Construction and Building Materials, 23*(11), 3359-3366. https://doi.org/10.1016/j.conbuildmat.2009.06.034

Pearson, R. G. (1972). The effect of duration of load on the bending strength of wood. *Holzforschung, 26*(4), 153-158. https://doi.org/10.1515/hfsg.1972.26.4.153

Reichel, S., & Kaliske, M. (2015). Hygro-mechanically coupled modelling of creep in wooden structures, Part I: Mechanics. *International Journal of Solids and Structures, 77*, 28-44. https://doi.org/10.1016/j.ijsolstr.2015.07.019

Resch, E., & Kaliske, M. (2010). Three-dimensional numerical analyses of load-bearing behavior and failure of multiple double-shear dowel-type connections in timber engineering. *Computers & Structures, 88*(3), 165-177. https://doi.org/10.1016/j.compstruc.2009.09.002

Sandhaas, G., Kuilen, J.-W. d., & Blass, H. J. (2012, July 15–19). *Constitutive model for wood based on continuum damage mechanics* [Conference presentation]. World Conference on Timber Engineering, Auckland, New Zealand.

Sandler, I., DiMaggio, F., & Barron, M. (1984). An extension of the cap model inclusion of pore pressure effects and kinematic hardening to represent an anisotropic wet clay. In Desai, C., & Gallagher, R. (Eds.), *Mechanics of engineering materials*. New York: Wiley.

SCC. (2014). CAN/ULC-S101: Standard methods of fire endurance tests of building construction and materials. Standards Council of Canada.

Schmidt, J., & Kaliske, M. (2007). Simulation of cracks in wood using a coupled material model for interface elements. *Holzforschung, 61*(4), 382-389. https://doi.org/10.1515/HF.2007.053

Schmidt, J., & Kaliske, M. (2009). Models for numerical failure analysis of wooden structures. *Engineering Structures, 31*(2), 571-579. https://doi.org/10.1016/j.engstruct.2008.11.001

Simo, J. C., & Ju, J. W. (1987). Strain- and stress-based continuum damage models—I. Formulation. *International Journal of Solids and Structures, 23*(7), 821-840. https://doi.org/10.1016/0020-7683(87)90083-7

Sirumbal-Zapata, L. F., Málaga-Chuquitaype, C., & Elghazouli, A. Y. (2018). A three-dimensional plasticity-damage constitutive model for timber under cyclic loads. *Computers & Structures, 195*, 47-63. https://doi.org/10.1016/j.compstruc.2017.09.010

Smith, I., Landis, E., & Gong, M. (2003). *Fracture and fatigue in wood*. John Wiley & Sons Ltd.

Svensson, S. (2009). Duration of load effects of solid wood: A review of methods and models. *Wood Material Science & Engineering, 4*(3-4), 115-124. https://doi.org/10.1080/17480270903326157

Tabarsa, T., & Chui, Y. (2000). Stress-strain response of wood under radial compression. Part I. Test method and influences of cellular properties. *Wood and Fiber Science, 32*(2), 144-152.

Tabarsa, T., & Chui, Y. (2001). Characterizing microscopic behavior of wood under transverse compression. Part II. Effect of species and loading direction. *Wood and Fiber Science, 33*(2), 223-232.

Thelandersson, S., & Honfi, D. (2009, September 21–22). *Behaviour and modelling of timber structures with reference to robustness* [Conference presentation]. Joint Workshop of COST Actions TU0601 and E55, Ljubljana, Slovenia.

Toratti, T. (1992). *Creep of timber beams in a variable environment*. [Doctoral dissertation, Helsinki University of Technology].

Tresca, H. (1864). *Mémoire sur l'écoulement des corps solides soumis à de fortes pressions*. Paris: Gauthier-Villars.

Tsai, S., & Wu, E. (1971). A general theory of strength for anisotropic materials. *Journal of Composite Materials, 5*, 58-80.

van der Put, T. A. C. M. (1989). *Deformation and damage processes in wood*. [Doctoral dissertation, Delft University Press].

Von Mises, R. (1913). Mechanik der festen Körper im plastischdeformablen Zustand [Mechanics of solid bodies in plastic deformation state]. *Nachrichten von der Gesellschaft der Wissenschaften zu Göttingen (Mathematisch-physikalische Klasse), 4*, 582–592.

Winandy, J. E. (1994). Wood Properties. *USDA-Forest Service, Forest Products Laboratory, Encyclopedia of Agricultural Science, 4*, 549-561.

Wood, L. W. (1947). Behavior of wood under continued loading. *Engineering New Record, 139*(24), 113–119.

Wood, L. W. (1951). *Relation of strength of wood to duration of load* (U. S. Department of Agriculture, Rep. No. 1916).

Xu, B.-H., Bouchaïr, A., & Racher, P. (2014). Appropriate wood constitutive law for simulation of nonlinear behavior of timber joints. *Journal of Materials in Civil Engineering, 26*(6), 04014004. https://doi.org/10.1061/(ASCE)MT.1943-5533.0000905

Yamada, S., & Sun, C. T. (1978). Analysis of laminate strength and its distribution. *Journal of Composite Materials, 12*(3), 275-284. https://doi.org/10.1177/002199837801200305

Zhu, E., Chen, Z., Pan, J., & Wang, L. (2010). *Finite element modelling of the structural performance of Dou-Gong brackets of Yingxian Wood Pagoda* [Conference presentation]. World Conference on Timber Engineering, Florence, Italy.

Zhu, E. C., Guan, Z. W., Rodd, P. D., & Pope, D. J. (2005). A constitutive model for OSB and its application in finite element analysis. *Holz als Roh- und Werkstoff, 63*(2), 87-93. https://doi.org/10.1007/s00107-004-0513-y

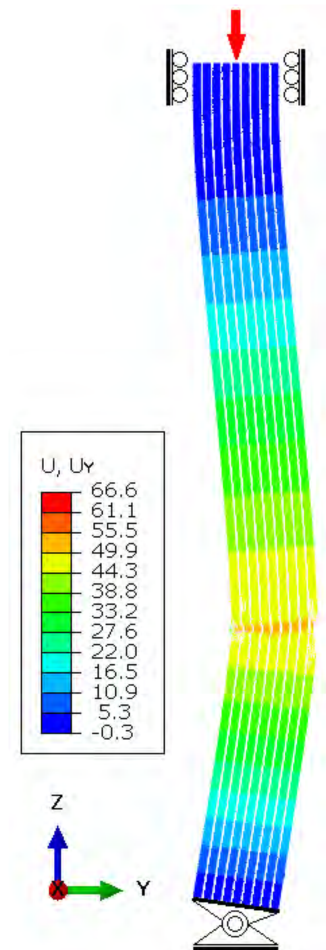


# CHAPTER 4.2

## Structural component analysis

**Authors**
Zhiyong Chen
Christian Dagenais
Yang Du

**Reviewers**
Sylvain Gagnon
Keven Durand
Zhongwei Guan

# TABLE OF CONTENTS

## 4.2.1 Introduction

Analysis of timber components under various loads is a classic topic. Numerous studies have been conducted on traditional wood-based products such as lumber. Corresponding design software packages, for example, WoodWorks®, are also available. However, there is little information on newer wood products such as cross-laminated timber (CLT), nail-laminated timber (NLT), dowel-laminated timber (DLT), and other types of composite components. This chapter introduces analysis methods and key considerations for modelling wood-based components as well as analytical and finite element (FE) methods that can be applied to various timber components. Analyses of strength, stability, and deflection are also covered.

## 4.2.2 Analysis Methods and Key Considerations for Modelling

### *4.2.2.1 Analysis Methods*

Of the two approaches used in the analysis and design of timber components, analytical models are very efficient for the specific cases for which the models have been developed. FE methods are capable of handling complex cases and can provide results that are more comprehensive than those provided by analytical methods. Eigenvalue buckling, linear load-displacement, and nonlinear load-displacement analyses are usually adopted to analyse timber components in FE modelling. Key input and output and applicable problems for different analysis methods are given in Table 1.

**Table 1. Typical analysis types for analysing timber components**

| Analysis method | Key input | Key output | Applicable problem |
|---|---|---|---|
| Eigenvalue buckling | Stiffness properties | Eigenvalues and buckling mode shapes | Elastic stability |
| Linear | Stiffness properties | Deformation, reaction, and stresses | Deflection |
| Nonlinear | Stiffness and strength properties | Deformation, stresses, yield/failure resistance and mode(s) | Strength and inelastic stability |

Linear analysis is the most common method to determine the deformation, reaction, and stresses when an element is in its elastic stage. With engineering adjustment, the lower bound of resistance and the corresponding failure mode of the components can be predicted manually based on the results of linear elastic analysis, for example, stress distribution and the highest stress, for simple cases. On the other hand, in order for the results to remain valid, linear analysis must ensure that the models are within the elastic range, that is, the stress components or stress combinations are lower than the material strength. This is difficult for some wood-based components with a complex composition because wood is anisotropic, with varying strengths and stiffness in different directions and under different load conditions (see Chapter 4.1).

Eigenvalue buckling analysis is commonly used to derive buckling resistances and mode shapes for beams and columns. This analysis is best suited for walls, slender beams, and columns where the members are likely to buckle in the elastic range. For beams and columns characterised by inelastic buckling, nonlinear analysis is preferrable in order to take into account the material nonlinearity, geometric nonlinearity, or both. Often, buckling modes obtained from eigenvalue buckling analysis can be used to generate imperfection in the models for post-buckling analysis (nonlinear analysis). It is worth noting that a timber beam with a high depth-to-width ratio could trigger compression buckling at the beam supports because the perpendicular-to-grain moduli of elasticity (MOEs) of wood-based components is much lower than the parallel-to-grain MOE.

Nonlinear analysis is capable of predicting the resistance, failure modes, and post-failure behaviour of analysed components, with or without imperfection (e.g., post-buckling analysis). This analysis requires more refined models, or comprehensive material models, for example, Wood$^{S}$ (Chen et al., 2011) and Wood$^{ST}$ (Chen et al., 2020), and specific input. In addition, it is essential that modellers are highly skilled at modelling, analysis, and result interpretation (see Chapter 3 for more information).

#### *4.2.2.2 Key Considerations for Modelling*

Although the basic methods of developing models for non-wood components can also be applied to wood-based components, some aspects are unique to wood-based components. The following are key considerations for modelling wood-based components:

- Wood is an anisotropic material, and its mechanical properties depend on various factors. Thus, a model must be adequate to the task of modelling wood-based components. (See Chapter 4.1 for more information.)
- Because material properties are strongly correlated with the wood grain (fibre direction), an adequate local coordinate system should be assigned to the wood-based components or the individual lumber or lamination.
- Wood is not homogeneous, but may have oblique fibre orientation (slope of grain), knots, and other growth characteristics which need to be taken into account (see Chapter 4.1).
- Engineered wood products, for example, laminated veneer lumber (LVL), and mass timber products, for example, glulam and CLT, usually possess bonding/glue surfaces between laminations. The adhesive in the bonding surfaces is usually very thin compared to each lamination. It is also stiff and strong enough to transfer the forces from one lamination to the other, and is commonly treated as rigid bonding. In cases where the adhesive or bonding surface is of interest, the adhesive layers should be modelled correctly, for example, using contact elements, with suitable stiffness and strength properties.
- Some mass timber products, such as CLT, are manufactured without edge gluing, so there are gaps between pieces of lumber in the same layer. If the products are simulated using 1D or 2D elements, the gaps should be taken into account by adopting effective mechanical properties. If the products are simulated using 3D elements, the gaps must be simulated to reflect their influence on the products' structural performance.
- Under uniform loads, where the individual pieces are assumed to deform to the same degree, or under small nonuniform loads, where the fasteners are engaged at a low-stress level, some mechanically laminated timber (MLT), for example, NLT and DLT, can be simplified as glued laminated timber (GLT), assuming infinite connections between individual pieces. In other cases, the influence of the connections between lumber members needs to be modelled accurately, for example, using springs or connection elements, because they play a crucial role in the structural performance. (See Chapter 5 for more information.)

## 4.2.3 Tension Components

Common tension (parallel to grain) components include webs and bottom chords of trusses (see Figure 1), bottom flanges in wood I-joists, chord members in diaphragms, end studs of shear walls, and occasionally bracing members. The bottom chords of trusses are often loaded in axial tension combined with bending. This section deals only with axially loaded members.

**Figure 1. Timber truss**

### *4.2.3.1 Analytical Methods*

Analysis of a component under axial tension is relatively straightforward. The tensile resistance, $T_r$, of the component can be calculated using Equation 1:

$$\boldsymbol{T_r = f_t A} \qquad [1]$$

where $f_t$ is the axial tensile strength of the component. This axial tensile strength must take into account the load-duration effect, service condition effect, size effect, treatment effect, and system effect according to the testing results or design standards, such as CSA O86 (CSA Group, 2019). $A$ is the cross-sectional area of the component. More than one cross-section is typically assessed when the cross-sectional area of components is not uniform or when cross-sections are weakened by, for example, fasteners.

CSA O86 only takes into account the size effect of the cross-section for sawn lumber and not the length effect. The design value of the gross section of glulam components has been decreased to compensate for the size effect. The National Design Specification (NDS) (American Wood Council, 2018) does take the size effect of the cross-section into account for sawn lumber, and both the size effect of the cross-section and the length effect, called volume effect, for glulam. EN 1995-1-1 (CEN, 2009) takes into account the size effect of the cross-section for sawn timber and for glulam, and both the size effect of the cross-section and the length effect for LVL.

The deformation, $\Delta$, of the component under axial tension force, $F$, can be calculated using Equation 2:

$$\Delta = \boldsymbol{\frac{FL}{AE}} \qquad [2]$$

where $E$ is the MOE of the component. This MOE must be adjusted by the service condition effect and treatment effect according to the testing results or design standards, such as CSA O86 (CSA Group, 2019). $L$ is the length of the component.

For composite components made of timber plus another material, forces usually transfer between different materials through specific mechanisms, such as, bonding. Such composite components can be simplified into a multiple spring model (see Figure 2) which includes the spring of the timber, $K_{timber}$, the spring of the other material, $K_{other}$, and the springs of the mechanism transferring the forces, $K_{tran}$. If the force-transferring mechanism is secured, it can be treated as rigid and the multiple spring model further simplified into a spring-in-parallel model.

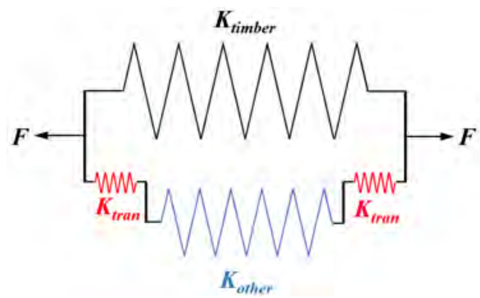


**Figure 2. Multiple spring model for a composite component**

#### *4.2.3.2 FE Methods*

Linear or nonlinear analysis can be conducted to analyse the deformation and resistance of components solicited in axial tension. MOE and Poisson's ratios are sufficient for the deformation analysis. Tension strength parallel to grain is required if the resistance of the components is of interest. In such a scenario, a suitable strength criterion and even a specific post-strength behaviour rule should be adopted.

Using FE models, the material properties can be homogeneous or assigned randomly according to a specific distribution function. With the later approach, the influence of the variability of wood-based products can be investigated directly using various stochastic FE modelling methods (Taylor & Bender, 1991) (see Chapter 3 for more information). The former approach can still be utilised to estimate this influence by varying the material input with the standard deviation of the material properties.

Tension components can be meshed with 3D solid, 2D plate/shell, and 1D bar elements, depending on the analysis requirements. The complexity of the models increases as the degree of freedom of elements is adopted. For components with notch(es) and/or opening(s), refined meshes should be applied to those locations if they are critical to the analysed components.

For composite components, the force-transferring mechanism between the timber and the other material must be modelled appropriately. To take as an example a glulam component with in-filled steel rods, the effect associated with the rod-timber interface, such as bond slip, should be modelled using proper contact elements or interaction models with specific stiffness and strength properties.

Boundary conditions of the models should represent the actual restrained situation for the tension components. The load should be applied to the designated area, rather than only at the single point (node) where significant concentrated stress and strain occur. Multiple point constraints techniques can be adopted.

As a practical or efficient solution, the multiple spring model (Figure 2) can be utilised for either pure wood components (for the length effect) or composite components. A more detailed spring model can be developed by combining a greater number of multiple spring models (as illustrated in Figure 3), each representing a section of the component, to better simulate the force-transferring mechanics between the timber and the other material.

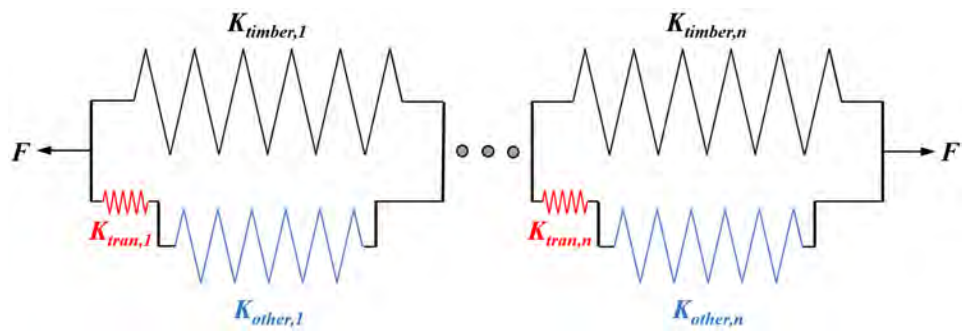


**Figure 3. Multiple spring models in series**

#### *4.2.3.3 Tension Perpendicular to Grain*

Designs that induce tensile stress perpendicular to grain are best avoided. If tensile stress perpendicular to grain cannot be avoided, mechanical reinforcement sufficient to resist all the resulting stresses should be considered. Therefore, it is essential to have FE models to verify if the components could fail due to perpendicular-to-grain tensile stress. Most of the rules for modelling timber components under parallel-to-grain tension are valid for analysing the stress perpendicular to grain and the potential failure of the components. MOE, Poisson's ratio, shear modulus, and tension strength perpendicular to grain are the required input. Refined meshes should be adopted where tension perpendicular to grain is most likely to occur.

### 4.2.4 Compression Components

Common axial compression components include sawn lumber studs, posts, webs and top chords of trusses (Figure 1), single member glulam and sawn timber columns (Figure 4), built-up sawn lumber columns, light wood-frame walls, and mass timber walls. The top chords of trusses are often loaded in compression combined with bending. This section deals only with axially loaded compression members.

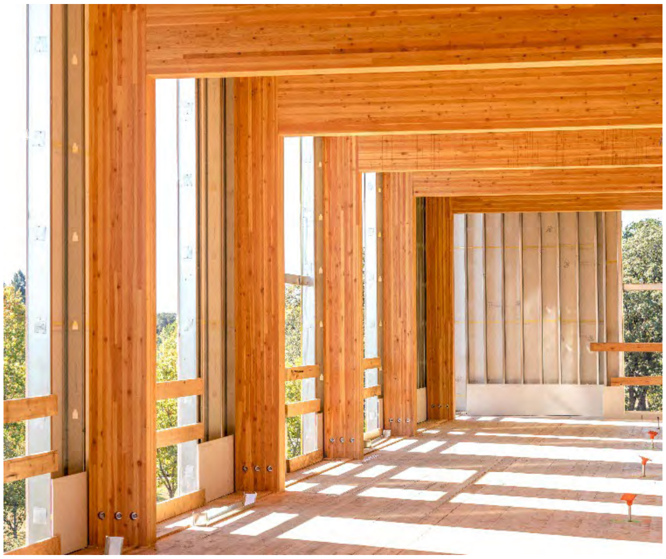

**Figure 4. Timber posts and beams**

#### *4.2.4.1 Analytical Methods*

Compression components are governed by strength, stability, or both, depending on the length-to-width ratio (as illustrated in Figure 5). Under an axial load, a short column, rather than buckling, is crushed by direct compression, while a long column will buckle and bend in a characteristic lateral movement. Buckling due to lateral deflection generally occurs before the axial compression stresses cause the material to fail. Intermediate-length columns fail via a combination of crushing and buckling. The length-to-width ratio is influenced by the boundary conditions and lateral supports of the components (Webber et al., 2015). Table 2 shows the influence of end restraints on the effective length.

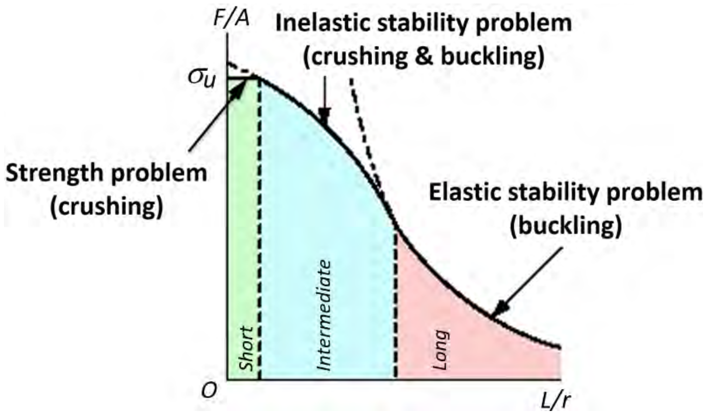


**Figure 5. Compression resistance versus slenderness (Courtesy of www.efunda.com).** ***Note: F is compression; A is cross-sectional area; $\sigma_u$ is the compression strength; L is effective length; and r is the radius of gyration of the cross-sectional area***

**Table 2. Minimum design values of effective-length factor, $K_e$, for compression members (CSA Group, 2019)**

| Degree of end restraint of compression member | $K_e$ | Symbol |
|---|---|---|
| Effectively held in position and restrained against rotation at both ends | 0.65 |  |
| Effectively held in position at both ends and restrained against rotation at one end | 0.80 |  |
| Effectively held in position at both ends but not restrained against rotation | 1.00 |  |
| Effectively held in position and restrained against rotation at one end, and restrained against rotation but not held in position at the other end | 1.20 | 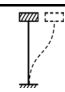 |
| Effectively held in position and restrained against rotation at one end, and partially restrained against rotation but not held in position at the other end | 1.50 |  |
| Effectively held in position but not restrained against rotation at one end, and restrained against rotation but not held in position at the other end | 2.00 | 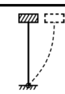 |
| Effectively held in position and restrained against rotation at one end but not held in position or restrained against rotation at the other end | 2.00 |  |

Note: Effective length $L = K_e L_o$, where $L_o$ is the distance between the centres of lateral supports of the compression member in the plane in which buckling is being assessed.

Traditionally, the analysis and design of columns is in three parts: a constant crushing capacity for short columns; an empirical curve for intermediate lengths; and a Euler formula for long columns (Johns, 2011). Nowadays, a single curve for the column stability (or slenderness) factor, aimed at reducing design strengths due to buckling, is typically adopted for all slenderness ratios. Take the CSA O86, for example: a formula based on the cubic Rankine-Gordon curve (Figure 6) is used to obtain the resistance of axial compression components.

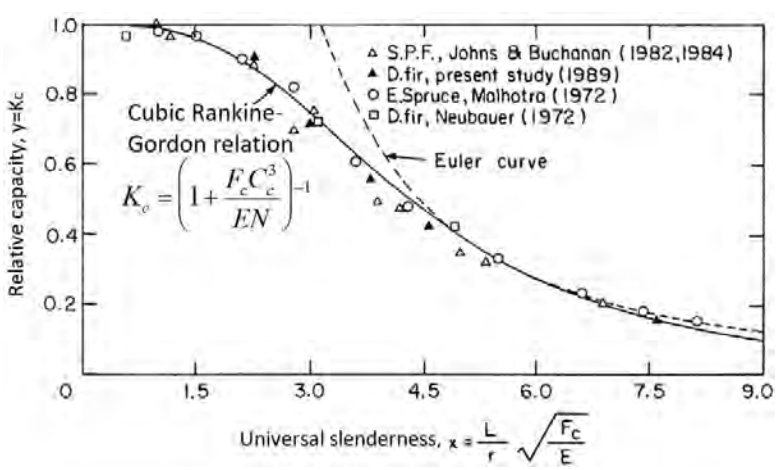


**Figure 6. Tangent cubic Rankine-Gordon and Euler formula versus column data (Zahn, 1989)**

The resistance, $P_r$, of the compression component can be calculated using Equation 3:

$$P_r = f_c A K_{Zc} K_C \qquad [3]$$

where $f_c$ is the compressive strength of the component. This compressive strength must take into account the load-duration effect, service condition effect, treatment effect, and system effect according to the testing results or design standards, such as CSA O86. $A$ is the cross-sectional area of the component. $K_{Zc}$ and $K_C$ are the size and slenderness factors, respectively, and are determined using different equations depending on the product and design standards. The deformation, $\Delta$, of the component before buckling under compression, *F*, can also be calculated using Equation 2.

Composite components under compression can be analysed using a transformed section analysis method (Brown & Suddarth, 1977). After transferring the non-timber material section into an equivalent timber section, a composite component can be treated as a pure timber component. Design standards such as CSA O86 and NDS provide specific methods (e.g., using strength-reduction factors) to design built-up columns connected with nails, bolts, and shear-plates with certain configurations. Other built-up columns, such as those connected using self-tapping screws, have to be analysed using FE methods.

#### *4.2.4.2 FE Methods*

Usually, eigenvalue buckling analysis is sufficient to determine the resistance of long compression components governed by elastic buckling. MOE and Poisson's ratios are the only required material input. With correct boundary conditions, for example, restraints at the ends of components and loading conditions, eigenvalue buckling analysis can be used to calculate the load magnitudes that cause buckling and associated buckling modes. Theoretically, it is possible to calculate as many buckling models as the number of degrees of freedom in the model. Most often, though, only the first buckling mode and the associated buckling-load factor, through which the buckling load is derived by multiplying the applying loads, need to be calculated. This is because higher buckling modes have no chance of occurring: buckling most often causes catastrophic failure or renders the structure unusable.

Determining the resistance of intermediate and short compression components governed or affected by material strength requires nonlinear analysis. The stiffness, tension, and compression strengths parallel to grain are required as material input. For some specific cases, for example, CLT panels which include transverse layers governed by rolling shear, shear strengths are also needed. Appropriate constitutive models such as Wood$^{ST}$ are best for such components. Moreover, geometric imperfection is required to determine the resistance of compression components using nonlinear analysis.

In FE modelling, there are two ways to introduce initial geometric imperfections. One introduces the lowest buckling mode or a linear combination of several buckling modes into the structure; the other introduces the initial geometric imperfections in an assumed form or in a random way. The amplitude of the imperfection is considered to be 1‰ of the length, or the tolerance of straightness specified in the corresponding product standards, for example, 6 mm for glulam equals or is less than 6 m in length (CSA Group, 2016).

The methods that take into account considering the influence of variability of wood-based products, and the modelling considerations for selecting elements, meshing notches and openings, simulating the force transferring mechanisms in composite components, and developing boundary conditions and loading (discussed in Section 4.2.3.2) also apply to compression components.

As an example, a simulated Spruce-Pine 12c-E glulam column 3.4 m long with a cross-section of 342 × 365 mm was analysed. The column was effectively held in position at both ends and restrained against rotation at the top. A 3D FE model was developed using ABAQUS with Wood[ST]. The first buckling mode obtained from eigenvalue buckling analysis with an amplitude of 6 mm (CSA Group, 2016) was assigned to the model as geometric imperfection. Under a vertical load, the column buckled and failed at about 1/3 of the height during the nonlinear analysis. Figure 7 shows the buckling deformation and failure of the glulam column model. Using material properties converted from the design values of CSA O86 (according to Section 4.1.2.7), the predicted compression resistance of the column was very close to the value estimated using the analytical method, with a difference of about 5%.

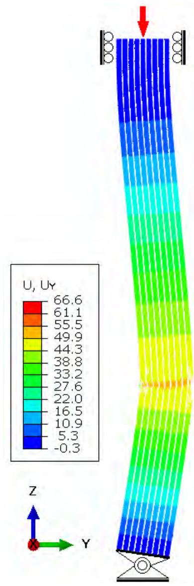


**Figure 7. Deformation (deformation scale factor = 3) of a glulam column under a vertical point load**

Most columns and walls under in-plane compression develop global flexural buckling, as illustrated in Figure 7. In some cases, like a long wall or a wall resisting both bending and compression forces (for example, wind and gravity loads) with low MOE in the loading direction (Pina et al., 2019), however, local buckling, e.g., the one shown in Figure 8, can occur before the global flexural buckling. As mentioned above, the column-buckling can also occur at the supports of a deep beam.

**Figure 8. Deformation of log-walls under vertical loads (Bedon & Fragiacomo, 2015)**

## 4.2.5 Bending Components

Common bending components, including beams (Figure 9), girders, joists, purlins, lintels, headers, sheathing, and decking, typically have loads applied perpendicular to their long axis. Many wood-based products, such as glulam, structural composite lumber, sawn lumber, built-up beams, and prefabricated wood I-joists, can be used as common bending components.

**Figure 9. Glulam beams**

### *4.2.5.1 Analytical Methods*

Bending components are governed by bending, shear, or deflection failure. Bending failure can be caused by material strength, instability, or a combination of both, depending on the slenderness of the component (see Figure 10). The slenderness is influenced by the beam cross-section sizes and the effective length, as determined by the type of load, lateral support spacing, and boundary conditions of the components (see Table 3). A stocky beam subjected to bending will fail before the beam buckles, while a slender beam loaded the same way will fail as a result of elastic buckling (lateral-torsional buckling) manifested by lateral movement and twist (or torsion) of the beam cross-section (Figure 11). For slender beams, buckling generally occurs before the stresses can cause the material to fail and, in such instances, the moment resistance is determined by the stiffness of the component. Beams with intermediate slenderness ratios fail as a result of inelastic buckling where the moment resistance is affected by both component strength and stiffness.

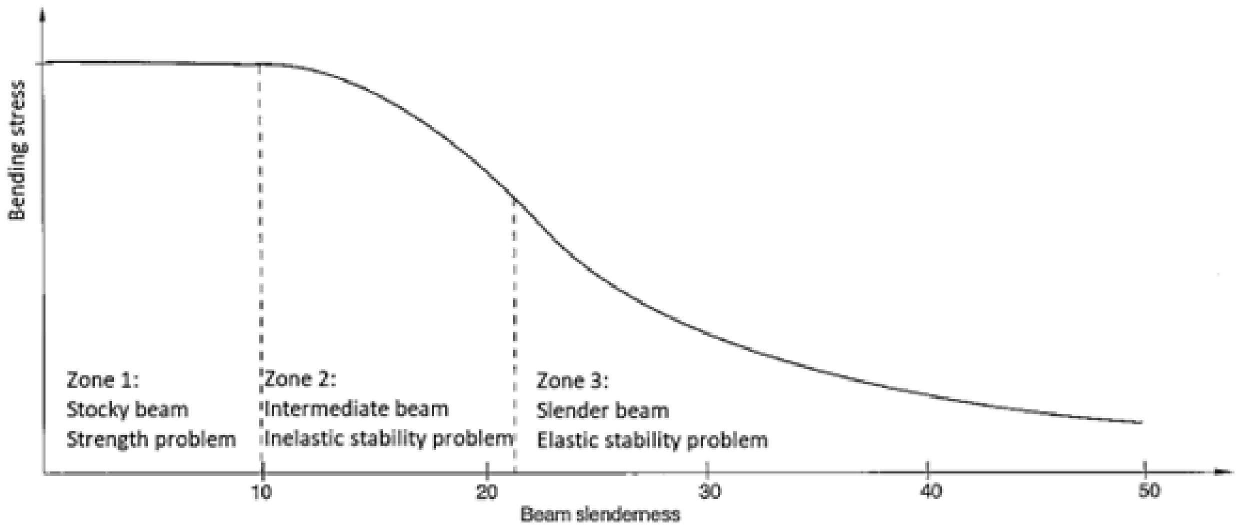


**Figure 10. Bending resistance versus slenderness**

**Table 3. Effective length, $L_e$, for bending members (CSA Group, 2019)**

| Type of load | Intermediate support | |
|---|---|---|
| | Yes | No |
| Beams | | |
| Any loading | 1.92a | $1.92l_u$ |
| Uniformly distributed load | 1.92a | $1.92l_u$ |
| Concentrated load at centre | 1.11a | $1.61l_u$ |
| Concentrated loads at 1/3 points | 1.68a | – |
| Concentrated loads at 1/4 points | 1.54a | – |
| Concentrated loads at 1/5 points | 1.68a | – |
| Concentrated loads at 1/6 points | 1.73a | – |
| Concentrated loads at 1/7 points | 1.78a | – |
| Concentrated loads at 1/8 points | 1.84a | – |
| Cantilevers | | |
| Any loading | – | $1.92l_u$ |
| Uniformly distributed load | – | $1.23l_u$ |
| Concentrated load at free end | – | $1.69l_u$ |

*Note:* $l_u$ *and* a *are the unsupported length and the maximum purlin spacing, respectively.*

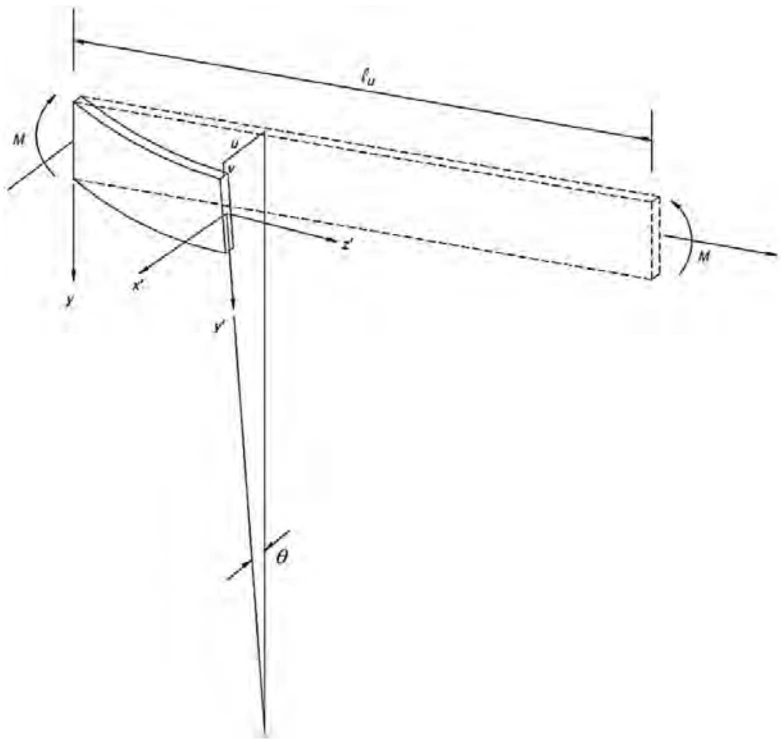


**Figure 11. Lateral-torsional buckling of a simply supported beam (Courtesy of American Wood Council)**

Unlike compression components, bending components sometimes have narrow cross-sections to resist shear forces, as in the case of prefabricated wood I-joists with oriented strand board (OSB) webs. The bending components then have to take into account global buckling (lateral-torsional buckling) as well as local buckling in the webs (see Figure 12). Analytical methods can usually take into account global buckling, but only rarely local buckling, which typically has to be analysed using FE methods.

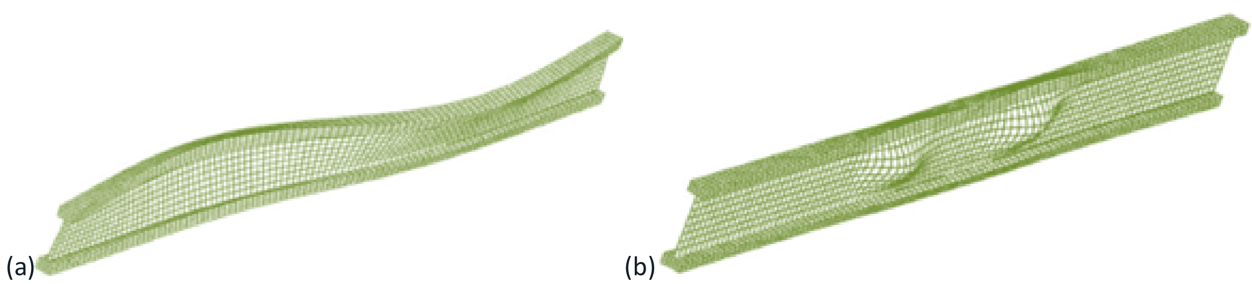

**Figure 12. Two typical buckling modes of I-joists (Zhu et al., 2005): (a) global; and (b) local buckling**

Typically, the analysis and design of the bending resistance of beams (e.g., using CSA O86) fall under one of the three parts: a constant material strength; a curve for the inelastic buckling; or a curve for linear buckling (Hooley & Madsen, 1964). NDS has adopted a similar approach. The bending moment resistance, $M_r$, of bending components can be calculated using Equation 4:

$$\boldsymbol{M_r = f_b S K_{Zb} K_L} \quad [4]$$

where $f_b$ is the bending strength of the component. This bending strength must take into account the load-duration effect, service condition effect, treatment effect, and system effect according to the testing results or design standards (e.g., CSA O86). $S$ is the section modulus of the component. $K_{Zb}$ and $K_L$ are the size factor and lateral stability factor, respectively, and are determined using different equations depending on the product type and design standards. Note that the $K_L$ factor was developed for simply-supported single-span beams with rectangular sections and an E/G ratio (MOE divided by the shear modulus) of 16, without taking into account the lateral bracing provided by sheathing or decking, under transverse loads applied on the top flange. When design conditions are not aligned with these assumptions, FE modelling is more favourable.

Aside from the bending resistance, the shear resistance of beams also needs to be analysed or verified. The shear resistance, $V_r$, of bending components can be calculated using Equation 5:

$$\boldsymbol{V_r = f_v \frac{2A_n}{3} K_{Zv}} \quad [5]$$

where $f_v$ is the shear strength of the component. This shear strength must take into account the load-duration effect, service condition effect, treatment effect, and system effect according to the testing results or design standards (e.g., CSA O86). $A_n$ is the net cross-sectional area of the component. $K_{Zv}$ is the size factor and is determined using different equations depending on the product type and design standards.

The deflection of the bending components can be calculated using engineering principles, for example, the moment theorem method, or the equations provided by some design handbooks, for example, *Wood Design Manual 2020* (Canadian Wood Council, 2021). When analysing most of the wood materials used in construction, deformation caused by shear is not commonly computed to simplify the analytical models. Except in special cases, the shear modulus for concrete and steel is high enough to assume that the shear deformation is too small to be relevant or worth computing. For most common wood products, the E/G ratio is approximately 16, far above the ratio of 2 to 3 observed in concrete and steel. For this reason, design standards such as CSA O86 and NDS (American Wood Council, 2018) provide an apparent MOE, which is historically reduced from the measured MOE to include shear deformation effects. These standards also specify how to get a shear-free (or true) MOE. This apparent MOE applies to simple-span beams with a span-to-depth ratio between 17:1 and 21:1 (See American Wood Council, NDS-2018 Appendix F.3). Proportion between shear deformation and bending deformation varies depending on loading and support conditions, beam geometry, span, and the effective shear stiffness. In some cases, such as a deep beam or a cantilever, it is better to compute shear deformations separately as the shear deformations calculated based on the apparent MOE may not be accurate.

Shear deformation of wood products such as CLT panels is higher than for other products, mainly because of the rolling shear of the transverse layers. The same is true of other engineered wood products with a low shear modulus. Both CSA O86 (Clause 8.5.2) and NDS (Clause 10.4.1) specify to compute both shear and bending deformation, but do not provide guidance or equations to cover all design cases. In addition, most of the beam deformation equations in the literature are for bending-only deformations; it is rare for these equations to show the shear part of the deformation. For these engineered wood products, it is important either to design with analytical models that include shear deformation or to use a software program capable of analysing shear deformation of materials. In all cases, when a software program with user-defined materials computes shear deformation, it is important to provide a shear-free MOE as an entry parameter.

Composite components can also be analysed using the transformed section analysis method (Brown & Suddarth, 1977). After transferring the non-timber material section into an equivalent timber section, a composite component can be treated as a pure timber component.

**Horizontal Holes in Beams**

Horizontal holes in beams are often required to allow for multiple heating, ventilation, air conditioning, plumbing and electricity pipes, ducts, and cables in multi-residential and industrial wood buildings. The Engineered Wood Association (APA) has guidelines for designing openings in glulam beams. APA Form S560 (APA, 2020a) has guidelines for notching and drilling glulam when end-notching and drilling of horizontal through-thickness holes cannot be avoided. With mass timber structures, larger holes are required and a design check needs to be performed. APA Form V700 (APA, 2020b) includes an analytical tool for when horizontal holes that exceed the guidance in S560 are necessary. However, this analytical procedure has limitations: it covers only circular holes (rectangular holes are outside of the scope) 16 in. (406 mm) in diameter, and the equations provided are limited to simple span and multiple span, subject to uniform load and/or concentrated load. This analytical method can be useful for light-frame residential and commercial applications, but should be used with caution for larger mass timber buildings. Similarly, APA Form G535 (APA, 2011) and V900 (APA, 2021) provide guidance for openings in LVL.

The analytical method does not provide guidance on how to compute splitting potentially occurring near the opening, a common failure mode observed while testing beams with unreinforced openings in bending. The method also does not provide guidance on how to reinforce openings with self-tapping screws, which is a common way to increase resistance to splitting near the openings. Of all the published standards, the most complete method for designing holes in beams is provided by the German national annex of the Eurocode 5 (European Committee for Standardization, 2009). DIN EN 1995-1-1/NA:2013-08 (Deutsches Institut für Normung e. V, 2013) provides guidance on the design of unreinforced openings (Clause NA.6.7) as well as on the design and reinforcement of both circular and rectangular openings (Clause NA.6.8.4). The provision also applies to LVL. This method is more conservative than the APA method.

### *4.2.5.2 FE Methods*

Eigenvalue buckling analysis is sufficient to determine the resistance of slender beams governed by elastic buckling, whereas the following three types of situations require nonlinear analysis: (1) stocky and intermediate beams governed or affected by material strength; (2) beams with initial imperfections which cannot be ignored; and (3) any beams where a detailed analysis is desired. The required material input, constitutive models, boundary conditions, loading conditions, buckling modes, and imperfections (discussed in Section 4.2.4.2) also apply to bending components.

The methods that take into account the influence of variability of wood-based products, and the modelling considerations for selecting elements, meshing notches and openings, simulating the force-transferring mechanisms in composite components, and developing boundary conditions and loading (discussed in Section 4.2.3.2) also apply to bending components.

Figure 13 shows the global and local buckling modes of I-joists with openings, as analysed by Zhu et al. (2005). In the FE models, the flanges and webs were meshed using solid and shell elements, respectively. Refined meshes were adopted at the transition zones between the openings and the rest of the web. In the nonlinear analysis of the I-joists (Guan & Zhu, 2009; Zhu et al., 2005), the top flange and the compression part of the OSB web were treated as elastoplastic orthotropic material, while the bottom flange and the tension part of the OSB web were treated as linear elastic orthotropic material. Hill's yield criterion was used to judge if the material yields, and Tsai-Hill criterion was used to judge if the material fails (cracks). The initial geometric imperfection was introduced into the beams using either the lowest buckling mode or a linear combination of several buckling modes. An amplitude of 2.5% of flange width was introduced in the global buckling analysis, and 10% of the web thickness was introduced in local web buckling analysis.

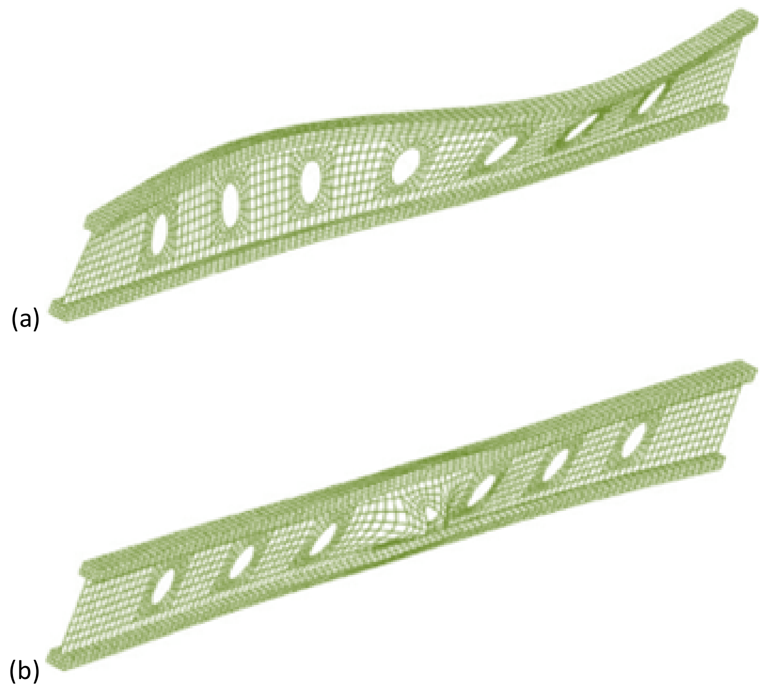


**Figure 13. Two typical buckling modes of I-joists with openings (Zhu et al., 2005): (a) global and (b) local buckling**

Figure 14 shows the stress distributions, at ultimate load, around the square opening and the circular opening. A comparison of experimentally failed modes and numerically simulated failed modes of a beam with circular openings or square openings is shown in Figure 15.

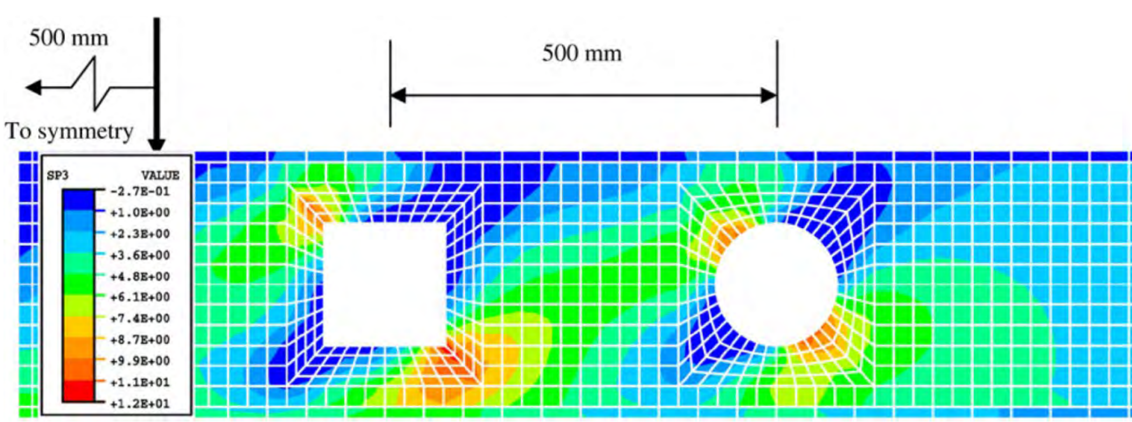


**Figure 14. Principal tensile stress (SP3, N/mm$^2$) in an I-joist web at ultimate load (Guan & Zhu, 2009)**

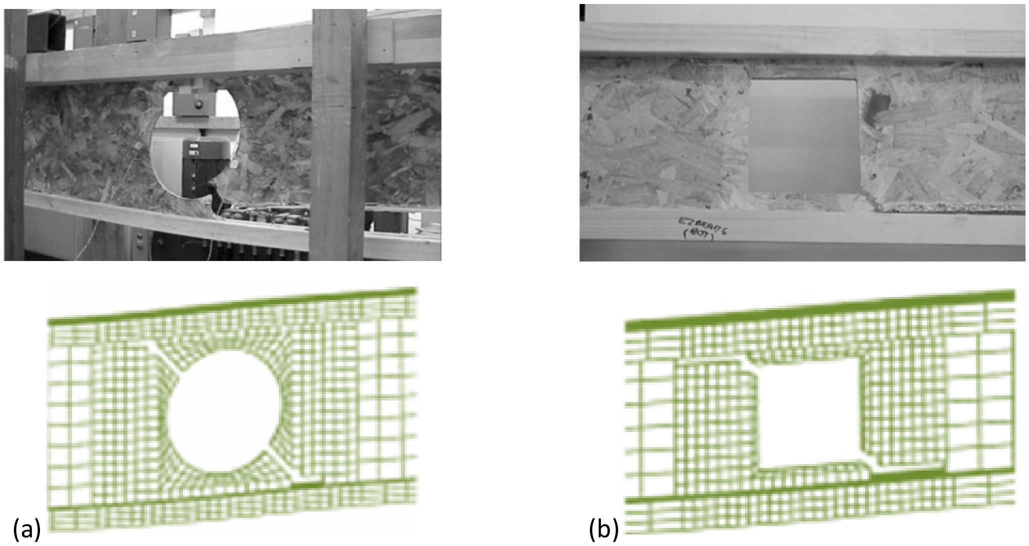


**Figure 15. Comparison of experimental failure modes and numerically simulated failure modes (Guan & Zhu, 2009): (a) I-joist with circular openings; and (b) I-joist with square openings**

## 4.2.6 Summary

Analyses of timber components under various loads are essential for structural design and product optimisation. In this chapter, analysis methods and key modelling considerations for wood-based components are introduced. Classic analytical methods are appropriate for specific wood-based products with limited configurations of loading and boundary conditions. FE methods can be utilised to analyse various wood-based products under any conditions. Described are analytical and FE methods for analysing the deflection and resistance, including strength and stability problems, of tension, compression, and bending components. The information in this chapter is intended to help practising engineers and researchers become better acquainted with analysis of wood-based components.

## 4.2.7 References

American Wood Council. (2018). *National design specification (NDS) for wood construction*. American Wood Council. https://www.awc.org/pdf/codes-standards/publications/nds/AWC-NDS2018-ViewOnly-171117.pdf

APA. (2011). *EWS G535: Field notching and drilling of laminated veneer lumber*. The Engineered Wood Association (APA).

APA. (2020a). *EWS S560J: Field notching and drilling of glued laminated timber beams*. The Engineered Wood Association (APA).

APA. (2020b). *V700: Effect of large diameter horizontal holes on the bending and shear properties of structural glued laminated timber*. The Engineered Wood Association (APA).

APA. (2021). *V900: Effect of large diameter horizontal holes on the bending and shear properties of laminated veneer lumber*. The Engineered Wood Association (APA).

Bedon, C., & Fragiacomo, M. (2015). Numerical and analytical assessment of the buckling behaviour of *Blockhaus* log-walls under in-plane compression. *Engineering Structures, 82*, 134-150. https://doi.org/10.1016/j.engstruct.2014.10.033

Brown, K. M., & Suddarth, S. K. (1977). *A glued laminated beam analyzer for conventional or reliability based engineering design*. Purdue University Agricultural Experiment Station.

Canadian Wood Council. (2021). *Wood design manual 2020*. Canadian Wood Council.

Chen, Z., Ni, C., Dagenais, C., & Kuan, S. (2020). Wood$^{ST}$: A temperature-dependent plastic-damage constitutive model used for numerical simulation of wood-based materials and connections. *Journal of Structural Engineering, 146*(3), 04019225. https://doi.org/10.1061/(ASCE)ST.1943-541X.0002524

Chen, Z., Zhu, E., & Pan, J. (2011). Numerical simulation of wood mechanical properties under complex state of stresses. *Chinese Journal of Computational Mechanics, 28*(4), 629-634, 640.

CSA Group. (2016). *CSA O122-16: Structural glued-laminated timber*. CSA Group.

CSA Group. (2019). *CSA O86:19*: *Engineering design in wood*. CSA Group.

Deutsches Institut für Normung e. V. (2013). *DIN EN 1995-1-1/NA: National Annex - Nationally determined parameters - Eurocode 5: Design of timber structures - Part 1-1: General - Common rules and rules for buildings*. DIN Deutsches Institut für Normung e.V.

European Committee for Standardization. (2009). EN 1995-1-1, 2009. *Eurocode 5: Design of timber structures - Part 1-1: General - Common rules and rules for buildings. In. Brussels, Belgium: European Committee for Standardization.*

Guan, Z. W., & Zhu, E. C. (2009). Finite element modelling of anisotropic elasto-plastic timber composite beams with openings. *Engineering Structures, 31*(2), 394-403. https://doi.org/10.1016/j.engstruct.2008.09.007

Hooley, R. F., & Madsen, B. (1964). Lateral buckling of glued laminated beams. *Journal of the Structural Division*, 90(ST3), 201-218. https://doi.org/10.1061/JSDEAG.0001088

Johns, K. (2011). A continuous design formula for timber columns. *Canadian Journal of Civil Engineering, 18*(4), 617-623.

Pina, J. C., Flores, E., I., S., & Saavedra, K. (2019). Numerical study on the elastic buckling of cross-laminated timber walls subject to compression. *Construction and Building Materials, 199*, 82-91. https://doi.org/10.1016/j.conbuildmat.2018.12.013

Taylor, S. E., & Bender, D. A. (1991). Stochastic-model for localized tensile-strength and modulus of elasticity in lumber. *Wood and Fiber Science, 23*(4), 501-519.

Webber, A., Orr, J. J., Shepherd, P., & Crothers, K. (2015). The effective length of columns in multi-storey frames. *Engineering Structures, 102*, 132-143. https://doi.org/10.1016/j.engstruct.2015.07.039

Zahn, J. J. (1989). *Progress report to NFPA on column research at FPL*. U.S. Department of Agriculture, Forest Service, Forest Products Laboratory.

Zhu, E. C., Guan, Z. W., Rodd, P. D., & Pope, D. J. (2005). Buckling of oriented strand board webbed wood I-joists. *Journal of Structural Engineering, 131*(10), 1629-1636. https://doi.org/10.1061/(ASCE)0733-9445(2005)131:10(1629)

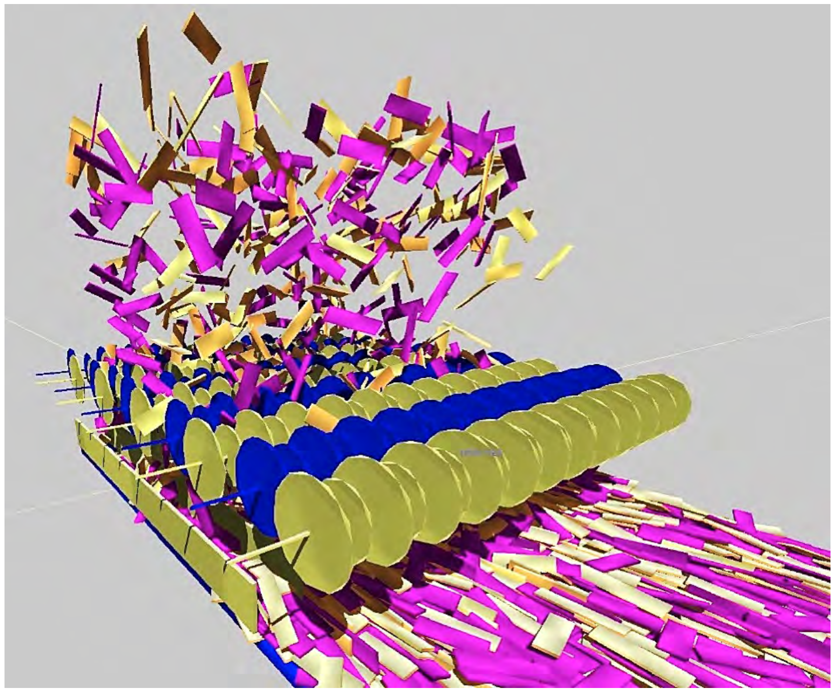

# CHAPTER 4.3

## Modelling processes and properties of structural wood products


**Authors**

Chunping Dai

Zhiyong Chen

**Reviewers**

Borjen Yeh

William Nguegang Nkeuwa

Markus Lukacevic

# TABLE OF CONTENTS

## 4.3.1 Introduction

Timber is an orthotropic material, and its properties vary significantly depending upon the grain orientation (van Beerschoten et al., 2014). The material properties are also affected to a large degree by the natural variability in wood (Winans, 2008). Engineered wood products are designed so that the natural defects in wood (e.g., cracks, low-strength material, and knots) are dispersed, resulting in mechanical and physical properties that are more consistent and uniform than those of solid sawn timber. This utilises the fibre resource more efficiently. Perhaps more important is the opportunity to refine and optimise the physical and mechanical properties of wood-based composites by controlling the production parameters.

Structural wood composites can be classified as one of three types: lumber, veneer, or strand based. Lumber-based products are mostly structural mass timber products such as glued laminated lumber (glulam) and cross-laminated timber (CLT). They are cold-pressed with structural adhesives, the density of which is an average of the undensified parent timbers used. Veneer- and strand-based products come under the umbrella terms structural composite lumber (SCL) and mass ply panel (MPP). These are hot-pressed and densified to a greater or lesser extent depending on element size and geometry. SCL products include laminated veneer lumber (LVL), parallel strand lumber (PSL), laminated strand lumber (LSL), and oriented strand lumber (OSL).

Plywood and LVL are made of veneers bonded together with continuous glue lines. The structure is simple and organised. The product is generally lighter and requires little (less than 10%) densification. In comparison, small discrete element (strands, particles, and fibres) composites, which represent a broad range of products including oriented strand board (OSB), OSL, Parallam™ particleboard, and medium density fibreboard (MDF), are much more complex in terms of their manufacture and their structure. The constituent elements are discontinuous, resulting in a highly porous and random spatial structure in mats. As such, a high degree of densification (usually 40–60%) is required to achieve sufficient bonding (Dai & Steiner, 1993; Dai et al., 2005). These products are generally much heavier and lower in volumetric recovery.

These newer engineered wood products are designed to have more consistent mechanical and physical properties than conventional lumber or sawn wood: the sophisticated manufacturing processes optimally arrange and bond thin wood veneers, strands, and flakes using thermoset adhesives under controlled heat and pressure. The ability to carefully calibrate properties and their variability through process control means that these newer wood products can be used in applications typically dominated by steel or concrete, such as long-span commercial roof trusses and shell structures (Clouston & Lam, 2001; Stürzenbecher et al., 2010).

The development of new wood-based products, plus the optimisation of existing products, plays a key role in the expansion of timber construction, especially for taller and larger structures. Manufacture of wood-based products, however, is complex, involving a variety of influencing factors—the properties of the constituents, the structure, and the many parameters of the manufacturing process. Traditional product development and optimisation usually uses trial-and-error laboratory experiments and mill trials, or empirical approaches. While they can offer direct and short-term solutions, experimental studies are generally time consuming and expensive to run; more importantly, they have limitations in providing fundamental understanding (Clouston & Lam, 2001; Gilbert et al., 2017). Modelling offers an efficient and cost-effective approach to advancing wood science and industrial composites manufacture. It applies mathematics, physics, and mechanics principles and computer numerical simulation techniques to the field of wood composites. Modelling also helps understand the complex manufacturing process and optimises the product performance by reducing the number and scope of experimental variables.

Three types of models have been developed for wood composites:

(1) *Analytical models*. Analytical models are based on elegant and often complex fundamental principles. They are very useful for improving understanding of underlying mechanisms and they can effectively tackle specific processing aspects and product properties. The solutions require knowing specific material properties, which may not be available in the literature. Testing highly variable materials, such as wood, is challenging, time consuming, and expensive. Processing can also exacerbate the variability in the properties. For example, stranding can cause so much damage and uncertainty in the grain angle in the cut strands that the exact mechanical properties of OSB strands have probably never been established. In addition, as the process evolves, the material structure and properties could easily become too complex and variable to track mathematically. Because of this, most analytical models often have limited practical uses. Most focus closely on only some individual aspects of manufacture or product property.

(2) *Computer simulation models.* Although largely based on fundamental principles, computer simulation models use numerical techniques such as the finite element method (FEM). Simulation also helps understand the complex manufacturing process and optimises product performance by reducing the number and scope of experimental variables. Computational models have been developed for mass timber and veneer as well as strand-based products. The most practical of these are simplified, semi-empirical models that only take into account the most basic principles. Barnes (2000) developed a good early example—an integrative foundation model for the effects of strand length, thickness, and orientation effect and other process parameters, including resin and fines content, and density, on mechanical properties of strand-based products such as PSL and OSB.

(3) *Statistical models.* These data-driven models are analogous to ‘black-box’ models (e.g., André et al., 2008; Noffsinger, 2004). Other data-mining methods include neutral network modelling and artificial intelligence. Although these models offer little or no insight into the processing mechanism or product performance, they have great potential for practical application, especially as more data are becoming available. As the big-data processing technology evolves, the statistical model will likely continue to develop as a modern manufacturing tool.

This chapter summarises analytical and computer simulation models that describe key processing operations and properties of lumber-, veneer-, and strand-based products. Many of the veneer- and strand-based models are a result of nearly 20 years of research by FPInnovations; the remainder are from published literature.

## 4.3.2 Lumber-based Products

Glulam and CLT, a variant of glulam developed in Austria in the 1980s to produce structural panels (Brandner et al., 2016, Wiesner et al., 2019), are thick laminate, cold-pressed bulk composites in which there is no viscoelastic compression of the wood substrate (see Figure 1).

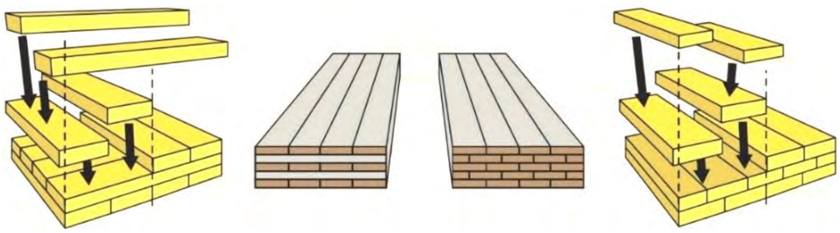

**Figure 1. CLT (left) and glulam (right) (BCFocus: www.bcfocus.com)**

#### *4.3.2.1 Process Modelling*

Figure 2 illustrates the process of manufacturing glulam and Figure 3 the process of manufacturing CLT. Both glulam and CLT use kiln-dried lumber where the moisture content is controlled to about 12%. Visually graded and stress-graded lamstocks are used for both glulam and CLT. Both also use structural resins, including phenol resorcinol formaldehyde, one-component polyurethane, catalysed melamine, and emulsion polymer isocyanate, applied by spraying or with a roller as a continuous film to freshly planed lumber surfaces. The production and quality control process are straightforward compared with hot-pressed veneer and strand composites, and in North America, are governed by ANSI/PRG 320 (APA, 2019).

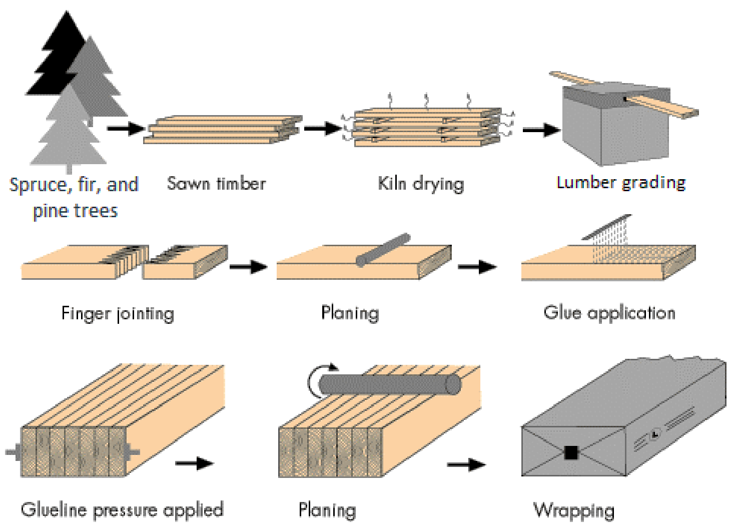


**Figure 2. Manufacturing process of glulam (Malo & Angst, 2008)**


**Figure 3. Manufacturing process of CLT (Karacabeyli & Gagnon, 2019)**

Lumber-based products are largely a function of the lumber grades and layup arrangement of graded lumber; the products are affected by species, density, and defects. Other important factors that influence the grades and other quality indicators are the dimensions of the lumber and numbers of layers; adhesive types and coverage; open assembly time; and pressure and pressing time (Wang et al., 2018). Although many structural models have been developed for glulam and CLT, very few process models are available for these products. Process models are needed to investigate the effects of resin type and coverage, assembly time, and pressure and time. The effects of lumber grade and layup can be determined using mechanical models.

### *4.3.2.2 Mechanical Models of Product Properties*

#### 4.3.2.2.1 Glulam

The mechanical properties of glulam depend, in general, on: (1) the combination of lamination grades in the beam layup; (2) the strength-reducing characteristics, such as knots and slope of grain, allowed in each lamination grade; (3) the E-rating or proof-loading or both of the individual laminations; (4) the strength and location of end joints; (5) the thickness of the laminations; and (6) the size of the beam and the distribution of stresses (Foschi & Barrett, 1980). The mechanical performance of glulam beams has been modelled using three major types of models: empirical models, probabilistic models, and advanced finite element (FE) models.

#### 4.3.2.2.2.1 Empirical Models

One method for predicting beam-bending strength is based on reducing the flexural strength of clear wood by a factor that takes into account the lamination grades in the layup and the knots within each lamination (Wilson & Cottingham, 1947; Freas & Selbo, 1954). Two moments of inertia are computed for the beam cross-section: $I_g$, the gross moment of inertia, and $I_k$, the sum of the moments of inertia for the knot areas within a prescribed beam length. The strength-reducing factor is expressed as a function of the ratio $I_k/I_g$.

A similar method has been developed to predict tensile strength of glued laminated beams (Freas & Selbo, 1954). This method uses a ratio, $K/b$, where $K$ is a knot area parameter and $b$ is the width of the laminations. The $I_k/I_g$ method is the basis for the industry standard, ASTM D 3737 (2018), and the Glulam Allowable Property (GAP) program (Williamson & Yeh, 2007; Yeh, 1996). However, this method does not predict statistical distributions of glulam beam strength and does not take into account the influence of end joints.

#### 4.3.2.2.1.1 Probabilistic Models

Foschi and Barrett (1980) were among the first to model the performance of glulam beams using a stochastic model, GLULAM (Figure 4). In their model, the laminations of the glulam beams were divided into elements, or cells. Their input consisted of generating clear wood densities and knot sizes and assigning them to each cell. Each cell was subsequently assigned a lumber modulus of elasticity (MOE) and tensile strength value that were correlated to the assigned density and knot size.

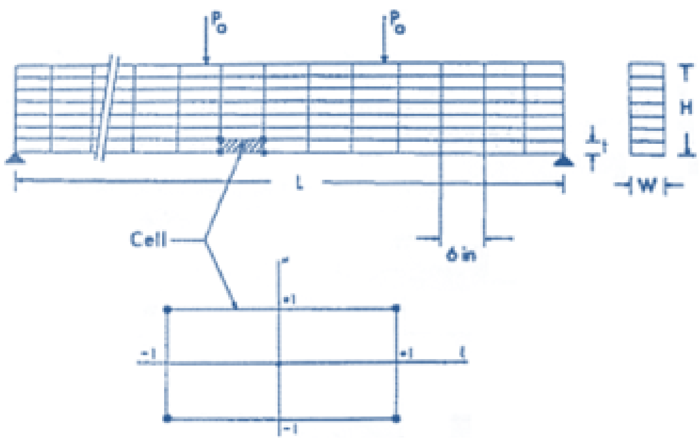


**Figure 4. GLULAM model (Foschi & Barrett, 1980)**

Several models have stemmed from the original Foschi and Barrett (1980) model. Ehlbeck et al. (1985) developed a similar model called the Karlsruhe calculation model. The two major improvements to the Foschi and Barrett (1980) model were the inclusion of end-joint effects and the ability to simulate progressive failures. The properties of end joints were simulated using a regression approach that generated tensile strength of the joints as a function of the lower density of the two jointed boards. Progressive failures were simulated by checking if the remaining adjacent cells, after the first failure, were able to support the redistributed stresses. Colling (1990) extended the Karlsruhe calculation model so that it distinguishes between finger-joint failure and failure within the lamellas themselves.

Another model that stemmed from Foschi and Barrett's (1980) original was devised by Govindarajoo (1989). Govindarajoo (1989) included a stochastic lumber properties model developed by Kline et al. (1986) to simulate correlated values of localised MOE within a piece of lumber. Regression models were added to simulate clear wood strength from the generated clear wood MOE values. Models developed by Burk and Bender (1989) were used to simulate end-joint stiffness and strength from the localised MOE values of the two jointed boards. Fink et at. (2013) characterised the stiffness of wooden lamellas with a weak-zone approach' (weak-zone model), where the lamella is modelled by the clear wood sections and weak zones representing knot clusters.

Bender et al. (1985) developed a model based on generating actual lumber properties rather than clear wood properties. The distributions were obtained by fitting probability density functions to actual long-span lumber MOE and using a regression approach to simulate lumber tensile strength. The long-span lumber tensile strength values were adjusted for length by using an independent weakest-link approach. Bender et al. (1985) modelled end-joint strengths using test data. Richburg (1988) refined the Bender et al. (1985) model in a pilot study to observe the effects of spatial correlation between localised lumber properties. Taylor (1988) developed a model that simulated spatially correlated localised lumber properties. Models developed by Burk (1988) were used to simulate end-joint properties as functions of the localised constituent lumber properties. Hernandez et al. (1992) refined the Bender et al. (1985) model by adding new features to calculate the beam stiffness, simulate the progressive failures, handle different loading conditions, and calculate the summary statistics.

The GLULAM model was also expanded by Folz and Foschi (1995) into the ULAG model (Figure 5). The ULAG model is used to predict the bending, shear, tension, and compression capacity of glulam using the tensile strength test data of the laminae and finger joints and the corresponding MOE values.

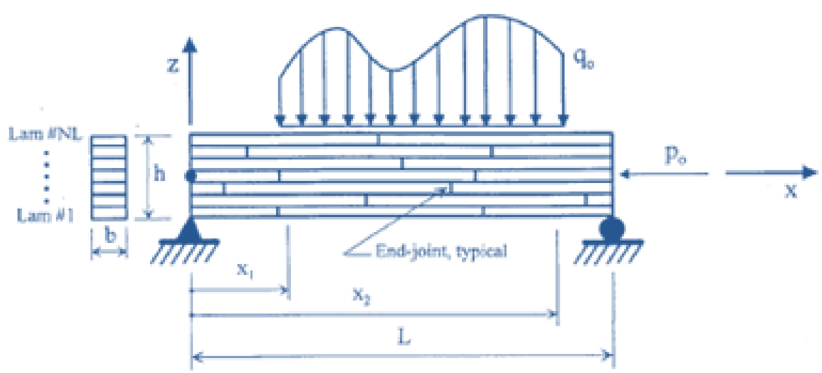


**Figure 5. ULAG model (Folz & Foschi, 1995)**

Below are the assumptions typically adopted in the probabilistic models:

- The laminae are assumed to be elastic.
- Although some compression failure can occur in the compression side of the beam, the models only assume tension failure and do not take into account the influence of compression.
- Manufacturers might make a finger joint when a knot is larger than visual quality restraint or when some serious defects/drying problem should be removed. In the models, if there is a larger knot than the predefined knot restraint, the portion of the knot in a lamina is removed and finger-jointed.
- The glue bond in between the laminae is stiff and strong enough to avoid sliding and delamination.

- The material properties of each lamella are described by profiles that vary only in the longitudinal direction.

The probabilistic models (Figure 6) usually contain three basic modules: (1) a module to reproduce the process of fabricating glulam beams; (2) a module to generate and allocate the material properties in the timber boards; and (3) a module to estimate the load-carrying capacity. In the first module, a geometric model is developed by assembling and meshing the laminae. Sometimes, the location of finger joints is also determined in this module. In the second module, the MOE and tensile strength of wood and finger joints are randomly generated based on the properties of clear wood or lumber, and of finger joints, using either a discrete parameter space approach or a continuous parameter space approach (Kandler, Füssl & Eberhardsteiner, 2015). The properties of laminae can be determined by conducting stress wave tests, static bending tests, or machine grading (Lee & Kim, 2000). In the third module, the GLULAM model is analysed using either FEM or the Transformed Section Analysis method (Brown & Suddarth, 1977) (Figure 7) based on beam theory. Monte Carlo simulation is usually adopted in the probabilistic models to characterise the probability distributions of beam strength and stiffness.

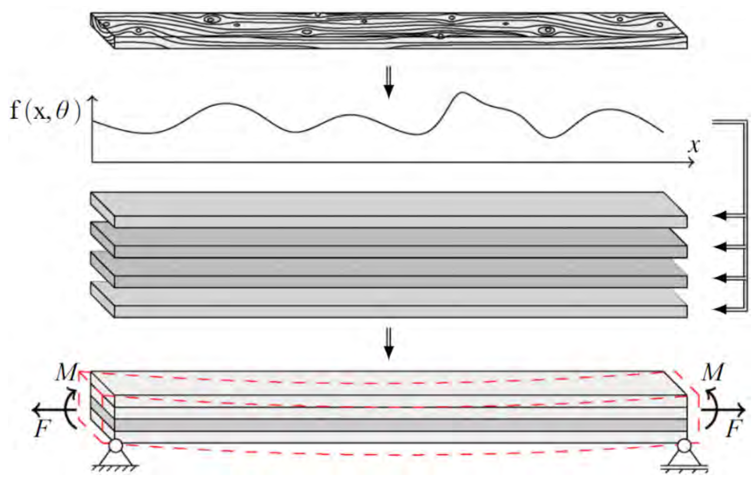


**Figure 6. Development of probabilistic models (Kandler, Füssl & Eberhardsteiner, 2015)**

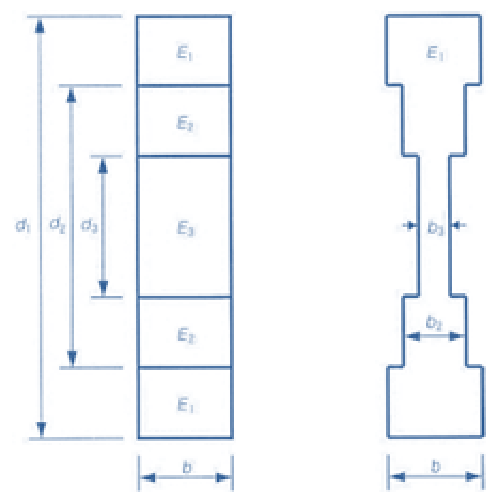


**Figure 7. Example of the Transformed Section Analysis method**

#### *4.3.2.2.1.2 Advanced FE Models*

Optical scanning devices can determine the orientation of fibre on the surface of lumber, as illustrated in Figure 8. The information on fibre angle in combination with a micromechanical model for wood can be used to generate longitudinal stiffness and strength profiles of each lamella. These property profiles can be used to develop an advanced FE modelling method for predicting the mechanical performance of glulam. This modelling approach includes four basic steps: (1) laser scanning; (2) reconstruction of 3D fibre and knot models; (3) determination of stiffness and strength profiles; and (4) analysis.

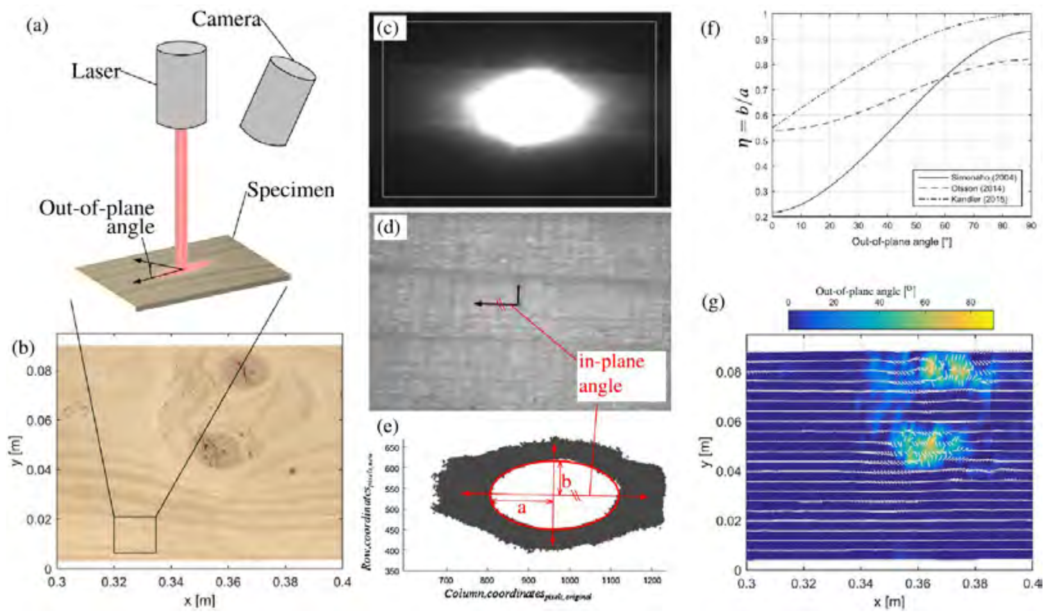


**Figure 8. Tracheid effect and its exploitation in laser scanning (Kandler, Lukacevic, Zechmeister, et al., 2018): (a) setup; (b) scanning the wooden surface; (c) visualisation of a recorded shape; (d) the wooden surface; (e) fitting of the ellipse; (f) estimating the out-of-plane component of the fibre; and (g) resultant vector file of fibre angle measurements**

The first step, laser scanning, describes propagation of light in wood, based on the tracheid effect. A simplified setup comprises a laser and a camera, as shown in Figure 8(a). Light travels further in a direction parallel to the fibre than perpendicular to the fibre in wood. Thus, projecting a laser dot onto a wooden surface and decomposing the spread of the light reveals the major material axis (see Figures 8[d] and 8[e]). While the in-plane fibre angle can be measured this way in principle only, Kandler, Füssl, Serrano & Eberhardsteiner (2015) presented approaches to deduct the out-of-plane angle from the same dataset (see Figures 8[f] and 8[g]) by using the ratio between the minor and major axes of the ellipse to estimate the out-of-plane component of the fibre.

A weak-zone approach (Fink et al., 2013) is used to construct the laminae. Each lamina is modelled using undisturbed, defect-free clear wood sections. These are interrupted by weak sections representing knot groups and defects. To reconstruct knot morphology, the resulting fibre angle values are used to automatically determine knot areas on all four surfaces of the board. The 3D knot geometry is reconstructed using an automated algorithm where the knots are modelled as rotationally symmetric cones (illustrated in Figure 9[a]).

The clear wood section can be reconstructed using a micromechanical multiscale model (Hofstetter et al., 2005) with mass density, moisture content, and fibre directions the main input factors.

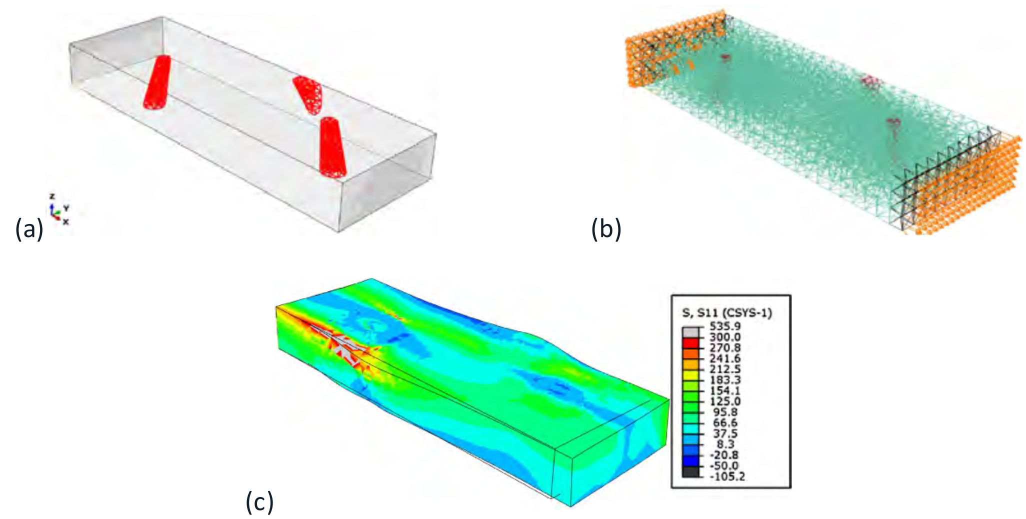


**Figure 9. FE model of an exemplary knot group (Kandler, Lukacevic, Zechmeister, et al., 2018): (a) geometric properties of the knots; (b) using tetrahedron FE mesh and geometric displacement boundary conditions; and (c) the effective stiffness computed from the resultant forces and the resulting stress field**

The stiffness of individual weak sections with knot groups and knot-free sections can be determined using a linear 3D FE model (see Figure 9). A model of each section is loaded in tension to estimate its effective tensile stiffness. A numerically based stiffness profile is derived by combining the stiffness values of knot groups and knot-free sections. With a 3D FE model, the tensile strength of an individual knot-free section is obtained using a density-based Tsai-Wu criterion (Tsai & Wu 1971). For the knot group, properties such as knot-area-ratio (Figure 10) can be used to estimate the tensile strength. As with the stiffness profile procedure, combining the strength values of knot groups and knot-free sections produces a strength profile for each lamina. The resulting stiffness profile sample is then used to determine a random process model; this model can randomly generate an arbitrary number of synthetic stiffness and strength profiles for the laminae of glulam.

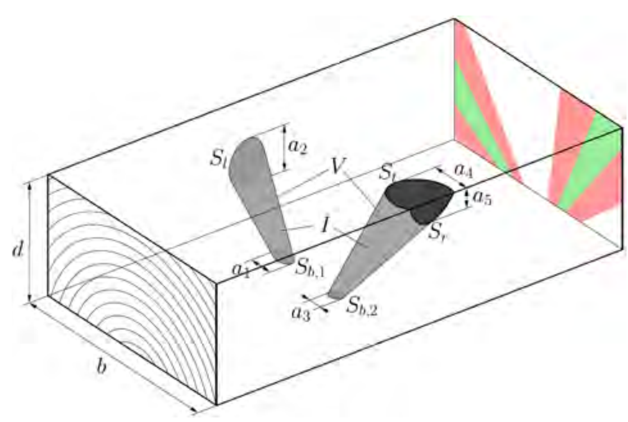

**Figure 10. Designation of geometric parameters used to calculate indicating properties, where green areas denote projected knot areas and red areas denote projected fibre deviation areas (Kandler, Lukacevic, Zechmeister, et al., 2018)**

Within the mechanical model, the glulam is procedurally generated using a constructive solid geometry method (Mäntylä, 1987). Because the available stiffness profiles have condensed the information into 1D curves, 2D FE computation is sufficient to model stress redistribution effects around weak zones formed by knot groups. As with the probabilistic models, the glue bonds can be ignored. The Tsai-Wu criterion (Tsai & Wu 1971) is also used to assess the utilisation level and load-bearing capacity of the glulam. Figure 11 shows an FE example of a glulam beam with an opening close to a support.

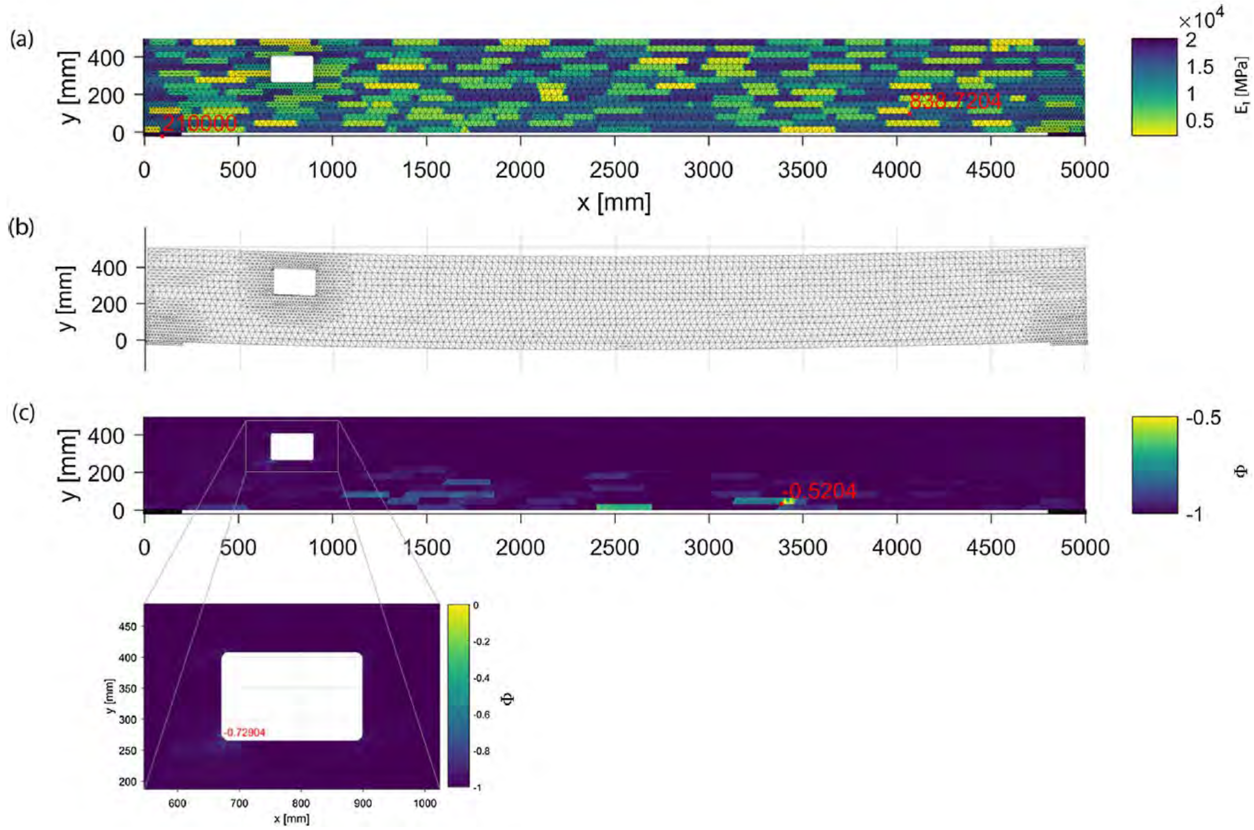


**Figure 11. Results of the mechanical model (Kandler, Lukacevic, Zechmeister, et al., 2018): (a) spatial distribution of longitudinal stiffness; (b) resulting displacements; and (c) evaluation of the Tsai-Wu failure criterion**

#### 4.3.2.2.2 CLT

The mechanical properties of a CLT panel depend, in general, on (1) the combination of lamination grades in the panel layup; (2) strength-reducing characteristics, such as knots and slope of grain, in each lamination grade; (3) strength and location of finger joints; (4) thickness of the laminations; (5) width-to-thickness ratio of lumber; (6) edge glue; and (7) the size of the panel and the particular distribution of stresses. Analytical models and FE models can model the mechanical performance of CLT panels. To the best of our knowledge, no probabilistic models have been developed for CLT panels. However, the methods for deriving the stiffness and strength profiles for laminae of glulam apply to the lumber in CLT panels (Li et al., 2018). In other words, probabilistic models of CLT panels can be developed by adding modules that use the CLT panel property profiles as input to analytical or FE models.

#### *4.3.2.2.2.2 Analytical Models*

During the last two decades, various types of analytical models have been developed to evaluate the basic mechanical properties of CLT panels or else existing models have been modified for use with CLT (Popovski et al., 2019). The most common analytical approach used in Europe is based on the Mechanically Jointed Beams theory, also called the $\gamma$ (gamma) method. As the name suggests, this method was originally developed for beams (e.g., I- or T-beams) connected using mechanical fasteners of a certain stiffness uniformly spaced along the length of the beams. According to this method, the stiffness of the mechanically jointed beams is defined using the effective bending stiffness, $(EI)_{eff}$, which depends on the properties of sections of the beams and the connection efficiency factor, $\gamma$. Factor $\gamma$ depends on the stiffness of the fasteners, with $\gamma = 1$ representing a completely glued member and $\gamma = 0$ representing no connection at all. This approach only provides a closed (exact) solution for the differential equation for simply supported beams or panels with a sinusoidal load distribution; however, the differences between the exact solution and those for uniformly distributed load or point loads are minimal and therefore acceptable engineering practice.

The Shear Analogy method (Kreuzinger, 1999), developed in Europe, is applicable to solid panels with cross layers. The methodology takes into account the shear deformation of the parallel and the cross layers and is not limited to a specific number of layers within a panel. Like the Gamma method, the Shear Analogy method also uses $(EI)_{eff}$ in calculating the bending stiffness. The shear deformation is introduced through a new shear stiffness term, $(GA)_{eff}$. Although this method does not provide a closed solution, it is adequate for CLT panels and also fairly accurate; for these reasons, the Shear Analogy method is used to determine the stiffness of CLT panels loaded perpendicular to the face in both the PRG 320 and CSA O86 standards.

Blass and Fellmoser (2004) applied the Composite theory (also called the k-method) to predict some of the design properties of CLT. However, this method does not account for shear deformation in individual layers. The k-method is reasonably accurate for panels with high span-to-depth ratio. Popovski et al. (2019) explain these methods in more detail.

The narrow edge glue bonds affect the structural performance of CLT panels, for example, stiffness and rolling shear. Free narrow edge glue bonds cause stress concentrations that lower the stiffness and strength of CLT panels under particular loads (Perret et al., 2019). To investigate CLT panels with narrow gaps and innovative lightweight panels with wide gaps (Figure 12), Franzoni et al. (2018) derived simplified closed-form solutions by applying a thick-plate homogenisation procedure. CLT and timber panels with gaps were modelled as a space frame of beams connected with wooden blocks (Figure 13). The researchers considered the contribution of both beams and blocks to the panel's mechanical response. The closed-form expressions can predict the panel's stiffnesses and maximum longitudinal and rolling shear stresses.

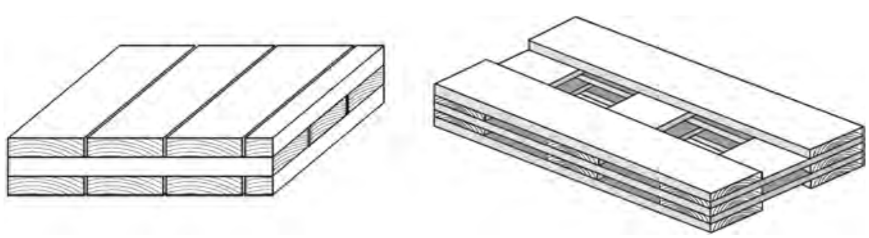

**Figure 12. CLT panel with narrow edge gaps (left) and innovative lightweight timber panel with wide gaps (right) (Franzoni et al., 2018)**

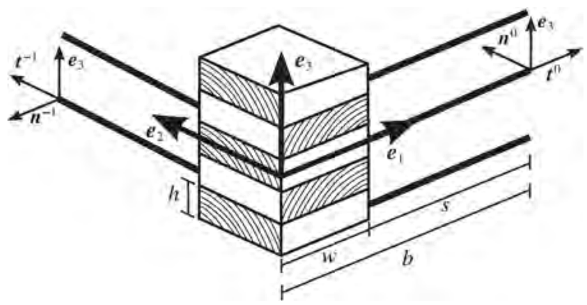


**Figure 13. Periodic unit cell of timber panel with gaps modelled as a space frame of beams connected with wooden blocks (Franzoni et al., 2018)**

### *4.3.2.2.2.3 FE Models*

To optimise CLT panels, a refined FE model can be developed with all pieces of lumber, glue bonds, and narrow edge gaps (if present). Comprehensive constitutive materials, which can accurately simulate the anisotropic behaviour of wood, for example, Wood$^{ST}$ (Chen et al., 2020), can be adopted. Contact elements, e.g., cohesive elements (Kawecki & Podgorski, 2018), can simulate the glue bonds between two pieces of lumber, since they can simulate the stiffness, strength, and even the damage of glue layers. Figure 14 shows a refined FE model for a CLT deck supported by two beams under two point-loads.

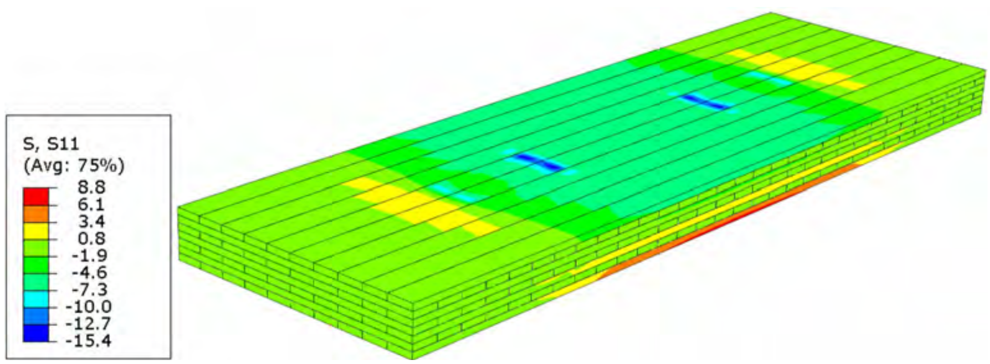


**Figure 14. FE model for a CLT deck**

Three-dimensional FE models are powerful but time consuming (Saavedra Flores et al., 2015, 2016). Alternatively, 2D models can be developed for some cases, such as the panels used in a single span floor.

## 4.3.3 Veneer-based Products

Veneer-based engineered products include plywood, LVL, and MPP. These products are made of veneers arranged in a crosswise or parallel fashion that are then glued and pressed together (see Figures 15, 16, and 17).

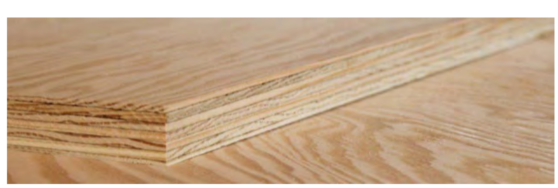

**Figure 15. Plywood (Courtesy of APA – The Engineered Wood Association)**

**Figure 16. LVL (Courtesy of Canadian Wood Council)**

**Figure 17. Mass plywood panel, MPP (Courtesy of Freres Lumber Co., Inc.)**

### *4.3.3.1 Process Modelling*

Several phases of veneer and veneer-based production require careful attention to material and process control as these feed into and affect subsequent steps as well as final product quality and performance. Such processes include log conditioning/heating, peeling, defect and moisture detection, veneer-ribbon clipping, veneer drying, glue application, panel layup, prepressing, and hot-pressing. Schematic representations of the process of plywood manufacture are shown in Figure 18.

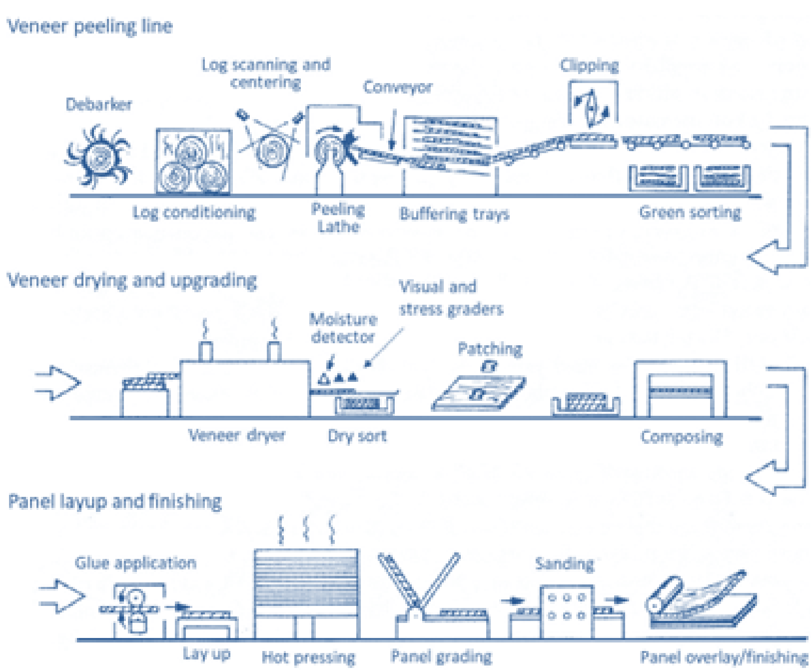


**Figure 18. Schematic flowchart of typical plywood manufacturing process**

Over the past 20 years, FPInnovations has developed a series of computer simulation and optimisation models for almost all stages of the process of veneer and veneer-based product manufacture—the log yard (modelling of log freshness with time, stacking, and seasonal parameters), log conditioning (thawing, heating, and softening for peeling), log peeling, veneer-clipping defect removal and optimal recovery, veneer drying, and veneer grading for tailoring of plywood/LVL mechanical properties. Based on fundamental principles governing the manufacturing operations and calibrated using extensive lab and mill trial data, these models have been widely used by mills across Canada for training, process optimisation, and product development.

Table 1 shows a list of the process models for veneer production for which Forintek/FPInnovations holds the copyright. Some of the models were the first simulation software packages developed anywhere in the world; they were designed for use in mills according to their operating parameters to help understand and progressively reduce operational inefficiencies.

**Table 1. List of process models developed for veneer production operations in Canada by Forintek/FPInnovations**

| Process | Process model | Manual/reference |
|---|---|---|
| Log drying | DryLog | Defo, M., & Brunette, G. (2007). Application of a mathematical model to the analysis of the influence of length and diameter on log drying rate. *Wood and Fiber Science*, *39*(1), 16-27 |
| Log conditioning | LOGCON | Dai, C., Chen, S., & Sallahuddin, U. (1996). LOGCON 2.0: Dynamic software for log conditioning |
| Log peeling | VPeel<br>VYield<br>SPINDLESS | Dai, C., Wang, B., & Chen, S. (1998). VPeel 2.0: Dynamic software for veneer peeling<br>Dai, C., & Wang, B. (1998). VYield 2.0: Computer software for veneer formation and recovery<br>Wang, B., & Dai, C. (1998). SPINDLESS 1.0: Dynamic software for spindless lathe peeling |
| Veneer clipping | VClip | Wang, B., Chow, G., & Dai C. (2015). VClip™: Veneer clipping simulator<br>Dai, C., Semple, K., Chow, G., & Allison, B. (2017). *Developing a veneer clip (VClip) simulator for clipping optimization*. Record #: FPIPRODUCT-173-1334 |
| Veneer drying | VDry | Dai, C., Yu, C., & Wang, B. (2003). VDry-L 1.0: Computer model of longitudinal veneer dryer<br>Dai, C., Yu, C., & Wang, B. (2003). VDry-J 1.0: Computer model of jet veneer dryer |
| Veneer grading | VGrader | Wang, B., & Dai, C. (2000). VGrader 1.0: Veneer grading and lay-up optimization |

#### 4.3.3.1.1 Log Drying and Log Conditioning

In most plywood/LVL plants, logs are acquired and stored in the yard for between a few weeks and 12 months. Keeping the logs fresh, that is, minimising moisture loss, is critical to the quality of veneer peeling and subsequent processing. The DryLog (Defo & Brunette, 2007) is an FE model based on the principles of heat and mass transfer. Extensive laboratory databases were developed to characterise the wood moisture–water potential relationships for this model. DryLog takes into account the effects of log-pile dimensions and alignments in relation to wind directions. One of the interesting features of this software is that it can use meteorological reports to predict the change in log moisture content with time at a given plant.

Log conditioning or heating is another critical process. Logs are thawed in the winter and heated to the temperatures necessary to soften the tissues and reduce the cutting forces during veneer peeling (Chen et al., 2021). Building upon some of the early work by Steinhagen et al. (1987), Dai et al. (1996) developed the LOGCON model based on the circular finite difference method and the assumption that heat is transferred solely through conduction (i.e., no mass flow). Experiments found only superficial (the outer 25 mm) change to the moisture content of logs even after 24 hours of hot water heating (Dai et al., 1996). LOGCON 2.0 software can model and plot heating and cooling dynamics for logs of different species and diameters, combinations of climatic and conditioning chamber temperatures, and time allowed for heating (a mill-throughput constraint). The software can also design and optimise log-conditioning processes. The key conditioning parameters include log species and diameter, heating temperature, weather temperature, and heating time. An example of typical outputs from LOGCON 2.0 is shown in Figure 19.

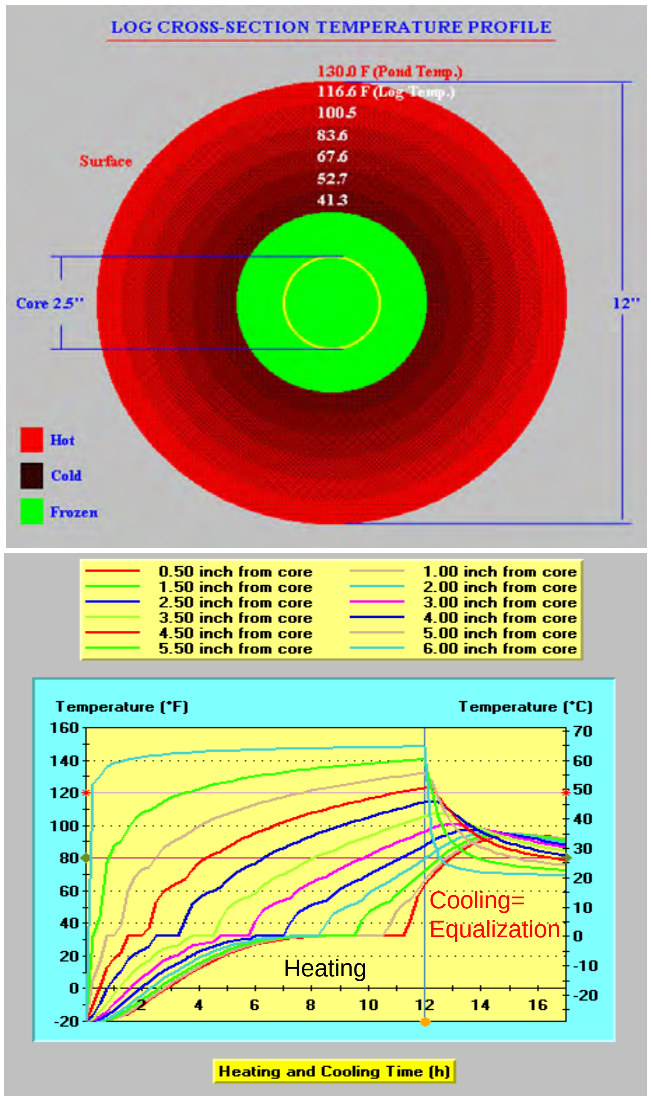


**Figure 19. Key outputs from LOGCON 2.0 log-conditioning simulation software: (left) log cross-section temperature profile; and (right) temperature versus time**

### 4.3.3.1.2 Veneer Peeling

Veneer peeling is arguably the most complex, mechanically dynamic process in the manufacture of veneer products. In modern plywood-processing plants, the veneer is cut and moves at speeds as high as 7.6 m/s (1500 ft/min). At such speeds, the peeling lathe components—the relative geometry of the knife, pressure/roller bar, and log/veneer positions—have to be precisely controlled to minimise vibration and maximise veneer quality and recovery. VPeel (Dai et al., 1998) is a Visual Basic program based on principles of 2D geometry to simulate the relative change of these lathe components at any given time during peeling.

Figure 20 is a screen shot of the VPeel interface showing the nonlinear decrease of the bar contact area (yellow) with the log and inner knife-rubbing area (red) with the log during peeling. Both parameters need to be adjusted to compensate for the change in geometry and log mass and the fact that the knife is also peeling lower density, weaker juvenile core. Lab and mill trial data were generated to take into account nongeometric factors. The VPeel simulator can be used by mills to understand how veneer peeling works and to program lathes by adjusting parameters such as knife pitch angle and bar gap to achieve best peeling quality. A similar simulation software SPINDLESS was also developed to simulate the relative geometry between log, knife and three spindles during peeling using a spindless lathe. The predicted geometry table can be used to program the dynamic movement of each spindle in order to control peel thickness.

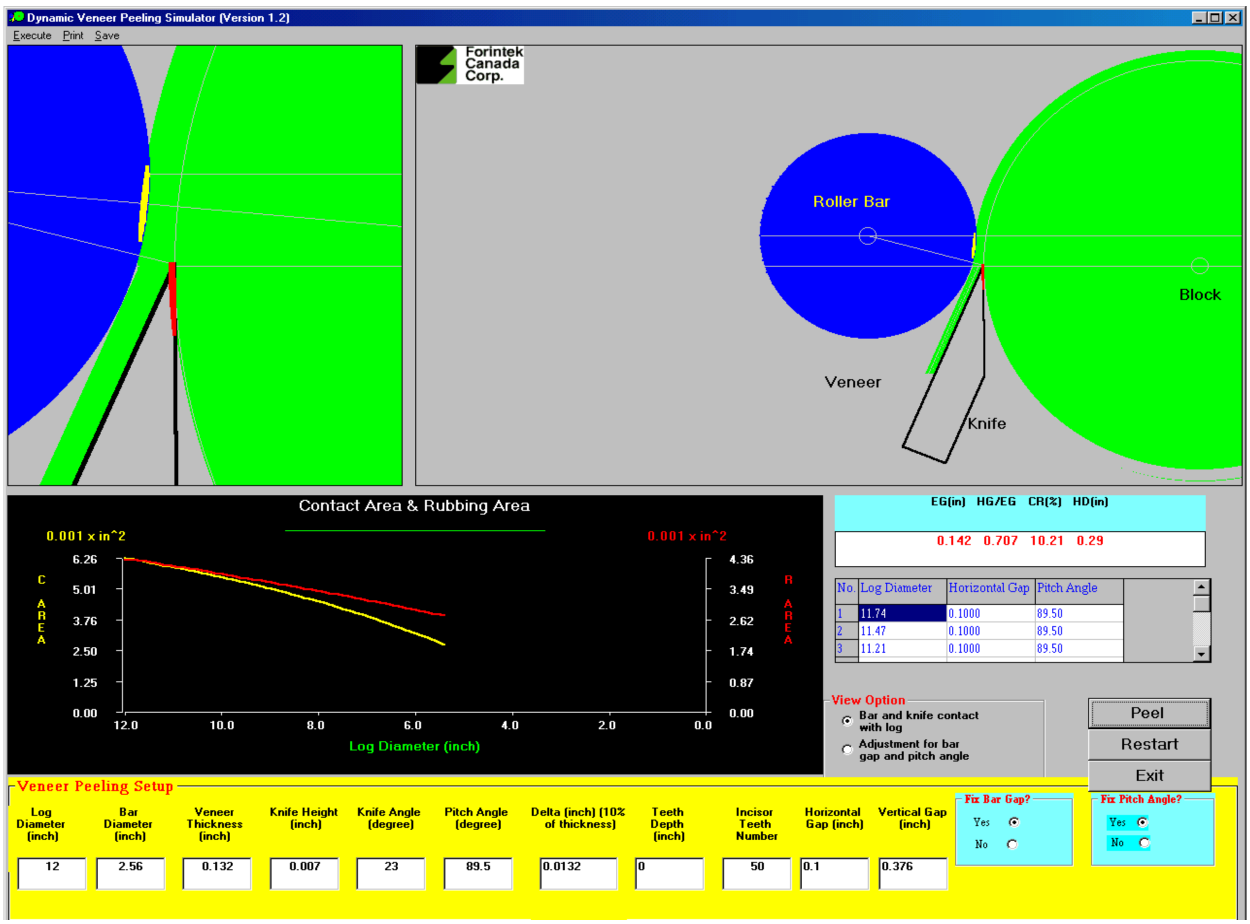


**Figure 20. Example of inputs and outputs from VPeel log-peeling simulation software**

To understand and predict veneer recovery, the VYield software package allows for prediction of volume, ribbon length, and area yields of veneer (plus recovery/waste ratios per block volume) by adjusting input log size (length, bottom, and top diameters), large- and small-end centring errors, veneer thickness, and core diameter settings. Based on earlier work by Foschi (1976), the 3D geometric model simulates the veneer sheet formation (veneer ribbon) on a Visual Basic platform with all input and output parameters conveniently listed in a single page, as shown in Figure 21(a). Figure 21(b) depicts a typical drastic fall in veneer-to-block-volume ratio (recovery) with larger centring inaccuracies. The effect is magnified with increase of diameter logs. This theoretical model needs to be calibrated to estimate realistic veneer recovery for mill applications. As with earlier models, extensive lab and mill trial data were collected to ensure the accuracy of the VYield model.

(a)

(b)

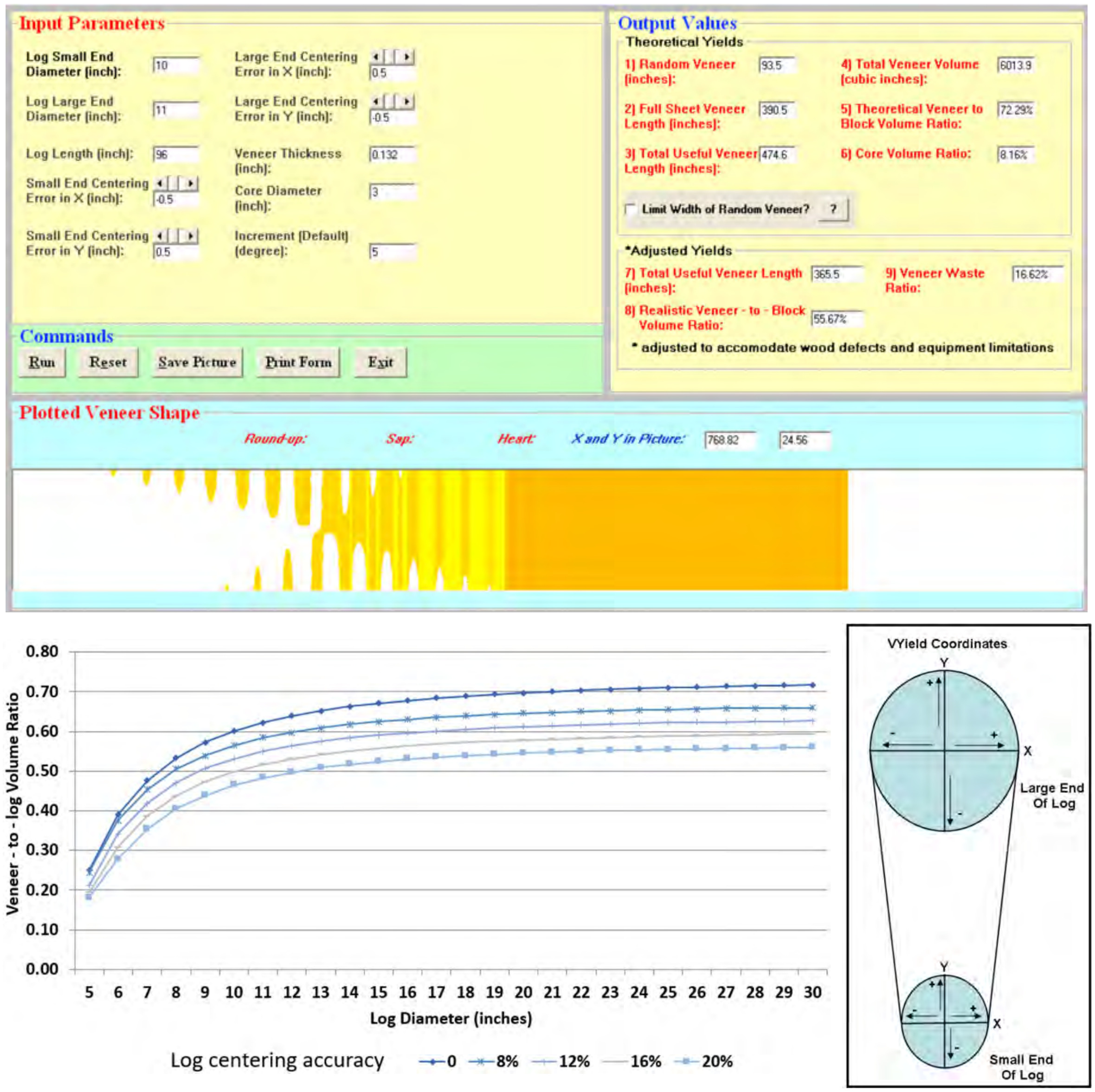


**Figure 21. VYield veneer recovery simulation software: (a) user interface; and (b) modelled effects of adjusting small- and large-end centring errors on recovery**

#### 4.3.3.1.3 Veneer Clipping Optimisation

Because of variations in log shape and defects, typical veneer ribbons contain defects such as knot holes or solid knots, fishtails, splits, and wanes. Knowing the ribbon shape and visual defects is essential when continuous sheets need to be cut into modular veneer size—typically 1.2 m by 2.4 m (4’ by 8’) for full sheets and 200 mm to 686 mm (8″ to 27″) for wide random sheets—for further processing. VClip software analyses images of peeled ribbons taken by mills and runs simulations of volume outturns based on adjusting settings of sheet length and permissible defect (length along and across the grain of the holes and edge defects termed fishtails). The veneer-clipping parameters include full sheet width, maximum hole size along and across the grain, lead/trail ribbon length, and edge defeat (maximum size along and across the grain). Figure 22 shows an image of a veneer ribbon used by VClip to run simulations for calculating recovery.

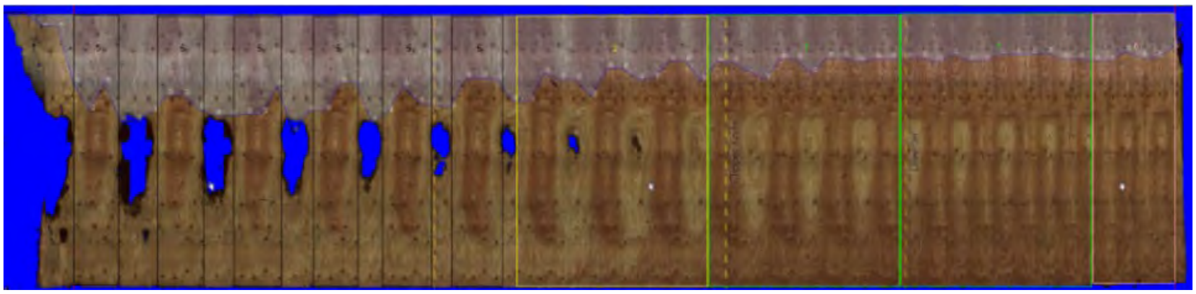

**Figure 22. Image of a veneer ribbon used by VClip to run simulations for calculating recovery**

Figure 23 shows an example of results of the VClip simulator examining the effects of adjusting the mininum allowable sheet width on recovery. The simulator and the mill trial data both show a 6% increase in recovery as the minimum clipping width setting is reduced from 24″ to 12″.

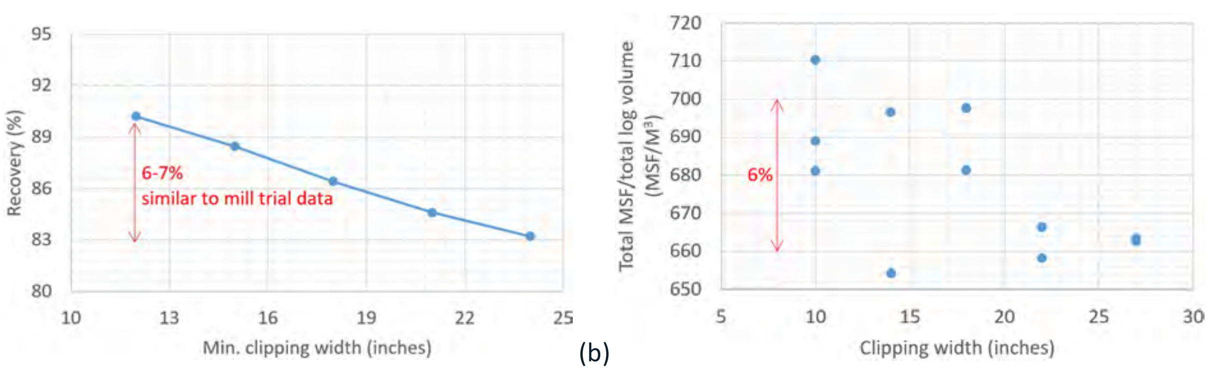


(a) (b)

**Figure 23. Example of using VClip to estimate the effect of minimum clipped sheet width between 12″ and 24″ on (a) percent recovery, and (b) million square feet (MSF) of 3/8″ thickness of veneer per log volume, with results compared to data collected from a mill trial**

Figure 24 shows an example of results of the VClip simulator modelling the effects of adjusting the allowable defect size for each mimimum clipping width setting. As might be expected, increasing the allowable void size increases recovery, and an overly conservative (too small) void size criterion is considerably magnified if the minimum clipping width setting is too high. These simulations help mills understand the less obvious effects of adjusting setting combinations at the clipper station, helping optimise recovery and value returns.

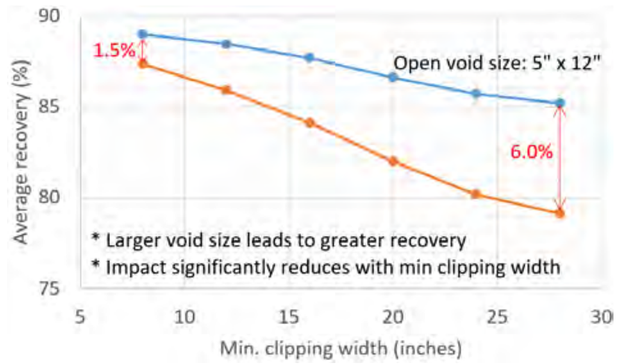


**Figure 24. Simulated effects of allowable defeat void size and clipping width on veneer recovery**

#### 4.3.3.1.4 Veneer Drying

As with of all wood composites, drying makes wet veneer, which usually has a highly variable moisture content, more-or-less uniformly dry (typically 2–4%). Low moisture content is needed for proper gluing. Low moisture content is also required to make sure less steam is generated during hot-pressing.

Drying represents over 80% of plant energy consumption, a major capital cost. VDry consists of two sub-models, VDry-J and VDry-L, simulating the physical and dynamic transport processes of veneer-drying operations in a jet airflow dryer and longitudinal airflow dryer, respectively. Based on the principles of heat and mass transfer, drying physics, and extensive experimental data, the models predict the in-situ variations of air temperature, humidity, veneer temperature, and moisture content. They are convenient tools for sensitivity analyses of key variables (such as veneer-sorting number, drying temperature, and feeding speed) on drying productivity and energy consumption.

As the jet dryer is the most commonly used dryer in the industry, the results presented here only focus on VDry-J. Figure 25 shows the output of simulated moisture content distribution of veneer sheets based on input species and the veneer thickness setting. The two peaks represent the moisture content of the average heartwood portion (around 40–50%) and of fresh sapwood (140–150%). Selecting a setting for a veneer-sorting and drying strategy (such as feed-forward control of veneer drying) is based on the moisture content statistics and distribution for a set of four groups. Toggling the boundaries of these groups adjusts the ratios in each batch.

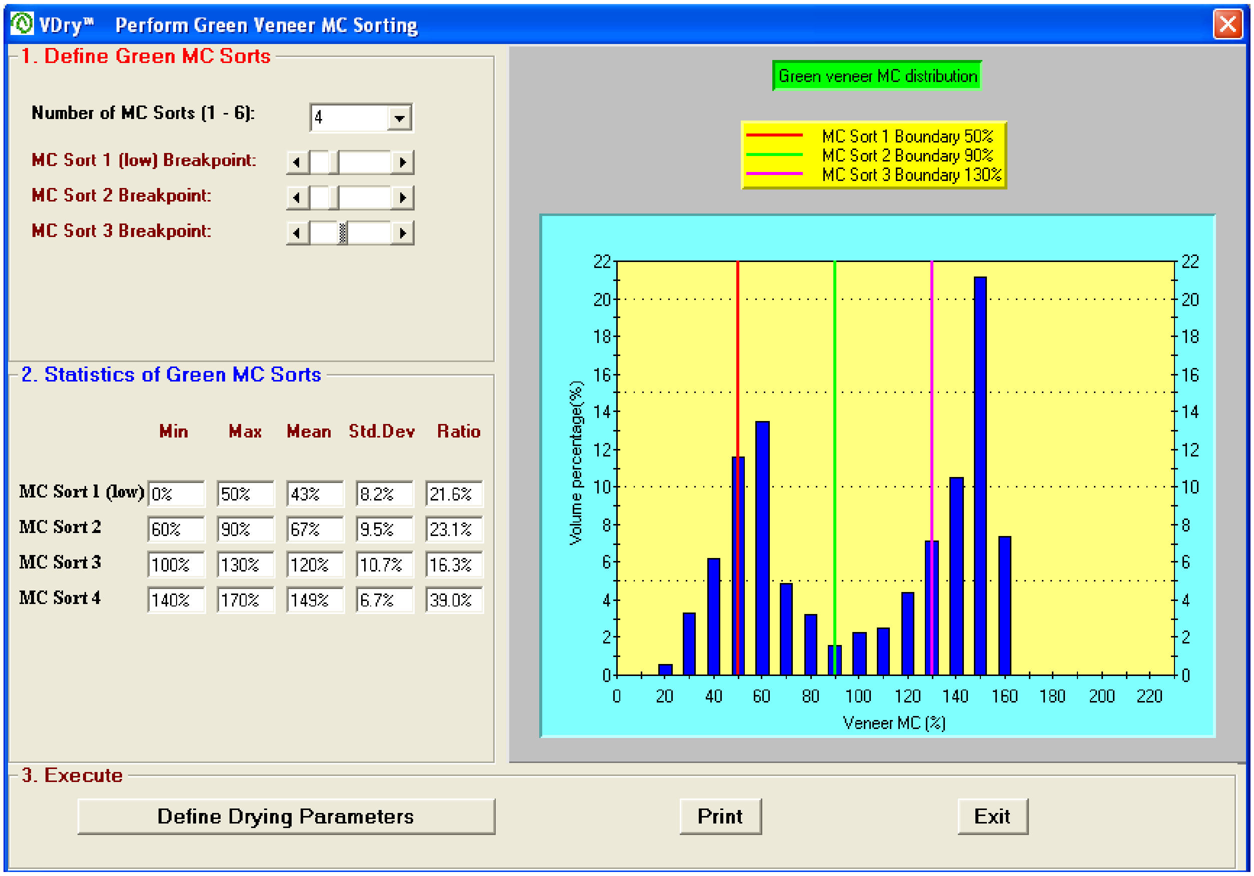


**Figure 25. Green veneer MC (moisture content) sorting and classification component of VDry simulation package**

The second component of the VDry simulation software involves input of dryer configuration (width and height, drying and cooling zone lengths); constraints (air velocity, stacker rate, dryer fill ratio, heat loss factor); dryer-operating details (hours of run per year, current energy costs, mill production costs); and the veneer parameters (sheet length and width, target dry density), as shown in Figure 26. Once these settings have been input, the simulator generates the percent volume of different prescribed dried moisture content groups (overdry, target, refeed, or redry) based on different settings for a range of parameters including veneer temperature inside the mill, ambient outside temperature, relative humidity, maximum attainable dryer temperature (reduced in winter), feed speed, the boundary moisture content for each group (target, redry, etc.), as well as toggles for temperature and relative humidity settings for the dryer zones (which can be preset at, for example, 190 °C and 35%). Apart from the percentage dried veneer classification by moisture content group, the output also includes estimates of production rate for dried veneer ($m^2$/h or sq. ft/h per given nominal thickness), and aspects of dryer energy consumption, efficiency, and production costs for the mill. An example of how adjusting the feed rate influences the productivity based on balancing feed rate with redry rates is shown in Figure 27. The VDry models have been used to help mills to understand and optimise the drying process and to design better dryers. Mill trials have shown that it is possible to consume less energy, be more productive, have higher fibre recovery, and produce better quality products by manipulating the zone temperatures, relative humidity, and percentages of redry/post-dry hot stacking veneers.

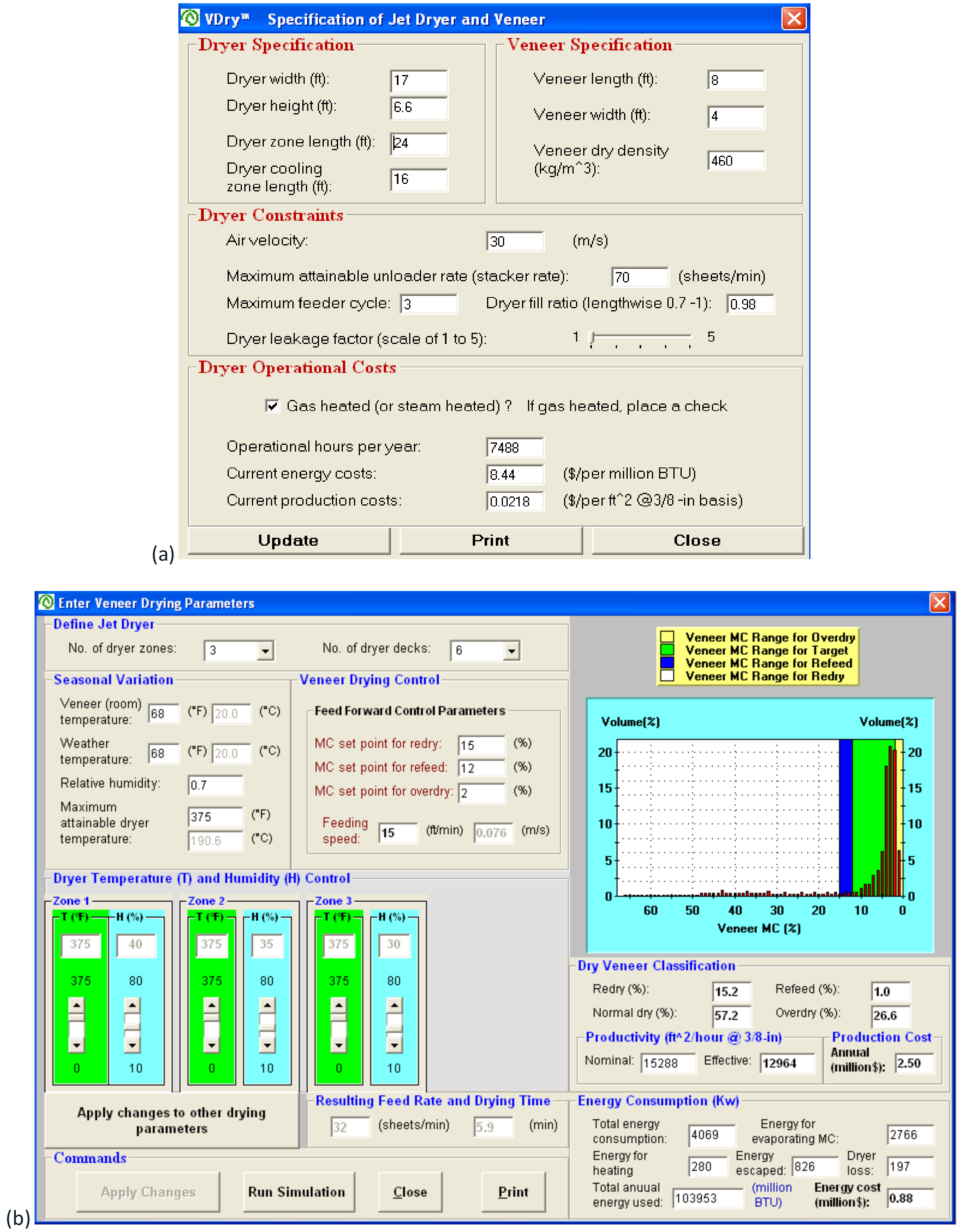


**Figure 26. VDry simulation software: (a) green MC (moisture content) classification; and (b) dry MC (moisture content) classification**

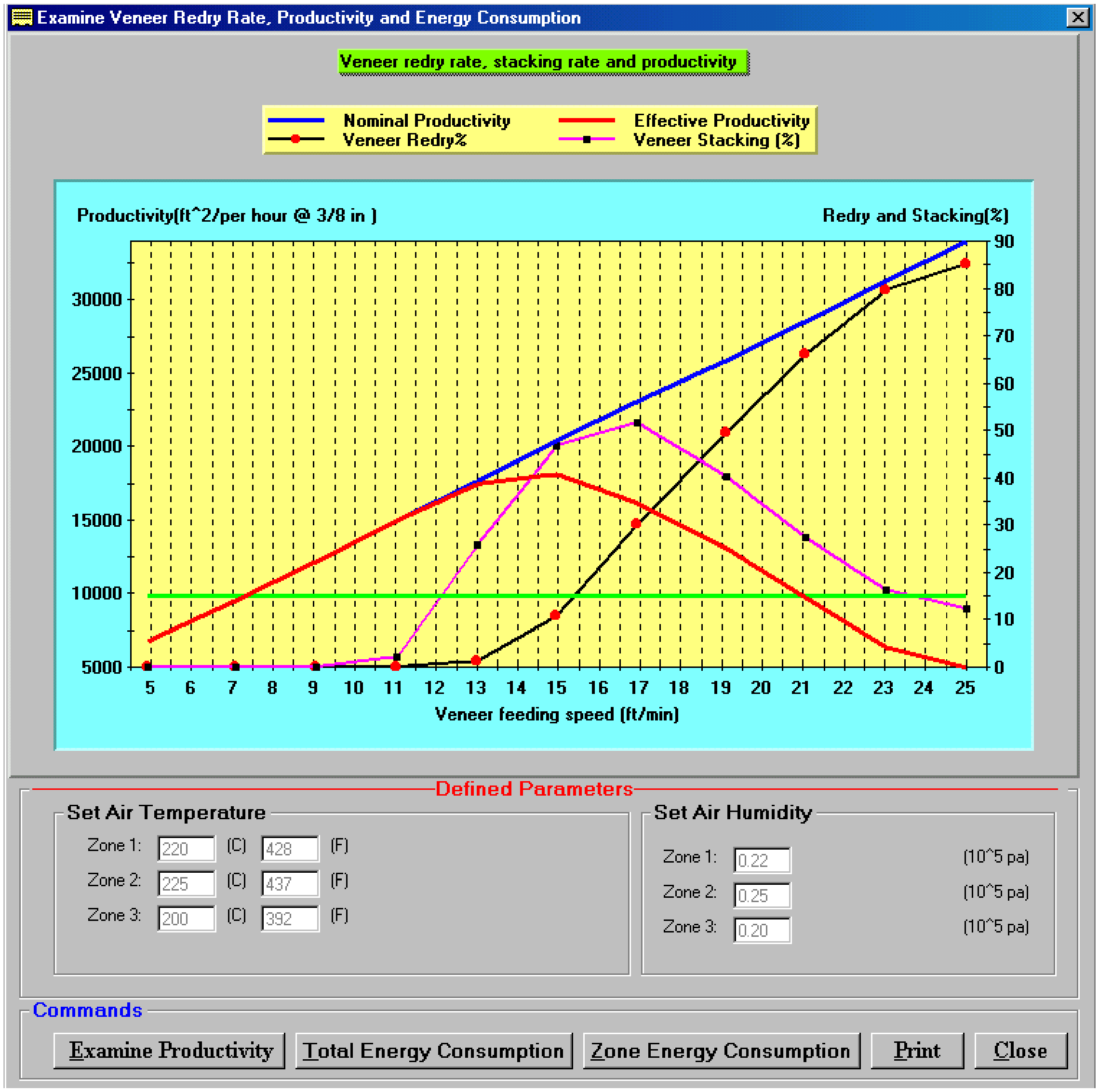


**Figure 27. Example of modelling the effect of feed rate on production efficiency using VDry**

### 4.3.3.1.5 Veneer Grading and Product Layup

For structural plywood and LVL products, veneer stress-grading is critical to ensure product properties conform to industry standards APA PS-1 (2010) and ASTM D5456 (2021). The stress grade of veneer depends mainly on grain angle and wood density. These characteristics are available for download when using an industry standard machine such as the Metriguard veneer scanner, which also measures veneer moisture content and temperature. The VGrader model inputs the data collected by the Metriguard scanner for each sheet (density, moisture content, temperature, ultrasonic propagation time [UPT]) to output the veneer MOE or E-grade based on density and grain orientation, which is directly correlated to UPT (Wang & Dai, 2013). The VGrader software also produces grade out-turn distributions based on input species, and E-grade or thresholds of UPT value straight from the Metriguard data, as illustrated in Figure 28.

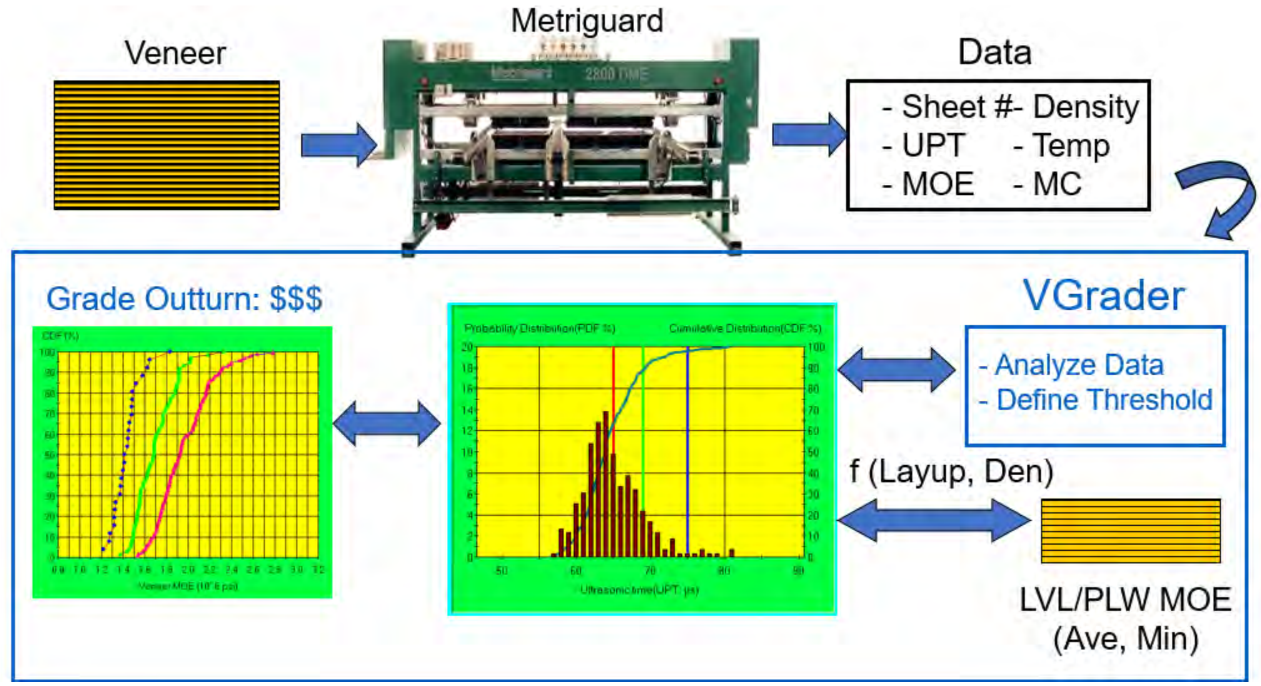


**Figure 28. Schematic of linkage between mill data from Metriguard veneer scanning and VGrader simulation software analyses: UPT stands for ultrasonic propagation time, Temp for temperature, MOE for modulus of elasticity, MC for moisture content, Den for density, Ave for average, Min for minimum, and PLW for plywood**

The VGrader simulator was designed to model the effects on average and variability (standard deviation, or stdev) of veneer MOE by toggling between veneer visual grade or MOE grade distributions (Figure 29[a]). Visual grade is generally no indicator of the MOE of a veneer, which is based on the UPT and density. Based on classical lamination theory, the VGrader predicts the product-bending MOE and modulus of rupture (MOR) of plywood or LVL by E-grade of veneer layers and their layup (Figure 29[b]). The standard practice is to locate the highest (G1) veneers in the surface layers and the lowest (G3) veneers in the core to maximise the panel-bending strength and usage of all veneer grades.

(a)

(b)

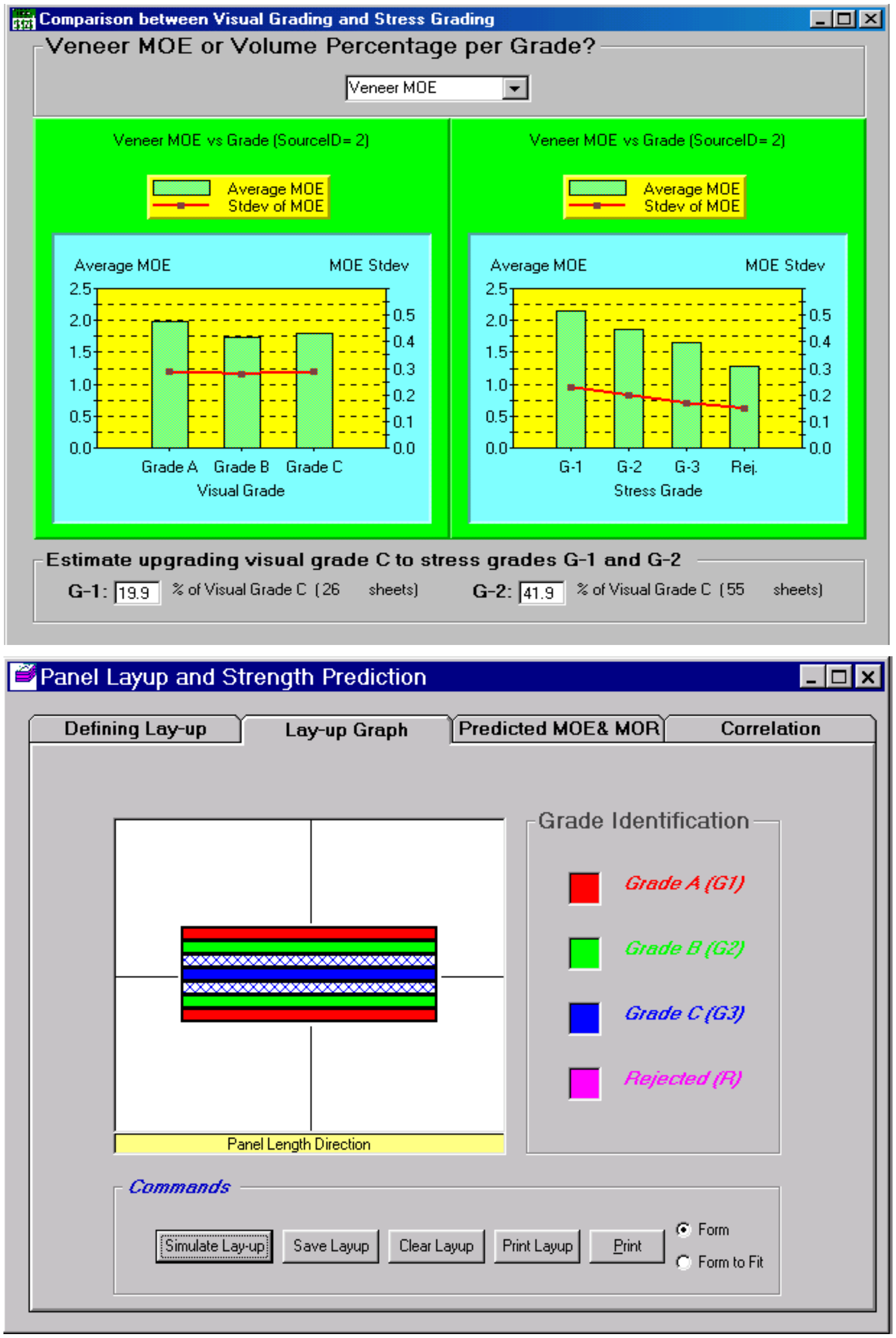


**Figure 29. Examples of applications of VGrade simulation software: (a) plotting the average and stdev (standard deviation) of veneer MOE by visual or stress grade; and (b) simulator estimates of product MOE and MOR based on grade layup**

All the models described in this section are stand-alone programs and have been utilised separately or in combination for training, process optimisation, and product development (Semple & Dai, 2016a, 2016b, 2017, 2018a, 2018b, 2018c; Wang & Dai, 2014). Further work is needed to create a fully integrated model from the process stages to the prediction of the final product mechanical properties and performance.

### *4.3.3.2 Mechanical Modelling of Product Properties*

#### 4.3.3.2.1 Plywood

Until fairly recently, comparatively little attention has been paid to the structural modelling of plywood, possibly because its development predates computers. This is not the case for strand-based engineered composites; modelling and computer simulation played a key role in their design and commercialisation. Although plywood is a low-cost, lightweight, and highly versatile building material, it exhibits complex progressive failure because of its non-isotropic layered biomaterials and combined polymer (resin) and biomass interlayers (Ivanov et al., 2008).

The modelling approaches described in this section also apply to MPP.

If only the elastic behaviour of plywood is of interest, it can usually be modelled two- or three-dimensionally so that each laminate is assigned with the corresponding material properties (Cha & Pearson, 1994; Merhar, 2020). Examples of the simulations for flexural, torsional, and longitudinal beech plywood (Merhar, 2020) are shown in Figure 30. Thick plywood, such as a 10-layer panel, can be modelled as single homogeneous, anisotropic block; the properties of such thick plywood can be reliably estimated following the rule of mixtures and classical lamination theory (De Oliveira et al., 2018). To take into account the variability of wood, the early VGrader simulator (Wang & Dai, 2013) (described in Section 4.3.3.1) combines classical lamination theory and composite rule of mixtures with stochastic modelling to predict the elastic bending modulus of plywood or LVL based on the known distribution and arrangement of veneer grades in the X-Y-Z directions. In effect, the simulator predicts the veneer E-grades from the online Metriguard scanning data and their layup configurations as the most important factors for governing the final composite stiffness.

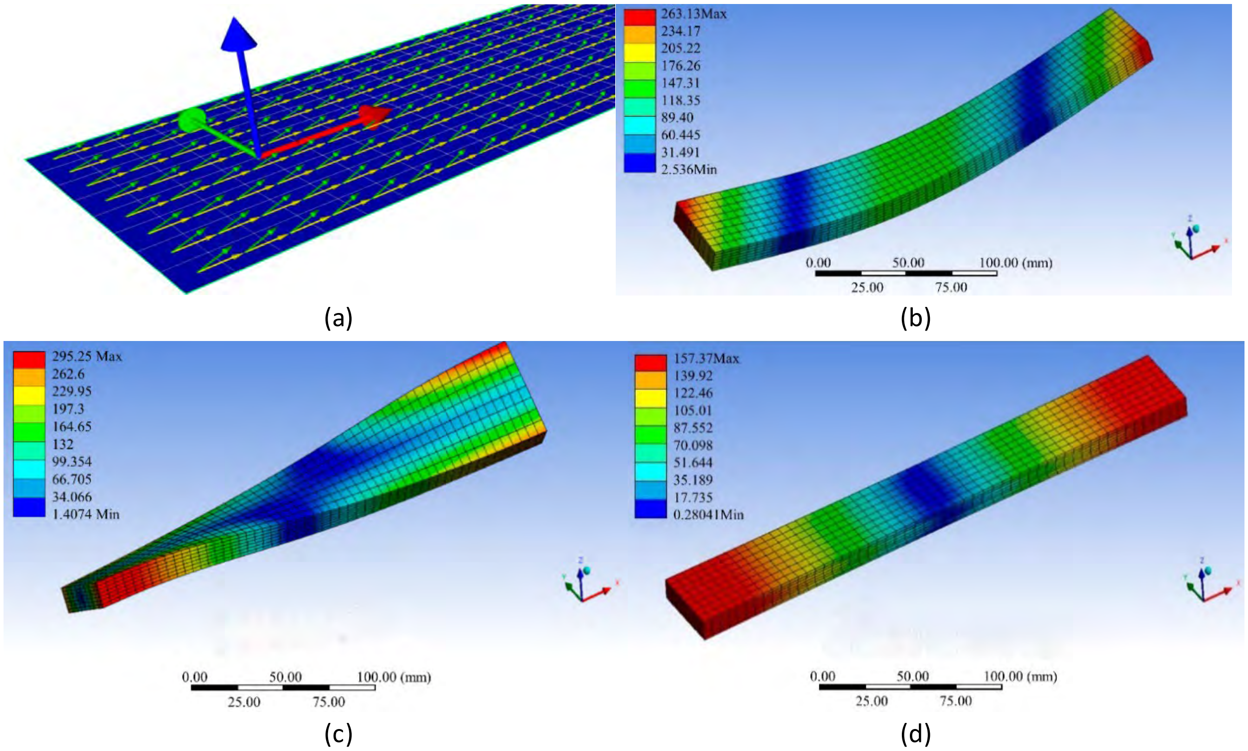


**Figure 30. Composite FE model using Ansys software: (a) first layer with specimen coordinate system; (b) relative deformation of the first flexural vibration mode; (c) relative deformation of the first torsional vibration mode; and (d) relative deformation of the first longitudinal vibration mode (Merhar, 2020)**

Apart from its elastic properties, the strength properties of plywood are important to simulate when the posted strength behaviour is of interest. Ivanov et al. (2008) modelled plywood as a layered cross-ply unidirectional fibre-reinforced composite akin to fibre-reinforced polymer-laminated composites. The researchers conducted compact tension tests in the outer-ply fibre direction and in the perpendicular-to-load (90°) and oblique-to-load (45°) directions, to categorise damage modes into fibre bundle rupture, matrix cracking along fibres, and delamination at the adhesive interlayers. FE modelling incorporating a material damage sub-model accurately simulated the experimental damage propagation behaviour in plywood specimens. The FE model can be extended to layup optimisation and development of very efficient large-scale computational simulations, thus avoiding the need for experimental fabrication.

Bonding is also an important aspect for modelling (Vratuša et al., 2017). El Moustaphaoui et al. (2020) modelled the stress-strain dynamics and fracture toughness at the bondlines in plywood. From a series of experimental tests for fracture toughness in modes I and II and mix mode delamination failure, the researchers employed numerical modelling to establish onset criteria for and identify a law governing propagation of delamination. They compared experimental and numerical results and used the compliance method to calculate the critical energy release rate and determine the resistance curve according to each mode of delamination.

Finally, little attention has been devoted to modelling dynamic loading of wood composites, despite that plywood is a cost-effective core material for high-performance impact-resistant sandwich structures made using higher density aluminium or fibre-reinforced polymer shells. Susainathan et al. (2020) used an explicit nonlinear numerical model based on constituent volume elements with a cohesive interlayer to simulate the low-velocity/low-energy impact behaviour of such structures. The researchers used a plastic wood behaviour sub-model in associated composite type damage criteria. Comparisons with experiments in terms of layer deformations and overall contact laws during impact provided good validation of numerical results, as shown in Figure 31.

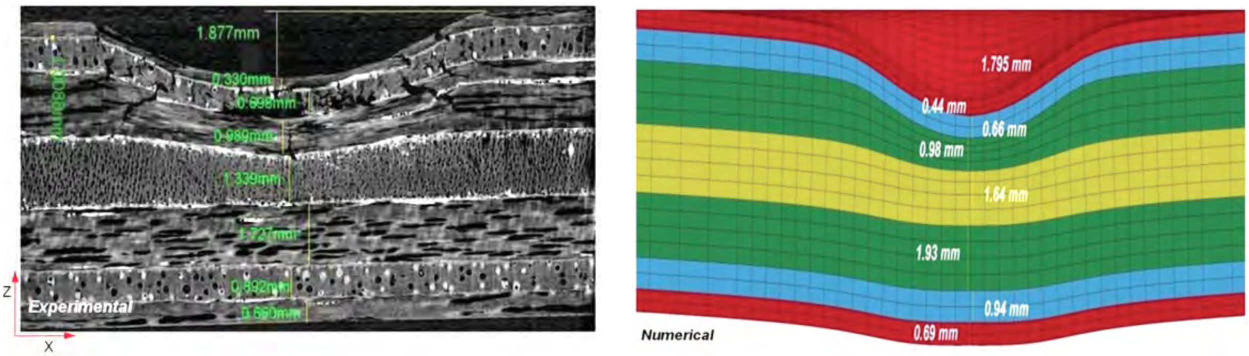


(a) (b)

**Figure 31. Impact layer deformation in plywood: (a) experimental, and (b) numerical simulation (Susainathan et al., 2020)**

### 4.3.3.2.2 LVL

There has been a large amount of recent research on modelling LVL, as this material has many high-performance structural applications, increasingly replacing concrete and steel. The modelling approaches described in Section 4.3.3.2.1 for plywood and MPP are also suitable for LVL, for example, the 3D orthotropic elastic models of LVL developed by van Beerschoten et al. (2014).

Clouston and Lam (2001) combined classical elastoplastic constitutive equations with a probabilistic strength prediction model of veneers to predict strength and stiffness distributions of veneer-based products. This approach was only recently applied to predicting design values for new LVL and structural plywood products based on information on the wood in the veneers; such information on wood is easier to obtain (Gilbert et al., 2017). Gilbert (2018) developed a predictive model for bending strength of LVL as well as the compressive strength for structural LVL products from a previously underutilised wood resource—early to mid-rotation (juvenile) subtropical hardwood plantation logs—with very close agreement with measured data.

Attempting to model stiffness parameters for LVL used in high-performance wind turbine towers, Ek and Norbäck (2020) found that classical laminate theory alone was insufficient to model the materials' elastic responses, particularly at the upper limit and beyond the materials' elastic response range to loading. Ek and Norbäck (2020) proposed a 3D linear-elastic FE model to account for variability in veneer properties and model the knots as $E = 0$ or voids in the structure. They used Monte Carlo simulation—simulating many model scenarios based on different statistically determined deviations in the material—to model the effects of size for thick LVL cross-sections. Increasing the number of veneers magnified the effect of variation between veneers and reduced the influence of knots. The researchers also concluded that wood and its laminated composites can, to some extent, redistribute stresses when loaded above the yield limit. In other words, if the yield stress is reached locally, it does not mean that the laminate will fail immediately.

Where brittle failure governs the structural performance of LVL (e.g., a curved LVL arch), the constitutive model of tensile and shear fracture can be adopted. Šmídová and Kabele (2018) conducted a nonlinear FE simulation of a four-point bending test of a curved LVL arch. The simulation applied a 2D homogeneous orthotropic constitutive model of tensile and shear fracture to the constituent yellow poplar wood. The model successfully reproduced the load-displacement response and captured the most distinctive features of the crack propagation pattern, as shown in Figure 32.

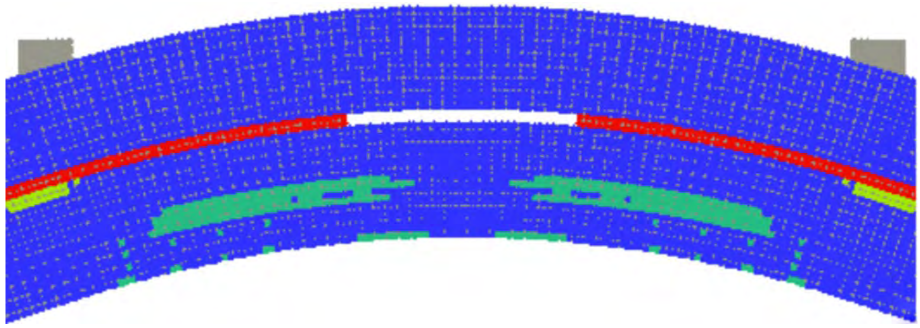

**Figure 32. LVL arch crown cracking under four-point bending in FE simulation: primary (red) and secondary (green) crack (Šmídová & Kabele, 2018)**

### 4.3.4 Strand-based Products

Strand-based composites, including LSL, PSL, and OSL (Figure 33), are far more complex in terms of structure and processing than lumber- and veneer-based products. Strand-based composites have many more layers and interlayers and more varied element sizes and orientation, mat-forming parameters, and mat-consolidation dynamics, particularly the development of vertical density profile during hot-pressing. The strand geometry (size and shape) and its distribution are critically important to simulate and optimise the strand orientation. Reliable models must take into account the variability within and across the wood elements, their preparation history (cutting and drying), and the processing stages (resin blending, mat forming, and hot-pressing).

**(a)** **(b)** **(c)**

**Figure 33. (a) LSL, (b) PSL, and (c) OSL (Courtesy of Canadian Wood Council)**

### *4.3.4.1 Modelling Structure-property Relationships*

Figure 34 illustrates the links between three essential parameter sets on which integrative models can be developed for the entire manufacturing process. The first parameter set defines the constituents from which wood composites are made: mainly wood, resin, and wax. The second parameter set defines the structure (the spatial organisation) of the constituents: density, strand orientation, porosity, and contact. The final parameter set concerns major processing steps: strand preparation, drying, blending, forming, and pressing. Developing the mat structure model is a key to providing comprehensive modelling of the entire composite process and all the properties.

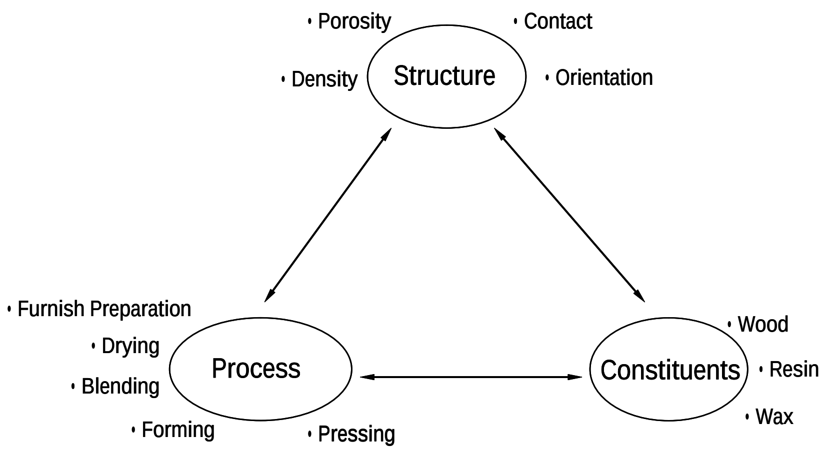


**Figure 34. Three parameter sets for modelling wood composites**

One of the earliest wood composite models is a conceptual model for particleboard structure by Suchsland (1959). Other early mathematical models focussed on random fibre networks to characterise paper structures (Dodson, 1971; Kallmes & Corte, 1960). Based on some of these early concepts and methods, subsequent work in the field involved developing a series of mathematical and computer models to characterise the mat formation, consolidation, and bonding properties of the wood composite. While some of the models are still in development, a summary of significant advances in understanding the mat formation and its relationship to product properties follows:

1. One of the early key discoveries was that the random mat formation in flakeboards (the precursor to OSB) mathematically follows a Poisson distribution (Dai, 1994; Dai & Steiner, 1994, 1997). The Poisson distribution allows for random overlaps of flakes (or longer strands) in a mat to be analytically defined. The average and the variance of strand overlaps are simply determined by the product of mat/panel compaction ratio and thickness ratio.

2. Defining the Poisson mat formation process has enabled analytical modelling of horizontal density distribution, allowing for calculation of local mat densities as a function of strand dimensions, wood density, panel density, and panel thickness (Dai & Steiner, 1997).

3. Combining this with prior deformation models of cellular solids (Gibson & Ashby, 1988) and wood (Wolcott, 1990) allows for the derivation of constitutive laws for mat consolidations based on

mechanisms of transverse wood compression (Dai, 2001; Dai & Steiner, 1993) and fibre bending (Zhou et al., 2008).

4. The mat structure model allows mat porosity and permeability to be analytically defined, which in turn leads to the ability to predict heat and mass transfer during pressing (Dai & Yu, 2004; Dai et al., 2005; Dai, Yu, & Zhou, 2007).

5. A mechanistic model was then developed to predict the internal bond strength of strand wood composites based on the mechanisms of inter-element contact (Wang et al., 2006; Dai, Yu, & Zhou, 2007), resin distribution (Dai, Yu, Groves, et al., 2007), inter-element bond strength (He et al., 2007), and localised bond failures (Dai et al., 2008).

6. Micromechanics models are also being developed to predict the elastic properties (bending MOE) (Dai et al., 2004) and the deflection/ultimate load of OSB under concentrated static loading (Dai & Yu, 2008).

7. Parallel to these analytical models, computer simulation models have been developed to simulate 2D and 3D mat structures and mat consolidations. These models, which use the discrete element method, Monte Carlo techniques, and 3D collision detection method between rigid bodies (van den Doel, 2008), complement the analytical models by permitting simulation of more realistic element shapes and spatial organisation.

8. The computer simulation models described above (see #7) have been combined with the material point method model to predict mechanical properties of strand composite products, such as OSL (Nairn, 2003). There is close agreement between the predicted model and the experimental results of flat bending MOE in the parallel direction. Both density profile and orientation play very significant roles in determining the elastic property of the final product. The model is capable of predicting the effects of other variables, such as species, resin content, and strand dimensions.

#### *4.3.4.2 Process Modelling*

Various physical models have been developed to simulate strand cutting (from bamboo culms) (Semple & Smith, 2017); particulate or strand drying (Kamke & Wilson, 1986; Noffsinger, 2004); resin blending (Dai, Yu, Groves et al., 2007; Smith, 2005; Tsai & Smith, 2014); mat forming and consolidation (Amini et al., 2017; Barnes, 2000; Dai & Chen, 2016; Dai, Semple, et al., 2017; Dai & Steiner, 1993; Lang & Wolcott, 1996; Zhou et al., 2008); and hot-pressing (Dai & Yu, 2004; Dai et al., 2005; Humphrey, 1989; Zombori et al., 2003). Table 2 shows the process models developed for strand-based composites at Forintek/FPInnovations.

**Table 2. List of computer simulation models for strand-based composites developed at Forintek/FPInnovations**

| Process | Simulation model/research report |
|---|---|
| Resin blending | Wang, X., Groves, K., & Chow, G. (2016). BlenderSim 1.0: Simulation of resin spray distribution in a rotary blender. |
| Mat formation/orientation | Dai, C., Wang, B., & Chen, S. (2000). MatForm 3.0: A 2D computer simulation model of OSB mat formation.<br>van den Doel, K., & Dai, C. (2014). SOS: Strand orientation simulator.<br>Dai, C., van den Doel, K., Semple, K., Groves, K., Greig, G., & Perraud, F. (2017). Development of strand orienting simulator (SOS) for engineered wood products. |
| Mat pressing | Dai, C., Yu, C., & Wang, B. (2004). MatPress 3.0: A 3D computer simulation of composite hot-pressing processes.<br>Dai, C., Yu, C., & Wang, B. (2004). ContiPress 1.0: Computer model for continuous pressing. |
| Mechanical properties | Dai, C., C. Yu, B. Wang and H. Xu. (2004). OSB-Pro 1.0: Computer model for OSB mechanical properties. Forintek.<br>Dai, C., & Chen, Z. (2016). OSB-Pro 2.0: Computer model for OSB/LSL mechanical properties. |

#### 4.3.4.2.1 Mat Formation

In strand-based wood composites, the presence and distribution of macro-voids (those between strands) critically influence the structural and physical properties and are generally governed by the random lengths of the wood strands and their partial random deposition during the formation process. Based on rigid body collision physics (Coumans, 2005, 2010), researchers developed a 3D strand orienting simulator (SOS) (Dai et al. 2017) to simulate the dynamic disc-strand forming and orienting processes (Figure 35). While the general angle distribution follows the von Mises distribution (Harris & Johnson, 1982), SOS predicts, for the first time, the orientation distribution as a function of former settings, for example, former height (strand free-fall distance), disc spacing, and strand dimensions. This relationship is essential for predicting the impact of strand length, width, and thickness on the final product mechanical properties of the final product.

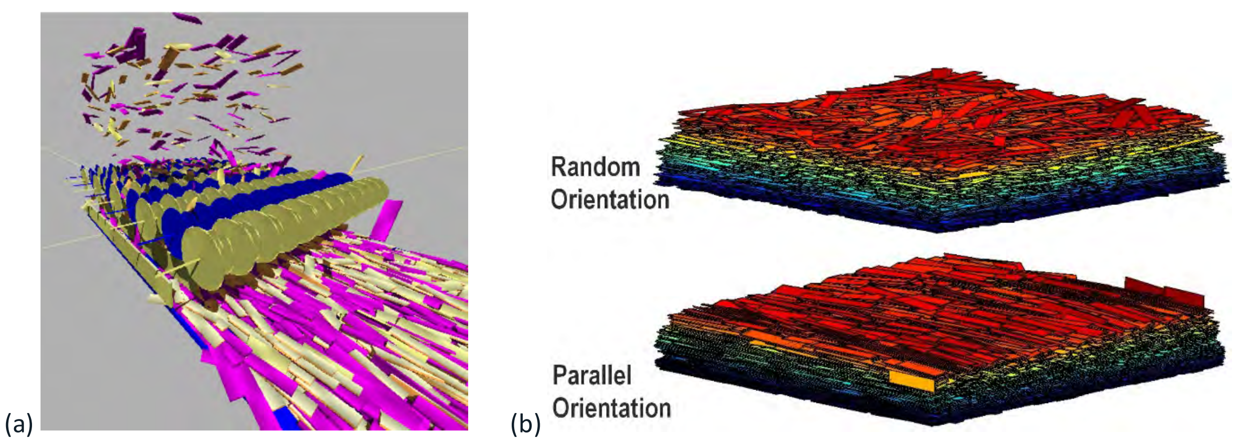


**Figure 35. Dynamic simulation, using SOS, of (a) strand orienting, and (b) mat-forming process**

Figure 36 shows an experimental strand mat and a 2D computer simulation package for laying down OSB mats (Dai et al., 2005). This simulation builds up a stochastic network of strands and overlaps from which horizontal density profiles can be generated (Pineda et al., 2021).

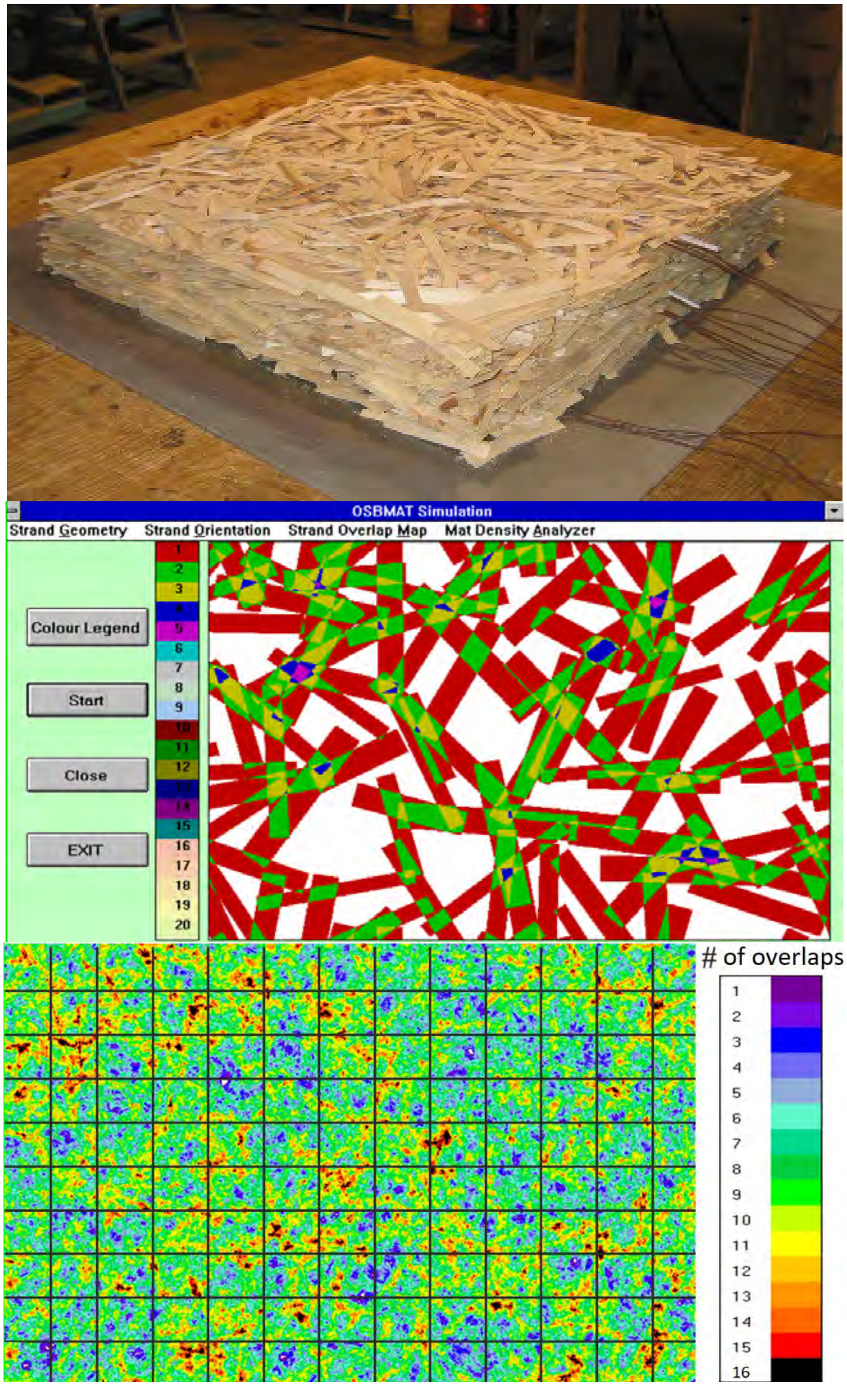


**Figure 36. Real and modelled strand distributions and prediction of the horizontal density profile in strand mats**

### 4.3.4.2.2 Mat Consolidation

Drolet and Dai (2010) developed a 3D mat consolidation model to illustrate strand compression or bending behaviour in a mat under pressure (Figure 37). Strand composite mats before pressing are usually very loose, containing a high percentage of void spaces. As wood is a cellular material, pores exist inside strands (cell lumens) and between strands. Figure 38 shows the structure of the predicted between-strand porosity in a consolidated strand mat where clear pathways exist despite the high degree of mat densification. The connected spaces remain, largely because voids along the strand edges are very difficult to eliminate during pressing. This type of pore structure makes strand-based composites very permeable to gases during hot-pressing (Dai et al., 2005). Optimum mat densification is needed to create intimate strand-to-strand contact for bond development with minimum volumetric loss (Dai, Yu, Groves, et al., 2007). These predictions lay the ground for modelling of mat hot-pressing and of bonding development (Dai et al., 2008).

(a) (b)

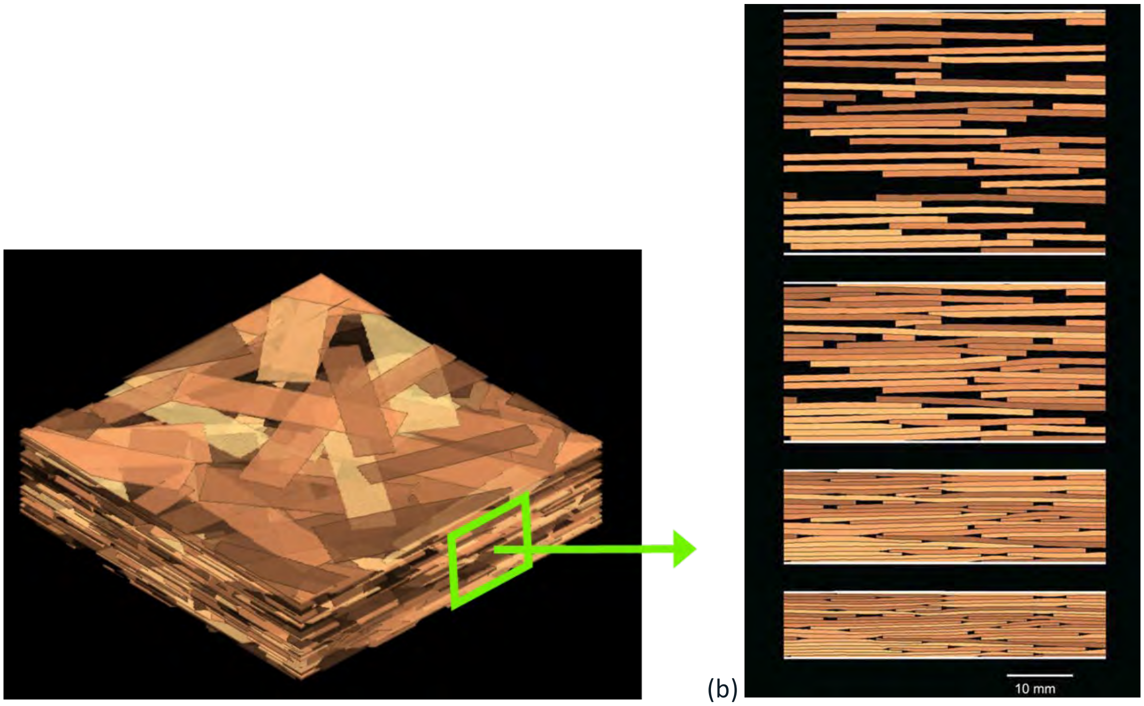


**Figure 37. MatPress simulation of strand mat consolidation: (a) 3D mat consolidation model; and b) simulated cross-section of a mat under progressive compression (Drolet & Dai, 2010)**

(a) (b)

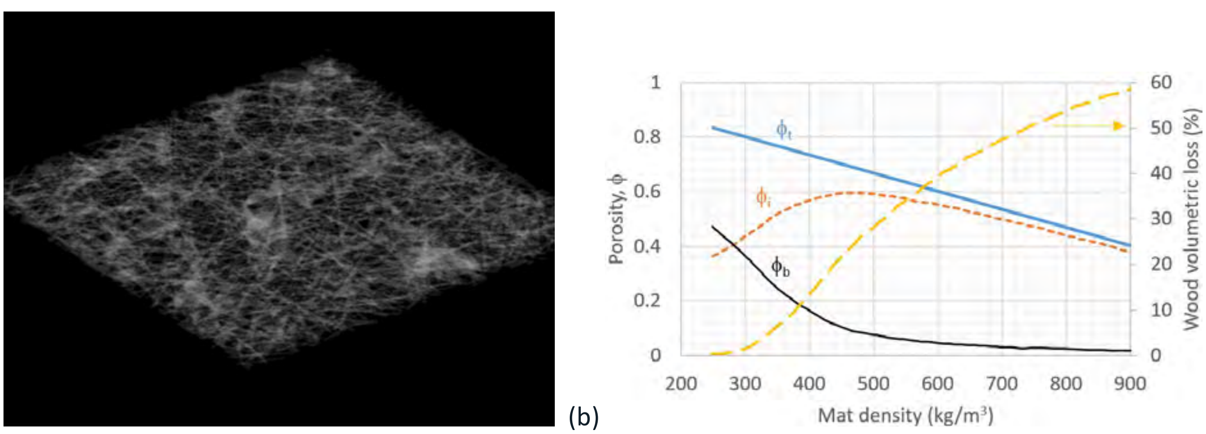


**Figure 38. Mat consolidation simulation: (a) simulated pore structure (void connectivity) in a consolidated strand board mat (Drolet & Dai, 2010); and (b) predicted porosity changes.** ***Note: $\phi_t$ is total porosity; $\phi_i$ is inside-strand porosity; $\phi_b$ is between-strand porosity and volumetric loss of wood during mat consolidation*** **(Dai et al., 2005)**

#### 4.3.4.2.3 Hot-pressing

Humphrey and Bolton (1989) pioneered the development of a heat-and-mass-transfer model for hot-pressing of wood composites (particleboard). Carvalho and Costa (1998) and Thoemen and Humphrey (2003) used similar approaches to develop models for MDF, as did Zombori et al. (2003) for strand boards. Hot-pressing of wood composites is a dynamic, interactive process involving three primary principles: (1) heat and mass transfer (physical); (2) mat consolidation (mechanical); and (3) resin curing (chemical process).

MatPress is a finite difference model based on these principles. It pays special attention to porous mat structure and permeability during formation and consolidation (Dai & Yu, 2004; Dai et al., 2000; Dai et al., 2005; Yu et al., 2007; Dai, Yu, Xu et al., 2007; Zhou et al., 2010). Figure 39 shows the MatPress-predicted spatial variations in temperature, moisture content, gas (air and steam), and density in an OSB mat during hot-pressing (Dai & Yu, 2004; Dai, Yu, Xu et al., 2007; Dai et al., 2005). The simulations are snapshots of MatPress predictions when reaching the target thickness during pressing. All profiles change with pressing time, and the degrees to which they change depend highly upon the parameters and the stage of pressing. While the density and temperature history have a strong impact on bonding, the gas/steam pressure needs to be carefully manipulated to minimise blows and delamination.

(a) (b) (c) (d)

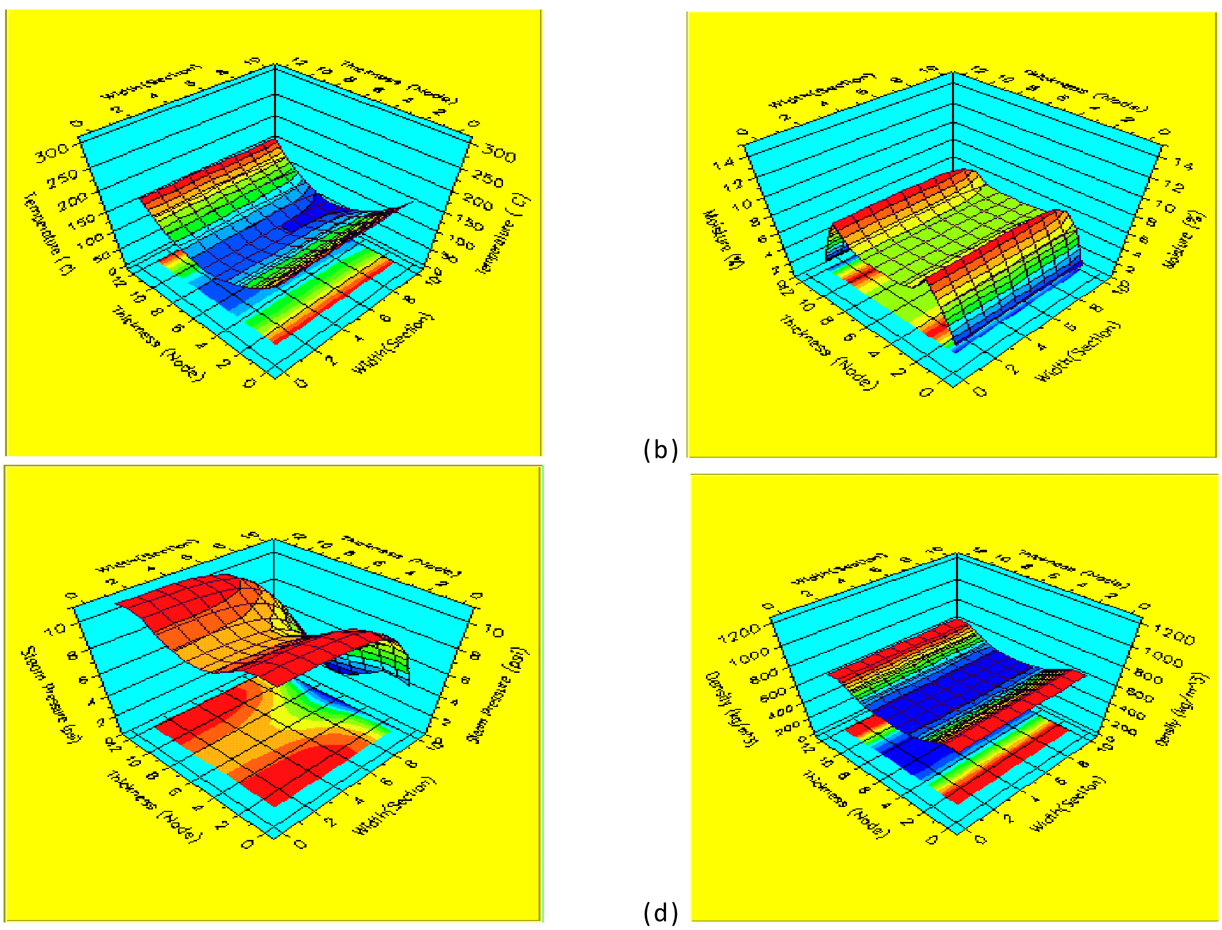


**Figure 39. MatPress simulation of strand composite hot-pressing process—variation of environment and densification from the centre position to the edge of panel: (a) temperature, (b) moisture content, (c) steam pressure, and (d) vertical density profile (VDP)**

### *4.3.4.3 Mechanical Modelling of Product Properties*

#### 4.3.4.3.1 FE Models

Most early modelling for strand-based composites focussed on predicting MOE and its distribution for design purposes, without taking into account strength. These models focus on the wood element properties and distribution. Earliest models for strand composites were for the precursor to OSB, that is, random and oriented flakeboards. Modelling by Hunt and Suddarth (1974) predicted tensile MOE and shear modulus of rigidity for flakeboard, while Shaler and Blankenhorn (1990) predicted the flexural MOE of oriented flakeboard. Subsequent studies have attempted to incorporate both elasticity and strength. For example, Triche and Hunt (1993) developed a linear-elastic FE model capable of predicting the tensile strength and MOE for a parallel-aligned strand composite. They used multiaxial failure criteria, including maximum stress theory and the Tsai-Wu theory (Tsai & Wu, 1971).

Several constitutive models have subsequently been developed for parallel strip-and-strand-based SCL based on the measured, known properties (mostly tensile strength and MOE) of the individual wood elements. For example, Wang and Lam (1998) developed a 3D nonlinear stochastic FE model to estimate the probabilistic distribution of the tensile strength of parallel-aligned wood strand composites based fundamentally upon longitudinal tensile strength and stiffness data of the individual strands.

Clouston and Lam (2001, 2002) developed early nonlinear stochastic models for the stress-strain behaviour in PSL based on the orthotropic and spatially variable constitutive properties of wood strands using probabilistic plasticity theory and the Tsai-Wu yield criterion. Their method combines classical composite mechanics modelling with stochastic modelling. From this, Clouston (2007) developed a constitutive model that predicted a materially nonlinear stress-strain curve for tension, compression, and bending in PSL, which was also based on the nonlinear constitutive properties of the individual strands, characterised within the framework of orthotropic elastoplasticity.

Bejo and Lang (2004) developed a probability-based model to study the effect of change in elastic properties on the performance of PSL, modelling the orthotropic behaviour of wood constituents relative to their position in the composite using theoretical and empirical equations. Winans (2008) used a probabilistic approach to model effective strength of PSL, accounting for grain angle variation within strips, the strip dimensions and effective properties of each element, biological defects such as voids, and the species mix in a PSL member. Arwade et al. (2009, 2010) proposed further models for spatial variation of MOE within a PSL member and for compressive strength in PSL (see Figure 40. Their computational models include adjustable factors for strand length, grain angle within strands, elastic constants, and parameters of the Tsai-Hill failure criterion.

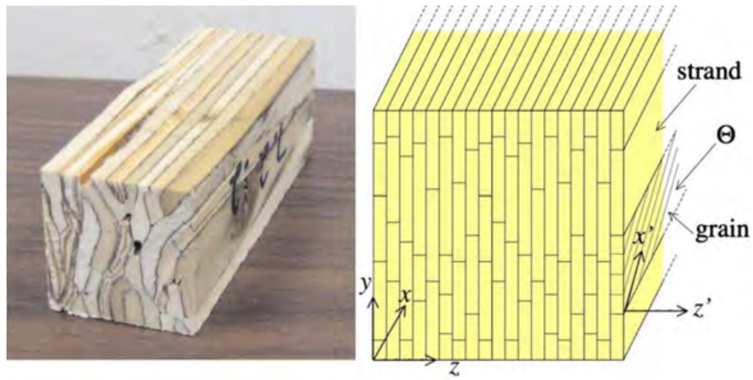


**Figure 40. Actual and idealised PSL mesostructure (Arwade et al., 2010).** ***Note: Θ is grain orientation angle***

#### 4.3.4.3.2 Integrated Model for Strand-based Products

Barnes (2000) developed a foundational semi-empirical model to predict the strength properties of oriented strand and particleboards using input wood properties (density, MOE, MOR) and eight parameters related to process: wood content; strand length; strand thickness; in-plane strand orientation; fines content; resin content; gaps between disc orienteer vanes; and strand free-fall distance from former surface to mat surface. Strand length and thickness interact strongly to affect the efficiency of the composite as it reaches solid parent wood strength (Figure 41[a]), showing how a high slenderness ratio is most effective, and the practical upper range of strand length is 6” (152 mm). The grain angle orientation in the mat is the other adjustable parameter that significantly affects the ability of the composites to approach parent wood MOE (Figure 41[b]). The model does not incorporate a VDP effect.

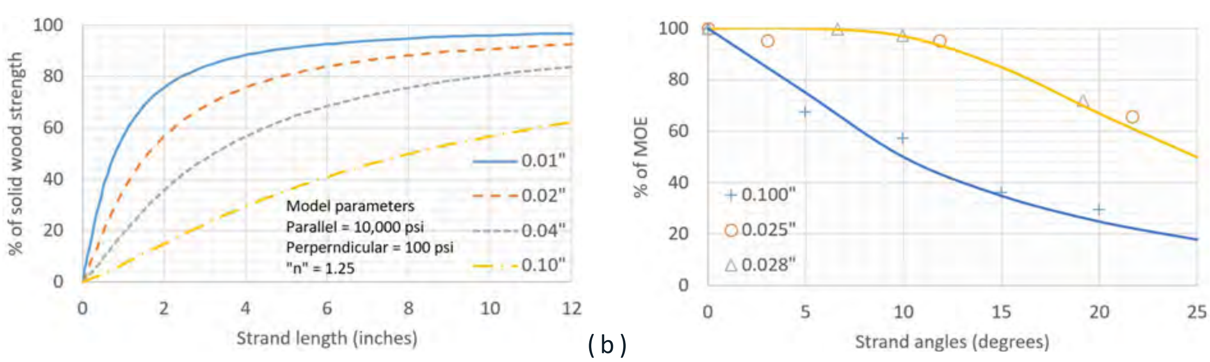


(a) (b)

**Figure 41. Examples of key process parameter effects on OSB composite efficiency: (a) strand length and thickness, and (b) in-plane orientation angle in mat (Barnes, 2000)**

Building on these process models, FPInnovations developed OSB-Pro, an integrated model for predicting the mechanical properties of strand composites of OSB/LSL. Key steps and factors involving strand preparation, strand orientation, mat forming, and mat consolidation in this model and the finished strand product are shown in the flowchart in Figure 42. The model contains nine modules including the input and output modules. For the model input, specific parameters related to raw materials and production processes are required: dimensions, density, and moisture content of panels; dimensions, density, and MOE of strands; number of layers; average angle of strands in each layer; VDP parameters; resin content; and fines content. Ultimately, the model can calculate mean values of axial, flatwise, and edgewise (in the case of LSL) bending MOEs.

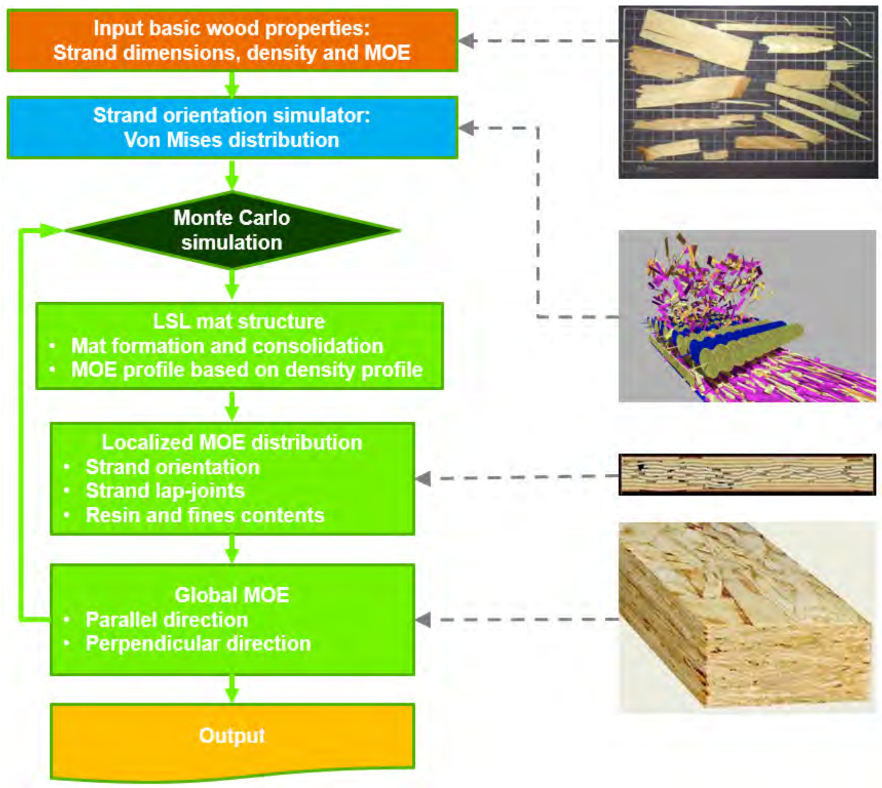


**Figure 42. Schematic diagram of an integrated model for predicting the MOE of LSL**

Using OSB-Pro, a 3D panel mesh was first generated using Monte Carlo simulations to derive statistical MOE values. The random variables are the location and the orientation of strands. These were assumed to either be uniform or correspond to a von Mises distribution (Harris & Johnson, 1982).

The parameters of the angle distribution were derived using the mat parameters, including number of layers and average angle of strands in each layer. The horizontal density profile in each layer was calculated once the strands were distributed to the panel mesh. The process model components also included VDP parameters, resin content, and fines content. In addition to strand orientation, the lap joints between strands, resin distribution, and fines content play a critical role in influencing the performance of LSL.

To account for these parameters, other sub-models incorporated a modified Hankinson equation (Barnes, 2000) for the strand overlaps, an inter-element contact model and a resin distribution model based on Dai, Yu, Groves et al. (2007), and a regression model for fines effect based on Han et al. (2007). OSB-Pro used a modified cosine function with two peaks to model VDP, and adjusted the average density of each layer according to empirical VDP data. Outputs include the mean values of MOE in axial, flatwise, and edgewise bending. Governed by the close correlation between density and MOE, a 3D MOE profile was generated based on the density profiles. Averaging and spring analogy methods were used to estimate the MOE of the model LSL under axial loads.

For the spring analogy method, the composite is seen as a series of springs (elements) connected in parallel and in series; the MOE of LSL is estimated based on calculating the average system stiffness. The process models have determined that parameters related to wood density, sieving, and classification (i.e., reducing variation in strand size and removing fines), strand size (particularly length) and orientation, and mat forming are the most important factors governing product performance indicators. In production, the two main process bottlenecks are drying the wood elements and pressing the product (be it plywood/LVL, strand composites, or even particleboard). Accomplishing this as quickly as possible underpins mill productivity. Models of these processes need to be further expanded to balance production efficiency with quality.

Of particular note is the incorporation of SOS into the FPInnovations OSB-Pro model. SOS enables predicting the practical effect of strand dimensions and former design/settings on orientation and hence final product properties. This is a significant advance compared with some of the early empirical models (Barnes, 2000). Figure 43 shows a good agreement between the model prediction and experimental data.

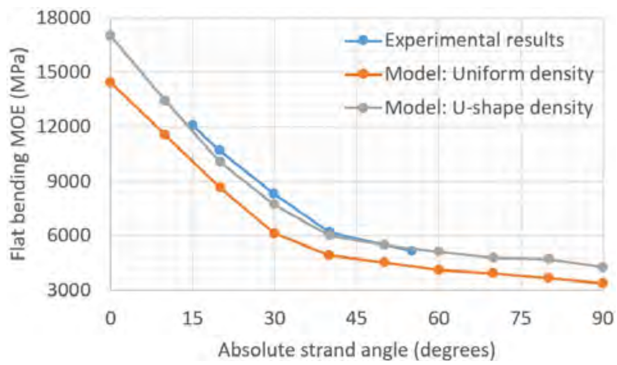


**Figure 43. Comparing predicted and measured flat bending MOE as affected by strand alignment and VDP (Data from Lau, 1980)**

Mills have used the OSB-Pro model to conduct sensitivity analyses of key parameters such as strand orientation, fines content, and product density in the development of LSL products (Figure 44). The SOS sub-model facilitates design and optimise the orienter system. The integrated model also helps mills minimise the number of trials and expedite the product development process.

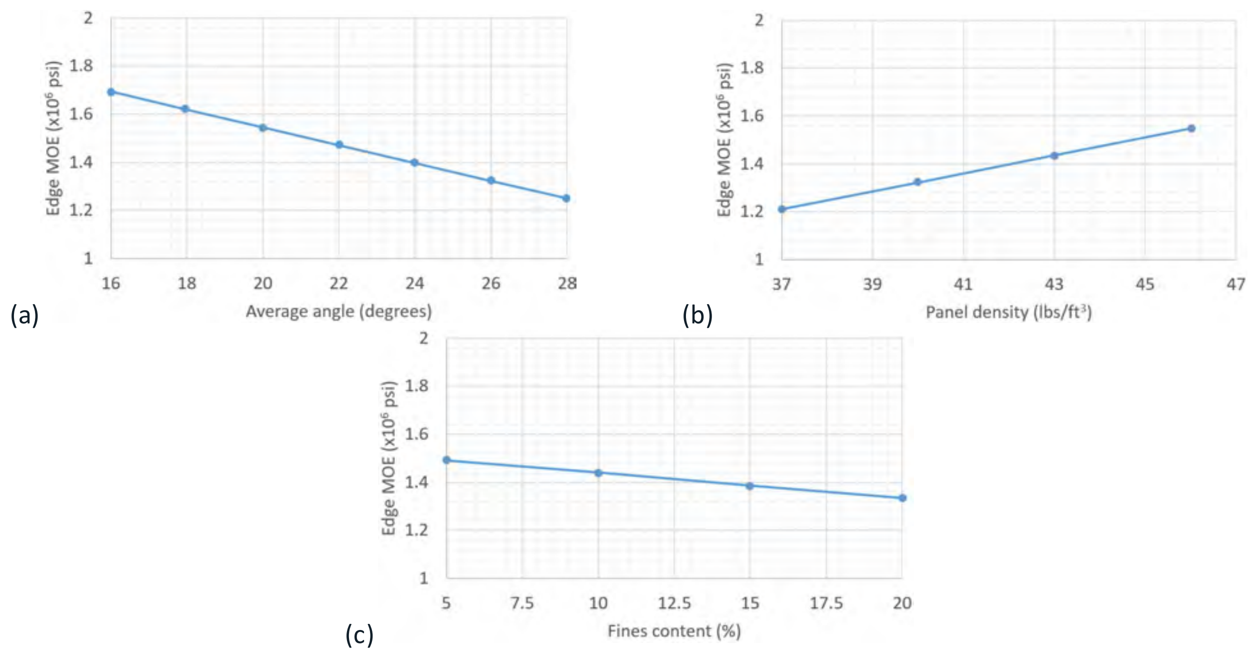


**Figure 44. Numerical simulations of edgewise bending MOE of LSL products with (a) average strand angle, (b) product density, and (c) fines content**

#### 4.3.4.3.3 Multiscale Modelling

In the last decade or so, the multiscale composite property approach has struck a balance between accuracy and efficiency and has been adapted and extended to wood composites. Having predictive tools capable of relating the material properties at micromechanic scales to large wood composite structures under complex loading conditions helps account for the fundamental and practical material properties of the structures (Gereke et al., 2012; Malek, Nadot-Martin et al., 2019; Stürzenbecher et al., 2010).

A multiscale model for strand boards (Stürzenbecher et al., 2010) was built up in two steps. In the first step, the elastic properties of homogeneous strand board material are estimated by means of continuum micromechanics from strand shape, strand orientation, elastic properties of the raw material, and mean board density. In the second step, also a homogenisation step, the effective stiffness of multilayer strand boards is determined based on classical laminate theory, which factors in the VDP and assembly of different layers (e.g., oriented surface layers, random core). Further refinements use multiscale modelling incorporating the material properties at different strategic scales (Gereke et al., 2012). Advances in multiscale modelling in other composites are well reviewed (Kanouté et al., 2009; Geers et al., 2010), and analytical micromechanics equations have been used successfully to predict the effective elastic properties of wood composites based on solid unidirectional circular fibres as well as rectangular strands or veneers (Malek, Nadot-Martin et al., 2019). Applications in the field of wood and bamboo strand composites have been growing over the past decade (Dixon et al., 2017).

Several researchers have applied the multiscale modelling approach to OSB. Figure 45 shows an example of multiscaling and the cell definition for rectangular resin-strand elements in PSL (Gereke et al., 2012; Malek, Nadot-Martin et al., 2019). The model developed by Malekmohammadi et al. (2014) incorporates discretized units within each strand as well as voids (incomplete resin coverage). Malekmohammadi et al. (2015) extended the Gereke et al. (2012) multiscale model for OSB by developing a more comprehensive multiscale analytical framework for predicting elastic response of strand-based composites under bending. They took into account several parameters, including wood species and their combination; strand dimensions, orientation, compaction, and density profile; void content; fines content; and resin type, content, and distribution. Dixon et al. (2017) applied the same methodology to laboratory-made bamboo OSB (Semple, Zhang, & Smith, 2015; Semple, Zhang, Smola, & Smith, 2015) to predict their flexural MOE by accounting for the different microstructures and properties of wood and bamboo. Malek, Zobeiry et al. (2019) developed a multiscale model with a sublaminate-based damage model to simulate the damage response of notched OSB panels, an approach that can be used to help tailor the properties of the area where holes or notches are machined for high-performance fasteners. A strain-softening approach was shown to be capable of accurately modelling the damage progression in notched OSB samples with acceptable agreement between the FEM simulations and experimental data.

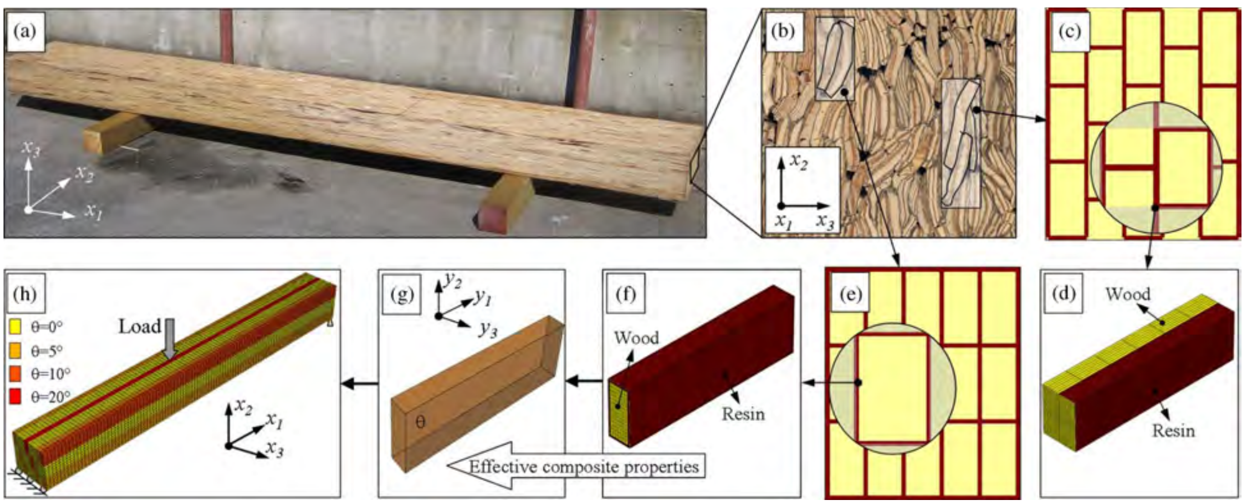


**Figure 45. Multiscale modelling scheme: (a) PSL beam; (b) PSL cross-section; (c) idealised microstructure, staggered array; (d) discretized unit cell, staggered array; (e) idealised microstructure, regular array; (f) discretized unit cell, regular array; (g) macroscopic homogenised element; (h) discretized PSL beam with randomly distributed grain orientation, $\vartheta$ (Gereke et al., 2012)**

The multiscale modelling approach is needed to predict the effective viscoelastic properties of composites over time under load (creep) or where one phase could become softer than the other, because of, for example, decay or temperature increase. Malek et al. (2018) proposed a 3D multiscale modelling approach (Figure 46) that allows engineers to simulate and predict the time-dependent viscoelastic behaviour of large, complex orthotropic composite structures (such as PSL) that consist of at least one viscoelastic phase under various loads at the macroscale (metres) using input parameters from micromechanical analyses at the microscale (millimetres). The example used in Figure 46 is an analysis of the time-dependent (creep) response of an orthotropic PSL beam under three-point loading. The approach is based on a computational homogenisation technique and a differential form of viscoelasticity proposed recently by Malek et al. (2018) for modelling the response of isotropic and transversely isotropic materials. FEMs were developed for different length scales using ABAQUS, incorporating the effect of microstructural parameters (such as wood strand size and orientation distributions, as well as resin area coverage, volume fraction, and relaxation modulus).

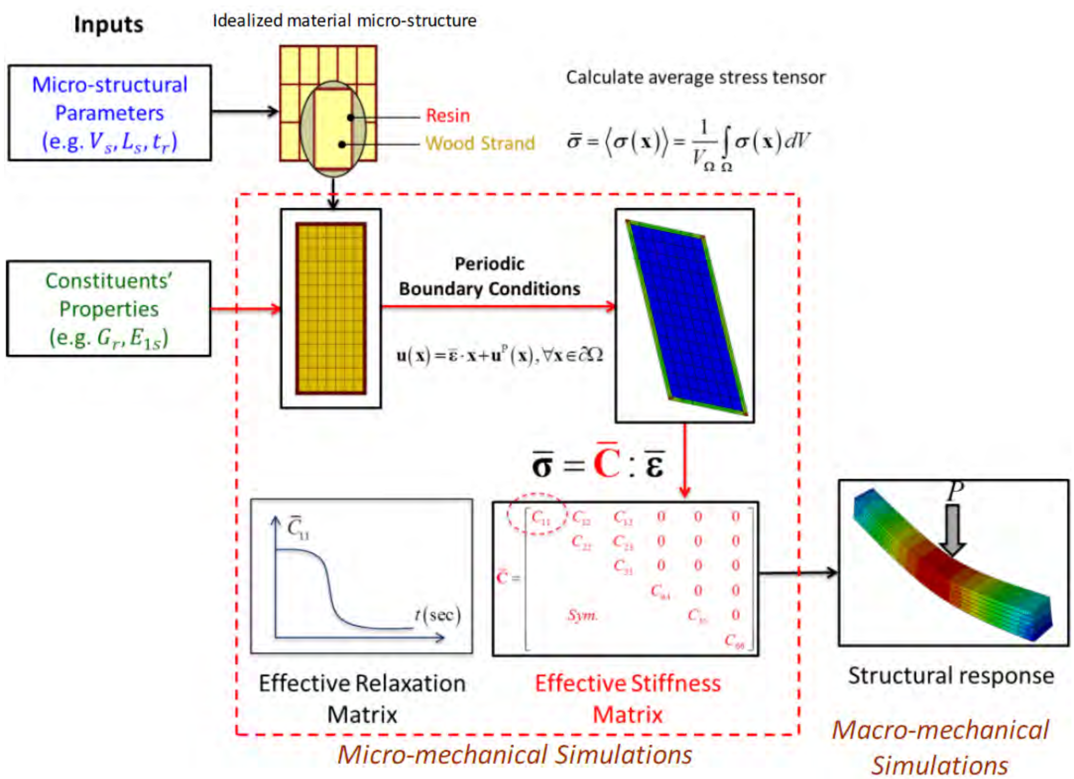


**Figure 46. Schematic of the multiscale modelling approach for simulating the structural behaviour of PSL (Malek et al., 2018)**

Malek, Nadot-Martin, et al. (2019) tested the morphological approach, developed for highly filled composites (Nadot-Martin et al., 2008; Dartois et al., 2013; Gereke et al., 2012; Malek et al., 2015, Malek, 2014). Morphological model predictions were found to be closer to the numerical reference solutions than previous analytical estimates for wood composites. The approach is a valuable alternative for computing the effective properties of strand-based composites made up of rectangular orthotropic strands or other large structural composites made from different wood or bamboo strands using less restrictive unit cells.

To incorporate intra-wood element microstructural variability and predict delaminations, Zerbst et al. (2020) developed a predictive microstructural FE model for moulded veneer products (see Figure 47). The researchers used a mapping tool, Envyo, to map digital greyscale images and discretize the oblique earlywood to latewood transitions in veneer surfaces that are prone to delaminating. These maps were converted to FE meshes. Local failure and damage modes were taken into account in simulating the veneer hot-moulding process. The numerical simulations provide very good agreement with the behaviour of measured tensile failure longitudinally and transversely to fibre orientation. The approach can be applied to incorporate material inhomogeneity into numerical simulations of larger bulk composites.

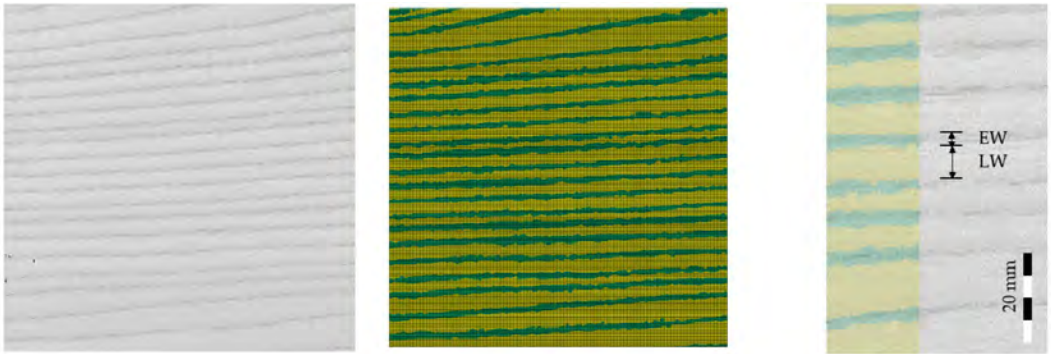


(a) (b) (c)

**Figure 47. (a) Original *pgm image for mapping; (b) FE mesh with allocated early wood (green) and latewood (yellow); and (c) borders of earlywood and latewood on mesh and image (Zerbst et al., 2020)**

### 4.3.5 Summary and Conclusions

This chapter introduces the process models and property models for lumber-, veneer-, and strand-based products. Modelling of lumber-based products mainly focussed on predicting the mechanical properties of lumber given the influence of defects (e.g., knots and slope of grain) and the end/finger joints in each lamination. The models have evolved from simple empirical and probabilistic methods to advanced FE methods that incorporate laser scanning and knot reconstruction technology. The modelling of veneer- and strand-based products has largely addressed the manufacturing processes. The veneer-based models developed at Forintek/FPInnovations simulate the processes of log conditioning, veneer peeling, veneer clipping, veneer drying, and veneer grading as well as the elastic properties of plywood and LVL products. Built upon the early analytical and computer simulation models developed by the senior author, the Forintek/FPInnovations models simulate and provide further insight into most stages of the strand-based wood composite production process, including mat formation, strand orientation, heat and mass transfer, and mat consolidation processes for strand-based wood composites. Structural models have also developed to specifically predict resin distribution, bonding strength, and mechanical properties of strand or short-fibre based wood composites.

The know-how in creating the veneer- and strand-based process models is built on nearly two decades of research by Forintek/FPInnovations. Based on fundamental principles and calibrated using extensive lab and mill trial data, these models have been widely used by engineered wood product mills across Canada for training, process optimisation, and product development. Mill trials have shown that the processing and product models can lead to significant benefits, including lower energy consumption, higher fibre recovery, greater productivity, better product quality, and less time spent in new product development.

In recent years, various multiscale models have been developed and described in the literature. They incorporate micromechanical equations for viscoelastic and other properties of the wood, resin components, and discretization of unit variations within wood elements based on earlywood and latewood zones, or bonding interfaces. This evolution has further increased the precision with which engineers can apply numerical simulations to predict the behaviour of large composite members in less costly and less time-consuming trials and tests. The process and product models have allowed wood composites to be engineered, manufactured, and designed for structural applications where material properties and variability need to be strictly controlled.

Future models should focus on accurately characterising material properties based on the structural, physical, and mechanical variations in raw materials, cutting-induced damage to wood constituents, and bonding and failure mechanism of the final products. Better knowledge in these areas will lead to more accurate model inputs and validations. Data-driven modelling, which we do not discuss in detail here, has great potential for practical applications, particularly in process optimisation.

### 4.3.6 Acknowledgements

The authors would like to acknowledge Dr. Kate Semple and Dr. Meiling Chen for their contributions to this chapter.

### 4.3.7 References

Amini, A., Arwade, S. R., & Clouston, P. L. (2017). Modeling the effect of void shapes on the compressive behavior of parallel-strand lumber. *Journal of Materials in Civil Engineering*, *29*(9), 04017129. https://doi.org/10.1061/(ASCE)MT.1943-5533.0001980

André, N., Cho, H. W., Baek, S. H., Jeong, M. K., & Young, T. M. (2008). Prediction of internal bond strength in a medium density fiberboard process using multivariate statistical methods and variable selection. *Wood Science and Technology*, *42*(7), 521-534. https://doi.org/10.1007/s00226-008-0204-7

APA. (2019). *ANSI/APA PRG 320: Standard for performance-rated cross-laminated timber*. The Engineered Wood Association (APA).

Arwade, S. R., Clouston, P. L., & Winans, R. (2009). Measurement and stochastic computational modeling of the elastic properties of parallel strand lumber. *Journal of Engineering Mechanics*, *135*(9), 897-905. https://doi.org/10.1061/(ASCE)EM.1943-7889.0000020

Arwade, S. R., Winans, R., & Clouston, P. L. (2010). Variability of the compressive strength of parallel strand lumber. *Journal of Engineering Mechanics*, *136*(4), 405-412. https://doi.org/10.1061/(ASCE)EM.1943-7889.0000079

APA. (2010). APA PS 1 Voluntary product standard, Structural plywood. Engineered Wood Association (APA).

ASTM. (2018). *ASTM D3737-18e1: Standard practice for establishing allowable properties for structural glued laminated timber (glulam).* ASTM International. https://doi.org/10.1520/D3737-18E01

ASTM. (2021). *ASTM D5456-21e1: Standard specification for evaluation of structural composite lumber products.* ASTM International.

Barnes, D. (2000). An integrated model of the effect of processing parameters on the strength properties of oriented strand wood products. *Forest Products Journal*, *50*(11/12), 33-42.

Bejo, L., & Lang, E. M. (2004). Simulation based modeling of the elastic properties of structural composite lumber. *Wood and Fiber Science*, *36*(3), 395-410.

Bender, D. A., Woestee, F. E., Schaffera, L., Marx, N. (1985). Reliability formulation for the strength and fire endurance of glued-laminated beams. *Research paper FPL-460, U.S.D.A. Forest Products Laboratory*.

Blass H. J., & Fellmoser, P. (2004, June 14–17). *Design of solid wood panels with cross layers* [Conference presentation]. World Conference on Timber Engineering, Lahti, Finland.

Brandner, R., Flatscher, G., Ringhofer, A., Schickhofer, G., & Thiel, A. (2016). Cross laminated timber (CLT): overview and development. *Holz als Roh- und Werkstoff*, *74*(3), 331-351.

Brown, K. M., & Suddarth, S. K. (1977). *A glued laminated beam analyzer for conventional or reliability based engineering design*. Purdue University Agricultural Experiment Station.

Burk, A. G. (1988). *Reliability models for finger joint strength and stiffness properties in Douglas-fir visual laminating grades*. [Master's thesis, Texas A&M University].

Burk, A. G., & D. A. Bender. (1989). Simulating finger-joint performance based on localized constituent lumber properties. *Forest Products Journal*, *39*(3), 45-50.

Carvalho, L. M. H., & Costa, C. A. V. (1998) Modeling and simulation of the hot-pressing process in the production of medium density fibreboard (MDF). *Chemical Engineering Communications, 170*(1), 1-21. https://doi.org/10.1080/00986449808912732

Cha, J. K., & Pearson, R. G. (1994). Stress analysis and prediction in 3-layer laminated veneer lumber: Response to crack and grain angle. *Wood and Fiber Science*, *26*(1), 97-106.

Chen, M., Troughton, G., & Dai, C. (2021). Optimum veneer peeling temperatures for selected softwood species using big roller bars. *Holz als Roh- und Werkstoff*, *79*(1), 151-159. https://doi.org/10.1007/s00107-020-01619-5

Chen, Z., Ni, C., Dagenais, C., & Kuan, S. (2020). Wood$^{ST}$: A temperature-dependent plastic-damage constitutive model used for numerical simulation of wood-based materials and connections. *Journal of Structural Engineering*, *146*(3), A04019225. https://doi.org/10.1061/(ASCE)ST.1943-541X.0002524

Clouston, P. (2007). Characterization and strength modeling of parallel-strand lumber. *Wood Research and technology*, *61*(4), 394-399. https://doi.org/10.1515/HF.2007.052

Clouston, P. L., & Lam, F. (2001). Computational modeling of strand-based wood composites. *Journal of Engineering Mechanics*, *127*(8), 844-851. https://doi.org/10.1061/(ASCE)0733-9399(2001)127:8(844)

Clouston, P. L., & Lam, F. (2002). A stochastic plasticity approach to strength modeling of strand-based wood composites. *Composites Science and Technology*, *62*(10-11), 1381-1395. https://doi.org/10.1016/S0266-3538(02)00086-6

Colling, F. (1990). Biegefestigkeit von brettschichtholzträgern in abhängigkeit von den festigkeitsrelevanten einflußgrößen [Bending strength of glulam beams. Development of a statistical model]. *Holz als Roh- und Werkstoff*, *48*, 269-273. https://doi.org/10.1007/BF02626515

Coumans, E. (2010). Bullet 2.76 Physics SDK Manual. Bullet Physics Library. http://bulletphysics.org

Coumans, E. (2015, August 9–11). *Bullet Physics Simulation: Introduction to rigid body dynamics and collision detection* [Conference presentation]. 42nd International Conference and Exhibition on Computer Graphics and Interactive Techniques, Los Angeles, California, USA.

Dai, C. (1994). *Modelling structure and processing characteristics of a randomly-formed wood-flake composite mat*. [Doctoral thesis, University of British Columbia].

Dai, C. (2001). Viscoelastic behavior of wood composite mats during consolidation. *Wood and Fibre Science*, *33*(3), 353-363.

Dai, C., Chen, S. and Sallahuddin, U. 1996. LOGCON 2.0: Dynamic software for log conditioning. Forintek copyright.

Dai, C., & Steiner, P. R. (1993). Compression behavior of randomly formed wood flake mats. *Wood and Fiber Science*, *25*(4), 349-358.

Dai, C., & Steiner, P. R. (1994). Spatial structure of wood composites in relation to processing and performance characteristics. *Wood Science and Technology*, *28*(3), 229-239. https://doi.org/10.1007/BF00193331

Dai, C., & Steiner, P. R. (1997). On horizontal density variation in randomly-formed short-fibre wood composite boards. *Composites. Part A: Applied Science and Manufacturing*, *28*(1), 57-64. https://doi.org/10.1016/S1359-835X(96)00094-2

Dai, C., & Yu, C. (2004). Heat and mass transfer in wood composite panels during hot-pressing: Part I. A physical-mathematical model. *Wood and Fiber Science*, *36*(4), 585-597.

Dai, C., & Yu, C. (2008). *Modeling concentrated static load (CSL) properties of OSB*. FPInnovations-Forintek report #4568. FPInnovations.

Dai, C., Semple, K., Chow, G., & Allison, B. (2017). *Developing a veneer clip (VClip) simulator for clipping optimization*. Record #: FPIPRODUCT-173-1334. FPInnovations.

Dai, C., van den Doel, K., Semple, K., Groves, K., Greig, G., & Perraud, F. (2017). *Development of strand orienting simulator (SOS) for engineered wood products*. Record #: FPIPRODUCT-173-1358. FPInnovations.

Dai, C., Yu, C., Groves, K., & Lohrasebi, H. (2007). Theoretical modeling of bonding characteristics and performance of wood composites: Part 2. Resin distribution. *Wood and Fiber Science*, *39*(1), 56-70.

Dai, C., Yu, C., & Hubert, P. (2000, December 10–13). *Modeling vertical density profile in wood composite boards* [Conference presentation]. Pacific Rim Bio-based Composites Symposium, Canberra, Australia.

Dai, C., Yu, C., & Jin, Q. (2008). Theoretical modeling of bonding characteristics and performance of wood composites: Part IV. Internal bond strength. *Wood and Fiber Science*, *40*(2), 146-160.

Dai, C., Yu, C., Wang, B., & Xu, H. (2004). Physical and mechanical models for wood strand composites. Canadian Forest Services.

Dai, C., Yu, C., Xu, C., & He, G. (2007). Heat and mass transfer in wood composite panels during hot pressing: Part IV. Experimental investigation and model validation. *Holzforschung*, *61*(1), 83-88. https://doi.org/10.1515/HF.2007.013

Dai, C., Yu, C., & Zhou, C. (2007). Theoretical modeling of bonding characteristics and performance of wood composites. Part I. Inter-element contact. *Wood and Fiber Science*, *39*(1), 48-55.

Dai, C., Yu, C., & Zhou, X. (2005). Heat and mass transfer in wood composite panels during hot pressing. Part II. Modeling void formation and mat permeability. *Wood and Fiber Science*, *37*(2), 242-257.

Dartois, S., Nadot-Martin, C., Halm, D., Dragon, A., Fanget, A., & Contesse, G. (2013). Micromechanical modelling of damage evolution in highly filled particulate composites–Induced effects at different scales. *International Journal of Damage Mechanics*, *22*(7), 927-966. https://doi.org/10.1177/1056789512468916

de Oliveira, S. J. C., Bolmin, O., Arrigoni, M., & Jochum, C. (2018). Plywood experimental investigation and modeling approach for static and dynamic structural applications. In A. Öchsner & H. Altenbach (Eds.), *Improved performance of materials*. Springer.

Defo, M., & Brunette, G. (2007). Application of a mathematical model to the analysis of the influence of length and diameter on log drying rate. *Wood and Fiber Science*, *39*(1), 16-27.

Dixon, P. G., Malek, S., Semple, K. E., Zhang, P. K., Smith, G. D., & Gibson, L. J. (2017). Multiscale modelling of moso bamboo oriented strand board. *BioResources*, *12*(2), 3166-3181. https://doi.org/10.15376/biores.12.2.3166-3181

Dodson, C. T. J. (1971). Spatial variability and the theory of sampling in random fibrous networks. *Journal of the Royal Statistical Society: Series B. Methodological*, 33(1), 88-94. https://doi.org/10.1111/j.2517-6161.1971.tb00859.x

Drolet, F., & Dai, C. (2010). Three-dimensional modeling of the structure formation and consolidation of wood composites. *Holzforschung*, *64*(5), 619-626. https://doi.org/10.1515/hf.2010.080

Ehlbeck, J., Colling, F., & Görlacher, R. (1985). Einfluß keilgezinkter lamellen auf die biegefestigkeit von brettschichtholzträgern [Influence of fingerjointed lamellae on the bending strength of glulam beams]. *Holz als Roh-und Werkstoff*, *43*, 333-337. https://doi.org/10.1007/BF02607817

Ek, J., & Norbäck, V. (2020). *Modeling of laminated veneer lumber: A study of the material properties for thick structural elements*. [Master's thesis, Chalmers University of Technology].

El Moustaphaoui, A., Chouaf, A., Kimakh, K., & Chergui, M. H. (2020). Determination of the onset and propagation criteria of delamination of Ceiba plywood by an experimental and numerical analysis. *Wood Material Science and Engineering*, *16*(5), 1-11. https://doi.org/10.1080/17480272.2020.1737963

Fink, G., Frangi, A., & Kohler, J. (2013, August 26–29). Modelling the bending strength of glued laminated timber - considering the natural growth characteristics of timber [Conference presentation]. W018 Meeting on Timber Structures, Vancouver, Canada.

Folz, B., & Foschi, R. O. (1995). ULAG: Ultimate load analysis of Glulam – User's manual, Version 1.0. Department of Civil Engineering, The University of British Columbia.

Foschi, R.O. (1976). Log centering errors and veneer yield. *Forest Products Journal*, *26*(2), 52-56.

Foschi, R. O., & Barrett, J. D. (1980). Glued-laminated beam strength: a model. *Journal of the Structural Division*, *106*(ST8), 1735-1754. https://doi.org/10.1061/JSDEAG.0005496

Franzoni, L., Lebée, A., Lyon, F., & Forêt, G. (2017). Elastic behavior of cross laminated timber and timber panels with regular gaps: Thick-plate modeling and experimental validation. *Engineering Structures*, *141*, 402-416. https://doi.org/10.1016/j.engstruct.2017.03.010

Freas, A. D., & Selbo, M. L. (1954). Fabrication and design of glued laminated wood structural members. *Technical Bulletin No. 1069. U.S.D.A. Forest Products Laboratory*.

Geers, M. G., Kouznetsova, V. G., & Brekelmans, W. A. M. (2010). Multi-scale computational homogenization: Trends and challenges. *Journal of Computational and Applied Mathematics*, *234*(7), 2175-2182. https://doi.org/10.1016/j.cam.2009.08.077

Gereke, T., Malekmohammadi, S., Nadot-Martin, C., Dai, C., Ellyin, F., & Vaziri, R. (2012). Multiscale stochastic modeling of the elastic properties of strand-based wood composites. *Journal of Engineering Mechanics*, *138*(7), 791-799. https://doi.org/10.1061/(ASCE)EM.1943-7889.0000381

Gibson, L. J., & Ashby M. F. (1988). *Cellular solids: Structure and Properties*. Pergamon Press. https://doi.org/10.1002/adv.1989.060090207

Gilbert, B. P. (2018). Compressive strength prediction of veneer-based structural products. *Journal of Materials in Civil Engineering*, *30*(9), 04018225. https://doi.org/10.1061/(ASCE)MT.1943-5533.0002417

Gilbert, B. P., Bailleres, H., Zhang, H., & McGavin, R. L. (2017). Strength modelling of laminated veneer lumber (LVL) beams. *Construction and Building Materials*, *149*, 763-777. https://doi.org/10.1016/j.conbuildmat.2017.05.153

Govindarajoo, R. (1989). *Simulation modeling and analyes of straight horizontally-laminated timber beams*. [Doctoral dissertation, Purdue University].

Harris, R. A., & Johnson, J. A. (1982). Characterization of flake orientation in flakeboard by the von Mises probability distribution function. *Wood and Fiber Science*, *14*(4), 254-266.

Han, G., Wu, Q., & Lu, J. Z. (2007). The influence of fines content and panel density on properties of mixed hardwood oriented strandboard. *Wood and Fiber Science*, *39*(1), 2-15.

He, G., Yu, C., & Dai, C. (2007). Theoretical modeling of bonding characteristics and performance of wood composites. Part 3: Bonding strength between two wood elements. *Wood and Fiber Science*, *39*(4), 566-577.

Hernandez, R., Bender, D. A., Richburg, B. A., & Kline, K. S. (1992). Probabilistic modeling of glued-laminated timber beams. *Wood and Fiber Science*, *24*(3), 294-306.

Hofstetter, K., Hellmich, C., & Eberhardsteiner, J. (2005). Development and experimental validation of a continuum micromechanics model for the elasticity of wood. *European Journal of Mechanics – A/Solids*, *24*(6), 1030-1053. https://doi.org/10.1016/j.euromechsol.2005.05.006

Humphrey, P.E. (1989). The hot pressing of dry-formed wood-based composites. Part II. A simulation model for heat and moisture transfer, and typical results. *Holzforschung*, *43*(3), 199-206. https://doi.org/10.1515/hfsg.1989.43.3.199

Hunt, M. O., & Suddarth, S. K. (1974). Prediction of elastic constants of particleboard. *Forest Products Journal*, *24*(5), 52-57.

Ivanov, I. V., Sadowski, T., Filipiak, M., & Knec, M. (2008). Experimental and numerical investigation of plywood progressive failure in CT tests. *Budownictwo i Architectura*, *2*(1), 79-94. https://doi.org/10.35784/bud-arch.2313

Karacabeyli, E., & Gagnon, S. (2019). *Canadian CLT Handbook 2019 Edition*. FPInnovations. Special publication SP-532E.

Kallmes, O., & Corte, H. (1960). The structure of paper, I. The statistical geometry of an ideal two dimensional fiber network. *Tappi Journal*, *43*(9), 737-752.

Kamke, F. A., & Wilson, J. B. (1986). Computer simulation of a rotary dryer. Part II: Heat and mass transfer. *AIChE Journal*, *32*(2), 269-275. https://doi.org/10.1002/aic.690320214

Kandler, G., Füssl, J., & Eberhardsteiner, J. (2015). Stochastic finite element approaches for wood-based products: theoretical framework and review of methods. *Wood Science and Technology*, *49*, 1055-1097. https://doi.org/10.1007/s00226-015-0737-5

Kandler, G., Füssl, J., Serrano, E., & Eberhardsteiner, J. (2015). Effective stiffness prediction of GLT beams based on stiffness distributions of individual lamellas. *Wood Science and Technology*, *49*, 1101-1121. https://doi.org/10.1007/s00226-015-0745-5

Kandler, G., Lukacevic, M., & Füssl, J. (2018). Experimental study on glued laminated timber beams with well-known knot morphology. *Holz als Roh- und Werkstoff*, *76*, 1435-1452. https://doi.org/10.1007/s00107-018-1328-6

Kandler, G., Lukacevic, M., Zechmeister, C., Wolff, S., & Füssl, J. (2018). Stochastic engineering framework for timber structural elements and its application to glued laminated timber beams. *Construction and Building Materials*, *190*, 573-592. https://doi.org/10.1016/j.conbuildmat.2018.09.129

Kanouté, P., Boso, D. P., Chaboche, J. L., & Schrefler, B. A. (2009). Multiscale methods for composites: a review. *Archives of Computational Methods in Engineering*, 16(1), 31-75. https://doi.org/10.1007/s11831-008-9028-8

Kawecki, B., & Podgorski, J. (2018). Numerical model of glulam beam delamination in dependence on cohesive strength. *AIP Conference Proceedings*, *1922*(1), 050005 (2018). https://doi.org/10.1063/1.5019059

Kline, D. E., Woeste, F. E., & Bendtsen, B. A. (1986). Stochastic model for modulus of elasticity of lumber. *Wood and Fiber Science*, *18*(2), 228-238.

Kreuzinger H. (1999). Platten, scheiben und schalen—ein berechnungsmodell für gängige statikprogramme. *Bauen mit Holz*, *1*, 34-39.

Lang, E. M., & Wolcott, M. P. (1996). A model for viscoelastic consolidation of wood-strand mats. Part II: Static Stress-Strain behavior of the mat. *Wood and Fiber Science*, *28*(3), 369-379.

Lee, J. J., & Kim, G. C. (2000). Study on the estimation of the strength properties of structural glued laminated timber I: determination of optimum MOE as input variable. *Journal of Wood Science*, *46*, 115-121. https://doi.org/10.1007/BF00777357

Li, M., Füssl, J., Lukacevic, M., Martin, C., & Eberhardsteiner, J. (2018). Bending strength predictions of cross-laminated timber plates subjected to concentrated loading using 3D finite-element-based limit analysis approaches. *Composite Structures*, *220*, 912-925. https://doi.org/10.1016/j.compstruct.2019.02.101

Malek, S. (2014). *Efficient multi-scale modelling of viscoelastic composites with different microstructures*. [Doctoral dissertation, University of British Columbia].

Malek, S., Gereke, T., Zobeiry, N., & Vaziri, R. (2018, January 31–February 2). *Multi-scale modelling of time-dependent response of composite structures made of orthotropic viscoelastic materials* [Conference presentation]. 13th International Conference on Steel, Space and Composite Structures, Perth, Australia.

Malek, S., Nadot-Martin, C., Tressou, B., Dai, C., & Vaziri, R. (2019). Micromechanical modeling of effective orthotropic elastic and viscoelastic properties of parallel strand lumber using the morphological approach. *Journal of Engineering Mechanics*, *145*(9), 04019066. https://doi.org/10.1061/(ASCE)EM.1943-7889.0001631

Malek, S., Zobeiry, N., Dai, C., & Vaziri, R. (2019). Strain-softening response and failure prediction in notched oriented strand board. *Journal of Materials in Civil Engineering*, *31*(6), 04019094. https://doi.org/10.1061/(ASCE)MT.1943-5533.0002737

Malek, S., Zobeiry, N., Gereke, T., Tressou, B., & Vaziri, R. (2015). A comprehensive multi-scale analytical modelling framework for predicting the mechanical properties of strand-based composites. *Wood Science and Technology*, *49*(1), 59-81. https://doi.org/10.1007/s00226-014-0682-8

Malekmohammadi, S., Tressou, B., Nadot-Martin, C., Ellyin, F., & Vaziri, R. (2014). Analytical micromechanics equations for elastic and viscoelastic properties of strand-based composites. *Journal of Composite Materials*, *48*(15), 1857-1874. https://doi.org/10.1177/0021998313490977

Malo, K.A. & Angst, V. (2008). Glued laminated timber. In Leonardo da Vinci Pilot Project, *Handbook 1 - Timber Structures*, CZ/06/B/F/PP/168007.

Mäntylä, M. (1988). An introduction to solid modelling. In Principles of computer science principles, *Computer Science Press*.

Merhar, M. (2020). Determination of elastic properties of beech plywood by analytical, experimental and numerical methods. *Forests*, *11*(11), 1221. https://doi.org/10.3390/f11111221

Nadot-Martin, C., Touboul, M., Dragon, A., & Fanget, A. (2008). Direct scale transition approach for highly-filled viscohyperelastic particulate composites: Computational study. In: Cazacu O (Ed.) *Multiscale modeling of heterogenous materials: From microstructure to macro-scale properties*, London: ISTE/Wiley.

Nairn, J. A. (2003). Material point method calculations with explicit cracks. Computer Modeling in Engineering and Sciences, 4(6), 649-664.

Noffsinger, J.R. (2004). *Modeling the oriented strandboard manufacturing process and the oriented strandboard continuous rotary drying system*. [Doctoral thesis, West Virginia University]. https://doi.org/10.33915/etd.2104

Perret, O., Lebée, A., Douthe, C., & Sab, K. (2019). Equivalent stiffness of timber used in CLT: closed-form estimates and numerical validation. *Holz als Roh- und Werkstoff*, 77, 367-379. https://doi.org/10.1007/s00107-019-01395-x

Pineda, H., Hu, Y., Semple, K., Chen, M., & Dai, C. (2021). Computer simulation of the mat formation of bamboo fibre composites. *Composites Part A: Applied Science and Manufacturing*, *149*, 106542. https://doi.org/10.1016/j.compositesa.2021.106542

Popovski, M., Gagnon, S., Mohammad, M., & Chen, Z. (2019). Chapter 3: Structural design of cross-laminated timber elements. In E. Karacabeyli & S. Gagnon (Eds.), *Canadian CLT handbook*. FPInnovations.

Richburg, B. A. (1988.) *Optimization of glued-laminated beam performance*. [Undergraduate fellows thesis, Texas A&M University].

Saavedra Flores, E., Dayyani, I., Ajaj, R. M., Castro-Triguero, R., DiazDelaO, F. A., Das, R., & González Soto, P. (2015). Analysis of cross-laminated timber by computational homogenisation and experimental validation. *Composite Structures*, *121*, 386-394. https://doi.org/10.1016/j.compstruct.2014.11.042

Saavedra Flores, E., Saavedra, K., Hinojosa, J., Chandra, Y., & Das, R. (2016). Multi-scale modelling of rolling shear failure in cross-laminated timber structures by homogenisation and cohesive zone models. *International Journal of Solids and Structures*, *81*, 219-232. https://doi.org/10.1016/j.ijsolstr.2015.11.027

Semple, K., & Dai, C. (2016a). *Log temperature conditioning simulations for Douglas fir and spruce peeler blocks*. FPInnovations.

Semple, K., & Dai, C. (2016b). *LogCon™ log conditioning time study for Lodgepole pine peeler logs*. FPInnovations.

Semple, K., & Dai, C. (2017). *Moisture evaluation and veneer peeling of Douglas fir and spruce logs from different mills and log yard age inventories*. Record #: FPIPRODUCT-173-1271. FPInnovations.

Semple, K. & Dai, C. (2018a). *Mill trial of log storage age effects on veneer productivity and using Logdry™ to predict Douglas fir residual moisture levels*. FPInnovations.

Semple, K., & Dai, C. (2018b). *Analyses and comparison of historic mill production data from two plywood mills*. FPInnovations.

Semple, K., & Dai, C. (2018c). *Log conditioning relating theoretical data to real time data from mills and comparing conditioning systems between two mills by species and season*. FPInnovations.

Semple, K. E., & Smith, G. D. (2017). Recovery modeling for OSB strand production from hollow bamboo culms. *BioResources*, *12*(4), 7841-7858.

Semple, K. E., Zhang, P. K., & Smith, G. D. (2015). Hybrid oriented strand boards made from Moso bamboo (*Phyllostachys pubescens* Mazel) and Aspen (*Populus tremuloides* Michx.): Species-separated three-layer boards. *Holz als Roh- und Werkstoff*, *73*(4), 527-536. https://doi.org/10.1007/s00107-015-0914-0

Semple, K. E., Zhang, P. K., Smola, M., & Smith, G. D. (2015). Hybrid oriented strand boards made from Moso bamboo (*Phyllostachys pubescens* Mazel) and Aspen (*Populus tremuloides* Michx.): uniformly mixed single layer uni-directional boards. *Holz als Roh- und Werkstoff*, *73*(4), 515-525. https://doi.org/10.1007/s00107-015-0913-1

Shaler, S. M., & Blankenhorn, P. R. (1990). Composite model prediction of elastic moduli for flakeboard. *Wood and Fiber Science*, *22*(3), 246-261.

Šmídová E, & Kabele P. (2018). Constitutive model for timber fracture used for FE simulation of LVL arch. *Acta Polytechnica CTU Proceedings*, *15*, 109-13. https://doi.org/10.14311/APP.2018.15.0109

Smith, G. D. (2005). Direct observation of the tumbling of OSB strands in an industrial scale coil blender. *Wood and Fiber Science*, *37*(1), 147-159.

Steinhagen, H. P., Lee, H. W. & Loehnertz, S.P. (1987). LOGHEAT: a computer program for determining log heating times for frozen and nonfrozen logs. *Forest Products Journal*, *37*(11/12), 60-64.

Stürzenbecher, R., Hofstetter, K., Schickhofer, G., & Eberhardsteiner, J. (2010). Development of high-performance strand boards: multiscale modeling of anisotropic elasticity. *Wood Science and Technology*, *44*(2), 205-223. https://doi.org/10.1007/s00226-009-0259-0

Suchsland, O. (1959). An analysis of the particle board process. *Michigan Quarterly Bulletin*, *42*(2), 350-372.

Susainathan, J., Eyma, F., De Luycker, E., Cantarel, A., & Castanie, B. (2020). Numerical modeling of impact on wood-based sandwich structures. *Mechanics of Advanced Materials and Structures*, *27*(18), 1583-1598. https://doi.org/10.1080/15376494.2018.1519619

Taylor, S. E. (1988). *Modeling spatially correlated localized lumber properties*. [Doctoral dissertation, Texas A&M University].

Thoemen, H., Humphrey, P. E. (2003). Modeling continuous pressing for wood-based composites. *Wood and Fiber Science*, *35*, 456-468.

Triche, M. H., & Hunt, M. O. (1993). Modeling of parallel-aligned wood strand composites. *Forest Products Journal*, *43*(11/12), 33-44.

Tsai, S. W., & Wu, E. M. (1971). A general theory of strength for anisotropic materials. *Journal of Composite Materials*, *5*(1), 58-80. https://doi.org/10.1177/002199837100500106

Tsai, Y-L., & Smith, G. (2014, June 4–7). *The impact of different strand configurations on the surging for a discrete element model of oriented strand board rotary drum blender* [Conference presentation]. BIOCOMP 2014, Beijing, China.

van Beerschoten, W. A., Carradine, D. M., & Carr, A. (2014). Development of constitutive model for laminated veneer lumber using digital image correlation technique. *Wood Science and Technology*, *48*(4), 755-772. https://doi.org/10.1007/s00226-014-0638-z

van den Doel, K., & Dai, C. (2014). SOS: Strand orientation simulator. FPInnovations.

Vratuša, S., Kariž, M., Ayrilmis, N., & Kuzman, M. K. (2017). Finite element simulations of the loading and deformation of plywood seat shells. *Holz als Roh- und Werkstoff*, *75*(5), 729-738. https://doi.org/10.1007/s00107-017-1160-4

Wang, B., & Dai, C. (2013). Development of structural laminated veneer lumber from stress graded short-rotation hem-fir veneer. *Construction and Building Material*, *47*, 902-909. https://doi.org/10.1016/j.conbuildmat.2013.05.096

Wang, B., & Dai, C. (2014). Optimum log conditioning temperature pertaining to veneer peeling for four softwood species. Research report. W-3123 Record #: FPIPRODUCT-1-7015. FPInnovations.

Wang, B. J., Ellis, S., & Dai, C. (2006). Veneer surface roughness and compressibility pertaining to plywood/LVL manufacturing. Part II. Optimum panel densification. *Wood and Fiber Science*, *38*(4), 727-735.

Wang, J. B., Wei, P., Gao, Z., & Dai, C. (2018). The evaluation of panel bond quality and durability of hem-fir cross-laminated timber (CLT). *Holz als Roh- und Werkstoff*, *76*(3), 833-841.

Wang, Y-T., & Lam, F. (1998). Computational modeling of material failure for parallel-aligned strand based wood composites. *Computational Materials Science*, *11*(3), 157-165.

Wiesner, F., Bisby, L. A., Bartlett, A. I., Hidalgo, J. P., Santamaria, S., Deeny, S., & Hadden, R. M. (2019). Structural capacity in fire of laminated timber elements in compartments with exposed timber surfaces. *Engineering Structures*, *179*, 284-295. https://doi.org/10.1016/j.engstruct.2018.10.084

Williamson, T., & Yeh, B. (2007, August 27–30). *Standard practice for the derivation of design properties of structural glued laminated timber in the United States* [Conference presentation]. International Council for Research and Innovation in Building and Construction, Bled, Slovenia.

Wilson, T. R. C., & W. S. Cottingham. (1947). Tests of glued-laminated wood beams and columns and development of principle of design. *Report No. R1687, U.S.D.A. Forest Products Laboratory*.

Winans, R. S. (2008). *Measurement and computational modeling of the mechanical properties of parallel strand lumber*. [Master's theses, University of Massachusetts Amherst].

Yeh, B. J. (1996, October 28–31). *Using computer models to predict the performance of structural glued laminated timber* [Conference presentation]. International Wood Engineering Conference, New Orleans, Louisiana, USA.

Yu, C., Dai, C., & Wang, B. (2007). Heat and mass transfer in wood composite panels during hot pressing: Part III. Predicted variations and interactions of the pressing variables. *Holzforschung*, *61*, 74-82. https://doi.org/10.1515/HF.2007.012

Zerbst, D., Liebold, C., Gereke, T., Haufe, A., Clauß, S., & Cherif, C. (2020). Modelling inhomogeneity of veneer laminates with a finite element mapping method based on arbitrary grayscale images. *Materials*, *13*(13), 2993. https://doi.org/10.3390/ma13132993

Zhou, C., Dai, C., & Smith, G. D. (2008). A generalized mat consolidation model for wood composites. *Holzforschung*, *62*(2), 201-208. https://doi.org/10.1515/HF.2008.053

Zhou, C., Smith, G., & Dai, C. (2010). Characterizing hydro-thermal compression behavior of aspen wood strands. *Holzforschung*, *63*(5), 609-617.

Zombori, B. G., Kamke, F. A., & Watson, L. T. (2003). Simulation of the internal conditions during the hot-pressing process. *Wood and Fiber Science*, *35*(1), 2-23.

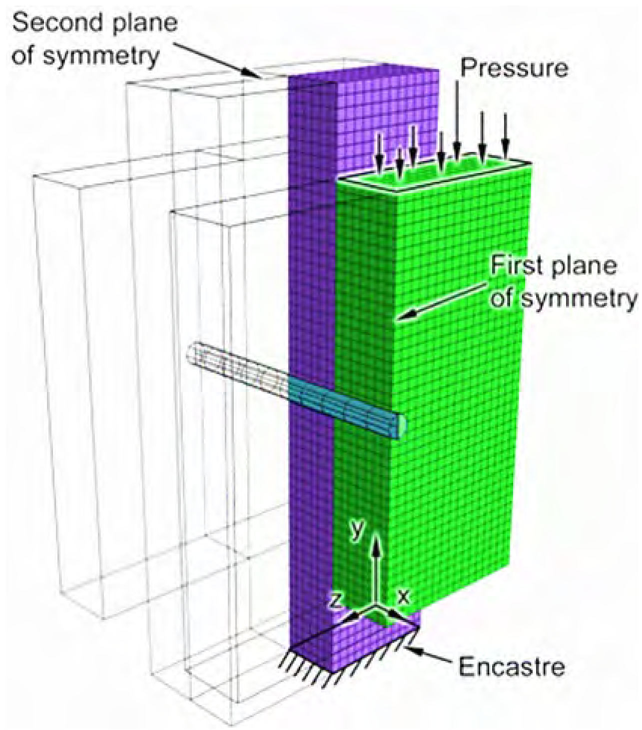


Image courtesy of González Fueyo et al. (2009)

# CHAPTER 5

## Connections

**Authors**
Pierre Quenneville
Zhiyong Chen
Carla Dickof
Mohammad Mohammad

**Reviewers**
Alexander Salenikovich
Chun Ni
Jean-Philippe Letarte
Jake Estok

## TABLE OF CONTENTS

## 5.1 INTRODUCTION

Connections play a crucial role in the integrity and load-resisting mechanism of structures. Due to the inherent characteristics of wood, timber connections are sensitive to construction details and various actions (e.g., gravity and lateral loads, fire, and moisture aspects) which may result in various failure modes, including some undesired ones. Timber connections are complex systems and include wood-based and non–wood-based components and fasteners. Well-designed connections with mechanical fasteners are usually characterised by highly nonlinear behaviour, strength and stiffness degradation, and pinching effect on their hysteresis loops. All these aspects may pose significant challenges for modelling of timber connections and how they interact with other elements in the structure. This chapter introduces the common concepts for modelling of timber connections in the design and analysis of timber structures, and the development and optimisation of timber connections, along with specific modelling considerations for key influencing factors.

## 5.2 DESIGN AND ANALYSIS OF CONNECTIONS IN TIMBER STRUCTURES

### 5.2.1 Introduction to Timber Connections

Timber and hybrid structures always include connections between members and to the supporting foundation, making the approach to the transfer of forces at these connections a critical part of timber engineering. Timber member sizes and lengths are impacted by manufacturing and shipping limits, which also impact the number and types of connections required. Various connection typologies exist to provide efficient force transfer using factory prefabrication and on-site assembly.

Timber structures have been used since the beginning of time, and builders have devised very clever means of transferring forces between structural members and between timber parts forming a structural element. Before the advent of steel on an industrial scale and structural adhesives that enabled timber to be assembled into bigger members, carpentry joints were used to transfer axial forces and shear along the grain. Moments were transferred with triangular systems (as braces). With the industrial revolution, nails, screws, bolts, and other metal connectors became more common, which encouraged the development of connection details to transfer larger forces and achieve greater spans.

It is important to consider all the forces and moments transferred at a connection (Figure 1). Detailing the transfer of large forces and moments or geometrically complex connections can be costly. Designing to simplify connections (e.g., pinned versus fixed moment transfer connections) is desirable for simple and cost-effective structures. To model a timber structure, a structural analysis is done either through a simple hand calculation or a sophisticated software package. In its simplest form, a timber connection is modelled as a connection that transfers axial and shear forces. Moment connections in timber structures are not impossible; however, this needs to be done through proper detailing to minimise costs and avoid wood splitting. If a moment connection is needed in a structural model, one should first get an appreciation of what this connection would look like in a real structure. Figure 2 shows various examples of pinned and moment connections that have been used in practice.

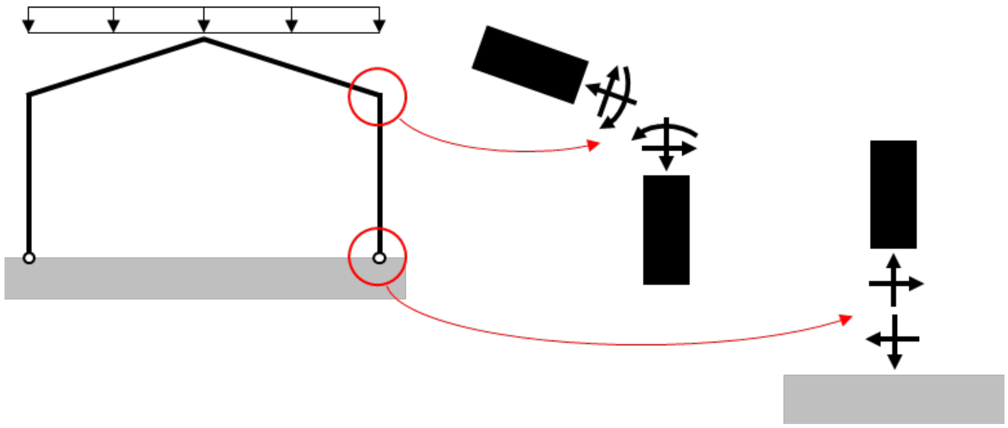

Figure 1. Load transfer of forces at connections

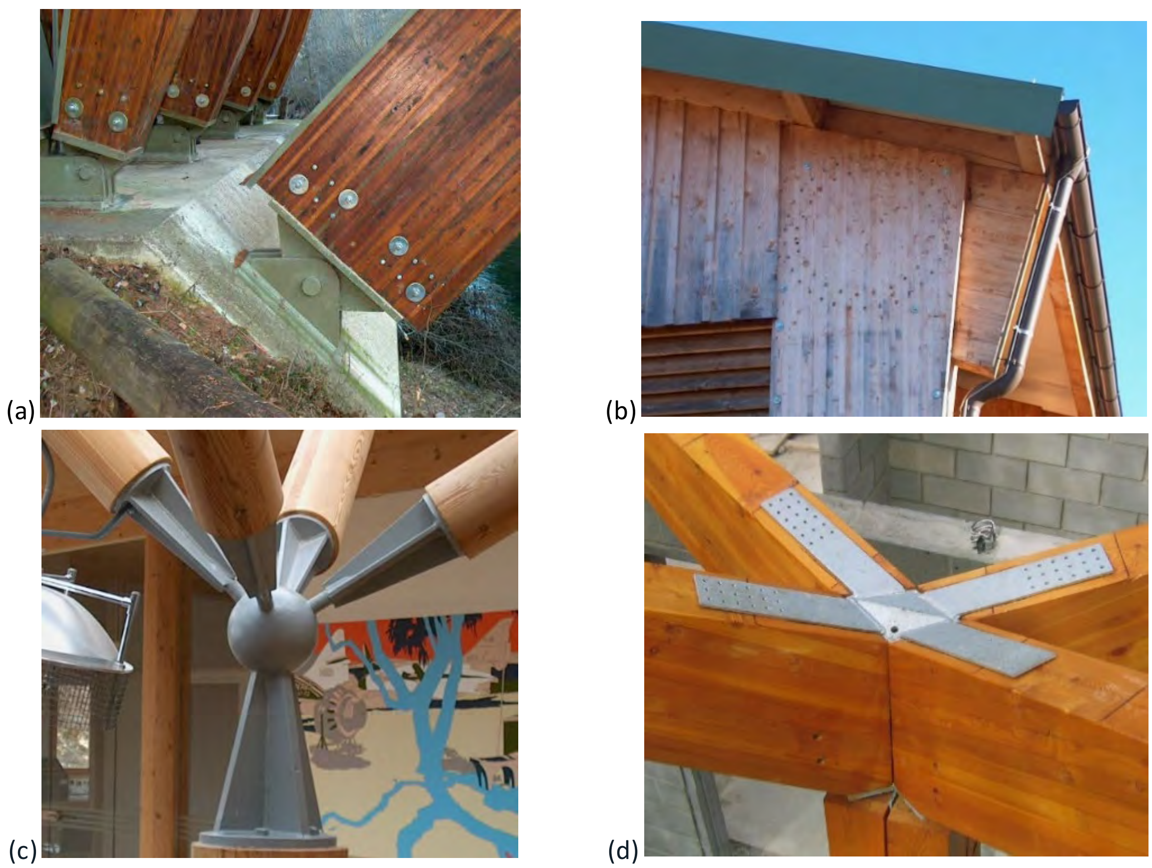


**Figure 2. (a) Bridge glued laminated timber (glulam) pinned support connection. (b) A moment connection between a glulam rafter and columns using dowels in a circular pattern. (c) A pinned truss connection using the reduction in moment of inertia. (d) A moment connection where the tensile force from a force couple is taken by a rivet connection (rivets to be installed). (Photo courtesy of Timber Systems.)**

It is also important to take into account the effect of the service conditions on the connecting members and the connections. High moisture content in the wood members in service can result in localised decay (Figure 3) and significantly reduced resistance and stiffness of a connection. Swelling and shrinkage will induce dimensional changes that can result in stress concentrations that can in turn lead to localised failures or cracks that can compromise the long-term performance of the connections even if they are not significant (Figure 4).

**Figure 3. Moisture and the absence of protection lead to the demise of a connection**

**Figure 4. Shrinkage of this glulam beam under service conditions, combined with the restraint imposed by a tall and stiff internal steel plate, resulted in localised cracks in line with the dowels**

In some cases, timber members are designed as brittle elements while the connections can be designed to provide a certain amount of ductility to the structural system. Attention to detail is important as timber connections have the potential to fail in either a ductile or a brittle manner, depending on the configurations of connections and types of fasteners. If the connections are to provide ductility to the overall structural system, then it is imperative that the connection details be such that each connection can accommodate a relatively large deformation without failing. Ultimately, there is a limit to the ductility of a structure that can be provided by timber connections, even if they are designed to be ductile (Chen & Popovski, 2020).

The resistance of a dowel type connection is governed by either the brittle resistance of the wood fibres engaged in resisting the load (in longitudinal shear, transverse or longitudinal tension, or a combination of the two) or the ductile resistance which is associated with bending of the fasteners and localised crushing of the wood fibres at the fasteners. As Figure 5 shows, the former results in a brittle failure, while the latter results in a ductile behaviour prior to failure. However, following the onset of crushing of the fibres and bending of the fasteners, there is always a possibility that a brittle failure occurs after large deformation. The occurrence of this secondary failure (the brittle failure following the ductile failure) governs the amount of ductility that the connection can provide to the structure and can also govern the maximum load that a connection can be designed for.

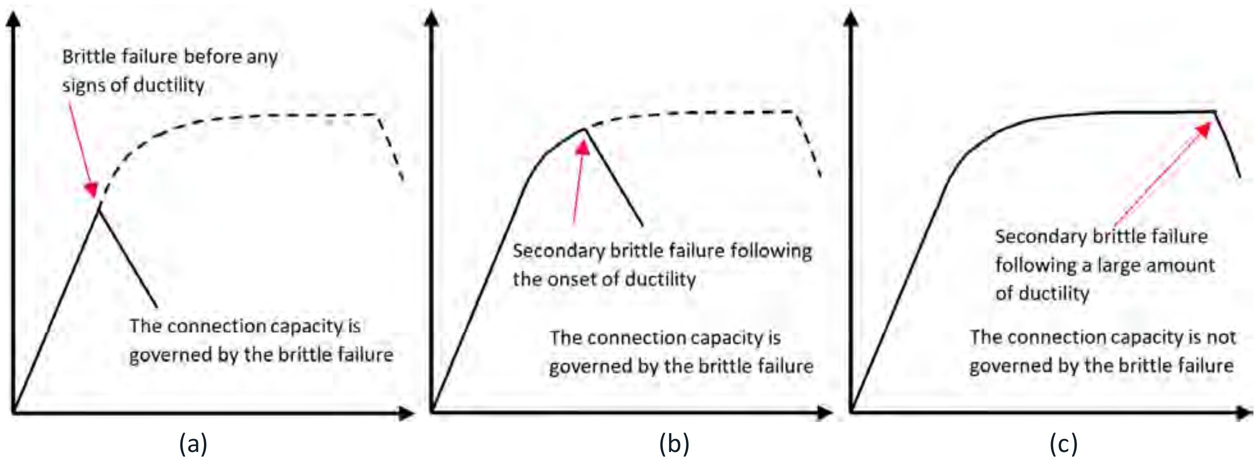


**Figure 5. Load deformation curves for brittle ([a] and [b]) and ductile (c) connection failure. The amount of ductility in a connection is governed by the onset of the secondary brittle failure**

With the development of advanced seismic engineering concepts and analysis, a designer must identify the hierarchy of structural elements that would provide the ductility in a structure. The seismic fuses or energy-dissipative elements must be designed to provide the targeted ductility in the system. The energy-dissipation capacity of connections can be compromised by the inherent variability in the performance of wood elements resulting from variations in material characteristics (i.e., the 5th percentile resistance is used in the design) and variations in construction tolerances (stronger dissipative elements are used during construction instead of the ones specified). This is because the targeted seismic fuse behaviour may be triggered at a much higher load and may change the behaviour of the entire system. To prevent the failure of non-dissipative structural elements, all structural elements and connections that are not part of the hierarchy of the identified seismic fuses must be capacity-protected. Capacity-protected elements must be designed to accommodate the full deformation of the dissipative elements; this is commonly achieved by ensuring their design resistance is higher than the ultimate resistance of the seismic fuse by multiplying by an overstrength factor. The value of the overstrength factor depends on the variability of the load that triggers the seismic fuse. It should be noted that within a dissipating fuse, it is also important to capacity-protect brittle failure modes.

### 5.2.2 Modelling of Connections in Timber Structures

Connections are a critical component of structural systems, particularly those involving timber. Most of the designer's time is often spent designing and detailing timber connections to meet strength, stiffness, ductility, and geometric requirements. In any mass timber buildings, connections are typically found in two types of locations:

(1) Continuous connections between mass timber panels (e.g., splines, drag straps, and chords); or

(2) Localised connections of liner members (e.g., glulam member connections).

Where finite element (FE) models are used, connections can be implemented in various ways. While in some cases timber connections are considered either fully fixed or fully released, in other cases it is important to provide accurate hysteretic forms for connections, including the yield strength and deformation, probable ultimate strength and deformation, and mode of failure. The extent of connection modelling depends on:

- The intended use of the model (gravity design, footfall vibration, seismic design, connection design or review);
- The intended use of the connection (dissipative or non-dissipative connection, primary gravity connection, etc.); and
- The type of analysis being performed (linear versus nonlinear analysis, static versus dynamic analysis).

When implementing connection modelling in an FE method, it is important to determine how best to evaluate the behaviour of the connection. In some cases, connections can be modelled using link elements with the relevant nonlinear or linear properties of the connection. In other cases, connections can be incorporated with nodal releases at the ends of member elements or line releases at the ends of shell elements.

When determining how to model the connection, it is critical to understand what information is required for a given FE model (e.g., the results that can be extracted from the analysis). For example, several programs model rigid link elements by assigning one node as the slave to another, preventing the extraction of specific forces transferred by such elements. In cases where the specific forces transferred is a key output, the required link element would need to be modelled with a specified stiffness – even if very high or very low.

It is also important to assess whether linear, nonlinear, or fully hysteretic behaviour should be incorporated in the connection element. Depending on the analysis software, there may be limitations on the implementation of nonlinear or hysteretic behaviour in releases. In most cases, it is possible to implement nonlinear and hysteretic behaviour into specialised link elements. The following sections discuss specific considerations for modelling connections in gravity and lateral load-resisting systems (LLRS).

#### *5.2.2.1 Connections in Gravity Load-Resisting Systems*

Typical gravity connections in mass timber construction include traditional post-and-beam construction joints, such as beam-column connections, as well as cross-laminated timber (CLT) panel construction (i.e., panel-beam connections or floor-wall connections). For more information on typical CLT floor and wall connections, refer to the *Canadian CLT Handbook* (Karacabeyli & Gagnon, 2019).

FE models intended for gravity analysis for ultimate limit states and serviceability limit states typically use a simplified approach for connection modelling. Depending on the type of stress, connections may be modelled as either fully rigid or fully released. For example, beam-column connections (e.g., beam-column hangers) are typically modelled as rigidly connected for shear and axial loads, and fully released for rotation (i.e., pinned). This allows a reasonable estimation of the stresses in the members and deflections of the system. This is a common approach for gravity modelling and for gravity elements in LLRS modelling. It is, however, important to ensure that the connections can tolerate lateral drifts associated with wind or seismic loadings, as noted in the National Building Code of Canada (National Research Council of Canada, 2020), Clause 4.1.8.3.5: "All structural framing elements not considered to be part of the SFRS must be investigated and shown to behave elastically or to have sufficient non-linear capacity to support their gravity loads while undergoing earthquake-induced deformations." Regardless of the connection type, including traditional bearing hangers, dowelled hangers, or proprietary form-fitted hangers (Figure 6), it is important to assess the drift capacity of these connectors.

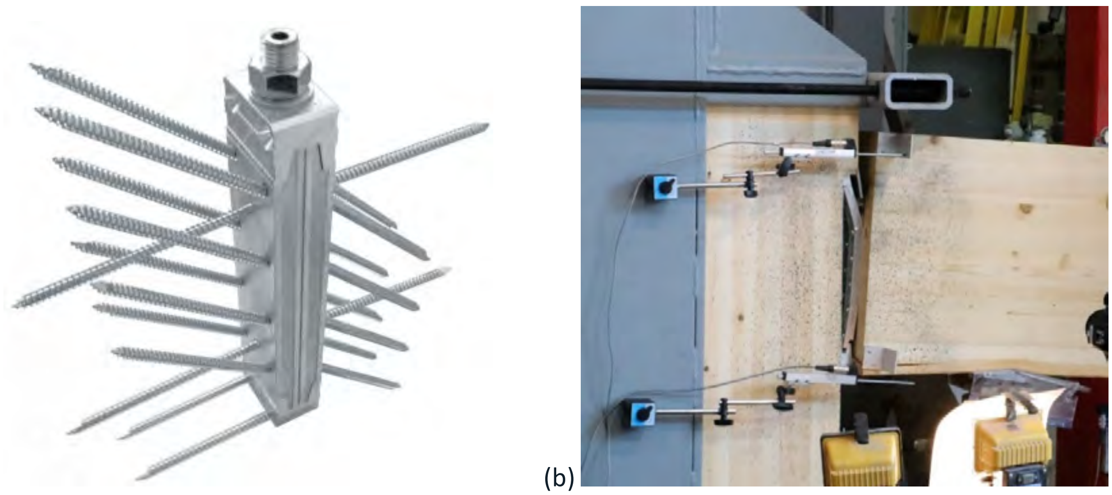

(a) (b)

**Figure 6. (a) Hanger connector (image courtesy of MTC Solutions), and (b) typical connection behaviour**

Similarly, beam-panel connections in floors are often modelled as fully released (i.e., no composite action). This can be done by providing an axial release in the shear direction between the elements. However, it is more commonly approached by simulating the floors using modified shell elements that capture the combined stiffness of the noncomposite panel and beam. For FE models intended for footfall vibration analysis, on the other hand, either the average stiffness of connections is used or connections are assumed fully rigid, as a higher stiffness provides for the worst-case scenarios. See Chapter 6.1 for more discussion of modelling practices for mass timber in vibration.

### *5.2.2.2 Connections in an LLRS*

In a timber LLRS, connections typically contribute significant deformation to the system and are the only source of energy dissipation. Therefore, it is important that the connections provide sufficient stiffness, ductility, and post-elastic yield to the system. For models used in wind design, it is critical that the stiffness of connections is taken into account; for seismic design, the energy-dissipative connections should be modelled accurately with post-elastic behaviour.

Depending on the analysis approach and intended application, several options are proposed for dissipative connections, among them:

- For linear analysis, dissipative connections should be modelled with an accurate stiffness; nonlinear post-yield information is not required. This type of modelling applies to FE models used in any equivalent static force procedure design, modal response spectrum analysis, or linear time-history analysis.
- For nonlinear analysis, it is important to provide accurate backbone curves and the hysteretic form for the dissipative connections. These dissipative connections must account for the stiffness and post-strength behaviour of the connection in all 6 degrees of freedom. This type of modelling applies to FE models used in pushover or nonlinear time-history analysis.

For connections that are not intended to dissipate energy, the need to model the connection will vary depending on the intent of the model and the level of accuracy required. These can be grouped into two categories: connections that do not form part of the LLRS and connections that are capacity-protected within an LLRS.

Although connections that do not form part of the LLRS often contribute in a small way to the overall stiffness of a building, they are often simplified in a model to ease calculation and to ensure that the LLRS is designed to carry the entirety of the lateral loads of the building and to provide the most conservative estimate of overall drift in the building. A classic example is providing rotational releases at beam ends of gravity frames and at column ends even though most connections provide some stiffness.

Connections that are not intended to dissipate energy but do form part of the vertical LLRS must be designed to be capacity-protected. The most accurate models include the elastic stiffness of these connections but often do not include the overall hysteretic behaviour. Because the design resistance of these connections is based on the probable ultimate capacity of the dissipative connections, it is generally not necessary to include their nonlinear behaviour. However, it is important to ensure that analysis results fall within the design strength and deformation capacity of these connections. In cases where a connection is engaged primarily in only one direction (e.g., a column bearing on a foundation in compression but held down with a dowelled connection in tension), it is necessary to provide a bilinear connection to capture the difference in stiffness in the two directions (tension and compression) (Figure 7).

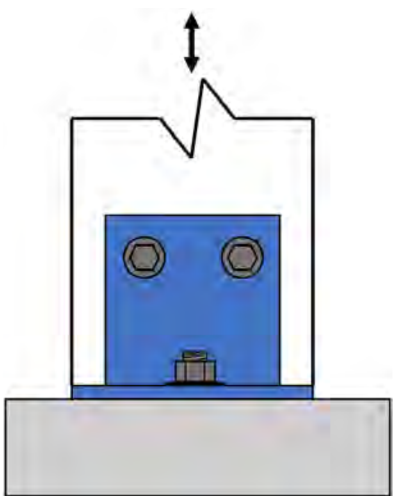
(a)

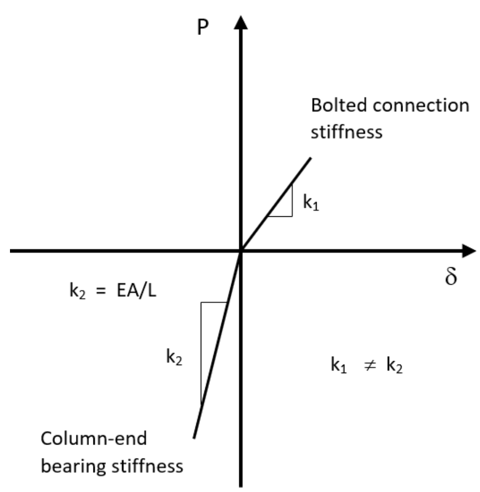

(b)

**Figure 7. (a) Timber connection and (b) load-deformation model**

Connections in horizontal diaphragms are typically capacity-protected similar to non-dissipative components of a vertical LLRS. Where complex models are used to evaluate the diaphragm behaviour, the connections should be modelled elastically, similar to vertical LLRS non-dissipative connections. These typically apply to:

- Spline connections between panels (in-plane axial and shear loads);
- Connections between chord and diaphragm; and
- Connections between diaphragm and the vertical LLRS.

The spline connections between panels may need to be represented as axially elastic in tension (i.e., panels pulling apart) but rigid in compression (i.e., panels pushing together), requiring a bilinear connection at these locations, like that discussed for a vertical LLRS.

#### *5.2.2.3 Rigidity of Moment-Resisting Connections*

In structural systems that are indeterminate, the rigidity of the connections affect the deformations and forces in the systems. For example, in the case of a portal frame with moment connections, for computational simplicity of the structural analysis, it is often assumed that the structural members are connected with a rigid moment connection to determine member forces and system deformations. In doing so, a rotational stiffness of the moment connection much higher than the bending stiffness of the adjoining members is assumed. In reality, a timber moment connection exhibits a nonrigid behaviour; its rotational flexibility results in larger system deformations and different member forces and moments. Figure 8 illustrates two types of models for portal frames. The portal frame model shown in Figure 8(a), assuming that the moment connections are infinitely rigid, will have smaller deformations and smaller moments at the knee connections, while the model shown in Figure 8(b), assuming that the moment connections have some flexibility, will have larger deformations, smaller apex moment, and larger moments at the knee connections.

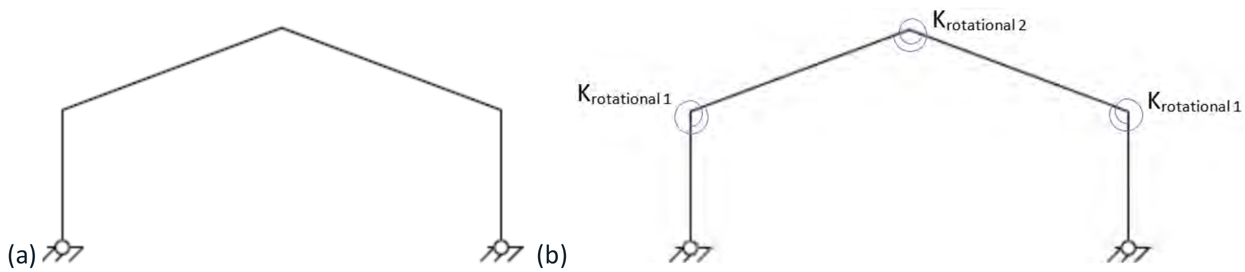


**Figure 8. Models for portal frames with moment connections with (a) infinite rigidity and (b) some flexibility**

For example, portal frames with laminated veneer lumber (LVL) rafters are common in Australasia. To speed the erection process, moment connections using rods within screwed LVL sleeves are utilised. This type of connection permits the transfer of moments between the LVL and a steel column (Figure 9). That connection system, with the rotational stiffness as a function of the sum of the axial deformations from the rod, sleeve, and screw connection system, has been studied by Scheibmair and Quenneville (2014). If detailed correctly, this moment connection can develop a moment greater than the actual LVL moment capacity, with a purely ductile failure mode if the rods are designed to be the weak link in the system.

(a)  (b)  (c) 

**Figure 9. Portal frame with LVL rafter and moment connection**

#### *5.2.2.4 Backbone Curves and Hysteresis Loops*

The calculated design resistance of the system can often be much lower than the yield resistance determined from test data. Depending on the purpose of the model, it may be necessary to model the response of the connections, providing upper and lower bounds, particularly for the yielding resistance. These are often built-in to typical backbone curve forms provided in analysis software. Figure 10 shows an example of the idealised curve profile commonly used in ETABS. When considering modelling stability, it is often useful to implement a post-failure tail to ensure model stability. For model stability, it can also be useful to include a slight post-yield slope.

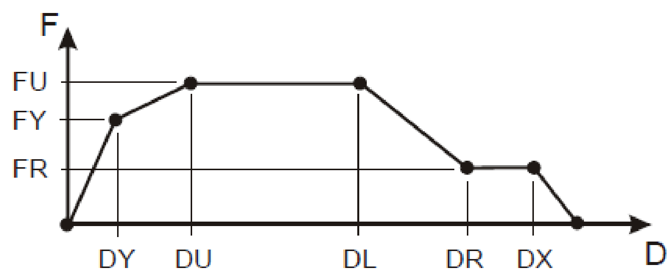


**Figure 10. Idealised monotonic backbone curve. (Computers and Structures, Inc., 2021)**

Where a nonlinear time-history analysis is required, it is also important to properly implement the correct hysteresis form. Figure 11 shows some examples; pinching is typically an accurate representation of a dowelled dissipative connection. In comparison, a nondegrading hysteresis is commonly used for steel yield, and buckling is commonly used for buckling steel braces. If using modelling software with limited built-in hysteresis forms, it is important to choose the modelling software suitable to implement the correct hysteresis form. Some software programs, such as ETABS, cannot implement the pinched hysteresis form required for these common hysteresis shapes. Software such as Abaqus, Ansys, SAP2000, and OpenSees provide more extensive hysteresis forms, or in some cases, the ability to create custom forms.

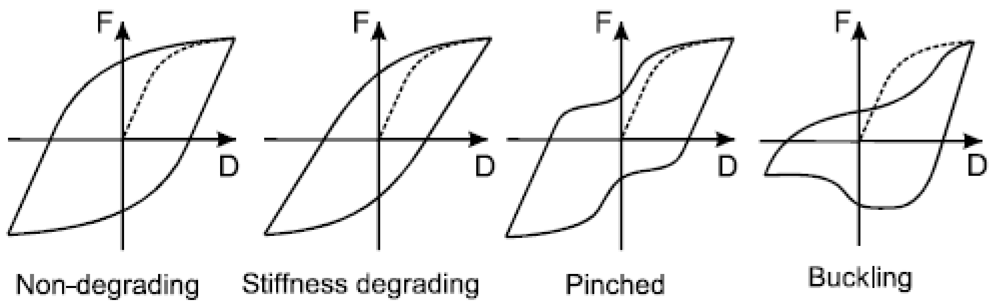


**Figure 11. Hysteresis loop types. (Computers and Structures, Inc., 2021)**

Figure 12 shows the typical hysteresis loops obtained during a reversed cyclic test on a nailed timber connection. The main features shown in Figure 12 include (a) nonlinear connection behaviour, (b) slightly asymmetric loops, (c) indistinct yield point, (d) stiffness degradation with increasing load cycles, (e) relatively fat initial hysteresis loops that imply large amounts of energy dissipation, (f) narrowed loop areas (pinching effect) in the middle of the hysteretic loops after the first load cycle, (g) strength degradation at the same deformation level for repeating loading cycles, (h) strength degradation for larger deformations, and (i) relatively high values of ductility.

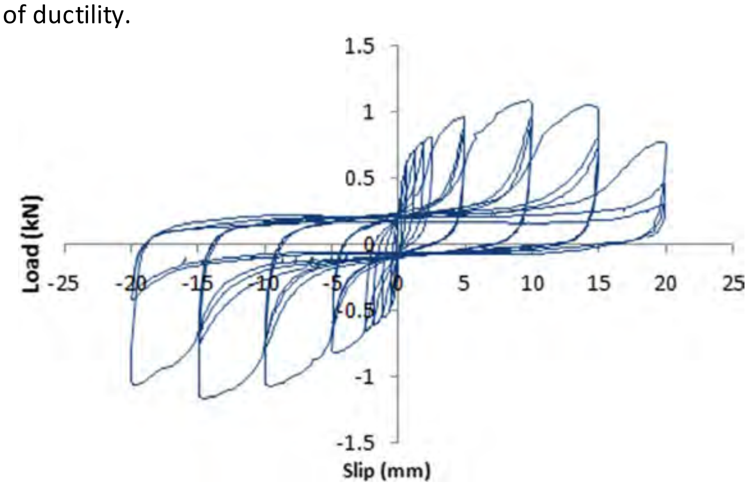


**Figure 12. Experimental load deformation hysteresis loops of a nailed connection (Li et al., 2012)**

The so-called pinching effect is due to the formation of a cavity around the fasteners resulting from the irrecoverable crushing of wood. This effect occurs after the first loading cycle at each deformation level, as the connection stiffness at that point is reduced due to the sole contribution of the metallic fasteners. As soon as the contact with the surrounding wood is re-established at higher deformation levels, the stiffness rapidly increases, which leads to the typical pinched shape of hysteretic curves. Therefore, a hysteretic model capable of predicting stiffness and strength degradation, along with the pinching effect, is desirable for timber connections. During the past several decades, various types of hysteretic models have been developed for dynamic analysis of timber connections and structures. Generally, they can be categorised as three major types: mechanics-based models, piecewise linear functions models, and mathematical models. Chapter 7.1 discusses the model types in more detail.

### *5.2.2.5 Innovative Connections*

Innovative fasteners and connectors are constantly being proposed to overcome some of the limitations of generic timber connections. These proprietary solutions typically target an increase in stiffness, strength, ductility, constructability, prefabrication, and aesthetics, or any combination of the six. Over the last two to three decades, fasteners such as self-tapping screws and self-drilling dowels have been used extensively in timber construction (Figure 13).

(a) 
(b) 
(c) 

**Figure 13. (a) Hanger connector (Sherpa Connection Systems, 2019), (b) self-drilling dowel, and (c) self-tapping screw**

Self-tapping screws are made of high-strength steel and are furnished with proprietary tips and threads; they come in many lengths and are typically larger in diameter than common wood screws but smaller in diameter than lag screws and offer significantly higher withdrawal resistance. Self-drilling dowels are made of ductile steel and are furnished with proprietary tips intended to self-drill through internal steel plates of a limited thickness. Their slenderness and ductile steel properties allow significant deformation to take place when used in shear to provide a desirable ductile load-deformation response.

These fasteners can offer significant advantages in the fabrication and erection of timber structures. Their impact on design has been limited as current North American design standards do not capture the full strength and ductility advantages. For example, self-tapping screws show a significant increase in resistance compared to the design standard approach for lag screws as a result of the rope effect. Another advantage of self-tapping screws has been their greater length, allowing large timbers to be connected together or reinforced against splitting, longitudinal shear, or compression perpendicular to the grain. They provide this advantage while behaving in a ductile manner. Note that self-tapping screws can be designed to be engaged primarily in tension by being installed parallel to the load direction or at an angle to the load (i.e., inclined screws). The high withdrawal capacity of these screws results in a performance governed by the strength of the screw steel; they provide a stronger and stiffer connection than that achieved using screws loaded in shear, but with very little ductility. Self-tapping screws may be ductile when loaded laterally.

Plate connectors, such as wood-concrete composite (HBV) or wood-steel composite (HSK) plates (Figure 14), or form-fitted connectors, such as Sherpa (Figure 15) or Knapp (Figure 6) connectors, have also been developed to allow for quick on-site erection and provide a concealed connection, which also enhances the fire performance of the assembly (Figure 13[a]). These types of connectors are generally proprietary and their design and behaviour should be provided by the supplier or confirmed through testing.

(a)
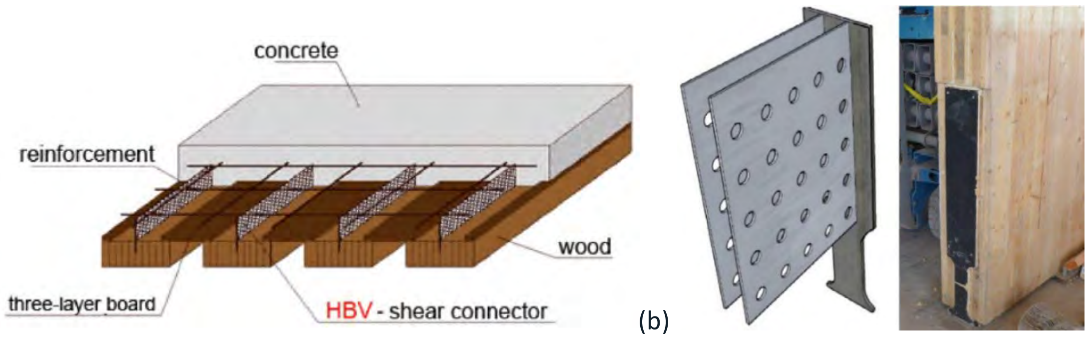


**Figure 14. (a) HBV used in a timber-concrete composite floor (TiComTec GmbH, 2011), and (b) HSK used as a hold-down in a shear wall (Zhang et al., 2018)**

**Figure 15. Hanger connection system (Sherpa Connection Systems, 2019)**

Note that not all connections in a structure require ductility. Energy-dissipative connections require ductility, but other connections need to meet only the strength, stiffness, and drift requirements to accommodate the response induced by gravity and lateral loads.

Because the height of timber structures is constantly increasing with innovation, it is necessary to adapt to the higher seismic demands in earthquake-prone zones and decrease the earthquake loadings by increasing ductility, energy dissipation, or both, through adopting different systems. As these systems are beyond the standard design solutions covered by timber design codes, they are defined as alternative solutions and require special attention. Examples of such innovative systems are buckling-restrained braces and resilient (or not) friction dampers. These systems are used to increase the timber structure's resilience and decrease the earthquake load demand. Figure 16 shows examples of these systems with their associated load-deformation responses.

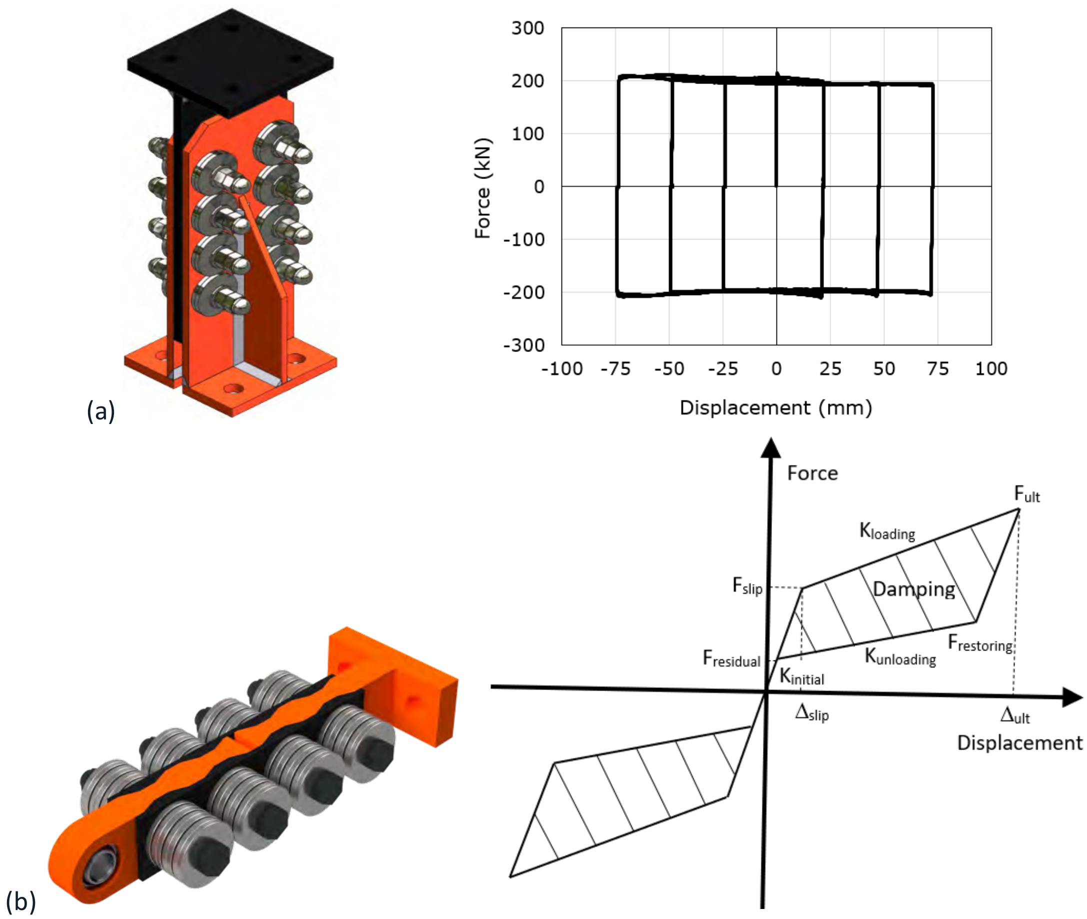


**Figure 16. (a) Friction damper and (b) resilient friction damper, with their respective load-deformation responses**

Analysis of timber structures incorporating these innovative energy-dissipative connection systems becomes an iterative process. These systems increase resilience as their behaviour is nonlinear. Some of the systems provide nonlinearity through material nonlinearity, others through geometric nonlinearity. Regardless, the analysis process is somewhat the same. As with any nonlinear system, the ability to reach the optimised solution using the fewest iterations depends on the accuracy of the first assumption. Whatever the system is, a possible procedure to achieve a solution to the structural analysis with an earthquake loading is as follows (Hashemi et al., 2020):

(1) Model the structure assuming rigid connections and estimate the earthquake loadings using a force-based method. Analyse the rigid structure subjected to these loads and determine the demands of the members and connections from the earthquake loads.
(2) Modify the rigid model by inserting the nonlinear systems as links. The loadings obtained at step (1) provide a good assessment of the maximum load demands on the systems. It is best to assume no limit to the displacement at this point.
(3) Analyse the nonlinear model using either a pushover analysis or a nonlinear time-history analysis. Appropriate scaled earthquake records should be considered. From these results, verify that the structure's target drift is respected. Make adjustments to the systems' characteristics by optimising the strength, stiffness, and displacement characteristics of the members and connections.

Depending on the overall model structural response, one may need to increase the system's strength or secondary stiffness, or both. More than one iteration is usually required, but an optimised solution is often achieved within two or three iterations.

With regard to seismic dampers and any other defined energy-dissipative device available on the market, it is of the utmost importance that they be connected to the timber structural element with the stiffest and strongest connections possible. This is to ensure that any deformation is concentrated in the damper and that the maximum earthquake energy is absorbed. A poorly detailed connection will result in slack and will decrease the efficiency of the damping system. For this reason, in any structural analysis that looks at the effect of seismic dampers on a structural response, it is advisable to connect the structural element of the seismic fuse (usually using a link having a distinct load-deformation response) to another link that accounts for the actual stiffness of the connection between the damper and the remaining timber structural element (Figure 17).

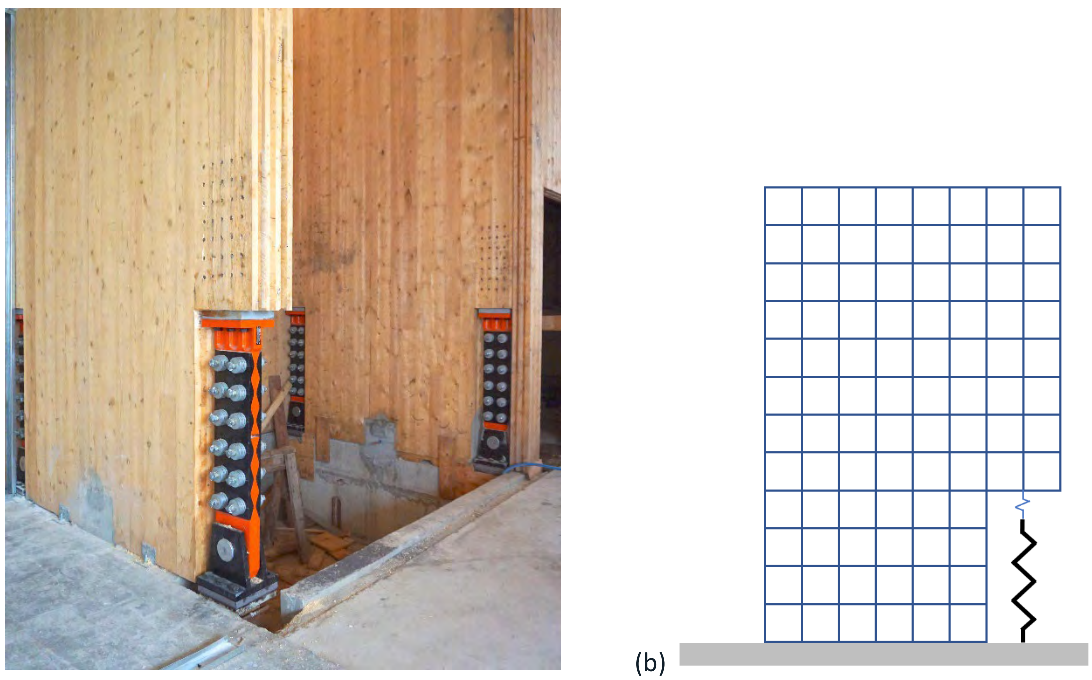

(a) (b)

**Figure 17. (a) Rocking CLT shear wall with a seismic damper at its bottom corner and a dowelled connection linking the damper to the CLT panel, with (b) its numerical model equivalent**

### 5.2.2.6 Sensitivity Studies for Connection Failure Modes

Timber connections fail in two distinctive manners: ductile or brittle, depending on the configuration, and connections may show a combination of both. Figure 18 illustrates various modes of failure for connections with dowels installed perpendicular to the face of a wood member. The bearing failure is specific to a dowelled connection and can occur at any angle to the grain; brittle wood failure can occur with any type of fastener. Typical brittle failure modes include splitting failure, which occurs only when a load perpendicular (or at an angle) to the grain is applied, while row shear, group tear-out, and net tension occur under a tensile load parallel to the grain. For a dowelled connection, only bearing failure can represent a ductile failure mode. A ductile failure provides the highest load for the number of dowelled fasteners specified. It also requires the greatest volume of wood with regard to fastener spacing, edge and end distance, and thickness of the member to prevent a wood shear or tension failure.

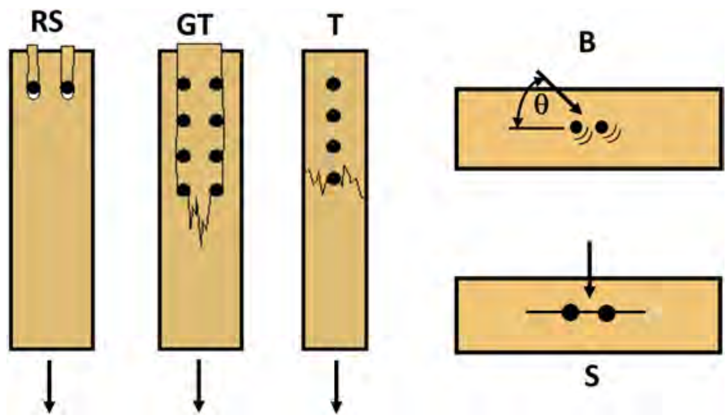


**Figure 18. Various failure modes (ductile and brittle) in a timber connection with dowels: row shear (RS), group tear-out (GT), net tension (T), bearing (B), and splitting (S)**

When modelling the hysteresis of a connection, a designer assumes that a ductile fastener bearing mode will govern the connection. However, this may not always be the case, as discussed in Section 5.2.1 and shown in Figure 5. It is also important to understand that the design strength resistance of a connection as determined from design standards is often significantly lower than its ultimate resistance. If a sensitivity study on the influence of the types of failures that may occur in a timber structure is to be carried out using structural analysis software, a link can be used at the connection, and the load-deformation curves shown in Figure 5 can be replicated. This type of analysis would allow an investigation of the robustness of a structural system under collapse or seismic events.

It is also important to understand that timber failure can be complex (Chen et al., 2020; Chen et al., 2011; Sandhaas et al., 2012). It is not necessary to look at complicated moment-resisting connections to start realising that even simple timber-to-timber connections can become somewhat complicated to analyse. For example, in the case of the connection shown in Figure 19, between a middle vertical member and two horizontal side members, there are several potential yield modes that can be predicted using the European yield model (EYM) (European Committee for Standardization, 2004) and up to four brittle failure modes in the side and middle members.

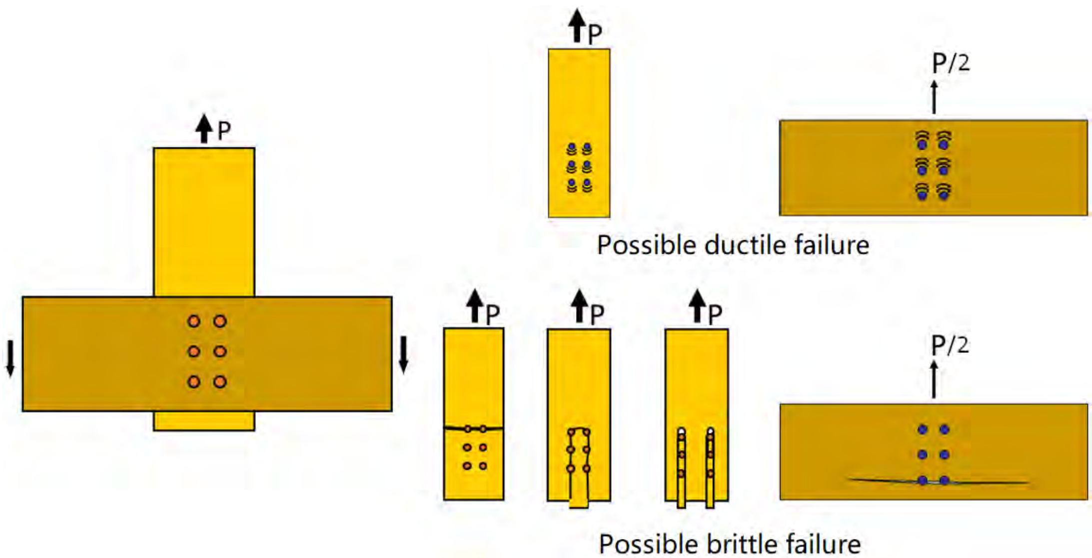


**Figure 19. Potential ductile and brittle failure modes**

For dissipative connections, brittle failure modes within the connection should be capacity-protected, like the surrounding non-dissipative elements and connections. Refer to Section 5.2.2.2 for further discussion of capacity protection.

## 5.3 DEVELOPMENT AND OPTIMISATION OF CONNECTIONS

A variety of connections, including generic and innovative connections, are available for timber structures. They can be categorised as (a) steel dowel type without threads (e.g., dowels, nails, bolts, tight-fit pins, drift pines, and rivets), (b) steel dowel type with threads (e.g., wood screws, lag screws, and self-tapping or self-drilling screws), (c) glued-in-rod type, (d) steel plate type (e.g., HSK, HBV, perforated plate, and shear fuses), (e) steel bar type (e.g., axial energy dissipator, buckling-restrained braces), and (f) slip friction type, among others. The focus of this section is on the steel dowel type and glued-in-rod type connections, which involve timber and steel materials and are more complex than the other types of connections composed primarily of steel. However, the modelling approaches discussed in this section also apply to other types of connections, with additional considerations.

This section discusses how to analyse a connection configuration and predict load-deformation behaviour, taking into account all possible modes of failure, and how to determine the maximum resistance and deformation capacity (Figure 20).

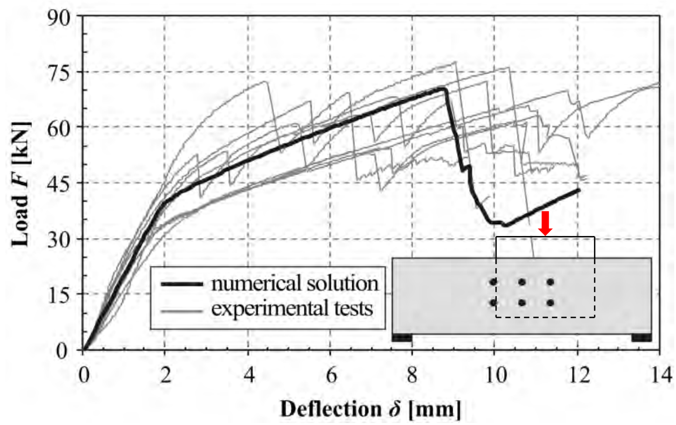


**Figure 20. Comparison of experimental load-deformation curves and one obtained through a numerical model incorporating realistic material behaviours**

### 5.3.1 Steel Dowel Type Connections under Shear

Dowel type connections using steel fasteners loaded in shear are probably the most common in contemporary timber structures. They vary from the simplest of nail or common bolt connections to tight-fitting pins, lag bolts, rivets, and screws. Numerous other proprietary fasteners that more or less have the shape of a dowel behave in a similar manner. Because all these fasteners load the surrounding timber in a similar way, the following section on their modelling, analysis, and optimisation applies to all of them.

#### *5.3.1.1 Behaviour and Mechanism*

The behaviour of timber connections loaded in shear is affected by many variables, including size and shape, embedment length, withdrawal strength, wood density, and construction method. A combination of the bearing, withdrawal, and friction determine the resistance of the connection; the resistance components are also impacted by the construction method, as predrilled holes offer different characteristics compared to fasteners hammered or screwed without a predrilled hole. For example, rivets provide the highest initial connection stiffness. Conversely, bolted connections require a larger construction tolerance in the hole through wood and the steel plate members to facilitate erection of the structure on site. The result is an initial slip (i.e., take-off) in the connection leading to a smaller effective stiffness as the oversized hole results in only a portion of the bolt bearing on the wood fibres at the start. Figure 21 shows a typical experimental load-deformation curve. This is the result of the experimental conditions in which the load on the timber connection is applied gradually from zero to the maximum, and the bolt is bearing on a small portion of its circumference at first until enough bearing deformation develops in the wood to allow the full bearing. This initial deformation, or slip, is more pronounced for fasteners that require larger tolerance for erection, such as bolts through steel plates.

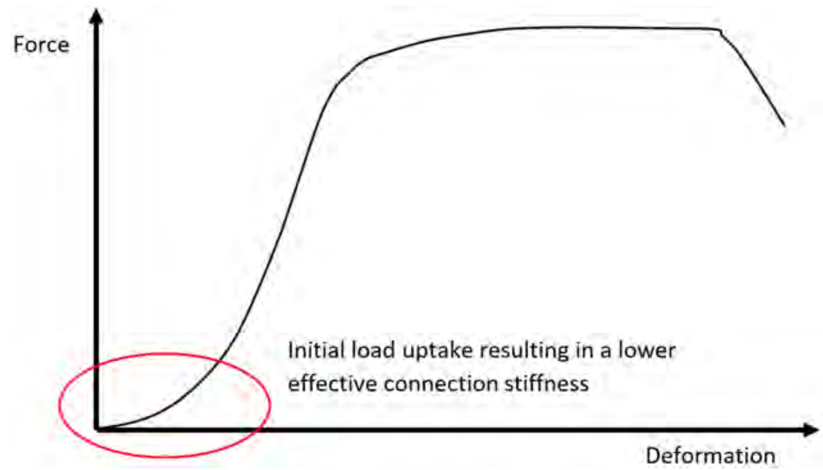


**Figure 21. Schematic force-deformation curve for a fastener with a fabrication tolerance**

Total deformations are smaller for connections that fail in a brittle manner and can be significant for connections that fail in a ductile manner. Connection deformations in the order of 40 mm have been observed for ductile bolted connections with a very large volume of wood surrounding the fasteners. Typically, small dowel type fasteners such as nails, screws, rivets, and self-tapping screws exhibit a load-deformation curve that reaches a maximum and then show a decrease in capacity (Figure 22). The reduced load resistance is the result of the excessive bending of the fastener and the pull-out of the fastener point end from the timber or steel side members. In addition, the stiffness of connections loaded perpendicular to the grain is generally smaller than that of connections loaded parallel to the grain.

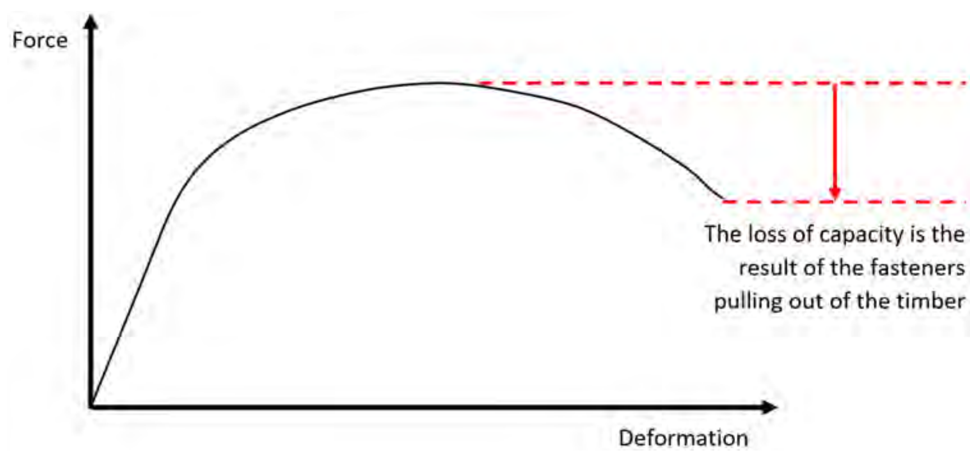


**Figure 22. Typical load-deformation curve for fasteners that can pull out of a timber main member following excessive deformation**

If the fastener resists separation of the side and main members, the rope effect can be developed (using bolts, screws, and nails with a deep penetration in the point side member) to increase the residual ultimate resistance (Figure 23). In European design equations, the resistance developed when the rope effect is mobilised is smaller or equal to the resistance determined from the yield modes. However, in laboratory tests this resistance can be considerably higher as friction can be developed between members. As this friction is somewhat unreliable due to potential shrinkage in the wood members, it is normally not relied on. Thus, the resistance of mode 1 in which the side member yields under crushing is then the upper bound of the EYM.

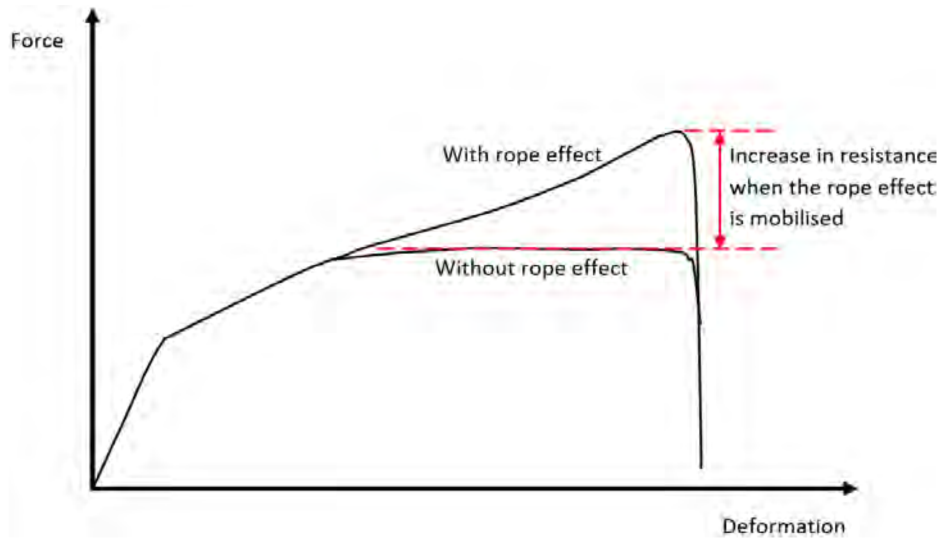


**Figure 23. Potential load-deformation curves for fasteners with and without the rope effect**

Traditionally, timber connections designed to act as seismic fuses are detailed with small dowel type fasteners. This design philosophy has the advantage of providing a residual strength and stiffness to the connection after each subsequent displacement cycle during a seismic event, as the bending dowels would ultimately crush the timber fibres. Typically, the resistance of dowel type fasteners with a small diameter is governed by the yield modes (EYM model 3) characterised by one or two plastic hinges developed in the fastener per connection shear plane combined with the crushing of timber, depending on the connection configuration. As shown in Figure 5, it is imperative to ensure that the secondary brittle failure in the seismic fuse connection is avoided before a non-dissipative structural element fails. This is achieved by ensuring that the connection detailing allows the connection resistance to reach EYM mode 1 by increasing spacing between fasteners and avoiding timber failure in shear, tension, or a combination of both. Figure 24 illustrates the required design targets for energy-dissipative connections in timber structures.

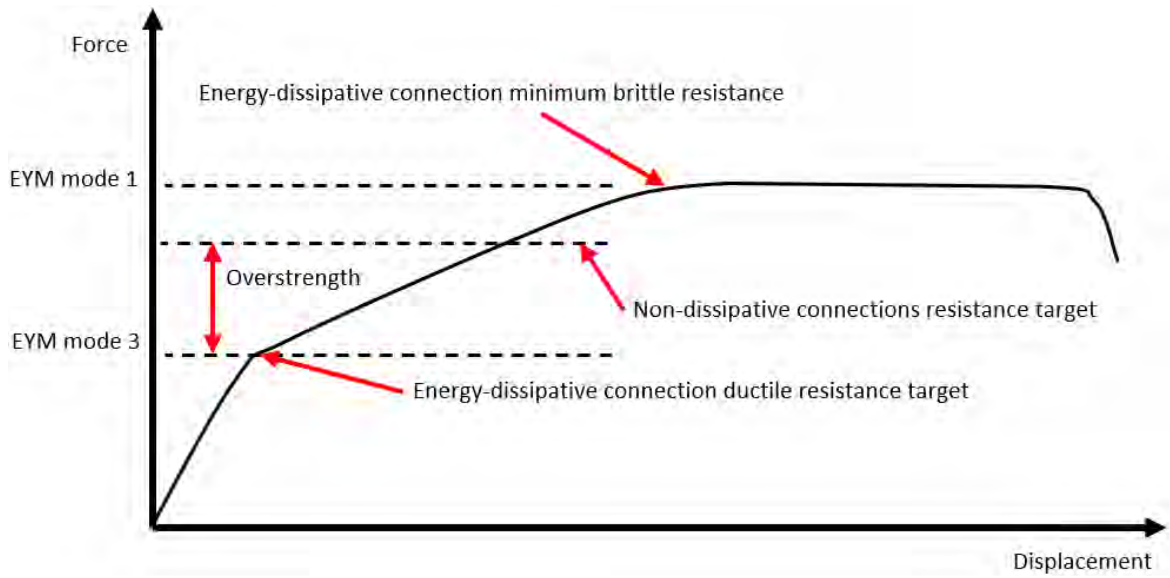


**Figure 24. Energy-dissipative connection resistance targets**

### *5.3.1.2 Modelling Methods*

#### 5.3.1.2.1 Efficient Model for Ductile Failure Modes

In general, bolts, dowels, nails, tight-fit pins, and screws behave like dowel type fasteners. Wood design standards, such as CSA O86:19 (CSA Group, 2019), approach the design methodology of all of these connectors using the EYM as shown in Figure 25.

(a) $f_1 d_F t_1$

(b) $f_2 d_F t_2$

(c) $\frac{1}{2} f_2 d_F t_2$

(d) $f_1 {d_F}^2 \left( \sqrt{\frac{1}{6} \frac{f_2}{(f_1 + f_2)} \frac{f_y}{f_1}} + \frac{1}{5} \frac{t_1}{d_F} \right)$

(e) $f_1 {d_F}^2 \left( \sqrt{\frac{1}{6} \frac{f_2}{(f_1 + f_2)} \frac{f_y}{f_1}} + \frac{1}{5} \frac{t_2}{d_F} \right)$

(f) $f_1 {d_F}^2 \frac{1}{5} \left( \frac{t_1}{d_F} + \frac{f_2}{t_1} \frac{t_2}{d_F} \right)$

(g) $f_1 {d_F}^2 \sqrt{\frac{2}{3} \frac{f_2}{(f_1 + f_2)} \frac{f_y}{f_1}}$

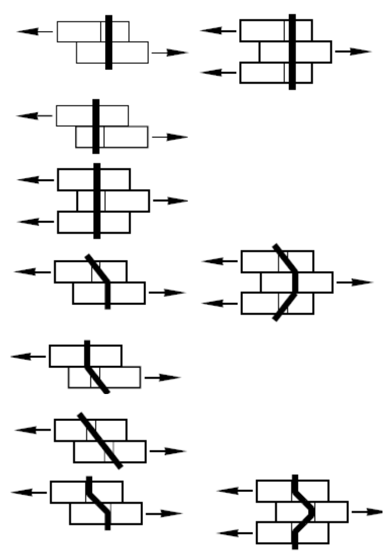

**Figure 25. Yield modes of dowel type connections specified in CSA O86 (CSA Group, 2019)**

In general, modes (d), (e), and (g) provide some ductility in a connection, with mode (g) providing the highest amount, resulting from a larger number of hinges per shear plane developed in the steel fastener. Dowel type fasteners yielding in other modes show more severe pinching of the hysteretic loops, resulting from localised embedment/crushing failure of the timber at the fasteners. In general, a slender fastener results in a more ductile controlling mode, and more small-diameter fasteners provide more ductility than fewer large-diameter fasteners.

Additionally, where connection slack (Figure 21) may occur, such as any steel-wood connection where the hole through the plate may be oversized, it is important to include the slack separately. When modelling, this initial slack can be incorporated separately with a specific nonlinear curve or a linear line with an effective stiffness accounting for the initial slip.

Load-deformation curves for connections failing in a ductile manner can be obtained using a simple 2D model (Figure 26). In this model, line elements are used to represent the fastener and the wood fibres. The material definitions for the wood and the steel elements are defined as elastoplastic. To represent the rope effect, restraints can be imposed along the axis of the fastener. Good results have been obtained using this approach (Erki, 1991). However, the model is incapable of accounting for brittle failure due to a wood failure in shear or tension.

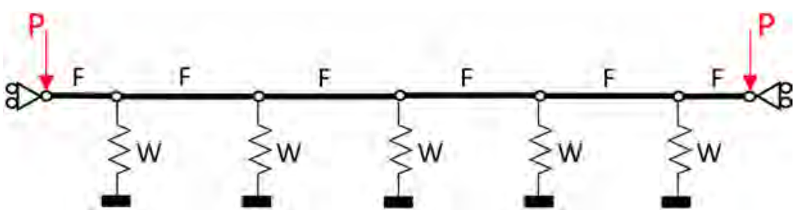


**Figure 26. Two-dimensional model with line elements to determine the load-deformation response of a fastener with a ductile behaviour. Both the fastener (F) and the wood (W) have elastoplastic behaviours**

#### 5.3.1.2.2 Advanced FE Models

To account for all key characteristics of wood (ductile and brittle), a 3D FE model of the connection is required, with the material defined for all loading directions. Timber and steel connection parts are modelled separately and interact using contact elements that are triggered when displacements fill the gaps (Figure 27). This is an important part of a connection model as parts are typically fabricated “loose” to allow the connection installation, and thus, not all surfaces are in contact in the same proportion at the onset of loading.

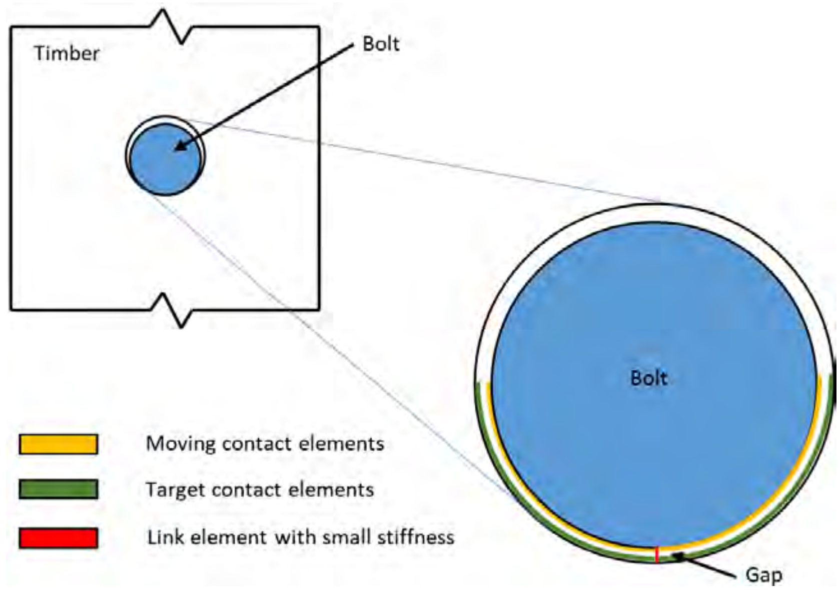


**Figure 27. Example where contact elements are used between fastener and timber**

These gaps are an intrinsic part of a connection and influence the load distribution among different fasteners of a connection. Optimising the model to the next level, gap sizes can be randomised and their effects analysed to determine the resulting variability in connection behaviour. Advanced FE software allows for this type of randomised model definition, and it is now possible to carry out multiple models with random features. Of course, the model should be simplified as much as possible to reduce the number of elements. This can be done by modelling only one-half of a volume if there is a plane of symmetry. However, one must use caution if there is a potential failure plane that can occur on this plane of symmetry.

When modelling a connection with a certain type of fastener, it is important to understand the potential modes of failure so that the modelling features allow all the failure modes to occur and that the connection behaviour is as realistic as possible. There is no point in modelling a connection if the occurrence of the brittle or ductile failure modes is prevented by using material characteristics that only assume an elastic behaviour.

A timber connection poses a structural problem where bearing stress parallel and perpendicular to the grain interacts with stress in tension perpendicular to the grain and shear stress parallel to the grain. The effectiveness of the FE model depends on how close to reality the materials are defined. Steel is easily modelled as an isotropic elastoplastic material. Wood, an anisotropic material, is normally modelled as an orthotropic material. However, not only is there different stiffness in three (longitudinal, radial, and tangential) directions, the resistance in tension and compression in each direction is different. At best, timber material will be defined as elastoplastic in compression in each direction with the stiffness and resistance being different, and the tension characteristic will be as an elastic-brittle material, again very different in the longitudinal and transverse directions. In addition to the normal stress, the material definition needs to consider the effect of shear stress. Table 1 lists all the material characteristics that must be taken into account to accurately model a connection.

**Table 1. Material characteristics to be used in modelling**

| Material | Loading direction | Material characteristic | | Load-deformation curve |
|---|---|---|---|---|
| Steel | Any | Elastoplastic | | 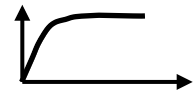 |
| Timber | Longitudinal | Compression | Elastoplastic | 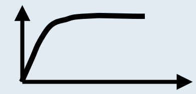 |
| | | Tension | Elastic-brittle | 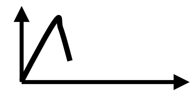 |
| | | Shear | Elastic-brittle[a] | 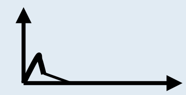 |
| | Transverse | Compression | Elastoplastic | 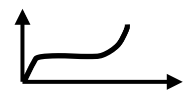 |
| | | Tension | Elastic-brittle[b] | 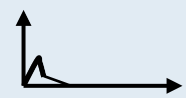 |
| | | Shear | Elastic-brittle | 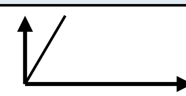 |

[a] In elements with cohesive material definition for shear

[b] In elements with cohesive material definition for tension perpendicular to the grain

The constitutive models incorporated in commercial FE software packages are often limited, which renders the general FE software unsuitable for modelling of wood-based materials. Without appropriate constitutive models, FE models cannot accurately predict the mechanical behaviour and failure modes. As a result, researchers have developed specific constitutive models for wood-based materials (Chen et al., 2011; Danielsson & Gustafsson, 2013; Franke & Quenneville, 2011; Khelifa et al., 2016; Khennane et al., 2014; Sandhaas et al., 2012). Among the developed models, the Wood$^{S}$ model developed by Chen et al. (2011) is a structural orthotropic elastoplastic damage constitutive model for wood. The model incorporates the effects of orthotropic elasticity and linear softening (damage), anisotropic plasticity with kinematic hardening, large plastic deformation, and densification. The constitutive model takes into account eight types of brittle and ductile failure modes, each associated with a different failure criterion. Wood$^{S}$ is one of the first constitutive models capable of simulating the complete stress-strain behaviour and various failure modes of wood-based members under different loading conditions, thus providing an important approach for numerical modelling of timber connections. The Wood$^{S}$ model has recently been upgraded to Wood$^{ST}$ for simulating the structural response of wood-based members and connections subjected to the thermal effects of fire (Chen et al., 2020).

When a comprehensive constitutive model is unavailable, an elastoplastic material behaviour must be used to capture the potential ductile failure modes as per the EYM; however, it is still not sufficient to capture the brittle failure modes. Alternatively, various techniques can capture the brittle longitudinal shear or tension perpendicular-to-grain failures, including using strategically located elements with a cohesive material definition (Figure 28). These elements are finite in their dimensions, and their existence is solely to allow a brittle failure to be generated at that location if it is to occur. Thus, prior knowledge of connection failure modes is necessary to save time. Otherwise, an elastic model needs to be analysed, and highly stressed elements in tension perpendicular to the grain and longitudinal shear must be identified. Figure 29 shows a bolted connection in an LVL beam loaded perpendicular to the grain failing by splitting. All timber elements can be assigned an elastoplastic material behaviour if cohesive material elements are located along the splits.

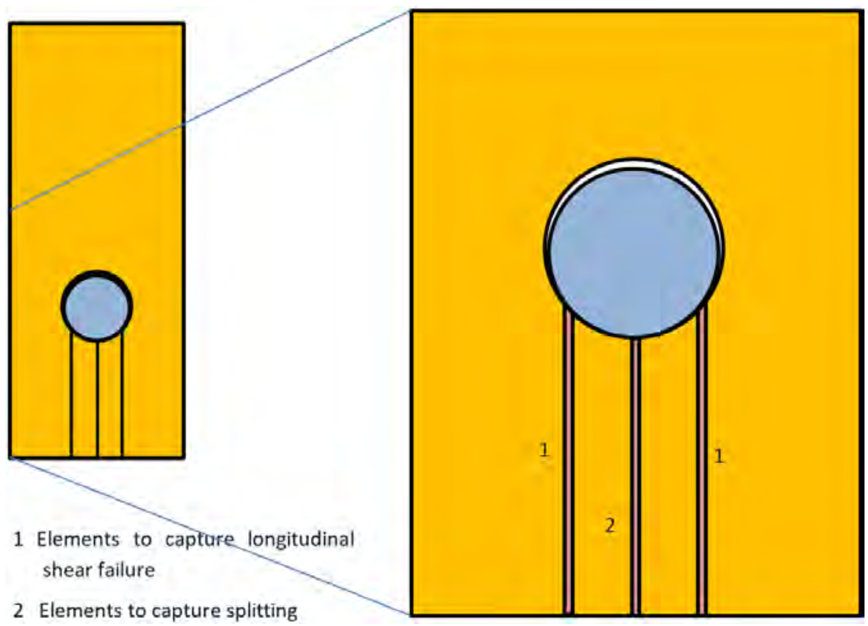


**Figure 28. Model using strategically positioned elements with cohesive material definitions to capture brittle failure (row shear and/or splitting). Elements in 1 would be checked for longitudinal shear failure and elements in 2 would be checked for tension perpendicular to the grain. The remaining timber elements would have an elastoplastic material behaviour**

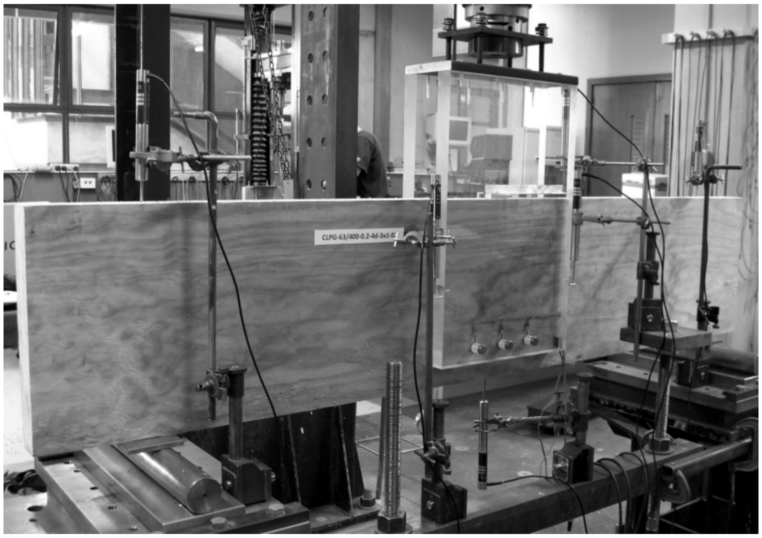
(a)

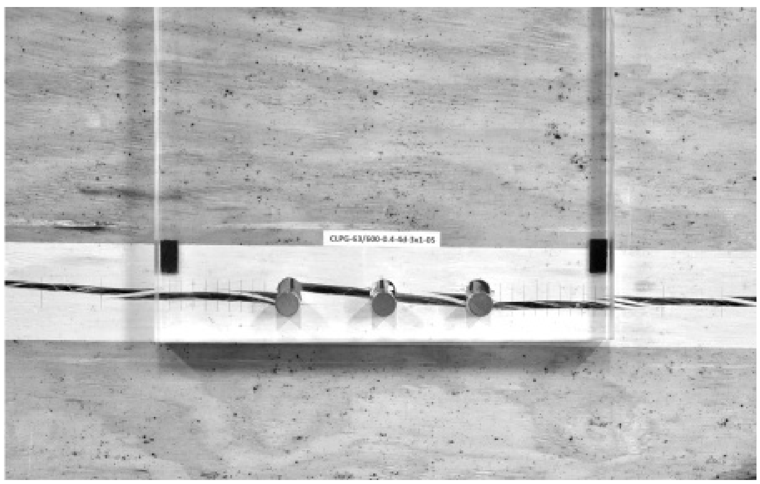
(b)

**Figure 29. Radiata pine LVL beam loaded perpendicular to the grain with splitting failure. The splitting indicates where the cohesive material elements should be located in a numerical model**

To observe the potential variability of a connection, material properties that are within a potential range should be assigned to the numerical model. It is typically implemented by establishing the average of all material properties and the variability within them, and then programming the numerical analysis to conduct multiple runs with randomly assigned material properties. Results of each run are then compiled, and the cumulative average response and variation are monitored. It is then possible to allow the runs to continue until the average and variability of the results converge (Figure 30). For added reliability to the previous results, further analyses with different starting random material definitions should be run and the results compared with the previous ones. If results are not changing, it can be concluded that the model is capturing all the randomness of the gaps and material variability.

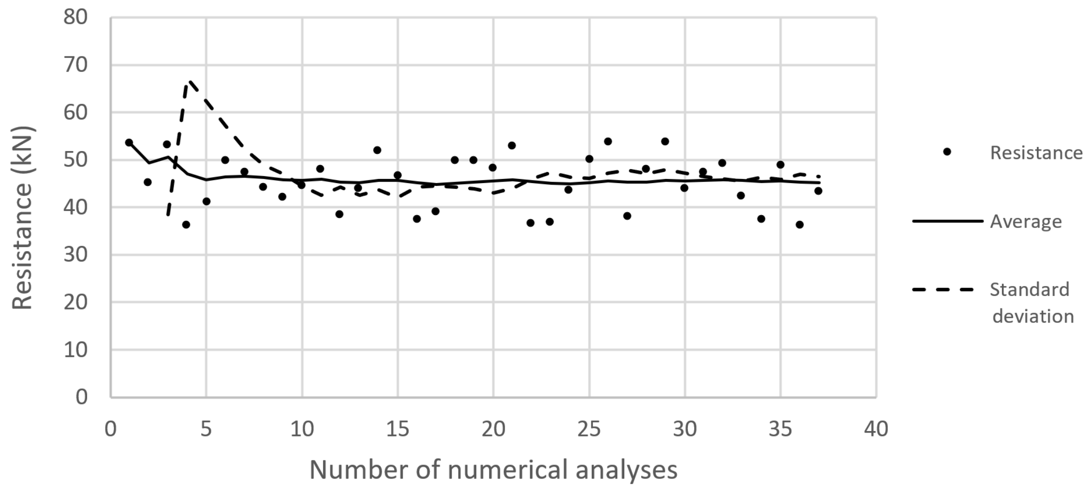


**Figure 30. Average connection maximum load and coefficient of variation versus number of numerical analyses**

In a connection with multiple fasteners, the variability of the wood density surrounding each fastener and the tolerance between the fastener and the hole (e.g., for a bolted connection) influences the overall connection load deformation. There is an element of randomness in the load transfer between the fasteners and the timber, and only a numerical analysis in which the randomness of the parameters is taken into account could reveal the possible average load-deformation response of a group of fasteners. Bickerdike (2006) conducted such an analysis and assessed the sensitivity of the connection response to different variables.

In cases where the load-deformation response of the fasteners in a connection is highly variable as a result of the connection configuration (e.g., the moment connection shown in Figure 2[b]), each dowel has a distinct load-deformation relationship. The ends of the dowels are loading the column, and the middle is loading the rafter. The column and rafter being at more or less 90 degrees to each other, and each dowel loading the column and rafter at a specific angle to the grain, make the numerical analysis somewhat elaborated. Chui and Li (2005) studied a similar connection geometry assuming a purely ductile behaviour with some success but without considering the potential for any brittle wood failure (splitting or shear) to occur. Ultimately, one would need to either consider the potential failure of the wood in the column or the rafter to be the result of tension perpendicular to the grain stress or plainly prevent this by reinforcing the column and rafter members to prevent splitting.

### 5.3.2 Screw and Glued-in-Rod Connections under Withdrawal

Self-tapping screws and glued-in-rods loaded in withdrawal are types of fasteners with a significant axial resistance. In this section, screws that resist lateral shear are not covered as these connections would be modelled in the same manner as steel dowels, discussed in Section 5.3.1. This section covers the axial resistance of the fasteners. The considerations discussed in this section and Section 5.3.1 should be applied to screws which are loaded laterally and axially.

There are three types of screws used in wood construction in general: wood screws, lag screws, and proprietary self-tapping screws (Figure 31). The design rules for wood screws and lag screws are included in the current Canadian wood design standard (CSA O86:19). Proprietary self-tapping screws are not covered in the current standard, but provisions are currently in development for potential inclusion in the 2024 edition.

Before the new provisions are adopted, it has been recommended that self-tapping screws be designed based on the lag screw provisions, with some adjustments to account for the characteristics of the self-tapping screws.


**Figure 31. Different types of screws: (a) wood screw, (b) lag screw, and (c) self-tapping screw**

Screws are often implemented in either shear (Figure 32[a]) or withdrawal (Figure 32[b]). Although using lag screws or wood screws in pure withdrawal is uncommon, using self-tapping screws in withdrawal configurations is common and reliable. This application results in a brittle failure mode, either in withdrawal for shorter threaded embedment lengths, or screw steel failure in tension for longer threaded embedment lengths. One common approach is to use inclined self-tapping screws to provide a stronger and stiffer shear connection than a typical shear connection. Fully threaded self-tapping screws can be used to reinforce wood in areas of high stress perpendicular to the grain as well, although no provisions for this are currently provided in Canadian standards.

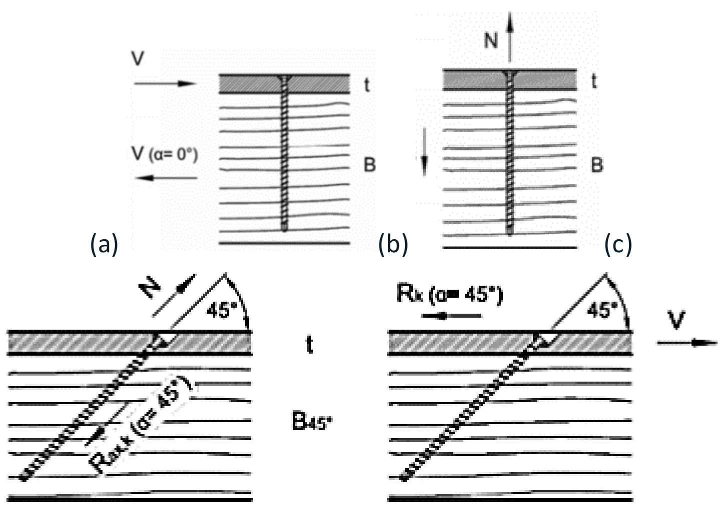


**Figure 32. (a) Self-tapping wood screw, (b) screw in withdrawal, and (c) inclined screw in withdrawal**

Glued-in rods (Serrano, 2001) are used for primarily two purposes in timber engineering: to join structural elements (Figure 33) or to reinforce wood in areas of high tensile stress perpendicular to the grain, similar to fully threaded self-tapping screws. Glued-in rods have been used for many years, especially for glulam — in Europe, mainly in Nordic countries, Germany, and Russia. A glued-in-rod connection makes it possible to obtain strong and stiff joints with excellent performance in load transfer without the need for large metal plates (i.e., often used for other dowel type fasteners). Architects prefer concealed connection hardware for aesthetic reasons and for enhancing the fire resistance of the assembly.

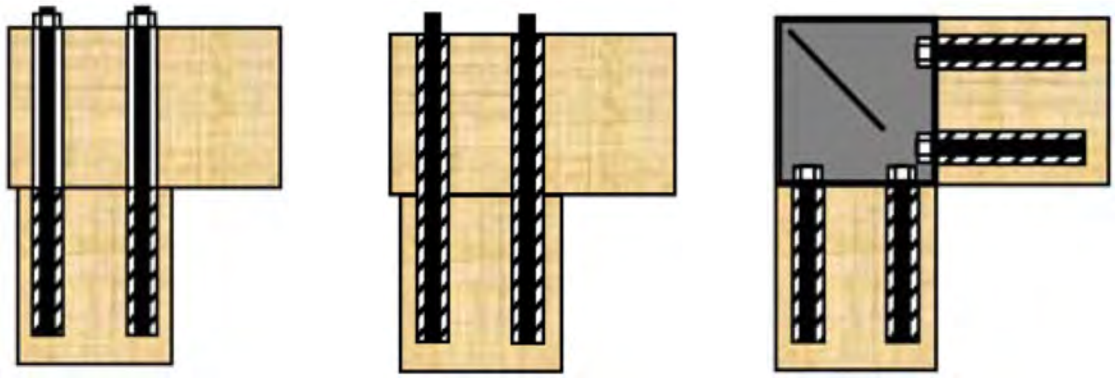

**Figure 33. Common configurations using glued-in steel rods (Fragiacomo et al., 2010)**

Similar to the discussion of modelling shear-loaded dowel type connections, it is imperative that the potential failures, both brittle and ductile, are accounted for. The potential modes of failure are the yielding of the glued-in steel rod or shank of the screw, followed by the brittle failure at the interface of the wood block and the steel shank, and then brittle failure of the wood (tensile and splitting failure). For the screw, the fibres surrounding the threads fail in shear, either in the longitudinal or transverse direction, depending on the orientation of the screw in the timber. For the glued-in rod, the glued interface separates from the timber fibres.

For a 2D efficient model similar to that discussed in Section 5.3.1.2.1, the general assumption is that the governing failure mode would be that of the steel in the rod or screw shank. It is the designer's responsibility to ensure that the screw withdrawal strength or glue interface strength is sufficient to prevent this type of failure, similar to all other brittle timber failure modes.

For more detailed 3D models, similar to those discussed in Section 5.3.1.2.2, for screw and glued dowelled connections, the interface between the steel shank and the fibres surrounding the fastener is the component that requires the modeller's attention. The steel and the timber away from the fastener can be modelled and defined as elastoplastic and elastic materials, respectively. The interface between the screw threads and the timber and between the glue of the glued-in rod and the timber fibres is best modelled using cohesive material defined to capture the failure of these two interfaces. These cohesive material elements should be located on the outside diameter of the screw or rod threads or on the outside of the glue diameter. As for the steel rod modelling, these special elements are finite in size. Figure 34 shows a possible FE model of a glued-in rod with different material elements.

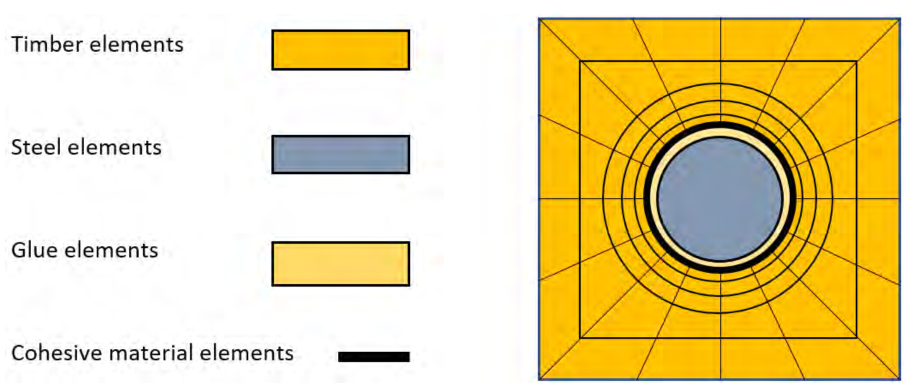


**Figure 34. FE model of a glued-in rod with different materials (end view)**

## 5.4 SUMMARY

Connections are essential elements for timber structures. This chapter discusses the structural behaviour, failure mechanism, and design considerations of timber connections. Modelling methods and key considerations are introduced for generic and innovative timber connections in structures that resist gravity and lateral loads. Efficient analytical and advanced FE modelling methods are discussed for analysing deflection, resistance, and failure modes of dowel type connections under shear, and screw and glued-in-rod connections under withdrawal. The information presented in this chapter is intended to help practising engineers and researchers become more acquainted with the analysis of timber connections.

## 5.5 REFERENCES

Bickerdike, M. (2006). *Predicting the row shear failure mode and strength of bolted timber connections loaded parallel-to-grain* [Unpublished master's thesis]. Royal Military College of Canada.

Chen, Z., & Popovski, M. (2020). Connection and system ductility relationship for braced timber frames. *Journal of Structural Engineering, 146*(12), 4020257. https://doi.org/10.1061/(ASCE)ST.1943-541X.0002839

Chen, Z., Ni, C., Dagenais, C., & Kuan, S. (2020). Wood[ST]: A temperature-dependent plastic-damage constitutive model used for numerical simulation of wood-based materials and connections. *Journal of Structural Engineering, 146*(3), 04019225. https://doi.org/10.1061/(ASCE)ST.1943-541X.0002524

Chen, Z., Zhu, E., & Pan, J. (2011). Numerical simulation of wood mechanical properties under complex state of stress. *Chinese Journal of Computational Mechanics, 28*(4), 629-634, 640.

Chui, Y. H., & Li, Y. (2005). Modeling timber moment connection under reversed cyclic loading, *Journal of Structural Engineering, 131*(11). https://doi.org/10.1061/(ASCE)0733-9445(2005)131:11(1757)

Computers and Structures, Inc. (2021). Material nonlinearity. Retrieved from https://wiki.csiamerica.com/display/kb/Material+nonlinearity

CSA Group. (2019). *Engineering design in wood* (CSA O86:19).

Danielsson, H., & Gustafsson, P. J. (2013). A three dimensional plasticity model for perpendicular to grain cohesive fracture in wood. *Engineering Fracture Mechanics, 98*, 137-152. https://doi.org/10.1016/j.engfracmech.2012.12.008

Erki, M.-A. (1991). Modelling the load-slip behaviour of timber joints with mechanical fasteners. *Canadian Journal of Civil Engineering, 18*(4). https://doi.org/10.1139/l91-074

European Committee for Standardization. (2004). *Eurocode 5: Design of timber structures - Part 1-1: General - Common rules and rules for buildings* (EN 1995-1-1:2004).

Fragiacomo, M., Batchelar, M. L., Wallington, C., & Buchanan, A. (2010, June 20–24). *Moment joints in timber frames using glued-in steel rods: experimental investigation of long-term performance* [Conference presentation]. World Conference on Timber Engineering, Riva del Garda, Italy.

Franke, B., & Quenneville, P. (2011). Numerical modeling of the failure behavior of dowel connections in wood. *Journal of Engineering Mechanics, 137*(3), 186-195. https://doi.org/10.1061/(ASCE)EM.1943-7889.0000217

González Fueyo, J. L, Dominguez, M., Cabezas, J. A., & Rubio, M. P. (2009). Design of connections with metal dowel-type fasteners in double shear. *Materials and Structures*, 42, 385-397. https://doi.org/10.1617/s11527-008-9389-3

Hashemi, A., Bagheri, H., Yousef-Beik, S. M. M., Mohammadi Darani, F., Valadbeigi, A., Zarnani, P., & Quenneville, P. (2020). Enhanced seismic performance of timber structures using resilient connections: Full-scale testing and design procedure. *Journal of Structural Engineering, 146*(9). https://doi.org/10.1061/(ASCE)ST.1943-541X.0002749

Karacabeyli, E., & Gagnon, S. (Eds.) (2019). *Canadian CLT handbook* (2nd ed.). FPInnovations.

Khelifa, M., Khennane, A., El Ganaoui, M., & Celzard, A. (2016). Numerical damage prediction in dowel connections of wooden structures. *Materials and Structures, 49*(5), 1829-1840. https://doi.org/10.1617/s11527-015-0615-5

Khennane, A., Khelifa, M., Bleron, L., & Viguier, J. (2014). Numerical modelling of ductile damage evolution in tensile and bending tests of timber structures. *Mechanics of Materials, 68,* 228-236. https://doi.org/10.1016/j.mechmat.2013.09.004

Li, M., Foschi, R. O., & Lam, F. (2012). Modeling hysteretic behavior of wood shear walls with a protocol-independent nail connection algorithm. *Journal of Structural Engineering, 138*(1), 99-108. https://doi.org/10.1061/(ASCE)ST.1943-541X.0000438

National Research Council of Canada. (2020). *National Building Code of Canada*.

Sandhaas, G., Van de Kuilen, J.-W., & Blass, H. J. (2012, July 15–19). *Constitutive model for wood based on continuum damage mechanics* [Conference presentation]. World Conference on Timber Engineering, Auckland, New Zealand. http://resolver.tudelft.nl/uuid:55c1c5e5-9902-43ad-a724-62bb063c3c80

Scheibmair, F., & Quenneville, P. (2014). Moment connection for quick assembly of timber portal frame buildings: Theory and validation. *Journal of Structural Engineering, 140*(1). https://doi.org/10.1061/(ASCE)ST.1943-541X.0000728

Serrano, E. (2001). Glued-in rods for timber structures — A 3D model and finite element parameter studies. *International Journal of Adhesion and Adhesives, 21*(2), 115-127. https://doi.org/10.1016/S0143-7496(00)00043-9

Sherpa Connection Systems. (2019). Design Guide. Retrieved from https://www.sherpa-connector.com/data/082019_Bemessungsguide_EN_web.pdf

TiComTec GmbH. (2011). *Load bearing constructions using wood-concrete-composite technique with glued-in HBV-shear connector*s (Technical Dossier).

Zhang, X., Popovski, M., & Tannert, T. (2018). High-capacity hold-down for mass-timber buildings. *Construction and Building Materials, 164*, 688-703. https://doi.org/10.1016/j.conbuildmat.2018.01.019

# CHAPTER 6

Floors and diaphragms

# TABLE OF CONTENTS

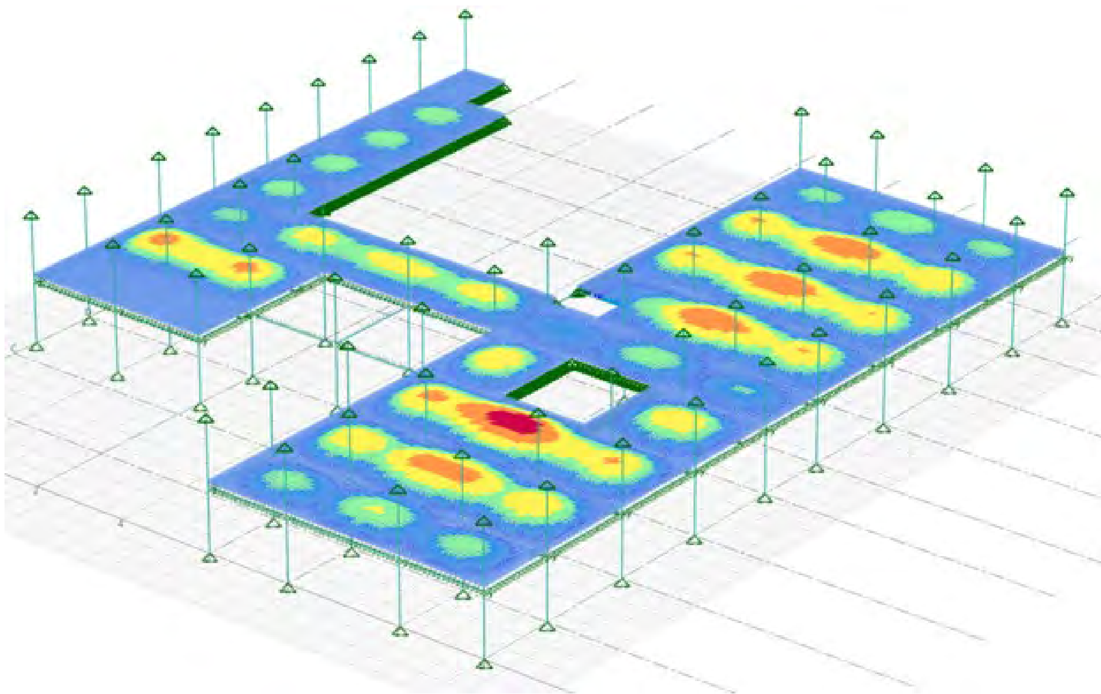

Image courtesy of Hercend Mpidi Bita, Timber Engineering Inc.

# CHAPTER 6.1

## Floors and roofs

**Authors**

Ying Hei Chui

Zhiyong Chen

**Reviewers**

Samuel Cuerrier Auclair

David Moses

Keith Crews

Lin Hu

## TABLE OF CONTENTS

## 6.1.1 Introduction

Floors and roofs have numerous structural and nonstructural functions. Structural functions include resistance against permanent dead load, loads due to use and occupancy, and snow accumulation.

The nonstructural functions of roofs include thermal insulation and building envelope protection. The nonstructural functions of floors include sound insulation and fire separation. Construction detailing to address these nonstructural issues may impact the structural performance of floor and roof systems and should be accounted for when determining the system response to the structural loads. For instance, an acoustic mat placed between a concrete slab and a mass timber panel (MTP) in a composite floor affects the stiffness of the shear connection between the concrete slab and timber panel, reducing the effective bending stiffness of the composite floor system.

From a structural loading perspective, out-of-plane loads on floors arise from live loads due to use and occupancy as well as self-weight of the structure and any permanent attachments. In the case of roofs, snow and wind are also major sources of out-of-plane loading. Figure 1 illustrates the action of out-of-plane snow, dead and wind loads on a roof and of out-of-plane dead and live loads on a floor. Under out-of-plane loading, the primary concerns in the design of roof and floor systems are the stresses in materials, forces in connections, and deflections of structural assemblies. For floor systems, an additional serviceability design check to ensure that the floor does not vibrate excessively under normal service conditions can prevent occupant discomfort.

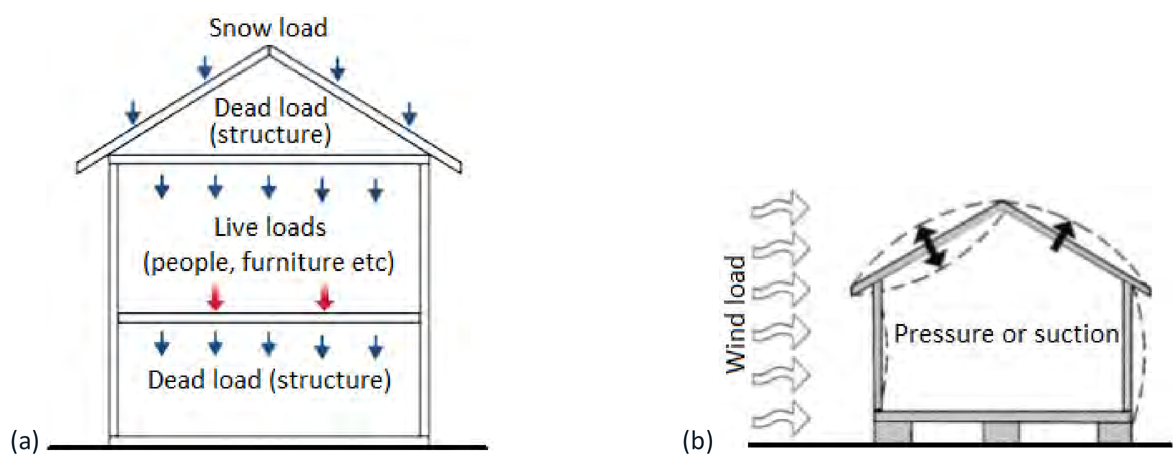


**Figure 1. Action of out-of-plane (a) static loads on floors and a roof; and (b) dynamic wind loads on a roof**

Timber-based roofs and floors, whether light wood-frame or mass timber systems, are complex structures to analyse despite their relatively simple construction. This is because they are constructed with multiple components and, in some cases (e.g., timber-concrete composite floors), multiple materials that are often connected by mechanical fasteners, leading to semi-rigid connections between components.

This chapter introduces analytical models for timber-based floors and roofs that are subject to out-of-plane loads. The focus is on floors, but the methods also apply to roofs. The types of system this chapter covers include light wood-frame, mass timber, and composite systems. These models allow users to calculate stresses in materials, forces in connections, deflections, and dynamic properties (such as fundamental natural frequencies) of the full assemblies when subjected to out-of-plane loads. In addition, given the increased use of finite element (FE) models in design, this chapter introduces FE modelling approaches for roof and floor systems.

## 6.1.2 Light Wood-Frame Systems

### *6.1.2.1 Behaviour and Mechanism*

Light wood-frame floor (LWFF) systems are among the most common floor systems in residential and nonresidential sectors the world over (Leichti et al., 1990). In most cases, LWFFs consist of wood-based joists, equally spaced over the width of the floor, that span one or more fields. A sheathing material is connected to the top of the joists by mechanical fasteners (see Figure 2). Different types of topping and ceiling materials may also be used to improve acoustic and fire performance. This system may be further reinforced in the across-joist direction with lateral components, such as blocking, strongback, cross bridging, bracing, and strapping (Jiang et al., 2004), as shown in Figure 3. These lateral reinforcements are usually attached to joists by mechanical fasteners.

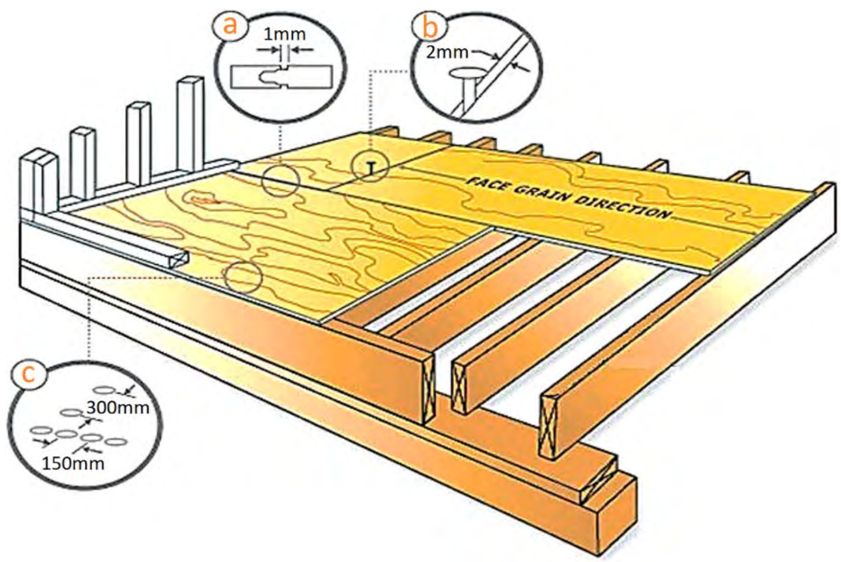


**Figure 2. LWFF (Fitzgerald, 2017): (a) tongue and groove joints between panels; (b) panel gap; and (c) nail spacing**

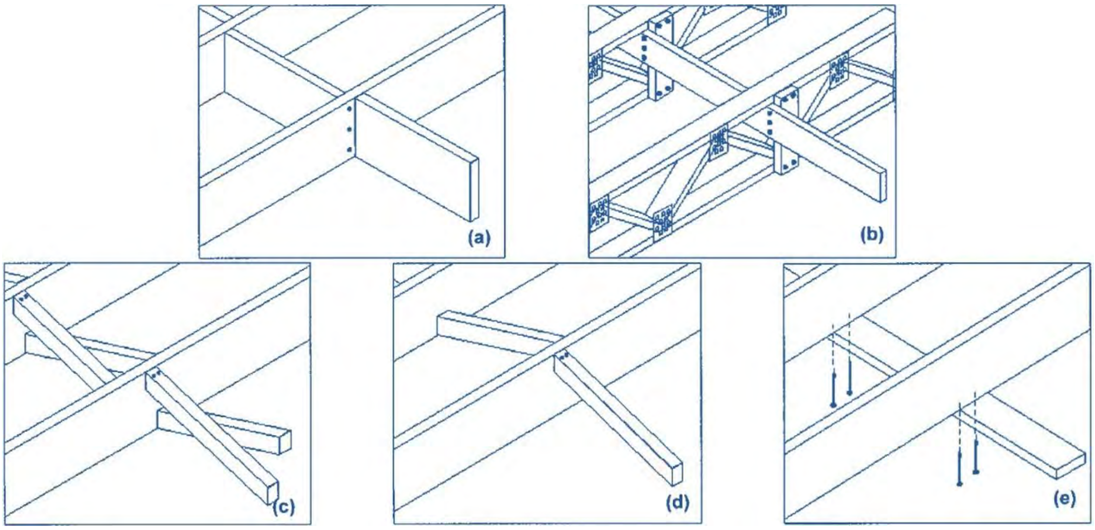


**Figure 3. Typical lateral reinforcements (Jiang et al., 2004): (a) blocking; (b) strongback; (c) cross bridging; (d) diagonal bracing; and (e) strapping**

The main function of joists in LWFFs is to resist out-of-plane loading such as gravity load. Depending mainly on the loads and spans, floor joists can be installed with or without lateral bracing members. In braced floors, the joists are braced against each other to increase their lateral stability and assist in load sharing. Joists are either sawn lumber or engineered wood products, for example, laminated strand lumber (LSL), laminated veneer lumber (LVL), wood I-joists (wooden flanges with structural panel web), or parallel chord trusses (wooden chords with diagonal lumber or light-gauge steel elements). The selection of floor joists depends on the strength and stiffness, with stiffness being the more dominant property in most cases due to the fact that serviceability criteria often dictate the allowable floor span. Different floor layouts are considered for efficiency and cost-effectiveness. For example, 2 × 10 lumber joists are twice as stiff as 2 × 8 lumber joists and use 25% more lumber for the same span and spacing. Conversely, 2 × 10 lumber joists at 610 mm (24”) spacing are 38% stiffer and use 16% less lumber than 2 × 8 lumber joists at 406 mm (16”) spacing (Jones & Spies, 1978).

Sheathing transfers and spreads out-of-plane loading to more floor joists. Common sheathing materials are oriented strand board (OSB) and plywood, but diagonally arranged lumber boards can also be used. The connections between sheathing and joists ensure loads are transferred between the different components through composite actions and without excessive deformation. Spacing of fasteners (e.g., nails) is one of the key factors affecting the strength, stiffness, and dynamic characteristics of LWFFs.

Under out-of-plane loading, floors must be designed to withstand bending and shear stresses, strain, and out-of-plane deformation. In addition, dynamic out-of-plane loading leads to vibrational excitation, which must be limited. Design criteria are relatively straightforward for floor systems with regular and homogeneous cross-sections. As mentioned above, LWFF systems commonly consist of equally spaced joists and sheathing material connected to the joists by some type of connections. In most cases, sheathing material is placed on top of the joists (Figure 4[a]), but box-type assemblies (Figure 4[b]), where sheathing material is positioned under and on top of the joists, are not uncommon. The assembly of different materials leads to a composite cross-section with flexible, semi-rigid, or rigid connections between the individual components. The stiffness and strengths of the different components and the connections have to be considered as they influence the stress distribution and stiffness of the composite cross-section.

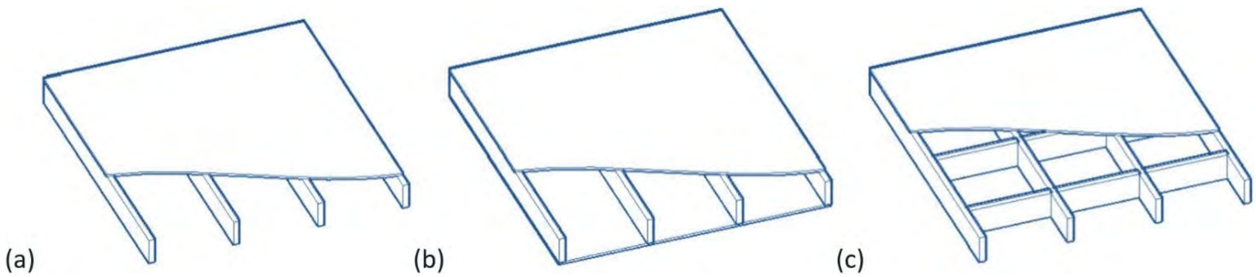


**Figure 4. LWFF systems: (a) T-beam; (b) I-beam; and (c) ribbed plate**

These flooring systems are most often designed to be beam-like one-way systems where loads are transferred to supports along the main direction of the joists. LWFF systems can also be designed as two-way systems, for example, ribbed-plate systems (Figure 4[c]), but these are less common. Besides the joist-and-sheathing-based LWFFs, wooden crossover jointed laminated systems, that is, raised wood access floors (Bocquet et al., 2007), can be used to form LWFFs.

The following sections address the analysis of joist-and-sheathing-based LWFFs in out-of-plane loading. Typical types of such joist-and-sheathing-based LWFFs, shown in Figure 4, are:

- Joists with a sheathing layer installed on top of the joists, treated as a series of T-beams;
- Joists with sheathing layers installed on top of and beneath the joists, treated as a series of I-beams; and
- Joists with sheathing layer installed on top of joists with lateral bracing elements running perpendicular to the joists, treated as a ribbed plate.

Analytical methods are described in Section 6.1.2.2 and numerical modelling (FE modelling approaches) in Section 6.1.2.3. Using either of these methods will provide more accurate and detailed results, especially for composite systems, like the sandwich panels, when there is a composite action with flanges and web. Alternatively, a simple and conservative design can be obtained by ignoring the composite action.

### *6.1.2.2 Analytical Methods*

The following sections describe 1D composite beam models and 2D ribbed-plate models.

#### 6.1.2.2.1 Beam Models

##### *6.1.2.2.1.1 Overview of Beam Models*

There are two main categories of beam models in composite systems: continuous bond models and discrete bond models. The continuous bond models, where the connections are modelled as evenly distributed, include the Gamma method (Möhler, 1956) and the Shear Analogy method (Kreuzinger, 1999), among others. The discrete bond models, where the connections are modelled as individual members, include beam models with rigid-perfectly plastic connections (Frangi & Fontana, 2003) or elastic-perfectly plastic connections (also called progressive yielding model [Zhang & Gauvreau, 2015], release-and-restore method [Zhang, Zhang & Chui, 2021], etc.). Continuous bond models are more suited for composite systems with continuous connections or uniformly distributed connections that are closely spaced, for example, LWFFs, while the discrete bond models are more suited for discontinuous connections. Because of their complexity and efficiency, discrete bond models are usually applied to composite systems with nonuniformly and widely spaced distributed connections, for example, timber-concrete composite (TCC) floors. Continuous bond models are discussed in this section because they can be applied to light wood-frame systems with great accuracy and are more efficient. For more information on discrete bond models, see Section 6.1.3.

The most common analytical method for LWFF design is the Gamma method (Möhler, 1956), modified versions of which have since been adopted into various design standards, for example, Eurocode 5 (European Committee for Standardization, 2004) and the German timber design standard DIN 1052 (Deutsches Institut für Normung e. V., 2008). In the Gamma method, a gamma ($\gamma$) factor represents the influence of the load-slip behaviours of the connections between the different sections of the composite on the overall stiffness of the composite. The Gamma method applies to both T-shape and I-shape beam floor systems. Note that the Gamma method only yields the exact solution for simply supported beams with sinusoidal loading; however, the accuracy of solutions is acceptable for almost all other loading situations for a simply supported beam.

The Shear Analogy method, developed by Kreuzinger (1999), has been adopted by national standards such as the German national annex to Eurocode 5 (Deutsches Institute für Normung e. V., 2013). In the Shear Analogy method, composite structures are modelled as two beam elements (beams A and B) connected to each other over the length of the beams by rigid truss elements pinned to the beams (see Figure 5). Beam A represents the stiffness values of the different layers and is considered to be shear rigid; beam B represents the inertia of the layers as well as their shear stiffness. The influence of the connectors is incorporated into the shear stiffness of beam B. The coupling of the two beams achieved through the truss elements ensures that the beams experience the same deflection during loading. For systems where the connections between the different layers are rigid, the Shear Analogy method can produce analytical results using fairly simple equations. Because of the flexibility of the connections in LWFFs and the truss elements in the idealised beam structure, the resulting system is statically indeterminate and usually requires computation.

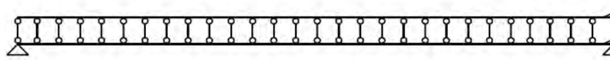


**Figure 5. Illustration of the Shear Analogy model: $E_A$ and $E_B$ are the modulus of elasticity of beam A and B, respectively, and $S_{XY}$ is the section modulus**

Compared to the Shear Analogy method, the Gamma method (discussed in detail in Section 6.1.2.2.1.2) analyses the deflections and stresses more efficiently. Moreover, the gamma factor allows a convenient qualification and comparison of the couple effect of different connections.

#### *6.1.2.2.1.2 Gamma Method*

According to the Gamma method, the effective bending stiffness of the full cross-section is calculated by summing the bending stiffness of each individual layer and adding the bending stiffness given by the parallel axis theorem factored by the gamma factor, which is directly related to the degree of connection between the layers. Deformations and stresses are calculated using the effective bending stiffness of the full cross-section. The different steps of an LWFF analysis using the Gamma method are shown next. The equations are applicable to both T-beam and I-beam floor sections (Figure 6). For T-beam calculations, the variables associated with the bottom section (indicated by subscript 3) are set to zero.

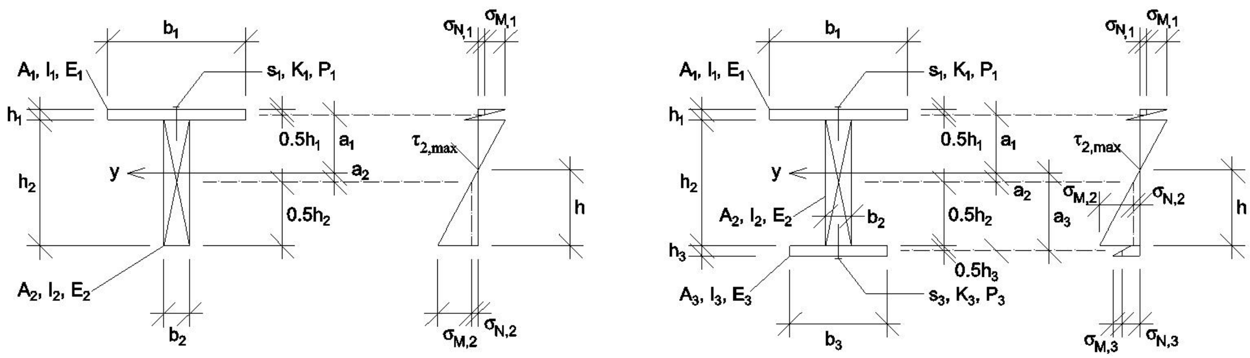


**Figure 6. Cross-sections and bending stress distributions of a T-beam (left) and an I-beam (right) (European Committee for Standardization, 2004)**

*(1) Effective Bending Stiffness,* $(EI)_{eff}$

The load-slip behaviour of the connectors between the components influences the effective bending stiffness of the cross-section. This is addressed by the gamma factor ($\gamma$). The effective bending stiffness, $(EI)_{eff}$, of the cross-sections shown in Figure 6 can be calculated using Equation 1:

$$\boldsymbol{(EI)_{eff} = \sum_{i=1}^{3}(E_i I_i + \gamma_i E_i A_i a_i{}^2)} \qquad [1]$$

where

$(EI)_{eff}$ = Effective bending stiffness of T-beam or I-beam with width equal to the joist spacing

$E_i$ = Modulus of elasticity of layer $i$

For T-sections $E_3 = 0$

$I_i$ = Second moment of inertia of layer $i$

$= \dfrac{b_i h_i{}^3}{12}$

with

$b_i =$ Width of layer $i$

$b_1$ is the joist spacing

$h_i =$ Height of layer $i$

For T-sections $I_3 = 0$

$\gamma_i$ = Gamma factor

$= 1$ for $i = 2$

$= \left[1 + \frac{\pi^2 E_i A_i s_i}{K_i L^2}\right]^{-1}$ for $i = 1$ and 3

with

$s_i =$ Connector spacing of connection $i$

For unequally spaced connectors

$s_{i,eff} = 0.75 s_{min} + 0.25 s_{max}$

$K_i =$ Slip modulus of connection $i$ ($K_i$ can depend on serviceability or ultimate limit state)

$L =$ Span of joists

For T-sections $\gamma_3 = 0$

$A_i$ = Cross-sectional area of layer $i$
$= b_i h_i$
For T-sections $A_3 = 0$

$a_i$ = Distance of the centroid of layer $i$ to the neutral axis
The distance of the centroid of layer 2 to the neutral axis can be calculated based on
$= \frac{\gamma_1 E_1 A_1 (h_1 + h_2) - \gamma_3 E_3 A_3 (h_2 + h_3)}{2 \sum_{i=1}^{3} \gamma_i E_i A_i} \qquad (0 \leq a_2 \leq h_2/2)$
The distances of layer 1 (and 3) to the neutral axis can be determined based on the geometry of the floor shown in Figure 6.

Appendix A shows an example of this calculation.

If different slip moduli ($K_i$) are used for serviceability limit state and ultimate limit state designs, two different gamma factors and, thereby, two different effective bending stiffness values are determined and used for the respective designs.

*(2) Maximum Stresses and Connection Forces*

This section shows equations for determining the maximum stress levels within the cross-sections and the forces on the connectors from the applied loads. These applied forces and bending moments need to be checked against the cross-sectional strength and the connector resistance; these are provided in material design standards such as CSA O86:19 (CSA Group, 2019). The following equations are based on ones that can be found in the German timber design standard DIN 1052 (Deutsches Institut für Normung e. V., 2008).

The maximum normal stresses within the cross-sections, $\sigma_i$, are at the outer fibres of the individual layers. Because of the flexibility of the connections, the maximum normal stresses within the layers cannot simply be determined based on stress equations for composite sections with rigid connections. Note that the maximum bending stress within each individual layer is due to the combined stresses of the bending moment and the axial forces. In Figure 6, $\sigma_{M,i}$ and $\sigma_{M,i}$ are the stresses due to bending moments and normal (axial) forces, respectively. The gamma factors address the influence of the connections, which affect the magnitude of the stresses due to normal loading component within the layers. The maximum normal stress of the individual layers can be determined using Equation 2 where the following sign nomenclature is assumed: (a) a positive bending moment induces tension in the bottom layer, and (b) a tension induces positive stress.

$$\boldsymbol{\sigma_i} = \pm \frac{\mathbf{0.5} \boldsymbol{E_i h_i M}}{(\boldsymbol{EI})_{\boldsymbol{eff}}} \pm \frac{\boldsymbol{\gamma_i E_i a_i M}}{(\boldsymbol{EI})_{\boldsymbol{eff}}} \qquad [2]$$

where

$\sigma_i$ = Normal stress within layer $i$
$M$ = Overall bending moment acting on the cross-section

Alternatively, the bending moment can be assigned to the joist member (layer 2) only. This approach is simpler but produces more conservative results. The maximum shear stress in the joist (layer 2) of the LWFF ($\tau_{2,max}$) caused by a shear force acting in a cross-section, *V*, can be calculated using Equation 3:

$$\boldsymbol{\tau_{2,max}} = \frac{(\gamma_3 E_3 A_3 a_3 + 0.5 E_2 b_2 h^2)}{(EI)_{eff} b_2} \boldsymbol{V} \qquad [3]$$

where

$\tau_{2,max}$ = Maximum shear stress in the joist
$V$ = Shear force acting on the cross-section
$h$ = Height of the neutral axis in the joist, $\frac{h_2}{2} + a_2$ (see Figure 6)

The shear load resisted by a connector in layer *i*, $P_i$, can be determined using Equation 4:

$$\boldsymbol{P_i} = \begin{cases} \frac{\gamma_i E_i A_i a_i s_i}{(EI)_{eff}} V & i = 1 \text{ and } 3 \\ 0 & i = 2 \end{cases} \qquad [4]$$

In Equation 4, $V$ is the shear force in the plane of the connectors.

*(3) Deflection*

The effective bending stiffness, $(EI)_{eff}$, is input into standard beam equations to calculate short-term deflections of an LWFF that reflect the loading applied onto the LWFF and its support conditions. For example, the mid-span deflection of a composite beam under a uniformly distributed load, $w$, can be calculated using

$$\Delta = \frac{5wL^4}{384\,(EI)_{eff}} \qquad [5]$$

The long-term effects and behaviour of the LWFF systems is influenced by creep deformation, which can be considered to be a reduction in the material properties and the connection stiffness. Eurocode 5 provides guidance on the reduction of the material and connection properties via the long-term loading deformation factor, which depends on the material as well as the service conditions, and via load combination factors (European Committee for Standardization, 2004). The reduced modulus of elasticity and connection stiffness influence the gamma factor and hence the overall effective bending stiffness. Because the service conditions, load combination factors, and materials referenced in Eurocode 5 are based on European classifications, a direct transfer of the creep coefficients to North American standards and products is not possible. Nevertheless, an adoption of the procedure in Eurocode 5 seems reasonable if designers choose appropriate creep coefficients.

Philpot et al. (1995) used various analytical models to investigate the reliability of wood joist floor systems in terms of serviceability and strength as well as the effects of creep. While creep does not affect the strength of the components, it affects the load-carrying capacity of a floor system because of redistribution of loading, increasing the probability of failure by over 50%. Fridley et al. (1997) studied the time-dependent deflection and time-dependent load distribution behaviour of wood floor systems in tests. While the components themselves experienced a significant increase in deformation due to creep (lumber, 10–60%; sheathing, 18%; no significant increase in nail connections), deformation in the assembled floors was less time-dependent (9–21%). The researchers concluded that system effects reduced the creep effects as well as the variability. The associated time-dependent load distribution changed by 7–12% compared to the initial elastically distributed load (Fridley et al., 1997). Wisniewski and Manbeck (2003) conducted a long-term test of a full-scale floor system made from composite wood I-joists and OSB sheathing under a uniformly distributed load. They recorded deflections of the individual joists and the environmental conditions for 508 days. The authors reported that the creep deflection stabilised after 168 days regardless of environmental condition changes. They reported a final creep deflection to initial deflection ratio of 1.66, which was higher than those considered in most design standards.

*(4) Floor Vibration*

The fundamental natural frequency, in Hz, of a simply supported composite beam can be determined using Equation 6:

$$\boldsymbol{f} = \frac{9.87}{2\pi L^2}\sqrt{\frac{(EI)_{eff}}{m_a}} \qquad [6]$$

where

$L$ = Span of floor in m

$m_a$ = Mass per metre length of LWFF with the width taken to be the joist spacing (including self-weight) in kg/m

The natural frequencies of LWFF systems should be controlled to prevent troublesome vibrations under normal service conditions. If the natural frequencies of an LWFF are too close to the excitation frequency induced by the occupants, the vibration of the floor can be amplified, leading to discomfort for the occupants. At least the first natural frequency of an LWFF should be above 4–8 Hz, the range of human perception. Other higher vibration modes may also lead to LWFF problems as human comfort and tolerability is related to accelerations and velocities of motions as well as frequency (Ohlsson, 1988). Furthermore, it is important that the natural frequencies of the LWFF system do not match the excitation frequencies of external impacts (e.g., heavy machinery) as this would cause resonance and potential damage to the structure.

Design criteria involve limiting the static deflection under a 1 kN concentrated load at the centre of the floor to either a deflection of 1 mm (Foschi & Gupta, 1987) or a ratio of the deflection to the floor span (Onysko, 1988). Ohlsson (1991) proposed a three-stipulation approach, with a static deflection limit of 1.5 mm/kN for a concentrated load at mid-span, a minimum natural frequency of 8 Hz, and a peak velocity that is dependent on the damping of the floor. After testing human perception of floor behaviours, and evaluating and correlating the results, Hu and Chui (2006) proposed a design criterion based on the natural frequency of the floor and its static deflection under a 1 kN concentrated load at mid-span, as shown in Equation 7:

$$\frac{f}{{d_{1kN}}^{0.44}} > \mathbf{18.7} \qquad [7]$$

where

$d_{1kN}$ = Calculated static deflection under a 1 kN concentrated load at mid-span.

It is worth noting that the frequency and deflection were calculated using a ribbed-plate mode (presented in Section 6.1.2.2.2). This design criterion was revised by using the calculated frequency and deflection from simple beam models that account for the stiffness contribution from lateral stiffness of the floor components, see CSA O86 Clause A.5.4.5 for the calculations of the frequency and deflection. The revised design criterion along with the simple beam equations for the frequency and deflection form the final design method for LWFF floors. This design method is now in the CSA O86:19 standard for evaluating vibrational serviceability of joisted floor systems (CSA Group, 2019).

The nonstructural aspects of the overall building may also affect floor vibration behaviour. Weckendorf et al. (2014) investigated the influence of construction methods and floor location within a structure on floor vibrations and found that architectural and construction detailing significantly influence floor vibration serviceability performance. Energy transmission between different areas can occur if no enhanced construction details are used.

*(5) Toppings*

Toppings (e.g., concrete) can be added to the floor systems in three different ways: as a floating topping; as a structural topping directly connected to the joists with the subfloor; or as a structural topping connected only to the subfloor, which in turn is connected to the joists.

While a floating topping does not connect structurally to the floor system, it affects natural frequencies because of the added weight; damping also has an effect. A floating topping can also contribute to floor stiffness, especially in the secondary direction, because of the generally low stiffness of the floor in this direction.

The effects of toppings that are directly connected to the joist elements via the subfloor can be considered using the Gamma method. Here the stiffness of the subfloor is usually ignored because its contribution to the overall stiffness is marginal compared to that of the topping, which usually has a significantly higher compression stiffness. Note that the connection stiffness is often affected when connecting a topping to a joist element through a subfloor. Jorge et al. (2011) showed that interlayers, such as subfloors, reduce connection stiffness in timber-lightweight aggregate concrete composite structures. Berardinucci et al. (2017) and Mirdad and Chui (2019) made similar observations. The Gamma method can be used in cases where each layer is structurally connected to the adjacent layers.

Structural toppings also add weight to the floor. As with the floating topping, the additional weight reduces the floor frequency. Human perception of floor vibration is a function of frequency: the lower the frequency, the lower the occupant's tolerance to floor vibration. Thus, a topping has a positive effect on floor vibration in that it increases stiffness, but also a negative effect, in that it increases mass and reduces the floor frequency. The final effect on the floor vibration is a summation of the negative and positive effects.

#### 6.1.2.2.2 Ribbed-Plate Model

An LWFF can be analysed as a 2D system to account for its two-way action. As part of the research work to develop design methods that address vibration problems in LWFF systems, Chui (2002) developed analytical models to predict static deflection under a point load and fundamental natural frequency, based on the ribbed-plate theory proposed by Timoshenko and Woinowsky-Krieger (1959). The derivation of this analytical solution was based on representation of the deflected shape of the floor by a Fourier series. The ribbed-plate model (Figure 7) is effective at accounting for the contributions of lateral bracing elements because the ribs in the ribbed-plate system can run along the span (the joists) and across the span (the lateral bracing members).

Khokhar and Chui (2019) applied the ribbed-plate model to evaluate the effectiveness of lateral bracing members such as cross bridging and lumber blocking. The assumptions made in the derivation of the ribbed-plate models presented in this section are summarised below:

- All four sides of the floor are simply supported.
- The sheathing is thin relative to the depth of the joists.
- The sheathing is semi-rigidly connected to the joists.
- The rotational stiffness of the bracing elements, such as blocking, is taken into account.

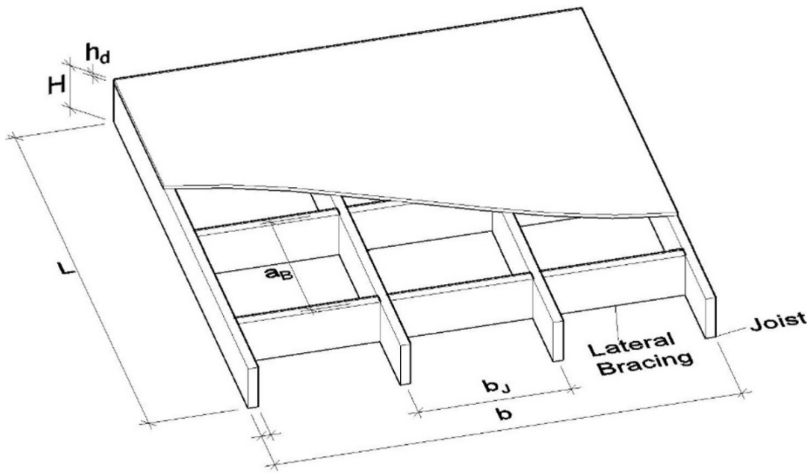


**Figure 7. Ribbed-plate model of a typical wood-based floor system showing joists, floor decking composed of topping and subfloor, and lateral bracing**

*(1) Deflection, Δ*

For the LWFF shown in Figure 7, the static deflection, $\Delta$, at floor centre under a point load $P$ can be calculated using the series-type solution shown in Equation 8. It can be implemented in a Microsoft Excel spreadsheet or a simple computer program.

$$\Delta = \frac{4P}{Lb\pi^4} \sum_{m=1,3,5..} \sum_{n=1,3,5..} \left( \frac{1}{D_x\left(\frac{m}{L}\right)^4 + 4D_{xy}\left(\frac{mn}{Lb}\right)^2 + D_y\left(\frac{n}{b}\right)^4} \right) \qquad [8]$$

where

| | | |
|---|---|---|
| $\Delta$ | = | Deflection of the floor at the centre in m |
| $P$ | = | Point load at the centre of the floor in N |
| $L$ | = | Span of the floor in m |
| $b$ | = | Width of the floor in m (for the floor design application, assume an aspect ratio of approximately one, i.e., $b$ is equal to a multiple of joist spacing and with a value close to $L$). |
| $m$ | = | Convergence term; it is recommended that 3 terms be used for $m$ = 1, 3, and 5 |
| $n$ | = | Convergence term; it is recommended that 17 terms be used for $n$ = 1,3,5, ⋯, and 33 |

$D_x$ = Bending stiffness of the system in the $x$ (span) direction of the floor in N·m

$= \frac{(EI)_{CJ}}{b_J}$

with

$(EI)_{CJ}$ = Composite bending stiffness of the joists in N·m$^2$, can be calculated using the Gamma method or the procedure in CSA O86:19 (CSA Group, 2019)

$b_J$ = Spacing of the joists in m

$D_y$ = Bending stiffness of the system in the $y$ (width) direction of the floor in N·m

$= \frac{\sum_i^j (EI)_{b,i}}{L} + \frac{(EI)_p b_J}{b_J - t + (h_d/H)^3 t}$

with

$(EI)_{b,i}$ = Bending stiffness of $i$-th lateral bracing member in N·m$^2$

$j$ = Total number of rows of lateral bracing elements

$(EI)_p$ = Bending stiffness of multilayered floor deck in N·m$^2$

$t$ = Width of the joists in m

$h_d$ = Thickness of multilayer floor deck in m

$H$ = Height of floor system (joist depth + floor deck thickness) in m

$D_{xy}$ = Shear and torsional stiffness of the system in N·m

$= \frac{G_p h_d^3}{12} + \frac{C}{2b_J}$

with

$G_p$ = Shear modulus of multilayered floor deck in N/m$^2$

$C$ = Joist torsional constant in N·m$^2$

*(2) Fundamental Natural Frequency, f*

The fundamental natural frequency of an LWFF system ($f$), in Hz, can be calculated using Equation 9:

$$\boldsymbol{f = \frac{\pi}{2\sqrt{m_f}}\sqrt{D_x\left(\frac{1}{L}\right)^4 + 4D_{xy}\left(\frac{1}{Lb}\right)^2 + D_y\left(\frac{1}{b}\right)^4}} \qquad [9]$$

where

$m_f$ = Mass per square metre of the LWFF

$= \frac{m_J}{b_J} + \rho_s t_s + \rho_c t_c$

with

$m_J$ = Mass per unit length of joists in kg/m

$b_J$ = Spacing of the joists in m

$\rho_s$ = Density of subfloor in kg/m$^3$

$t_s$ = Thickness of subfloor in m (see Figure 8)

$\rho_c$ = Density of topping in kg/m$^3$

$t_c$ = Thickness of topping in m

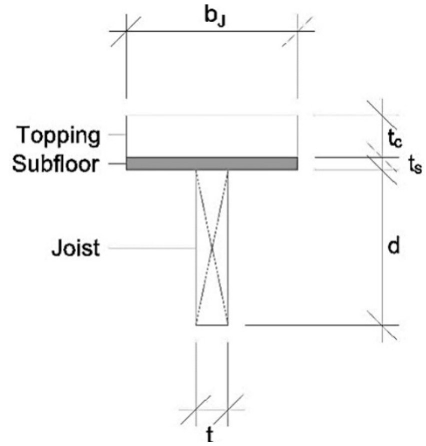


**Figure 8. Nomenclature of a T-beam section**

*(3) Bending Stiffness of Lateral Bracing Member,* $(EI)_b$

Using the ribbed-plate theory, a row of lateral bracing members can be treated as a beam running perpendicular to the joists. There are two types of bracing members: discrete bracing members, for example, cross bridging and blocking; and continuous bracing elements, for example, strapping and strongback. Both types of bracing member are fastened to the joists using mechanical fasteners. The derivation of bracing member bending stiffness is shown below.

***Discrete Bracing Systems***

For a discrete-element type bracing member, one row of the elements can be treated as a rib and the equivalent bending stiffness, $(EI)_b$ can be determined using Equation 10:

$$\boldsymbol{(EI)_{b,i} = K_r b_J} \quad [10]$$

where

$(EI)_{b,i}$ = Equivalent bending stiffness of *i*-th lateral bracing member in N·m$^2$

$K_r$ = Rotational stiffness of single bracing element, defined as the bending moment required to rotate a single element by a unit angle relative to the joist

Figure 9 illustrates a test method developed by Khokhar (2004) to measure the rotational stiffness of a bracing element. By applying a load at the centre of the test specimen, the rotational stiffness, $K_r$, can be calculated from the measured deflection, rotation, and applied load, as shown in Equation 11 (Khokhar & Chui, 2019):

$$\boldsymbol{K_r = P\left(\frac{\Delta}{\theta}\right)} \quad [11]$$

where

$P$ = Applied point load in N

$\Delta$ = Deflection at the centre of the test specimen at load $P$ in m

$\theta$ = Rotation of the bracing element at load $P$

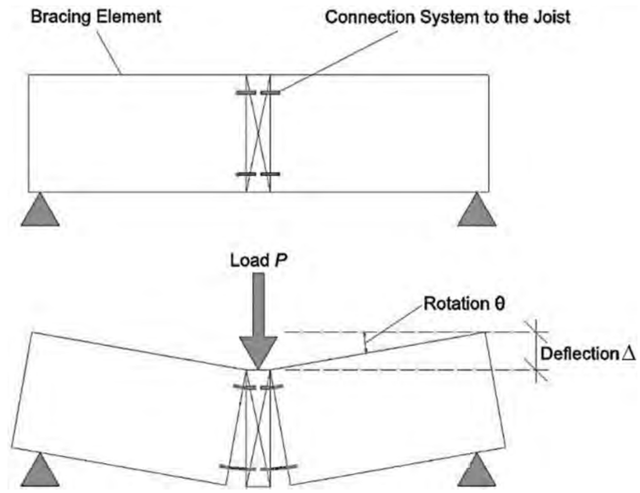


**Figure 9. Test set-up to measure rotational stiffness, $K_r$ (top: unloaded joist; bottom: loaded joist)**

Note that the rotational stiffness measured in this manner is applicable to the specific connection details, joist, and joist depth. The $K_r$ and $(EI)_b$ values for some common lateral bracing elements are shown in Table 1. These are based on the work by Khokhar and Chui (2019).

**Table 1. Rotational stiffness $K_r$ and equivalent bending stiffness $(EI)_b$ of selected cross bridging and solid blocking**

| Type of element | Joist spacing (mm) | Joist depth (mm) | Construction details | $K_r$ (kN·m) | $(EI)_b$ (kN·m²) |
|---|---|---|---|---|---|
| Cross bridging | 610 | 241 | 38 mm × 51 mm lumber toenailed to joist using two 4.19 mm × 63 mm nails at each end | 73.8 | 45 |
| Solid blocking | 610 | 241 | 38 mm × 241 mm lumber toenailed to joist using two 4.19 mm × 63 mm nails at each end | 93.4 | 57 |

***Continuous bracing system***

Strongback is effective when the joists are open-web trusses that allow a continuous lumber member to pass through the open web. With this type of construction, bending stiffness of the transverse rib can be taken as the bending stiffness of the lumber strongback member.

Equation 12, derived from Smith (1980), can be used to estimate bending stiffness of thin lumber strapping of sectional size ($b_s \times t_{cs}$) semi-rigidly connected to the bottom of the joists, taking into consideration the load-slip modulus of the nailed connection:

$$(EI)_b = \frac{\frac{E_{strap}I_s}{z^2}}{1-\frac{}{\left(\beta+\frac{\pi^2}{Kcl_{strap}{}^2}\right)E_{strap}I_s}} \qquad [12]$$

where

| | | |
|---|---|---|
| $(EI)_b$ | = | Equivalent bending stiffness of strapping in N·m$^2$ |
| $E_{strap}$ | = | Modulus of elasticity of the strapping material in N/m$^2$ |
| $I_s$ | = | Second moment of inertia of section $i$ in m$^4$<br>$= \frac{b_s t_{cs}{}^3}{12}$<br>with<br>$b_s$ = Width of strapping in m<br>$t_{cs}$ = Height of strapping in m |
| $Z$ | = | $(d + t_{cs})/2$<br>with<br>$d$ = Joist depth in m |
| $\beta$ | = | $\frac{1}{E_{strap} b_s t_{cs}} + \frac{Z^2}{E_{strap} I_s}$ |
| $K_c$ | = | Load-slip modulus of strapping-to-joist connection in N/m/m |
| $l_{strap}$ | = | Length of the shortest strapping in m |

In research on lateral bracing elements from more than 20 laboratory floors, Hu (2002) reported mechanical data on strongback, lumber strapping, and various types of bridging.

*(4) Bending Stiffness and Shear Rigidity of Multilayered Floor Deck*

Assuming there is no composite action between subfloor and topping, they can be treated as separate. Equation 13 gives the bending stiffness of the multilayer deck, $(EI)_p$:

$$\boldsymbol{(EI)_p = \frac{E_c t_c{}^3}{12} + (EI)_{s\parallel}} \qquad [13]$$

where

| | | |
|---|---|---|
| $(EI)_p$ | = | Bending stiffness of multilayered floor deck bending stiffness in N·m |
| $E_c$ | = | Modulus of elasticity of the topping material in N/m$^2$ |
| $t_c$ | = | Thickness of the topping in m |
| $(EI)_{s\parallel}$ | = | Unit bending stiffness of subfloor across joists, i.e., parallel to major panel axis, in N·m |

The shear rigidity of the multilayer deck, $(G_p h_d^3/12)$, can be obtained by summing the individual contribution from subfloor and topping, as shown in Equation 14:

$$\boldsymbol{\frac{G_p h_d^3}{12} = \frac{G_c t_c{}^3}{12} + \frac{G_s t_s{}^3}{12}} \qquad [14]$$

where

| | | |
|---|---|---|
| $G_c$ | = | Shear modulus of topping material in N/m$^2$ |
| $G_p$ | = | Shear modulus of multilayered floor deck in N·m |
| $G_s$ | = | Shear modulus of subfloor material in N/m$^2$ |
| $t_c$ | = | Thickness of the topping in m |
| $t_s$ | = | Thickness of the subfloor in m |

*(5) Torsional rigidity of joist, C*

The torsional rigidity of the joist, $C$, can be calculated using Equation 15:

$$\boldsymbol{C = G_f J_p} \quad [15]$$

where

$G_f$ = *Shear modulus of the joist* material in N/m$^2$
$\approx E_f/16$
with
$E_f$ = modulus of elasticity of the joist (flange of I-joist) material in N/m$^2$

$J_p$ = Torsional constant in m$^4$
For a rectangular cross-section, the following approximate equation can be used:
$J_p = \frac{db^3}{3}$
with
$d$ = Depth in m
$b$ = Width in m
For joist products consisting of two flanges (see Figure 10) such as wood I-joists or parallel chord trusses, $J_p$ can be estimated using the following equation:
$J_p = \frac{2b_f c_f^{\,3}}{3}$
with
$b_f$ = Flange width in m
$c_f$ = Flange thickness in m

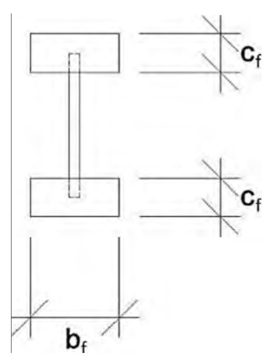


**Figure 10. Nomenclature for cross-sectional dimensions of flanges**

### *6.1.2.3 Numerical Methods*

6.1.2.3.1 Computer-based Models

Before commercial FE programs had become widely available, a number of computer-based modelling programs had been developed. Thompson et al. (1977) developed an FE program called FEAFLO (Finite Element Analysis of FLOors). FEAFLO is based on the analysis of a cross beam with T-beam elements connected to each other by a sheathing strip. The model takes into account the variability of individual beams as well as the load-sharing and two-way action due to the sheathing panels that connect the beams elements. The sheathing beam can include gaps and can consist of one or two layers depending on the floor configurations. The approach ignores the contribution of the torsional stiffness of the sheathing, which the authors felt was reasonable because of the ratios of modulus of elasticity to shear modulus of wood-based materials. Foschi (1982) developed a combined Fourier series and FE analysis procedure that addressed the lateral and torsional joist deformations. This procedure allows for the influence of joist bridging on deformation behaviour and stress distribution. The program also considers the plate behaviour of the sheathing.

Further developing the T-beam method, McCutcheon (1984) presented a beam-spring floor model. The model consists of a beam, representing the sheathing running across the joists, resting on vertical springs, which represent the bending behaviour of the T-section of the joists and sheathing at mid-span. The time-dependent behaviour of wood floor systems can be modelled using viscoelastic springs as the support of the sheathing beam (Fridley et al., 1998), see Figure 11.

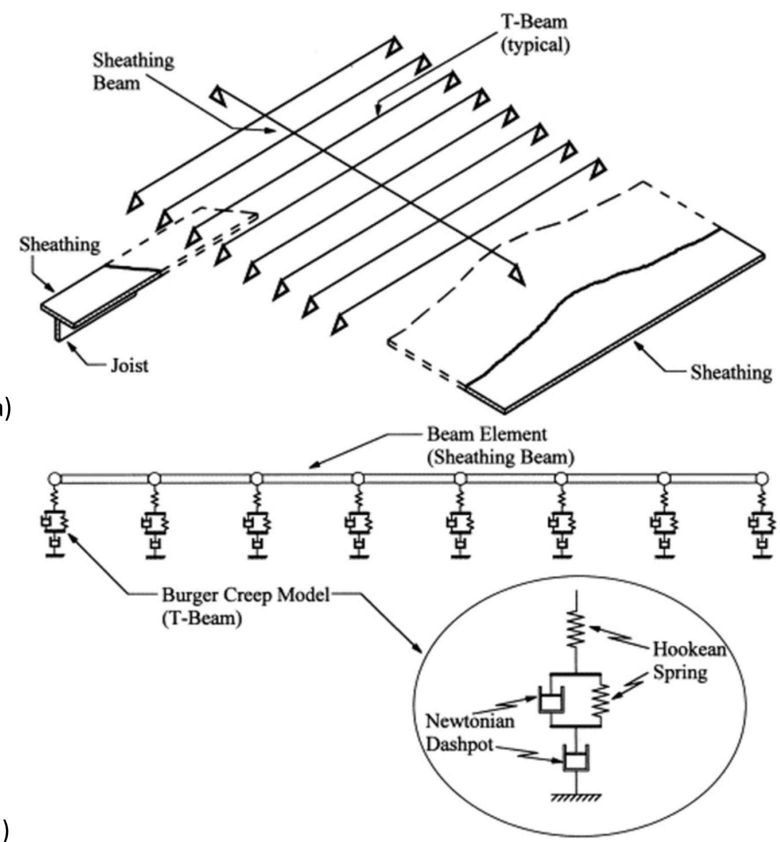


(a)

(b)

**Figure 11. Idealisation of viscoelastic system model (Fridley et al., 1998): (a) intermediate model; and (b) final model**

6.1.2.3.2 FE Models

While most LWFFs can be designed using the analytical approaches and the computer-based tools described in Section 6.1.2.3.1, more complicated floor layouts might require advanced methods like FE modelling. FE modelling is the most common numerical method used in construction and engineering today. Because they are capable of predicting the stresses, deflections, and natural frequencies of wood-based floor structures, FE models are used as a design tool as well as for benchmarking the simplified design equations design engineers routinely use. Furthermore, these models are powerful tools for the development of innovative floor components and systems. When used to determine the behaviour of LWFFs, it is important that the FE models developed represent the LWFF characteristics accurately. Because several commercial FE programs can be used to model LWFFs, this section describes critical elements of FE models of LWFFs rather than a detailed step-by-step guide for the development of such models.

To develop an FE model that represents an LWFF system, it is critical to determine the type of LWFF system and its components, the boundary and support conditions, and the desired output of the FE model. While the type of LWFF system and its particular components and boundary conditions directly influence the behaviour of the LWFF, the desired output of the FE model influences how detailed such a model has to be. A well-defined desired output can therefore help to reduce the time needed to develop an FE model and the associated computational time. For example, if the only goal of an FE model is to determine the deflection and/or natural frequency of an LWFF system, it might be feasible to model the floor as a beam or plate with dimensions and equivalent stiffness properties of the LWFF system. These stiffness properties could be determined using the methods described in Section 6.1.2.2. On the other hand, if the desired output relates to component capacities and failure modes or local stresses and deformations, a corresponding FE model would require a significantly higher level of detail to be able to predict these failures or local behaviours accurately.

As mentioned above, the type of LWFF system and its components directly influence the behaviour of the LWFF. The overall system selected determines if the floor acts as a beam-like structure with a one-way load transfer or if the floor is able to transfer loads in both directions of the panel (such as ribbed plates). Accordingly, an FE model must be capable of simulating these behaviours. Depending on the desired output, beam-like structures can be modelled by a single beam element or as multiple beam elements that are connected to each other by connectors and the sheathing. LWFF systems that allow for a two-way load transfer can be modelled as solid plate elements or as a grid of beam elements connected to each other by appropriate connector elements. For both type of systems, material properties or equivalent properties have to be used in order to allow the FE model to predict the behaviour of the floor systems. Here the term 'equivalent properties' represents the overall behaviour of an FE element that is equivalent to the behaviour of one or several floor components, such as effective bending stiffness, $(EI)_{eff}$. Note that input properties should be appropriate for the design purpose, for example, ultimate limit state design or serviceability limit state design. These equivalent properties are obtained either from testing or from modelling of the subsystem or assembly.

As with material properties, appropriate connection properties should be used. In either beam- or plate-like structures, the connections between the different floor components influence the behaviour of the floor because they influence its composite behaviour. Therefore, the connection elements chosen for the FE model should accurately represent the behaviour of the connections (including yielding and failure loads). These behaviours may include the bending and axial behaviour of a fastener (e.g., for a nail connection between a beam and sheathing), and rotational behaviour (e.g., for an angle bracket connecting two perpendicular beam elements in a ribbed-plate floor). While some commercial FE programs provide connector elements to which the desired properties can be assigned, connectors in FE programs are generally nonlinear springs (axial, lateral, and/or rotational) reflecting the behaviour of the connections. Input properties for materials and connections can be found in the literature or can be determined based on testing.

In addition, information on the contact between different elements needs to be provided. This information represents how different elements interact with each other when they are in contact. Contact information can include behaviour normal to the elements, indicating the transfer of compression forces, and tangential to the elements, indicating friction forces. Information on all contacts (beam-to-sheathing and sheathing-to-sheathing) should be provided. Figure 12 shows the connectors and contact conditions for a T-beam floor and a ribbed-plate model.

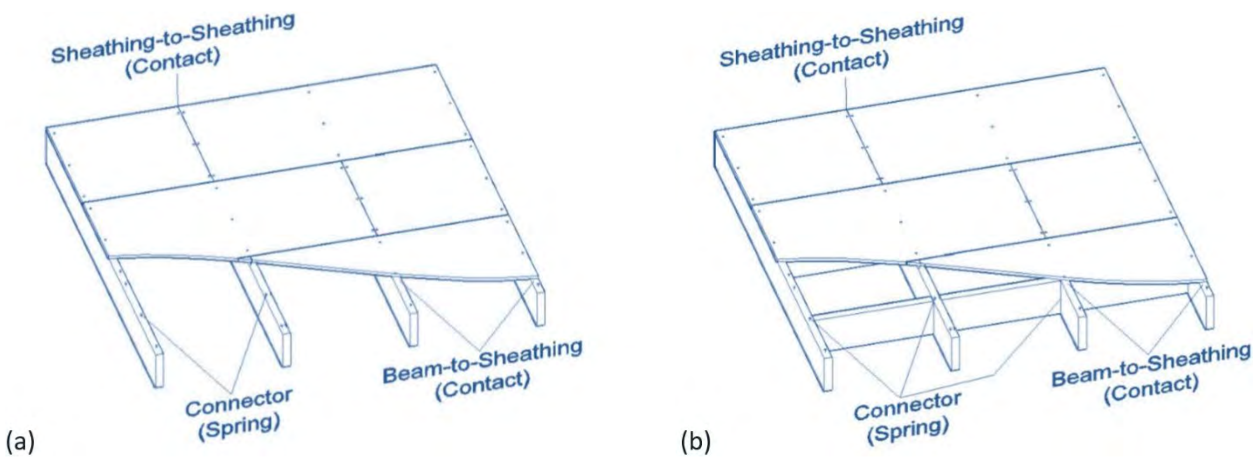


**Figure 12. LWFFs with indications of connector elements and contact conditions for FE models: (a) T-beam; and (b) ribbed plate**

Besides the LWFF structural system, the boundary conditions are important as they directly affect the internal forces and stresses as well as deformations. The boundary conditions should be selected based on the given structural system and additional conditions. Based on the structural system, that is, beam- or plate-like behaviour, the FE model should reflect the locations and restrains of support elements. In most cases, the boundary conditions associated with idealised conditions such as simple supports are sufficient for the design of LWFFs. More complex boundary conditions may be required to accurately reflect the support conditions in the real structure. Complex conditions that may need to be taken into account include support flexibility and the need for additional restraining conditions that increase rotational stiffness at the support from connections between the floor and the supports or from wall elements installed on top of the floor elements. In platform construction, loads from walls above could add rotational restraint to the floor, leading to a semi- or fully clamped support instead of a simple support.

In addition, symmetry conditions can be applied to reduce the size of an FE model. Because of the large number of components in an LWFF system, the size of an FE model can be reduced to half (for beam-like structures) or a quarter (for plate-like structures) if symmetry in terms of structural system and loading is applied. Such reductions in size can help to reduce the computational effort, especially for a highly detailed FE model. Note that the symmetry conditions should be used with caution in a frequency analysis, because they will ignore any asymmetric modes that actually exist in the full model.

As processes in FE calculations are hard to follow, validation procedures should be implemented to check if the results are reasonable. The development of an FE model generally follows the following steps:

- Determine the desired output of the FE model and the required level of detail of the model.
- Determine the structural system, boundary conditions (e.g., one-way beam versus two-way plate and eventual additional boundary conditions), and loading action.
- Adopt the appropriate material model with necessary properties or equivalent properties.

- Adopt the appropriate connection model with properties which can be based on analytical models, FE models, and tests. The size effect and spacing effect of connections should be considered when modelling or testing the connection.
- Adopt the appropriate contact properties.
- Check if symmetry conditions can be used and if they are beneficial.
- Develop the FE model with required level of detail based on the desired output.
- Select the appropriate type and size of elements for the floor components, especially the connectors.
- Conduct convergence studies on the element types and sizes, and the connector properties to finalise the element types and size, and the connector properties as input. Also note that a more refined FE mesh leads to a closer agreement to the fully converged result. In reality, a fully converged result is not achievable, and users should apply judgement to determine if the accuracy of the model results are acceptable.
- Verify the results with the test data.

Figure 13 shows an example of a detailed FE model of a T-beam floor with I-joists and sheathing. (Note that such a detailed model is usually not needed and is only shown here for illustration purposes.) The model was built in the commercial software Abaqus 2020 (Dassault Systèmes, 2019). The figure shows I-joists around the boundaries of the floor as well as sheathing elements on top of the I-joists. For the purpose of illustration, some sheathing elements are not shown. The green checks in Figure 13 represent connector elements along the edges and within the sheathing elements. The four side I-joists bear on supports; the internal I-joists are supported at their ends by the end joists. Pressure is applied to the top surface of the sheathing. Besides input properties of the materials, material orientation, and behaviour of the connectors in the different directions, the contacts between elements need to be precisely defined. In a model like the one shown in Figure 13, contact and contact surfaces between the following have to be defined:

- Joists that are oriented perpendicular to each other;
- Joist surfaces and adjacent sheathing surfaces; and
- Edge surfaces of sheathing elements and adjacent sheathing elements.

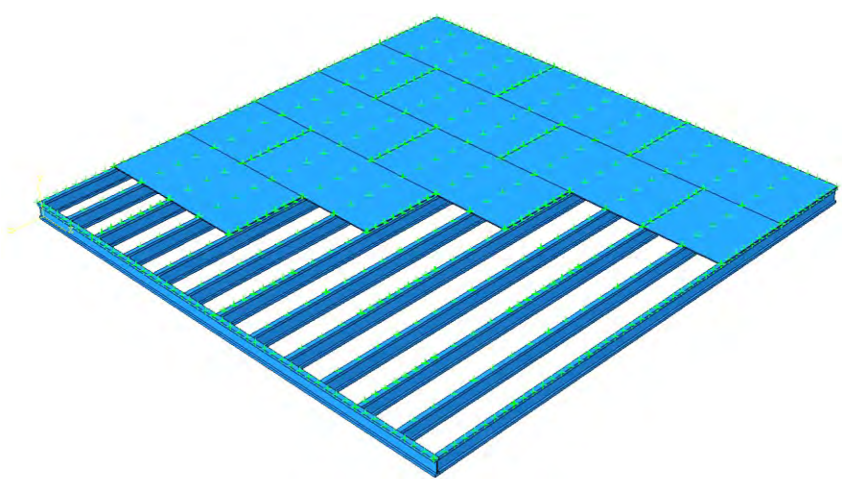

**Figure 13. A T-beam FE floor model with I-joists and sheathing (some sheathing elements are not shown)**

After creating and determining the response of the FE model to applied loads, various types of information can be extracted from FE model output. Figure 14 shows the displacement field of the modelled floor; for illustration purposes, only half of the floor is shown. Figure 15 shows the first three natural vibrational modes of the modelled floor. Other possible results can include stresses and strain as well as connector forces and displacements.

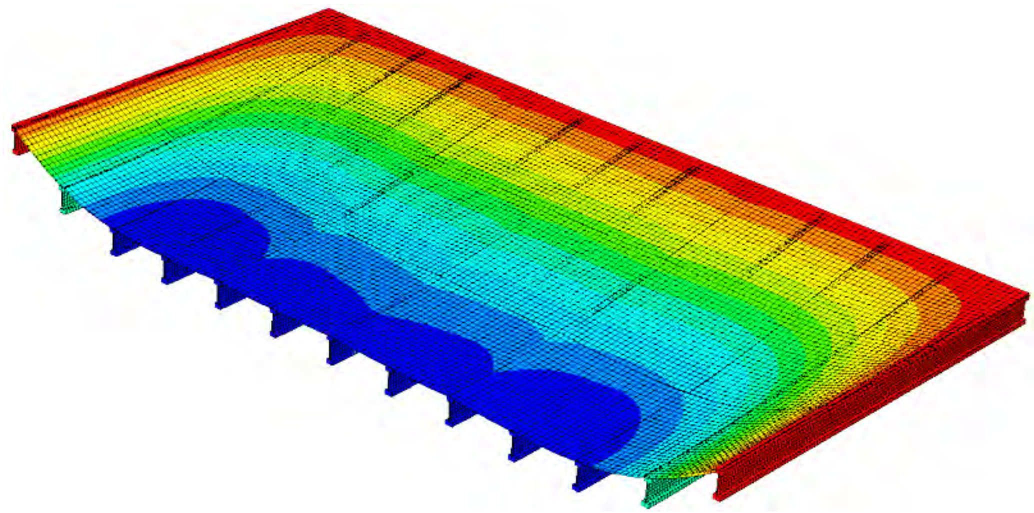

**Figure 14. Displacement field of modelled floor under uniform surface pressure: Only half of the floor is displayed, and deflection is amplified for illustration purposes**

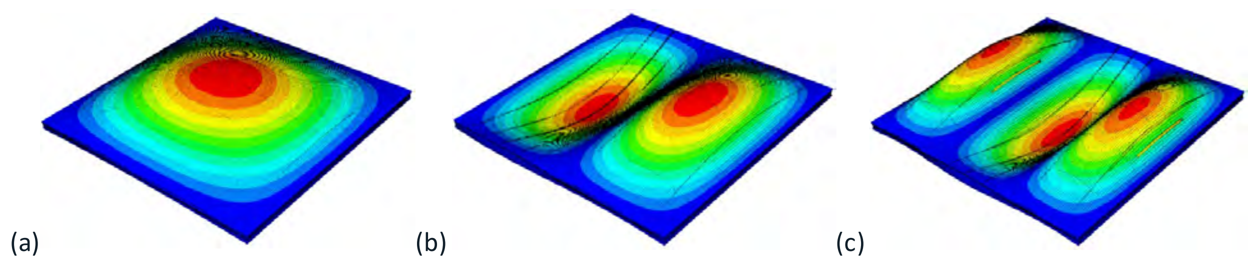


**Figure 15. Vibration modes of modelled floor: (a) first; (b) second; and (c) third**

### 6.1.3 Mass Timber and Composite Systems

With the development of new engineered wood products, especially the mass timber products, more options have become available for floors and roofs. MTPs that have been used in floors and roofs include cross-laminated timber (CLT), glued laminated timber (GLT, or Glulam), nail-laminated timber (NLT), dowel-laminated timber (DLT), LVL, and LSL, among others (Figure 16).

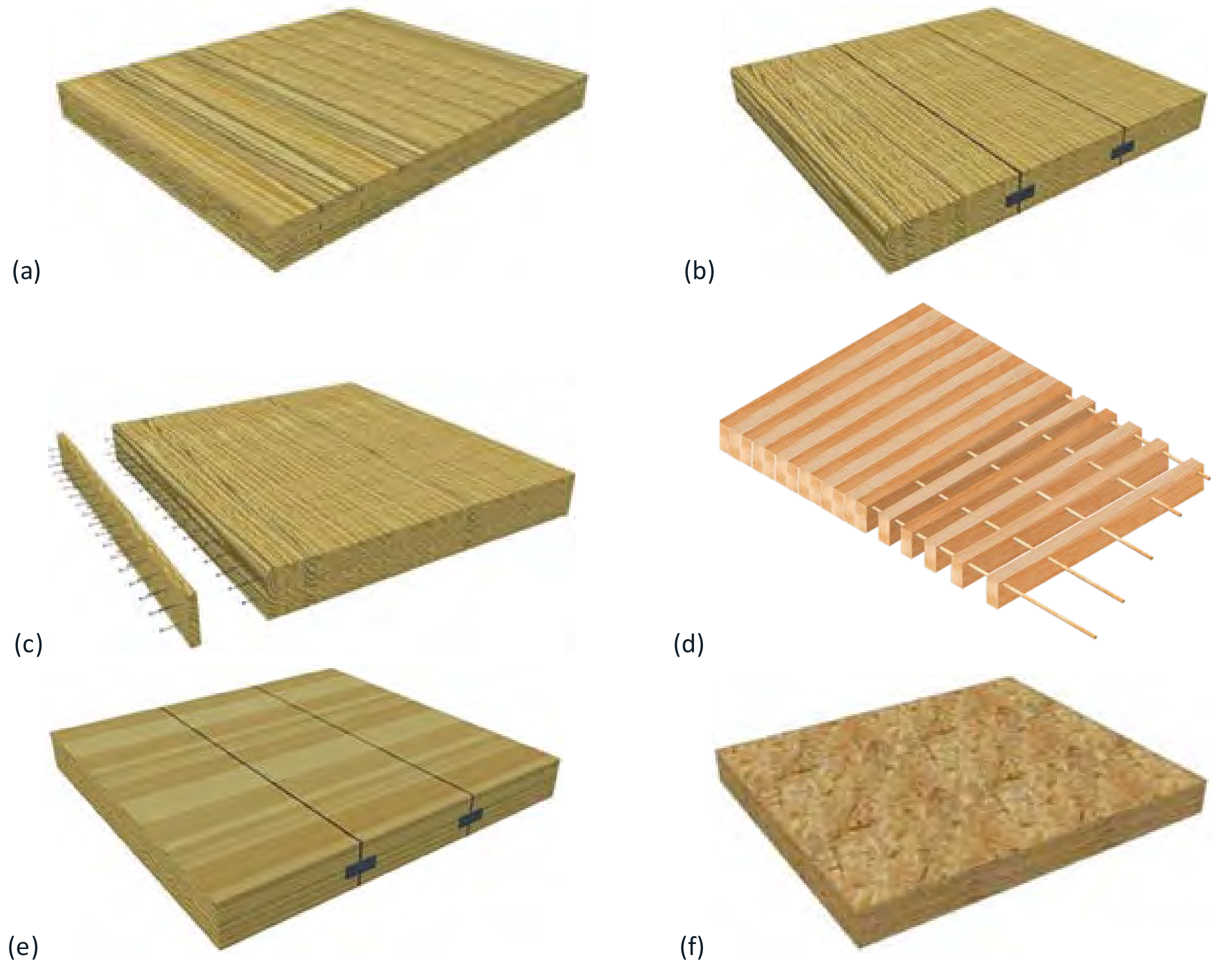


**Figure 16. Mass timber floors (Jackson et al., 2017): (a) CLT; (b) Glulam; (c) NLT; (d) DLT; (e) LVL; and (f) LSL**

MTPs can be used in floors with decking (hardwood, ceramic, floating, carpet, etc.) alone or with a concrete topping 50 to 125 mm thick plus decking. Mass timber floors with a concrete topping are more common because they are more cost-effective, and the focus of this section is on TCC systems (Figure 17). However, the analytical models and numerical modelling methods can be easily applied to mass timber systems with flooring alone by replacing the properties of concrete with those of the flooring materials. Alternatively, the mass timber floors and roofs can be conservatively analysed using the traditional beam theory without taking into account composite actions.

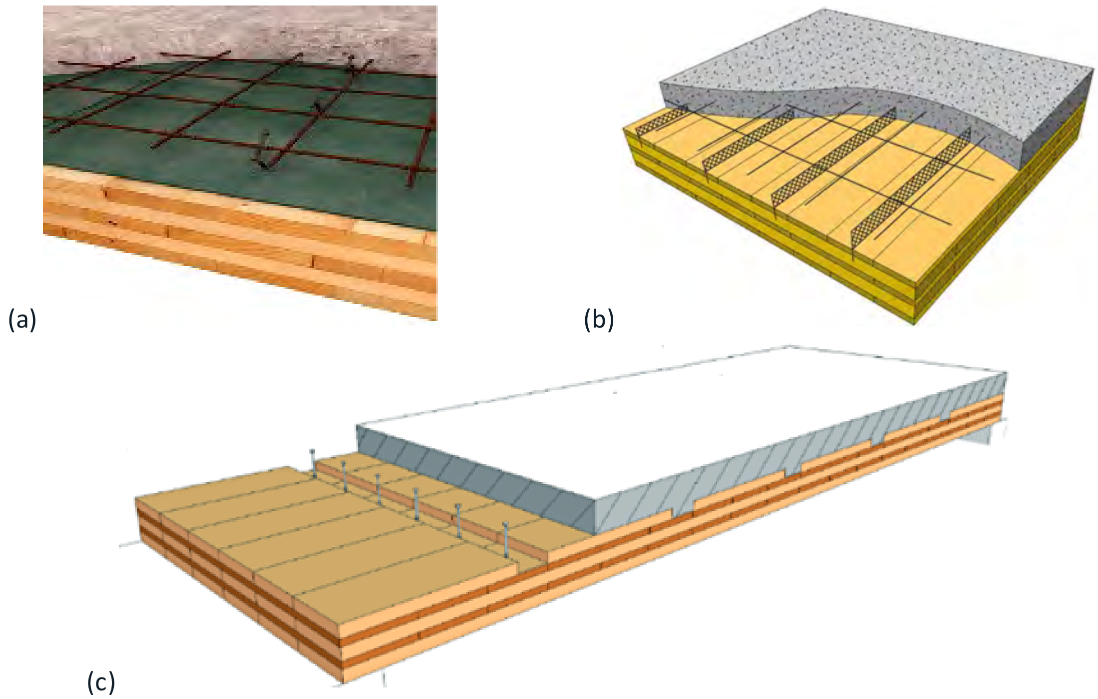


**Figure 17. Mass TCC floor system: (a) dowel-type mechanical connectors (Rothoblaas, 2021); (b) HBV mesh (Setragian & Kusuma, 2018); and (c) notched connection (Courtesy of the University of Melbourne)**

#### *6.1.3.1 Behaviour and Mechanism*

TCC is a timber-based hybrid system in which mass timber beams (e.g., glulam), MTPs (e.g., CLT, DLT, NLT, massive plywood panel, etc.), or structural composite lumber (SCL, e.g., oriented strand lumber, LSL, LVL, etc.) are connected to a reinforced concrete slab with mechanical connection. There may be a gap between the timber and concrete because of soft insulation layers or rigid timber planks. The majority of the timber-concrete shear connections can be classified into the following categories:

a) **Dowel-type fasteners**: Dowel-type fasteners include nails, bolts, dowels, wood screws, coach/lag screws, steel rebars, steel rebars with hooks, self-tapping screws (STSs), and shear stud connectors with crampons (Cuerrier-Auclair, 2020; Dias et al., 2018; Yeoh, Fragiacomo, De Franceschi, & Heng Boon, 2011). Dowel-type fasteners are the most common connection systems used for TCC system because of its high ductility.
b) **Longitudinal connectors**: The types of longitudinal connectors are one-sided truss plates; nail plates bent at 90°; double-sided nail plates; perforated steel plates glued to timber; and steel mesh plates glued to timber (HBV mesh). The HBV (Holz–Beton–Verbund) mesh has the advantage of depending less on the properties of the wood and has a high stiffness (Gerber, 2016; Hong, 2017). Longitudinal connectors have the advantage of limiting local stresses; this increases the potential stiffness and strength of the shear connector because there is less deformation with the wood. Longitudinal connectors can be continuous along the beam, if required.
c) **Notched connections**: Notches are cut directly into the timber beam or slab, and the concrete fills the notches upon casting, creating a tight-fitting connection, with the concrete bearing directly on the timber in the parallel-to-grain direction. These connections are recommended for their high strength

and stiffness, but they are often governed by brittle failure modes. To prevent brittle failure and uplift of the concrete, a dowel-type fastener (e.g., lag/coach screws or STSs) may be needed at each notch.

d) **Glued connections**: Glued connections in TCC are simple and convenient solutions that provide almost full composite action. The major disadvantages are the brittle behaviour, sensitivity to hydrothermal and temperature changes, and uncertainty under long-term loading. The moisture content of wood and freshly poured concrete also strongly influences the performance of the glue, and detailed inspection of the effectiveness of this connection is necessary (Loulou, 2013; Negrão, et al., 2010; Pham, 2007).

For illustration purpose, a longitudinal section of a TCC system with dowel, notched, or proprietary connections is shown in Figure 18. These TCC systems are efficient in the construction of modern multi-storey mass timber buildings because of their higher strength and stiffness-to-weight ratios, larger span-to-total depth ratios, higher in-plane rigidity, and acoustic, thermal, and fire performances when compared with the conventional timber-only system (Ceccotti, 2002; Dias et al., 2016, 2018; Yeoh, Fragiacomo, De Franceschi & Heng Boon, 2011). In this section, the focus is on TCC systems with dowel-type fasteners or notched connections because longitudinal connectors are mostly proprietary products and glued connections are uncommon.

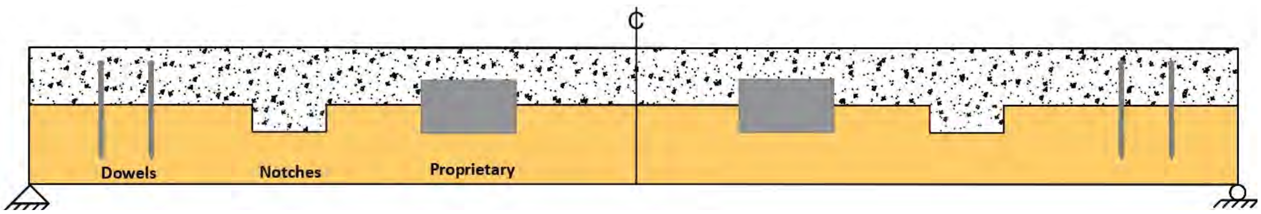


**Figure 18. Longitudinal section of a TCC system with dowel, notched, and proprietary connectors**

#### 6.1.3.1.1 Systems with Dowel-type Fasteners

The mechanical shear connectors connect the concrete slab to the timber element, which allows for partial shear transfer and therefore partial composite behaviour of the system. The connectors must be strong, stiff, and ductile enough to transfer the shear force between the timber and concrete components in order to provide an adequate partial composite action. The structural efficiency of this composite system largely depends on the performance of the shear connections. By avoiding failures in the connections, it is possible to maximise the load-carrying capacity and increase the effective bending stiffness of the system (Deam et al., 2008; Dias et al., 2007, 2010, 2018).

Allowable floor spans for TCC systems are often governed by serviceability performance requirements, such as deflection and vibration, which depend directly on effective bending stiffness. A layer sandwiched between the concrete slab and MTP or SCL is often insulation used to enhance acoustic or thermal performance of a TCC system. This interlayer negatively affects the strength and stiffness of the connection (Mirdad & Chui, 2019). Due to the flexibility of the mechanical shear connectors, relative slip between the bottom fibre of concrete and the top fibre of timber will occur. This violates the Euler-Bernoulli beam theory assumption that ’plane sections remain plane’. Therefore, the transformed section method, from the conventional principle of structural analysis for determining composite bending stiffness and stress distribution, widely used for reinforced concrete, cannot be used in the design of TCC beams. Also, in such a partial composite system, the interlayer slip leads to two neutral axes (see Figure 19).

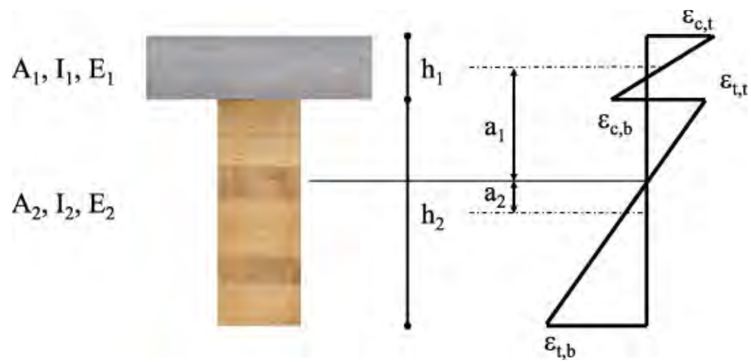


**Figure 19. Approximation of a TCC system as a strain distribution with two neutral axes based on the Gamma method (Hadigheh et al., 2021)**

The most common dowel-type fastener used in modern mass timber construction, including composite floor systems, is STS (Dietsch & Brandner, 2015). Fully threaded screws with wide countersunk heads are efficient in TCC systems, as the full thread provides a better load transfer in timber and better bonding with concrete, while the countersunk head provides pull-out resistance in concrete (Mirdad & Chui, 2019). Besides, several screws with cylindrical countersunk heads (ETA-Danmark, 2019) or hexagonal heads (ETA-Danmark, 2018) have been developed specifically for TCC systems. Many experimental and theoretical studies of STS concrete-to-timber connections have concluded that the strength and stiffness of an STS connection increases substantially if the screw is installed at an angle (e.g., 45° or 30°) to the surface of the timber member, instead of the normal perpendicular (90°) to the surface (Gerber, 2016; Kavaliauskas et al., 2007; Marchi et al., 2017). For concrete-to-timber STS connections, Mirdad and Chui (2019) experimentally and analytically (2020a; 2020b) proved that there is a significant increase in strength and stiffness of the connection when the screws are inserted at a 30° angle to the timber member surface compared to a 45° angle.

Figure 20 shows a few potential failure modes of TCC with dowel-type fasteners. They include (a) a timber fracture in the tension zone; (b) withdrawal of fasteners when there is thick insulation; (c) a rolling shear in CLT; and (d) cracking of concrete. The behaviour of joints with inclined mechanical connectors is more complex because load transfer involves bending of the fasteners and embedment of the wood as well as the withdrawal resistance of the fasteners and the friction between the elements (see Figure 21).

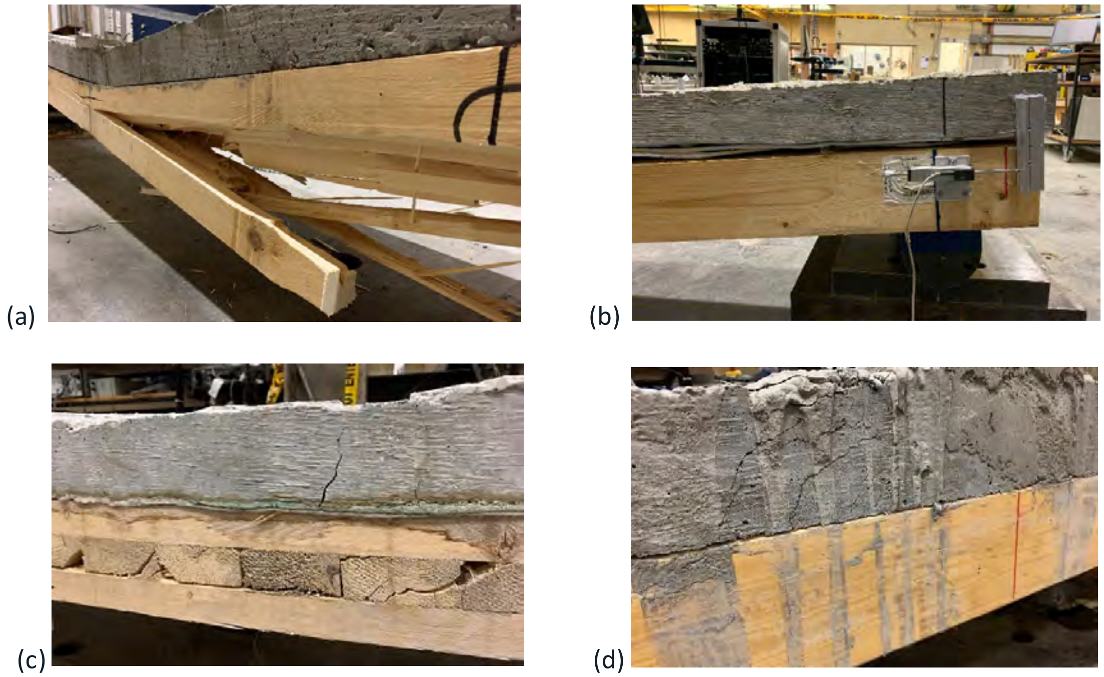


**Figure 20. TCC system failure modes: (a) timber fracture in the bending zone; (b) withdrawal of fasteners where there is thick insulation; (c) rolling shear in a CLT specimen; and (d) cracking of concrete**

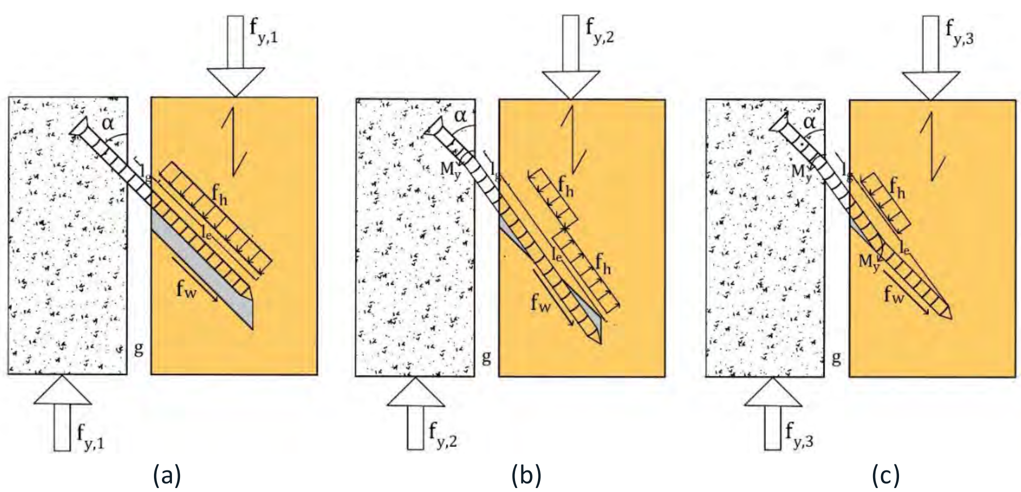


**Figure 21. Stress distributions in concrete-to-timber connections with an inclined dowel-type fastener: (a) embedment of fastener; (b) embedment of fastener plus single plastic hinge; and (c) embedment of fastener plus double plastic hinge**

#### 6.1.3.1.2 Systems with Notched Connections

Notched connections in TCC floors are mechanical connections that provide shear resistance from the compression between timber and concrete. Notched connections are usually made by cutting grooves in the timber and filling them with concrete. The grooves can also be made by gluing timber blocks on the top of timber panels or beams (Dias et al., 2018). Grooving the timber element to distribute the shear force on a larger surface increases the stiffness and the strength of the shear connection. Notched connections in two types of TCC floor systems are shown in Figure 22.

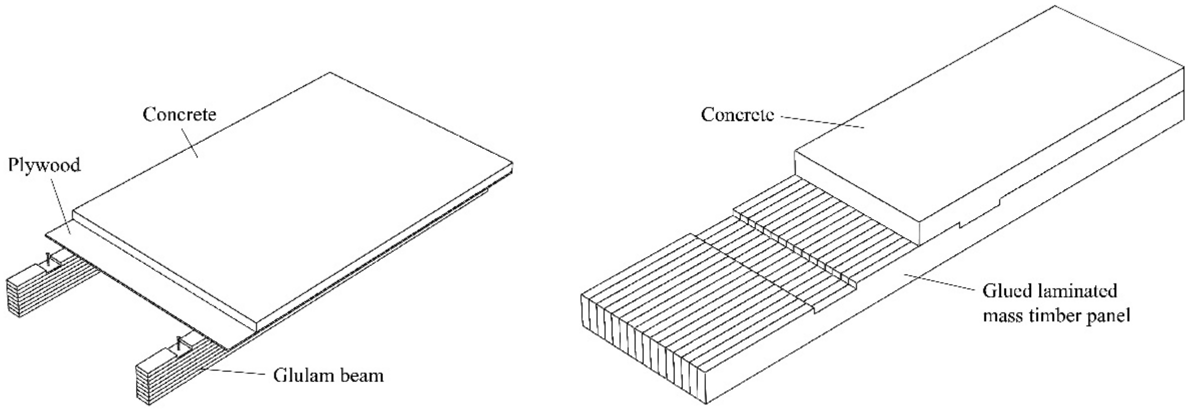


(a) Ribbed ceiling system

(b) Flat slab system

**Figure 22. Notched connections in two types of TCC floors (Zhang et al., 2020)**

Compared with steel fasteners and adhesives, notched connections are cost-effective and labour-saving when constructing TCC floor systems. Notches can be rectangular (Zhang et al., 2020), triangular (Yeoh, Fragiacomo, De Franceschi & Buchanan, 2011; Yeoh, Fragiacomo & Deam, 2011), trapezoidal (Gutkowski et al., 2008), and round (Cuerrier-Auclair et al., 2016a) shapes. The notches are cut in certain sizes and spaced regularly along the composite floor. The spacing of the notched connections in the composite floor is usually larger than that for steel fasteners such as STS. One of the most important characteristics of the TCC floors with notched connections is that timber and concrete layers are discretely connected; thus, the shear forces are only transmitted at these discrete locations. However, notched connections can also be cut as a continuous notched curve (Boccadoro & Frangi, 2014) or continuous minor notches (Müller & Frangi, 2018). In the case of micro notches, the notches act as friction that bonds timber and concrete together (Müller & Frangi, 2018).

The notched connections are usually very stiff and effective at resisting shear forces generated at the interface of timber and concrete, but they have little or no capacity to prevent the timber and concrete from separating vertically. Other reinforcing techniques are therefore often used in the notches to prevent the concrete from uplifting. The existing reinforcing techniques include STSs (Zhang et al., 2020), coach screws or lag screws (Jiang & Crocetti, 2019; Yeoh, Fragiacomo, De Franceschi & Buchanan, 2011; Yeoh, Fragiacomo & Deam, 2011), post-tensioned dowel connectors (Gutkowski et al., 2008; LeBorgne & Gutkowski, 2010), and end-to-end rods (Boccadoro et al., 2017) (see Figure 23).

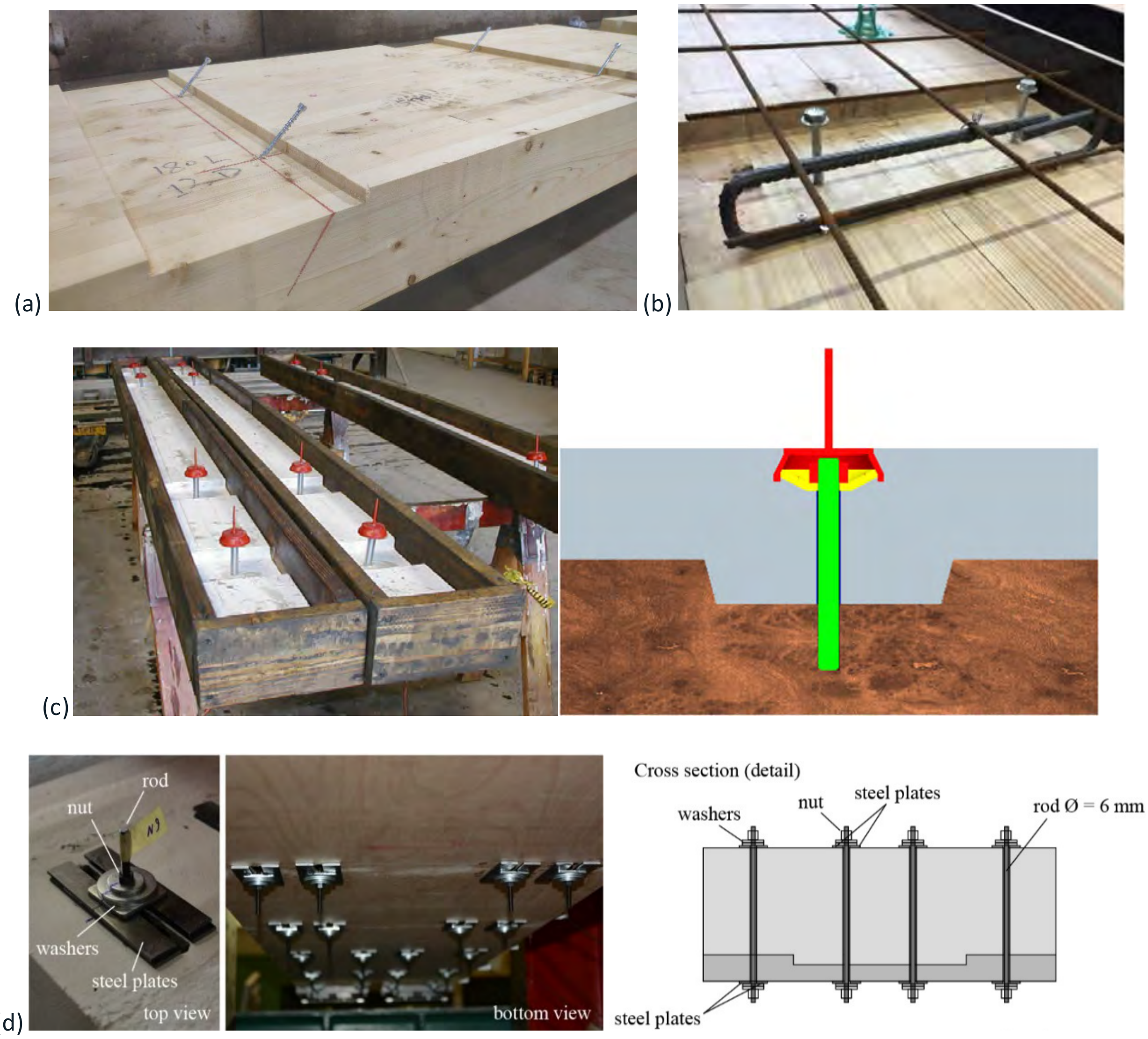


**Figure 23. Reinforcing techniques for TCC floors with notches: (a) STSs; (b) lag screws and stirrup (Jiang & Crocetti, 2019); (c) post-tensioned dowels (LeBorgne & Gutkowski, 2010); and (d) end-to-end rods (Boccadoro et al., 2017)**

The STSs and lag screws are cost-effective and relatively easy to install. The post-tensioned dowels and end-to-end rods facilitate deconstruction because the post-tension can be removed and removing the concrete from the timber is easier. These connections are more efficient in restricting gap openings but are expensive and less practical during installation. Irrespective of which type of steel fastener is used, when the number and size of steel fasteners are small compared with the configuration of the notch, the steel fasteners only contribute to the axial load-carrying capacity with negligible shear resistance.

Irrespective of the notch shape, the stress concentration effect always exists at the notched corners. Thus, cracking of concrete under the shear load can be expected in the serviceability limit state. If the load keeps increasing, the notched connection can fail in one of the following ways: (a) longitudinal shear failure in the timber in front of the notch; (b) longitudinal compression failure in the timber in front of the notch; (c) shear failure in the concrete as a result of shear crack propagation; and (d) compression failure in the concrete (Schönborn et al., 2011; see Figure 24).

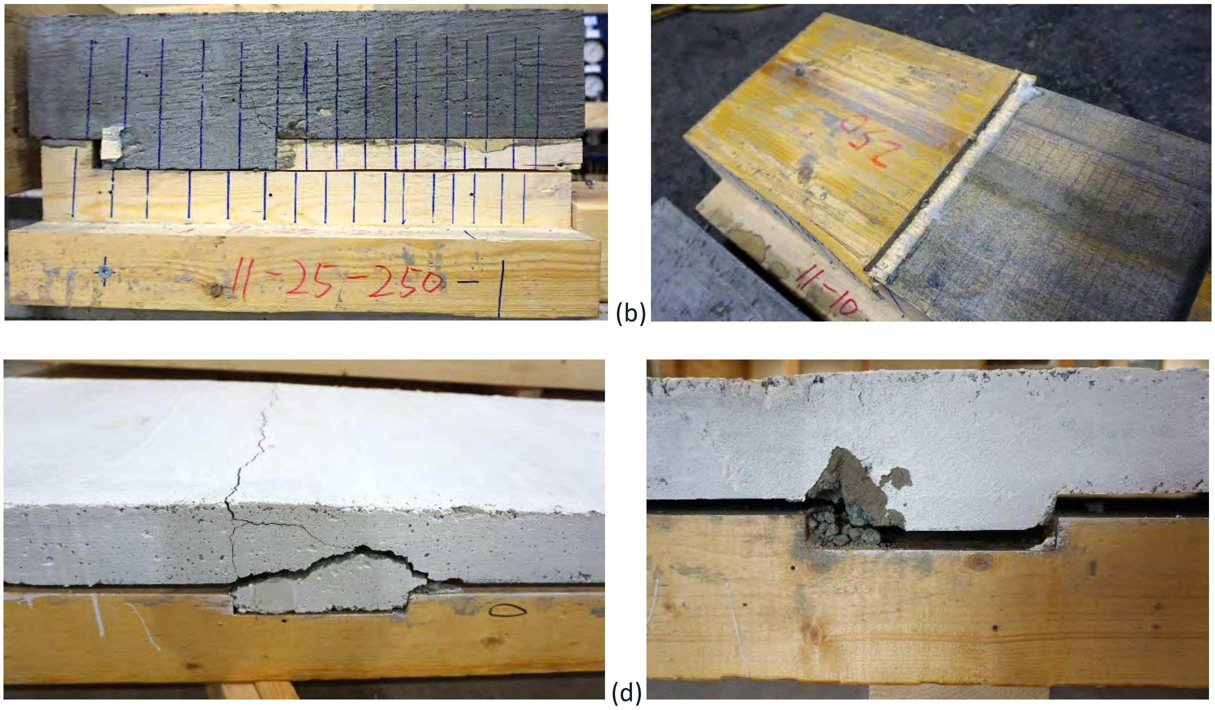


**Figure 24. Typical failure modes of notched connections: (a) longitudinal shear failure in the timber in front of the notch; (b) longitudinal compression failure in the timber in front of the notch; (c) shear failure in the concrete because of shear crack propagation; and (d) compression failure in the concrete**

All these failure modes, except compression failure in timber, are brittle and should be avoided. Shear failure of timber can be prevented by spacing the notched connections far apart. Compression failure of concrete can be prevented by choosing a higher-grade concrete and controlling material quality during concrete casting. Shear failure of concrete can often be prevented by providing sufficient notch width—at least 150 mm, according to Dias et al. (2018)—and adding additional steel fasteners to the notch.

Failure of a composite floor under an external load does not necessarily happen at the notched connections. If the notched connections are overly reinforced, or the connections are too flexible to provide enough composite action, the timber and concrete components can fail under bending before the notched connection failure. The components of composite floors with notched connections have slightly different failure characteristics: bending failure of timber often happens around the notched regions where the cross-section of the timber is reduced, as shown in Figure 25(a); or shear failure of the concrete component can be triggered by the shear cracks developed around notches, as shown in Figure 25(b). The ideal failure pattern of composite floors is the notched connection ductile failure, that is, timber compression failure at the contact area of the notch, followed by failure of the generally brittle components (timber or concrete).

(a)  (b) 

**Figure 25. Two typical component failure modes of TCC floors with notches: (a) bending failure of timber underneath the notch; and (b) shear failure of concrete**

### *6.1.3.2 Analytical Methods*

Mass timber and TCC floors are usually analysed as one-way action systems although they can behave as two-way action systems. This is because experimentally supported analytical models for the two-way action of this composite system have not been well developed. The focus of this section is the one-way action systems. Two-way action systems can be analysed using numerical methods. The application of continuous bond models and discrete bond models to TCC floor systems are discussed in Section 6.1.3.2.1 and Section 6.1.3.2.2, respectively.

#### 6.1.3.2.1 Continuous Bond Models

As discussed in Section 6.1.2.2.1, the continuous bond models such as Gamma method, Newmark's composite beam model (Newmark et al., 1951), and the frozen shear force model (Van der Linden, 1999) are suitable for composite systems with continuous connections or uniformly distributed closely spaced connections, for example, TCC floor systems with longitudinal connectors or dowel-type fasteners. Grosse and colleagues (Grosse, Hartnack, Lehmann & Rautenstrauch, 2003; Grosse, Hartnack & Rautenstrauch, 2003) suggested that the distance between discrete connectors should not exceed 3% of the beam span if a continuous bond is to be assumed. Because of its simplicity and efficiency, this category of models can also be applied to TCC floor systems with discontinuous connections, for example, TCC floor systems with notched connections, if certain simplifications are applied.

The Gamma method presented in Eurocode 5 (European Committee for Standardization, 2004) is the most widely used simplified design method for partial composite systems. In certain conditions, the Gamma method can be safely used to estimate the deflection of floors with discrete connections, especially when the floor is simply supported and has closely spaced connections. The Gamma method should be used with caution to estimate the stress distribution in composite floors with discrete connections as it can underestimate stresses in the floors. The Gamma method for LWFFs was described in detail in Section 6.1.2.2.1.2; precautions for applying the Gamma method to TCC systems are summarised below.

(1) Effective Bending Stiffness, $(EI)_{eff}$

The effective bending stiffness, $(EI)_{eff}$, of TCC floor systems based on the Gamma method can be calculated using Equation 1, with the effective width, effective connector spacing, modulus of elasticity of concrete, and concrete cracking taken into account, as discussed below. Figure 26 shows a longitudinal section, a cross-section with timber beam, and a cross-section with MTP/SCL of a TCC system with dowel-type fasteners. The primary geometric and material parameters are defined as follows: $h$, depth; $A$, cross-sectional area; $I$, moment of inertia; $E$, modulus of elasticity; $L$, span; and $b$, width of the cross-section of the concrete slab, insulation, and timber with the subscript $c$, $in$, and $t$, respectively.

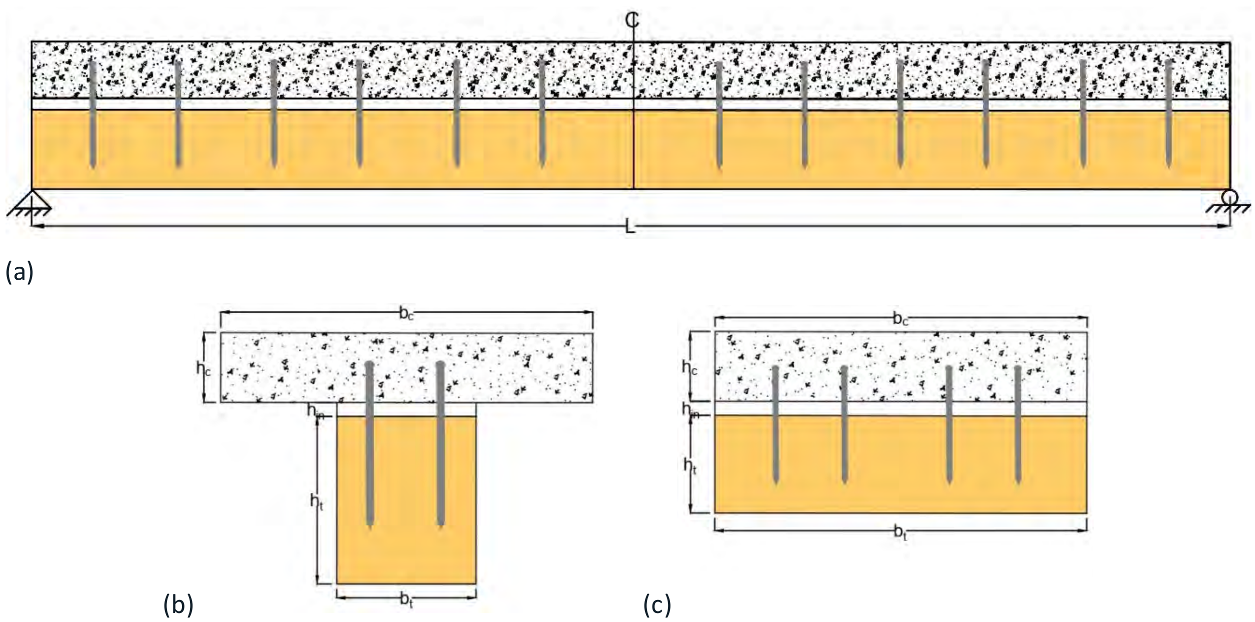


**Figure 26. TCC system with dowel-type mechanical fasteners: (a) longitudinal section; (b) cross-section with timber beam; and (c) cross-section with MTP/SCL**

(a) Effective Width, $b_c$

In the case of TCC with MTP at the bottom, the effective width, $b_c$, of the concrete slab equals the width of the MTP and needs to be designed to a standard unit width. In the case of TCC with timber beams, the effective width of the concrete slab may be based on the Canadian steel design standard CSA S16-14 (CSA Group, 2014a). This is considered to be conservative because of the lower composite action in TCC compared to steel-concrete composite. The effective width of the concrete slab is calculated, based on Cuerrier-Auclair (2020), using Equations 16 and 17 as follows:

$$\boldsymbol{b_{c,e}} = \mathbf{min}(\mathbf{0.1}\boldsymbol{L};\ \mathbf{12}\boldsymbol{h_c};\ \boldsymbol{b}_{\mathbf{e}}) \qquad [16]$$

$$\boldsymbol{b_{c,i}} = \mathbf{min}(\mathbf{0.25}\boldsymbol{L};\ \mathbf{24}\boldsymbol{h_c};\ \boldsymbol{b}_{\mathbf{m}}) \qquad [17]$$

where

| | | |
|---|---|---|
| $b_{c,e}$ | = | Effective width of an edge beam in mm |
| $b_{c,i}$ | = | Effective width of an internal beam in mm |
| $L$ | = | Span of system in mm |
| $h_c$ | = | Thickness of the concrete slab in mm |
| $b_e$ | = | The sum of the spacing between edge beam and internal beam, and half width of the edge beam in mm |
| $b_m$ | = | Actual spacing of the middle beams in mm |

The effective widths of concrete slabs in TCC with timber beams is illustrated in Figure 27.

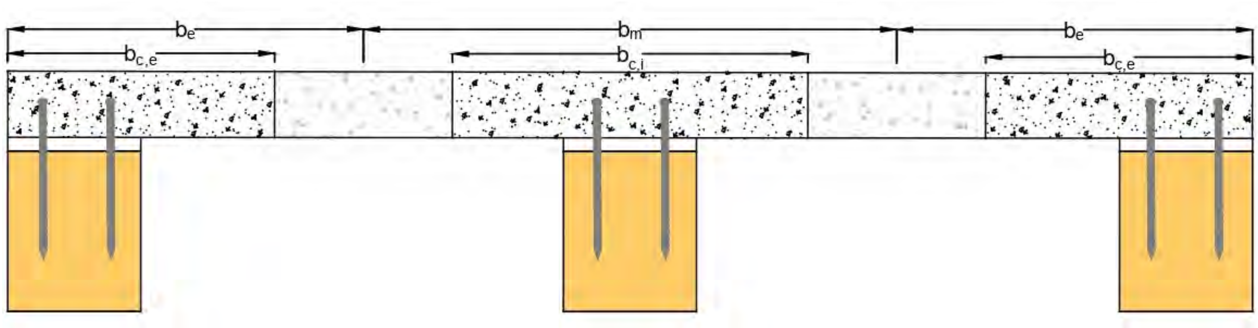


**Figure 27. Effective width of concrete slab in TCC with timber beams**

(b) Effective Connector Spacing, $\boldsymbol{s_{eff}}$

For uniformly distributed connectors, the effective spacing is considered to be the actual spacing. For nonuniformly distributed connectors, typical for a single-span TCC floor, the spacing is smaller at the end quarters of the single-span beam and larger in the middle. The effective spacing, $s_{eff}$, of nonuniformly distributed connectors can be calculated as

$$\boldsymbol{s_{eff} = 0.75 s_{min} + 0.25 s_{max}} \quad [18]$$

where

| | | |
|---|---|---|
| $s_{min}$ | = | Minimum connector spacing, e.g., at the ends, in mm |
| $s_{max}$ | = | Maximum connector spacing, e.g., in the middle of the beam, in mm |

(c) Modulus of Elasticity of Concrete, $\boldsymbol{E_c}$

The modulus of elasticity of concrete, $E_c$, is an input parameter for the Gamma method. It can be determined according to tests or standards. The following is an example for determining $E_c$ in accordance with the Canadian concrete design standard, CSA-A23.3-14 (CSA Group, 2014b). The modulus of elasticity of normal density concrete with compressive strength ($f_c'$) between 20 and 40 MPa can be calculated as

$$\boldsymbol{E_c = 4500\sqrt{f_c'}} \quad [19]$$

For concrete density ($\rho_c$) between 1500 and 2500 kg/m$^3$, the modulus of elasticity according to CSA-A23.3-14 (CSA Group, 2014b) can be calculated as

$$\boldsymbol{E_c = (3300\sqrt{f_c'} + 6900)\left(\frac{\rho_c}{2300}\right)^{1.5}} \quad [20]$$

(d) Concrete Cracking

Concrete cracks that develop during curing as a result of shrinkage are usually controlled with the minimum reinforcement specified in codes. In the case of CSA-A23.3-14 (CSA Group, 2014b), for example, the minimum reinforcement is 0.2% of the gross area of concrete. Cracks can also appear after the load is applied, with the concrete starting to crack and the neutral axis moving towards the geometric centroid of the remaining cross-section, where the cracked portion is neglected, resulting in a decrease in the bending stiffness of the system and an increase in deflection (Mirdad, 2020). Cracking of concrete in the TCC system is important and should be considered in the design. Cuerrier-Auclair et al. (2016b) present a moment-curvature method to account for the influence of concrete cracking on the load-carrying capacity of a TCC beam. This method is based on a 1D FE analysis of the composite beam where the stiffness parameters of the concrete are updated at each load increment using a secant method by assuming a material law, that is, the stress-strain relationship, for the concrete and the steel reinforcement.

More practical methods to account for the influence of concrete cracking are given in material design standards, for example, CSA A23.3-14 (CSA Group, 2014b) and CSA S16-14 (CSA Group, 2014a). CSA A23.3-14 provides a simple empirical procedure to consider concrete cracking without reducing the concrete area by excluding concrete in tension. For normal weight concrete, the steel standard CSA S16-14 neglects the contribution of the tensile resistance of concrete when calculating the strength and stiffness of steel-concrete composite beams. A similar approach can be used in TCC beam design. According to CSA A23.3-14, the gross moment of inertia ($I_g$) of concrete is permitted in elastic analysis to check ultimate limit state designs. To account for reduced capacity after concrete cracking, a reduction factor of 0.35 is applied to the gross moment of inertia, as shown in Equation 21,

$$\boldsymbol{I_c = 0.35 I_g} \quad [21]$$

where

| | | |
|---|---|---|
| $I_c$ | = | Reduced second moment of inertia of cracked concrete |
| $I_g$ | = | Gross second moment of inertia of concrete |

This factor was conservatively enforced by various standards to account for capacity loss due to concrete cracking. A similar approach to account for concrete cracking can be adopted for TCC systems.

(2) Maximum Stresses and Connection Forces

The maximum normal stresses in a TCC system can be calculated using Equation 2. Figure 28 shows the stress distribution in a TCC system with beams. The shear stress in the wood-based panel or beams can be estimated using Equation 3. The stress limit needs to be checked for timber and concrete resistance.

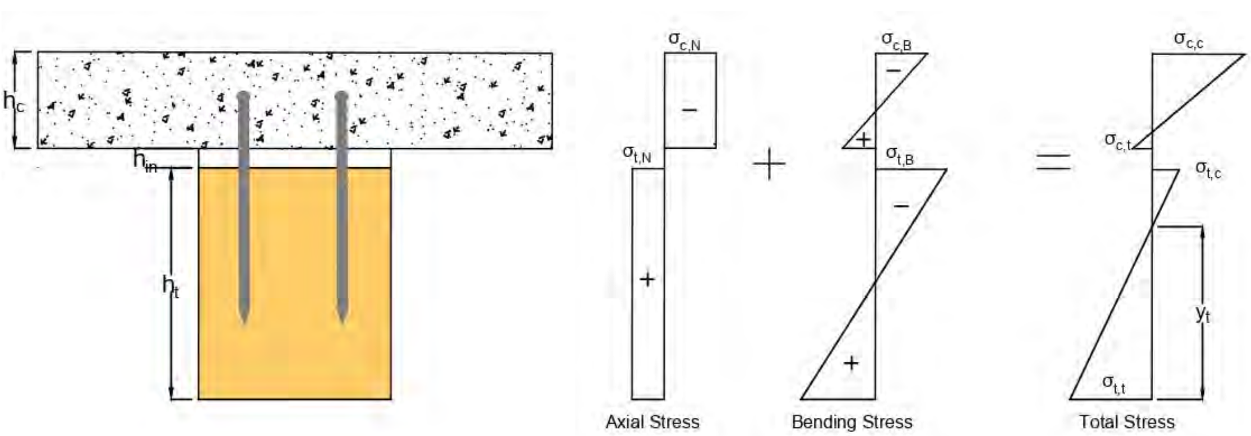


**Figure 28. Stress distributions of TCC system based on Gamma method**

Taking the Canadian concrete standard CSA A23.3-14 (CSA Group, 2014b) as an example, the top extreme fibre stress of concrete in compression must not be greater than its factored compressive strength, as follows:

$$\boldsymbol{\sigma_{c,c} \leq 0.9\phi_c f_c'} \tag{22}$$

where

| | | |
|---|---|---|
| $\sigma_{c,c}$ | = | Concrete compressive stress at the top in N/mm$^2$ |
| $\phi_c$ | = | Resistance factor for concrete |
| $f_c'$ | = | Specified compressive strength of concrete in N/mm$^2$ |

No specific verification needs to be made for the concrete in tension because its contributions are neglected. If the designer wants to minimise the concrete cracking in tension, the bottom extreme fibre stress of concrete in tension can be limited to its factored modulus of rupture, as follows:

$$\boldsymbol{\sigma_{c,t} \leq \phi_c(0.6\lambda\sqrt{f_c'})} \tag{23}$$

where

| | | |
|---|---|---|
| $\sigma_{c,t}$ | = | Concrete tensile stress at bottom in N/mm$^2$ |
| $\lambda$ | = | Modification factor for concrete density according to CSA A23.3-14 (CSA Group, 2014b) |

Based on CSA A23.3-14, the resistance of the concrete needs to be checked to determine whether there is a small tensile stress or full compressive stress in the concrete (CSA Group, 2014b). For the design load, it is necessary to ensure that the concrete has sufficient compressive strength to avoid failure before the connectors fail, that is, that the compressive resistance of the concrete exceeds the sum of shear forces in all the connectors between the zero and the maximum bending moment locations.

The concrete resistance for each possible case is shown in Figure 29 and can be calculated as follows:

Case 1: The neutral axis is in the cross-section, $y_c \leq h_c$, that is, a tensile stress is induced in the bottom portion:

$$\boldsymbol{X_{sum} \leq \alpha_1\beta_1 b_c y_c f_c'} \tag{24}$$

Case 2: The neutral axis is beyond the cross-section, $y_c > h_c$, that is, full compressive stress is induced in the cross-section:

$$\boldsymbol{X_{sum} \leq \alpha_1\beta_1 b_c h_c f_c'} \tag{25}$$

where

| | | |
|---|---|---|
| $h_c$ | = | Concrete thickness in mm |
| $y_c$ | = | Distance of the neutral axis of concrete to the compression edge in mm<br>$= \frac{h_c(\sigma_{c,N} + \sigma_{c,B})}{2\sigma_{c,B}}$<br>with<br>$\sigma_{c,N}$ = compressive stress in concrete induced by axial force in N/mm$^2$<br>$\sigma_{c,B}$ = tensile stress of concrete at bottom in N/mm$^2$ |
| $\alpha_1$ | = | $0.85 - 0.0015 f_c'$ |
| $\beta_1$ | = | $0.97 - 0.0025 f_c'$ |

$b_c$ = Width of concrete in mm
$f_c'$ = Compressive strength of concrete in N/mm$^2$
$X_{sum}$ = Sum of shear forces in all the connectors between the zero and the maximum bending moment locations, in N

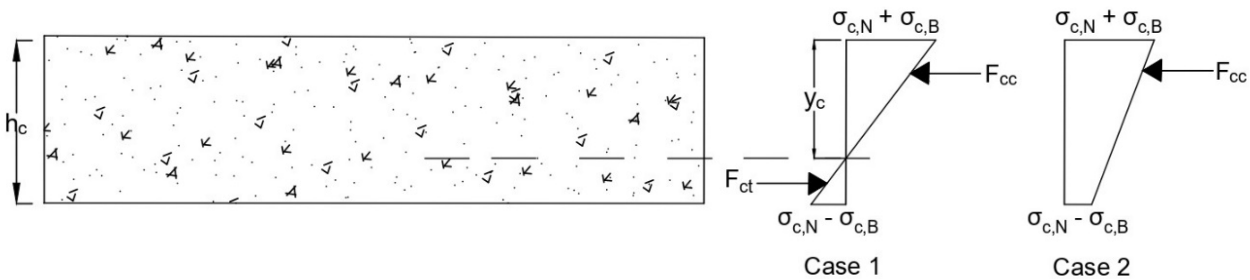


**Figure 29. Stress distributions in concrete**

The shear load on a connector can be determined using Equation 4. It should be smaller than the yield capacity of the connector.

(3) Deflection

For mid- to large-span TCC systems, the short- and long-term deflections related to serviceability limit state are usually the most critical principles. The short-term deflection of the TCC system can be estimated using the standard beam equations, for example, Equation 5, with the effective bending stiffness calculated using Equation 1 as input. In the extended service period of the system, long-term behaviour such as creep, mechanosorptive creep, and shrinkage may occur; these will influence the internal forces and stresses on the components.

Shrinkage in concrete induces tensile stress in the concrete slab, which is usually balanced by compression in the timber element. This tensile stress can propagate cracks in concrete, which reduces the deflection due to shrinkage. In the long term, the stress due to shrinkage can be relaxed due to the creep phenomena, which also reduces the deflection due to shrinkage. Accounting for all these phenomena is complex and, to promote this system with a more realistic implication, conservative creep adjustment factors can be applied for the effective long-term modulus of each component by neglecting shrinkage. The long-term deflection due to shrinkage of concrete can be reduced by shoring the TCC system before casting the concrete in the prefabrication or on-site application (Fragiacomo & Lukaszewska, 2015). According to Cuerrier-Auclair (2020), the specified modulus of elasticity of the concrete, $E_{c,LT}$, modulus of elasticity of timber, $E_{t,LT}$, and stiffness of the shear connectors, $k_{LT}$, may be multiplied by the creep adjustment factor for long-term load duration for both serviceability and ultimate limit states, as follows:

$$\boldsymbol{E_{c,LT} = 0.35E_c} \quad [26]$$

$$\boldsymbol{E_{t,LT} = 0.5E_t} \quad [27]$$

$$\boldsymbol{k_{LT} = 0.25k} \quad [28]$$

In the case of a soft insulation and thin timber planks, the bending stiffness, $E_{in} I_{in}$, is small compared with those of concrete and timber and can be ignored in the design.

(4) Vibration

TCC floors should be evaluated to prevent objectionable vibrations. According to Hu et al. (2016), the vibration-controlled span of a TCC floor can be directly calculated using Equation 29:

$$\boldsymbol{L \leq 0.329 \frac{((EI)_{eff}^{1m})^{0.264}}{(m_a^{1m})^{0.207}}} \qquad [29]$$

where

$(EI)_{eff}^{1m}$ = Effective bending stiffness of a 1 m wide strip composite beam in N·m$^2$

$m_a^{1m}$ = Mass per unit length of a 1 m wide strip of TCC beam in kg/m

(5) Limitations of Gamma method for TCC systems

This simplified method is particularly accurate for predicting the structural performance of the composite beams in which all materials remain linear-elastic (Yeoh, Fragiacomo, De Franceschi, & Heng Boon, 2011). However, there are some limitations in the application:

- The shear forces between timber and concrete are assumed to be uniformly transferred, which is valid for continuous connections such as adhesives, continuous HBV plates, and closely spaced STSs. The connections must be uniformly stiff and equally spaced so that the connection stiffness can be smeared along the beam axis. For widely spaced connections, this assumption could lead to unacceptable errors.

- This method assumes a simply supported beam subjected to a sinusoidal distributed load with a deflection also in a sinusoidal shape. For other supporting conditions and load forms, this method may yield predictions that are nonconservative.

- This method is based on the theory of linear elasticity; cracking of concrete and plasticity of connections are therefore not considered. Van der Linden (1999) modified the Gamma method to the frozen shear force model by considering, in part, the ductility of the connection. Once the applied load approaches the elastic limit load, the connectors closest to the support yield first. At this point, the model assumes the entire system has yielded. This approach significantly underestimates the load-carrying capacity of composite systems.

To overcome these limitations, discrete bond models (discussed in Section 6.1.3.2.2) can be suitable alternatives.

### 6.1.3.2.2 Discrete Bond Models

#### *6.1.3.2.2.1 Overview of Discrete Bond Models*

For a composite floor with widely spaced connections, the components are only connected at discrete locations. Using a continuous bond model may lead to unacceptable errors, and discrete bond models should be used instead. The following composite beam models can be used to model the discrete connected composite floors.

(1) Composite Beam Model with Rigid-Perfectly Plastic Connections (Frangi & Fontana, 2003)

In this model, the connections are assumed to be rigid-perfectly plastic. In the elastic stage, the connections are assumed to be rigid and the relative slip between two layers is assumed to be zero. After the ultimate load-carrying capacity of the connection has been reached, the connection will sustain a fixed load without unloading. Since most of the connections cannot be perfectly rigid, this composite beam model tends to overestimate the stiffness of the composite floors under the serviceability limit state and the resistance under the ultimate limit state.

(2) Progressive Yielding Models (Mirdad, Chui & Tomlinson, 2021; Mirdad, Chui, Tomlinson & Chen, 2021; Zhang & Gauvreau, 2015)

This model can predict the structural performance of discrete connected composite beams at the elastic stage and after the connections have yielded. The connections are assumed to be elastic-perfectly plastic, yielding consecutively under the shear load. The model can only be applied to simple support conditions, and the connections in the composite floor must be identical and symmetrically spaced about the mid-span. The progressive yielding method is suitable for the design of different composite floor systems with mechanical connectors.

(3) Release-and-Restore Model (Byfield, 2002; Zhang, Zhang & Chui, 2021)

This composite beam model is built with the release-and-restore method, which is similar to the force method in structural analysis. The connections in the composite floors can be randomly spaced and have different stiffness. The boundary conditions and load forms of the composite beam are not restricted. The composite beam model can be further extended to the post-elastic stage. The release-and-restore method is suitable for the design of different composite floor system with notched connections.

Sections 6.1.3.2.2.2 and 6.1.3.2.2.3, respectively, describe in detail the use of a progressive yielding model to analyse TCC with mechanical connections and a release-and-restore model to analyse TCC with notched connections. The precautions recommended for modelling TCC—effective width, effective connector spacing, modulus of elasticity of concrete, concrete cracking, and long-term deflection—discussed in Section 6.1.3.2.1 also apply to discrete bond models.

###### *6.1.3.2.2.2 Application of Progressive Yielding Method in Analysis TCC with Mechanical Connections*

The progressive yielding model developed by Mirdad (2020) and Mirdad and colleagues (Mirdad, Chui & Tomlinson, 2021; Mirdad, Chui, Tomlinson & Chen, 2021) can, based on superposition and compatibility conditions, predict the load-carrying capacity and effective bending stiffness of TCC floor systems with the following conditions:

- The beam is simply supported in one-way action under uniformly distributed load.
- The cross-section consists of mass timber beams or MTPs at the bottom and a concrete slab at the top, possibly with insulation layers or planks between the timber and the concrete slab.

- The concrete and timber exhibit linear-elastic behaviour and remain in contact with the shear connections at all points along the beam.
- The horizontal load transfer between timber and concrete is entirely by the linear elastic-perfectly plastic mechanical fasteners arranged symmetrically from the mid-span.

According to the superposition method, a simply supported TCC beam under a uniform load can be subdivided into two fictitious subsystems, as shown in Figure 30. For subsystem 1, after releasing the connectors, the fully noncomposite system is analysed under a uniformly applied load equal to the real uniformly applied load. In subsystem 2, the connectors are replaced by a redundant shear force that acts opposite to the slip caused by the subsystem 1. The unknown shear force between concrete and timber is found by applying compatibility conditions when the two subsystems are combined. In Figure 30, a uniform load $w$ is applied over the span $L$. The distance between the connectors is $n_i$ . Based on the superposition and compatibility conditions, the unknown shear forces in $r$ pairs of shear connectors arranged symmetrically about the mid-span can be calculated based on the slips in subsystem 1 and subsystem 2. Here, the index of the outermost connector pair can be referred to as "1", and the index will increase with decrease in connector distance from the mid-span. Similarly, the vertical deflection of TCC at mid-span due to the applied load can be calculated using the superposition method based on subsystem 1 and subsystem 2.

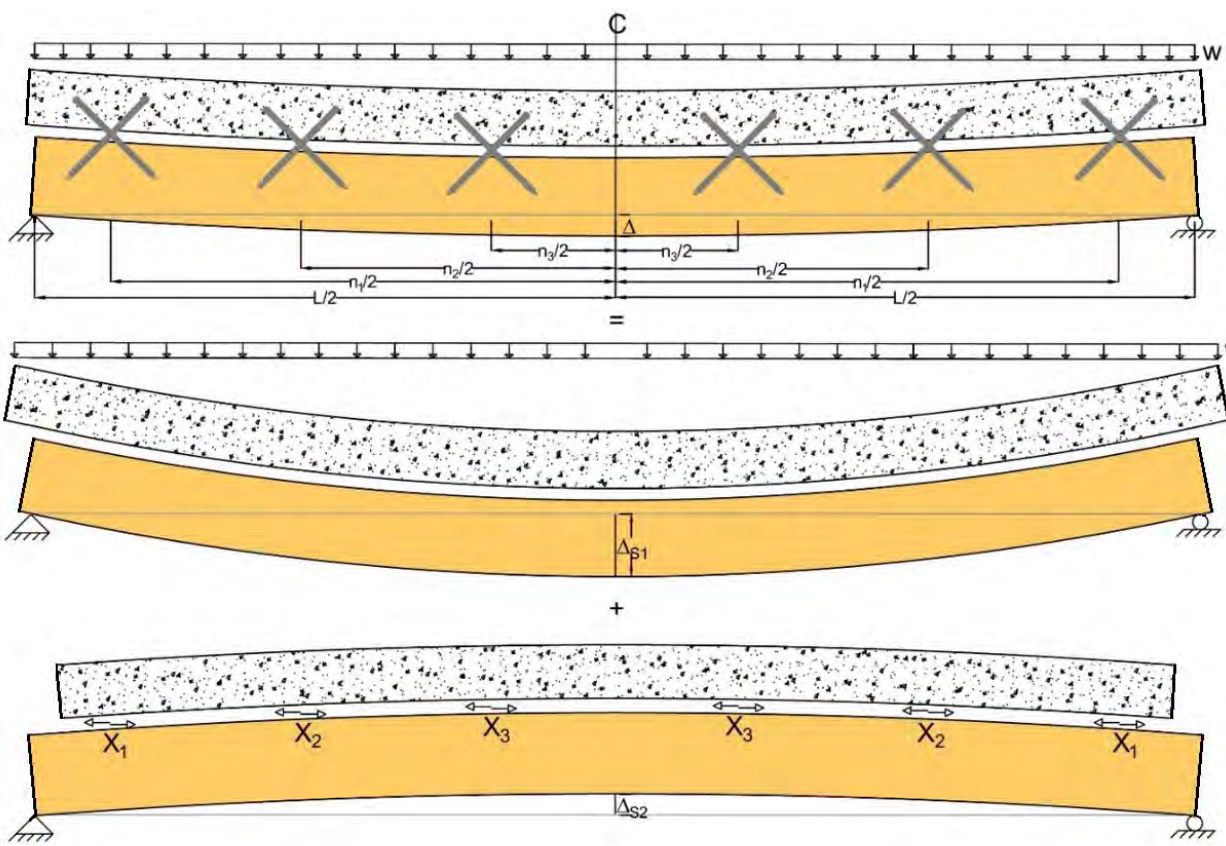


**Figure 30. TCC system response: primary system with uniform load (top); subsystem 1 with fully noncomposite action (middle); and subsystem 2 with unknown shear forces (bottom)**

Under the external applied load, the connectors near the support will reach their yield strength first because of the higher shear forces, given that all connectors are of the same type. Once the connectors near the supports yield, the load will be redistributed to the remaining elastic connectors until they also yield. A yielded connector does not contribute to resisting a load greater than its yield load, which is the basis for an incremental method to calculate the shear force in the concrete-timber connection. As a result, the nonlinear calculation for the connector force can be performed by combining the linear calculation with incremental loading. The incremental loading and deflection can be calculated because of the load redistributions in the system after each connector has yielded.

(1) Effective Bending Stiffness, $(\mathrm{EI})_{eff}$

The effective bending stiffness, $(EI)_{eff}$, of the TCC system can be directly calculated from the closed-form solution shown in Equation 30.

$$(\mathrm{EI})_{eff} = \frac{L^4(E_cI_c+E_tI_t)^2\left[\left[\frac{(E_cA_c+E_tA_t)}{2E_cA_cE_tA_t}+\frac{H^2-h_i^2}{8(E_cI_c+E_tI_t)}\right]\sum_{i=1}^{r} n_i + {}^{1}/_{k}\right]}{L^4(E_cI_c+E_tI_t)\left[\left[\frac{(E_cA_c+E_tA_t)}{2E_cA_cE_tA_t}+\frac{H^2-h_{in}^2}{8(E_cI_c+E_tI_t)}\right]\sum_{i=1}^{r} n_i + {}^{1}/_{k}\right] - 0.032rH(H+h_{in})(2Ln_1-n_1^2)(3L^2n_1-n_1^3)} \quad [30]$$

where

| | | |
|---|---|---|
| $E_c$ | = | Modulus of elasticity of concrete in N/mm$^2$ |
| $E_t$ | = | Modulus of elasticity of timber in N/mm$^2$ |
| $I_c$ | = | Moment of inertia of concrete in mm$^4$ |
| $I_t$ | = | Moment of inertia of timber in mm$^4$ |
| $A_c$ | = | Cross-sectional area of concrete in mm$^2$ |
| $A_t$ | = | Cross-sectional area of timber in mm$^2$ |
| $H$ | = | Height of TCC section including timber, concrete, and insulation gap, in mm |
| $h_{in}$ | = | Thickness of insulation gap in mm |
| $n_i$ | = | Distance of the connector from mid-span in mm |
| $n_1$ | = | Distance of the first connector from mid-span in mm |
| $r$ | = | Number of connector rows from mid-span to the support |
| $k$ | = | Stiffness of the connector obtained from testing or from the analytical model, in N/mm |

For timber-concrete joints with inclined mechanical connectors, for example, STSs, the analytical models developed by Mirdad and Chui (2020a; 2020b) can be used to estimate the stiffness and strength. If the slip modulus ($k_u$) for ultimate limit states calculation is required, it can be assumed as two-thirds of the initial slip modulus (European Committee for Standardization, 2004).

(2) Connector Forces

The effective force of the first outermost connector, $F_{y,eff}$, can be calculated as follows:

$$\boldsymbol{F_{y,eff}} = \boldsymbol{X_1} = \frac{wH(3L^2n_1-n_1^3)}{76.8(E_cI_c+E_tI_t)\left[\left[\frac{(E_cA_c+E_tA_t)}{2E_cA_cE_tA_t}+\frac{H^2-h_{in}^2}{8(E_cI_c+E_tI_t)}\right]\sum_{i=1}^{r} n_i + {}^{1}/_{k}\right]} \quad [31]$$

The sum of shear forces in all the connectors between the mid-span and a support, $X_{sum}$, is equal to the resultant normal force at a given cross-section under applied load $w$. $X_{sum}$ for a given load can be calculated using the closed-form formula shown in Equation 32:

$$\boldsymbol{X_{sum}} = \sum_{i=1}^{r} \boldsymbol{X_i} = \frac{rwH\left(3L^2 n_1 - n_1^3\right)}{120\left(E_c I_c + E_t I_t\right)\left[\left[\frac{\left(E_c A_c + E_t A_t\right)}{2E_c A_c E_t A_t} + \frac{H^2 - h_{in}^2}{8\left(E_c I_c + E_t I_t\right)}\right]\sum_{i=1}^{r} n_i + {}^{1}/_{k}\right]} \qquad [32]$$

This sum of the shear forces, $X_{sum}$, is required to calculate the stresses in the TCC components and the deflection under load, $w$.

(3) Maximum Stresses in Timber and Concrete

The stresses in concrete and timber under the applied load (e.g., concrete compression, timber tension, and/or shear) should be checked to determine if either fails before the yielding of the first outermost connectors. As illustrated in Figures 31 and 32, the total stress at each position in a cross-section can be calculated by summing the axial stress from subsystem 1 due to bending and the axial stress from subsystem 2 due to the normal force and bending.

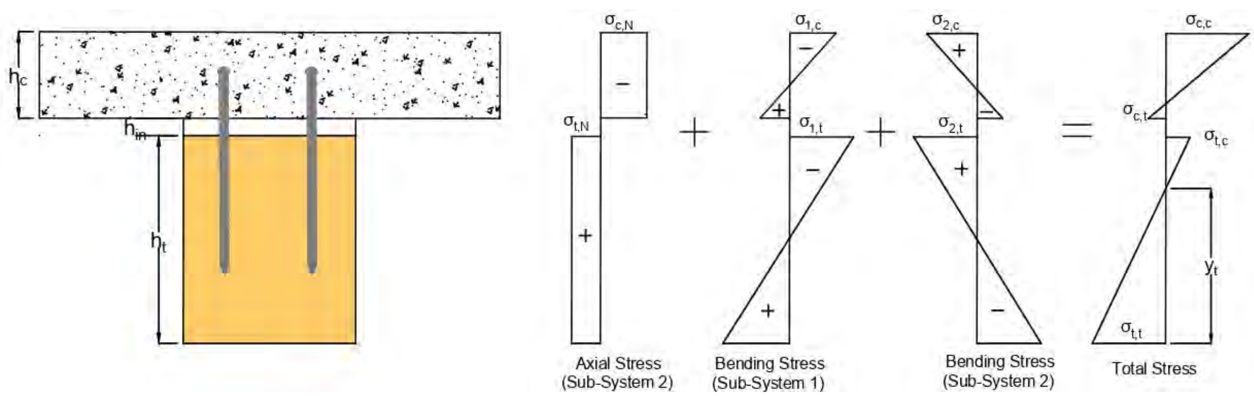


**Figure 31. Stress distributions in TCC systems with mass timber beam and concrete slab**

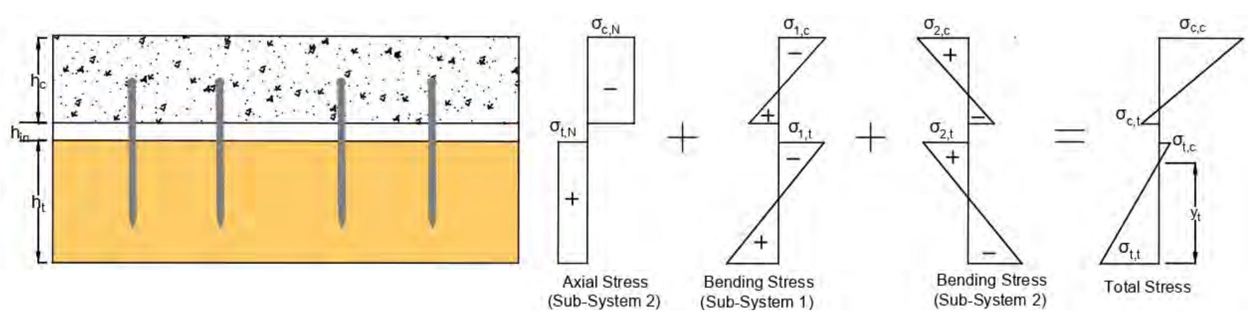


**Figure 32. Stress distributions in TCC systems with MTP or SCL and concrete slabs**

According to the equilibrium condition, the resultant normal force applied in the timber and concrete at a given cross-section is equal to the sum of shear forces, $X_{sum}$, in all the connectors between the mid-span and support. Therefore, the axial stress in the members is

$$\boldsymbol{\sigma_{t,N}} = \frac{\boldsymbol{X_{sum}}}{\boldsymbol{A_t}} \tag{33}$$

$$\boldsymbol{\sigma_{c,N}} = \frac{\boldsymbol{X_{sum}}}{\boldsymbol{A_c}} \tag{34}$$

where

$\sigma_{t,N}$ = Tensile stress in timber induced by axial forces in N/mm$^2$

The resultant axial stress due to bending at a position in the cross-section is the sum of the bending stresses obtained from the two subsystems, as shown below:

$$\boldsymbol{\sigma_{t,B} = \sigma_{1,t} + \sigma_{2,t}} \tag{35}$$

$$\boldsymbol{\sigma_{c,B} = \sigma_{1,c} + \sigma_{2,c}} \tag{36}$$

where

$\sigma_{t,B}$ = Normal stress in timber induced by bending moment in timber
$\sigma_{c,B}$ = Normal stress in concrete induced by bending moment in concrete
$\sigma_{i,t}$ = Bending stress in timber in subsystem *i* in N/mm$^2$
$\sigma_{i,c}$ = Bending stress in concrete in subsystem *i* in N/mm$^2$

In subsystem 1, the normal stress in the member is caused by the bending moment assuming the concrete and timber are unconnected, while in subsystem 2, the normal stress is caused by the bending moment induced by the eccentric normal force. The stresses can be written as follows,

$$\boldsymbol{\sigma_{1,t}} = \frac{\boldsymbol{3w \cdot E_t I_t (L^2 - n_i^2)}}{\boldsymbol{4 b_t h_t^2 (E_c I_c + E_t I_t)}} \tag{37}$$

$$\boldsymbol{\sigma_{1,c}} = \frac{\boldsymbol{3w \cdot E_c I_c (L^2 - n_i^2)}}{\boldsymbol{4 b_c h_c^2 (E_c I_c + E_t I_t)}} \tag{38}$$

$$\boldsymbol{\sigma_{2,t}} = \frac{\boldsymbol{3X_{sum} E_t I_t (H + h_{in})}}{\boldsymbol{b_t h_t^2 (E_c I_c + E_t I_t)}} \tag{39}$$

$$\boldsymbol{\sigma_{2,c}} = \frac{\boldsymbol{3X_{sum} E_c I_c (H + h_{in})}}{\boldsymbol{b_c h_c^2 (E_c I_c + E_t I_t)}} \tag{40}$$

The total axial stress for the member is the sum of the stresses in the subsystems and can be written as

$$\boldsymbol{\sigma_{t,z} = \sigma_{t,N} + \sigma_{t,B}} \tag{41}$$

$$\boldsymbol{\sigma_{c,z} = \sigma_{c,N} + \sigma_{c,B}} \tag{42}$$

where

$\sigma_{t,z}$ = Total tensile stress $\sigma_{t,t}$ or total compressive stress $\sigma_{t,c}$ of timber in N/mm$^2$
$\sigma_{c,z}$ = Total tensile stress $\sigma_{c,t}$ or total compressive stress $\sigma_{c,c}$ of concrete in N/mm$^2$

The shear stress is most critical in the timber member, and the maximum stress happens at the neutral axis of the timber member where flexural stress is zero. The shear stress of timber, $\tau_t$, can be calculated using the neutral axis of timber, as shown in Equation 43:

$$\tau_t = \frac{h_t{}^2(\sigma_{t,N}+\sigma_{t,B})^2 E_t V}{8\sigma_{t,B}^2 (EI)_{eff}} \quad [43]$$

where

| | | |
|---|---|---|
| $h_t$ | = | Height of timber in mm |
| $V$ | = | Shear force in the composite cross-section of interest in N |

Note that the neutral axes move further apart from each other and towards the centroid of each member as the degree of composite action decreases.

The superposition method can also be applied to mass timber floors. The stress distribution of a ribbed-plate system is shown in Figure 33. In the case of a ribbed-plate system with timber beams and MTP, the stresses in the MTP as well as the timber beams need to be checked separately.

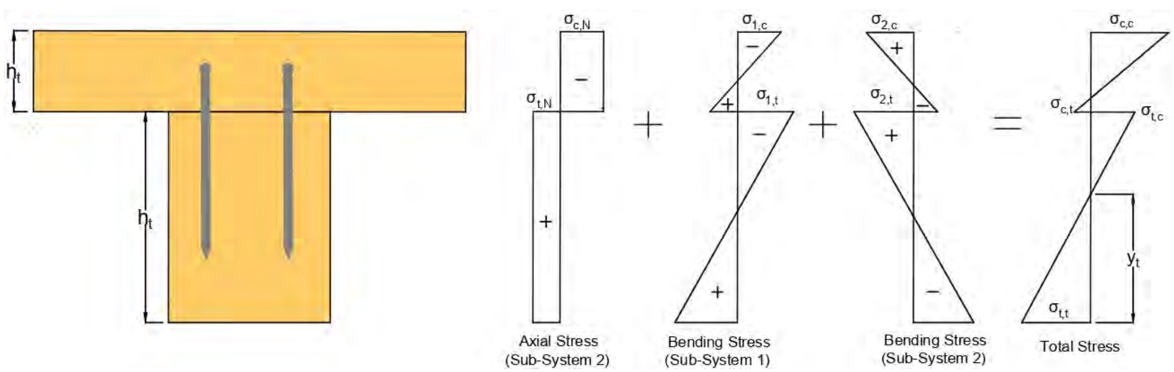


**Figure 33. Stress distributions in composite systems with mass timber beams and MTP or SCL**

(4) Deflection, Δ

The vertical deflection of the TCC system under a uniformly distributed load, $w$, can be calculated using Equation 44:

$$\Delta = \frac{5wL^4 - 19.2X_{sum}n_1(2L-n_r)(H+h_{in})}{384(E_cI_c+E_tI_t)} \quad [44]$$

To calculate the long-term deflection, the modulus of elasticity of the concrete ($E_{c,LT}$), modulus of elasticity of timber ($E_{t,LT}$), and stiffness of the shear connectors ($k_{LT}$) may be multiplied by the creep adjustment factors for long-term load duration for both serviceability and ultimate limit states, as given in Equations 26 to 28.

(5) Vibration

TCC floors should be evaluated to prevent objectionable vibrations, as shown in Equation 29. An example of a TCC floor system with an MTP is shown in Appendix B.

###### *6.1.3.2.2.3 Application of Release-and-Restore Method in Analysis of TCC with Notched Connections*

The release-and-restore method developed by Zhang, Zhang and Chui (2021), based on a concept of released structure, can predict the structural performance of TCC floor systems where the spacing between connectors is large, as with notched connections. The underlying assumptions for this model are as follows:

- There is no separation between concrete and timber. The vertical deflection and curvature for both components are treated as equal.
- Friction between timber and concrete is neglected and all the shear forces are resisted by the notched connections.
- Euler-Bernoulli beam theory holds for timber and concrete components and their shear deformation is thus not considered.
- Concrete is assumed to mainly resist compression and cracking of concrete is not considered.
- The size of the notch is considered to be small compared to the timber component, so the presence of the notch is ignored when calculating the overall sectional properties of the timber. However, the presence of the notch should be considered when calculating the shear strength capacity of the timber.

The analytical solution can be used for cases without restriction on the boundary conditions, loading conditions, connection stiffness, and connection locations.

The release-and-restore method has four steps: partition, release, restore, and combine. The first step is to partition the composite beam in accordance with the positions of bearing surfaces in the notched connections (see Figure 34). It is assumed that the composite beam is divided into $n$ segments. In most cases, the composite beams with notches are not connected at the supports, but for universality and consistency of the solution, the two ends of the beam are assumed to be connected. Thus, $n$+1 connections exist in the beam. The free-body diagram for each segment under the external load is illustrated in Figure 34. In the second step, the axial forces in timber and concrete in each segment are released. Since friction is neglected, the two components can have free slip under the external load. Since no separation between timber and concrete is considered, the curvature of timber and concrete at any point along the beam is assumed to be equal. In the third step, the axial forces acting on timber and concrete are considered. Timber is assumed to resist tension and concrete is subject to compression. The axial forces induce bending moment in the composite cross-section. In the fourth step, the internal forces of the segment from the release-and-restore steps are combined to calculate its actual internal forces. The partitioned segments then need to be assembled to form the continuous beam by applying the compatibility conditions. The slips at two sides of each segment should be compatible with the slips of the adjacent segments. When combining adjacent segments, the connections (in this case, notches) have to be taken into account.

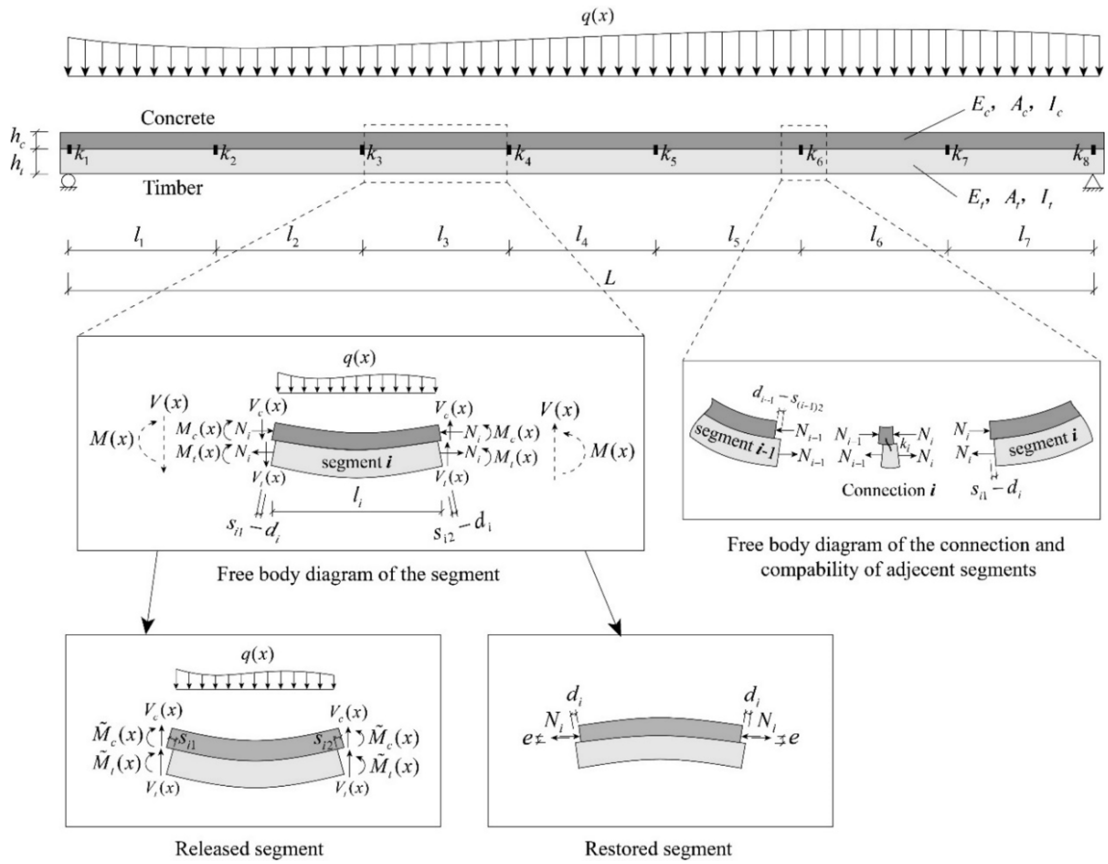


**Figure 34. Solving the internal actions in the composite beam with discrete connections using the release-and-restore method (Zhang, Zhang & Chui, 2021)**

where

| | | |
|---|---|---|
| $A_i$ | = | Cross-sectional area of concrete or timber layer |
| $d_i$ | = | Relative slip at two sides of the restored segment between timber and concrete |
| $E_i$ | = | Modulus of elasticity of concrete or timber layer |
| $e$ | = | Eccentricity of axial forces in the restored segment |
| $I_i$ | = | Second moment of inertia of concrete or timber |
| $h_i$ | = | Height of concrete or timber layer in the composite beam |
| $k_i$ | = | Connection stiffness |
| $l_i$ | = | Length of each segment |
| $L$ | = | Beam span |
| $M_i$ | = | Overall external bending moment acting on the beam |
| $\bar{M}_i$ | = | Average external moment in partitioned segment $i$ |
| $N_i$ | = | Axial force in the $i$-th partitioned segment |
| $q$ | = | Line load |
| $s_{i1}$ | = | Relative slip at the left side of the released segment between timber and concrete |
| $s_{i2}$ | = | Relative slip at the right side of the released segment between timber and concrete |
| $V_i$ | = | Shear force |

This release-and-restore method was conducted using the matrix method. Presented below are the governing equations and solution for a TCC beam with simple supports, as illustrated in Figure 34. For support conditions other than the simple support, see Zhang, Zhang and Chui (2021).

The unknown slip vectors are

$$\{\boldsymbol{S_1}\} = [\boldsymbol{s_{11}}, \boldsymbol{s_{21}}, \boldsymbol{s_{31}}, \dots, \boldsymbol{s_{n1}}]^T \quad [45]$$

$$\{\boldsymbol{S_2}\} = [\boldsymbol{s_{12}}, \boldsymbol{s_{22}}, \boldsymbol{s_{32}}, \dots, \boldsymbol{s_{n2}}]^T \quad [46]$$

$$\{\boldsymbol{D}\} = [\boldsymbol{d_1}, \boldsymbol{d_2}, \boldsymbol{d_3}, \dots, \boldsymbol{d_n}]^T \quad [47]$$

Under the simple support conditions, the slip vector $\{S_1\}$ can be solved and expressed as

$$\{\boldsymbol{S_1}\} = [(\boldsymbol{W_2} - \boldsymbol{W_1}) + (\boldsymbol{W_1} + \boldsymbol{W_2})(2\boldsymbol{I} + \boldsymbol{\Theta K})^{-1}\boldsymbol{\Theta K}]^{-1}\boldsymbol{W_2}\{\boldsymbol{\Lambda}\} \quad [48]$$

where $I$ is the identity matrix

$$\boldsymbol{I} = \begin{bmatrix} \mathbf{1} & & & & \\ & \mathbf{1} & & & \\ & & \mathbf{1} & & \\ & & & \ddots & \\ & & & & \mathbf{1} \end{bmatrix}_{n\times n} \quad [49]$$

Vector $\{\Lambda\}$ is

$$\{\boldsymbol{\Lambda}\} = [\boldsymbol{\lambda_1}, \boldsymbol{\lambda_2}, \boldsymbol{\lambda_3}, \dots, \boldsymbol{\lambda_n}]^T \quad [50]$$

in which $\lambda_i$, the difference of length change between the bottom of the concrete and the top of timber in the released segment,

$$\boldsymbol{\lambda_i} = \frac{(\boldsymbol{h_c} + \boldsymbol{h_t})}{2(\boldsymbol{E_c I_c} + \boldsymbol{E_t I_t})}\boldsymbol{l_i \bar{M}_i} \quad [51]$$

and $\bar{M}_i$ is the average external bending moment in segment $i$

$$\boldsymbol{\bar{M}_i} = \frac{1}{l_i}\int_{x_i}^{x_i+l_i} \boldsymbol{M(x)dx} \quad [52]$$

Matrix $\Theta$ is the parameter matrix

$$\boldsymbol{\Theta} = \begin{bmatrix} \boldsymbol{\theta_1} & & & & \\ & \boldsymbol{\theta_2} & & & \\ & & \boldsymbol{\theta_3} & & \\ & & & \ddots & \\ & & & & \boldsymbol{\theta_n} \end{bmatrix}_{n\times n} \quad [53]$$

in which

$$\boldsymbol{\theta_i} = \frac{l_i}{E_t}\left[\frac{\left(\frac{h_t}{2}+e\right)h_t}{2I_t} + \frac{1}{A_t}\right] + \frac{l_i}{E_c}\left[\frac{\left(\frac{h_c}{2}+e\right)h_c}{2I_c} + \frac{1}{A_c}\right] \quad [54]$$

and $e$ is the eccentricity of axial forces in the restored segment

$$e = \frac{E_t I_t h_c - E_c I_c h_t}{2(E_c I_c + E_t I_t)} \quad [55]$$

The stiffness matrix $K$ can be expressed as

$$K = \begin{bmatrix} k_1 & & & & \\ k_1 & k_2 & & & \\ k_1 & k_2 & k_3 & & \\ \vdots & \vdots & \vdots & \ddots & \\ k_1 & k_2 & k_3 & \cdots & k_n \end{bmatrix}_{n\times n} \quad [56]$$

Matrices $W_1$ and $W_2$ are expressed as

$$W_1 = \begin{bmatrix} 0 & 1 & 0 & \cdots & 0 \\ 0 & 0 & 1 & \cdots & 0 \\ \vdots & \vdots & \vdots & \ddots & \vdots \\ 0 & 0 & 0 & \cdots & 1 \\ k_1 & k_2 & k_3 & \cdots & k_n \end{bmatrix}_{n\times n} \quad [57]$$

$$W_2 = \begin{bmatrix} 1 & & & & \\ & 1 & & & \\ & & \ddots & & \\ & & & 1 & \\ & & & & -k_{n-1} \end{bmatrix}_{n\times n} \quad [58]$$

The slip vectors $\{S_2\}$ and $\{D\}$ can be determined from

$$\{S_2\} = \{\Lambda\} - \{S_1\} \quad [59]$$

$$\{D\} = (2I + \Theta K)^{-1}\Theta K\{S_1\} \quad [60]$$

The axial forces in each segment can be determined from

$$\{N\} = [N_1, N_2, N_3, \ldots, N_n]^T = 2\Theta^{-1}\{D\} \quad [61]$$

The bending moments in the timber and concrete in each segment are given as

$$M_c(x) = \frac{E_c I_c}{E_c I_c + E_t I_t} M(x) - N_i\left(\frac{h_c}{2} - e\right) \quad [62]$$

$$M_t(x) = \frac{E_t I_t}{E_c I_c + E_t I_t} M(x) - N_i\left(\frac{h_t}{2} - e\right) \quad [63]$$

The shear forces in the timber and concrete can be stated as

$$V_c(x) = \frac{E_c I_c}{E_c I_c + E_t I_t} V(x) \quad [64]$$

$$V_t(x) = \frac{E_t I_t}{E_c I_c + E_t I_t} V(x) \quad [65]$$

Stresses at the top and bottom of the concrete are

$$\sigma_{c,c}(x) = -\frac{E_c h_c M(x)}{2(E_c I_c + E_t I_t)} + \frac{N_i\left(\frac{h_c}{2} - e\right)h_c}{2I_c} - \frac{N_i}{A_c} \tag{66}$$

$$\sigma_{c,t}(x) = \frac{E_c h_c M(x)}{2(E_c I_c + E_t I_t)} - \frac{N_i\left(\frac{h_c}{2} - e\right)h_c}{2I_c} - \frac{N_i}{A_c} \tag{67}$$

Stresses at the top and bottom of the timber are

$$\sigma_{t,c}(x) = -\frac{E_t h_t M(x)}{2(E_c I_c + E_t I_t)} + \frac{N_i\left(\frac{h_t}{2} - e\right)h_t}{2I_t} + \frac{N_i}{A_t} \tag{68}$$

$$\sigma_{t,t}(x) = \frac{E_t h_t M(x)}{2(E_c I_c + E_t I_t)} - \frac{N_i\left(\frac{h_t}{2} - e\right)h_t}{2I_t} + \frac{N_i}{A_t} \tag{69}$$

The deflection of the beam can be determined using the Mohr integral method

$$\Delta(t) = \int_0^L \frac{\widehat{M}(x,t) M^{tot}(x)}{E_c I_c + E_t I_t} dx \tag{70}$$

where $\widehat{M}(x,t)$ is the moment distribution when a unit force is acting at the position of $x = t$, and $M^{tot}(x)$ is the sum of moments in timber and concrete under the external load. The sum of moments in timber and concrete is

$$M^{tot}(x) = M(x) - \frac{(h_c + h_t)}{2} N(x) \tag{71}$$

### *6.1.3.3 Numerical Methods*

#### 6.1.3.3.1 General Rules

While most TCC and mass timber floor systems can be analysed using the analytical methods described in Section 6.1.3.2, advanced modelling methods such as FE models can be used for cases beyond the scope of the analytical methods and the system development and optimisation. The modelling guidelines discussed in Section 6.1.2.3, for light wood-frame systems, apply to the numerical modelling of TCC and mass timber floor systems. In addition, the following additional guidelines are applicable:

- Adopt appropriate or equivalent material properties for concrete and timber based on experiments or appropriate literature, and account for concrete cracking in the material model.
- Consider the orthotropic nature of timber and the constitutive model to describe the nonlinear behaviour. See, for example, Wood$^{S}$ (Chen et al., 2011) or Wood$^{ST}$ (Chen et al., 2020).
- Model shear connectors using the smeared or discrete contact elements, depending on the connection type and the layout of shear connectors.
- Adopt appropriate connection properties (load-slip response) based on experimental results or modelling (for example, Mirdad & Chui, 2019).

Several researchers have conducted FE modelling of TCC floor systems to evaluate their behaviour under out-of-plane load (Fragiacomo, 2005; Fragiacomo & Ceccotti, 2006; Fragiacomo et al., 2014; Gutkowski et al., 2010; Khorsandnia et al., 2014; Liu, 2016; Lopes et al., 2012; Lukaszewska et al., 2010; Persaud & Symons, 2006; Van der Linden, 1999). Similar approaches can be adopted to study the specific composite floor system, such as concrete -timber beam/MTP or ribbed-plate system connected by dowel-type fasteners. Figure 35 shows an FE model of a TCC system developed by Liu (2016) using Vector-2.

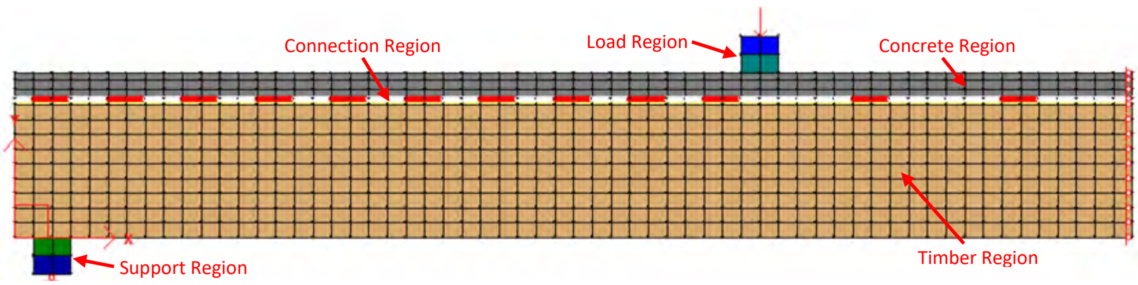


**Figure 35. FE model of a TCC system developed using Vector-2 (Liu, 2016)**

The composite floors with notched connections can be modelled with 2D or 3D solid elements or simplified beam elements. When using solid elements, the notched connections are often easier to model than mechanical steel fasteners as the exact geometries of notches can easily be meshed (Jiang & Crocetti, 2019; Monteiro et al., 2013). The nonlinear behaviours of the composite system can be directly implemented into the constitutive laws of timber and concrete. However, the interaction between timber and concrete at the interface should be defined precisely. The contact stiffness between timber and concrete needs to be carefully calibrated to prevent the elements from penetrating into each other. Any penetration would cause low connection stiffness, while overly stiff contact would induce unrealistically high stiffness. The solid-element model is suitable for modelling local nonlinear behaviours of notched connections, such as timber plasticity and concrete cracking. The cracking of timber can be modelled by a cohesive layer that can take into account the occurrence of longitudinal shear or fracture in tension perpendicular to the grain. Accurate calibration of the input parameters, however, is necessary for realistic FE predictions. The plasticity of and damage to concrete are often modelled by the concrete-damaged plasticity model (Bedon & Fragiacomo, 2017).

The simplicity of the notched connection motivates its popularity. However, the standardisation of notched connections is not well developed because the notch geometries and reinforcing techniques vary. The variability of the notched connection properties arises from (1) the material properties of the concrete and timber; (2) the geometry and sizes of the notches; and (3) the presence of additional mechanical fasteners. There are no well-accepted models for accurately predicting the stiffness and strength of notched connections. Refined FE modelling with suitable constitutive models of wood, for example, Wood$^{ST}$ (Chen et al., 2020), and reinforcing concrete can be adopted. Conducting laboratory connection tests would be desirable to validate prediction models.

#### 6.1.3.3.2 Framework or Truss Model

When a large composite floor is to be modelled and the overall behaviour of the system is of interest, a solid-element model is often overly complicated and inefficient. Another way to model the composite floors with discrete notched connections is the framework model (Grosse, Hartnack, Lehmann & Rautenstrauch, 2003; Grosse, Hartnack & Rautenstrauch, 2003). The framework model is built with a rigorous analytical derivation that is easier to implement than solid-element models. Timber and concrete components in the framework model are represented with beam elements located at the centres of two components, as shown in Figure 36.

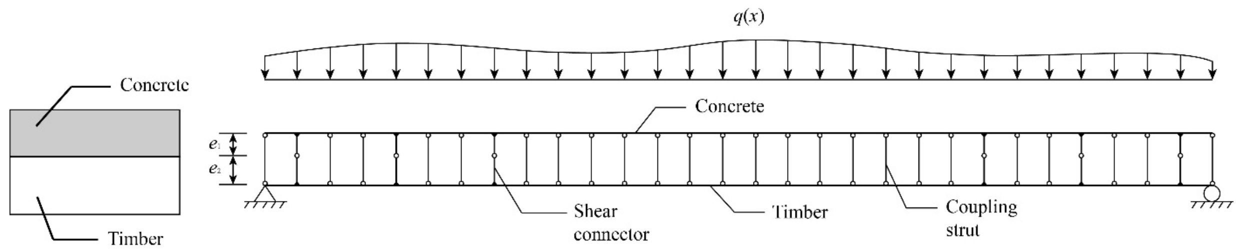


**Figure 36. Framework model**

The shear connections are represented by hinged cantilevers that are rigidly connected to the timber and concrete. The shear stiffness of the original connection is mimicked by adjusting the bending stiffness of the cantilevers. As shown in Figure 37, the bending stiffness of cantilevers can be determined from:

$$(\boldsymbol{EI})_{\boldsymbol{cantilever}} = \frac{\boldsymbol{k}}{3}(\boldsymbol{e_1}^3 + \boldsymbol{e_2}^3) \qquad [72]$$

where

| | | |
|---|---|---|
| $(EI)_{cantilever}$ | = | Bending stiffness of the cantilever |
| $k$ | = | Shear stiffness of the original connection |
| $e_1$ | = | Distance between the centroid of concrete to the joint |
| $e_2$ | = | Distance between the centroid of timber to the joint |

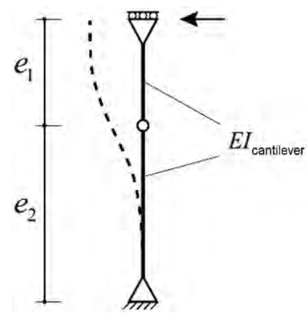


**Figure 37. Shear connection represented by hinged cantilevers in the framework model**

Closely spaced short struts need to be built in the framework model to connect timber and concrete and ensure the same vertical displacement of the two layers. The struts should be modelled as rigid bars that cannot deform under the vertical (axial) load.

#### 6.1.3.3.3 Space-Exact Element Model

Nguyen et al. (2010; 2011) proposed an exact FE model for the linear static analysis of two-layer beams with an interlayer slip. The layers are connected discontinuously and therefore the shear connections are modelled using concentrated spring elements at each connector location (Figure 38[a]). It is assumed that no uplift can occur at the top layer. Thus, both layers have the same transversal deflection but different rotations and curvatures. The effect of friction at the interface is accounted for by assuming that the friction force is proportional to the normal force at the interface. Based on these key assumptions, the governing equations are established and an original closed-form solution is derived. From the analytical expressions for the displacement and force fields, the space-exact stiffness matrix (Figure 38[b]) for a generic two-layer beam element can be deduced and incorporated into any displacement-based FE code for the linear static analysis of two-layer beams with an interlayer slip and arbitrary loading and support conditions. The model can also incorporate a time-discretised solution to consider the effects of time, such as creep and shrinkage of the concrete slab.

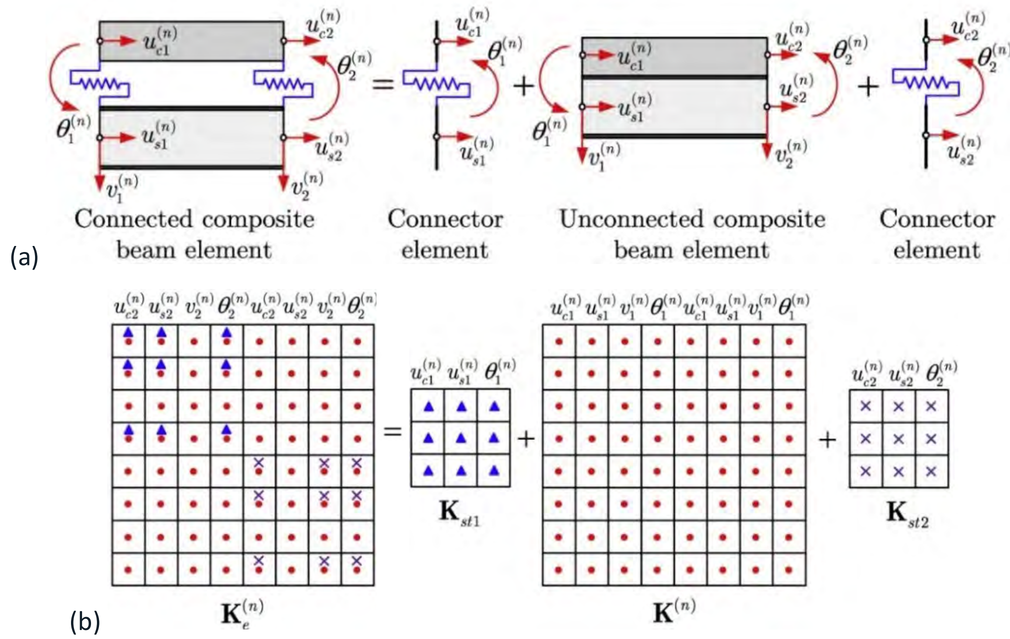


**Figure 38. (a) FE model; and (b) corresponding stiffness assembly procedure for a connected composite beam element (Nguyen et al., 2010): $K_e$ and $K$ are the stiffness matrix of the connected and unconnected composite beam element, respectively; $K_{st1}$ and $K_{st2}$ are the stiffness matrix of connector elements**

6.1.3.3.4 Case Study

Zhang, Zhang and Chui (2021) provide an example of numerical and analytical modelling on an MTP–concrete composite floor strip with notched connections. The dimensions, material properties of timber and concrete, and magnitude of the load are shown in Figure 39. The notched connections are 25 mm deep and the stiffness was assumed to be 600 kN/mm. Appendix C shows the procedure for determining the deflection, relative slip, and stress distributions in the composite floor according to the discrete bond model.

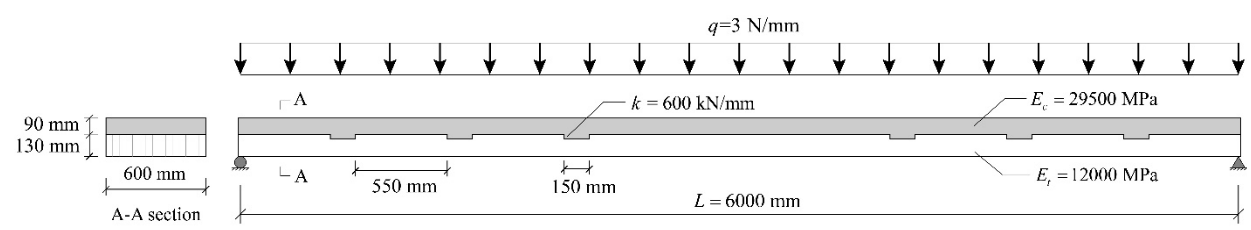


**Figure 39. MTP–concrete composite floor strip**

A 2D model was built in the general purpose FE modelling software, Abaqus 2020 (Dassault Systèmes, 2019), to compare with the discrete bond model. Only half of the floor was built in the model because the floor was symmetric. Four-node bilinear plane stress quadrilateral (CPS4) elements were used to model timber and concrete. The nominal element size was about 10 mm in most of the areas, while a denser mesh with 5 mm nominal element size was used in the region of concrete protrusions. A frictionless behaviour between timber and concrete was defined in the tangential direction, and a hard contact was defined in the normal direction. However, to reduce the element penetration effect and mesh sensitivity issues, the stiffness scale factor in the normal direction was adjusted to 5. Figure 40 compares the discrete bond model results with the FE modelling results.

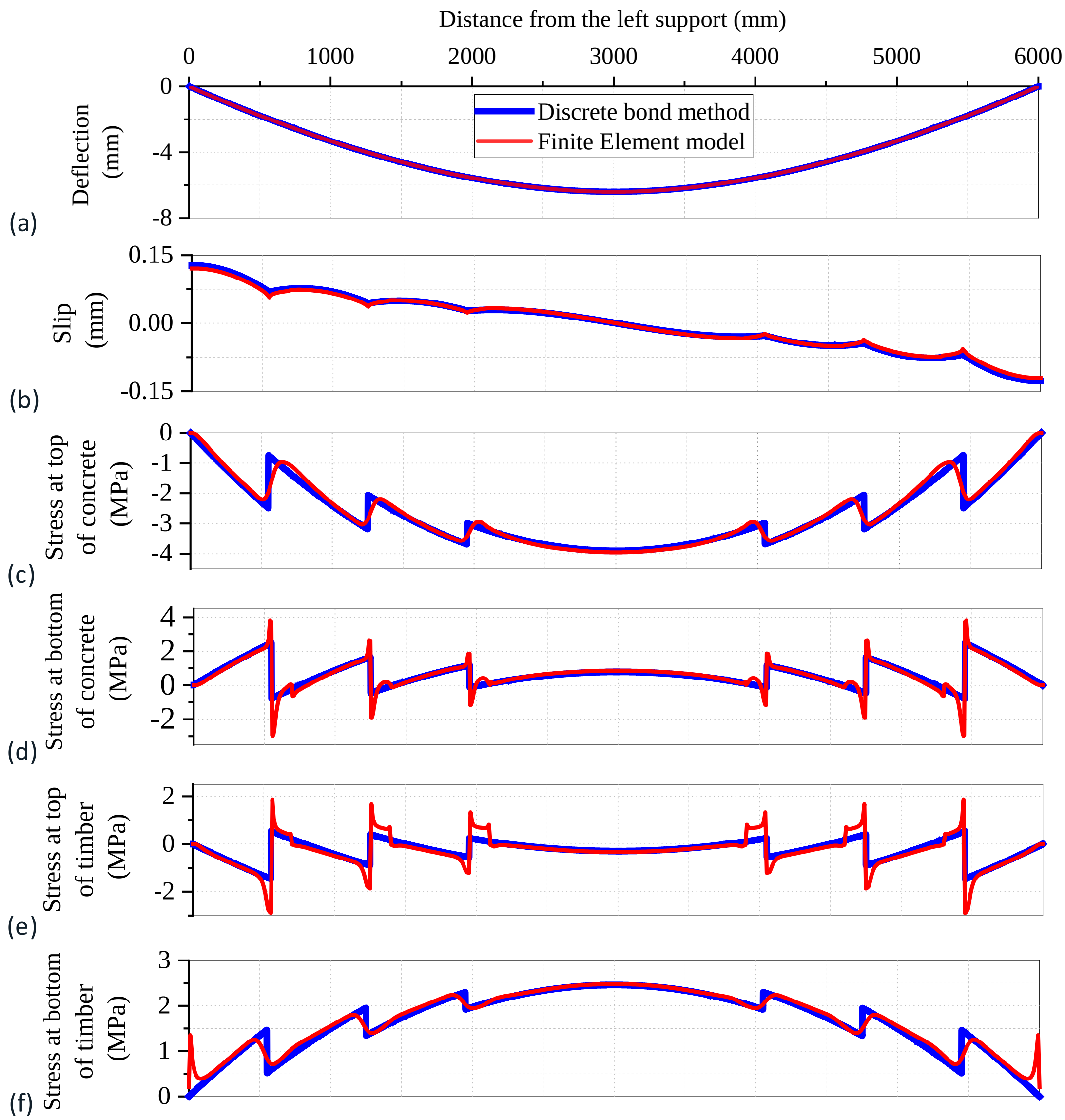


**Figure 40. Comparison of FE and analytical modelling results: (a) Deflection; (b) relative slip between timber and concrete; (c) stress at top of concrete; (d) stress at bottom of concrete; (e) stress at top of timber; and (f) stress at bottom of timber**

The two models yielded very similar results in terms of deflection, relative slip, and stress distributions. Relative slip does not uniformly increase from mid-span to the supports; rather, it is constrained at the regions around the notched connections and released at locations far away from connections. Note that the stress distribution in the composite floor fluctuates around the connections because of the discontinuity of axial forces in the floor. The FE model generates peak stress values around the notch as a result of stress singularity of the sharp corners.

## 6.1.4 Summary

In this chapter, the behaviour and mechanism of the light wood-frame, mass timber, and TCC floor systems are discussed. Generally speaking, most of the timber floors and roofs are complex composite systems of which the connectors or connections play an essential role in governing the composite effect among different layers of materials. Continuous bond models, discrete bond models, and ribbed-plate models for analysing the stresses, deformations, and frequencies of composite floor systems are introduced along with specific applications for different types of floor systems. Computer-based models, FE models, framework/truss model, and space-exact element model are also introduced. General rules and specific consideration for developing FE models for different types of floor systems are also provided. The information presented in this chapter is intended to help practising engineers and researchers become more acquainted with the modelling and analysis of timber floors and roofs subject to the out-of-plane loads.

## 6.1.5 Acknowledgements

The authors would like to acknowledge Dr. Jan Niederwestberg, Dr. Md Abdul Hamid Mirdad, and Dr. Lei Zhang for their contributions to this chapter.

## 6.1.6 Nomenclature

| | |
|---|---|
| $A_i$ | Cross-sectional area of layer $i$ in a composite beam/floor, $i = 1,2,3$ |
| $A_c$ | Cross-sectional area of concrete in timber-concrete composite floor/beam |
| $A_t$ | Cross-sectional area of timber in timber-concrete composite floor/beam |
| $a_i$ | Distance between the centre of layer $i$ in a composite floor/beam to the neutral axis of the composite cross-section, $i = 1,2,3$ |
| $b$ | Width of the floor/beam |
| $b_c$ | Width of concrete in the composite floor |
| $b_{c,e}$ | Effective width of an edge beam in the composite floor |
| $b_{c,i}$ | Effective width of an internal beam in the composite floor |
| $b_e$ | The sum of the spacing between edge beam and internal beam, and half width of the edge beam |
| $b_f$ | Width of the flange |
| $b_i$ | Width of layer $i$ in a composite beam/floor, $i = 1,2,3$ |
| $b_{in}$ | Width of insulation in the composite floor |
| $b_J$ | Spacing of the joists in the composite floor |
| $b_m$ | Actual spacing of the middle beams |
| $b_s$ | Width of strapping in the ribbed plate |
| $b_t$ | Width of timber in the composite floor |
| $C$ | Joist torsional constant |
| $c_f$ | Thickness of the flange |
| $D$ | Slip vector |
| $D_x$ | Bending stiffness of the ribbed floor in the span ($x$) direction |
| $D_y$ | Bending stiffness of the ribbed floor in the width ($y$) direction |
| $D_{xy}$ | Shear and torsional stiffness of the ribbed floor system |
| $d$ | Joist depth |

| | |
|---|---|
| $d_{1kN}$ | Calculated static deflection of floor under 1 kN concentrated load at mid-span |
| $d_i$ | Relative slip at two sides of the restored segment between timber and concrete in the release-and-restore model |
| $E$ | Modulus of elasticity |
| $E_A$ | Modulus of elasticity of beam A in Shear Analogy model |
| $E_B$ | Modulus of elasticity of beam B in Shear Analogy model |
| $E_c$ | Modulus of elasticity of concrete/topping |
| $E_{c,LT}$ | Modulus of elasticity of concrete in the long term |
| $E_f$ | Modulus of elasticity of the flange material |
| $E_i$ | Modulus of elasticity of layer $i$ in a composite floor/beam, $i = 1{,}2{,}3$ |
| $E_{in}$ | Modulus of elasticity of insulation |
| $E_t$ | Modulus of elasticity of timber |
| $E_{t,LT}$ | Modulus of elasticity of timber in the long term |
| $E_{strap}$ | Modulus of elasticity of the strapping material in the ribbed plate |
| $e$ | Eccentricity of axial forces in the restored segment in the release-and-restore model |
| $e_1$ | Distance between the centroid of concrete to the joint in the framework model |
| $e_2$ | Distance between the centroid of timber to the joint in the framework model |
| $(EI)_b$ | Equivalent bending stiffness of strapping |
| $(EI)_{b,i}$ | Bending stiffness of the $i$-th lateral bracing member in the ribbed plate |
| $(EI)_{cantilever}$ | Bending stiffness of the cantilever in the framework model |
| $(EI)_{CJ}$ | Composite bending stiffness of the joist in the ribbed plate |
| $(EI)_{eff}$ | Effective bending stiffness of a composite cross-section |
| $(EI)_{eff}^{1m}$ | Effective bending stiffness of a 1 m wide strip composite beam |
| $(EI)_p$ | Bending stiffness of multilayered floor deck in the ribbed plate |
| $(EI)_{s\|\|}$ | Unit bending stiffness of subfloor across joists |
| $F_{cc}$ | Compression in concrete |
| $F_{ct}$ | Tension in concrete |
| $F_y$ | Yield strength of one row of connectors |
| $F_{y,eff}$ | Effective connector force |
| $f$ | Fundamental natural frequency |
| $f_c'$ | Specified compressive strength of concrete |
| $f_b$ | Timber bending strength |
| $f_v$ | Timber shear strength |
| $G_c$ | Shear modulus of topping material |
| $G_f$ | Shear modulus of the joist material |
| $G_p$ | Shear modulus of multilayered floor deck in the ribbed plate |
| $G_s$ | Shear modulus of subfloor material |
| $H$ | Total height of floor system |
| $h$ | Height of the neutral axis in the joist |
| $h_c$ | Thickness of concrete |
| $h_d$ | Thickness of multilayer floor deck in the ribbed plate |
| $h_i$ | Height of layer $i$ in the composite beam/floor, $i = 1{,}2{,}3$ |

| | |
|---|---|
| $h_{in}$ | Thickness of the insulation layer |
| $h_t$ | Thickness of timber |
| $I$ | Identity matrix |
| $I_c$ | Second moment of inertia of concrete |
| $I_g$ | Gross second moment of inertia of concrete |
| $I_i$ | Second moment of inertia of layer $i$ in a composite floor/beam, $i = 1,2,3$ |
| $I_{in}$ | Second moment of inertia of insulation |
| $I_s$ | Second moment of inertia of strapping in ribbed plate |
| $I_t$ | Second moment of inertia of timber |
| $J_p$ | Torsional constant |
| $j$ | Total number of rows of lateral bracing elements in the ribbed plate |
| $K$ | Stiffness matrix in the release-and-restore model |
| $K_c$ | Load-slip modulus of strapping-to-joist connection |
| $K_i$ | Slip modulus of connections in layer $i$ in a composite floor/beam, $i = 1,3$ |
| $K_r$ | Rotational stiffness of single bracing element in a ribbed plate |
| $k$ | Shear stiffness of the original connection |
| $k_i$ | Connection stiffness of the *i*-th connection counted from left to right |
| $k_{LT}$ | Long-term connection stiffness |
| $L$ | Span of beam/joist/floor/system |
| $l_i$ | Length of the *i*-th partitioned segment in the release-and-restore model |
| $l_{strap}$ | Length of the shortest strapping in the ribbed plate |
| $M$ | Overall external bending moment acting on the floor/beam |
| $M_c$ | Bending moment in concrete |
| $M_t$ | Bending moment in timber |
| $M^{tot}$ | Sum of bending moments in timber and concrete |
| $\widehat{M}$ | Moment distribution when a unit force is acting on the beam/floor |
| $\overline{M}_i$ | Average external bending moment in the partitioned segment $i$ |
| $m$ | Convergence term |
| $m_a$ | Mass per unit length |
| $m_a^{1m}$ | Mass per unit length of a 1 m wide strip of timber-concrete composite floor |
| $m_f$ | Mass per square metre of the floor |
| $m_J$ | Mass per unit length of joist |
| $N$ | Axial force vector |
| $N_i$ | Axial force in the *i*-th partitioned segment in the release-and-restore model |
| $n$ | Convergence term |
| $n_i$ | Distant between a pair of connectors that are symmetric about the mid-span |
| $P$ | Point load |
| $P_i$ | Shear load on connector in layer $i$, $i = 1,3$ |
| $q$ | Line load |
| $r$ | Number of connector rows from mid-span to the support |
| $S_1$ | Slip vector at the left side of the released segment |
| $S_2$ | Slip vector at the right side of the released segment |
| $S_c$ | Section modulus of concrete |

| | |
|---|---|
| $S_t$ | Section modulus of timber |
| $S_{XY}$ | Section modulus in Shear Analogy model |
| $s_{eff}$ | Effective spacing of nonuniformly spaced connectors |
| $s_i$ | Connector spacing in layer $i$ in a composite floor/beam, $i = 1,3$ |
| $s_{i1}$ | Relative slip at the left side of the released segment between timber and concrete in the release-and-restore model |
| $s_{i2}$ | Relative slip at the right side of the released segment between timber and concrete in the release-and-restore model |
| $s_{max}$ | Maximum connector spacing |
| $s_{min}$ | Minimal connector spacing |
| $t$ | Width of the joists in ribbed plate |
| $t_c$ | Thickness of topping |
| $t_{cs}$ | Height of strapping in the ribbed plate |
| $t_s$ | Thickness of subfloor |
| $V$ | Overall shear force in the cross-section |
| $V_c$ | Shear force in concrete |
| $V_t$ | Shear force in timber |
| $W_1$ | Coefficient matrix |
| $W_2$ | Coefficient matrix |
| $w$ | Uniformly distributed load |
| $X_i$ | Shear force in connector $i$ |
| $X_{sum}$ | Sum of shear forces in all the connectors between mid-span and the support |
| $y_c$ | Distance of the neutral axis of concrete to the compression edge |
| $y_t$ | Distance of the neutral axis of cross-section to the tension edge |
| $Z$ | Parameter in the ribbed-plate model |
| $\alpha_1$ | Parameter for calculating concrete compression force |
| $\beta_1$ | Parameter for calculating concrete compression force |
| $\beta$ | Parameter in the ribbed-plate model |
| $\gamma_i$ | Gamma factor for layer $i$ in a composite floor/beam |
| $\Delta$ | Deflection of the beam/floor |
| $\Delta_a$ | Deflection limit |
| $\delta$ | Relative slip between timber and concrete |
| $\varepsilon_{c,t}$ | Normal strain at top of concrete |
| $\varepsilon_{c,b}$ | Normal strain at bottom of concrete |
| $\varepsilon_{t,t}$ | Normal strain at top of timber |
| $\varepsilon_{t,b}$ | Normal strain at bottom of timber |
| $\mathit{\Theta}$ | Parameter matrix |
| $\theta$ | Rotation |
| $\theta_i$ | Parameter in the release-and-restore model |
| $\mathit{\Lambda}$ | Parameter vector in the release-and-restore model |
| $\lambda$ | Modification factor for concrete density |
| $\lambda_i$ | Difference of length change between the bottom of concrete and top of timber in the released segment $i$ in the release-and-restore model |

| | |
|---|---|
| $\rho_c$ | Density of topping/concrete |
| $\rho_s$ | Density of subfloor |
| $\rho_t$ | Density of timber |
| $\sigma_{c,B}$ | Normal stress in concrete induced by bending moment in concrete |
| $\sigma_{c,c}$ | Concrete compressive stress at top |
| $\sigma_{c,N}$ | Compressive stress in concrete induced by axial force |
| $\sigma_{c,t}$ | Concrete tensile stress at bottom |
| $\sigma_{c,z}$ | Total tensile stress or total compressive stress of concrete |
| $\sigma_i$ | Normal stress at the top or bottom of layer $i$ in the composite floor/beam |
| $\sigma_{i,c}$ | Bending stress of concrete in subsystem $i$ |
| $\sigma_{i,t}$ | Bending stress of timber in subsystem $i$ |
| $\sigma_{M,i}$ | Maximum normal stress induced by bending moment in layer $i$ of a composite beam/floor |
| $\sigma_{N,i}$ | Normal stress induced by axial force in layer $i$ of a composite beam/floor |
| $\sigma_{t,B}$ | Normal stress in timber induced by bending moment in timber |
| $\sigma_{t,c}$ | Timber compressive stress at top |
| $\sigma_{t,N}$ | Tensile stress in timber induced by axial forces |
| $\sigma_{t,t}$ | Timber tensile stress at bottom |
| $\sigma_{t,z}$ | total tensile stress or total compressive stress of timber |
| $\tau_t$ | Shear stress in timber |
| $\tau_{i,max}$ | Maximum shear stress in layer $i$ in a composite cross-section |
| $\phi_c$ | Resistance factor for concrete |

### 6.1.7 References


Bedon, C., & Fragiacomo, M. (2017). Three-dimensional modelling of notched connections for timber–concrete composite beams. *Structural Engineering International, 27*(2), 184-196. https://doi.org/10.2749/101686617X14881932435295

Berardinucci, B., Di Nino, S., Gregori, A., & Fragiacomo, M. (2017). Mechanical behavior of timber–concrete connections with inclined screws. *International Journal of Computational Methods and Experimental Measurements, 5*(6), 807-820. https://doi.org/10.2495/CMEM-V5-N6-807-820

Boccadoro, L., & Frangi, A. (2014). Experimental analysis of the structural behavior of timber-concrete composite slabs made of beech-laminated veneer lumber. *Journal of Performance of Constructed Facilities, 28*(6), A4014006. https://doi.org/10.1061/(ASCE)CF.1943-5509.0000552

Boccadoro, L., Zweidler, S., Steiger, R., & Frangi, A. (2017). Bending tests on timber-concrete composite members made of beech laminated veneer lumber with notched connection. *Engineering Structures, 132*, 14-28. https://doi.org/10.1016/j.engstruct.2016.11.029

Bocquet, J. F., Pizzi, A., & Resch, L. (2007). Full-scale industrial wood floor assembly and structures by welded-through dowels. *Holz als Roh- und Werkstoff*, *65*(2), 149-155. https://doi.org/10.1007/s00107-006-0170-4

Byfield, M. P. (2002). Analysis of composite beam with widely spaced shear connectors. *Structural Engineering*, *80*(13):31-3.

CSA Group. (2014a). *CSA S16-14: Design of steel structures*. CSA Group.

CSA Group. (2014b). *CSA-A23.3-14: Design of concrete structures*. CSA Group.

CSA Group. (2019). *CSA O86:19: Engineering design in wood*. CSA Group.

Ceccotti, A. (2002). Composite concrete-timber structures. *Progress in Structural Engineering and Materials*, *2002*(4), 264-275. https://doi.org/10.1002/pse.126

Chen, Z., Zhu, E., & Pan, J. (2011). Numerical simulation of wood mechanical properties under complex state of stress. *Chinese Journal of Computational Mechanics*, *28*(04), 629-634, 640.

Chen, Z., Ni, C., Dagenais, C., & Kuan, S. (2020). Wood$^{ST}$: A temperature-dependent plastic-damage constitutive model used for numerical simulation of wood-based materials and connections. *Journal of Structural Engineering*, *146*(3): A04019225. https://doi.org/10.1061/(ASCE)ST.1943-541X.0002524

Chui, Y. H. (2002). Application of ribbed-plate theory to predict vibrational serviceability of timber floor systems. In Majid, W., M., W., A., Ahmad, Z., & Malik, A., R., A (Eds.), *Proceedings of 7$^{th}$ World Conference on Timber Engineering, WCTE 2002*.

Cuerrier-Auclair, S. (2020). *Design guide for timber-concrete composite floors in Canada*. Special Publication SP-540E. FPInnovations.

Cuerrier-Auclair, S., Sorelli, L., & Salenikovich, A. (2016a). A new composite connector for timber-concrete composite structures. *Construction and Building Materials, 112*, 84-92. https://doi.org/10.1016/j.conbuildmat.2016.02.025

Cuerrier-Auclair, S., Sorelli, L., & Salenikovich, A. (2016b). Simplified nonlinear model for timber-concrete composite beams. *International Journal of Mechanical Sciences, 117*, 30-42. https://doi.org/10.1016/j.ijmecsci.2016.07.019

Dassault Systèmes. (2019). *Abaqus 2020*. [Computer software].

Deam, B. L., Fragiacomo, M., & Buchanan, A. H. (2008). Connections for composite concrete slab and LVL flooring systems. *Materials and Structures, 41*(3), 495-507. https://doi.org/10.1617/s11527-007-9261-x

Deutsches Institut für Normung e. V. (2008). *DIN 1052:2008-12: Design of timber structures - General rules and rules for buildings*. DIN Deutsches Institut für Normung e. V.

Dias, A. M. P. G., Cruz, H. M. P., Lopes, S. M. R., & van de Kuilen, J. W. (2010). Stiffness of dowel-type fasteners in timber-concrete joints. *Structures and Buildings, 163*(4), 257-266. https://doi.org/10.1680/stbu.2010.163.4.257

Dias, A. M. P. G., Lopes, S. M. R., Van de Kuilen, J. W. G., & Cruz, H. M. P. (2007). Load-carrying capacity of timber-concrete joints with dowel-type fasteners. *Journal of Structural Engineering, 133*(5), 720–727. https://doi.org/10.1061/(ASCE)0733-9445(2007)133:5(720)

Dias, A. M. P. G., Schänzlin, J., & Dietsch, P. (2018). *Design of timber-concrete composite structures: A state-of-the-art report by COST Action FP1402/WG 4*. Shaker Verlag. https://doi.org/10.2370/9783844061451

Dias, A., Skinner, J., Crews, K., & Tannert, T. (2016). Timber-concrete-composites increasing the use of timber in construction. *European Journal of Wood and Wood Products, 74*, 443-451. https://doi.org/10.1007/s00107-015-0975-0

Dietsch, P., & Brandner, R. (2015). Self-tapping screw and threaded rods as reinforcement for structural timber elements—A state-of-the-art report. *Construction and Building Materials, 97*, 78-89. https://doi.org/10.1016/j.conbuildmat.2015.04.028

European Committee for Standardization. (2004). EN 1995-1-1:2004 + A2:2014 - *Eurocode 5: Design of timber structure*. European Committee for Standardization.

ETA-Danmark. (2018). *SFS VB Screws, SFS vb screws as fasteners in wood-concrete composite slab kit*. European Technical Assessment, ETA-13/0699.

ETA-Danmark. (2019). *Rotho Blaas CTC Screw, Self-Tapping Screws for use in Wood-Concrete Slab Kits*. European Technical Assessment ETA-19/0244.

Fitzgerald, S. (2017, August 09). Floor System Sizes and Materials - ppt video online download. Slideplayer. https://slideplayer.com/slide/11413043/

Foschi, R. O. (1982). Structural analysis of wood floor systems. *Journal of the Structural Division, 108*(7), 1557-1574. https://doi.org/10.1061/JSDEAG.0005988

Foschi, R. O., & Gupta, A. (1987). Reliability of floors under impact vibration. *Canadian Journal of Civil Engineering*, *14*(5), 683-689. https://doi.org/10.1139/l87-098

Fragiacomo, M. (2005). A finite element model for long-term analysis of timber-concrete composite beams. *Structural Engineering and Mechanics, 20*(2), 173-189. https://doi.org/10.12989/sem.2005.20.2.173

Fragiacomo, M., & Ceccotti, A. (2006). Long-term behavior of timber-concrete composite beams. I: Finite element modeling and validation. *Journal of Structural Engineering, 132*(1),13-22. https://doi.org/10.1061/(ASCE)0733-9445(2006)132:1(13)

Fragiacomo, M., & Lukaszewska, E. (2015). Influence of the construction method on the long-term behavior of timber-concrete composite beams. *Journal of Structural Engineering, 141*(10), 04015013. https://doi.org/10.1061/(ASCE)ST.1943-541X.0001247

Fragiacomo, M., Balogh, J., To, L., & Gutkowski, R. M. (2014). Three-dimensional modeling of long-term structural behavior of wood-concrete composite beams. *Journal of Structural Engineering, 140*(8), A4014006. https://doi.org/10.1061/(ASCE)ST.1943-541X.000090

Frangi, A., & Fontana, M. (2003). Elasto-plastic model for timber-concrete composite beams with ductile connection. *Structural Engineering International, 13*, 47-57. https://doi.org/10.2749/101686603777964856

Fridley, K. J., Hong, P., & Rosowsky, D. V. (1997). Time-dependent service-load behavior of wood floors: Experimental results. *Journal of Structural Engineering, 123*(6), 836-843. https://doi.org/10.1061/(ASCE)0733-9445(1997)123:6(836)

Fridley, K. J., Rosowsky, D. V., & Hong, P. (1998). Time-dependent service-load behavior of wood floors: Analytical model. *Computers & Structures, 66*(6), 847-860. https://doi.org/10.1016/S0045-7949(97)00074-6

Gerber, A. R. (2016). *Timber-concrete composite connectors in flat-plate engineered wood products*. [Master's thesis, University of British Columbia]. https://doi.org/10.14288/1.0300229

Grosse, M., Hartnack, R., Lehmann, S., & Rautenstrauch, K. (2003). Modellierung von diskontinuierlich verbundenen Holz-Beton-Verbundkonstruktionen / Teil 1: Kurzzeittragverhalten [Modelling of discontinuously connected wood-concrete composite structures / Part 1: Short-term load-bearing behavior]. *Bautechnik, 80*(8), 534-541. https://doi.org/10.1002/bate.200304120

Grosse, M., Hartnack, R., & Rautenstrauch, K. (2003). Modellierung von diskontinuierlich verbundenen Holz-Beton-Verbunddecken / Teil 2: Langzeittragverhalten [Modelling of discontinuously connected wood-concrete composite structures / Part 1: Long-term load-bearing behavior]. *Bautechnik, 80*(10), 693-701. https://doi.org/10.1002/bate.200305110

Gutkowski, R. M., Balogh, J., & To, L. G. (2010). Finite-element modeling of short-term field response of composite wood-concrete floors/decks. *Journal of Structural Engineering, 136*(6), 707-714. https://doi.org/10.1061/(ASCE)ST.1943-541X.0000117

Gutkowski, R. M., Brown, K., Shigidi, A., & Natterer, J. (2008). Laboratory tests of composite wood–concrete beams. *Construction and Building Materials, 22*(6), 1059-1066. https://doi.org/10.1016/j.conbuildmat.2007.03.013

Hadigheh, S. A., McDougall, R., Wiseman, C., & Reid, L. (2021). Evaluation of composite action in cross laminated timber-concrete composite beams with CFRP reinforcing bar and plate connectors using Digital Image Correlation (DIC). *Engineering Structures*, 232: 111791. https://doi.org/10.1016/j.engstruct.2020.111791

Hong, K. E. M. (2017). *Structural performance of nail-laminated timber-concrete composite floors*. [Master's thesis, University of British Columbia].

Hu, L. (2002). Implementation of a new serviceability design procedure for wood based floors. *Canadian Forest Service Report No. 9*. Forintek Canada Corp.

Hu, L. J., & Chui, Y. H. (2006). Development of a design method to control vibrations induced by normal walking action in wood-based floors. In *Proceedings of the 8th World Conference on Timber Engineering* (Vol. 2, pp. 217-222).

Hu, L., Audair, S. C., Chui, Y. H., Ramzi, R., Gagnon, S., Mohammad, M., Ni, C., & Popovski, M. (2016). Design method for controlling vibrations of wood-concrete composite floor systems. In *Proceedings of World Conference on Timber Engineering*.

Jackson, R., Luthi, T., and Boyle, I. (2017). Mass timber: Knowing your options. STRUCTURE magazine: 22-25. https://www.structuremag.org/?p=10916

Jiang, L., Hu, L., & Chui, Y. H. (2004). Finite-element model for wood-based floors with lateral reinforcements. *Journal of Structural Engineering*, *130*(7), 1097-1107. https://doi.org/10.1061/(ASCE)0733-9445(2004)130:7(1097)

Jiang, Y., & Crocetti, R. (2019). CLT-concrete composite floors with notched shear connectors. *Construction and Building Materials, 195*, 127-139. https://doi.org/10.1016/j.conbuildmat.2018.11.066

Jones, R. A., & Spies, H. R. (1978). Wood frame floor systems. *Council Notes, 03(01), 2-8*.

Jorge, L. F. C., Lopes, S. M. R., & Cruz, H. M. P. (2011). Interlayer influence on timber-LWAC composite structures with screw connections. *Journal of Structural Engineering, 137*(5), 618-624. https://doi.org/10.1061/(ASCE)ST.1943-541X.0000299

Kavaliauskas, S., Kazimieras Kvedaras, A., & Valiunas, B. (2007). Mechanical behaviour of timber-to-concrete connections with inclined screws. *Journal of Civil Engineering and Management, 13*(3), 193-199. https://doi.org/10.3846/13923730.2007.9636437

Khorsandnia, N., Valipour, H., & Crews, K. (2014). Structural response of timber-concrete composite beams predicted by finite element models and manual calculations. *Advances in Structural Engineering, 17*(11), 1601-1621. https://doi.org/10.1260/1369-4332.17.11.1601

Khokhar, A. M. (2004). *Influence of bracing stiffness on performance of wooden floors*. [Master's thesis, University of New Brunswick].

Khokhar, A., & Chui, Y. H. (2019). Ribbed-plate approach to predict static and dynamic responses of timber floor with between-joist bracing. In *Proceedings of World Conference of Timber Engineering, WCTE 2016*.

Kreuzinger, H. (1999). Platten, scheiben und schalen–ein berechnungsmodell für gängige statikprogramme. *Bauen mit Holz, 1*, 34-39.

LeBorgne, M. R., & Gutkowski, R. M. (2010). Effects of various admixtures and shear keys in wood–concrete composite beams. *Construction and Building Materials, 24*(9), 1730-1738. https://doi.org/10.1016/j.conbuildmat.2010.02.016

Leichti, R. J., Falk, R. H., & Laufenberg, T. L. (1990). Prefabricated wood I-Joists: An industry overview. *Forest Products Journal, 40*(3), 15-20.

Liu, C. (2016). *Modelling of timber-concrete composite structures subjected to short-term monotonic loading*. [Master's thesis, University of Toronto].

Lopes, S., Jorge, L., & Cruz, H. (2012). Evaluation of non-linear behavior of timber–concrete composite structures using FE Model. *Materials and Structures, 45*(5), 653-662. https://doi.org/10.1617/s11527-011-9787-9

Loulou, L. (2013). *Durability of a mixed wood-concrete assembly bonded under water loading*. [Doctoral thesis, Université Paris-Es].

Lukaszewska, E., Fragiacomo, M., & Johnsson, H. (2010). Laboratory tests and numerical analyses of prefabricated timber-concrete composite floors. *Journal of Structural Engineering, 136*(1), 46-55. https://doi.org/10.1061/(ASCE)ST.1943-541X.0000080

Marchi, L., Scotta, R., & Pozza, L. (2017). Experimental and theoretical evaluation of TCC connections with inclined self-tapping screws. *Materials and Structures, 50*(3):180. https://doi.org/10.1617/s11527-017-1047-1

McCutcheon, W. J. (1984). Defections of uniformly loaded floors: A beam-spring analog. *Research Paper FPL449*, U.S.D.A. Forest Product Laboratory.

Mirdad, M. A. H. (2020). *Structural performance of mass timber panel-concrete (MTPC) composite floor system with inclined self-tapping screws and an insulation layer*. [Doctoral thesis, University of Alberta].

Mirdad, M. A. H., & Chui, Y. H. (2019). Load-slip performance of mass timber panel-concrete (MTPC) composite connection with self-tapping screws and insulation layer. *Construction and Building Materials, 213*, 696-708. https://doi.org/10.1016/j.conbuildmat.2019.04.117

Mirdad, M. A. H., & Chui, Y. H. (2020a). Strength prediction of mass-timber panel-concrete composite connection with inclined screws and a gap. *Journal of Structural Engineering, 146*(8), 04020140. https://doi.org/10.1061/(ASCE)ST.1943-541X.0002678

Mirdad, M. A. H., & Chui, Y. H. (2020b). stiffness prediction of mass timber panel-concrete (MTPC) composite connection with inclined screws and a gap. *Engineering Structures, 207*, 110215 https://doi.org/10.1016/j.engstruct.2020.110215

Mirdad, M. A. H., Chui, Y. H. & Tomlinson, D. (2021). Capacity and failure mode prediction of mass timber panel-concrete composite floor system with mechanical connectors. *Journal of Structural Engineering*, *147*(2), 04020338. https://doi.org/10.1061/(ASCE)ST.1943-541X.0002909

Mirdad, M. A. H., Chui, Y. H., Tomlinson, D., & Chen, Y. (2021). Bending stiffness and load-deflection response prediction of mass timber panel-concrete composite floor system with mechanical connectors. *Journal of Performance of Constructed Facilities*, *35*, 04021052. https://doi.org/10.1061/(ASCE)CF.1943-5509.0001620

Möhler, K. (1956). *Über das Tragverhalten von Biegeträgern und Druckstäben mit zusammengesetzten Querschnitten und nachgiebigen Verbindungsmitteln*. Technical University of Karlsruhe.

Monteiro, S. R. S., Dias, A. M. P. G., & Negrão, J. H. J. O. (2013). Assessment of timber-concrete connections made with glued notches: test set-up and numerical modeling. *Experimental Techniques, 37*(2), 50-65. https://doi.org/10.1111/j.1747-1567.2011.00804.x

Müller, K., & Frangi, A. (2018). 4-Point bending tests of timber-concrete composite slabs with micro-notches. In *Proceedings of World Conference on Timber Engineering, WCTE 2018*.

Negrão, J. H. J., Leitão de Oliveira, C. A., Maia de Oliveira, F. M., & Cachim, P. B. (2010). Glued composite timber-concrete beams. I: Interlayer connection specimen tests. *Journal of Structural Engineering*, *136*(10), 1236-1245. https://doi.org/10.1061/(ASCE)ST.1943-541X.0000228

Newmark, N. M., Siess, C. P., & Viest, I. M. (1951). Test and analysis of composite beams with incomplete interaction. *Proceedings of the Society for Experimental Stress Analysis, 9*(1), 75-92.

Nguyen, Q. H., Hjiaj, M., & Aribert, J. M. (2010). A space-exact beam element for time-dependent analysis of composite members with discrete shear connection. *Journal of Constructional Steel Research, 66*(11), 1330-1338. https://doi.org/10.1016/j.jcsr.2010.04.007

Nguyen, Q. H., Hjiaj, M., & Guezouli, S. (2011). Exact finite element model for shear-deformable two-layer beams with discrete shear connection. *Finite Elements in Analysis and Design, 47*(7), 718-727. https://doi.org/10.1016/j.finel.2011.02.003

Ohlsson, S.V. (1988). *Springiness and human induced floor vibration: A design guide: Document no. D-12*. Swedish Council for Building Research.

Ohlsson, S. V. (1991). Serviceability criteria – Especially floor vibration criteria. In J. Marcroft (Ed.), *Proceedings of the 1991 International Timber Engineering Conference, Volume I*. TRADA Technology Ltd.

Onysko, D. M. (1988). Performance and acceptability of wood floors – Forintek Studies. *National Research Council of Canada. Publication 28822*, Forintek Canada Corp.

Persaud, R., & Symons, D. (2006). Design and testing of a composite timber and concrete floor system. *The Structural Engineer, 21*, 22-30.

Pham, H. S. (2007). *Optimization and fatigue behavior of the wood-UHPFRC connection for new composite bridges, s.l.* [Doctoral thesis, École nationale des ponts et chaussées].

Philpot, T. A., Rosowsky, D. V., & Fridley, K. J. (1995). Reliability of wood joist floor systems with creep. *Journal of Structural Engineering*, *121*(6), 946-954. https://doi.org/10.1061/(ASCE)0733-9445(1995)121:6(946)

Rothoblaas. (2021). Silent floor-resilient underscreed foil made of bitumen and polyester felt. Rothoblaas. https://www.rothoblaas.com/products/soundproofing/soundproofing-layers/silent-floor

Setragian, Z. B. & Kusuma, C. C. (2018). *Moisture safety evaluation of CLT-concrete composite slab*. [Master's thesis, Chalmers University of Technology].

Schönborn, F., Flach, M., & Feix, J. (2011). Bemessungsregeln und ausführungshinweise für schubkerven im holz-beton-verbundbau [Design rules and details for construction of grooves in timber-concrete-composite constructions]. *Beton- und Stahlbetonbau, 106*(6), 385-393. https://doi.org/10.1002/best.201100013

Smith, I. (1980). Series type solutions for built-up beams with semi-rigid connections. In *Proceedings of Institution of Civil Engineers*. Part 2, 69(3):707-719. https://doi.org/10.1680/iicep.1980.2372

Thompson, E. G., Vanderbilt, M. D., & Goodman, J. R. (1977). FEAFLO: A program for the analysis of layered wood systems. *Computers & Structures*, *7*(2), 237-248. https://doi.org/10.1016/0045-7949(77)90042-6

Timoshenko, S., & Woinowsky-Krieger, S. (1959). *Theory of plates and shells*. McGraw Hill.

Van der Linden, M., L., R. (1999). *Timber-concrete composite floor systems*. [Doctoral thesis, Delft University of Technology]. http://resolver.tudelft.nl/uuid:6b2807c2-258b-45b0-bb83-31c7c3d8b6cd

Weckendorf, J., Hafeez, G., Doudak, G., & Smith, I. (2014). Floor vibration serviceability problems in wood light-frame buildings. *Journal of Performance of Constructed Facilities, 28*(6), A4014003. https://doi.org/10.1061/(ASCE)CF.1943-5509.0000538

Wisniewski, B., & Manbeck, H. B. (2003). Residential floor systems: Wood I-Joist creep behavior. *Journal of Architectural Engineering, 9*(1), 41-45. https://doi.org/10.1061/(ASCE)1076-0431(2003)9:1(41)

Yeoh, D., Fragiacomo, M., & Deam, B. (2011). Experimental behaviour of LVL–concrete composite floor beams at strength limit state. *Engineering Structures, 33*(9), 2697-2707. https://doi.org/10.1016/j.engstruct.2011.05.021

Yeoh, D., Fragiacomo, M., De Franceschi, M., & Buchanan, A. H. (2011). Experimental tests of notched and plate connectors for LVL-concrete composite beams. *Journal of Structural Engineering, 137*(2), 261-269. https://doi.org/10.1061/(ASCE)ST.1943-541X.0000288

Yeoh, D., Fragiacomo, M., De Franceschi, M., & Heng Boon, K. (2011). State of the art on timber-concrete composite structures: Literature review. *Journal of Structural Engineering, 137*(10), 1085-1095. https://doi.org/10.1061/(ASCE)ST.1943-541X.0000353

Zhang, C., & Gauvreau, P. (2015). Timber-concrete composite system with ductile connections. *Journal of Structural Engineering, 141*(7), 04014179. https://doi.org/10.1061/(ASCE)ST.1943-541X.0001144

Zhang, L., Chui, Y. H., & Tomlinson, D. (2020). Experimental investigation on the shear properties of notched connections in mass timber panel-concrete composite floors. *Construction and Building Materials, 234*, 117375. https://doi.org/10.1016/j.conbuildmat.2019.117375

Zhang, L., Zhang, S., & Chui, Y. H. (2021). Analytical evaluation to the timber-concrete composite beam connected with notched connections. *Engineering Structures, 227*, 111466. https://doi.org/10.1016/j.engstruct.2020.111466

# Appendix A – Gamma Method

***Effective bending stiffness (Section 6.1.2.2.1.2)***

The following is an example showing the determination of the effective bending stiffness of a 6 m long LWFF with a T-section:

Floor length:

$$L = 6000 \text{ mm}$$

Sheathing: Canadian softwood plywood 6 ply

$$b_1 = 610 \text{ mm}; h_1 = 18.5 \text{ mm}$$

$$E_1 I_1 = 1.3 \times 10^6 \text{ MPa/mm} \cdot 610 \text{ mm} = 7.9 \times 10^8 \text{ N} \cdot \text{mm}^2$$

$$E_1 A_1 = 47\,000 \text{ N/mm} \cdot 610 \text{ mm} = 2.9 \times 10^7 \text{ N}$$

Joist: Lumber SPF No. 2, 2x10, spaced at 610 mm

$$E_2 = 9500\text{MPa}; b_2 = 38 \text{ mm}; h_2 = 235 \text{ mm}$$

$$A_2 = b_2 h_2 = 4940 \text{ mm}^2; I_2 = b_2 {h_2}^3/12 = 7.0 \times 10^6 \text{ mm}^4$$

$$E_2 I_2 = 3.9 \times 10^{11} \text{ N} \cdot \text{mm}^2$$

$$E_2 A_2 = 8.5 \times 10^7 \text{ N}$$

Connection: Nails

$$s_1 = 300 \text{ mm}; K_1 = 3680 \text{ N/mm}$$

Gamma factor:

$$\gamma_1 = \left[1 + \frac{\pi^2 E_1 A_1 s_1}{K_1 l^2}\right]^{-1} = \left[1 + \frac{\pi^2 (2.9 \times 10^7 \text{ N})(300 \text{ mm})}{(3680 \text{ N/mm})(6000 \text{ mm})^2}\right]^{-1} = 0.6$$

Distance of the centre of the sections to the neutral axis:

$$a_2 = \frac{\gamma_1 E_1 A_1 (h_1 + h_2)}{2 \sum_{i=1}^{2} \gamma_i E_i A_i} = 21.7 \text{ mm}; a_1 = \frac{(h_1 + h_2)}{2} - a_2 = 105.1 \text{ mm}$$

Effective bending stiffness:

$$(EI)_{eff} = \sum_{i=1}^{3} (E_i I_i + \gamma_i E_i A_i {a_i}^2) = 6.2 \times 10^{11} \text{N} \cdot \text{mm}^2$$

This is equal to:

$$(EI)_{eff} = \frac{6.2 \times 10^{11} \text{ N} \cdot \text{mm}^2}{0.61 \text{ m}} = 1.0 \times 10^{12} \text{ N} \cdot \text{mm}^2/\text{m}$$

# Appendix B – Progressive Yielding Method

***Timber-concrete composite floor system design with mechanical connectors (Section 6.1.3.2.2.2)***

This appendix shows an example of designing a timber-concrete composite (TCC) system with mass timber panels (MTP) according to the progressive yielding method for long-term load duration, taking into account creep. This is described in Section 6.1.3.2.2.2, with the numerical values of geometric and material properties according to Figures 26 and 30.

Span and connector spacing:
Number of connector rows from mid-span, $r = 4$, at 500 mm spacing of span, $L = 4000\ \mathrm{mm}$
Therefore, $n_1 = 3500\ \mathrm{mm}$, $n_2 = 2500\ \mathrm{mm}$, $n_3 = 1500\ \mathrm{mm}$, $n_4 = 500\ \mathrm{mm}$

Concrete:
Dimensions: $h_c = 100\ \mathrm{mm}$, $b_c = 600\ \mathrm{mm}$
Therefore, $A_c = 60000\ \mathrm{mm}^2$, $I_c = 17.5 \times 10^6\ \mathrm{mm}^4$ (including cracking factor), $S_c = 10 \times 10^5\ \mathrm{mm}^3$,
Properties: $f_c' = 35\ \mathrm{MPa}$, $E_c = 26\,622 \times 0.35 = 9318\ \mathrm{MPa}$

Insulation thickness: $h_{in} = 0\ \mathrm{mm}$ (no insulation)

Mass timber:
Dimensions: $h_t = 130\ \mathrm{mm}$, $b_t = 600\ \mathrm{mm}$
Therefore, $A_t = 78\,000\ \mathrm{mm}^2$, $I_t = 110 \times 10^6\ \mathrm{mm}^4$, $S_t = 16.9 \times 10^5\ \mathrm{mm}^3$
Properties: $f_b = 18.3\ \mathrm{MPa}$, $f_v = 1.5\ \mathrm{N/mm}^2$, $E_t = 9500 \times 0.25 = 4750\ \mathrm{MPa}$

Connectors:
2 Cross-pairs of screws ($n = 4$) at an insertion angle of $45°$ and penetration length of $100\ \mathrm{mm}$ in the width of the beam. The yield force per screw is 15.3 kN, according to Mirdad and Chui (2019).
Therefore, the yield force $F_y = 4 \times 15.3\ \mathrm{kN} = 61.4\ \mathrm{kN}$,
and the elastic stiffness $k = 4 \times 0.25 \times 15.2\ \mathrm{kN/mm} = 15.2\ \mathrm{kN/mm}$.

Load:
Total factored load (dead and live load) is $w = 7.5\ \mathrm{kN/m}$.

Solution with the progressive yielding method:
The effective bending stiffness of the TCC system can be calculated using Equation 30 of the progressive yielding method: $EI_{eff} = 1300.3\ \mathrm{kNm}^2$.

Deflection limit:
For the specified load $w = 7.5\ \mathrm{kN/m}$, based on Equation 32, the sum of all the connector forces at cross-section, $X_{sum} = 65.3\ \mathrm{kN}$.

According to Equation 44, the vertical deflection of TCC under a specified load is $\Delta = 19.2\ \mathrm{mm}$. This is less than the deflection limit of $\Delta_a = L/180 = 22.2\ \mathrm{mm}$. Therefore, the deflection of TCC is within the allowable limit.

Connector capacity:
The effective connector force based on Equation 31 is $F_{y,eff} = X_1 = 25.5\ \mathrm{kN} < F_y = 61.4\ \mathrm{kN}$. Therefore, the first outermost connector will not yield for the specified applied load.

Member stress:
Based on Equations 33 to 42, the stresses in the concrete and timber are as follows:

Timber compression stress, $\sigma_{t,c} = -0.96\ \mathrm{N/mm^2}$,

Timber tension stress, $\sigma_{t,t} = 2.64\ \mathrm{N/mm^2}$,

Concrete compression stress, $\sigma_{c,c} = -2.04\ \mathrm{N/\ mm^2}$, and

Concrete tension stress, $\sigma_{c,t} = -0.14\ \mathrm{N/mm^2}$ (still in compression).

Timber resistance:
Bottom extreme fibre stress of timber, $\sigma_{t,t} = 2.64\ \mathrm{N/mm^2}$ is less than the timber bending strength, $f_b = 11.8\ \mathrm{N/mm^2}$. Therefore, the tensile stress of timber is within the limit of specified bending strength of timber.

Based on Equation 43, the shear stress of timber, $\tau_t = 0.22\ \mathrm{N/mm^2}$, is less than the timber shear strength, $f_v = 1.5\ \mathrm{N/mm^2}$. Therefore, the shear stress of timber is within the limit of specified shear strength of timber.

Concrete resistance:
Based on Equations 22 and 23, the top extreme fibre stress of concrete, $\sigma_{c,c} = -2.04\ \mathrm{N/mm^2}$, is less than the specified compressive strength of concrete, $f_c' = -35\ \mathrm{N/mm^2}$, and the bottom extreme fibre stress of concrete, $\sigma_{c,t} = -0.14\ \mathrm{N/\ mm^2} < 0.6\lambda\sqrt{f_c'} = 3.55\ \mathrm{N/mm^2}$. Therefore, the concrete compression and tension stress are within the limit of specified compression and modulus of rupture strength.

The distance of the neutral axis of concrete to the compression edge, $y_c = 107.2\ \mathrm{mm} > h_c = 100\ \mathrm{mm}$. Therefore, the concrete will be compressed at the bottom and will follow Case 2.

According to Equation 25, the resistance of concrete against the connector force, $X_{sum} = 65.3\ \mathrm{kN} < \alpha_1\beta_1 b_c h_c f_c' = 1029.9\ \mathrm{kN}$. As a result, the concrete will not crack under the normal force of the connector.

Vibration limit:
According to Equation 29, the allowable vibration control span is 5.4 m, which is larger than the designed TCC span of 4 m. Therefore, the TCC span under specified load is within the vibration limit.

Comparison with the Gamma method:
If the Gamma method is used to calculate the effective bending stiffness, based on Equation 1 $EI_{eff} = 1219.7\ \mathrm{kNm^2}$, which is within 6% of the effective bending stiffness calculated using the progressive yielding method.

Based on the calculated effective bending stiffness, the mid-span deflection can be calculated using Equation 5, the stresses in the member using Equation 2, and the connector capacity using Equation 4.

## Appendix C – Discrete Bond Model

***Internal actions in discrete connected composite floors (Section 6.1.3.3.4)***

The procedure used to solve the deflection, relative slip, and internal actions in the composite floor in Figure 39 is shown here using the discrete bond model (Zhang, Zhang & Chui, 2021). The geometry and material properties of timber, concrete, and connections are as follows:

| **Timber** | **Concrete** | **Connections** |
|---|---|---|
| $E_t = 12\,000$ MPa | $E_c = 29\,500$ MPa | $k_1 = 0$ |
| $h_t = 130$ mm | $h_c = 90$ mm | $k_{2-7} = 6 \times 10^5$ N/mm |
| $A_t = 78\,000$ mm$^2$ | $A_c = 54\,000$ mm$^2$ | $k_8 = 0$ |
| $I_t = 1.0985 \times 10^8$ mm$^4$ | $I_c = 3.645 \times 10^7$ mm$^4$ | |

The floor span is $L = 6000$ mm.

As the floor has six connections, it can be partitioned into seven segments, as shown in Figure 41. The lengths for the segments are as follows:

$$l_1 = 550 \text{ mm}, \quad l_2 = 700 \text{ mm}, \quad l_3 = 700 \text{ mm}, \quad l_4 = 2100 \text{ mm},$$
$$l_5 = 700 \text{ mm}, \quad l_6 = 700 \text{ mm}, \quad l_7 = 550 \text{ mm}$$

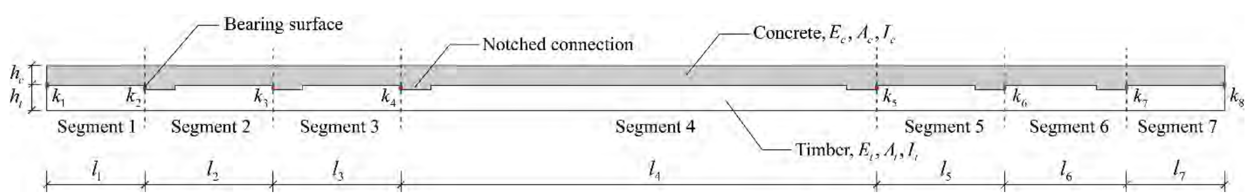


**Figure 41. Partitioning of the composite beam with notches**

The uniformly distributed load acting on the floor strip is

$$w = 3 \text{ N/mm}$$

The bending moment distribution along the floor under the uniformly distributed load can be expressed as

$$M(x) = \frac{wx}{2}(L - x)$$

The average external bending moment in each segment can be determined as follows:

$$M_1 = \frac{1}{l_1}\int_0^{l_1} M(x)dx = 2.32 \times 10^6 \text{ N/mm}, \qquad M_2 = \frac{1}{l_2}\int_{l_1}^{l_2} M(x)dx = 6.82 \times 10^6 \text{ N/mm},$$

$$M_3 = \frac{1}{l_3}\int_{l_2}^{l_3} M(x)\,dx = 10.50 \times 10^6 \text{ N/mm}, \qquad M_4 = \frac{1}{l_4}\int_{l_3}^{l_4} M(x)\,dx = 12.95 \times 10^6 \text{ N/mm},$$

$$M_5 = \frac{1}{l_5}\int_{l_4}^{l_5} M(x)\,dx = 10.50 \times 10^6 \text{ N/mm}, \qquad M_6 = \frac{1}{l_6}\int_{l_5}^{l_6} M(x)dx = 6.82 \times 10^6 \text{ N/mm},$$

$$M_7 = \frac{1}{l_7}\int_{l_6}^{l_7} M(x)\,dx = 2.32 \times 10^6 \text{ N/mm}$$

The eccentricity of axial forces is

$$e = \frac{E_t I_t h_c - E_c I_c h_t}{2(E_c I_c + E_t I_t)} = -4.42 \text{ mm}$$

The parameter matrix $\Theta$ can be determined as

$$\Theta = \begin{bmatrix} 3.71 & & & & & & \\ & 4.73 & & & & & \\ & & 4.73 & & & & \\ & & & 14.18 & & & \\ & & & & 4.73 & & \\ & & & & & 4.73 & \\ & & & & & & 3.71 \end{bmatrix} \times 10^{-6} \frac{\text{mm}}{\text{N}}$$

The vector $\{\Lambda\}$ can be determined as

$$\{\Lambda\} = [0.059 \quad 0.220 \quad 0.338 \quad 1.250 \quad 0.338 \quad 0.220 \quad 0.059]^T \text{ mm}$$

The matrices $W_1$ and $W_2$ can be expressed as

$$W_1 = \begin{bmatrix} 0 & 1 & 0 & 0 & 0 & 0 & 0 \\ 0 & 0 & 1 & 0 & 0 & 0 & 0 \\ 0 & 0 & 0 & 1 & 0 & 0 & 0 \\ 0 & 0 & 0 & 0 & 1 & 0 & 0 \\ 0 & 0 & 0 & 0 & 0 & 1 & 0 \\ 0 & 0 & 0 & 0 & 0 & 0 & 1 \\ 0 & 6 \times 10^5 & 6 \times 10^5 & 6 \times 10^5 & 6 \times 10^5 & 6 \times 10^5 & 6 \times 10^5 \end{bmatrix}$$

$$W_2 = \begin{bmatrix} 1 & & & & & & \\ & 1 & & & & & \\ & & 1 & & & & \\ & & & 1 & & & \\ & & & & 1 & & \\ & & & & & 1 & \\ & & & & & & -6 \times 10^5 \end{bmatrix}$$

The stiffness matrix $K$ is

$$K = \begin{bmatrix} 0 & & & & & & \\ 0 & 1 & & & & & \\ 0 & 1 & 1 & & & & \\ 0 & 1 & 1 & 1 & & & \\ 0 & 1 & 1 & 1 & 1 & & \\ 0 & 1 & 1 & 1 & 1 & 1 & \\ 0 & 1 & 1 & 1 & 1 & 1 & 1 \end{bmatrix} \times 6 \times 10^5 \text{ N/mm}$$

According to Equations 48, 59, and 60, the slip vectors $S_1$, $S_2$, and $D$ can be solved as

$$\{S_1\} = [0.1275 \quad 0.1663 \quad 0.2047 \quad 0.6249 \quad 0.1330 \quad 0.0532 \quad -0.0688]^T \text{ mm}$$

$$\{S_2\} = [-0.0688 \quad 0.0532 \quad 0.1330 \quad 0.6249 \quad 0.2047 \quad 0.1663 \quad 0.1275]^T \text{ mm}$$

$$\{D\} = [0 \quad 0.0975 \quad 0.1604 \quad 0.5975 \quad 0.1604 \quad 0.0975 \quad 0]^T \text{ mm}$$

The axial forces in each segment can be determined using Equation 61 as

$$\{N\} = [0 \quad 41274 \quad 67873 \quad 84285 \quad 67873 \quad 41274 \quad 0]^T \text{ N}$$

Once the axial forces in the segments have been determined, the sum of bending moments in timber and concrete $M^{tot}(x)$ can be determined using Equation 71. The deflection of the floor can then be determined using Equation 70 where the moment distribution of the floor under a unit force acting at the location of $x = t$ is expressed as

$$\widehat{M}(x,t) = \begin{cases} (L-t)x/L, & 0 \le x \le t \\ (L-x)t/L, & t \le x \le L \end{cases}$$

The mid-span deflection of the floor is

$$\Delta(L/2) = \int_0^L \frac{\widehat{M}(x, L/2)M^{tot}(x)}{E_c I_c + E_t I_t} dx = 6.4 \text{ mm}$$

The relative slip between two layers at the left end of the floor is

$$\delta(0) = S_{11} - D_1 = 0.128 \text{ mm}$$

The relative slip between timber and concrete at any location along the floor is

$$\delta(t) = \delta(0) - \frac{h_c + h_t}{2(E_c I_c + E_t I_t)} \int_0^t M(x) dx + \left[ \frac{1}{E_c A_c} + \frac{1}{E_t A_t} + \frac{\left(\frac{h_c}{2} - e\right) h_c}{2E_c I_c} + \frac{\left(\frac{h_t}{2} - e\right) h_t}{2E_t I_t} \right] \int_0^t N(x) dx$$

The moment distributions in timber and concrete can be determined using Equations 62 and 63, and the stress distributions in timber and concrete can be determined using Equations 66, 67, 68, and 69.

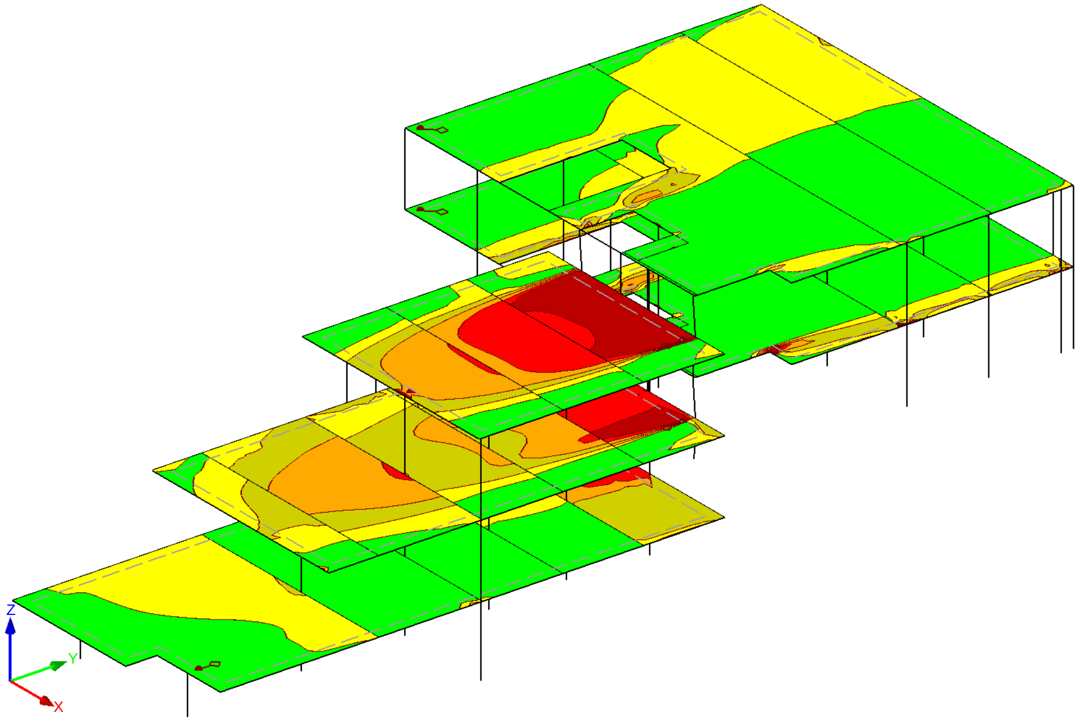


# CHAPTER 6.2

## Diaphragms


**Authors**

Daniel Moroder

Zhiyong Chen

**Reviewers**

Philip Line

Ghasan Doudak

Hans-Eric Blomgren

Jeremy Church

Andy Buchanan

# TABLE OF CONTENTS

## 6.2.1 Introduction

Floors and roofs mainly carry gravity loads by providing out-of-plane strength and stiffness (Chapter 6.1). They typically also possess in-plane strength and stiffness to allow for diaphragm action, thus being called diaphragms. Diaphragms are critical components of all buildings. They play a fundamental role in the framework of a structure, independent of the material used and the type of external action. Diaphragms not only transfer any horizontal load to the vertical lateral load-resisting system (LLRS) but also tie all structural and nonstructural elements together, providing integrity to a building. A loss of diaphragm action could lead to the partial or total collapse of a building due to instabilities among vertical load-resisting elements or due to a lack of horizontal load distribution into the LLRS. The following list summarises the roles of diaphragms (Moehle et al., 2010; Standards New Zealand, 2015), shown graphically in Figure 1.

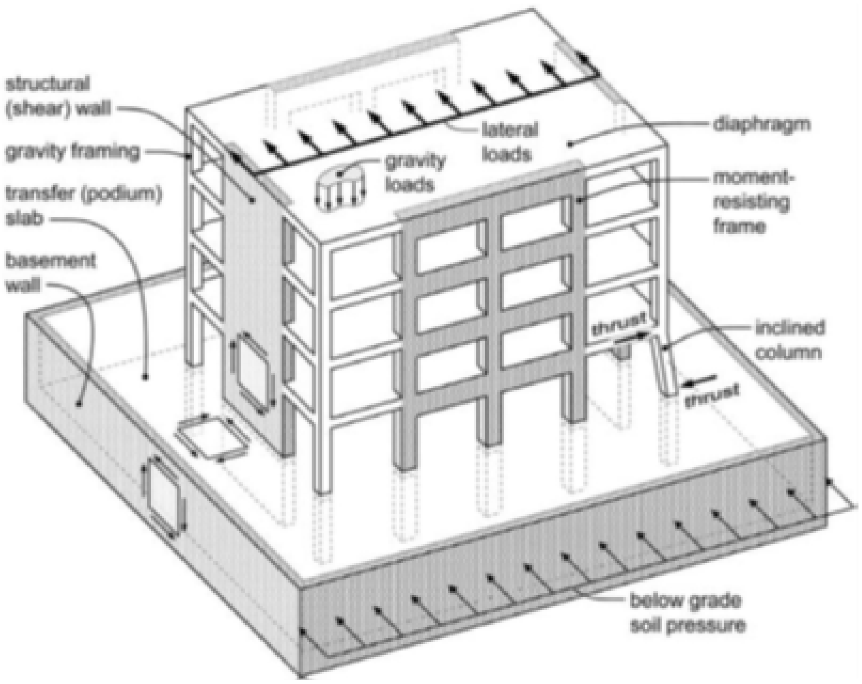


**Figure 1. Roles of diaphragms (Moehle et al., 2010)**

The roles of diaphragms are to

- **Transfer horizontal forces to the lateral load-resisting system**—such forces can be generated by wind actions or the seismic acceleration of floor masses or other elements connected to the floors;
- **Provide lateral support for vertical elements** to prevent columns buckling and walls running over several stories, as well as the torsional buckling of gravity beams;
- **Resist wall and façade out-of-plane forces** from the inertial forces generated by the mass within the elements, as well as wind pressures acting on the façade and other components attached to it;
- **Resist horizontal thrust** from inclined columns, ramps, and stairs;
- **Resist transfer forces** from displacement incompatibilities in the LLRS or due to changes in the vertical geometry of the structure, like setbacks or podiums, as well as concentrated forces;

- **Provide pull-back** forces to gravity- and lateral load-resisting elements during earthquake reversal; and
- **Resist soil loads** from walls bearing against slopes, or levels below grade.

This chapter introduces analytical models for wood-based diaphragms (i.e., wood frame, mass timber, and composite diaphragms) subjected to in-plane loads. These models allow users to assess the performance of the system and determine forces in the connections and deflections of the full assemblies when subjected to in-plane loads. Also, given the increased use of finite element (FE) models in design, this chapter additionally introduces appropriate FE modelling approaches for diaphragms.

## 6.2.2 Diaphragm Analysis

### *6.2.2.1 Diaphragms and Components*

Diaphragms can typically be categorised by their construction materials, as summarised in Figure 2. In the presence of concrete topping, which is typically monolithically poured in the field, diaphragms are typically categorised by the contribution of the concrete topping to the diaphragm action, as shown in Table 1.

| Timber diaphragms | Concrete diaphragms | Steel diaphrams | Composite diaphrams |
|---|---|---|---|
| • Wooden boards (traditional)<br>• Wood frame with wood sheathing<br>• Mass timber panels | • Cast-in-situ<br>• Pre-cast concrete | • Steel decks (mostly roofs) | • Timber-concrete composite<br>• Steel-concrete composite |

**Figure 2. Diaphragms categorised by materials**

**Table 1. Diaphragms categorised by concrete topping**

| Nonstructural topping | Structural topping |
|---|---|
| The concrete topping does not provide any diaphragm action and is merely used to add mass (i.e., to increase acoustic and vibration performance), to incorporate services, or to provide a level surface | The concrete topping resists the diaphragm action. Normally, the presence of concrete is used with composite action to resist gravity forces |

Past and current timber diaphragm types include

- **Transverse single boards (traditional)**: boards run perpendicular to the framing elements and are fixed with at least two nails at each crossing;
- **Diagonal boards (traditional)**: same as above, but the boards are inclined at 45° with respect to the framing elements. The board orientation and the use of two or more nails make this kind of diaphragm stronger and stiffer;
- **Double diagonal boards (traditional)**: boards are placed in two layers, the second running at 90° to the first. This layout provides much higher stiffness and strength than single diagonal boards;

- **Wood sheathing**: large plywood panels or Oriented Strand Board (OSB) nailed to framing elements, commonly known as light wood framing.
- **Mass timber panels**: engineered wood panels like Cross-Laminated Timber (CLT), Glued Laminated Timber (glulam), Laminated Veneer Lumber (LVL), Nail-Laminated Lumber (NLT), and Dowel-Laminated Lumber (DLT). Larger element dimensions and high strength values make these diaphragms well suited for multi-storey timber buildings.
- **Timber-concrete composite:** timber floors made of wood panels on joists or mass timber panels with a concrete topping, which act together as a diaphragm.

Framing elements of the above-mentioned diaphragms can be made of sawn lumber, glulam, or structural composite lumber, as well as built-up members like I-beams, trusses, etc. Individual panels are connected by metal fasteners like nails, screws, and staples; by adhesives; or by a combination of both. Information regarding the performance and design principles of traditional diaphragms, which are not the focus of this chapter, appears in Elliott (1979), Jephcott and Dewdney (1979), and Dean (1982). However, some of the modelling methods and considerations discussed in this chapter also apply to traditional diaphragms.

The recent availability of engineered mass timber products has led to new diaphragm systems, referred to in the following pages as 'mass timber' diaphragms. Wood frame diaphragms involve nailing individual boards or sheeting panels to framing elements (Figure 3, left), while mass timber diaphragms connect together large mass timber panels (Figure 3, right). The mass timber panels carry both gravity and horizontal loads and do not require additional framing elements to resist vertical loads, to transfer shear forces between panels, or to introduce axial loads into a diaphragm. For the diaphragm action, panels can be connected via a myriad of connection details (refer to Section 6.2.6; Karacabeyli & Gagnon, 2019). Because of their larger available size and increased strength and stiffness, mass timber panels open the possibility of building larger and taller timber buildings.

**Figure 3. Examples of wood frame diaphragm (Courtesy of www.continuingeducation.construction.com) and mass timber diaphragm (Courtesy of www.xlam.co.nz), with schematic cross sections**

Diaphragms can be made from many different materials (Figure 2), but their main components can be grouped as follows (see Figures 4 and 5): (a) plate elements, e.g., panels; (b) chord beams; (c) collectors; (d) drag/strut beams; and (e) connections to the lateral load-resisting system. These diaphragm components are best explained on the basis of the horizontal girder analogy (Figure 6), where the 'web' of the girder is made of plate elements and the 'flanges' consist of the chord beams. The plate elements, with possible openings, transfer the unit shear forces (forces per unit length), while the chord beams resist bending in the diaphragm via compression and tension forces. Timber diaphragms made of several single panels need to be connected by fasteners to guarantee the force transfer.

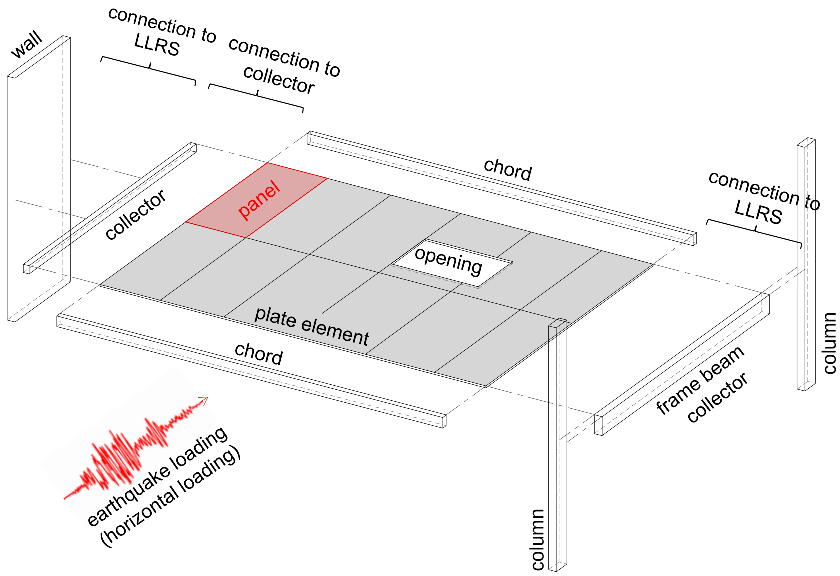


**Figure 4. Definitions of diaphragm components**

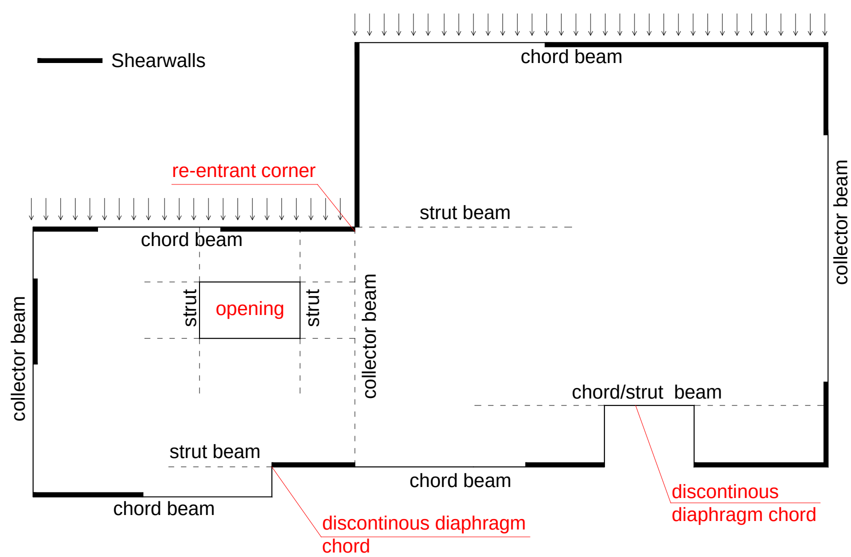


**Figure 5. Irregular floor geometry with typical diaphragm components**

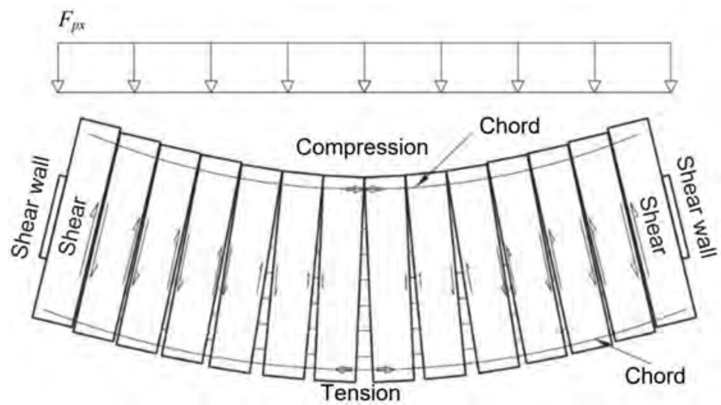


**Figure 6. Beam analogy for a diaphragm (Ghosh et al., 2017)**

Around openings and re-entrant corners, strut (or drag) beams collect shear forces from the disturbed area and anchor them to adjacent parts of the diaphragm. These parts are commonly referred to as sub-diaphragms or transfer diaphragms, as shown in Figure 7 (not to be confused with diaphragms which resist transfer forces from displacement incompatibilities. See Diekmann, 1995; Malone and Rice, 2012; Fanella and Mota, 2018; and Section 6.2.2.4). Irregularities often require reduced fastener spacing, increased reinforcement, or the use of thicker framing elements, but the sub-diaphragms are essentially designed as regular diaphragms. The resultant shear forces in the diaphragm have to be collected and transferred to the LLRS via the collectors (i.e., collector regions or beams). The connections of the collector to the LLRS must be designed properly, as it is an essential part of the load path into the foundations.

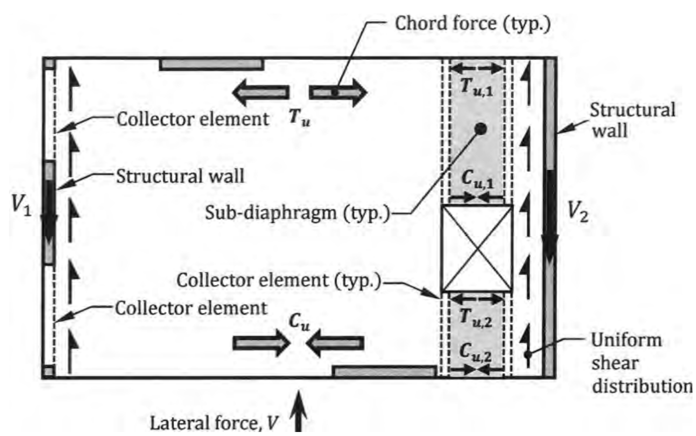


**Figure 7. Force distribution in a diaphragm with an opening (Fanella and Mota, 2018)**

### 6.2.2.2 Diaphragm Loads

Typically, diaphragm loads can be categorised as seismic loads, wind loads, or transfer forces, as well as concentrated forces from inclined columns or from the restraint of vertical elements in general. Transfer forces can be treated like imposed displacements from the LLRS and have the same effects as concentrated forces. One can further differentiate these actions by the type of load application: area (surface) loads, line loads, and concentrated loads. When using FE models, the actual force application should be modelled. Table 2 summarises how to model common loads on diaphragms for purposes of analysis.

**Table 2. Sources of loads on diaphragms with corresponding idealised load type on diaphragm**

| Load type | Concentrated loads [force] | Uniformly distributed line load [1] [force per length] | Uniformly distributed area load [force per area] |
|---|---|---|---|
| Seismic action | | √ | √ |
| Transfer/Compatibility | √ [2] | | |
| Wind | √ | √ | |
| Soil/water pressure | √ | √ | |
| Buckling restrain | √ [2] | | |
| Sloping columns | √ [2] | | |

[1] Uniformly distributed line loads applied on the compression and/or tension edge of the diaphragm. Some standards, like ASCE 7-16 (American Society of Civil Engineers, 2016), specifically require wind loads to be applied at both the tension and compression edges.

[2] If the force is introduced via a collector beam, then it can be idealised as a uniformly distributed line load along the ends of the diaphragm.

A comparative study by Moroder (2016) shows that in wood frame diaphragms, the type of load application does not influence the load path as long as forces are introduced and distributed via the framing members (see Section 6.2.2.3). In mass timber diaphragms, force introductions along the diaphragm edges generate longitudinal stresses in the diaphragm panels and create force components perpendicular to the panel edges, to be resisted by the connections. Also, longitudinal stresses must be transferred along the panels to activate diaphragm portions away from the point of force introduction.

### 6.2.2.3 Complexities in the Wind Design of Diaphragms

Loads applied to a diaphragm edge, from a combination of wind suction and internal pressure, for example, do not necessarily activate the whole diaphragm. The load paths between framing elements must be guaranteed, as otherwise the force components perpendicular to the panel edges can pull the diaphragm elements apart. Establishing load paths from the diaphragm edges into the diaphragm body can be done in one of the following ways, as illustrated in Figure 8:

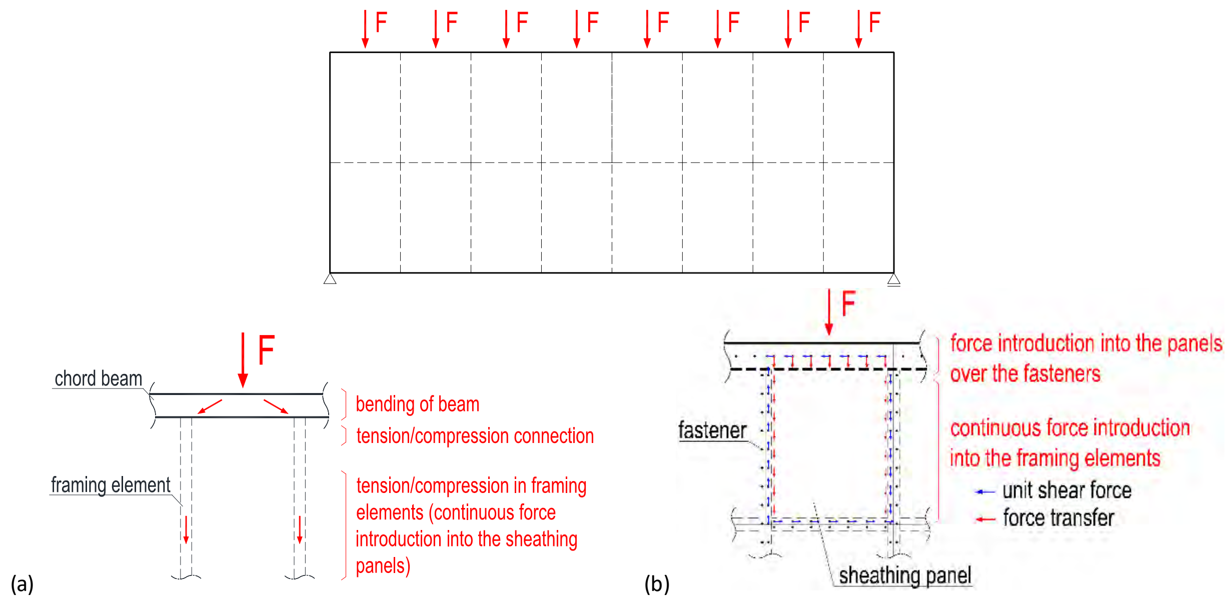


**Figure 8. Force transfer of wind loads in the diaphragm via (a) chord beam and (b) panels**

**Force transfer via chord beam (wood frame diaphragms only) (see Figure 8[a]):**

The chord beam resists the forces in bending (in the diaphragm in-plane direction) and transfers these forces into the framing members parallel to the load direction. Since this force can act in both tension and compression, there must also be a tension connection between the chord beam and the framing members. The framing elements continuously transfer the axial load into the sheathing panels. Splices in the joists or blocking elements are designed to account for the demand from both the tension and compression forces.

**Force transfer via sheathing panels (wood frame and mass timber diaphragms) (see Figure 8[b])**:

Force is introduced from the chord beam directly into the sheathing panels, requiring the fasteners to resist forces perpendicular to the panel edges. Since the fasteners already need to resist the unit shear force (blue arrows) from the diaphragm action, it is necessary to check if they can also resist the additional load component (red arrows) from the direct load introduction. The additional force component normally also requires an increased edge distance among the fasteners. This mechanism also creates normal panel stresses, which need to be accounted for in design.

A simple approach to account for the resultant force, which covers both the unit shear force and the additional transfer force component, is to reduce the diagram depth and therefore increase the unit shear force in the panel fasteners. The National Appendix to Eurocode 5 (Deutsches Institut für Normung, 2010) adopts this approach, which requires the reduction of the effective diaphragm depth to half the actual depth for force introductions along one edge or to a quarter of the actual depth for force introduction along both edges.

### *6.2.2.4 Complexities in the Seismic Design of Diaphragms*

Table 3 summarises the three key aspects of the seismic design of timber diaphragms according to loading codes and timber design standards for different jurisdictions.

**Table 3. Comparison of design codes for the seismic design of timber diaphragms**

| | Europe EN 1995:2008 and EN 1998:2010 | Italy NTC 2018 | Switzerland SIA 265:2003 and SIA 261:2003 | New Zealand NZS3603:1993 and NZS1170.5: 2004 | Canada O86-19 and NBCC 2015 | USA ASCE 7-16, IBC 2021 and SDPWS 2021 |
|---|---|---|---|---|---|---|
| Elastic/ yielding diaphragms | No explicit provisions | Allows diaphragms to be designed to yield, as long as diaphragm fasteners follow ductile behaviour (provides prescriptive rules to achieve this) | No explicit provisions | Elastic only | Elastic only | Elastic and yielding |
| Capacity design provisions | No explicit overstrength factors | Overstrength factors for high and medium ductile structures | Overstrength factor of 1.2 | Overstrength factor of 1.6 | No explicit overstrength factors | Overstrength factors for collector beams [2]; special provisions for the anchorage details |
| Flexible diaphragm definition [1] | $\Delta_{diaphragm} \geq 1.1\ \Delta_{LLRS}$ | | No information provided | $\Delta_{diaphragm} \geq 2\ \Delta_{LLRS}$ | No information provided | $\Delta_{diaphragm} \geq 2\ \Delta_{LLRS}$ |

[1] $\Delta_{diaphragm}$ = deformation of the diaphragm at the storey of interest; $\Delta_{LLRS}$ = interstorey deformation of the LLRS at the storey of interest;
[2] Structures with light-frame shear walls are exempt from this rule, i.e., collector beams are designed with the standard load combination.

### Elastic or ductile diaphragm design

In most countries, as indicated in Table 3, diaphragms should be designed elastically. This implies that they should be able to resist probable design loads and redistribute these loads within themselves in a manner compatible with the assumptions used for LLRS design. Some localised plasticity in the diaphragm may be acceptable, if it does not alter the basic assumption of the diaphragm mechanism and if the gravity resisting functions of the diaphragm elements are not compromised to prevent progressive collapse.

### Capacity design

All the above codes and standards require the application of capacity design principles for the design of seismic resistant buildings, but do not always provide specific overstrength factors (Table 3).

To guarantee that local plasticity in diaphragms occurs in ductile elements only if needed and does not cause any detrimental effects, all non-ductile diaphragm components (wooden sheathing, chord and collector beams, connections with stocky bolts or cold drawn/hardened steel like type 17 screws, etc.) must theoretically be designed based on capacity design principles (i.e., for the overstrength of the ductile fasteners of the diaphragm panel splices). However, the practical application of these principles is complex. Therefore, there should be some margins between the ductile sheathing fasteners and the non-ductile capacity-protected elements, even if not adhering to strict capacity design principles. To do this, either 1.2 times the value of the ductile floor forces or the full elastic floor forces, whichever are less, can help establish the demand on non-ductile diaphragm components. Using this second level of capacity protection might lead to high demand in the capacity protected diaphragm elements. This demand need not be larger than that derived from an elastic analysis.

**Diaphragm flexibility**

The definition of flexible and rigid floor diaphragm behaviour (Figure 9) has always been a point of discussion, especially for wood frame construction. The flexibility of the floor diaphragm can change the dynamic response of the whole building (Chen, Chui, & Ni, 2013; Moroder, 2016), as well as the impacts on the distribution of lateral forces into the LLRS, as known from first principles (Chen, Chui, Mohammad et al., 2013; Chen, Chui, Mohammad et al., 2014; Chen, Chui, Ni et al., 2014). The standard assumption is that flexible diaphragms distribute loads in proportion to tributary areas, whereas rigid diaphragms distribute loads to the lateral load-resisting elements in proportion to their stiffness. For the latter, one must also consider torsional effects because of possible eccentricities between the centre of stiffness and the centre of mass. Figure 9 schematically shows the diaphragm behaviour as rigid, flexible, or semirigid, as a function of its deflection relative to the vertical LLRS.

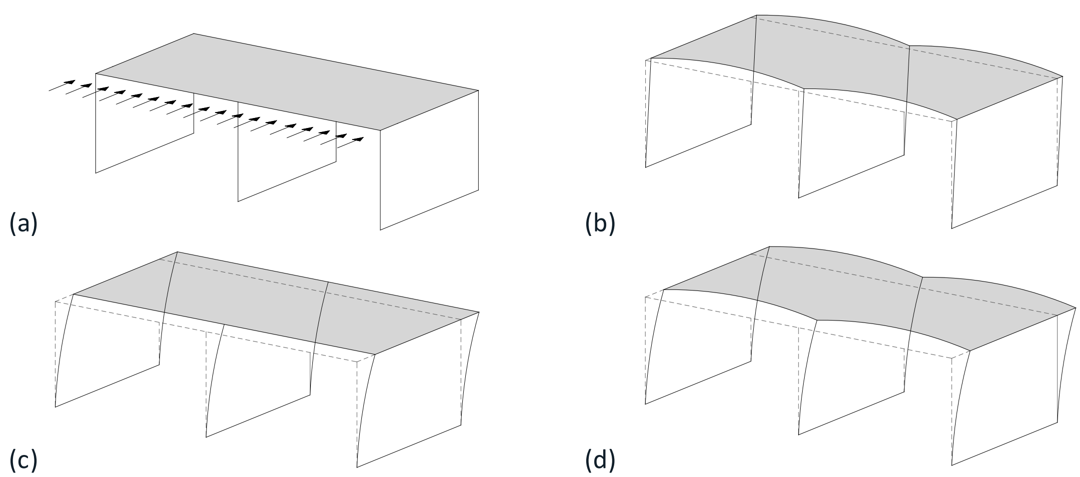

**Figure 9. Diaphragm behaviour: (a) diaphragm loading, (b) flexible diaphragm ($\Delta_{diap} \gg \Delta_{LLRS}$), (c) rigid diaphragm ($\Delta_{diap} \ll \Delta_{LLRS}$), and (d) semirigid diaphragm ($\Delta_{diap} \cong \Delta_{LLRS}$)**

Definitions of diaphragm flexibility vary widely (see Table 3 and Figure 10), and the rationales for the limits are mostly unknown (Sadashiva et al., 2012). Some timber design standards provide prescriptive detailing rules for rigid diaphragms, but they do not necessarily apply to modern floor materials and panel layouts. Since interstorey drifts and individual diaphragm deflections vary along the height of a building, diaphragms could be defined as flexible for some storeys and rigid for others. This causes some complexity in designing taller structures, and its actual application by practitioners is questionable. It is also unclear for which force demand to calculate the diaphragm deflections, considering that a static analysis normally under-predicts the values determined from nonlinear time history analysis. Code provisions typically apply to single-storey structures, with more sophisticated analysis methods required to analyse taller ones. A possible alternative is a global definition of diaphragm stiffness based on the diaphragm deflection and interstorey drift at the mid-height of the structure, as suggested by Fleischman and Farrow (2001). This provides an average value of flexibility which could be used for design.

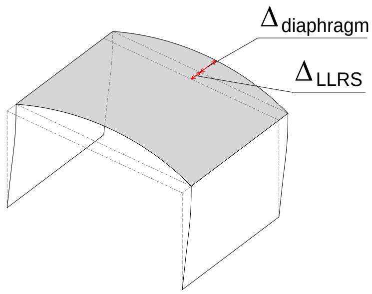


A diaphragm is flexible if

ASCE 7-16, NZS 1170.5:2004:
$\Delta_{diaphragm} \geq 2\ \Delta_{LLRS}$

Eurocode 8, NTC 2008:
$\Delta_{diaphragm} \geq 1.1\ \Delta_{LLRS}$

**Figure 10. Diaphragm flexibility according to international seismic codes**

Since the force distribution in the diaphragm and the LLRS is affected by the diaphragm flexibility, both stiffnesses must be assessed and the forces distributed as mentioned above. Timber diaphragms normally behave in a semirigid manner and can be designed by either an envelope method (Karacabeyli & Gagnon, 2019; Karacabeyli & Lum, 2022) or a specific analysis (Chen, Chui, Mohammad, et al., 2014).

In addition to the three key aspects mentioned above, higher mode effects, transfer forces, and displacement incompatibilities must also be considered in the design and analysis of diaphragms.

**Higher mode effects**

One difficulty in determining the inertial force demand in diaphragms is that static methods are based on a first mode response and therefore are unable to predict the effects of higher modes. Hence, higher mode effects are often ignored, or in the best case, accounted for with amplification factors providing peak responses along the building height (Rodriguez et al., 2002; Standards New Zealand, 2006; Priestley et al., 2007). More research is still required to define dynamic amplification factors for taller timber buildings. Meanwhile, designers must depend on more sophisticated analysis methods, like modal response spectrum or time history analysis, to adequately consider these effects, or alternatively rely on the limited literature available to determine any amplification factors. For example, the pseudo equivalent static analysis described in Standards New Zealand (2004b) considers the effect of higher modes by multiplying the equivalent static forces by the building overstrength for upper storeys and the peak ground acceleration for lower storeys.

**Transfer forces and displacement incompatibilities**

In seismic design, most forces are generated by the inertia of the diaphragms and contents. Inertial forces, however, are not the only action to be considered in diaphragms. Structures with nonuniform LLRSs up the building height can generate large transfer forces in diaphragms. These arise from the force redistribution and displacement incompatibilities between LLRSs with different stiffnesses. This effect is visible in podium structures, structures with dual LLRSs with walls and frames (see Figure 11), structures with walls of different lengths at different levels, or structures where walls are horizontally offset or missing between one floor and the next. Transfer forces cannot be determined directly from peak inertial forces using a modal response spectrum or time history analysis, since the obtained forces are not in equilibrium and do not maintain their sign. At the time of writing, there are no generally accepted diaphragm design methods which consider all the factors mentioned above. The few existing methods have yet to be validated for timber structures.

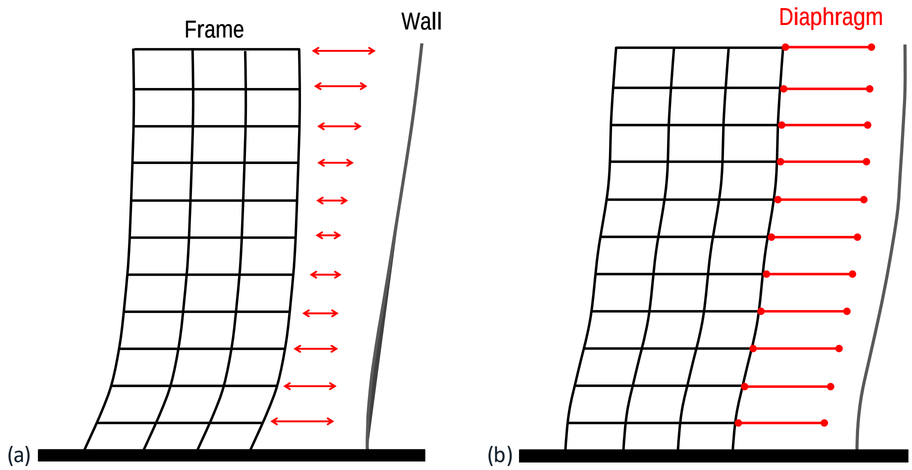


**Figure 11. Deformation shape of a frame and a wall: (a) under equivalent static earthquake loads and relative displacements, and (b) with the diaphragm acting as a link element**

Researchers have been investigating the effects of displacement incompatibilities between LLRSs and reinforced concrete diaphragms for many years (Fenwick and Fong, 1979; Matthews et al., 2003; Bull, 2004; Fenwick et al., 2010). Such incompatibilities can come from multiple sources: double curvature deflection of frame beams versus the simply supported beam deflection of the floors, beam elongation in frame beams, uplift and rocking or raking of walls, torsion of frame beams, etc. These incompatibilities could potentially lead to damage to the floors, including column separation or column push-out, and hence loss of support; wide cracks along the diaphragm perimeters; diaphragm topping delamination; and failure of diaphragm reinforcement. They can also prevent walls from rocking or raking, thus creating a stiffer structure and allowing for larger seismic loads. While these issues are prevalent in stiff diaphragms, such as those in concrete, they are of less importance in timber diaphragms, which tend to have enough local flexibility for localised displacement demands (Moroder, 2016; Moroder et al., 2014). Section 6.2.6 provides more information on diaphragm connections to the LLRS and associated displacement incompatibilities.

### *6.2.2.5 Synopsis of Diaphragm Analysis Methods*

Several different analysis methods and approaches listed in this guide can serve to analyse diaphragms. Designers need to decide which approach best suits the given problem and what level of accuracy is required. Table 4 provides a quick overview of available analysis methods applicable to timber diaphragms and the features that can be accounted for.

**Table 4. Requirements, allowed irregularities, and deformation estimation of different analysis methods**

| Analysis method | Continuous chord beams | Unsupported edges | Concentrated loads | Openings/re-entrant corners | Deformations |
|---|---|---|---|---|---|
| Deep beam/girder analogy | Required | Typically not allowed (certain standards provide specific guidance or tabulated reduced capacities) | Allowed | Not allowed | Calculated through equation for uniformly distributed loads |
| Shear field analogy | Required | Allowed under certain circumstances | Not allowed | Allowed | Not determined |
| Truss analogy | Required | Allowed under certain circumstances | Allowed | Allowed | Determined |
| FE analysis | Not required (panel elements can transfer chord forces) | Allowed | Allowed | Allowed | Determined |

### Simplified diaphragm analysis according to the deep beam or girder analogy

Both timber and concrete diaphragms are normally analysed according to the deep beam or girder analogy (shown schematically in Figure 12 and discussed further in Sections 6.2.3.2.1 and 6.2.5.2.1 for timber and concrete diaphragms, respectively). Such simplified analysis methods provide satisfactory results, as long as the floor is rectangular and does not contain substantial irregularities, such as floor openings, re-entrant corners, and concentrated forces. These influence the load path, leading to stress concentrations, and therefore require more specific designs. Although it is well known to engineers that steel and timber beams with openings, cut outs, concentrated forces, etc. (see Figure 12[b] and [c]), need local reinforcement because of stress concentrations, such effects in the design of irregular diaphragms are often neglected by designers. Like irregular beams, diaphragms need collector and strut beams to redistribute stresses to other parts of the diaphragms, as shown in Figure 12(d). In addition, such diaphragms are weakened and therefore more flexible, another effect often neglected in design.

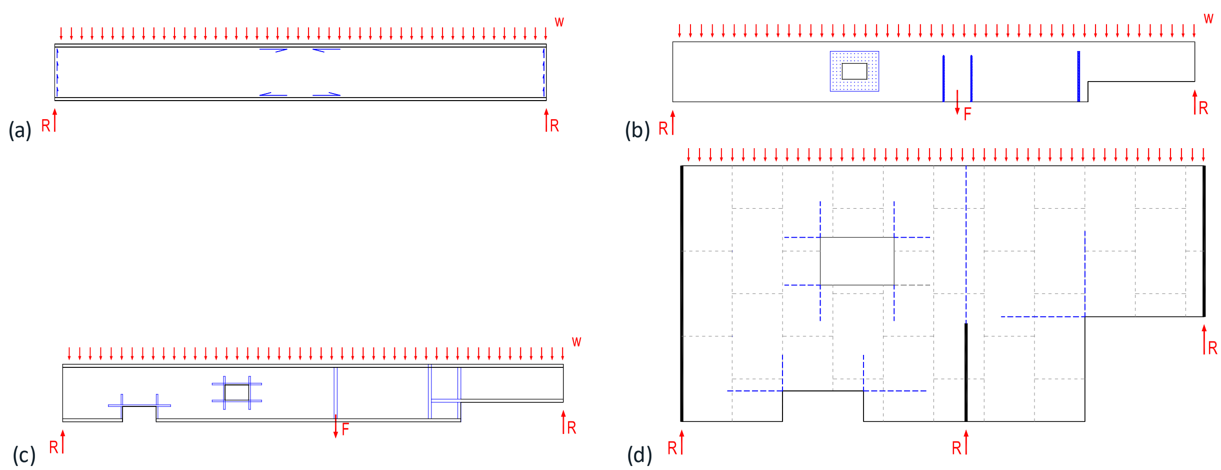


**Figure 12. Beam analogy (modified and adapted from Scarry [2015]): (a) steel beam; (b) reinforced timber beam and (c) reinforced steel with notches, openings, and concentrated forces; and (d) timber diaphragm with re-entrant corners, openings, and concentrated forces, as well as respective drag/strut beams**

Some irregular diaphragms can easily be solved with rational engineering methods, like subdividing diaphragms into regular sub-diaphragms or using the superposition of the forces from an equivalent regular diaphragm while adding forces from irregularities and discrete force introductions. Multiple irregularities will soon make this too complex, and more sophisticated analysis methods will be required.

**Shear field analogy**

The shear field analogy originates in aeronautical engineering and has been subsequently introduced into civil engineering. Nielsen introduced the method in 1979 for use with concrete walls (Kærn, 1979). Schulze and Schönhoff (1989) further applied its principles to the calculation of wood frame diaphragms. Eurocode 5 (European Committee for Standardization, 2008), its German National Appendix (Deutsches Institut für Normung, 2010), and the Swiss Timber Code SIA 265 (Swiss Society of Engineers and Architects, 2003b) are all explicitly based on the shear field analogy. Both the report by Kessel and Schönhoff (2001) and the Commentary on the former German Timber Standard DIN1052:2004 (Blaß et al., 2004) explain the method and its advantages and provide some practical examples.

**Equivalent truss model**

Before the widespread availability of FE software packages, there were several attempts to develop equivalent truss models to analyse diaphragms. The advantages of a truss model are that they allow the modelling of irregularities and concentrated forces and can account for the stiffness of the diaphragm.

Early methods for the analysis of diaphragms and shear walls with wooden sheathing panels assumed that the panel could act as a tension tie. These methods were later abandoned and refined through the shear field analogy, as described in Section 6.2.3.2.3; this, however, does not fall under the definition of a truss model. Further attempts have used equivalent tension or compression diagonals which simulate the panel shear stiffness, as well as the stiffness of the fasteners used in the panel splices. This leads to more realistic load paths, but requires the back-calculation of the shear forces in the individual sheathing panels from the axial forces in the diagonals. This method was later extended by Moroder (2016) for use in mass timber panels, by subdividing the larger panels with orthogonal and diagonal members; see Section 6.2.3.2.4.

Equivalent truss models have had a wider uptake in the analysis of concrete diaphragms than for timber. As early as the 1940s, Hrennikoff (1940) proposed the first method for such models: a grillage model, discussed in greater detail in Section 6.2.5.2.3. The approach is based on what is nowadays known as strut-and-tie analysis, an approach that found more widespread application only after its publication by Schlaich et al. (1987) and its subsequent adoption in concrete design standards (American Concrete Institute, 2019; European Committee for Standardization, 2005; Standards Australia, 2009; Standards New Zealand, 2006).

Strut-and-tie and grillage models consist of orthogonal and diagonal members, simulating concrete compression members and reinforcing steel resisting tension. Whereas simple strut-and-tie models can be carried out as desktop studies, more complex diaphragms soon need more refined grillage models, typically requiring analysis software. As a lower-bound kinematic model, the strut-and-tie analysis guarantees equilibrium, but the diaphragm might have undergone significant deformation, with concrete cracking and steel yielding, to reach the load path assumed in the model. The only approach that better approximates this nonlinear behaviour is nonlinear FE analysis.

**FE analysis**

FE analysis of diaphragms provides the most realistic load path and information on the general performance of the diaphragms, but it also requires a high degree of knowledge about the specific software package and a larger number of input parameters. Any FE analysis also requires a certain degree of post-processing to adequately determine the forces and displacement of components and connections.

For both concrete and timber diaphragms, a designer must determine the level of analysis required for the specific diaphragm. For timber diaphragms, this can range from elastic models with homogenous material parameters that have reduced shear stiffness to account for fastener stiffness to orthotropic panels connected with discrete nonlinear links to model the individual fasteners. Similarly, one can analyse concrete diaphragms elastically, typically leading to conservative results, or with multi-layered shell elements which also account for the nonlinear behaviour of both the concrete and the steel bars.

Although FE analysis is now commonly used in design offices, it is good design practice to predict or check the load paths and magnitude of forces with simplified desktop studies to ensure the analysis provides reasonable answers.

## 6.2.3 Wood Frame Diaphragms

### *6.2.3.1 Behaviour*

Typical wood frame floor assemblies consist of joists supported by main beams, which are then covered with wooden panels. Under diaphragm action, the typical assumption is that bending is taken by the chord beams acting as *flanges* and shear is resisted by the panels (diaphragm sheathing acting as *webs*). Experimental evidence has shown that assumed constant shear distribution along the depth of the diaphragm, as opposed to a parabolic constant shear distribution found according to first principles, is appropriate for the design of timber diaphragms (Applied Technology Council, 1981; Smith et al., 1986). To guarantee that the sheathing panels work as a splicing plate, all panel edges need to be connected to each other (blocked diaphragm). Typically, these connections use metallic fasteners like nails, screws, or staples in framing elements or specific blocking elements. Unblocked diaphragms withstand loads with a completely different mechanism, like the '*moment couple series'* normally used to design diaphragms made of transverse boards based on a Vierendeel truss analogy.

The aspect ratios (span to width) of diaphragms normally range from 1 to 5. For aspect ratios smaller than 1, sheathing panels and joists substantially contribute to bending resistance. Because of the high diaphragm depth, however, the resulting tension and compression forces will be relatively small, yielding to a conservative design (Prion & Lam, 2003). The upper limit of the aspect ratio normally aims to limit flexible diaphragm designs, rather than to set a limit to the analysis method itself.

The limiting factor in many timber diaphragms is the design of the sheathing-to-framing connections. These connections determine the ability of the diaphragm to resist loads and transfer them to the vertical LLRS. The fasteners in the panel splices can contribute to about 80% of diaphragm deflection and hence influence the load distribution in both the diaphragm and vertical LLRS (refer to Section 6.2.3.5). Forces in chord and collector beams are typically small, especially as compared to the out-of-plane gravity loads carried by the same members. Any splices, however, must still be detailed to transfer axial loads from diaphragm action.

### 6.2.3.2 Analytical Methods

#### 6.2.3.2.1 Girder Analogy

The deep beam or girder analogy commonly serves to analyse timber diaphragms with regular geometries. In this approach, the chord beams running along the diaphragm edges perpendicular to the load direction resist flexural tension and compression forces, while the diaphragm panels resist shear forces, as shown in Figure 13.

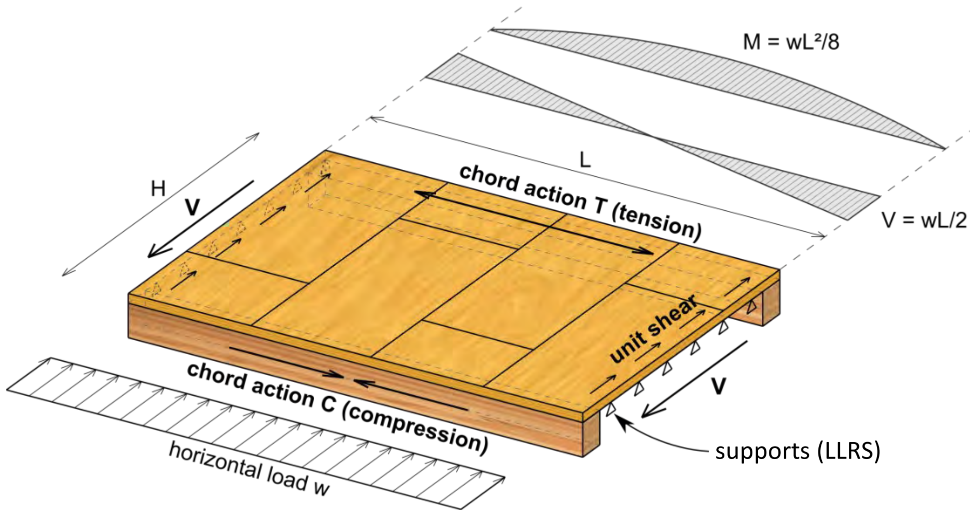


**Figure 13. Girder analogy**

The number, nature, and size of diaphragm irregularities, which would make this simplified method nonconservative, are seldom defined or quantified. In general, the diaphragm must be free of re-entrant corners, concentrated loads, big openings, or other irregularities causing stress concentrations for the girder analogy to fully apply. In spite of this, the girder analogy is commonly applied to irregular diaphragms, leading to local or global diaphragm damage due to stress concentrations and excessive diaphragm deformations.

The following equation determines the tension and compression forces in the chord beams:

$$\boldsymbol{T = C = \frac{M}{H} = \frac{wL^2}{8H}} \qquad [1]$$

where *T* is the tension force in the chord beam; *C* is the compression force in the chord beam; *w* is the uniformly distributed load; *L* is the diaphragm span; *H* is the diaphragm depth; and *M* is the moment from the uniformly distributed load.

The unit shear force, defined as the shear force per unit length (or shear flow), can be calculated as

$$\boldsymbol{v = \frac{V}{H} = \frac{wL}{2H}} \qquad [2]$$

where *v* is the unit shear force; and *V* is the shear force at diaphragm supports.

These equations can be modified to account for loads different from the uniformly distributed load. For diaphragms with a limited number of irregularities, hand methods based on first principles are still a feasible way to determine unit shear forces and axial forces in framing elements. Refer to Malone and Rice (2012) for the analysis of irregular wood frame diaphragms from first principles.

**Limitations of the girder analogy**

A large majority of structures require far from regular floor geometries. Setbacks, openings, re-entrant corners, concentrated force introduction, etc., limit the use of the deep beam analogy. Because of the lack of simple analysis methods and the fact that many designers pay little attention to diaphragm design, however, this procedure is still applied to most diaphragm designs, thereby ignoring stress concentrations.

One can account for openings and other irregularities by additional calculations based on first principles. A number of publications (Dean et al., 1984; Diekmann, 1982; Elliott, 1979; Jephcott & Dewdney, 1979; Kessel & Schönhoff, 2001; Prion & Lam, 2003; Tissell & Elliott, 2004) provide the theory and methods for openings in timber diaphragms. Not all methods have been verified against experimental evidence, and some can quickly become complex, depending on the number of equations involved.

#### 6.2.3.2.2 Shear Field Analogy

The shear field analogy overcomes the disadvantages of the ‘diagonal analogy’ referred to in the former German Timber Standard DIN1052:1988 (Deutsches Institut für Normung, 1988) and the strut-and-tie methods (Schlaich et al., 1987). Timber diaphragms cannot provide node force transfer, as assumed by these methods (see Section 6.2.3.2.3). The shear field analogy also calculates the constant unit shear force along the diaphragm edges and the linear force distribution along the frame and boundary beams, which the girder analogy does not explain.

Figure 14 shows the derivation of the shear field analogy from the superposition of several equivalent trusses. All diagonals inclined in one direction have the same force in tension, and the diagonals inclined in the other direction have the same force in compression. The resultant forces along the panel edge are constant and parallel to it. The framing elements therefore only transfer axial loads, which are linearly distributed in the ideal case of an infinite number of equivalent diagonals. Since the fasteners are only loaded by shear forces parallel to the panel edge, the use of the minimum nailing distances for unloaded edges is acceptable.

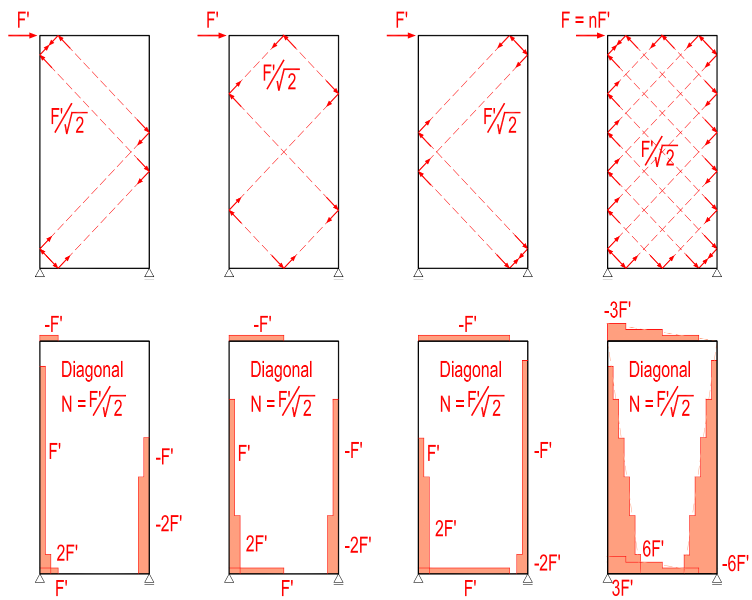


**Figure 14. Derivation of the shear field analogy as a superposition of truss models (modified from Kessel and Schönhoff [2001])**

The requirements and basic assumptions of the shear field analogy can be summarised as follows:

- The diaphragm must consist of sheathing panels fixed using metallic fasteners to framing elements along all edges (blocked wood frame diaphragm);
- Loads can only be introduced along the framing elements parallel to the load direction;
- The fastener stiffness must be smaller than the shear stiffness of the sheathing panels and the axial stiffness of the framing elements;
- The capacity of the diaphragms is dictated by the (ductile) failure of the connections.

### Limitations of the shear field theory

The shear field analogy provides a reasonably easy method to analyse wood frame diaphragms with irregularities like openings or re-entrant corners. As the number of irregularities increases, however, this method, based on hand calculations, soon becomes too complex. The assumptions of the shear field analogy are very often violated in real structures. Loads not applied via the framing elements in their axial direction, as well as displacement incompatibilities, cause inconsistencies in the method. Such incongruencies include the following:

- The actual axial and shear stiffness of the framing elements and sheathing panels are not considered;
- Because of floor irregularities and load applications perpendicular to the framing elements, fasteners are activated perpendicular to the panel edge. Because fasteners normally provide strength and stiffness in this direction, framing elements activated in bending and sheathing panels need to resist axial stresses;

- Framing elements, especially chord beams, are continuous over several panels and are activated in bending because of the displacement relative to adjacent panels;
- Connections between framing elements are activated under the deformation of the panels, providing additional stiffness;
- Framing elements are not continuous over the whole diaphragm because of limited commercially available lengths or because they are interrupted by orthogonal elements. The analogy does not consider the stiffness of splices;
- Under larger deformations, panel edges can touch each other, thus providing a wedging effect which makes the diaphragm notably stiffer.

Construction economy often dictates that not all panel edges are connected to each other (unblocked diaphragm), and therefore that they cannot transfer the shear forces. This creates an additional force demand in the remaining fasteners and generates force components perpendicular to the framing elements, as shown in Figure 15 (blue arrows). Meyer (2006) showed that concentrated fasteners can partially solve this problem. However, the fastener spacing must increase accordingly and the torsional shear of the framing element needs to be taken into account. Because of the high loads, the fasteners at the unsupported edge might yield, leading to large deflections. Unblocked diaphragms should thus only be used for limited span and reduced loads. The German National Appendix to Eurocode 5 (Deutsches Institut für Normung, 2010) allows for unblocked diaphragms under certain geometric conditions and load limitations by reducing its nominal strength by 33%.

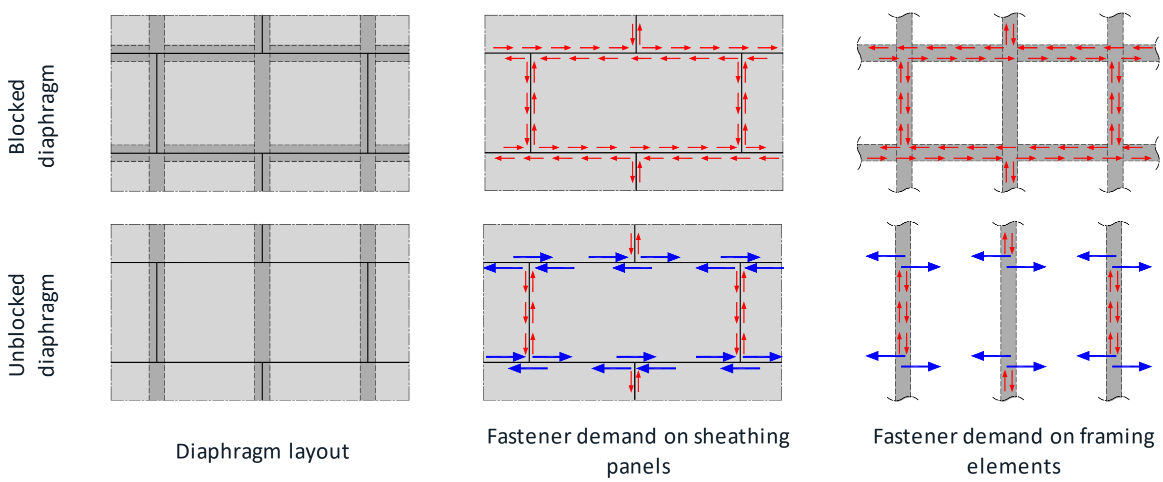


**Figure 15. Blocked (top) and unblocked (bottom) diaphragms, and fastener demands on sheathing panels and framing elements (modified from Kessel and Schönhoff [2001])**

There is a very similar method for concrete diaphragms, known as the stringer-panel method (Blaauwendraad & Hoogenboom, 1996). The method is not well known, has therefore found little application, and is not discussed herein.

#### 6.2.3.2.3 Equivalent Truss Method

The former German Timber Standard DIN1052:1988 (Deutsches Institut für Normung, 1988) allowed for the design of wood frame walls and diaphragms by using equivalent tension diagonals. In this initial form of an equivalent truss, the sheathing panel was verified by only considering a relatively narrow strip of it, as shown in Figure 16. The tension force was assumed to be connected to the surrounding framing elements along the full length of the panel edges. The fastener capacity was verified by considering the force components parallel to the framing members. Not only was the fastener check not compatible with the statical model chosen, but the principles of the '*tension-field theory*' were not admissible for wood frame diaphragms (Colling, 2011). This theory, introduced by Wagner (1929), only applies to thin webbed members after buckling occurs, which generally does not happen in designs with standard panel thicknesses and spacing of framing elements. Furthermore, the force demand in a panel joint, as shown in Figure 16(b), is very difficult to design. The shear field analogy discussed previously could show that such force transfer does not occur in wood frame diaphragms.

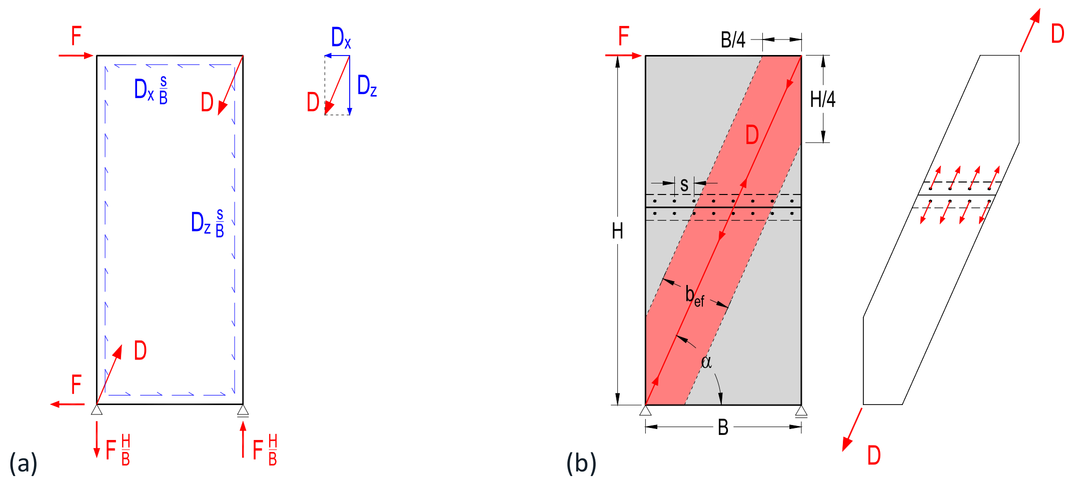


**Figure 16. Basic truss model for walls, according to DIN 1052:1988 (Deutsches Institut für Normung, 1988) (modified from Kessel and Schönhoff [2001])**

By using the same basic assumptions as in the shear field analogy, Kamiya (1990) derived the stiffness of an equivalent diagonal to reproduce the membrane effect of wood frame walls. Kessel & Schönhoff (2001) later fully elaborated upon and explained this idea. In this analogy, the stiffness of the equivalent diagonal represents both the sheathing panel stiffness and the fastener stiffness and can therefore serve as the actual stiffness of the diaphragm. Kamiya and Itani (1998) compared the deflections of a tested wood frame diaphragm and the truss analysis, observing an error of 28%.

**Limitations of the truss analogy**

The truss analogy can be seen as a compromise between a simple approach like the girder analogy and a sophisticated FE analysis. It allows for irregular geometries and provides a clear force path through all involved members. Complex geometries might need a refined mesh, resulting in a number of different diagonals. Because the forces are introduced as concentrated loads in the nodes, some calculated results (like the axial force in framing members) require post-processing to account for the real force distribution along the member length.

For timber diaphragms, the diagonal stiffness depends on fastener stiffness and spacing. These values need to be iterated on an initial assumption. To obtain shear stresses and axial forces in framing members, some additional calculations are necessary.

### 6.2.3.2.4 Modified Equivalent Truss Method

For blocked light wood framing and mass timber diaphragms, the equivalent truss method is recommended. The truss analogy allows the analysis of statically indeterminate diaphragms in the presence of irregularities and concentrated forces. If the deflected shape of the LLRSs is imposed on the diaphragm, it is also possible to evaluate transfer forces.

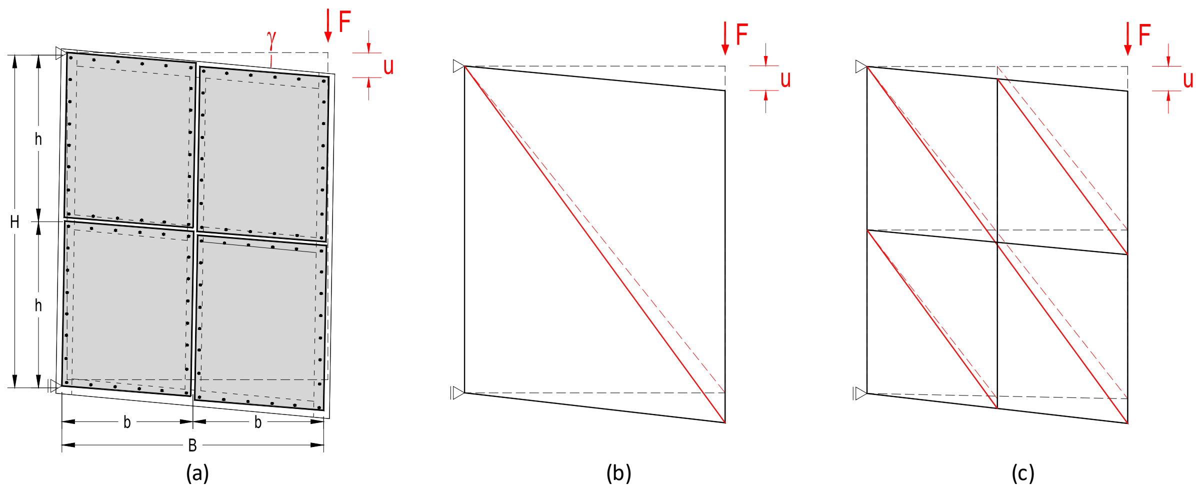


**Figure 17. Truss model solutions for a shear panel with multiple sheathing panels: a) shear panel with multiple sheathing panels connected on blocking elements; b) truss model with one diagonal for the whole shear panel (implicitly considers the internal connection stiffness); and c) truss model with one diagonal for each sheathing panel**

With the equivalent truss method, the horizontal diaphragm is modelled by a grillage of elements representing framing elements and beams, as well as the axial stiffness of each panel, which in turn includes the fastener stiffness perpendicular to the panel edges. For each panel, the shear stiffness and fastener flexibility are modelled by equivalent diagonals, characterised by the following properties:

$$(Gd)_{ef} = \frac{1}{\frac{1}{Gd} + \frac{2s}{K_{ser\,||}}\left(\frac{1}{b} + \frac{1}{h}\right)} \quad [3]$$

$$E_{ef} = \frac{(Gd)_{ef}\, l^2}{hb} \quad [4]$$

$$A_{ef} = l = \sqrt{h^2 + b^2} \quad [5]$$

where $(Gd)_{ef}$ is the equivalent shear through thickness rigidity of the panel; $G$ is the shear modulus of the sheathing panel; $d$ is the sheathing panel thickness; $E_{ef}$ is the equivalent modulus of elasticity of the diagonal; $A_{ef}$ is the equivalent cross-sectional area of the diagonal; $K_{ser\,||}$ is the slip modulus of the fastener parallel to the panel edge; $s$ is the fastener spacing; $b$ is the panel width; $h$ is the panel height; and $l$ is the diagonal length.

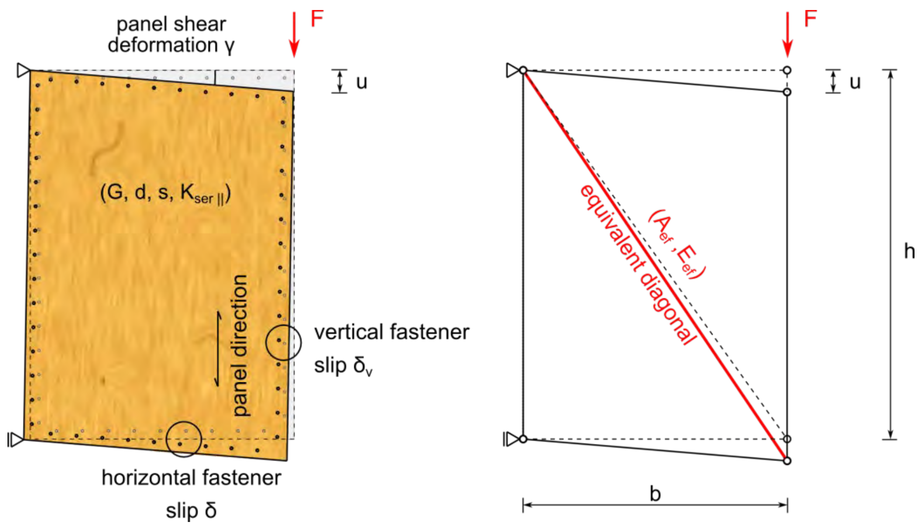


**Figure 18. Shear panel with fastener stiffness and equivalent truss diagonal**

By mathematically setting the equivalent diagonal cross-sectional area $A_{ef}$ equal to the diagonal length $l$ (this step does not have any physical meaning, but somewhat simplifies the method), it is possible to calculate the unit shear force $t$ in the panel (that is, the shear force per length) as the normal stress in the diagonal:

$$\boldsymbol{v = \sigma = \frac{F_{diagonal}}{A_{ef}} = \frac{F_{diagonal}}{l}} \qquad [6]$$

where $v$ is the unit shear force in the panel; $\sigma$ is the axial stress in the diagonal; $F_{diagonal}$ is the force in the diagonal; and $A_{ef}$ is the diagonal area, which equals to the diagonal length $l$.

To obtain the tension/compression forces in the chord and collector beams, add the integration of the unit shear forces along the element length (i.e., the result of multiplying the unit shear force by the length along the framing element) to the axial forces from the truss elements. This is because the diagonal introduces the equivalent panel force in the nodes, even though, in reality, it is introduced gradually through the fasteners along the panel edge. Although typically not required in wood frame diaphragms due to the limited size of the sheathing panels, the equivalent trusses can also be subdivided into sub-diagonals with the procedure and equations used in Section 6.2.4.2.

For the transverse truss element (along the panel width $b$) not corresponding to beams or framing elements, the stiffness of the tributary panel strip is summed (in series) with the fastener stiffness perpendicular to the panel edge ($K_{ser\perp}$). Considering a common subdivision of two diagonals along the panel width, the equivalent stiffness (in force per length) of the transverse member for a wood frame diaphragm is

$$\boldsymbol{K_{ef,transverse\ truss} = \frac{1}{\frac{1}{\frac{E_{90}A'}{b'}} + \frac{1}{n' K_{ser\perp}}}} \qquad [7]$$

where $E_{90}$ is the panel stiffness perpendicular to the panel direction; $A'$ is the tributary cross section of the transverse truss element = $h'd$; $d$ is the panel thickness; $b'$ is the tributary width of the longitudinal truss element = $(b_i + b_{i+1})/2$; $h'$ is the tributary width of the transverse truss element = $(h_i + h_{i+1})/2$; $n'$ is the number of fasteners along $h'$; and $K_{ser\perp}$ is the slip modulus of the fasteners perpendicular to the panel edge. Refer to Figure 26 for an explanation of the annotations used in the equation above.

### 6.2.3.3 FE Methods

#### 6.2.3.3.1 Modelling Techniques and Software

FE analysis can provide a very powerful tool to describe the behaviour of wood-framed structural assemblies loaded in-plane. Stresses in the sheathing panels and framing elements, as well as forces in the connections and the deformation of all the elements involved, can be determined under monotonic and cyclic loading. However, the accuracy of the results is in proportion to the model complexity, which in turn is in proportion to the knowledge and time required to set up the model and post-process the results.

Foschi (1977) and Falk and Itani (1989) conducted pioneering work in the use of computer analysis for panelised structures. A series of stand-alone analysis programs or subroutines for commercial software have since arisen to solve timber diaphragms. Table 5 provides a non-exhaustive list of specialised software for the analysis of wood frame systems.

**Table 5. Specialised FEM models or routines for the analysis of wood frame shear walls and diaphragms**

| Name | Description | Reference |
|---|---|---|
| DAP-3D | Diaphragm analysis program for wooden houses subjected to wind loads, later extended by including the pinching effects of nails. | Foschi (1999) |
| HYST | Studies the hysteretic behaviour of connections in light-frame wood construction. | Foschi (2000), expanded by Li et al. (2012) |
| CASHEW | Cyclic analysis of shear walls. | Folz and Filiatrault (2000a) |
| SAWS | Seismic analysis of wood frame structures. | Folz and Filiatrault (2000b) |
| LightFrame3D | Nonlinear finite-element model to study 3D timber light-frame buildings under static loading conditions. | He et al. (2001) |
| FLOOR2D | Analysis of light wood frame diaphragms under static cyclic loading with smeared connections. | Li and Foschi (2004) |
| WoodFrameMesh, WoodFrameSolver | Meshes and solves wood frame structures. | Pathak (2008) |
| M-Cashew2 | Extended version of CASHEW (Matlab routine). | Pang and Hassanzadeh (2010) |
| SAPWood | Nonlinear seismic structural analysis and loss analysis of wood frame structures. | Lindt et al. (2010) |

Aside from the above-mentioned specialised software tools, commercially available software like Dlubal RFem (Dlubal, 2016), SAP2000 (CSI, 2004), or Abaqus (Dassault Systèmes HQ, 2011) and research software like OpenSees (McKenna et al., 2000) or Ruaumoko (Carr, 2006) can model wood-framed structures. Although membrane and beam elements can model panel and frame elements, respectively, fasteners are still the weak point in the model definition. Commonly, each fastener is modelled using a linear or nonlinear link element with stiffnesses obtained by code provisions or fitted from experimental data. Research by Judd and Fonseca (2005) and Winkel (2006) shows that uncoupled spring pairs overestimate model stiffness. To overcome this, one could consider oriented springs which follow the orientation of the resultant force in the element, but these are not available in most software packages.

#### 6.2.3.3.2 Simplified FE Approach with Single Membrane and Equivalent Shear Stiffness

For most diaphragm designs, a simplified approach is of use when modelling diaphragms with commercial FE software. Since a diaphragm's behaviour is governed by its stiffness and the largest source of flexibility is in the diaphragm panel splices, one must consider the connection behaviour. Unless a more specific diaphragm analysis is warranted, a single shell or membrane element with an equivalent shear stiffness, which accounts for the panel splices, serves to analyse the load path in diaphragms and the load demand in the various diaphragm components. The base assumptions and procedure for this method are explained in the following paragraphs.

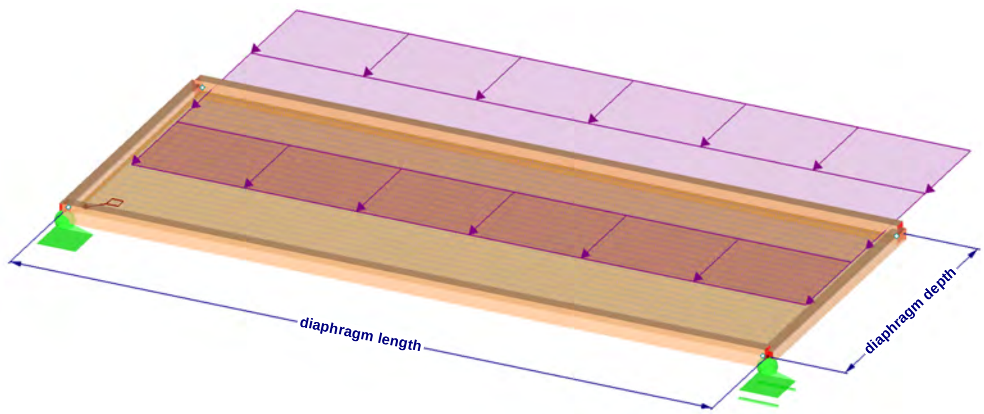


**Figure 19. Simplified diaphragm model, with a single membrane with reduced shear stiffness and collectors/chords**

**Defining the equivalent shear stiffness of timber diaphragms**

Although timber has orthotropic properties, these are typically not required in timber diaphragms, as the material (i.e., plywood, glulam, LVL, or CLT) has approximately the same shear strength and stiffness in the two plane directions. The axial stiffnesses in the longitudinal and transverse directions do not typically affect the analysis. As a rule, joists in plywood diaphragms do not participate in diaphragm action, instead preventing shear buckling of the plywood panels. Joists only need to be considered if they participate in transferring axial loads, as chords or collectors. It is best, however, to verify these assumptions on a case-by-case basis and consider a sensitivity analysis.

Except for CLT (as will be discussed in Section 6.2.4.3), the shear stiffness of the shell element should be taken as the shear modulus of the base timber material, as provided in the relevant material standard or from the manufacturer's literature. The largest sources of flexibility in timber diaphragms are the panel fasteners in the sheathing panel splices; hence, the in-plane stiffness needs to be reduced accordingly. This reduced or effective shear stiffness can be determined by Equation 3.

The slip modulus $K_{ser}$ is typically taken as an elastic stiffness value of a specific fastener, as, for example, provided in Eurocode 5 (European Committee for Standardization, 2008). For the simplified analysis, it is not possible to use a nonlinear force-displacement curve, as provided in some material standards, like the Canadian and New Zealand timber design standards, or from test data. In these cases, consider a linearization with a secant stiffness instead. The secant stiffness can be taken from the origin point to the yield point or at the design capacity of the fastener. This approach is a rough approximation of the fastener's force-displacement behaviour, but it provides a workable value, given the large uncertainties that arise when determining the stiffness properties of fasteners in timber joints in general (Jockwer & Jorissen, 2018). When considering the stiffness of connections, it is always prudent to consider a sensitivity analysis. When structural glue has been used, one can assume the connections are rigid.

Typically, the effective shear stiffness of wood-framed diaphragms with panel sheathing is in the range of 20% to 40% of the timber shear stiffness. This range is affected by the diaphragm geometry, as well as the timber material and fastener selection.

**FE modelling of the diaphragm**

All relevant beam elements (chord and collector beams) can be modelled with their real section sizes and material properties. The panel elements are modelled as a membrane element by using the in-plane effective shear stiffness, defined as above. Panel splices and the connections between the panels and the beam elements need not be modelled separately and can instead be meshed together. The reduced shear stiffness already considers the connection stiffness between the panel and beams.

After running the structural analysis with appropriate loads and load combinations, it is possible to directly read the shear force per metre (unit shear force or shear flow) from the model output. This value can help verify the sheathing panel thickness or type and the type and spacing of fasteners.

Dealing with axial stresses or forces in the two principal directions requires some post-processing of the model output, as well as a degree of engineering judgment. In regular timber diaphragms, the chord and collector beams resist most or all axial forces in the form of tension and compression forces. Since the membrane element with its timber properties has an intrinsic axial stiffness, the computer model will show that it assists in transferring and resisting axial forces. Unless panel splices are designed to carry these forces, all axial forces in the panel should be resisted only by the chords and collector beams. Most software packages allow users to integrate the resultant axial stresses in a certain area or section of the structure, thus allowing them to quickly determine the additional force demand to be assigned to the beam elements.

If there is no dedicated beam element to carry the axial forces, or when axial stresses occur in the membrane element due to diaphragm irregularities, these forces need to be resisted by the panel elements themselves and transferred over any panel splices. After determining the resultant force in the affected area, one can verify the axial load demand in the panel element and design any force transfer over the splice. The panel splices themselves can resist this force transfer, as long as they have sufficient capacity for the additional load demand and sufficient edge distance for a load perpendicular to the panel edge. Alternatively, tension loads can be assigned to discrete or continuous steel straps or brackets. Compression loads are usually transferable via compression and bearing, but this might require additional blocking members for diaphragms with thinner panels, like plywood and OSB.

Note that if the fastener diameter or spacing needs to be changed during the design, it is necessary to update the equivalent shear stiffness of the shell and run the model again. This process could require a few iterations.

#### 6.2.3.3.3 'Complex' Modelling with Individual Panels and Fasteners, Each with Respective Stiffness

When there is a need for a higher level of detail or a more accurate diaphragm analysis, one must model the fastener properties (e.g., stiffness and strength) with greater detail. This allows the designer to capture the idealised behaviour of the fasteners used to connect the various diaphragm components. Typically, the panel-to-panel and panel-to-beam connections are modelled with both their shear and axial stiffness. If the beam elements (chords or collectors) are spliced, one must then model the splice stiffness as well.

The orthotropic material properties should be used in specifying the shell element, while taking care to consider the correct orientation of the panel direction, which will affect the orthotropic nature of the material.

Modelling the stiffness of the fasteners perpendicular to the shearing panel edge makes it possible to account for more realistic behaviour among any axial forces in the diaphragm. In all simplified diaphragm analysis methods, the typical assumption is that any axial tension and compression forces are resisted by beam elements rather than sheathing panels. This behaviour is typically appropriate for light wood framing diaphragm, but mass timber diaphragms can attract significant axial forces.

It requires engineering judgment to decide the level of detail to which to model the connections. Depending on the expected behaviour of the diaphragm (elastic or yielding), the force-displacement behaviour of the connections needs to be modelled as linear or nonlinear springs. In the axial direction, one can use a higher compression stiffness, to simulate the fact that the panels will be bearing in contact after closing any tolerance gaps. Depending on the software package used, continuous (line) hinges (see Figure 20) or discrete spring or link elements (see Figure 21) can simulate the connection behaviour. The latter makes it possible to directly model additional fasteners or different types of fasteners in specific regions of the diaphragm, as well as to determine any force concentrations in individual fasteners. The time required to set up and interpret the model is, however, also greatly increased when using individual fasteners. As mentioned above, most software packages only include 'orthogonal' stiffness properties, not allowing for the orientation of the resultant force and hence for oriented spring properties.

Although the model can calculate both axial forces in beam elements and fastener forces, any stresses in the shell element might require integration over the specific area under consideration. Some software packages allow for the representation of force integrations over an ideal section through the shell element.

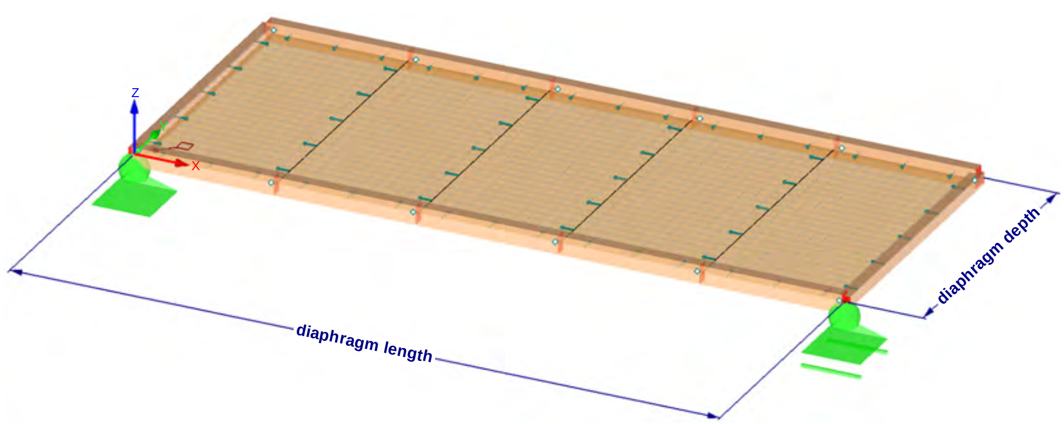


**Figure 20. Diaphragm model with line hinges to model panel splices and connections to chords and collectors**

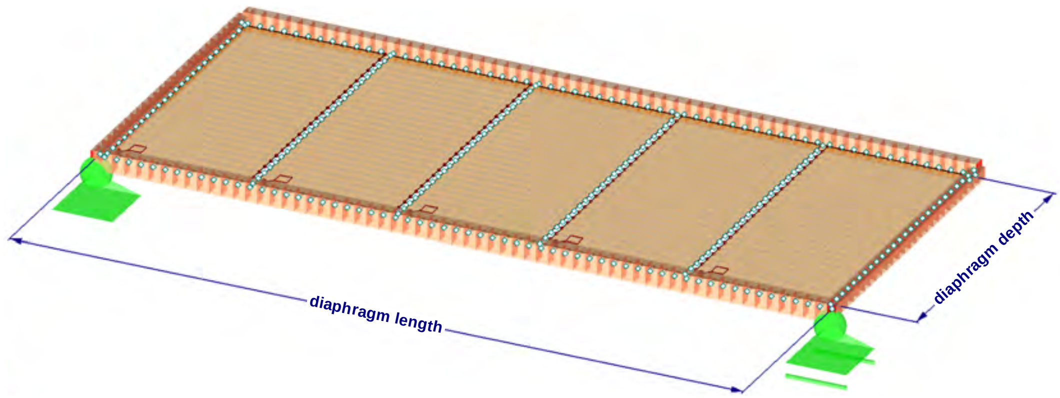


**Figure 21. Diaphragm model with discrete fasteners to model panel splices and connections to chords and collectors**

#### *6.2.3.4 Component Capacity*

All diaphragm elements, like sheathing panels, fasteners, frame elements, and chord/collector/strut beams, need to be verified, as does the connection of the collector beams to the LLRS. The latter must also allow for displacement incompatibilities between the LLRS and the floor (see Section 6.2.6).

##### 6.2.3.4.1 Sheathing Panels, Panel Connections and Framing Elements

Sheathing panels must resist the unit shear force in the diaphragm, which is a function of the panel thickness and shear strength. Even though the panel is continuously fixed to framing members, one must also consider panel shear buckling. Of all the codes reviewed in this guide, only the Canadian timber design standard (CSA, 2019) and the German National Appendix to Eurocode 5 (Deutsches Institut für Normung, 2010) consider panel buckling.

The panel connection needs to be checked for fastener capacity and spacing. For load components perpendicular to the panel edge, one must not only verify the resultant force against the fastener capacity but also respect the minimum distance to the loaded edge.

Frame elements do not normally need to be verified, since their axial load is generally relatively small. When framing elements introduce large concentrated forces into the diaphragm (for example, large wind loads from the façade), compression or tension checks might be required. Buckling can normally be ignored, since the sheathing panels prevent lateral displacements.

The German National Appendix to Eurocode 5 provides the most comprehensive guidance for the design of panelised systems. Reduction factors account for the eccentricities between the centre of the framing elements and the mid-height of the panels, as well as for concentrated forces applied perpendicular to framing elements. Another reduction factor allows unblocked diaphragms to consider the additional fastener demand and increased flexibility. The Appendix also provides a number of prescriptive rules to prevent the lateral buckling of framing elements.

##### 6.2.3.4.2 Chord Beams and Collector Beams

Tension and compression forces in chord beams must be verified in accordance with code equations. Like the frame elements, compression chords are normally not subject to buckling, since the diaphragm restrains any lateral displacements. A conservative design is preferable for chord splices, since a loss in chord capacity could compromise the whole building's behaviour. Flexible splices can also significantly increase diaphragm deflection and should therefore be avoided. Blaß et al. (2004) suggest designing the splice for a chord force equal to 1.5 times the actual demand.

Collector and strut beams collect all shear forces and either transfer them to the LLRS or redistribute them to other parts of the diaphragm. As such, they carry tension and compression forces, something their design must take into account.

The load demand from both gravity and horizontal forces must be used with the appropriate load combination to verify any beam element.

##### 6.2.3.4.3 Connection of the Diaphragm to the Lateral Load-Resisting System

There must be appropriate connection details to introduce forces from the collector beams into the LLRS. These details obviously depend on the material and the structural system adopted with guidance provided in Section 6.2.6.

##### 6.2.3.4.4 Dependency of the Design Capacity and Load Direction

It is common practice to consider horizontal loads along the two principal directions of the building. For certain analysis methods or expected structural ductility levels, some codes require the application of a full load in one direction and 30% of the load in the orthogonal direction (Consiglio Superiore dei Lavori Pubblici, 2008; European Committee for Standardization, 2004; Standards New Zealand, 2004a). Also, considering the reversal action of wind and seismic loads, as well as the natural and accidental torsional eccentricities of structures, one must consider a number of load combinations when designing the LLRS.

Panels and panel fasteners must be able to handle for the maximum unit shear force from all combinations. Depending on the loading direction considered (i.e., one of the two principal directions of the building), the functions of chord and collector beams are reversed. For load applications in an arbitrary direction, boundary beams must resist both chord and collector actions.

#### *6.2.3.5 Diaphragm Deflection*

The first comprehensive publication about the design of timber diaphragms was the *Guidelines for the Design of Horizontal Wood Diaphragms* (Applied Technology Council, 1981). It contains some considerations about diaphragm deflections and shows the derivation of a four-term deflection equation. The deflection equation, based on first principles, is still in use in a number of timber design codes, as shown below. The deflection of a diaphragm derives from the following four contributions: bending deformation (of the chord beams), shear deformation (of the sheathing panels), fastener slip, and chord splice slip.

As when evaluating the strength of the diaphragm, the assumption is that the chord beams resist all bending of the diaphragm and that the sheathing panels have negligible axial stiffness. Likewise, the shear deformations are purely attributed to the sheathing elements. The fastener slip provides the largest deflection contribution, as discussed in Section 6.2.3.5.1. Because of the limited available beam lengths, chords need to be spliced. An additional term can account for the splice slip on the diaphragm deflection. To prevent large deformation contributions from the chord splice, the former German Timber Standard DIN1052:2008 (Deutsches Institut für Normung, 2008) required chord splices to be designed as stiff as possible by increasing the chord demand by 1.5.

For regular diaphragms spanning two supports, the mid-span deflection $\Delta$ is

$$\Delta = \Delta_{bending} + \Delta_{shear} + \Delta_{fastener\ slip} + \Delta_{splice} \quad [8]$$

where $\Delta_{bending}$ is the flexural deflection of the diaphragm, considering the chords acting as a moment-resisting couple; $\Delta_{shear}$ is the deflection of the diaphragm resulting from the shear deformation of the sheathing panel; $\Delta_{fastener\ slip}$ is the deflection of the diaphragm due to fastener slip; and $\Delta_{splice}$ is the deflection of the diaphragm due to chord connection slip.

$$\Delta_{bending} = \frac{5WL^3}{192EAH^2} \quad [9]$$

$$\Delta_{shear} = \frac{WL}{8GHd} \quad [10]$$

$$\Delta_{fastener\ slip} = \frac{1}{2}\delta(1+\alpha)m \quad [11]$$

$$\Delta_{splice} = \frac{\sum \delta_s x}{2H} \quad [12]$$

where $W$ is the lateral uniformly distributed load applied to the diaphragm; $L$ is the span of the diaphragm; $E$ is the modulus of elasticity of the chord members; $A$ is the cross-sectional area of one chord; $H$ is the distance between chord members (diaphragm height); $d$ is the sheathing panel thickness; $G$ is the shear modulus of the sheathing; $m$ is the number of sheathing panels along the length of the chord member; α is the sheathing panel aspect ratio, $\alpha = b/h$ (where $b$ is the length in chord direction); $\delta$ is the fastener slip of the panel-to-panel connection at the diaphragm support, from code provisions or experimental data; $x$ is the distance of the splice from the origin; and $\delta_s$ is the splice slip in the chord.

Equations 9 and 10 are identical in the timber design standards used in New Zealand (Standards New Zealand, 1993), Canada (Standards Council of Canada, 2014), and the US (American Wood Council, 2008). Equation 11 is specific to the New Zealand timber design standard NZS3603 (Standards New Zealand (1993), with other international standards having a more simplified term. This fastener slip term in the New Zealand standard provides the most general equation, as it is possible to choose the panel dimension arbitrarily. It is dependent on the slip of the single fastener $e_n$, and also on the panel aspect ratio $\alpha = b/h$ (where $b$ = panel length along the chord beam). This accounts for the fastener slip on both the vertical and horizontal joints of the single panels. Using standard plywood sizes of 1.2x2.5m (i.e., 4 x 8 feet) allows the derivation of the equation in the Canadian standard:

$$\Delta_{fastener\ slip} = 0.000614\ L\ e_n \quad [13]$$

Similarly, the term in the Special Design Provisions for Wind and Seismic SDPWS 2008 is

$$\Delta_{fastener\ slip} = 0.188\ L\ e_n \quad [14]$$

which is equivalent to the Canadian standard, except for use of the imperial units. Converted to SI units, the fastener slip constant 0.188 from Equation 14 becomes 1/1,627, which is the value, 0.000614, used in Equation 18. Although the New Zealand timber design standard provides the fastener slip $e_n$ as a force-displacement relationship for nails, the North American codes provide empirical formulas for different fastener types, sizes, and sheathing materials.

The contribution of the chord splice term [12] appears only in the Canadian and US standards, but at the time of writing is about to be introduced in the forthcoming update to the New Zealand timber design standard, currently available as the draft standard DZ 1720.1 (Standards New Zealand, 2020).

#### 6.2.3.5.1 Parameters Influencing the Diaphragm Deflection

Considering the three fundamental deflection contributions of bending, shear, and fastener slip in their most general form, as in Equation 8, leads to the following inverse linear relationships:

- the bending stiffness is in proportion to the elastic modulus and the cross-sectional area of the chord material;
- the shear stiffness is in proportion to the shear modulus and the thickness of the sheathing panel material; and
- the fastener slip is in proportion to the slip modulus and the spacing of the fasteners.

$$u_{diaphragm} = \frac{5}{192}\frac{W}{EA}\frac{L^3}{H^2} + \frac{1}{8}\frac{W}{Gt}\frac{L}{H} + \frac{1}{4}\frac{Ws}{K_{ser}}\left(1+\frac{b}{h}\right)\frac{1}{b}\frac{L}{H} \qquad [15]$$

Aside from these linear dependencies, the length-to-width ratio *L/H* most influences the diaphragm deflection. The ratio depends linearly on the shear and fastener slip terms, but is nonlinearly proportional to the bending term.

The graph shown in Figure 22 considers a typical blocked wood frame diaphragm with plywood sheathing panels of 1.2 x 2.4 m and 2.8 mm diameter nails to evaluate the deflection contributions, with the additional assumptions that the diaphragm is loaded with a uniformly distributed load and all fasteners are equally spaced.

Figure 22 shows these values for a range of *L/H* values, considering a diaphragm depth of 5 m.

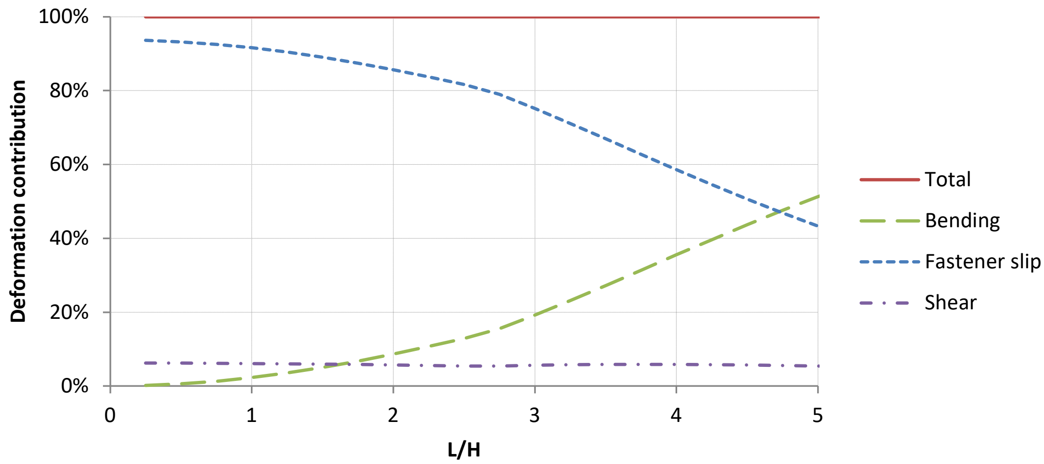


**Figure 22. Diaphragm panel deflection due to panel shear deformation, vertical connector slip, and horizontal connection**

Although the shear deflection has a limited influence for all ratios, the bending term becomes more dominant for longer-span diaphragms. This is to be expected, since such diaphragms' behaviour moves away from typical deep beam behaviour. The figure also explains why diaphragm ratios are limited to an upper value of 5, where diaphragm behaviour no longer adheres to the assumptions of a deep beam and excessive diaphragm flexibility would be achieved.

The equivalent truss method, outlined above, can directly determine the deflection of timber diaphragms.

#### 6.2.3.5.2 Deflection of Unblocked Diaphragms

According to Kessel & Schönhoff (2001) and Schulze and Schönhoff (1989), unblocked diaphragms have a displacement 4 times larger than an equivalent blocked diaphragm. The stiffness should therefore be taken as 25% of that of a blocked diaphragm. Research by the American Plywood Association similarly suggests that the overall diaphragm deflection should be multiplied by 2.5 or 3, depending on the spacing of the framing elements (APA – The Engineered Wood Association, 2007). Because of the high loads, the connectors close to the unsupported edge might undergo extensive yielding, leading to large deformations. Eventually, the forces are transferred by contact between the panels which are wedged together. This mechanism does not lead to immediate brittle failure, but does lead to very large displacements.

## 6.2.4 Mass Timber Diaphragms

### *6.2.4.1 Behaviour*

Wallner-Novak et al. (2013) discuss the design of diaphragms made from CLT panels and refer also to the deep beam analogy, as shown in Figure 23(a) and (b). The panels and panel connections which resist the shear and tension/compression forces along the edges are resisted by chord beams or by appropriate panel connectors. For loading perpendicular to the panel length (Figure 23[c]), one can assume the diaphragm works as a series of beams in parallel. An FE analysis by Ashtari (2009) also confirmed the shear force distribution in Figure 23(a), but it did not evaluate the tension and compression forces in Figure 23(b) because the panels were connected with rigid links perpendicular to the panel edges. Both documents studied regular diaphragms with one row of panels.

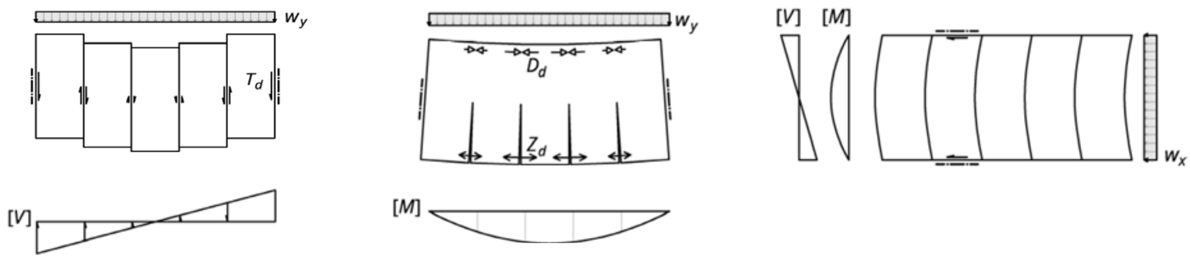


**Figure 23. Mechanism of floor diaphragms: a) shear along panel connection, b) chord forces, c) diaphragms as series of beams (Wallner-Novak et al., 2013)**

FE analysis comparisons by Moroder (2016) confirm the deep beam behaviour of mass timber diaphragms in terms of the unit shear distribution. Yet, results also show that longitudinal stresses play a major role for certain load conditions. This behaviour becomes even more obvious for diaphragms with multiple panel rows or with irregularities.

Because mass timber diaphragms lack framing elements, panel axial forces are activated in the load direction. For forces applied to diaphragm edges, this is the only mechanism available to transfer the loads into the diaphragm. In addition, the panels also contribute to the bending stiffness of the diaphragm, which activates stresses perpendicular to the load direction. Such effects should not be neglected, since panels without cross layers are activated in tension perpendicular to the grain, and fasteners also need to resist force components perpendicular to the panel edge. In the absence of special reinforcing elements (i.e., drag/strut beams, metal brackets, etc.), mass timber panels carry not only unit shear forces but also additional longitudinal forces.

Wallner-Novak et al. (2013) suggested that tension and compression forces can also be resisted by the panel fasteners instead of the chord beams. Although this approach is technically feasible, as long as panels and fasteners are designed for these forces, such diaphragms are not as efficient as those with chord beams. Concentrated stresses must not be able to ‘unzip’ joints, so be mindful when averaging stresses / forces at joints. Figure 24 shows the SAP2000 analysis results of a 1.2 m x 4.8 m diaphragm consisting of 8 CLT panels with and without chord beams under a load of 3.5 kN/m$^2$. Chord beams, if present, had a cross section of 189 mm x 400 mm, with a modulus of elasticity of 11,000 MPa. The panel fasteners were modelled with a stiffness of 3,000 N/mm, increasing to infinity in compression after 1 mm of displacement when assuming the panels bear against each other. For the diaphragm without chord beams, Figure 24 shows not only that the fasteners are heavily loaded perpendicular to the panel edge (compared to the maximum fastener force from the unit shear force of 2.5 kN), but that the diaphragm deflection also increases by 250%. Shear stresses compare reasonably well, with a slightly less uniform distribution. The measured tension stress in the panels, 1.0 N/mm$^2$, reached the tension strength perpendicular to grain for some timber species.

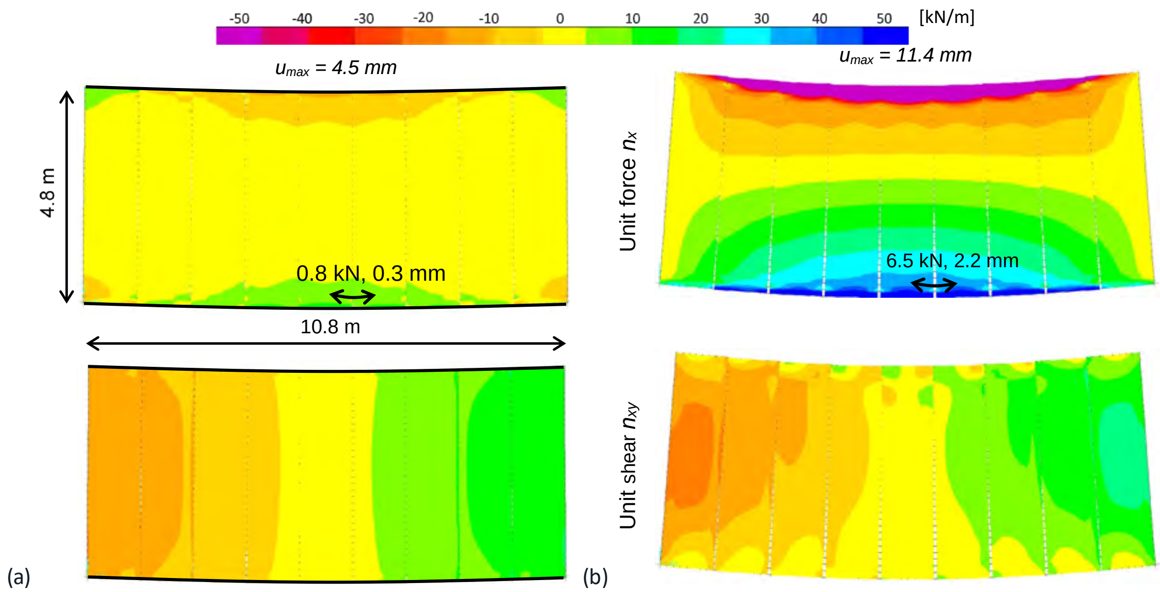


**Figure 24. Simply supported diaphragms (a) with and (b) without chord beams**

Despite the assumption that, in the presence of chord beams, the diaphragm panels do not resist any tension and compression forces, as shown in Figure 25(a), connections must still carry nominal tension forces, as shown in Figure 25(b). The analysis found a connection load component perpendicular to the panel edge of about 30% of the unit shear force component. This effect can also be seen in the chord forces, which are reduced by 15% when compared to the value obtained by the girder analogy.

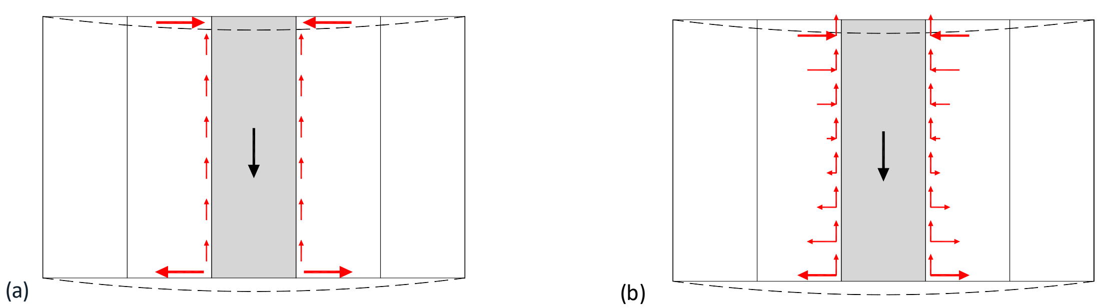


**Figure 25. Force distribution in diaphragm panel connections with mass timber panels: (a) idealised force distribution, and (b) real force distribution**

Mass timber diaphragms can be analysed with the girder or shear field analogy, as long as the loads are appropriately transferred into the diaphragm. This is always guaranteed for area loads, but panel connections must be specifically designed for these longitudinal loads. Mass timber diaphragms without chord beams are relatively flexible and require connections and panels to be carefully designed, since high axial forces arise from the required bending strength.

### *6.2.4.2 Analytical Methods*

#### 6.2.4.2.1 Girder Analogy

As discussed above, the girder analogy can be used to analyse mass timber diaphragms, as their behaviour is similar to that of wood frame diaphragms (Section 6.2.3.2.1).

### 6.2.4.2.2 Equivalent Truss Model for Mass Timber Diaphragms

As with the analysis of wood frame diaphragms, the truss analogy can be used for mass timber diaphragms. Even though not all assumptions of the shear field analogy strictly apply to this kind of diaphragm, the same procedure can be used to determine the effective shear through thickness rigidity. Depending on the types of connection between the individual panels and between the panels and beams, the equivalent shear through thickness rigidity $(Gd)_{ef}$ for mass timber diaphragms becomes

$$(Gd)_{ef} = \frac{1}{\frac{1}{Gd}+\frac{s}{K_{ser}}\left(\frac{c_1}{b}+\frac{c_2}{h}\right)} \qquad [16]$$

where $(Gd)_{ef}$ is the equivalent shear through thickness rigidity of the panel; $G$ is the shear modulus of the mass timber panel; $d$ is the mass timber panel thickness; $K_{ser}$ is the slip modulus of the fastener parallel to the panel edge; $c_i$ is the number of connections rows along the sheathing panel edge; $c_1$ is the number of lines of fasteners between adjacent panels along the sheathing panel height $h$; and $c_2$ is the number of lines of fasteners between adjacent panels along the sheathing panel length $b$.

For mass timber panels, no framing elements are necessary along the longitudinal panel edge; $c_1$ is therefore typically 1 (or, if a connection with a splice plate is used, 2). The heads of the panels sit normally on a beam, requiring two lines of fasteners to transfer the forces; therefore $c_2$ = 2.

- Mass timber diaphragm with lap joint and screws, $c$ = 1

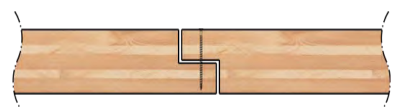

- Mass timber diaphragm with single spline joint and screws/nails, $c$ = 2

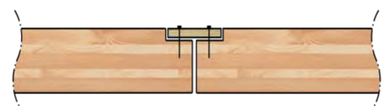

To derive the effective area $A_{ef}$ and modulus of elasticity $E_{ef}$ of the equivalent diagonal, use the same equations as for wood frame diaphragms, outlined in Section 6.2.3.2.4.

According to the shear field analogy for wood frame diaphragms, sheathing panels must connect to framing elements with flexible metallic fasteners. For mass timber panels, framing elements are partly missing and the high axial stiffness and thickness of the panel elements activates longitudinal stresses. Moroder (2016) and Wallner-Novak et al. (2013) show that the girder analogy still provides an adequate method to predict demand in mass timber diaphragms. To use the truss analogy for mass timber diaphragms, apply the assumptions and modifications to the analogy shown in the next paragraph.

Mass timber panels normally span two or more gravity beams and connect to them to guarantee diaphragm action. These beams are the truss elements running along the short length of the panels. An equivalent truss element needs to be placed along the panel-to-panel edge. The stiffness of this element is the same as the panel stiffness in this direction, and the cross-sectional area is the sum of half of the cross-section areas of each of the two panels. In this way, the equivalent truss model can capture the longitudinal forces in the panel direction.

Because mass timber panels possess relatively high axial stiffness compared to plywood panels, one must account for normal stresses along the two main directions. Additionally, fasteners will transfer forces not only parallel to the panel edges but also perpendicular to them. By dividing the panels into multiple diagonals, as shown in Figure 26, the transverse truss elements (along the panel width *b*) can account for these effects by including the fastener stiffness perpendicular to the panel edges.

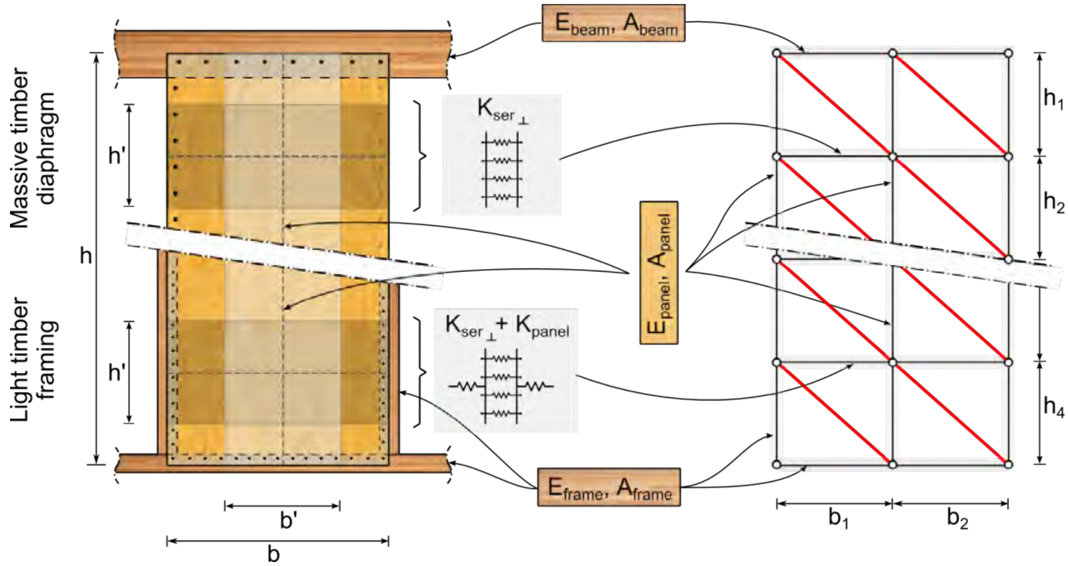


**Figure 26. Timber panels and idealization thereof in the equivalent truss model for multiple diagonals for wood frame and mass timber diaphragms**

Because of stiffness considerations, if panels are subdivided into multiple diagonals, higher forces are attracted close to stiffer elements like beams or supports. In such cases, consider the average of all diagonals belonging to one panel element.

The individual diaphragm panel can be subdivided in a regular pattern of *m* x *n* equivalent diagonals or by diagonals with varying lengths, according to Table 6 and Figure 27.

**Table 6. Diaphragms categorised by materials**

| m x n regular diagonals | irregular diagonals |
|---|---|
| $E_{ef,mxn} = mn\frac{(Gd)_{ef} l_{mxn}^{2}}{bh}$ | $E_{ef,ij} = \frac{(Gd)_{ef} l_{ij}^{2}}{b_j h_i}$ |
| $A_{ef,mxn} = l_{mxn} = \sqrt{\left(\frac{b}{n}\right)^2 + \left(\frac{h}{m}\right)^2}$ | $A_{ef,ij} = l_{ij} = \sqrt{b_i^{2} + h_j^{2}}$ |

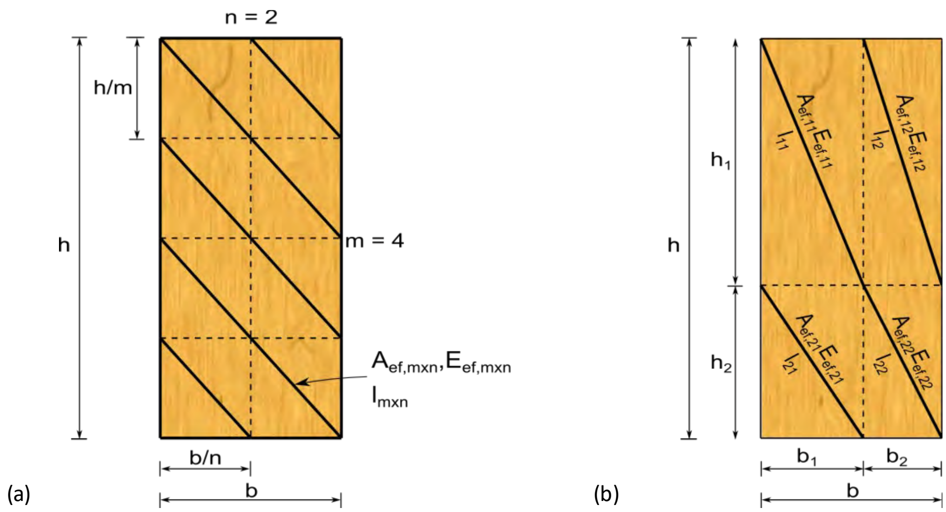


**Figure 27. Shear panel with fastener stiffness and equivalent truss diagonal**

All beams (collector, chord, strut) and framing elements, as well as other reinforcing elements, are modelled with their real axial stiffness. The remaining longitudinal truss elements (along the panel height *h*) are to be modelled with axial panel stiffness corresponding to the tributary width *b′* of the truss element, as shown in Figure 26.

For the transverse truss element (along the panel width *b*) not corresponding to beams or framing elements, the stiffness of the tributary panel strip is summed (in series) with the fastener stiffness perpendicular to the panel edge ($K_{ser\perp}$). For a mass timber diaphragm, the axial stiffness of the transverse truss element is much greater than that of the fasteners and can normally be ignored. For a common subdivision of two diagonals along the panel width, the equivalent stiffness of the transverse member in a mass timber panel can be calculated as

$$K_{ef,transverse\ truss,mass} = \frac{1}{\frac{1}{\frac{E_{90}A'}{b'}} + \frac{1}{(3-c)\,n'\,K_{ser\perp}}} \cong (3-c)\,n'\,K_{ser\perp} \qquad [17]$$

where *c* is the number of fastener lines that transfer the unit shear force from one panel to the other.

### 6.2.4.3 FE Methods

FE analysis of mass timber diaphragms is very similar to the analysis of wood frame diaphragms. Three types of models discussed by Breneman et al. (2016) can apply: homogenous models (Figure 28[a]), discrete panel and lumped connection models (Figure 28[b], [c]), and discrete panel and distributed connection models (Figure 28[d]).

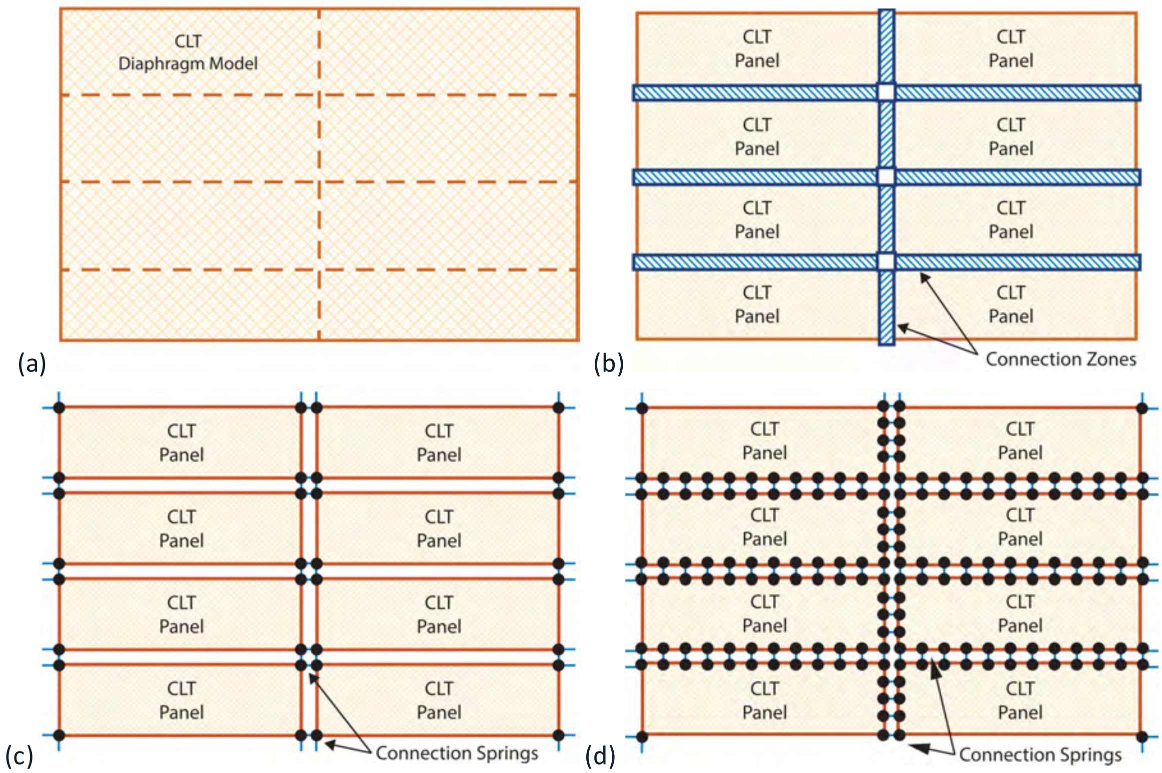


**Figure 28. Models for diaphragms (Breneman et al., 2016): (a) homogenous model; (b) discrete panel model with 2D connection zones; (c) discrete panel model with corner connections; and (d) discrete panel model with spaced connections**

For a simplified diaphragm analysis (Figure 28[a]), refer to the considerations in Section 6.2.3.3.2, but with the effective shear stiffness from Equation 16. For CLT diaphragms, one must also consider the reduced shear stiffness of the crosswise glued laminates. The reduced shear modulus is typically provided by the supplier or is calculable based on the geometry and panel layup (ProHolz, 2014). For the purposes of the simplified diaphragm analysis, the following approximation can be used:

$$\boldsymbol{G_{CLT} = 0.75\ G_{mean}} \qquad [18]$$

$G_{CLT}$ can be used in Equation 16 to determine the effective shear stiffness. Note that when using $G_{CLT}$, one can use the gross area (or full depth) of the CLT when modelling diaphragms, as the reduction factor already considers the orthogonal orientation of laminates.

For more 'complex' FE analysis (Figure 28[b] to [d]), the same considerations apply as in Section 6.2.3.3.3. For mass timber diaphragms, the orthotropic material properties can have a more noticeable impact on diaphragm behaviour than for wooden sheathing. This is because mass timber panels made of glulam or LVL have quite substantial differences in stiffness in the two principal directions. This behaviour is less pronounced in CLT panels, due to the crosswise orientation of the laminates; however, this affects the shear stiffness as noted above. Some software packages, like Dlubal RFEM (Dlubal, 2016), have specific modules which determine the orthotropic material properties of CLT based on the panel layup and laminate material properties. Line hinges or discrete fasteners can serve to model panel splices or connections to beam elements.

Due to the significantly higher axial stiffness of mass timber panels, the respective fasteners between panels will likely attract forces perpendicular to the panel edges. If these forces are to be transferred via the panel fasteners, one also needs to consider the increased edge distance to the loaded edge. In addition, for large force introductions into the panels around diaphragm irregularities, one must consider the low-tension perpendicular to grain capacity for glulam or LVL panels.

#### 6.2.4.4 Component Capacity

Mass timber diaphragms require the same design verification as wood frame diaphragms, with some additional considerations. Spickler et al. (2015) provided a practical design method to determine the strength of a CLT horizontal diaphragm due to lateral wind or seismic loads. Panel shear buckling can normally be ignored because of the increased panel thickness. Due to the missing framing elements, only the mass timber panels and their connections carry longitudinal forces. It is therefore important to check axial buckling. Panel splices are typically executed as half lap joints or with wooden splines recessed into the tops of the panels. Typically, screwed connections are preferable for mass timber diaphragms. For a more exhaustive list of mass timber connection details, see the CLT Handbook (Karacabeyli & Gagnon, 2019).

Because there are both shear and axial forces, mass timber panels should be verified for this combined load. This can involve a suitable constitutive model, e.g., Wood$^{S}$ (Chen et al., 2011) and Wood$^{ST}$ (Chen et al., 2020), or a simple strength criterion, e.g., the Norris criterion, which allows for the verification of a generic stress state in a timber element (Thelandersson & Larsen, 2003). Stress levels are normally relatively small, making such verification redundant. Brittle failures in tension perpendicular to the grain must be avoided independently from the approach taken. Connectors must account for the forces parallel and perpendicular to the panel edges, and increased minimum distances to the loaded edge must be respected.

#### 6.2.4.5 Diaphragm Deflection

Assuming the same design assumptions apply to mass timber diaphragms as to wood frame diaphragms, it is possible to assess their deflection based on the same first principles. Spickler et al. (2015) provided a practical design method to determine the deflection of a CLT horizontal diaphragm due to lateral wind or seismic loads. Aside from the thickness of the panels involved, the main difference between the two diaphragm types are the missing frame elements to connect the individual sheathing panels together. For mass timber diaphragms, the panel elements are most commonly directly connected to each other with screws. The deflection equation for mass timber diaphragms is

$$\boldsymbol{u = \frac{5WL^3}{192EAH^2} + \frac{WL}{8GHd} + \frac{1}{4}e_n(c_1 + c_2\alpha)m} \tag{19}$$

where the fastener slip term differs from Equation 11 to account for the fact that the unit shear force is normally transferred from one panel directly to the adjacent one. Thus, only the connection slip along one line of fasteners needs to be considered; $c_1$ is therefore typically 1. If, however, the mass timber panels are connected by a strip of plywood, placed in a recess, and nailed to both panels, then the same equation can be used as for wood frame diaphragms ($c_1$ = 2). Mass timber diaphragms are normally supported by gravity beams at their ends; the same beams also serve to transfer the shear force between adjacent panels, resulting in $c_2$ = 2. One can therefore account for the connection slip along the panel heads in the same manner as for wood frame diaphragms. The fastener slip $e_n$ is calculated for the maximum unit shear force at the support.

Add the deflection component $\Delta_{splice}$ of the diaphragm due to chord connection, as used in Equation 12, if appropriate.

## 6.2.5 Timber-Concrete Composite Diaphragms

### 6.2.5.1 Behaviour

For regular reinforced concrete floors, concrete diaphragms act as horizontal beams, spanning the load-resisting walls. The resulting moment demand is resisted by the tension and compression couple. The forces from the moment demand are resisted by the chord members, which consist of the steel reinforcing and concrete. For timber-concrete composite floors, where the concrete is structurally connected to the timber, the supporting timber members can transfer tension and compression forces and therefore act as collector or chord beams. The horizontal load is transferred to the LLRS via a uniformly distributed shear force along the ends of the diaphragm.

Although this simplified model follows the deep beam or girder analogy, as described below, irregularities in the floor plan will result in disturbed areas, requiring a more rigorous analysis. Strut-and-tie models can be applied around this disturbed area, allowing an analysis of the load path in the diaphragm with tension and compression struts.

### 6.2.5.2 Analytical Methods

#### 6.2.5.2.1 Deep Beam Analogy

The design of timber-concrete composite diaphragms follows either classical beam theory, where plane sections remain plane, or deep beam theory (Figure 29). In either case, chord beams, which consist of either gravity beams or specially reinforced strips in the slab itself, are designed using Equation 1 to resist tension and compression forces. The shear stress is considered constant along the end of the diaphragm and calculated according to Equation 2.

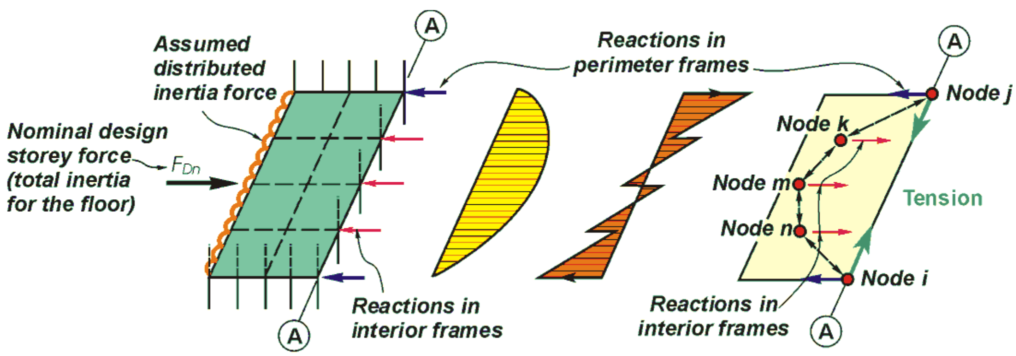


**Figure 29. Deep beam analogy for a typical timber-concrete composite diaphragm with a frame structure (modified from Park et al. [1997]): (a) forces, (b) moments, (c) shear forces, and (d) internal forces**

For usual diaphragm sizes, the concrete can resist most of the shear force, and the reinforcement required to resist gravity loads or for crack control additionally contributes to the shear strength. For tension chords, one must guarantee that the axial force can be resisted by the reinforcement provided; this requires appropriate curtailment in case of splices.

**Limitations of the Deep Beam Analogy**

As for the girder analogy for timber diaphragms described in Section 6.2.3.2.1, complex floor geometries create irregular load paths and stress concentrations, which cannot be captured with the deep beam analogy.

For diaphragms in high seismic areas, where transfer forces and other displacement incompatibilities are likely, it is best not to use the deep beam analogy. This is because not all diaphragm forces can be accurately predicted, and the assumed load distributions might not be compatible with the general building behaviour (Bull, 2004).

Research has shown that for topped and non-topped precast diaphragms, the girder analogy requires a certain degree of plastic redistribution. To activate the flexural reinforcement in the chords, the shear reinforcement (or connectors) in the web may need to undergo tensile stresses. This force combination cannot be predicted with the deep beam analogy and might cause premature failure in the diaphragm (International Federation for Structural Concrete, 2003).

#### 6.2.5.2.2 Strut-and-Tie Method for Simple Diaphragms (Desktop Analysis)

The strut-and-tie method, developed for concrete members, relies on the compression strength of concrete and the tensile strength of reinforcement bars. It has found wide application since its formal definition by Schlaich et al. (1987), even though it found earlier use in the truss analogy for concrete beams (Mörsch, 1912; Ritter, 1899). The method is especially suited for the study and detailing of disturbed regions (D-regions) in reinforced concrete structures—that is, areas or sections where the Bernoulli hypothesis of plane sections (beam theory) is no longer valid. The strut-and-tie method can serve to design entire members, given both disturbed and Bernoulli regions.

The method guarantees equilibrium at each node and provides an admissible load path in the structural element by setting up a truss-like system. Compression struts and tension ties are assigned so as to guarantee the shortest possible load path with the minimum strain energy (International Federation for Structural Concrete, 2011). This normally neglects the tension strength of concrete, and concrete struts do not intersect except at nodes. For tension ties, there must be sufficient steel reinforcement; for compression struts, the concrete cross section must be verified, taking into consideration possible transverse tensile strains (i.e., for bottle struts, struts in tension regions). Verifying nodes depends on the number of ties and/or struts connected and is the most delicate part of the procedure. Coefficients normally provide reduced concrete strength in case of tensile stresses in the nodal area. Most international concrete codes (American Concrete Institute, 2019; European Committee for Standardization, 2005; Standards Australia, 2009; Standards New Zealand, 2006) provide guidelines and provisions for the use of strut-and-tie models. In New Zealand, this model has been the preferred method of design for concrete diaphragms over the last two decades (Bull, 2004; Park et al., 1997; Paulay, 1996).

Most floor diaphragms are irregular and, due to typical aspects ratios, lack any Bernoulli regions. This means all diaphragms are best considered as disturbed areas, to be designed with strut-and-tie models. There are no unique strut-and-tie models for a given load combination, but one should consider the following when analysing a diaphragm (Gardiner, 2011):

- The load path should be shortest possible, with the least amount of strain energy;
- Equilibrium at each node is to be maintained;
- Compression struts should never cross each other;
- Tension ties should be arranged following typical reinforcement layouts.

Figure 30(a) is a representation of the force flow in a diaphragm, as assumed in the deep beam analogy. For the load reversal in (b), struts and ties are similar to those for typical truss models. The models shown in (c) and (d) assume diagonal tension fields, achieved by the rebars in the floor.

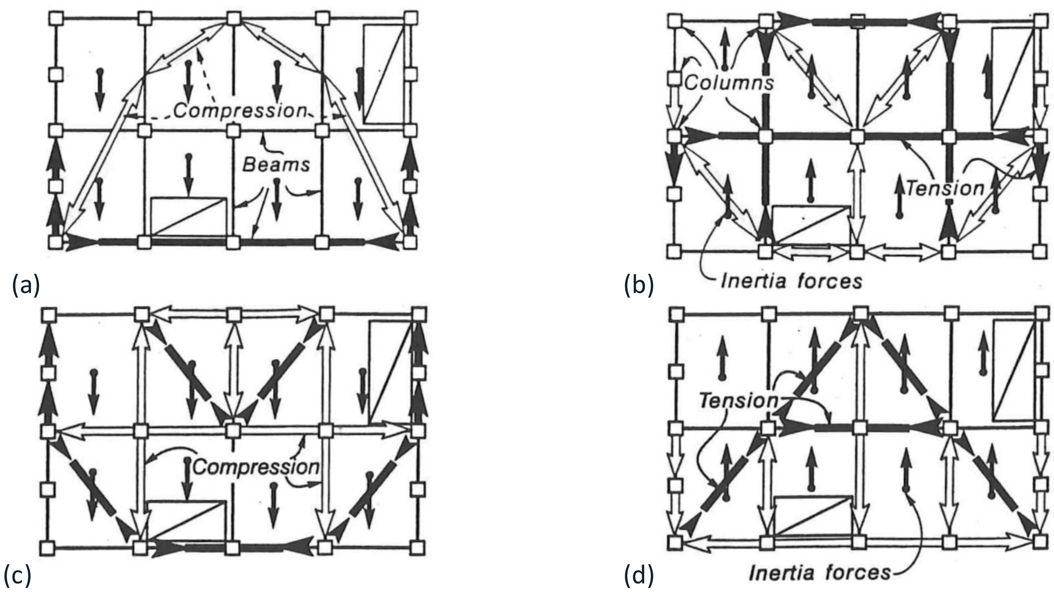


**Figure 30. Strut-and-tie models for a floor diaphragm with openings: a) and b) using compression fields, c) and d) using tension fields (Park et al., 1997; Paulay, 1996)**

Tension ties often correspond to the tension chords or specially designed internal beams with continuous reinforcement. Small tension forces are normally resisted by the reinforcement meshes required by gravity design or for crack control. If the tension force becomes too large, for example around floor openings, it might be necessary to provide some additional ties in the form of drag bars.

**Limitations of the strut-and-tie method**

The choice of the strut-and-tie model geometry is not unique. Although forces prefer the load path with the greatest stiffness, designers sometimes choose scenarios with a quite tortuous load path. Even though statically admissible, such load paths imply force redistribution, which is often accompanied by extensive cracking. This may lead to excessive diaphragm damage and the failure of other structural elements attached to the diaphragm. One should therefore choose the most appropriate and adequate strut-and-tie model, based on stress trajectories from an elastic FE analysis, or on design experience.

The localised tension ties may require concentrated reinforcement in specific positions. Diaphragm reinforcement, however, normally consists of steel mesh or a grillage of reinforcement bars, providing distributed reinforcement across the diaphragm. This can influence the load path and in extreme cases lead to bar yielding before the activation of drag ties or chords.

One of the major disadvantages of the strut-and-tie method is that the chosen model geometry depends on a specific applied load. A different loading condition or even a load reversal might require a new analysis, with a completely different load path. This can result in multiple analyses of irregular floor geometries with a number of loading conditions.

Because the strut-and-tie method is based on force equilibrium at the nodes, it cannot distribute the horizontal loads as a function of the stiffness of the diaphragm and the LLRS. Designers must decide the force distribution method early in the design process, according to the assumption of a flexible or rigid diaphragm. This assumption always needs verification, and the load path should be adjusted accordingly.

###### 6.2.5.2.3 Grillage or Lattice (Refined Strut-and-tie) Method, after Hrennikoff (1940)

Ritter (1899) and Mörsch (1912) used lattice models in their earliest form in their truss analogy of concrete beams; these models also found application in the '*Framework Method*' by Hrennikoff (1941). The elastic continuum was described as a framework of bars arranged in a specific pattern, to successfully represent deformations, stresses, and unit shears. At that time, design software for such models did not exist; it only became possible to verify the method with the development of FE methods. The framework method therefore remained purely theoretical for many years, and practitioners preferred simpler approaches, like the strut-and-tie method.

Several researchers have used lattice models based on beam or truss elements to represent concrete elements on a micro or macro scale. Ilgadi (2013) completed a comprehensive summary and study of such models with various levels of complexity, including compression nonlinearity, tensile fracture, interaction with concrete steel, concrete cracking, and loading complexities.

Equivalent trusses (sometimes described as grillages, meshes, etc.) have found a wider acceptance over the last decades in New Zealand. Based on Hrennikoff's work, Gardiner (2011) shows the applicability of equivalent trusses to the design of irregular concrete diaphragms. Bull and Henry (2014) and Scarry (2014) have further promoted the use of equivalent trusses to analyse diaphragms. Figure 31 shows a possible definition of compression and tension elements, which can be implemented in any structural analysis program that can solve trusses. The truss not only provides tension and compression forces for any possible loading conditions but also considers the load distribution according to the diaphragm stiffness, and if modelled, the stiffness of the LLRS. The struts and ties, as well as the nodal areas, can be designed as for the strut-and-tie method.

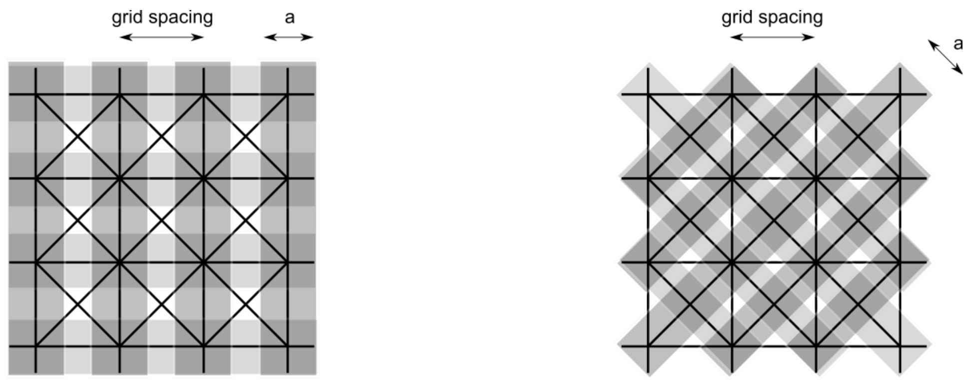


Orthogonal compression & tension width
a = ¾ grid spacing

Diagonal compression width
b = 0.4 grid spacing

Diagonal tension width
b = 0

**Figure 31. Width of truss elements in concrete diaphragms (modified from Bull and Henry [2014], based on Hrennikoff [1940])**

### *6.2.5.3 FE Methods*

For simplified analyses, a concrete floor can be modelled as a linear elastic and isotropic shell element, meshed with smaller elements to guarantee accurate details. It is possible to obtain principal stresses and verify maximum compression stresses against code values. Reinforcement is necessary to account for tension forces. Since floor diaphragms should remain elastic, this approach often provides satisfactory results for simple designs. Note that this simple approach cannot account for displacement incompatibilities due to the ductile behaviour of the LLRS or load redistribution because of cracking around floor openings. Some limited research has shown that elastic FE models provide a conservative comparison to an inelastic FE model in estimating tension demands. Compression demand, however, is generally underestimated, as the cracking of the concrete changes the strut angles. Yet, this is typically not of major concern, as the compression strength of the concrete struts typically exceeds the demand (Gardiner, 2011). The effect of cracking can be considered by reducing the stiffness of the cracked concrete, as is typical for concrete beams. Nakaki (2000) suggests a stiffness reduction of 0.15 to 0.5 to the in-plane gross section when analysing a building under ultimate limit state seismic events.

For a more comprehensive approach, one must model both concrete and reinforcing steel with their relative constitutive laws, to account for concrete cracking, tension stiffening, the nonlinear response of concrete in compression, and the nonlinear behaviour of the reinforcement, including strain hardening. This can result in a complex nonlinear model if predefined reinforced concrete elements are not provided in the analysis software. It may require relatively small meshing, also necessitating a sensitive analysis to define the most appropriate meshing size until convergence is achieved. This approach can be very time-consuming and requires an in-deep knowledge of the software package being used.

FE analysis allows the modelling of the continuous nature of concrete diaphragms, in contrast to strut-and-tie models which consider discrete tension and compression elements. FE methods also allow the study of the (localised) stress concentrations around re-entrant corners and openings. The modelling approach and considerations for the timber components and the connections between two components, discussed in Sections 6.2.3.3 and 6.2.4.3, also apply to composite diaphragms.

#### *6.2.5.4 Component Capacity*

The design of the individual components of concrete slab diaphragms is strongly influenced by the structural system. Chord and collector beams can be made of timber elements connected to the concrete slab or can be integrated into the concrete slab itself. Depending on the solution adopted, the relevant material codes will provide guidance for verifying beams.

When using the deep beam analogy, the concrete slab must carry the unit shear forces. This can be verified by checking the concrete shear strength (with or without the contribution from diaphragm reinforcement/mesh). Tension forces in chord and collector beams can be verified based on the tension capacity of the reinforcement in the concrete. Compression forces do not typically govern the design of concrete, but should be considered for large forces or very slender members (due to the risk of out-of-plane buckling).

When using the strut-and-tie model or a grillage analysis, one must verify the tension and compression forces in the ties and struts, respectively, using the appropriate material standard. Nodal zones need to be designed carefully, with special attention to reinforcement anchoring.

### 6.2.6 Connections within Diaphragms, and Connections to Lateral Load-Resisting Systems

This section offers guidance for designing and modelling connections between diaphragm panels or between diaphragms and gravity load-resisting systems or LLRSs. It focuses mainly on mass timber diaphragms.

#### *6.2.6.1 Connections with Mass Timber Diaphragms*

##### 6.2.6.1.1 Connections between Single Mass Timber Diaphragm Elements

To connect two single wood panels together, use the typical connection systems shown in Figure 32:

(a) adjacent panels nailed with half-lapped joints;

(b) wooden spline in recess between panels with screws or nails;

(c) inclined fully threaded screws or regular screws at 90° between floor joists;

(d) panel nailed to the next joist/framing member;

(e) double inclined screws in shear between solid panels;

(f) tongue and groove with double inclined, fully threaded screws.

These connections show typical details designed in accordance with code provisions or the manufacturer's information to guarantee adequate shear transfer. Note that some configurations, e.g., those using inclined screws, are not suitable for energy dissipative connections. In general, it is not recommended to rely on energy dissipation from the diaphragm, as discussed in Section 6.2.2.4.

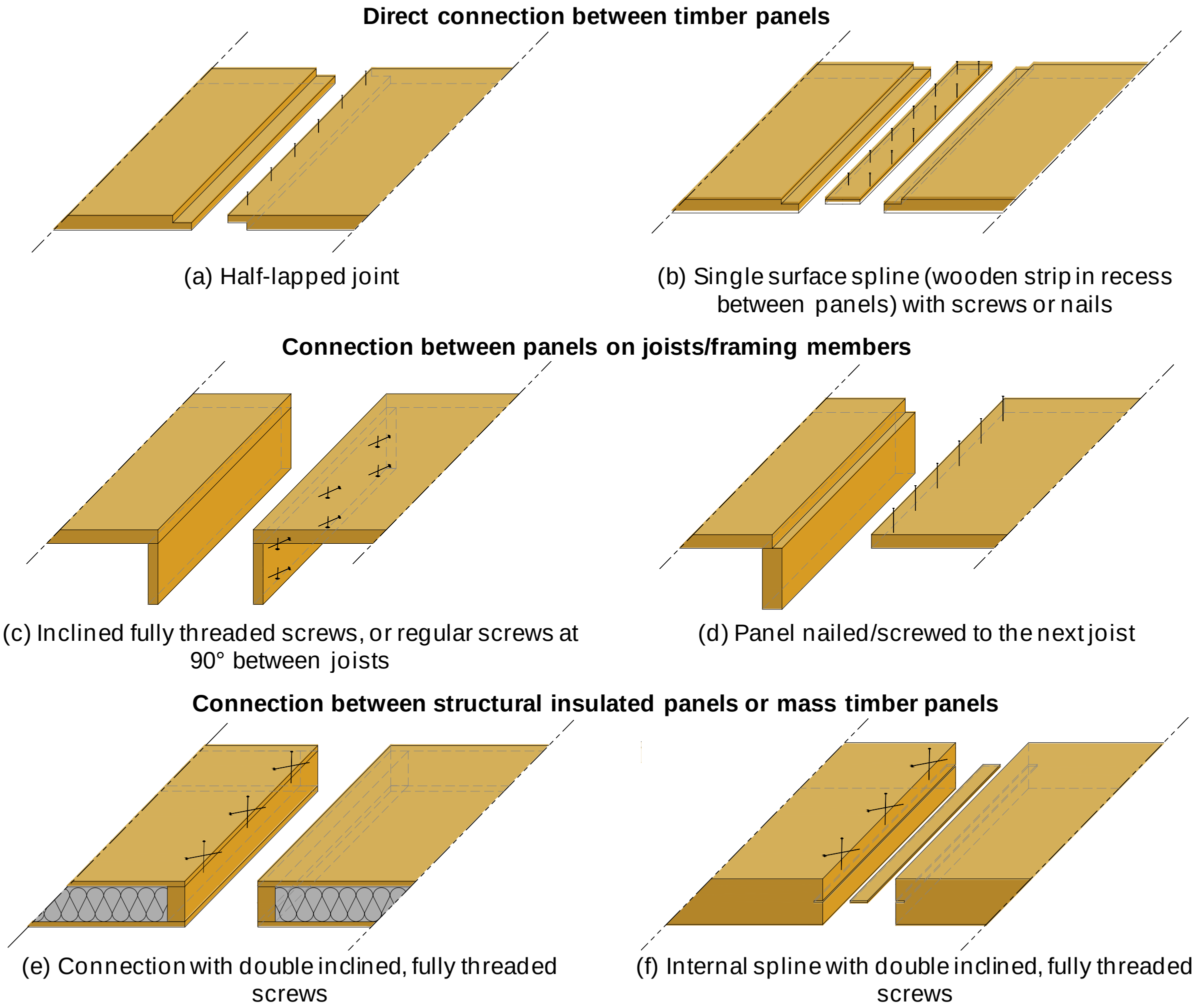


**Figure 32. Connection details between floor elements**

It is best not to glue diaphragm panels, as this would result in very brittle failure modes. If panels are glued to the framing elements/joists, then the connection between the joints, at least, should be designed with metallic fasteners (see Figure 32[c]). In general, use connections with yielding failure mechanisms to prevent brittle diaphragm failure in cases of higher than predicted seismic loading, even if the diaphragms are not otherwise designed to be energy dissipative.

Because of the possible displacement incompatibilities, as discussed in Section 6.2.6.3, special detailing for floor panel connections close to the beam-column joints of structural frames may be necessary.

#### 6.2.6.1.2 Chord Beams

Chord beams must resist diaphragm bending in the form of tension and compression forces. Any splices in the chord beams absolutely must be designed correctly for both tension and compression forces due to load reversals. Chord splices also influence the diaphragm stiffness and should be designed to be as stiff as possible.

For re-entrant corners or diaphragm setbacks, the forces in the chords need to be transferred via the panel elements to the next chord or strut beam, as shown in Figure 33, to provide force continuity. Stress concentrations in the panels and the forces in the beams can be determined with the equivalent truss method. Alternatively, it is possible to ignore the discontinuous chord and consider the next continuous internal beam acting as the chord. The internal chord beam needs to carry higher forces because of the smaller lever arm. With this approach, one must consider higher displacements and therefore potential damage at the discontinuities.

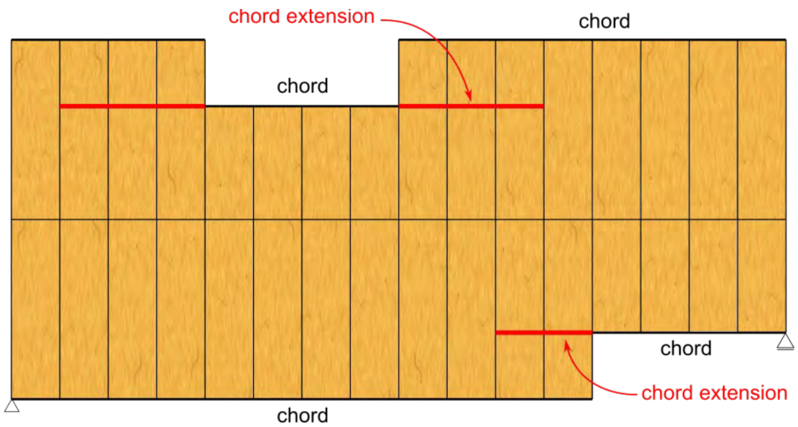


**Figure 33. Chord discontinuities**

#### 6.2.6.1.3 Collector and Strut Beams

Collector beams collect the unit shear forces along the ends of the diaphragm and transfer them to the next lateral load-resisting element. The collector beams therefore need to work in tension and compression. Because of openings and other floor irregularities, additional strut/drag beams may be necessary to transfer the forces from the disturbed areas to the remaining diaphragm. The forces in these members need to be determined with rational analysis, like the equivalent truss method.

The biggest challenge in designing these collector and strut beams is any potential intersection with other members. Since it is of paramount importance to transfer the axial forces correctly, connections need to be designed accordingly. Figure 34[a] shows a connection for smaller axial forces for two orthogonally running beams. Tension forces are transferred by the bolt and the steel angles, and compression forces by compression. For mass timber panels, it is sometimes possible to avoid dedicated strut beams by transferring tension forces trough a nailed steel strip to the adjacent panel or panels, as in Figure 34[b]. For such cases, one must consider possible tension forces perpendicular to grain. Figure 35 shows two examples of chord/strut beam splices.

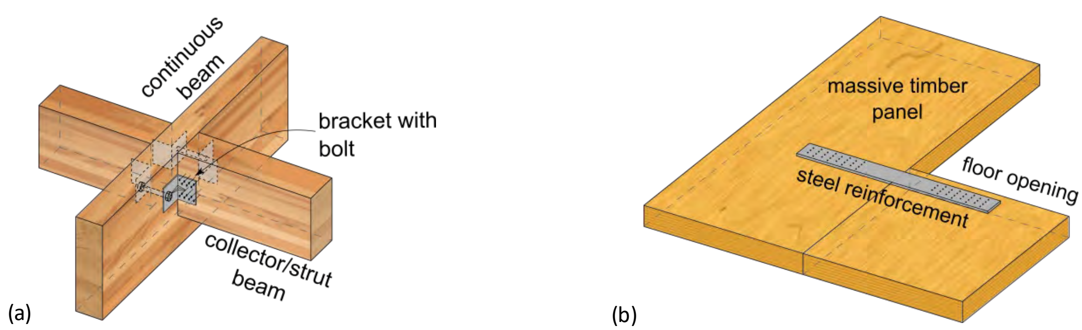


**Figure 34. Force transfer in timber diaphragms due to irregularities: (a) connection for collector or strut beams with small axial forces, and (b) connection on mass timber panels with small axial forces**

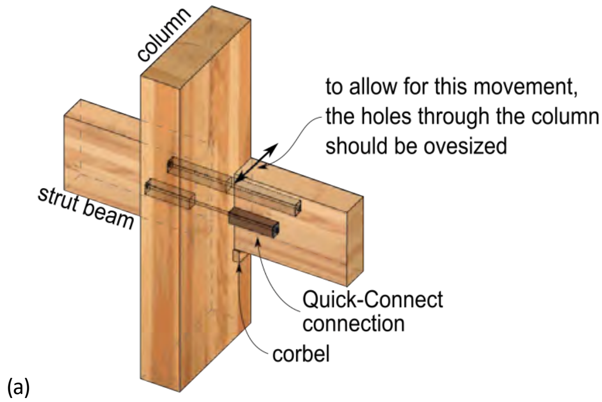


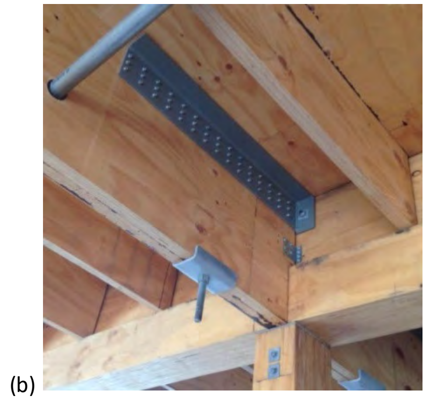


**Figure 35. Possible details of a chord/strut beam splice: a) sketch of a timber Quick-Connect connection (Quenneville et al., 2011), and (b) steel connection in the Kaikoura District Council Building**

Depending on the direction of the horizontal load application, chord and collector beams swap their functions, i.e., collector beams become parallel and chord beams become perpendicular to the load applied. It is therefore necessary to determine the force demand in the elements from all possible load scenarios (line of attack and direction), to determine appropriate section sizes and to design splices accordingly. Most collector and strut beams also carry gravity loads, so their section size and connection design must arise from the respective load combinations.

### *6.2.6.2 Connections of Diaphragms to Walls*

All cantilevered shear walls, whether post-tensioned rocking walls, wood frame walls, mass timber walls with ductile hold downs, or walls connected with ductile fasteners along their vertical joints, will rotate and uplift under design earthquakes. Such behaviour is desired, as the resulting gap opening between wall and foundation leads to the yielding of the hold-downs or the small dowel fasteners (nails, screws, staples) along the vertical joints, providing the required ductile link in the LLRS. Because of their diaphragm-to-wall connections, which are necessary to transfer the horizontal forces, floor diaphragms are often subjected to out-of-plane bending due to rotation and uplift from the foundation, as shown in Figure 36.

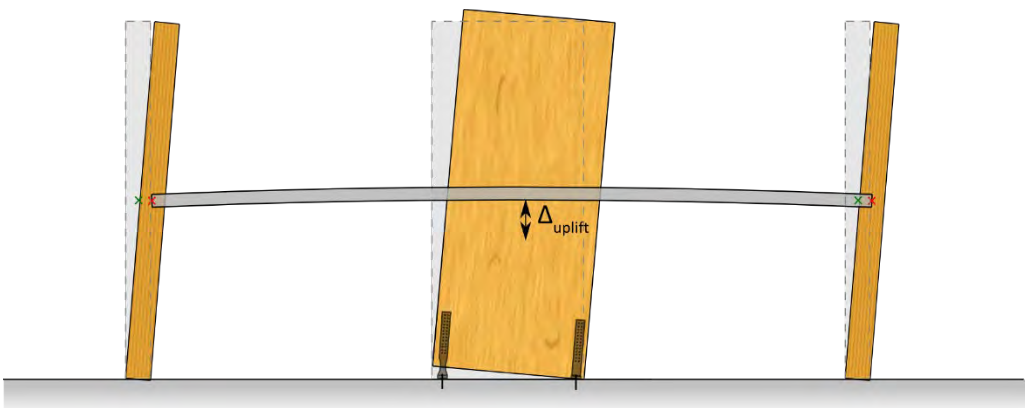


**Figure 36. Floor out-of-plane bending due to wall rotation and uplift**

In certain design situations, this imposed deformation demand may damage the floor slab, and as it also makes the wall stronger and stiffer, this tends to increase axial forces in the wall and other connected gravity-resisting elements. The out-of-plane flexibility of the floor and the flexibility of the connection can often accommodate such displacement incompatibility. Ideally, releasing the rotational or vertical movement degrees of freedom will remove incompatibilities.

#### 6.2.6.2.1 Connection to Single Walls

For wall structures, the diaphragm (horizontal) forces and possible gravity (vertical) forces may be transferred via the collector beam to the LLRS, as shown in Figure 37. The diaphragm panels connect directly to the collector beam with nails or screws; see Section 6.2.6.3. The most appropriate connection between the collector beam and the walls depends on the span direction and out-of-plane stiffness of the floor.

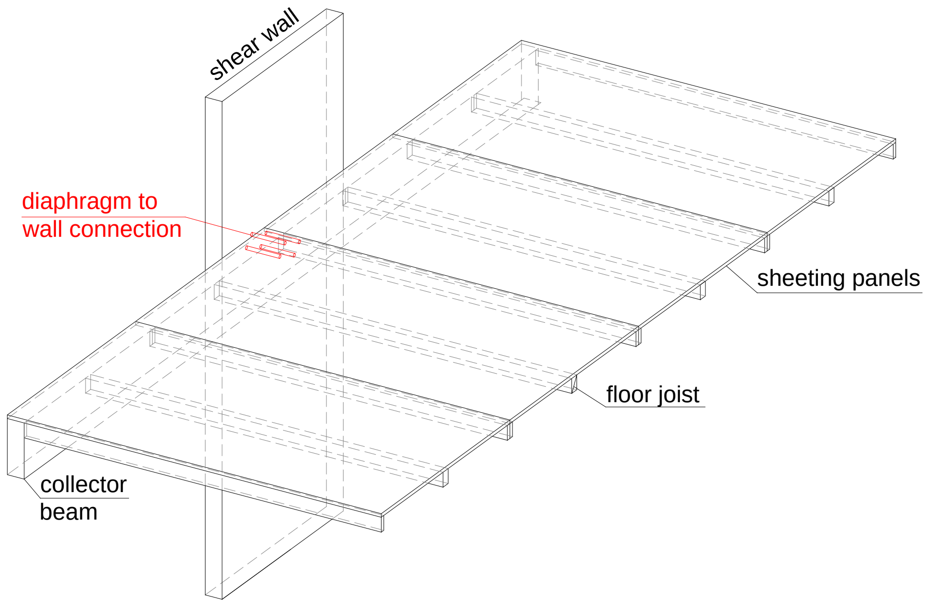


**Figure 37. Scheme of a typical diaphragm to wall connection**

Floor elements running parallel to the wall only have to transfer horizontal forces; otherwise, they would have to resist gravity forces as well. To minimise the effects of displacement incompatibilities, the collector beam should be connected to the wall by a single connection near the centre of the wall. An eccentric connection will induce bigger rotations and uplifts in one direction as the wall rocks. Because the vertical displacement incompatibility is normally much smaller than the deflection limit under serviceability loads, it generally does not create any damage to structural or nonstructural elements.

For flexible floors with relatively low out-of-plane stiffness, one can use economical connections with closely spaced bolts, inclined fully threaded screws, or large diameter dowels. For stiffer floors, a steel-to-steel solution with a pin in a slotted hole will help avoid displacement incompatibilities. To minimise friction, use brass shims or polytetrafluoroethylene (PTFL) pads at areas of contact. Boundary columns at each end of the wall can reduce interaction between the floor diaphragm and the wall, in which case the collector beams should be pin-connected to these boundary columns via closely spaced bolts or a large diameter dowel.

These solutions apply to all floor systems, including timber-only diaphragms and timber-concrete composite diaphragms. Recommended solutions are listed in Table 7 in order of reduced interaction between wall and floor.

**Table 7. Possible connections between walls and collector beams**

| Connection type | Force transfer | Displacement incompatibilities | | Comments |
|---|---|---|---|---|
| Large diameter dowel | Horizontal shear and gravity | Rotation is allowed | Uplift is not allowed | Makes it necessary to determine embedment strength carefully and avoid splitting of timber. |
| Closely spaced bolts | Horizontal shear and gravity | Rotation is partially allowed [1)] | Uplift is not allowed | Simple and cost-effective solution; the flexibility of the connection allows for some rotation. |
| Inclined fully threaded screws | Horizontal force only | Rotation is allowed | Uplift is allowed | Screws might behave inelastically; damaged screws can be replaced, or additional screws added. Very economical solution. |
| Slotted steel plate | Horizontal force only | Rotation is allowed | Uplift is allowed [2)] | Relatively expensive and laborious connection, significantly reducing interaction. |
| Wall end-columns and pinned connection | Horizontal shear and gravity | Rotation is allowed | Uplift is allowed | Essentially eliminates interaction; increases the construction cost significantly. |

1) Given the possibility of using oversized holes in timber and accounting for a relatively flexible dowel connection, it is normally possible to accommodate wall rotation for limited drift ratios.

2) This requires special measures to reduce friction at the contact interface.

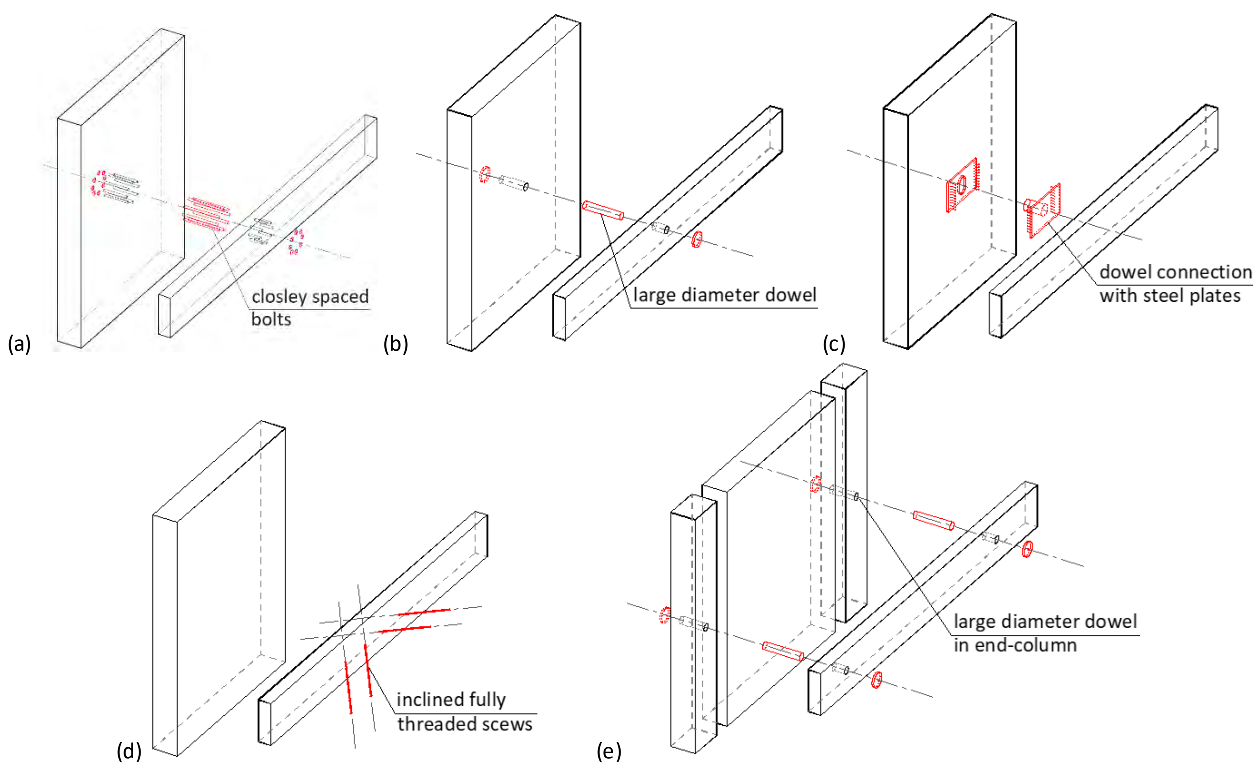


**Figure 38. Recommended beam-to-wall connections: (a) closely spaced bolts, (b) large diameter dowel, (c) steel plates with slotted hole and pin, (d) inclined fully threaded screws, and (e) large diameter dowel in end-columns**

Without appropriate connection detailing to avoid displacement incompatibilities between the wall and the diaphragms beams, one must consider the interaction between the two, since both the strength and the stiffness of the LLRS will increase. This is because the beams counteract the imposed rotation and uplift, providing additional recentring forces and moments to the wall, as shown in Figure 39.

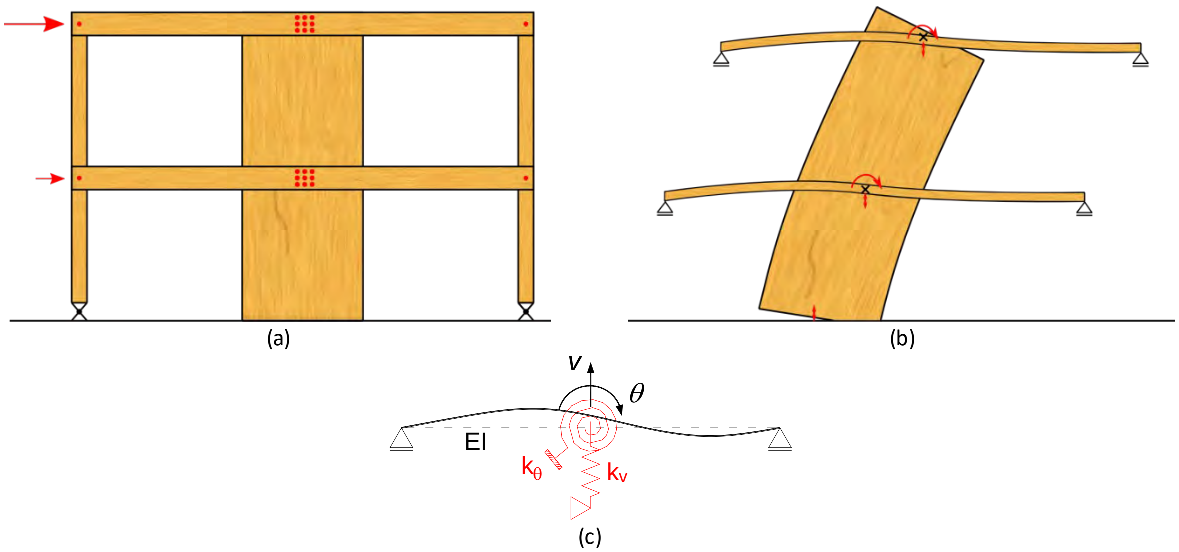


**Figure 39. Wall-to-beam assembly with statical system: a) wall-beam-column system, b) wall-beam interaction, and c) statical system**

A number of software packages allow pushover analysis of possible wall-to-beam assemblies, like those shown in Figure 40. Although it is possible to model approximate compression stiffness with single compression springs, to obtain realistic wall rotations and uplifts, one must model the wall-foundation interface with multi-springs or other elements.

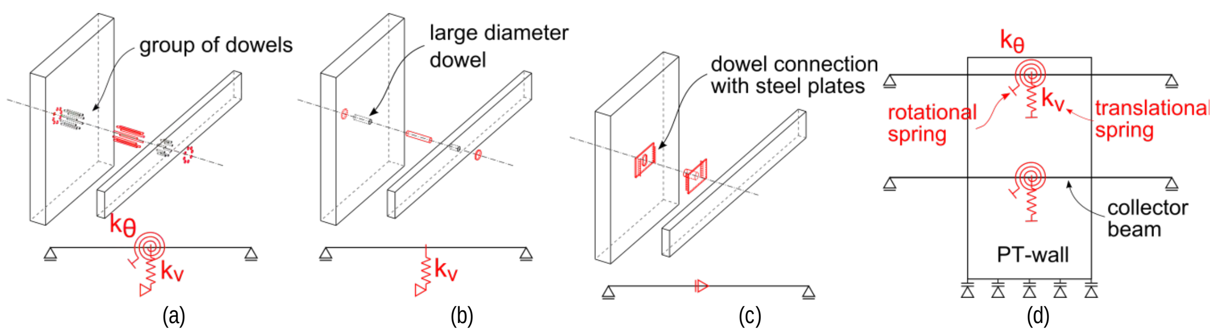


**Figure 40. Summary of three proposed wall-to-beam connections: (a) translational and rotational interaction, (b) translational interaction, and (c) no interaction with the collector beam; (d) shows the complete statical model**

An analytical procedure can also provide a pushover analysis of the wall-to-beam system. For each imposed rotation in the wall, obtain the force and moment equilibrium at the wall-foundation interface by iteration. For the given deformed shape, determine the vertical force and moment at the wall-to-beam connection due to the displacement incompatibility (Moroder, 2016). These recentring actions, which are a function of the beam bending stiffness $EI$ and the connection rotational and translational stiffness, $k_{\vartheta}$ and $k_v$ respectively, need to be considered in the equilibrium conditions.

#### 6.2.6.2.2 Connection to Core-Walls

The same design recommendations regarding the diaphragm-to-wall connections apply to core-wall systems as to single walls. More attention must be paid to the displacement incompatibilities arising from the out-of-plane rotations of the walls, however.

Because core-wall systems normally resist horizontal loads in both principal directions, collector beams in both directions must connect to the walls, with connection details that allow for displacement incompatibilities. Because of height constraints, collector beams are normally placed at the same height and need to be spliced at their intersection at the core-wall. To allow for both the axial force transfer in the beams and the vertical displacement imposed by the orthogonal walls, thin, out-of-plane flexible steel plates, as shown in Figure 41, are preferable. Steel plates fixed at the tops and bottoms of the beams can be connected by nails, rivets, or fasteners sufficiently far from the intersection to allow for the elastic bending of the plates. The flexibility of the beam-to-wall connection, the bending of the beams, and the flexible splice plate must allow for the expected displacements.

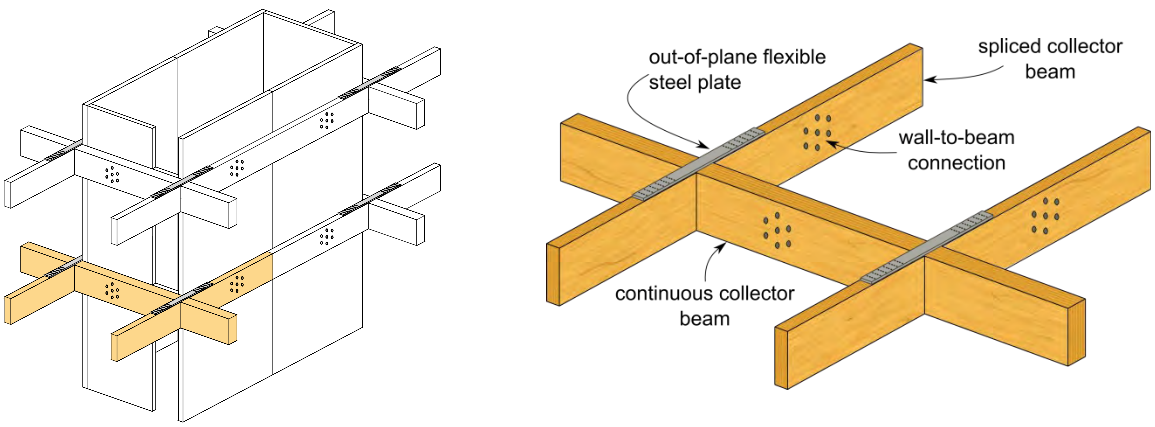


**Figure 41. Collector beam connection with out-of-plane flexible steel plates**

The unit shear forces from the diaphragm should be introduced to the collector beams at a distance from the intersection point of the collector beams, because the relative vertical movement of the beams in these disturbed areas might pull out the panel fasteners. One should not rely on shear transfer in this area and should ideally avoid panel connections, as shown in Figure 42, by transferring forces to the collectors at remote locations.

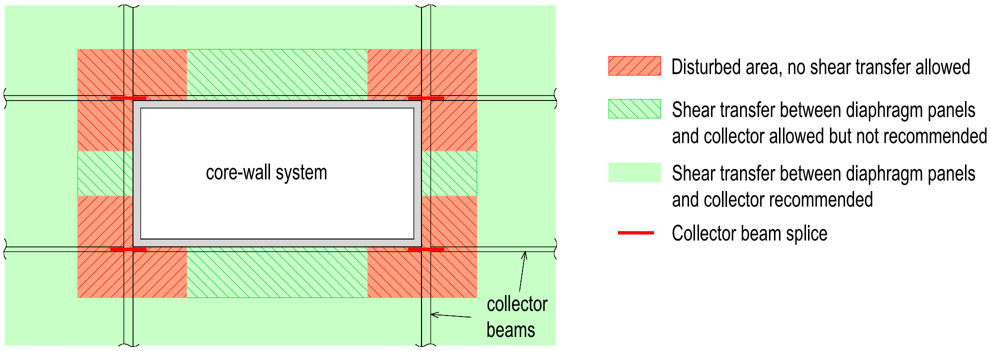


**Figure 42. Recommended and prohibited areas for shear force transfer between the core and the floor diaphragms**

For rigid out-of-plane diaphragms, it is recommended to use a design solution with boundary columns at the corner of the core-wall system. This reduces imposed vertical uplift and rotation from the rocking walls and means the collector beam splices need only allow for the out-of-plane rotation of the walls.

### *6.2.6.3 Connections of Diaphragms to Timber Frames*

This section considers timber diaphragms running perpendicular to the seismic and gravity frames. The diaphragms transfer vertical gravity forces and horizontal shear forces to the frame beam, which acts as a collector or strut. For diaphragms sitting between the beams, gravity loads can be transferred by a timber corbel, a pocket in the main beam, or steel hanger brackets, as shown in Figure 43. The horizontal shear forces in the diaphragm can be transferred directly by nailing or screwing the sheeting panels to the top of the beam.

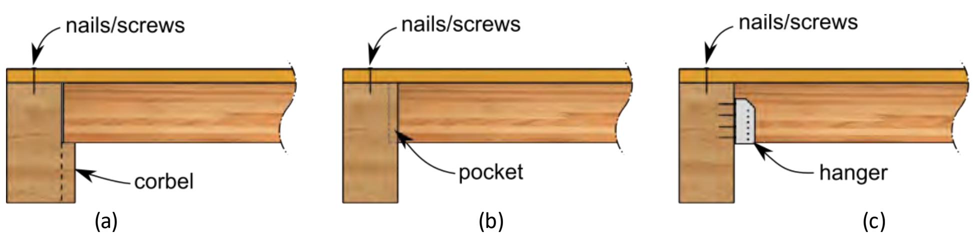


**Figure 43. Suggested floor to frame connections (floor joists flush with beam): (a) floor joist on corbel, (b) floor joist in pocket, and (c) steel bracket/hanger**

Where the floor panels sit atop the beams, gravity forces are transferred by direct contact. Shear forces can be transferred by using inclined fully threaded screws or by connecting the sheathing panels to blocking elements, which again connect to the beam by screws or steel plate elements (see Figure 44).

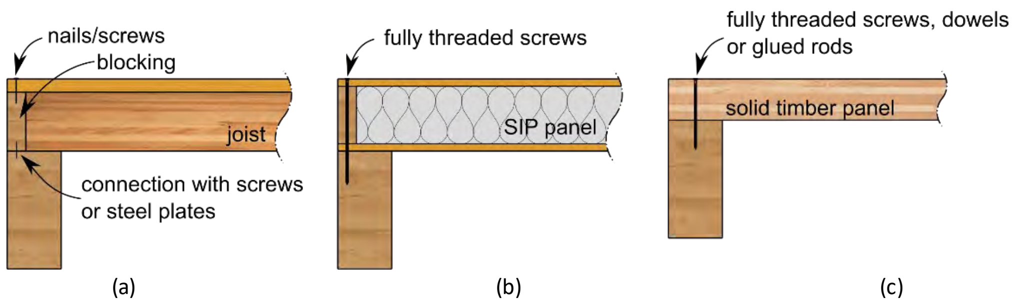


**Figure 44. Suggested diaphragm to frame connections (floor joists on top of beam): (a) floor joist sitting – additional blocking required, (b) Structural Insulated Panel, and (c) solid timber floor**

Independently of the seating detail, there must be enough bearing surface in case of a gap opening at a beam column interface due to geometric beam elongation.

**Floor panel connections to accommodate frame elongation**

Ductile timber frames will experience beam elongation under design earthquakes as geometric gaps open (e.g., in post-tensioned Pres-Lam frames) or the steel elements (the glued rod, external steel plate, etc.) yield at the beam-column interface. Although this effect is desirable, helping achieve ductility and/or damping, the displacement demand may lead to the floor tearing, as shown in Figure 45.

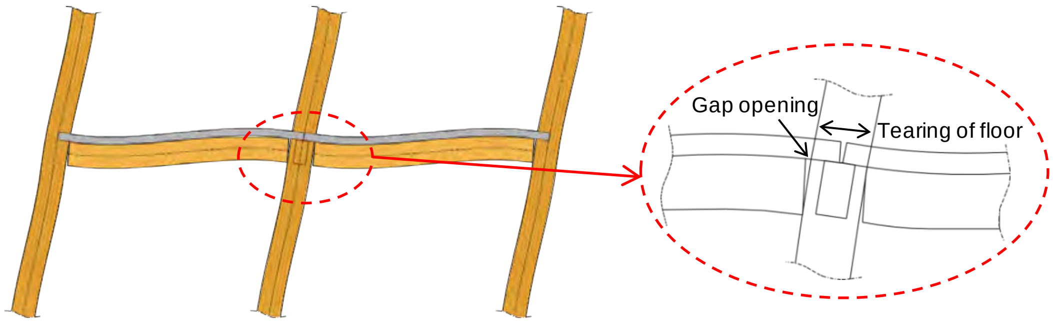


**Figure 45. Tearing of the floor due to frame elongation**

One must allow for this elongation of the floor without causing a brittle tear in the plate element, as that would cause permanent damage and compromise the shear transfer. The flexibility of the timber elements and the low stiffness of the steel connections allow for two simple design solutions for engineered timber floor panels:

***Solution 1 - Concentrated gap*** (see Figure 46):

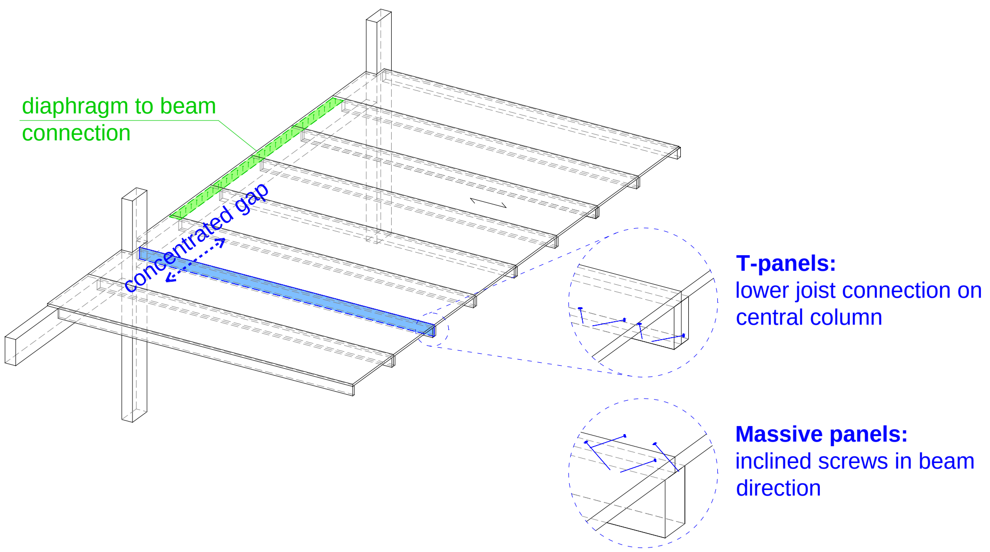


**Figure 46. Sample design for a concentrated floor gap**

As the required deformation at the floor level occurs only at the beam-column joint, a joint between two adjacent floor panels should be positioned accordingly. All other panel joints further away can be designed without any specific deformation considerations.

- For diaphragms with sheathing panels and slender joists, connect only the lower part of the joist, so that it can bend up its height but still guarantee shear transfer (see Figure 47[a]). Design the connection between the sheathing panel and joist with sufficient capacity and appropriate minimum distances to allow for the joist bending (i.e., the additional forces perpendicular to the joist edges need to be considered in addition to the shear forces acting parallel to the panel edges).
- For diaphragms with stiff joists, one can use special steel elements. These should allow the panels to move apart from each other but still transfer shear forces (an example is shown in Figure 47[b]). Provide seismic gaps in the floor finishing and wall linings to allow these deformations to occur.
- For a diaphragm with mass timber panels running perpendicular to the frame direction, the connection of the panels to the transverse beam is the main source of flexibility to accommodate the displacement demand. This can involve a connection with inclined screws between the panel and the beam, as shown in Figure 46. If a gap opens, the screws will deform elastically in dowel action but keep transferring shear when the seismic action runs perpendicular to the frame direction.

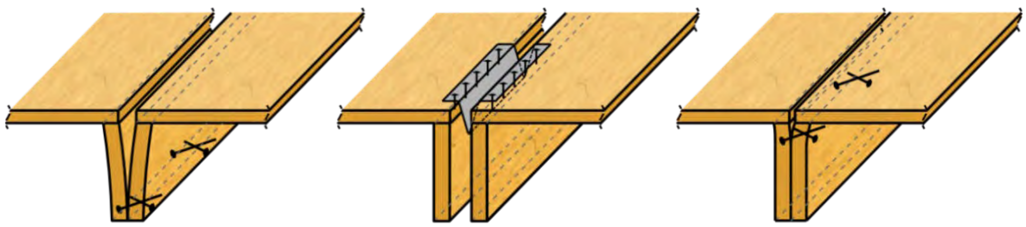


**Figure 47. Details for a concentrated floor gap: (a) lower joist connection, (b) connection with thin steel plate, and (c) upper joist connection**

***Solution 2: Spread floor gaps and panel elongation*** (see Figure 48):

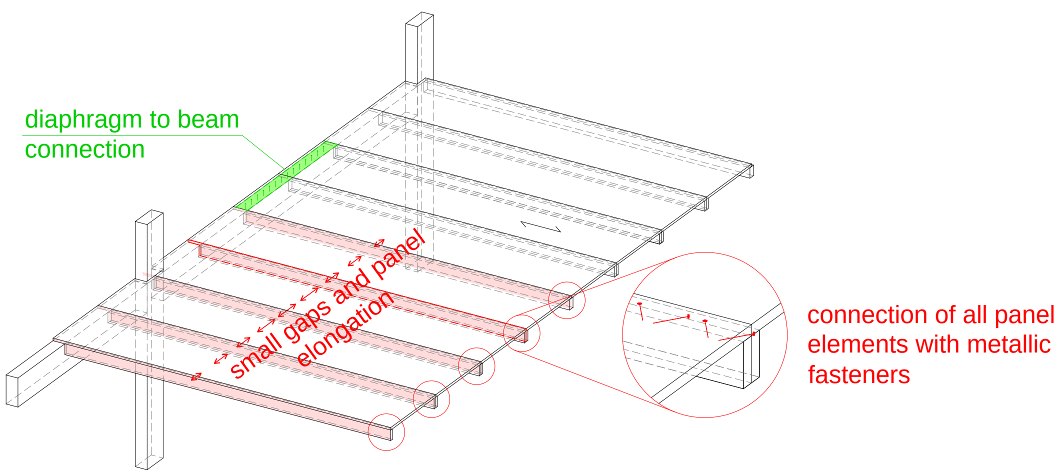


**Figure 48. Sample design for a spread floor gap**

An alternative to a concentrated gap at each column location is detailing for spread gaps. A number of small panel gap openings and the elongation of the sheeting panel itself will accommodate the required deformation.

Two to three floor elements on each side of the beam-column joint should connect to each other via metallic connectors like nails or screws (for example, an upper joist connection, shown in Figure 47[c] or a connection with a nailed spline, as in Figure 47[b]). The connection needs to guarantee full shear transfer between the elements but should be flexible enough to allow for a small displacement. Small gaps will hence open in several panel joints, and the sheeting panels will elongate. The panels close to the beam-column joint(s) should not be connected to the beam to transfer diaphragm forces, as this would prevent floor gap openings and panel elongations further away from the area of interest.

Regardless of the type of panel connection, there should be a tolerance gap in the panels around all the frame columns to further prevent interaction and potential damage to the columns and/or floor elements. One can estimate the size of the gap from the calculated gap opening at the beam column joint.

Another solution to avoid frame elongation on a multi-bay frame is to connect the diaphragm only to one bay and let it slide over the remaining beams. However, this might result in high shear forces at the connection between the diaphragm and the beam and would require specific detailing to allow the diaphragm to slide in respect to all other elements.

### *6.2.6.4 Connections with Timber-Concrete Composite Diaphragms*

This section gives guidance for the design of timber-concrete composite diaphragms. In some cases, these may be reinforced concrete topping on plywood on wood frame floors or mass timber floors.

#### 6.2.6.4.1 Connections within Timber-Concrete Composite Diaphragms

Except for precast concrete panels with discrete connectors, cast-in-situ concrete diaphragms do not require any specific connections inside them. When using the deep beam analogy, diaphragm forces are transferred via the shear capacity of the concrete, with the aid of the diaphragm reinforcement if required. Tension forces in the chords and collector beams are transferred via the steel reinforcing, and compression forces via the concrete.

With a strut-and-tie analysis, tension and compression struts are well defined and the corresponding forces are resisted by the reinforcing steel and concrete, respectively. Many international concrete standards, like Eurocode Eurocode 2 (European Committee for Standardization, 2005), NZS 3101 (Standards New Zealand, 2006), or ACI 318 (American Concrete Institute, 2014), provide specific provisions for the design of nodal zones.

#### 6.2.6.4.2 Connection of Timber-Concrete Composite Diaphragms to Timber Walls

In general, do not to connect a concrete slab directly to the timber walls; instead, transfer horizontal forces first along a timber collector beam. The force transfer thus occurs between the wall and the collector beams and the connections can be designed following the recommendations discussed above.

The connection between a concrete slab and a collector beam can follow Figure 49. The diaphragm shear force is introduced to the beam via notched connections used for the timber-concrete composite floor design (see Gerber et al., 2012). If the concrete topping connects to the beam directly, the beams have to be designed as a composite section.

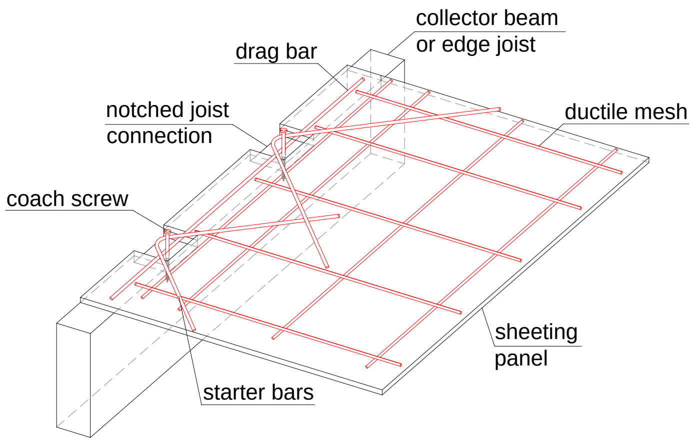


**Figure 49. Suggested connection between the concrete topping and the timber beam**

The diaphragm force is then transferred from the timber beam to the wall with the type of connection outlined in Section 6.2.6.2.1. This results in a solution such as that outlined in Figure 50, which assumes a bolted connection to act as a pin.

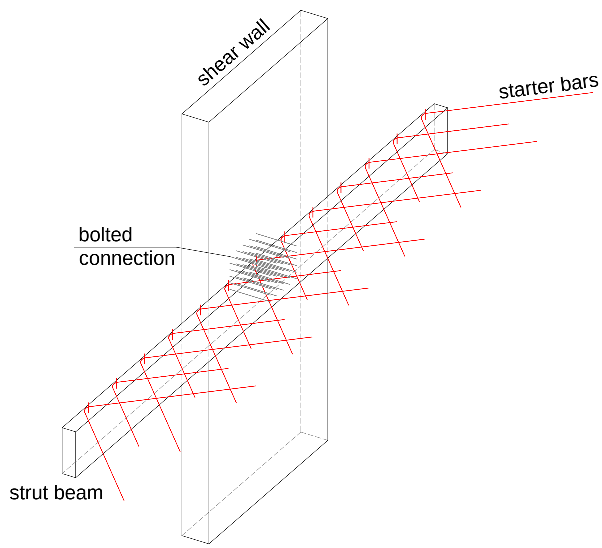


**Figure 50. Conceptual connection of the diaphragm to the timber strut beam and its connection to the wall**

### 6.2.6.4.3 Connections to Accommodate Frame Elongation for Concrete Topping

The introduction of concrete topping in a ductile timber frame structure requires more attention in diaphragm design because displacement incompatibilities cannot be accommodated as in engineered timber. The low tensile strength of concrete means that tearing forces due to frame elongation and bending forces due to uplift and wall rotation tend to crack the diaphragm topping. Large cracks can interrupt the force transfer and compromise the diaphragm action (Bull, 2004).

For timber frame structures with timber-concrete composite floors, it is possible to accommodate the displacement incompatibility required of the beam-column gap opening, like the concentrated floor gap solution already described for timber diaphragms. An example for hybrid concrete floors with a concentrated gap is shown in Figure 51.

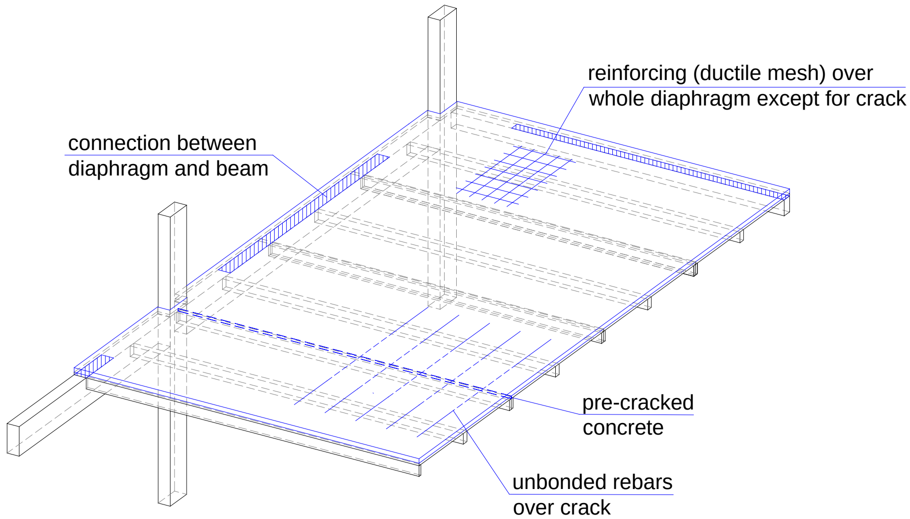


**Figure 51. Suggested detailing for a hybrid timber-concrete floor in a frame system**

To guarantee the shear transfer between the sub-diaphragms, which is needed for the diaphragm action in the transverse direction and to link the single sub-diaphragms together, place unbonded rebars over the potential crack line. Choose the unbonded length so as to have only elastic deformation if the crack opens along the entire line. After a crack occurs and activating the shear-friction mechanism becomes impossible, the reinforcing bars can still transfer shear in dowel action. As suggested in Figure 51, one should pre-crack the concrete along the line of the beam-column joint.

Note that this solution for timber-concrete composite diaphragms is only based on theoretical considerations. Even though already implemented in real constructions like the Trimble Navigation Building (Brown et al., 2012), further investigation and some experimental testing is recommended. If large gaps open, dowel action may not occur until a kinking effect allows for the shear transfer. However, this implies the plasticization of the unbonded rebars and, potentially, large deformations.

The diaphragms have to be tied appropriately to the timber collector beams. One way of doing this is shown in Figure 49, with staggered starter bars cast into the concrete slab. This should guarantee the force transfer from the diaphragm to the beam in the central portion of the beams, leaving it unconnected close to the beam-column joints (in the disturbed areas shown in Figure 52). Frame elongation will thus not compromise the force transfer, which starts away from the disturbed areas where the displacement incompatibility is concentrated.

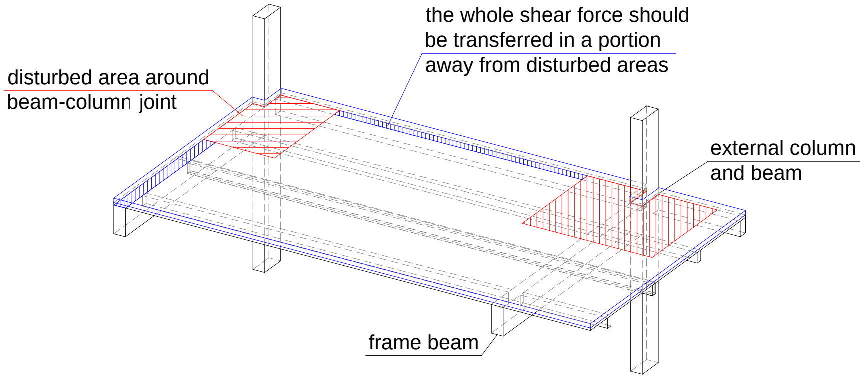


**Figure 52. Shear transfer between the concrete topping and beams**

Take care if a floor gap opens along a collector or tie beam, as the cracking of the concrete can compromise the force transfer. Ideally, place the pre-crack away from any connection to the beams.

For the design of all concrete diaphragms, consider the design recommendations given in Bull and Henry (2014).

## 6.2.7 Summary

This chapter introduces the types and components of diaphragms, along with their structural role. It highlights and discusses the complexities in the design of diaphragms for wind and seismic loads. It summarises and compares typical analysis methods for diaphragms, i.e., deep beam/girder analogy, shear field analogy, truss analogy, and FE methods. For three types of diaphragms, i.e., light-wood frame, mass timber, and timber-concrete composite diaphragms, it discusses first their behaviour and then the analytical and FE methods that can help model them. It also introduces the calculation of component capacity and diaphragm deflection and discusses the design and modelling of connections within diaphragms and connections to lateral load-resisting systems. The information presented in this chapter aims to help practising engineers and researchers become better acquainted with the modelling and analysis of timber diaphragms subject to in-plane loads.

## 6.2.8 References

American Concrete Institute. (2019). *Building code requirements for structural concrete and commentary* (ACI CODE-318-19).

American Forest & Paper Association - American Wood Council (2021). *Special design provisions for wind and seismic with commentary* (ANSI/AF&PA SDPWS-2021).

American Society of Civil Engineers (2016). *Minimum design loads for buildings and other structures* (ASCE 7-16).

American Wood Council. (2008). *ASD/LRFD: Wind & seismic: special design provisions for wind and seismic* (ANSI/AF&PA SDPWS-2008).

APA – The Engineered Wood Association. (2007). *Diaphragms and shear walls*.

Applied Technology Council. (1981). *Guidelines for the design of horizontal wood diaphragms* (ATC 7).

Ashtari, S. (2009). *In-plane stiffness of cross-laminated timber floors* [Master's Thesis, University of British Columbia]. UBC Theses and Dissertations. https://open.library.ubc.ca/soa/cIRcle/collections/ubctheses/24/items/1.0073342

Blaauwendraad, J., & Hoogenboom, P. C. J. (1996). Stringer panel model for structural concrete design. *Structural Journal, 93*(3), 295–305. https://doi.org/10.14359/9689

Blaß, H. J., Ehlbeck, J., Kreuzinger, G., & Steck, G. (2004). *Erläuterungen zur DIN 1052:2004-08. Entwurf, Berechnung und Bemessung von Holzbauwerken [Commentary on the DIN 1052:2004-08. Design of timber structures]*. DGfH Innovations- und Service GmbH.

Breneman, S., McDonnell, E., & Zimmerman, R. (2016). An approach to CLT diaphragm modelling for seismic design with application to a US high-rise project. In Eberhardsteiner, J., Winter, W., Fadai, A., & Pöll, M. (Eds.). *WCTE 2016 e-book : containing all full papers submitted to the World Conference on Timber Engineering (WCTE 2016), August 22–25, 2016, Vienna, Austria*. TU Verlag Wien. https://resolver.obvsg.at/urn:nbn:at:at-ubtuw:3-2204

Brown, A., Lester, J., Pampanin, S., & Pietra, D. (2012). *Pres-Lam in practice: A damage-limiting rebuild project* [Conference presentation]. SESOC Conference 2012, Auckland, New Zealand.

Bull, D. (2004). Understanding the complexities of designing diaphragms in buildings for earthquakes. *Bulletin of the New Zealand Society for Earthquake Engineering, 37*(2), 70–88. https://doi.org/10.5459/bnzsee.37.2.70-88

Bull, D. & Henry, R. (2014). *Strut & tie: Seminar notes (TR57)*. The New Zealand Concrete Society.

Carr, A. (2006). Ruaumoko 3D. Christchurch, New Zealand.

Chen, Z., Chui, Y., Ni, C., Doudak, G., & Mohammad, M. (2013). Influence of diaphragm flexibility on lateral load distribution between shear walls in light wood frame buildings. In C. Brebbia & S. Hernández (Eds.), *Earthquake Resistant Engineering Structures IX* (pp. 157–166). WIT Press.

Chen, Z., Chui, Y. H., Mohammad, M., Doudak, G., & Ni, C. (2014). *Load distribution in lateral load resisting elements of timber structures* [Conference presentation]. World Conference on Timber Engineering, Québec City, Québec, Canada.

Chen, Z., Chui, Y. H., & Ni, C. (2013). Seismic performance of mid-rise hybrid light wood frame buildings and influence of diaphragm flexibility. *Structures Congress 2013*, 1229-1241. https://doi.org/10.1061/9780784412848.109

Chen, Z., Chui, Y. H., Ni, C., Doudak, G., & Mohammad, M. (2014). Load distribution in timber structures consisting of multiple lateral load resisting elements with different stiffnesses. *Journal of Performance of Constructed Facilities, 28*(6), A4014011. https://doi.org/10.1061/(ASCE)CF.1943-5509.0000587

Chen, Z., Ni, C., Dagenais, C., & Kuan, S. (2020). Wood$^{ST}$: A temperature-dependent plastic-damage constitutive model used for numerical simulation of wood-based materials and connections. *Journal of Structural Engineering, 146*(3), 04019225. https://doi.org/10.1061/(ASCE)ST.1943-541X.0002524

Chen, Z., Zhu, E., & Pan, J. (2011). Numerical simulation of wood mechanical properties under complex state of stress. *Chinese Journal of Computational Mechanics, 28*(4), 629-634, 640.

Colling, F. (2011). *Building bracing for buildings in timber panel construction. Fundamentals, stresses, verifications according to DIN and EUROCODE.* Karlsruhe Ingenieurbüro Holzbau.

Consiglio Superiore dei Lavori Pubblici (2008). Norme tecniche per le costruzioni ("Design code for structures"), Rome, Italy.

Consiglio Superiore dei Lavori Pubblici (2018). Update of the "Technical standards for construction. Ordinary supplement to the "Official Gazette" No. 42 of February 20, 2018 - General Series. Ministero Delle Infrastrutture E Dei Trasporti, Italy.

CSI. (2004). SAP2000: Static and Dynamic Finite Analysis of Structures. USA.

Dassault Systèmes HQ. (2011). Abaqus FEA. France.

Dean, J.A. (1982). Sheathed Construction. Timber Engineering Seminar.

Dean, J. A., Moss, P. J., & Stewart, W. (1984). *A design procedure for rectangular openings in shearwalls and diaphragms* [Conference presentation]. Pacific Timber Engineering Conference, Auckland, New Zealand.

Deutsches Institut für Normung (1988). *Structural use of timber; design and construction* (DIN 1052-1:1988-04).

Deutsches Institut für Normung. (2008). *Design of timber structures - general rules and rules for buildings* (DIN 1052:2008-10).

Deutsches Institut für Normung. (2010). *National Annex - Nationally determined parameters - Eurocode 5: Design of timber structures. Part 1-1: General - Common rules and rules for buildings* (DIN EN 1995-1-1:NA:2010).

Diekmann, E. F. (1982). Design of wood diaphragms. Fourth Clark C. Heritage Memorial Workshop, University of Madison.

Diekmann, E.F. (1995). Diaphragms and Shear Walls. In K. F. Faherty and T. G. Williamson (Eds.), *Wood Engineering and Construction Handbook* (8.1–8.68), McGraw-Hill.

Dlubal. (2016). RFEM Structural Analysis Software. Dlubal Software GmbH, Germany.

Elliott, J. R. (1979). *Wood diaphragm testing - past, present, planned*. Paper presented at the Proceedings on a Workshop on Design of Horizontal wood diaphragms, Berkeley, California.

Eurocode 2 (2005). EN 1992:2004. Design of concrete structures - Part 1-1: General rules and rules for buildings. European Committee for Standardization.

Eurocode 8 (2004). EN 1998-1:2004/AC:2009. Design of structures for earthquake resistance. Part 1: General rules, seismic actions and rules for buildings. European Committee for Standardization.

Eurocode National Annex - Nationally determined parameters - Eurocode 5: Design of timber structures. Part 1-1: General - Common rules and rules for buildings, DIN EN 1995-1-1:NA:2010 C.F.R. (2010).

European Committee for Standardization. (2005). *Eurocode 2: Design of concrete structures - Part 1-1: General rules and rules for buildings* (Eurocode Standard EN 1992:2004 C.F.R.).

European Committee for Standardization. (2008). *Eurocode 5: Design of timber structures. Part 1-1: General - Common rules and rules for buildings* (Eurocode Standard EN 1995-1-1:2004/A1:2008).

European Committee for Standardization. (2004). *Eurocode 8: Design of structures for earthquake resistance. Part 1: General rules, seismic actions and rules for buildings* (Eurocode Standard EN 1998-1:2004/AC:2009).

Falk, R. H., & Itani, R. Y. (1989). Finite-element modeling of wood diaphragms. *Journal of Structural Engineering-ASCE, 115*(3), 543-559. https://doi.org/10.1061/(ASCE)0733-9445(1989)115:3(543)

Fanella, D. A., & Mota, M. (2018, April). Design of reinforced concrete diaphragms for wind. *Structure*. www.structuremag.org/?p=12970.

Fenwick, R.C. and Fong, A. (1979). The Behaviour of Reinforced Concrete Beams under Cyclic Loading. *Bulletin of the New Zealand Society for Earthquake Engineering, 12*(1): 158–167.

Fenwick, R., Bull, D.K. and Gardiner, D. (2010). Assessment of hollow-core floors for seismic performance. Research Report, Civil and Natural Resources Engineering, University of Canterbury.

Fleischman, R.B. and Farrow, K.T. (2001). Dynamic behavior of perimeter lateral-system structures with flexible diaphragms. *Earthquake Engineering & Structural Dynamics, 30*(5): 745–763.

Folz, B., & Filiatrault, A. (2000a). CASHEW: A Computer Program for Cyclic Analysis of Wood Shear Walls. USA

Folz, B., & Filiatrault, A. (2000b). SAWS: A Computer Program for Seismic Analysis of Woodframe Structures. USA

Foschi, R. O. (1977). Analysis of wood diaphragms and trusses. Part I: Diaphragms. *Canadian Journal of Civil Engineering, 4*(3), 345–352. https://doi.org/10.1139/l77-043

Foschi, R. O. (1999). DAP3D shear wall/diaphragm analysis program. University of British Columbia. Canada

Foschi, R. O. (2000). *Modeling the hysteretic response of mechanical connections for wood structures* [Conference presentation]. World Conference on Timber Engineering, Whistler, British Columbia, Canada.

Gardiner, D. (2011). *Design recommendations and methods for reinforced concrete floor diaphragms subjected to seismic forces* [Doctoral dissertation, University of Canterbury]. UC Research Repository. http://hdl.handle.net/10092/6993

Gerber, C., Crews, K., & Shrestha, S. (2012). *Design guide Australia and New Zealand: Timber concrete composite floor systems*. Structural Timber Innovation Company.

Ghosh, S. K., Cleland, N. M., & Naito, C. J. (2017). *Seismic design of precast concrete diaphragms: A guide for practicing engineers* (GCR 17-917-47). National Institute of Standards and Technology, US Department of Commerce.

He, M., Lam, F., & Foschi, R. O. (2001). Modeling three-dimensional timber light-frame buildings. *Journal of Structural Engineering-ASCE, 127*(8), 901–913. https://doi.org/10.1061/(ASCE)0733-9445(2001)127:8(901)

Hrennikoff, A. P. (1940). *Plane stress and bending of plates by method of articulated framework* [Doctoral dissertation, Massachusetts Institute of Technology]. DSpace. http://hdl.handle.net/1721.1/64833

Hrennikoff, A. P. (1941). Solution of problems of elasticity by the framework method. *Journal of Applied Mechanics, 8*(4), A169–175. https://doi.org/10.1115/1.4009129

Ilgadi, O. B. (2013). *Advanced three-dimensional analysis of concrete structures using nonlinear truss models* [Doctoral dissertation, Colorado School of Mines]. Mountain Scholar. http://hdl.handle.net/11124/80357

International Code Council (2021). 2021 International Building Code (IBC).

International Federation for Structural Concrete. (2003). *Seismic design of precast concrete building structures: state-of-art report* (*fib* bulletin no. 27).

International Federation for Structural Concrete. (2011). *Design examples for strut-and-tie models: technical report* (*fib* bulletin no. 61.).

Jephcott, D. K., & Dewdney, H. S. (1979). *Analysis methods for horizontal wood diaphragms*. Paper presented at the Proceedings on a Workshop on Design of Horizontal wood diaphragms, Berkeley, California.

Jockwer R., & Jorissen A. (2018). Stiffness and deformation of connections with dowel-type fasteners. In C. Sandhaas, J. Munch-Andersen, & P. Dietsch (Eds.), *Design of connections in timber structures: A state-of-the-art report by COST Action FP1402 / WG3* (pp. 95–126). Shaker Verlag.

Judd, J., & Fonseca, F. (2005). Analytical model for sheathing-to-framing connections in wood shear walls and diaphragms. *Journal of Structural Engineering, 131*(2), 345–352. https://doi.org/10.1061/(ASCE)0733-9445(2005)131:2(345)

Kærn, J. C. (1979). *The stringer method applied to discs with holes*. Final Report, IABSE Colloquium, Plasticity in Reinforced Concrete, Copenhagen, Denmark.

Kamiya, F. (1990). Horizontal plywood sheathed diaphragms with openings: static loading tests and analysis. *Proceedings of the 1990 International Timber Engineering Conference, Tokyo, Japan* 2, 502–509.

Kamiya, F., & Itani, R. Y. (1998). Design of wood diaphragms with openings. *Journal of Structural Engineering, 124*(7), 839–848. https://doi.org/10.1061/(ASCE)0733-9445(1998)124:7(839)

Karacabeyli, E., & Gagnon, S. (Eds.). (2019). *CLT handbook, 2019 edition* (Vols. 1–2). FPInnovations.

Karacabeyli, E., & Lum, C. (Eds.). (2022). *Technical guide for the design and construction of tall wood buildings in Canada* (2nd ed.). FPInnovations.

Kessel, M. H., & Schönhoff, T. (2001). *Entwicklung eines Nachweisverfahrens für Scheiben auf der Grundlage von Eurocode 5 und DIN 1052 neu [Development of a design methodology for diaphragms based on Eurocode 5 and DIN 1052]*, TU Braunschweig, Institut für Baukonstruktion und Holzbau.

Li, M., Foschi, R. O., & Lam, F. (2012). Modeling hysteretic behavior of wood shear walls with a protocol-independent nail connection algorithm. *Journal of Structural Engineering, 138*(1), 99–108. https://doi.org/10.1061/(ASCE)ST.1943-541X.0000438

Li, M., & Foschi, R. O. (2004). *FLOOR2D User's Manual*. University of British Columbia. Vancouver, Canada

Malone, R.T. & Rice, R.W. (2012). *The analysis of irregular shaped structures: Diaphragms and shear walls*. McGraw Hill.

Matthews, J.G., Bull, D.K. and Mander, J.B. (2003). Preliminary results from the testing of a precast hollowcore floor slab building. Proceedings, 2003 Pacific Conference on Earthquake Engineering, Christchurch, New Zealand.

McKenna, F., Fenves, G. L., Scott, M. H., & Jeremic, B. (2000). Open System for Earthquake Engineering Simulation (OpenSees). Berkeley, USA.

Meyer, M. (2006). *Deckentafeln mit freien Plattenrändern [Diaphragms with unsupported edges]*. Paper presented at the Forschungskolloqium, Holzbau Forschung und Praxis, Stuttgart, Germany.

Moehle, J.P., Hooper, J.D., Kelly, D.J. and Meyer, T.R. (2010). *Seismic design of cast-in-place concrete diaphragms, chords, and collectors: a guide for practicing engineers*. NEHRP Seismic Design Technical Brief No. 3. National Institute of Standards and Technology, US Department of Commerce.

Moroder, D. (2016). *Floor diaphragms in multi-storey timber buildings* [Doctoral dissertation, University of Canterbury]. UC Research Repository. http://hdl.handle.net/10092/11893

Moroder, D., Smith, T., Simonetti, M., Ponzo, F.C., Cesare, A.D., Nigro, D., Pampanin, S. and Buchanan, A.H. (2014). Experimental behaviour of diaphragms in post-tensioned timber frame buildings. European Conference on Earthquake Engineering and Seismology, Istanbul, Turkey.

Mörsch, E. (1912). *Der Eisenbetonbau, seine Theorie und Anwendung [Reinforced concrete, theory and application]*. Verlag Konrad Wittwer.

Nakaki, S.D. (2000). *Design guidelines for precast and cast-in-place concrete diaphragms*. NEHRP Professional Fellowship Report. Earthquake Engineering Research Institute.

Pang, W., & Hassanzadeh, M. (2010). *Next generation numerical model for non-linear in-plane analysis of wood-frame shear walls* [Conference presentation]. World Conference on Timber Engineering, Riva del Garda, Italy.

Park, R., Bull, D. K., & Paulay, T. (1997). *Seismic design of reinforced concrete structures* (Technical report no. 21). New Zealand Concrete Society.

Pathak, R. (2008). *The effects of diaphragm flexibility on the seismic performance of light frame wood structures* [Doctoral dissertation, Virginia Polytechnic Institute and State University]. VTechWorks.

Paulay, T. (1996). *Seismic design of concrete structures: the present needs of societies (Paper No 2001)* [Conference presentation]. World Conference on Earthquake Engineering, Acapulco, Mexico.

Prion, H. G. L., & Lam, F. (2003). Shear walls and diaphragms. In S. Thelandersson & H. J. Larsen (Eds.), *Timber engineering* (pp. 383–408). Wiley.

Quenneville, P., Franke, S., & Swager, T. (2011). *Design guide New Zealand: Timber portal frames*. Structural Timber Innovation Company.

Ritter, W. (1899, February 18). Die Bauweise Hennebique [The Hennebique System]. *Schweizerische Bauzeitung, XXXIII*(7), 59–61.

Rodriguez, M.E., Restrepo, J.I. and Carr, A.J. (2002). Earthquake-induced floor horizontal accelerations in buildings. *Earthquake Engineering & Structural Dynamics, 31*(3): 693–718.

Sadashiva, V.K., MacRae, G.A., Deam, B.L. and Spooner, M.S. (2012). Quantifying the seismic response of structures with flexible diaphragms. *Earthquake Engineering & Structural Dynamics*, *41*(10): 1365–1389.

Scarry, J. M. (2014). *Floor diaphragms – Seismic bulwark or Achilles' heel* [Conference presentation]. New Zealand Society for Earthquake Engineering Conference 2014, Wellington, New Zealand.

Scarry, J.M. (2015). Floor Diaphragms and a Truss Method for their Analysis. *Bulletin of the New Zealand Society for Earthquake Engineering*, *48*(1): 41–62.

Schlaich, J., Schafer, K., & Jennewein, M. (1987). Toward a consistent design of structural concrete. *Prestressed Concrete Institute Journal, 32*(3), 74–150.

Schulze, H., & Schönhoff, T. (1989). *Bemessungsvorschläge für Deckenscheiben in Holzbauart mit dreiseitiger Lagerung [Design recommendations for timber diaphragms with three-sided support]*. IRB-Verlag.

Smith, P. C., Dowrick, D. J., & Dean, J. A. (1986). Horizontal timber diaphragms for wind and earthquake resistance. *Bulletin of the New Zealand Society for Earthquake Engineering, 19*(2), 135–142. https://doi.org/10.5459/bnzsee.19.2.135-142

Spickler, K., Closen, M., Line, P., and Pohll, M. (2015). *Cross laminated timber: Horizontal diaphragm design example* [White paper]. Structurlam. https://www.structurlam.com/wp-content/uploads/2016/10/Structurlam-CrossLam-CLT-White-Paper-on-Diaphragms-SLP-Oct-2015.pdf

Standards Australia (2009). *Concrete Structures* (AS 3600).

Standards Council of Canada (2014). O86-14. Engineering design in wood, Ottawa, Canada.

Standards New Zealand. (1993). *Timber structures standard* (NZS 3603).

Standards New Zealand. (2004a). *Structural design actions part 5: Earthquake actions - New Zealand* (NZS 1170.5).

Standards New Zealand. (2004b). *Supp structural design actions part 5: Earthquake actions - New Zealand – commentary* (NZS 1170.5).

Standards New Zealand. (2006). *Concrete structures standard: The design of concrete structures* (NZS 3101).

Standards New Zealand (2015). *Structural Design Actions – Part 5: Earthquake actions – New Zealand Commentary* (DZ 1170.5 Commentary A1 - Public Comment Draft NZS 1170.5 Supp1:2004).

Standards New Zealand. (2020). *Timber structures - Part 1: Design methods. Public consultation draft - New Zealand* (DZ NZS AS 1720.1/V6.0.).

Steel Deck Institute. (2016). *Diaphragm design manual - No. DDM04* (4th ed.).

STIC (2013). Design Guide Australia and New Zealand - Post-Tensioned Timber Buildings. Structural Timber Innovation Company, Christchurch, New Zealand.

Swiss Society of Engineers and Architects. (2003a). *Actions on structures* (SIA 261:2003).

Swiss Society of Engineers and Architects. (2003b). *Timber structures* (SIA 265:2003).

Thelandersson, S., & Larsen, H. J. (Eds.) (2003). *Timber engineering*. Wiley.

Tissell, J.R. & Elliott, J.R. (2004). *Plywood diaphragms* (Research Report 138). APA - The Engineered Wood Association.

van de Lindt, J. and Pei, S. (2010). SAPWood. https://nees.org/resources/sapwood.

Wagner, H. (1929). Ebene Blechwandträger mit dünnem Stegblech [Flat sheet metal girders with very thin metal webs] (4 parts). *Zeitschrift für Flugtechnik und Motorluftschiffahrt, 20*(8-12). NASA Technical Reports Server, Reports NACA-TM 604, 605 and 606, 1931.

Wallner-Novak, M., Koppelhuber, J., & Pock, K. (2013). *Brettsperrholz Bemessung - Grundlagen für Statik und Konstruktion nach Eurocode [Cross laminated timber design - Construction and design according to Eurocode]*. proHolz Austria.

Winkel, M. H. (2006). *Behaviour of light-frame walls subject to combined in-plane and out of plane loads* [Master's Thesis, The University of New Brunswick].

# CHAPTER 7

Load-resisting systems

## TABLE OF CONTENTS

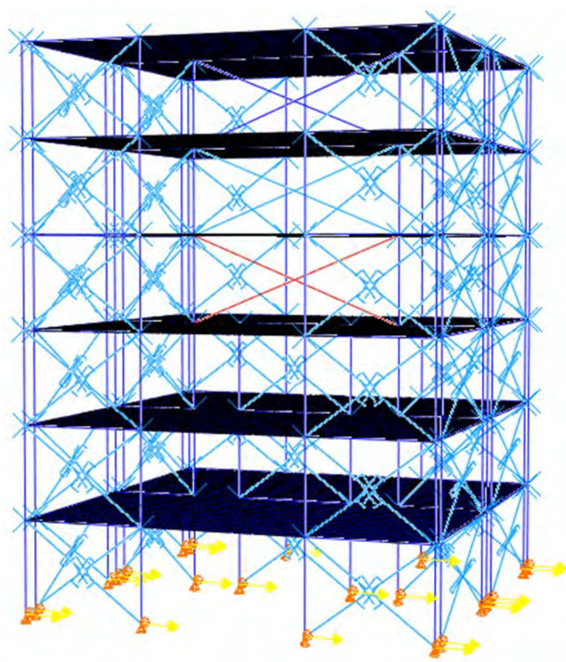

# CHAPTER 7.1

## Light wood-frame structures


**Authors**
Zhiyong Chen
Daniel Dolan
David Moses

**Reviewers**
Chun Ni
Robert Jonkman
Minghao Li
Weichiang Pang

# TABLE OF CONTENTS

## 7.1.1 Introduction

Wood-frame construction is the dominant structural system for single- and multi-family housing in low-rise (up to 4 storeys) buildings in North America (Ni & Popovski, 2015). Commonly, these buildings are engineered using hand calculations or spreadsheets. However, since building codes have increased the maximum allowable number of storeys in wood-frame buildings, they now require more complex modelling techniques. Updates to standards, such as CSA O86 (Canadian Standards Association (CSA), 2019), provide additional analytical requirements for designing mid-rise light wood-frame buildings and wood-frame buildings on podiums (Chen & Ni, 2017). Numerical modelling for both types of buildings serves to model the added complexity of these structures while accounting for irregularities. This chapter discusses the behaviour and mechanisms of light wood-frame structures under lateral loading, including analytical models, advanced and practical finite element (FE) models for shear walls, and key modelling and analysis considerations.

## 7.1.2 Behaviour and Mechanisms

### *7.1.2.1 Whole Buildings*

Light wood-frame buildings are constructed using dimensional lumber framing and wood-based sheathing connected to each other with metal fasteners, e.g., nails. Figure 1 shows a light wood-frame building under construction. Wood framing has a dual purpose, supporting both gravity and lateral loads. Gravity loads are resisted in light wood-frame buildings by floor and roof plates made from sheathing on joists or on trusses which transfer their loads into vertical wall elements made from studs and sheathing. Lateral loads (from wind or seismic events) are resisted using these same systems: the floor and roof plates are diaphragms and the wall assemblies are shear walls. This chapter focuses on modelling wall behaviour under lateral loads. Chapter 6 introduces and discusses the analysis and modelling of floors and roofs under in-plane and out-of-plane loads.

**Figure 1. A light wood-frame building under construction**

The lateral load path for a light-frame timber building (Figure 2) is modelled with forces concentrated at the floor and roof levels from seismic inertial force or wind blowing on the windward wall of the building. Note that in an actual construction, wind would exert pressures on all exterior and interior walls; in the figure, the concept is simplified to windward walls only. The windward wall sheathing acts as a one-way plate between the studs in the wall to distribute pressure to the studs as a line load. The studs then act as simply supported, vertically oriented beams that distribute the load (beam reactions) to the edges of the floor or roof diaphragms. Assuming the studs are simply supported will transfer 50% of the load up to the diaphragm above the studs and 50% to the diaphragm below the studs. Since the studs are numerous and closely spaced, the loads on the diaphragms are effectively uniform line loads along the edge of the diaphragm, similar to what is illustrated in Figure 3.

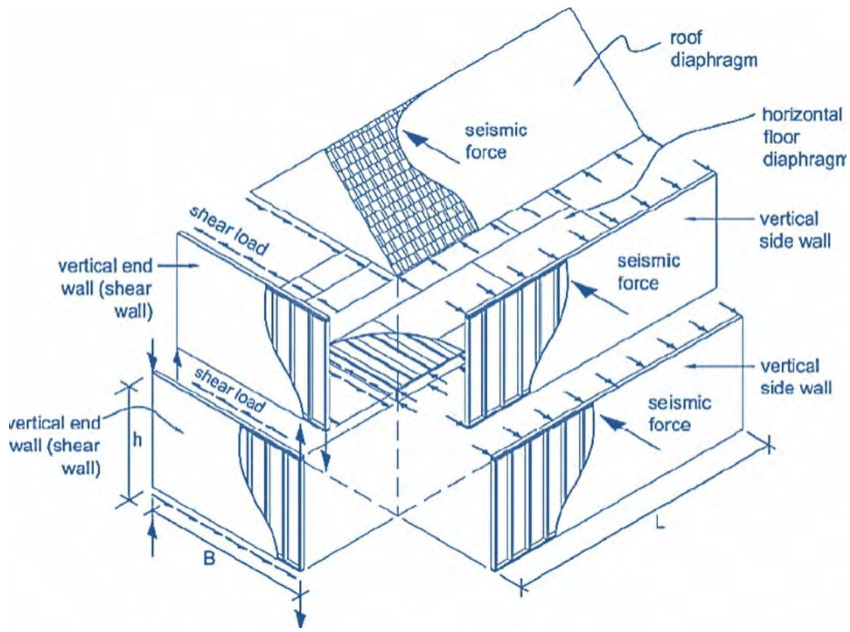


**Figure 2. Concept of lateral load path under seismic (or wind) loading for light-frame timber buildings (Building Seismic Safety Council (BSSC), 2006)**

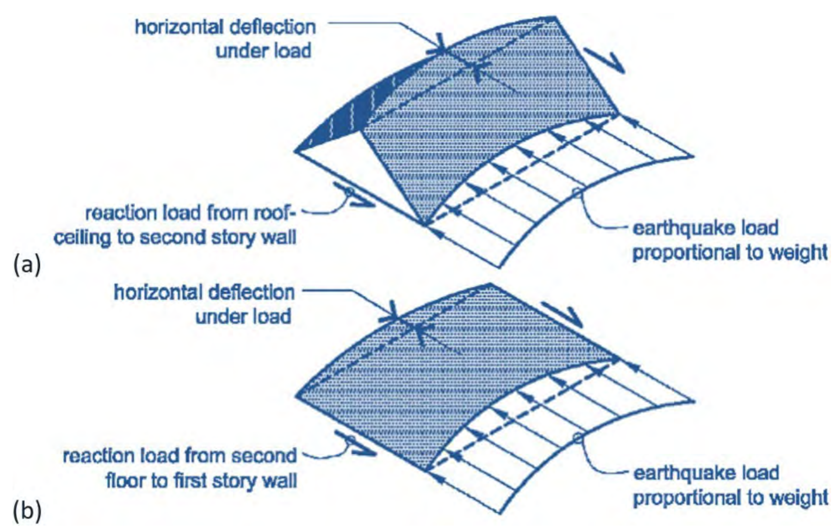


**Figure 3. Application of uniform line load on the edge of the (a) roof and (b) floor diaphragms resulting from lateral earthquake (or wind) reactions from wall studs attached to the diaphragm (BSSC, 2006)**

The diaphragm in turn acts as a simply supported deep beam that spans horizontally between the shear walls below. The loads from the shear walls are added to the diaphragm below, while the shear walls supporting the diaphragm from below resist its reactions (Figure 4). The deep beam behaviour of the diaphragm allows its edges to transfer its loads as uniformly distributed tractions to the shear walls below it.

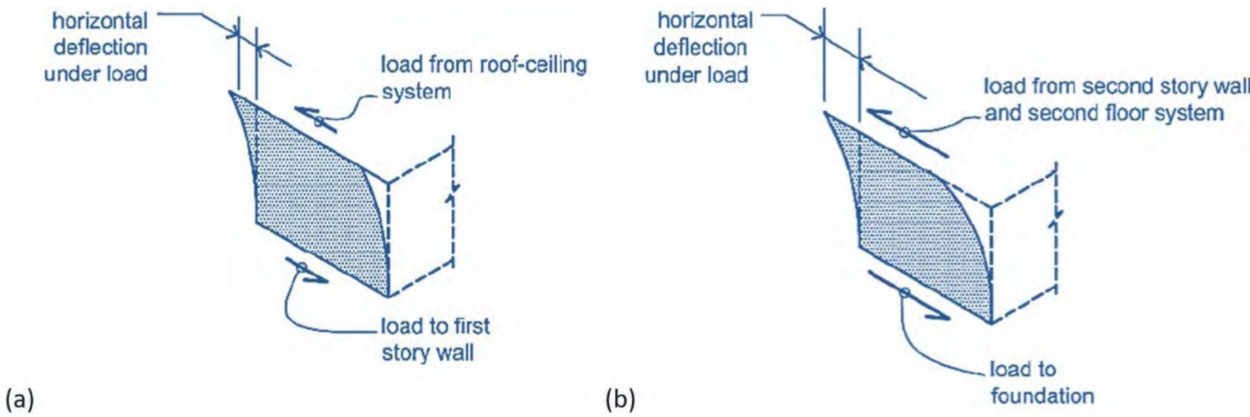


**Figure 4. Load distribution along the top of a shear wall supporting a diaphragm under wind or seismic loads: (a) second-storey wall and (b) first-storey wall**

Notice that the resultant force from the upper level across the transfer is equal (but opposite in direction) to the resultant force below, to keep the forces in equilibrium. These reactions from the ends of the diaphragm are based on the simply supported deep beam assumption. However, Wagemann Herrera (2021) has recently shown that there are certain structural requirements for realising these assumptions in practice. First, as outlined in ASCE 7 (American Society of Civil Engineers (ASCE), 2016) and other load design standards used around the world, the assumption that the loads are distributed according to the tributary area of the wall is only valid if the diaphragm is *flexible* in relation to the wall lines supporting it. This assumption is common for light-frame wood structures, but modern structures of this type utilise adhesives between the diaphragm sheathing and framing to eliminate floor squeaks. This in turn significantly increases the stiffness of the diaphragm, beyond the flexible diaphragm assumption. As the stiffness of the diaphragm increases, the reactions at the supports will be related to the stiffness thereof (that is the stiffness of the shear walls). If the diaphragm is relatively stiff, then use either a full elastic analysis or a rigid diaphragm analysis to account for the actual stiffness of the diaphragm and shear walls. However, simply assuming either flexible or rigid diaphragm analysis will under- or overestimate the loads distributed to the wall lines by as much as 60% (Chen, Chui, Mohammad, et al., 2014; Chen, Chui, Ni, Doudak, & Mohammad, 2014a; Wagemann Herrera, 2021). Therefore, diaphragms should be modelled in a way that properly reflects their stiffness using whole building models.

A second assumption made in the design of diaphragms that also adversely affects the load path analysis lies in the design of the struts used to distribute the loads from the diaphragms to the wall lines and in turn to the individual wall piers in the wall line. Most designers only assume that the strut can act as a simple beam between wall piers and that it will distribute the load equally to the two adjacent wall piers. This is a mistake if the wall piers have different stiffnesses, in which case the analysis should be made as if the strut were a continuous beam along the entire length of the wall line and the loading a uniformly distributed axial traction along the length of the strut. The reaction forces for the strut are the individual wall piers, and each wall pier has a different stiffness depending on the length, sheathing type, and fastening schedule. This provides a significantly different distribution of forces to the individual wall piers.

An additional standard design assumption is that all the wall piers in the wall line will displace equally when subjected to the loads from the diaphragm. In light wood-frame shear walls, this might be close to correct, but if the axial stiffness of the strut is not at least 60% of the lateral stiffness of the shear wall pier with the lowest aspect ratio (height/length), the assumption is incorrect. In this case, there will again be a significant additional error, of as much as 40%, in the loads applied to the wall line and individual piers, in addition to the error from the incorrect assumption about the diaphragm's flexibility (Wagemann Herrera, 2021).

So, the designer should be aware when designing light-frame buildings that the effective stiffness of the diaphragm and the axial stiffness of the strut element are important considerations to accurately determine the loads in the shear walls. When modelling the entire building, the modeller must accurately tie the mechanical properties used to the experimental data about the conditions being considered. The most difficult parameter to model correctly will be the diaphragm stiffness, especially if adhesives are used but not counted as structural adhesives. The reinforcing effect on the diaphragm can increase its stiffness by as much as a factor of 10.

### *7.1.2.2 Shear Walls*

Light wood-frame shear walls (LWFSWs) consist of dimensional lumber framing and wood structural panels (WSPs, plywood or oriented strand board). The WSPs are fastened to the framing using nails, or occasionally wood screws (Chen & Ni, 2021). The components and assembly of a typical LWFSW are illustrated in Figure 5.

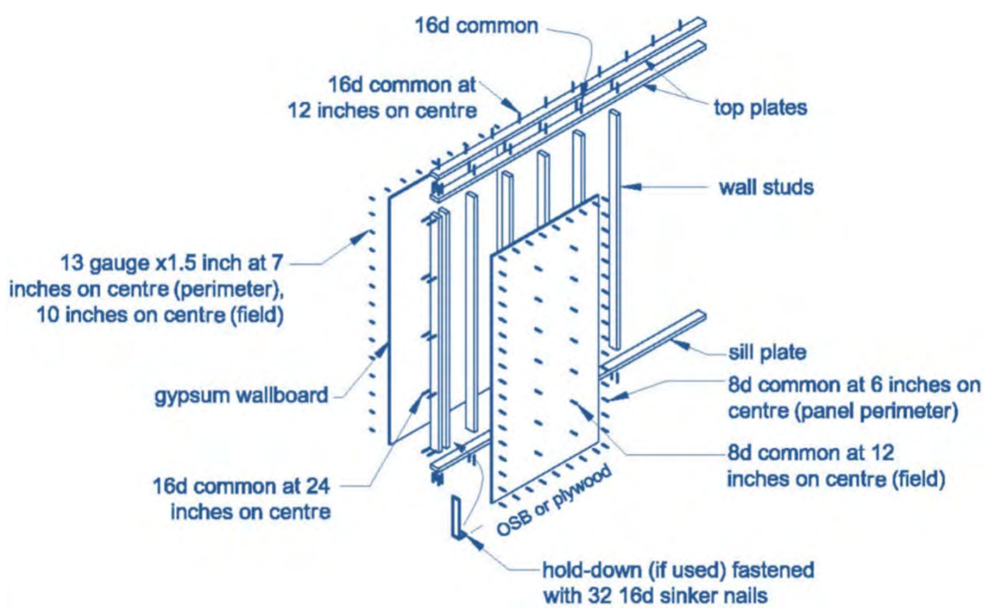


**Figure 5. Example of LWFSW nails for wood-based sheathing and screws for gypsum wallboards (FEMA, 2006)**

The mechanical response of an LWFSW is very well understood due to the large database of experimental tests on and numerical models of this structure (Chen et al., 2016; Serrette et al., 1997). The response of a typical LWFSW is mainly controlled by the connections between the sheathing and the framing. When the shear wall is loaded in plane, the wall framing will distort into a parallelogram, and the WSPs will rotate about the individual panel centre if the sheathing is symmetrically nailed around its perimeter, as illustrated in Figure 6. The deformation of the sheathing-to-framing connections provides energy dissipation in the shear walls.

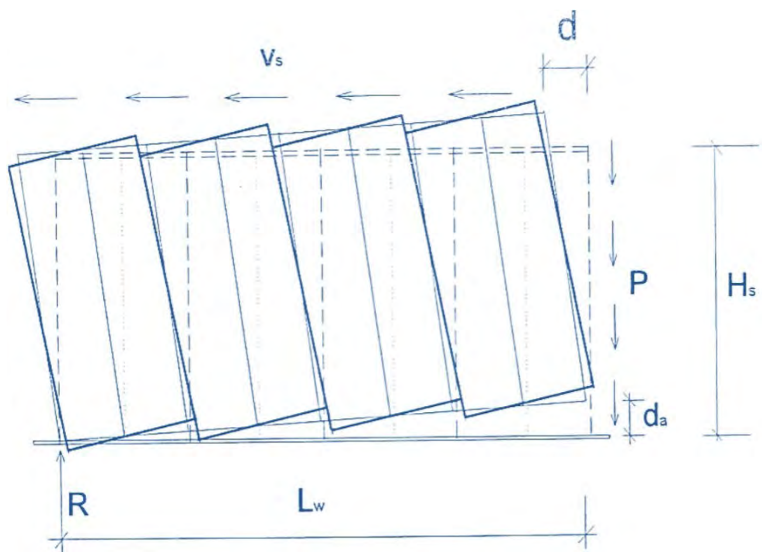


**Figure 6. Rotation of sheathing panels in a shear wall without hold-downs**

Wood-frame shear walls are characterised by their strength and deformation behaviour. This behaviour is highly dependent on the use of sheathing-to-framing connections and the hold-downs at the bottom corners at the ends of the shear wall.

<u>Strength behaviour</u>

Hold-downs help limit deflections in shear walls, but their most significant contribution is increasing the strength of these walls (Ni & Karacabeyli, 2011). For example, shear walls with WSP sheathing attached using nails at 150 mm (6 inches) have a lateral design strength of around 391 N/m (440 plf) when hold-down connections resist the overturning forces. The same wall without hold-downs would have a design strength reduction of around 75%, to approximately 89 N/m (100 plf). To further strengthen shear walls, one can increase the nail density around the perimeter of the sheet of sheathing and use larger nails. For example, a shear wall with hold-downs and tighter perimeter nail spacing could achieve a capacity of approximately 925 N/m (1040 plf), more than double that of standard nail spacing. Note that the capacity of a shear wall without hold-downs is severely limited even with tighter nail spacing because the nails resist both the lateral forces and the overturning forces, as discussed in the following paragraphs.

Hold-downs to resist uplift are installed by attaching them to the end studs (the *chords*) and to the foundation or shear wall below this level, as shown in Figure 7. When applying the lateral load to the top of the shear wall, the resulting uplift force on the chord is transferred through the hold-down to resist the uplift. The nail in the sheathing only resists the racking (shear) forces in the wall. As the hold-down becomes engaged, the chord element lifts and the nails attached to the chord element transfer the overturning force into the sheathing, as shown in Figure 7.

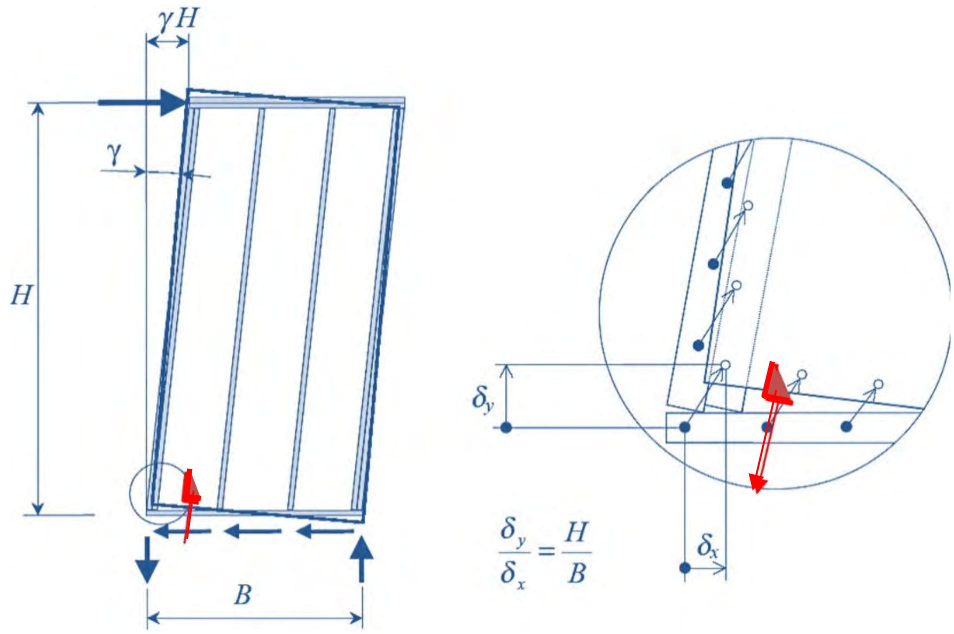


**Figure 7. Load path of a shear wall with hold-downs to resist overturning forces that limit load transfer in nails; $\delta_x$ and $\delta_y$ represent the deformations of a corner nail**

With no hold-down, the nails along the bottom plate resist both the lateral and uplift forces, as shown in Figure 8. This causes early failure of the nails along the bottom plate of the wall as they tear out the sheathing, resulting in significant strength loss. Increasing the edge distance of the nails along the bottom plate to 19 mm (¾-inch) significantly improves the displacement capacity of the wall, but not its strength.

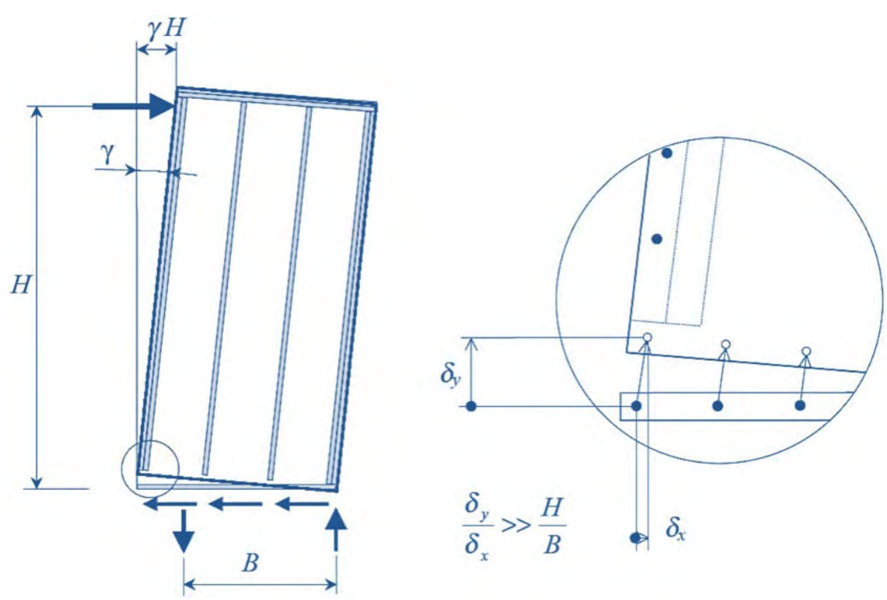


**Figure 8. Load path of a shear wall without hold-downs and with nailed connections resisting the overturning forces**

Deformation behaviour

The deformation behaviour of shear walls is the result of contributions from four components, listed in order of significance: sheathing connections, hold-downs, wood-frame bending, and the shear of the sheathing. Design codes and models for shear wall behaviour account for these four factors, as discussed in detail in Section 7.1.3.4.

Connections between the sheathing and the framing are the primary factor controlling shear wall behaviour. Nails typically attach the WSP to the framing, while screws attach the gypsum wallboard sheathing on the opposite side, as shown in Figure 5. In this discussion, the WSP side of the wall controls the deformation behaviour at loads close to design. The second most important factor is whether there are mechanical hold-downs (in the form of either individual hold-down connections or continuous rod hold-downs). The third and fourth main components contributing to deformation are the bending of the framing elements and the shear deformation of the wood sheathing panels. It is typically assumed that the connections between the floor or roof diaphragms and the top and bottom plate elements of the framing are sufficiently strong and stiff to fully transfer the loads into the shear wall at the top and out of it at the bottom, without slippage.

Note that the compression of the top and bottom plates also contributes to the deformation of the wood-frame shear wall. Since the top and bottom plates are compressed under the compression chord of the shear wall, the bottom plate will deform in compression perpendicular to grain. This compression is often considered a secondary effect in the overall displacement. However, narrow shear walls see the compression deformation of the bottom plate become pronounced. For instance, a wall with a 2:1 aspect ratio (wall height/length = 2) will experience lateral deflections that are twice the vertical compression displacement of the bottom plate under the chord element (end studs). For example, if the compressive deformation in the bottom plate is 6 mm (0.25 inch), the lateral displacement of the wall due to the bottom plate will be 12 mm (0.5 inch). In this example of a 2:1 aspect ratio shear wall, the bottom plate could account for 21% of the allowable drift limit of 2.5% storey height in a typical light-frame shear wall design.

Other wood-frame shear wall configurations

Typically, WSPs are nailed to one or both sides of the framing in a standard light-frame shear wall, as shown in Figure 9(a). Another configuration of wood-frame shear walls is the Midply shear wall, where the framing is nailed to both sides of WSPs. Midply shear walls, shown in Figure 9(b), were developed in the 1990s by researchers at Forintek Canada Corp. (the predecessor of FPInnovations) and the University of British Columbia (Varoglu et al., 2006; Varoglu et al., 2007). There is now also a new configuration of Midply shear walls (Chen et al., 2020; Ni & Chen, 2021), as shown in Figure 9(c). Midply is a high-capacity lateral load resisting system suitable for high wind and seismic loads. Midply shear walls consist of structural components used in standard shear walls, but re-arranged so the lateral resistance and the dissipated energy of the system significantly exceed those in standard shear wall arrangements. The nailed connections in Midply shear walls work in double shear, as shown in Figure 10. This results in approximately double the lateral resistance of a standard single-sided wood-frame shear wall with the same nailing schedule and wall length (Varoglu et al., 2006; Varoglu et al., 2007).

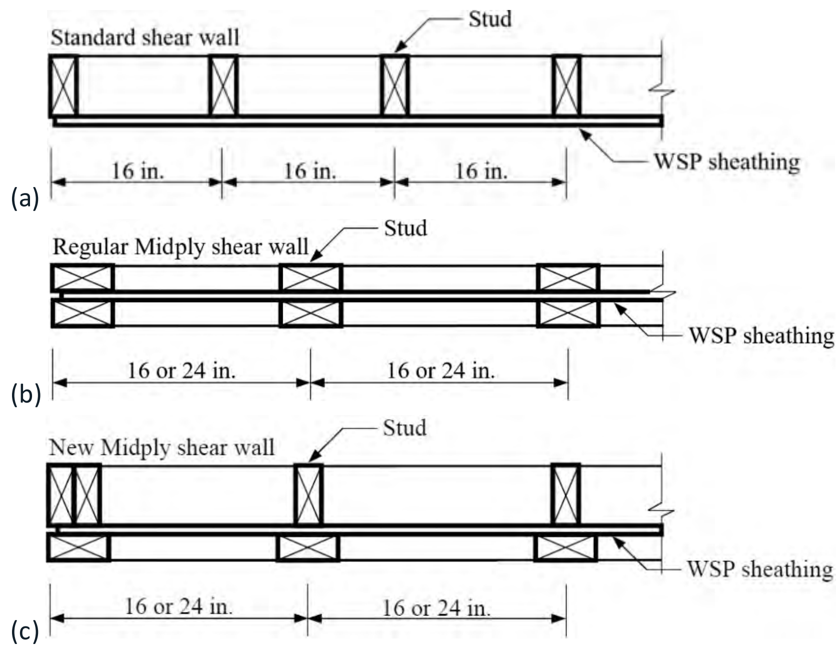


**Figure 9. Cross-sections of (a) a standard shear wall, (b) and (c) Midply shear walls**

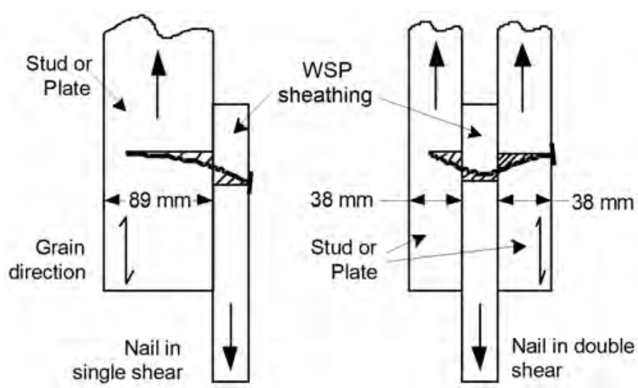


**Figure 10. Nailed connection working in single shear in standard shear wall (left) and double shear in Midply (right)**

### *7.1.2.3 Platform and Balloon Framing*

Platform and balloon framing are framing techniques used for light wood-frame construction, as illustrated in Figure 11. Platform construction is the predominant technique in most of the world. In this approach, the order of assembly after the foundations are placed is to start by building the first floor (platform) and then erecting its walls. The second-floor platform is then constructed on top of the first-floor walls, followed by the walls for the second floor. This process is then repeated until the building is completed. This became the predominant form of light-frame construction in the late nineteenth and early twentieth centuries to simplify shipping with uniform standard material lengths. Balloon framing, used prior to the adoption of platform construction, follows a different procedure. After completing the foundation, the walls of the building are erected to their full height and then the floors are constructed by hanging them on the side of the walls, as shown in Figure 11.

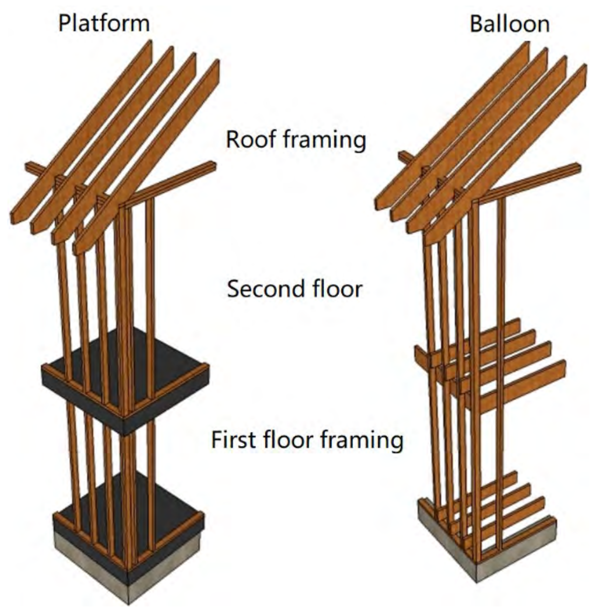


**Figure 11. Comparison of Platform (left) and Balloon (right) framing in light wood-frame construction**

Shear walls behave differently in these two framing types. In platform construction, they behave as described in Section 7.1.2.2. The behaviour of balloon frame shear walls is similar, except for the influence of the intermediate floor(s) and the wall sheathing layout. The attachment of the intermediate floor level to the wall studs affects the lateral translation of the framing. Since sheathing is not manufactured in lengths sufficient to extend from the foundation to the roof (the full height of the balloon frame), the discontinuity at the intermediate floor level will affect the behaviour of the walls. Models must reflect the interaction between the intermediate floor diaphragm(s) and the shear wall, as well as the effect of the sheathing layout.

The authors are unaware of any analysis of or experimental tests on balloon-framed shear walls to aid in this type of modelling. This chapter will focus on platform shear walls. Modelling balloon-framed shear walls requires the following additional considerations:

1) Allow the continuous wall studs to translate horizontally and develop reverse bending.
2) Apply a pinned-fixed translation to the studs on the first floor, a fixed-fixed one between intermediate floors, and a fixed-pinned one on the top floor.
3) Allow the sheathing to deflect, with each sheet initially rotating around its centre due to the symmetrical nailing at the perimeter.
4) Account for the fact that horizontally stacked sheathing increases the shear wall stiffness due to the reverse bending of the studs. Horizontally staggered sheathing will likely impinge on adjacent panels as they rotate under a load (similar to the behaviour of large diaphragms) and significantly increase the stiffness and strength of the shear wall. This may occur as the centre of rotation of the staggered panels moves for each panel, thereby changing the lever arms from the centre of rotation to the individual nails.

### 7.1.3 Analytical Models

There has been extensive research on light wood-frame shear walls since the late 1920s. Analytical models for hand calculations (Åkerlund, 1984; Burgess, 1976; Easley et al., 1982; Källsner, 1984; McCutcheon, 1985; Tuomi & McCutcheon, 1978) account for nail spacing and the global displacement and rotation of the shear wall, as shown in Figure 12. These models are often based on semiempirical assumptions. Most assume elastic behaviour, with the full anchorage of the wall to the floor/foundation and with the studs connected by pins to the top and bottom plates. They further assume the framing members and sheathing are rigid. There are proposed formulations based on both linear elastic and nonlinear elastic-plastic properties. While most models apply only to shear walls fully anchored to the floor/foundation, a few, like that developed by Salenikovich (2000), allow for the uplift of the studs and/or bottom plate. Ni and Karacabeyli (2000) and Ni and Karacabeyli (2002) developed a mechanics-based method to account for the effects of vertical loads and perpendicular walls on the performance of shear walls without hold-down connections. Other shear wall models include a truss system (Steinmetz, 1988) or a composite cantilever with partial interaction (Henrici, 1984).

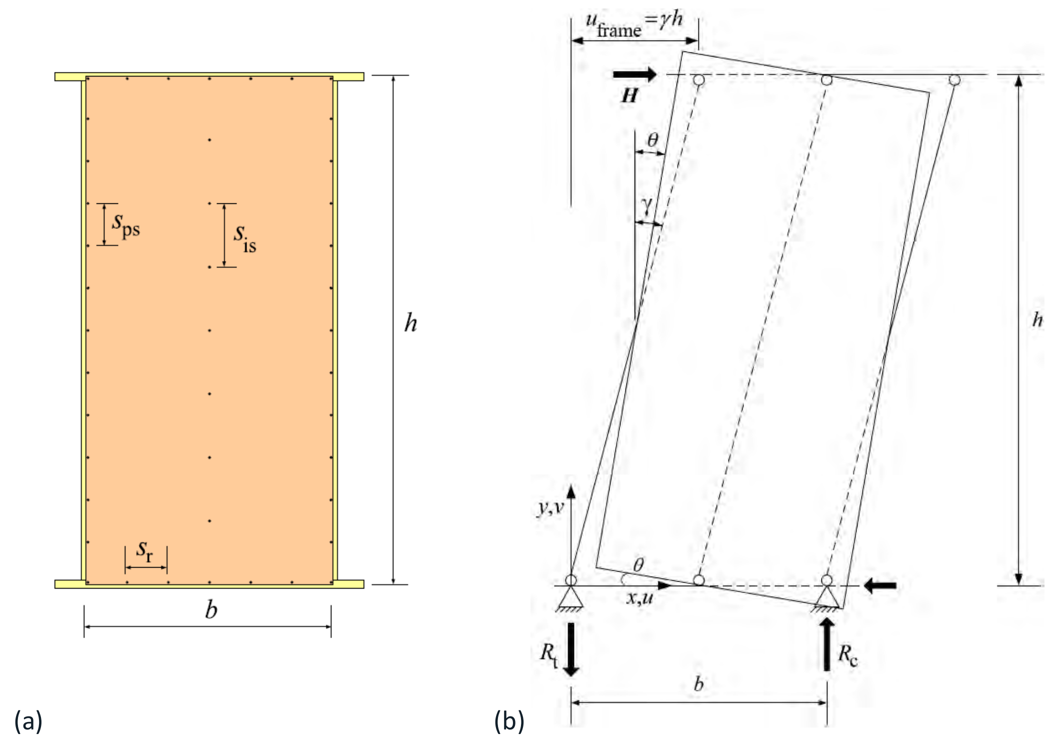


**Figure 12. (a) A shear wall unit built from wood framing and a sheathing panel; (b) a static model of a fully anchored shear wall unit in a deformed state: $\gamma$ is the rotation of vertical frame members and $\theta$ is the rotation of sheathing. (Källsner & Girhammar, 2009b)**

This section will focus on analytical techniques which explicitly model nailed connections.

### *7.1.3.1 Elastic Models*

Elastic models developed by Källsner and others (Åkerlund, 1984; Källsner, 1984; Källsner & Girhammar, 2009a) can analyse statically loaded fully anchored shear walls without openings. These models are based on the linear elastic properties of the mechanical sheathing-to-framing connections of the shear walls. The method of minimum potential energy serves to derive expressions for both the horizontal load-carrying capacity and the horizontal displacement of the shear walls, based on the following assumptions:

(1) Framing members and sheathing are rigid bodies.

(2) There is no contact between adjacent sheets or between sheets and surrounding structures (that is sheathing is free to rotate).

(3) Framing joints act as hinges.

(4) Sheathing-to-framing connections have linear elastic load-slip characteristics up to failure. The slip modulus (stiffness) of the connections is constant and the same in all joints. Connection stiffness is independent of the force direction and of the orientation of the sheathing relative to the framing members.

(5) Displacements of the wall are smaller than the width and height of the sheathing.

(6) The edge distances of the sheathing-to-framing connections are smaller than the width and height of the sheathing, that is the fasteners are approximately located along the edges of the sheathing.

Figure 13 illustrates the force distribution on the sheathing panel, while Figure 14 shows the stress distribution on the sheathing and framing members in a fully anchored shear wall, in accordance with linear elastic theory.

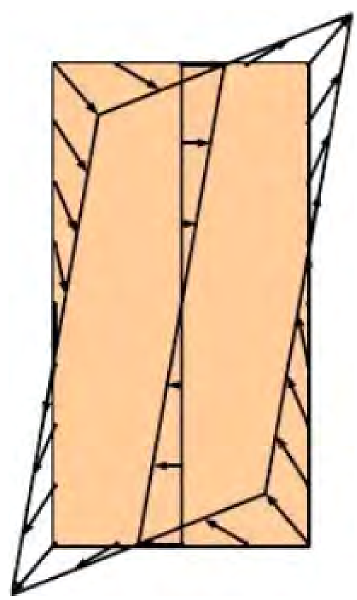

**Figure 13. Force distribution on the sheathing panel in a fully anchored shear wall, in accordance with linear elastic theory (Girhammar & Källsner, 2008)**

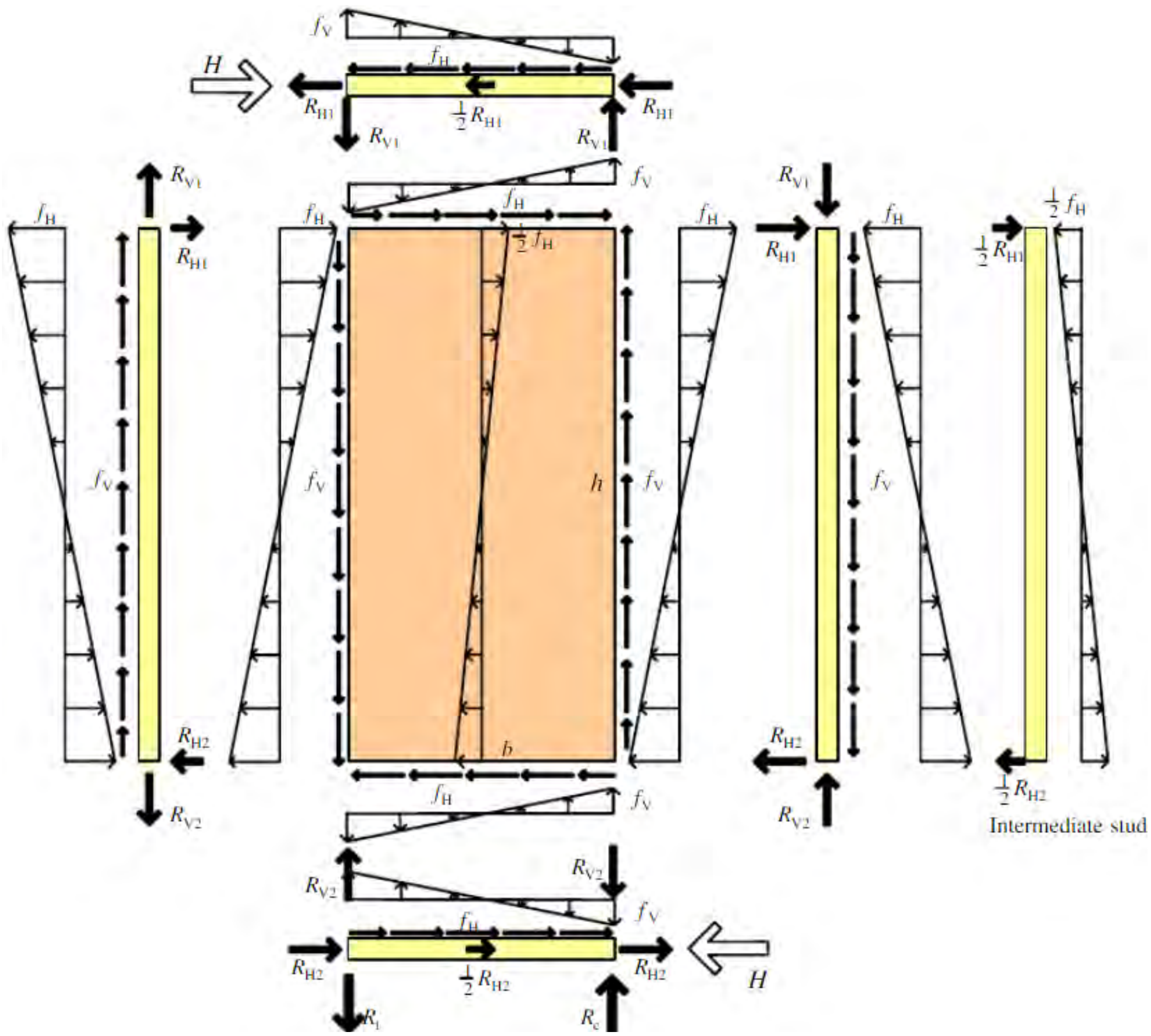


**Figure 14. Stress distribution on a sheathing panel and framing members in a fully anchored shear wall, in accordance with linear elastic theory (Girhammar & Källsner, 2008)**

The horizontal shear capacity of a wall unit, $H$, is calculated as follows:

$$\boldsymbol{H} = \frac{\boldsymbol{F_v}}{\boldsymbol{h}\sqrt{\left[\frac{\hat{x}_{corner}}{\sum_{i=1}^{n}\hat{x}_i^2}\right]^2 + \left[\frac{\hat{y}_{corner}}{\sum_{i=1}^{n}\hat{y}_i^2}\right]^2}}, \tag{1}$$

where $F_v$ is the shear capacity of a single nailed connection; $h$ is the height of the wall unit; $\hat{x}_i$ and $\hat{y}_i$ are the coordinates of each nail in the coordinate axes relative to the centres of the fasteners; and $\hat{x}_{corner}$ and $\hat{y}_{corner}$ are half of the width and height of the wall unit, respectively. The load-carrying capacity of a shear wall consisting of several wall units (wall segments) is the sum of the load-carrying capacity of the individual parts. For shear walls with sheathing of the same type and thickness on both sides, assume the load-carrying capacity is the sum of the calculated contributions.

The horizontal displacement of the top plate of a wall unit, $u_{frame}$, is calculated as follows:

$$\boldsymbol{u_{frame}} = \frac{\boldsymbol{Hh^2}}{\boldsymbol{k}}\left[\frac{\boldsymbol{1}}{\sum_{i=1}^{n}\hat{x}_i^2} + \frac{\boldsymbol{1}}{\sum_{i=1}^{n}\hat{y}_i^2}\right] \qquad [2]$$

where $k$ is the stiffness of one nailed connection.

A common observation in the full-scale testing of shear walls is the sinusoidal bending of the vertical framing members (studs) (Chen et al., 2016). This is especially true when the spacing between the fasteners is small or when the sheathing is nailed to both sides of a shear wall. The rigid member assumption leads to an overprediction of shear wall stiffness in the elastic model. Assuming rigid sheathing in the elastic model is a good approximation in the ultimate limit state. However, to more accurately predict deformations for serviceability limit states requires shear deformations of the sheathing.

Since framing joints should act as hinges, significant shear forces must be transmitted in the framing joints of the vertical studs where two sheets meet. These forces become significant in shear walls with sheathing on both faces. All studs subjected to tensile forces should be fully anchored to the floor or foundation. Hinges in the model prevent horizontal and vertical displacement, meaning that the elastic model predicts high stiffness. Since the true behaviour of the sheathing-to-framing connections is nonlinear, one can improve model predictions of displacements using the secant slip modulus of the connections.

#### *7.1.3.2 Plastic Models*

Tests of nailed connections show that load-slip curves are characterised by plastic deformations. Methods for determining the upper and lower bounds of the plastic load-carrying capacity of shear walls appear in Källsner and Girhammar (2009b), Källsner et al. (2001), and Källsner and Lam (1995).

The upper bound method is based on the kinematic theorem and gives load-carrying capacities higher than or equal to the exact plastic load-carrying capacity. The lower bound method is based on the static theorem and gives capacities lower than or equal to the exact value (Neal, 1978). Both models assume that the load-displacement relationships of the sheathing-to-framing connections are completely plastic. Most of the assumptions of the elastic model (Section 7.1.3.1) also apply to the plastic methods, with the following exception:

- Sheathing-to-framing connections are completely plastic, with identical properties for all connections: they are independent of the force direction and of the orientation of the sheathing panels relative to the framing members.

**Upper Bound Method – Kinematic Theorem**

The kinematic theorem for determining an upper bound to plastic load-carrying capacity is based on choosing a geometrically possible pattern of deformations. The principle of virtual work serves to make the internal work of all the fasteners equal to the work of the external forces. In the formulation of the internal work, each timber member can be regarded as a rigid body rotating around its own centre of rotation (CR) relative to the sheathing.

For a wall unit, as shown in Figure 12(a), and for the same wall segment in a deformed state, as illustrated in Figure 12(b), it is possible to develop the force distribution. This is demonstrated in Figure 15, which shows the assumed positions of the CR and the matching fastener forces, with the following subscripts: *r* represents the horizontal top and bottom plates (*rails*), *ps* represents the perimeter studs, and *is* represents the vertical intermediate studs. All connections with shear capacity, $F_v$, are assumed to have reached the plastic capacity, $F_v = F_p$. The true plastic load-carrying capacity of the shear wall is obtained when the internal work of all the fasteners reaches its minimum value.

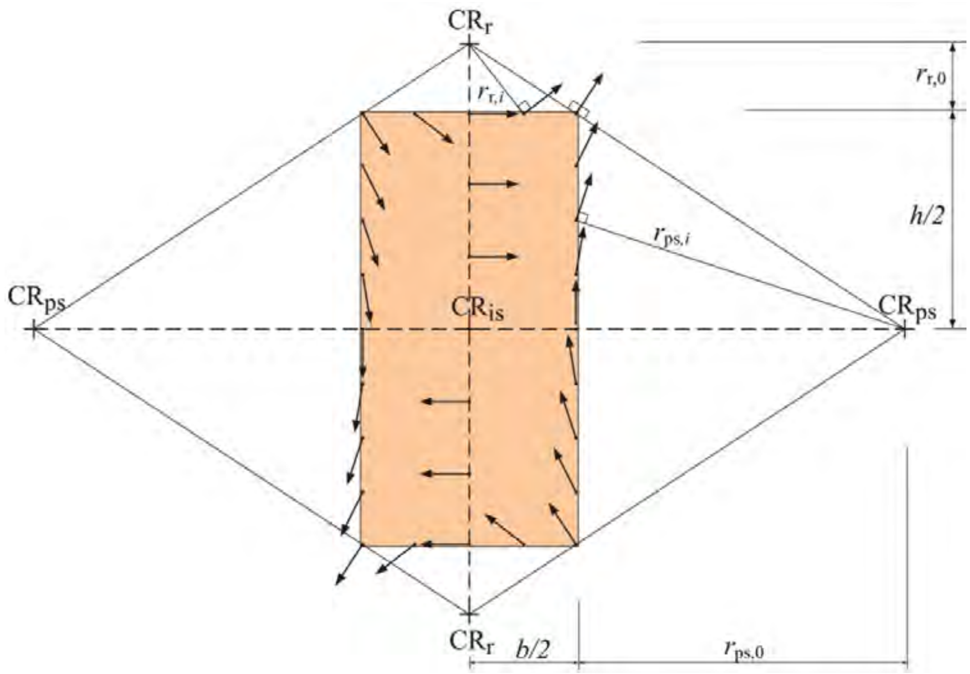


**Figure 15. Force distribution on the sheathing panel according to the plastic upper bound theory (Källsner & Girhammar, 2009b)**

The horizontal load-carrying capacity of a wall unit, $H$, is

$$\boldsymbol{H} = \frac{2F_p \sum_r r_{r,i} + F_p \frac{2r_{r,0}}{h}\left[2\sum_{ps} r_{ps,i} + \sum_{is} r_{is,i}\right]}{h\left(1+\frac{2r_{r,0}}{h}\right)} \qquad [3]$$

where $r_i$ is the distance from each fastener to its CR along the different framing members, $\Sigma_r$ is the summation of the fastener distances in the horizontal top and bottom plates, $\Sigma_{ps}$ is the summation of the fastener distances in the vertical perimeter studs, and $\Sigma_{is}$ is the summation of the fastener distances in the vertical intermediate studs. The unknown quantity $r_{r,0}/h$ must be estimated before calculating the capacity *H*. For a reasonable estimate of $r_{r,0}/h$, determine the centres of rotation for elastic conditions, that is use the $\gamma/\theta$-value from the elastic model according to Källsner and Girhammar (2009a) and then calculate $r_{r,0}/h$ using

$$\frac{\gamma}{\theta} = 1 + \frac{2r_{r,0}}{h} \qquad [4]$$

The positions of the other CRs can be determined graphically, as shown in Figure 15. Given all the CRs, it becomes possible to calculate the force *H*.

The horizontal displacement of the top plate of a wall unit, $u_{frame}$, can be calculated as

$$u_{frame} = 2u_{corner} + 2\frac{h}{b}v_{corner} \quad [5]$$

where $u_{\text{corner}}$ and $v_{\text{corner}}$ are the displacements of the corner fasteners in the horizontal and vertical directions, respectively.

**Lower Bound Method – Static Theorem**

To obtain the lower bound of the plastic load-carrying capacity of a shear wall, assume a force distribution that fulfils the conditions of force and moment equilibrium and where the force on each fastener is at most equal to the plastic capacity of the fastener. At the same time, the constituent materials in the structure (wood members, sheathing, and connections) must be able to transfer the internal and external forces without exceeding the strength and deformation limits of the materials.

The lower bound model assumes the framing members are completely flexible. This implies that the force distribution along the perimeter fasteners will be parallel to the framing members, as shown in Figure 16. Each edge fastener, except those in the corners, may be assumed to carry the same plastic load $f_p$ parallel to the edge. The model assumes each corner fastener carries a load $F_p/2$ ($F_p = f_p \times S_r$) parallel to each of the associated sides of the sheathing, and that the nails in the centre stud(s) do not carry any load. For the chosen force distribution, there are no force components perpendicular to the length or grain direction of the wood members. Consequently, there is no demand on any of the framing joints between the wood members to transfer the sheathing forces transferred by the sheathing-to-framing connections.

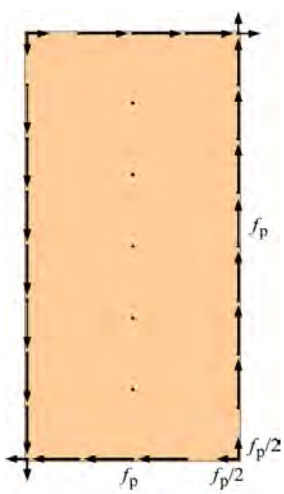

(a)

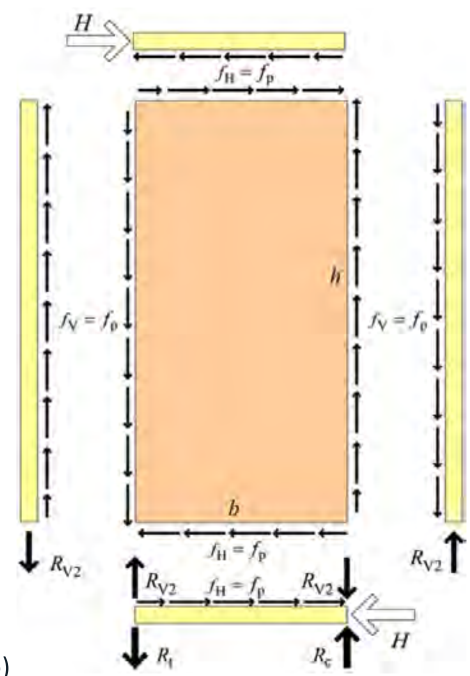

(b)

**Figure 16. (a) Force distribution on the sheathing panel and (b) stress distribution on the sheathing and the framing members in a fully anchored shear wall according to the plastic lower bound theory, assuming pure shear flow ($f_p$) (Källsner & Girhammar, 2009b)**

With the chosen force distribution, which corresponds to a pure shear flow along the edges of the sheathing, $f_p$, the horizontal load-carrying capacity, $H$, is

$$H = f_p b \tag{6}$$

It is evident that the elastic capacity is almost the same as the plastic capacity that uses a lower bound method (Källsner & Girhammar, 2009b). The load-carrying capacity of a shear wall consisting of several wall units is the sum of the load-carrying capacity of the individual parts. For shear walls with the same sheathing on both sides, one can assume the load-carrying capacity is the sum of the calculated contributions. Design standards, for example CSA O86:2019 (CSA, 2019), use the plastic capacity calculated according to the lower bound method.

The horizontal displacement of the top plate of a wall unit, $u_{frame}$, can be calculated as

$$u_{frame} = 2\left(1 + \frac{h}{b}\right)\frac{s_r}{b}\frac{H}{k} \tag{7}$$

where $s_r$ is the nail spacing in the top and bottom plates.

**Summary**

All assumptions for the elastic and plastic models are the same, except for the properties of the sheathing-to-framing connections. Elastic models assume that all connections have the same stiffness properties and that this stiffness is independent of the load direction and of the orientation between the sheathing relative to the framing members. In addition to the comments at the end of Section 7.1.3.1. for elastic models, plastic models require the sheathing-to-framing connections to be modelled as plastic. Also, calculating the displacements of the shear wall requires the secant modulus of the sheathing-to-framing connections for both the elastic and plastic models. Note that the force distribution in the plastic lower bound model results in there being no force component perpendicular to the length or grain direction of the wood members; therefore, there are no shearing forces to be transferred by the framing joints between the wood members.

Many design standards, for example CSA O86 (CSA, 2019), Eurocode 5 (European Committee for Standardization <CEN>, 2004), and NZS 3603 (Standards New Zealand, 1993), use the lower bound method with an added requirement to consider the buckling of the sheathing.

### *7.1.3.3 Sheathing Buckling*

A possible failure mode in shear walls under lateral load is for the sheathing panels to buckle before the nailed connections along the panel edges reach their capacities. For an orthotropic, homogeneous, and elastic sheathing material like plywood, the critical shear stress for a sheet with simply supported boundaries along all edges subjected to uniform in-plane shear stress along the panel edges is

$$\tau_{cr} = k_{\tau,ort}\frac{\pi^2}{3}\sqrt[4]{E_x E_y^3}\left(\frac{t}{b/2}\right)^2, \tag{8}$$

where $t$ and $b$ are the thickness and width of the sheet, respectively; $E_x$ and $E_y$ are the axial stiffness of the panel in the x and y directions, respectively; and $k_{\tau,ort}$ is the panel buckling factor, which depends on the length-to-width ratio of the panel and boundary conditions. For shear walls, in practice, the boundary conditions of the sheathing are somewhere between simply supported and clamped along all four edges. $k_{\tau,ort}$

appears in, for example, von Halász and Cziesielski (1966), Larsson and Wästlund (1953), Dekker et al. (1978). This method ignores the contribution of the intermediate stud support and is therefore conservative. Various standards use it, e.g., CSA O86 (CSA, 2019) and Eurocode 5 (CEN, 2018).

### *7.1.3.4 Deflection*

The above-mentioned elastic models (Section 7.1.3.1) and plastic models (Section 7.1.3.2) can calculate the lateral deflection of single-storey shear walls. However, three- (AWC, 2018) or four-term formulas (APA – The Engineered Wood Association, 2001; Applied Technology Council, 1981; Carradine, 2019; CSA, 2019; International Code Council, 2021; Newfield et al., 2013a, 2013c) are more common to estimate deflections in design standards. The three- and four-term formulas consider the four deformation components described briefly in Section 7.1.2.2: connections, hold-downs, wood-frame bending, and the shear of the sheathing, though the three-term formula combines the sheathing shear deformation and the slip of connections into one term. As noted in Section 7.1.2.2, deformations for most shear walls occur due to connection slip and anchorage deformation.

In CSA O86 (CSA, 2019), for example, the static deflection at the top of a blocked shear wall segment with WSPs and gypsum, $\Delta_{sw}$, is calculated with four terms, respectively representing chord bending deformation, shear deformation, connection slip, and anchorage deformation, as follows:

$$\Delta_{sw} = \frac{2vH_s^3}{3EAL_s} + \frac{vH_s}{B_v} + 0.0025H_s e_n + \frac{H_s}{L_s} d_a \qquad [9]$$

where $v$ is maximum shear due to the specified loads at the top of the wall; $H_s$ is the height of the shear wall segment; $E$ is the modulus of elasticity of the vertical boundary framing members; $A$ is the cross-sectional area of the chord member; $L_s$ is the horizontal length of the shear wall segment; $B_v$ is the shear-through-thickness rigidity of the sheathing; $e_n$ is the sheathing-to-framing connection deformation; and $d_a$ is the total vertical elongation of the system for wall overturning restraint (including fastener slip, hold-down device elongation, and anchor or rod elongation).

To derive the deflection of an unblocked shear wall segment with WSPs, scale the deflection calculated by the above equation using an adjustment factor (CSA, 2019).

For multi-storey shear walls, models must consider the multi-storey effects on shear wall deflection. One methodology is based on engineering mechanics, with the assumption that the shear wall is cantilevered from its base and stacked for the full height of the building (Newfield et al., 2013c). Deflection due to bending and wall anchorage system elongation, which represent flexural behaviour, will result in a rotation at the top of each wall segment. This in turn causes an increase in lateral drifts and deflections for each storey above, as shown in Figure 17. For more information, see Newfield et al. (2013c) and CSA O86 (CSA, 2019).

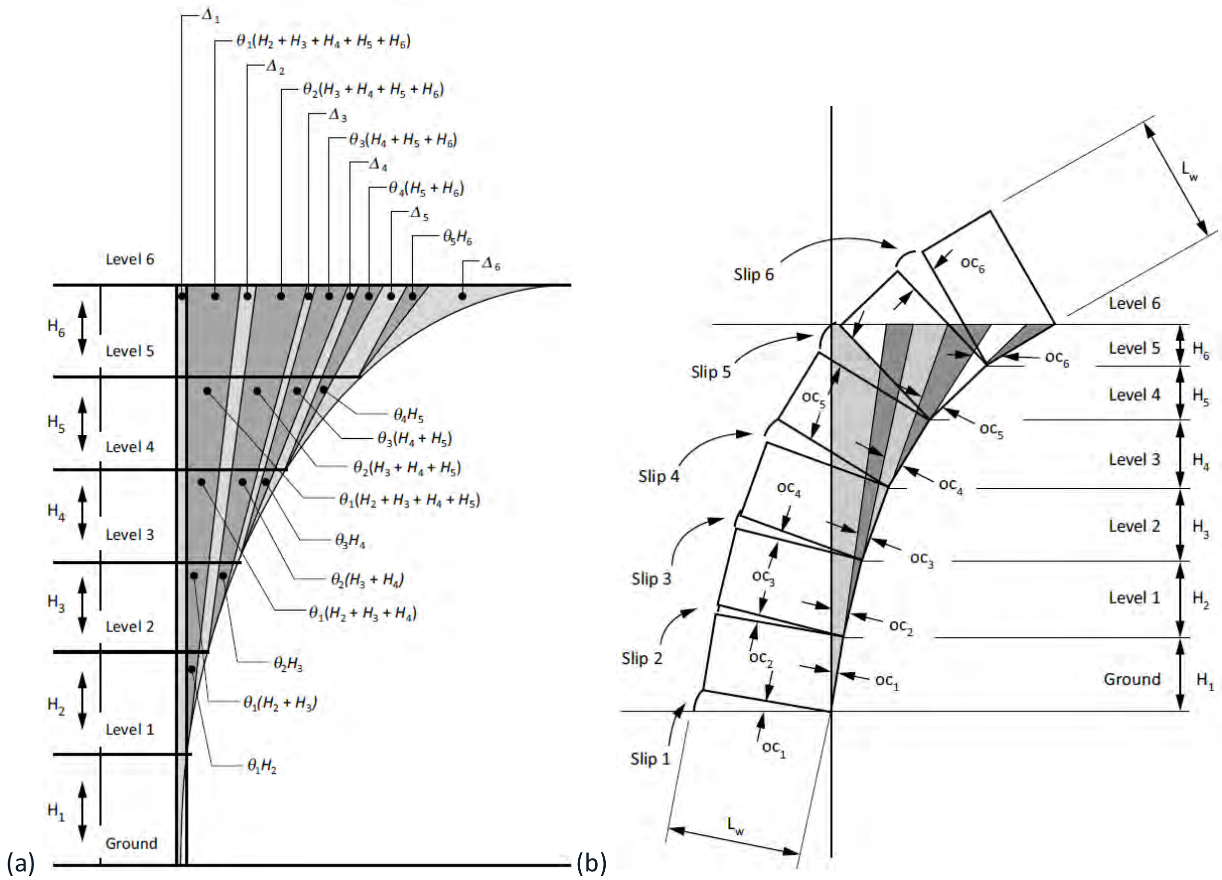


**Figure 17. (a) Cumulative rotation due to bending and (b) cumulative rotation due to wall anchorage system elongation (CSA, 2019)**

## 7.1.4 Numerical Models

### *7.1.4.1 General Considerations*

Computer-based numerical models, usually involving the FE method, have existed since the late 1960s. Studies have proposed a number of methods to model shear walls in light wood-frame platform construction. The choice of model depends on whether a static or dynamic analysis is necessary to achieve the intended goal.

If only a static analysis is required, it can be limited to investigating the force and stress distribution within a wall element or expanded to account for the overall load distribution between diaphragms and shear walls. If the goal is a detailed distribution of the forces and stresses within a wall element, then a detailed FE model would be appropriate. If aiming for a full-building response, then a macro model is more appropriate, assuming the macro elements can be calibrated to simulate individual wall panels or entire wall lines based on experimental results and simplified assumptions related to aspect ratio and wall segment lengths.

If a dynamic analysis is necessary, then, as with static modelling, one can develop either a detailed or a macro model. However, any model used must also include mass distribution characteristics in the components. One can address this issue with simple assumptions about stiffness, strength, mass, redundancy, etc., as well as their respective distribution in the structure. Most designers assume that the mass is lumped at the diaphragm levels (floors and roof) and that the mass associated with the walls is distributed, with 50% added to the floor below and 50% to the roof or floor above for each level of the building. If the walls and general building configuration are somewhat uniform (which is usually the case), then the mass can be uniformly distributed across the diaphragm.

For general analysis (static or dynamic), one should first decide whether linear elastic analysis will be sufficient, or if nonlinear (sometimes called plastic) analysis is required. Elastic analysis applies only up to design load levels. An analysis of performance above design levels must be nonlinear.

For reference, there are currently no commercial programs that reasonably simulate the hysteretic response of timber connections or assemblies. Commercial software can achieve reasonable results if modelling monotonic linear or nonlinear behaviour, but not for hysteretic behaviour. Advanced commercial software, such as ABAQUS (Dassault Systèmes, 2016), allows the user to define the nonlinear and hysteretic response of elements and connections. Otherwise, without hysteric models, the analysis can only be approximate. Some noncommercial software packages incorporate hysteretic behaviour for wood construction, such as CASHEW (Cyclic Analysis of wood SHEar Walls; Folz and Filiatrault, 2002a, 2002b), SAPWood (Seismic Analysis Program for Woodframe buildings; Pei and van de Lindt, 2010), Timber 3D (Pang, 2015), and MCASHEW2 (Pang & Shirazi, 2010). This software packages have been developed primarily for research purposes rather than design level investigations, and are capable of both detailed and full-structural analysis.

### *7.1.4.2 Advanced FE Methods*

Advanced FE methods usually include two types of models: detailed models and macro-element models. The force-displacement relationships of connection elements in a detailed model or macro-spring elements in a macro-element model are key to the structural behaviour of shear walls. Sections 7.1.4.2.1 through 7.1.4.2.4 introduce detailed and macro-element models for light wood-frame shear walls, along with their respective force-displacement relationships (that is backbone curves and hysteresis loops).

#### 7.1.4.2.1 Detailed Models

An accurate model of shear walls must consider all element behaviours. The more detailed the analysis goal, the more important the individual element models. A detailed FE model for light wood-frame shear walls, as illustrated in Figure 18, typically includes shell elements for sheathing, beam elements for framing members, and spring elements for connections (Christovasilis & Filiatrault, 2010; Di Gangi et al., 2018; Rinaldin & Fragiacomo, 2016; Xu & Dolan, 2009b; Zhu et al., 2010). These models can be created on both commercial FE software, e.g., ABAQUS, and noncommercial computer programs, e.g., MCASHEW2 (Pang & Shirazi, 2010). Figure 19 and Figure 20 respectively illustrate connection models using springs and a deformed shear wall, both modelled in MCASHEW2.

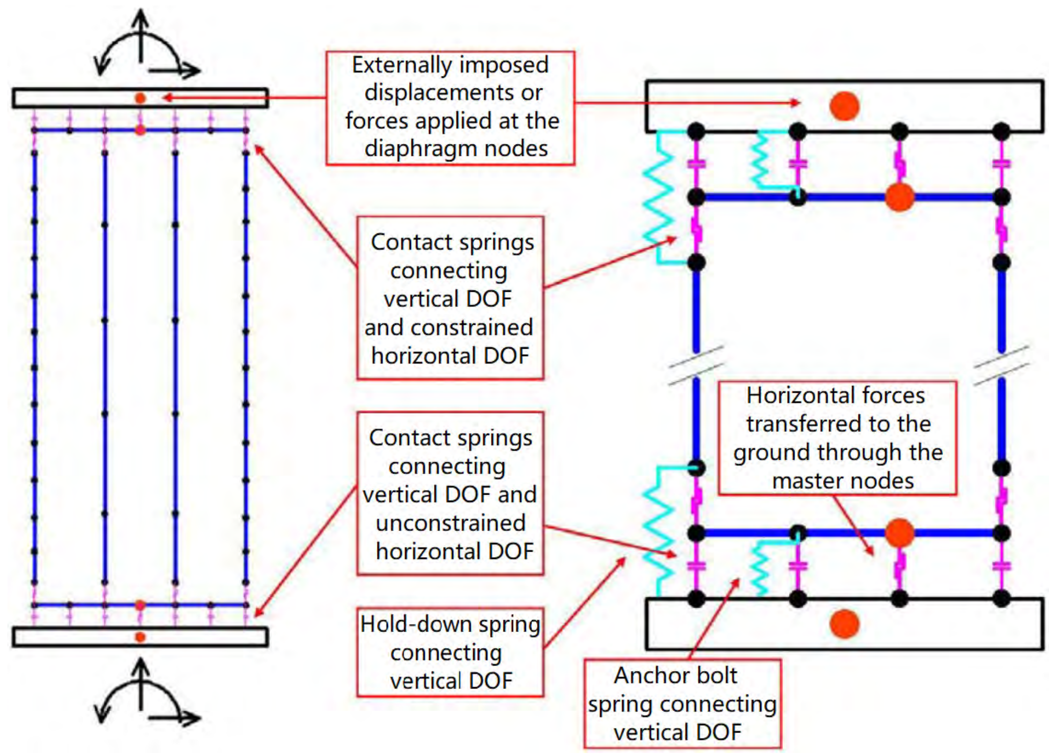


**Figure 18. Detailed numerical model of a light wood-frame shear wall (Christovasilis & Filiatrault, 2010)**

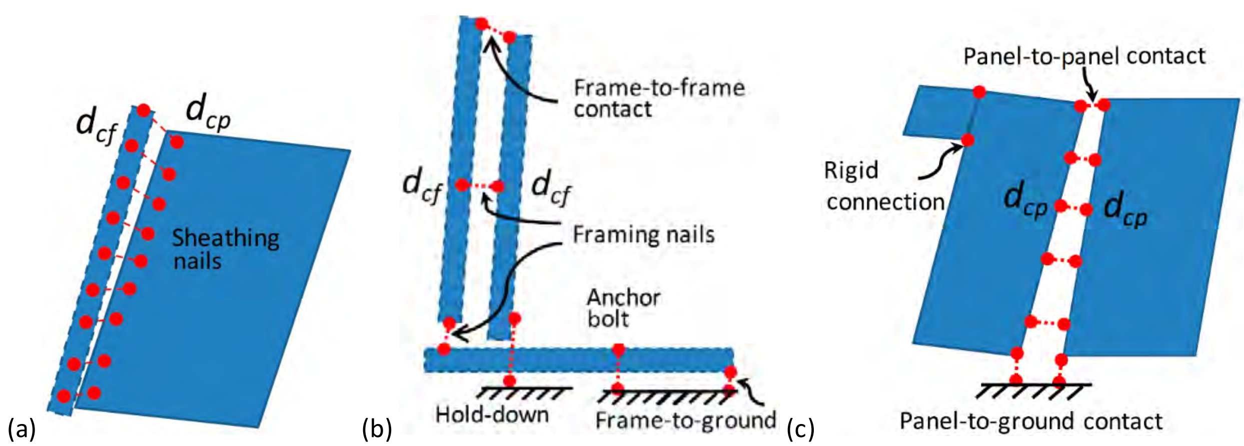


**Figure 19. Connection (spring) elements (Pang & Shirazi, 2010): (a) sheathing-to-framing; (b) framing-to-framing; and (c) panel-to-panel**

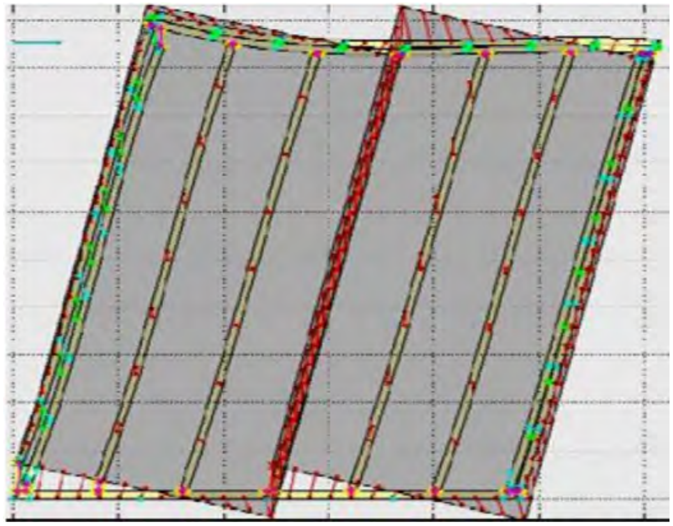

**Figure 20. Deformed shear wall in MCASHEW2 (Pang & Shirazi, 2010)**

Sheathing-to-framing nailed connections are crucial to the performance of light wood-frame structures under various loading conditions. In most cases, especially for seismic loads, connections are the weakest points of the structural system and thus govern its stiffness, strength, deformation, and ductility. Therefore, an analysis must include detailed load-displacement (slip) models. Figure 21 shows typical hysteresis loops obtained from a reversed cyclic test on a nailed connection. A nonlinear FE analysis using this behaviour for each nailed connection will provide realistic results. The main features of hysteresis loops, as shown in Figure 21, include (a) nonlinear connection behaviour; (b) slightly asymmetric loops; (c) indistinct yield points; (d) stiffness degradation with increasing load cycles; (e) relatively fat initial hysteresis loops that imply large amounts of energy dissipation; (f) narrowed loop areas (that is the 'pinching effect') in the middle of hysteretic loops after the first load cycle; (g) strength degradation at the same deformation level for repeating loading cycles; (h) strength degradation for larger deformations; and (i) relatively high ductility. The so-called pinching effect refers to loops narrowing after multiple cycles and occurs due to the formation of gaps around the fasteners (nails) because of the irreparable crushing of wood (mainly in the framing member). This effect occurs after the first loading cycle at each deformation level, as the sole contribution of the fasteners reduces the connection stiffness at that point. As soon as contact with the surrounding wood is re-established at higher deformation levels, the stiffness rapidly increases, leading to the typical pinched shape of hysteretic curves. For linear analyses, an equivalent stiffness can be used as input for the springs; nonlinear analyses, meanwhile, requires a backbone curve model or even a hysteretic model which can represent the hysteretic behaviour of nailed connections. Sections 7.1.4.2.4 and 7.1.4.2.3 discuss specific options for hysteresis loops and backbone curves, respectively.

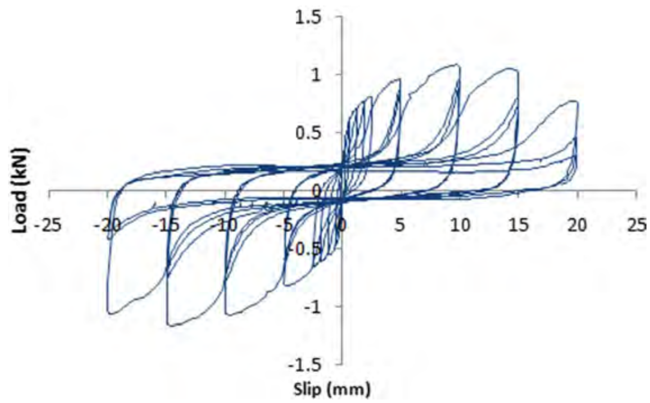


**Figure 21. Experimental load-deformation hysteresis loops for a nailed connection (Li et al., 2012)**

If using commercial software to investigate the forces and stresses within a shear wall, then the spring elements, as shown in Figure 19, will be located at the positions of the individual nails in the physical wall. The springs connect the nodes of the shell elements (representing the sheathing) to the beam elements (representing the framing). Most commercial software packages require mesh refinement for the local sheathing and framing around these nodes. All framing connections (for vertical studs to the horizontal top and bottom plates) can be modelled as pinned connections, since the physical connections involved are usually smooth-shank nails driven into the end grain of the stud.

Boundary conditions must be provided for anchoring the framing. If modelling conventional construction, then there will be no hold-down connections present to resist the uplift of the end studs (chords). The anchorage consists of bolts or nails distributed along the bottom plate and nails connecting the top of the wall to the upper floor or roof diaphragm—it is possible to model this using pinned boundary restraints. It is very difficult to construct a fixed connection in wood, and designers very rarely attempt to do so. Most connections between structural elements involve either nails or bolts, modelled as pins in FE analysis. Models of engineered construction must include the hold-down connectors. If the goal is a detailed response within the wall element, it is important to locate the connection between the hold-down anchor and the end stud of the wall segment at the proper height and on the correct side of the chord element. Proprietary testing has shown that attaching the hold-down connection in such a way results in significant bending stresses in the chord element, since the hold-down cannot rotate as the wall segment racks under load. In such a scenario, the spring or connector elements for the hold-down should provide both axial and bending stiffness. The sheathing-to-framing nail connection and the rotation of the connector itself counter the induced moment in the chord. To model continuous rod hold-downs, use additional elements with material properties representing steel rods. MCASHEW2 (Pang & Shirazi, 2010) also assigns nonlinear behaviour to non-sheathing-to-framing connections for more detailed and sophisticated models.

### 7.1.4.2.2 Macro-Wall Element Models

Models of full structures serve to investigate full-building response, including modes of vibration, natural frequencies, force distributions among shear walls, and deformations. Wall segments are usually modelled as horizontal- or diagonal-spring elements attaching the upper diaphragm to the lower one (Chen & Ni, 2020; Filiatrault, Isoda, & Folz, 2003; Xu & Dolan, 2009a), as in Figure 22. A typical macro-wall element consists of three rigid truss framing elements and one or two spring elements pinned to each other. To consider rotation, one can add two more springs to the bottom of the rigid truss element, as shown in Figure 23. The spring constants must have mechanical properties that represent the lateral stiffness and nonlinear behaviour of the wall element (Chen, Chui, Ni, Doudak, & Mohammad, 2014b). The boundary conditions are usually pinned-pinned, and the models can adjust the stiffness to represent either the engineered or the conventional construction condition. Figure 24 shows a tested two-storey light wood-frame building and its mode, while Figure 25 shows a 6-storey light wood-frame building with portal frames using macro-wall elements (Chen, Chui, Ni, & Xu, 2014).

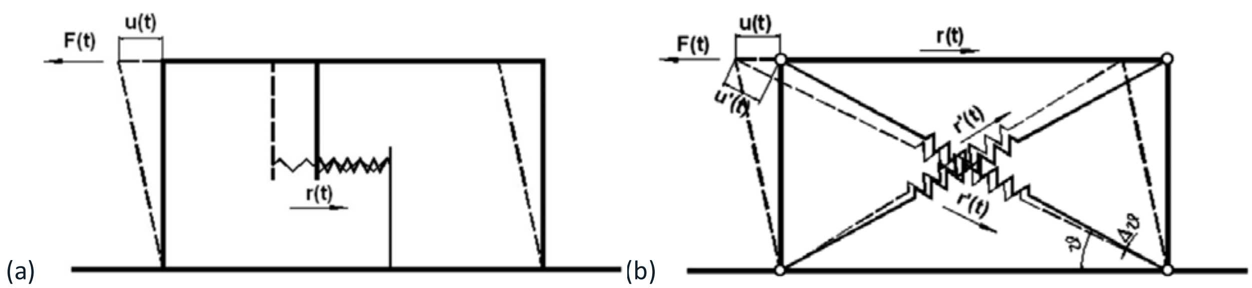


**Figure 22. Macro-element models for wood-frame shear walls (Xu & Dolan, 2009a) : (a) single-spring model and (b) diagonal-spring model**

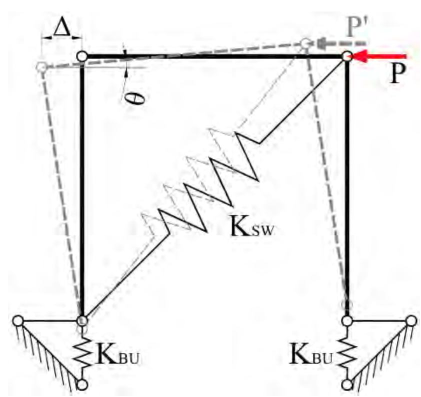


**Figure 23. Macro-element models for wood-frame shear walls modified to consider rotation (Chen, Chui, Ni, Doudak, & Mohammad, 2014b)**

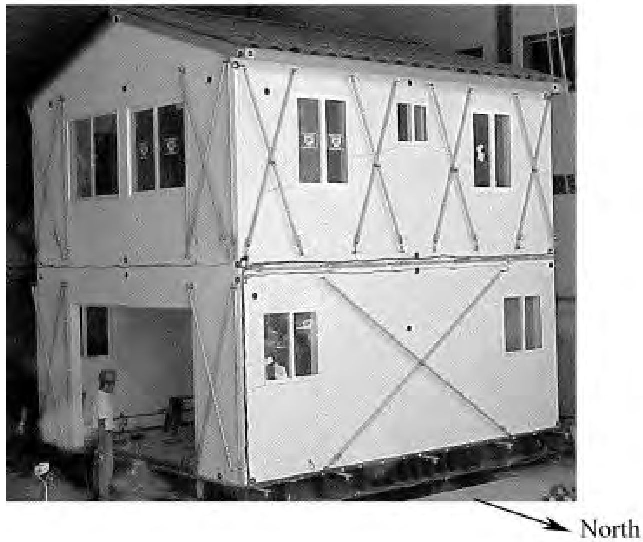


(a)

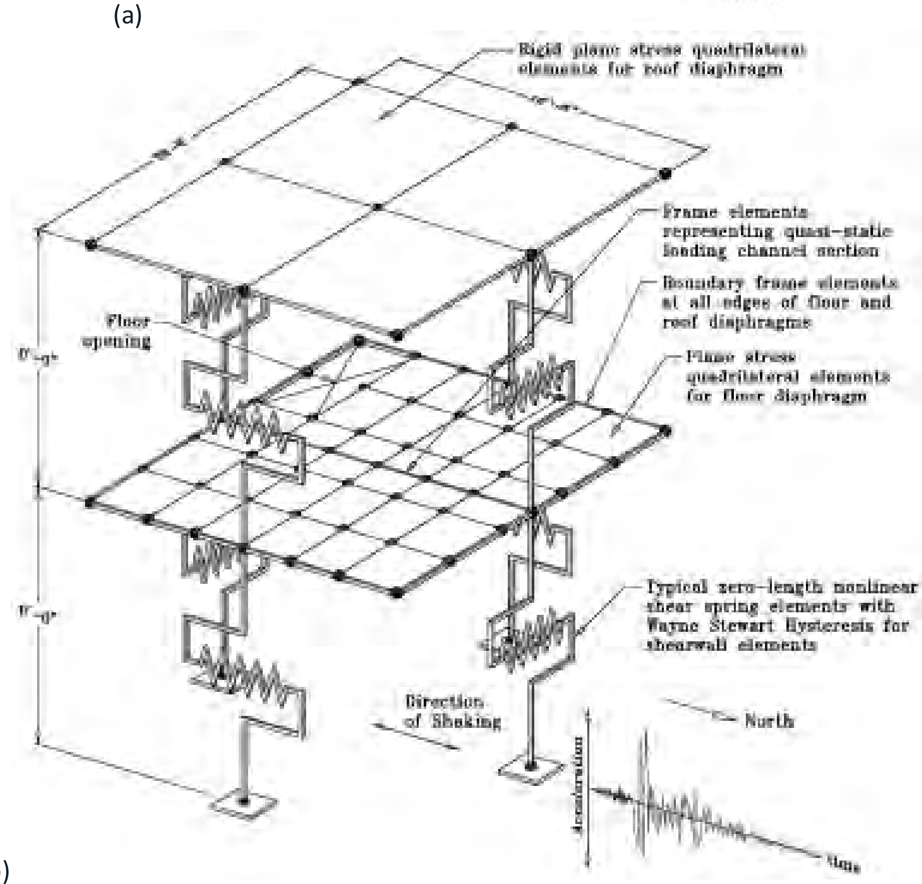


(b)

**Figure 24. Two-storey wood-frame test structure (Filiatrault et al., 2003): (a) test structure; and (b) Pancake model**

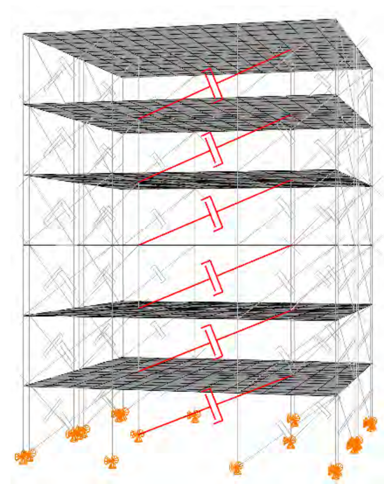

**Figure 25. FE model of a 6-storey light wood-frame building (Chen, Chui, Ni, & Xu, 2014)**

The lateral behaviour of light wood-frame buildings is similar to that of the nailed connections that make up the shear walls. As shown in Figure 26, the hysteresis loops of a wood-frame shear wall are similar to those of the sheathing-to-framing connections shown in Figure 21. Krawinkler et al. (2000) defined four deterioration modes for wood-frame shear walls, namely basic strength deterioration, post-peak strength deterioration, unloading stiffness degradation, and accelerated reloading stiffness degradation. Therefore, a hysteretic model capable of predicting stiffness and strength degradation, along with the pinching effect, is desirable for the nonlinear dynamic analysis, e.g., seismic response analysis, of light wood-frame buildings. For linear analysis, the equivalent stiffness of the shear wall is sufficient for each spring; a backbone curve model which can represent the envelope of load-displacement curves is required for nonlinear static analysis. Sections 7.1.4.2.3 and 7.1.4.2.4 discuss specific hysteretic models and backbone curve models, respectively.

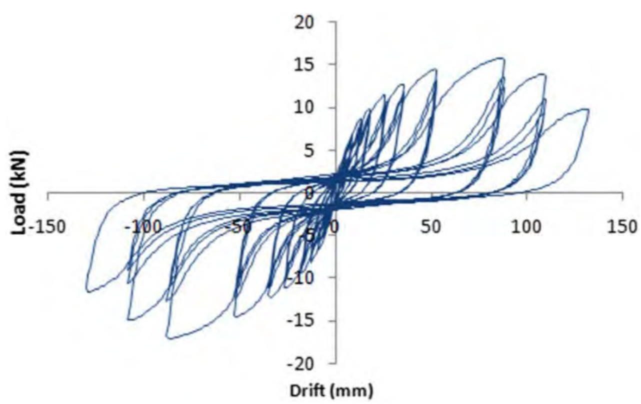


**Figure 26. Experimental hysteresis loops of a wood-frame shear wall (Li et al., 2012)**

One important issue to consider is whether the model represents the nonstructural sheathing materials correctly. Experimental results for both wall and full-building testing, such as Chen et al. (2016), Fischer et al. (2001), Gatto and Uang (2002), McMullin and Merrick (2002), Mosalam et al. (2003), Deierlein and Kanvinde (2003), and Pardoen et al. (2003) report that finish materials such as gypsum wallboard and stucco increase the stiffness of the wall segments by as much as a factor of 10. However, the incompatibility of the stiffness and failure mechanism of the finish materials and WSPs mean that the finish materials control performance until they begin to fail. As a result, the WSP response at the location where the finish material fails must resist the local deflection demands that result from the sudden drop in local stiffness. Therefore, linear models should not be used to simulate behaviour past the point at which the more brittle finish materials begin to fail. The Federal Emergency Management Agency (FEMA; 2012) and Chen et al. (2016) proposed combination rules for wood-frame shear walls that incorporate different sheathing materials.

Three-dimensional models of light wood-frame buildings assume the diaphragms to be either rigid elements or shell elements with equivalent in-plane stiffness (not fully rigid). With respect to the 2D modelling of light wood-frame buildings, which analyses shear walls in a selected line of resistance, one can consider the effect of diaphragm flexibility in the out-of-plane direction by adding either a rigid linking beam, if the diaphragm is assumed to be rigid, or a pinned rigid link bar, if the diaphragm is assumed to be flexible (Chen & Ni, 2021). This is illustrated in Figure 27.

(a)

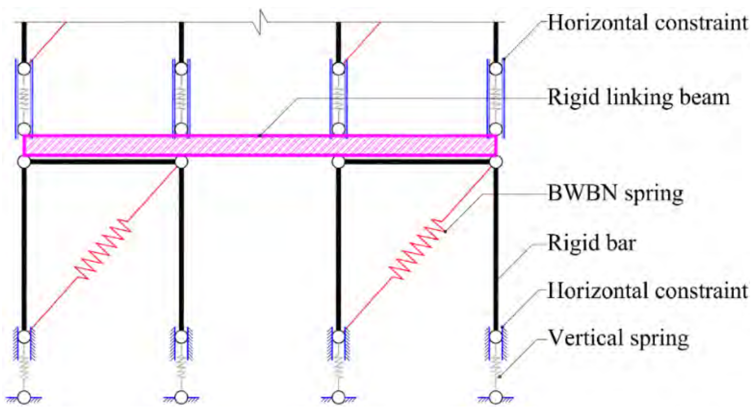


(b)

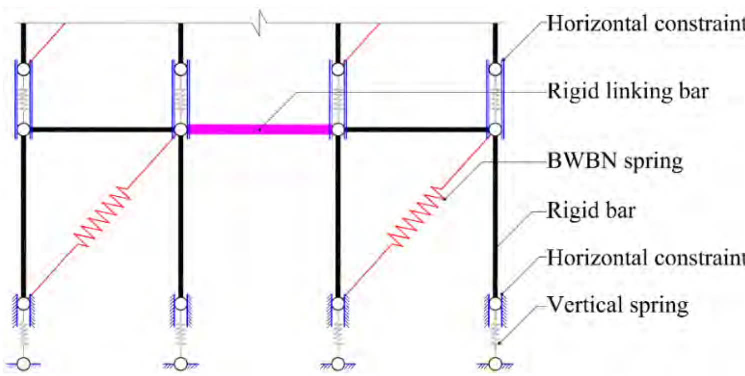


**Figure 27. Light wood-frame building models with (a) rigid or (b) flexible diaphragms in out-of-plane direction (Chen & Ni, 2021)**

#### 7.1.4.2.3 Hysteresis Loops

Nonlinear dynamic (response history) analysis involves the explicit modelling of inelastic response, accounting for stiffness and strength degradation, hysteretic energy dissipation, the inclusion of viscous damping and second-order effects, and the selection and scaling of earthquake ground motions. Hysteretic models are the essential parts for such an analysis. The past several decades have seen various types of hysteretic models developed for the dynamic analysis of timber connections and structures. Generally, these models can be categorised into three major types, discussed in the following sections: mechanics-based models, empirical models, and mathematical (phenomenological) models.

**Mechanics-based models**

Mechanics-based models represent fasteners and wood members using specific structural elements. For nailed connections, for example, as shown in Figure 28 and Figure 29(a), Chui et al. (1998) and Foschi (2000) modelled the nail and the wood as an elastoplastic beam on a nonlinear foundation. There are also analysis techniques based on large displacement theory.

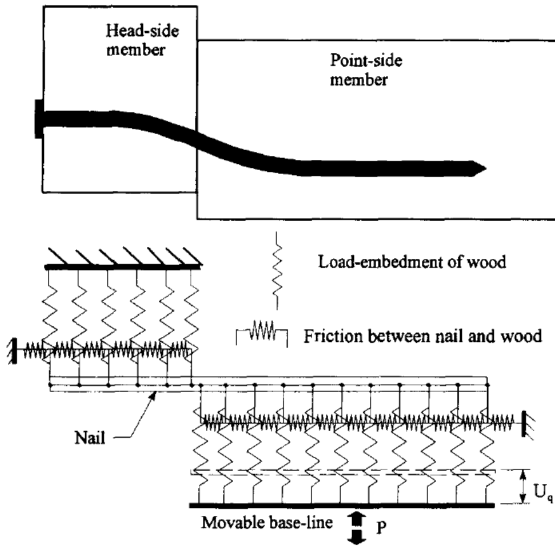


**Figure 28**. **Assemblage of elements to model a nailed wood joint (Chui et al., 1998)**

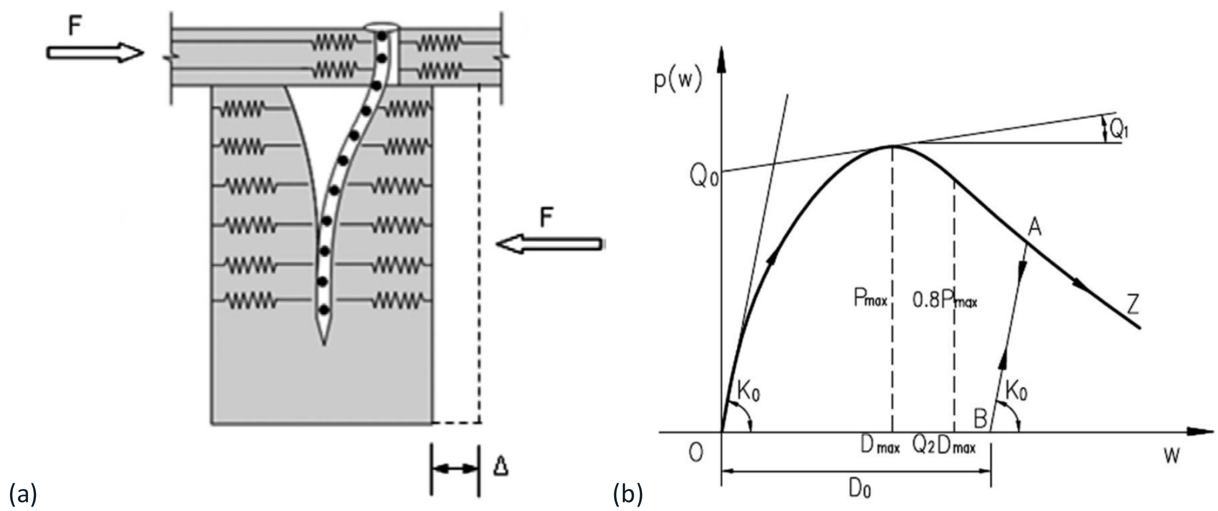


**Figure 29. HYST panel-frame nailed connection (Foschi, 2000; Li et al., 2012): (a) Schematics of HYST model; and (b) Embedment properties of wood medium**

In Foschi's (2000) HYST algorithm, the nail shank is modelled using elastoplastic beam elements, with each node having five degrees of freedom (DOFs). If $u$ = the axial displacement of the cross-sectional centroid of the beam and w = the lateral displacement, the DOFs used at each node are u and its derivative $u'$, $w$, the rotation $w'$, and the curvature $w''$. Thus, the shape functions of $u$ and $w$ are cubic and fifth-order polynomials, respectively. This representation minimises the number of required elements and is computationally efficient, given that the connection model is for a multiple connection model of a frame or wall.

The hysteresis of the steel nail shank should obey a simple elastoplastic constitutive relation that considers strain hardening. When the nail deforms laterally, it compresses but cannot pull the wood medium. As shown in Figure 29(a), this behaviour is modelled by a bed of continuous, compression-only nonlinear springs smeared along the nail shank. Equation 10 represents the relationship between the applied pressure $p$(w) and the wood deformation $w$, corresponding to a monotonic increase in $w$. This assumes that the compressive behaviour shows a peak $P_{max}$, (Equation 11), followed by a softening trend. The pressure $p(w)$ is thus represented by two exponential curves connected at the peak load, as shown in Figure 29(b). $K_0$ is the initial stiffness of the embedment relationship; $Q_0$ and $Q_1$ are, respectively, the intercept and the slope of the asymptote that the deformation $w$ approaches as it nears infinity. However, $w$ is constrained to not exceed $D_{max}$, the value at which the pressure $p(w)$ reaches the maximum $P_{max}$. $Q_2$ gives the fraction of $D_{max}$ at which the pressure drops to 80%$P_{max}$ during the softening phase. $Q_3$ can be calculated using Equation 12.

$$\boldsymbol{p(w)} = \begin{cases} (\boldsymbol{Q_0} + \boldsymbol{Q_1 w})\left(\boldsymbol{1} - \boldsymbol{e}^{-\boldsymbol{K_0 w/Q_0}}\right) & \boldsymbol{if\, w \leq D_{max}} \\ \boldsymbol{P_{max} e^{Q_3 (w - D_{max})^2}} & \boldsymbol{if\, w > D_{max}} \end{cases} \qquad [10]$$

$$\boldsymbol{P_{max}} = (\boldsymbol{Q_0} + \boldsymbol{Q_1 D_{max}})\left(\boldsymbol{1} - \boldsymbol{e}^{-\boldsymbol{K_0 D_{max}/Q_0}}\right) \qquad [11]$$

$$\boldsymbol{Q_3} = \frac{\boldsymbol{log(0.8)}}{[(\boldsymbol{Q_2} - \boldsymbol{1.0})\boldsymbol{D_{max}}]^2} \qquad [12]$$

Figure 29(b) also shows how to implement loading and reloading in the HYST algorithm. If the wood medium is unloaded at A, the pressure decreases following line AB, with a constant unloading stiffness which is assumed as equal to the initial $K_0$. Further unloading, or a further decrease in the displacement $w$, proceeds from B to O at zero pressure. That is, the nail shank releases from the wood surface and travels through a gap of magnitude $D_0$. This gap remains, and during the reloading, the shank will travel through it until it touches the wood again at Point B. A further increase in $w$ will require a further increase in pressure. The pressure should increase linearly, with the same stiffness $K_0$, until it reaches Point A. Further increases in $w$ correspond to the pressures along the softening path from point A. The HYST algorithm has been included in a shear wall model (Figure 30) by Dolan (1989) and a 3D building model, LightFrame3D, by He (2002).

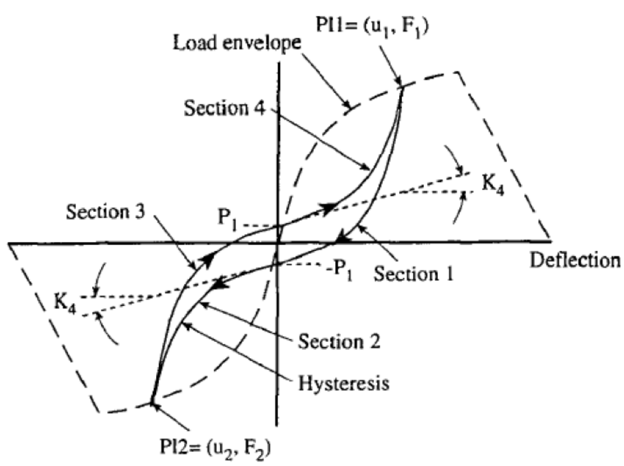


**Figure 30. Dolan model (Dolan, 1989)**

The HYST model has since been upgraded by Li et al. (2012), who reduced the number of DOFs to the standard three per node (*u*, *w*, and *w'*), with linear and cubic polynomial shape functions for *u* and *w*, respectively. This showed that computational efficiency can be greatly improved without significantly affecting numerical accuracy, if one models the nail shank with a sufficient number of beam elements (e.g., 10). The parameters that characterise the embedment's load-deformation relationship can be calibrated by an optimization algorithm using the test results of the nail connections under either monotonic or cyclic loading. The reloading assumption now represents strength and stiffness degradation. The modified HYST, as shown in Figure 31, assumes that reloading from Point B also follows a straight line, but now with reduced stiffness $K_{RL}$, which is related to the initial $K_0$ and the gap size $D_0$. It also adds the effect of nail withdrawal.

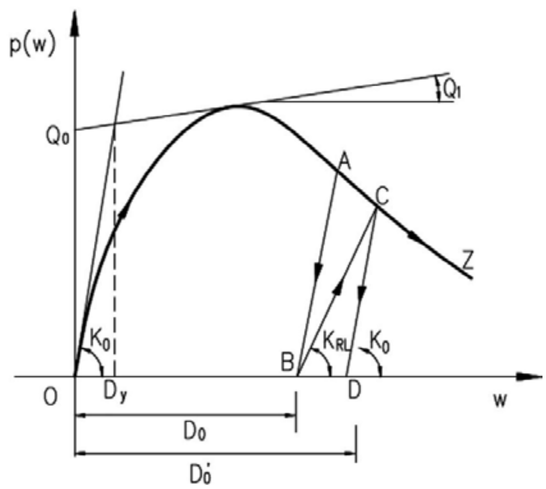


**Figure 31. Loading and unloading of wood medium in modified HYST algorithm (Li et al., 2012)**

The model developed by Chui et al. (1998) is similar to the HYST model, with the addition of an empirical set of rules for the loading and unloading paths of the wood medium, as illustrated in Figure 32. The model's input properties include the load-embedment behaviour of the wood and the nail bending properties. It also considers the effects of the cyclic response of the fastener material, the shear deformation in the fastener, the friction between fastener and wood, and the withdrawal effect of the fastener. These rules implicitly embody the formation of gaps, which was not explicitly considered, and require fitting the parameters as in a full empirical model.

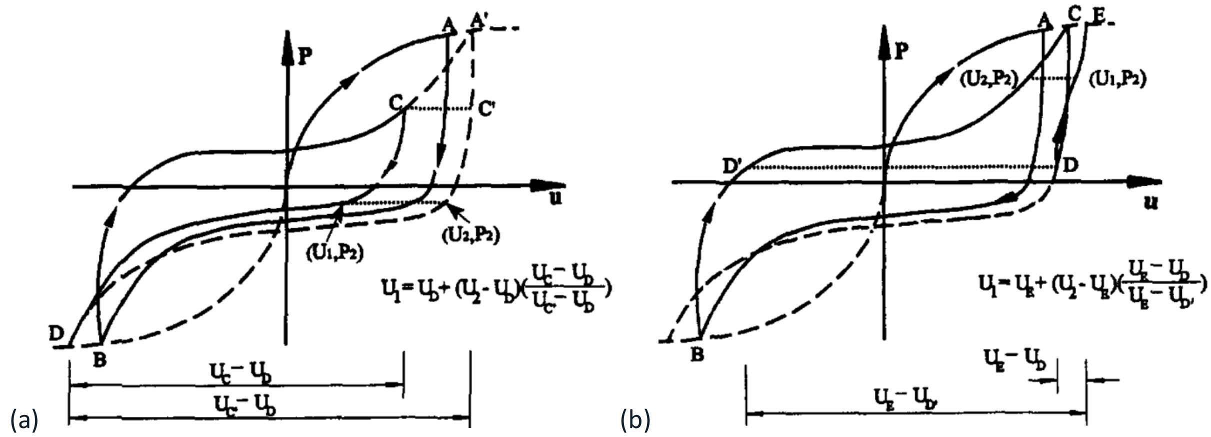


**Figure 32. Path rules for the load-embedment responses of wood, proposed by Chui et al. (1998): (a) when the load direction reverses during loading; and (b) when the load reverses direction at D during unloading before it reaches the zero slip location**

### Empirical Models

Empirical hysteretic models, also called piecewise linear function models or parameter hysteretic models, are commonly used in structural engineering. They function by specifying a set of rules for loading and unloading paths. These rules usually involve a set of parameters which are calibrated to the observed experimental response of a connection or assembly for a given load or displacement history. There have been a number of attempts to empirically model timber connections and structures under reversed cyclic loading, e.g., the Kivell model (Kivell et al., 1981) (Figure 33), Stewart model (Stewart, 1987) (Figure 34), Ceccotti model (Ceccotti & Vignoli, 1990) (Figure 35); Modified Stewart model or MSTEW model (Folz & Filiatrault, 2001b) (Figure 36), Rinaldin model (Rinaldin et al., 2013) (Figure 37); and Pinching4 model (Lowes et al., 2003; Mazzoni et al., 2006) (Figure 38). For deformations larger than those already occurring in the connection, all the models follow the envelope or skeleton curve describing the behaviour of the connection under static loading. Other researchers have used improved versions of these models in their work.

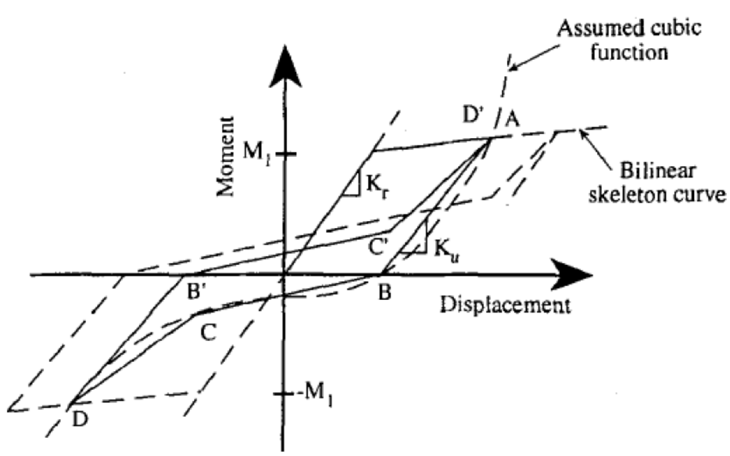


**Figure 33. Kivell model (Kivell et al., 1981)**

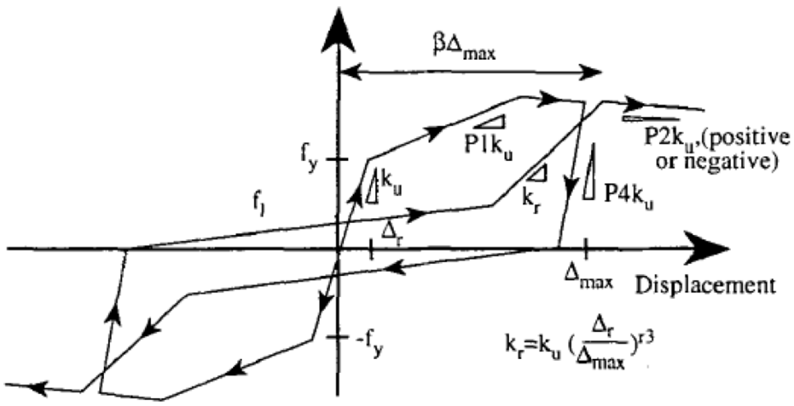


**Figure 34. Stewart model (Stewart, 1987)**

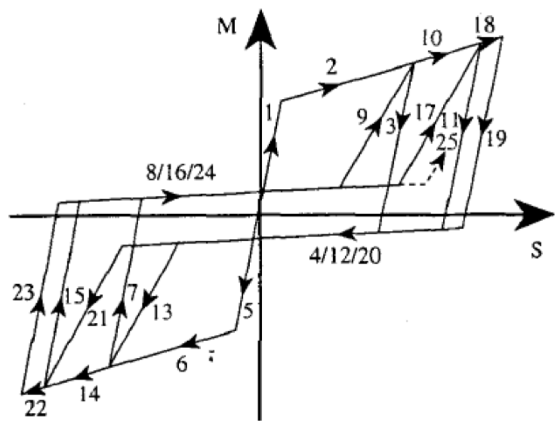


**Figure 35. Ceccotti model (Ceccotti & Vignoli, 1990)**

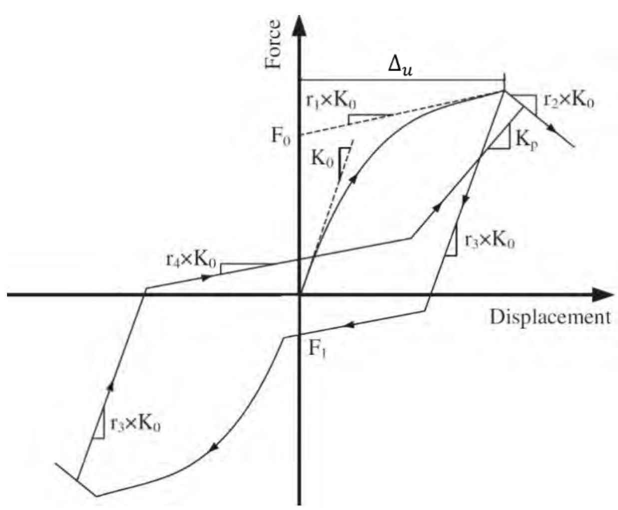


**Figure 36. Modified Stewart model, MSTEW (Folz & Filiatrault, 2001a)**

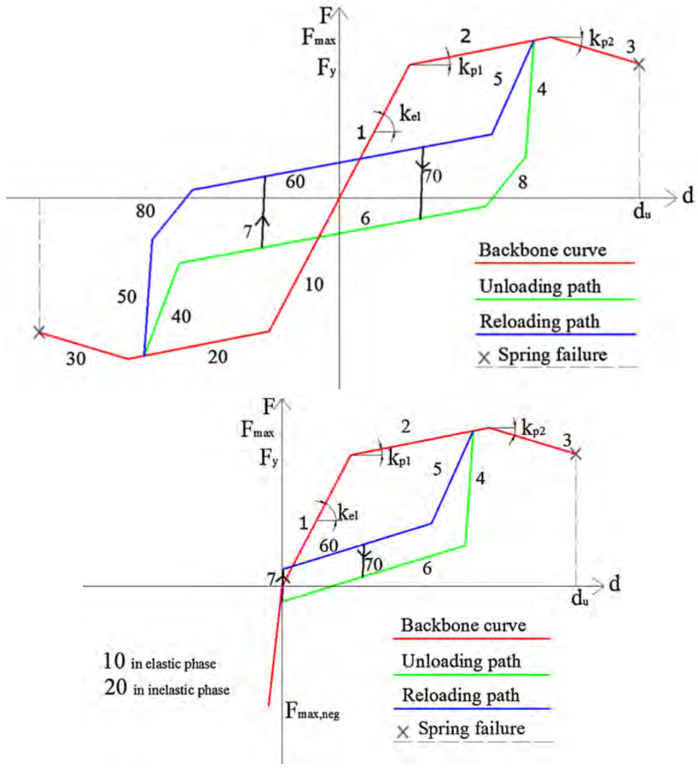


**Figure 37. Rinaldin model (Rinaldin et al., 2013): Left – Shear hysteresis law; Right – Axial hysteresis law**

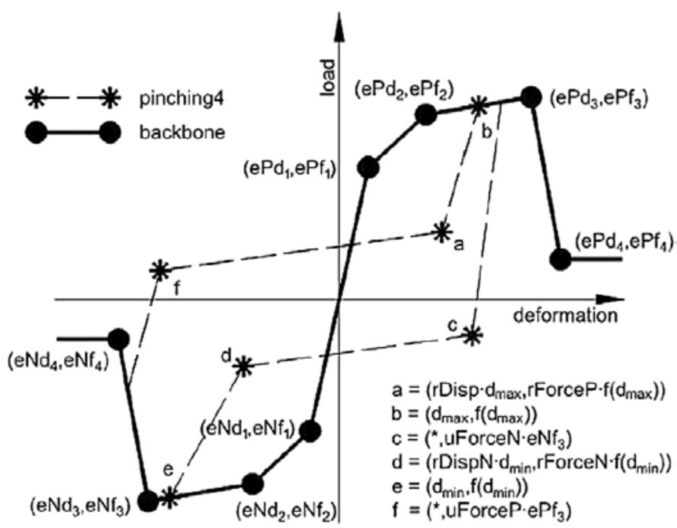


**Figure 38. Pinching4 model (Lowes et al., 2003; Mazzoni et al., 2006)**

Empirical hysteretic models typically use a series of piecewise linear or exponential functions for the backbone or envelope curve, the loading path, and the unloading path. This involves straight segments between any changes in the displacement direction. For example, the MSTEW model (Folz & Filiatrault, 2001b) (Figure 36), which is widely accepted in both the wood engineering and research communities (Pang et al., 2007), consists of a nonlinear path for the envelope curve and a series of linear segments to model the loading and unloading paths off the envelope curve. It requires a total of 10 parameters (Table 1) to capture the nonlinear hysteretic responses of timber structures.

**Table 1. Definition of hysteretic parameters of MSTEW model**

| Parameter | Definition |
|---|---|
| $K_0$ | Initial stiffness |
| $F_0$ | Force intercept of the asymptotic stiffness at ultimate strength |
| $F_I$ | Zero-displacement load intercept |
| $\Delta_u$ | Displacement at ultimate load |
| $r_1$ | Asymptotic stiffness ratio under monotonic load |
| $r_2$ | Post-capping strength stiffness ratio under monotonic load |
| $r_3$ | Unloading stiffness ratio |
| $r_4$ | Reloading pinched stiffness ratio |
| $\alpha$ | Hysteretic parameter for stiffness degradation |
| $b$ | Hysteretic parameter for stiffness and strength degradation |
| *F0* | Initial stiffness |

The modelling of the monotonic pushover response of the shear wall combines an exponential and a linear function. These two functions (Equation 13) define the ascending and descending envelopes for the lateral load-displacement relation of the shear wall (Figure 36).

$$\boldsymbol{F}(\Delta) = \begin{cases} \mathbf{sgn}(\Delta)(\boldsymbol{F_0} + \boldsymbol{r_1 K_0}|\Delta|)\left(\mathbf{1} - \boldsymbol{e}^{-\boldsymbol{K_0}|\Delta|/\boldsymbol{F_0}}\right) & \boldsymbol{if}\ |\Delta| \leq |\Delta_{\boldsymbol{u}}| \\ \mathbf{sgn}(\Delta)\boldsymbol{F_u} + \boldsymbol{r_2 K_0}[\Delta - \mathbf{sgn}(\Delta)\Delta_{\boldsymbol{u}}] & \boldsymbol{if}\ |\Delta| > |\Delta_{\boldsymbol{u}}| \end{cases} \quad [13]$$

The envelope curve is defined by five physically identifiable static parameters: $K_0$, $F_0$, $r_1$, $r_2$, and $\Delta_u$; see Table 1. Phenomenologically, Equation 13 captures the crushing of the framing members and sheathing, along with the yielding of the connectors. Beyond the displacement $\Delta_u$, which is associated with the ultimate load $F_u$, the load-carrying capacity decreases.

For a shear wall under cyclic loading, as illustrated in Figure 39, the load-displacement Paths OA and CD follow the monotonic envelope curve, Equation 13. All other paths are assumed to exhibit a linear load-displacement relationship. Unloading off the envelope curve follows a path such as AB with a stiffness of $r_3 K_0$. Here, the wall unloads elastically. Under continued unloading, the response moves onto Path BC, which has reduced stiffness $r_4 K_0$. The low stiffness along this path exemplifies the pinched hysteretic response displayed by wood-frame shear walls under cyclic loading. This occurs because of the previously induced crushing of the wood material of the framing members in the sheathing-to-framing nailed connections (Path BC). Loading in the opposite direction for the first time forces the response onto the Envelope Curve CD. Unloading off this curve is assumed to be elastic along Path DE, followed by a pinched response along Path EF which passes through the zero-displacement intercept $F_I$ with slope $r_4 K_0$. Continued reloading follows Path FG with degrading stiffness $K_p$, as given by

$$\boldsymbol{K_p} = \boldsymbol{K_0}\left(\frac{\Delta_0}{\Delta_{max}}\right)^{\boldsymbol{\alpha}} \quad [14]$$

with $\Delta_0 = F_0 / K_0$. Note (from Equation 14) that $K_p$ is a function of the previous loading history through the last unloading displacement $\Delta_{un}$ off the envelope curve (corresponding to Point A in Figure 39). Thus,

$$\Delta_{max} = \boldsymbol{\beta}\Delta_{un} \quad [15]$$

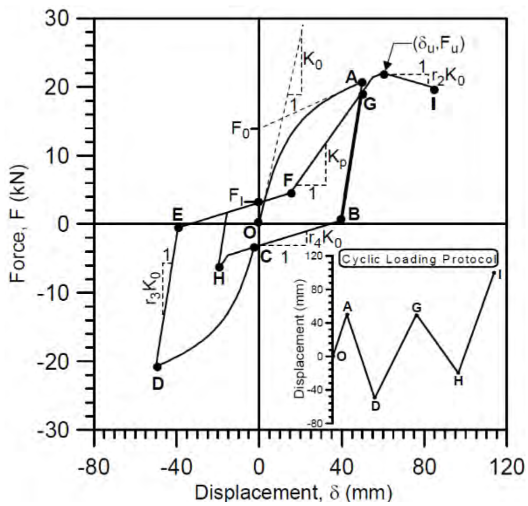


**Figure 39. Force-displacement response of a shear wall under cyclic loading (Folz & Filiatrault, 2001b, 2002a)**

If the shear wall is displaced to $\Delta_{un}$ during another cycle, then the corresponding force will be less than $F_{un}$, the value that was previously achieved. This strength degradation is shown in Figure 39 by comparing the respective force levels reached at points A and G. In this model, under continued cycling to the same displacement level, the force and energy dissipated per cycle is assumed to stabilise. To obtain the 10 parameters (Table 1), fit the model to a connection or to the shear wall test data by using trial-and-error methods or specific tools, e.g., the CASHEW (Cyclic Analysis of wood SHEar Walls) program (Folz & Filiatrault, 2000).

The empirical hysteretic models with static parameters discussed above cannot capture the damage process in timber structures. Richard et al. (2002) proposed a strength reduction based on a cumulative factor calculated in one direction with respect to the previously achieved strength in the opposite direction. Collins et al. (2005) defined a similar damage calculation process. Although most of these constitutive laws use exponential functions for the pre-peak backbone curve and hysteresis loops, that of Ayoub (2007) uses trilinear functions. This model describes the damage process in detail, dividing it into four degradation phenomena: strength reduction, decrease in unloading stiffness, decrease in accelerated stiffness, and cap degradation.

The Pang et al. (2007) evolutionary parameter hysteretic model (EPHM, Figure 40) is only defined by exponential functions (pre and post-peak backbone; unloading and loading hysteretic loops); damage is not cumulative. The Humbert (2010) model (Figure 41) can be considered an improvement of the Richard et al. (2002) and Yasumura et al. (2006) models and is capable of modelling asymmetric behaviour (Humbert et al., 2014).

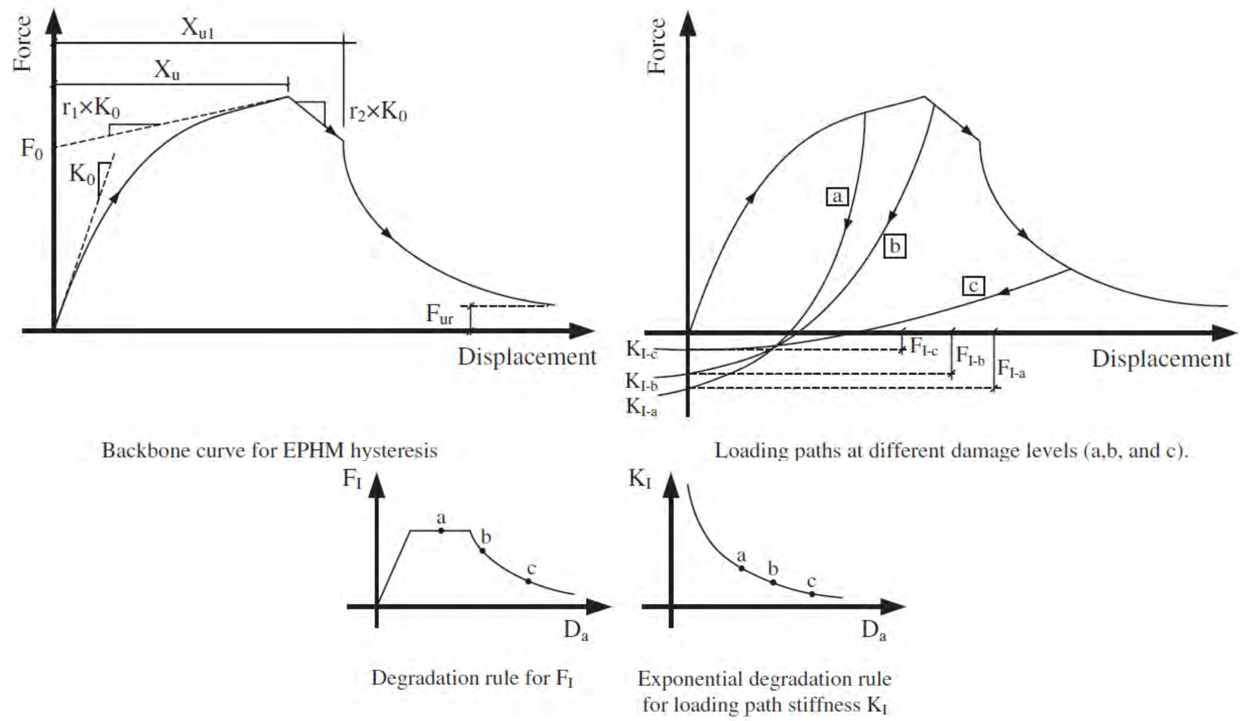


**Figure 40. EPHM 16-parameter hysteretic model (Pei & van de Lindt, 2008)**

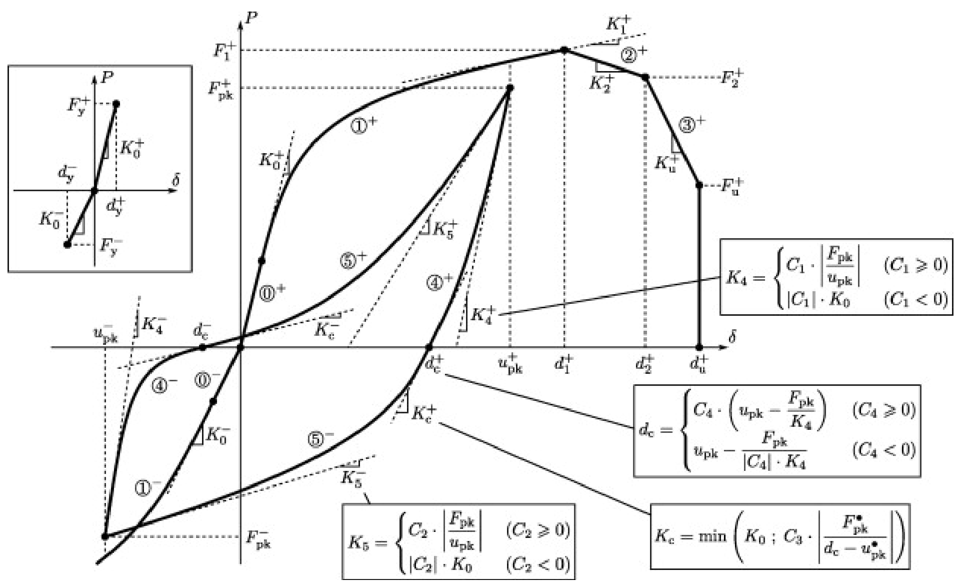

**Figure 41. Humbert model (Humbert, 2010)**

The empirical hysteresis can use piecewise linear segments or exponential curves. In most commercial software packages, such as Ansys, SAP2000, and DRAIN-2DX, piecewise linear segments serve to define the hysteresis. Other software, such as CASHEW (Filiatrault et al., 2003), has adopted the Stewart model. SAWS (Seismic Analysis of Woodframe Structures; Folz & Filiatrault, 2001b), SAPWood (Pei & van de Lindt, 2007; 2008), and Timber3D (Pang et al., 2012) all use the Stewart model and MSTEW. OpenSees includes the MSTEW and Pinching4 models (Franco et al., 2019; Lowes et al., 2003; Mazzoni et al., 2006).

**Mathematical Models**

Mathematical models are also called semi-physical or phenomenological models (Ismail et al., 2009; Ma et al., 2004). In general, they do not involve a detailed analysis of the physical behavior of a system through its hysteresis loops; instead, they combine some physical understanding of the hysteretic system with some form of black-box modelling (Ismail et al., 2009). The past few decades have seen proposals for various mathematical models of hysteresis. One of the most widely accepted is a differential model originally proposed by Bouc (1967) and subsequently generalised by Wen (1976) and other researchers. This model is known as the Bouc–Wen model and has seen extensive use to mathematically describe the hysteretic behavior of components and devices in civil and mechanical engineering. It connects the restoring force and deformation through a first-order nonlinear differential equation with unspecified parameters. By choosing suitable parameters, it is possible to generate a large variety of different shapes for the hysteresis loops to account for strength degradation, stiffness degradation, and even the pinching characteristics of an inelastic structure. Foliente (1995) modified the Bouc–Wen–Baber–Noori (BWBN) model to characterise the general features of the hysteretic behaviour of wood joints and structural systems.

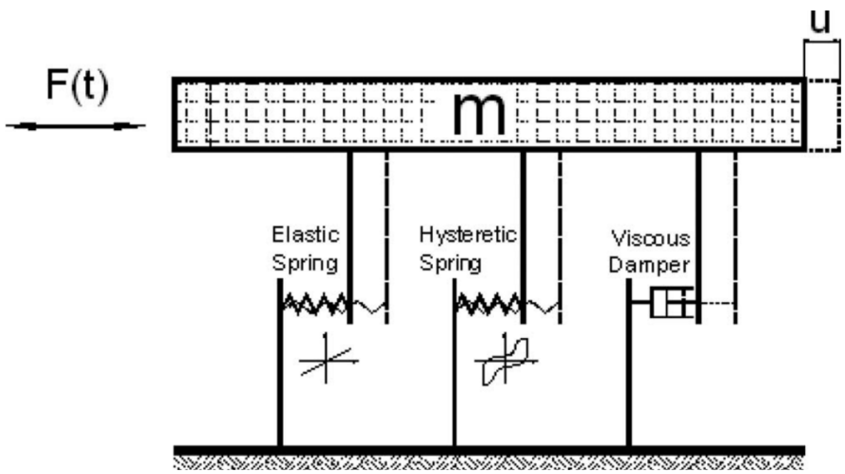


**Figure 42. Schematic diagram of an inelastic system (Foliente, 1993; Ma et al., 2004)**

The basis of the modified BWBN model (Figure 42) is the mass-normalised equation of motion for a single degree of freedom system consisting of a mass connected in parallel to a nonlinear hysteretic spring, a linear spring, and a viscous damper (see Equation 16):

$$\ddot{u}(t) + 2 \cdot \xi_0 \cdot \omega \cdot \dot{u}(t) + \alpha \cdot \omega^2 \cdot u(t) + (1-\alpha) \cdot \omega^2 \cdot z(t) = f(t) \qquad [16]$$

where $u$ is relative displacement of the mass to the base; $\xi_0$ is the linear viscous damping ratio, which equals $cm\omega/2$, where $c$ is linear viscous damping coefficient, $m$ is mass, $\omega$ is the pseudo-natural frequency of the nonlinear system, and $\omega^2$ is mass-normalised stiffness; $\alpha$ is a rigidity ratio that determines the ratio of the final asymptote tangent stiffness to the initial stiffness; $f(t) = F(t)/m$, where $F(t)$ is the force applied to the mass; and $z(t)$ is hysteretic displacement, expressed with the differential equation shown in Equation 17:

$$\dot{z}(t) = \frac{\dot{u}(t) - v\left(\beta \cdot |\dot{u}(t)| \cdot |z(t)|^{n-1} \cdot z(t) + \gamma \cdot \dot{u}(t) \cdot |z(t)|^{n}\right)}{\eta} h(z) \qquad [17]$$

where $\beta$ and $\gamma$ act as a couple and determine whether the curve is hardening or softening; $n$ is a parameter which determines the sharpness of the transition from the initial slope to the slope of the asymptote; $\eta$ and $v$ are the linearly energy-based stiffness and strength degradation parameters, respectively; and $h(z)$ is the pinching function given in Equation 18:

$$\boldsymbol{h(z) = 1 - \xi_1 \cdot e^{\left\{-[z \cdot sgn(\dot{u}(t)) - q \cdot z_u]^2 / \xi_2^2\right\}}} \quad [18]$$

where $sgn$ is the signum function; $\xi_1$ and $\xi_2$ control the pinching stiffness and pinching range, respectively; and $q$ controls the residual force. This model can therefore represent a wide variety of hardening or softening hysteresis loops with a considerable range of cyclic energy dissipation. It includes the system degradation (stiffness and/or strength) as a function of the hysteretic energy dissipation and pinching.

This modified BWBN model of the hysteretic behaviour of timber connections and structures is governed by 13 different identifiable parameters in Eqs. (16) to (18) (Chen et al., 2014; Xu and Dolan, 2009a, b). It calibrates the BWBN parameters by using the response to a particular cyclic displacement history, and then evaluates the responses for other histories or seismic excitations. Identifying the Bouc–Wen model parameters involves proposing a signal input (or several) and an identification algorithm that uses the measured output of the model along with this input to determine the unknown model parameters. This question has stirred a lot of research due to its difficulty as a nonlinear and nondifferentiable problem. Some proposed identification methods involve a rigorous analysis of the convergence of the parameters to their true values, while others rely on numerical simulations and experimentation. Available options (Ismail et al., 2009) include (a) Least-squares identification; (b) Kalman filter identification; (c) Genetic algorithm identification; (d) Gauss-Newton iterative Identification; (e) Bootstrap filter identification; (f) Identification using periodic signals; (f) Simplex method identification; (g) Support vector regression identification; and (h) Constrained nonlinear optimization identification.

To simulate the highly asymmetric hysteresis of specific timber connections, e.g., hold-downs, Aloisio et al. (2020) developed an extended energy-dependent generalised Bouc–Wen model (Song & Kiureghian, 2006) by adding two energy-based parameters. Structural analysis software like SAP2000 and OpenSees implements the Bouc–Wen, Baber–Noori–Wen, and BWBN models, in a simplified form, to predict the nonlinear responses of spring elements (Mazzoni et al., 2006). They have also been incorporated into the general-purpose FEsoftware ABAQUS through subroutines (Xu & Dolan, 2009a, 2009b), and also into MATLAB (Aloisio et al., 2021).

**Model Comparison**

Although each has its own features, most models of the same type share similar advantages and limitations. Table 2 compares the three major types of hysteretic models for timber structures, discussed in the preceding pages of this section and summarised below.

Table 2. Comparison of three major types of hysteretic models and their use

| Item | Mechanics-based model | Empirical model | Mathematical model |
|---|---|---|---|
| Input/parameter acquisition | Engineering material properties | Curve fitting | Curve fitting |
| Challenging part | Solution of a nonlinear problem at each time step | Parameter acquisition | Parameter acquisition |
| Pushover analysis | Yes | Yes | No |
| Cyclic analysis | Yes | Yes | Yes |
| Dynamic analysis | Yes | Yes | Yes |
| Protocol dependency | No | Yes | Yes |
| Loading rate sensitivity | No | No | Yes |

**Mechanics-based models** rely on the basic material properties of the fastener and the embedment characteristics of the surrounding wood medium. They provide fair fitting accuracy for the hysteresis loops of timber connections and structures. Instead of calibration parameters, to which it may sometimes be difficult to assign a physical meaning, this approach uses constraints with which engineers are more familiar: moduli of elasticity, yield stress, etc. Such models automatically adapt to any input history, whether force or displacement, and develop pinching loops as the gaps form, which makes the models protocol independent. The more general procedure used in mechanics-based models is more computationally intensive than the fitted tools in other models, since it requires the solution of a nonlinear problem at each time step.

**Empirical models** provide good fitting accuracy for the hysteresis loops of timber connections and structures, but do not rely on mechanical properties. Although they do depend on physical parameters, e.g., displacements, forces, and stiffnesses, the model parameters must derive from calibration to existing test results, that is hysteresis loops. This implies that most models can only be used in specified cases where the hysteretic behaviour of timber connections and/or structures is known. It is also uncertain whether the fitted set of parameters properly represents loops for histories other than the one used in the calibration, given that this loop represents a specific structural response to a corresponding loading history.

**Mathematical models** provide good fitting accuracy for the hysteresis loops of timber connections and structures, but do not directly rely on mechanical properties and physical parameters. The model parameters must be calibrated to the test results, that is force and displacement history. Although the computation time is very short, the process of calibrating the parameters may be lengthy. If the experimental displacements do not provide sufficient information, such as pinching or stiffness degradation, the parameters controlling them may not be properly calibrated.

#### 7.1.4.2.4 Backbone Curves

For nonlinear static analysis (pushover), the structure is subjected to gravity loads with monotonically increasing lateral loading until reaching the model's maximum capacity to deform. This requires a backbone curve accounting for the elastic and plastic behaviour of nailed connections or shear walls, as well as residual strength and displacement.

The nonlinear analysis provisions of ASCE 41 (ASCE, 2017) involve modelling light wood-frame shear walls that incorporate certain nonlinear force-deformation characteristics. The generalised ASCE 41 backbone curve accounts for strength degradation and residual strength and is defined in terms of elastic and plastic regions.

Figure 43 provides a schematic representation of this curve, for which Point B is the yield drift ($\Delta_y$) point, Point C is the onset of strength degradation, and Point E is the maximum deformation point. For deformation levels larger than drifts corresponding to Point E, the shear wall strength is assumed to be zero. Parameter *c*, identified in the plot of Figure 43, refers to the residual strength of the system, parameter *d* represents the ultimate drift ($\Delta_u$) until the onset of strength degradation (Point C), and parameter *e* refers to the maximum drift up to failure of the shear wall at Point E. The ASCE 41 documentation provides values for the parameters *c*, *d*, and *e* for different sheathing combinations of shear walls. The parameters that construct the ASCE curve (e.g., $\Delta_y$, $\Delta_u$, *c*, *d*, and *e*) are based on the judgment of engineers and researchers involved in the development of this standard. A recent extensive study of short-period buildings focused on the effects of the residual strength of light wood-frame shear walls on the collapse performance of a wide range of light wood-frame archetypes (FEMA, 2020). The characterisation of these parameters is extremely important if modelling the performance of walls or buildings past the peak resistance. Currently, there is little data for the wall testing of high displacements due to restrictions on the stroke length of most laboratory actuators. More data is becoming available as laboratories add longer stroke actuators to their testing equipment.

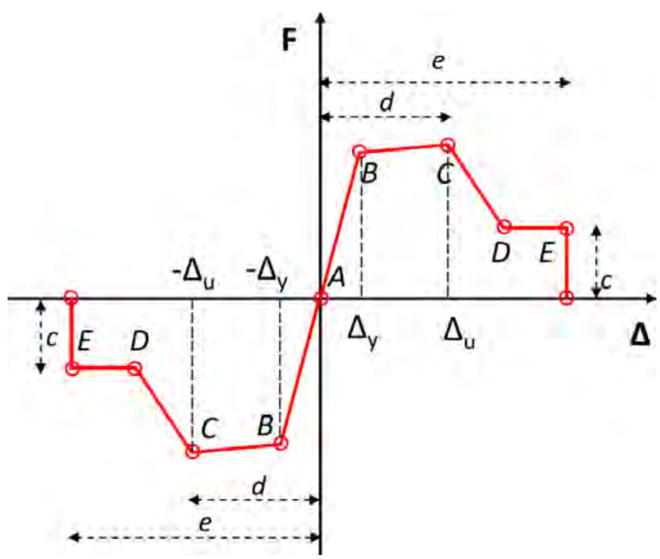


**Figure 43. Generalised force-deformation relation per ASCE 41 for light-frame wood systems (Koliou et al., 2018)**

Koliou et al. (2018) proposed an envelope curve to model light wood-frame shear walls by connecting the parameters of the generalised force-deformation relationship to those of the hysteretic model used in the CUREE-Caltech Woodframe project (Fischer et al., 2001). Figure 44. Schematically shows the shape of the proposed envelope backbone curve from cyclic data. The parameters that define the shape of this curve are well aligned with a few of the parameters of the hysteretic model ($F_o$, $k_o$, $r_1$, $r_2$, and $\delta_u$) (see Section 7.1.4.2.3). Koliou et al. (2018) identified the parameters of the proposed backbone curves for shear walls with different material combinations.

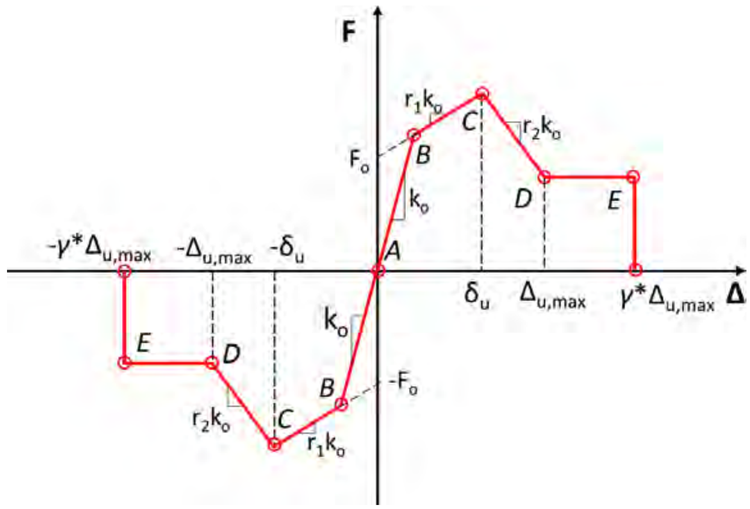


**Figure 44. Monotonic backbone curve envelope for modelling light wood-frame shear walls, proposed by Koliou et al. (2018)**

An important aspect of the proposed envelope curve is that it includes residual strength and displacements for the wood-frame shear walls as a factor of the ultimate displacement ($\Delta_{u,max}$). The inclusion of residual strength and displacements in the range of 6–7% ($\gamma\Delta_{u,max}$) drift for WSPs is based on a number of reversed cyclic tests and shake-table testing that demonstrated that these drift levels are achievable even without considering bearing and building system-level effects (considering the building as a system rather than focusing on a component, e.g., wall response) (Pei et al., 2013). Taking into account building effects, drifts can easily exceed 10% (van de Lindt et al., 2016). WSPs ideally require a $\gamma$ factor of 1.4–1.5; while for other panels, a $\gamma$ factor of 1.2–1.5 will suffice.

### *7.1.4.3 Practical FE Methods*

The structural linear analysis of light wood-frame buildings usually adopts practical FE Methods. Two typical examples are a wall model comprising a stick element and a rotational spring and a wall model consisting of a beam element. Such models are usually adopted for linear dynamic analysis.

#### 7.1.4.3.1 Stick and Rotational Spring Model

Carradine (2019) introduced a model comprising stick elements and rotational springs, as illustrated in Figure 45. The stick elements have an effective flexural stiffness to account for chord shortening and elongation (due to the bending of the wall) and an effective shear stiffness to account for panel stiffness and fastener slip. Rotational springs at the base of each wall represent the stiffness of the anchorage system. The principal of equivalence can help determine the equivalent flexural stiffness, effective shear stiffness, and rotational wall stiffness (Carradine, 2019) based on the corresponding deformations, estimated using the analytical models discussed in Section 7.1.3.

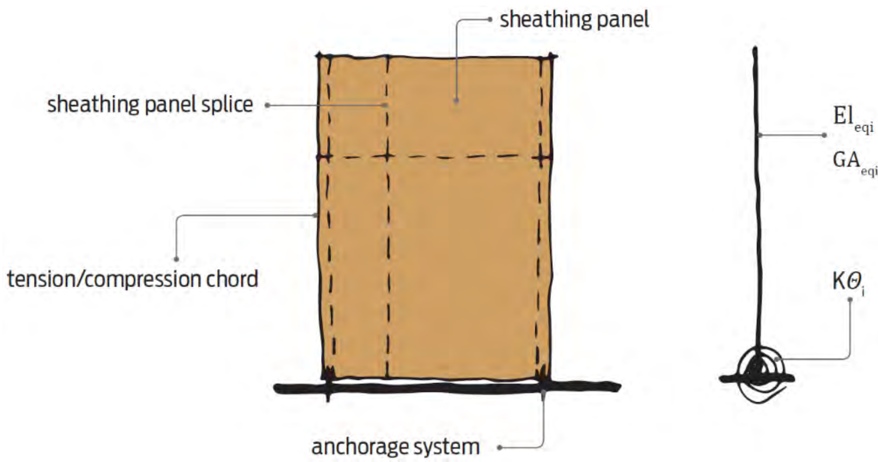


**Figure 45. Spring and stick representation of a light wood-frame shear wall (Carradine, 2019)**

#### 7.1.4.3.2 Equivalent Beam Model

The equivalent beam model (Newfield et al., 2013b, 2014; Ni & Popovski, 2015) is simpler than the stick and rotational spring model because it removes the rotational spring at the bottom (Figure 45). The model has an effective flexural stiffness to account for chord shortening and elongation (due to the bending of the wall), bearing compression in wood plates, and anchorage slip, as well as an effective shear stiffness to account for panel stiffness and fastener slip. Compared with the stick and spring model, the equivalent beam model accounts for the bending compression in wood plates and anchorage slip in the effective flexural stiffness. The principle of equivalence can help determine the effective flexural stiffness and effective shear stiffness (Newfield et al., 2013b, 2014; Ni & Popovski, 2015) based on the corresponding deformations, estimated using the analytical models discussed in Section 7.1.3.

## 7.1.5 Summary

Light wood-frame buildings are the most common timber structures. This chapter discusses their behaviour and mechanisms at the system level (entire structures) and assembly level (shear walls). It summarises analytical models, both elastic and plastic, along with methods for calculating the sheathing buckling and lateral deflection. It provides advanced and practical FE modelling with corresponding recommendations and considerations. The information presented in this chapter is intended to help practising engineers and researchers become better acquainted with the modelling of light wood-frame buildings.

The hysteretic models and backbone curve models discussed in this chapter can be of use in different types of timber connections discussed in Chapter 5 and in timber structures discussed in Chapters 7.2 to 7.5.

## 7.1.6 References

Åkerlund, S. (1984). A simple calculation model for sheathed wood-framed shear walls. *Bygg Teknik, 1*:45–48.

Aloisio, A., Alaggio, R., & Fragiacomo, M. (2021). Equivalent viscous damping of cross-laminated timber structural archetypes. *Journal of Structural Engineering, 147*(4), 04021012. https://doi.org/10.1061/(ASCE)ST.1943-541X.0002947

Aloisio, A., Alaggio, R., & Fragiacomo, M. (2020). Extension of generalized Bouc–Wen hysteresis modeling of wood joints and structural systems. *Journal of Engineering Mechanics, 146*(3), 04020001 . https://doi.org/10.1061/(ASCE)EM.1943-7889.0001722

American Society of Civil Engineers (ASCE). (2016). *Minimum design loads and associated criteria for buildings and other structures*.

American Society of Civil Engineers (ASCE). (2017). *Seismic evaluation and retrofit of existing buildings (ASCE/SEI, 41-17)*.

American Wood Council (AWC). (2018). *National design specification for wood construction*.

APA – The Engineered Wood Association. (2001). *Wood structural panel shear wall and diaphragm - Allowable stress design manual for engineered wood construction*.

Applied Technology Council (ATC). (1981). *Guidelines for the design of horizontal wood diaphragms* (ATC-07).

Ayoub, A. (2007). Seismic analysis of wood building structures. *Engineering Structures, 29*(2), 213–223. https://doi.org/10.1016/j.engstruct.2006.04.011

Bouc, R. (1967). *Force vibration of mechanical systems with hysteresis* [Conference presentation]. 4th Conf. on Nonlinear Oscillation, Prague, Czechoslovakia.

Building Seismic Safety Council (BSSC). (2006). *Homebuilders' guide to earthquake resistance design and construction – FEMA P-232*. Report prepared for the Federal Emergency Management Agency (FEMA) of the United States Department of Homeland Security. National Institute of Building Sciences, Washington, D.C.

Burgess, H. J. (1976). *Derivation of the wall racking formulae in TRADA's design guide for timber frame housing* (Research Report E/RR/36). Timber Research and Development Association (TRADA).

Carradine, D. M. (2019). *Multi-storey light timber-framed buildings in New Zealand - Engineering design*. Building Research Association of New Zealand (BRANZ).

Ceccotti, A., & Vignoli, A. (1990). Engineered timber structures: An evaluation of their seismic behaviour. In H. Sugiyama (ed)., *Proceedings of the International Timber Engineering Conference, Tokyo, Japan* (pp. 946–953).

Chen, Z., Chui, Y.-H., Doudak, G., & Nott, A. (2016). Contribution of type-X gypsum wall board to the racking performance of light-frame wood shear walls. *Journal of Structural Engineering, 142*(5), 04016008. https://doi.org/10.1061/(ASCE)ST.1943-541X.0001468

Chen, Z., Chui, Y. H., Mohammad, M., Doudak, G., & Ni, C. (2014). *Load distribution in lateral load resisting elements of timber structures* [Conference presentation]. World Conference on Timber Engineering, Québec City, Québec, Canada.

Chen, Z., Chui, Y. H., Ni, C., Doudak, G., & Mohammad, M. (2014a). Load distribution in timber structures consisting of multiple lateral load resisting elements with different stiffnesses. *Journal of Performance of Constructed Facilities, 28*(6), A4014011. https://doi.org/10.1061/(ASCE)CF.1943-5509.0000587

Chen, Z., Chui, Y. H., Ni, C., Doudak, G., & Mohammad, M. (2014b). Simulation of the lateral drift of multi-storey light wood frame buildings based on a modified macro-element model. In A. Salenikovich (Ed.), *World Conference on Timber Engineering (WCTE 2014)*.

Chen, Z., Chui, Y. H., Ni, C., & Xu, J. (2014). Seismic response of midrise wood light-frame buildings with portal frames. *Journal of Structural Engineering, 140*(8), A4013003. https://doi.org/10.1061/(ASCE)ST.1943-541X.0000882

Chen, Z., & Ni, C. (2017). *Seismic response of mid-rise wood-frame buildings on podium*. FPInnovations.

Chen, Z., & Ni, C. (2020). Criterion for applying two-step analysis procedure to seismic design of wood-frame buildings on concrete podium. *Journal of Structural Engineering, 146*(1), 04019178. https://doi.org/10.1061/(ASCE)ST.1943-541X.0002405

Chen, Z., & Ni, C. (2021). Seismic force-modification factors for mid-rise wood-frame buildings with shearwalls using wood screws. *Bulletin of Earthquake Engineering, 19*, 1337–1364. https://doi.org/10.1007/s10518-020-01031-7

Chen, Z., Ni, C., Karacabeyli, E., Yeh, B., & Line, P. (2020). *Expanding wood use towards 2025: Seismic performance of midply shear walls*. FPInnovations.

Christovasilis, I., & Filiatrault, A. (2010). A two-dimensional numerical model for the seismic collapse assessment of light-frame wood structures. In S. Senapathi, K. Casey, & M. Hoit (eds.), *Structures Congress 2010* (pp. 832–843).

Chui, Y. H., Ni, C., & Jiang, L. (1998). Finite-element model for nailed wood joints under reversed cyclic load. *Journal of Structural Engineering, 124*(1), 96–103. https://doi.org/10.1061/(ASCE)0733-9445(1998)124:1(96)

Collins, M., Kasal, B., Paevere, P., & Foliente, G. C. (2005). Three-dimensional model of light frame wood buildings. I: Model description. *Journal of Structural Engineering, 131*(4), 676–683. https://doi.org/10.1061/(ASCE)0733-9445(2005)131:4(676)

Canadian Standards Association (CSA). (2019). *Engineering Design in Wood*. (CSA O86:19).

Dassault Systèmes. (2016). *Abaqus analysis user's manual*.

Deierlein, G., & Kanvinde, A. (2003). *Woodframe project report W-23*: *Seismic performance of gypsum walls - Analytical investigation*. Consortium of Universities for Research in Earthquake Engineering (CUREE).

Dekker, J., Kuipers, J., & Ploos van Amstel, H. (1978). Buckling strength of plywood, results of tests and design recommendations. *HERON, 23*(4), 5–59.

Di Gangi, G., Demartino, C., Quaranta, G., Vailati, M., & Liotta, M. A. (2018). Timber shear walls: Numerical assessment of the equivalent viscous damping. In G. R. Liu & P. Trovalusci (Ed.), *Proceedings of the International Conference on Computation Methods, vol. 5, 2018* (pp. 929–938).

Dolan, J. D. (1989). *The dynamic response of timber shear walls.* [Doctoral dissertation, University of British Columbia]. UBC Theses and Dissertations. https://dx.doi.org/10.14288/1.0062552

Easley, J. T., Foomani, M., & Dodds, R. H. (1982). Formulas for wood shear walls. *Journal of the Structural Division, 108*(11), 2460–2478. https://doi.org/10.1061/JSDEAG.0006075

European Committee for Standardization (CEN). (2004). *Eurocode 5: Design of timber structures – Part 1-2: General rules – structural fire design*. (Eurocode Standard EN 1995-1-2).

European Committee for Standardization (CEN). (2018). *Eurocode 5: Design of timber structures - Part 1-1: General - Common rules and rules for buildings.* (Eurocode Standard EN 1995-1-1)

Federal Emergency Management Agency (FEMA). (2006). *Homebuilders' guide to earthquake-resistant design and construction*. FEMA 232. https://nehrpsearch.nist.gov/static/files/FEMA/PB2007111287.pdf

Federal Emergency Management Agency (FEMA). (2012). *Seismic evaluation and retrofit of multi-unit wood-frame buildings with weak first stories*. FEMA P-807. https://store.atcouncil.org/index.php?dispatch=products.view&product_id=241

Federal Emergency Management Agency (FEMA) (2020). *Short-period building collapse performance and recommendations for improving seismic design: Volume 2 - Study of one-to-four story wood light-frame buildings*. FEMA P-2139-2. https://atcouncil.org/docman/fema/293-fema-p-2139-2-wood/file

Filiatrault, A., Isoda, H., & Folz, B. (2003). Hysteretic damping of wood framed buildings. *Engineering Structures, 25*(4), 461–471. https://doi.org/10.1016/S0141-0296(02)00187-6

Fischer, D., Filiatrault, A., Folz, B., Uang, C.-M., & Seible, F. (2001). *CUREE woodframe project report W-06: Shake table tests of a two-story woodframe house*. Consortium of Universities for Research in Earthquake Engineering (CUREE).

Foliente, G. C. (1993). *Stochastic dynamic response of wood structural systems* [Doctoral dissertation, Virginia Polytechnic Institute and State University]. VTechWorks. http://hdl.handle.net/10919/27532

Foliente, G. C. (1995). Hysteresis modeling of wood joints and structural systems. *Journal of Structural Engineering, 121*(6), 1013–1022. https://doi.org/10.1061/(ASCE)0733-9445(1995)121:6(1013)

Folz, B., & Filiatrault, A. (2000). *CASHEW - Version 1.0: A computer program for cyclic analysis of wood shear walls*. University of California, San Diego.

Folz, B., & Filiatrault, A. (2001a). Cyclic analysis of wood shear walls. *Journal of Structural Engineering, 127*(4), 433–441. https://doi.org/10.1061/(ASCE)0733-9445(2001)127:4(433)

Folz, B., & Filiatrault, A. (2001b). *SAWS - Version 1.0: A computer program for the seismic analysis of woodframe structures*. University of California, San Diego.

Folz, B., & Filiatrault, A. (2002a). *A computer program for seismic analysis of woodframe structures*. Consortium of Universities for Research in Earthquake Engineering. (CUREE)

Folz, B., & Filiatrault, A. (2002b). *CASHEW: A computer program for the cyclic analysis of wood shear walls*. Consortium of Universities for Research in Earthquake Engineering (CUREE).

Foschi, R. (2000). Modeling the hysteretic response of mechanical connections for wood structures. In *WCTE 2000: World Conference on Timber Engineering, Whistler Resort, British Columbia, Canada, July 31–August 3, 2000*.

Franco, L., Pozza, L., Saetta, A., Savoia, M., & Talledo, D. (2019). Strategies for structural modelling of CLT panels under cyclic loading conditions. *Engineering Structures, 198*(1), 109476. https://doi.org/10.1016/j.engstruct.2019.109476

Gatto, K., & Uang, C.-M. (2002). *Woodframe project report W-13: Cyclic response of woodframe shearwalls: Loading protocol and rate of loading effects*. Consortium of Universities for Research in Earthquake Engineering (CUREE).

Girhammar, U. A., & Källsner, B. (2008). Analysis of influence of imperfections on stiffness of fully anchored light-frame timber shear walls—elastic model. *Materials and Structures, 42*(3), 321. https://doi.org/10.1617/s11527-008-9458-7

He, M. (2002). *Numerical modeling of three-dimensional light wood-framed buildings* [Doctoral dissertation, University of British Columbia]. UBC Theses and Dissertations. http://hdl.handle.net/2429/13092

Henrici, D. (1984). Zur Bemessung Windaussteifender Hölzerner Wandscheibe [On the design of wind-bracing wooden wall slabs]. *Bauen mit holz, 86*(12), 873–877.

Humbert, J. (2010). *Characterization of the behavior of timber structures with metal fasteners undergoing seismic loadings* [Doctoral dissertation, Grenoble University].

Humbert, J., Boudaud, C., Baroth, J., Hameury, S., & Daudeville, L. (2014). Joints and wood shear walls modelling I: Constitutive law, experimental tests and FE model under quasi-static loading. *Engineering Structures, 65*, 52–61. https://doi.org/10.1016/j.engstruct.2014.01.047

International Code Council (ICC). (2021). The International Building Code (IBC).

Ismail, M., Ikhouane, F., & Rodellar, J. (2009). The hysteresis Bouc–Wen model, a survey. *Archives of Computational Methods in Engineering, 16*(2), 161–188. https://doi.org/10.1007/s11831-009-9031-8

Källsner, B. (1984). *Skivor som vindstabiliserande element vid träregelväggar* [Panels as wind-bracing elements in timber-framed walls]. TräteknikRapport no. 56. TräteknikCentrum.

Källsner, B., & Girhammar, U. A. (2009a). Analysis of fully anchored light-frame timber shear walls—Elastic model. *Materials and Structures, 42*(3), 301–320. https://doi.org/10.1617/s11527-008-9463-x

Källsner, B., & Girhammar, U. A. (2009b). Plastic models for analysis of fully anchored light-frame timber shear walls. *Engineering Structures, 31*(9), 2171–2181. https://doi.org/10.1016/j.engstruct.2009.03.023

Källsner, B., Girhammar, U. A., & Wu, L. (2001). A simplified plastic model for design of partially anchored wood-framed shear walls. In *CIB-W18, Meeting Thirty-Four, Venice, Italy, August 2001*.

Källsner, B., & Lam, F. (1995). Diaphragms and shear walls. *Holzbauwerke nach Eurocode 5 - STEP 3.* Arbeitsgemeinschaft Holz.

Kivell, B. T., Moss, P. J., & Carr, A. J. (1981). Hysteretic modelling of moment-resisting nailed timber joints. *Bulletin of the New Zealand National Society for Earthquake Engineering, 14*(4), 233–245. https://doi.org/10.5459/bnzsee.14.4.233-243

Koliou, M., van de Lindt, J. W., & Hamburger, R. O. (2018). Nonlinear modeling of wood-frame shear wall systems for performance-based earthquake engineering: Recommendations for the ASCE 41 standard. *Journal of Structural Engineering, 144*(8), 04018095. https://doi.org/10.1061/(ASCE)ST.1943-541X.0002083

Krawinkler, H., Parisi, F., Ibarra, L., Ayoub, A., & Medina, R. (2000). *Woodframe project report W-02: Development of a testing protocol for woodframe structures*. Consortium of Universities for Research in Earthquake Engineering (CUREE).

Larsson, G., & Wästlund, G. (1953). *Plywood som konstruktionsmaterial* [Plywood as a structural material]. Statens kommitté för byggnadsforskning, Bulletin 21. Petterson.

Li, M., Foschi, R. O., & Lam, F. (2012). Modeling hysteretic behavior of wood shear walls with a protocol-independent nail connection algorithm. *Journal of Structural Engineering, 138*(1), 99–108. https://doi.org/10.1061/(ASCE)ST.1943-541X.0000438

Lowes, L. N., Mitra, N., & Altoontash, A. (2003). *A beam-column joint model for simulating the earthquake response of reinforced concrete frames* (PEER Report 2003/10). Pacific Earthquake Engineering Center (PEER), University of California, Berkeley.

Ma, F., Zhang , H., Bockstedte, A., Foliente , G. C., & Paevere, P. (2004). Parameter analysis of the differential model of hysteresis. *Journal of Applied Mechanics, 71*(3), 342–349. https://doi.org/10.1115/1.1668082

Mazzoni, S., McKenna, F., Scott, M. H., & Fenves, G. L. (2006). *The open system for earthquake engineering simulation (OpenSEES) user command-language manual*. Pacific Earthquake Engineering Center (PEER), University of California, Berkeley.

McCutcheon, W. J. (1985). Racking deformations in wood shear walls. *Journal of Structural Engineering, 111*(2), 257–269. https://doi.org/10.1061/(ASCE)0733-9445(1985)111:2(257)

McMullin, K. & Merrick, D. (2002). *Woodframe project report W-15: Seismic performance of gypsum walls: Experimental test program*. Consortium of Universities for Research in Earthquake Engineering (CUREE).

Mosalam, K. M., Machado, C., Gliniorz, K.-U., Naito, C., Kunzel, E., & Mahin, S. (2003). *Woodframe project report W-19: Seismic evaluation of an asymmetric three-story woodframe building*. Consortium of Universities for Research in Earthquake Engineering (CUREE).

Neal, B. G. (Ed.) (1978). *Plastic methods of structural analysis* (3rd ed.). Chapman and Hall.

Newfield, G., Ni, C., & Wang, J. (2013a). *Design example: Design of stacked multi-storey wood-based shear walls using a mechanics-based approach*. FPInnovations and Canadian Wood Council.

Newfield, G., Ni, C., & Wang, J. (2013b). *Linear dynamic analysis for wood-based shear walls and podium structures*. FPInnovations and Canadian Wood Council.

Newfield, G., Ni, C., & Wang, J. (2013c). *A mechanics-based approach for determining deflections of stacked multi-storey wood-based shear walls*. FPInnovations and Canadian Wood Council.

Newfield, G., Ni, C., & Wang, J. (2014). Design of wood frame and podium structures using linear dynamic analysis. In, A. Salenikovich (Ed.), *World Conference on Timber Engineering (WCTE 2014)* (pp. 1426–1433).

Ni, C., & Chen, Z. (2021). *Expanding wood use towards 2025: Seismic performance of midply shear wall - Year 2*. FPInnovations.

Ni, C., & Karacabeyli, E. (2000). Effect of overturning restraint on performance of shear walls. In *WCTE 2000: World Conference on Timber Engineering, Whistler Resort, British Columbia, Canada, July 31–August 3, 2000*.

Ni, C., & Karacabeyli, E. (2002). Capacity of shear wall segments without hold-downs. *Wood Design Focus, 12*(2), 10–17.

Ni, C., & Karacabeyli, E. (2005). *Design of shear walls without hold-downs* (CIB-W18/38-15-4). CIB-W18 Meeting Thirty-Eight, Karlsruhe, Germany, August 2005.

Ni, C., & Popovski, M. (2015). *Mid-rise wood-frame construction handbook*. FPInnovations.

Pang, W. (2015). *Timber3D: Dynamic finite element analysis for timber structures*. Clemson University.

Pang, W., & Shirazi, M. (2010). Next generation numerical model for non-linear in-plane analysis of wood-frame shear walls. In *11th World Conference on Timber Engineering 2010 (WCTE 2010)* (pp. 2255–2260).

Pang, W., Ziaei, E., & Filiatrault, A. (2012). *A 3d Model for Collapse Analysis of Soft-Story Light-Frame Wood Buildings.* Proceedings of the World Conference on Timber Engineering, Auckland, New Zealand.

Pang, W. C., Rosowsky, D. V., Pei, S., & van de Lindt, J. W. (2007). Evolutionary parameter hysteretic model for wood shear walls. *Journal of Structural Engineering, 133*(8), 1118–1129. https://doi.org/10.1061/(ASCE)0733-9445(2007)133:8(1118)

Pardoen, G., Waltman, A., Kazanjy, R., Freund, E., & Hamilton, C. (2003). *Woodframe project report W-25: Testing and analysis of one-story and two-story shear walls under cyclic loading*. Consortium of Universities for Research in Earthquake Engineering (CUREE).

Pei, S., van de Lindt, J. W., Wehbe, N., & Liu, H. (2013). Experimental study of collapse limits for wood frame shear walls. *Journal of Structural Engineering, 139*(9), 1489–1497. https://doi.org/10.1061/(ASCE)ST.1943-541X.0000730

Pei, S., & van de Lindt, J. W. (2007). *Seismic analysis package for woodframe structures – Version 1.0, users manual for SAPWood for Windows*. Department of Civil and Environmental Engineering, Colorado State University.

Pei, S., & van de Lindt, J. W. (2008). *SAPWood: Seismic analysis program for woodframe buildings*.

Pei, S., & van de Lindt, J. W. (2010). *SAPWood for Windows, seismic analysis package for woodframe structures*. Colorado State University.

Richard, N., Daudeville, L., Prion, H., & Lam, F. (2002). Timber shear walls with large openings: Experimental and numerical prediction of the structural behaviour. *Canadian Journal of Civil Engineering, 29*, 713–724. https://doi.org/10.1139/L02-050

Rinaldin, G., Amadio, C., & Fragiacomo, M. (2013). A component approach for the hysteretic behaviour of connections in cross-laminated wooden structures. *Earthquake Engineering and Structural Dynamics, 42*(13), 2023–2042. https://doi.org/10.1002/eqe.2310

Rinaldin, G., & Fragiacomo, M. (2016). Non-linear simulation of shaking-table tests on 3- and 7-storey X-Lam timber buildings. *Engineering Structures, 113*, 133–148. https://doi.org/10.1016/j.engstruct.2016.01.055

Salenikovich, A. J. (2000). *The racking performance of light-frame shear walls* [Doctoral dissertation, Virginia Polytechnic and State University]. VTechWorks. http://hdl.handle.net/10919/28963

Serrette, R. L., Encalada, J., Juadines, M., & Nguyen, H. (1997). Static racking behavior of plywood, OSB, gypsum, and FiberBond walls with metal framing. *Journal of Structural Engineering, 123*(8), 1079–1086. https://doi.org/10.1061/(ASCE)0733-9445(1997)123:8(1079)

Song, J., & Der Kiureghian, A. (2006). Generalized Bouc–Wen model for highly asymmetric hysteresis. *Journal of Engineering Mechanics, 132*(6), 610–618. https://doi.org/10.1061/(ASCE)0733-9399(2006)132:6(610)

Standards New Zealand. (1993). *Timber Structures Standard* (NZS 3603).

Steinmetz, D. (1988). Die Aussteifung von Holzhäusern am Beispiel des Holzrahmenbaus [The bracing of wooden houses using the example of timber frame construction]. *Bauen mit holz, 90*(12), 842–851.

Stewart, W. (1987). *The seismic design of plywood sheathed shear walls* [Doctoral dissertation, University of Canterbury]. UC Research Repository. http://hdl.handle.net/10092/2458

Tuomi, R. L., & McCutcheon, W. J. (1978). Racking strength of light-frame nailed walls. *Journal of the Structural Division, 104*(7), 1131–1140. https://doi.org/10.1061/JSDEAG.0004955

van de Lindt, J. W., Bahmani, P., Mochizuki, G., Pryor, S. E., Gershfeld, M., Tian, J., Symans, M.D., & Rammer, D. (2016). Experimental seismic behavior of a full-scale four-story soft-story wood-frame building with retrofits. II: Shake table test results. *Journal of Structural Engineering, 142*(4), E4014004. https://doi.org/10.1061/(ASCE)ST.1943-541X.0001206

Varoglu, E., Karacabeyli, E., Stiemer, S., & Ni, C. (2006). Midply wood shear wall system: Concept and performance in static and cyclic testing. *Journal of Structural Engineering, 132*(9), 1417–1425. https://doi.org/10.1061/(ASCE)0733-9445(2006)132:9(1417)

Varoglu, E., Karacabeyli, E., Stiemer, S., Ni, C., Buitelaar, M., & Lungu, D. (2007). Midply wood shear wall system: Performance in dynamic testing. *Journal of Structural Engineering, 133*(7), 1035–1042. https://doi.org/10.1061/(ASCE)0733-9445(2007)133:7(1035)

von Halász, R., & Cziesielski, E. (1966). Berechnung und Konstruktion geleimter Träger mit Stegen aus Furnierplatten [Calculation and design of glued beams with webs of veneer panels]. *Berichte aus der Bauforschung, 47*.

Wagemann Herrera, M. A. (2021). Effect of diaphragm flexibility and strut axial stiffness on the load distribution in the lateral force resisting system [Master's thesis, Universidad de Concepción]. Repositorio Bibliotecas UdeC. http://repositorio.udec.cl/jspui/handle/11594/6534

Wen, Y.-K. (1976). Method for random vibration of hysteretic systems. *Journal of the Engineering Mechanics Division 102*(2), 249–263. https://doi.org/10.1061/JMCEA3.0002106

Xu, J., & Dolan, J. D. (2009a). Development of a wood-frame shear wall model in ABAQUS. *Journal of Structural Engineering, 135*(8), 977–984. https://doi.org/10.1061/(ASCE)ST.1943-541X.0000031

Xu, J., & Dolan, J. D. (2009b). Development of nailed wood joint element in ABAQUS. *Journal of Structural Engineering, 135*(8), 968–976. https://doi.org/10.1061/(ASCE)ST.1943-541X.0000030

Yasumura, M., Kamada, T., Imura, Y., Uesugi, M., & Daudeville, L. (2006). Pseudodynamic tests and earthquake response analysis of timber structures II: Two-level conventional wooden structures with plywood sheathed shear walls. *Journal of Wood Science, 52*(1), 69–74. https://doi.org/10.1007/s10086-005-0729-4

Zhu, E., Chen, Z., Chen, Y., & Yan, X. (2010). Testing and FE modelling of lateral resistance of shearwalls in light wood frame structures. *Journal of Harbin Institute of Technology, 42*(10), 1548–1554.

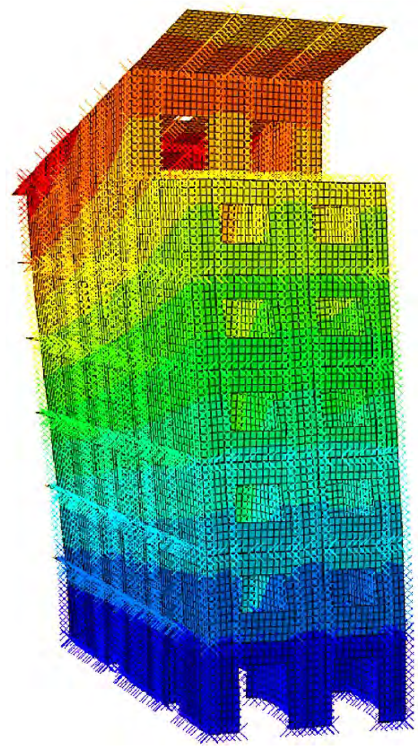

Image courtesy of Rinaldin & Fragiacomo (2016)

# CHAPTER 7.2

## Mass timber structures

**Authors**
Zhiyong Chen
Marjan Popovski
Robert Jackson
Lucas Epp
Dlubal Software

**Reviewers**
Scott Breneman
Maurizio Follesa
Nicholas Sills
Jean-Philippe Carrier

# TABLE OF CONTENTS

## 7.2.1 Introduction

Global interest in using engineered wood products in residential and commercial buildings has increased due to their 'green' credentials and high strength-to-weight ratio. Mass timber (MT) products (Appendix A), e.g.,

- Cross-laminated timber (CLT)
- Dowel-laminated timber (DLT)
- Glued laminated timber (glulam or GLT)
- Laminated strand lumber (LSL)
- Laminated veneer lumber (LVL)
- Mass plywood panels (MPP)
- Nail-laminated timber (NLT)
- Parallel strand lumber (PSL)

provide options for creative and cost-efficient structural systems as alternatives to concrete and steel construction. While post and beam timber frame buildings have been around for centuries, new mass timber products have begun to change how we build with timber. Practising engineers, however, are not always familiar with the structural performance and use of models for analysing mass timber structural systems, leaving these efficient systems out of the market space. This chapter introduces the promising structural systems built from MT products, as well as the corresponding analytical and numerical models that assist in their analysis and design, to provide technical information to convince engineers to adopt them.

## 7.2.2 Gravity Load-Resisting Systems

Mass timber can involve many potential gravity load-resisting systems, the most common of which are the following:

- Timber post and beam frames
- Hybrid post and beam frames
- Wall systems

The following sections identify key modelling considerations for these gravity systems, while additional commentary on the progressive collapse of gravity systems appears in Chapter 8.

### *7.2.2.1 Compounding Deflections*

Compounding deflections can be a critical issue in longer-span timber post and beam frame systems. A typical gravity load-resisting frame consists of a girder, purlin, and deck system, with the final deflection at the midspan of the grid bay compounding the respective deflections of the girder, the purlins, and the deck itself.

Standard component-by-component design in software that treats each component separately, like WoodWorks Sizer (CWC, 2020), usually ignores this phenomenon. A 3D model with appropriate panel splices, panel hinges, and beam-end hinges, as shown in Figure 1 below, is highly recommended to fully understand compounding deflections. This will often control the final sizing of the members, given specific performance criteria.

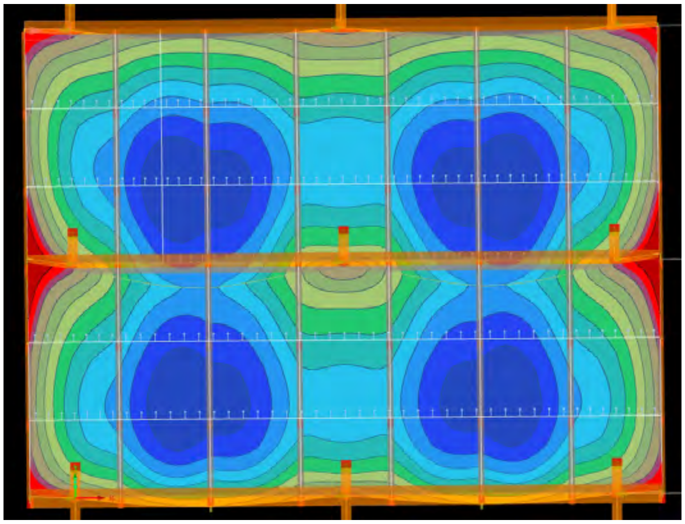

**Figure 1. Out-of-plane deflection in an MT floor showing compounding deflections (Red and blue indicate minimum and maximum deflection, respectively, while other colours represent transition zones)**

### *7.2.2.2 Multispan Panel Load Amplification*

Most MT floor and roof panels are between 20 ft. (6.1 m) and 60 ft. (18.3 m) long. Such long panels reduce the need for connections and allow their use in multispan applications. This is highly desirable, improving overall deflection and vibration performance, sometimes reducing bending moments, and providing better overall redundancy. However, simple engineering mechanics mean that multispan panels also increase the loading on central supporting members such as purlins or walls, as shown in Figure 2 below. This is often lost or ignored in simple component-based software that determine the size of the members based on tributary width alone. This issue can also become pronounced because panel ends are often staggered, creating multiple reaction loads on supporting elements across their lengths.

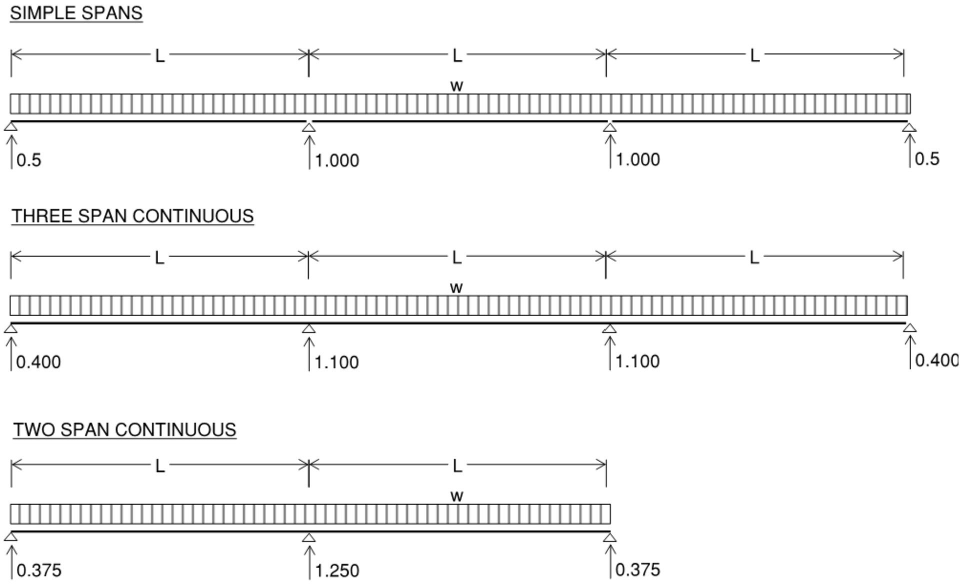


**Figure 2. Multispan panel load amplification (Reaction Forces for Decks)**

As with the compounding deflection issue described above, models for even simple gravity systems should consider seams and staggered panel layouts. Such models can help engineers properly understand the intensity of the bending moments and shear forces in a system. As seen in Figure 2, some common conditions can result in middle purlins having a 25% higher load than that calculated using a simplified component-based analysis.

### *7.2.2.3 Human-Induced Vibrations*

Human-induced vibrations are often a controlling factor in mass timber floor designs and are best understood through detailed modelling. More on this can be found in Chapter 6 of this guide, as well as the US Mass Timber Vibration Design Guide (WoodWorks – Wood Products Council, 2021).

Basic dynamic modelling often ignores the conventional screwed connection between mass timber decks and supporting members. However, accounting for it can slightly increase overall stiffness by creating a series of 'T' beams, which engages the panel as a compression flange. This is particularly suitable for CLT, as support is possible from both purlins and girders either parallel or perpendicular to the deck span. To appropriately capture this stiffness, one should set the member eccentricities as shown in Figure 3 below, so members sit directly below mass timber panel surfaces. When eccentricities are paired with line springs quantifying the stiffness of the screwed connections, overall system stiffness and vibration performance can increase.

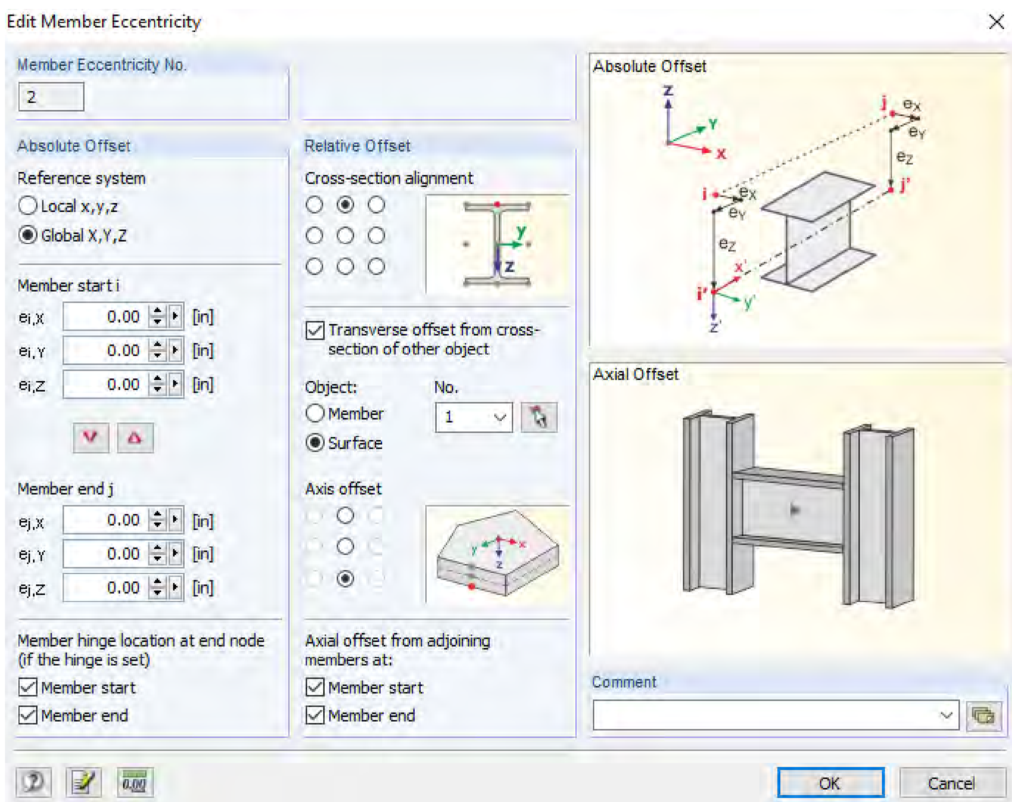


**Figure 3. Member eccentricity in Dlubal RFEM**

### *7.2.2.4 End Conditions and Connections*

When modelling gravity systems, appropriate hinges or end releases are one of the simplest but perhaps the most important consideration. For most timber-to-timber connections, one should idealise them within a model setting as pins. When it comes to the specific design of the connection, one must carefully consider eccentricities from the shear load to the member shear centre. Chapter 5 further discusses modelling considerations for connections.

### *7.2.2.5 Support Conditions*

In a model setting, most beam, purlin, and column support conditions can be idealised as simple 'nodal supports', and most panel support conditions as simple 'line supports'. However, 'surface supports' should sometimes be utilised for the latter, particularly in point-supported CLT systems, to avoid singularities at nodal supports. Dividing the panel surface at the location of the support and adding a 'surface support' to the panel, with a spring stiffness equal to the stiffness of the member below (the bending stiffness of a steel plate, for example), as shown in Figure 4, can drastically impact the concentrated force distribution around these support points. Finite Element Mesh Refinement zones are also highly recommended in instances like this, where panel stresses are concentrated in a tight region.

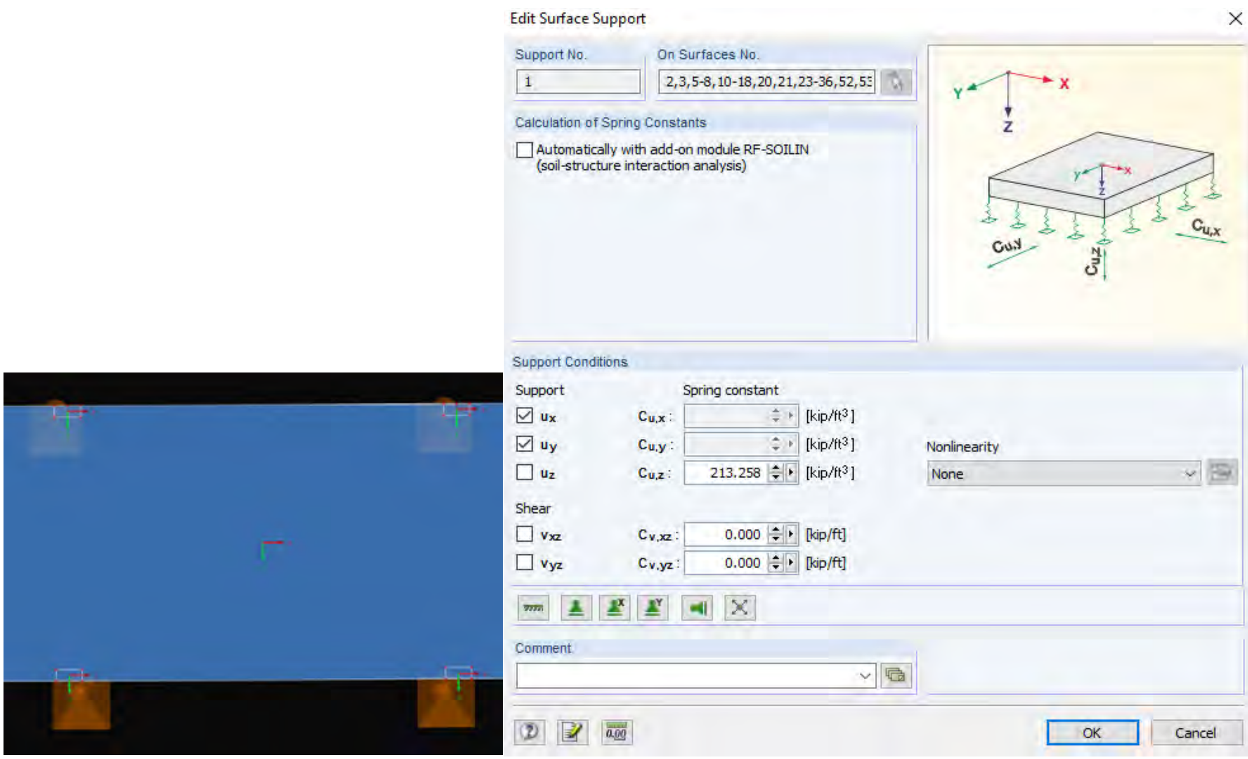


**Figure 4. Spring surface supports in point-supported CLT panels**

## 7.2.3 Lateral Load-Resisting Systems

Most modern mass timber buildings are hybrid in nature. Very often, a mass timber gravity system is paired with a lateral system of cast-in-place reinforced concrete shear walls or steel braced frames. However, several 'pure' mass timber lateral load-resisting systems exist:

- Platform-type shear walls
- Balloon-type shear walls
- Braced frames
- Moment frames

The following sections offer some key modelling recommendations for these systems.

### *7.2.3.1 Platform-Type Shear Walls*

#### 7.2.3.1.1 Structural Behaviour and Mechanisms

MT structures are typically built using a platform-type approach, with the floor at each storey used as a base for erecting the MT walls of the storey above, as illustrated in Figure 5. The height of the MT walls is therefore equal to the storey height. At each storey, gravity loads are transferred through MT floor panels. Because gravity loads are cumulative, the maximum building height usually depends on the perpendicular-to-grain compression resistance of the MT floor panels at the lowest storey. Otherwise, there must be specific solutions to efficiently transfer gravity loads between wall panels in adjacent storeys. Figure 6 shows a typical storey of a multistorey platform-type CLT building.

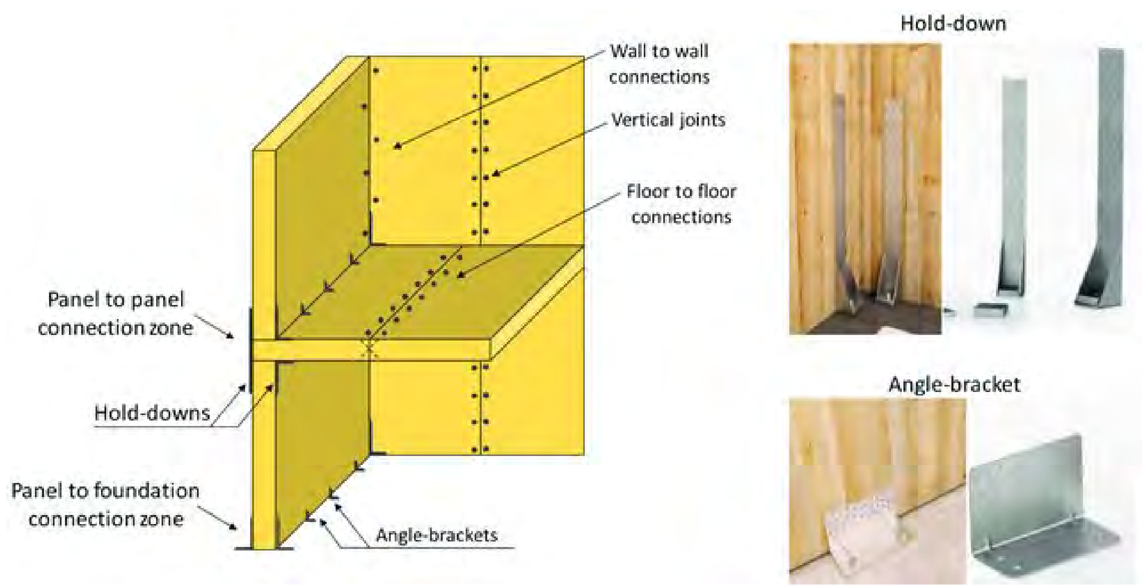


**Figure 5. Platform-type system with typical connections (Sandoli et al., 2021)**

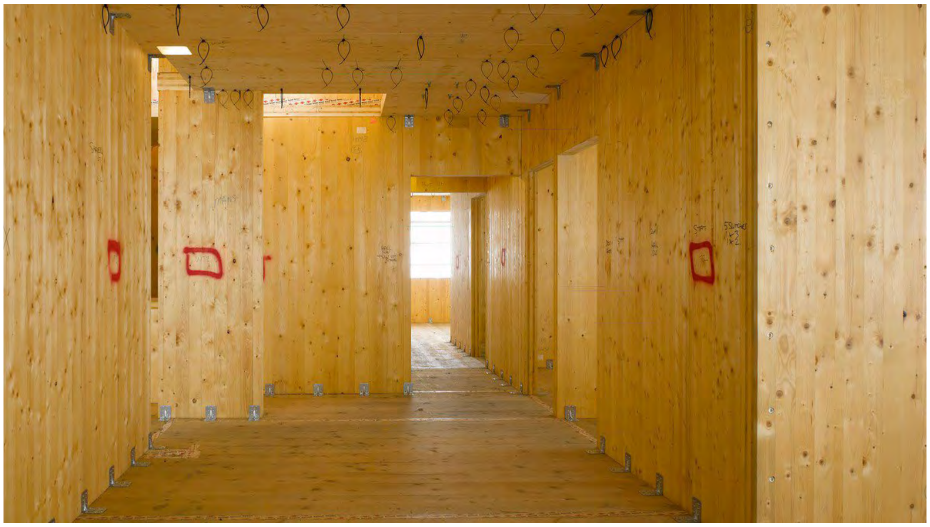

**Figure 6. CLT shear walls with floors in Murray Grove (Photo: Will Pryce. Courtesy of Waugh Thistleton Architects)**

As illustrated in Figure 5, the MT walls connect to the foundation or MT floors using metal brackets, which act mostly as shear connectors, and hold-downs. Both connectors typically use fasteners such as nails or screws. The uplift forces induced by the overturning moments are mostly resisted by the hold-downs. Typical shear connectors also provide some uplift resistance, although not all models account for their contribution. With special designs, like the one shown in Figure 7, the shear connectors can resist only pure shear forces, thus avoiding shear-uplift interaction. Vertical joints (Figure 5) or splines with fasteners usually connect panels together to form a longer shear wall.

**Figure 7. Shear connector with ovalised holes to resist only pure shear forces (Hashemi et al., 2018)**

To quantify the performance of platform-type MT shear walls, FPInnovations has conducted a series of monotonic and cyclic tests of CLT walls with various configurations and connection details (Popovski et al., 2010), as have other research institutions (Gavric et al., 2015; van de Lindt et al., 2020; Vassallo et al., 2018).

As illustrated in Figure 8, the lateral load-carrying capacity and deflection of CLT shear walls depend on (a) the rigid rocking of the panel over the corners, along with the partial crushing of the timber in compression and the extension of the hold-down in tension, (b) the slip of the wall relative to the foundation due to the shear flexibility of the hold-downs and shear stiffness of the bracket connectors, (c) the shear deformation of the panel, (d) the bending deformation of the panel, and (e) the slip in the vertical joints between panels. The shear and bending deformations of the panel are generally negligible, except in walls with openings. Since the connection deformation provides the greatest contribution to shear wall deflection, stiffer connections lead to better wind-induced response on the part of the MT shear wall system (Chen & Chui, 2017; Chen et al., 2015). Note that without specific solutions to efficiently transfer gravity loads between wall panels in adjacent storeys, MT floor panels would reduce the lateral deformation of the storeys due to compression perpendicular-to-grain.

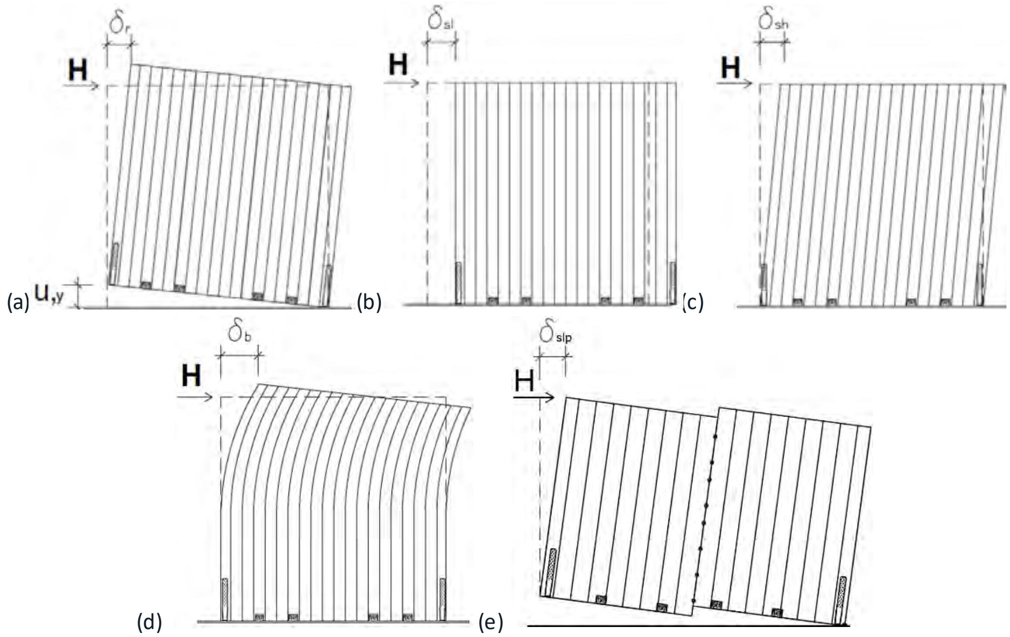

**Figure 8. Deflection components of platform-type CLT walls (Gavric et al., 2015): (a) rocking; (b) sliding; (c) shear; (d) bending; and (e) slip**

For coupled-panel CLT shear walls, there are three possible types of kinematic behaviour: (a) coupled-wall behaviour, when each wall panel (segment) rocks about its lower corner as an independent, individual panel; (b) single-coupled wall behaviour, when the wall panels behave as partly fixed panels with semirigid connections between them; and (c) single wall behaviour, when the wall panels behave as a single wall with rigid connections between them. In the first case, the vertical joint between wall panels is less stiff than the anchoring connections, thus allowing the necessary slip between individual wall panels. When loaded with lateral forces, connected panels behave like individual panels, rocking about each individual lower corner (Figure 9[a]). The second possibility is an intermediate or combined behaviour: as vertical connections between coupled-wall panels are semirigid, small deformations (slip) of the vertical connection are possible (Figure 9[b]). Conversely, if the vertical connection between coupled-wall panels is very stiff, the coupled walls behave virtually the same as a single, monolithic wall panel (Figure 9[c]).

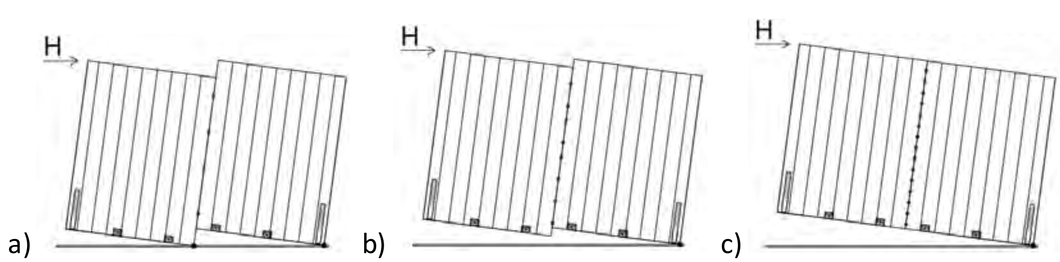

**Figure 9. Types of behaviour for adjacent wall panels (Gavric et al., 2015): (a) coupled-panel behaviour; (b) combined single–coupled panel behaviour; and (c) single-panel behaviour**

Figure 10 shows potential failure modes of CLT shear walls, which include brittle failure, like cracking at an opening; CLT block-shear failure; bracket fracture; and ductile yielding, i.e., fastener yielding and wood crushing in hold-downs and shear connectors. MT shear walls under seismic loads should use the capacity design approach, where panels and the nondissipative parts of connections are capacity protected (Follesa et al., 2018), while the energy dissipative parts of the connections should yield and dissipate energy. The resistance and energy dissipation capacity of the MT shear walls will then be governed by the energy dissipative connections, i.e., hold-downs, shear connectors, and vertical joints (if present). Therefore, connections with high resistance and a large ductility and/or decent energy dissipation capacity can improve the seismic response of an MT shear wall system.

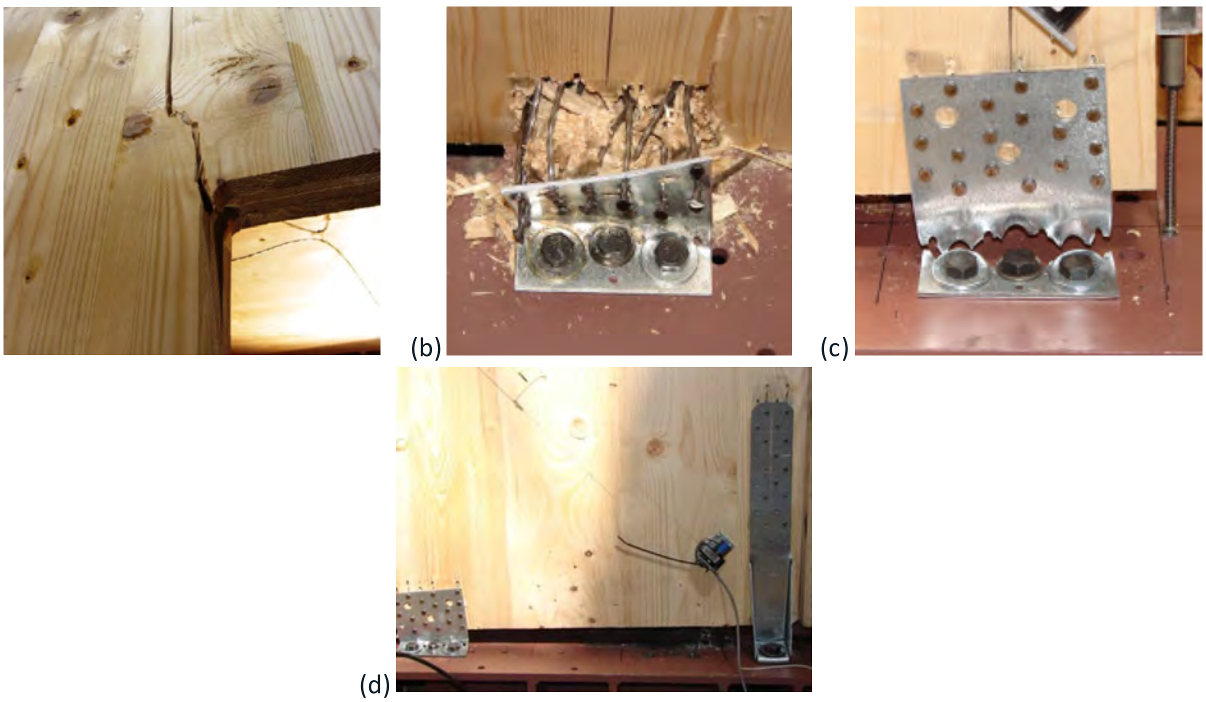

(a) (b) (c) (d)

**Figure 10. Potential failure modes of CLT walls: (a) cracking at opening; (b) CLT block-shear failure; (c) bracket fracture; and (d) fastener yielding and wood crushing in hold-down and shear connector**

7.2.3.1.2 Analytical Methods

There exist several analytical methods that can evaluate the design parameters of CLT shear walls, including internal forces in connectors and the rotation and lateral displacement of the walls (Lukacs et al., 2019).

**Lateral Resistance**

With respect to strength assessment, the analytical models generally fall into three groups: (a) tension-compression couple models, Figure 11; (b) rectangular-pattern uplift-force models, Figure 12; and (c) triangular-pattern uplift-deformation models, Figure 13. All these methods are mainly based on static equilibrium equations, and most consider the wall panel to be rigid, i.e., they disregard the deformation of the CLT panel itself in favour of the connections. Tension-compression couple models only consider the internal level arm between the tensile bracing and the compression zone, whose length mainly varies depending on the size of the compression zone. To consider the effect of the compression zone, one can use a reduction coefficient zone (Casagrande, et al., 2018; Casagrande et al., 2016; Nolet et al., 2019), a rectangular 'stress block' (Tomasi, 2014; Wallner-Novak et al., 2013), or a triangular compression zone (Schickhofer et al., 2010). In rectangular-pattern uplift-force models, hold-downs and shear connectors within the 'tensile zone' (Figure 12[a]) or outside the compression zone (Figure 12[b]) can resist uplift forces equal to the tensile strength of the hold-down. Triangular-pattern uplift-deformation models consider a triangular distribution of the connector displacement, based on the displacement when the hold-down reaches its strength. Analyses can either consider (Reynolds et al., 2017; Tamagnone et al., 2018) or ignore (Gavric et al., 2015; Gavric & Popovski, 2014; Masroor et al., 2020; Pei et al., 2013) the compression zone.

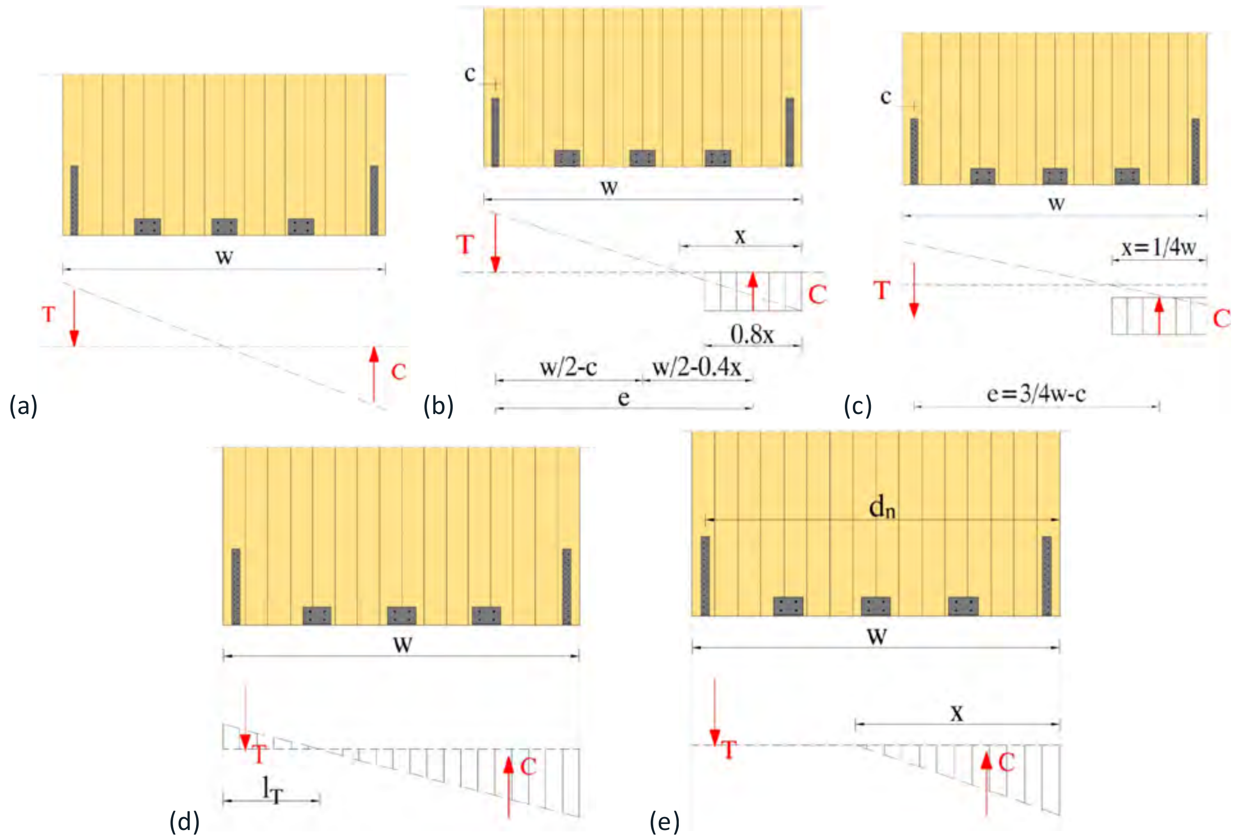


**Figure 11. Tension-compression couple models: (a) Casagrande et al. (2016); (b) Tomasi (2014); (c) Wallner-Novak et al. (2013); (d) G Schickhofer et al. (2010), model I; and (e) G Schickhofer et al., model II (2010)**

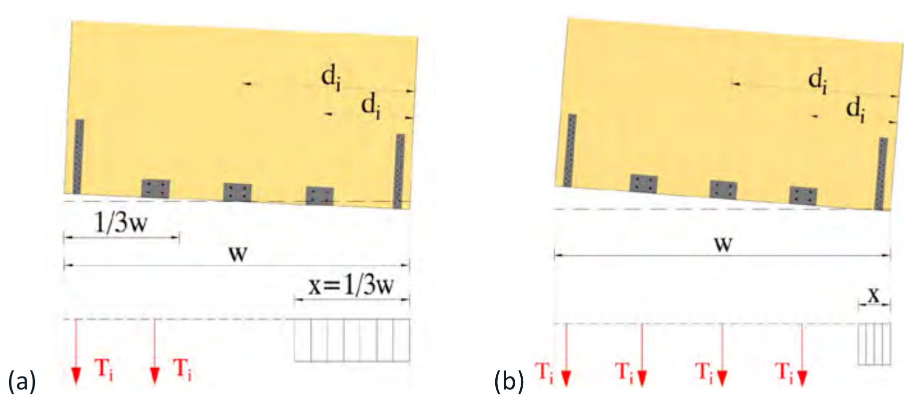


**Figure 12. Rectangular-pattern uplift-force models (a) with and (b) without tensile zone (Reynolds et al., 2017)**

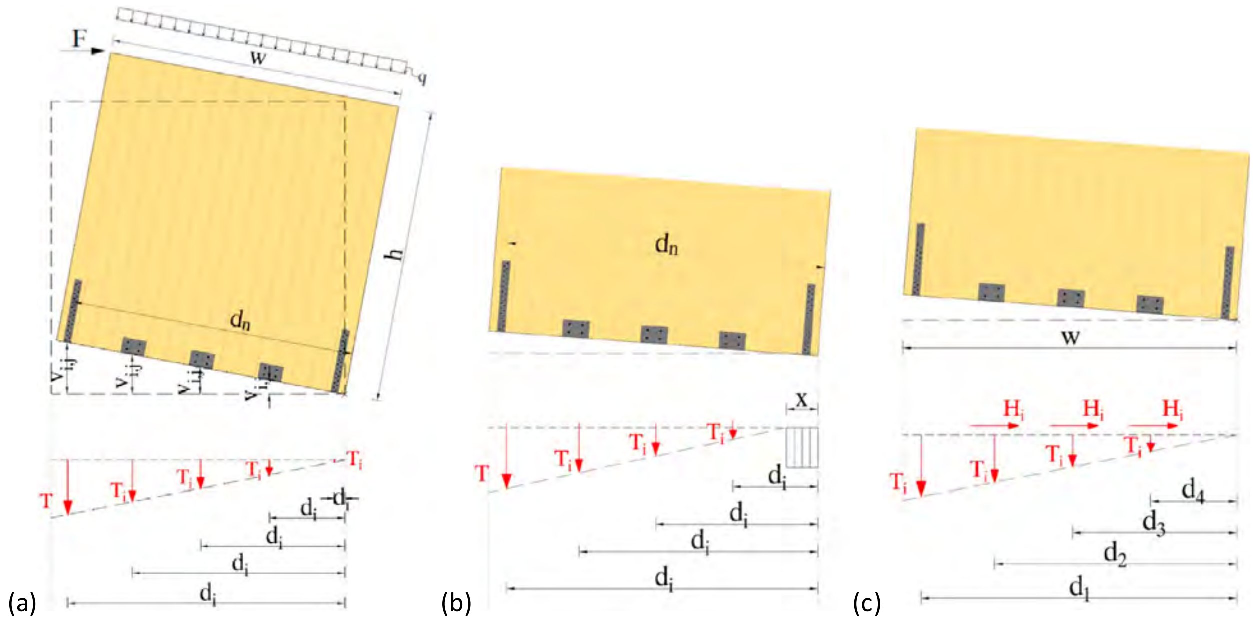


**Figure 13. Triangular-pattern uplift-deformation models: (a) Pei et al. (2013); (b) Reynolds et al. (2017); and (c) Gavric and Popovski (2014)**

Typically, the load-carrying capacity of single-panel walls is that arising either from the pure rotation or from the pure translation of the wall, whichever is less. The tension-compression couple models consider only the hold-downs as resisting rotation (uplift) and design shear connectors as exclusively resisting sliding. The rectangular-pattern uplift-force models and triangular-pattern uplift-deformation models, in addition to an internal lever arm, also consider the vertical capacity of the shear connectors. Few models consider the shear-uplift interaction of the forces specifically in the shear connectors (Gavric & Popovski, 2014), friction as an addition to the shear capacity (Gavric et al., 2015; Reynolds et al., 2017; Wallner-Novak et al., 2013), or a nonrigid base (Ringhofer, 2010; Gerhard Schickhofer & Ringhofer, 2012), e.g., a deformable CLT flooring under the wall. For coupled- (Figure 14) or multipanel (Figure 15) CLT shear walls, the load-carrying capacity must also account for the shear resistance of the vertical joints. Models developed by Casagrande et al. (2018), Flatscher and Schickhofer (2016), Gavric et al. (2015), Masroor et al. (2020), and Nolet et al. (2019) can help evaluate load-carrying capacity. Note that different models define single-panel behaviour slightly differently. For example, Gavric et al. (2015) defined single-panel behaviour as what occurs when there is no or almost no slip in the vertical joints connecting two panels (Figure 9[c]), while Masroor et al. (2020) define it as only one panel touching the foundation at the corner (Figure 15[b]).

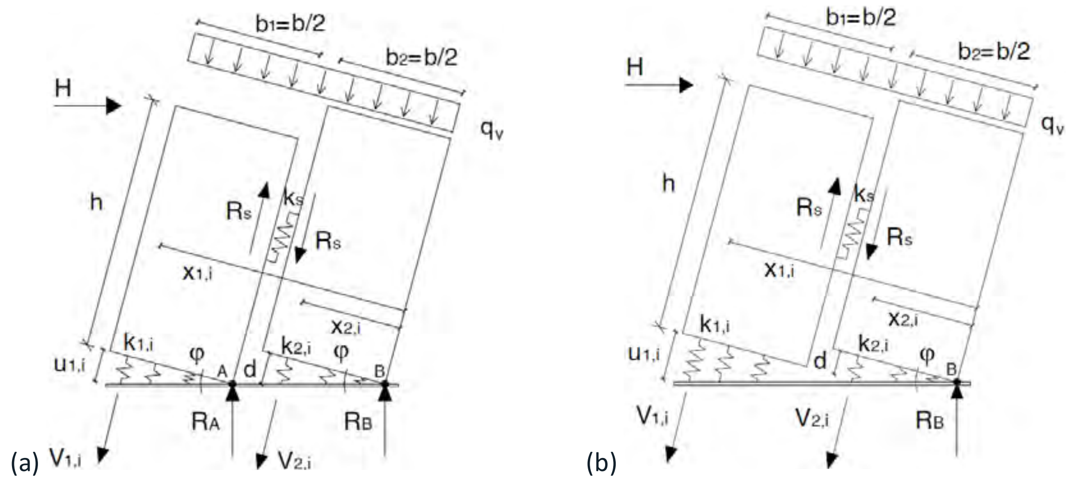


**Figure 14. Schematic of coupled-wall models (Gavric et al., 2015): (a) coupled-wall behaviour; (b) combined single–coupled behaviour**

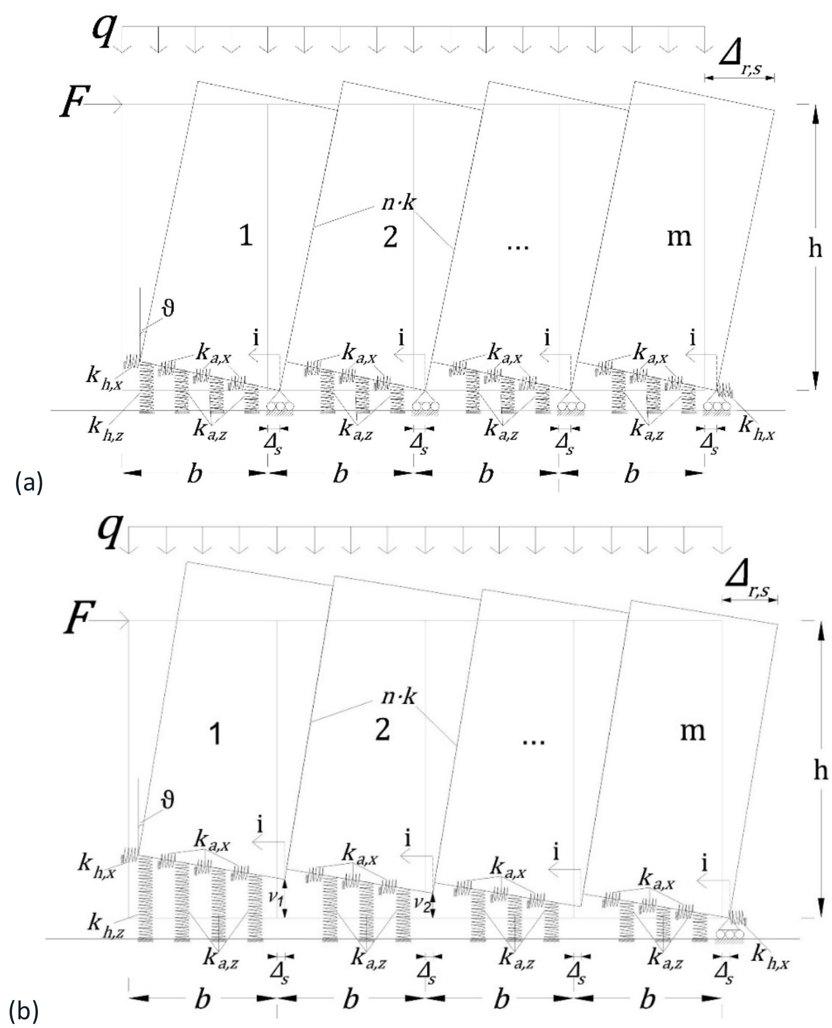


**Figure 15. CLT multipanel shear walls (Masroor et al., 2020): (a) coupled-panel behaviour; (b) single-panel behaviour**

### Lateral Deflection

The total lateral deflection of CLT walls is the sum of the rocking (anchorage deformation), sliding, panel shear, panel bending, and slip in the vertical joints (for coupled walls only), as shown in Figure 8.

Some models to determine lateral resistance, like the triangular-pattern uplift-deformation models, can also derive the rocking, sliding, and slip deformation in shear walls under lateral loads, if they account for the stiffness of connections. Note, however, that the model developed by Flatscher and Schickhofer (2016) is a displacement-based method. Thus, unlike with the force-based methods used in other models, one must analyse the sliding and rocking behaviour together, as illustrated in Figure 16(a). Meanwhile, the model developed by Hummel, Seim, and Otto (2016) considers the increased panel flexibility due to an elastic foundation, as shown in Figure 16(b).

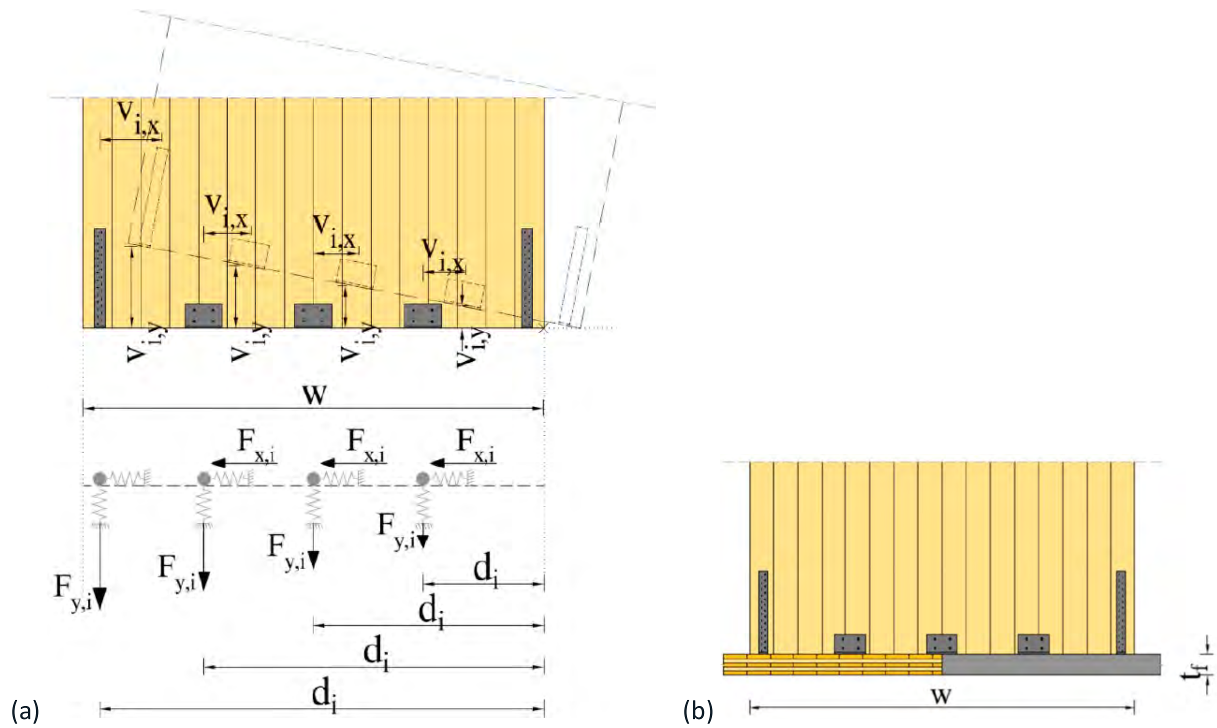


**Figure 16. (a) Rocking and sliding deformation in displacement-based method (Flatscher & Schickhofer, 2016); (b) a CLT wall showing different foundations (Left – CLT; Right – concrete) (Hummel et al., 2016)**

Fundamental engineering mechanics can help determine the bending and shear deformation in the panels, i.e., by using the deformation calculation of a cantilever beam under a point load. The bending and shear stiffness properties play a key role in the calculation. Several proposed methods can help estimate these two parameters (Popovski et al., 2019), including the simplified design method (Gavric et al., 2015) and *k* method (composite theory) (Blass & Fellmoser, 2004) for the effective bending stiffness of CLT panels; and the simplified design method (Gavric et al., 2015) and representative volume element method (Moosbrugger et al., 2006) for effective shear stiffness. Gavric et al. (2015) considered a shape reduction factor of 1.2 for the shear deformation, though other models have not followed suit (Casagrande et al., 2016; Flatscher & Schickhofer, 2016; Hummel et al., 2016; Wallner-Novak et al., 2013).

#### 7.2.3.1.3 Finite Element Methods

Different types of FE models have been proposed for modelling CLT shear walls (Pozza et al., 2017; Rinaldi, Casagrande, Cimini, Follesa, Sciomenta, et al., 2021; Tran & Jeong, 2021). These can be as simple as using a single translational or rotational spring (Figure 17) for the entire wall or as complex as using numerous shell elements for panels and multiple springs for connections (Figure 18).

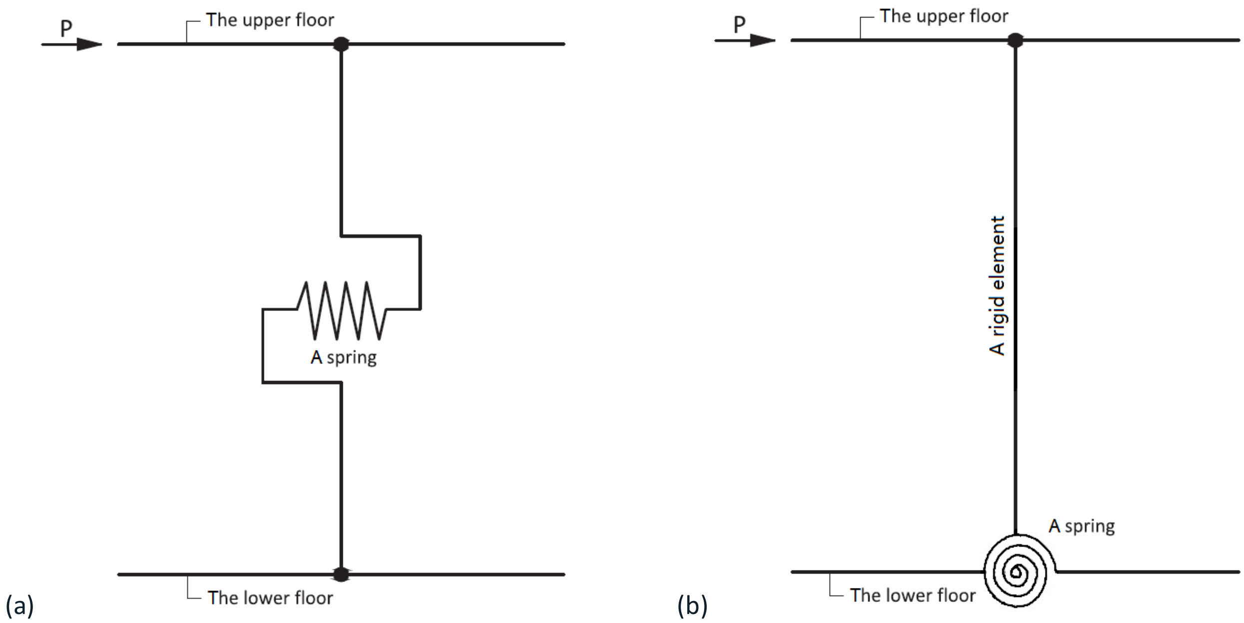


**Figure 17. Macro models: (a) Translational spring; (b) Rotational spring**

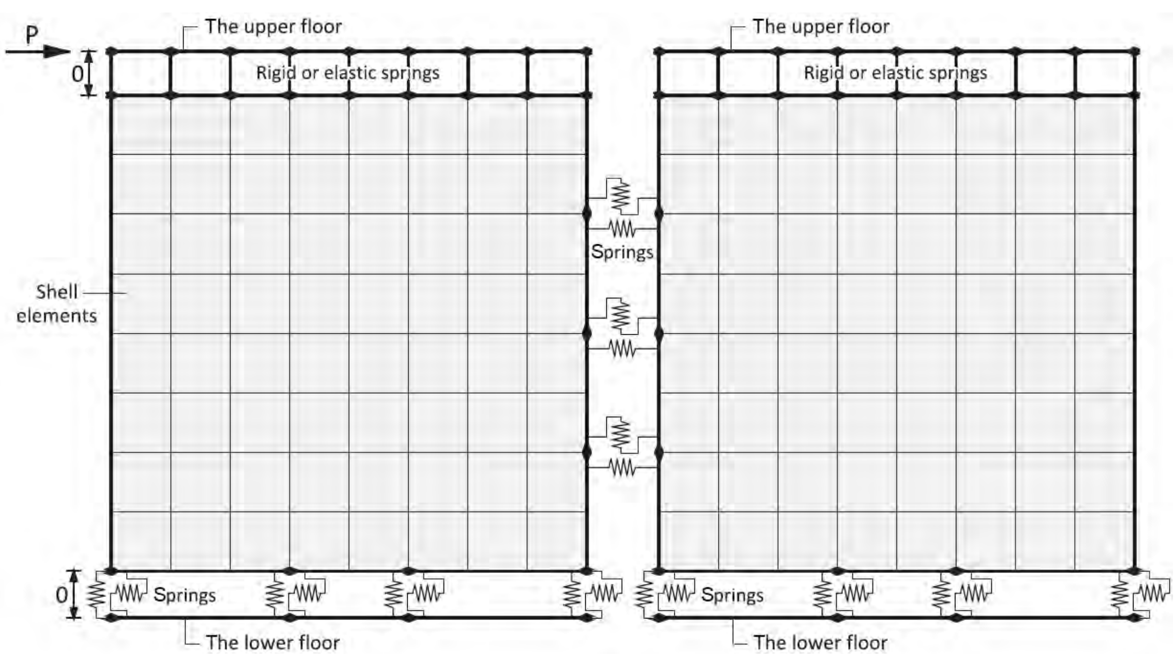


**Figure 18. Component-based model for a coupled-panel CLT wall**

The models shown in Figure 17 are called macro, super element, or phenomenological models. Their aim is to faithfully reproduce the global response of the shear walls (Chen & Popovski, 2021c). Consequently, users must calibrate the spring of the model to test results for a shear wall or to simulation results for a detailed wall model. Different analyses require different input properties: an equivalent stiffness for linear analyses, parameters describing a backbone curve for static pushover analyses, and those describing hysteresis loops for nonlinear dynamic analyses. Chapter 7.1 discusses backbone curve models or hysteretic models that can be used in the springs. A macro model with a transitional spring (Figure 17[a]) is suitable for shear walls with a low aspect ratio or limited storeys without a prominent wall rotational effect, while one with a rotational spring (Figure 17[b]) can consider the wall rotational effect. The advantages of such macro models are simplicity and efficiency. The main drawback is that the representativeness of the model is limited to the specific wall configuration used to calibrate the model.

The model shown in Figure 18 is called a micro or component-based model. Since it incorporates all components, such a model can reproduce the global response of the shear walls based on individual component response. These models must calibrate the constitutive law for each component based on the results from experimental tests or on proper analytical assessments. As illustrated in Figure 18, it simulates CLT panels using multi-layer or homogenous equivalent shell elements; shear connectors, hold-downs, and vertical joints using spring elements; and the connections between the wall and the upper floor using rigid or elastic springs. The modelling input relies on many factors, such as modelling objectives and types of analysis. Generally, CLT panels are assigned orthotropic elastic properties (Popovski et al., 2019) because they are designed to be capacity protected, while the connections require input on stiffness and strength. FPInnovations' CLT Handbook provides CLT material properties (Karacabeyli & Gagnon, 2019), which are also available in some design software programs, e.g., Dlubal (Dlubal Software, 2021). The stiffness and strength of a connection can be obtained by either calibrating the test results or using the equations provided by material standards, e.g., CSA O86 (CSA, 2019b) and Eurocode 5 (CEN, 2018). Nonlinear time-history analysis of timber connections requires a hysteretic model (see Chapter 7.1) capable of predicting the stiffness and strength degradation, as well as the pinching effect. These types of models generally require an accurate calibration of the elements that reproduce the structural behaviour of the connections. After calibration, it is possible to simulate the structural behaviour of any structure assembled with the calibrated connections, regardless of the geometrical configuration of the wall and the arrangement of the connections. The main drawback is the need for numerous input parameters that may not be available.

Other existing models are more or less similar to the component-based model, albeit with various simplifications. For example, one can model panels as an isotropic material, with an equivalent modulus of elasticity (Polastri et al., 2016; Pozza & Scotta, 2015) derived from the weighted mean values of the moduli both parallel to and perpendicular to the grain, corresponding to the glued crosswise-alternated timber of the panel; the panels are modelled using one or two springs or truss elements within a hinged frame (Mestar et al., 2020; Pozza et al., 2015), as shown in Figure 19. The literature has proposed three main ways to simplify the connections. As shown in Figure 19, a set of springs can simulate multiple shear connectors or vertical joints. Figure 20 shows how all connections can be simulated using vertical and horizontal truss elements (Follesa et al., 2013), while in Figure 21, connection zones with shell elements simulate the connections in specific zones (Christovasilis et al., 2020; Rinaldi, Casagrande, Cimini, Follesa, & Fragiacomo, 2021). The connection zone models can assign orthotopic material properties to these zones. With the zone for bottom connections, for example, the equivalent shear modulus considers the sliding deformation of the connections (e.g., shear connections), whereas the modulus of elasticity in the vertical direction considers the uplift deformation of the connections (e.g., hold-downs). To derive the equivalent stiffness of the truss elements in Figure 20 and the connection zones in Figure 21, one can use the equations provided by Follesa et al. (2013) and Rinaldi, Casagrande, Cimini, Follesa, and Fragiacomo (2021), respectively. Note that the rocking mechanism in these two models is limited due to the nature of the modelling strategies.

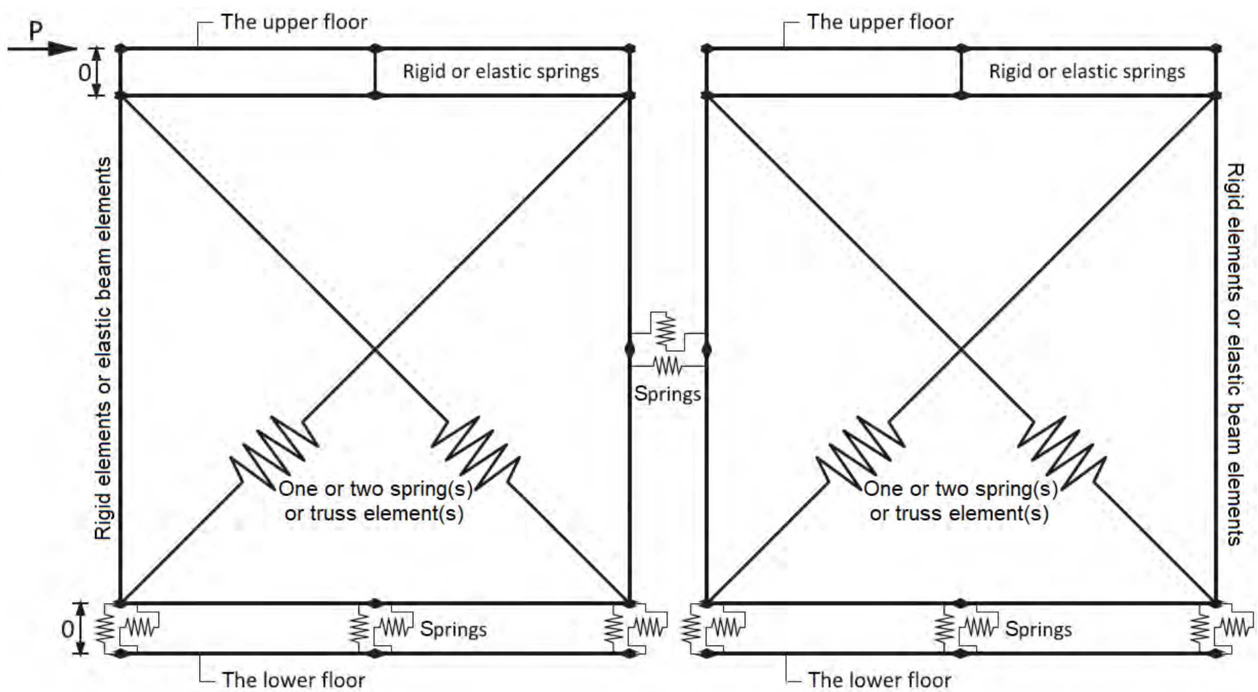


**Figure 19. Truss analogy panel model for a coupled CLT shear wall**

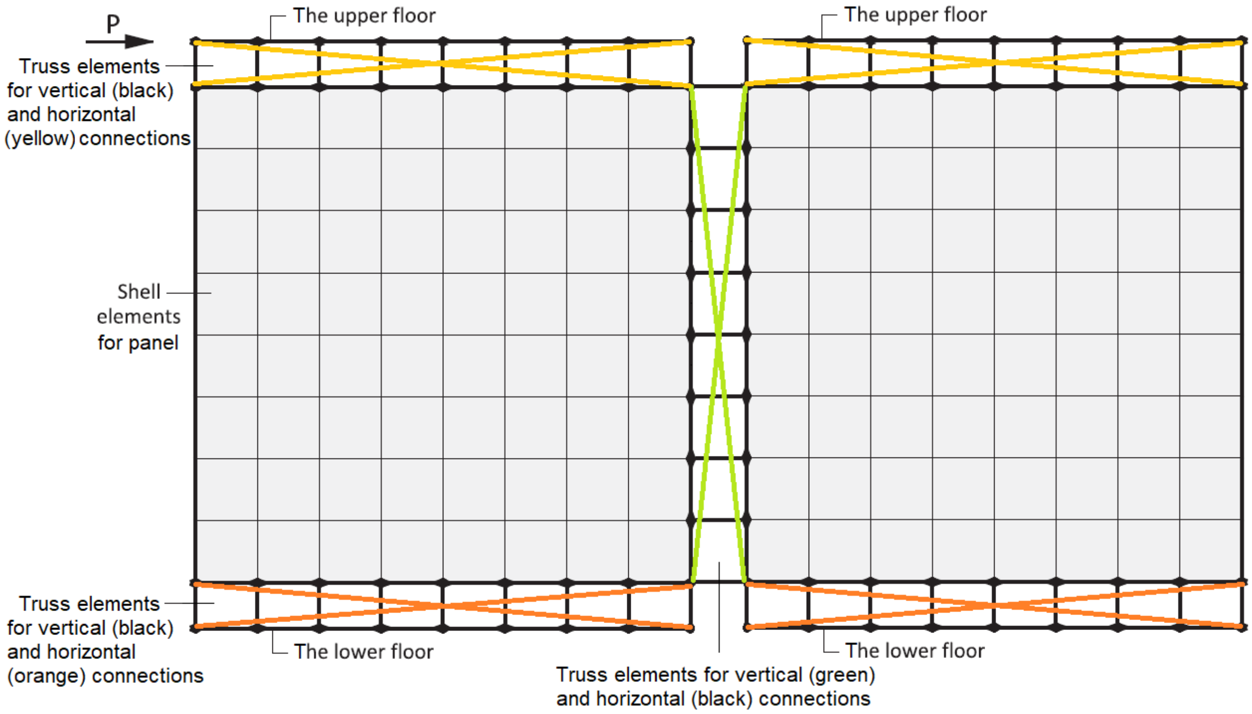


**Figure 20. Truss analogy connection model for a coupled CLT shear wall**

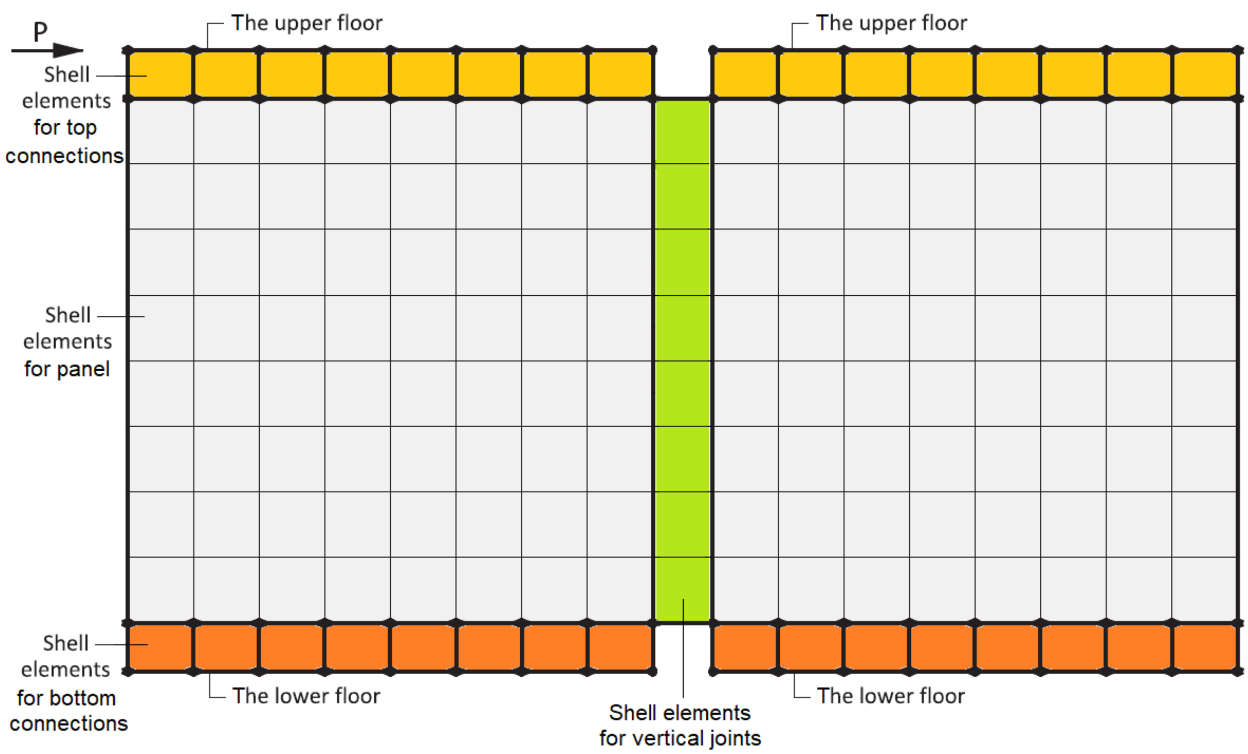


**Figure 21. Connection zone model for a coupled CLT shear wall**

The friction between the walls and the floor panels (or the foundation) should be ignored in most cases, as earthquakes usually have vertical components that can reduce this effect. If this is impossible, the developed models should include these friction effects in the stiffness of either the shear connections or the vertical joints. For multistorey buildings, wall models should also consider the influence of the floor panels between two vertical walls, e.g., using elastoplastic springs or other equivalent methods, in order to account for the compression deformation in the floor panels. Not doing so may lead to an overestimate of the lateral deflection of the multistorey walls, resulting in an uneconomical design.

### *7.2.3.2 Balloon-Type Shear Walls*

#### 7.2.3.2.1 Structural Behaviour and Mechanisms

Besides the platform-type method discussed in the previous section (Figure 5 and Figure 22[a]), another common approach to constructing MT buildings is the balloon-type method (Figure 22[b]) (Chen & Popovski, 2020c). Here, walls are continuous over multiple storeys and floor panels are attached to the sides of the walls at each storey. This alleviates the accumulation of compression perpendicular-to-grain on the floor panels. It also takes advantage of MT panels, which are manufactured at up to 20 m in length. Figure 23 shows a balloon-type CLT building under construction.

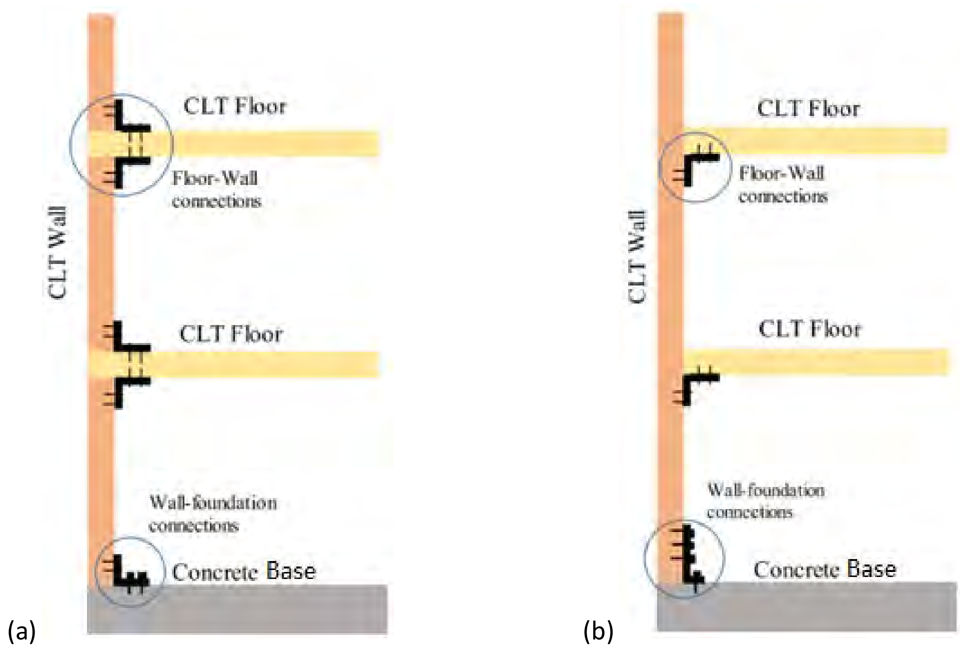


**Figure 22. Simplified schematics of (a) platform-type and (b) balloon-type CLT walls**

**Figure 23. Balloon-type CLT building under construction (Courtesy of Nordic Structures)**

As with platform-type MT shear walls, balloon-type MT shear walls connect to the foundation (Figure 24) using hold-downs and shear connectors with fasteners, which resist the shear and uplift force induced by the overturning moment. As shown in Figure 23 and illustrated in Figure 24, vertical joints connect panels together to form a longer shear wall, while panel extension connections form a taller shear wall.

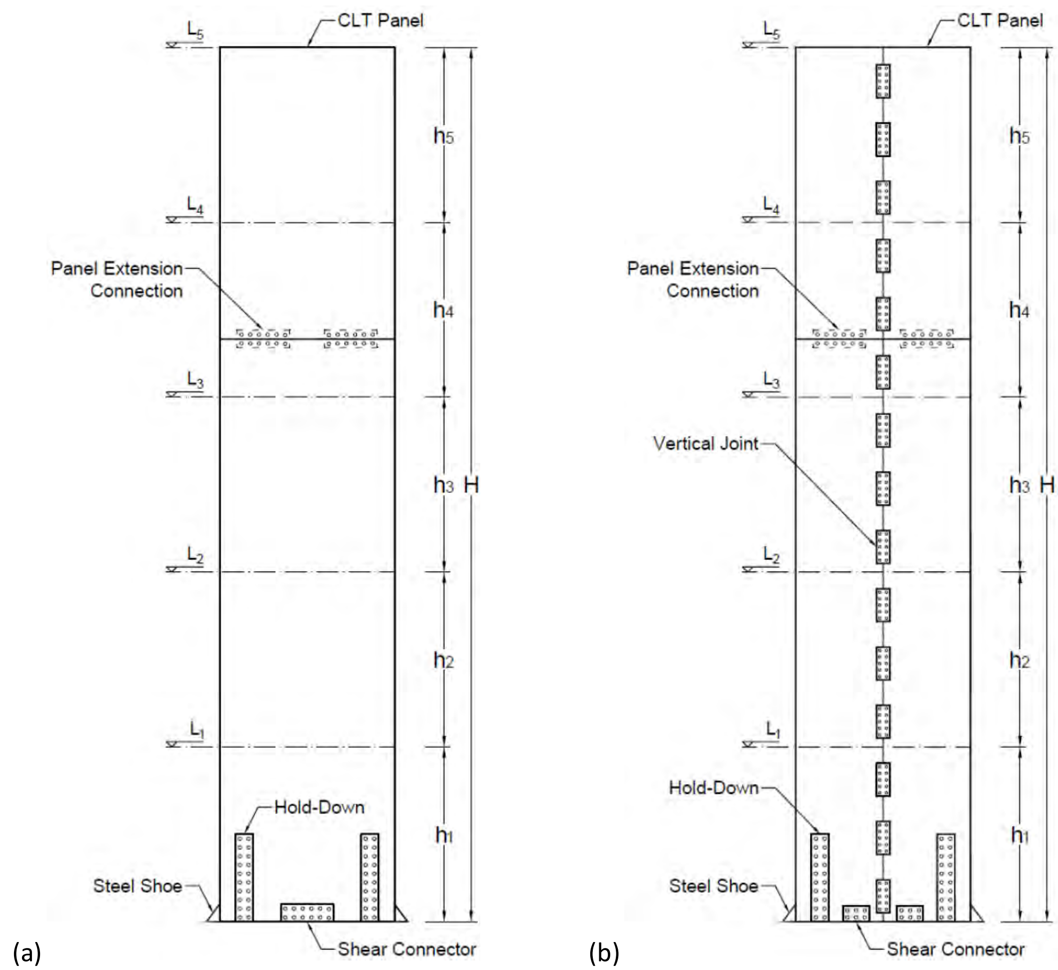


**Figure 24. Simplified schematics of (a) a single- and (b) coupled-panel balloon-type CLT walls**

FPInnovations has conducted a series of monotonic and cyclic tests of MT connections and walls with various configurations and parameters (Chen et al., 2018; Chen & Popovski, 2020c), as have other research institutions (Shahnewaz et al., 2021), to quantify the seismic performance of balloon-type single-panel and coupled-panel MT shear walls (Figure 24). The total lateral deflection at any height is comprised of bending, shear, rocking, sliding, and slip (for coupled-panel walls only), as illustrated in Figure 25. Rocking and bending are the major contributors to the total deflection of a single-panel balloon-type wall, while slip and bending dominate the deflection of coupled-panel walls (Chen & Popovski, 2020c). The contribution of bending deflection increases with the aspect ratio (height to length) of the panel (Chen & Popovski, 2021b). As in platform-type construction, stiffer connections can improve the wind-induced response of a balloon-type MT shear wall system (Chen & Chui, 2017; Chen et al., 2015; Chen & Popovski, 2021b).

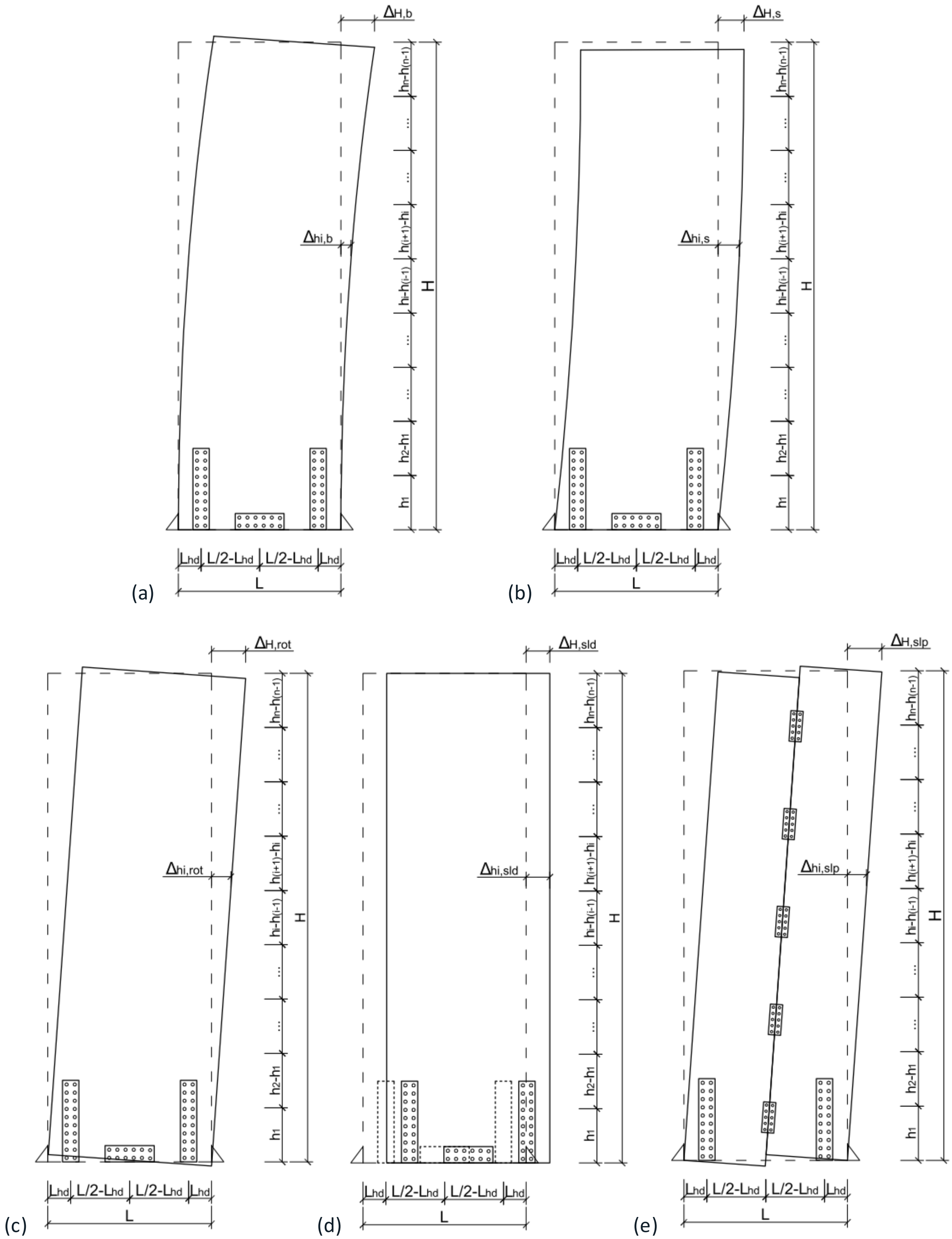


**Figure 25. Components contributing to the lateral deflection of balloon-type walls: (a) bending; (b) shear; (c) rocking; (d) sliding; and (e) slip**

Failure modes similar to those for platform-type CLT shear walls (Figure 10) can also occur in balloon-type CLT shear walls. For seismic design, balloon-type MT shear walls should follow the capacity design approach. The panels and the nondissipative part of the connections should be capacity protected to avoid brittle failure, e.g., cracking at openings, CLT block-shear failure, or bracket fracture. The energy dissipative part of the connections should be yielding in order to dissipate the seismic input energy, as shown in Figure 10 and Figure 26. Correspondingly, the resistance and energy dissipation capacity of the MT shear walls are governed by the energy dissipative connections, i.e., the hold-downs and vertical joints (if present). As with the platform-type MT shear wall, connections with high strength and a large ductility and energy dissipation capacity can improve the seismic response of a balloon-type MT shear wall system.

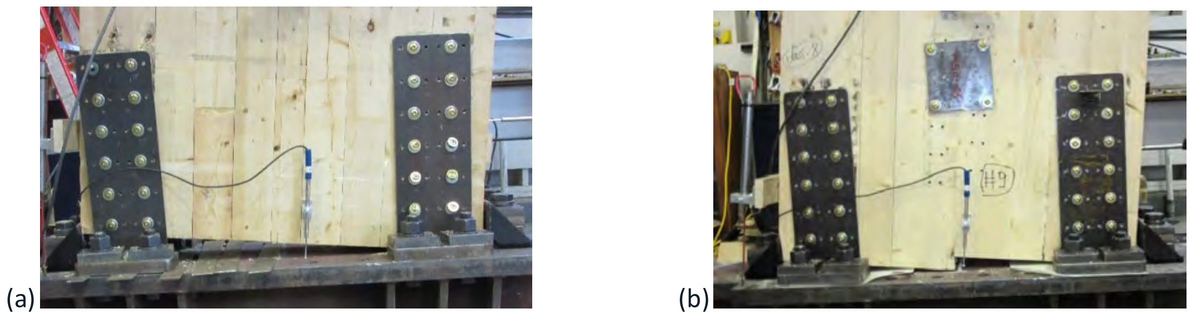
(a) (b)

**Figure 26. Failure modes of balloon-type CLT shear walls: (a) yielding of hold-downs in a single-panel wall; and (b) yielding of hold-downs and vertical joints in a coupled-panel wall**

#### 7.2.3.2.2 Analytical Methods

FPInnovations has developed two analytical models (rigid base and elastic base) (Chen & Popovski, 2020c, 2021d) based on engineering principles and mechanics to predict the lateral deflection and resistance of single- and coupled-panel balloon-type CLT shear walls, as illustrated in Figure 27.

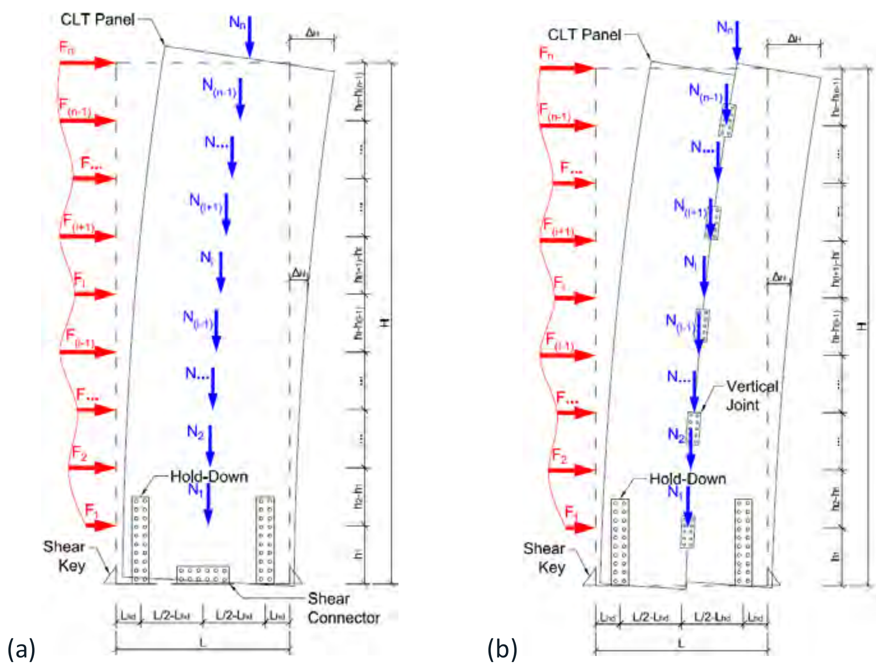


**Figure 27. Analytical models of (a) single- and (b) coupled-panel balloon-type CLT shear walls**

**Lateral Deflection**

As with platform-type CLT shear walls, one can assume the total lateral deflection of balloon-type CLT shear walls (Figure 27) comprises five deflection components: panel bending, panel shear, rotation (hold-down deformation), sliding, and slip in vertical joints (for coupled-panel wall only); see Figure 25.

Fundamental engineering mechanics can help determine the bending and shear deformation in the panels, i.e., by using the deformation calculation of a cantilever beam under multiple point loads. As is the case for platform-type walls, there are various methods of estimating the bending and shear stiffness of the panels: (a) the simplified design method (Gavric et al., 2015) and *k* method (composite theory) (Blass & Fellmoser, 2004), for the effective bending stiffness of CLT panels; and (b) the simplified design method (Gavric et al., 2015) and representative volume element method (Moosbrugger et al., 2006), for the effective shear stiffness. The deflections induced by the sliding of the shear walls and the slip in the vertical joints (for coupled-panel walls only) consider not only the stiffness of the connections but also the friction between the wall panel and the foundation or the floor, or between panels.

The deflection due to the rigid-body rotation of timber shear walls can be derived in various ways by assuming different behaviour at the base of the panel. Models for calculating the rotation deformation of the shear walls assume either a 'rigid panel base', where the bottoms of CLT panels are also not deformable, or an 'elastic panel base', where the bottoms of CLT panels deform elastically under compression. With the former assumption, the CLT panel is free to rotate about its corner under lateral loads. To calculate the rotation deformation, one solves sets of force equilibrium equations, deformation coordination equations, and material constitutive equations. With the latter assumption, a certain length of CLT panel will be compressed and the wall panel will rotate around a certain point along the length of the wall. The length of the compression area decreases and the location of the zero-compression point moves from one end of the wall to the other as the lateral load increases. There are several cases to analyse, with different connections depending on the lateral and vertical loads. Upon determining the case for a specific lateral and vertical load using trial and error, it is possible to derive the rotation deformation of a CLT shear wall accordingly.

**Lateral Resistance**

The developed models assume that the lateral resistance of balloon-type CLT shear walls is governed by the strength of the hold-downs, the shear connector(s), the wood in contact with the shear keys, and the vertical joints (if present). In such cases, one can assume the lateral resistance of this system to be the minimum resistance derived in the three scenarios (i.e., shear failure of connections at the bottom of the wall, overturning failure of single-panel walls, and overturning failure of coupled-panel walls). The friction and bi-axial behaviour of the connections (Izzi et al., 2018) help determine the lateral resistance.

#### 7.2.3.2.3 FE Methods

The modelling approaches for platform-type CLT shear walls (discussed in Section 7.2.3.1.3) can also apply to balloon-type shear walls. Figure 28 illustrates a component-based model of a coupled-panel balloon-type CLT shear wall. Shell elements simulate CLT panels, while connector or spring elements simulate shear connectors, hold-downs, and vertical joints. In general, CLT panels have orthotropic elastic properties because they are capacity designed, while the connections require stiffness and strength. For the timber connections, a nonlinear time-history analysis should use a hysteretic model that can account for stiffness and strength deterioration, as well as for pinching effect. For walls with high gravity loads or a large aspect ratio, it is also necessary to consider the compressive strength of the CLT panels in the material model, especially at the bottom of the wall, in order to accurately calculate the pivot point, the moment arm of overturning resistance, and hence the lateral resistance and deflection of the walls.

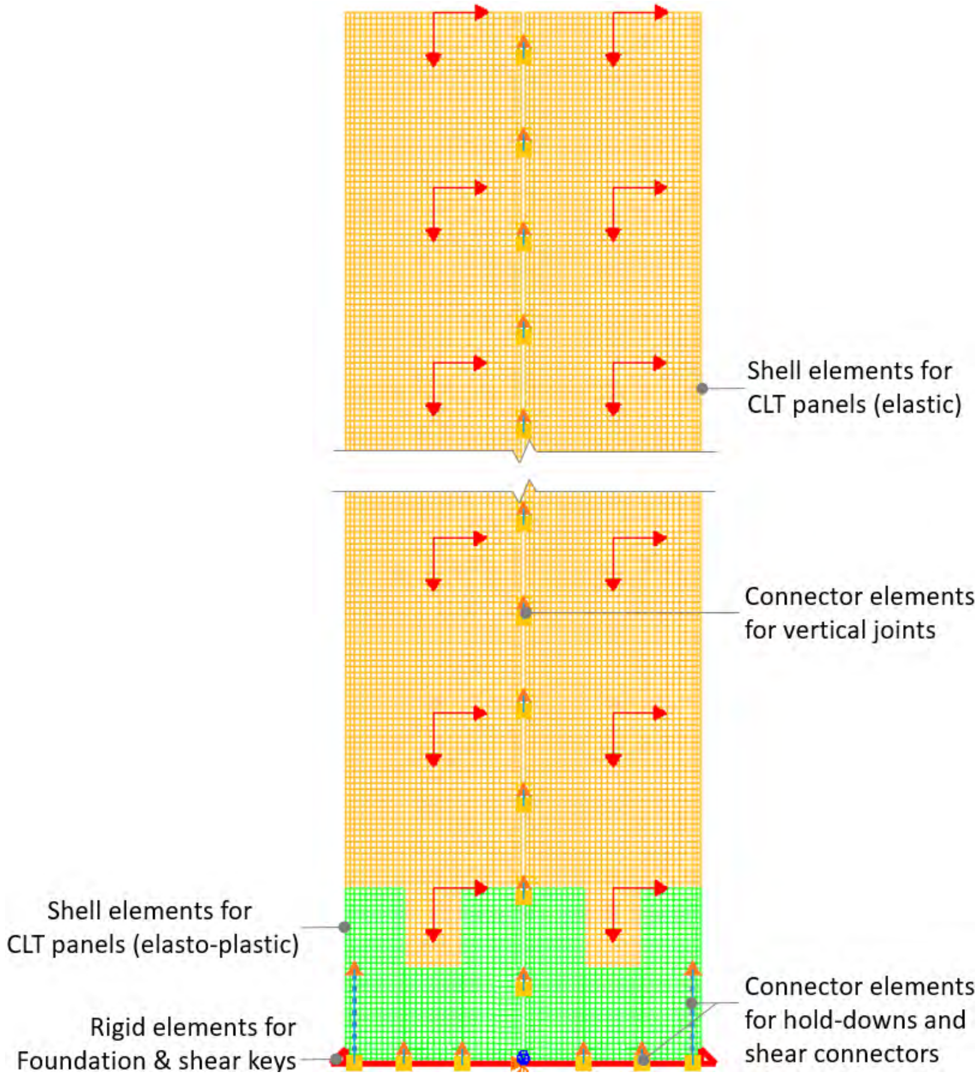


**Figure 28. Finite element models of (a) single- and (b) coupled-panel balloon-type CLT shear walls**

### *7.2.3.3 Braced Frames*

#### 7.2.3.3.1 Structural Behaviour and Mechanisms

Braced MT frames (BMTFs) are essentially vertically cantilevered planar trusses (Bruneau et al., 2011). Because of their high strength and stiffness to resist lateral loads, BMTFs are one of the most efficient seismic force–resisting systems (SFRSs). Recent constructions have incorporated BMTFs into tall timber structures in high wind areas (e.g., the 18-storey Mjøstårnet building in Brumunddal, Norway) and high seismic zones (e.g., the UBC Earth Sciences Building in Vancouver, Canada), as shown in Figure 29.

(a)  (b) 

**Figure 29. Braced frame buildings: (a) Mjøstårnet (Abrahamsen, 2018) and (b) Earth Sciences Building (Courtesy of naturallywood.com)**

BMTFs consist of columns, beams, and braces that attach to each other using connections. Depending on the configuration, BMTFs can mainly be classified into concentrically braced frames (CBFs) (NIST, 2013), Figure 30, buckling-restrained braced frames (BRBFs) (NIST, 2015), Figure 31, and eccentrically braced frames (EBFs) (Bruneau et al., 2011), Figure 32.

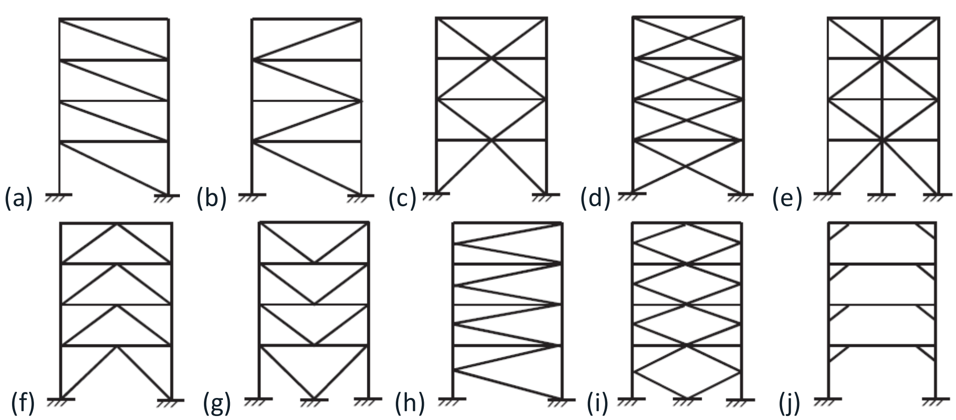


**Figure 30. Concentrically braced frame configurations: (a and b) single diagonal braced frames; (c to e) X-braced frames; (f and g) inverted V-braced frames (inverted chevron and chevron braced frames, respectively); (h and i) K-braced and double K-braced frames, respectively; and (j) knee-braced frames**

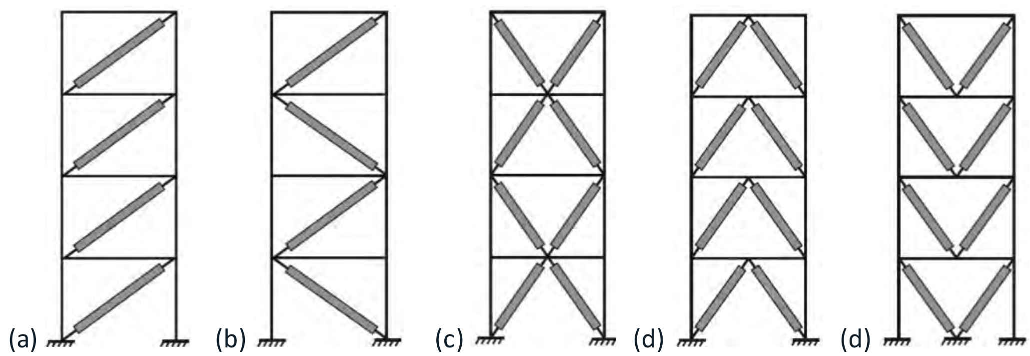


**Figure 31. Typical BRBF configurations with BRBs: (a) Diagonal bracing (one way); (b) Diagonal bracing (zig-zag); (c) Multistorey X-bracing; (d) Inverted V-bracing (chevron); and (e) V-bracing**

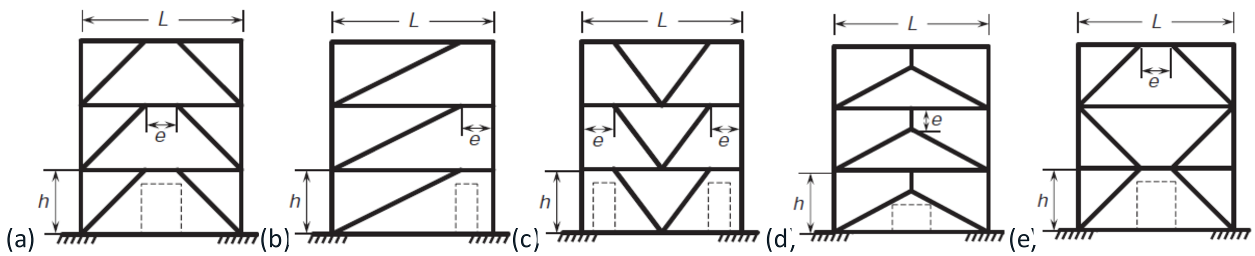


**Figure 32. Eccentrically braced frame configurations: the link is designated by a length, e.**

### Concentrically Braced Frames

CBFs (Figure 30) resist lateral loads through a vertical concentric truss system where the longitudinal axes of the members align concentrically at the joints. CBFs provide high stiffness in the linear range of their response, thus reducing deformations for serviceability limit state design. This is why they were originally developed to resist wind loads. Single diagonal braced frames (Figure 30[a] and [b]) and X-braced frames (Figure 30[c] to [e]), with energy dissipative connections at both ends of the braces, can usually take seismic loads, while the configurations in Figure 30(f) to (j) are usually not recommended for seismic regions because they exhibit relatively poor cyclic inelastic response or induce undesirable demands in beam or column elements. From the perspective of seismic design, the diagonal braces in V or inverted-V (chevron) frame configurations, as well as those in K or double K configurations, impose large, concentrated loads on the beams or columns that need to be capacity protected. For X-braces, the capacity loads imposed on the beams from the brace tensile and compressive resistance imbalance are usually minimal and can thus be ignored. This is especially true when the cross-sections of the braces are uniform for every two storeys or more.

All members of CBFs should be triangularly connected, with the diagonal braces within 30° to 60° of the horizontal beam. Where possible, diagonal braces should be inclined at approximately 45°. This provides an efficient system with lower member forces than other arrangements. Narrow braced frames with steeply inclined braces are less stiff and are more sensitive to bending-type deformations of the entire frame. Wider braced frames on the other hand are more stable structures but have more shear-type response under lateral loads.

FPInnovations has conducted a series of monotonic and cyclic tests of braces with end connections, mechanics analysis of connection and system ductility, and seismic response analysis of BMTFs with various design parameters (Chen & Popovski, 2020a, 2020b; Chen et al., 2019). As the concept of capacity design is signally important for the seismic design of any SFRS, all nonlinear deformations and energy dissipation for BMTFs should occur in the connections at both ends of a brace. These connections should be able to yield by a combination of wood crushing and fastener bending. Brace connections on the column side, as well as other connections, should remain elastic, with strength higher than the probable strength of the energy dissipative zones.

Correspondingly, the primary source of lateral drift capacity in BTFs is the introduction of ductile energy dissipative connections. Proportioning and detailing rules for connections can ensure adequate axial ductility in the braces, which translates into lateral drift capacity for the entire system. Special design and detailing rules for connections, beams, and columns can prevent less ductile modes of response that might result in reduced lateral drift capacity (Chen & Popovski, 2021a).

**Buckling-Restrained Braced Frames**

With increasing emphasis on performance-based design, the diagonal braces of CBFs can be replaced by buckling-restrained bars (BRBs) to achieve higher levels of ductility and energy dissipation (Figure 31). BRBs act as replaceable fuses, which minimise damage to other elements and can be replaced if damaged after a major seismic event (Dong et al. 2021). Such BRBFs are primarily used in steel structures and provide economical installation, with bolted or pinned connections to the rest of the frame. BRBFs also offer design flexibility because both the strength and the stiffness of the braces is easily tuned. Furthermore, it is also simple to model the cyclic behaviour of BRBs for inelastic analysis. Due to their enhanced energy dissipation and ductility capacity, steel BRBFs have higher seismic force modification factors for seismic design in the National Building Code of Canada (NBCC; NRC, 2022), thus leading to smaller member sections. BRBFs are of potential use in timber-based systems where all components except the BRBs are made of timber. However, there are also some innovative hybrid timber–steel BRBs, as shown Figure 33 (Blomgren et al., 2016).

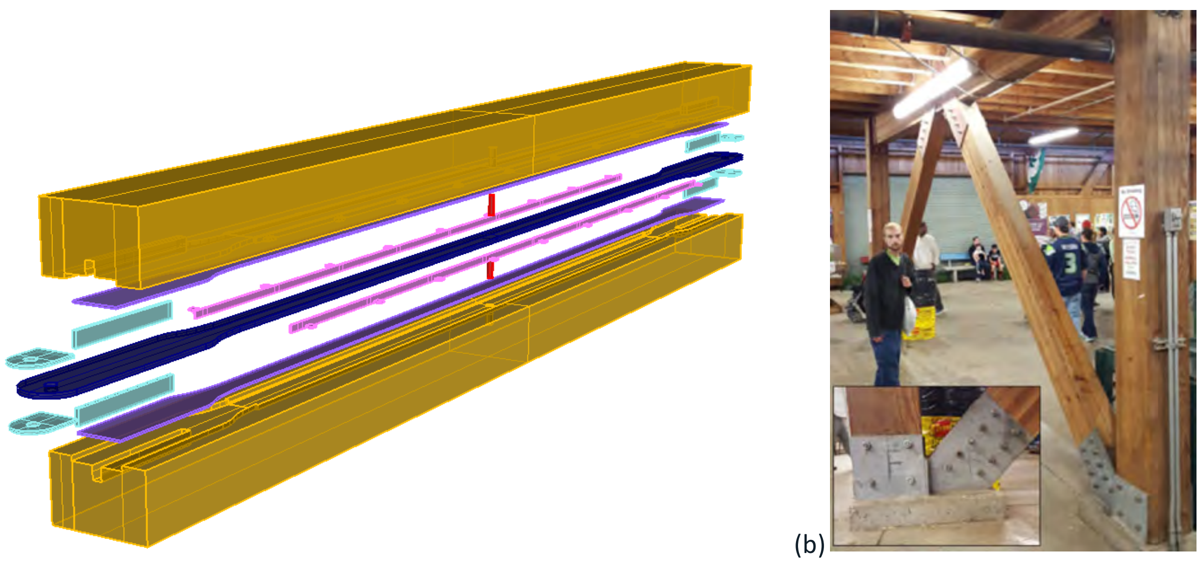

(a) (b)

**Figure 33. (a) Hybrid-timber BRB, (b) as used in a BMTF (Blomgren et al., 2016)**

**Eccentrically Braced Frames**

EBFs (Figure 32) in steel structures combine the advantages of high elastic stiffness and ductility at large storey drifts (Fujimoto et al., 1972; Tanabashi et al., 1974). An EBF is a framing system in which the axial forces induced in the braces are transferred either to a column or another brace through shear and bending in a small segment of the beam. This type of framing system dissipates seismic energy by controlled shear or flexural yielding in those same small segments of the beams, called 'links'. Architecturally, EBFs also provide more freedom for door opening than CBFs and BRBRs. Figure 32(e) shows an EBF without links on every floor. The links in Figure 32(d) are oriented vertically; therefore, unlike in other configurations, they are not integral parts of the beams.

EBFs are best avoided in pure timber BTFs because the wood components cannot act as links to dissipate the seismic energy. However, they can be considered for hybrid BTFs in which the links or the beams with links are steel elements. The links in Figure 32(b) and (c) connect to the columns. Bruneau et al. (2011) have shown that beam-to-column moment connections are vulnerable to brittle fracture. Meanwhile, link-to-column moment connections are subject to both high moments and shear forces, making them even more vulnerable to the same failure mode. It is thus highly desirable to avoid these two configurations.

In a CBF, either the diagonal braces themselves or their end connections are designed and detailed to dissipate energy. For an EBF, however, links must be properly designed and detailed for adequate strength and ductility. All other structural components (beams outside the links, braces, columns, and connections) follow capacity design principles (capacity protected) to remain essentially elastic during seismic response.

This chapter addresses the modelling of BTFs in typical building applications. While the emphasis here is on CBFs and BRBRs, which will be discussed below, some aspects also apply to other types of BTFs.

#### 7.2.3.3.2 Analytical Methods

There are no specific analytical models for braced timber frames, especially when considering the bending stiffness of columns. However, the matrix method can analyse the forces and deflection of the braced frames (Chen & Popovski, 2021a), e.g., in MATLAB (Chandrasekaran, 2019). Given the availability of various software, including general-purpose finite element (FE) software and design-oriented structural analysis software, the FE methods discussed below (Section 7.2.3.3.3) are recommended for the analysis of braced timber frames. If one needs to develop analytical models for such frames, e.g., when there is a need to analyse the repetitive modelling of numerous configurations, some considerations discussed in Section 7.2.3.3.3, e.g., how to account for the stiffness of connections, can also apply to the development of analytical models.

#### 7.2.3.3.3 FE Methods

Chen et al. (2019) proposed two types of FE models for braced timber frames (Figure 34), a continuous column model and a pinned connection model. The continuous column model (Figure 34[a]) assumes the columns are continuous elements from the top to the bottom. It models the columns and horizontal beams using beam and truss elements, respectively, both with linear elastic properties because they are typically capacity protected. For the brace assemblies, each including a diagonal brace and two end connections, the model uses springs with equivalent mechanical properties determined using springs in series theory. The horizontal beams are pinned to the columns. Meanwhile, the pinned connection model (Figure 34[b]) uses elastic truss elements for both columns and horizontal beams, while modelling the brace assemblies with equivalent springs.

Intersections among all members are modelled as pins. The columns in both models connect to the ground using pin connections. The analysis results (Chen & Popovski, 2020a; Chen et al., 2019) showed that the pinned connection model underestimated the stiffness and fundamental frequency of the braced frames due to the structural characteristics of the model itself, and that it concentrated the failure in a single storey/tier, thus underestimating the strength and ductility of the BTFs. Similar findings occur in the analyses of braced steel frames by Bruneau et al. (2011), MacRae et al. (2004), MacRae (2010), and Wada et al. (2009). Consequently, one should use models with continuous columns (Figure 34[a]) to analyse and design BTFs. These models can estimate the potential drift concentration in frames of different heights, which in turn can estimate the column stiffness required to achieve the desired performance. For preliminary analyses or an initial sizing of the components, the pinned connection model can still be an efficient solution.

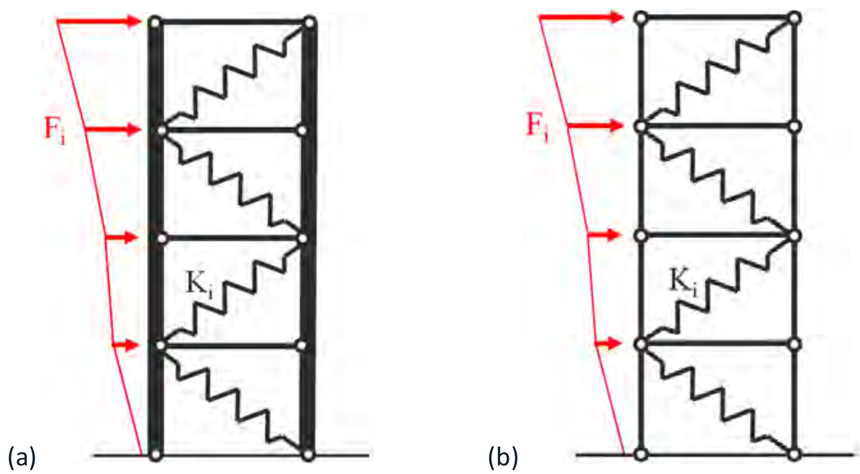


**Figure 34. Schematics of the FE models for multistorey BTFs: (a) continuous column model and (b) pinned connection model**

The brace assemblies play a key role in the structural performance of braced timber frames. Linear analyses, which ignore the displacement in the energy dissipators, would provide relatively conservative results, e.g., lower period, higher seismic loads, and higher component forces/stresses. Nonlinear analyses, which do consider the displacement in the energy dissipators, would provide more reliable and accurate results, including the interstorey drift and the P-Delta effects. A conventional modelling approach for nonlinear analyses models the brace using a linear elastic truss element, with a nonlinear spring for the connection at each end. The material properties and geometric parameters of the brace serve as input for the truss element, and the full backbone curves or hysteresis loops of the connections provide input for the nonlinear springs. The two end connections are usually assumed to behave identically, e.g., to yield at the same time. The test results for a brace with riveted connections (4 × 5 rivets of 65 mm length) at two ends (Popovski, 2004), Figure 35, however, have shown that the top and bottom connections of the brace experience significantly different deformation levels due to a number of factors, including variability in wood strength properties. Once nonlinear deformations started to develop in one of the connections, its reduced stiffness increased the deformation demand on it, leading to a failure of that particular connection, usually referred to as 'the weak connection'. Neither failure nor any large deformation occurred in the other brace connection, often referred to as the 'strong connection', or in the brace member itself. Figure 36 shows the hysteresis loops of the weak connection, the strong connection, and the brace member of a typical glulam brace with two riveted connections. To more accurately model the behaviour of the three components, one should use an equivalent nonlinear spring element to simulate the performance of a brace assembly. One first scales the backbone curves or hysteresis loops of the brace and end connections, then combines them at the same load level. The combined hysteresis loops will serve as the input for the spring representing the whole brace assembly.

**Figure 35. Testing of a glulam brace with riveted connections**

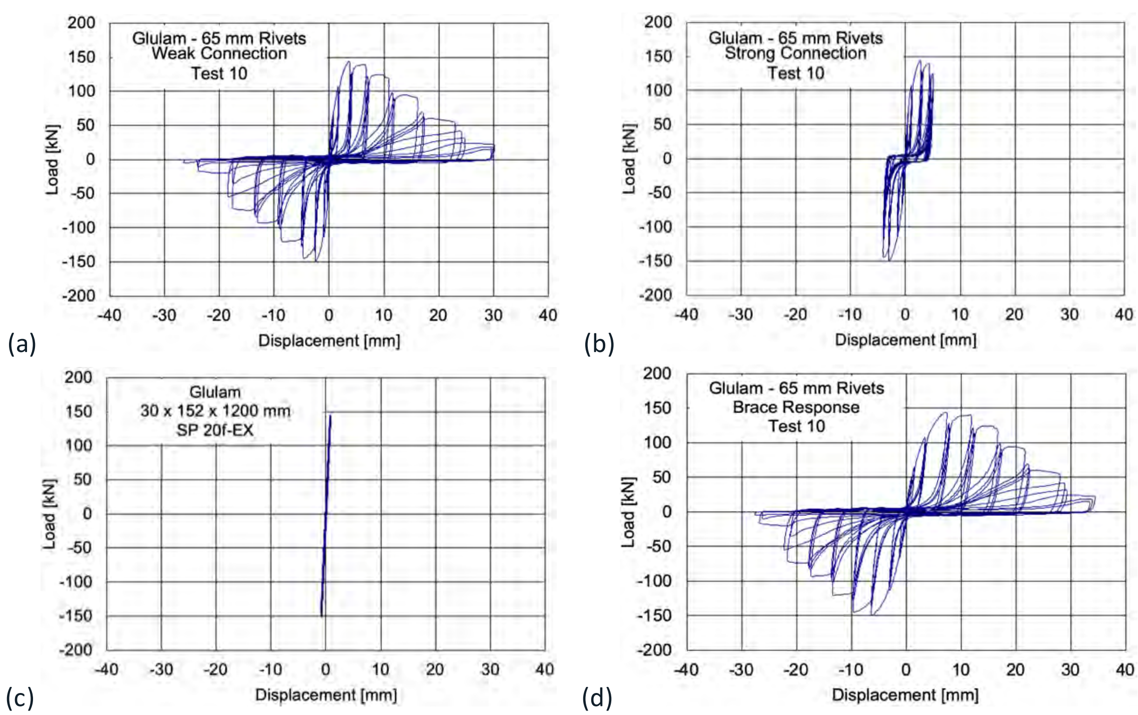


**Figure 36. Hysteresis loops for (a) the weak connection; (b) the strong connection; (c) the brace member; and (d) a combination of all three, each for a glulam brace with riveted connections**

Unlike the conventional braces discussed in previous paragraph, buckling-restrained braces are straightforward to model with uniaxial linear or nonlinear springs, depending on the analysis type and brace properties. Yield strength, cyclic strain hardening, and low-cycle fatigue endurance data are generally available from the brace manufacturers or from experiments (Murphy et al., 2021). Bilinear force-deformation models are sufficiently accurate to capture their behaviour. Acceptance criteria for the brace elements, based on peak deformations and cumulative deformations, can be extrapolated from the qualification testing requirements for buckling restrained braces, e.g., AISC 341 (AISC, 2016).

In models that assume diaphragms to be rigid, it is also important to consider the isolation of the SFRS from the diaphragms to adequately model the axial force distribution in the collectors. This can be done, for example, by using gap-contact elements at each floor level to attach the braced frame to the adjacent nodes that form part of the rigid floor system.

### *7.2.3.4 Moment Frames*

#### 7.2.3.4.1 Structural Behaviour and Mechanism

Moment-resisting frames (moment frames for short), shown in Figure 37, are rectilinear assemblages of beams and columns which rigidly connect to each other. Moment frames typically carry vertical and horizontal loads in the same plane (2-D), however, three-dimensional arrangements, where beams and columns are connected in two orthogonal directions, are also possible. The lateral load resistance is provided primarily by rigid frame action—that is, by the development of bending moment and shear forces in the frame elements and joints. By virtue of the rigid beam-column connections, a moment frame cannot displace laterally without bending the beams, columns, and connections. The bending rigidity of the frame elements and connections is therefore the primary source of lateral stiffness for the entire frame, while the connection resistance governs the strength of the frames.

**Figure 37. Moment frames using circular pattern of dowels in LVL beam and columns (Courtesy of Metsä Wood)**

In general, moment-resisting frames have more deformation capacity and less stiffness than other structural systems, such as shear walls and braced frames. In some cases, therefore, the deformation requirements, rather than the strength requirements, can govern the design, especially in multistorey frames. Since they allow for larger movements during an earthquake, inflexible elements attached to the frame, such as the cladding, must accommodate this additional movement to avoid damage.

The analysis and design of moment-resisting connections in timber is usually complex, and such connections may be expensive to construct. Consequently, the design process must carefully account for the connection strength, stiffness, and rotational ductility. Common connections for moment frames are dowel-type fasteners, e.g., dowels (Figure 37 and Figure 38); nails (Figure 39[a]); rivets (Figure 39[b] and [c]); steel tubes (Figure 40), with or without insert or gusset plate(s); and glued-in rod connections (Figure 41). Some special connections, like steel nail plates (Figure 42), quick-connect moment connections (Figure 43), and self-tapping screws (Figure 44), can also help reduce the time and resources required for assembly. There are also hybrid solutions (Figure 45 to Figure 47) where timber elements connect to each other through a steel part with higher stiffness and ductility. This chapter, however, will focus on moment-resisting connections with dowel-type fasteners.

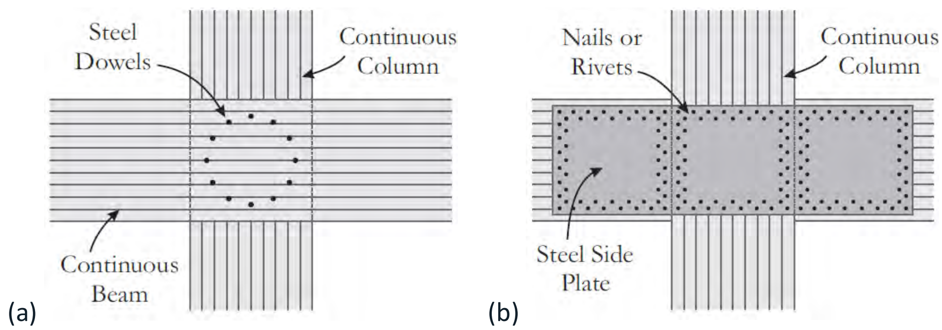


**Figure 38. Beam-to-column moment connections with (a) dowels and (b) steel side plates (Gohlich, 2015)**

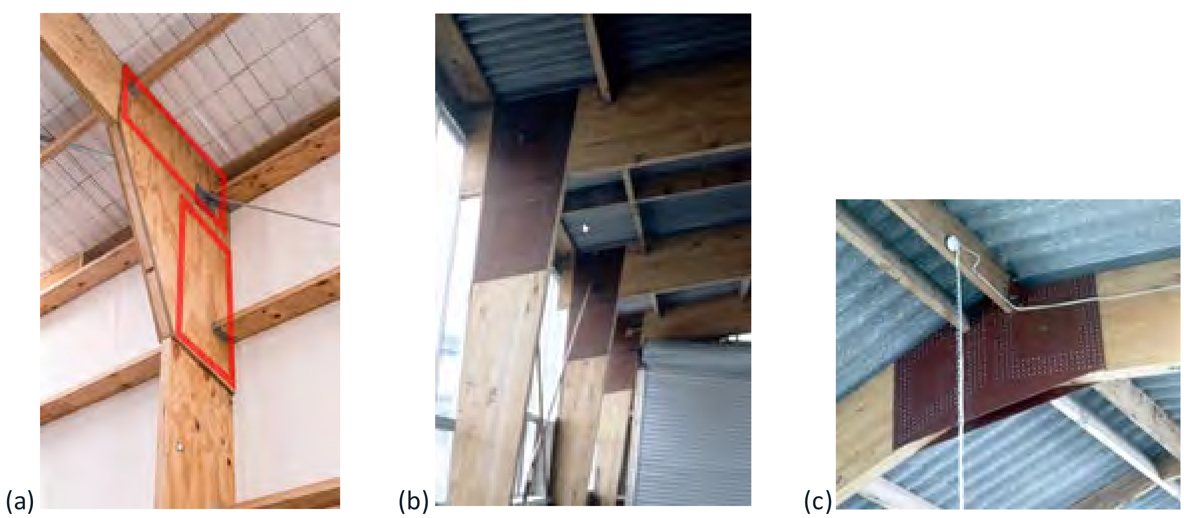


**Figure 39. Portal frame connections with (a) nails and plywood gusset plates and (b) rivets and steel gusset plates for the knee connection; and (c) the apex connection. (Courtesy of Dr. Minghao Li)**

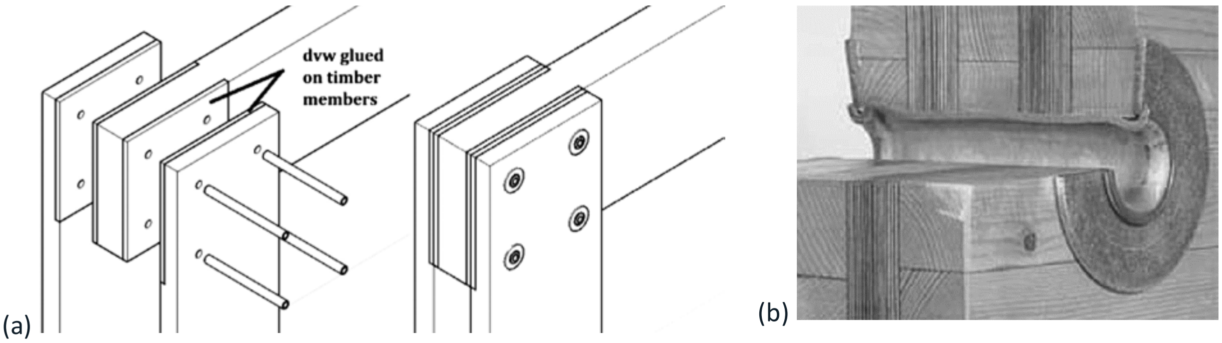


**Figure 40. (a) Densified veneer wood reinforced timber connection with expanded tube fasteners before and after assembly (van Bakel et al. 2017); (b) Cut-open specimen of steel tube inserted into glulam, with densified veneer wood (Leijten et al., 2006)**

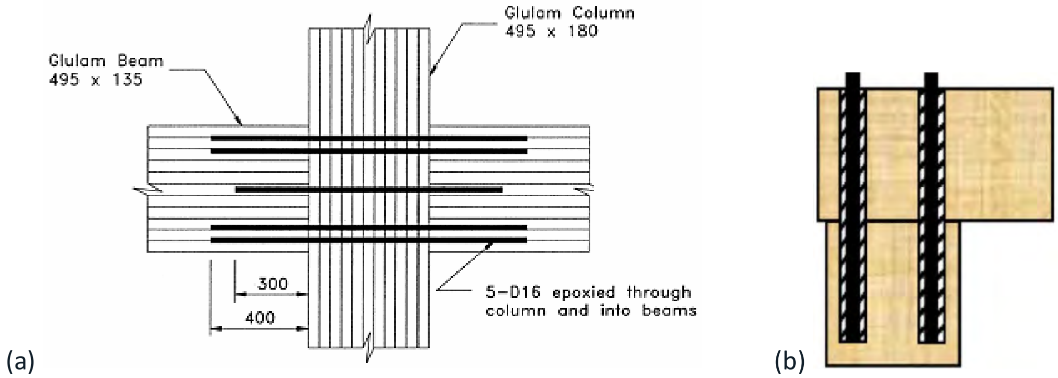


**Figure 41. Common configurations of glued-in rod connections for (a) portal frames (Fragiacomo and Batchelar, 2012) and (b) multistorey buildings (Buchanan and Fairweather, 1993)**

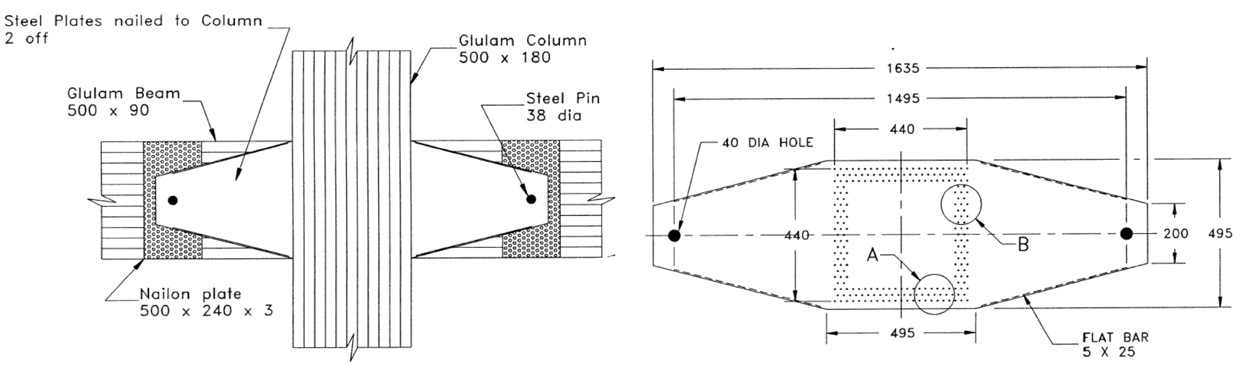


**Figure 42. Glulam connection with steel nail plates (Buchanan and Fairweather, 1993)**

(a)

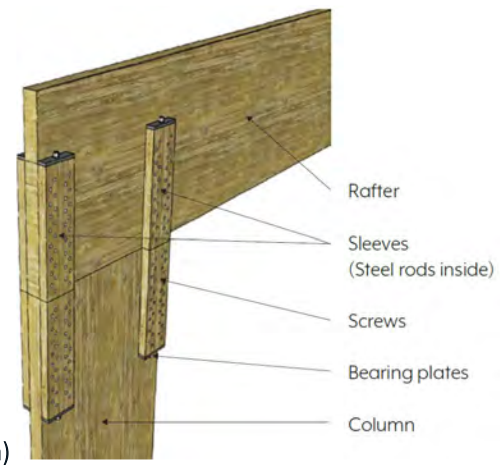


(b)

**Figure 43. (a) Quick-connect moment connection between the column and a rafter in a portal frame; and (b) its application in the Netball Central facility in New South Wales, Australia, using LVL portals**

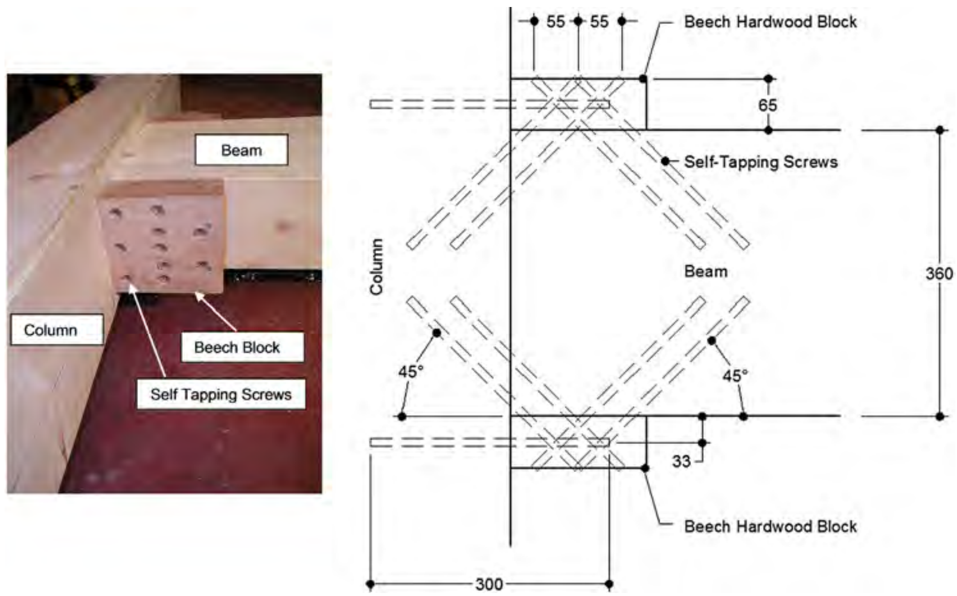


**Figure 44. Heavy timber frame beam-column connection, view and details (Kasal et al., 2014)**

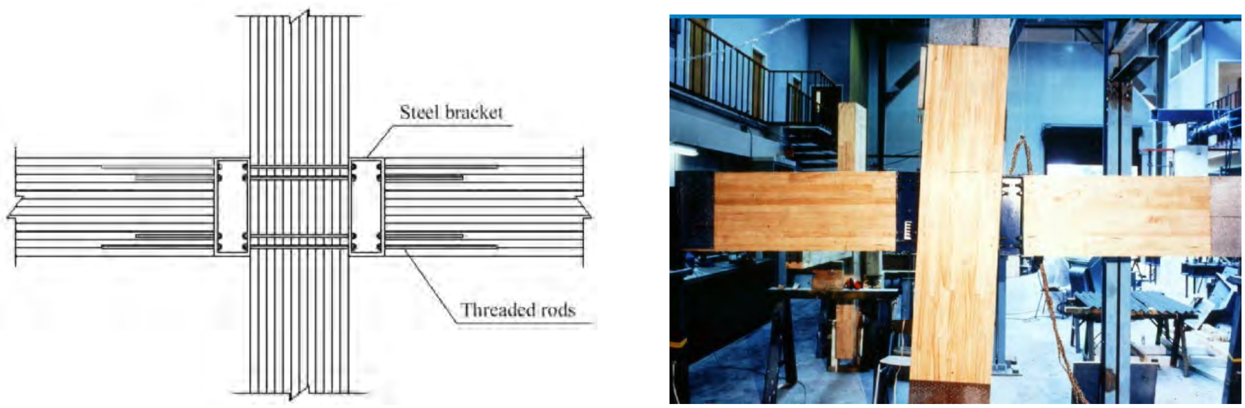


**Figure 45. Epoxied dowelled connection (Buchanan and Fairweather, 1993)**

(a) 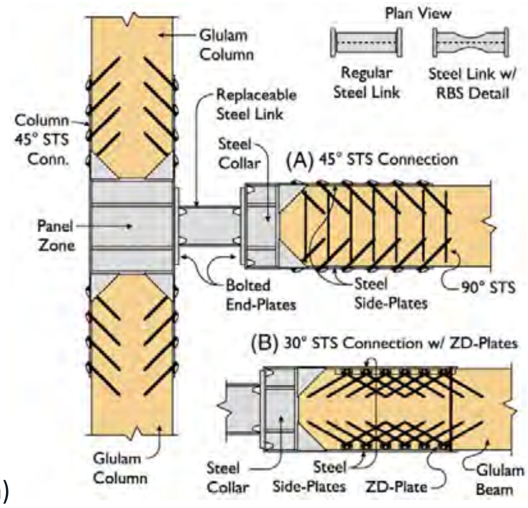

(b) 

**Figure 46. Typical hybrid connection details: (a) type A, with 45° STS, and type B, with 30° STS with ZD-plates; (b) the test setup (Gohlich et. al., 2018)**

(a) 
(b) 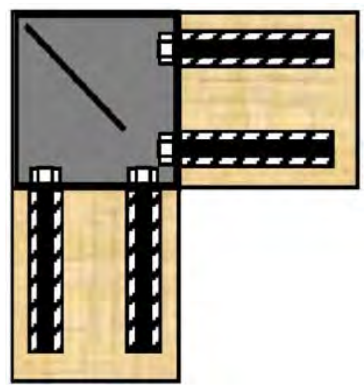

**Figure 47. (a) The metal box connection used in UBC Bioenergy Research Demonstration Facility, and (b) Common configurations of glued-in rod connections for portal frames (Fragiacomo and Batchelar, 2012)**

When moment connections use steel dowels, they should be placed in one or more circular patterns around the centre of the connection (Blaß & Schädle, 2011; Branco & Neves, 2011;). To adjust the stiffness and strength of the connections, one should vary the radius and number of the circular fastener patterns, the number of fasteners, the thickness of the side and middle timber, the quality of the timber (embedment strength), and the diameter and material properties of the fasteners. Designers should be aware that stresses perpendicular to the grain can develop in moment connections of this type, and a careful design is necessary to prevent the timber members from splitting. Cracking perpendicular-to-grain may also occur due to induced swelling or shrinkage across the confined connection section. To reduce the stresses near the end-grain of the members, it is possible to control the mechanical behaviour of the connection by positioning a high-diameter bolt or rod in the centre of the connection. Note that placing the fasteners in rectangular pattern causes a worse combination of shear and tension perpendicular-to-grain stresses in the members; be certain to avoid such arrangements.

In all cases, dowelled connections should fail in yielding mode. According to the European yield model (CEN, 2004), there are three failure modes for three-element connections: embedment of the side or middle timber member, one plastic hinge in the fastener or two plastic hinges in the fastener along with timber crushing. Moment connections with two plastic hinges as a failure mode are ideal for seismic areas because they result in the highest energy dissipation. Timber connections with slender or semirigid fasteners have a higher equivalent energy ratio than those with nonslender or rigid fasteners (Rinaldin et al., 2013). In timber connections with slender fasteners, the steel fasteners must deform plastically before the timber element fails. One brittle failure mechanism that can occur when using a moment connection is for the timber near the connection to split.

If moment connections serve as part of an SFRS in a seismically active region, the design must use capacity design procedures. According to these design principles, the moment connections should serve as the ductile part of the structure (dissipative zones), while all other members should have sufficient overstrength to allow a ductile response in them. The moment connections should fail in ductile failure mode and should possess sufficient deformation capability for the SFRS to reach its assumed deformation capacity. The moment connection and SFRS ductility are closely linked, as a capacity for connection rotational ductility is necessary for system ductility; the former is usually much higher in numerical terms than the latter, and is also, in most cases, the highest of all types of ductility (Chen & Popovski, 2020a).

Moment connections need to minimise the initial slip and provide adequate stiffness during the elastic response. This is especially important for tall timber buildings, whose design is usually governed by the wind serviceability limit state. In these cases, connections with inadequate elastic stiffness can govern the overall design under lateral loads. Regardless of the building height, excessive elastic deformations can lead to unintended load paths in the structure, which may violate the stability limit state.

#### 7.2.3.4.2 Analytical Methods

As with braced timber frames, there are no specific analytical models for moment timber frames, especially ones that account for the bending stiffness of the beam-column connections. However, software such as MATLAB can use the matrix method to analyse the forces and deflection of the moment frames (Chandrasekaran, 2019). Given the availability of general-purpose FE software and design-oriented structural analysis software, the FE methods discussed below (Section 7.2.3.4.3) are the best option for analysing moment timber frames, though one can also develop other analytical models that apply some considerations discussed in Section 7.2.3.4.3.

#### 7.2.3.4.3 FE Methods

The beams and columns in moment frames typically follow capacity design principles to avoid inelastic effects, such as element shear failure, bending failure, and element instability due to local or lateral-torsional buckling. Inelastic deformations should occur primarily in the beam-column connections. The modelling of beams and columns commonly involves beam elements with linear elastic mechanical properties. While the columns are typically pinned to the ground, the beam-column connections are modelled using multiple spring sets, each composed of a rotational spring ($K_\theta$) for the bending resistance, a horizontal spring ($K_H$) for the axial resistance, and a vertical spring ($K_V$) for the shear resistance, as illustrated in Figure 48(a). Usually, it is safe to omit the two axial degrees of freedom (DOF) and focus entirely on the rotational DOF with a single spring, as shown in Figure 48(b). In other cases, one can express the rotational DOF as coupled axial springs ($K_T$ and $K_B$), as seen in Figure 48(c). For linear analyses, stiffness is the only input for the spring models; for nonlinear analyses, spring models have to reproduce the backbone curves or hysteresis loops of connections. More information regarding the backbone curve and hysteresis loops models appears in Chapter 7.1. For detailed FE models of wood-based components, one should adopt a specific material model of wood that can represent its anisotropic behaviour and predict various failure modes, such as Wood$^{S}$ (Chen et al., 2011) or Wood$^{ST}$ (Chen et al., 2020); see Chapter 4.1.

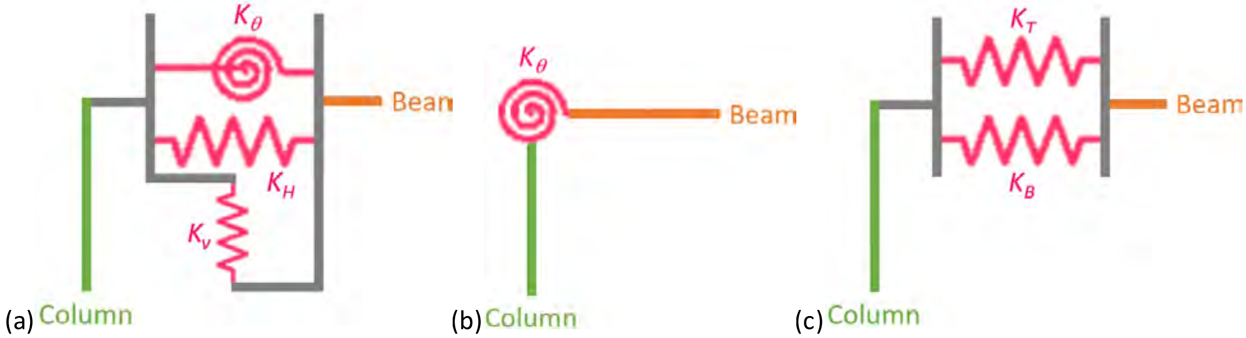


**Figure 48. Models for beam-column connections: (a) multiple spring set; (b) single spring; (c) coupled springs**

## 7.2.4 Additional Modelling Considerations

### *7.2.4.1 Nonstructural Elements*

Nonstructural components are often ignored when modelling structural systems; however, there are cases where they should be considered.

The last few cycles of building codes have had increasing requirements for the performance of nonstructural (secondary) components. There is a long history of such responsibilities being delegated to secondary (supporting) structural engineers, leaving these components forgotten or disorganised. However, the primary structural engineers of record now bear more responsibility for addressing this issue. This is primarily related to the seismic restraint of ceiling-hung mechanical and electrical services: nonstructural components falling from ceilings are a key cause of harm to building occupants in a seismic event.

Also, nonstructural partition wall and façade elements add stiffness to the SFRS and decrease a building's fundamental period (Chen et al., 2016; FEMA, 2012; Lafontaine et al., 2017; Niederwestberg et al., 2021). In addition to the stiffness, these components can also impact the damping properties of a building. The stiffness of the partition walls and façade elements is quite hard to quantify, so it is common practice to ignore them when designing an SFRS. However, the design community generally understands that partition walls and façades can impact the building period, especially for long buildings with lots of them in one direction. Chen et al. (2016) and FEMA (2012) have proposed specific methods to include the contributions of nonstructural walls. In addition, one should carefully consider the damping value assigned when reviewing dynamic wind-induced vibrations for a serviceability limit state, particularly in taller timber buildings; this can control the design of the SFRS. Research and monitoring are underway to determine the actual, in-situ fundamental period and damping values of built mass timber structures through Ambient Vibration Testing (service wind loads) with accelerometers. This will hopefully clarify the reasons for the differences between structural models and in-situ building performance.

### *7.2.4.2 Structural Non-SFRS elements*

It is critical to consider structural components that resist gravity loads, such as mass timber panels, glulam beams, glulam columns, and all their associated connections, when designing an SFRS. Review gravity components for interstorey drift compatibility, so that the members themselves, and more specifically their connections, can handle imparted rotations due to the overall building interstorey drift while maintaining their gravity load-carrying capacity under any relevant load case. This requirement is clearly laid out in the 2020 NBCC (NRC, 2022), Clause 4.1.8.3.5: 'all structural framing elements not considered to be part of the SFRS must be investigated and shown to behave elastically or to have sufficient nonlinear capacity to support their gravity loads while undergoing earthquake induced deformations'.

In addition to maintaining their gravity load-carrying capacity, in some cases, beam-to-column connections which should be pinned can have significant rotational capacity—something the designers may need to consider. For instance, if a beam-to-column connection with some nominal rotational capacity is modelled as a spring, it can engage some modest moment frame behaviour, particularly in longer frames. This moment frame behaviour can in turn reduce the modal periods of the global structure, and perhaps even the demands within the primary SFRS components. This phenomenon can impact the—quite important—accuracy of the design force within the 'fuse' component, and the 2020 NBCC (NRC, 2022), Clause 4.1.8.3.7, clearly lays out the requirement to review it:

> stiffness imparted to the structure from elements not part of the SFRS, other than those described in sentence (6) [Walls], shall not be used to resist earthquake deflections, but shall be accounted for… a) in calculating the period … b) in determining the irregularity of the structure … and c), in designing the SFRS if inclusion of the elements not part of the SFRS in the analysis has an adverse effect on the SFRS.

In practice, designers often ignore this phenomenon of secondary stiffness added by the gravity load-resisting frame or fail to give it the proper attention. It is certainly important to consider when heavy beam-end connections have moment capacity and, in turn, can alter the lateral demand in the primary SFRS. While this may seem onerous to consider, there is certainly precedent for such a check in standard Canadian and US structural engineering practice. For example, there are similar provisions in the concrete material standard, CSA A23.3-19 (CSA, 2019a), under Clause 21.11, which outlines the requirements for 'Members Not Considered Part of the Seismic-Force-Resting-System Rd=1.5, 2.0, 2.5, 3.5, or 4.0)'. Clause 21.11.3 outlines requirements for gravity load-resisting frames, and Clause 21.11.3.4 outlines requirements for slab-to-column connections. Some primary requirements are related to the aspect ratios of members, ensuring they do not attract too much load from the primary SFRS components, and to the ductility requirements in detailing, to avoid brittle failures in these gravity load-resisting components. There is very little commentary on this issue in the current version of CSA O86-19 (CSA, 2019b). Clarity must be added in CSA O86, to bring it in line with the NBCC provisions on how to explicitly consider this issue in the modelling and design of timber components and connections.

### *7.2.4.3 Diaphragm Stiffness Effects*

For more detailed information on the modelling of various diaphragm effects, see Chapter 6.2. The structural engineering community has long discussed the complex issue of the stiffness of mass timber diaphragms. The assumptions underlying the modelling of the diaphragm can drastically impact the vertical SFRS components, as they directly affect the distribution of forces. For modelling/analysis purposes, the options are essentially as follows:

- Option 1: Fully Flexible
- Option 2: Semirigid Shells
- Option 3: Fully Rigid Shells
- Option 4: Enveloped Flexible and Rigid
- Option 5: Enveloped Semirigid and Rigid
- Option 6: Semirigid Shells with Detailed Modelling of Splines

Unfortunately, the choice of modelling software will constrain many of these approaches.

Option 1, the fully flexible approach, assumes that the forces are based on tributary area. This would apply to most light wood-frame diaphragms sheathed with plywood or OSB, including those with sheathing over NLT, DLT, or GLT decks. The latter diaphragms should be considered 'blocked'.

For large mass timber panels with higher in-plane shear capacity, such as those with CLT, MPP, and TCC, Option 5 often provides a pragmatic approach with engineering judgement. The idea is to model the diaphragms first as rigid and then as semirigid, giving the appropriate EA and GA values to the homogenous membrane surface, and then to take an envelope of the forces imparted into the vertical SFRS components. This approach fails to consider the yielding of the fasteners in the splines, but it is very efficient from a modelling perspective because it uses one homogenous membrane or shell element, as shown in Figure 49 (Breneman et al., 2016).

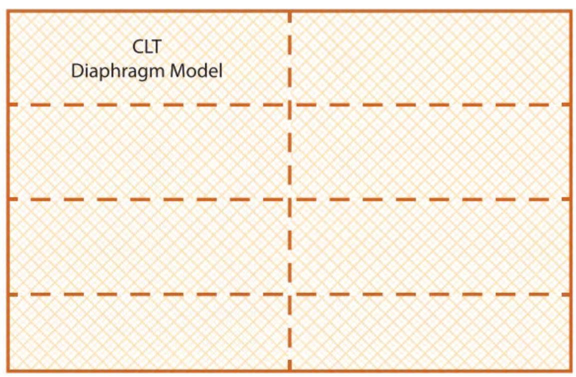


**Figure 49. Homogeneous diaphragm surface model without springs**

Option 6 (Figure 50) is perhaps the most accurate, but can be difficult to use in a full-scale model. Its use also depends on the choice of modelling software. Breneman et al. (2016) provide an overview of several different methods for modelling CLT diaphragms. Utilizing in-plane springs at the spline locations is perhaps the most reasonable choice, especially when using the Dlubal RFEM software for lateral analysis. See Chapter 6.2 for a more detailed discussion of the modelling of timber diaphragms.

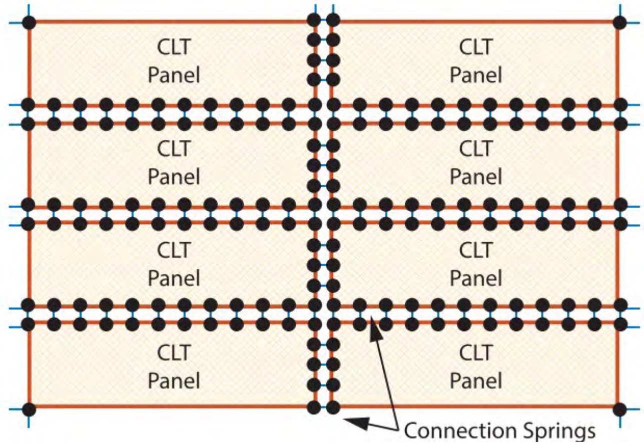


**Figure 50. Diaphragm surface model with panel delineation and line-type springs**

When linear line-type springs represent the stiffness of CLT spline, CLT-to-steel drag, or CLT-to-chord connections, it is important to specifically review each connection. One method for determining the stiffnesses of these connections is to use the slip information for screwed connections in Eurocode 5 (EN 1995-1-1:2004+A1), as described in clause 7 (CEN, 2004), which determines the stiffness of the connection $K_{ser}$ based on the density of the timber material $\rho_m$ and the diameter of the fastener d, as shown in Equation 1:

$$K_{ser} = \rho_m^{1.5}\, d/23 \qquad [1]$$

One should define the line springs relative to the panel's local axes, in the same locations where the flexural hinge or release will be defined. Figure 51 shows an example RFEM dialog box.

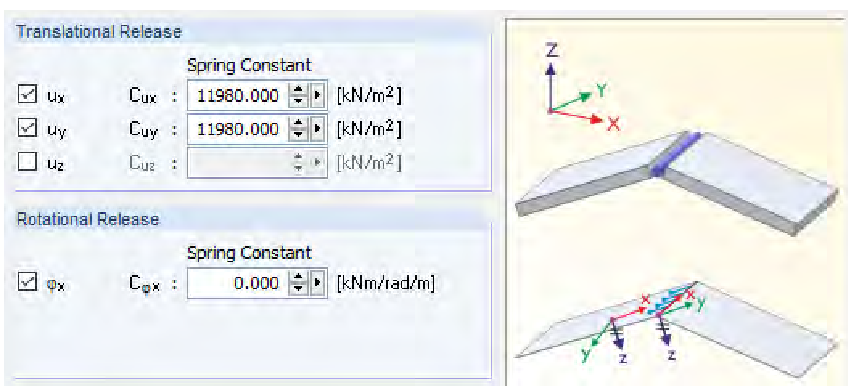


**Figure 51. RFEM line spring element input**

Finally, note that there has been much debate on this topic, particularly for the design of CLT diaphragms. New, simplified guidance on the issue appears in the updated *2021 Special Provisions for the Design of Wind and Seismic (SPDWS) with Commentary* (AWC, 2021). Section 4.5 of the SPDWS offers a simplified approach with a nominal shear capacity (kN/m or kip/ft) for the diaphragm that considers dowel-type fastener connections between the CLT panels. These fasteners require ductile failure behaviour. The SPDWS also states that wood elements, steel drags, and chord members are to be designed for 2.0 times the forces induced from design loads for capacity protection. These provisions however do not clarify how to model the diaphragm. ASCE-7-16 (ASCE, 2016) and IBC 2021 (ICC, 2021) provide recommendations on modelling, but essentially refer to engineering mechanics.

#### *7.2.4.4 Supports and Foundation Effects*

A restraint is a limit placed on the movement corresponding to a specific DOF of a model, in relation to the reference system. For a fixed restraint, the movement is set to zero, whereas a spring restraint normally has a linear elastic spring connection to the fixed reference system. A reaction force corresponds to each restrained DOF in the structure. These reaction forces must at least form a statically determinate set. Conventional restraints include horizontal rollers, pins, fixed/rigid, vertical rollers (nonrotation, at axis of symmetry), and translational and rotational springs. Neglecting fixity where there is a degree of restraint will provide a conservative estimate of the deformation and internal forces. Friction in the roller and pin supports can generate some forces (induce partial restraint), even if the supports are real pins or rollers.

The two main types of 'ground' that the models offer are soil and rock. The model of a structure is more likely to be realistic if it neglects the deformation of a rock support than if it neglects the effect of a soil support. Soil tends to be nonhomogeneous, with potentially time-dependent mechanical properties. Its properties are also dependent on the water content and are nonlinear in relation to stress and strain. To address these features requires advanced analysis outside the scope of this document. Taking into account the structure and the soil in a single analysis is known as conducting an analysis that includes soil-structure interaction properties.

There are four basic ways of defining the supports for a structure:

- Support fixity model – this ignores deformations of the ground and shows the nodes for the structure that are in contact with the ground fixed restraints.
- Winkler model – this models the ground using linear elastic springs at the structure-soil interface. The springs are not coupled, i.e., when one spring deforms, the other springs are not affected by shear transfer in the ground.
- Half space model – this models the ground using coupled springs at the structure-soil interface, i.e., it considers shear transfer in the ground.
- Element model for the ground – this model the ground as finite elements with fixities at distances from the structure.

While 'garbage in, garbage out' needs to be avoided in soil-structure interaction modelling, an approximate model (such as the Winkler model) may be better than no model at all.

### 7.2.5 Summary

This chapter introduces key modelling considerations for gravity load-resisting systems. It also discusses the behaviour and mechanism of specific mass timber lateral load-resisting systems, i.e., platform- and balloon-type shear walls, braced frames, and moment frames. It provides analytical models and advanced and practical FE models, accompanied by corresponding recommendations and considerations. Finally, Appendix A will briefly introduce various mass timber products. The information presented in this chapter is intended to help practising engineers and researchers become better acquainted with the modelling of mass timber structures.

## 7.2.6 References


Abrahamsen, R. (2018). Mjøstårnet – 18 storey timber building completed. *Internationales Holzbau-Forum IHF 2018*. https://www.forum-holzbau.com/pdf/32_IHF2018_Abrahamsen.pdf

American Institute of Steel Construction (AISC). (2016). *Seismic provisions for structural steel buildings* (ANSI/AISC 341-16).

American Society of Civil Engineers (ASCE). (2016). *Minimum design loads and associated criteria for buildings and other structures* (ASCE/SEI 7-16).

American Wood Council (AWC). (2021). *Special design provisions for wind and seismic with commentary* (ANSI/AWC SDPWS-2021).

ANSI & APA. (2019). *Standard for performance-rated cross-laminated timber* (ANSI/APA PRG 320-2019).

Blass, H. J., & Fellmoser, P. (2004). *Design of solid wood panels with cross layers*.

Blass, H., & Schädle, P. (2011). Ductility aspects of reinforced and non-reinforced timber joints. *Engineering Structures, 33*(11), 3018–3026.

Blomgren, H.-E., Koppitz, J.-P., Valdés, A., & Ko, E. (2016). *The heavy timber buckling-restrained braced frame as a solution for commercial buildings in regions of high seismicity* [Conference presentation]. World Conference on Timber Engineering, Vienna, Austria.

Branco, J. M., & Neves, L. A. C. (2011). Robustness of timber structures in seismic areas. *Engineering Structures, 33*(11), 3099–3105.

Breneman, S., McDonnell, E., & Zimmerman, R. (2016). An approach to CLT diaphragm modelling for seismic design with application to a US high-rise project. In J. Eberhardsteiner, W. Winter, A. Fadai, & M. Pöll. (Eds.), *WCTE 2016 e-book: containing all full papers submitted to the World Conference on Timber Engineering (WCTE 2016), August 22–25, 2016, Vienna, Austria*. TU Verlag Wien. https://resolver.obvsg.at/urn:nbn:at:at-ubtuw:3-2204

Bruneau, M., Uang, C.-M., & Sabelli, R. (2011). *Ductile design of steel structures* (2nd ed.). McGraw-Hill.

Buchanan, A. H. & Fairweather R. H. (1993). Seismic design of glulam structures, *Bulletin of the New Zealand National Society for Earthquake Engineering*, *26*(4), 415–436. http://dx.doi.org/10.5459/bnzsee.26.4.415-436

Canadian Standards Association (CSA). (2016). *Structural glued-laminated timber* (CAN/CSA-O122-16).

Canadian Standards Association (CSA). (2019a). *Design of concrete structures* (CSA A23.3:19).

Canadian Standards Association (CSA). (2019b). *Engineering design in wood* (CSA O86:19).

Canadian Wood Council (CWC). (2020). WoodWorks Sizer (Version 2020, v. 11).

Casagrande, D., Doudak, G., Mauro, L., & Polastri, A. (2018). Analytical approach to establishing the elastic behavior of multipanel CLT shear walls subjected to lateral loads. *Journal of Structural Engineering, 144*(2), Article 04017193. https://doi.org/10.1061/(ASCE)ST.1943-541X.0001948

Casagrande, D., Rossi, S., Sartori, T., & Tomasi, R. (2016). Proposal of an analytical procedure and a simplified numerical model for elastic response of single-storey timber shear-walls. *Construction and Building Materials, 102*(2), 1101–1112. https://doi.org/10.1016/j.conbuildmat.2014.12.114

Chandrasekaran, S. (2019). *Advanced structural analysis with MATLAB*. CRC Press.

Chen, Z., & Chui, Y.-H. (2017). Lateral load-resisting system using mass timber panel for high-rise buildings. *Frontiers in Built Environment, 3*(40). https://doi.org/10.3389/fbuil.2017.00040

Chen, Z., Chui, Y.-H., Doudak, G., & Nott, A. (2016). Contribution of type-X gypsum wall board to the racking performance of light-frame wood shear walls. *Journal of Structural Engineering, 142*(5), Article 04016008. https://doi.org/10.1061/(ASCE)ST.1943-541X.0001468

Chen, Z., Chui, Y.-H., & Popovski, M. (2015). Chapter 2 – Development of lateral load resisting system. In Y. H. Chui (Ed.), *Application of analysis tools from NEWBuildS research network in design of a high-rise wood building* (pp. 15–36). NEWBuildS and FPInnovations. https://www.bcfii.ca/wp-content/uploads/2021/02/fii415-2014-15-newbuilds-application-of-analysis-tools-in-design-of-high-rise-wood-building-1.pdf

Chen, Z., Cuerrier-Auclair, S., & Popovski, M. (2018). *Advanced wood-based solutions for mid-rise and high-rise construction: Analytical prediction models for balloon-type CLT shear walls* (Project 301012205). FPInnovations. https://library.fpinnovations.ca/en/permalink/fpipub52680

Chen, Z., Ni, C., Dagenais, C., & Kuan, S. (2020). Wood$^{ST}$: A temperature-dependent plastic-damage constitutive model used for numerical simulation of wood-based materials and connections. *Journal of Structural Engineering, 146*(3), Article 04019225. https://doi.org/10.1061/(ASCE)ST.1943-541X.0002524

Chen, Z., & Popovski, M. (2020a). Connection and system ductility relationship for braced timber frames. *Journal of Structural Engineering, 146*(12), Article 04020257. https://doi.org/10.1061/(ASCE)ST.1943-541X.0002839

Chen, Z., & Popovski, M. (2020b). *Expanding wood use towards 2025: Seismic performance of braced mass timber frames, year 2*. FPInnovations. https://library.fpinnovations.ca/en/permalink/fpipub52921

Chen, Z., & Popovski, M. (2020c). Mechanics-based analytical models for balloon-type cross-laminated timber (CLT) shear walls under lateral loads. *Engineering Structures, 208*, Article 109916. https://doi.org/10.1016/j.engstruct.2019.109916

Chen, Z., & Popovski, M. (2021a). *Expanding wood use towards 2025: Performance and draft design guidelines for braced timber frames under lateral loads* (Project 301014059). FPInnovations.

Chen, Z., & Popovski, M. (2021b). *Expanding wood use towards 2025: Seismic performance of balloon mass timber wall, year 2* (Project 301014059). FPInnovations.

Chen, Z., & Popovski, M. (2021c). *Modelling of mass timber seismic force resisting systems* (Infonote no. 06). FPInnovations.

Chen, Z., & Popovski, M. (2021d). *Seismic performance of CLT balloon walls made of larch in mid-rise and high-rise construction in Korea, Year 1* (Project 301014346). FPInnovations.

Chen, Z., Popovski, M., & Symons, P. (2019). *Solutions for upper mid-rise and high-rise mass timber construction: Seismic performance of braced mass timber frames – Year 1* (Project 301013067). FPInnovations. https://library.fpinnovations.ca/en/permalink/fpipub52818

Chen, Z., Zhu, E., & Pan, J. (2011). Numerical simulation of wood mechanical properties under complex state of stress. *Chinese Journal of Computational Mechanics, 28*(4), 629–634, 640.

Christovasilis, I. P., Riparbelli, L., Rinaldin, G., & Tamagnone, G. (2020). Methods for practice-oriented linear analysis in seismic design of Cross Laminated Timber buildings. *Soil Dynamics and Earthquake Engineering, 128*, Article 105869. https://doi.org/10.1016/j.soildyn.2019.105869

Dlubal Software. (2021). RFEM 5. https://www.dlubal.com/en-US/downloads-and-information/documents/online-manuals/rfem-5/01/01

Dong, W., Li, M., Lee, C, & MacRae, G. (2021). Numerical modelling of glulam frames with buckling restrained braces. *Engineering Structures*, 239, Article 112338. https://doi.org/10.1016/j.engstruct.2021.112338

European Committee for Standardization (CEN). (2004). *Eurocode 5: Design of timber structures – Part 1-2: General rules – structural fire design*. (Eurocode Standard EN 1995-1-2).

European Committee for Standardization (CEN). (2018). *Eurocode 5: Design of timber structures - Part 1-1: General - Common rules and rules for buildings.* (Eurocode Standard EN 1995-1-1)

Federal Emergency Management Agency (FEMA). (2012). *Seismic evaluation and retrofit of multi-unit wood-frame buildings with weak first stories* (FEMA P807). https://www.loc.gov/item/2012515987/

Flatscher, G., & Schickhofer, G. (2016). *Displacement-based determination of laterally loaded cross laminated timber (CLT) wall systems* [Conference presentation]. 3rd International Network on Timber Engineering Research (INTER) Meeting, Graz, Austria.

Follesa, M., Christovasilis, I., Vassallo, D., Fragiacomo, M., & Ceccotti, A. (2013). Seismic design of multi-storey cross laminated timber buildings according to Eurocode 8. *Ingegneria Sismica, 30*(4), 27–53.

Follesa, M., Fragiacomo, M., Casagrande, D., Tomasi, R., Piazza, M., Vassallo, D., Canetti, D., & Rossi, S. (2018). The new provisions for the seismic design of timber buildings in Europe. *Engineering Structures, 168*, 736–747. https://doi.org/10.1016/j.engstruct.2018.04.090

Fragiacomo, M., & Batchelar, M. (2012). Timber frame moment joints with glued-in steel rods. I: Design. *Journal of Structural Engineering*, *138*(6), 789–801. https://doi.org/10.1061/(ASCE)ST.1943-541X.0000419

Fujimoto, M., Aoyagi, T., Ukai, K., Wada, A., & Saito, K. (1972). Structural characteristics of eccentric K-braced frames. *Transactions of the Architectural Institute of Japan, 195*(5), 39–49. https://doi.org/10.3130/aijsaxx.195.0_39

Gavric, I., Fragiacomo, M., & Ceccotti, A. (2015). Cyclic behavior of CLT wall systems: Experimental tests and analytical prediction models. *Journal of Structural Engineering, 141*(11), Article 04015034. https://doi.org/10.1061/(ASCE)ST.1943-541X.0001246

Gavric, I., & Popovski, M. (2014). *Design models for CLT shearwalls and assemblies based on connection properties* [Conference presentation]. 47th Meeting – INTER (International Network on Timber Engineering), Bath, UK. https://doi.org/10.13140/RG.2.1.3845.0728

Gohlich, R. J. (2015). *Development of an innovative hybrid timber-steel moment-resisting frame for seismic-resistant heavy timber structures* [Masters' thesis, Carleton University]. Carleton University Research Virtual Environment (CURVE). https://doi.org/10.22215/etd/2016-11310

Gohlich, R., Erochko, J., & Woods, J. E. (2018). Experimental testing and numerical modelling of a heavy timber moment-resisting frame with ductile steel links. *Earthquake Engineering & Structural Dynamics, 47*(6), 1460–1477.

Hashemi, A., Zarnani, P., Masoudnia, R., & Quenneville, P. (2018). Experimental testing of rocking cross-laminated timber walls with resilient slip friction joints. *Journal of Structural Engineering, 144*(1), Article 04017180. https://doi.org/10.1061/(ASCE)ST.1943-541X.0001931

Holt, R., Luthi, T., & Dickof, C. (Eds.). (2017). *Nail-laminated timber: U.S. design & construction guide v 1.0*. Binational Softwood Lumber Council (BSLC).

Hummel, J., Seim, W., & Otto, S. (2016). Steifigkeit und Eigenfrequenzen im mehrgeschossigen Holzbau [Stiffness and natural frequencies in multi-storey timber construction]. *Bautechnik, 93*(11), 781–794. https://doi.org/10.1002/bate.201500105

International Code Council (ICC). (2021). *International building code* (ICC IBC-2021).

Izzi, M., Polastri, A., & Fragiacomo, M. (2018). Modelling the mechanical behaviour of typical wall-to-floor connection systems for cross-laminated timber structures. *Engineering Structures, 162*, 270–282. https://doi.org/10.1016/j.engstruct.2018.02.045

Karacabeyli, E., & Gagnon, S. (Eds.) (2019). *Canadian CLT Handbook*. FPInnovations.

Kasal, B., Guindos, P., Polocoser, T., Heiduschke, A., Urushadze, S., & Pospisil, S. (2014). Heavy laminated timber frames with rigid three-dimensional beam-to-column connections, *Journal of Performance of Constructed Facilities*, *28*(6), Article A4014014. https://doi.org/10.1061/(ASCE)CF.1943-5509.0000594

Lafontaine, A., Chen, Z., Doudak, G., & Chui, Y. H. (2017). Lateral behavior of light wood-frame shear walls with gypsum wall board. *Journal of Structural Engineering, 143*(8), Article 04017069. https://doi.org/10.1061/(ASCE)ST.1943-541X.0001798

Leijten, A. J. M., Ruxton, S., Prion. H., & Lam, F. (2006). Reversed-cyclic behavior of a novel heavy timber tube connection. *Journal of Structural Engineering, 132*(8):1314–1319. https://doi.org/10.1061/(ASCE)0733-9445(2006)132:8(1314)

Lukacs, I., Björnfot, A., & Tomasi, R. (2019). Strength and stiffness of cross-laminated timber (CLT) shear walls: State-of-the-art of analytical approaches. *Engineering Structures, 178*, 136–147. https://doi.org/10.1016/j.engstruct.2018.05.126

MacRae, G. (2010). *The development and use of the continuous column concept* [Conference presentation]. Joint Proceeding of the 7th International Conference on Urban Earthquake Engineering & 5th International Conference on Earthquake Engineering, Tokyo, Japan.

MacRae, G. A., Kimura, Y., & Roeder, C. (2004). Effect of column stiffness on braced frame seismic behavior. *Journal of Structural Engineering, 130*(3), 381–391. https://doi.org/10.1061/(ASCE)0733-9445(2004)130:3(381)

Masroor, M., Doudak, G., & Casagrande, D. (2020). The effect of bi-axial behaviour of mechanical anchors on the lateral response of multi-panel CLT shearwalls. *Engineering Structures, 224*, Article 111202. https://doi.org/10.1016/j.engstruct.2020.111202

Mestar, M., Doudak, G., Caola, M., & Casagrande, D. (2020). Equivalent-frame model for elastic behaviour of cross-laminated timber walls with openings. *Proceedings of the Institution of Civil Engineers - Structures and Buildings, 173*(5), 363–378. https://doi.org/10.1680/jstbu.19.00057

Moosbrugger, T., Guggenberger, W., & Bogensperger, T. (2006). *Cross-laminated timber wall segments under homogeneous shear - with and without openings* [Conference presentation]. 9th World Conference on Timber Engineering, Portland, Oregon, United States.

Murphy, C., Pantelides, C. P., Blomgren, H.-E., & Rammer, D. (2021). Development of timber buckling restrained brace for mass timber-braced frames. *Journal of Structural Engineering, 147*(5), Article 04021050. https://doi.org/10.1061/(ASCE)ST.1943-541X.0002996

National Institute of Standards and Technology (NIST). (2013). *Seismic design of steel special concentrically braced frame systems: A guide for practicing engineers* (GCR 13-917-24).

National Institute of Standards and Technology (NIST). (2015). *Seismic design of steel buckling-restrained braced frames: A guide for practicing engineers* (GCR 15-917-34).

Niederwestberg, J., Daneshvar, H., Chui, Y. H., & Chen, Z. (2021). Contribution of partition walls in lateral load-resisting systems of low-rise light wood frame buildings. *Journal of Structural Engineering, 147*(4), Article 04021010. https://doi.org/10.1061/(ASCE)ST.1943-541X.0002960

Nolet, V., Casagrande, D., & Doudak, G. (2019). Multipanel CLT shearwalls: an analytical methodology to predict the elastic-plastic behaviour. *Engineering Structures, 179*, 640–654. https://doi.org/10.1016/j.engstruct.2018.11.017

National Research Council (NRC). (2022). *National Building Code of Canada 2020*.

Pei, S., van de Lindt, J. W., & Popovski, M. (2013). Approximate R-factor for cross-laminated timber walls in multistory buildings. *Journal of Architectural Engineering, 19*(4), 245-255. https://doi.org/10.1061/(ASCE)AE.1943-5568.0000117

Polastri, A., Loss, C., Pozza, L., & Smith, I. (2016). *CLT buildings braced with cores and additional shear walls* [Conference presentation]. 14th World Conference on Timber Engineering (14WCTE), Vienna, Austria.

Popovski, M. (2004). *Structural systems with riveted connections for non-residential buildings.* (Project 3279). Forintek Canada Corp.

Popovski, M., Gagnon, S., Mohammad, M., & Chen, Z. (2019). Chapter 3 – Structural design of CLT elements. In E. Karacabeyli & S. Gagnon (Eds.), *CLT Handbook (2019 edition)*. FPInnovations.

Popovski, M., Schneider, J., & Schweinsteiger, M. (2010). *Lateral load resistance of cross-laminated wood panels* [Conference presentation]. 11th World Conference on Timber Engineering, Riva del Garda, Italy.

Pozza, L., Savoia, M., Franco, L., Saetta, A., & Talledo, D. (2017). Effect of different modelling approaches on the prediction of the seismic response of multi-storey CLT buildings. *The International Journal of Computational Methods and Experimental Measurements, 5*(6), 953–965. https://doi.org/10.2495/CMEM-V5-N6-953-965

Pozza, L., & Scotta, R. (2015). Influence of wall assembly on behaviour of cross-laminated timber buildings. *Proceedings of the Institution of Civil Engineers - Structures and Buildings, 168*(4), 275–286. https://doi.org/10.1680/stbu.13.00081

Pozza, L., Scotta, R., Trutalli, D., & Polastri, A. (2015). Behaviour factor for innovative massive timber shear walls. *Bulletin of Earthquake Engineering, 13*(11), 3449–3469. https://doi.org/10.1007/s10518-015-9765-7

Reynolds, T., Foster, R., Bregulla, J., Chang, W.-S., Harris, R., & Ramage, M. (2017). Lateral-load resistance of cross-laminated timber shear walls. *Journal of Structural Engineering, 143*(12), Article 06017006. https://doi.org/10.1061/(ASCE)ST.1943-541X.0001912

Rinaldi, V., Casagrande, D., Cimini, C., Follesa, M., & Fragiacomo, M. (2021). An upgrade of existing practice-oriented FE design models for the seismic analysis of CLT buildings. *Soil Dynamics and Earthquake Engineering, 149*, Article 106802. https://doi.org/10.1016/j.soildyn.2021.106802

Rinaldi, V., Casagrande, D., Cimini, C., Follesa, M., Sciomenta, M., Spera, L., & Fragiacomo, M. (2021). *Simplified strategies for the numerical modelling of CLT buildings subjected to lateral loads* [Conference presentation]. World Conference on Timber Engineering, Santiago, Chile.

Rinaldin, G., Amadio, C., & Fragiacomo, M. (2013). A component approach for the hysteretic behaviour of connections in cross-laminated wooden structures. *Earthquake Engineering & Structural Dynamics, 42*(13), 2023–2042. https://doi.org/10.1002/eqe.2310

Rinaldin, G., & Fragiacomo, M. (2016). Non-linear simulation of shaking-table tests on 3- and 7-storey X-Lam timber buildings. *Engineering Structures*, 113, 133-148. https://doi.org/10.1016/j.engstruct.2016.01.055

Ringhofer, A. (2010). *Erdbebennormung in Europa und deren Anwendung auf Wohnbauten in Holz-Massivbauweise* [Seismic standardisation in Europe and their application to residential buildings erected in solid timber construction] [Master's Thesis, Graz University of Technology].

Sandoli, A., D'Ambra, C., Ceraldi, C., Calderoni, B., & Prota, A. (2021). Sustainable cross-laminated timber structures in a seismic area: Overview and future trends. *Applied Sciences, 11*(5), Article 2078. https://doi.org/10.3390/app11052078

Schickhofer, G., Bogensperger, T., Moosbrugger, T., Augustin, M., Blaß, H., & Ebner, H. (2010). *BSPhandbuch: Holz-Massivbauweise in Brettsperrholz: Nachweise auf Basis des neuen europäischen Normenkonzepts* [CLT manual: Solid wood construction in cross laminated timber: Evidence based on the new European standards]. Verlag der Technischen Universität Graz.

Schickhofer, G., & Ringhofer, A. (2012). *The seismic behaviour of buildings erected in solid timber construction: Seismic design according to EN 1998 for a 5-storey reference building in CLT*. Institute of Timber Engineering and Wood Technology, Graz University of Technology.

Shahnewaz, M., Dickof, C., & Tannert, T. (2021). Seismic behavior of balloon frame CLT shear walls with different ledgers. *Journal of Structural Engineering, 147*(9), Article 04021137. https://doi.org/10.1061/(ASCE)ST.1943-541X.0003106

Tamagnone, G., Rinaldin, G., & Fragiacomo, M. (2018). A novel method for non-linear design of CLT wall systems. *Engineering Structures, 167*, 760–771. https://doi.org/10.1016/j.engstruct.2017.09.010

Tanabashi, R., Naneta, K., & Ishida, T. (1974). *On the rigidity and ductility of steel bracing assemblage* [Conference presentation]. 5th World Conference on Earthquake Engineering, Rome, Italy.

Tomasi, R. (2014). CLT course at 'FPS COST Action FP1004 – Enhance mechanical properties of timber, engineered wood products and timber structures'. CLT Training School, University of Trento April 15–17, 2014.

Tran, D. K., & Jeong, G. Y. (2021). Effects of wood species, connection system, and wall-support interface type on cyclic behaviors of cross-laminated timber (CLT) walls under lateral loads. *Construction and Building Materials, 280*, Article 122450. https://doi.org/10.1016/j.conbuildmat.2021.122450

van Bakel, R., Rinaldin, G., Leijten, A. J. M., & Fragiacomo., M. (2017). Experimental–numerical investigation on the seismic behaviour of moment-resisting timber frames with densified veneer wood reinforced timber joints and expanded tube fasteners. *Earthquake Engineering and Structural Dynamics*, *46*(8), 1307–1324. https://doi.org/10.1002/eqe.2857

van de Lindt, J. W., Amini, M. O., Rammer, D., Line, P., Pei, S., & Popovski, M. (2020). Seismic performance factors for cross-laminated timber shear wall systems in the United States. *Journal of Structural Engineering, 146*(9), 04020172. https://doi.org/10.1061/(ASCE)ST.1943-541X.0002718

Vassallo, D., Follesa, M., & Fragiacomo, M. (2018). Seismic design of a six-storey CLT building in Italy. *Engineering Structures, 175*, 322–338. https://doi.org/10.1016/j.engstruct.2018.08.025

Wada, A., Qu, Z., Ito, H., Motoyui, S., Sakata, H., & Kasai, K. (2009). Seismic retrofit using rocking walls and steel dampers. In B. Goodno (Ed.), *Improving the Seismic Performance of Existing Buildings and Other Structures* (pp. 1010–1021).

Wallner-Novak, M., Pock, K., & Koppelhuber, J. (2013). *Brettsperrholz Bemessung* [Cross laminated timber dimensioning]. proHolz Austria.

WoodWorks – Wood Products Council. (2021). *U.S. Mass Timber Floor Vibration Design Guide*. https://www.woodworks.org/wp-content/uploads/wood_solution_paper-Mass-Timber-Floor-Vibration.pdf

# Appendix A – Mass Timber Products

## *A.1 Cross-Laminated Timber (CLT)*

CLT panels were developed in Europe in the early 1990s and are now considered the most versatile and robust product for use in mass timber buildings. CLT can be used for floor, roof, and wall panels. CLT panels comprise 2X stock that is laminated together in an alternating crosswise pattern, similar to plywood veneers. Typical species used in CLT include Spruce-Pine-Fir, Douglas Fir, or Black Spruce. Due to CLT's cross laminations, the panels afford significant in-plane shear capacity and can serve as diaphragms or shear walls in building lateral systems. In these cases, one must carefully detail panel-to-panel joints for in-plane shear transfer.

A number of fabrication plants in North America currently produce CLT panels to the ANSI/APA PRG-320 (ANSI & APA, 2019) standard. In-plane panel dimensions are generally quite stable due to the cross laminations, but the thickness of the panels remains susceptible to swelling and shrinkage. For buildings that load CLT perpendicular-to-grain over multiple stories, it is important to consider the shrinkage and compression that can occur through the depth of the panel as they accumulate over the height of the building.

CLT is a standardised product often used in a one-way decking capacity. However, it can also function as a two-way bending member. The most common use of CLT is for horizontal floor and roof panels, and it is also commonly used as a bearing wall or shear wall element.

## *A.2 Dowel-Laminated Timber (DLT)*

DLT is very similar to NLT, discussed below, with the key difference that the lam stock is often finger jointed and run through a shaper, creating a better refined and cleaner product. Also, wood dowels, rather than nails, hold together the vertical laminations. This leads to opportunities for acoustic baffle integration and profiling. The most standard use of DLT is for horizontal floor and roof panels, but it can also serve in bearing wall applications, or in shear wall applications when plywood is fastened to one face.

## *A.3 Glued Laminated Timber (glulam or GLT)*

**Post and Beam Glulam Members**

The industry has used glulam post and beam members for many years. Glulam components often pair with mass timber panelised components in timber structures. Glulam is a standardised product covered by the American National Standards Institute Standard for Glued Laminated Timber and by CSA-O122 (CSA, 2016).

**GLT Used as Panels**

Glulam beams can also be placed on the flat side with the lamination lines running vertical for use as floor and roof panels. Typical species used in glulam include Spruce-Pine-Fir, Douglas Fir, Black Spruce, or in special cases, Alaskan Yellow Cedar. Similar to NLT and DLT, plywood stitches the panels together and acts as a diaphragm. When used without sheathing, the diaphragm resistance should be determined based on the properties of the connectors between the GLT and the beams below. Most glulam suppliers can produce glulam beams for use as panels and ship them to site as a prefabricated product. Some can provide a fluted soffit, which can help with acoustics and provide a unique visual appearance.

GLT panels also require robust moisture protection during erection, as they are susceptible to swelling perpendicular-to-grain. One way to mitigate this is to add a ¼" gap between each 2' panel, leaving room for expansion and contraction throughout the construction phase and the first few drying seasons. GLT is a standardised, one-way panel system for use in horizontal floor and roof panels and, in the US, is covered by the ANSI/APA Standard A190.1 for Glued Laminated Timber (ANSI & APA, 2022).

### *A.4 Laminated Strand Lumber (LSL)*

LSL panels are a one-way system made from flaked wood strands with a length-to-thickness ratio of approximately 150. Combined with adhesive, the strands are oriented, formed into a large mat or billet, and pressed together. Typically, the billets are cut into smaller beams and rim-boards for light wood-frame construction, but they can also be left in their larger panel form.

Aspen is the fibre of choice for LSL panels among most larger North American suppliers. Plywood typically sheathes the panels, providing in-plane stiffness and shear resistance for lateral diaphragm loads. Although there is some in-plane member stiffness due to the semi-random orientation of the flakes, the material standards for diaphragm applications neither recommend nor recognise it. In-plane panel dimensions are generally stable due to the fibre orientation; however, as with CLT, the thickness of the panels remains susceptible to swelling and shrinkage.

### *A.5 Laminated Veneer Lumber (LVL)*

LVL panels are a one-way system of glued plywood veneers stacked in parallel: essentially, a thicker, single-direction plywood. Typically, the billets are cut into smaller beams for light wood-frame construction, but like LSL panels, they can also be left in their larger panel form.

Douglas Fir serves as the veneer in LVL panels. Many suppliers in North America can supply LVL beams and billets. Plywood typically sheathes the panels, providing in-plane stiffness for lateral diaphragm loads. The use of use LVL panels in diaphragm applications is not recommended, as the product is not cross-laminated. As with LSL, the in-plane panel dimensions are generally stable but the thickness of the panels remains susceptible to swelling and shrinkage. Some Canadian and European suppliers also laminate LVL beams on edge into panels, which exposes the end and edge grain of the veneers rather than the face grain, as in a typical exposed LVL billet. This technique offers a clean visual aesthetic and can produce a larger range of thicknesses.

### *A.6 Mass Plywood Panels (MPP)*

MPP panels are a veneer-based panel product fabricated in Oregon. Analogous to typical plywood, the veneers alternate to provide planar stability. However, most of the fibre is in one primary direction. Panels come in large billets of up to 12' x 60' and in various thicknesses. The most common use of MPP is for horizontal floor and roof panels, but as with CLT, MPP can also be used as a bearing wall or shear wall element. In-plane panel dimensions are generally very stable due to the fibre orientation, but as with CLT, the thickness of the panels remains susceptible to swelling and shrinkage.

### *A.7 Nail-Laminated Timber (NLT)*

NLT panels have been in use since the early 1900s. They are typically composed of 2X lumber stock, stood on edge and nailed together side by side, and are mostly used in floor applications (Holt et al., 2017). Spruce-Pine-

Fir and Douglas Fir are most common materials for NLT panels, but any wood species can be used for the lamination stock. Plywood sheathes the panels on the top, providing in-plane stiffness and shear resistance for lateral diaphragm loads. The panels can be prefabricated in a shop environment or nailed together on-site by a carpenter. Robust moisture protection during fabrication and erection is a must for NLT panels, as they are susceptible to swelling perpendicular-to-grain. To mitigate these potential swelling issues, a 2X lamination should be left out every 20 feet and reinstalled after the panels have acclimatised.

NLT is a nonstandardised, one-way panel system. Standards for the base material exist in the form of typical dimensional lumber grading rules. The most common use of NLT is for horizontal floor and roof panels. Less typically, NLT can also be used in bearing wall applications, or in shear wall applications when plywood is fastened to one face.

### *A.8 Parallel Strand Lumber (PSL)*

Similar to LSL and oriented strand lumber (OSL), PSL is made from flaked wood strands arranged parallel to the longitudinal axis of the member, with a length-to-thickness ratio of approximately 300. The wood strands in PSL are longer than those in LSL and OSL. Combined with an exterior, waterproof phenol-formaldehyde adhesive, the strands are oriented and formed into a large billet, then pressed together and cured using microwave radiation. PSL beams are available in thicknesses ranging from 68 mm to 178 mm, with a maximum depth of 457 mm. PSL columns are available in square or rectangular dimensions of 89 mm, 133 mm, and 178 mm. PSL elements can be long but transportation constraints usually limit them to 20 m.

PSL is a solid, highly predictable, uniform mass timber product because natural defects such as knots, slope of grain, and splits are dispersed throughout the material or removed altogether during the manufacturing process. Like the other Structural Composite Lumber products (LVL, LSL, and OSL), PSL offers predictable strength and stiffness and dimensional stability. Manufactured at a moisture content of 11%, PSL is less prone to shrinking, warping, cupping, bowing, and splitting. In modern mass timber buildings, it is mostly used in gravity-resisting elements such as beams and columns.

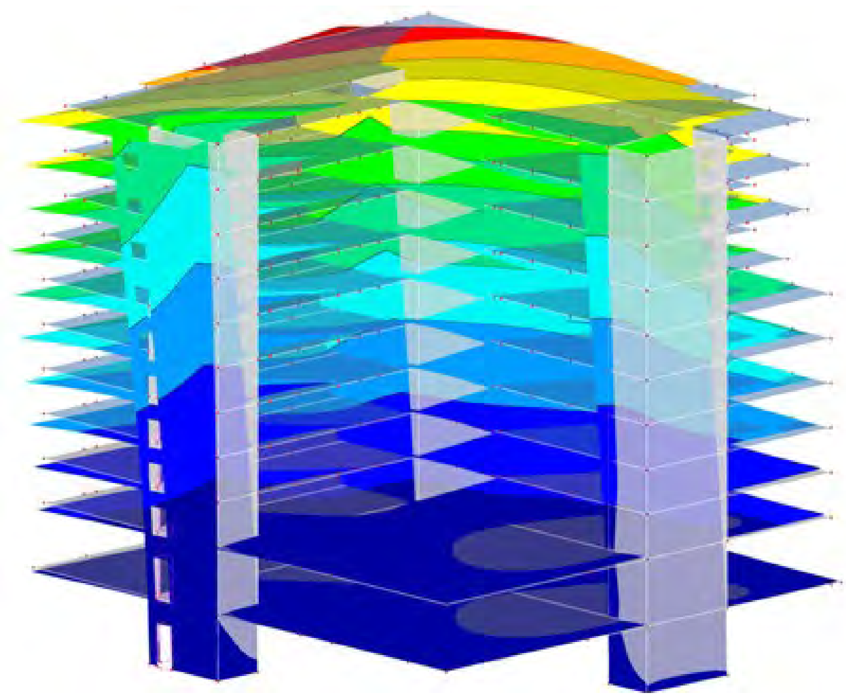

# CHAPTER 7.3

## Hybrid timber structures


**Authors**

Hercend Mpidi Bita

Robert Malczyk

Thomas Tannert

Dorian Tung

**Reviewers**

Cameron Ritchie

Hiroshi Isoda

# TABLE OF CONTENTS

## 7.3.1 Introduction

Innovative structural materials, connections, and components have allowed the potential extension of wood-based systems to high-rise construction (Karacabeyli & Lum, 2021; Popovski et al., 2019; Popovski et al., 2022). Recent research has led to the 'designing and building of tall timber structures, also in earthquake-prone regions, being part of regular timber engineering practice' (NRC, 2022). Therefore, low-value commodities in low-rise residential construction are no longer the dominant structural application for wood products, which are instead being used in large, tall residential, office, and commercial mixed-use buildings. These are also of high importance category, and both the 2020 National Building Code of Canada (NBCC; NRC, 2022) and ASCE-7 22 (ASCE, 2022) rank all of them as high-risk categories.

One solution with significant potential for the increased use of wood beyond previous limitations, e.g., building height, involves 'hybrid structures' that integrate wood with different materials (Chen et al., 2021; Tannert et al., 2018). Hybridisation is the process of combining two or more materials to form a system that makes use of the strength of each material and simultaneously overcomes their individual weaknesses. Novel structural solutions, which peak in multifunctional hybrid structures, balance architectural form, structural function, and building physics functionality. The hybrid design framework is also interesting for its ease of assembly, which results in reduced construction time and improved building physics performance. Engineers consider hybrid timber structural systems a cost-effective solution that maximises the application of individual structural material, e.g., mass timber, concrete, steel, and masonry, based on individual and collective structural performance, architectural and constructability advantages, and cost.

Hybridisation is possible at two levels: i) the component level, such as in glulam-steel columns (MTC Solutions, 2020) or timber-concrete-composite floors (Leach, 2018), and ii) the system level, which is the focus of this chapter. One major structural advantage of hybrid timber structures for seismic design is their lesser weight, which attracts lower seismic forces than a concrete structure since base shear is directly proportional to weight. However, since hybrid systems involve two or more materials, corresponding design procedures usually overlap multiple engineering standards, making design a challenge and requiring additional research effort (Fast & Jackson, 2017). The success of a hybrid structure relies on adequately addressing compatibility in deformation and stiffness. An example of the former is hybridising concrete lateral walls with timber gravity columns, where they deform differently under axial load. To address compatibility, decouple any unnecessary load interactions and avoid complex numerical models. An example of the latter is the case of hybridising concrete lateral walls with a timber diaphragm floor: with properly justified model stiffness for both walls and floor (calibrated against test data) and simple load transfer detail at the interface, the numerical model can both reasonably capture the behaviour of the hybrid timber structure and provide analysis force for design purposes.

This chapter introduces examples of hybrid structures and typical connection details, as well as special considerations for the design and analysis of such structures, as technical information in support of their adoption. Other chapters discuss the modelling of timber structures in detail, such as Chapters 7.1, 7.2, 7.4, and 7.5 for light wood-frame structures, mass timber structures, and timber structures with advanced seismic protection, long-span timber structures, respectively, and Chapter 6 for floor diaphragms; meanwhile, the modelling of structures using non-wood materials, though not the focus of this guide, is briefly discussed in Chapter 2.

## 7.3.2 Examples of Hybrid Buildings and Connections

The last decade has seen the investigation and construction of several hybrid timber structural systems in actual buildings (Quintana Gallo et al., 2021). A common application of hybrid timber structure is a mixed-use 'podium building' (Chen & Ni, 2020), with a residential or office wood structure built on top of a commercial or parking concrete (Figure 1[a]) or steel (Figure 1[b]) structure. In North America, the interface is known as podium slab or transfer slab, because the upper portion sits on a concrete or steel slab designed as a transfer floor. Typically, the upper, wood building is up to six storeys with a light wood frame. With recent code updates for mass timber construction, the upper part of the building can now reach up 12 storeys in Canada (NRC, 2022) and 18 in the USA (ICC, 2021). The lower part is typically two to three storeys above ground level.

(a)  (b) 

**Figure 1. UBC Brock Commons: (a) Concrete cores; (b) mass timber on concrete podium**

Tesfamariam et al. (2014) developed a lateral load-resisting system (LLRS) combining steel moment frames and cross-laminated timber (CLT) infill walls. They varied infill configurations to provide a parametric analysis for a fictitious case study building and performed nonlinear dynamic analyses to compute fragility curves. Green and Karsh (2012) proposed, and Zhang et al. (2017) experimentally and numerically investigated, a mass timber balloon-wall with steel link beams, dubbed 'Finding Forest Through Trees' (FFTT). One of the world's tallest hybrid timber buildings (https://www.ctbuh.org/mass-timber-data), the 18-storey Brock Commons in Vancouver, Canada, shown in Figure 2(a), comprises a cast-in-place concrete ground floor and two concrete elevator cores with CLT floors and glulam columns (CWC, 2017; Huber et al., 2020). The 17 storeys of mass timber superstructure carry all gravity loads, while the two concrete cores act as LLRSs. The 14-storey Treet in Bergen, Norway, uses braced glulam frames as the primary LLRS, with reinforced concrete topping slab and prefabricated wood modules (Mpidi Bita et al., 2018). The glulam trusses give the building the necessary stiffness; the independent CLT walls do not contribute to the building's lateral stability. Prefabricated modules are stacked up to four storeys high and do not connect to the surrounding LLRS (Chen et al., 2020). Levels 5 and 10, denoted 'power storeys', are strengthened glulam storeys topped with a prefabricated concrete slab. They connect to the façade trusses and do not rest on the building modules below. A very similar concept occurs in 'Mjøstårnet', the world's tallest timber building. The main load bearing consists of glulam trusses along the façades and internal columns and beams. CLT cores serve as the secondary load bearing for vertical circulation and do not contribute to the building's lateral stability. In contrast to Treet, Mjøstårnet has prefabricated floor and wall elements. The 4-storey ON5 in Vancouver, Canada, shown in Figure 2(b), uses a concrete core, masonry shear walls, and a concrete floor at the podium level, with CLT shear walls, steel moment frames, and CLT floors above.

(a)  (b) 

**Figure 2. Hybrid timber buildings: (a) Brock Commons during construction; (b) ON5 during construction**

#### *7.3.2.1 Load-Resisting Systems*

Gravity load-resisting systems (GLRSs) for hybrid timber structures are typically wood-based: i) post and beam with floor system, ii) flat-slab or point-supported system, and iii) load-bearing wall and floor system. The first system uses mass timber beams and columns, e.g., glue laminated timber (glulam or GL), with a mass timber floor plate, e.g., CLT. The second system includes a mass timber floor plate, typically CLT, point-supported at minimum by glulam columns, at all the corners or edges of the panels. Residential, office, and commercial mixed-use buildings up to 18 storeys all use both post and beam systems and flat-slab systems. An example of the third system is the novel hybrid of cold-formed steel (CFS) walls and CLT floors developed by Timber Engineering Inc (Malczyk & Mpidi Bita, 2021), also referred to as the CLT/CFS system; this is currently in use for residential buildings up to 12 storeys in North America and provides a cost-effective solution for buildings with micro-units (e.g., loadbearing walls, typically at 12 on centre). This GLRS uses CFS loadbearing walls in a platform-type construction, as well as CLT floors and roof. All aforementioned systems add structural or nonstructural concrete on top of mass timber panels to improve fire, acoustics, and vibration performance.

In the current North American market for residential buildings up to six storeys, the LLRS is dominated by light wood-frame shear walls. In contrast, LLRSs for hybrid timber structures are not typically wood-based. The choice of material depends on lateral load demands and constructability; typical options are concrete cores or shear walls (Figure 3[a]) or steel-braced frames (Figure 3[b]). In North America, low-rise buildings may also use reinforced masonry or CFS, depending on lateral load demands. With respect to seismic design, concrete cores or shear walls can be of use in all regions, regardless of building height. Steel-braced frames in high seismic zones typically use buckling-restrained braces (BRB), whereas low seismic and wind-governed regions, or low-rise buildings, typically adopt concentrically braced frames. With respect to constructability, steel-braced frames offer advantages over concrete cores or shear walls because they allow the installation of the frames in parallel to the GLRS, hence increasing the speed of construction and shortening the overall project schedule. Steel-braced frames are also often located at the perimeter of a building, providing flexibility for elevator and stair locations. Buildings with masonry, CFS, and light wood-frame shear walls as LLRSs are limited to six storeys and to designs not requiring high ductility.

(a)  (b) 

**Figure 3. (a) GLRS composed of glulam posts and beams with CLT floors, LLRS composed of concrete shear walls (Photo credit: Marta Maj – Equilibrium Consulting Inc.); (b) GLRS composed of glulam posts and beams with CLT floors, LLRS composed of BRB frames (Photo credit: Omer Mohammed – Equilibrium Consulting Inc.)**

#### *7.3.2.2 Typical Connections*

As for any structure, the design of a hybrid timber building should ensure continuous load paths with adequate strength and stiffness on structural members and their connections to transfer all forces from the point of application to the final point of resistance. Since hybrid timber structures have different materials for the GLRS and LLRS, the load paths and responses can be affected by factors such as drift compatibility between the two systems, differential movement due to temperature, moisture, as well as load and load duration. There must be adequate connection details to carefully assess these points, as they affect all disciplines across the entire project.

Figure 4 shows a typical connection between a CLT floor panel and a concrete core. This detail uses steel angles to support CLT floor panels and transfer the gravity load. Self-tapping screws (STSs) connect the CLT to the steel angle, which is anchored to the concrete by mechanical fasteners. When using the CLT floor as a diaphragm, this detail is designed for in-plane shear demands. Figure 5 shows a connection between the steel components of a moment frame and the CLT panels of the floor and wall. This detail, at which the CLT panels come directly in contact with the steel components, uses STSs as fasteners. Figure 6(a) and Figure 6(b) show a typical glulam beam-to-column bearing connection using a steel hanger. The steel hanger connects to the column with STSs. When connecting to a concrete wall, the hanger is welded to a steel embed, as shown in Figure 6(c). The beam stays in place thanks to a knife plate, connecting via STSs from the bottom (Figure 6[a]) or top (Figure 6[b]) or by through bolts from the side (Figure 6[c]). In Figure 6(a), the STSs connecting the CLT panel to the beam may extend to the concrete topping when the topping serves as part of the diaphragm to resist the vertical acceleration of the floor. Section 7.3.4.3 further elaborates on this.

(a) 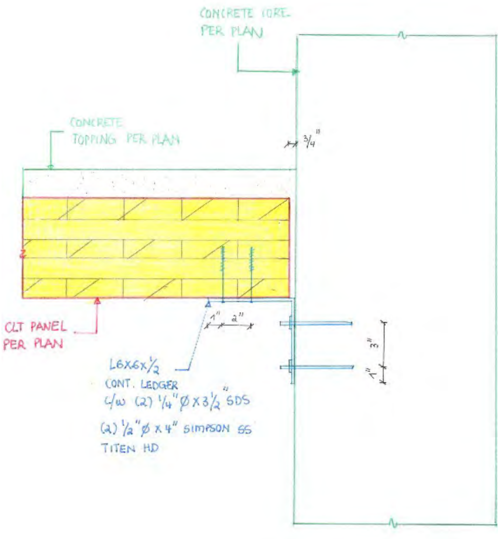

(b) 

**Figure 4. CLT to concrete core: (a) structural sketch; (b) site photo (with steel angle)**

(a) 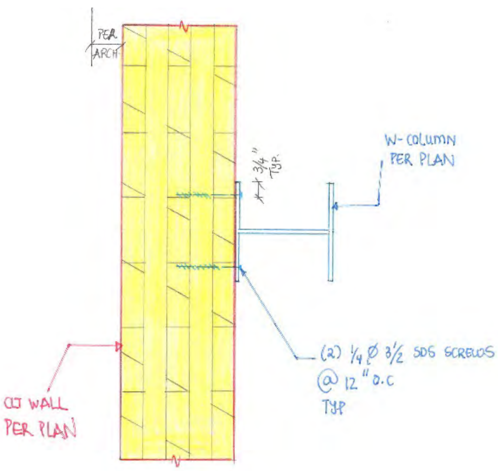

(b) 

**Figure 5. CLT to steel column: (a) structural sketch; (b) site photo (with moment frame)**


**Figure 6. (a) Encapsulated beam-to-column steel hanger; (b) exposed beam-to-column steel hanger; and (c) exposed beam-to-concrete wall steel hanger**

## 7.3.3 Special Structural and Modelling Considerations

### *7.3.3.1 Building Vertical Movements*

Considerations of vertical movements are prerequisite for buildings taller than six storeys. The main contributing factors are i) elastic axial shortening due to gravity loads; ii) shrinkage; iii) creep; iv) joint settlement; and v) construction tolerances. For hybrid timber structures, vertical movements become significant because these factors have different effects on different structural materials, e.g., wood, concrete, steel, and others. For platform-type construction, where a floor acts as a platform for the next level, vertical deformations accumulate over building height. Vertical movements negatively impact both the immediate and long-term performance of a building, as well as such nonstructural elements as partition walls, doors, windows, and glazing. Detailing usually helps deal with vertical movements. In terms of analysis, hand calculations that consider all these contributing factors are typically sufficient. Some scenarios, such as those in which the hybrid systems are complex, however, require FE modelling (Chen et al., 2015). Chapter 4.1 discusses the modelling of wood-based products exposed to various actions, such as forces, moisture, and time effects.

The 18-storey University of British Columbia (UBC) Brock Commons residence uses CLT floor panels point-supported on glulam columns as the GLRS and concrete cores as the LLRS. The detail shown in Figure 7(a) mitigates the effects of differential vertical movements between the supports, i.e., the axial shortening of the mass timber column and stiff concrete core (Fast & Jackson, 2017; Jackson, 2017). At the time of installation, the column was higher than the concrete core at certain levels in order to accommodate the vertical deformation of glulam. This was achieved by shimming the column with a series of 1.6mm steel plates (Fast & Jackson, 2017).

(a) 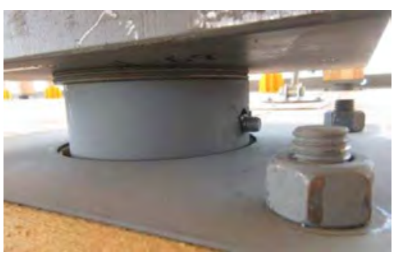 (b) 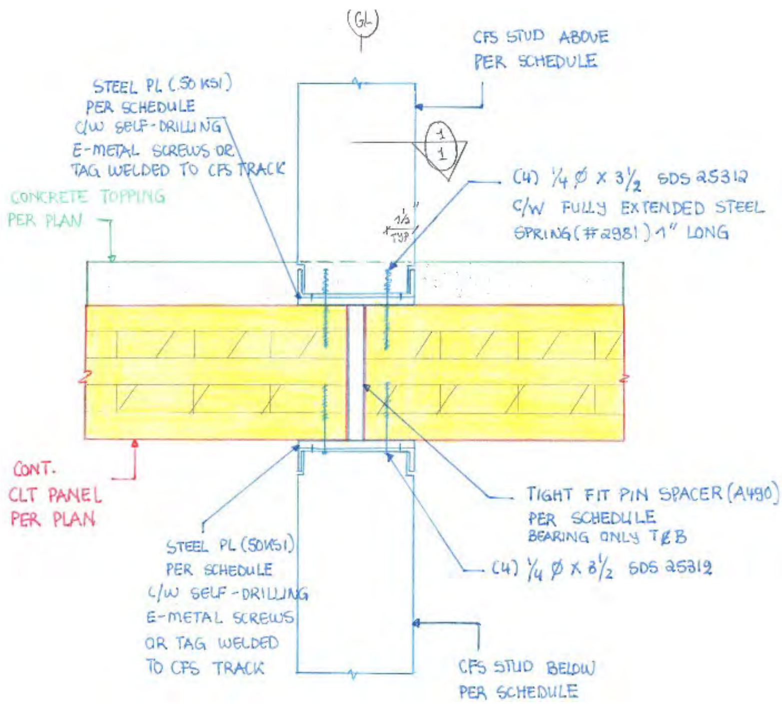


**Figure 7. (a) Steel shim at top of column in UBC Brock Commons building (Jackson, 2017); (b) CLT/CFS system connection detail**

A system with CFS walls and CLT floor panels in a platform-type construction must consider vertical movements. Figure 7(b) illustrates a novel detail developed by Timber Engineering Inc. to ensure a dimensionally stable structural system that contains vertical movements within an individual level: a tight-fit pin or spacer in the CLT panel at the location of the CFS studs to enable direct gravity-load transfer between adjacent levels. After any floor movement due to CLT panel shrinkage, the addition of the steel plates to the CFS walls above and below the CLT panels ensures an even vertical load distribution. The top steel plate uses screws with springs to ensure the robustness of the CFS wall above by keeping the wall in place during and after movements, i.e., the initially fully extended screw compresses as the CLT panel shrinks.

### *7.3.3.2 Lateral Drift Compatibility*

Buildings typically allow an interstorey drift up to 0.025h, where h is the storey height. Therefore, GLRS members are required to maintain their gravity load-carrying capacities with additional drift-induced stresses. One must model the structural members of the GLRS in such a way that they do not contribute to the lateral resistance of a hybrid timber structure, i.e., those with pinned connections at both ends. Although models do not explicitly include these connections, their design and detailing must accommodate the drift demands and corresponding stresses to ensure the structural members remain elastic, as assumed in models.

Typical wood bearing-type connections have negligible rotational stiffness and should theoretically be pinned. These include angle-bearing wood-to-wood or wood-to-steel connections with construction tolerances to prevent full moment fixity. They can therefore meet the drift demands, with negligible additional stresses on the connecting members. Experimental testing has shown that tight-fit connectors such as those produced by KNAPP, which have little to no construction tolerance, can meet rotational demands while maintaining load-carrying capacity (Leach, 2018). Similar tests have shown that MEGANT and RICON connectors can resist gravity loads when subjected to cyclic drift demand above 0.02h (MTC, 2020). Nevertheless, designers should always check any possible additional stresses induced onto the connecting members.

Figure 8 illustrates a simplified 2D structural idealisation that models the drift compatibility of GLRS, as well as additional drift-induced stresses. This idealisation uses 2-noded 1D elements with linear elastic material properties for the columns and beams, and can model the CLT floor as a 2-noded 1D or 4-noded 2D element, with corresponding in-plane stiffness and negligible out-of-plane stiffness. The CLT floor and beam are offset in elevation with respect to the floor level, defined as the top node of the column. The CLT floor is also offset with respect to the beam. To transfer gravity loads from the CLT floor to the beam, this idealisation models an axial- and shear-only $k_1$ spring or rigid element along the length of the floor and beam.

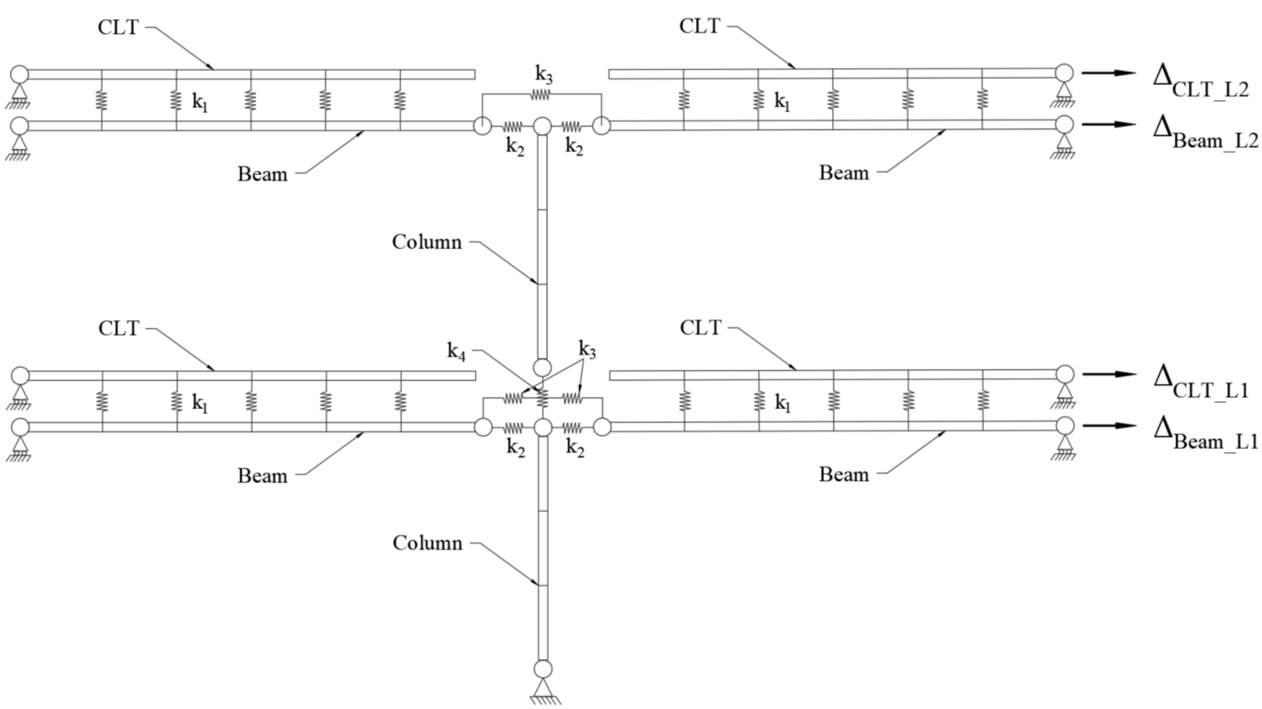


**Figure 8. Structural idealisation for drift compatibility**

The beam connects to the column using a $k_2$ spring or rigid element, to transfer both shear and axial forces due to gravity. For continuous beams and systems, where moment restraints can occur due to connection detail, a $k_3$ spring models the moment transfer between the sections on either side of the column. The connection between columns is idealised using a $k_4$ spring or rigid element transferring both gravity and shear forces without interfering with the beam and CLT elements. This idealised model typically applies the lateral load at the floor level under consideration as a lateral deformation on the beam ($\Delta_{Beam\_Li}$) and CLT ($\Delta_{CLT\_Li}$) elements to evaluate the lateral drift on the GLRS, as well as the corresponding additional stresses, e.g., the combined gravity and moment on the connections.

## 7.3.4 Special Analysis Considerations

### *7.3.4.1 Gravity Analysis*

The GLRS and LLRS of a hybrid timber structure are typically analysed separately. A main reason for this is to simplify the design by limiting the model contribution of the GLRS to the LLRS, and vice-versa. This simplification needs to be followed through connection details. A GLRS model helps capture the appropriate load paths between slabs, beams, columns, and walls, as well as possible live load reductions and live load patterns for continuous members. Designers must not only ensure that connections are detailed to form a continuous load path but also consider how they may impact other design criteria, such as building movements, disproportionate collapse prevention, and footfall-induced vibrations.

The typical bearing-type connections between structural members should account for construction tolerances. In other words, they should allow some movements to accommodate assembly. These tolerances also minimise rotational stiffness to achieve pinned connections. Therefore, when constructing models at the component level, i.e., beams, columns/walls, and slabs, one can simplify the connections between the elements into pins, as shown in Figure 9. There is no need to explicitly model the connections; a simple moment release would be sufficient. Nevertheless, it is also necessary to pay attention to the possible contribution of the floor if it is explicitly modelled, e.g., using a 2D 4-node element. Unless one includes additional considerations, e.g., appropriate releases or offsets or a reduction to the stiffness of the floor plate, an analysis that explicitly models the floor will affect the load distribution on the beams though composite action between the floor and the beams, as shown in Figure 9. Consequently, models commonly analyse beams and columns at the component level, without the floor plate, by applying the loads from the CLT directly on the beam as a uniformly distributed load. Chapter 6.1 offers detailed information on the modelling and analysis of floors.

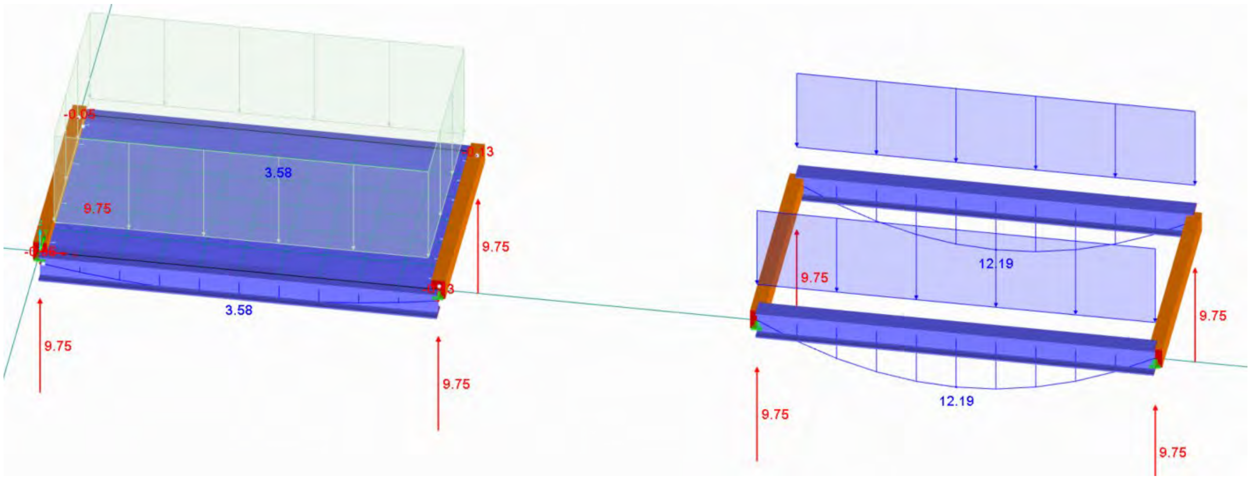


**Figure 9. Modelling elements at component level**

Figure 10 shows an example of a system-level model, i.e., an entire building, with all beams, columns, and walls. Similar to beams and slabs, the column bases are typically pinned, since they use bearing-type connections. Nonetheless, for the system model, LLRS should be explicitly modelled for stability, i.e., second order-effects. This is because, as Figure 10 shows, the two central cores provide the required stability. The system-level model offers the advantage of being able to track the loads from the roof down to the base of the building. Nevertheless, designers should account for additional design considerations, such as live load reduction, live load patterns for continuous members, and the local lateral buckling of members.

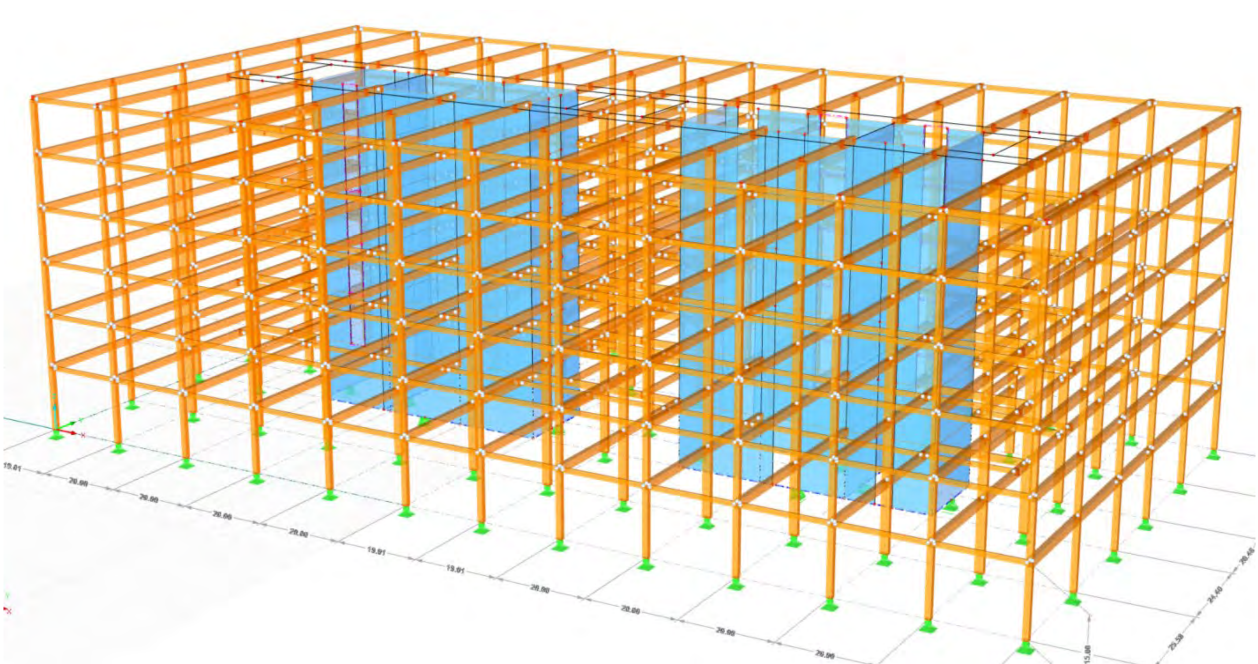

**Figure 10. Modelling elements at system level**

Disproportionate collapse prevention for hybrid timber structures is a relevant design criterion due to the increasing height and occupancy level of these buildings (Huber et al., 2020). The mitigation strategies against such catastrophic failure include i) reducing the building's exposure to extreme events; ii) reducing the vulnerability of the structural components following an extreme event; and iii) ensuring structural robustness, a structural property of the building that prevents collapse propagation. Previous research (Huber et al., 2020; Mpidi Bita et al., 2018) showed that structural robustness is a practical and economical approach for wood buildings, as it enables a collapse-resistance mechanism or alternative load path (ALP). For hybrid timber structures, as for any other structural system, one can conduct an analysis for disproportionate collapse prevention at three different structural levels or idealisations (Mpidi Bita et al., 2018): i) micro or connection level; ii) macro or component level; and iii) global level.

In design practice, ALP analysis requires a complete 3D FE model of a building, including all primary structural components, as shown in Figure 11 (Mpidi Bita et al., 2018; Mpidi Bita & Tannert, 2019). Depending on the level of nonlinearity, 2-noded 1D elements can model all the beams and columns, while 4-noded 2D elements with both bending and membrane stiffness can model the mass timber floors. Unless the floor is a timber composite floor system, the analysis can neglect the stiffness of the nonstructural concrete topping while considering its mass in the dead load estimation. Chapter 8 offers more information regarding the modelling and analysis of progressive/disproportionate collapse.

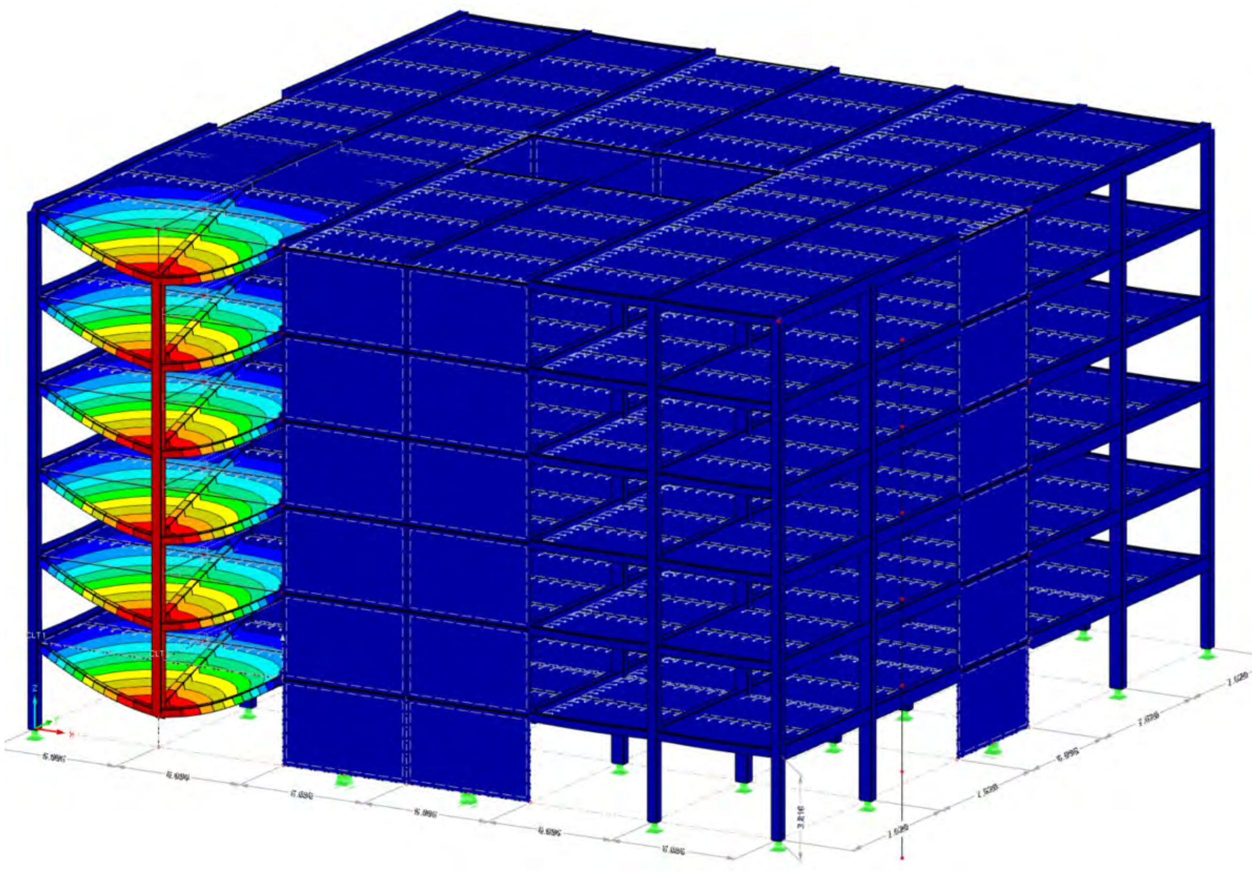

**Figure 11. 3D model of six-storey building following ground-floor edge column removal**

#### 7.3.4.2 Wind Analysis

Per NBCC 2020 (NRC, 2022), either static, dynamic, or wind tunnel procedures help determine wind loads, depending on the dynamic properties of a building. A building is dynamically sensitive if its lowest frequency ($f_1$) is 0.25Hz < $f_1$ < 1Hz and its height is above 60m and more than 4 times its minimum width. Very dynamically sensitive buildings have $f_1 \leq 0.25$Hz and a height more than 6 times the minimum effective width. ASCE-7 22 (ASCE, 2022) considers buildings with $f_1$ < 1Hz flexible or dynamically sensitive. The design of tall hybrid mass timber structures is often governed by lateral deformation under the serviceability limit state (Chen & Chui, 2017). In other words, designers should always ensure that lateral deformation due to wind is below the code limit, typically h/400, where h is the storey height.

Low- and mid-rise hybrid timber structures are often dynamically insensitive. One can apply the forces obtained from the static procedure as point loads or uniformly distributed loads. This analysis is linear static, with the LLRS modelled as elastic. High-rise hybrid timber structures, on the other hand, are typically dynamically sensitive due to the lightweight nature of the wood components. To perform wind-induced vibration on a building requires a full building model, with all lateral wind loads carried by the LLRS and the GLRS pinned at both ends without contributing to the lateral resistance. The modelling assumptions described in Section 7.3.4.3 also apply to wind analysis. Chapter 9 offers more information regarding the modelling and analysis of wind-induced response.

#### 7.3.4.3 Seismic Analysis

According to NBCC 2020 (NRC, 2022), one should analyse and design LLRSs for seismic loads using either a linear or nonlinear dynamic procedure. The code also gives the conditions in which it is possible to use the equivalent static force procedure (ESFP), depending on the period, height, and irregularities of a building, as well as the design seismic spectral acceleration at 0.2s based on the building's location and importance. Similarly, ASCE-7 22 (ASCE, 2022) also provides conditions allowing the use of the ESFP. Given that hybrid timber structures are currently restricted to 12 (NRC, 2022) or 18 storeys (ICC, 2021), the ESFP and the linear dynamic procedure apply mostly in design practice. The former is better for mid-rise buildings up to 8 storeys without structural irregularities, where one can follow the seismic force distributions and load paths using hand calculations.

The floor diaphragm for hybrid timber structures requires careful consideration because it links a GLRS that is typically wood based to an LLRS that is normally not wood based. Models typically assume floor build-ups with light wood frames are flexible and treat mass timber floor systems with nonstructural concrete topping as rigid, even though a semi-rigid assumption is recommended. In addition, the in-plane diaphragm stiffness is a function of the connection within the diaphragm as well to the supporting element. Using appropriate in-plane elastic and shear moduli based on connection details is essential to estimating the force distribution to the LLRS. This is especially critical for buildings with a nonsymmetric LLRS layout, i.e., torsionally sensitive buildings. Without explicitly modelling diaphragm in-plane stiffness to capture its deformation, it is common practice to create an envelope for force distribution using both flexible and rigid assumptions. Most models assume the connection between the CLT floor panels and the LLRS—typically a bearing-type connection with construction tolerances—is pinned, without rotational stiffness. When assuming that the concrete topping fully carries the diaphragm loads, i.e., with a minimum thickness of 3" (75mm), one can treat the diaphragm itself, as well as the wall connection, as rigid. As shown in Figure 5(a), STSs with 2"–3" washer heads at nominal spacing can connect the CLT panels and beams to the concrete topping. These screws not only allow the CLT panels and beams to go along with the ride during a seismic event, but they also prevent possible uplift from the vertical acceleration of an earthquake. Chapter 6.2 offers more information regarding the modelling and analyses of diaphragms.

To conduct a seismic analysis of hybrid timber structures using FE models, it is possible to consider i) the LLRS only; ii) LLRS with connecting GLRS only using appropriate boundary conditions; and iii) both the LLRS and GLRS. For the first approach, one should apply the seismic forces calculated by the ESFP, distributed to the individual lateral load-resisting components (LLRC) based on diaphragm flexibility, as a lateral point load at each level. This approach can work for hybrid timber structures regardless of the selected LLRS, e.g., steel-braced frames, concrete shear walls, CFS, or masonry shear walls. Figure 12(a) shows the applied lateral and gravity (self-weight and favourable dead) loads at each level on a single shear wall. It models the shear wall with 2D 4-noded elements with in-plane stiffness and negligible out-of-plane stiffness. For discontinuous LLRSs at every level, apply appropriate boundary conditions, e.g., release moments and axial restraints for possible discrete hold-downs. Chapters 7.1, 7.2, 7.4, and 7.5 provide more information regarding the modelling of different timber structures. The analysis that designs the individual LLRC and obtains the corresponding lateral shears and interstorey drifts may be linear or nonlinear static.

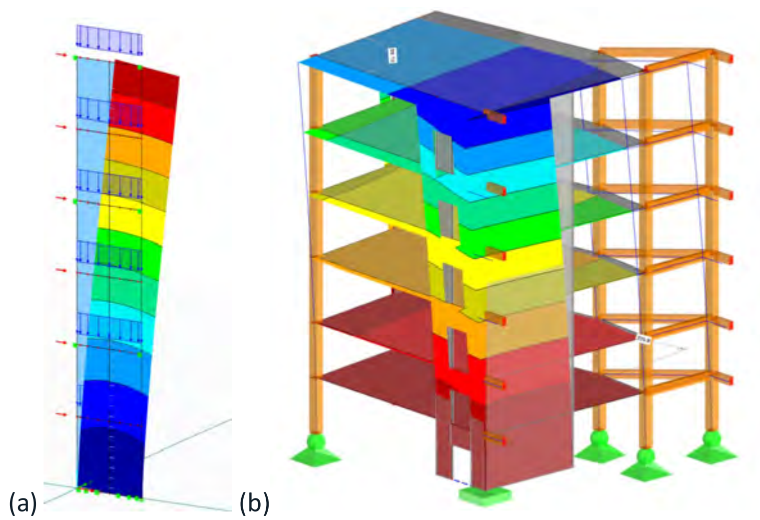


**Figure 12. Lateral loads applied to LLRS: (a) individual LLRC; (b) LLRS with connecting GLRS**

For buildings with core or irregularly shaped LLRSs, the second approach, which includes the LLRS and the connecting GLRS, as shown in Figure 12(b), is generally better for determining complex lateral force distribution. This models the concrete core with openings to better estimate the in-plane stiffness of the LLRS, and it captures the diaphragm stiffness contribution using 2D 4-noded elements with in-plane stiffness and negligible out-of-plane stiffness for better lateral load distribution to the individual wall. Although they are not necessary, the model may include surrounding columns and beams for global stability, with the appropriate boundary conditions. Nonetheless, to obtain realistic results, the fundamental period of the partial building model must be within 15% of that of the full model.

The third approach for seismic analysis considers the full building with a complete LLRS, with or without a GLRS, as shown in Figure 13(a) and Figure 13(b), respectively. To estimate force distribution and building drift, regardless of the selected LLRS, one should model the floor diaphragm in-plane stiffness as semi-rigid, which is typical for CLT diaphragms, or as rigid, which is typical for concrete diaphragm. For CFS walls with concrete cores and CLT floors, as shown in Figure 13(a), the FE model may only include the LLRS, without the CFS walls. Nevertheless, one should ensure that the difference in building period with and without the CFS walls is not greater than 15%. In Figure 13(b), the FE model includes both the GLRS, composed of glulam posts and beams with CLT floors, and the LLRS, composed of steel braces. As Section 7.3.4.1 notes, the GLRS in a hybrid mass timber structure typically has moment release at both ends, based on bearing-type connections with sufficient construction tolerance. Therefore, it is possible to model the beams and columns with pins at both ends so as to not contribute to lateral resistance. FE models may include advanced modelling assumptions, such as material and geometric nonlinearities. In this case, the nonlinearities should only be considered at specific locations that are likely to experience energy dissipation, e.g., BRB braces or shear wall hold-downs. The requirements for nonlinear behaviour and energy dissipation appear in codes and standards, e.g., NBCC 2015 or ASCE-7 22. Chapter 10 offers more information regarding the modelling and analyses of seismic-induced response.

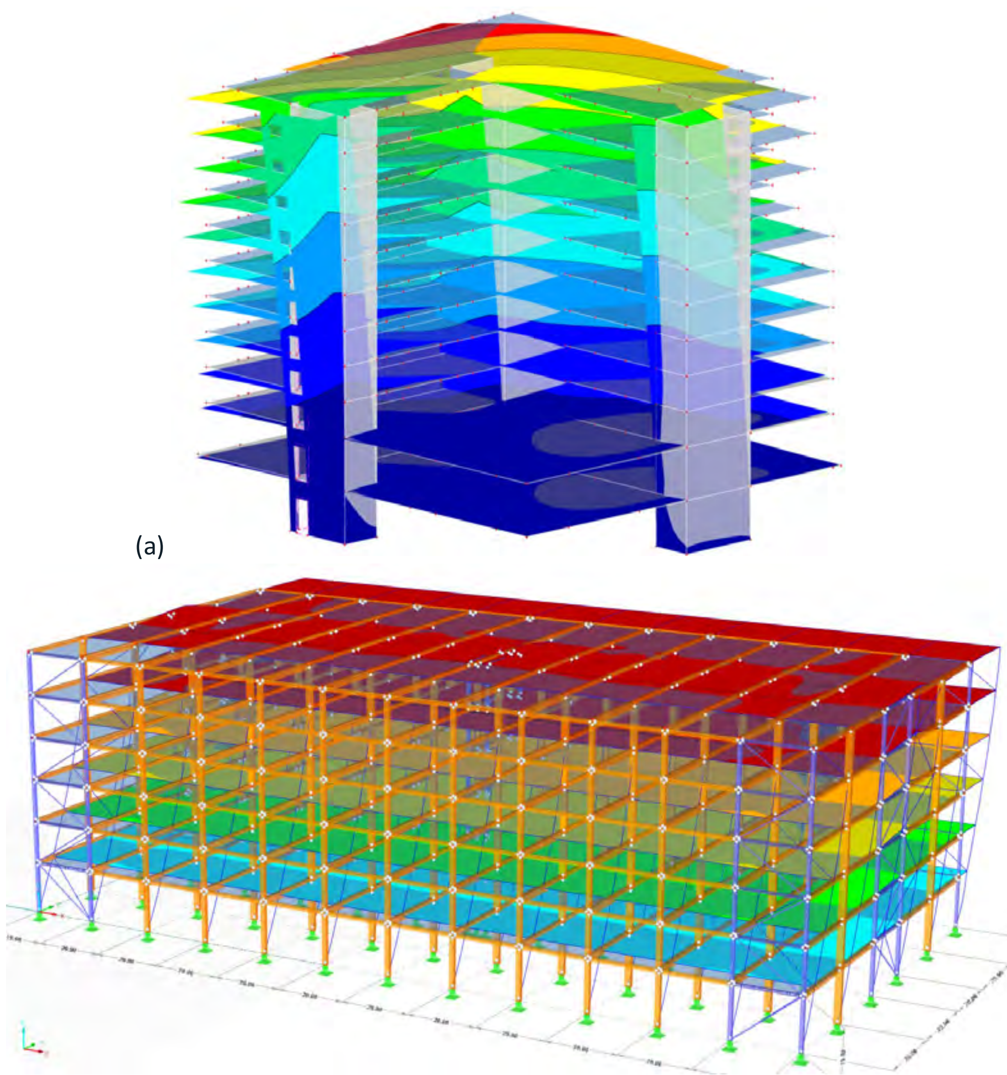

(a)

(b)

**Figure 13. (a) Full building model with LLRS only; (b) full building model with both LLRS and GLRS**

## 7.3.5 Summary

A hybrid timber structure integrates wood with different materials to make better use of the individual strength of each. To provide technical information to support the design and analysis of hybrid timber structures, this chapter introduces examples of such structures, the typical connection details, and special considerations on the design and analysis of hybrid structures. Chapters 7.1, 7.2, 7.4, and 7.5, respectively, discuss the modelling of light wood-frame structures, mass timber structures, timber structures with advanced seismic protection, and long-span timber structures, while Chapter 6 discusses that of floor diaphragms and Chapter 2 briefly covers that of structures using non-wood materials.

## 7.3.6 References

American Society of Civil Engineering (ASCE). (2022). *Minimum design loads for buildings and other structures* (ASCE/SEI 7).

Chen, Z., & Chui, Y.-H. (2017). Lateral load-resisting system using mass timber panel for high-rise buildings. *Frontiers in Built Environment, 3*(40). https://doi.org/10.3389/fbuil.2017.00040

Chen, Z., Li, M., Chui, Y.-H., & Popovski, M. (2015). Chapter 3 – Analysis and design of concrete – glulam floor system and gravity load resisting system. In Y. H. Chui (Ed.), *Application of analysis tools from NEWBuildS research network in design of a high-rise wood building* (pp. 37–47). NEWBuildS and FPInnovations. https://www.bcfii.ca/wp-content/uploads/2021/02/fii415-2014-15-newbuilds-application-of-analysis-tools-in-design-of-high-rise-wood-building-1.pdf.

Chen, Z., & Ni, C. (2020). Criterion for applying two-step analysis procedure to seismic design of wood-frame buildings on concrete podium. *Journal of Structural Engineering, 146*(1), Article 04019178. https://doi.org/10.1061/(ASCE)ST.1943-541X.0002405

Chen, Z., Ni, C., Dagenais, C., & Lin, H. (2021). *Expending wood use towards 2025: Development of mass timber midply wall systems, Year 1* (Project 301014059). FPInnovations.

Chen, Z., Popovski, M., & Ni, C. (2020). A novel floor-isolated re-centering system for prefabricated modular mass timber construction – Concept development and preliminary evaluation. *Engineering Structures, 222*, Article 111168. https://doi.org/10.1016/j.engstruct.2020.111168

Canadian Wood Council (CWC). (2017). *Wood design manual 2017* (Vols. 1–2).

Fast, P. & Jackson, R. (2017). *Case Study: University of British Columbia's 18-storey Tall Wood House at Brock Commons* [Conference presentation]. IABSE Symposium: Engineering the Future, Vancouver, Canada. https://doi.org/10.2749/vancouver.2017.2322

Green, M. C., & Karsh, J. E. (2012). *TALL WOOD – The case for tall wood buildings: How mass timber offers a safe, economical, and environmentally friendly alternative for tall building structures*. mgb. https://cwc.ca/wp-content/uploads/publications-Tall-Wood.pdf

Huber, J. A. J., Ekevad, M., Girhammar, U. A., & Berg, S. (2020). Finite element analysis of alternative load paths in a platform-framed CLT building. *Structures & Buildings*, *173*(5), 379–390. https://doi.org/10.1680/jstbu.19.00136

International Code Council (ICC). (2021). *2021 International building code* (ICC IBC-2021).

Jackson, R. (2017). *Case study: TallWood house at Brock Commons, the University of British Columbia* [PDF slides]. https://www.woodworks.org/wp-content/uploads/WEB118-JACKSON-TallWood-House-Webinar-170125.pdf

Karacabeyli, E., & Lum, C. (Eds.) (2021). *Technical guide for the design and construction of tall wood buildings in Canada* (2nd ed.). FPInnovations.

Leach, H. (2018). *Interstorey drift performance of timber beam-hanger connections* [Master's thesis, Queen's University]. Queen's Graduate Theses and Dissertations. http://hdl.handle.net/1974/24879

Malczyk, R., & Mpidi Bita, H. (2021). Cross-laminated timber and cold-formed steel hybrid system: A new approach. Timber Engineering Inc. https://www.timberengineering.ca/s/Cross-Laminated-Timber-and-Cold-Formed-Steel-Hybrid-System-A-New-Approach-updated-November-17.pdf

Mpidi Bita, H., Currie, N., & Tannert, T. (2018). Disproportionate collapse analysis of mid-rise cross-laminated timber buildings. *Structures and Infrastructure Engineering*, *14*(11), 1547–1560. https://doi.org/10.1080/15732479.2018.1456553

Mpidi Bita, H., & Tannert, T. (2019). Disproportionate collapse prevention analysis for a mid-rise flat-plate cross-laminated timber building. *Engineering Structures*, *178*, 460–471. https://doi.org/10.1016/j.engstruct.2018.10.048

MTC Solutions. (2020). *Inter-story drift testing of KNAPP RICON S VS connectors*. https://mtcsolutions.com/wp-content/uploads/2019/04/WP_-_Inter-story_Drift_Performance_of_Pre-engineered_Connectors.pdf

National Research Council Canada (NRC). (2022). *National Building Code of Canada 2020*.

Popovski, M., Gagnon, S., Mohammad, M., & Chen, Z. (2019). Chapter 3: Structural design of cross-laminated timber elements. In E. Karacabeyli & S. Gagnon (Eds.), *CLT Handbook: 2019 edition*. FPInnovations.

Popovski, M., Tung, D., & Chen, Z. (2022). 5.3: Structural analysis and design. In E. Karacabeyli & C. Lum (Eds.), *Technical guide for the design and construction of tall wood buildings in Canada* (2nd ed). FPInnovations.

Quintana Gallo, P., Carradine, D. M., & Bazaez, R. (2021). State of the art and practice of seismic-resistant hybrid timber structures. *European Journal of Wood and Wood Products, 79*(1), 5–28. https://doi.org/10.1007/s00107-020-01556-3

Tannert, T., Follesa, M., Frangiacomo, M., Gonzalez, P., Isoda, H., Moroder, D., Xiong, H., & van de Lindt, J. (2018). Seismic design of cross-laminated timber buildings. *Wood and Fiber Science*, *50*(Special Issue – CLT/Mass Timber), 3–26.

Tesfamariam, S., Stiemer, S. F., Dickof, C., & Bezabeh, M. A. (2014). Seismic vulnerability assessment of hybrid steel-timber structure: Steel moment-resisting frames with CLT infill. *Journal of Earthquake Engineering, 18*(6), 929–944. https://doi.org/10.1080/13632469.2014.916240

Zhang, X., Azim, M. R., Bhat, P., Popovski, M., & Tannert, T. (2017). Seismic performance of embedded steel beam connection in cross-laminated timber panels for tall-wood hybrid system. *Canadian Journal of Civil Engineering, 44*(8), 611–618. https://doi.org/10.1139/cjce-2016-0386

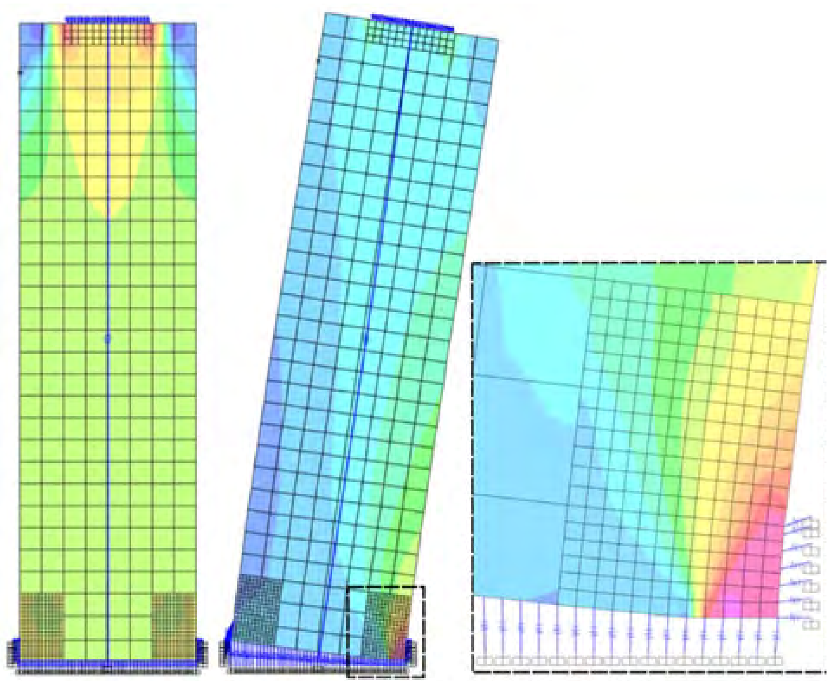

Image courtesy of Wilson et al. (2019)

# CHAPTER 7.4

## Timber structures with advanced seismic protection


**Authors**

Francesco Sarti
Zhiyong Chen
Keri Ryan
Marjan Popovski

**Reviewers**

Chun Ni
Shiling Pei
Asif Iqbal
Ashkan Hashemi

# TABLE OF CONTENTS

## 7.4.1 Introduction

Timber structures traditionally provided satisfactory seismic performance due to such features as a light weight, high strength-to-weight ratio, structural redundancy, elastic deformation capacity, and the ductility of connections (Ugalde et al., 2019). Nowadays, however, they aim for greater heights and longer spans, resulting in challenging seismic designs. Rather than increasing the seismic resistance of a structure, more recent work applies advanced seismic protection technologies to reduce the seismic demand from other structures on those made of timber. Such seismic protection technologies can be grouped into supplemental damping, rocking systems, and seismic isolation (Chen et al., 2020).

Seismic protection by means of supplemental damping aims to decrease structural demands (potential energy – elastic deformation). To this end, it increases inherent energy dissipation (damping) by adding supplemental devices called dampers. The total energy dissipated during a vibration cycle due to inherent damping and inelastic behaviour (if present) is given by the area under a force-displacement or moment-rotation hysteretic curve, as illustrated in Figure 1(a). For equivalent displacements, supplemental damping typically increases lateral stiffness, enlarging the forces and shortening the fundamental period but also dissipating much more energy. The increase in damping reduces not only potential but also kinetic energy, thus decreasing both the acceleration and displacement demands. Period shortening usually implies larger accelerations but leads to smaller displacement, so supplemental damping is in general quite effective for reducing drift (Figures 1[b] and 1[c]). This is especially beneficial for timber structures, as structural damage shows much larger correlations with interstorey drifts than with structural forces (Priestley et al., 2007).

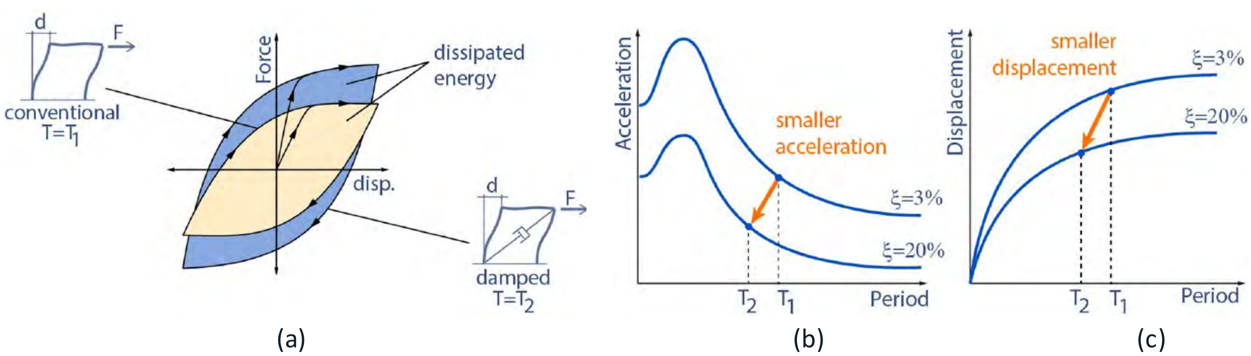


**Figure 1. (a) Idealised force-displacement hysteretic behaviour of conventional and damped system. Effects of greater damping and stiffness in the structural response of (b) acceleration and (c) displacement (Ugalde et al., 2019)**

A rocking system is a seismic protection method in which one or more structural parts rotate relative to each other, like rigid bodies allowing the entire structure to rock when under seismic loads. In some systems, methods like post-tensioning can control the rocking. The controlled rocking systems also use supplemental damping. The structural demands on timber members are reduced by increasing the elastic deformation of the post-tensioning system, its kinetic energy (rocking movement), and the damping capability. A typical configuration of rocking walls containing a post-tensioning tendon and supplemental dampers is illustrated in Figure 2, along with its force-displacement relationships. The timber assembly and tendons are expected to behave solely elastically, thus providing restoration (self-aligning) force; the dissipative behaviour is provided by dampers, typically metallic or friction. In the entire system, a large amount of energy is dissipated when the force or moment is activated, resulting in two symmetric, flag-shaped hysteresis loops.

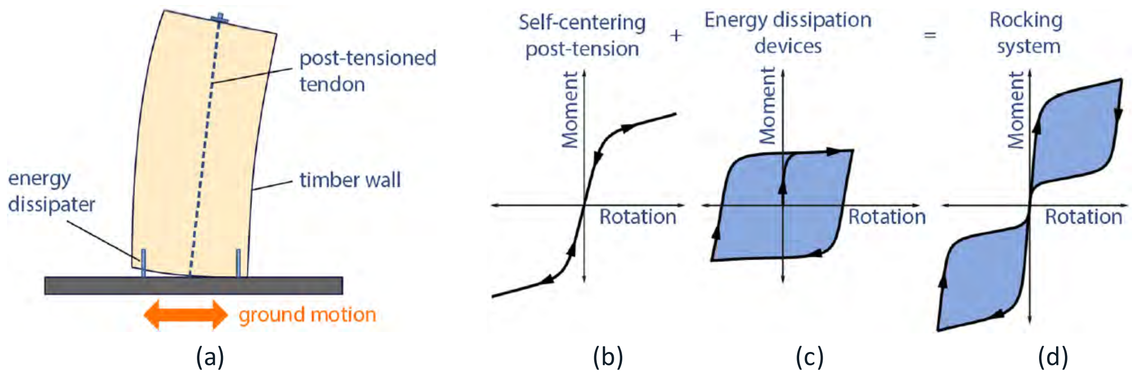


**Figure 2. (a) Schematic configuration of a typical post-tensioning rocking wall with energy dissipators. Hysteretic behaviour of (b) an elastic self-centring system, (c) an energy dissipation system, and (d) the resulting rocking system (Ugalde et al., 2019)**

Unlike supplemental damping and rocking systems, which modify energetic balance, seismic isolation aims to reduce the seismic input energy to prevent damage. This uses a flexible interface (isolators) beneath the supports of the structure (superstructure), such that the structural response is uncoupled from the ground motion, as illustrated in Figure 3(b) compared to traditionally fixed in Figure 3(a). This seismic protection technology results in much more flexible structures with significantly increased periods. These are subject to much smaller lateral demands, as seen in the decreased acceleration of the superstructure (Figure 3[c]), which keeps acceleration-sensitive members undamaged. Unlike supplemental damping, period shifting increases the total displacement during an earthquake (Figure 3[d]). However, most of this displacement is concentrated in the isolation system (Figure 3[b]), while the superstructure typically shows much smaller relative deformations and less damage to structural and nonstructural components.

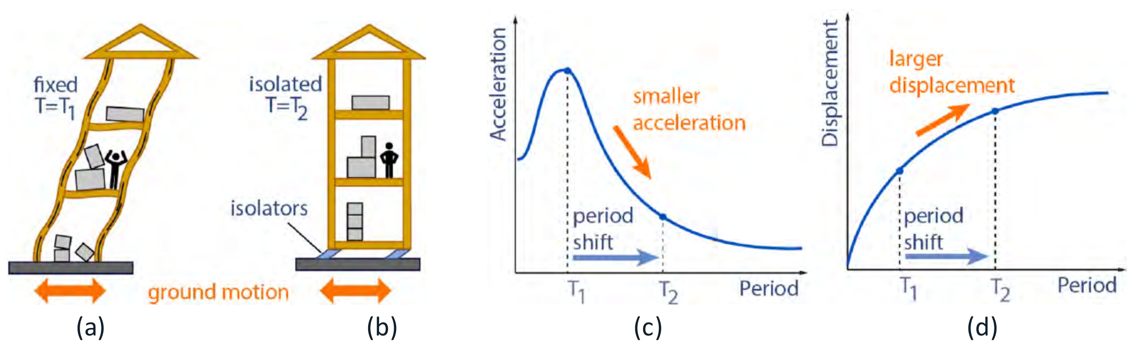


**Figure 3. Schematic seismic response for structures with (a) fixed base and (b) isolated base. Effects of the period shift in structural response for (c) acceleration and (d) displacement (Ugalde et al., 2019)**

Many types of seismic protection technology and corresponding devices have been proposed to date. This chapter is, however, limited to rocking systems, systems with resilient slip friction joints, and seismic isolation systems, which currently fall within the scope of performance-based seismic design with peer-review and special approval. This chapter discusses the behaviour and mechanism for each type of seismic protection timber system, then introduces corresponding advanced and practical modelling methods.

## 7.4.2 Controlled Rocking Systems

### *7.4.2.1 The Pres-Lam Concept*

In the late 1990s, the US PRESSS (PREcast Structural Seismic Systems) program conducted the first research into the development of post-tensioned rocking systems. This involved experimental research on several structural systems. Of the different technologies developed and tested, hybrid technology proved the most stable and promising. It combines recentring and dissipation, provided respectively by post-tensioning and mild steel reinforcement, as illustrated in Figure 4. This generates a flag-shaped hysteresis loop (Figure 2[b]–2[d]), which ensures that the residual displacements are minimised; in addition, the use of mild steel reinforcement provides significant dissipation, concentrating the damage at the connection interface.

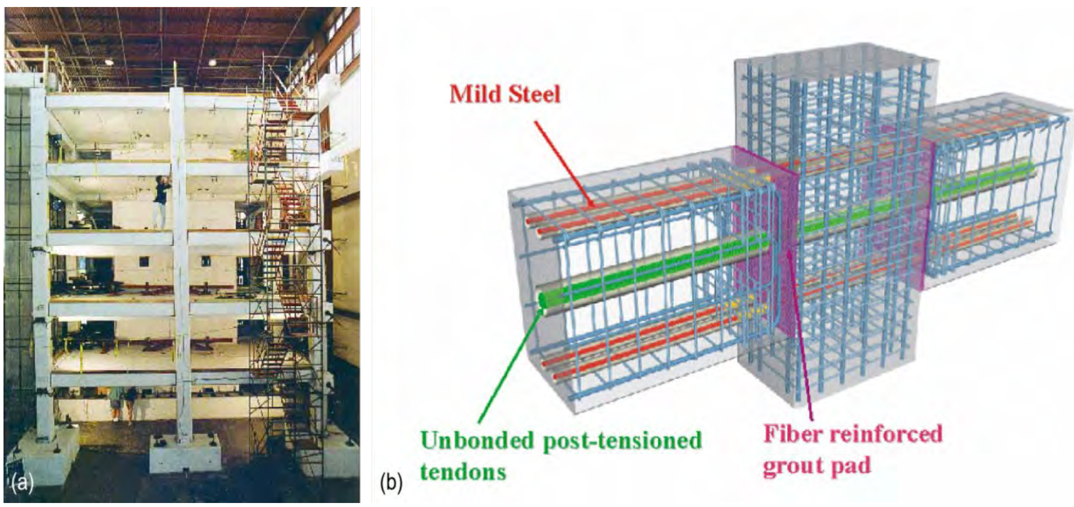


**Figure 4. (a) PRESSS five-storey building (Priestley et al., 1999) and (b) rocking beam-column joint (Courtesy of Miss. S. Nakaki)**

Palermo et al. (2005) extended the rocking concept to timber structures. It can be applied to both moment-resisting frames (Smith, 2014) and shear walls (Sarti, 2015), Figure 5, and is referred to as Pres-Lam (Prestressed Laminated Timber).

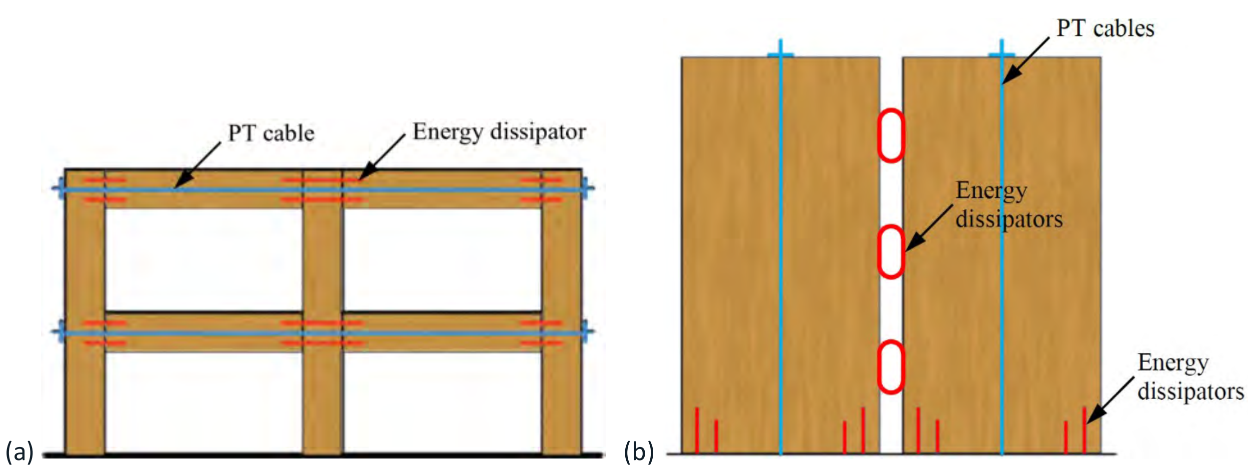


**Figure 5. Illustration of Pres-Lam system used in (a) moment-resisting frame and (b) wall-based system**

A ‘controlled rocking’ motion occurs in hybrid jointed ductile connections, as shown in Figure 6 for a typical frame beam-column subassembly. A similar conceptual mechanism can be developed in timber walls. Unlike traditional solutions (i.e., nailed or steel dowel connections), the inelastic demand in a hybrid rocking solution is accommodated at the column-to-beam interface (wall-to-foundation for wall systems) by opening and closing an existing gap and through the yielding of the mild steel or the dissipation devices (internal or external). If correctly designed and detailed, there should be negligible crushing of the wood material in the beam-column (or wall) elements (Palermo et al., 2005). The lack of damage to the structural elements, the appropriate energy dissipation capacity of the dissipators, and the self-centring properties of the unbonded post-tensioned tendons can guarantee improved seismic performance in comparison to the traditional solutions for timber construction. High levels of ductility can be achieved without degrading strength and stiffness or leaving any residual deformation and structural damage. This greatly reduces the repair costs (including downtime) after a significant seismic event (Palermo et al., 2005).

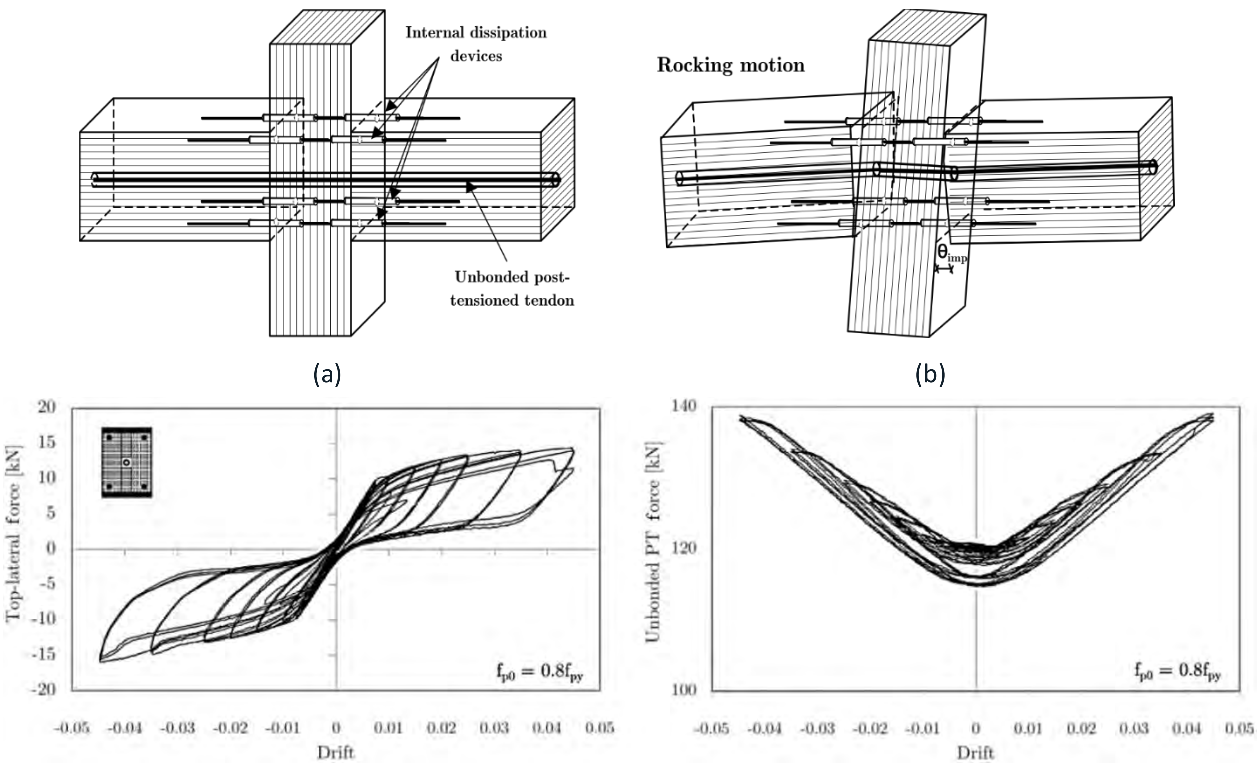


(a) (b)

(c) (d)

**Figure 6. Rocking concept applied to laminated veneer lumber frame systems (Palermo et al., 2005): (a) undeformed, (b) with rocking motion, (c) hysteresis loops, and (d) post-tensioning force-drift**

After successful validation through testing, numerous Pres-Lam buildings have been constructed throughout the world. Figures 8 and 9 show examples of framed and wall buildings constructed with Pres-Lam technology.

**Figure 7. A Pres-Lam frame building under construction in Christchurch, New Zealand**

**Figure 8. A Pres-Lam wall building, Peavy Hall, in Corvallis, Oregon (Photo courtesy of StructureCraft)**

### 7.4.2.2 Behaviour and Mechanism

The basic concept of a post-tensioned rocking system is to activate a controlled rocking motion between two structural members (i.e., beam-column or wall-foundation). This is generally achieved by subjecting the element to a compressive load. The post-tensioning load enables a moment-resisting connection at the element end, but it allows separation between either the beam-column or wall-foundation interface. Separation between elements occurs as the connection moment increases beyond the decompression value, $M_{dec}$. This corresponds to zero compression at one end of the cross-section, as shown in Figure 9.

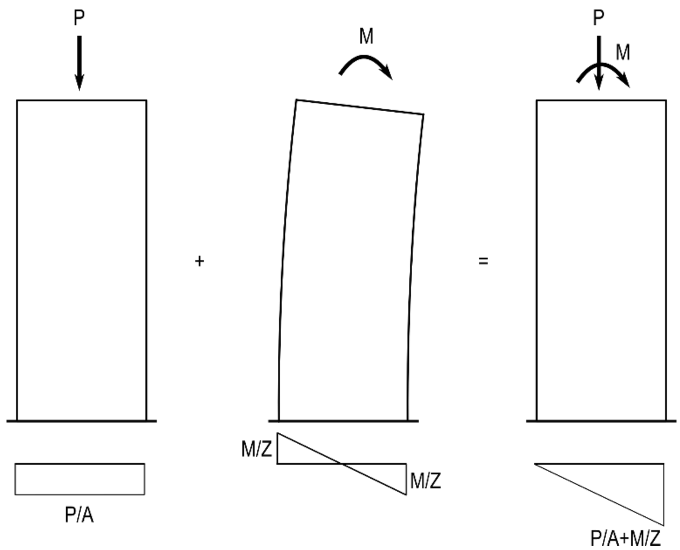


**Figure 9. Decompression point**

In general, the axial load is imposed using post-tensioned high-strength steel bars. In walls, gravity loads may also contribute. From this, load *P* in Figure 9 can be obtained from the sum of the initial post-tensioning force, $T_{pt0}$, and the gravity load, *N*. Therefore, the decompression moment, $M_{dec}$, can be derived as

$$\frac{M}{Z} - \frac{P}{A} = 0 \rightarrow M_{dec} = \left(T_{pt0} + N\right)\frac{Z}{A} \qquad [1]$$

where P is the total axial load acting on the cross-section; M is the connection moment; Z is the section modulus; and A is the cross-section area.

Figure 10 illustrates the rocking mechanism of post-tensioned systems without energy dissipators. Before decompression, the deformation of the element is purely elastic, resulting from the bending and shear deformation of the wall panel or frame system. This is highlighted by the linear elastic behaviour seen in the force-displacement response (Figure 10[b]). After the gap has opened (i.e., with nonzero connection rotation, $\theta$), however, the compression zone depth (*c*), referred to as neutral axis depth, varies with a decreasing negative slope, as shown in Figure 10(c). This results in a nonlinear trend towards low connection rotation values for both the force-displacement and the moment-rotation response. For small values, the neutral axis depth is larger than the half-section depth (*h*) and there is no post-tensioning force increase. When the neutral axis depth reaches *h*/2, the increase in post-tensioning force results in linear behaviour, as shown in Figure 10(d) ($T_{pt}$-θ chart). The increase in post-tensioning force, as well as the decrease in the neutral axis depth, affects the post-decompression stiffness of the connection, as shown in Figure 10(d) (M-θ chart). Using pure post-tensioned rocking sections leads to multilinear elastic hysteresis, and the system provides very limited hysteretic damping.

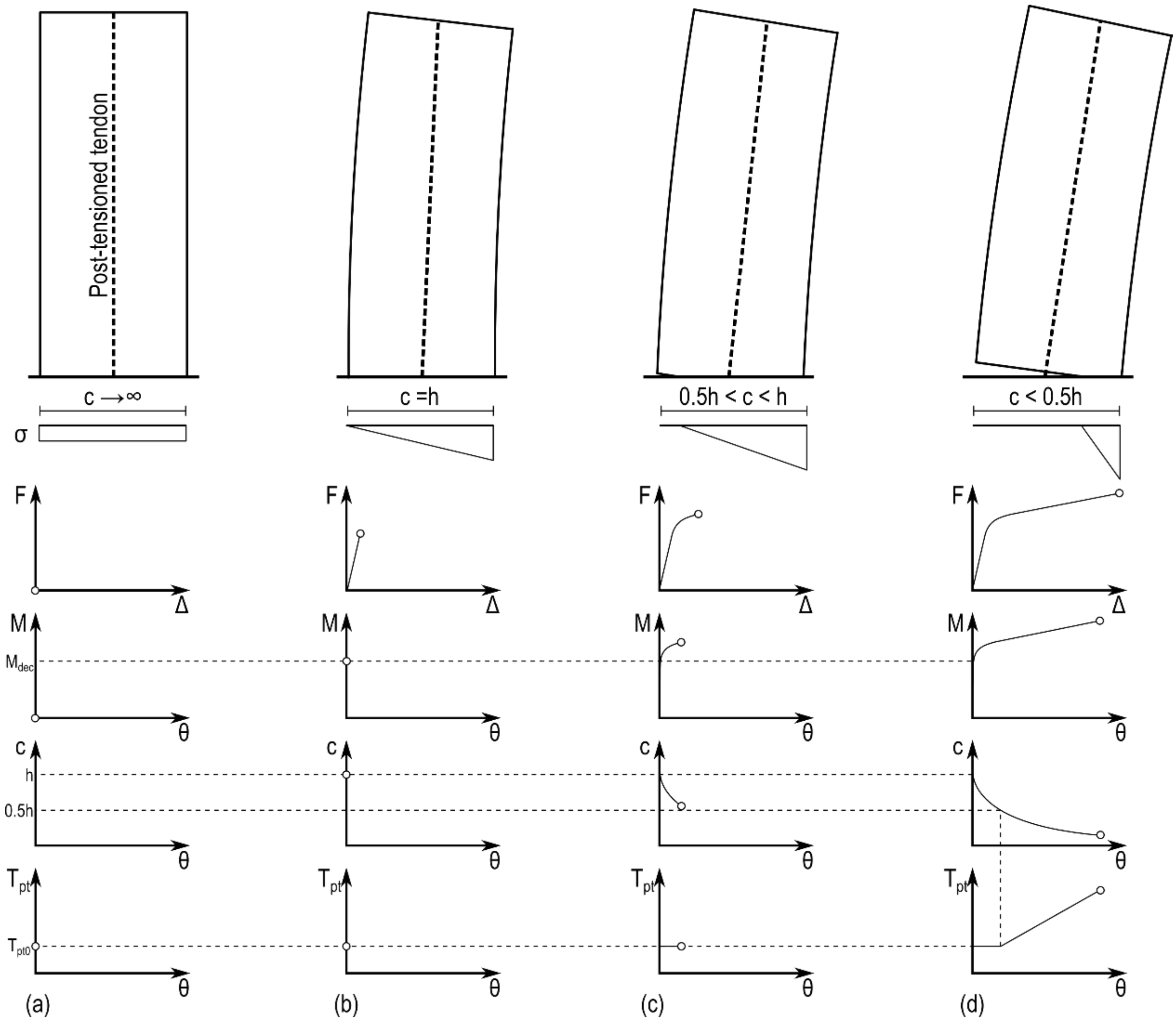


**Figure 10. Post-tensioned rocking mechanism: (a) initial state, (b) decompression, (c) nonlinearity, and (d) tendon elongation**

*Note: F, $T_{pt0}$, and $T_{pt}$ represent the lateral load on the wall, the initial post-tensioning force, and the post-tensioning force in the rod, respectively. M and $M_{dec}$ represent the moment applied at the bottom of the wall and the decompression moment, respectively. C and h represent the neutral axis depth and the length of the wall, respectively. The deflection of the wall is designated as $\Delta$, while $\theta$ is the wall rotation.*

When using a dissipative post-tensioned rocking system, damping devices are connected to the element and provide the hysteretic energy dissipation. The system's mechanics, shown in Figure 11, are similar to the pure post-tensioned rocking connection. At the decompression point (Figure 11[a]), no connection rotation develops and the dissipators do not activate. As soon as the gap opens and the yielding displacement of the dissipators occurs, the dissipators yield in tension (Figure 11[b]). As connection rotations increase, the tendons elongate and the dissipators further extend, displaying ductile behaviour and developing hysteretic damping. Under reversed loading, the dissipators yield in compression (Figure 11[d]) and the system recentres, revealing a typical flag-shaped hysteresis (Figure 6[c]). The neutral axis depth trend is similar to that for the post-tensioned only solution, and is not strongly influenced by the use of dissipation devices. In fact, these devices usually develop similar forces once they yield, with a negligible influence on the force balance which governs the depth value of the neutral axis.

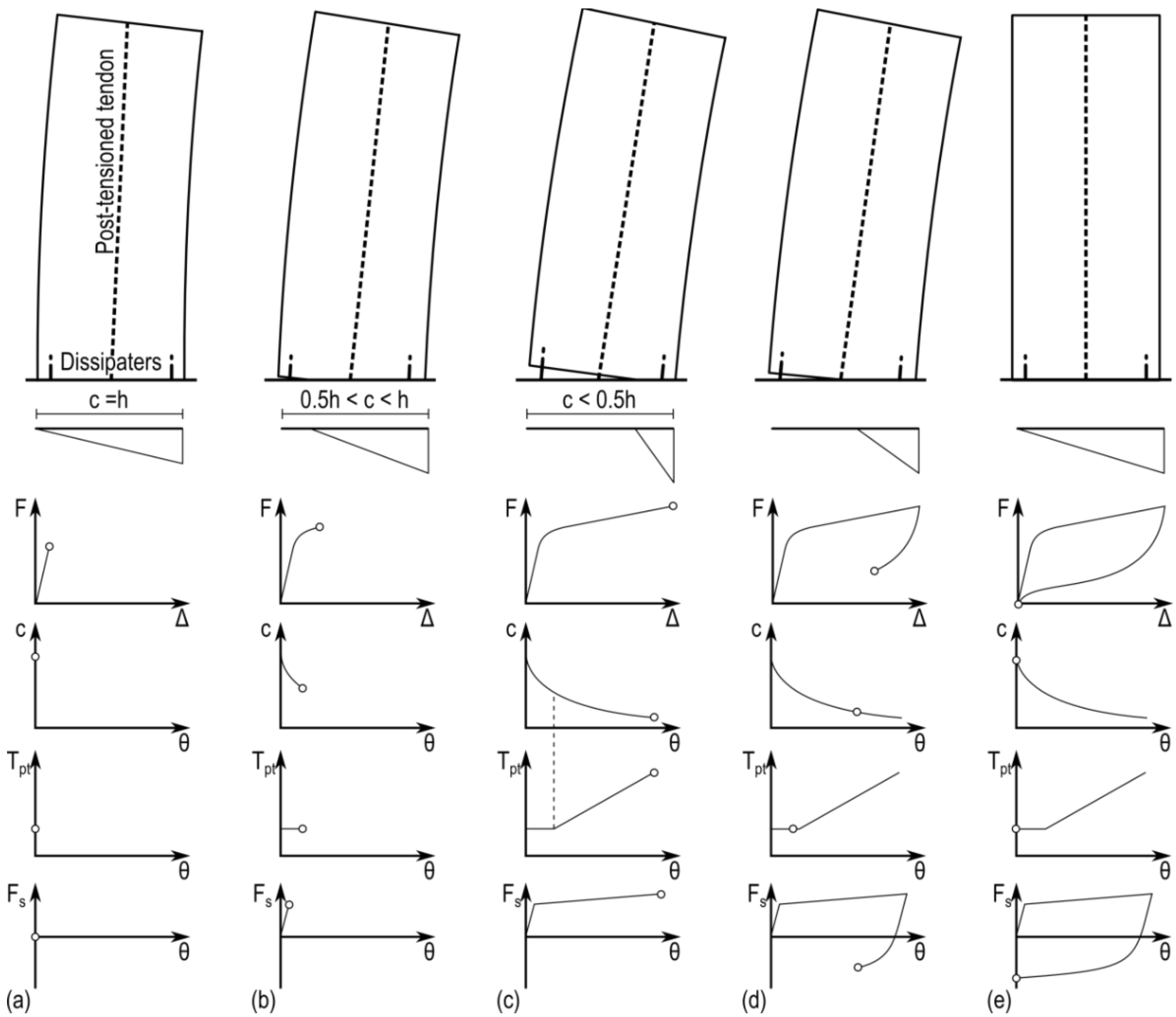


**Figure 11. Dissipative post-tensioned rocking mechanism: (a) decompression, (b) tensile yielding, (c) tendon elongation, (d) compressive yielding, and (e) recentring**

*Note: F and $T_{pt}$ represent the lateral load on the wall and the post-tensioning force in the rod, respectively. C represents the neutral axis depth of the wall, while $F_s$ represents the force resisted by the fuses. The deflection of the wall is designated as $\Delta$ while $\theta$ is the wall rotation.*

The typical force-displacement loop of a dissipative post-tensioned rocking connection is a flag-shaped hysteresis. This derives from a combination of multilinear elastic and bilinear hysteresis rules, as shown in Figure 12(a).

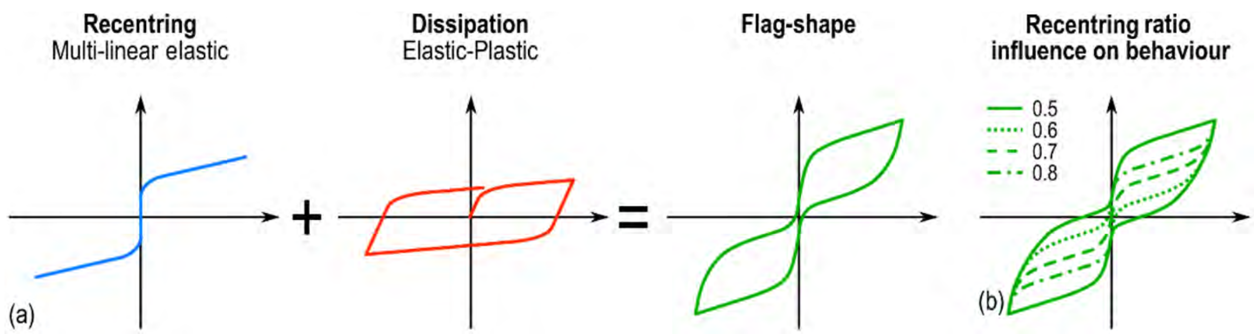


**Figure 12. (a) Flag-shaped hysteresis, (b) influence of the recentring ratio on behaviour**

The hysteretic shape is governed by the recentring ratio, β or λ, as defined by Equation 2.

$$\boldsymbol{\beta = \frac{M_{pt}}{M_{tot}}; \lambda = \frac{M_{pt}}{M_s}} \quad [2]$$

where $M_{pt}$ is the post-tensioning moment contribution; $M_s$ is the dissipative moment contribution; and $M_{tot}$ is the total moment distribution, = $M_{pt} + M_s$.

Figure 12(b) qualitatively shows the influence of this parameter on the hysteretic behaviour. For a unit value of β, the connection follows a multilinear elastic (post-tensioned only) relationship, with almost no energy dissipation; instead, for β = *0* (*λ* = 0), the connection is a mild steel–only option with very high hysteretic damping and significant residual displacement. A minimum value of β = 0.55 (λ = 1.15) is suggested in theory, ensuring acceptable levels of dissipation and negligible residual displacement (Standards New Zealand, 2006). In reality, however, post-tensioned timber systems tend to target high values of β.

### *7.4.2.3 Analytical Models*

#### 7.4.2.3.1 *M-θ* Relationship

The moment-rotation analysis of post-tensioned rocking sections (Figure 13) follows an iterative procedure proposed by Pampanin et al. (2001) and modified by Palermo and Pampanin (2008) for precast concrete post-tensioned elements. This procedure, referred to as Modified Monolithic Beam Analogy (MMBA), was adapted to Pres-Lam systems by Newcombe et al. (2008). This analysis can calculate displacement due to gap opening (i.e., rigid body rotation), see Section 7.4.2.3.2, and calibrate rotational spring models, see Section 7.4.2.4.1.1. The MMBA comprises a step-by-step iterative procedure based on global strain compatibility and assumes that the total displacement of the rocking element is equal to that of an analogic monolithic element. The step-by-step procedure is summarised in Figure 14.

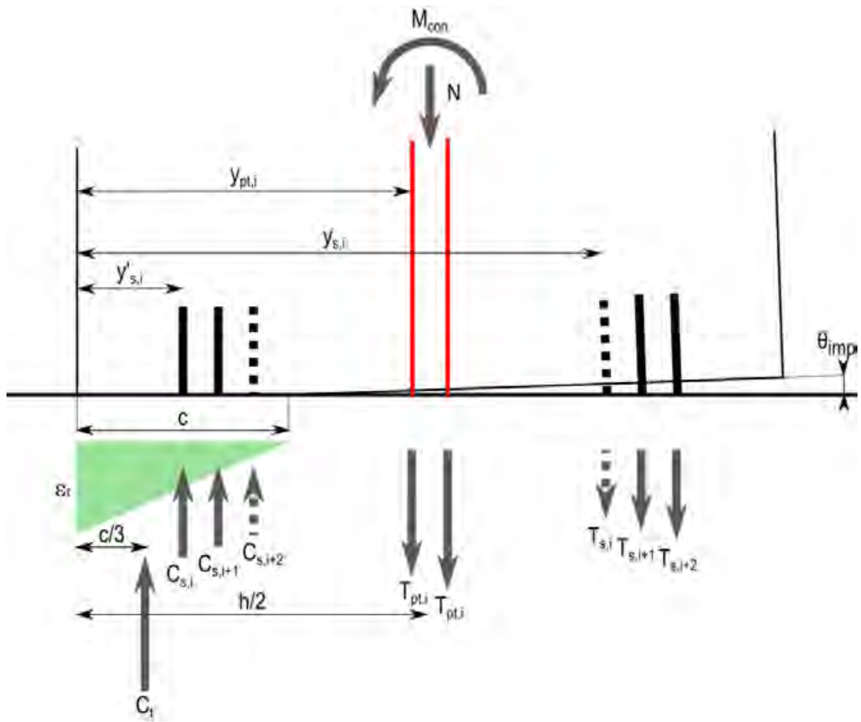


**Figure 13. Section analysis nomenclature**

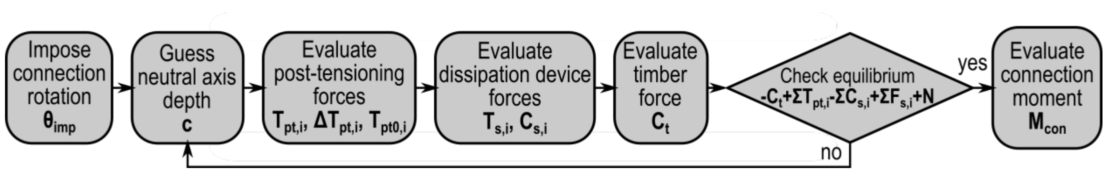


**Figure 14. Moment-rotation MMBA, step-by-step procedure**

The general moment-rotation behaviour of the post-tensioned timber connection can be divided into two situations, depending on the decompression moment. When the connection moment is lower than the decompression moment, the gap is not expected to open and the rotation is zero; once the decompression moment is overcome, the rotation increases with the connection moment. The moment-rotation response past the decompression moment is as follows, and is shown in Figure 14.

**Step 1 – Impose the connection rotation**

Impose a base connection rotation, $\theta_{imp}$, while considering lateral load design and the elastic contributions of the cantilevered wall or frame system.

**Step 2 – Propose initial neutral axis depth**

As part of the iterative procedure, guess an initial natural axis depth value, *c*, then iterate it to achieve vertical force equilibrium for the section.

**Step 3 – Evaluate post-tensioning forces**

For the imposed rotation, $\theta_{imp}$, and the initial neutral axis depth, c, tendon elongation due to the gap opening in the *i*-th reinforcement layer is

$$\boldsymbol{\Delta_{pt,i} = \theta_{imp}\left(y_{pt,i} - c\right)} \tag{3}$$

where $\Delta_{pt,i}$ is the elongation of the *i*-th post-tensioning reinforcement layer; and $y_{pt,i}$ is the edge distance of the *i*-th post-tensioning reinforcement layer.

The strain and post-tensioning force increment of the *i*-th post-tensioning layer are then evaluated as

$$\boldsymbol{\Delta\varepsilon_{pt,i} = \frac{\Delta_{pt,i}}{l_{ub,i}}} \tag{4}$$

$$\boldsymbol{\Delta T_{pt,i} = \Delta\varepsilon_{pt,i} E_{pt} A_{pt,i}} \tag{5}$$

where $l_{ub,i}$ is the unbonded length of the *i*-th post-tensioning reinforcement layer; $E_{pt}$ is the post-tensioning steel elastic modulus; and $A_{pt,i}$ is the cross-section area of the *i*-th post-tensioning reinforcement layer.

Finally, the total post-tensioning force, $T_{pt,i}$, can be evaluated:

$$\boldsymbol{T_{pt,i} = T_{pt0,i} + \Delta T_{pt,i}} \tag{6}$$

where $T_{pt0,i}$ is the initial post-tensioning force of the *i*-th post-tensioning reinforcement layer.

**Step 4 – Evaluate the forces in the dissipation devices**

The displacement due to the gap opening of the *i*-th tension dissipative layer, $\Delta_{s,i}$, and the compression dissipative layer, $\Delta'_{s,i}$, is given by

$$\boldsymbol{\Delta_{s,i} = \theta_{imp}\left(y_{s,i} - c\right); \Delta'_{s,i} = \theta_{imp}\left(c - y'_{s,i}\right)} \tag{7}$$

where $y_{s,i}$ is the edge distance of the *i*-th mild steel reinforcement tension layer and $y'_{s,i}$ is edge distance of the *i*-th mild steel reinforcement compressive layer.

A number of dissipative devices can be used in Pres-Lam systems. These can be mild steel devices, such as tension-compression yielding mild steel bars (Sarti, 2015), U-Shaped flexural steel plates (Skinner et al., 1974), or dissipative angles (Di Cesare et al., 2013), or others, such as friction devices (Morgen and Kurama, 2007) or velocity-dependant dissipators (Marriott et al., 2008). The dissipative design forces, $T_{s,i}$ and $C_{s,i}$, depend on the dissipative device used. They can be worked out as follows:

$$\boldsymbol{T_{s,i} = F_{s,i}\left(\Delta_{s,i}\right); C_{s,i} = F_{sy,i}\left(\Delta'_{s,i}\right),} \tag{8}$$

where $F_{s,i}(\Delta_{s,i})$ is dissipative device force as a function of the device tension displacement and $F_{s,i}(\Delta'_{s,i})$ is dissipative device force as a function of the device compression displacement.

This guide does not discuss the calibration of the force-displacement functions for these devices. This information can be found in the relevant literature referenced above.

### Step 5 – Evaluate the force in the timber members

To evaluate the strain $\varepsilon_t$ in the timber member, apply the strain compatibility condition and assume the displacement of the rocking element is the same as that of the analogic monolithic element. This leads to

$$\boldsymbol{\varepsilon_t = c\left(\phi_{dec} + \frac{3\theta_{imp}}{L_{cant}}\right)} \qquad [9]$$

where $\phi_{dec}$ is decompression curvature.

$$\boldsymbol{\phi_{dec} = \frac{M_{dec}}{E_{con}I}} \qquad [10]$$

where $E_{con}$ is the connection modulus (equal to $k_{gap}E_t$ for post-tensioned timber [STIC, 2013]). This reduced modulus of elasticity accounts for the reduction in stiffness during material testing due to timber end effects observed in experimental tests by Newcombe (2007). $E_t$ is the timber modulus of elasticity; $k_{gap}$ gives values for post-tensioned timber structures, as shown in Table 1; $I$ is the second moment of area for the section; and $L_{cant}$ is the effective cantilever length.

**Table 1. $K_{gap}$ values**

| Situation | Occurrence | $K_{gap}$ |
|---|---|---|
| No perpendicular to the grain action | Wall-foundation, column-foundation connection, beam-column connections with concrete columns | 0.7 |
| Perpendicular to grain action with adequate measures to protect against the perp to grain crushing of timber | Beam-column joints reinforced with screws, epoxied-in rods etc | 0.55 |
| Perpendicular to grain action with no effort to protect against the perp to grain crushing of timber | Unreinforced beam-column joints (not recommended) | 0.1 |

The effective cantilever length for wall systems depends on the force distribution acting on the structure. For wall systems, this is the centroid of the force distribution (Figure 15):

$$\boldsymbol{L_{cant} = \frac{\sum_{i=1}^{n} F_i h_i}{\sum_{i=1}^{n} F_i}} \qquad [11]$$

where $F_i$ is force acting at the $i$-th storey; $h_i$ is $i$-th story height; and $n$ is total number of storeys.

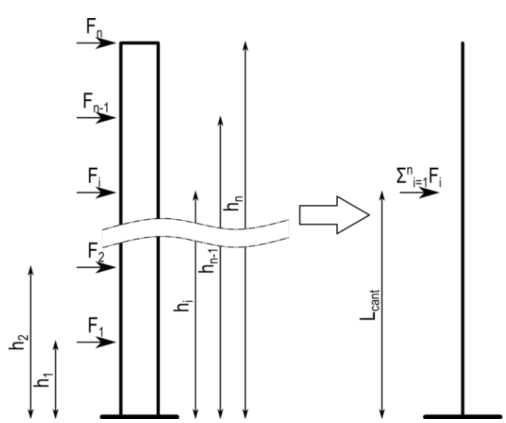


**Figure 15. Effective cantilever length**

Generally, when designing for earthquake loading, the force distribution can be assumed as triangular. In this case, the effective cantilever length is equal to 75% of the total building height.

In frame systems, $L_{cant}$ is the distance from the face of the column to the point of contra-flexure. For seismic-only loading, it is half the beam length.

The force in the timber members can then be evaluated by assuming a triangular stress distribution:

$$\boldsymbol{C_t = 0.5E_{con}\varepsilon_t bc} \qquad [12]$$

where b is section width.

**Step 6 – Check the equilibrium and evaluate the connection moment**

Once the force contributions are evaluated, the vertical force equilibrium must be assessed according to Equation 13:

$$\boldsymbol{-C_t + \sum_{i=1}^{n_s} T_{s,i} - \sum_{i=1}^{n_s} C_{s,i} + \sum_{i=1}^{n_{pt}} T_{pt,i} + N = 0} \qquad [13]$$

If the equilibrium is not satisfied, the neutral axis depth value must be iterated; otherwise, the connection moment can be evaluated around the timber compression centroid.

$$\boldsymbol{M_{con} = \sum_{i=1}^{n_{pt}} T_{pt,i}\frac{h}{2} + \sum_{i=1}^{n_s} T_{s,i}\left(d_{s,i} - \frac{c}{3}\right) - \sum_{i=1}^{n_s} C_{s,i}\left(d'_{s,i} - \frac{c}{3}\right) + N\left(\frac{h}{2} - \frac{c}{3}\right)} \qquad [14]$$

7.4.2.3.2 *Displacement/Rotation Response of Pres-Lam Systems*

##### *7.4.2.3.2.1 Walls*

The total displacement, $\delta_{tot}$, at the top of the wall panel is a combination of displacement due to gap opening (i.e., rigid body rotation), $\delta_{gap}$, and the contributions from elastic bending, $\delta_b$, and shear, $\delta_s$, due to the elastic deformation of the wall panel, as. This is illustrated in Figure 16.

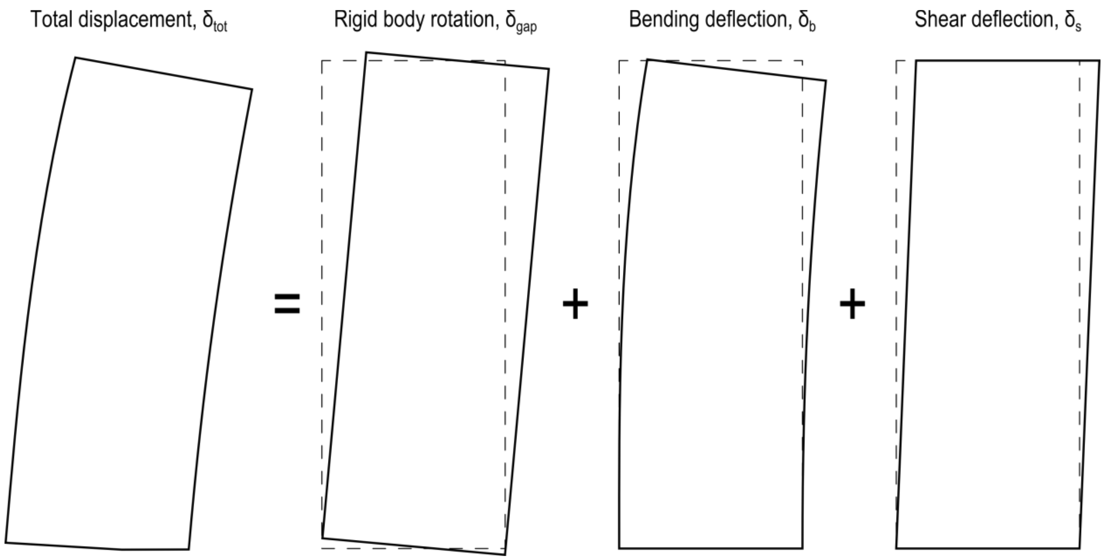


**Figure 16. Displacement contributions in a post-tensioned rocking wall**

$$\boldsymbol{\delta_{tot} = \delta_{gap} + \delta_b + \delta_s} \tag{15}$$

The rigid body rotation of the wall panel results in the displacement contribution, $\delta_{gap}$:

$$\boldsymbol{\delta_{gap} = \theta_{imp} h_n} \tag{16}$$

where $\theta_{imp}$ is the base connection rotation and $h_n$ is the top storey height.

Although the gap opening contribution, $\delta_{gap}$, can be derived from the moment-rotation analysis in Section 7.4.2.3.1, for a general type of loading, the bending and shear contributions, $\delta_b$ and $\delta_s$, respectively, can be evaluated as

$$\boldsymbol{\delta_b = \int \frac{M(z)}{E_t I} dz} \tag{17}$$

$$\boldsymbol{\delta_s = \int \frac{V(z)}{G_t A_{ts}} dz} \tag{18}$$

where $z$ is the height coordinate; $M(z)$ is moment distribution along the cantilever; $V(z)$ is shear distribution along the cantilever; $E_t$ is elastic modulus; $G_t$ is shear modulus; $I$ is the second moment of area; $A_{ts}$ is shear area (i.e., 2A/3 for timber rectangular sections); and $h_n$ is the height at top level $n$.

#### *7.4.2.3.2.2 Frames*

The total rotation, $\theta_{tot}$, of the frame connections is the combination of the contributions due to beam rotation, $\theta_b$, column rotation, $\theta_c$, joint panel rotation, $\theta_j$, interface compression deformation, $\theta_{int}$, and gap opening deformation, $\theta_{gap}$.

$$\boldsymbol{\theta_{tot} = \theta_b + \theta_c + \theta_j + \theta_{int} + \theta_{gap}} \tag{19}$$

The elastic deformation of a frame system contains several contributors do not present in walls. These must be included to accurately predict the response analytically, as shown in Figure 17. The gap opening contribution, $\delta_{gap}$, can be derived from the moment-rotation analysis in Section 7.4.2.3.1, while the derivation of the beam rotation, $\theta_b$; column rotation, $\theta_c$; joint panel rotation, $\theta_j$; and interface compression deformation, $\theta_{int}$, are discussed below.

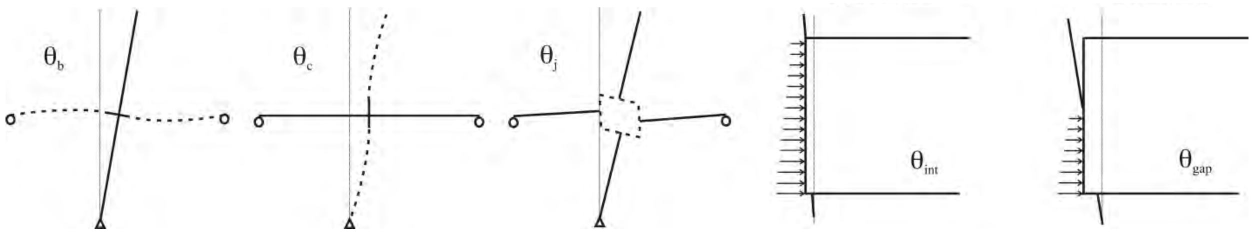


**Figure 17. Rotation contributions to a Pres-Lam frame (from left to right): beam deformation, column deformation, joint panel deformation, interface compression deformation, and gap opening deformation**

### Beam rotation, $\theta_b$

Calculations of flexural and shear deformations of beams are based on the following cantilever arrangement (Figure 18):

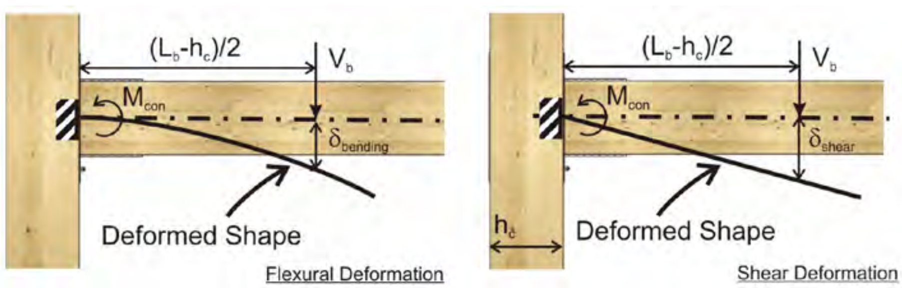


**Figure 18. Flexural and shear deformations of a cantilever beam**

The total rotation of the section in relation to the column face, $\theta_{b,con}$, is

$$\boldsymbol{\theta_{b,con} = M_{con}\left[\frac{L_b-h_c}{6E_{t,para}I_b} + \frac{2\alpha_{s,ci}}{G_t A_b(L_b-h_c)}\right]} \qquad [20]$$

where $E_{t,para}$ is the timber elastic modulus; $I_b$ is the second moment of inertia of the beam; $\alpha_{s,cl}$ is the shear coefficient, to convert average shear to centroidal shear ($\alpha_{s,cl}$ can be taken as 3/2 for rectangles); $G_t$ is the timber shear modulus; $A_b$ is the area of the beam; $L_b$ is the length of the beam; and $h_c$ is the width of the column.

During design, however, all elastic rotation contributions must be calculated about a common point. In this case, the common point is the centre line of the beam-column joint, and the beam rotation contribution of the column is

$$\boldsymbol{\theta_b = \frac{M_{con}}{L_b}\left[\frac{(L_b-h_c)^2}{6E_{t,para}I_b} + \frac{2\alpha_{s,cl}}{G_t A_b}\right]} \qquad [21]$$

**Column rotation, $\theta_c$**

The calculations of the flexural and shear deformations of the internal column are based on the cantilever arrangement shown in Figure 19.

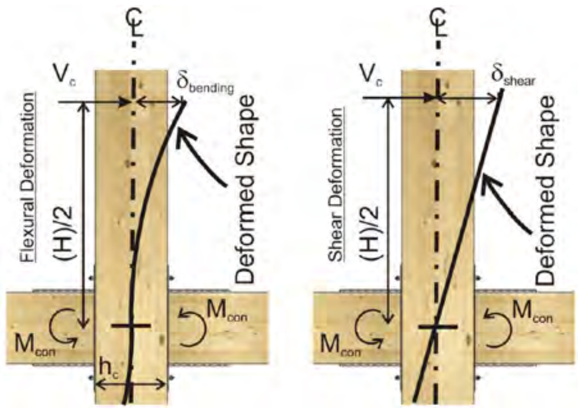


**Figure 19. Flexural and shear deformations of a cantilever column**

The total rotation of the column section, $\theta_c$, can be calculated as shown in Equation 22:

$$\boldsymbol{\theta_c = \frac{M_{con}L_b}{(L_b - h_c)}\left(\frac{H}{6E_{t,para}I_c} + \frac{2\alpha_{s,cl}}{G_t A_c H}\right)} \qquad [22]$$

where $I_c$ is the second moment of inertia of the column; $A_c$ is the area of the column; $L_b$ is the length of the beam; and H is the height of the column.

Since this rotation already occurs about the centre line of the column, it does not need to be converted. For an external column, on the other hand, the equation must be divided by two (2.0) due to the moment at the column centre line being half of that given above.

**Joint panel rotation, $\theta_j$**

Due to the low shear modulus of timber, the calculation of the total beam-column joint rotation contributions must account for the panel rotations of the column joints. Shear rotation in the joint panel is due to the change in force created by the addition of shear stresses in the columns due to the force couple, $V_{jp}$, created by the moment at the connection, $M_{con}$, as shown in Figure 20. When decompression occurs for an approximately full rectangular section, such as a typical beam in a post-tensioned seismic frame, the moment $M_{con}$ can be decoupled by the lever arm:

$$\boldsymbol{V_{jp} = \frac{3M_{con}}{2h_b}} \qquad [23]$$

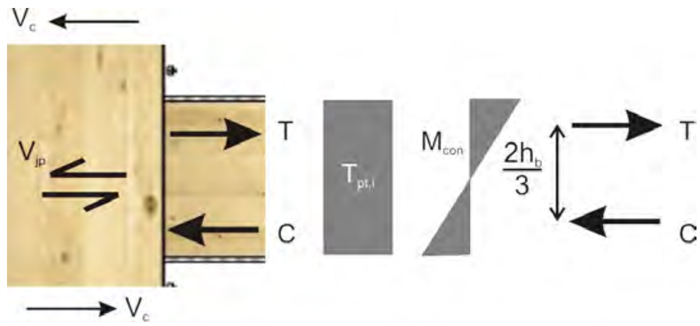


**Figure 20. Joint panel moment couple for an external joint**

After decompression, this lever arm increases towards the full section height ($h_b$). This is also the case when the reinforcement (dissipation) devices are added, but the design does not account for it. The following procedure thus provides a conservative estimate of joint rotation. The shear stress ($\tau_{jp}$) in the column is calculated as

$$\boldsymbol{\tau_{jp} = \frac{V_{jp}}{\alpha_{s,ave} A_c}} \qquad [24]$$

where $\alpha_{s,ave}$ is the shear coefficient needed to determine the shear rigidity of the section. For a rectangular section, the factor $\alpha_{s,ave}$ is

$$\boldsymbol{\alpha_{s,ave} = \frac{10(1+\nu)}{12+11\nu}} \qquad [25]$$

where $\nu$ is Poisson's ratio (taken as 0.55 for timber).

The rotation in the column joint panel is then simply the shear stress, $\tau_{jp}$, divided by the shear modulus, G. taking his equation for joint panel rotation and combining Equations 24 and 25 provides an equation for the calculation of the joint panel rotation, $\theta_j$, in terms of the connection moment, $M_{con}$:

$$\boldsymbol{\theta_j = \frac{3M_{con}}{2\alpha_{s,ave} A_c h_b G_t}} \qquad [26]$$

Figure 20 shows the case of an external beam-column joint, for which Equation 26 was developed. For an internal joint, the equation remains the same when there is no dissipative reinforcement. Otherwise, the moment couple increases by a factor of $(2 – \beta)$, where $\beta$ is the recentring ratio ($\beta = M_{pt}/M_t$) of the beam-column joint. The reasons for this are given in Figure 21. As shown, since the post-tensioning tendon is unbonded and passes through the column without transferring any force to it, the force couples are provided by the two compression contributions of each beam. To calculate these force couples, the connection moment, $M_{con}$, is again conservatively divided by a lever arm of $2h_b/3$. When dissipation is added to the beams and columns, the steel contribution to the total moment capacity, $M_{con,s} = (1 – \beta)M_{con}$, must be added to the single connection contribution provided by $M_{con}$. The total contribution to the joint panel deformation is thus $M_{con} + (1- \beta)M_{con} = (2 – \beta)M_{con}$.

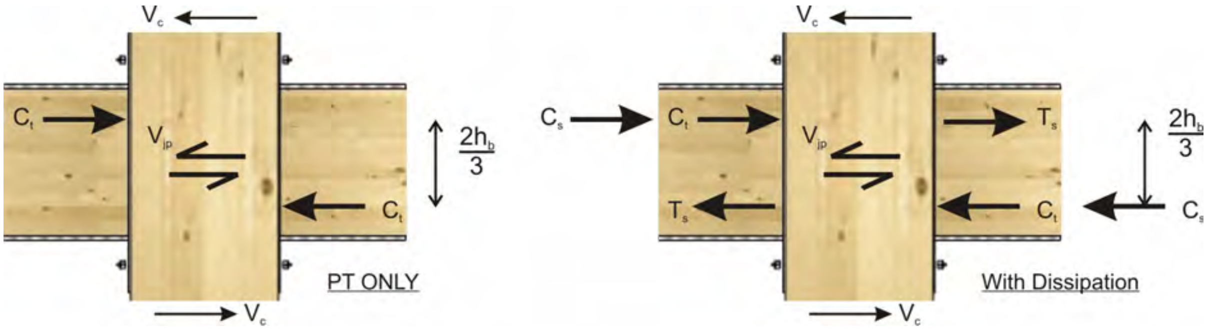


**Figure 21. Shear deformation contributions for an internal beam-column joint, with and without dissipation**

### Interface compression deformation $\theta_{int}$

Unlike post-tensioned walls on stiff foundations (e.g., concrete), the beams of the post-tensioned frames are connected to the columns, which are under compression perpendicular to grain. Figure 22 illustrates this effect. An initial compression is applied to a ridged block on a softer surface, then the rigid block representing the beam is translated sideways at its end, simulating movement due to seismic motion. An interface compression deformation ($\theta_{int}$), which indicates an additional rotational component due to compression perpendicular to grain deformation at the column face (van Beerschoten et al., 2011), must be considered in the post-tensioned frames.

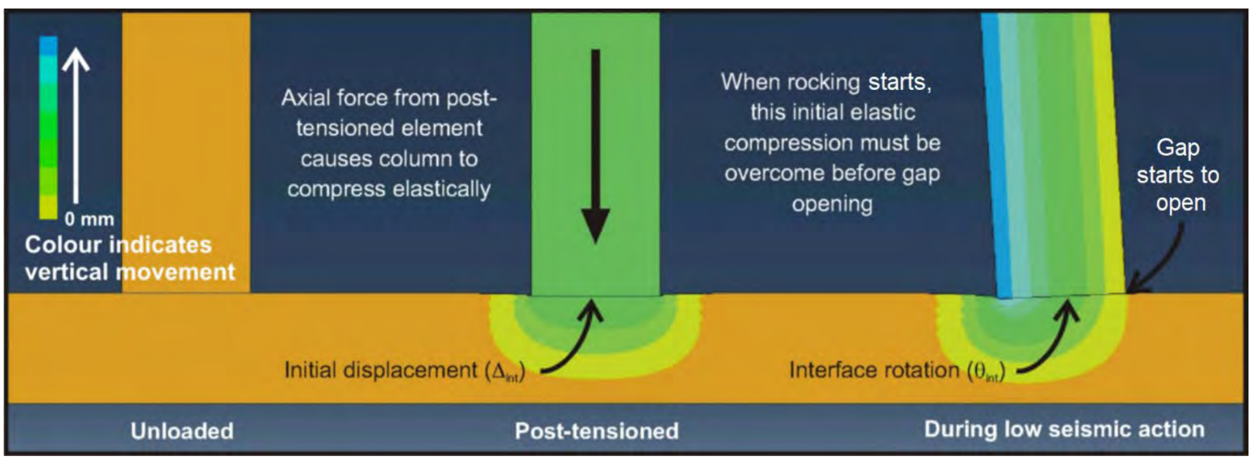


**Figure 22. Interface compression deformation simulation**

*Note: $\Delta_{int}$ is the initial displacement of the beam face into the column under stress (m); $\theta_{int}$ is the initial rotation of the beam face into the column under stress.*

In any timber post-tensioned system, the interface deformation shown in Figure 22 has a more significant effect than for concrete or steel. This is because of the low elastic modulus of timber perpendicular to the grain, which is 55 times less than that of concrete and 430 times less than for steel. The interface rotation is elastic and thus relatively simple to calculate using the following equation:

$$\theta_{int} = k_{int} \frac{T_{pt,i} h_c}{E_{t,perp} h_b^2 b_b} \quad [27]$$

where $k_{int}$ is the Interface compression factor, which accounts for load shearing and interface reinforcement and is discussed later in this section; $T_{pt,i}$ is the initial post-tensioning force; $E_{t,perp}$ is the beam bearing modulus perpendicular to grain; $h_c$ is column height; $h_b$ is beam height; and $b_b$ is beam width.

Tests have investigated the displacement of a timber block loaded perpendicular to the grain to understand the effects of stress-spreading (Blass and Görlacher, 2004) and screw reinforcement (Watson et al., 2013). A simplified model was then developed to compare the test case (reinforced and long enough to allow stress spreading to occur, as shown in Figure 23[a]) and a block of timber with uniform compressive stress and no reinforcement, as shown in Figure 23(b).

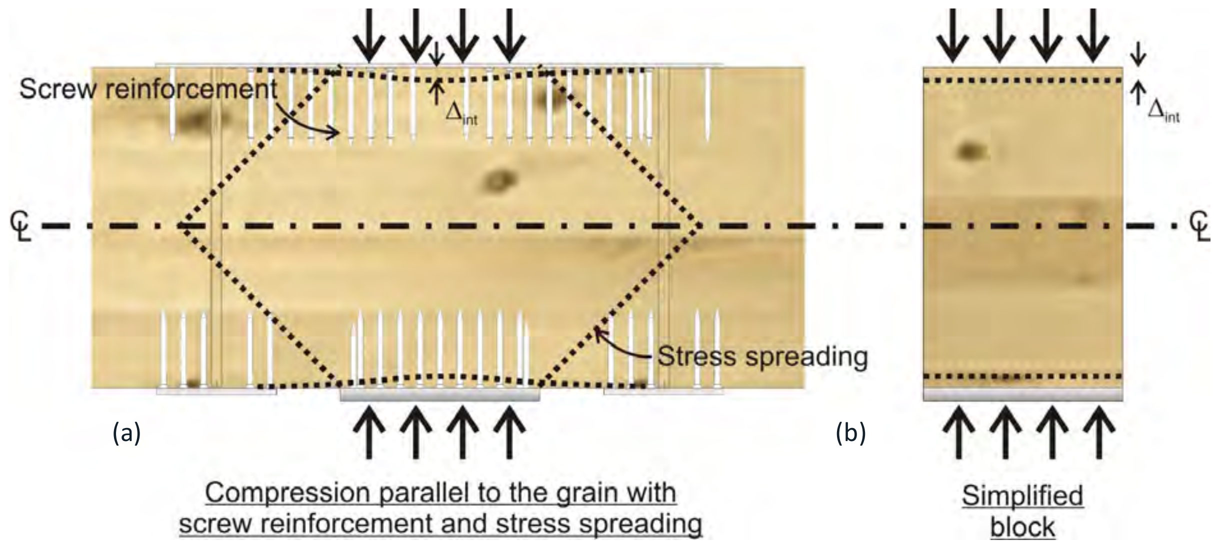


**Figure 23. Deformation of a timber block under perpendicular to the grain compression loading (a) with and (b) without stress spreading and screw reinforcement**

Watson et al. (2013) defined two formulas to account for stress spreading ($k_{ss}$) and screw reinforcement ($k_{scr}$). The first was based on the work performed by Blaβ and Görlacher (2004) and is defined as

$$\boldsymbol{k_{ss}} = \frac{\boldsymbol{h_c}}{\boldsymbol{b_L\, ln\left(\frac{h_c}{b_L}+1\right)}} \tag{28}$$

where $b_L$ is the length of the loaded area, taken as the beam height, $h_b$ (m).

The second equation, which accounts for the screw reinforcement, was derived by Watson et al. (2013):

$$\boldsymbol{k_{scr} = 1 + 54\,\frac{A_{scr}}{A_t}\left(\frac{l_s}{h_c}\right)^{1.26}} \tag{29}$$

where $A_t$ is the total area in compression (m$^2$); $A_{scr}$ is the total area of screw reinforcement (m$^2$); and $l_s$ is the total length of the screw (m).

The interface compression factor, $k_{int}$, is calculated by multiplying the stress spreading factor, $k_{ss}$, and the screw reinforcement factor, $k_{scr}$:

$$k_{int} = \frac{1}{k_{scr}k_{ss}} \qquad [30]$$

#### 7.4.2.4 Numerical Models

Modelling post-tensioned rocking systems can involve two main categories of model. The first are spring type models, including the rotational spring model and multi-spring model (Marriott, 2009; Newcombe, 2012; Palermo et al., 2005), with either the rocking connections or the gap opening mechanics simulated using spring elements. The second are material- or component-based models (Chen & Popovski, 2020; Wilson et al., 2019), with geometric and material properties as input.

##### 7.4.2.4.1 Spring Models

The most convenient model, in terms of calibration as well as computational efficiency, concentrates the system behaviour at the rocking connection (i.e., wall base or beam-column joint) via two parallel rotational springs. This is a rotational spring model. The contribution of the post-tensioning (recentring) moment is modelled using a multilinear elastic hysteresis, while the dissipative contribution can be modelled using a bilinear moment-rotation relationship. This represents a simplified and very convenient modelling technique, but it cannot provide detailed information about the system—which cannot simulate gap opening (and consequent uplifting)—and it does not model the actual elongation of the post-tensioning and mild steel reinforcements.

When a more detailed analysis is needed, a multi-spring model can instead be used for Pres-Lam walls. The detailed modelling approach makes use of a base contact element (a multi-spring element) to simulate the gap opening and variation in the neutral axis. This allows physically simulation of the system behaviour using truss (or spring) elements to model the post-tensioning and mild steel dissipators. The multi-spring model can be implemented in the modelling software RUAUMOKO (Carr, 2004), which has been widely used in past research on post-tensioned rocking systems (Marriott, 2009; Newcombe, 2012; Palermo et al., 2005), or in other general finite element software, such as ABAQUS and OpenSees (McKenna, 2011). OpenSees does not have a multi-spring element implemented, one can be developed within the code.

The multi-spring modelling approach, however, is not suitable for Pres-Lam frames: the frame shortening creates a difficulty. During the construction of a Pres-Lam frame building, it is common to stress the frames on the ground and then lift them into place. This avoids placing shear loading on the columns. However, this is not easily replicated in a numerical model, as loading would need to occur and the column boundary conditions would need to be set. As such, rotational spring models are more common for Pres-Lam frames.

###### *7.4.2.4.1.1 Rotational Spring Model*

When modelling post-tensioned walls and frames, a simplified modelling approach concentrates the system behaviour on a pair of rotational springs calibrated on the moment-rotation analysis presented in Section 7.4.2.3. The recentring and dissipative contributions are provided by the post-tensioning and mild steel reinforcements, respectively. Those contributions can be modelled using a multilinear elastic hysteresis for the recentring rotational spring and an elastoplastic relationship for the dissipative contributions, as illustrated in Figures 24(a) and 25. A similar approach can be adopted for coupled systems. The storey nodal points are then connected to the corresponding nodes of the wall elastic elements by rigid trusses. This couples the horizontal displacement of those nodes (i.e., no relative horizontal displacement is allowed), as shown in Figure 24(b). To account for the flexibility of the column base connection (Figure 26), an additional rotational spring can be used and calibrated, depending on the connection type used (Figure 24[c]). When defining the wall and frame elements, elastic elements are usually input by defining the elastic material and assigning the cross-sectional area, $A_t$, or shear area, $A_{st}$, as well as the second moment of the area, $I_t$.

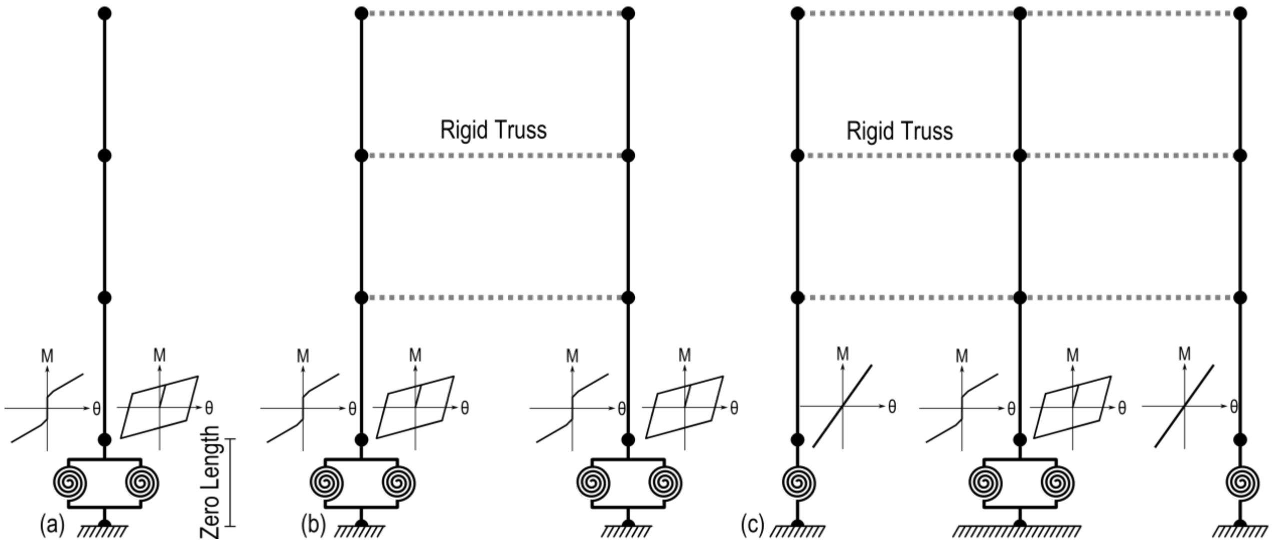


**Figure 24. Rotational spring wall model overview: (a) single wall, (b) coupled walls, and (c) column-wall-column system**

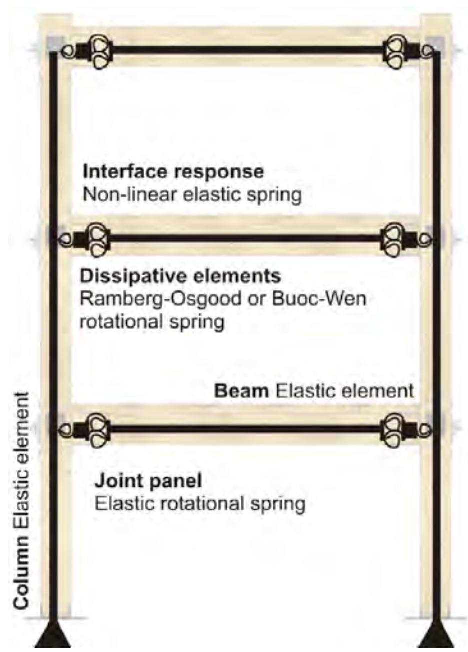


**Figure 25. Rotational spring frame model overview**

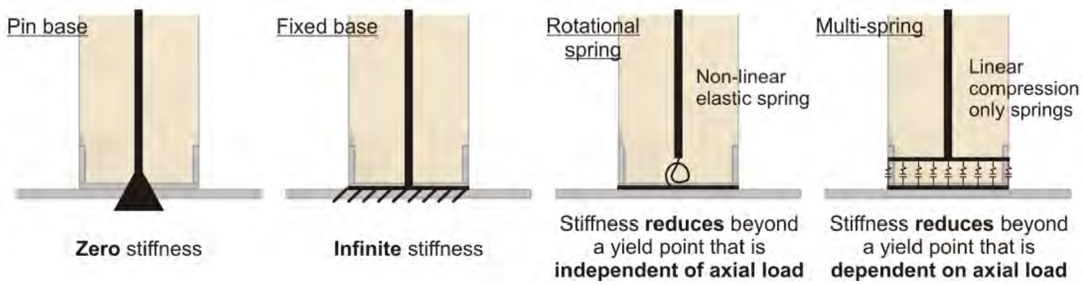


**Figure 26. Base connection modelling options considered for frame model**

When using rotational springs, calibration simply consists of matching the analytical moment-rotation results. The combination of hysteresis required is a multilinear elastic relationship for the recentring ratio, and an elastoplastic rule for the dissipative contribution. The multilinear elastic behaviour of a post-tensioned only solution usually involves a curved transition from the decompression moment and a linear trend after the 'yield' point moment $M_0$ (Figure 27[a]). For practical purposes, a secant branch from the decompression moment to the yield point, identified by the coordinates $M_0$ and $\theta_0$, can approximate the curved transition. Although the decompression point should be defined at zero connection rotation to ensure the numerical stability of the model, a nonzero rotation must be defined. In general, a value equal to 1/10 of the rotation $\theta_0$ gives stable and satisfactory results. The dissipative contribution (see Figure 27[b]) is defined by the yielding coordinates (i.e., rotation and moment) that result from the analytical moment-rotation. A post-yield stiffness ratio, r, must also be provided.

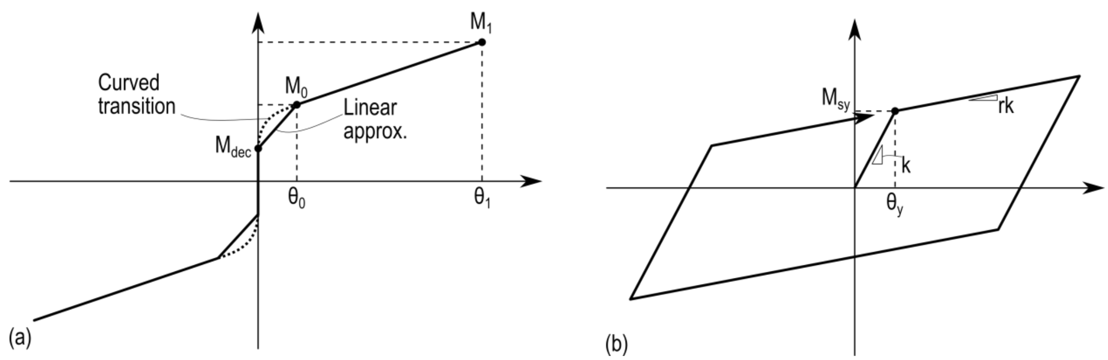


**Figure 27. Rotational spring model calibration: (a) multilinear elastic and (b) elastoplastic**

Given a coupled system, the base connection shall be calibrated in accordance with the moment-rotation analysis of each wall, as shown by Iqbal (2011). In column-wall-column systems the coupled elements are boundary columns which can have several end conditions (i.e., moment connection or pin; Figure 26). If there is some connection stiffness, it can be modelled using an elastic rotational spring at the base of the column element, calibrated to account for the particular fastening method used.

When designing post-tensioned timber frames, it is important to understand the amount of rotation that occurs at the beam-column connection, as this is linked to the connection moment capacity and the global frame behaviour. As discussed in Section 7.4.2.3.2.2, the total displacement of a post-tensioned timber frame comprises several contributing displacement sources (Figure 17): the elastic beam rotation, the elastic column rotation, the joint panel rotation, the interface compression deformation, and the gap deformation. The latter two are already incorporated into the rotational spring, while the former two are calculated directly using the numerical model. Finally, to model the joint panel deformation, a rotational spring is added in the joint panel region. The stiffness of the rotational spring, $k_{jp}$, is

$$\boldsymbol{k_{jp}} = \frac{2\alpha_{s,ave}A_c h_b G_t}{3}\frac{L_b}{L_b - h_c} \quad [31]$$

The final term in Equation 31, $L_b/(L_b-h_c)$, is necessary because standard practice is to place the spring representing the joint rotation at the beam-column centre line (shown in Figure 28). The joint rotation is related to the connection moment, $M_{con}$; therefore, there must be an increase in stiffness to account for the fact that in its position, the model will be subjected to the moment at the centre line, $M_{cl}$, rather than $M_{con}$; $M_{cl} = M_{con}L_b/(L_b-h_c)$.

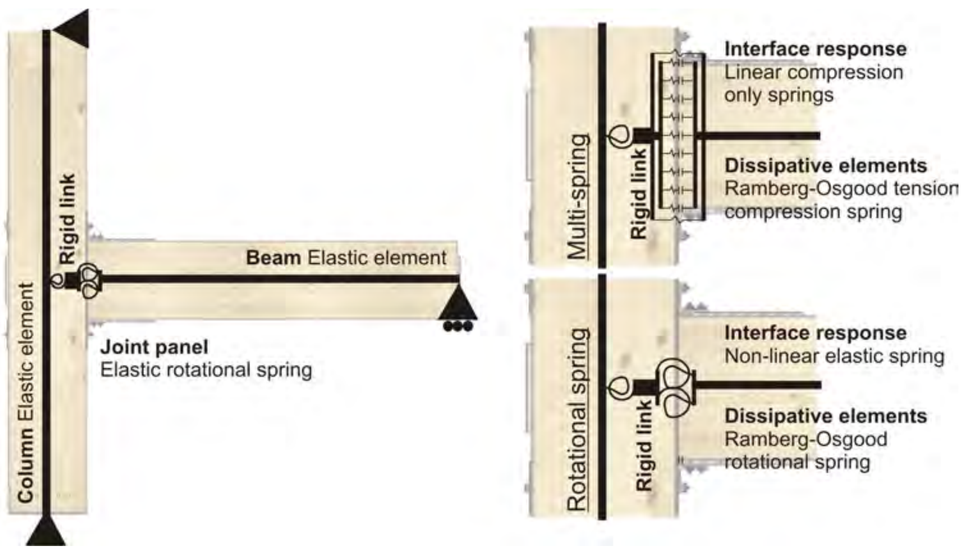


**Figure 28. Summary of rotational spring and multi-spring models for use in local beam-column numerical modelling prediction for post-tensioned timber frame connections**

### *7.4.2.4.1.2 Multi-spring Models*

The main advantage of the multi-spring model is that it simulates the base connection using a contact element at the base nodes for uplift and rotation. Since the gap opening is modelled, the post-tensioning tendons and dissipators are modelled using spring or truss elements. To account for shear deformations, the wall elastic elements are modelled using nonlinear beam-column elements, each of which is in turn modelled as an elastic section. The shear behaviour is then incorporated using a section aggregator (McKenna, 2011). The base multi-spring element consists of several parallel springs connected to the master nodes via rigid link elements. Compression-only material allows the gap opening. Finally, the post-tensioning is modelled using truss elements connected at the wall element with rigid links at the anchorage height, allowing for the unbonded length of the post-tensioning tendons. The initial preload of the post-tensioning springs must be input while taking into account the elastic losses of the model. After applying the preload and evaluating the shortening of the wall elements and multi-spring unit, the dissipating elements are connected to avoid initial compressive stresses.

For a single wall option (Figure 29[a]), the dissipation is concentrated at the wall-foundation interface. The dissipative reinforcement can be modelled using either zero-length spring elements or trusses. For the truss elements, the node distance from the base must account for the unbonded length of the dissipator. With zero-length spring elements, the connection nodes must be at zero distance and axial stiffness given as input. When modelling coupled systems, the wall is coupled either to another wall or to boundary columns (Figure 29[b] and [c]). The model can consist of a multi-spring unit and post-tensioning springs/trusses, as in the case of a single wall with the dissipators distributed along the height of the element. This can be done by creating a set of nodes at the depth distance of a half-section from the multi-spring centre line, connected via rigid links to the elastic wall elements. The nodes are then connected to the dissipator springs.

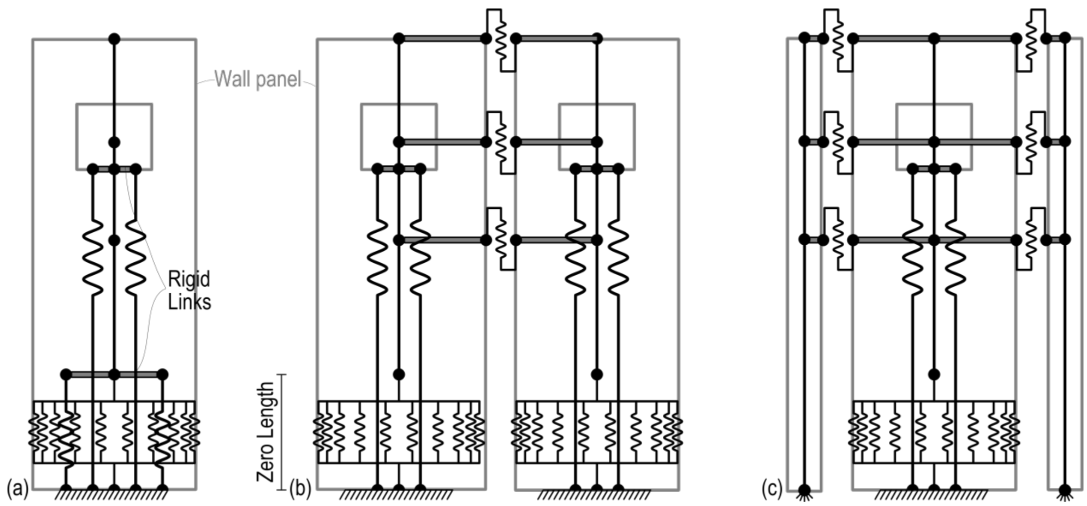


**Figure 29. Multi-spring models overview: (a) single wall, (b) coupled walls, and (c) column-wall-column system**

Like rotational spring models, multi-spring models must be calibrated against the analytical results. This process starts by calibrating the multi-spring axial stiffness using the results of the moment rotation analysis, followed by the prestress post-tensioned spring or truss elements, and the mechanical properties of the dissipators. The post-tensioning and the dissipative spring modelling should be calibrated against the material stress-strain relationships, as shown in the next section.

**Post-tensioning reinforcement material and initial force calibration**

The post-tensioning reinforcement can be modelled using either an elastoplastic or Menegotto-Pinto (Menegotto & Pinto, 1973) relationship, depending on the type of post-tensioning device used. An elastoplastic hysteresis is suitable for post-tensioning strands, while a Menegotto-Pinto rule is more appropriate for post-tensioning bars. In fact, the hysteresis can model the transition curve typical of hardened steel and can be calibrated to fit the post-tensioning stress-strain relationship for steel.

An issue with the multi-spring approach is that some post-tensioning elastic losses occur as a result of the axial flexibility of the wall elements, as well as the axial stiffness of the multi-spring unit. If the static analysis includes the initial preload in the post-tensioning springs/trusses, the elastic shortening of the wall and the multi-spring unit induce a force loss. Considering different stiffness contributions can help address this problem. The system can be represented by a spring system, as shown in Figure 30(b).

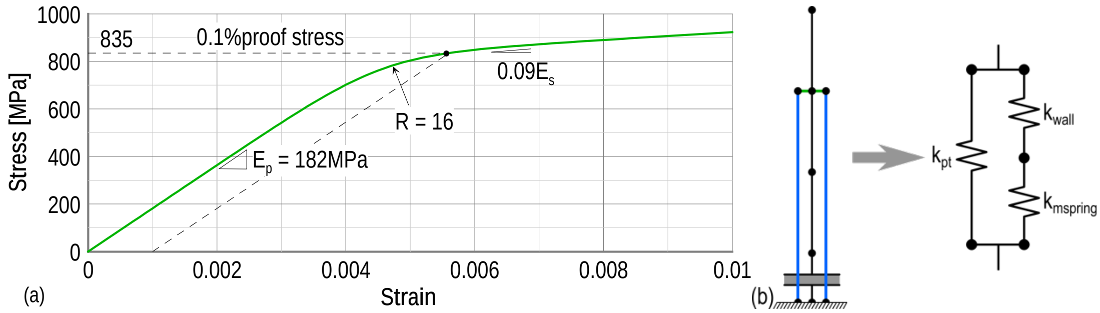


**Figure 30. Post-tensioning reinforcement calibration: (a) stress-strain relationship and (b) spring system for initial force calibration**

The shortening of the system, $\delta_{initial}$, due to the preload force in the spring, $T^*_{pt0}$, can be evaluated as

$$\delta_{initial} = \frac{T^*_{pt0} - \Delta T_{pt}(\delta_{initial})}{k_{pt} + \left(\frac{1}{k_{mspring}} + \frac{1}{k_{wall}}\right)^{-1}} \quad [32]$$

where $k_{pt}$ is post-tensioning spring stiffness and $k_{mspring}$ is the total stiffness of the multi-spring element. The loss of preload in the spring also depends on the initial shortening:

$$\Delta T_{pt}(\delta_{initial}) = k_{pt}\delta_{initial} \quad [33]$$

Based on the preceding equations, the initial preload in the spring necessary to achieve the required initial post-tensioning force $T_{pt0}$, or $T^*_{pt0}$, can be derived as follows:

$$T^*_{pt0} = \frac{T_{pt0}}{1 - \frac{k_{pt}}{2k_{pt} + \left(\frac{1}{k_{mspring}} + \frac{1}{k_{wall}}\right)^{-1}}} \quad [34]$$

**Dissipative reinforcement calibration and connection stiffness**

A zero-length spring can be used to model dissipative reinforcement. This should be calibrated while considering the appropriate hysteretic rule for the specific dissipative device used, as illustrated in Figure 31.

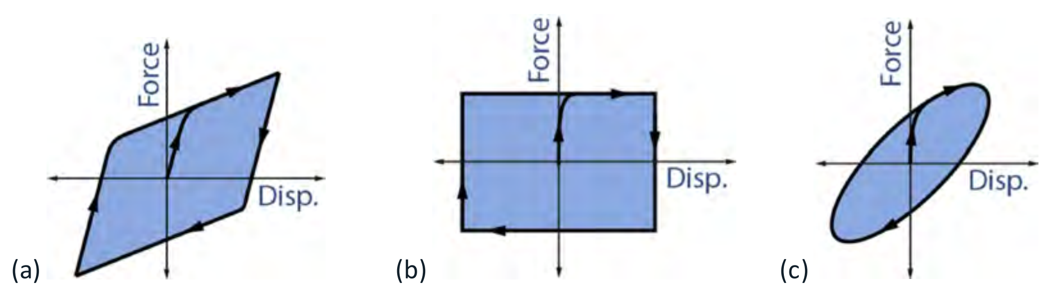


**Figure 31. Idealised hysteretic behaviour: (a) bilinear hysteresis for metallic dissipators, (b) rectangular hysteresis for friction dissipators, and (c) elliptic for viscous (Ugalde et al., 2019)**

The elastic stiffness of the dissipators' connections can have a significant influence on the overall behaviour of the system. When the dissipator is simulated using a single spring calibrated using the effective length, pulling the system back to its initial position should in theory push the dissipator back to zero displacement. As observed during experimental testing, however, this is not a realistic assumption. The compressive stresses in the dissipator push the connection in the opposite direction, causing the dissipator not to go to zero displacement after cyclic yielding (Figure 32). To account for this, the dissipator can be connected in series with an additional elastic spring.

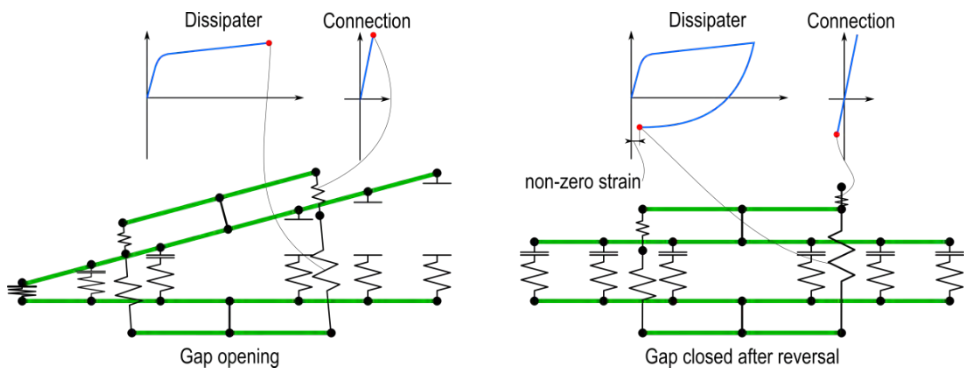


**Figure 32. Dissipator behaviour, accounting for connection stiffness**

As discussed earlier in this section, applying an initial post-tensioning force shortens the multi-spring unit. This leads the dissipators to compressive stresses before any lateral load is applied. Depending on the geometric characteristics of the dissipators, this could also result in compressive yielding before any gap opens. To solve the issue, the model should first define the structure nodes (including those connecting the dissipators) and connect the base contact element, the rigid links, and the post-tensioning springs/trusses into a post-tensioned only solution; a static analysis is then performed, applying the compressive forces from the post-tensioning springs to the model. Once the static analysis is performed, the dissipators and connection springs can be connected. This helps avoid initial compressive stresses in the dissipators.

7.4.2.4.2 Material- or Component-based Models

The Pres-Lam system can also be simulated using a material- or component-based modelling approach. Such an approach is demonstrated on a coupled Pres-Lam CLT (cross-laminated timber) shear wall, shown in Figure 33.

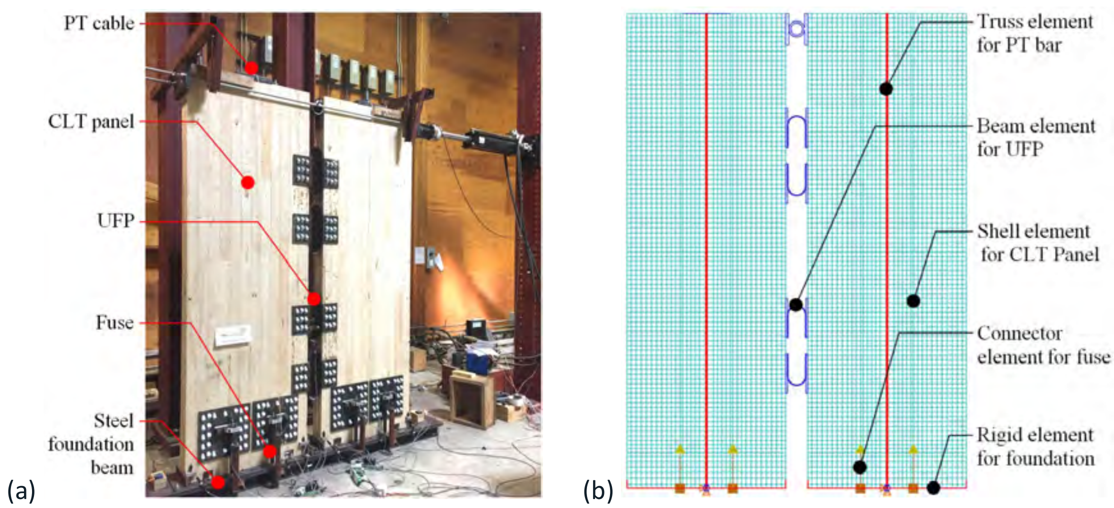


**Figure 33. Coupled Pres-Lam CLT shear wall: (a) testing specimen and (b) FE model**

### Structural components

CLT panels consist of several layers of boards stacked crosswise (typically at 90 degrees) and glued together on the wide faces and sometimes on the narrow faces (Karacabeyli and Gagnon, 2019). Generally, CLT walls under in-plane loading present a very complex stress state and many failure modes need to be considered (Danielsson and Serrano, 2018). As a result, detailed 3D finite element (FE) models with a comprehensive constitutive model of wood (e.g., Wood$^{ST}$; see Chen, Ni, et al., 2020) are desirable. The post-tensioning walls should be designed following capacity design methodology, such that only low damage (e.g., a certain amount of crushing) occurs at the bottom of the CLT panels. In such cases, the CLT panels can be modelled using shell elements with adequate stiffness and strength properties in each orthogonal direction. The material properties of the CLT panels can be derived by testing or from the existing results (e.g., Chen et al., 2018).

The steel post-tensioning cables are typically modelled using truss elements. Each cable can be meshed using a 2D thermally coupled truss element with an element length equal to the wall height and the corresponding diameter. The modulus of elasticity (MOE), and yield and ultimate strength can be derived from testing, or from the information provided by the manufacturer (e.g., DSI, 2018). The post-tensioning force applied to the wall can be achieved by lowering the temperature of the cable that caused the corresponding shortening (Dang et al., 2014). The physical and thermal properties of the cable can be taken according to test results or standards, such as the Eurocode 5 standard EN 1993-1-2 (European Committee for Standardization, 2005). The foundation and the steel plates connected to the cable at the top, for applying the post-tensioning force to the wall panel, can be modelled using rigid elements.

### Energy dissipators and connections

The ‘plug and play’ fuse is composed of a steel bar, covered by a steel tube, with a reduced cross-section in the centre for yielding and two half-steel-tubes filling the gap between the reduced section and the outer tube. It is in itself a relative complex system. Usually, the hysteresis loops of the fuses can be obtained through a refined (microscale level) FE simulation (Rahmzadeh and Iqbal, 2018). Another option is to consider the steel bar in this system as a buckling restrained element. Alternatively, the fuses can be modelled using truss elements or connector elements without considering buckling. A U-shape flexural plate (UFP) is a U-shaped steel plate, much simpler to model than such fuses. It can be simulated using a very detailed solid element model (Baird et al., 2014), a less detailed shell element model (Chen and Popovski, 2020), or a simplified beam element model. The specific dimensions (diameter and length of the reduced cross-section) and material properties (e.g., MOE and yield strength) of the steel bars and UFPs are needed as input.

The bracketed steel plates to connect the fuses to the wall, brackets to connect the UFPs to the CLT panels, and connections between the steel parts and the CLT panel or energy dissipator should include adequate overstrength factors, following the capacity design method. The loads from fuses or UFPs can thus be transferred to the panels efficiently and without any damage to the steel parts and CLT panels. Such connections between the panel and the energy dissipators can be treated as rigid constraints. To prevent unrealistic stress concentration from developing in the model, multiple point constraint technique can help connect the fuses and UFPs to the CLT panels.

The shear keys at the bottom of both ends of each panel prevent sliding between the wall and the foundation beam; the roller is installed at the top of the two panels to transfer the lateral load between them. These connections are typically designed with sufficient stiffness and strength to be modelled using rigid elements.

### Contact zones

Usually, the wall panel touches the foundation, the steel plate at the top, and the shear keys unevenly due to the manufacturing tolerance of the CLT panels and steel plates. An initial gap of 2 mm can be considered for these interactions, according to the tolerance requirement of PRG 320 (APA, 2019). This gap effect usually accounted for by downsizing the MOE of the wall panels with a modification factor (Newcombe, 2007); this can be simulated using 'softened' contact with friction (Dassault Systèmes Simulia Corp., 2016). The CLT panel can penetrate the foundation, the steel plate, and the shear key by a maximum of 2 mm. Contact stiffness, the ratio between the pressure transferred and the penetration, can be taken as 1% of the stiffness of the CLT panel in the longitudinal direction for contact between the CLT panel and the foundation or between the CLT panel and the steel panel on the top, and as 1% of the stiffness of the CLT panel in the transverse direction for contact between the CLT panel and the shear keys. The coefficient of friction can be taken as 0.2 for wood–steel contact (Engineering ToolBox, 2004).

The multiple point constraint technique can connect the steel plates between the CLT panel and the roller, or the UFPs to the CLT panels. The tie constraint can be used to fix the roller to one steel plate. 'Hard' contact can be applied to the interaction between the steel plate and a UFP or roller. The hard contact relationship minimises the penetration of the slave surface into the master surface at the constraint locations and does not allow the transfer of tensile stress across the interface. This approach ignores the friction in these contact pairs.

Wilson et al. (2019) developed FE models (Figure 34) for post-tensioned CLT walls using a similar approach. These models require only the physical and mechanical properties of wood and steel (post-tensioning cables, UFPs and fuses) as input.

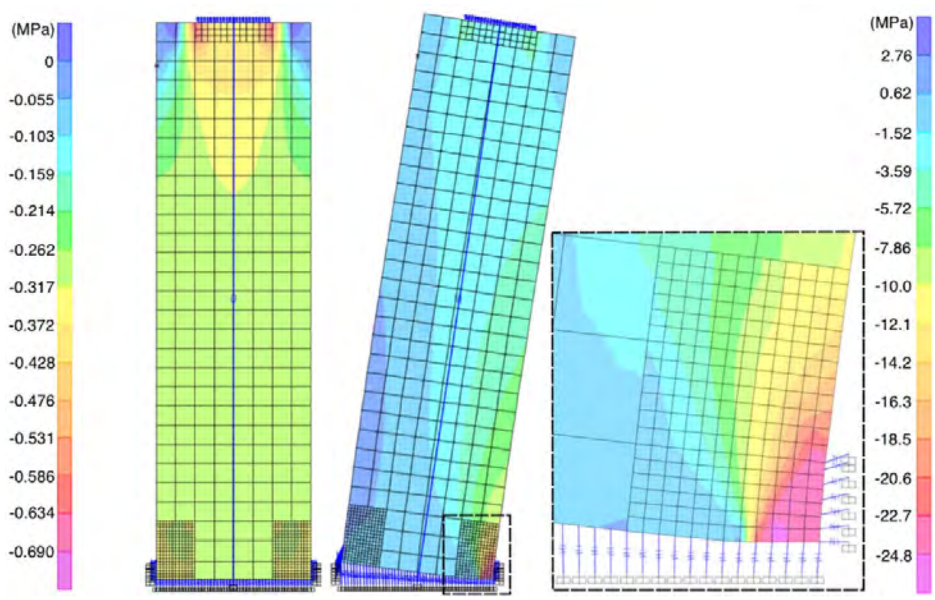


**Figure 34. Vertical stress in a post-tensioned shear wall (left) after initial post-tensioning force is applied and (right) at 3% drift, with close-up view of toe stresses (Wilson, 2019)**

## 7.4.3 Timber Systems with RSFJ Connections

Designed to slip before structural members yield, friction dampers (Figure 35) act as a reusable fuse that dissipates the seismic input energy without the need for replacement after an earthquake. In doing so, they allow a building to withstand an earthquake without sustaining significant damage to its structure. The inline friction damper dissipates energy as its elements slide relative to one another in both tension and compression, converting an earthquake's kinetic energy directly into thermal energy in a nondestructive process. Benefits of friction dampers include relatively low cost and maintenance, relative ease of design and installation, and velocity and temperature independence. Some have a rectangular hysteretic loop (Figure 35), which provides the highest possible energy dissipation per cycle. They can be installed in parallel to develop large loads and can act as load limiting devices (slip load limits buckling, column and foundation loads).

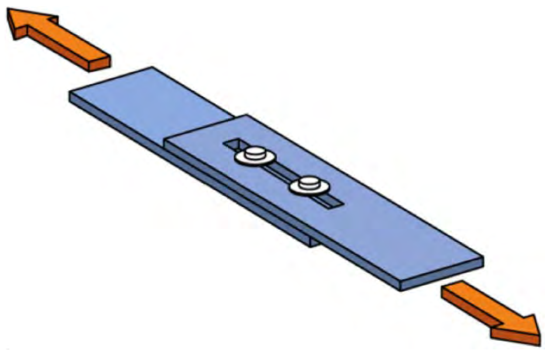

(a)

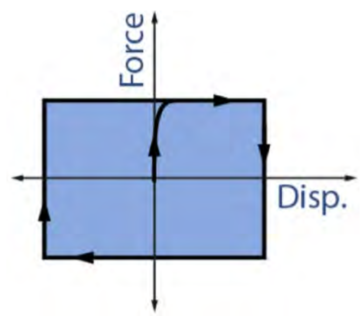


(b)

**Figure 35. (a) Schematic configuration and (b) idealised force-displacement hysteretic behaviour of a friction dissipator (Ugalde et al., 2019)**

One friction damper (connection) designed to avoid damage in timber structures during seismic events is the Resilient Slip Friction Joint (RSFJ), developed at the University of Auckland in New Zealand. An RSFJ (Figure 36) consists of two outer plates (black) and two centre plates with elongated holes (orange). The outer cap plates and the centre slotted plates are grooved and clamped together with high-strength bolts and disc springs. RSFJs can not only provide damping through friction but also self-centre due to their inherent configuration. The combination of this friction damping capability and self-centring ability makes these devices both ideal ductile fuses and damage avoidant. The RSFJ can be used in all possible Seismic Force–Resisting Systems (SFRSs), such as braced frames (Figure 37, left), shear walls (Figure 37, right), and moment-resisting frames.

(a)

(b)

**Figure 36. Schematic of a typical RSFJ (a) and its profiled plates (b)**

(a) (b)

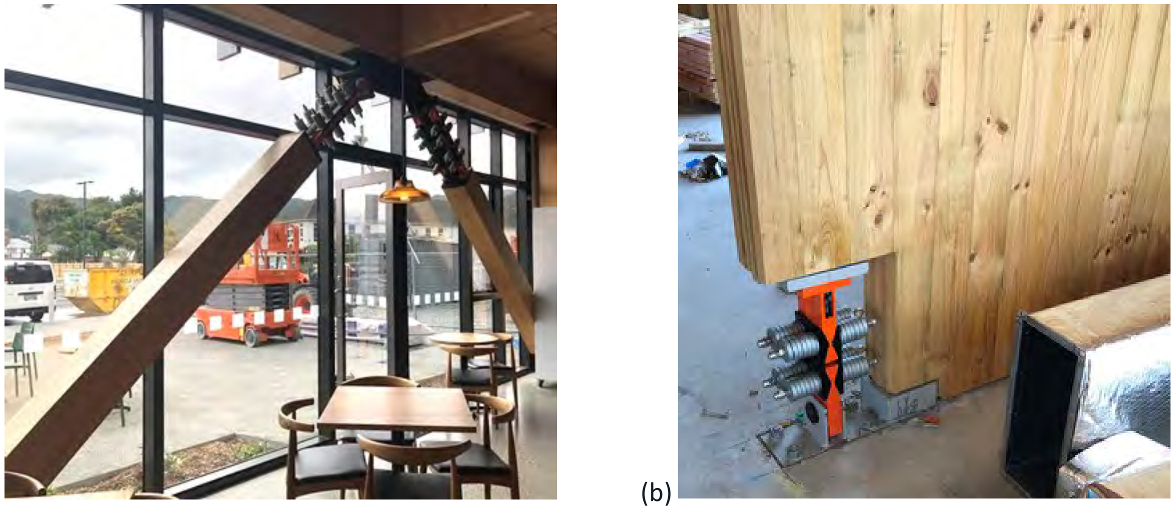

**Figure 37. (a) RSFJs in a braced bay and (b) an RSFJ used as a hold-down for a CLT wall**

### *7.4.3.1 Behaviour and Mechanism*

A certain level of friction is generated between the outer cap plates and the centre slotted plates of an RSFJ, which are clamped together with high-strength bolts and disc springs, as shown in Figure 37. Before the applied joint force overcomes the sloped beaming surfaces, the RSFJ is at rest (Figure 38[a]) and provides full stiffness. When the applied joint force overcomes the frictional resistance between the sloped bearing surfaces, the centre slotted plates start to slide (Figure 38[b], [c]) and energy is dissipated through friction during cycles of sliding. The patented shape of the plate ridges, along with the use of disc springs and high-strength bolts, allows the system to self-centre. The angle of the grooves is designed so, at the time of unloading, the reversing force from the elastically compacted disc springs is larger than the friction force acting between the facing surfaces. Therefore, the system recentres upon unloading. In its normal operation, no component yields. The fuse resets itself after the completion of an earthquake sequence, eliminating any loss of stiffness and restoring the building to its initial position, as shown by the hysteresis loop in Figure 39.

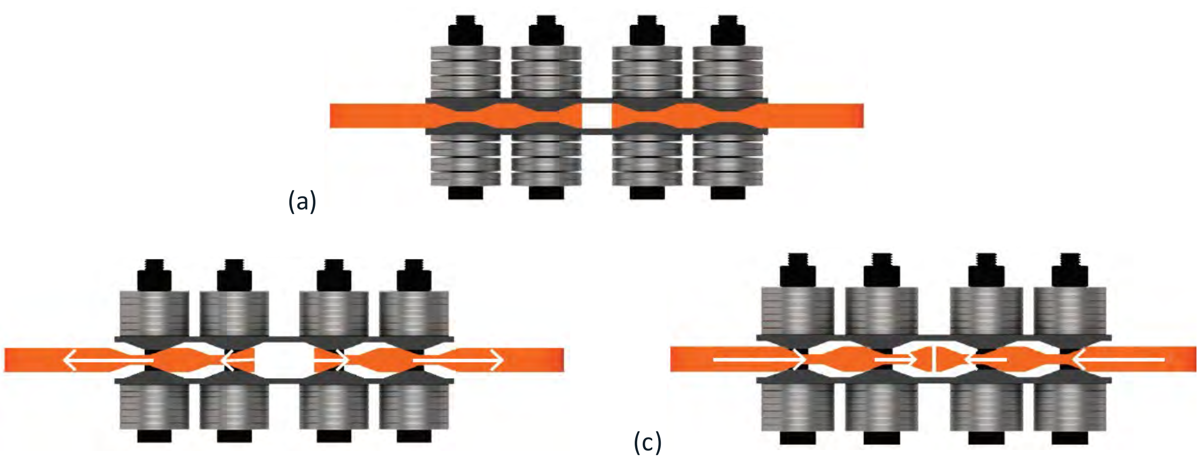

(a) (b) (c)

**Figure 38. RSFJ (a) at rest, (b) in tension, and (c) in compression (Courtesy of TECTONUS)**

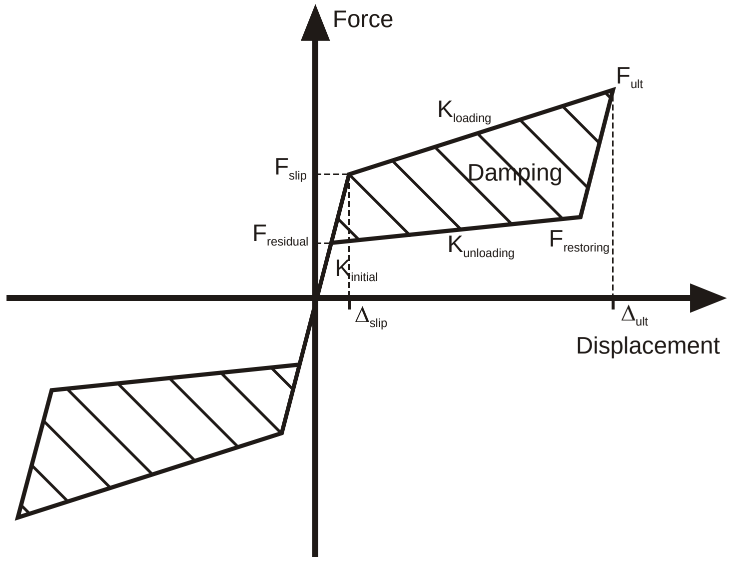


**Figure 39. Flag-shaped load-deformation response of the RSFJ**

The RSFJ connects one structural timber member to another (or to the foundation) through its middle plates. The bolts and disc springs have been prestressed to give the device an initial rigidity that prevents any movement under small load demands (wind or small earthquakes). When an earthquake of a certain level strikes, it imposes a displacement demand on the device, and the middle plates are either pulled apart or pushed closer together. Because of the shape of the plates, the two cap plates are pushed apart, and the outside disc springs are compressed. These compressed disc springs provide a restoring force that bring the device back to its initial position following the earthquake loading. This can be repeated as many times as required, if the force demand remains within the design load of the RSFJ.

The dimensions and configuration can vary to provide different levels of resistance and damping. Typically, the device damping ranges between 15% and 20%, depending on the amount of displacement provided. The damping ratio provided by this technology is one of the highest among available self-centring systems. The number of bolts, the angle of the grooves, the level of prestress of the bolts/disc spring assembly, and the number of discs springs are all design variables that allow the device to be customised for a range of demands. This variability in configuration results in a multitude of potential flag-shaped load-deformation relationships (Figure 39), accommodating different load and displacement levels.

For braced timber frames (Figure 37 [left]), it is important to ensure that the brace retained its required out-of-plane stability. Within the damper, a male/female anti-buckling tube assembly serves to ensure this. For rocking shear walls (Figure 37 [right]), the tension RSFJ connection provides the ductility while the wall horizontal shear connections remain rigid. For such applications, since the wall deformation can occur in all directions, there is a pin connection at the bottom along with a swivel bearing to eliminate internal bending moments, providing true deformation compatibility. The design philosophy for seismic resistant timber structures with RSFJs is based on the principle that the ductility comes from the RSFJ units; the other components, including the timber elements, remain linear elastic with minimised damage. This allows the structure to return to service following a quick inspection after a major seismic event.

### *7.4.3.2 Numerical Models*

The modelling methods for mass timber structures discussed in Chapter 7.2 are applicable to timber structures with RSFJs, but RSFJs are different from common timber connections. The models should properly simulate the RSFJ's flag-shaped hysteresis loops. These loops' key parameters include the slip force, $F_{slip}$; ultimate force, $F_{ult}$; restoring force, $F_{restoring}$; residual force at the end of unloading, $F_{residual}$; initial elastic deflection before slip, $\Delta_{slip}$; ultimate displacement, $\Delta_{ult}$; initial stiffness, $K_{intial}$; loading stiffness, $K_{loading}$; and unloading stiffness, $K_{unloading}$, as illustrated in Figure 39. The RSFJs can be modelled in commercially available design software such as ETABS or SAP2000, which both have a built-in link element (Damper-Friction Spring) that can accurately represent the load-deformation behaviour of the RSFJ. The parameters of the link element are initial (nonslipping) stiffness, slipping stiffness (loading), slipping stiffness (unloading), stop displacement, and pre-compression displacement. The precise values of the first four parameters are $K_{intial}$, $K_{loading}$, $K_{unloading}$, and $\Delta_{ult}$; the last parameter can be taken as $\Delta_{slip}$ - $F_{slip}/K_{loading}$.

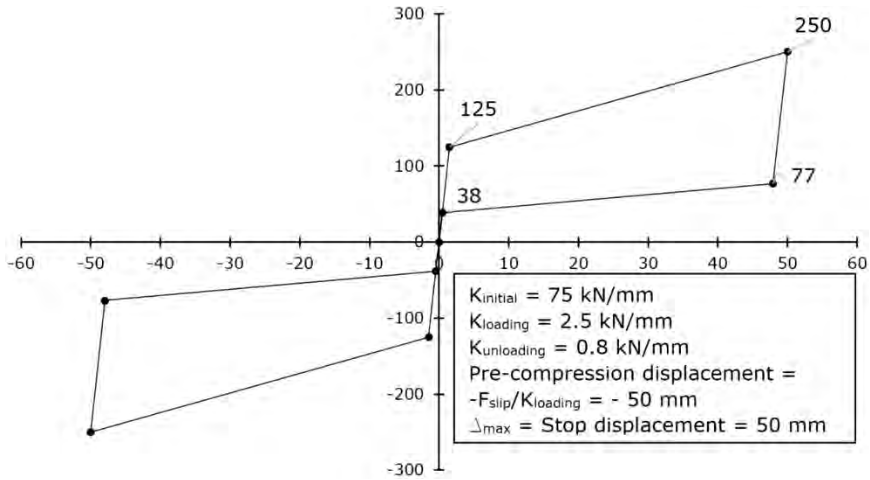


**Figure 40. Parameters for an RSFJ**

An FE model for a braced timber frame with an RSFJ for each diagonal brace is illustrated in Figure 41(a). The beams, diagonal braces and columns can be modelled using truss and beam element with corresponding geometric and mechanical properties. The former two should be pinned to the columns. The link element defined for the axial translational degree of freedom should be fixed to the diagonal brace and pinned to the column. If two RSFJs are used for each diagonal brace, one can either add another link element to the other end of the diagonal brace or just combine the two into one. To further simplify the model, a single link element can be adopted to simulate the diagonal brace assembly, which includes a brace and one or two RSFJ(s) in series. In such a case, the input stiffness value needs to be modified to account for the elastic stiffness of the whole brace assembly (i.e., $K_{total} = (n/K_{RSFJ} + 1/K_{brace})$, where n is the number of RSFJs and $K_{brace}$ is the stiffness of the diagonal brace). Figure 41(b) shows an FE model for a shear wall with RSFJs as hold-downs. The wall can be modelled using shell elements with the corresponding mechanical properties. The wall should be pinned to the foundation at the centre of its base in the horizontal direction and connected to the foundation with contact elements at the two conners of the base. The contact elements should be able to simulate the compression transfer and gap opening.

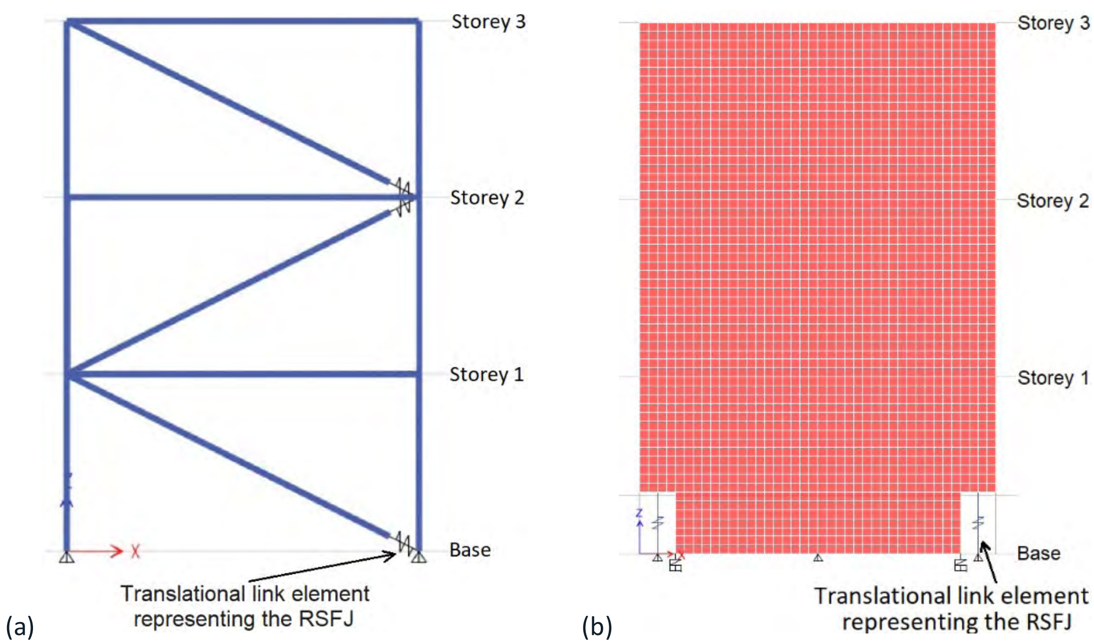


**Figure 41. FE models for timber structures with RSFJs: (a) braced timber frame and (b) shear wall**

This type of seismic damper, and any other defined energy-dissipative device, must be connected to the timber structural element with the stiffest possible connection. This ensures that any deformation is concentrated in the friction damper, and the maximum earthquake energy is damped. A poorly detailed connection results in slackness and decrease the efficiency of the damping system. Thus, in any structural analysis that looks at the effect of seismic dampers on structural response, it is advisable to connect the structural element of the seismic fuse (usually with a link having a distinct load-deformation response) to another link that accounts for the actual stiffness of the connection between the damper and the remaining timber structural element. This is shown in Figure 42.

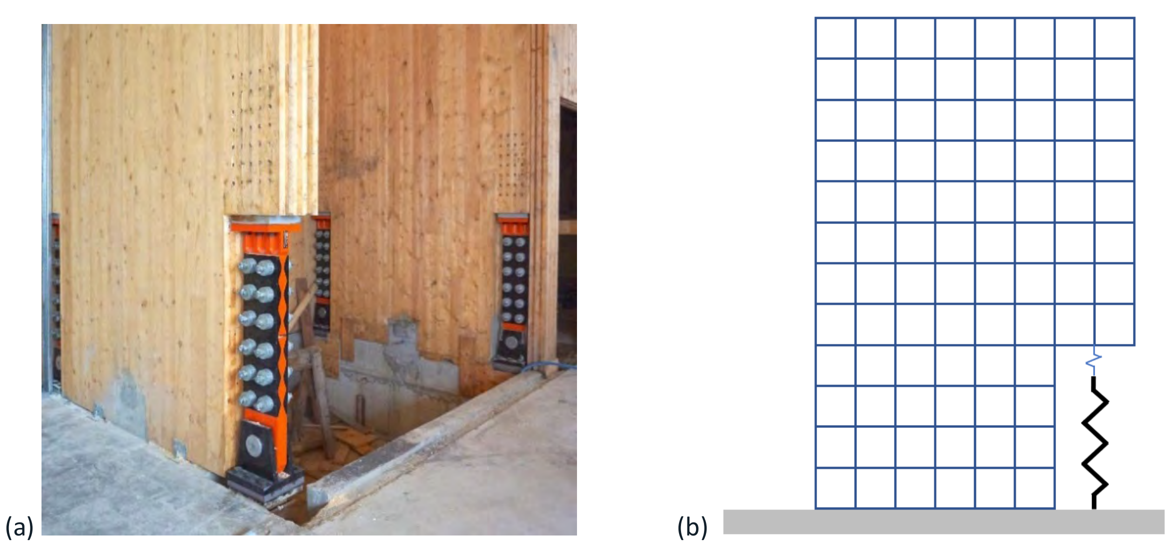


**Figure 42. (a) Rocking CLT shear wall with seismic damper at its bottom corner and a dowelled connection linking the damper to the CLT panel; (b) the numerical model equivalent**

## 7.4.4 Seismic Isolation and Applications

### *7.4.4.1 Theoretical Basis of Seismic Isolation*

Seismic isolation has evolved as a superior method to protect an entire building from the damaging effects of earthquakes, and this applies to timber structures as much as to any others. It is the only known technique that can simultaneously reduce interstorey drift (protection of the structure) and floor accelerations (protection of contents). Stated simply, seismic isolation is a dynamic response modification strategy that serves to reduce demands on the structure rather than to increase its capacity. In traditional base isolation, the building is supported on flexible devices or isolators at its base. The devices together create a flexible layer that separates the building from the input ground motion. When designed effectively, the isolation layer is substantially more flexible than the structure above it, or superstructure, effectively making the latter rigid (Figure 43[a]).

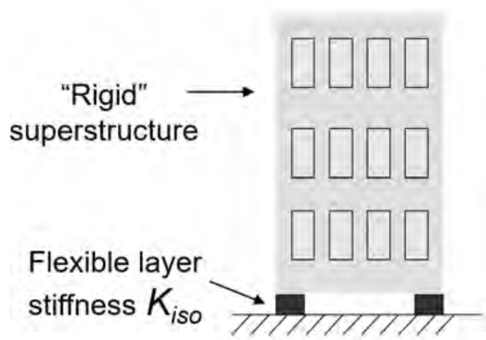


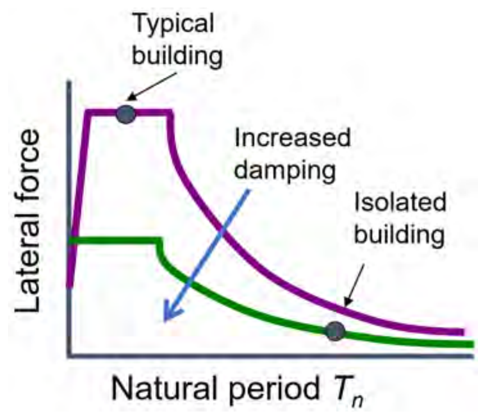


**Figure 43. (a) Rigid superstructure on flexible isolation, and (b) design spectrum for conventional and isolated structure**

The overall effect of the isolation layer is to lengthen the natural period of the structure. A desired period can be achieved by selecting the isolation system parameters. Using spectral design principles, elongating the period results in a significant reduction in lateral force or design base shear. Whereas a typical, low- to mid-rise building falls in the constant acceleration region of the design spectrum, an isolated building can be tuned in the region where the spectral acceleration is inversely proportional to period, as shown in Figure 43(b). While the design base shear decreases, the trade-off is a substantial increase in deformation demand. However, these deformations are mostly accommodated by the isolation devices, due to their flexibility. The isolator deformations are further controlled through energy dissipation, which leads to a reduction in the design forces (Figure 43[b]). Popular isolation devices have substantial energy dissipation capacity, and the isolation system may be accompanied by supplemental damping devices such as viscous fluid dampers or hysteretic steel dampers.

Modal analysis shows that the natural period of well-isolated building is only slightly longer than the 'isolation period,' as the stiffness of the isolation system supports a rigid mass. The first mode shape is close to uniform (i.e., is the rigid structure response mentioned earlier). Even more than in a typical building, the dynamic response under earthquake loading is dominated by the first mode response, because this mode is nearly identical to the input acceleration vector. Higher modes, which are nearly orthogonal to the input acceleration vector, do not get expressed (Chopra, 2016). Compared to a fixed-base building, in which deformation demands are distributed over the height, the deformation demands in an isolated building resemble the first mode shape, with deformations concentrated in the isolation system (Figure 44).

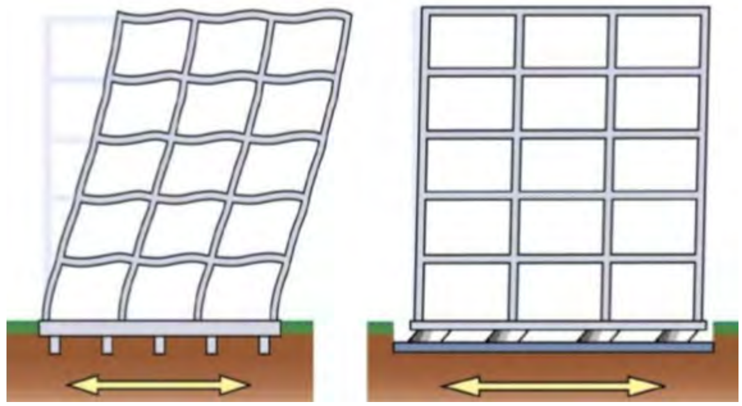

**Figure 44. Distribution of deformation demands in fixed vs isolated building (Courtesy of Dynamic Isolation Systems)**

Seismic isolation loses some effectiveness if the superstructure is too flexible, and the isolation system cannot induce a sufficient period shift. In this case, the fundamental period of the isolated structure is noticeably longer than the isolation period, and the first mode shape includes noticeable structural deformation. However, such a condition is more acceptable and even expected when isolating a tall building. While it is not usually possible to achieve total isolation in rigid superstructures, in tall structures, the isolation system can help substantially reduce drift demands throughout the height of the structure.

The preceding discussion assumes that the isolation plane is located at the base or foundation level. Base isolation is most effective because the entire mass of the building is isolated. When applied at the base, isolators are installed on pedestals or footings on the foundation, and base level framing is erected on top of them. All utilities that extend into the foundation and thus cross the isolation plane must be detailed for the seismic gap, including plumbing for water and wastewater, natural gas, and electrical lines. Flexible piping with large loops or bends is a common feature. Some components, like stairs and elevator shafts, may be extended into the isolation plane. The isolation plane is commonly at ground level or below, in which case the building is surrounded by a moat the width of the isolation gap. A sacrificial moat cover often surrounds the building and hides the isolation moat.

Moving the isolation plane to the top of the first story does not affect the effectiveness of the system (because there is no significant mass below this level), and it theoretically reduces costs. In this scenario, isolators may be installed directly atop the first story columns. There is no need for an additional floor level at the foundation just above the isolators, or for a costly moat and moat covers. However, additional building components must be detailed to cross the isolation interface, such as an exterior façade, interior partition walls, and stair systems. The new Justice and Emergency Services Precinct Buildings in Christchurch, New Zealand, adopt this approach. Other circumstances can motivate the placement of the isolation plane at various levels in a structure. For instance, in mid- to high-rise buildings in Japan, interstorey systems at mid-level served to separate lower and upper occupancies in both structure and form (Tasaka et al., 2008). Roof isolation as a retrofit strategy is much less intrusive than base isolation. Interestingly, 185 Berry Street in San Francisco, California, US, was retrofitted with two additional stories on top of an isolation system.

Ryan and Earl (2010) investigated the trends in the dynamic response of a six-story building as the plane of isolation was systematically varied from the base level to the roof, while keeping the fundamental period of the isolated building constant. They found that isolation systems at various levels are similarly effective in mitigating the force demands above the isolators, but do little to mitigate the force demands at levels below the isolation system. As such, overall effectiveness decreases as the location of the isolation system moves up the structure. The roof isolation system was found to be the least effective location, but it still reduced force demands throughout the structure by about 30% as compared to the reference fixed-base structure. The effectiveness of the roof isolation system increases by maximizing the isolated roof mass.

#### *7.4.4.2 Isolation Device and Mechanics-based Models*

Two classes of isolation devices are in common use today: elastomeric and spherical sliding bearings. These two classes of bearings are briefly introduced below, along with their specific mechanics-based models.

**Bearing Class 1: Elastomeric Bearings**

Elastomeric bearings comprise the class of bearings that utilises rubber elastomers for lateral flexibility. The basic composition of these devices is well-represented by the natural rubber bearing (Figure 45). This is composed of alternating layers of rubber elastomer and thin steel shims. All layers are bonded together, as well as to top and bottom cover plates. The rubber layers provide lateral flexibility, while the intermediate steel shims provide vertical rigidity/stability and prevent excessive bulging of the rubber. An outer layer of cover rubber protects the bearing components.

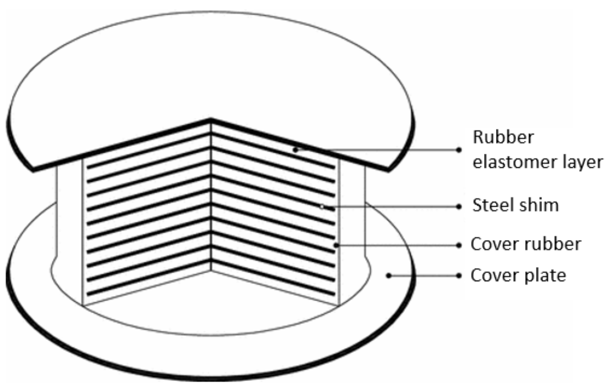


**Figure 45. Natural rubber bearing**

Natural rubber bearings have no inherent energy dissipation and thus are generally accompanied by independent energy dissipation devices, such as fluid viscous, steel, or lead dampers. For efficiency and economy, alternative devices package energy dissipation within the elastomeric bearing. The most common is the lead-rubber bearing, which has a lead core press fitted into the centre of the bearing (Figure 46). When subjected to lateral force demands, the lead yields (flows) and dissipates energy.

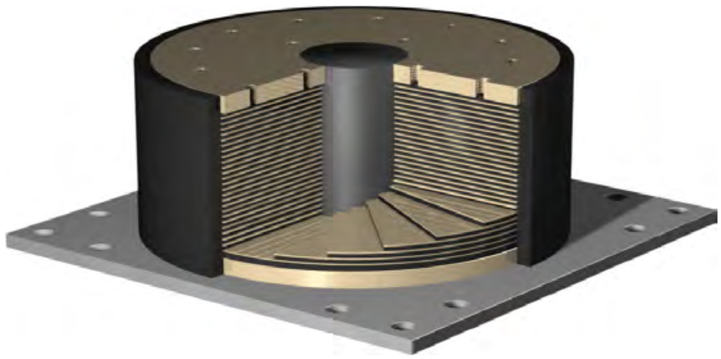

**Figure 46. Lead-rubber bearing (Courtesy of Dynamic Isolation Systems)**

Another alternative is a high-damping rubber bearing, made from specially formulated rubber compounds that provide intrinsic damping associated with strain in the elastomer. High-damping rubber bearings can provide 8 to 16% of critical damping during a design level earthquake (ASCE, 2004). High damping rubber bearings have nonlinear stiffness, with a tendency to stiffen at large shear strains. They are also subject to stiffness degradation (scragging) after multiple cycles of loading. Modelling them is more complex than other rubber bearings, and they are not widely used outside Japan.

The basic mechanical properties of elastomeric bearings are essentially the same for each bearing type. The lateral stiffness of the bearing (based on the properties of the elastomer) is given by

$$k_r = \frac{GA_r}{\sum t_r} \qquad [35]$$

where $G$ is the shear modulus of the rubber; $A_r$ is the bonded cross-sectional area of rubber; and $t_r$ is the thickness of a single rubber layer. The summation over $t_r$ represents the total thickness of rubber. The cover rubber is not included in the bonded area. The lateral resistance for most elastomeric bearings is essentially linear even for large shear strains in the rubber, except in the case of the high-damping rubber bearing.

The vertical stiffness of an elastomeric bearing is given by

$$k_V = \frac{E_c A_r}{\sum t_r} \qquad [36]$$

where $E_c$ is the compression modulus of the rubber-steel composite. Kelly (1997) showed that the compression modulus of a multilayer bearing depends on its shape factor $S$, which is the ratio of the loaded area to the force-free area of a single rubber layer. For instance, for a circular bearing, $S = R_r/2t_r$ ($R_r$ is the bearing radius) and $E_c = 6GS^2$. Kelly (1997) gives derivations for bearings with different geometry.

The rotational or bending stiffness of a bearing is given by $P_E h_b$, where $h_b$ is the total bearing height, including steel layers, and $P_E$ is the Euler buckling load:

$$P_E = \frac{\pi^2 (EI)_S}{h_b^2} \qquad [37]$$

where $(EI)_S$ is the effective bending stiffness (moment versus curvature) of the multilayer bearing, given by

$$(EI)_S = \frac{1}{3} E_c I \frac{h_b}{\Sigma t_r} \tag{38}$$

and $I$ is the conventional bending moment of inertia, based on bearing geometry (Kelly, 1997; Ryan et al., 2005). The torsional stiffness of an individual bearing can usually be neglected in favour of the torsional resistance of the whole structure.

The lateral force-deformation must be modified in a lead-rubber bearing to account for the effects of the lead core, which exhibits high stiffness until it yields and begins to flow. The yield force $Q$ of the lead core is

$$Q = A_{lead}\sigma_{y,lead} \tag{39}$$

where $A_{lead}$ is the cross-sectional area of the lead core and $\sigma_{y,lead}$ is the yield strength of the lead. Combining the effects of the linear stiffness of the elastomer and the resistance of the lead core (elastic-perfectly plastic), the lateral resistance of the lead-rubber bearing can be idealised as bilinear, with yield force $Q$ (y-intercept value) and post-yield stiffness $k_r$ (Figure 47). The instantaneous force $F_b$ in the post-yield region can be represented by

$$F_b = Q + k_r U_b \tag{40}$$

where $U_b$ is the bearing deformation. The circular bearing exhibits the same response to deformation in any radial direction. The force-deformation response replicated from test data shows that the bearing response gradual transitions from the initial to the post-yield region; there are vary modelling strategies to represent this behaviour. The initial stiffness $k_i$ is usually taken as 10 to 20 times the post-yield stiffness $k_r$ (Figure 47).

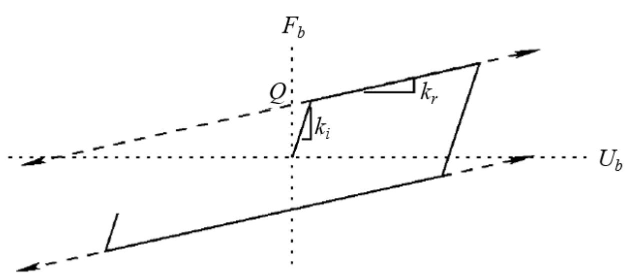


**Figure 47. Bilinear force-deformation of a lead-rubber bearing**

**Bearing Class 2: Flat and Spherical Sliding Bearings**

The second class of bearings include all friction based-devices, which includes flat sliding bearing, rolling bearings, and spherical sliding bearings. Bearings in this class use friction between the sliding surfaces to resist movement in an earthquake. The friction component is mathematically represented as

$$Q = \mu N \tag{41}$$

where $N$ is the instantaneous normal force on the bearing and $\mu$ is the sliding coefficient of friction. The normal force is sometimes represented as the weight carried by the bearing; however, the normal force on a sliding bearing can vary when the building is subjected to vertical acceleration and overturning, which has important implications for the modelling.

Flat sliding bearings may be designed with a very low friction sliding surface (Figure 48[a]). Comparable rolling bearings use nearly frictionless ball bearings that roll within guide rails (Figure 48[b]). Flat sliding/rolling bearings are not used alone in an isolation system due to their lack of a restoring force (i.e., they have no tendency to recentre after a large earthquake event). However, these devices may be used in combination with elastomeric bearings to provide additional stability to the system without increasing the overall base shear.

(a) 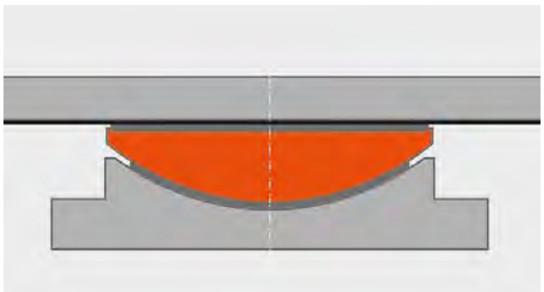 (b) 

**Figure 48. (a) Sliding bearing with a top flat surface (Courtesy of MAURER), and (b) cross-linear bearing with perpendicular guide plates that constrain movement along top and bottom rails**

The original spherical sliding bearing was manufactured by Earthquake Protection Systems as the Friction Pendulum System™, and is now referred to as the Single Pendulum™ bearing. In this bearing system, an articulated slider rests on a concave surface (Figure 49). The details of the sliding interfaces that control the friction coefficient are proprietary but believed to be stainless steel sliding on a polytetrafluoroethylene (PTFE; more commonly known as Teflon) or woven PTFE surface. Sliding friction coefficients can range from 0.02 to 0.15. The instantaneous friction coefficient also depends on velocity.

**Figure 49. Single pendulum bearing (Courtesy of Earthquake Protection Systems)**

While flat sliding bearings have no restoring force, the curvature of a single pendulum bearing provides a linear restoring force inversely proportional to the radius of the curvature. Thus, the restoring force in the bearing can be represented by

$$F_b = \mu N \, sgn(\dot{U}_b) + \frac{N}{R_c} U_b \qquad [42]$$

where $R_c$ is the radius of the curvature, and the stiffness associated with the restoring force is $N/R_c$. The total force deformation response is represented by Figure 50. It combines the effects of friction resistance (rigid plastic) with the linear restoring force. Conceptually, the initial stiffness is much greater than in a lead-rubber bearing and should correspond to a yield deformation on the order of 2.5 to 5mm (0.1 to 0.2 inches).

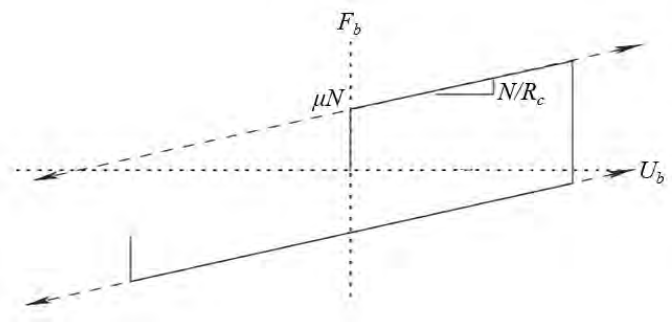


**Figure 50. Bilinear (rigid-plastic) force deformation response of a single pendulum bearing**

The vertical stiffness of a friction pendulum bearing can be computed as

$$k_V = \frac{1}{2}\frac{E_S A_S}{h_b} \quad [43]$$

where $E_s$ is the elastic modulus of steel; $A_s$ is the area of the inner slider; and $h_b$ is the total bearing height (Sarlis and Constantinou, 2010). The rotational and torsional stiffness of the bearing is essentially zero (Sarlis and Constantinou, 2010), as the isolator has insignificant resistance to both forms of motion.

Multi-spherical sliding bearings incorporate the concept of multiple sliding surfaces. This has two advantages: first, the bearings can then offer a comparable displacement capacity in a more compact and economic package with less steel; second, the properties of the sliding surfaces can be tuned for multiple performance objectives (i.e., targeted response to service-, design-, and maximum considered earthquake-level events).

A double pendulum bearing comprises an articulated slider between top and bottom spherical sliding surfaces (Figure 51). Sliding can occur on both surfaces, and the friction coefficients $\mu_1$, $\mu_2$ and radii of curvature $R_1$, $R_2$ can be selected independently for each. A Triple Pendulum™ bearing incorporates one double pendulum mechanism within another, larger one (Figure 52). Sliding occurs over the four unique surfaces, and again, friction coefficients $\mu_1$, $\mu_2$, $\mu_3$, $\mu_4$ and radii $R_1$, $R_2$, $R_3$, $R_4$ can all be selected independently. Generally, the inner sliders have lower friction coefficients and smaller radii of curvature than the outer sliders and engage in lower-level events. The properties of the outer set of sliders are optimised for a design-level event.

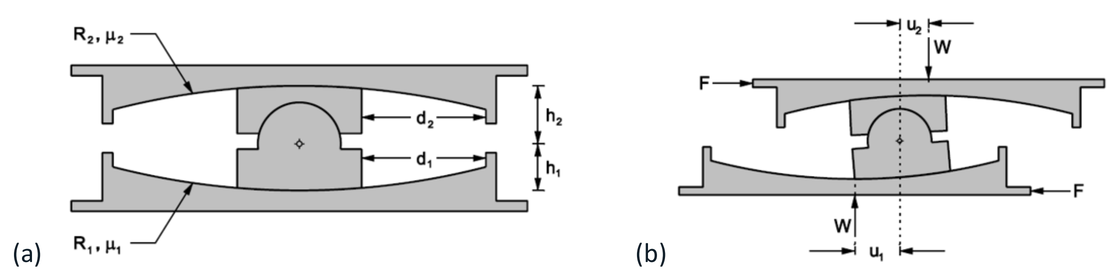


**Figure 51. Double pendulum bearing: (a) undeformed, and (b) during sliding**

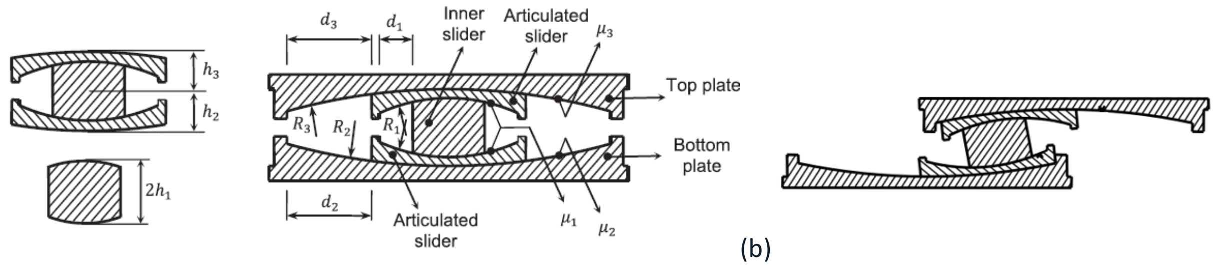


**Figure 52. Triple pendulum bearing: (a) undeformed, and (b) during sliding**

Several sources describe the generalised force-deformation response of double and triple pendulum bearings with multiple stages of sliding that depend on the sliding surfaces engaged (Fenz and Constantinou, 2008a; 2008b; Morgan and Mahin, 2011). Figures 53 and 54 illustrate these stages. The hysteretic response of each stage is controlled by the friction coefficient and effective radius of the activated surface. In many practical applications, $\mu_1 = \mu_2$ and $R_1 = R_2$ for the double pendulum bearing, so the three stages of sliding (Figure 53) reduce to a single one. Likewise, in a triple pendulum bearing, the inner double pendulum mechanism is nearly always defined with the same friction $\mu_1$ and radius $R_1$ on both surfaces, while the outer double pendulum mechanism is often defined such that $\mu_2 = \mu_3$ and $R_2 = R_3$ (Figure 52). In this case, the five stages of sliding (Figure 54) reduce to three unique stages.

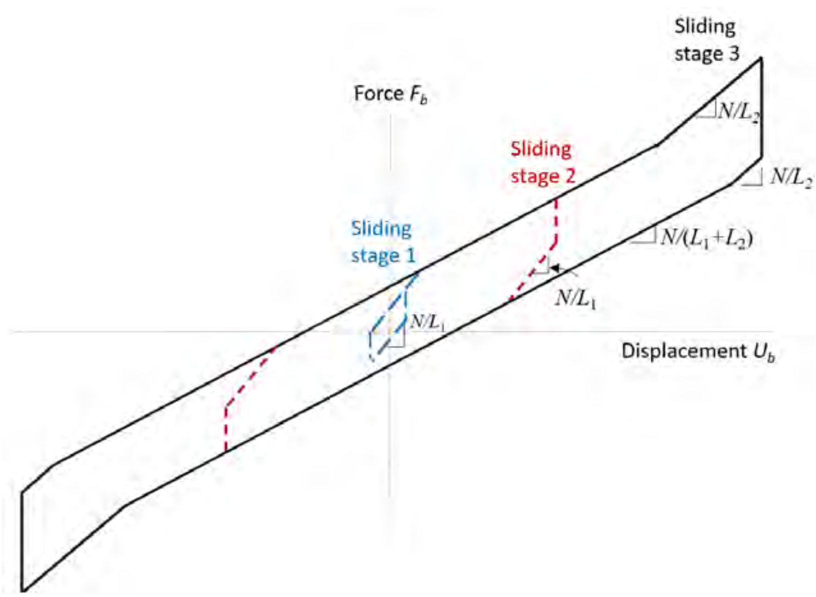


**Figure 53. Sliding stages for a generalised double pendulum bearing ($L_i = R_i - h_i$)**

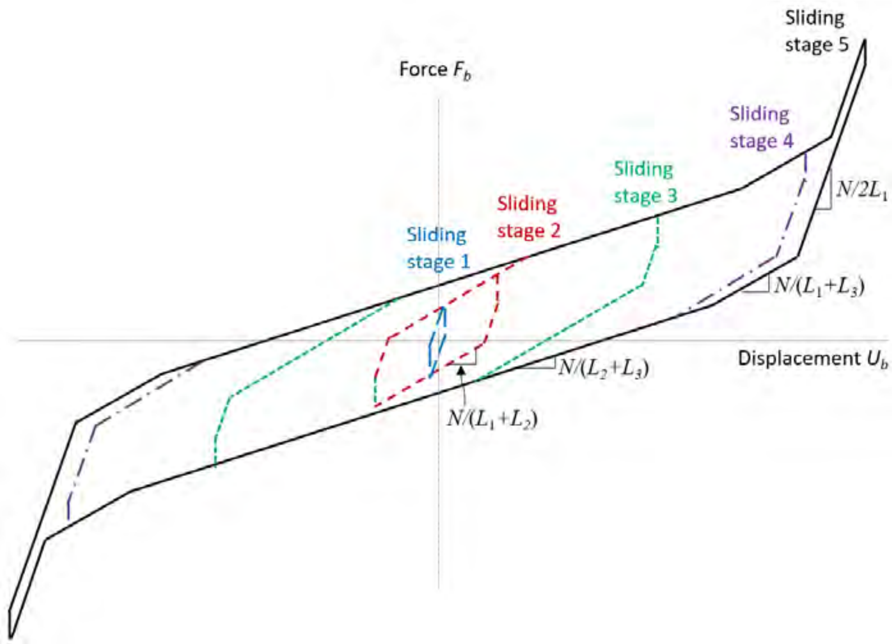


**Figure 54. Sliding stages for a generalised triple pendulum bearing ($L_i = R_i - h_i$)**

A tension-capable double pendulum bearing is a slight variant of a traditional double pendulum bearing with some unique features. The bearing consists of two orthogonally oriented concave beams connected through a sliding rail mechanism that allows independent sliding in each direction (Figure 55). Unlike all the other bearings described thus far, the movement in the two orthogonal directions is uncoupled, so design parameters (both pendulum radius and friction coefficient) may be optimised for independent response parameters in each direction. The rail system also provides an effective uplift restraint.

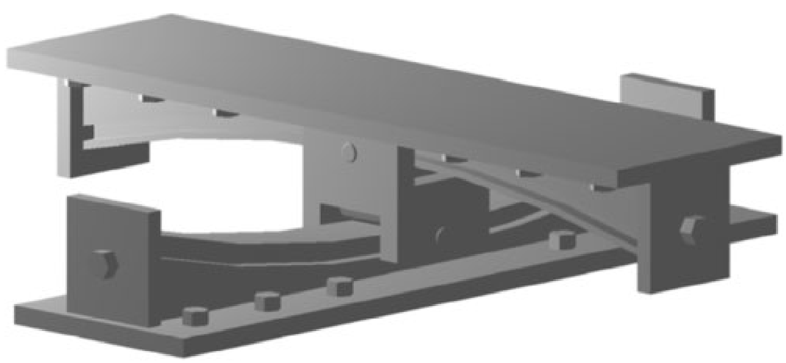

**Figure 55. Tension capable double pendulum bearing (Roussis & Constantinou, 2006)**

### *7.4.4.3 Numerical Models*

7.4.4.3.1 Equivalent Spring-Damper Models

The response of a typical seismic isolation device can be modelled using a discrete element approach or a continuum finite element approach. The latter can be accomplished with general-purpose finite element programs; however, this is only recommended if studying the behaviour of an individual isolator. It is not necessary or efficient for design when a full dynamic model of the structure is required to predict the interaction between the flexible structure and the nonlinear isolation devices.

Design employs equivalent spring-damper models. These use a series of multi-directional ‘springs’ or zero-length elements that physically represent the composite force-deformation, moment versus rotation, and torsional behaviour of the devices, with appropriate interactions as needed. In most model formulations, the shear force-deformation response of the bearings is coupled in the lateral direction, while springs representing the remaining components (axial, bending, and torsional response) are uncoupled. Given the necessary software capabilities, a savvy user who knows the basic spring formulations in each direction can build a multi-spring isolator model from basic elements. However, many software packages, including design-oriented and general-purpose finite element software, allow users to specify material and geometric properties directly in multi-directional isolator elements.

For example, OpenSees includes a variety of bearing elements contributed by users. Its code is open source, so anyone may review the element formulations. Some of these allow free selection of material models for response in the non-shear direction. Some formulations allow users to specify a physical height and calculate *P-Δ* moments. In SAP2000, isolation bearings are implemented as link/support elements. These can be implemented as either one-joint links (isolator fixed at the base) or two-joint links (isolators connected to moving parts of the model at both ends). The links generally specify linear behaviour with a user-defined stiffness for all non-shear directions and allow fixity in any direction. LS-DYNA implements isolator elements using a material model applied to a discrete beam element. The Material Type 197 is referred to as *MAT_SEISMIC_ISOLATOR. Several different element formulations are available within this material, each specified through ITYPE. Some ITYPEs may have unique user input data. The following sections describe various element formulations, with samples of implementation.

***Plasticity Model for Coupled Shear Behaviour***

Under realistic earthquake loading, a bearing may move bidirectionally from its origin or undeformed configuration, with instantaneous x- and y-components of displacement $U_{bx}$ and $U_{by}$. Expanding on Equation 40 for a lead-rubber bearing, the bearing force components are then

$$\begin{Bmatrix} F_{bx} \\ F_{by} \end{Bmatrix} = (1-\alpha) f_y \begin{Bmatrix} Z_x \\ Z_y \end{Bmatrix} + \alpha k_i \begin{Bmatrix} U_{bx} \\ U_{by} \end{Bmatrix} \quad [44]$$

where $\alpha$ is the ratio of the post-yield to initial stiffness; $k_i$ is the initial stiffness; and $f_y$ is the yield force in the bearing. The first term in Equation 44 represents the plastic component, and $(1-\alpha)f_y$ is numerically equivalent to the yield force $Q$ of the lead core. The components $Z_x$ and $Z_y$ comprise a vector $\boldsymbol{Z}$ with magnitude $\leq 1$.

The evolution of the bearing’s movement can be represented by a rate-independent plasticity model incorporating a constitutive law and flow rule. Yielding occurs when the bearing displacement reaches the yield displacement in any direction; this is physically modelled by a circular interaction surface. During plastic flow, the magnitude of $\boldsymbol{Z}$ remains 1 (bearing movement persists on the yield surface) and its direction is determined by the flow rule. The associative flow rule states that the rate of change of plastic flow is in the same direction as the plastic force. Magnitude $\boldsymbol{Z} < 1$ indicates movement inside the yield surface (i.e., unloading). One well-known and robust algorithm to represent such rate independent plasticity is the return mapping algorithm

(Simo and Hughes, 1998). Numerically, this produces a sharp transition from the elastic to post-yield region. This is not representative of all devices and can induce artificial higher mode effects.

*Examples of Implementation*: In this form, the model is most directly applicable to an elastomeric bearing. A representative implementation is the *Elastomeric Bearing (Plasticity) Element in OpenSees*. In addition to the features outlined immediately above, the bidirectional shear behaviour in this element is somewhat capable of large strain hardening. To use the model, one must specify initial stiffness, characteristic strength $Q$, and post-yield stiffness ratios for linear hardening and large strain nonlinear hardening. Based on the nodal coordinates, the element can include a physical height, and *P-Δ* moments are distributed to the joints according to a user-defined *sDratio*. The user can also implement independent springs for vertical, rotational, and torsional stiffness. The element is omitted from the Rayleigh damping formulation by default, but can be included.

***Bouc-Wen Model for Coupled Shear Behaviour***

An alternative model for the bidirectionally coupled response provides a smooth transition from pre- to post-yield. The Bouc-Wen differential model was originally proposed by Bouc (1967) and subsequently generalised by Wen (1976). Park et al. (1986) extended the model for bidirectionally coupled behaviour. While the equations can take on a variety of forms, their presentation here parallels Nagarajaiah et al. (1991). The generalised force-deformation response is consistent with Equation 44, but the components of ***Z*** are evaluated at each time step by solving the following coupled first order differential equations, as a function of the components of bearing deformation $U_{bx}$ and $U_{by}$:

$$\begin{Bmatrix} \dot{Z}_x \\ \dot{Z}_y \end{Bmatrix} u_y = A \begin{Bmatrix} \dot{U}_{bx} \\ \dot{U}_{by} \end{Bmatrix} - \begin{pmatrix} Z_x^2(\gamma\, sgn(\dot{U}_{bx} Z_x) + \beta) & Z_x Z_y(\gamma\, sgn(\dot{U}_{by} Z_y) + \beta) \\ Z_x Z_y(\gamma\, sgn(\dot{U}_{bx} Z_x) + \beta) & Z_y^2(\gamma\, sgn(\dot{U}_{by} Z_y) + \beta) \end{pmatrix} \begin{Bmatrix} \dot{U}_{bx} \\ \dot{U}_{by} \end{Bmatrix} \quad [45]$$

Here $u_y$ is the yield deformation, and $A$, γ, β are dimensionless variables that control the shape of the hysteresis loop. Conventionally, $A$ = 1 and γ+β=1 to constrain ***Z*** to a vector of unit magnitude.

*Examples of Implementation*: OpenSees implements this model as part of the *Elastomeric Bearing (Bouc-Wen) Element*. The element is almost identical to the comparably named plasticity element in OpenSees, but uses the Bouc-Wen model formulation rather than the plasticity formulation for the bidirectionally coupled lateral force deformation. SAP2000 also implements this model as part of the *Hysteretic (Rubber) Isolator Property*, for use with a Link/Support element. Like the OpenSees implementation, this property permits bidirectionally coupled bilinear hysteretic behaviour to be assigned in the bearing lateral directions, and uncoupled linear stiffnesses in the remaining directions (vertical, rotational, and torsional). Movement in any of these remaining directions can be fixed (equivalent to infinite stiffness). For bilinear hysteretic properties, the user specifies initial stiffness, yield strength, and a post-yield stiffness ratio. Finally, a variant of this model is available in LS-DYNA: *MAT_SEISMIC_ISOLATOR, with option ITYPE = 1.

***Advanced Model for Elastomeric and Lead-Rubber Bearings* (*Kumar et al., 2014*)**

These models were motivated by a need for advanced formulations to represent large strain/large deformation behaviour and by possible demands on elastomeric isolation bearings in nuclear structures subject to extreme ‘beyond design basis’ ground shaking. These models have been selected to represent elastomeric bearings that include stability effects—an important aspect of their response that basic models do not capture. They have also been successfully implemented in widely used programs.

Based on stability analysis, bearing behaviour is coupled in the horizontal and vertical directions (Ryan et al., 2005). While the bearing is vertically stiff in the undeformed configuration, this stiffness decreases under lateral deformation as the bearing shear layers rotate, leading to greater vertical flexibility. If the bearing is too slender or has a low shape factor, it may buckle. At the same time, the axial load can lead to a substantial decrease in horizontal or shear stiffness in the deformed configuration.

The basic formulation of the bidirectionally coupled shear force-deformation behaviour is the same as in the Bouc-Wen model discussed immediately above. The coupling of vertical and horizontal response is considered indirectly using stiffness expressions that depend on the response in the other direction (Kumar et al., 2014). Instantaneous horizontal stiffness is computed from the current axial or normal force $N$ on the bearing:

$$k_r = \frac{G_r A_r}{\sum t_r}\left(1-\left(\frac{N}{P_{cr}}\right)^2\right) = k_{ro}\left(1-\left(\frac{N}{P_{cr}}\right)^2\right) \quad [46]$$

where $k_{ro}$ is the basic stiffness of rubber at zero axial load (Equation 35). $P_{cr}$ is the critical buckling load of the bearing, given by

$$P_{cr} = \sqrt{k_{ro} h_b P_E} \quad [47]$$

with $P_E$ defined as in Equation 37. Likewise, the instantaneous vertical stiffness of the bearing is a function of the magnitude of the bearing deformation $U_b$:

$$k_v = \frac{E_c A_r}{\sum t_r}\frac{1}{\left[1+\frac{3}{\pi^2}\left(\frac{U_b}{r}\right)^2\right]} = k_{vo}\frac{1}{\left[1+\frac{3}{\pi^2}\left(\frac{U_b}{r}\right)^2\right]} \quad [48]$$

where $k_{vo}$ is the vertical stiffness of the bearing in the undeformed configuration (Equation 36) and $r$ is the radius of gyration of the bonded rubber area. Equations 46–48 approximate the stability formulation based on a two-spring mechanical model that has been experimentally validated.

Besides the stability formulation, the model includes an advanced formulation for the tensile response of the bearing, including cavitation (the formation of cavities in the rubber volume at a critical hydrostatic stress), post-cavitation, and strength degradation under cyclic tensile loading. The formulation is presented in detail in Kumar et al. (2014). Figure 56(a) shows the representative cyclic tensile force-deformation response of the model in red, compared against the experimentally observed response in black. Another advanced feature of the model is the option to modify the horizontal force-deformation response of the lead-rubber bearings to include strength degradation due to the heating of the lead core. This formulation, originally developed by Kalpakidis et al. (2010), models the temperature change in the bearing over time using a first order differential equation that depends on the horizontal movement of the bearing. Subsequently, the yield strength of the lead core degrades exponentially as temperature increases. Again, this formulation is summarised in Kumar et al. (2014). Figure 56(b) shows the representative cyclic response of the model under sustained cyclic loading that induces significant heating of the lead core (in red), as compared to experimental data (in blue).

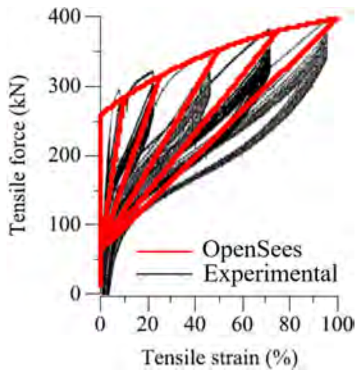


(a)

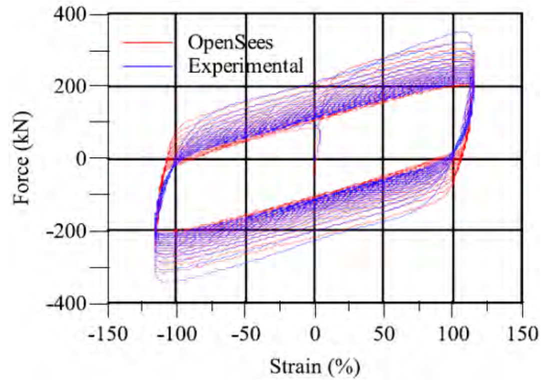


(b)

**Figure 56. (a) Hysteretic cyclic tensile force-deformation, including post-cavitation response; (b) cyclic shear force-deformation, including strength degradation due to the heating of the lead core (Kumar, Whittaker, & Constantinou, 2014)**

*Examples of Implementation*: OpenSees implements this model as ElastomericX and LeadRubberX for formulations without and with the strength degradation formulation, respectively. A third option, HDR, uses a model proposed by Grant et al. (2004) to capture the nonlinear shear behaviour in high-damping rubber bearings. Unlike the models described earlier, the user directly inputs the shear and bulk moduli of the rubber and the geometric properties of the bearing. The stiffness in each direction is computed within the software using the mechanics formulations. In the LeadRubberX, the user can turn off various advanced capabilities of the model, such as cavitation, horizontal-vertical coupling effects, and strength variation. This model formulation is also available in LS-DYNA as *MAT_SEISMIC_ISOLATOR, with option ITYPE = 3.

***Extension of Bidirectionally Coupled Models to Friction Pendulum Behaviour***

Comparing Figures 47 and 50 shows the fundamental response of Friction Pendulum bearings is similar to that of elastomeric bearings. With some additions, both the plasticity and Bouc-Wen formulations given earlier in this section are readily extended to Friction Pendulum bearings, as described later in this section. Equation 44, which represents the fundamental bidirectionally coupled force-deformation equations, can be recast for a single pendulum bearing as follows:

$$\begin{Bmatrix} F_{bx} \\ F_{by} \end{Bmatrix} = N\mu \begin{Bmatrix} Z_x \\ Z_y \end{Bmatrix} + \frac{N}{R_c} \begin{Bmatrix} U_{bx} \\ U_{by} \end{Bmatrix} \qquad [49a]$$

$$N = k_v U_{bz} + c_v \dot{U}_{bz} \geq 0 \qquad [49b]$$

In Equation 49a, $\mu$ is the friction coefficient; $R_c$ is the radius of curvature; and $N$ is the instantaneous normal or axial force on the bearing. $N$ is computed independently at each time step, assuming a linear viscous relation with the bearing vertical deformation $U_{bz}$ (Equation 49b). It should be calibrated initially from a gravity analysis of the system. The normal force $N$ and displacement $U_{bz}$ are positive for downward movement (engaged compression). $N$ is zero during upward displacement, to represent unconstrained uplift or a lack of tension response. The stiffness $k_v$ is as given in Equation 43, and optional vertical viscous damping can be included through a coefficient $c_v$.

The following model (Constantinou et al., 1990) is commonly used to account for the velocity dependence of the friction coefficient:

$$\mu = \mu_{max} - (\mu_{max} - \mu_{min})\, exp(-\, a\dot{U}_b) \quad [50]$$

where $\mu_{max}$ and $\mu_{min}$ are the friction coefficients at high velocity and at rest, respectively; $a$ is a coefficient equal to the inverse of the characteristic sliding velocity; and $\dot{U}_b$ is the magnitude of the current bearing velocity vector.

*Examples of Implementation*: OpenSees implements this model with a plasticity formulation as *Single Friction Pendulum Bearing Element*. The user specifies the initial stiffness of the bearing (usually calibrated to a small yield deformation on the order of 2 mm), bearing radius $R_c$, and a friction model. Options include Coulomb friction (constant friction coefficient), velocity-dependent friction as per Equation 50, and several combined velocity and pressure dependent friction models. The *P-Δ* moment is distributed entirely to the concave surface as defined by the user. The user can also implement independent springs for vertical, rotational, and torsional stiffness. The element is omitted from Rayleigh damping by default, but can be included. SAP2000 implements the model with a Bouc-Wen formulation as part of *Friction Pendulum Isolator Property*, for use with a Link/Support element. The velocity-dependent friction formulation is included (Equation 50). Finally, a variant of this model is available in LS-DYNA as *MAT_SEISMIC_ISOLATOR, with option ITYPE = 0.

***Model for Tension-Capable Double Pendulum Bearing***

The model for the tension-capable double pendulum bearing is based on Roussis and Constantinou (2006). Its distinctive features can be represented with only a slight modification of the model for the single pendulum bearing (Equation 49). Recall that the response of this bearing is uncoupled in the X- and Y-directions; thus, the force-deformation relation is rewritten as

$$F_{bx} = N\mu_1 Z_x + \frac{N}{R_1} U_{bx} \quad [51a]$$

$$F_{by} = N\mu_2 Z_y + \frac{N}{R_2} U_{by} \quad [51b]$$

with no interaction between X-direction components (Equation 51a) and Y-direction components (Equation 51b). In this equation, X and Y directions are to be oriented along the sliding rails (Figure 55). If this is not the case, a force transformation must convert the response components to the principal directions of the model. In addition, Equation 51 reflects that sliding along the rails may have unique friction coefficients and pendulum radii in each direction (e.g., $\mu_1$, $R_1$ for X-direction and $\mu_2$, $R_2$ for Y-direction). In addition, the normal force equation (Equation 49b) is modified to reflect the tension-capable rail system:

$$N = \begin{cases} k_{vc} U_{bz} + c_v \dot{U}_{bz} \text{ if } U_{bz} > 0 \\ k_{vt} U_{bz} + c_v \dot{U}_{bz} \text{ if } U_{bz} < 0 \end{cases} \quad [52]$$

where normal force $N$ and displacement $U_{bz}$ are again positive for downward (compressive) response. The formulation allows for different vertical stiffnesses for compression $k_{vc}$ and tension $k_{vt}$.

*Examples of Implementation*: SAP2000 implements this model with a Bouc-Wen formulation as *Double-Acting Friction-Pendulum Isolator Property*, for use with a Link/Support element. It includes the velocity-dependent friction formulation (Equation 50). The axial force formulation can include a gap in the normal force equation before engaging the axial resistance in either the compressive or tensile direction. The components *of Z* are evaluated from the first order differential equation

$$\dot{Z}u_y = \begin{cases} \dot{U}_b(1 - Z^2) & \text{if } U_b \cdot Z > 0 \\ \dot{U}_b & \text{otherwise} \end{cases} \quad [53]$$

where $Z$, $U_b$ represent $Z_x$, $U_{bx}$ for the X direction and $Z_y$, $U_{by}$ are their equivalents for the Y direction. Equation 53 is a simplification of Equation 45 for uncoupled behaviour.

***Model for Triple Pendulum Bearing***

A modelling approach developed for the triple pendulum bearing aims to replicate its generalised multi-stage backbone curve (Figure 57), which is derived from the stages of sliding (Figure 54). The backbone curve is replicated by three elements in a series (Fenz and Constantinou, 2008c; Morgan and Mahin, 2011). Each element is essentially a single pendulum bearing element (friction coefficient $\mu_i$ and effective radius $R_{ie}$) that represents the *i*-th sliding interface, and is implemented alongside a gap element to represent the finite displacement capacity $u_i$ along that surface (Figure 58). Although the components of the series model do not accurately reflect the movement on the individual sliding surfaces, the model has been shown to give the correct composite force-deformation response of the bearing. Based on the bearing geometry shown in Figure 52, the parameters of the individual elements of the series spring model should be chosen as specified in Table 2.

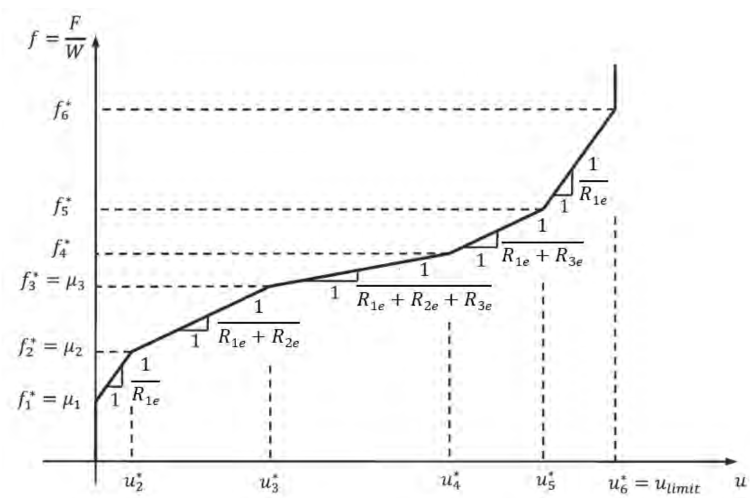


**Figure 57. Normalised force-displacement backbone curve for triple pendulum bearing**

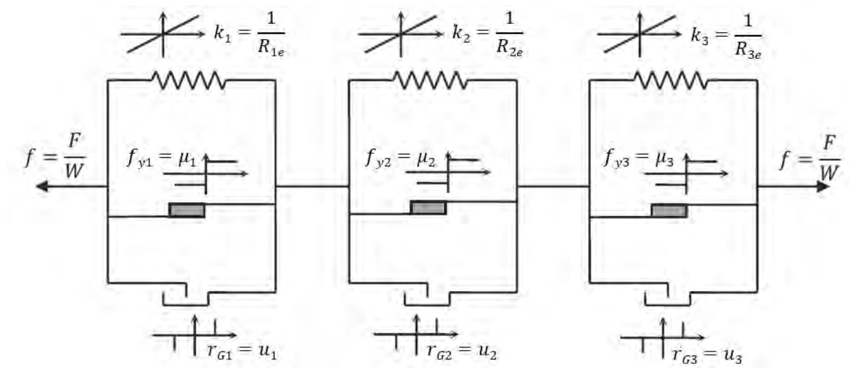

**Figure 58. Components of the series spring model for triple pendulum bearing**

**Table 2. Properties of Triple Pendulum Bearing Series Spring Model**

| Element | Pendulum effective radius | Friction coefficient | Gap length (displacement limit) |
|---|---|---|---|
| Inner sliders, Surfaces 1 in Figure 52 | $R_{1e} = 2(R_1\text{-}h_1)$ | $\mu_1$ | $u_1 = u_{limit} - u_2 - u_3$ |
| Bottom concave slider, Surface 2 in Figure 52 | $R_{2e} = R_2\text{-}R_1 - (h_2\text{-}h_1)$ | $\mu_2$ | $u_2 = (1\text{-}R_{1e}/R_{2e})d_2$ |
| Top concave slider, Surface 3 in Figure 52 | $R_{3e} = R_3\text{-}R_1 - (h_3\text{-}h_1)$ | $\mu_3$ | $u_3 = (1\text{-}R_{1e}/R_{3e})d_3$ |

*Examples of Implementation*: OpenSees implements the series spring model as the self-contained *Triple Friction Pendulum Element*. The individual elements of the series model incorporate a plasticity formulation to numerically evaluate the single pendulum bearing, and a circular gap element to represent the finite displacement capacity when moving bidirectionally (Dao et al., 2013). The element can also incorporate any of the friction models in OpenSees, including a velocity- and normal force–dependent friction model developed to represent the friction response observed in a large-scale shake table test of a building isolated with triple pendulum bearings (Dao et al. 2013). The series spring model is also implemented as a standalone *Triple-Pendulum Isolator Property* in SAP2000, for use with a Link/Support element that follows the implementation of the *Friction-Pendulum Isolator Property*. In LS-DYNA, the user can implement the series spring model by combining single pendulum bearings in series.

7.4.4.3.2 Analysis Methods and Superstructure Damping Considerations

The models discussed in Section 7.4.4.3.1 inherently include the effects of energy dissipation in the isolators. It is unnecessary and undesirable to apply additional damping to the isolation system. In this context, a global approach such as Rayleigh damping can apply damping to the superstructure elements alone, but the influence of the damping parameters on the overall drift and acceleration responses of the isolated structure has some important nuances. Rayleigh damping involves constructing a damping matrix *C* proportional to both the mass matrix *M* and the stiffness matrix *K* of the superstructure:

$$\boldsymbol{C = a_o M + a_1 K} \qquad [54]$$

The constants $a_o$ and $a_1$ can be used to select or specify damping ratios in two modes. After a modal decomposition, the result is that the damping ratio in any mode $n$, or $\xi_n$ is given by

$$\xi_n = a_o \frac{1}{2\omega_n} + a_1 \frac{\omega_n}{2} \tag{55}$$

where $\omega_n$ is the frequency of mode $n$. In Equation 55, the mass proportional component is inversely proportional, and the stiffness proportional component is directly proportional, to the modal frequency. This can be graphically represented by the Rayleigh damping curve shown in Figure 59. Constants $a_o$ and $a_1$ are commonly selected to achieve approximately constant and bounded damping in the primary operating modes of the structure (e.g., mode 1 and mode $n$, where $n$ is the highest mode with noticeable mass participation). Hall (2006) pointed out that when damping is selected based on the first $n$ superstructure modes, effective damping in the first or isolation modes can become very large (Figure 59). This occurs regardless of any stiffness proportional damping to the isolators and can be physically interpreted as a uniform air damping that suppresses the entire movement of the building. The net effect is to grossly overestimate the damping in the isolation mode and thus artificially suppress the displacement demand in the isolators, which is unconservative for design.

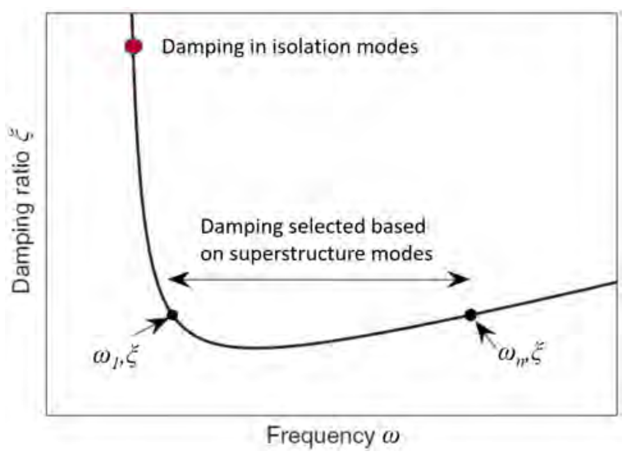


**Figure 59. Rayleigh damping curve showing variation in damping ratio as a function of frequency**

To solve this problem, Ryan and Polanco (2008) recommended using stiffness proportional damping for the superstructure (eliminating the mass proportional component), which has little influence on the damping in the isolation mode. This is satisfactory if higher mode response is insignificant, as expected in well-designed base-isolated buildings. However, a later shake table test on a large-scale base-isolated building with triple pendulum bearings showed that higher modes were significant due to lateral-vertical coupling effects (Dao and Ryan, 2014). In this case, stiffness proportional damping undesirably suppressed the response of higher modes. Assigning a low level of Rayleigh damping calibrated to the frequencies of the isolation modes (effective frequency observed during shaking) and the second superstructure mode, with a supplemental dashpot from roof to base for the first superstructure mode, achieved an acceptable balance.

As mentioned, these solutions are satisfactory if the program allows the user to not assign any stiffness proportional damping to the isolator elements. The appropriate strategy also depends on how the coupled system of equations for nonlinear response history analysis is solved. In the more common direct integration method, the coupled equations are evaluated at every time step; thus, a full damping matrix must be built explicitly. Substructure approaches that allow one to exclude the isolators from any applied stiffness proportional damping should be utilised if available; OpenSees, for instance, offers this capability. SAP2000 does not permit the user to 'turn off' damping to the isolators or exclude the isolator elements when constructing the stiffness proportional component of a global damping matrix, which has been shown to lead to artificially high viscous damping from the isolators. Sarlis and Constantinou (2010) coined the phrase 'damping leakage' to describe this problem. Anajafi et al. (2020) offered an alternative strategy to avoid the issue, building a stiffness proportional superstructure damping matrix indirectly instead of using a built-in global damping feature. They did so successfully in SAP2000 in two different ways: (1) by applying interstorey viscous dampers, and (2) by using material damping. They also recommended calibrating the superstructure damping coefficient based on the second mode of the isolated structure (first structural mode) in each direction.

SAP2000 also offers the fast nonlinear analysis (FNA) method, which is widely used to evaluate base-isolated structures. The FNA approach is intended for systems with nonlinearities limited to a few link elements, which well describes an isolated building modelled with a linear superstructure and a few nonlinear isolators. The FNA approach is recommended whenever link elements are used for isolators in SAP2000 (Sarlis and Constantinou, 2010). FNA applies modal decomposition based on effective linear stiffness, and treats the nonlinear element forces as unbalanced forces grouped with external loads. FNA also specifies damping to individual modes based on the modal decomposition rather than formulating a global damping matrix. While traditional methods like Rayleigh damping can still be employed, the explicit control over the damping in each mode afforded by the modal decomposition is beneficial. The recommended approach is to specify a constant level of damping in each mode (2–5%), except for the first three 'rigid body' modes, which are primarily deformation in the isolation system. The damping override feature in SAP2000 can help assign a damping ratio of 0% to the first three modes, thus eliminating any suppression of the isolator movement through artificial viscous or air damping (Sarlis and Constantinou, 2010).

### 7.4.5 Summary

Because of their inherent characteristics (e.g., light weight, high strength-to-weight ratio, structural redundancy, elastic deformation capacity, and ductility of connections), timber structures usually have satisfactory seismic performance. Taller and larger timber structures that face greater seismic demands perform better with advanced seismic protection technologies that reduce the seismic demand. This chapter discusses the behaviour and mechanisms of three types of advanced seismic protection timber systems: rocking (Pres-lam) systems, systems with resilient slip friction joints, and seismic isolation systems. It provides both mechanics-based modelling and advanced modelling methods, along with corresponding recommendations. The information presented in this chapter aims to help practising engineers and researchers become better acquainted with modelling timber systems with advanced seismic protection devices.

### 7.4.6 References

Anajafi, H., Medina, R. A., & Santini‐Bell, E. (2020). Effects of the improper modeling of viscous damping on the first‐mode and higher‐mode dominated responses of base‐isolated buildings. *Earthquake Engineering & Structural Dynamics, 49*(1), 51–73. https://doi.org/10.1002/eqe.3223

APA. (2019). *ANSI/APA PRG 320 Standard for performance-rated cross-laminated timber* (ANSI standard PRG 320-2019). The Engineered Wood Association, USA. https://www.apawood.org/ansi-apa-prg-320

ASCE Task Committee on Seismic Isolation. (2004). *Primer on seismic isolation*. American Society of Civil Engineers.

Blass, H. J., Görlacher, R. (2004). Compression perpendicular to the grain. *Proceedings of the 8th World Conference of Timber Engineering,* 2,435–440. Finnish Association of Civil Engineers RIL.

Bouc, R. (1967, September 5–9). *Force vibration of mechanical systems with hysteresis* [Conference presentation]. 4th Conf. on Nonlinear Oscillation, Prague, Czechoslovakia.

Carr, A. (2004). *Ruaumoko programme for inelastic dynamic analysis - user manual.* Department of Civil Engineering, University of Canterbury.

Chen, Z., Ni, C., Dagenais, C., & Kuan, S. (2020). Wood$^{ST}$: A temperature-dependent plastic-damage constitutive model used for numerical simulation of wood-based materials and connections. *Journal of Structural Engineering, 146*(3), 04019225. https://doi.org/10.1061/(ASCE)ST.1943-541X.0002524

Chen, Z., & Popovski, M. (2020). Material-based models for post-tensioned shear wall system with energy dissipators. *Engineering Structures*, *213*, 110543. https://doi.org/10.1016/j.engstruct.2020.110543

Chen, Z., Popovski, M., & Ni, C. (2020). A novel floor-isolated re-centering system for prefabricated modular mass timber construction – Concept development and preliminary evaluation. *Engineering Structures, 222*, 111168. https://doi.org/10.1016/j.engstruct.2020.111168

Chen, Z., Popovski, M., & Symons, P. (2018). *Advanced wood-based solutions for mid-rise and high-rise construction: Structural performance of post-tensioned CLT shear walls with energy dissipators*. Technical Report (301012204). FPInnovations.

Chopra, A. K. (2016). *Dynamics of structures: Theory and applications to earthquake engineering* (5th ed.). Prentice-Hall.

Constantinou, M., Mokha, A., & Reinhorn, A. (1990). Teflon bearings in base isolation II: Modeling. *Journal of Structural Engineering, 116*(2), 455–474. https://doi.org/10.1061/(ASCE)0733-9445(1990)116:2(455)

Dang, X., Lu, X., Qiang, J., & Jiang, H. (2014). Finite element analysis with solid and plane element of seismic performance of self-centering pre-stressed shear walls. *Journal of Building Structures, 35*(5), 17–24.

Danielsson, H., & Serrano, E. (2018). Cross laminated timber at in-plane beam loading – prediction of shear stresses in crossing areas. *Engineering Structures, 171*, 921–927. https://doi.org/10.1016/j.engstruct.2018.03.018

Dao, N. D., Ryan, K. L., Sato, E., & Sasaki, T. (2013). Predicting the displacement of triple pendulum™ bearings in a full‐scale shaking experiment using a three‐dimensional element. *Earthquake Engineering & Structural Dynamics, 42*(11), 1677–1695. https://doi.org/10.1002/eqe.2293

Dao, N. D., & Ryan, K. L. (2014). Computational simulation of a full-scale, fixed-base, and isolated-base steel moment frame building tested at E-Defense. *Journal of Structural Engineering, 140*(8), A4014005. https://doi.org/10.1061/(ASCE)ST.1943-541X.0000922

Dassault Systèmes Simulia Corp. (2016). *ABAQUS analysis user's manual (version 6.14)*. Dassault Systèmes Simulia Corp.

Di Cesare, A., Ponzo, F. C., Nigro, D., Simonetti, M., Smith, T., & Pampanin, S. (2013). Experimental testing and numerical analysis of steel angles as hysteretic energy dissipating devices. In *XV Convegno ANIDIS-L'Ingegneria Sismica in Italia*. Padova University Press.

DSI. (2018). Dywidag threadbar® – Technical data [metric units] [Fact sheet]. Dywidag-Systems International (DSI). https://www.ebsgeo.com/ModuleFile?id=550

Engineering ToolBox. (2004). *Friction and friction coefficients*. The Engineering Toolbox. https://www.engineeringtoolbox.com/friction-coefficients-d_778.html

European Committee for Standardization. (2005). *Eurocode 3: Design of steel structures – Part 1-2: General rules – Structural fire design* (Eurocode Standard EN 1993-1-2). https://www.phd.eng.br/wp-content/uploads/2015/12/en.1993.1.1.2005.pdf

Fenz, D. M., & Constantinou, M. C. (2008a). *Mechanical behavior of multi-spherical sliding bearings* (Technical Report No. MCEER-08-0007). Multidisciplinary Center for Earthquake Engineering Research. https://nehrpsearch.nist.gov/static/files/NSF/PB2008112236.pdf

Fenz, D. M., & Constantinou, M. C. (2008b). Spherical sliding isolation bearings with adaptive behavior: Theory. *Earthquake Engineering & Structural Dynamics, 37*(2), 163–183. https://doi.org/10.1002/eqe.751

Fenz, D. M., & Constantinou, M. C. (2008c). Modeling triple friction pendulum bearings for response-history analysis. *Earthquake Spectra, 24*(4), 1011–1028. https://doi.org/10.1193/1.2982531

Grant, D. N., Fenves, G. L., & Whittaker, A. S. (2004). Bidirectional modelling of high-damping rubber bearings. *Journal of Earthquake Engineering, 8*(spec01), 161–185. https://doi.org/10.1080/13632460409350524

Hall, J. F. (2006). Problems encountered from the use (or misuse) of Rayleigh damping. *Earthquake engineering & structural dynamics, 35*(5), 525–545. https://doi.org/10.1002/eqe.541

Iqbal, M. A. (2011). *Seismic response and design of subassemblies for multi-storey prestressed timber buildings* [Doctoral dissertation, University of Canterbury, Christchurch, New Zealand]. UC Research Repository. https://ir.canterbury.ac.nz/handle/10092/5379

Kalpakidis, I. V., Constantinou, M. C., & Whittaker, A. S. (2010). Modeling strength degradation in lead–rubber bearings under earthquake shaking. *Earthquake Engineering & Structural Dynamics, 39*(13), 1533–1549. https://doi.org/10.1002/eqe.1039

Karacabeyli, E., & Gagnon, S. (2019). *Canadian CLT handbook* (2nd ed.). FPInnovations.

Kelly, J. M. (1997). *Earthquake-resistant design with rubber* (2nd ed.). Springer-Verlag.

Kumar, M., Whittaker, A. S., & Constantinou, M. C. (2014). An advanced numerical model of elastomeric seismic isolation bearings. *Earthquake Engineering & Structural Dynamics, 43*(13), 1955–1974. https://doi.org/10.1002/eqe.2431

Marriott, D. J. (2009). *The development of high-performance post-tensioned rocking systems for the seismic design of structures* [Doctoral dissertation, University of Canterbury, Christchurch, New Zealand]. UC Research Repository. https://ir.canterbury.ac.nz/handle/10092/2678

Marriott, D., Pampanin, S., Bull, D., & Palermo, A. (2008). Dynamic testing of precast, post-tensioned rocking walls systems with alternative dissipating solutions. *Bulletin of the New Zealand Society for Earthquake Engineering*, *41*(2), 90–103. https://doi.org/10.5459/bnzsee.41.2.90-103

McKenna, F. (2011). OpenSees: A framework for earthquake engineering simulation. *Computing in Science & Engineering, 13*(4), 58–66. https://doi.org/10.1109/MCSE.2011.66

Menegotto, M., & Pinto, P. E. (1973). *Method of analysis for cyclically loaded reinforced concrete plane frames including changes in geometry and non-elastic behavior of elements under combined normal force and bending* [Conference presentation]. IABSE Symposium on the Resistance and Ultimate Deformability of Structures Acted on by Well-Defined Repeated Loads, Lisbon, Portugal.

Morgan, T. A. & Mahin, S.A. (2011). *The use of innovative base isolation systems to achieve complex seismic performance objectives* (Technical Report PEER 2011/06). Pacific Earthquake Engineering Research Center, University of California, Berkeley.

Morgen, B. G. & Kurama, Y. C. (2007). Seismic design of friction-damped precast concrete frame structures. *J Struct Eng*, *133*(11), 1501-1511. https://doi.org/10.1061/(ASCE)0733-9445(2007)133:11(1501)

Nagarajaiah, S., Reinhorn, A. M., & Constantinou, M. C. (1991). Nonlinear dynamic analysis of 3-D-base-isolated structures. *Journal of Structural Engineering, 117*(7), 2035–2054. https://doi.org/10.1061/(ASCE)0733-9445(1991)117:7(2035)

Newcombe, M. (2012). *Seismic design of post-tensioned timber frame and wall buildings* [Doctoral dissertation, University of Canterbury, Christchurch, New Zealand]. UC Research Repository. https://ir.canterbury.ac.nz/handle/10092/6399

Newcombe, M. P., Pampanin, S., Buchanan, A. H., & Palermo, A. (2008). Section analysis and cyclic behavior of post-tensioned jointed ductile connections for multi-story timber buildings. *Journal of Earthquake Engineering, 12*(S1), 83–110. https://doi.org/10.1080/13632460801925632

Palermo, A., Pampanin, S., Buchanan, A. H., & Newcombe, M. P. (2005). *Seismic design of multi-storey buildings using laminated veneer lumber (LVL)* [Conference presentation]. New Zealand Society of Earthquake Engineering Annual Conference, Wairakei, New Zealand.

Palermo, A., Pampanin, S., & Carr, A. (2005, 23–25 May). *Efficiency of simplified alternative modeling approaches to predict the seismic response of precast concrete hybrid systems* [Conference presentation]. Fib Symposium: Keep Concrete Attractive, Budapest, Hungary.

Pampanin, S., Priestley, M. J. N., & Sritharan, S. (2001). Analytical modelling of the seicmic behaviour of precast concrete frames designed with ductile connections. *Journal of Earthquake Engineering, 5*(3), 329–367. https://doi.org/10.1080/13632460109350397

Park, Y. J., Wen, Y. K., & Ang, A. H. S. (1986). Random vibration of hysteretic systems under bi‐directional ground motions. *Earthquake Engineering & Structural Dynamics, 14*(4), 543–557. https://doi.org/10.1002/eqe.4290140405

Priestley, M. J. N., Calvi, G. M., & Kowalsky, M. J. (2007). *Displacement-based seismic design of structures*. IUSS Press.

Priestley, M. J. N., Sritharan, S., Conley, J. R., & Pampanin, S. (1999). Preliminary results and conclusions from the PRESSS five-story precast concrete test building. *PCI Journal, 44*(6), 42–67. https://doi.org/10.15554/pcij.11011999.42.67

Rahmzadeh, A., & Iqbal, A. (2018). *Study of replaceable energy dissipators for self-centering structures* [Conference presentation]. Eleventh U.S. National Conference on Earthquake Engineering, Integrating Science, Engineering & Policy, Los Angeles, USA.

Roussis, P. C., & Constantinou, M. C. (2006). Uplift‐restraining friction pendulum seismic isolation system. *Earthquake Engineering & Structural Dynamics, 35*(5), 577–593. https://doi.org/10.1002/eqe.545

Ryan, K. L., Kelly, J. M., & Chopra, A. K. (2005). Nonlinear model for lead–rubber bearings including axial-load effects. *Journal of Engineering Mechanics, 131*(12), 1270–1278. https://doi.org/10.1061/(ASCE)0733-9399(2005)131:12(1270)

Ryan, K. L., & Polanco, J. (2008). Problems with Rayleigh damping in base-isolated buildings. *Journal of Structural Engineering, 134*(11), 1780–1784. https://doi.org/10.1061/(ASCE)0733-9445(2008)134:11(1780)

Ryan, K. L., & Earl, C. L. (2010). Analysis and design of inter-story isolation systems with nonlinear devices. *Journal of Earthquake Engineering, 14*(7), 1044–1062. https://doi.org/10.1080/13632461003668020

Sarlis, A. A., & Constantinou, M. C., (2010). *Modeling of triple friction pendulum isolators in program SAP2000*. Supplement to MCEER Report 05-009. University at Buffalo.

Sarti, F. (2015). *Seismic design of low-damage post-tensioned timber wall systems* [Doctoral dissertation, University of Canterbury, Christchurch, New Zealand]. UC Research Repository. https://ir.canterbury.ac.nz/handle/10092/11335

Simo, J. C. & Hughes, T. J. R. (1998). *Computational inelasticity*. Springer.

Skinner, R. I., Kelly, J. M., & Heine, A. J. (1974). Hysteretic dampers for earthquake-resistant structures. *Earthquake Engineering and Structural Dynamics, 3*(3), 287-296. https://doi.org/10.1002/eqe.4290030307

Smith, T. (2014). *Post-tensioned timber frames with supplemental damping devices* [Doctoral dissertation, University of Canterbury, Christchurch, New Zealand]. IC Research Repository. https://ir.canterbury.ac.nz/handle/10092/9217

Spieth, H. A., Carr, A. J., Pampanin, S., Murahidy, A. G., & Mander, J. B. (2004). *Modelling of precast prestressed concrete frame structures with rocking beam-column connections*. Research Report, Department of Civil Engineering., University of Canterbury, Christchurch, New Zealand.

Standards New Zealand. (2006). *Concrete structures standard* (NZS 3101.1&2:2006). https://www.standards.govt.nz/shop/nzs-3101-1-and-22006/

STIC. (2013). *Design guide Australia and New Zealand - Post-tensioned timber buildings*. Structural Timber Innovation Company.

Tasaka, M., Mori, N., Yamamoto, H., Murakami, K., & Sueoka, T. (2008, April 18–20). *Applying seismic isolation to buildings in Japan – retrofitting and middle-story isolation* [Conference presentation]. 18th Analysis and Computation Specialty Conference, ASCE Structures Congress, Vancouver, B.C., Canada.

Ugalde, D., Almazán, J. L., Santa María, H., & Guindos, P. (2019). Seismic protection technologies for timber structures: a review. *European Journal of Wood and Wood Products, 77*(2), 173–194. https://doi.org/10.1007/s00107-019-01389-9

van Beerschoten, W., Smith, T., Palermo, A., Pampanin, S., & Ponzo, F. C. (2011). The stiffness of beam to column connections in post-tensioned timber frames. *Proceedings of the International Council for Research and Innovation in Building and Construction: Working Commission W18 – Timber Structures,* Meeting 44, Italy. Karlsruhe Institute of Technology.

Watson, C. P., van Beerschoten, W., Smith, T., Pampanin, S., & Buchanan, A. H. (2013). Stiffness of screw reinforced LVL in compression perpendicular to the grain. *Proceedings of the International Council for Research and Innovation in Building and Construction: Working Commission W18 – Timber Structures,* Meeting 47, Vancouver. Karlsruhe Institute of Technology.

Wen, Y-K. (1976). Method for random vibration of hysteretic systems. *Journal of the Engineering Mechanics Division, 102*(2), 249–263. https://doi.org/10.1061/JMCEA3.0002106

Wilson, A. W., Motter, C. J., Phillips, A. R., & Dolan, J. D. (2019). Modeling techniques for post-tensioned cross-laminated timber rocking walls. *Engineering Structures, 195*, 299–308. https://doi.org/10.1016/j.engstruct.2019.06.011

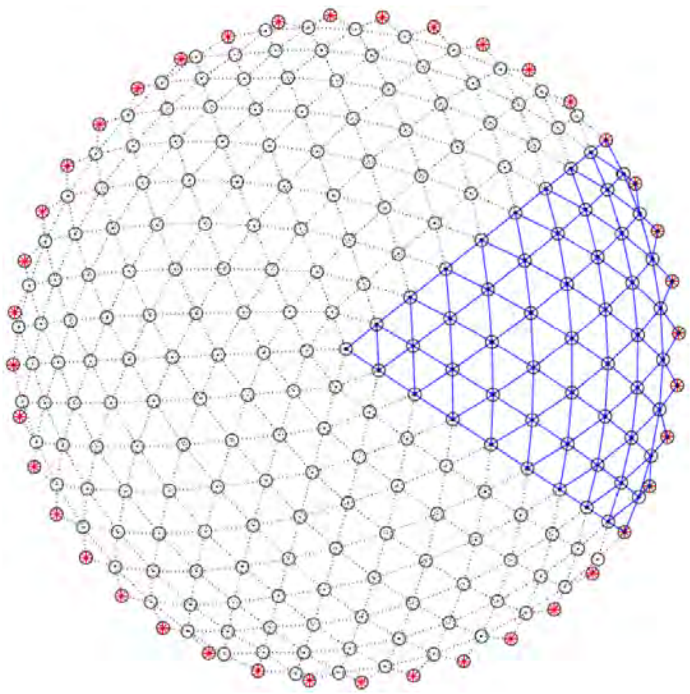

Image courtesy of Fredriksson and Herrström (2017)

# CHAPTER 7.5

## Long-span timber structures


**Authors**

Roberto Crocetti

Zhiyong Chen

Rune Abrahamsen

Gerald Epp

Lucas Epp

**Reviewers**

Mohammad Mohammad

Richard Harris

# TABLE OF CONTENTS

## 7.5.1 Introduction to Long-Span Timber Structures

A few points should be kept in mind when designing long-span structures (Crocetti, 2016; Farreyre & Journot, 2005):

- as the span increases in load-bearing structures, the cross-section increases at a faster rate,
- tension and compression members are structurally more efficient than bending members,
- the higher the strength-to-weight ratio of a given material, the higher its structural efficiency,
- sensitivity to buckling increases primarily with the span of the structure.

After a short historical overview of long-span timber structures, this chapter discusses these and other relevant aspects of design, along with the analysis and modelling of different structural types typical for timber structures.

### *7.5.1.1 Historical Background*

Bridges may have been the first examples of manufactured long-span timber structures. The need to overcome obstacles, such as rivers and valleys, has always challenged humans to find suitable structures to span long distances. Until the first half of the 19th century, wood was essentially the only material available for such a purpose. Especially after the 16th century, bridges of considerable engineering interest were built using wood. Some remarkable examples are the timber bridges designed and built by the Swiss brothers Hans Ulrich Grubenmann and Johannes Grubenmann in the 18th century. The brothers' ingenious combination of the arch and truss principles allowed them to construct longer and better timber bridges than ever before (Crocetti, 2016a, b). Another example of a long-span timber structure is the Colossus Bridge; built in 1812 with a clear span of approximately 104 m, it far exceeded any bridge (of any other material) of its time. The load-carrying structure consisted of three parallel trussed timber arches that also included a number of iron diagonal members. From a structural point of view, the Colossus Bridge behaved similarly to a fixed (hingeless) arch (Crocetti, 2016a, b) (Figure 1).

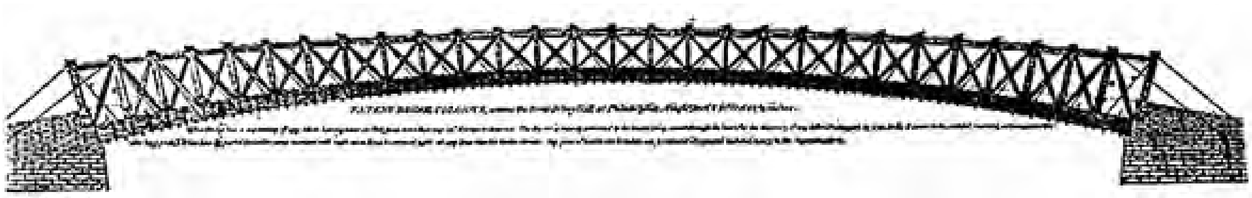

**Figure 1. The Colossus Bridge over the Schuylkill River near Philadelphia, USA, 1812**

Since the second half of the 19th century, with the advent of steel and reinforced concrete, wood "fell out of fashion" among builders and designers, possibly because of durability and fire issues. Recently, however, wood has come back in a number of ways: as traditional lumber, in various reconstituted forms of engineered wood, bonded by structural adhesives, and in combination with such other materials as steel, concrete, and composites. This "renaissance" probably arose from the development (and sometimes rediscovery) of (Crocetti, 2016a, b)

- New wood-based materials, such as glued laminated timber (glulam), laminated veneer lumber (LVL), and cross-laminated timber (CLT)

- New types of connectors/fasteners and connections, such as self-tapping screws, slotted-in plates and dowels, bonded-in rods, plates, etc.
- New chemical and structural-constructive methods of wood protection

Environmental and sustainability concerns have been additional key drivers for this renaissance in wood.

Remarkable timber structures with long spans have been constructed over the past 30–40 years. Two representative examples, the Superior Dome and Viking Ship, are shown in Figures 2 and 3, respectively. The Superior Dome (Figure 2), the world's largest wooden dome, opened on September 14, 1991 (Superior Dome, 2020). It is a stadium on the campus of Northern Michigan University in Marquette, Michigan, USA. It has a diameter of 163 m and a height (rise) of 49 m. The structure is a geodesic dome with glulam ribs made of Douglas fir. The Viking Ship (Figure 3) was built for the Olympic Games in Lillehammer, Norway, in 1994. The architects were inspired by the Oselver, a small wooden rowing boat traditionally built and used along the west coast of Norway. The structure consists of a number of parallel, three-hinged, trussed arches, with a longest span of 96.4 m (Figure 3 [right]). A dorsal arch gives the boat its characteristic roof. This arch, whose purpose is mainly aesthetic, is supported by the other arches (Farreyre & Journot, 2005).

**Figure 2. The Superior Dome, Marquette, USA, built in 1991 (Courtesy of TMP Architecture)**

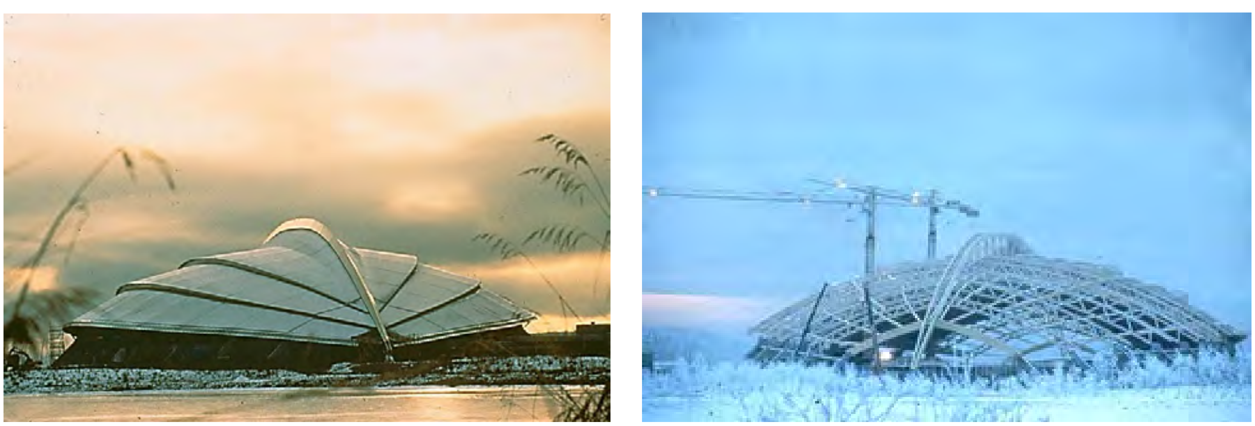

**Figure 3. The Viking Ship in Hamar, Norway, built in 1992 (Courtesy of NIELSTORP+)**

Long-span timber structures have also recently been constructed with hybrid timber systems. The Tianfu Agriculture Expo in China is a series of five vaults built to create enclosures over internal buildings, museums, and open-air markets forming a large agriculture exposition. At 80,000 m$^2$, these comprise one of Asia's largest timber structures. They use a unique, hybrid timber-steel Vierendeel truss arch to achieve clear spans of up to 115 m and heights of up to 45 m. Hybrid structures combining shell action with discretized or truss elements are also common (Figure 5), and can be quite structurally efficient. When combining timber and steel, one must carefully consider the relative thermal and moisture performance of the two materials for both structural design and construction.


**Figure 4. Tianfu Agriculture Expo, China, under construction in 2021**

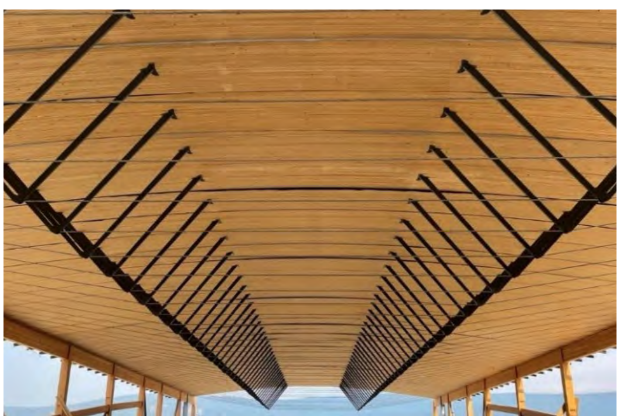


**Figure 5. Hybrid structural forms: a slender timber compression shell with discretized steel elements as trussing (KF Aerospace Centre for Excellence) (left), and hybrid timber-steel trusses in the form of a portal frame and king-post roof trusses (University of Idaho Basketball Arena) (right)**

### *7.5.1.2 Material*

In designing structures, one must bear in mind the influence of scale, particularly that the self-weight of a load-bearing structure increases with its span. All structures have weight, and this weight—that is, their own weight—is one of the loads they must carry. The longer the span of a structure of a given type, the more important its self-weight becomes in relation to other loads; eventually, the structure reaches a span at which it can only just support its own weight. The efficiency of different materials can be estimated by means of a notional experiment comparing how long bars of different materials, with constant cross-section and hanging freely under their own weight, can become before they break off at the top. To determine the material efficiency, one simply sets the weight of the bar as equal to its tensile strength. Simple calculations show that the highest maximum length is achieved by the material with the highest tensile strength-to-density (f/ρ) value. This is true not only in the very simple case of stress (tension), as explained above, but also in bending and more complex stress situations. Every type of structure, in fact, has a maximum possible length, beyond which it cannot carry even its own weight (Francis, 1980).

In this sense, timber shows excellent performance. In fact, the f/ρ ratio of, for example, common structural members made of softwood, is similar to (or even higher than) that of mild steel members. For this reason—and because it is economic and environmentally friendly—mid- to long-span applications often make use of timber, especially when live loads are light.

#### *7.5.1.3 Structural Form*

It is vital for the designer to understand structural action—how, in other words, forces pass through the structure of a given configuration. In general, structures are more efficient when loads cause axial forces in the system rather than bending. This is primarily because the internal stress distribution in axially loaded structures or structural members is constant; this uniform stress level allows the material to be stressed to the limit. This obviously not the case for structures in bending, where stress distribution reaches its maximum at the top and/or bottom fibres while being zero at the neutral axis. In terms of serviceability, structures predominantly subjected to axial forces also resist deformations more efficiently than flexural loaded structures. Deformations resulting from bending, in fact, are commonly considerably larger than those resulting from purely axial forces. These are the main reasons why long-span structures of any material are often designed to take an applied load primarily in tension and compression. Long-span timber structures are typically constructed using the truss, the arch, the catenary, or the dome. Timber structures that work predominantly in tension are not very common, though some examples exist, such as the so-called cable-shaped timber structures (see Section 7.5.4.3). Also, individual members of various timber structures work in tension, e.g., the tension tie of a tied arch or the bottom chord and some of the web members in a truss structure. Note that although members in tension are in general more efficient than members in compression, the opposite is usually true for their connections.

Figure 6 illustrates how different structural systems provide an internal bending moment to counterbalance the external applied loads. In all cases, the basic mechanisms are the same: a force couple is formed between compression and tension zones whose magnitude exactly equals the applied bending moment. For a given applied moment, the magnitude of the internal forces developed in the compression and tension zones depends directly on the magnitude of the lever arm. The deeper the structure, the greater the lever arm and the smaller the tension and compression forces. Designing an appropriate structure for a given span range is directly related to choosing a system with appropriate internal moment resistance (Schodek & Bechthold, 2013).

In short spans, the design moments are low. Therefore, in principle, such constructions can use any structural system. As spans lengthen, however, design moments increase so rapidly that only a few structural systems remain feasible. Constant-depth members, such as beams, are relatively shallow; increases in span lengths quickly lead to large tensile and compressive stresses that provide the internal resisting moment. Because the depth of these members is inherently limited, increasing the lever arm of the resisting force couple cannot entirely compensate for the span increase. Therefore, members such as beams cannot have very long spans because, past a certain point, the internal compression and tension forces become too large for efficient handling.

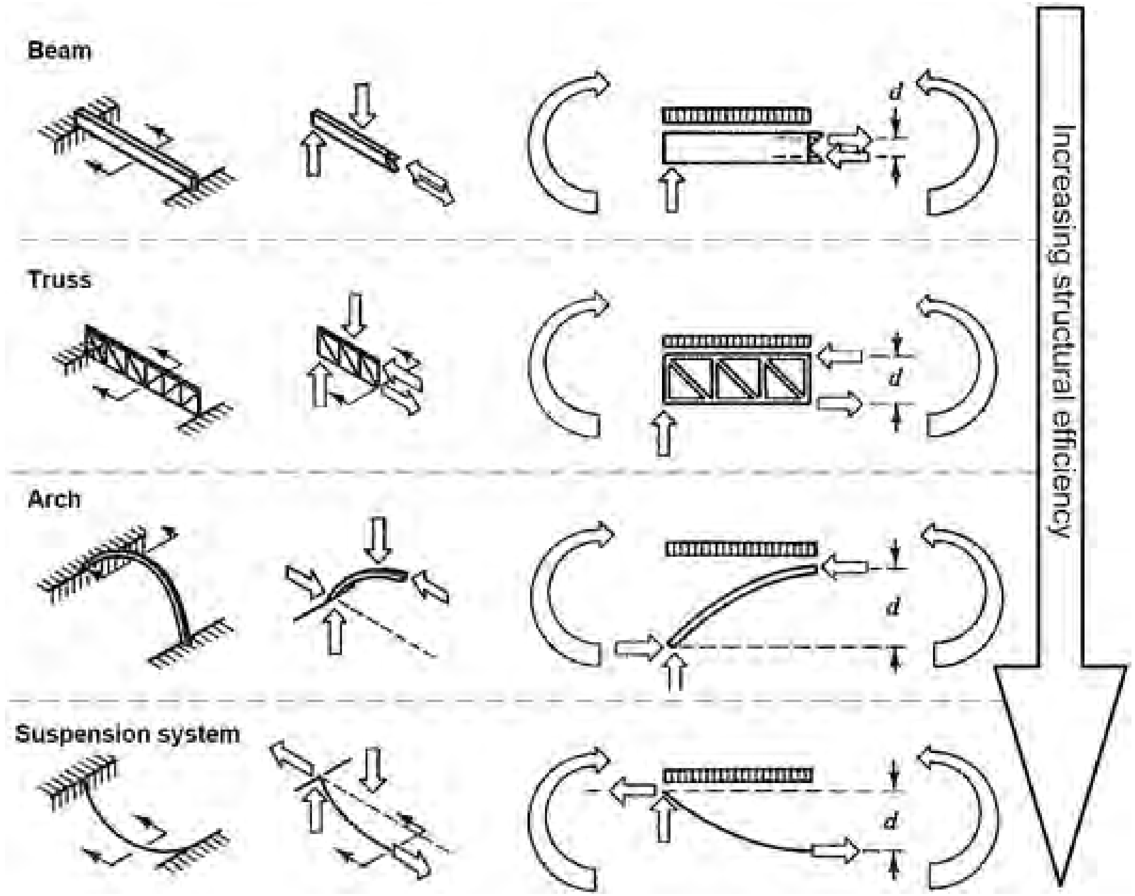


**Figure 6. Principle of load-bearing behaviour of different (planar) load-bearing systems**

The truss is more efficient than the beam for long spans for the reasons given earlier in this section and due to the "internal lever arm." This is typically larger in trusses than in beams (Figure 6), as it can be assembled from smaller elements. Suspension system and arches shaped according to the funicular of loads are both very efficient structural systems, similarly. If these two systems are subjected to the same set of external loads, only axial forces will develop in both. The magnitude of these forces is the same in both cases if the rise of the arch equals the sag of the suspension system. However, there is a fundamental discrepancy between the axial force generated in the suspension system and that generated in the arch: the former is tension and the latter is compression (Figure 6). Therefore, the possibility of premature failure due to buckling (i.e., before the ultimate strength of the material has been reached) makes arches less efficient than suspension systems (Schodek & Bechthold, 2013).

However strong and stiff a material, it is of little use unless it can be formed into structurally economical shapes that meet the functional requirements of the construction. Although materials like concrete (and to some extent steel) can be shaped into virtually any form, the very high manufacturing costs, such as the price of the formwork of curved concrete members, limit the use of statically optimized structural shapes to special applications. On the other hand, glued timber can be shaped into a large variety of forms relatively simply, and thus at a reasonable cost. The production cost of a curved glulam member, for example, does not significantly differ from that of a similar straight member. Thus, timber is particularly suitable for long-span structures such as arch-shaped and suspended systems.

Note, however, that although the consumption of material decreases as the efficiency of the structure increases, the structure's complexity and construction follow the opposite trend. Generally speaking, the elements and construction both tend to become more expensive as the structure become more efficient. This is one of the main reasons why only special applications, such as long-span structures, typically use statically optimised shapes.

#### *7.5.1.4 Typical Structural Systems*

The choice of structural system is often influenced by such factors as boundary conditions, production possibilities, transportation limitations, building functionality, and cost considerations. Table 1 illustrates some typical one- and two-way systems suitable for long-span structures and indicates the economic span ranges and corresponding structural depths for each structural system. The maximum spans provided do not represent the maximum possible spans (most of the systems could be made to span farther). The minimum limitations are intended to represent a system's lower feasibility range, based on construction or economic considerations. These values seek to suggest the relationships between structural systems, spans, and corresponding structural depths (Swedish Wood, 2018; parts 1). The figure does not include the width of the members. As a rule of thumb, however, the ratio between the depth *h* and width *b* of a member should be $h/b \approx 5$ for members with significant bending moments and $h/b \approx 1$ for members working mainly in tension and/or compression. If needed, some of the systems shown in Table 1 can be given a pre-camber to compensate for part of the final deflection. In general, all structures must be braced to prevent lateral buckling and/or to withstand horizontal loads (see Section 7.5.3.1).

**Table 1. Typical structural systems for timber structures, with suggested suitable (economic) span and structural depth**

| Name | Static system | Suitable span (m) | Depth |
|---|---|---|---|
| Straight or Double-pitched beam | 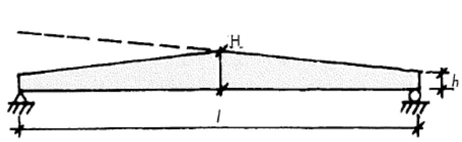  | ≤30 | $h \approx \frac{l}{20}$ <br> $H \approx \frac{l}{15}$ |
| Trussed beam | 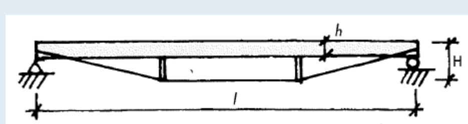  | 25–50 | $h \approx \frac{l}{30}$ <br> $H \approx \frac{l}{10}$ |
| Straight truss on two supports | 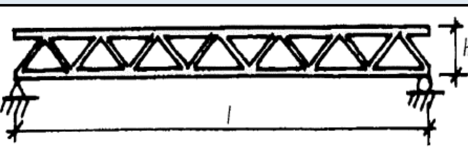  | 25–70 | $h \approx \frac{l}{10}$ |

| Name | Static system | Suitable span (m) | Depth |
|---|---|---|---|
| Orthogonal grid | 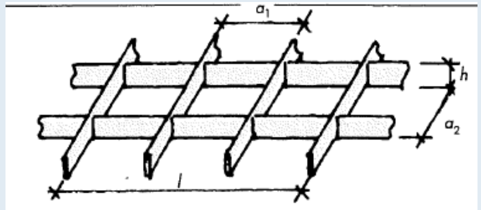  | 10–30 | $h \approx \frac{l}{20}$ |
| Three-pin truss, with or without tie | 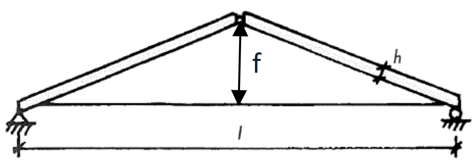  | 15–40 | $h \approx \frac{l}{30}$ <br> $\frac{f}{l} \geq \frac{1}{8}$ |
| Three-pin (or two-pin) arch, with or without tension tie | 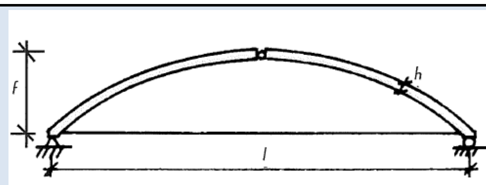  | 30–60 | $h \approx \frac{l}{40}$ <br> $\frac{f}{l} \geq \frac{1}{7}$ |
| Three-pin (or two-pin) trussed arch, with or without tension tie | 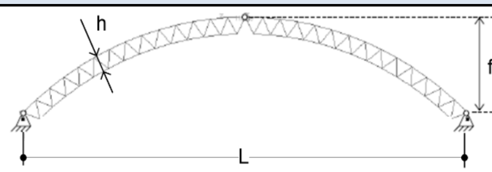  | 50–150 | $h \approx \frac{l}{30}$ <br> $\frac{f}{l} \geq \frac{1}{7}$ |
| Three-pin portal frame with moment-resisting haunch connections | 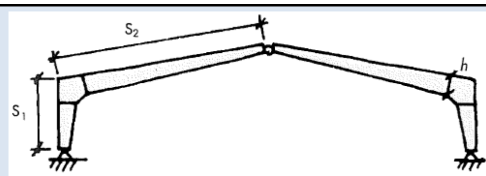  | 15–25 | $h \approx \frac{s_1 + s_2}{13}$ |
| Three-pin portal frame with curved haunches | 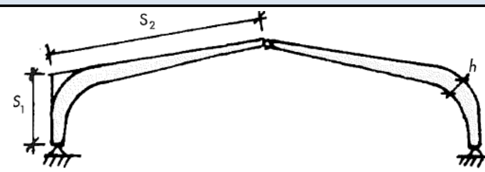  | 15–50 | $h \approx \frac{s_1 + s_2}{15}$ |
| Stress ribbon | 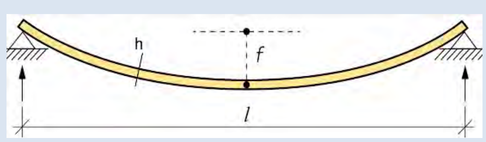  | 40–80 | $h \approx \frac{l}{200}$ <br> $\frac{f}{L} \approx \frac{1}{10}$ |
| Dome (geodesic or other) | 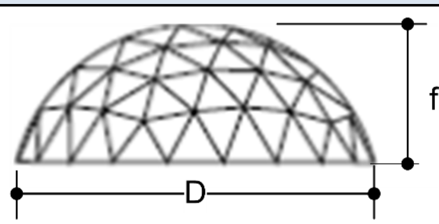  | 50–200 | $h \approx \frac{l}{180}$ <br> $\frac{f}{D} \geq \frac{1}{5}$ |

When supports are available on all sides of a long-span structure, and the ratio of the long- to short-span direction is less than approximately 1.5, it may be useful to consider a structural system with elements spanning both directions. Pay careful attention to the following:

- a structural analysis comparing the efficiency of one-way elements only with a two-way system.
- the increased complexity of connections between the elements.
- the erection complexity and speed.
- the presence of local construction expertise, and an early approximate costing.

The load-bearing systems of many structures consist of a number of identical parallel structural systems (one-way systems). As a rule, the price per square metre of the primary structures of a load-bearing system, such as trusses or arches, decreases as the spacing between these structures increases. On the other hand, the price of the secondary structures, such as purlins or other roof structural elements, follows the opposite trend: it increases as the spacing between the primary structures increases. A theoretical optimum spacing could hence minimize the total cost of the structure, as illustrated in Figure 7.

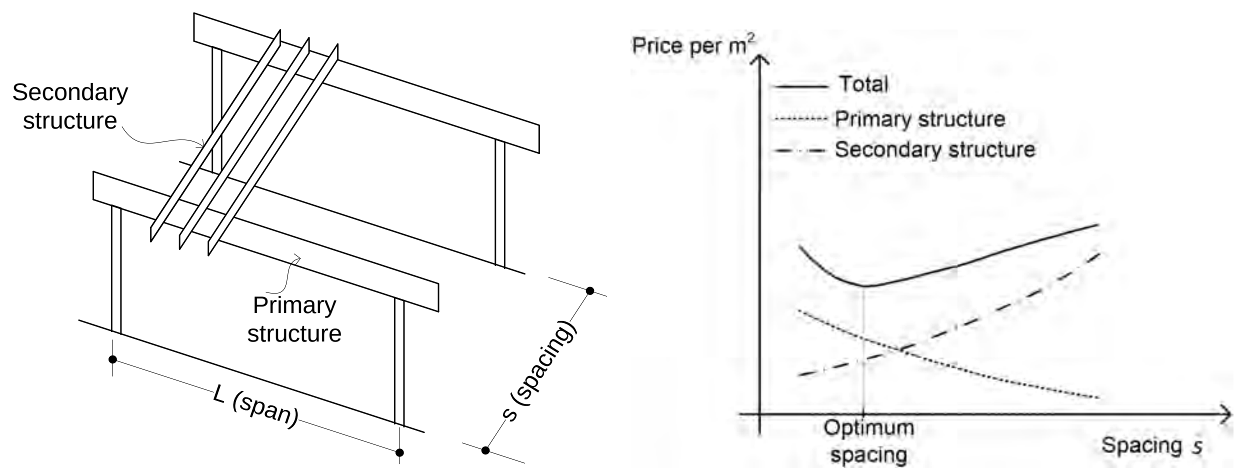


**Figure 7. Qualitative trends for price per square metre for a primary load-bearing structure, a secondary load-bearing structure, and their total (Riberholt, 1985)**

For example, when glulam serves as a structural material for both primary and secondary load-bearing structures—the latter consisting of purlins—the optimum spacing *s* can be approximately derived via Equation 1 (Riberholt, 1985):

$$s \approx \sqrt{L}, \qquad [1]$$

where s = spacing between primary load-bearing structures; and L = span of the primary load-bearing structures.

However, when the secondary load-bearing system consists of prefabricated roof elements rather than purlins, other considerations apply. Such elements often span longer than purlins, so the most economical choice is not as obvious.

### *7.5.1.5 Free-Form Timber Structures*

There is a long history of designing and building complex or free-form shapes and structures of varying sizes with timber as a natural material. The flexibility and workability of the material makes it ideal for shaping and milling, but its natural defects and variability make the results unpredictable. Perhaps the earliest structures built using wood curved into given shapes are indigenous dwellings constructed with bamboo, reed, and hardwoods in places like southern Iraq (Mudhif houses), Ethiopia (Dorze tribe houses), and Brazil (Oca houses).

In the 1960s, Frei Otto pioneered the use of timber for free-form gridshell structures. He used the so-called bending-active technique: a lattice of initially straight timber lathes is laid flat on the ground then curved up into place on-site. After success with smaller structures at Expo 67 in Montreal, his crowning achievement was the Mannheim Multihalle (1975), an interconnected series of spaces created by a bidirectional, double-layer grid of 2”x2” timber lathes, with clear spans up to 200 ft—a span-to-depth ratio thinner than that of an eggshell. In the 1990s, Julius Natterer explored timber gridshells using elements initially curved in one direction then allowed to torque about their long axis during installation. This allowed structures with larger structural depths and spans, culminating in the Expodach Hanover in 2000.

Both these approaches, however, limit the geometrical form of the roof because an initially straight timber element can only be curved or twisted to a certain degree. The Swatch Headquarters by Shigeru Ban, shown in Figure 8, involved another approach to truly free-form roof structures. Instead of using small, initially straight cross-section lathes, the design used much larger straight elements. Each piece was three-dimensionally computer numerical control (CNC) milled into the required twisted, curved shape to suit the geometry of the roof (albeit with significant cost and material waste). Since this project, further advances in glue lamination have enabled the automated production of glulam elements that are doubly curved from the beginning, removing much of the wasted material created by CNC milling an initially straight element. Several timber gridshells have been built worldwide using a similar strategy.

**Figure 8. Swatch Headquarters**

The Taiyuan Botanical Garden in China (Figure 9) contains three timber dome gridshells, with unique seashell-like geometry and a parabaloid rather than spherical shape. These gridshells use continuous spliced glulam elements in two directions, running above each other. One direction is geodesic, to minimize the volume of doubly-curved glulam. All layers in the gridshell are moment-fixed to each other using a bespoke hidden connection, allowing the removal of a third direction gridshell element in all but the largest dome (a 90 m span). This dome uses a series of diagonal cables below the glulam shell to create in-plane shear stiffness.

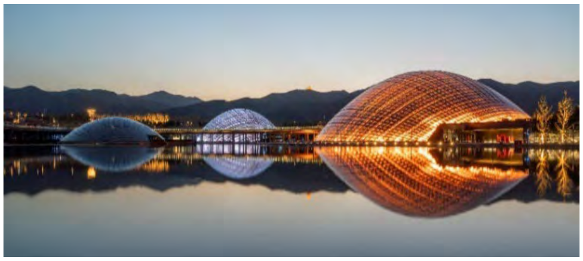

**Figure 9. Taiyuan botanical Garden**

## 7.5.2 General Aspects of Long-Span Structure Analysis

In essence, structurally modelling long-span structures is similar to doing the same for any other kind of structure, with the transformation of a complex real-world construction into an idealized model. This model can then be elaborated with different degrees of sophistication, depending on the importance of the application.

This chapter focuses on the design of long-span structures for roof applications. Roofs are typically designed based on a static analysis (except for a very slender roof, which may be prone to aerodynamic instability). However, it should be kept in mind that—although not treated in this chapter—dynamics often govern the design of some types of long-span structure, e.g., pedestrian bridges and floors.

Before discussing different analysis strategies for long-span structures, note that there are some uncertainties related to design. Construction materials, even when homogeneous, can differ substantially from the elastic (or plastic) idealization. This is particularly true for timber, whose stiffness and strength can vary widely owing to its natural composition and to site and life histories when incorporated into a structure. Structural analysis almost inevitably simplifies the geometry of a structure; for example, it typically ignores construction joints, site imperfections, and other details. Moreover, the design loadings for live load, creep, settlements, etc., are mere idealizations based on statistical studies, often rough. Thus, larger inaccuracies in results are likely regardless of the method of analysis used. Therefore, greater emphasis should be given to considering the physical behaviour of the structure and designers should try to anticipate the consequence of a calculation being in error (by approximately 20%), rather than refining analysis models to achieve an apparently accurate result (Hambly, 2019).

In general, errors have greater consequences in long-span structures than in short-span ones. Thus, regardless of the material selected for the project, one must consider the following issues carefully when designing a long-span structure:

- The engineer must be rigorously correct, determine accurate load paths, and consider what happens if something goes wrong in fabrication or use.
- In a short-span structure, structural behaviour is typically “assumed”; a long-span structure, on the other hand, requires measures to ensure that the design assumptions are correct. Either a) consider a range of worst-case scenarios and then model and design for the extremes, or b) detail to ensure behaviour happens as predicted (e.g., for a connection, either consider a range of behaviours from fully fixed to fully pinned, or formally detail a pin).
- A lack of bracing against instability, both in the finished structure and during construction.

Furthermore, there are some particular issues which are typical for timber:

- Timber is inhomogeneous, anisotropic, only durable in certain conditions, and weaker at connections.
- Failures in timber typically arise from design errors, happen soon after construction, and occur due to basic errors in understanding timber behaviour (Frühwald et al., 2007). Common faults include the following:
    - A risk of perpendicular to grain failure (anisotropy)
    - Misjudgement or disregard of moisture effects (shrinking and swelling)
    - Poor joint design
    - A lack of fire safety
    - Poor communication among design and building team

### *7.5.2.1 General Rules*

#### 7.5.2.1.1 Choice of finite elements

In a numerical analysis, one can choose among 1D elements (beam elements), 2D elements (surface elements), and 3D elements (volume elements). All line elements, straight or curved, are 1D elements with translational and rotational displacement functions. Examples include the truss element and the beam element. The 2D elements are typically surface elements with a triangle or quadrilateral as their basic shape. They are commonly used for plate-type members, such as slabs, bridge decks, and shells, where the two dimensions perpendicular to the thickness are considered much larger than the thickness itself. Finally, 3D elements mesh volumes.

It is possible to model most long-span timber structures using 1D elements. The use of such elements, in the form of grillage or a space frame, also allows the analysis of plate-like structures and shells with enough accuracy. For manifestly two-dimensional structural behaviour, such stress-laminated deck plates subjected to concentred loads, 2D elements could give more accurate results than 1D elements. On the other hand, 3D elements are very seldom employed for the structural analysis of long-span timber structures.

#### 7.5.2.1.2 Global Structural Analysis

The structural analysis of long-span structures should always follow a preliminary calculation performed either by hand or by numerical simulation with a simplified model that adequately reflects the behaviour of the real structure. For example, a preliminary analysis of the in-plane behaviour of large roof construction consisting of a number of parallel load-bearing systems can use a two-dimensional model consisting of a single load-bearing system loaded according to its tributary loading area. Analogously, the preliminary design of plate or shell structures can adopt simpler methods of grillage and/or a space frame.

The final design of a long-span structure comprising a series of identical, parallel load-bearing systems can involve modelling either one isolated two-dimensional system or the entire structure, the latter as a three-dimensional system. There are both pros and cons to either approach. The two-dimensional approach is fast and gives most of the data necessary for the final design of the structure. It must, however, deal with the following by means of a separate structural model:

- the design of secondary load-bearing structures,
- the out-of-plane stability of the isolated systems, and
- the design of the bracing members.

The three-dimensional approach, meanwhile, gives the necessary information to design the entire structure but increases a) the time required for the modelling and b) the complexity of processing the results.

#### 7.5.2.1.3 Three Levels of Theory

Structural analysis of long-span structures commonly assumes that timber and any possible members made of other materials have linear properties throughout and that all strains are small. Hooke's Law always applies, and any nonlinear effects will therefore be of a geometric nature. Generally, there are three levels of theory (Bell, 2017):

- Linear or first-order theory: Displacements and rotations of elements are small in comparison to their characteristic length, and equilibrium equations exist for undeformed (ideal) geometry. Therefore, the principle of superposition has unlimited validity.
- (Nonlinear) Second-order theory: Small displacements are still assumed, but equilibrium equations are now established with respect to deformed geometry. The principle of superposition has only limited validity and is generally not used.
- (Nonlinear) Third-order theory*:* Displacements are no longer small, and equilibrium refers to deformed geometry. The principle of superposition is not valid.

These fundamental theories can be explained by studying a simply supported beam with an elastic support, subject to the simultaneous action of an axial and transverse force, as illustrated in Figure 10. The three simple structures shown in the figure have the same geometry, material, and cross-section, and are subject to the same set of forces (P and F). The only difference among the three structures is the stiffness k of the vertical elastic spring at the right-hand support, which is high in case (a), low in case (b), and very low in case (c).


**Figure 10. Illustration of (a) first-, (b) second-, and (c) third-order theory by means of three simply supported beams; k decreases from (a) to (c)**

The stiffness k influences the magnitude of the vertical displacement at the elastic support. In case (a), the displacement is very small, and can thus be assumed to be zero; here, first-order theory applies. In case (b), the vertical displacement is small but not negligible; here, second-order theory applies. The vertical displacement being small, the following approximation applies: $\cos(\theta) \approx 1$ and $\sin(\theta) \approx \theta$. In case (c), the vertical displacement is large and no geometric approximations are possible; here, third-order theory applies. Studying the rotational equilibrium about point A for the three different systems allows the derivation of the following relationship between the applied vertical force F and the corresponding vertical stiffness of the system:

$$\text{Case (a)} \Rightarrow F = k \cdot u \tag{2a}$$

$$\text{Case (b)} \Rightarrow F = \left(k - \frac{P}{L}\right) \cdot u \tag{2b}$$

$$\text{Case (c)} \Rightarrow F = \left[k - \frac{P}{L\sqrt{1-(u/L)^2}}\right] \cdot u \tag{2c}$$

Equation 2 shows that the vertical stiffness of the structure is linear and not affected by the axial force P in a first-order analysis (i.e., case [a]). In case (b), second-order analysis, the stiffness is still linear but the axial force P reduces it. In case (c), third-order analysis, the axial force P also reduces the stiffness. Moreover, the stiffness is nonlinear and lower than in the other two cases. Generally, the strength and stiffness of long-span structures can often be adequately handled by linear (first-order) theory—however, stability and special types of structures cannot.

For most of these structures, second-order analysis is normally sufficient unless they are very slender, in which case third-order analysis would be more appropriate. However, timber and/or timber-based hybrid structures are rarely this slender; thus, third-order theory is not generally necessary.

#### *7.5.2.2 Stability Analysis*

Dealing with stability problems commonly requires one of the following techniques:

- **Linear buckling (or eigenvalue) analysis**
  This is the most common type of analysis and is easy to implement, but the results that it can provide are limited. Linear buckling analysis (LBA) determines both the buckling load magnitudes and the corresponding buckling modes based on an initially undeformed shape of the structure. Finite element (FE) programs typically calculate many buckling modes and the associated load multiplier. Normally, the lowest load multiplier and its corresponding buckling mode are of interest. LBA gives no information about the numerical values of either displacements or stresses associated with the different buckling modes.

- **Nonlinear buckling analysis**
  This typically requires a load to be applied gradually in multiple steps on a structure with a given initial imperfection. Each load increment modifies the structure's shape, and this in turn modifies the structure's stiffness. Therefore, the stiffness of the structure must be updated at each load increment. In nonlinear buckling analysis (NLBA), load steps are defined so the difference in displacement between two consecutive steps is not too large.

In LBA, the lowest (Euler) buckling load serves as a basis for deriving the relative slenderness ratio $\lambda_{rel}$, (i.e., the square root of the ratio between the characteristic compression strength and the buckling load of the member). The next stage in the analysis then calculates a reduction factor $k_c$ as a function of the relative slenderness ratio (for very slender members, $k_c \approx \lambda_{rel}^{-2}$). The factor $k_c$ considers the risk for buckling and is applied to reduce the compression strength of the member, thus eliminating the risk of failure due to instability.

NLBA, on the other hand, has no need for buckling reduction factors. The resulting axial forces and bending moments in the member, as calculated using NLBA, can be used directly (without reduction factors) to design the member. Section 7.5.4.2.4 provides more details about applying LBA and NLBA to analyse arch structures.

Although LBA uses 1D FEs to analyse any type of instability, including flexural, torsional, and lateral-torsional buckling of members, this is not the case for NLBA. Indeed, NLBA uses 1D FEs only when analysing axially loaded members with symmetric cross-sections (flexural buckling). For other types of instability, such as lateral-torsional buckling, which involves bidirectional bending and torsion of the member, NLBA cannot be performed with 1D FEs but only with 2D or 3D FEs.

When large deformations are likely to occur during loading (typically for slender structures and those with deformable joints), nonlinear analysis is normally necessary. Structures typically analysed in this manner include:

- shallow arches and frames;
- slender spatial frames and shells, including segmental lattice roofs; and
- cable-shaped structures.

#### *7.5.2.3 Form-Finding*

Choice of form is intrinsic to creating efficient structures. For structures with longer spans or more complex geometry, the question of structural form and topology is often pivotal to the success of both architecture and structure.

As the name suggests, form finding involves finding a 2D or 3D geometry for a structure that respects anticipated boundary conditions and forces, while also meeting the aesthetic and functional requirements of the built environment. Current practice typically uses two methods of form-finding: funicular form and minimal surfaces. The geometry of a surface or shell structure is often based on the principal of funicularity—a funicular form will tend to create geometry which acts primarily in either compression or tension under a given set of loads and boundary conditions. Compression and tension are the most structurally efficient ways to transmit loads over long spans.

*As hangs the flexible line, so but inverted will stand the rigid arch.*
*Robert Hooke, 1675*

Funicular shape can be described with the diagram in Figure 11. When a point load is applied on a simply supported cable, it undergoes deformation, inducing tension across the cable. The shape achieved is called a funicular shape. When increasing the resolution of point loads at an equal distance across the cable, the form clearly tends towards a catenary curve with only tension across the structure. If one flips this curve upside-down into an arch, a structure with the curve as a thrust line becomes a compression-only structure; the magnitudes of tension and compression in these two structures are inversely identical (Figure 11). A catenary cable is a funicular geometry for uniformly distributed loads (e.g., self-weight). However, under any other imposed loading (e.g., a wind load or point load), the catenary shape will no longer be funicular, and the cable geometry will deform to find a new funicular equilibrium state. Form-finding is often regarded as the process of determining funicular or approximately funicular shapes for a given structure and set of boundary conditions.

**Figure 11. Change in funicular shape of cable structure with increasing resolution of point loads**

The same concept can also apply to three-dimensional geometry. As shown in Figure 12, when a uniform load is applied on a 2D grid of elements with corner supports, it deforms into a funicular (cable-net like) form, with all elements in tension. The elements close to the supports have comparatively higher magnitudes of tensile force. Rotating this geometry upside-down generates a compression-only shell for uniform vertical loads.

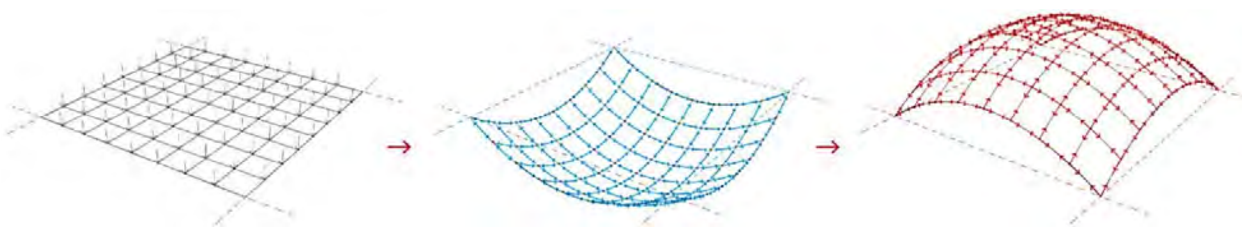

**Figure 12. Form finding of funicular shell from**

A prominent method of form finding for tensile structures uses the concept of minimal surfaces for a particular set of boundary constraints. This concept arose in Frei Otto's seminal research at the Institute for Lightweight Structures at the University of Stuttgart. Otto experimented with sets of closed curves dipped in liquid soap, forming a minimal surface that connects the set of boundary curves. This surface represents a geometry that minimizes the energy in the surface and thus represents the minimum possible surface area to connect the boundary curve(s). In an ideal state, minimal surfaces only carry tension, while the boundary elements carry compression and bending. This method's property of surface tension makes it useful when exploring form for tensile structures. However, the concept of minimal surfaces does not provide ideal geometry for compression structures. Digital form-finding techniques often use analysis methods which can represent both minimal surfaces and funicular/compression structures.

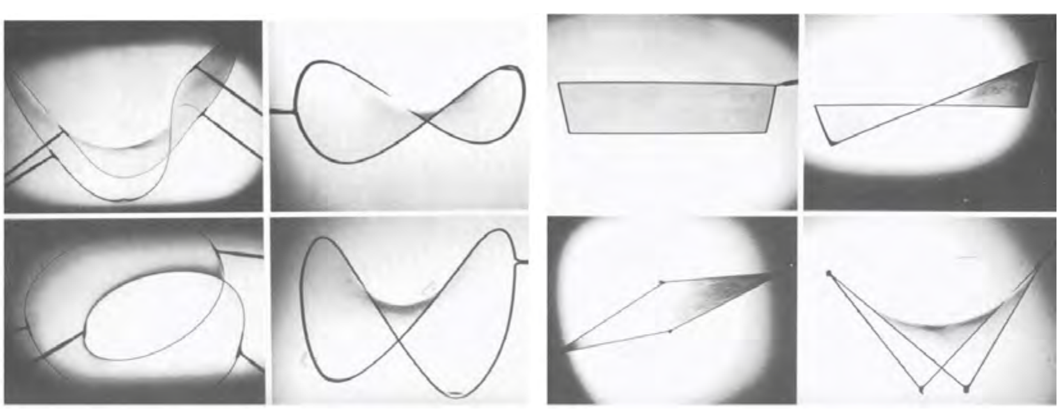

**Figure 13. Form finding for minimal surface (IL 1 – Minimalnet, Frei Otto)**

Pioneers in modern form-found structures included architects and engineers such as Vladimir Shukhov, Antoni Gaudí, Frei Otto, Felix Candela, Heinz Isler, and Pier Luigi Nervi (for examples of their work, see Figure 14). One of the earliest explorers of modern gridshell structures was Vladimir Shukhov, who introduced diagrid (lattice) structure at the end of the 19th century. Mainly using steel, he introduced the advantage of free-form surfaces to create lightweight, long-span structures; due to the rational distribution of material along the shape, the grids were two to three times lighter than roofs with conventional frames. During the 1896 All-Russia industrial and art exhibition, he presented this concept in the form of towers, suspension structures, and doubly-curved vaulted structures. His contemporary, architect Antoni Gaudí, introduced the use of hanging chains as a physical modelling technique to explore funicular shapes. This technique transformed how modern forms are designed and analysed. Gaudí used it to derive the geometry of the iconic La Sagrada Familia, using hanging grids of chains and applying weights via sandbags, then altering the geometry by changing either the cable lengths or the sandbag weights. Construction of the structure then started using a scaled-up version of this model geometry.

**Figure 14. Examples of early form-found structures. From left to right: tensile steel lattice shell of Oval Pavilion; hanging chain model for La Sagrada Familia; Mannheim gridshell hanging chain-net model; compressive steel gridshell for All-Russia industrial and art exhibition 1896; La Sagrada Familia; Mannheim gridshell seen from inside**

Frei Otto built on this technique when designing the Mannheim timber gridshell. Instead of individual cables, he explored the geometry of this temporary shelter by suspending a 2D grid whose density and boundary conditions represented the actual project constraints, then flipping it upside down to create the compression geometry for the timber gridshell. Structural engineers Ian Liddell and Ted Happold (Happold and Liddell, 1975) then used dimensional analysis and custom finite element formulations to correlate measured deformations in the scale model to the behaviour of the real structure. This made the stresses in the gridshell predictable, and helped explain the real buckling behaviour of the gridshell.

Contemporary form-finding processes have adapted these techniques and evolved them into more sophisticated digital tools using analysis techniques such as the Force Density method and the concept of Dynamic relaxation, pioneered by Alistair Day. This software allows real-time investigation of funicular and minimal shapes, without physical modelling.

Form-found shapes can be categorized into two main types, based on curvature: singly-curved surfaces and doubly-curved surfaces, as illustrated in Figure 15. Singly-curved surfaces (also known as ruled surfaces), curve in one direction, while the other direction can be described by straight lines (the rulings). The gaussian curvature at any point on a singly-curved surface is thus zero. Doubly-curved surfaces curve in both directions, and can be simplistically further categorised into two shape types: synclastic and anticlastic. In a synclastic surface, the curvature in both directions has the same sign, and the gaussian curvature is always positive. In an anticlastic surface, the curvatures in each direction have opposite signs, and the gaussian curvature is always negative.

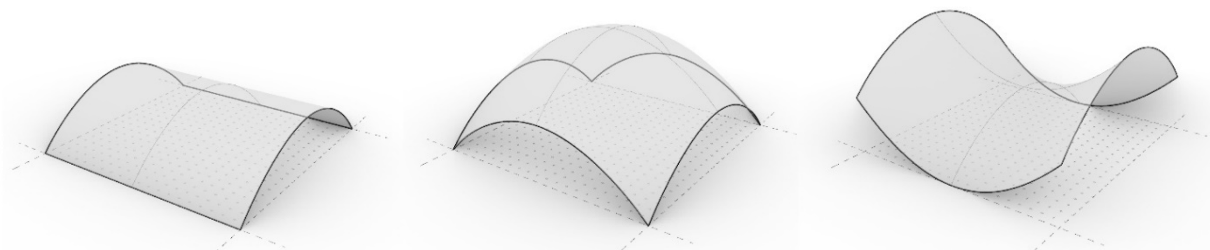

**Figure 15. Types of shell surfaces. From left to right: ruled surface, synclastic surface, anticlastic surface**

Force follows stiffness, and form is what creates this stiffness. Thus, it is crucial to understand how these geometrical forms affect structural behaviour when conceiving efficient long-span structures. Each geometrical type and its derivatives have different structural performance, as well as key advantages and disadvantages in construction and fabrication complexity.

Long-span timber structures can have timber shells of uniform thickness in either compression or tension, using materials such as glulam, CLT, or LVL, as shown in Figure 16 (left). However, they are often discretized into structural forms such as arches, trusses, and gridshells, reducing the material required and increasing structural efficiency, as shown in Figure 16 (right). Figure 17 illustrates the discretization of a free-form surface shell into a gridshell.

**Figure 16. (left) An example of uniform shell structures – BUGA Pavilion and (right) an example of discretized gridshell structures – Expo Roof**

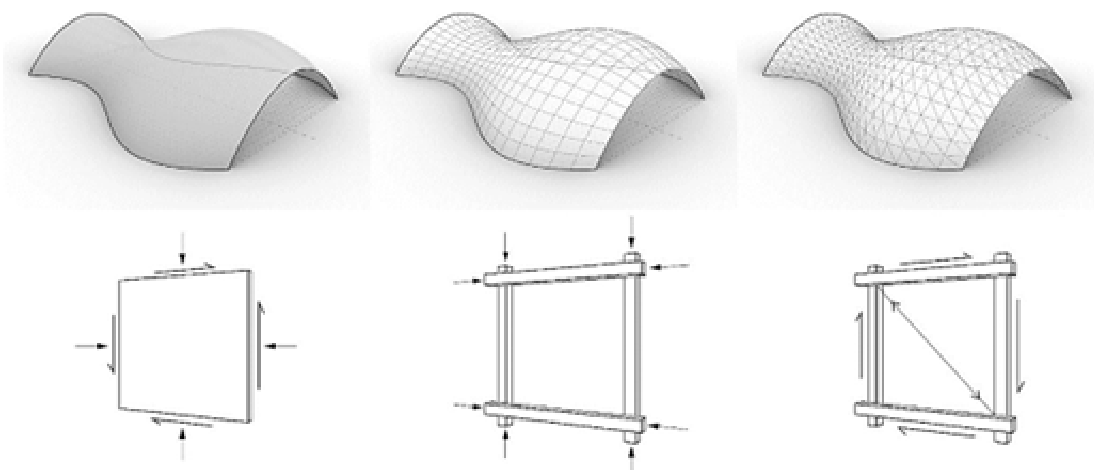

**Figure 17. Discretization of a free-form surface shell into a gridshell. From left to right: shell Action; gridshell (not diagonalised); gridshell (diagonalised)**

Timber gridshells discretize a surface into two or more directions. The surface geometry is often chosen to match a funicular shape, meaning the gridshell primarily carries compression or tension under its own self-weight. Architectural considerations often lean towards a two-directional or quadrilateral gridshell. This poses a unique structural challenge, as in-plane shear buckling quickly dominates the structural performance. In steel gridshells, this is not an issue, as it is simple to create moment-stiff connections between crossing layers using welds or tight-fit bolted connections. Not so with timber: moment connections are both expensive and difficult to fabricate / install. Many engineers thus introduce opaque sheathing or a third direction in the gridshell to create the desired in-plane stiffness. In the Mannheim Multihalle this involved a diagonalised grid of steel cables; in many timber gridshells, the third direction is created with full-size structural elements, adding to the visual density and complexity of the construction (e.g., Tacoma Dome, Superior Dome, Exeter University Forum). However, recent progress in the field of timber connections allows some timber quadrilateral gridshells to be built without requiring a third direction (e.g., Taiyuan Domes, China, as shown in Figure 18).

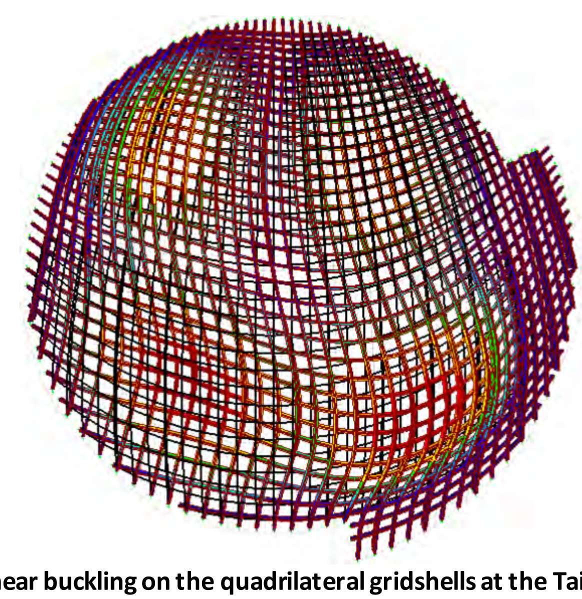

**Figure 18. In-plane shear buckling on the quadrilateral gridshells at the Taiyuan Botanical Gardens**

### 7.5.2.4 Dynamic Relaxation

Central to creating software tools which mimic the hanging chains approach of Gaudí and Otto is a robust analysis algorithm which can simulate the behaviour of these highly dynamic systems during form-finding.

Dynamic relaxation is an analysis technique created by Alistair Day in 1960, initially for use in predicting surge tidal profiles and then applied to structures, starting with buildings such as the Sydney Opera Hall. Dynamic relaxation analyses a static structure dynamically, using small time steps, and minimises the energy state of a given system of particles and springs at each step. It is incredibly powerful, as it can accurately analyse highly nonlinear systems and, unlike the finite element method, shows strong convergence even with structures which have significant form changes or lose entire elements. Dynamic relaxation also allows the investigation of optimal forms, as it naturally lends itself to simulating dynamic physical systems such as hanging chains or soap films. Mathematically, the dynamic relaxation technique is deceptively simple. The basic technique can be understood by considering a single mass hanging from a spring (Figure 19).

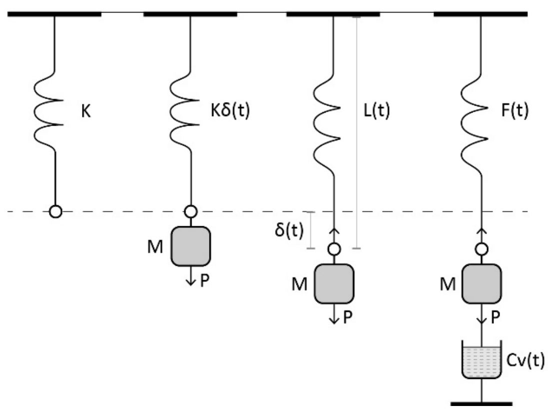


**Figure 19. Illustration of a single mass hanging from a spring: $P$ is the constant load applied at node *i* in direction *x* (i.e., the external load on the system); $Cv(t)$ is the viscous damping of the system at time t; and $F(t)$ is the Spring Force acting on node *i* at time t**

Newton's second law and Hooke's law provide the sum of forces at time $t$:

$$P - K\delta(t) - Cv(t) = Ma(t) \qquad [3]$$

This can be re-written as

$$R(t) = Ma(t) + Cv(t) \qquad [4]$$

where $R$ is the resultant force on the node. We can express this in Central Finite Difference form (Euler method):

$$R(t) = M\left(\frac{v\left(t+\frac{\Delta t}{2}\right)-v\left(t-\frac{\Delta t}{2}\right)}{\Delta t}\right) + Cv\left(\frac{v\left(t+\frac{\Delta t}{2}\right)-v\left(t-\frac{\Delta t}{2}\right)}{\Delta t}\right) \qquad [5]$$

Then, we can rearrange this and express it as a recurrence equation for nodal velocity at time $t + \frac{\Delta t}{2}$ with constants A and B:

$$v\left(t+\frac{\Delta t}{2}\right) = A\frac{\Delta t}{M}R(t) + Bv\left(t-\frac{\Delta t}{2}\right) \qquad [6]$$

Finally, the updated geometry and resultant spring forces at time $t + \Delta t$ can be expressed:

$$\boldsymbol{\delta}(\boldsymbol{t} + \Delta \boldsymbol{t}) = \boldsymbol{\delta}(\boldsymbol{t}) + \boldsymbol{v}(\boldsymbol{t} + \tfrac{\Delta t}{2})\Delta \boldsymbol{t} \quad [7]$$

and

$$\boldsymbol{R}(\boldsymbol{t} + \Delta \boldsymbol{t}) = \boldsymbol{P} + \sum_{m} \left(\tfrac{F}{L}\right)(\boldsymbol{t} + \boldsymbol{\Delta t})(\boldsymbol{\delta}_{j} - \boldsymbol{\delta}_{i})(\boldsymbol{t} + \boldsymbol{\Delta t}) \quad [8]$$

In simpler terms, this algorithm is effectively as follows. Given a system of springs and node masses (springs representing structural elements or constraints):

(1) Set the external loads on each node equal to the applied loads on the system
(2) Calculate the internal spring forces from the springs connected to each node, as a result of these external loads
(3) Sum both external loads and internal spring forces and calculate a resultant force vector
(4) Move each particle slightly in the direction of this force vector
(5) Recalculate spring forces, and repeat steps 3–5 until the particle system converges
(6) Convergence happens when the resultant of the external forces and the internal spring forces is zero.

This algorithm, while simple in concept, can be applied to highly complex and nonlinear structural systems such as bending-active gridshells without loss of accuracy. It predicts the forces inside the timber lathes at each step as the gridshell is raised from a position flat on the ground to its final curved shape.

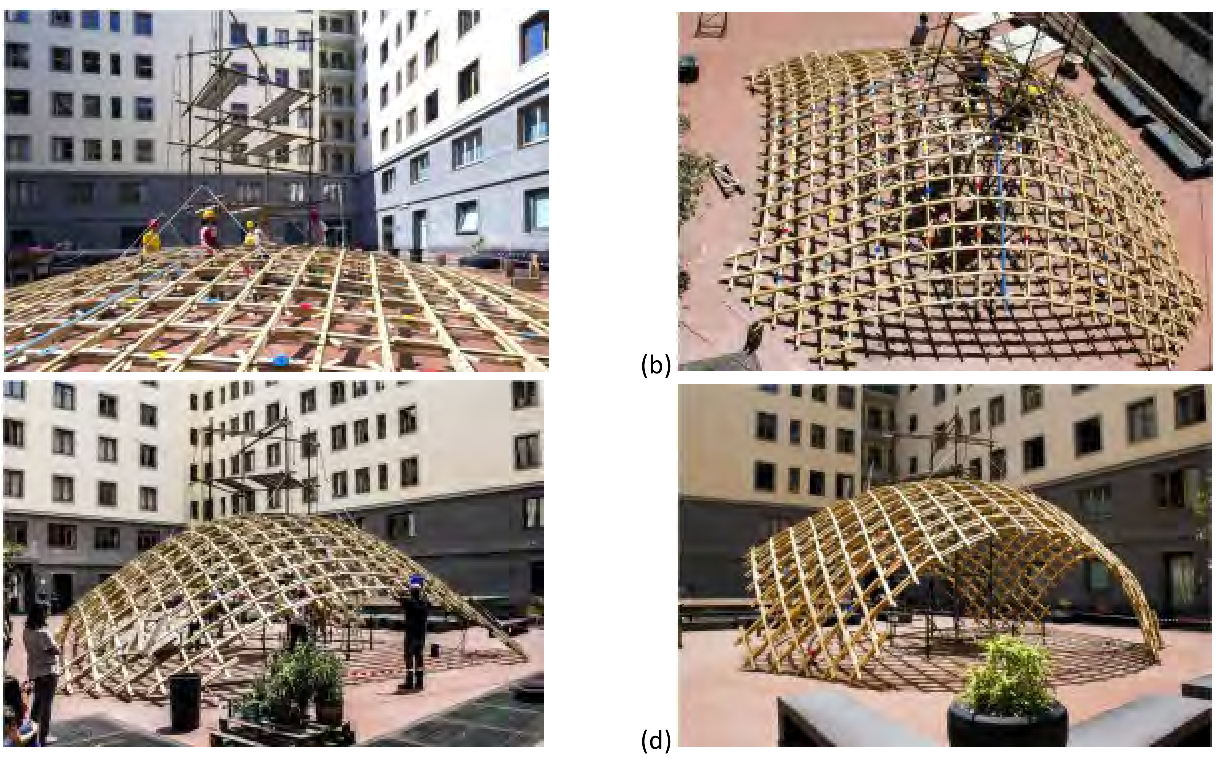
(a) (b) (c) (d)

**Figure 20. Toledo gridshell 2.0. Construction process (D'Amico et al., 2015): (a–c) The central nodes are pulled up using cables; (d) additional horizontal thrust is added to the corner nodes in order to reach the final shape**

## 7.5.3 Influence of the Span on Structural Design

This section introduces the influence of the span on the stability, bracing, and joints of a structure.

### *7.5.3.1 Structural Stability*

Sensitivity to problems of stability, such as flexural buckling (both in-plane and out-of-plane) and lateral-torsional buckling, increases with the span of the structure. This can be explained by studying the in-plane buckling of the two-hinged arch shown in Figure 21. We assume that the arch is shaped according to the funicular of a uniformly distributed gravity load (i.e., the parabola).

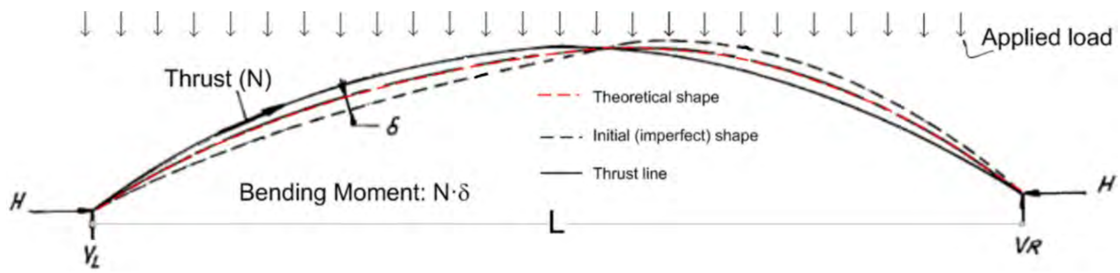


**Figure 21. The bending moments that occur in an arch due to an initial imperfection**

To begin with, one must bear in mind that real structures always have geometric imperfections. Assuming that the initial imperfection for the arch in Figure 21 is shaped according to the first buckling mode (the dotted line), the maximum bending moment in the arch caused by the initial imperfection is $M=N\cdot\delta$. This occurs at approximately 0.2 to 0.25 of the span, depending on the static system of the arch. If one compares arches made of the same timber material with different spans—all loaded by a uniformly distributed gravity load, with a constant rise-to-span ratio and a constant slenderness ratio (i.e., constant critical Euler buckling stress)—both the thrust N and the magnitude of the initial imperfection $\delta$ increase linearly with the span L. Therefore, the bending moment in the arch M, governing the arch's sensitivity to in-plane buckling, increases with the square of the span. Consequently, the resistance against in-plane buckling decreases with the span. A similar model could help study the effect of the distance between lateral restraints on the out-of-plane buckling of the arch in Figure 21.

### *7.5.3.2 Structural Bracing*

Bracing against buckling is important for any type of slender structure and is thus crucial to long-span structures, except suspended ones which work predominantly in tension. To understand this, consider the magnitude of the brace forces in a compression strut laterally restrained at its end and elastically restrained at its mid-length. A similar situation can occur in the out-of-plane direction of the arch in Figure 21 or in the compression chord of a truss when they are laterally braced against buckling (Figure 22).

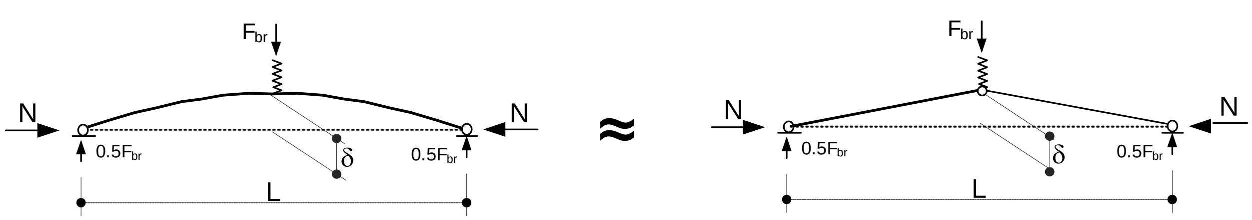


**Figure 22. Compression strut with an initial imperfection, laterally restrained at the ends and braced at the mid-length: (left) real member, and (right) idealized member for approximate evaluation of the bracing force $F_{br}$**

The simple equilibrium considerations for the strut's initially deformed shape (Figure 22) show that the brace force $F_{br}$ is:

$$F_{br} = \frac{4 \cdot N}{L} \cdot \delta, \quad [9]$$

where $F_{br}$ is the brace force; N is the applied compression force in the member; L is the length of the member; and $\delta$ is the initial imperfection's maximum amplitude. In Equation 9, observe that the ratio between the initial imperfection and the length of the span, $\delta$/L, is roughly constant regardless of the magnitude of the span (as explained above). Thus, the brace force $F_{br}$ is governed by the axial force N for different spans. In turn, N typically increases with the span of the structure (e.g., an arch or the compression chord of a truss), so increasing spans require larger lateral bracing forces. In other words, the requirements concerning the strength, stiffness, and number of bracing systems increase with the span of the structure.

#### *7.5.3.3 Joints and Connections*

In long-span timber structures, connections and joints between members often need substantial strength, mainly due to the magnitude of the forces transmitted between members, and are thus typically very large. Further, for production and transportation demands always limit the maximum size of the individual members of a structure. For example, for economical transportation in Sweden, the maximum length of timber members should be such that the total length of the vehicle does not exceed 30 m, as illustrated in Figure 23. This means, in practice, that the maximum length of the timber members should be approximately 24 m, while the maximum height and width should not exceed 4.5 m and 2.6 m, respectively. These rules are valid in Sweden at the time of writing and might be different in other countries (Swedish Wood, 2018; parts 3–4).

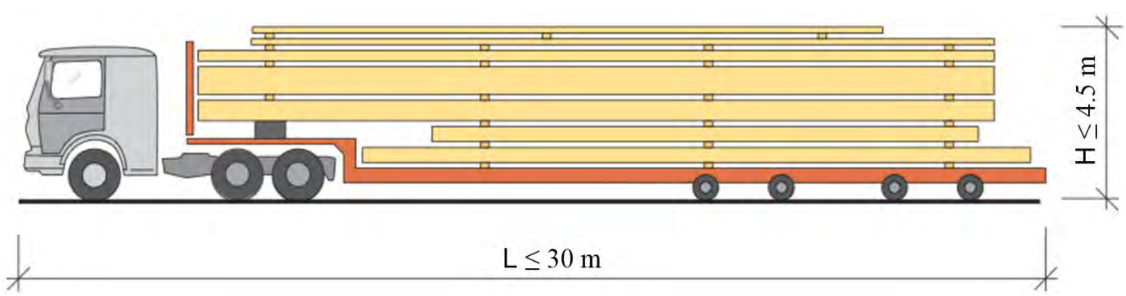


**Figure 23. Overall dimensions of a lorry for economical transportation without needing particular permissions from the roadway administration**

The size limitations of the members generally make splices unavoidable in long-span structures; thus, joints become necessary even at very highly stressed parts of the structure, such as in the chords of a truss. Standard, off-the-shelf connections are not typically adequate to transmit very large forces, so long-span structure applications normally require customized designed connections. Few connection types are suitable for transmitting very large forces from one member to another, the most common being the following:

- connections with multiple slotted-in steel plates and dowels;
- bonded-in rods; and
- steel plates with predrilled inclined holes and inclined fully-threaded screws.

Chapter 5 thoroughly discusses the analysis of these types of connections; therefore, this section only covers some important issues related to long-span structures.

7.5.3.3.1 Anisotropy of Wood

Due to its structure, wood has substantially different mechanical properties in different directions. The tensile strength in loading perpendicular to the grain, for example, is in the order of only 2% of the strength in loading along the grain. There is also a large difference in failure modes. Regardless of the direction of the load in relation to that of the grain, failures in tension are in general brittle, while failures in compression are in general ductile, when buckling is not an issue. Timber is weakest in tension perpendicular to the grain, and connections should avoid such loading modes (Swedish Wood, 2018; part 2). Figure 24(a) shows a truss node configuration allowing potential tension perpendicular to the grain due to the bending moment resisted by the connection. This may lead to the web members cracking (splitting); Figures 12(b) and (c) show possible modifications of Figure 12(a) that considerably reduce the risk of splitting failure.

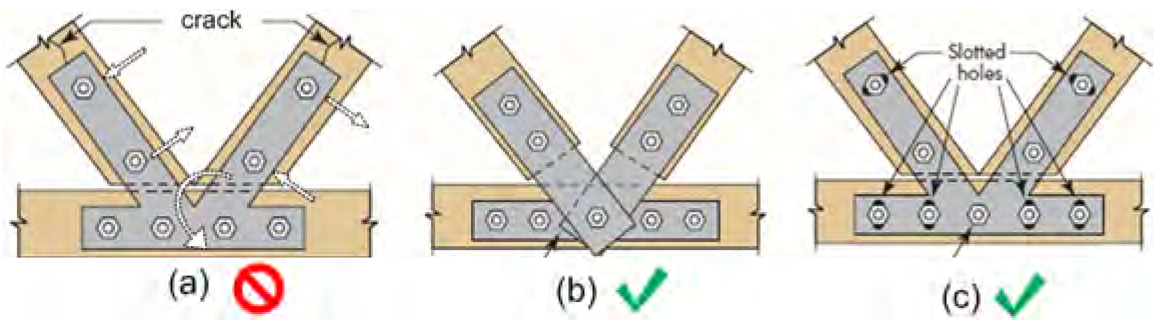


**Figure 24. Truss nodes with external steel plates and bolts: (a) fixed-angle gusset plates prevent timber truss members from rotating under load; (b) node with separate plates to joint truss members, with pinned connection at the intersection point; and (c) node with slotted holes to allow for unrestrained rotation of members (Swedish Wood, 2018; part 2)**

7.5.3.3.2 Hygroscopicity of Wood

One must carefully consider the moisture-related expansion and contraction features of wood when detailing connections to reduce tension perpendicular-to-grain stresses. Changes in moisture content will cause the timber to swell and shrink. The dimensional changes in the direction parallel to the grain can be ignored in most cases. Dimensional changes in perpendicular-to-grain direction cannot, especially in members with large cross-sectional dimensions, which are typical in long-span structures. For example, Figure 25 shows how to connect knee-jointed frames made with dowels passing through three timber members that overlap in the knee joint. If the moisture in the timber decreases after installation, as is normal for indoor structures, shrinkage occurs in both the column and the rafter, mainly in the cross-grain direction. Since the connectors restrain such a shrinkage, excessive tension perpendicular to the grain may occur at both the column and rafter parts of the connections, causing the timber to split. Splitting at the knee joints negative affects both the moment-resisting capacity of the joints and the shear strength of the members. To avoid splitting in such types of structures, one can use finger-jointed haunches or adopt rafter and column members made of more form-stable timber products, such as cross-glued LVL. For long spans, glulam is typically the structural material chosen, and for reasons of transportation, it is often convenient to assemble the parts of the frame at the building site. This can be done as shown in Figures 13(b) and (c), which illustrate how the rafter and column parts of a glulam frame can be assembled accounting for hygroscopicity. More specifically, Figure 25(b) shows a knee consisting of a steel bracket connected to the rafter and column by bonded-in rods. Figure 25(c) shows a knee joint with one or more slotted-in steel plates and dowels.

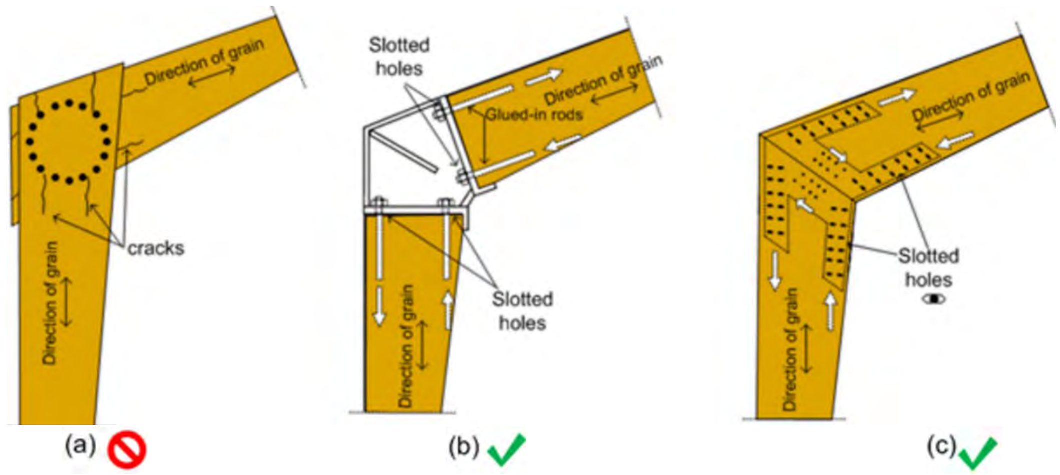


**Figure 25. Different solutions for knee joints of glulam frames: (a) dowel connection with stocky fasteners passing through the rafter (a single beam) and column (double parallel members on each side of the rafter); (b) knee joint consisting of a steel bracket connected to the rafter and column by bonded-in rods; and (c) slotted-in plates and dowels (Swedish Wood, 2018; part 2)**

7.5.3.3.3 Connection Eccentricities

Since long-span structures generally have substantial axial forces, even a small eccentricity of the force in a connection would lead to a relatively large bending moment, which in turn would negatively affect the strength of both the jointed members and the connection itself. For example, if there is a bending moment in truss members due to a possible eccentricity at a node, this in turn may generate stresses perpendicular to the grain in the members. Eccentricity at the truss node may result if the centre lines of the chord and web members do not meet at the same point, as shown in Figure 26(a); it may also result even if they do meet at the same point, but the centre of rotation of the fastener group in the chord is located elsewhere, as shown in Figure 26(b). In most cases, however, it is possible to design a truss node without eccentricity, as shown in Figure 26(c).

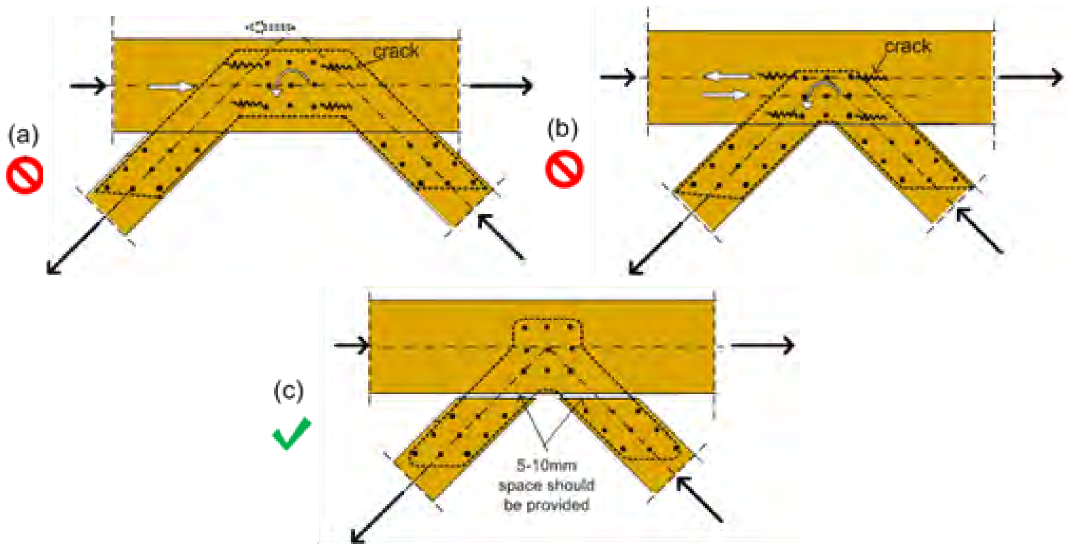


**Figure 26. A truss node with slotted-in steel plates and dowels: (a) the centre lines of the chord and the webs do not meet at the same point; (b) the rotation centre of the fastener group in the chord is located below the meeting point of the centre lines of the webs; and (c) node without eccentricities (Swedish Wood, 2018; part 2)**

At times, connections with centre lines converging to a single point may hide eccentricities. For example, Figure 27(a) schematically shows the connection between the arch and tension tie of a tied arch. Due to the particular arrangement of the fasteners in the tension tie, there is eccentricity between the centre of the fastener group and the axial force in the tie. This eccentricity can be eliminated by rearranging the fasteners in the tie, as illustrated in Figure 27(b).

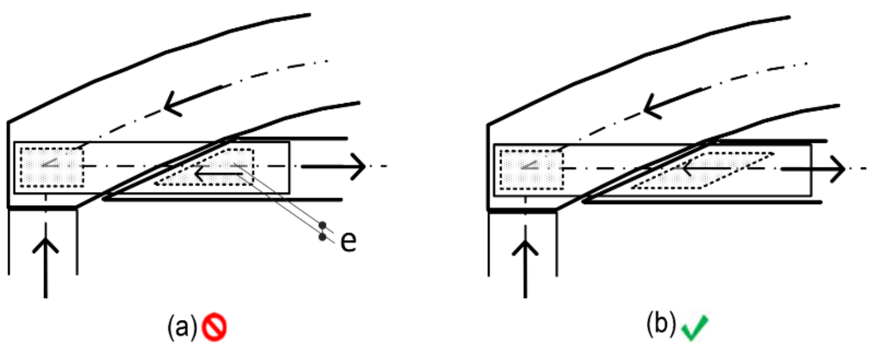


**Figure 27. Connection between the arch and the tension tie of a tied arch: (a) asymmetric (eccentric) arrangement of fasteners in the tie, and (b) symmetric (centric) arrangement of fasteners in the tie**

7.5.3.3.4 Ductile Behaviour of Connections

The design of connections, especially when they are part of long-span structures, should promote ductile rather than brittle failure modes. This is typically achieved by ensuring failure occurs in the steel parts before the timber parts. Usually, steel fails in a ductile manner after substantial yielding. For joints with multiple dowel-type fasteners, for example, ductile behaviour is typically achieved by designing the dowels so they undergo large bending deformations due to the formation of plastic hinges at one or several parts of the dowel, as illustrated in Figure 28.

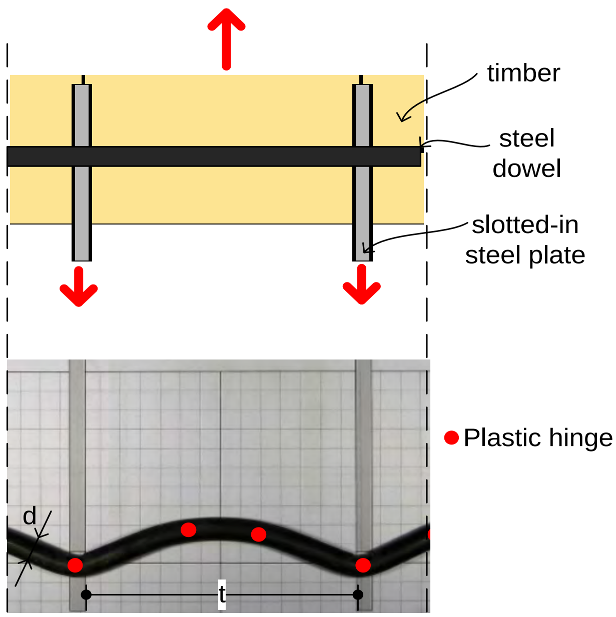


**Figure 28. Part of a connection with two slotted-in plates and a dowel (top), and the deformation of the dowel at yielding (bottom) (Rossi et al., 2016)**

The use of sufficiently slender fasteners can help attain this failure mode. To achieve the ductile failure mode shown in Figure 28, for example, the slenderness of the dowel, defined as $\lambda$=t/d, where t is the thickness of the wood member and d is the diameter of the dowel, should exceed the relative slenderness ratio of the dowel, $\overline{\lambda}$, which in turn can be defined as (Mischler et al., 2000)

$$\overline{\lambda} = 4 \cdot \sqrt{\frac{M_y}{f_h \cdot d^3}}, \qquad [10]$$

where $M_y$ is the dowel's yield moment and $f_h$ is the embedment strength of the timber.

Fabrication tolerances and local defects in timber significantly affect the load-carrying capacity of the joints. Slender dowels and larger dowel spacing can balance the effect of uneven load distribution among the fasteners. Thus, in connections that use several fasteners in the direction of the grain, the influence of the so-called group effect (i.e., the reduction of load-bearing capacity due to premature brittle failure) can be strongly mitigated thanks to fasteners with ductile behaviour.

## 7.5.4 Analysis and Modelling of Typical Structural Types

This section discusses the most common types of structural system suitable for long-span timber structures. It emphasises planar timber structures, but also mentions a few types of spatial (or space) structures. The main reference for the following sections concerning trusses, portal frames, and arches is *Limträhandbok* [Glulam handbook] part 2 (Swedish Wood, 2018).

### *7.5.4.1 Trusses*

Figure 29 shows three typical types of trusses. A truss is a structure that includes one or more triangular units constructed with straight (or nearly straight) members, whose ends are connected at joints referred to as nodes. These triangular units are geometrically stable shapes. Timber trusses generally give an economic solution for spans over 30 m. Long spans typically space trusses 5 to 12 m on centre, carrying purlins at intervals of 1.2 to 2.4 m and supporting light sheet elements of either timber or steel. Alternatively, one can omit purlins and apply heavier roof sheet elements directly on the trusses instead. To achieve economy, the spacing of trusses should increase with their span, as explained in Section 7.5.1.4.

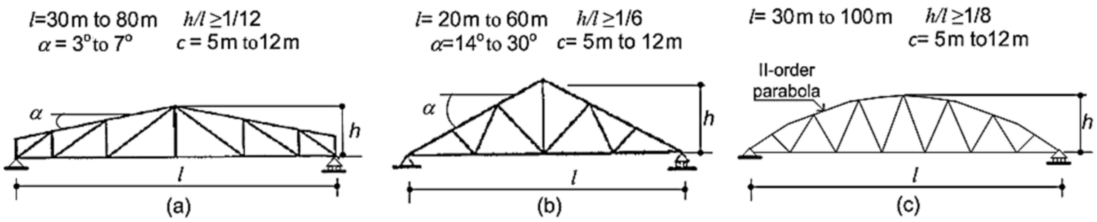


**Figure 29. Preliminary design of three different truss types (*c* refers to the spacing between adjacent trusses)**

If the required architectural profile conflicts with the optimal structural profile, this may introduce high stresses into the web system and the connections. Economy is then a matter of adopting the most suitable structural arrangement of web members for a reasonable balance between material consumption and workmanship. In order to achieve this:

- Keep the number of joints as low as possible, because the workmanship for each joint is expensive.
- Avoid excessive slenderness in the compression chords and the diagonal webs.
- Avoid making the local bending moments in the chord members too large.
- Keep the smallest of the angles created between a diagonal web member and the chord member within a given range, typically 45°±10°.

It is often economical to prefabricate as much of the truss as possible in the factory, provided the prefabricated truss parts are transportable. Glulam manufacturers in Norway have produced trusses up to 30 m long and 3.5 m deep and transported them using special trucks escorted by police. Although such transport is not cheap, it was nonetheless the most economical option. A large range of alternatives is available for the general shapes of trusses. The following sections describe some of the most common truss types.

#### 7.5.4.1.1 Parallel-Chord Trusses

Parallel-chord trusses frequently serve as an alternative to glulam beams for long spans (typically over 30 m), where beams may be uneconomical or impossible to produce at the required length. The loads in the web members are frequently very large, which causes some difficulties in providing adequate joints. Web configuration is usually either Howe, Pratt, or Warren type (see Figure 30).

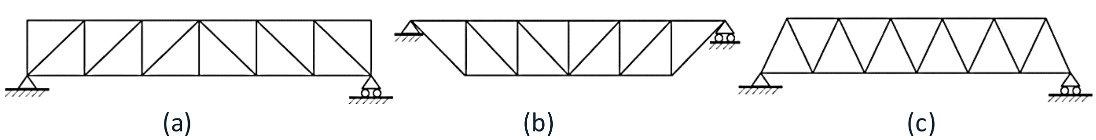


**Figure 30. Examples of parallel-chord trusses: (a) Howe (diagonal in compression), (b) Pratt (diagonal in tension), and (c) Warren (diagonals in alternating compression and tension)**

The advantage of a configuration with diagonal webs in compression rather than in tension is that the joints between webs and chords are relatively simple to construct, since they can transmit loads by bearing stress.

The disadvantage is that the relatively long diagonals are prone to buckling when subjected to compression. The Pratt-type configuration has the advantage that it can also be supported at its upper chord, so the centre of gravity of the truss is below the line between the two supports. This simplifies erection, as the self-weight of the truss acts as a stabilising force against overturning, if the truss is initially out-of-plumb. Parallel-chord trusses often include a pre-camber that corresponds approximately to the deflection due to self-weight plus one-half of the main variable load (e.g., snow load).

#### 7.5.4.1.2 Pitched Trusses

The simplest pitched truss is the three-pin truss (Figure 31[a]), which consists of two inclined rafters (or upper chords) forming the slope of the roof, with a tie that must take the horizontal thrust. Lacking web members, this particular truss configuration gives rise to a large bending moment in the upper chords. Therefore, the cross-sectional depth of the upper chord is typically much larger than that those of similar trusses that include web members (Figure 31[b]). The roof slope for three-hinged trusses should preferably exceed 3:12 (14$^{o}$) to avoid excessive deflection of the ridge and limit horizontal displacements at the supports.

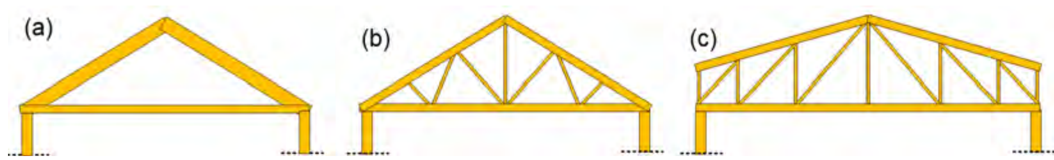


**Figure 31. Examples of double-pitched trusses: (a) simple three-pin truss, (b) double-pitched truss with web members, and (c) trapezoidal truss (Howe type)**

The shapes of the trusses shown in Figures 19(b) and (c) fit the bending moment diagram for uniformly distributed gravity loads fairly well, so the web members transfer relatively small to medium loads. Therefore, the joints can usually be designed to take these loads with little difficulty.

#### 7.5.4.1.3 Bowstring and Lenticular Trusses

For very long-span applications, both bowstring and lenticular trusses (Figure 32) are reasonable alternatives. When choosing a parabolic truss, given a uniformly distributed gravity load, the chords of the truss take virtually all the applied load, leaving the web members unstressed. For asymmetric load configurations, on the other hand, the web members are activated, but only moderately stressed. The connections between the web members and chords can therefore be made very simple and thus inexpensive. From the point of view of statics, a parabolic profile is most efficient for supporting uniform loading. However, practical manufacturing considerations usually make a circular contour for chord members more convenient or necessary. Steel rods or plates can serve as the bottom chords of both bowstring and lenticular trusses.

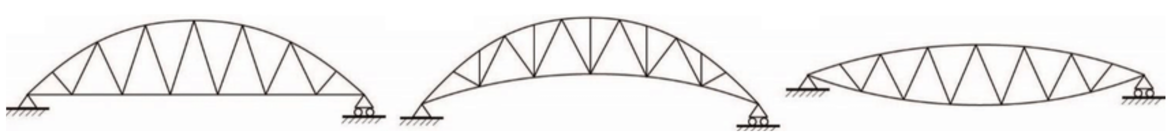

(a) (b) (c)

**Figure 32. Examples of bowstring and lenticular trusses: (a) bowstring with horizontal bottom chord, (b) bowstring with raised bottom chord, and (c) lenticular truss**

#### 7.5.4.1.4 Conceptual Design

Generally, architectural considerations determine the shape and possibly the slope of the roof. In addition, the need for services such as ventilation ducts, which pass through the truss, can influence the choice of the profile. Figure 29 offers preliminary designs of three typical truss types.

The choice of cross-section for the members should decide the type of connection which will be used for the nodes of the truss. For example, consider a connection made of slotted-in plates and dowels, typically used in the nodes of long-span trusses. In order to increase the load-bearing capacity of the nodes, it is often necessary to use a large number of slotted-in plates; this requires relatively wide cross-sections to accommodate all the plates. Figure 33 shows a glulam truss with a curved upper chord, part of the load-bearing structure of an Olympic sport hall built in Hamar, Norway, in 1992. The structure has a span of 70 m, and the design tension force in the lower chord of the truss is as high as 7000 kN. Due to the very large forces, the most stressed members of the truss used as many as nine slotted-in plates.

**Figure 33. (left) A glulam truss with a curved upper chord, part of the Olympic sport hall in Hamar, Norway. (right) Principle of truss node with slotted-in plates and dowels used in the nodes of the truss**

The bending stiffnesses of the single members in the plane of the truss should be kept reasonably small relative to that of the assembled truss. The bending moments at the nodes will then be small enough to ignore, and the truss can thus be analysed with satisfactory approximation by assuming all its members to be hinged at the ends. The assumption that the bending stiffness of the members is small compared to that of the assembled truss is normally fulfilled if the chord depths do not exceed 1/7 of the truss depth (see Figure 34).

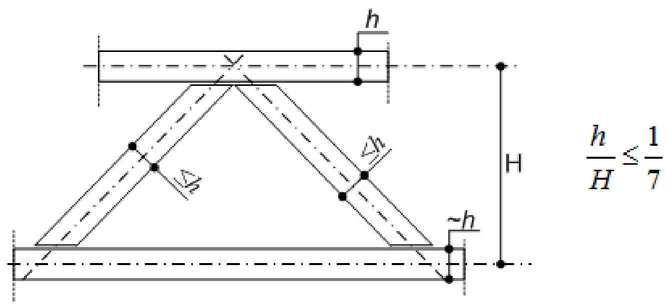


**Figure 34. Recommended ratio between member depths and truss depth to reduce the influence of bending moments**

To achieve this, chord members commonly have nearly square-shaped cross-sections, while web members have rectangular cross-sections, with the larger side in the out-of-plane of the truss. The choice of relatively shallow cross-sections in the plane of the truss also facilitates the design of nodes without eccentricities. During design, it is very important to account for the reduction in strength due to the presence of slots and dowel holes, particularly for members subjected to tension. As a rule, to consider holes and slots, preliminary designs can assume the net area $A_{net}$ is 60% to 80% of the gross area $A_{gross}$ of tension members; typically $A_{net} = 0.75A_{gross}$ in CAS O86 (Canadian Standards Association, 2019b). The required fire resistance for a given structure, typically fire class R60 (European Committee for Standardization, 2004) or 60 min (1 hour) (National Research Council of Canada, 2020), influences the cross-section size of the truss members and the connection types for the assembly of nodes. Considering the calculated charring of the exposed surfaces, the connection must still be able to transfer the necessary forces in case of a fire after 30, 60, 90, or 120 minutes.

7.5.4.1.5 Numerical Modelling

An ideal truss would be represented by a static system where each node has a perfect hinge and no eccentricities, and point loads are applied only at the nodes. This seldom occurs in timber structures, however. For example, at node positions, the joints give a certain degree of rotational restraint and slip occurs due to the deformability of the connections. Moreover, the upper and bottom chords of the truss are normally continuous members rather than hinged at their intersections with web members, as is ideal. An accurate model of the truss would include translational and rotational springs at the node positions (see Figure 35).

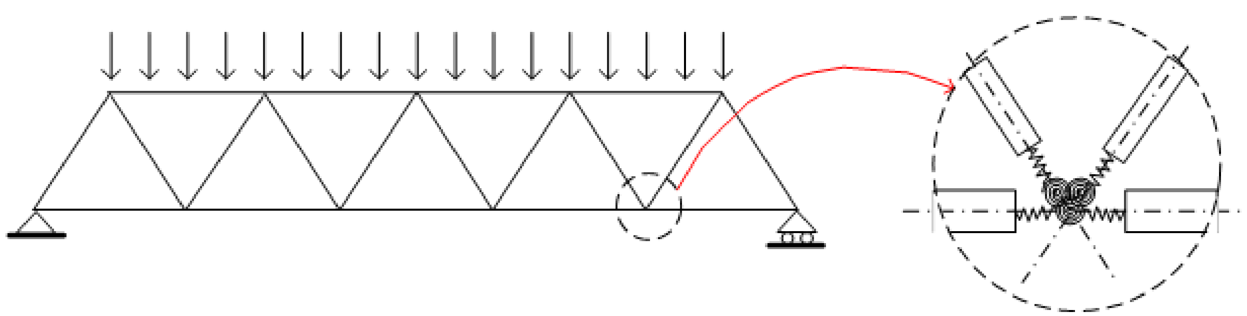

**Figure 35. Advanced truss model, with translational and rotational springs at the ends of the web members**

However, the accuracy of the available models for estimating the rotational and translational stiffness of the connections is usually rough. Further, the above recommendations, such as adopting springs at the ends of the truss members, do not significantly affect the magnitude of forces and bending moments. Therefore, when analysing trusses in the ultimate limit state, a model with continuous chords (Figure 36) gives sufficiently accurate results.

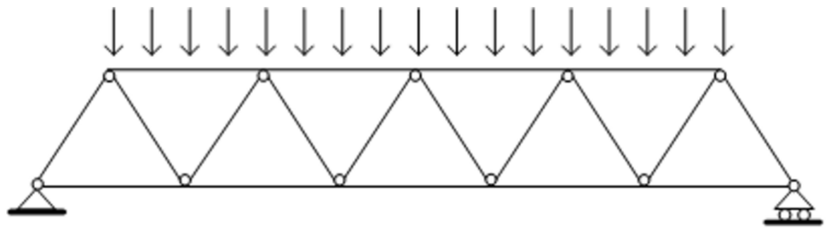

**Figure 36. Truss model, with hinges at the ends of the web members and continuous chord members**

A model like the one illustrated in Figure 36 gives pure axial forces in the web members. However, possible (unplanned) eccentricities and the potential rotational fixity provided by the connections generate some bending moment in the web members. Accounting for these moments typically involves increasing the calculated axial forces in the web members by approximately 10 to 15% when designing the node connections.

The model with fixed connections shown in Figure 37 can usually analyse the serviceability limit state of the truss—deflection check and vibration check, when needed; the analysis increases the calculated deflection by a given load or deflection factor to account for possible slip at the connections. The factor may be 1.1 to 1.2 for nodes assembled using dowels and 1.0 for those with bonded-in rods. To more accurately estimate the deflection of the truss, one can use a model with translational springs at the outermost nodes of the web members (the rotational springs do not contribute significantly to the overall bending stiffness of the truss).

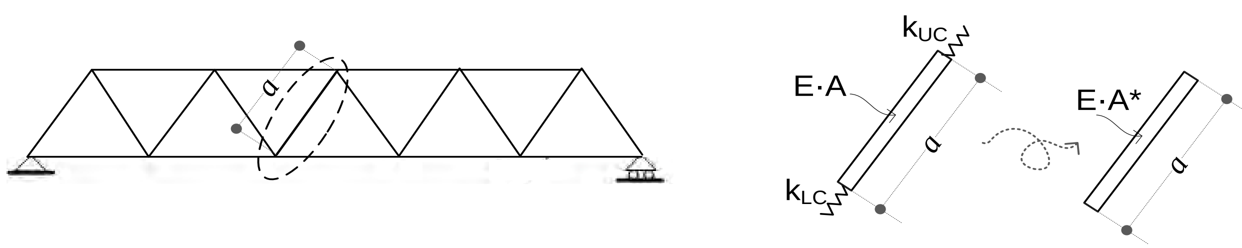


**Figure 37. Possible model for the web members of a truss in the serviceability limit state**

To account for the translational stiffness of the connections, which increases deflection, one can use the model adopted for an analysis in the ultimate limit state (Figure 36), but with a fictitious cross-sectional area A* (or a fictitious Young's modulus, if preferred) for the web members (see Figure 37):

$$A^* = \left( \frac{1}{A} + \frac{E}{a \cdot k_{LC}} + \frac{E}{a \cdot k_{UC}} \right)^{-1}, \quad [11]$$

where $A^*$ is the fictitious cross-sectional area of the web member; $A$ is the cross-sectional area of the web member; $E$ is the Young's modulus (parallel to the grain) of the web member; $a$ is the distance between the two outermost nodes of the web member; $k_{LC}$ is the translational stiffness of the connections between the web member and the lower chord; and $k_{UC}$ is the translational stiffness of the connections between the web member and the upper chord.

7.5.4.1.6 Buckling and Bracing of Compression Members

Addressing the buckling of the entire truss typically requires sufficient lateral bracing. The design of truss compression members and of members subjected to combined compression and bending, typically the upper chords of a truss, should for account the risk of both in-plane and out-of-plane buckling. In general, assume the buckling length of the truss members is the distance between the outermost nodes of the member for in-plane buckling and the distance between the lateral bracing points for out-of-plane buckling (Figure 38).

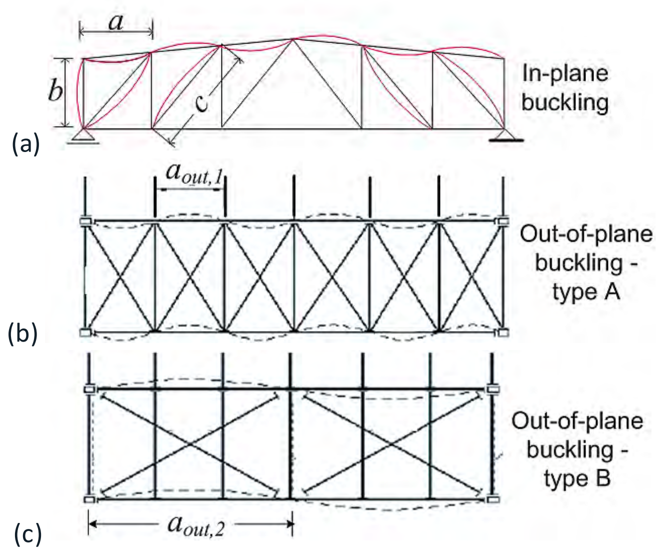


**Figure 38. Examples of theoretical buckling lengths in trusses: (a) an elevation of a truss, (b) a top view of two adjacent trusses with a type A bracing system, and (c) a top view of two adjacent trusses with a type B bracing system**

When the lateral bracing is not adequately stiff, the out-of-plane buckling length could be longer than that determined according to Figures 26(b) and (c). If so, FE models, where the bracing is modelled as an elastic spring, can better predict the buckling length.

### *7.5.4.2 Portal Frames and Arches*

Portal frames and arches are similar from the point of view of structural analysis. Therefore, this section gives only a general introduction to the former and discusses the latter in a more detailed fashion.

7.5.4.2.1 Portal Frames

Timber frames of relevant span are most often made of glulam, and occasionally of other timber products, such as LVL. When glulam serves as a building material, the haunch is typically either curved with continuous laminations (Figure 39[a]) or finger-jointed (Figure 39[b]). With other timber materials, the haunch is typically built up, as illustrated in Figure 39(c). Most often, portal frames have three hinges, making the structure statically determinate; thus, possible settlements do not generate significant bending moments. The roof slope must not be too small, in order to reduce excessive deflection of the ridge. Therefore, the angle between the rafter and the horizontal should not be less than 14°.

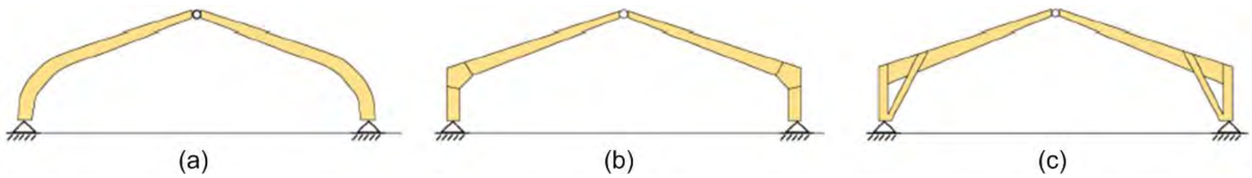


**Figure 39. Examples of three-hinged portal frames: a) frame with curved haunches, b) frame with finger-jointed haunches, and c) built-up frame (knee-braced frame)**

The form of the frame should follow the funicular of the main load combination, as far as functional and aesthetic considerations permit. Generally, curved (Figure 40[a]) and built-up (Figure 40[c]) haunches and knee-braced frames do this most easily and are therefore best suited for long spans.

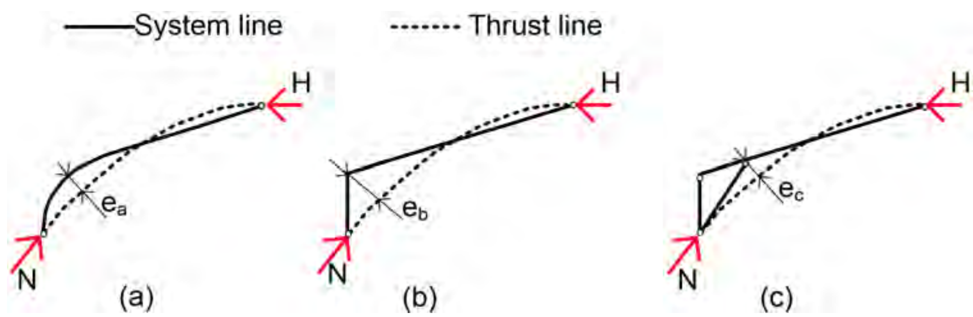


**Figure 40. System lines of different types of portal frames, with corresponding thrust lines for uniformly distributed gravity load (second-degree parabola passing through the hinges): the maximum bending moment in the frame is proportional to the maximum eccentricity $e_i$**

**Three-hinged portal frames** are suitable for spans up to 40 m. To make them transportable, the connecting line between ridge and foot should not exceed 24 m, and the distance at right angles from this line to the outer edge of the haunch should not be more than 3.7 m.

**Two-hinged portal frames** provide stiffer structures and allow the structure to be manufactured and transported in two, three, or more parts, which are connected with rigid joints on site. Joints can be placed at positions in the structure with small moments. Rigid joints demand more complicated workmanship than hinged ones, and will therefore cost more. On the other hand, the individual parts that form the two-hinged frame are smaller than those in a corresponding three-hinged frame and therefore easier to transport. This type of portal frame can in general span slightly more than the three-hinged portal frame.

7.5.4.2.2 Arches

Arches are very suitable for execution in timber, a material that can be produced in curved forms with varying depth without a great increase in price. As a rule, arches with solid sections of constant depth are most common, with glulam their principal structural material. However, composite sections of I- or box-shaped, as well as trussed, arches also occur, especially for long spans. Such cases can also use other timber-based products.

The form of the arch should ensure the bending moments are as small as possible. Thus, its geometry should follow the thrust line of the dominating loading combination. It is impossible to completely avoid the influence of moments, however, since the structure must account for several load combinations, each with its own thrust line. In general, the geometry of the arch is often parabolic; choosing a circle comparatively simplifies the production to some degree. Note that for the typical rise-to-span ratio $f/l \approx 0.15$, the geometries of the parabola and circle are very similar. For functional reasons, such as to increase the headroom near the supports, one can place the arch on the top of columns or walls, as illustrated in Figure 41. In this case, the arch needs a tension tie between its springing/supporting points to take the horizontal support reactions it causes.

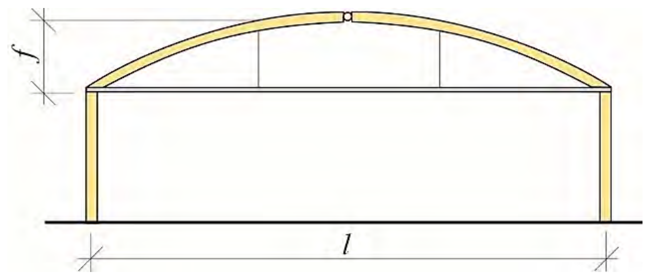


**Figure 41. Arch on top of columns or walls, with a tension tie**

When the springing points of the arch are directly on the ground or on abutments, as shown in Figure 42, the horizontal forces can be taken directly into the bedrock (if present); by passive earth pressure in the foundations, if ground conditions are good enough (Figure 42[b]); or by a tension tie under or within the floor (Figure 42[c]). In general, the latter solution is preferable when the horizontal thrust has substantial magnitude or when the mechanical properties of the soil are poor. To limit the magnitude of the horizontal reactions, the rise of the arch should be equal to or greater than 0.15 of its span. For a parabola or circle, this corresponds to an angle of spring of approximately 30°. Usually, timber arches are designed with a rise-to-span ratio in the range $0.14 \leq f/l \leq 0.30$.

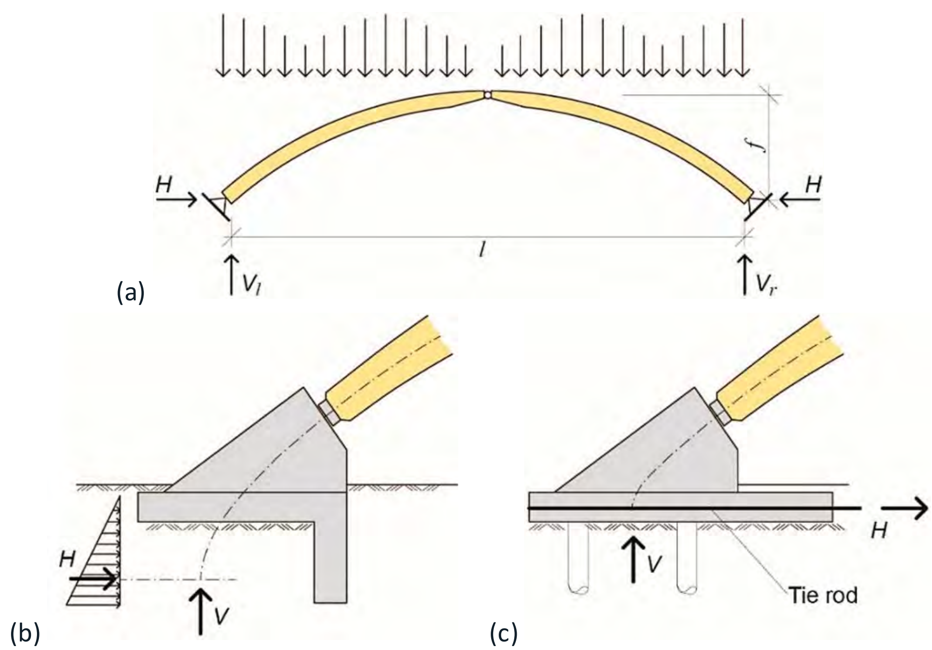


**Figure 42. Approaches for taking the thrust at the spring points of an arch: (a) arch structural, with springing points directly placed on the foundations; (b) horizontal thrust taken directly by passive earth pressure; and (c) horizontal force taken by a tension tie**

There are three primary types of arch, normally defined by their end conditions: the three-hinged arch, the two-hinged arch, and the fixed-ended arch, as illustrated in Figure 43. The figure optimises the depth of the arches with respect to the envelope of the bending moment diagrams for asymmetric gravity loads randomly applied on the top of an arch.

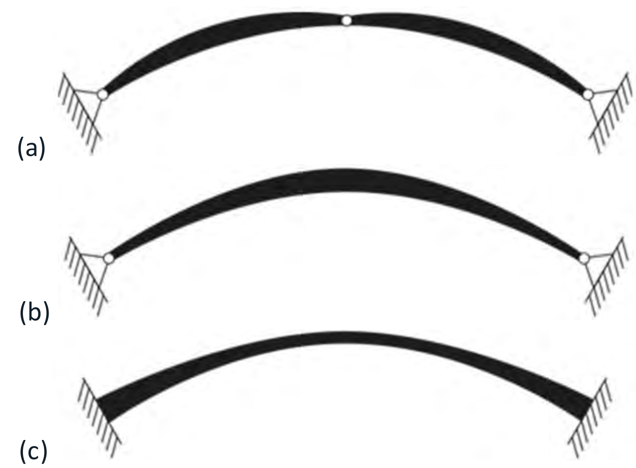


**Figure 43. Three typical types of arches: (a) three-hinged arch; (b) two-hinged arch; and (c) fixed (zero-hinged) arch**

Manufacturing and transportation considerations influence the choice of three-hinged, two-hinged, or fixed arch. The three-hinged arch is the most common structural type for arches made of timber and is often chosen for spans of up to 70 m. The two-hinged arch and the less common fixed arch generally serve for very long spans; the arch must usually be manufactured and transported in three or more parts, which are rigidly joined together on site. Moment stiff joints are unusual in massive arch members, but not unknown. For example, Figure 44 shows a moment stiff connection in the rib of a timber dome; an arch can use a similar solution.

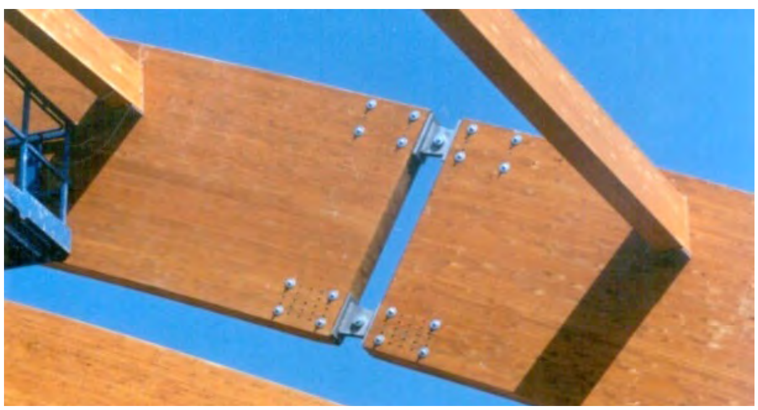

**Figure 44. Moment stiff connections in curved glulam members subjected to combined compression and bending. (Courtesy of Rubner Holzbau, Italy)**

In most cases, however, two-hinged and fixed timber arches are designed as trussed arches. The required moment stiff connections consist of two separate hinges: one at the upper chord of the truss and the other at the lower chord. The axial force at the hinge multiplied by the distance between the chords produces a couple that can counterbalance the bending moment generated by the applied loads. Figure 45 shows two road bridges with a load-bearing structure consisting of two-hinged and fixed trussed arches. Figure 46 shows the Richmond Olympic Oval, with two-hinged primary Glulam arches (100 m) and tied secondary arches (14 m).

(a)

(b)

**Figure 45. (a) A roadway bridge with a two-hinged trussed arch (span 70 m) in Tynset, Norway; and (b) a roadway bridge with a fixed trussed arch (span 32 m) in Matrand, Norway**

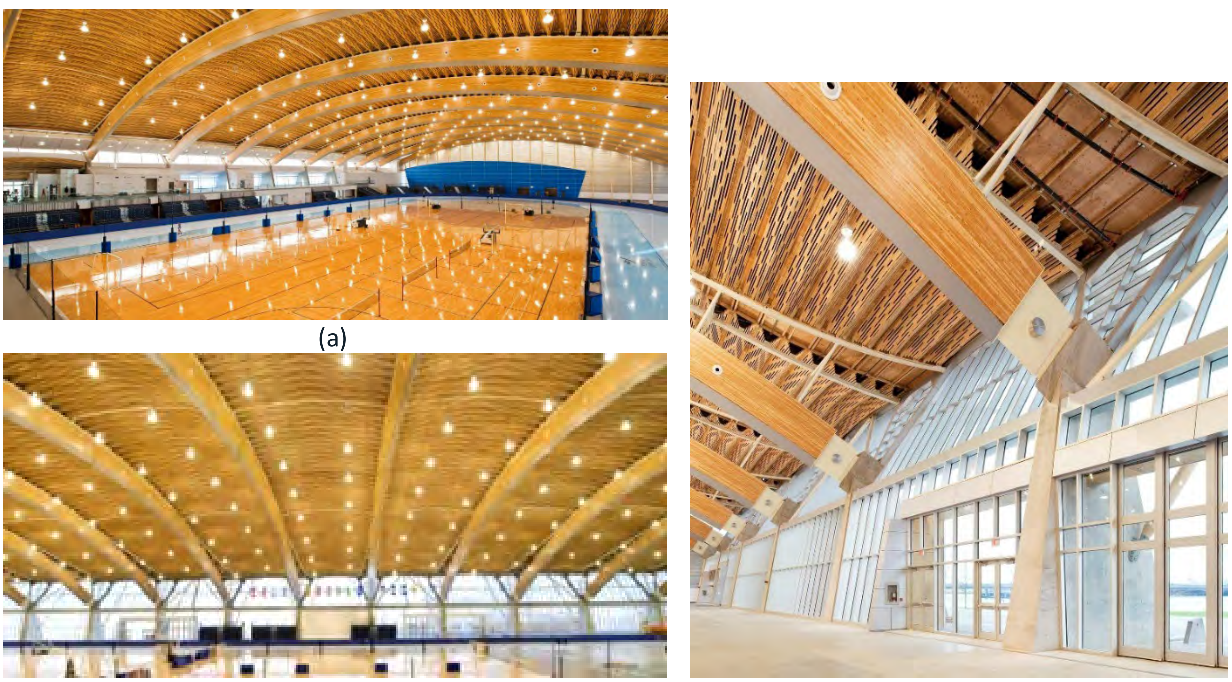

(a)

(b) (c)

**Figure 46. The Richmond Olympic Oval, Canada: (a) two-hinged primary glulam arches (100 m); (b) tied secondary arches (14 m); and (c) arch pin detail**

According to some building codes, such as Eurocode 1-3 (European Committee for Standardization, 2003) and CSA S6:19 (Canadian Standards Association, 2019a), one should consider drifted snow load arrangements, with triangular load distributions on each half of the arch, during design. Such load conditions give rise to relatively large bending moments in the arch, especially with a long span. To find the proper shape for an arch with given boundary conditions and randomly applied loads, observe the bending moment diagram for different asymmetric load cases. The envelope of the different bending moment diagrams will indicate how the cross-sectional depth of the arch should vary to reduce the stresses in the arch, as illustrated in Figure 47.

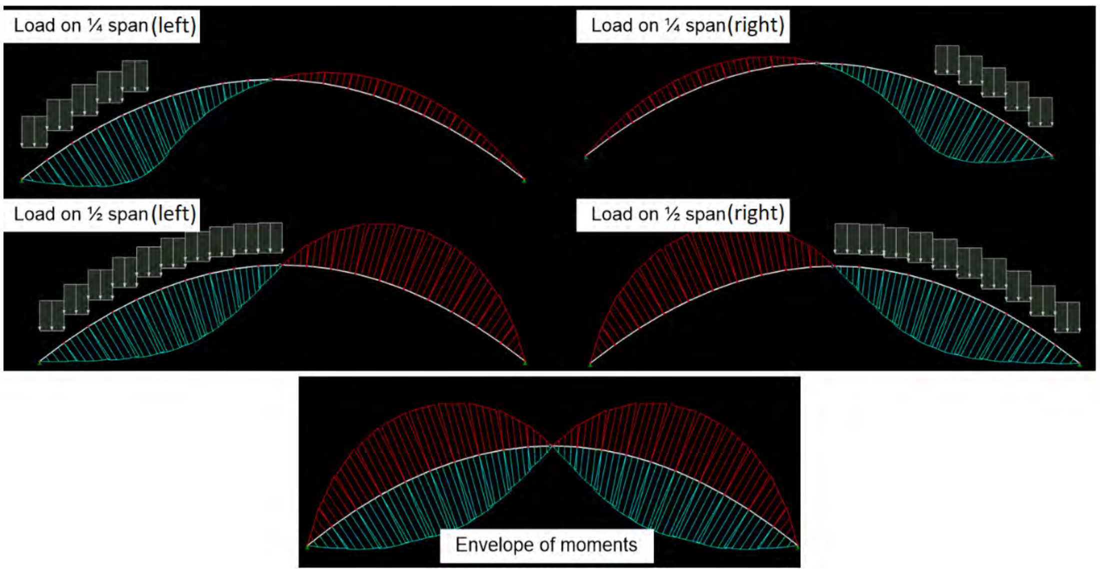


**Figure 47. Bending moment diagrams for a three-hinged parabolic arch: asymmetric load distribution applied at different locations (top); and envelope of all bending moment diagrams (bottom)**

It is difficult to achieve an arch with the profile suggested by the envelope of the bending moment diagrams (Figure 48[a]) using massive timber members. The stresses caused by the large local bending moments M can significantly decrease if one chooses a structure with a larger internal lever arm. Figure 48(b) shows how to create cross-sectional depth variation in the two halves of the arch using a trussed solution.

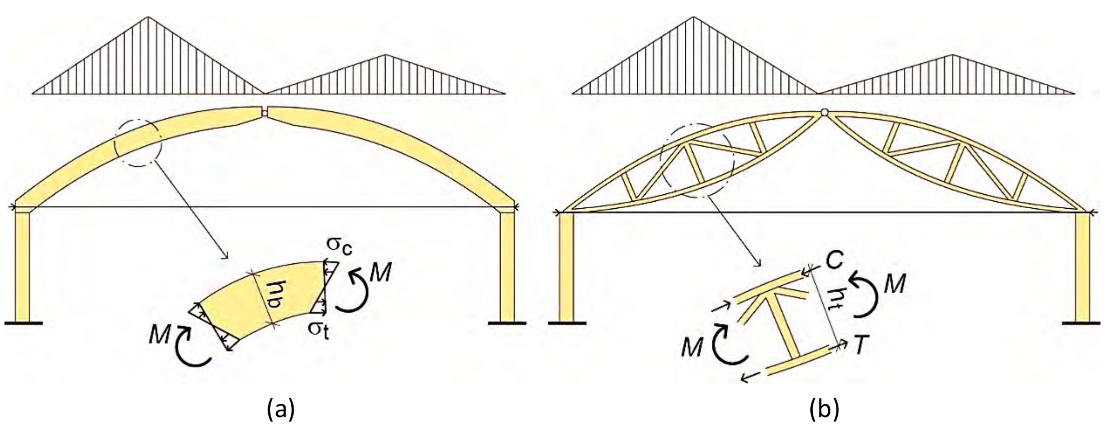


**Figure 48. Three-hinged arches subjected to asymmetric load distribution: (a) arch with massive cross-section and constant depth; and (b) trussed arch with varying depth**

A number of stadiums in Sweden have used configurations similar to Figure 48(b). These applications, however, use a straight lower chord for each half-arch. Although a curved lower chord gives higher strength and stiffness, it has the disadvantage of offering a complicated connection at the springing points and crown, where two timber members and a tension tie (typically steel rods) intersect. Figure 49 shows three-hinged trussed arches with a straight lower chord and a span of 75 m during construction in Nässjö, Sweden.

**Figure 49. Three-hinged arches during construction in Nässjö, Sweden (Courtesy of Sören Håkanlind)**

7.5.4.2.3 Conceptual Design

Generally, architectural considerations determine the shape and possibly the rise of the arch. However, for economic reasons and to limit the horizontal thrust, there are some rules of thumb concerning depth-to-span ratios, maximum span, etc.. Figure 50 provides preliminary designs for three typical arch types.

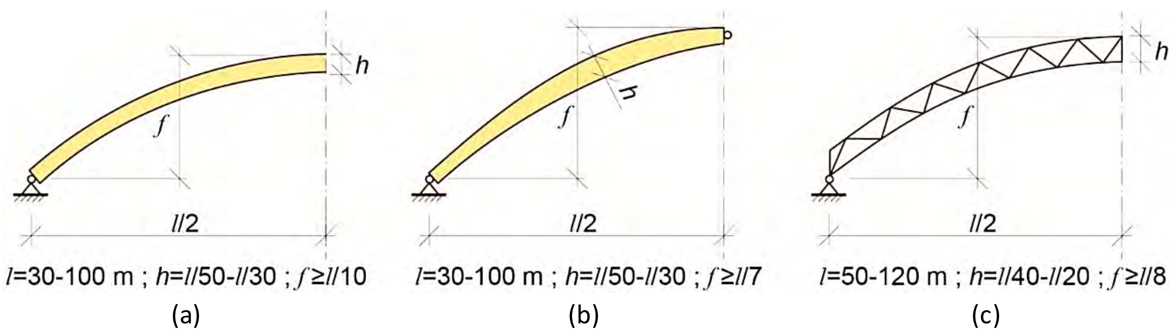


**Figure 50. Preliminary designs for three arch types: (a) two-hinged arch; (b) three-hinged arch; and (c) trussed arch (three-hinged, two-hinged, or fixed)**

The three-hinged arch is stable against horizontal forces in its own plane. It is also statically determinate, so the moment distribution is not significantly affected by uneven settlement of the foundations or by unforeseen deformations in joints and connections. Further, this arch has hinges at the springing points, which simplifies the construction of the foundations. In poor soil conditions, the horizontal reactions at the supports can be taken by tension members between the foundations located within or under the slab.

A lighter looking structure is possible if one takes advantage of the inherent bending stiffness of the arch chords and offsets the webs (Figure 4).

7.5.4.2.4 Stability and Numerical Modelling

As a rule, arches are slender, and a design must therefore consider the risk of both in-plane and out-of-plane buckling, to an even larger extent than for frames.

#### *7.5.4.2.4.1 Out-of-Plane Buckling*

An arch, which lies in one vertical plane, must not topple over sideways (Figure 51[a]), particularly during erection. There are three ways to prevent this by ensuring lateral stability during construction. First, have fixed connections at the base; however, this may be difficult to achieve and requires a massive foundation to prevent overturning, especially for large structures. Second, stabilise the arch using ties or ropes anchored to the ground or foundation. Third, and most commonly, erect two adjacent arches simultaneously. The arches are in this case furnished with temporary or permanent bracing, which prevents the structure from collapsing (Figure 51[b]).

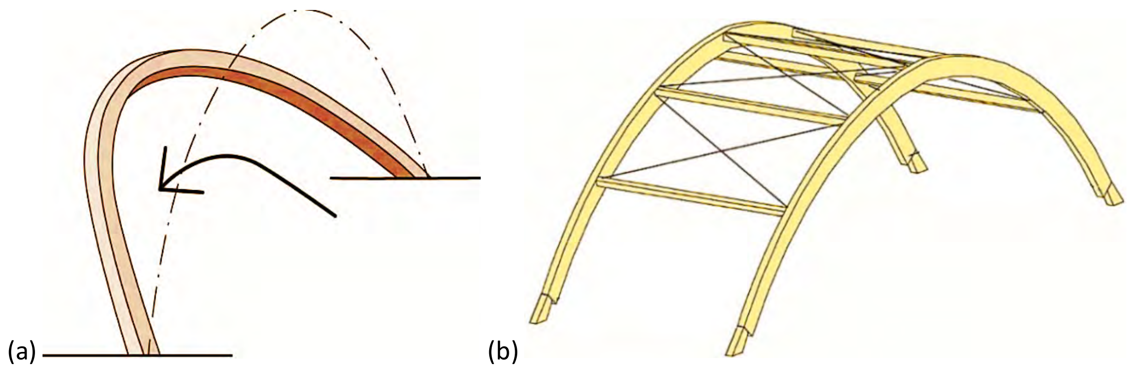


**Figure 51. Considerations during arch erection: (a) an arch toppling over sideways (overturning); and (b) lateral bracing of arches with purlins and cross-bracing**

Another major consideration with respect to the behaviour of frames and arches in a lateral direction is lateral buckling (i.e., out-of-plane buckling). Since timber elements can be fairly slender, this problem may, as illustrated in Figure 52, occur.

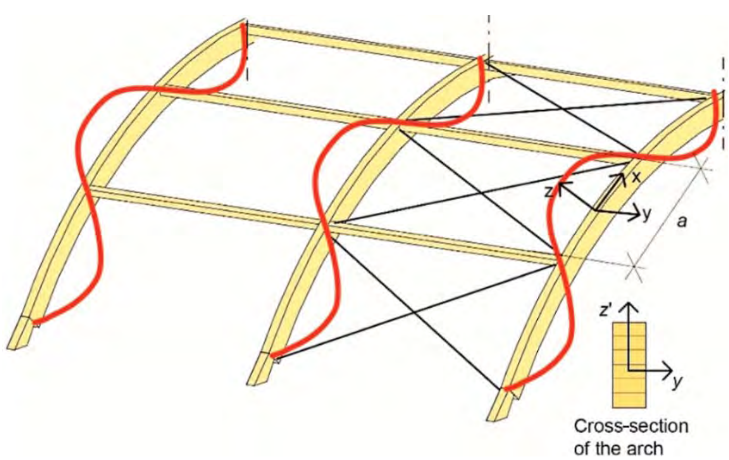


**Figure 52. Lateral (out-of-plane) buckling of braced arches**

The risk of out-of-plane buckling can be reduced by increasing the stiffness of the arch in the lateral direction, either by increasing the width of the arch cross-section or by reducing the distance between the compression struts of the bracing system. The roof sheeting itself, such as load-bearing roof panels between the arches, can also reduce or eliminate the danger of lateral buckling. When purlins are vital components in the bracing, the connection between the arch and the purlin must be able to transmit the bracing forces. For ordinary arches, the risk of out-of-plane buckling is checked as for a beam-column member; that is, the distance between the bracing points (distance a in Figure 52) serves as the effective length (buckling length). When the upper side of the arch is laterally braced, there is normally no significant risk of lateral-torsional buckling, even in zones of the arch subjected to a negative bending moment (i.e., a moment that produces compression stress at the bottom side of the arch, assuming that the arch springing points are secured against rotation about the z axis [Figure 52]). However, especially with slender arches (i.e., those with cross-sectional depth-to-width ratio of 6 or more), it is good practice to also brace the bottom of the arch. Figure 53 shows a bracing method that is effective, easy to execute, and not very invasive.

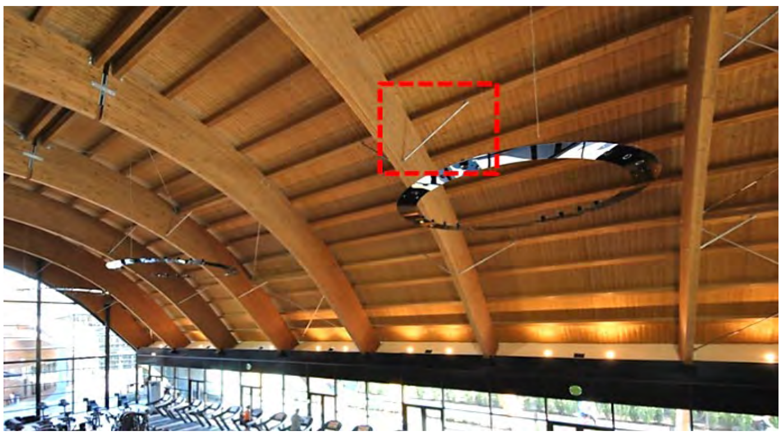

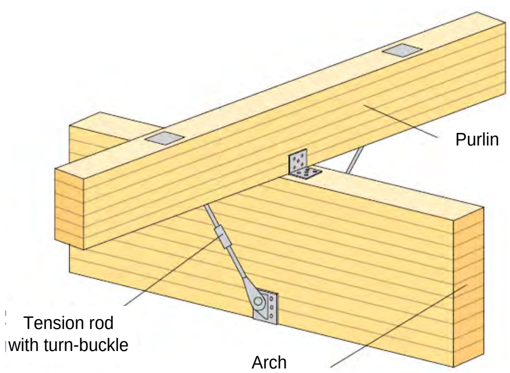


**Figure 53. A glulam arch sport hall (Courtesy of Rubner Holzbau): discrete bracing at the bottom side of arch (left) and clarification of the bracing method (right)**

### *7.5.4.2.4.2 In-Plane Buckling*

The common methods of analysis for buckling in the plane of the arch are Linear Buckling Analysis (LBA) and Nonlinear Buckling Analysis (NLBA), as discussed in Section 7.5.2.2. LBA can verify arches in the same manner as beam-columns (i.e., members subjected to simultaneous bending and compression). The calculation of stresses due to external loading is based on linear elastic theory and considers the equilibrium of the undeformed static system. To account for stresses caused by deflections from initial in-plane imperfections, multiply the compression strength values by buckling reduction factors, typically given in building codes as a function of the relative slenderness ratio (i.e., the square root of the ratio between parallel-to-grain compression strength and Euler critical stress).

Unless the crown is restrained against horizontal movements, arches always buckle in asymmetrical configurations, regardless of whether the load is symmetrical or not. The crown thus moves horizontally and becomes a point of contraflexure, as illustrated in Figure 54.

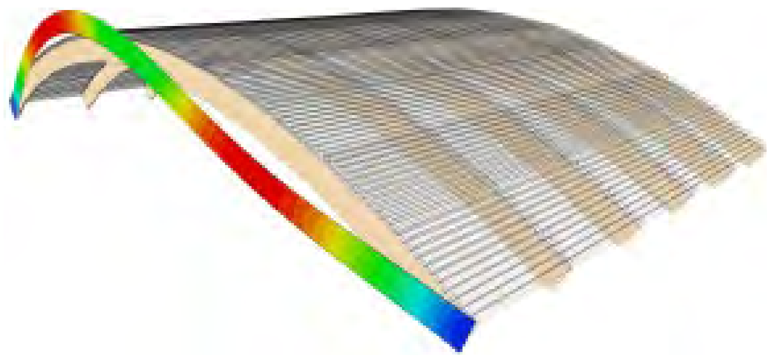

**Figure 54. Typical in-plane buckling mode for two- and three-hinged arches (Andersson & Larsson, 2014)**

To determine the buckling load according to LBA, $N_{cr}$, use the well-known Euler equation:

$$N_{cr} = \pi^2 \cdot \frac{E \cdot I}{l_{cr}^2}, \qquad [12]$$

where $E{\cdot}I$ is the bending stiffness in the plane of the arch; and $l_{cr}$ is the buckling length, i.e., the developed length of the part of the arch between the springing point and the point of contraflexure.

To determine the buckling length of the arch (or any component in an arbitrary planar structure)

(1) Perform a linear static analysis for the assumed design load combination and determine the axial forces in a cross-section of the arch. The critical section is usually at 0.20 to 0.25 of the arch span.
(2) Perform a linearized buckling calculation for the assumed design load combination, following the procedure from Section 7.5.2.2. This calculation gives one or more buckling factors (eigenvalues); these factors, when multiplied by the load, indicate what magnitude of load (with the assumed distribution) will cause instability. The calculation also gives the eigenvectors to the corresponding buckling factors; the eigenvectors indicate how the arch will buckle (in the form of different buckling shapes/modes).
(3) Select the lowest buckling factor and multiply the axial forces from step (1) by it. This provides the axial forces that can be considered the buckling load ($N_{cr}$).
(4) Given a known buckling load ($N_{cr}$), determine the corresponding buckling length $l_{cr}$ of the arch (the only unknown quantity) using Equation 12.

Upon determining the buckling length, it is possible to calculate the reduction factors. In the most common case, where there is only axial force and bending about the strong axis (with no bending about the weak axis), the design criterion will be

$$\frac{\sigma_m}{f_m}+\frac{\sigma_c}{k\cdot f_c}\leq 1, \quad [13]$$

where $\sigma_m$ is the bending stress at the chosen cross-section; $\sigma_c$ is the compression stress at the chosen cross-section; $f_m$ is the bending strength; $f_c$ is the (parallel-to-grain) compression strength; and $k$ is a reduction factor that considers the risk for buckling. The latter typically derives from the so-called slenderness ratio $\lambda_{rel}$, defined as the square root of the ratio between the characteristic compression strength ($N_{Rd}$) and the buckling load of the member ($N_{cr}$). Building codes, such as Eurocode 5, give the empirical relationship between $k$ and $\lambda_{rel}$ (European Committee for Standardization, 2018).

For two- and three-hinged arches, preliminary design can assume that the critical length is $l_{cr}$ = 1.25$s$, where $s$ is the curvilinear (true) length of one-half of the arch. In general, this assumption gives conservative values of the critical length (i.e., provides slightly longer lengths than a more accurate analysis) for arches with constant cross-sectional depth.

A nonlinear geometric calculation accounts not only for the displacements caused by loads but also for the geometric deviation of the structure from the ideal geometry, the so-called geometric imperfections. This analysis gives the "real" cross-sectional forces and moments for the design load, without k factors (i.e., the reduction factors for buckling recommended by the different building codes). The design checks therefore occur as in Equation 13 (i.e., combining bending and axial force). In this case, however, the buckling factor $k$=1, since the risk of buckling is incorporated into the analysis itself.

In the past, nonlinear analysis of structures was unthinkable, as there was no ready access to advanced software. Such tools are now freely available, and the modelling of geometric imperfections to some extent depends on what a particular program offers. Typically, lower buckling modes are good candidates for the actual shape of the geometric deviations (initial imperfections), as illustrated in Figure 55. Alternatively, one can use the deformed shapes generated by a given load case. The order of magnitude of the applied imperfections is approximately $l_i$/400 for glulam components (European Committee for Standardization, 2018), where $l_i$ is the (curvilinear) distance between two points of contraflexure or between a hinge and a point of contraflexure (Figure 55).

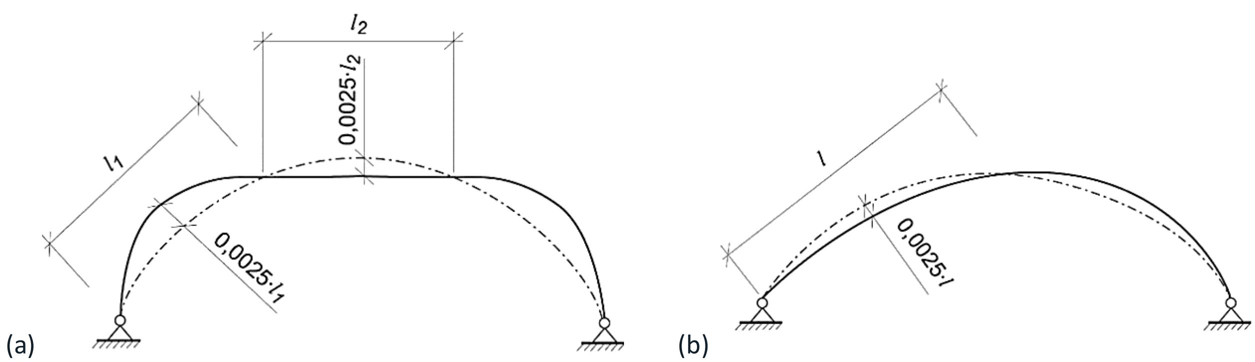


**Figure 55. Recommended initial imperfections for arches according to Eurocode 5: (a) symmetric shape affine with the second buckling mode of a two-hinged arch; and (b) asymmetric (or sway mode) shape affine with the first buckling mode (European Committee for Standardization, 2018)**

### *7.5.4.3 Suspended Structures*

7.5.4.3.1 General Issues and Solutions

In ordinary suspended structures, the primary load-bearing system typically consists of cables (or sometimes bars), which have very low inherent bending stiffness (Crocetti, 2017). The main features of such structures are that they work substantially in tension and carry loads by changing their original shape (i.e., they are so called form active structures).

The change in shape is often problematic, especially in roof constructions exposed to asymmetrical loads, such as an uneven snow load. Here, excessively large deflections of the roof are likely to occur. Sensitivity to wind-induced instability (i.e., wind oscillations generated by gusts of wind or by periodic vortex shedding) is also a potential problem with suspension structures, as illustrated in Figure 56 (left). Problems usually arise from lifting forces and dynamic instability due to wind load, or from large deformations due to asymmetric load. Figure 56 (right) illustrates some methods to stiffen suspended roof structures and thereby reduce the risk of both large deformations and wind-induced instability. To increase the bending stiffness of the roof, a) increase the dead weight of the roof, b) choose load-bearing elements with inherent bending stiffness (the so-called stress ribbon) (Hofverberg, 2016; Gustafsson & Ingvarsson, 2017), c) use double prestressed cable systems along with vertical compression struts, or d) connect the main cable to the base using prestressed vertical cables.

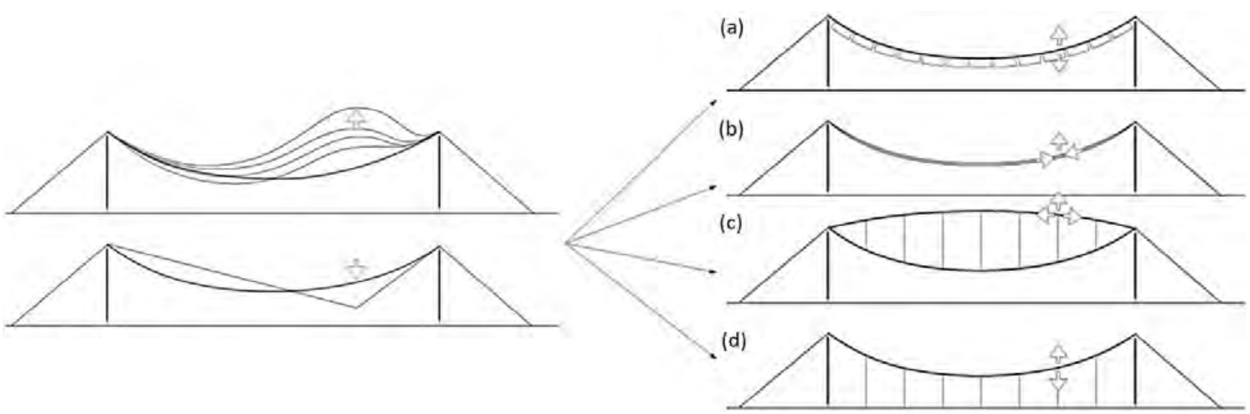


**Figure 56. Suspension roof systems: potential problems (left) and possible solutions (right)**

Suspension systems with timber as a load-bearing material generally follow principle (b), as shown in Figure 56 (right). Such a case makes use of curved glulam beams. The system is commonly referred to as the stress ribbon, with a similar structural behaviour to the cable but non-negligible bending stiffness. These roof structures commonly take the shape of the quadratic parabola, the circle, or at times, the catenary; these curves are not significantly different from one another, especially when the sag-to-span ratio is small (e.g., less than 0.15) (Persson, 2017). For uniformly distributed downward loads, such as permanent loads or snow, the stress ribbon works like a cable, taking the load primarily by tension. On the other hand, the bending stiffness of the stress ribbon is most beneficial when

- reducing deflections for asymmetric gravity loads,
- mitigating the risk of aerodynamic instability, or

- reducing deflections in cases of upward loads, such as those produced by wind suction. Here, the stress ribbon acts as an upside-down arch, taking the load primarily by compression. However, one must account for the risk of buckling in the stress ribbon, especially with small permanent loads.

Figure 57 shows the Grandview Heights Aquatic Centre, Surrey, Canada, the roof of which follows the shape of the catenary and can be considered a stress ribbon, in accordance with principle (b) in Figure 56. The load-bearing roof construction consists of curved double parallel glulam beams with a cross-section of 130 x 266 $mm^2$ and spacing of approximately 800 mm. The roof consists of two compartments with long spans ($L_1$ = 45 m and $L_2$ = 55 m). The ratio between the sag and the span is about 0.11.

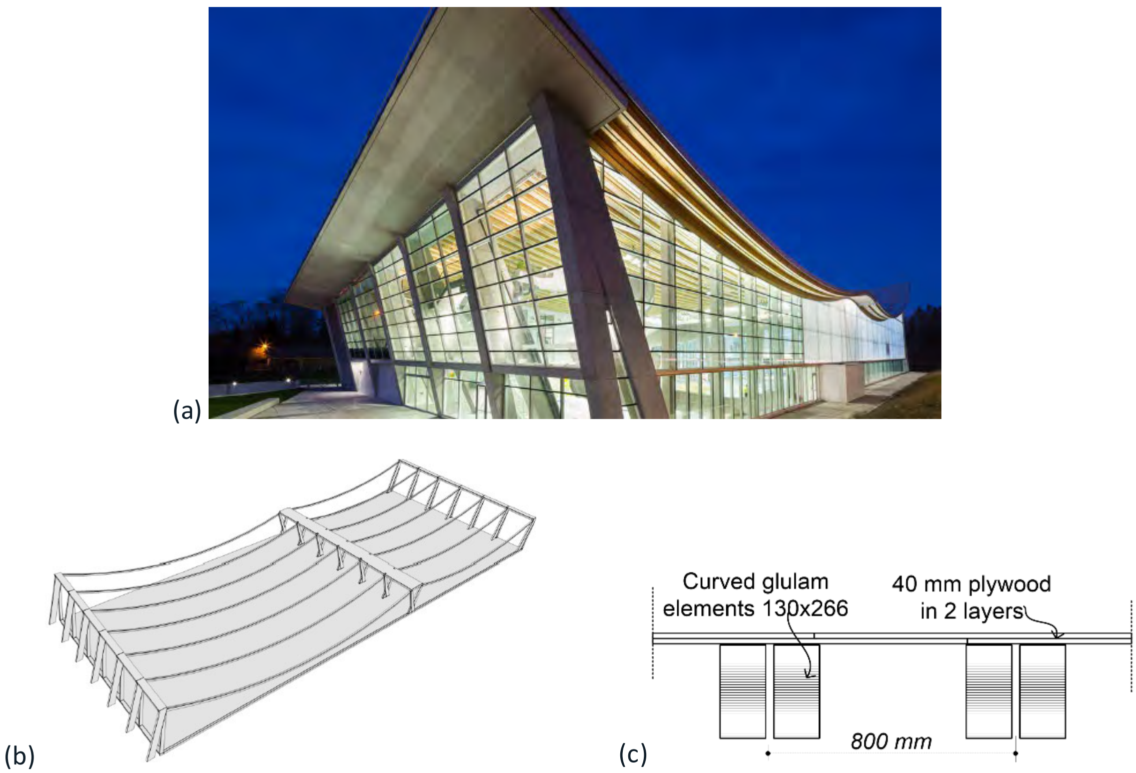


**Figure 57. Grandview Heights Aquatic Centre, Surrey, Canada ([http://www.surrey.ca/city-government/19392.aspx](http://www.surrey.ca/city-government/19392.aspx)): (a) view of the hall; (b) axonometry; and (c) cross-section of the suspended roof**

Suspension systems using principle (a) in Figure 56 are also possible with timber as a load-bearing material. Such cases use straight members with very low bending stiffness (e.g., laminated veneer lumber sheets). After being firmly anchored at the supports, the initially straight members deflect due to their self-weight and naturally assume the funicular shape of their self-weight (i.e., the catenary). These suspension systems can be classified as form-active structures, structural systems that take loads by altering the form of the structure. To reduce the risk of excessively high deflections caused by asymmetric loads, dead weight is often added on the top of these very slender load-bearing systems; increasing the permanent load of the roof generates pre-tension in the suspended structure, which in turn reduces the deflections, mainly generated by asymmetric loading. Figure 58 shows Hohenems municipal works yard, Austria. The roof consists of cross-glued laminated veneer lumber with a width of 1800 mm and a thickness of 39 mm. The span and sag are about 20 m and 1.7 m, respectively; the sag-to-span ratio is thus roughly 0.12. The roof follows the shape of the catenary. To increase the stiffness of the roof and counteract possible lifting forces due to upward wind, a layer of gravel was laid on the roof, in accordance with principle (a) in Figure 56.

**Figure 58. Hohenems municipal works yard, Austria (Courtesy of Wilfried Dechau, DETAIL inspiration)**

7.5.4.3.2 Short Theoretical Background

Figure 59(a) shows a cable suspended between two supports and subjected to an arbitrary distributed load. The assumption is that the cable has constant axial stiffness and no bending stiffness. An infinitesimal segment of the cable, with corresponding internal forces, appears in Figure 59(b).

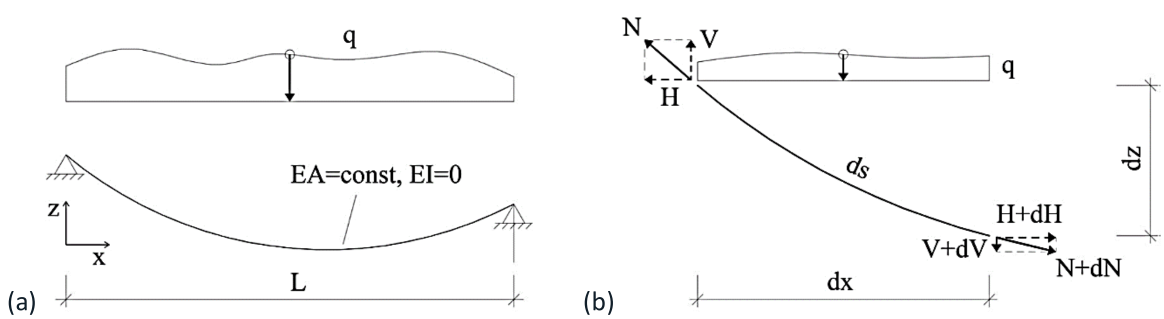


**Figure 59. (a) Cable suspended between two supports subjected to a distributed gravity load; and b) infinitesimal cable segment with internal forces**

Equilibrium considerations for the infinitesimal cable element lead to the following equation:

$$z'' = -\frac{q(x)}{H}, \qquad [14]$$

where *z* is the curve that describes the geometry of the cable, and *z''* is the second derivative of z with respect to x; *q (x)* is the gravity load; and *H* is the horizontal force in the cable.

For a cable suspended between two equally high supports subjected to a uniformly distributed load *q*, double integration of Equation 14 yields

$$H = \frac{q \cdot L^2}{8 \cdot f}, \qquad [15]$$

where *L* is the span; and *f* is the sag of the cable at mid-span.

When the system works not only in pure tension but also with a certain amount of bending stiffness (i.e., in the case of the stress ribbon), the equations above are generally no longer valid. To study the stress ribbon system analytically, one must therefore find expressions for the combination of both axial and bending actions. The equation for structural behaviour in such a circumstance is

$$E \cdot I \cdot w'''' - (H + \Delta H) \cdot (z + w)'' = q - g \cdot \frac{\Delta H}{H}, \qquad [16]$$

where *g* is the permanent load; *q* is the variable load; *E* is the modulus of elasticity; *I* is the moment of inertia; *z* is the curve that describes the shape of the undeformed structure; *w* is deflection; *H* is the horizontal force due to permanent load *g*; and *ΔH* is the horizontal force due to variable load *q*.

If the variable load *q* is uniformly distributed over the entire span, and the chosen shape for the stress ribbon is the parabola (or the catenary or the circle, in case the sag is small), the pure cable-like behaviour practically resists the load. The deflection *w* is thus very small, and one can, with satisfactory accuracy, assume it to be equal to zero. Consequently, all the derivatives of *w* and *ΔH* (which are proportional to *w*) will also be equal to zero. Therefore, Equation 16 reduces to the cable Equation 14. On the other hand, asymmetric load conditions lead to non-negligible deflections *w*, which in turn create both bending moments in the stress ribbon and additional horizontal force (*ΔH*).

#### 7.5.4.3.3 Key Parameters Affecting the Structural Behaviour of Suspended Structures

***Sag-to-Span Ratio***

The ratio between sag and span has a significant influence on the structural behaviour of suspended structures. As this ratio decreases, the horizontal force increases, as indicated by Equation 15. This translates into a larger cross-section of the stress ribbon and a more complicated design for the supports. Conversely, a larger sag-to-span ratio decreases the horizontal force, generally leading to economical and structurally efficient solutions. For pedestrian bridges, sag-to-span ratio also affects vibration characteristics and serviceability. The drawbacks of a large sag-to-span ratio for a pedestrian bridge might be a steeper walkway and lower frequency. Roof structures normally do not have such serviceability issues; thus, larger sags are acceptable. The natural frequencies of a vibrating cable are proportional to the square root of the ratio between the tensile force in it and its mass; therefore, excessively large sag-to-span ratios could result in very low natural frequencies in the structure. This may negatively affect wake-induced oscillations produced by wind forces. Moreover, excessively large sags also have the practical negative effect of reducing the usable indoor space. The ratio between the sag *s* and the span *l* of a timber stress ribbon is usually in the range of 0.10 to 0.12 for roof structures and somewhat lower for pedestrian bridges; if the gradient of the walkway is too steep, wheelchair users may have difficulty with it. (Note that stress ribbon footbridges whose tension force is taken by steel typically have smaller *s* to *l* ratios, typically around 0.015, than similar timber bridges. However, the smaller the *s* to *l* ratio, the higher the tension force in the structure. Timber does not easily handle very large tension forces, especially due to the unavoidable presence of joints, which significantly reduce the strength of the structure).

#### *Bending Stiffness*

As Section 7.5.4.3.1 explains, an increase in bending stiffness makes a suspended structure less sensitive to asymmetrical loads and wind-induced instability. Deflections and bending moments depend on the stiffness of the suspended structure. When the bending stiffness is very low, the deflection of the suspended structure is nearly the same as that of the cable, where the load is resisted in tension with negligible bending. Although increasing the bending stiffness of the suspended structure causes less deflection, it also gives rise to increasing bending moments. Therefore, for small permanent loads, the designer should adopt a cross-sectional depth that gives reasonable deflections with not overly large bending moments.

#### 7.5.4.3.4 Key Modelling Aspects

Timber-based suspended structures can use either very flexible members that adjust their final shape depending on the applied loads (form-active structure) or curved members with inherent bending stiffness. Nonlinear analysis is recommended in both cases. Second-order analysis typically gives reasonably accurate results, but third-order analysis is preferable when analysing form-active structures.

### *7.5.4.4 Domes*

A dome is synclastic with a positive Gaussian curvature, meaning that the curved surface is bent to the same side in every direction (Salvadori & Levy, 1967). By this definition, a dome is not necessarily accompanied by a circular bottom surface and might have an oval shape. When a portion of a sphere is cut off by a plane, the resulting shape is referred to as a spherical dome. This section primarily discusses such domes.

Timber structures are typically ribbed or reticulated domes (see Figure 60). Reticulated domes can have a number of designs, the most common being Schwedler, three-way grid, Kiewitt, lattice, and geodesic.

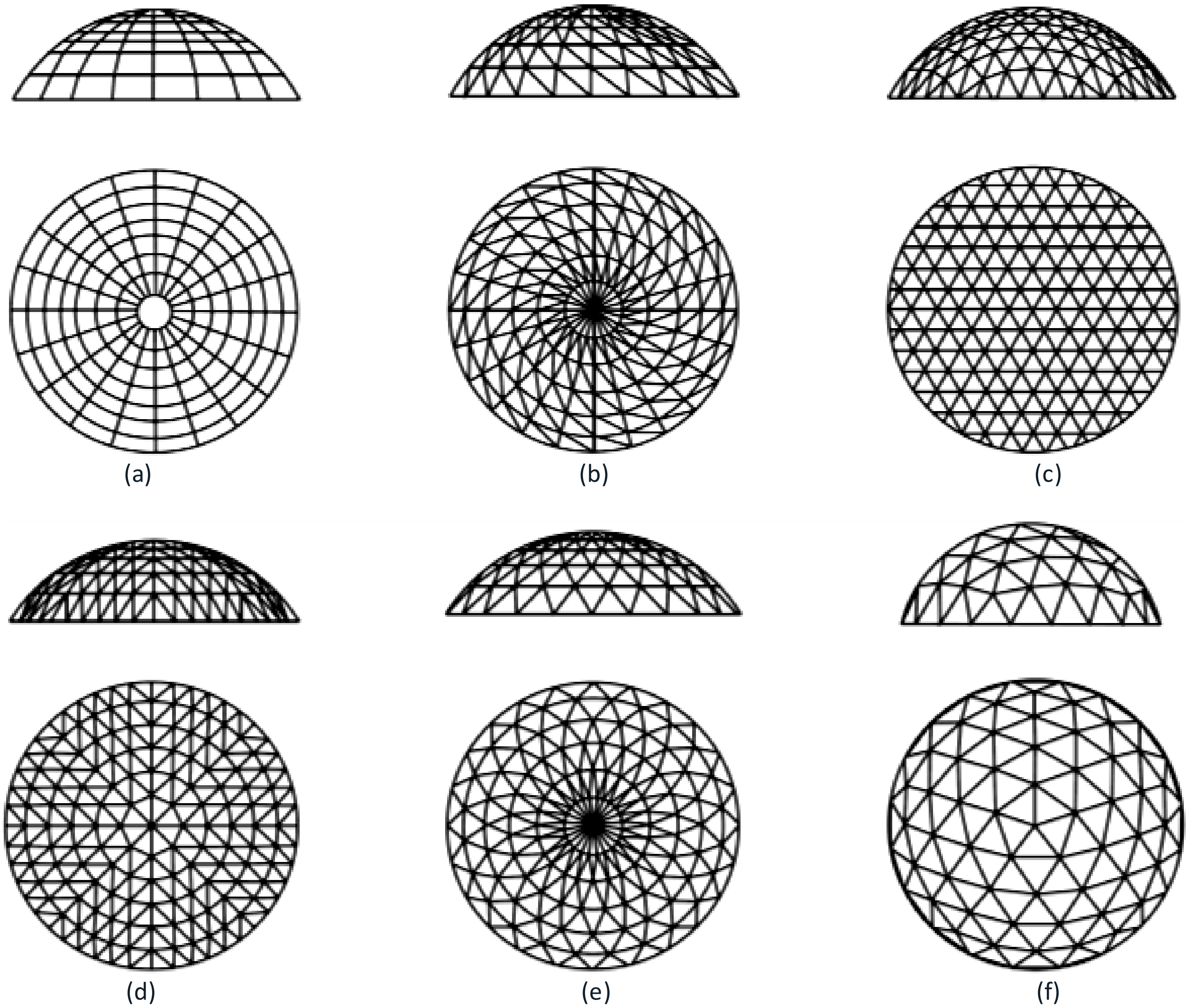


**Figure 60. Different dome patterns: (a) ribbed, (b) Schwedler, (c) three-way grid, (d) Kiewitt, (e) lattice, and (f) geodesic**

7.5.4.4.1 Ribbed Domes

Ribbed domes are in essence a system of two- or three-hinged arches (yet more efficient, because of two-way action) with bearings arranged along a circle, as illustrated in Figure 61. The spaces between the arches have purlins to support the roof. Moreover, there is diagonal bracing between the arches at a number of bays (typically every second bay). The thrust of the arch (*H*) can be taken either by distinct supports located at each springing point of the arch or by a bearing ring.

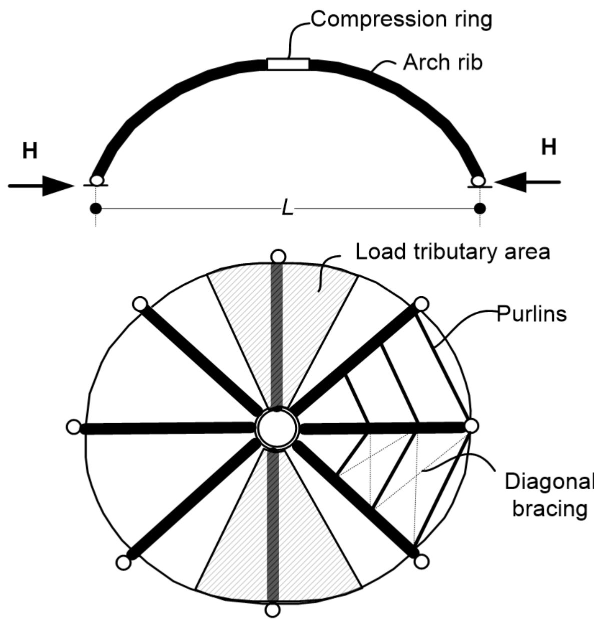


**Figure 61. Schematic illustration of a ribbed dome**

At the apex of a ribbed dome, the arch ribs are typically attached to a metal ring (compression ring) with moment stiff connections. The cross-section of the ring is subjected to compression, torsion, and bending. These forces are induced by the thrust forces, the bending moment, and shear forces in the arch ribs at the apex of the dome. It is important to pay particular attention to the possible buckling of the ring. Figure 62 shows a sport hall in Livorno, Italy. The structure is a ribbed dome with a diameter of 109 m and a rise of 33 m. Moment resisting connections connect the arch ribs and the compression ring at the apex of the dome.

**Figure 62. Sport hall in Livorno, Italy (Courtesy of Rubner Holzbau): (a) ribbed dome and (b) moment resisting connection**

As a rule, the purlins of a ribbed dome are attached to the arch ribs with a connection that can take only shear forces. If the connections between the purlins and the arch ribs can also take axial forces, it is better to adopt a spatial structure, with a number of circumferential rings acting as ties for the ribs. This will result in a lighter structure since individual members bear stress more uniformly than in the traditional ribbed dome described above. Figure 63 depicts a ribbed dome with four circumferential rings and, accordingly, four statically indeterminate quantities, $H_1$, $H_2$, $H_3$, and $H_4$.

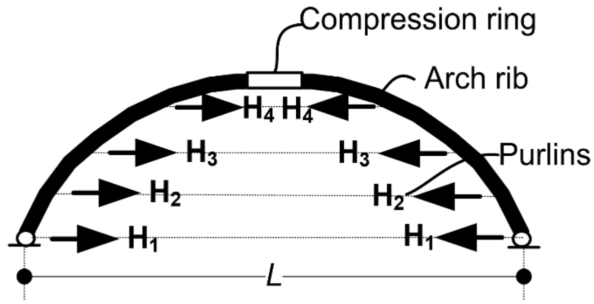


**Figure 63. Ribbed dome with purlins acting as ties**

7.5.4.4.2 Reticulated Domes

As noted in the previous section, the most common patterns for reticulated domes are Schwedler, three-way grid, Kiewitt, lattice, and geodesic.

- Schwedler domes (Figure 60[b]), introduced by the German engineer J.W. Schwedler, are characterized by meridional ribs and circumferential rings braced by diagonal bars. They are basically an evolution of the ribbed dome, with the addition of diagonals in the trapezoidal spaces.
- Three-way grid domes (Figure 60[c]) consist of an equilateral triangular plane projected onto the spherical surface. Theoretical analysis shows that this pattern seems to distribute forces well, even during asymmetrical loading, making these domes economical.
- Kiewitt domes (Figure 60[d]), introduced by G.R. Kiewitt, have a lamella pattern. Much like the ribbed and Schwedler configurations, this pattern is based on rings; it consists of several sectors, normally six or eight, in a circular plan. In each sector, an additional two-way rib system enhances the stiffness.
- Lattice domes (Figure 60[e]) also have a lamella pattern. To obtain the geometry of this pattern, start by rotating circles, both clockwise and counter-clockwise, that are tangent to the centre point of the dome. This will generate the curved lines seen in Figure 60(e). Adding circles in the horizontal plane completes the generations of the nodes.
- Geodesic domes (Figure 60[f]), patented by R. Buckminster Fuller, arise from an icosahedron, a polyhedron with 12 vertices, 20 faces, and 30 edges, as illustrated in Figure 64(a). Every face can be subdivided into smaller faces, which are then exploded to the sphere in which the icosahedron is encapsulated. The result is the spherical pattern shown in Fuller's patent in Figure 64(b).

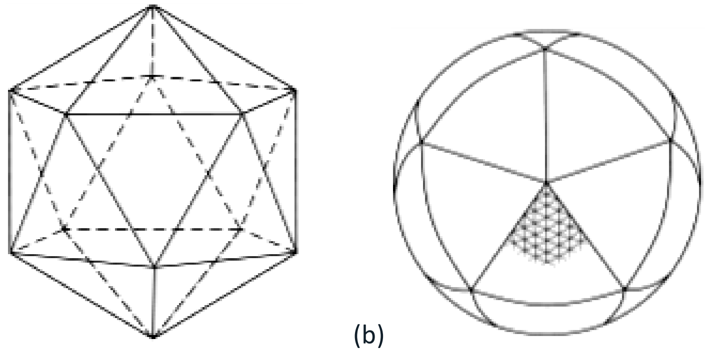
(a) (b)

**Figure 64. Development of a geodesic dome: (a) regular icosahedron; and (b) Fuller's patent**

In general, the most economic system for a dome occurs when the length of the members and the angle between them do not vary significantly, as this would require large labour requirements to erect the structure. The pattern that best fulfils these requirements is the geodesic grid. If all members are assigned the same size, a geodesic dome is in general more evenly stressed and thus lighter than other types of domes of a similar size.

Figure 65 shows the construction of one of the twin geodesic domes built for coal storage in Brindisi, Italy, in 2015. Each dome has a diameter of 143 m and a rise of 46 m. Note that they were erected without needing to build a temporary supporting tower in the centre of the dome area, as is typical for radial ribbed dome structures. This considerably reduces construction costs.

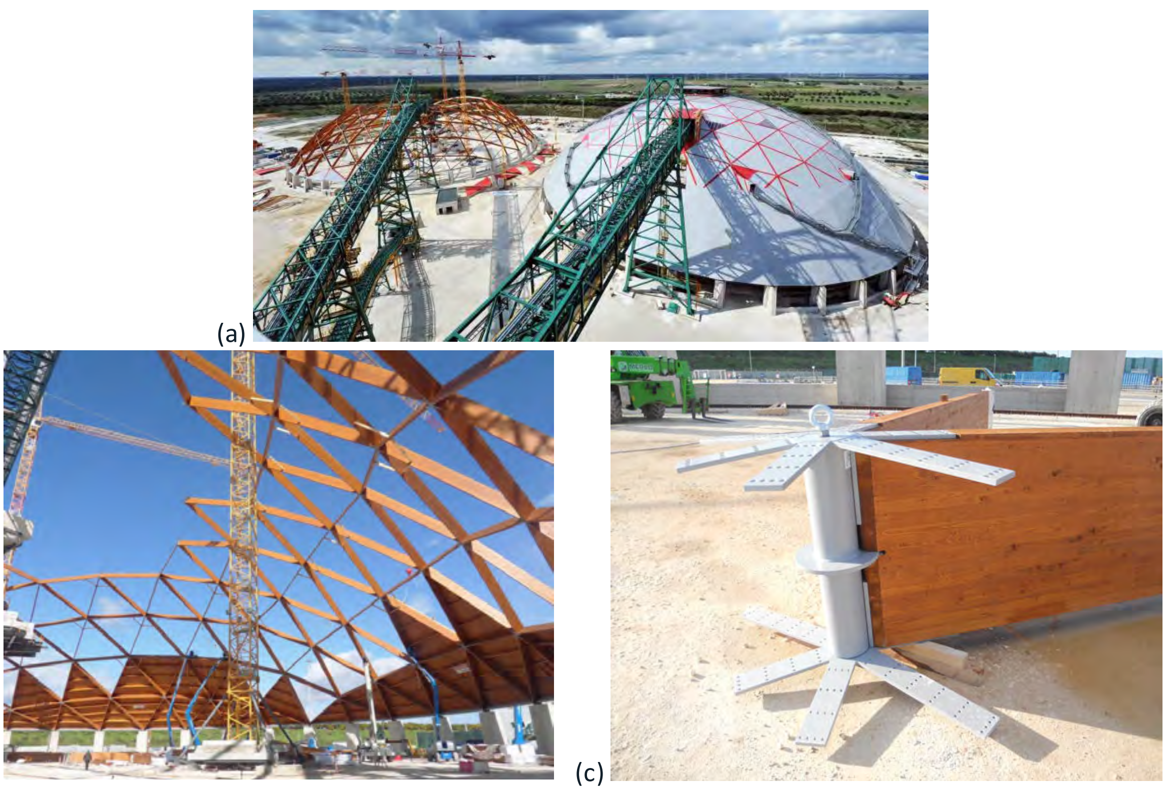
(a)
(b) (c)

**Figure 65. Twin geodesic domes in Brindisi, Italy (Courtesy of Rubner Holzbau): (a) two geodesic domes, (b) geodesic dome structure under erection, and (c) node details**

Nodes play an important role in large timber structures, particularly dome structures. Simple welded or plug-in connections, which are typical in steel structures, are not normally possible with timber. Connections must therefore be very adaptable and make it easy to erect the structure. To help simplify this process for the dome shown in Figure 65(b), the nodes have special joints. These joints (Figure 65[c]), which consist of steel plates and inclined self-tapping screws, are designed to resist bending moments and shear forces that arise during construction, when the members of the triangulated dome cantilever out.

#### *7.5.4.4.2.1 Method of Analysis*

There are two methods for analysing a reticulated dome (Fredriksson & Herrström, 2017): a) the equivalent continuous shell analogy and b) the discrete structure method. Method a) is suited for the preliminary design of a dome, as it is relatively easy to use and allows for hand calculations. It uses the properties of a continuous (thin) shell in membrane action, translating the computed stresses or unit forces into the corresponding axial forces in the reticulated grid. Due to their complex geometry, reticulated domes are highly indeterminate structures. Repetitive calculations with varying sections can be cumbersome, which makes the shell analogy a useful tool for estimating forces in the early design stage. It is also useful for validating the results obtained through more advanced methods. Method b) typically involves computational FE calculations for a model, including every single member of the reticulated structure. This approach directly analyses the structure and can thoroughly determine axial forces, shear forces, and bending moments. After a nonlinear analysis, the numerical model can accurately predict the failure modes and the magnitudes of the associated failure loads due to structural instability, which is often an issue for domes. This section describes the design method using the equivalent continuous shell analogy.

A simplified analysis considers the reticulated dome as a membrane. A membrane subjected to a uniformly distributed gravity load develops meridional and hoop (or parallel) forces, as shown in Figure 66.

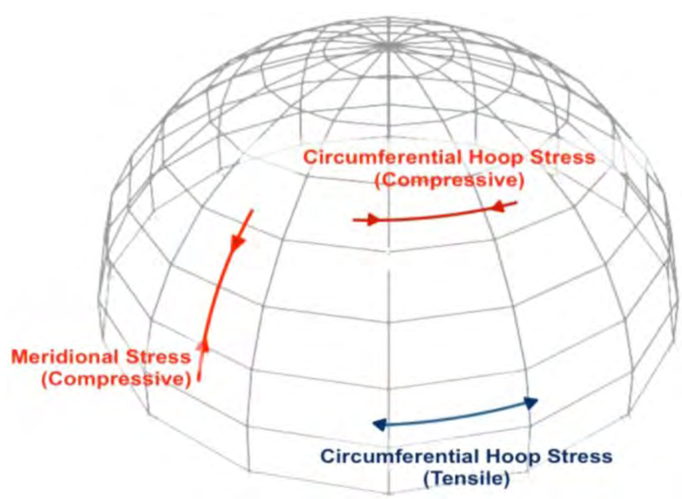


**Figure 66. Meridional and hoop (or parallel) forces in a dome structure subjected to uniformly distributed loads (Nayak et al., 2020)**

The meridional and parallel forces per unit length are indicated by $N_\varphi$ and $N_\theta$, respectively (Figure 67).

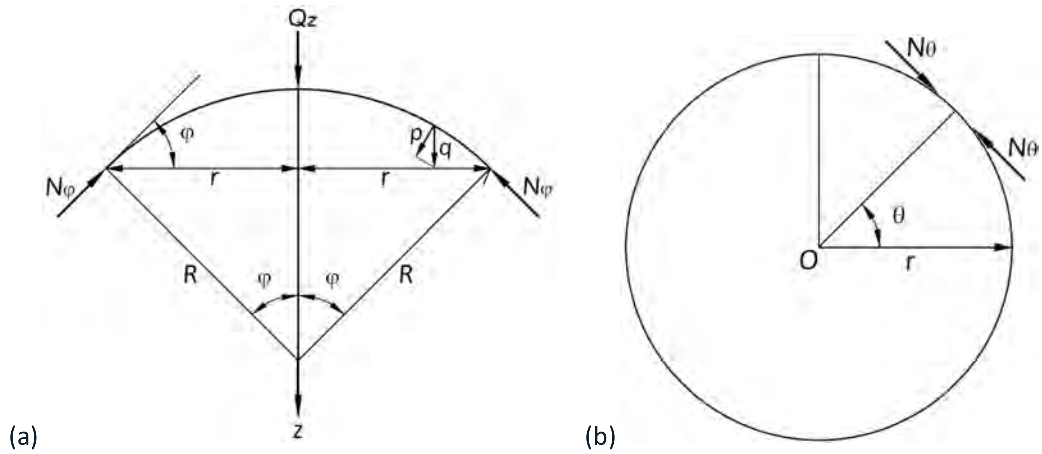


**Figure 67. Meridional and hoop forces in a dome structure: (a) cross-section and (b) top view**

The following equation can provide the meridional and parallel forces $N_\varphi$ *and* $N_\theta$ (in kN/m) for a spherical dome:

$$N_\varphi + N_\theta = p \cdot R \tag{17}$$

The meridional force can be calculated by stating the vertical equilibrium of the shell sector above the parallel φ (Figure 67).

$$N_\varphi = \frac{Q_z}{2 \cdot \pi \cdot R \cdot \sin^2 \varphi}, \tag{18}$$

where $p$ is the normal component of the load $q$ (kN/m²); and $Q_z$ is the resultant of all the loads above the parallel $\varphi$. Figure 68 shows a live load $q$ (e.g., snow) and a dead load $w$ acting on a spherical dome.

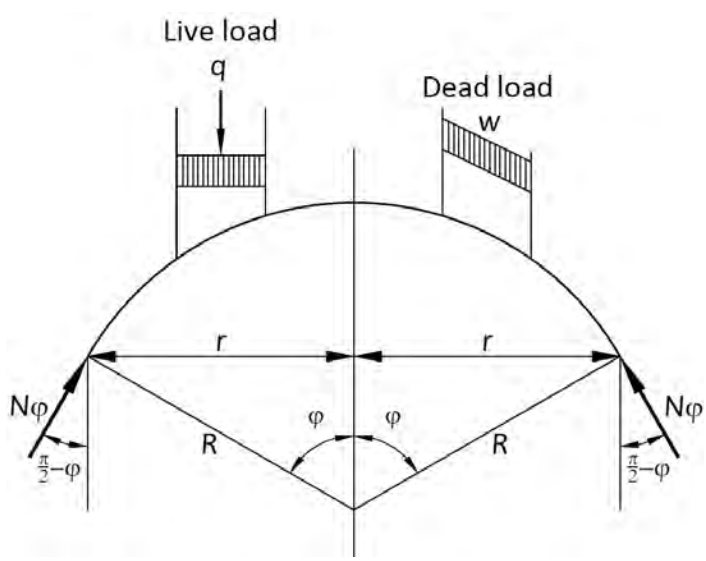


**Figure 68. Spherical dome subjected to both dead and live loads**

The membrane unit forces caused by the dead load *w* are

$$N_{\varphi,w} = \frac{w \cdot R}{1+\cos\varphi} \quad \text{and} \quad N_{\theta,w} = w \cdot R \cdot \left( \cos\varphi - \frac{1}{1+\cos\varphi} \right). \qquad [19]$$

Whereas the membrane unit forces caused by the live load *q* are

$$N_{\varphi,q} = \frac{1}{2} \cdot q \cdot R \quad \text{and} \quad N_{\theta,q} = \frac{1}{2} \cdot q \cdot R \cdot \cos(2 \cdot \varphi). \qquad [20]$$

The unit forces derived according to the continuous shell analogy can be translated into axial forces in a reticulated dome. To do so, the following conditions should ideally apply:

- The reticulated dome pattern should be of a regular uniform mesh.
- The members of the reticulated dome should all be approximately equal in cross-section and length
- The dome should not have any large openings or any other discontinuity in its pattern.

These conditions are seldom all fulfilled, but comparisons by hand calculation and numerical analysis show they give a fairly accurate result in most cases. For a geodesic dome meeting these conditions, as illustrated in Figure 69, one can determine the forces in the members that follow the ideal meridional trajectory by multiplying the meridional force $N_\varphi$ by the tributary width, *a*, which depends on mesh density. Likewise, to determine the force in any member that follows the annular direction, multiplying the annular force $N_\varphi$ by its tributary width *b*.

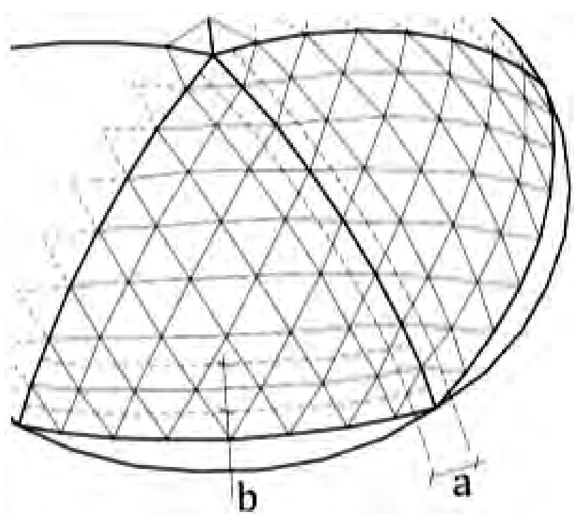


**Figure 69. Tributary widths a and b for calculating forces in meridional and hoop members in a geodesic dome**

###### *7.5.4.4.2.2 Design Recommendations for Reticulated Timber Domes*

When designing timber domes, the most relevant issues to considered are

- Which dome geometry is most suitable?
- How sensitive is a geodesic timber dome to geometric imperfections?
- How accurately can hand calculations predict failure loads?
- How does creep influence structural stability?
- How sensitive is the structure to settlements?

General answers to the above questions are as follows.

In general, if cross-sections are kept somewhat constant for all the main load-bearing members of the dome, the geodesic arrangement gives the best economy and structural efficiency of the configurations shown in Figure 60. This allows the lowest variation of member lengths and the highest buckling load.

Three different buckling mechanisms occur in reticulated dome structures: a) member buckling, b) nodal buckling (snap-through), and c) global buckling. In timber domes, members tend to be relatively stocky, so member buckling is in general unlikely to govern the design. If members were considered pinned at their ends, nodal buckling could give the lowest failure load. However, due to the large connections needed to connect the members of the dome to one another, relatively large rotational restrain is introduced at the ends of these members, mitigating the risk of nodal buckling. Therefore, global buckling is normally the governing buckling mechanism in timber reticulated domes. The buckling load (global buckling) of reticulated domes is significantly affected by geometric imperfections. For example, given an initial imperfection of approximately D/300, where D is diameter of the dome, the failure load of the dome may decrease by a factor of approximately 2.5, compared to the theoretical buckling load calculated by simple LBA.

A common method to account for the effect of imperfection in the analysis is to impose this imperfection in the shape of an eigenmode. This can involve single mode or a combination of several. In general, the first mode does not yield the lowest failure load; the imperfection could instead be the linear combination of several base shapes or simply a higher eigenmode.

The hand calculation method based on the continuous shell analogy accurately predicts the first buckling load, when the load is uniformly distributed. However, the buckling load due to asymmetric load configurations is not suitable for hand calculation.

Creep causes the members of the dome aligned with the meridional trajectories to shorten with time. This induces a global symmetrical deflection of the dome. Creep also makes the axial load in the most loaded members of the dome increase because of the decrease of the rise of the dome. This reduces the magnitude of the lever arm of the resisting couple generated by the compression and tensile forces at the top and bottom of the dome, respectively. This negatively affects the stability of the dome, as the buckling load diminishes with increasing creep. However, the reduction in buckling load due to creep is generally less severe than the corresponding reduction caused by geometric imperfections. The effect of the combined action of creep and initial imperfection decreases the resistance of the dome against buckling more than do the same actions in isolation.

The buckling loads of reticulated domes are not significantly affected by support settlement, even when it is relatively large in magnitude and differential.

7.5.4.4.3 Key Modelling Aspect

Timber domes can be simply ribbed or reticulated. Overall, the former provides simpler construction, but less structural efficiency. Of the reticulated systems, the geodesic arrangement gives the best economy and structural efficiency.

Typically, buckling governs the design of timber domes. Among the possible instability modes, global buckling is most likely in reticulated timber domes. Dome structures are very sensitive to geometric imperfections. Therefore, for the final design of a dome, a nonlinear (second-order) analysis, possibly including different initial geometric imperfections, is necessary. The imposed imperfections should be affine, with the shape of the buckling eigenmodes of the dome structure.

The analysis should also include long-term effects, since creep leads to increased compression forces in the members aligned with the meridional trajectories of the dome.

## 7.5.5 Summary

This chapter introduces the history and advantages of long-span timber structures, along with typical structural form and systems. It discusses general aspects of analysis for long-span timber structures, as well as the influence of the span on the structural design of long-span timber structures in terms of structural stability, bracing, and joints/connections. It describes in detail the analysis and modelling of the typical structural types of long-span timber structures (i.e., trusses, portal frames, arches, suspended structures, domes, and freeform structures), with corresponding recommendations. The information presented in this chapter is intended to help practising engineers and researchers become better acquainted with the modelling and analysis of long-span timber structures.

## 7.5.6 References

Andersson, B, & Larsson, G. (2014). *Verification of buckling analysis for glulam arches* [Master's thesis, Lund University, Sweden]. ISRN LUTVDG/TVSM--14/5195--SE (1-154) | ISSN 0281-6679.

Bell, K. (2017). *Dimensjonering av trekonstruksjoner* [Design of timber structures]. Fagbokforlaget.

Canadian Standards Association. (2019a). *Canadian highway bridge design code* (CSA standard CSA S6). https://www.csagroup.org/canadian-highway-bridge-design-code/

Canadian Standards Association. (2019b). *Engineering design in wood*. (CSA standard CSA O86). https://www.csagroup.org/store/product/2702965/

Crocetti, R. (2016a). *Large-span timber structures* [Conference presentation]. Proceedings of the World Congress on Civil, Structural, and Environmental Engineering (CSEE'16), Prague, Czech Republic.

Crocetti, R. (2016b). *Timber structures for large-span structures* [Keynote paper]. Proceedings of the World Congress on Civil, Structural, and Environmental Engineering (CSEE'16) Prague, Czech Republic. https://doi.org/10.11159/icsenm16.124

Crocetti, R. (2017). Hängtakskonstruktioner ger elegant spännvidd [Suspended roof structures give elegant spans]. Swedish Wood. https://www.svenskttra.se/publikationer-start/tidningen-tra/2017-4/hangtakskonstruktioner-ger-elegant-spannvidd/

D'Amico, B., Kermani, A., Zhang, H., Pugnale, A., Colabella, S., & Pone, S. (2015). Timber gridshells: Numerical simulation, design and construction of a full scale structure. *Structures*, 3: 227–235. http://doi.org/10.1016/j.istruc.2015.05.002

Dragicevic, P. (n.d.). Gaudí's Hanging Chain Models. In *Data Physicalization Wiki*. http://dataphys.org/list/gaudis-hanging-chain-models/

European Committee for Standardization. (2003). *Eurocode 1 - Actions on structures - Part 1-3: General actions - Snow loads* (Eurocode Standard EN 1991-1-3). https://www.phd.eng.br/wp-content/uploads/2015/12/en.1991.1.3.2003.pdf

European Committee for Standardization. (2004). *Eurocode 5: Design of timber structures. Part 1-2: General rules: Structural fire design* (Eurocode Standard EN1995-1-2). https://www.phd.eng.br/wp-content/uploads/2015/12/en.1995.1.2.2004.pdf

European Committee for Standardization. (2018). *Eurocode 5: Design of timber structures - Part 1-1: General - Common rules and rules for buildings* (Eurocode Standard EN 1995-1-1). https://www.phd.eng.br/wp-content/uploads/2015/12/en.1995.1.1.2004.pdf

Farreyre, A., & Journot, J.-B. (2005). *Timber trussed arch for long span* [Master's thesis, Chalmers University of Technology, Göteborg, Sweden]. Chalmers publication library. https://publications.lib.chalmers.se/records/fulltext/10772.pdf

Francis, A. J. (1980). *Introducing Structures, A Textbook for Students of Civil and Structural Engineering, Building and Architecture*. Elsevier.

Fredriksson, G., & Herrström, M. (2017). *Stability analysis of a large span timber dome* [Master's thesis, Lund University, Sweden]. Rapport TVBK-5258 ISSN 0349-4969 ISRN: LUTVDG/TVBK-17/5258+122p.

Frühwald, E., Serrano, E., Toratti, T., Emilsson, A., & Thelandersson, S. (2007). *Design of safe timber structures - how can we learn from structural failures in concrete, steel and timber?* Technical Report, Division of Structural Engineering, Lund University.

Gustafsson, D. & Ingvarsson, M. (2017). *Application of asymmetric loads on cable shaped structures - A load case study of timber roof stress ribbon structures* [Master's thesis, Chalmers University of Technology, Göteborg, Sweden]. Chalmers publication library. https://publications.lib.chalmers.se/records/fulltext/250144/250144.pdf

Hambly, E. C. (2019). *Bridge deck behavior*. CRC Press.

Happold, E., & Liddell, W. (1975). Timber lattice roof for the Mannheim Bundesgartenschau. *The Structural Engineer*, 3(53): 99–135.

Hofverberg, S. (2016). *Long-span tensile timber roof structures: Development of design proposals adopting the Stress Ribbon concept* [Master's thesis, Chalmers University of Technology, Göteborg, Sweden]. Chalmers open digital repository. https://hdl.handle.net/20.500.12380/240142

Lepida, C. (2018). *La Sagrada Familia; hidden secrets & mysteries!* Itinari. https://www.itinari.com/la-sagrada-familia-hidden-secrets-and-mysteries-ncd1

Mischler, A., Prion, H., & Lam, F. (2000). *Load-carrying behaviour of steel-to-timber dowel connections* [Conference presentation]. World Conference of Timber Engineering, Whistler, B.C., Canada.

National Research Council of Canada. (2020). National building code of Canada 2020. NRC.

Nayak, C. B., Jain, M. A., & Walke, S. B. (2020). Parametric study of dome with and without opening. *Journal of The Institution of Engineers (India): Series A,* 101(3), 463–475. http://doi.org/10.1007/s40030-020-00447-3

Persson, K. (2017). *Analysis of catenary shaped timber structures* [Master's thesis, Lund University, Sweden], Rapport TVBK-5262, ISSN 0349-4969, ISRN: LUTVDG/TVBK-17/5262+(pp129).

Riberholt, H. (1985). *Trækonstruktioner, eksempler* [Timber structures, Examples]. Danmarks Tekniske Højskole. https://bibliotek.dk/da/work/870970-basis:10061342

Rossi, S., Crocetti, R., Honfi, D., & Frühwald Hansson, E. (2016). *Load-bearing capacity of ductile multiple shear steel-to-timber connections* [Conference presentation]. World Conference of Timber Engineering, Vienna, Austria.

Salvadori, M. & Levy, M. (1967). *Structural design in architecture*. Prentice Hall.

Schlaich, J. & Bergermann, R. (1994). *Conceptual design of long-span roofs*. International Association for Bridge and Structural Engineering. https://www.e-periodica.ch/digbib/view?pid=bse-re-003:1994:71::21

Schodek, D., & Bechthold, M. (2013). *Structures* (7th Edition). Pearson.

Superior Dome. (2020). In *Wikipedia*. https://en.wikipedia.org/w/index.php?title=Superior_Dome&oldid=990179976

Swedish Wood. (2016). *Design of timber structures*: *Vol. 1. Structural aspects of timber construction.* https://www.svenskttra.se/siteassets/5-publikationer/pdfer/design-of-timber-structures-1-2016.pdf

Swedish Wood. (2018). *Limträhandbok* [Glulam handbook] (Vols. 1–4). https://www.svenskttra.se/publikationer-start/publikationer/limtrahandbok/

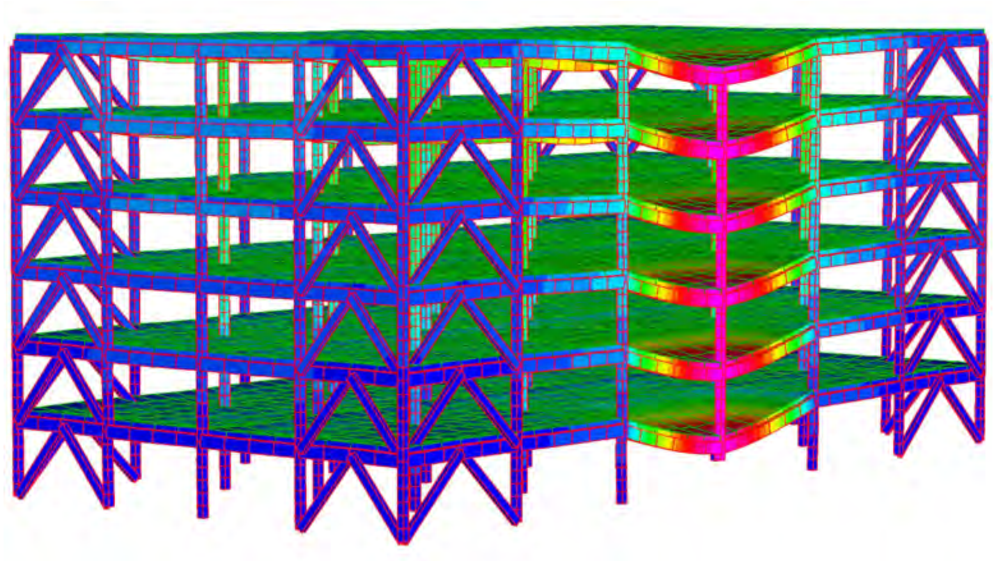

# CHAPTER 8

## Progressive/disproportionate collapse

**Authors**
Benoit Gilbert
Zhiyong Chen
Nathan Benbow

**Reviewers**
Marjan Popovski
Robert Jockwer
Alex Zecevic

# TABLE OF CONTENTS

## 8.1 INTRODUCTION TO PROGRESSIVE COLLAPSE OF TIMBER BUILDINGS

Progressive collapse is a phenomenon initiated by local damage to a structure that propagates throughout the structural system in a chain reaction, leading to the partial or entire collapse of the structure. It is characterised by a final state of damage that is disproportionate to the initial damage (American Society of Civil Engineers [ASCE], 2016; Ellingwood, 2006). Progressive collapse is triggered by an abnormal event, classified as a low-probability/high-consequence event, such as an explosion, vehicle impact, construction or design error, fire, or natural disaster (Adam et al., 2018). These events are rare (low probability) but often result in significant economic losses and human casualties (high consequences), especially for tall buildings (Rezai et al., 2014).

The most popular design procedure for progressive collapse consists of designing the building not to sustain the abnormal event, but rather to prevent the local damage from propagating throughout the building. To achieve this goal, the system needs to be designed to find alternative load paths (ALPs) and redistribute the loads after the initial damage, which depends on the level of structural redundancy (Adam et al., 2018). A building that provides such level of redundancy is referred to as being robust. The ALP is a design methodology (General Services Administration [GSA], 2016; Institution of Structural Engineers [IStructE], 2010; Department of Defense [DoD], 2016) commonly used for this purpose, in which load-bearing elements are removed systematically one at a time, and the ability of the structure to redistribute loads and bypass the missing element is assessed (see Section 8.2). However, if the ALP approach proves impractical, another methodology would be to consider the load-bearing members which could be exposed to the low-probability/high-consequence events as key elements and design them accordingly to withstand such events (IStructE, 2010).

A distinction can be made between progressive collapse and disproportionate collapse, with various definitions given in Adam et al. (2018). In summary, the former relates to the propagation of failure throughout the structural system and, therefore, the structural response to the abnormal event, while the latter relates to the final state of the damaged structure relative to the initial state of damage. In practice, however, the two terms are interchangeable in the context of structural robustness design. Using one term over the other varies between countries (Ellingwood et al., 2007). For instance, despite similarities in design methodologies, the DoD (2016) and GSA (2016) design guidelines mainly use the term progressive collapse, while the UK's IStructE guide (2010) mainly uses the term disproportionate collapse. Largely based on the definition of the *Minimum Design Loads and Associated Criteria for Buildings and Other Structures* standard (ASCE, 2005), Ellingwood et al. (2007) do not make a distinction between the two terms and have proposed the following definition to be adopted by the professional community:

> Progressive collapse – the spread of local damage from an initiating event, from element to element, resulting, eventually, in the collapse of an entire structure or a disproportionate large part of it; also known as disproportionate collapse.

Depending on the national design specifications in place, timber buildings shall be designed to withstand progressive collapse to the same extent as their reinforced concrete and steel counterparts. While the resistance of reinforced concrete and steel buildings to progressive collapse has been studied extensively, there are still only limited studies on timber buildings (Huber et al., 2019). In this chapter, a distinction is made between two types of timber buildings:

- Light wood-frame (stud frame) buildings: These refer to lightweight timber buildings with walls manufactured from closely spaced, small-section lumber studs sheathed with wood-based panels using nailed, screwed, or stapled connections. This type of construction is well suited for buildings up to six storeys. The robustness of wood-frame buildings has been experimentally studied on a full-scale six-storey building (Grantham et al., 2003). Grantham & Enjily (2004) found that this type of building, especially when designed with rim beams, commonly offers enough structural redundancy for a load to be redistributed over a removed stud wall. The relatively low self-weight of this type of structure also implies low loads in post-failure scenarios and reduced dynamic effects (Thelandersson & Honfi, 2009). These buildings are not covered in this chapter, but the UK Timber Frame Association (2008) provides guidance on detailing specifications for robustness.
- Mass timber buildings: These are assembled from engineered wood products, such as laminated veneer lumber (LVL), glued laminated timber (glulam), parallel strand lumber, cross-laminated timber (CLT), and mass plywood panels. These buildings are the focus of this chapter as their design requires more detailed analysis than light wood-frame buildings in terms of robustness.

Investigations into progressive collapse of reinforced concrete and steel buildings led to changes to improve robustness in relevant design standards, such as providing continuity of slab bottom reinforcing bars through columns (Hawkins & Mitchell, 1979; Mitchell & Cook, 1984) or tying detailing requirements (Adam et al., 2018). Many designers therefore believe that reinforced concrete and steel buildings are inherently robust, even if they are not designed against progressive collapse. It is a misconception to believe that the same intrinsic robustness systematically applies to all mass timber buildings. Due to the nature of prefabricated structural timber elements and the associated lack of continuity between these elements, the brittle failure mode of timber material in tension, shear, and bending (Thelandersson & Honfi, 2009), and the lack of ductility in some of the connections (Lyu et al., 2020; Masaeli et al., 2020), some mass timber buildings (e.g., post-and-beam systems and moment-resisting frames) are generally deemed to be more elastic and typically have fewer possibilities than reinforced concrete and steel buildings for finding ALPs (Hewson, 2016). If not adequately designed, mass timber buildings may therefore be more vulnerable to progressive collapse. Note that the ductility discussed in this chapter is different from the ductility of seismic force–resisting systems. Additionally, as the height of constructed mass timber buildings constantly increases (Karacabeyli & Lum, 2022)—currently the tallest mass timber building, the Mjøsa Tower in Brumunddal, Norway (completed in 2019), is 85.4 m high—the consequences associated with a progressive collapse event also dramatically increase. As a result, designers must pay special attention to ensure robustness is achieved (Popovski et al., 2021). Importantly, due to the common lack of structural redundancy in mass timber buildings, ALPs must be clearly identified and designed to sustain the loss of a load-bearing element.

In steel and reinforced concrete frame buildings, the loss of a load-bearing column is typically resisted by three mechanisms developed in the adjacent beams (Stylianidis et al., 2016), with the representative load-deformation curve illustrated in Figure 1. These mechanisms may not be encountered to the same magnitude in all mass timber buildings. The mechanisms are as follows:

- Flexural action: In the initial phase, the load is resisted by the beams or floors spanning over the lost load-bearing element in bending (Figure 2[a]). However, due to the low rotational stiffness of the connections usually encountered in some mass timber buildings (Masaeli et al., 2020), such as post-and-beam systems, and the discontinuity of the structural elements, the flexural action mechanism may not be predominant in the corresponding mass timber buildings.
- Compressive arch action: As the deformation increases, compression forces develop in the beams and floors as these elements try to deform between the fixed columns and push against them (Figure 2[b]). The maximum gravity load that is resisted by compressive arch action occurs up to a maximum displacement of the removed element equal to the depth of the beam or floor. Compressive arch action has been experimentally observed in post-and-beam mass timber buildings (Cheng et al., 2021; Lyu et al., 2020), but the amount of force resisted by this mechanism would depend on the construction gap between the beams and columns and the stiffness of these elements.
- Catenary action: If the connections are ductile enough, tension forces eventually develop in the beams or floors under large deformation and would efficiently resist the gravity load (Figure 2[c]). Most connections for mass timber buildings would often fail and not allow enough rotation to take place before catenary action could fully develop (Lyu et al., 2020). Post-tensioned frames, which use tensioned steel cables inside the beams, may be used to enhance the development of catenary action after column removal (Hewson, 2016).

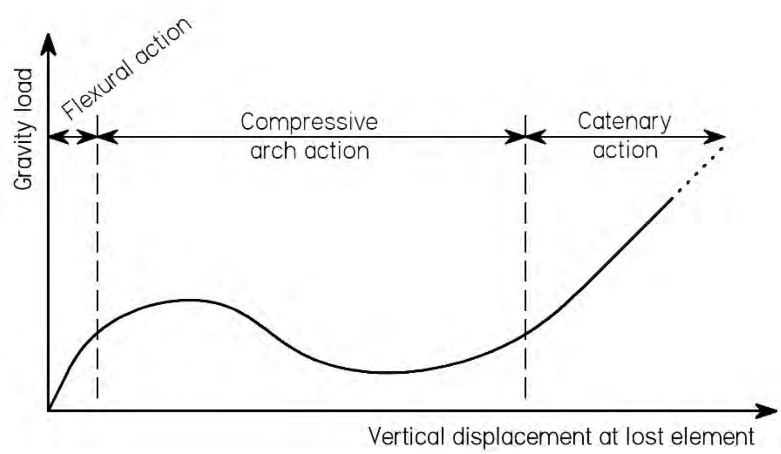


**Figure 1. Nonlinear deformation response by frame buildings after the loss of a load-bearing element. (Adapted from Stylianidis et al., 2016)**

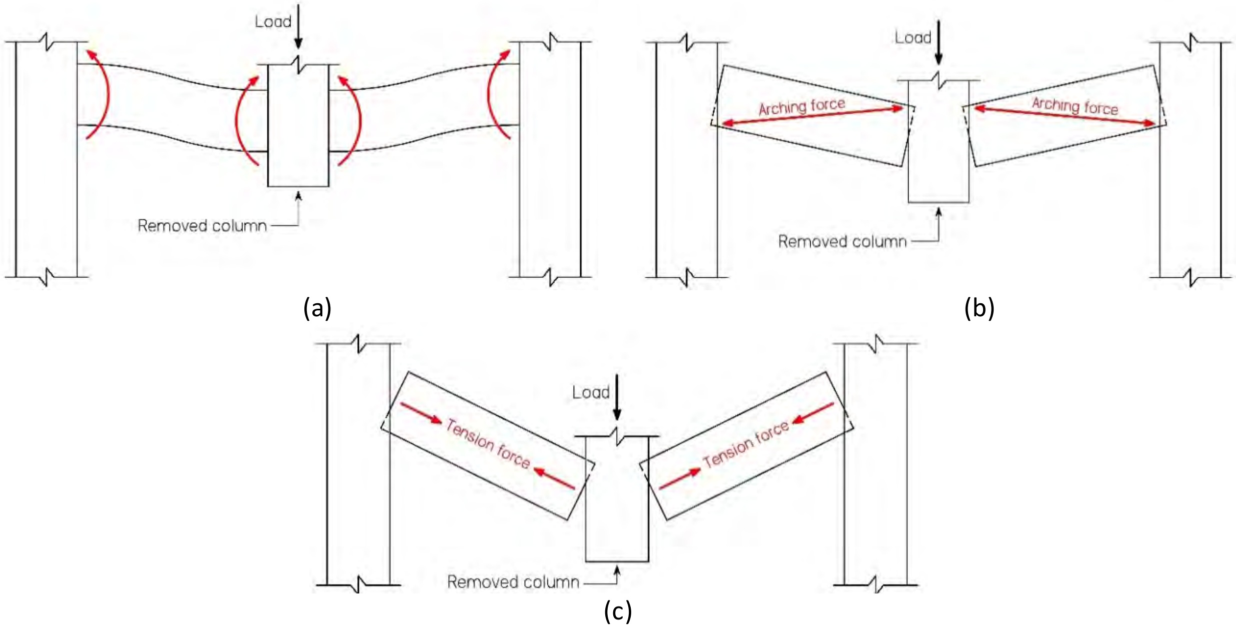


**Figure 2. Resisting mechanisms include (a) flexural, (b) compressive arch, and (c) catenary actions**

Horizontal and vertical ties are considered the strict minimum measure in design against progressive collapse (GSA, 2016; IStructE, 2010; DoD, 2016). They provide continuity throughout the structure, and they are designed under the assumption that large deformation will take place under the loss of a load-bearing element, enabling the load to be resisted through catenary action. Enough rotation must therefore develop at the connections, typically 0.2 rad (DoD, 2016), for ties to be efficient. This method is accordingly potentially unsound (Stylianidis et al., 2016) if the connections are not verified to allow the catenary action phase to be fully established (i.e., requiring both rotation capacity and tensile resistance). While this amount of rotation can be achieved in the more ductile reinforced concrete and steel buildings, recent research shows that this is more problematic for mass timber connections (Lyu et al., 2020; Masaeli et al., 2020). Despite connections being the key in ensuring buildings are robust (Jorissen & Fragiacomo, 2011), connectors available commercially are not always designed with robustness in mind and would allow catenary action to only partially develop. They are commonly optimised for specific loading cases (e.g., vertical shear load in beam-to-column connections) or high stiffness. Load reversal, rotation, tension load, etc., are not always considered in the optimisation of these joints. Therefore, extreme caution must be exercised for mass timber buildings when the design includes horizontal and vertical ties. Nevertheless, when connections are designed to enhance ductility, catenary action can be achieved in mass timber frames (Lyu et al., 2020).

This chapter introduces simplified and advanced modelling techniques of mass timber buildings under a load-bearing element removal scenario. It also shows how to identify the ALPs and design for them. Five types of mass timber buildings are discussed, namely, (1) shear wall systems, (2) post-and-beam systems, (3) hybrid systems, (4) long-span structures, and (5) prefabricated module structures. The general design approaches for robustness are introduced and explained in Section 8.2. The design approaches that best apply to various timber structural systems and the associated modelling techniques are then illustrated in Sections 8.3 to 8.5.

## 8.2 DESIGN AND ANALYSIS METHODS AND STRATEGIES FOR ROBUSTNESS

In general, the analysis and quantification of robustness may be based on (a) a risk analysis (Baker et al., 2008), (b) a reliability analysis (Köhler, 2007), or (c) a deterministic analysis (Brett & Lu, 2013). Risk and reliability analyses are probabilistic approaches and thus factor in probability distributions regarding building exposure or material parameters. A deterministic analysis may be conducted in a pragmatic manner and is needed as a complement to a probabilistic analysis (Starossek, 2006). Probabilistic and deterministic analyses may both yield measures to quantify robustness; however, deterministic analyses are typically adopted in design.

This section summarises the design methods and strategies to achieving robustness (Figure 3) that have been widely adopted in design guidelines (Adam et al., 2018). The recommendations relevant to each country usually implement one or more variations of these methods; however, the basic principles are the same (Arup, 2011). A detailed review of these methods, with differences between countries, can be found in Arup (2011) and Adam et al. (2018). The chosen design typically depends on the importance level (or building class) of the building and the degree of confidence the engineer wants to get out of the analysis. The accidental load combination for progressive collapse also depends on the recommendations relevant to each country and typically comprises the dead load in addition to a reduced live or snow load. A short-term load duration factor of 1.0 is also commonly used in practice.

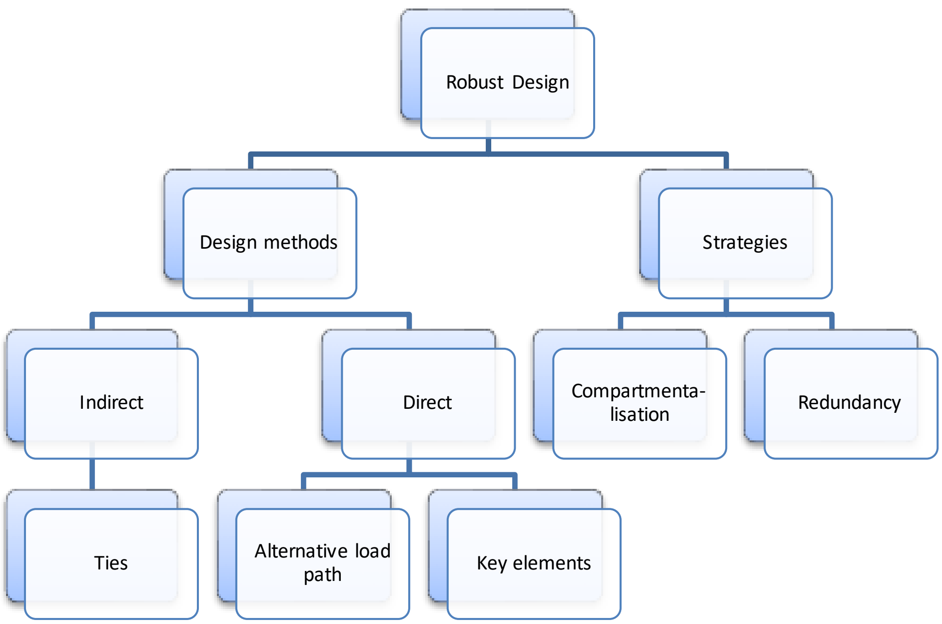


**Figure 3. Categorisation of design methods and strategies for robustness**

### 8.2.1 Tie Forces

The tie-force design approach is classified as an indirect design method (Ellingwood et al., 2007), meaning that the designer does not explicitly model the consequence of removing a load-bearing element, but rather applies a set of requirements to tie elements together. Tie forces are considered the minimum prerequisite against progressive collapse and would be applied without additional analysis to lower-importance level (or building class) structures (Arup, 2011). A more quantitative method would be needed, such as those presented in Sections 8.2.2 to 8.2.4, for higher-importance/class structures, often in addition to providing ties to the structure.

Ties can be classified as peripheral, internal horizontal, and vertical, as shown in Figure 4(a). Their purpose is to maintain the structural integrity of a building after the loss of a load-bearing element. The required tie strength varies between countries; for instance, information is provided in Annex A of Eurocode 1 (European Committee for Standardization [CEN], 2006), Section 3.1 of *Design of Buildings to Resist Progressive Collapse* (DoD, 2016), and Clause 6.2.3 of the *Structural design actions* standard (Standards New Zealand, 2002). As mentioned in Section 8.1, the implicit requirement of horizontal ties is that enough rotation can develop at the connections for catenary action to occur. In reference to Figure 4(b), structural integrity is provided if:

$$\boldsymbol{L_{ALC} \leq 2F_{TF}Sin(\theta)} \quad [1]$$

where $L_{ALC}$ is the accidental load combination, and $F_{TF}$ is the tie force. The higher the rotation at the connection, the lower the tie strength requirement. Typically, a rotation of 0.2 rad is recommended (DoD, 2016), and the designer must ensure that the axial tie strength is maintained after this level of rotation. Vertical ties are there to provide a minimum resistance to the vertical elements being removed and to facilitate the load redistribution between floors (IStructE, 2010).

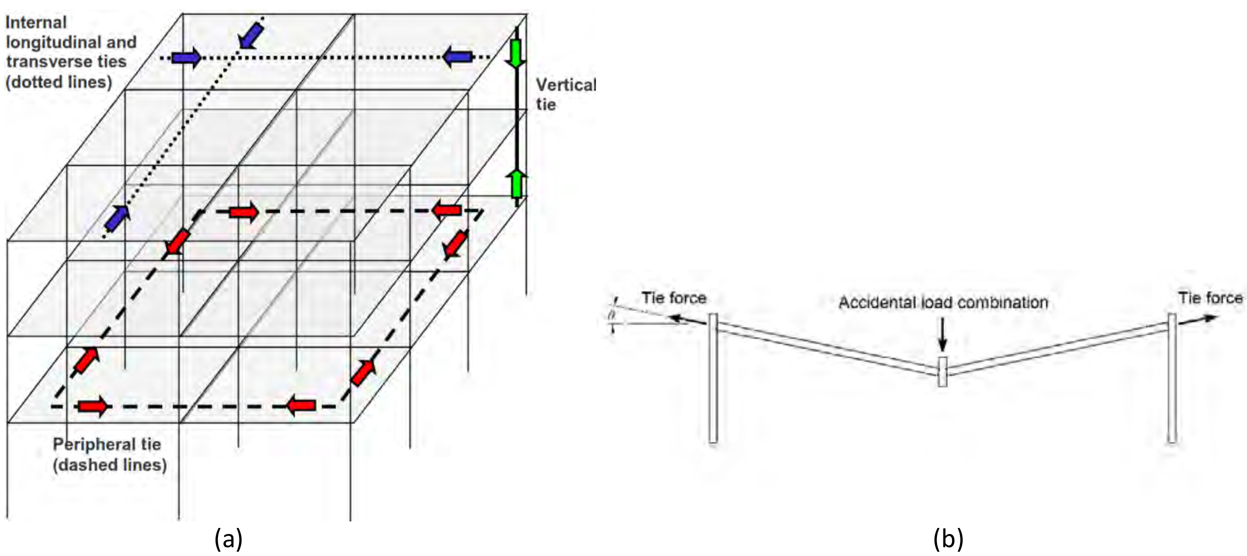


**Figure 4. (a) Tie forces in a frame structure (DoD, 2016). (b) Resisting mechanisms of horizontal ties**

In mass timber buildings, vertical tie forces are provided in practice to ensure vertical structural continuity; however, horizontal ties are not always straightforward to incorporate into the design. In post-and-beam buildings, for instance, the discontinuity of the beam elements, and often the presence of the continuous columns between beams, prove tying beams to beams challenging. Ties can also be provided through CLT floors, but this is challenging in practice as the designer still needs to ensure that all connections can rotate by at least 0.2 rad without failing. As a result, progressive collapse is typically best examined using one of the direct design methods introduced in the next sections in which the loss of a load-bearing element is explicitly accounted for in the analysis. However, providing continuity through a building using ties is generally good practice and is often required in design guides for all importance levels or building classes to achieve a 'satisfactory' level of robustness.

### 8.2.2 ALPs for Static Analysis

The ALP design methodology using static analysis is often considered one of the most practical and best-suited procedures to assess structural robustness (Adam et al., 2018; McKay et al., 2012). In this methodology, either linear static (Section 8.2.2.2) or nonlinear material and geometric (Section 8.2.2.3) analyses are run.

As mentioned in Section 8.1, the ALP is a threat-independent design procedure for which the ability of the system to bridge over a removed load-bearing element is structurally assessed (Adam et al., 2018). Load-bearing elements are removed systematically one at a time, and the structural integrity of the building is then checked. The location of the elements to be removed and the number of removal scenarios to be analysed must include all potential threats. The DoD (2016) and IStructE (2010) provide guidance for the minimum number of column and wall load-bearing elements to be removed. The recommendations provided by the IStructE (2010) can be summarised as follows:

- The removed elements are each supporting column, any nominal length of load-bearing walls, and each transfer beam (i.e., a beam supporting one or more of the previous elements).
- Elements should be removed one at a time, on each storey, unless it can be shown that element removal on different storeys leads to similar results.
- If several columns are located within a plan diameter of nominal length, they should be removed simultaneously.
- In corners, the length of load-bearing walls removed should be equal to the storey height in each direction, but not less than the distance between expansion or control joints.

The nominal length of load-bearing walls to be removed varies among guidelines and is between 1 to 2.25 times the storey height.

#### *8.2.2.1 Dynamic Increase Factors*

Due to the often sudden removal of a load-bearing element, progressive collapse is essentially a dynamic event. The structure is therefore subjected to inertial loads, on top of the gravity loads, which must be captured by the analysis to accurately assess the structural integrity. In practice, these inertial loads are accounted for in static analyses by amplifying the gravity loads by a dynamic increase factor (DIF) (Tsai, 2010). The value of the DIF is chosen so that under a given gravity load, the static displacement of a structural system from the amplified loads matches the peak dynamic displacement. In other words, if a structural system results in a peak dynamic displacement of 100 mm under a given gravity load, and if the gravity load must be increased by 1.4 for the structure to also deform 100 mm statically, then the DIF is equal to 1.4. From matching the displacements, the stresses resulting from the static analysis would therefore reflect those experienced by the structure during the dynamic event. This methodology, however, assumes that the dynamic and static deformed shapes are the same, which may not always be the case.

Theoretically, the upper value of the DIF is 2.0 and corresponds to a system behaving elastically. When energy is dissipated through plasticity, the DIF decreases, and using a value of 2.0 would be conservative (Ruth et al., 2006). However, some structural responses, such as concrete slabs separating due to uplift and re-seating on their supports, can lead to a DIF greater than 2.0 (Arup, 2011). Studies are still needed to develop relevant and accurate DIF values for timber structures. Palma et al. (2019) proposed that a DIF of 1.5 be incorporated in the second generation of Eurocode 5 (CEN, 2004) based on numerical and analytical studies performed on timber structures (Mpidi Bita et al., 2018; Dietsch & Kreuzinger, 2016) and values reported for steel and concrete (Stevens et al., 2011; Stevens et al., 2012). Preliminary experimental studies performed by Cheng et al. (2021) appear to confirm this value; however, the authors encountered experimental DIF values greater than 2.0 when brittle failure modes developed at the connections. Brittle failure modes must be avoided, and the designer must pay special attention to the failure modes that could develop under a load-bearing element removal scenario. While a failure mode may be ductile under service loads, radically different stress patterns may lead to a less ductile failure mode under accidental loads.

While it is essential to consider the dynamic effects in static analyses for the reasons mentioned above, they are not always explicitly accounted for in design guidelines. It is therefore up to the designer to make informed decisions regarding the inertial forces in the analyses and the DIF value to use. The DoD (2016) recommends that the theoretical upper value of 2.0 be used for timber structures. The DIF value is only added to loads applied to the floors that deform dynamically (corresponding to the bays adjacent to the removed load-bearing element).

#### *8.2.2.2 Linear Static Analysis*

In linear static analyses, all structural elements and materials are assumed to behave elastically. Linear static analyses are run, and the resistance of each structural element is then compared to the force induced in the element from the accidental design load combination, according to the relevant design specification. While this approach is simple and valid for minor levels of plasticity, it may be extremely conservative for systems that offer structural redundancy and load redistribution (Arup, 2011). Examples of models based on linear static analysis are provided in Sections 8.3 and 8.4.

#### *8.2.2.3 Nonlinear Static Analysis*

In nonlinear static analyses, the ductility of structural elements and connections is modelled through nonlinear load-deformation curves, such as linear elastic-perfectly plastic, linear elastic-multilinear plastic, or linear elastic-multilinear plastic with strength degradation (Figure 5). Note that the more nonlinearity is introduced in the model, the more the load is redistributed and the more precise the structural response is. However, considering that strength degradation is computationally expensive, it often leads to convergence issues and requires expertise. Moreover, strength degradation is only implemented in comprehensive finite element (FE) software packages, which are mainly used in academia and specialised industries. These programs are not always available in design offices. Strength degradation will not be accounted for in the examples covered in this chapter; however, Lyu (2021) details a model of post-and-beam mass timber buildings incorporating strength, for interested readers. In a design situation, linear elastic-perfectly plastic load-deformation curves would typically be inputted for ductile connections, both for simplicity and to work within the limitations of most commercial software, as mentioned above.

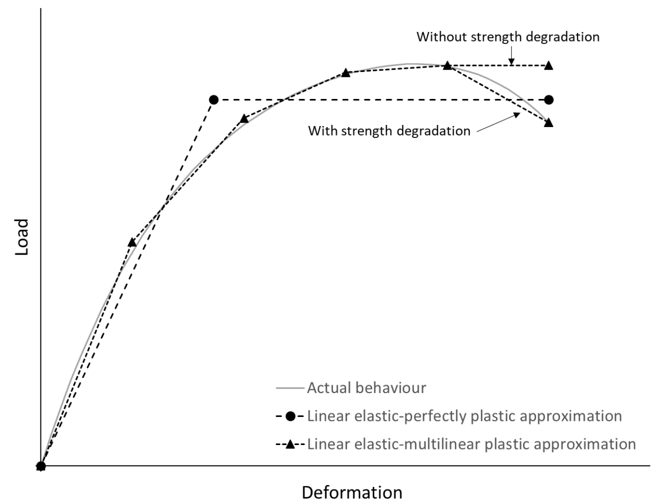


**Figure 5. Examples of linear elastic-perfectly plastic and linear elastic-multilinear plastic approximations**

Regarding timber structures, introducing nonlinearity would principally consist of modelling plasticity in the connections, as timber material in bending, shear, and tension is essentially brittle and thus best modelled elastically. However, in hybrid steel-timber structures, yielding of the steel would be typically accounted for using linear elastic-perfectly plastic stress-strain curves. This approach also implies that the ductile behaviour of the structural elements is known either through experimental testing, quantitative analysis, or other means. If data on ductility is not available, then the elements would have to be conservatively modelled as brittle. Brittle structural elements are considered to behave elastically in an analysis.

A structure should be modelled in three dimensions, and nonlinear material and geometric (i.e., accounting for second-order geometric nonlinearity, also known as the P-Δ effect) analyses shall be run. These types of analyses allow ductile elements to deform plastically and the load to be redistributed through the system. They also allow the load to be resisted through catenary action under large deformation. Enough sub-load increments must be computed for the structural response to be correctly captured, and FE software that incorporates both material and geometric nonlinearity must be used.

In terms of design, two types of demand-to-capacity structural checks must be performed:

(1) For ductile elements, the deformation of each element must not exceed the deformation capacity.

(2) For brittle elements, the loads must not exceed the design strength.

Both checks are performed in accordance with the relevant design specifications. Examples of deformation acceptance criteria for various timber components are provided in the *Seismic Evaluation and Retrofit of Existing Buildings* (ASCE/SEI 41-13) standard (ASCE, 2013).

### *8.2.2.4 Nonlinear Static Pushover Analysis with Simplified Dynamic Response*

The nonlinear static pushover analysis, also referred to as the pseudo-static response (Izzuddin et al., 2008), uses the static load-displacement response to determine the dynamic response of the system (Izzuddin et al., 2008). After removal of a load-bearing element, the energy balance between the gravitational energy release and energy absorption in the structure is used to calculate the dynamic response (Byfield et al., 2014). This method is not proposed in design guidelines and must be used with caution. Preliminary results performed on 2D post-and-beam timber frames by Cheng et al. (2021) found that the pseudo-static response inconsistently predicted the actual dynamic response.

Contrary to the static analyses described in Sections 8.2.2.2 and 8.2.2.3, in which the DIF value must be defined before the analysis and applied to the accidental load combination on the floors that deform dynamically, only the static accidental load combination (i.e., without a DIF) is applied to the building in the nonlinear static pushover analysis. The pseudo-static response is obtained in two steps, which are illustrated in Figure 6:

(1) The nonlinear static load versus displacement of the removed element response would be established by performing nonlinear geometric and material static analysis.

(2) The pseudo-static response (i.e., corresponding to the maximum nonlinear dynamic response [Izzuddin et al., 2008]) would be determined from the nonlinear load displacement curve. This is done by, for any given displacement, equating the work done by a constant gravity load *P* at its maximum dynamic displacement $U_{dyn}$ (hatched area in Figure 6) to the energy absorbed statically by the system under the same displacement (dotted area in Figure 6). If a solution cannot be found, the energy released after sudden removal of the element cannot be balanced by the internal energy, and collapse will occur at this applied load.

At a given displacement $U_{dyn}$, the difference between the two curves corresponds to the DIF, as shown in Figure 6. This calculation procedure considers dynamic effects as well as beneficial load redistribution mechanisms, but it does not require as great a computational effort as the non-linear dynamic procedure presented in the following section. Damping and material strain rate effects, however, are not considered by the procedure.

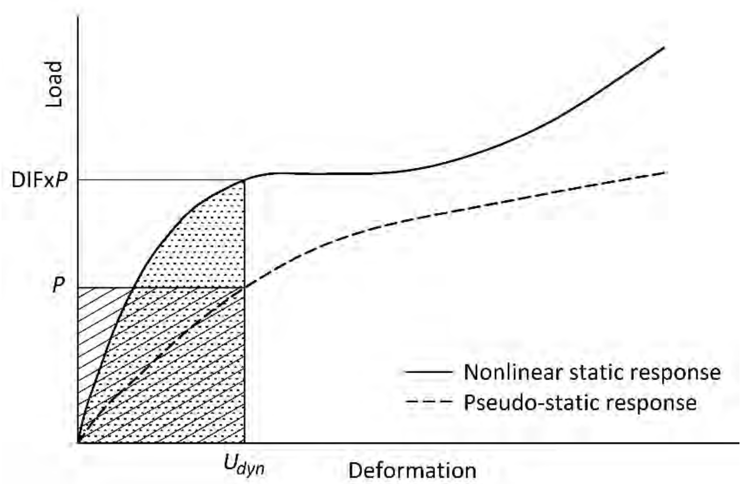


**Figure 6. Pseudo-static response**

### 8.2.3 ALPs for Dynamic Analysis

The FE model in this approach is similar to the one described in Section 8.2.2.3, but nonlinear material and geometric dynamic analyses are run. Strain rate enhancement can also be modelled. Gravity loads are first applied to the structure by allocating a density to the structural elements, with the value of the density calculated to match the dead and live loads. Alternatively, a gravity load can be simulated by applying masses to the system, which would be subjected to the gravity acceleration.

The analysis is typically run in two steps:

(1) The gravity load would first be applied quasi-statically to an undamaged building.

(2) A selected load-bearing element would then be suddenly removed, typically in a time less than 1/10 of the natural period of the structure (GSA, 2016; DoD, 2016), to let the structure dynamically deform freely. Energy absorption would typically be factored in using Rayleigh damping, with a critical damping ratio of 3% recommended for wood buildings with finish (Hu et al., 2019).

The nonlinear dynamic analysis approach is complex and requires significant expertise in structural dynamics (Arup, 2011). While it may not be the most commonly used design approach, it is considered the most rigorous (Arup, 2011; Byfield et al., 2014) and is more suited for academic purposes. It allows inertial forces to be captured correctly without the need for a DIF value, more accurately reproducing the dynamic response and structural deformation. This approach would enable, for instance, a better understanding of overall structural behaviour and ultimately the development of design recommendations. It has been reported widely in academic publications on steel and reinforced concrete buildings. Demand-to-capacity structural checks similar to those discussed in Section 8.2.2.3 would be performed at the maximum dynamic deformation or generated stress.

While this approach is not further detailed in this chapter, the models presented in the advanced analysis methods in Sections 8.3 and 8.4 can be expanded for dynamic analysis using the recommendations mentioned in the steps above. Examples of dynamic analysis for mass timber buildings can be found in Mpidi Bita et al. (2018) and Mpidi Bita & Tannert (2019a).

### 8.2.4 Key Elements

The second direct design method (Figure 3) is to design the load-bearing elements as key elements, and to make them strong enough to directly withstand a prescribed hazard loading and survive the event (IStructE, 2010). This approach would principally be used when:

- The loss of a load-bearing element would result in a large area (typically greater than 100 $m^2$, or 15% of the floor area across two adjacent storeys) of the building being damaged (i.e., disproportionate collapse, such as the loss of a transfer beam) (IStructE, 2010);
- A load-bearing element is carrying a large proportion of the total structure; or
- The ALP approach proved ineffective.

Despite the term ‘key elements’ being taken directly from the Eurocode standards, this approach is analogous to other international approaches that use differing terminology, such as ‘hardening’, ‘enhanced local resistance’, etc. (Huber et al., 2019). It is important to note that this approach generally applies to post-and-beam and post-and-plate building typologies as they offer a lesser degree of redundancy than other systems.

Eurocode likely covers the design of key elements the most explicitly and recommends that these elements be designed to withstand a design pressure of 34 kPa, in addition to the loads that the elements are already carrying under the accidental load case combination. The pressure is applied directly over the surface of the elements (in the horizontal and vertical directions, one direction at a time) and any attached items (CEN, 2006). This value comes from forensic investigations into the Ronan Point collapse (the partial collapse of a 22-storey apartment building in Canning Town, East London, UK), in which the findings estimated that the static equivalent of the explosion was 34 kPa (IStructE, 2010). Note that this is a recommended design pressure, and a specific blast pressure should be determined if necessary. Also, this maximum design pressure may not always result in the critical design actions to be accounted for in key elements due to the presence of ancillary building elements tied to the key element being examined. For example, if a column has full-height, non–load-bearing walls fixed to it, which are capable of resisting and transmitting loads resulting from a maximum of 10 kPa static pressure, then, subject to the geometry, the design actions may be higher than those for the 34 kPa pressure (wherein non–load-bearing walls would be 'blown away'). For scenarios like this, an iterative approach must be used to determine the critical design case. To avoid unreasonably high loads, IStructE (2010) recommends that 34 kPa be applied on a maximum area spanned by two nominal lengths of $2.25H$, where $H$ is the storey height (i.e., usually limited to an area of 6 m × 6 m for 2.7 m storey height).

In addition, the exposure and vulnerability determined during the robustness assessment of a building should be used to determine the appropriate loads to be applied to the elements being designed as key elements. For example, if there are columns that are exposed to heavy vehicle traffic, then a point load with a magnitude proportionate to the impact force of such vehicles should be applied to the columns (at a height deemed appropriate for the impact—0.5 m and between 0.5 and 1.5 m recommended for cars and trucks, respectively) (CEN, 2006). On the contrary, it would not be necessary to design columns on levels that are not exposed to such risks and therefore such design loads.

For transfer beams, the consequence of failure would generally be significant. If a transfer beam carries a large portion of a building, it is appropriate to design it as a key element.

Once the appropriate key element loads are determined, the analysis of the structure can be carried out using linear static principles and relevant codes and standards.

### 8.2.5 Redundancy

Redundancy is a design strategy that ensures the existence of ALPs, creating a structural system that is statically indeterminate, with several members acting in parallel when loaded (IStructE, 2010). Redundancy may be 'active', where the load is shared among parallel members already at low load levels, or 'passive or fail-safe', where the parallel members only take up loads after a certain amount of damage in the system (IStructE, 2010). Light wood-frame structures with numerous lumber and ductile nailed connections are an example with a significant amount of structural redundancy.

Redundancy may also have a detrimental effect on structural robustness. Munch-Andersen & Dietsch (2011) discuss the detrimental effects of structural redundancy by presenting two cases of timber building collapse.

By redistributing the load in a collapse situation, redundancy may promote progressive collapse. The authors claim that a less redundant design would have enhanced the robustness of one of the two analysed buildings. To avoid global redundancy and breaking continuity, building segments may be structurally isolated from each other, as discussed in Section 8.2.6.

### 8.2.6 Compartmentalisation

Compartmentalisation is a design strategy that consists of dividing a structure into independent structural compartments which are themselves robust. This is also referred to as 'isolation by segmentation' (Starossek & Haberland, 2010), or a second level of defence (Ellingwood et al., 2007). Compartment borders are either strengthened to sustain high loads (i.e., designed as key elements, discussed in Section 8.2.4, for effective compartment borders), or their continuity is reduced to allow large displacements (Starossek, 2006). Structural fuse elements may limit the transferred forces between compartments to a certain level and thus may be used to avoid collapse progression from one compartment to the next.

A compartmentalised design may be suitable if structural collapse resulting from local failure must be limited to an acceptable extent. For large, horizontally aligned timber structures (e.g., bridges and stadiums) with low height, horizontal progression of the collapse may be limited by compartmentalisation. In tall timber buildings, the design of intermittent strong floors may be a compartmentalisation approach which is suitable for arresting debris falling.

ALP design and compartmentalisation are conflicting design objectives. An ALP design may be more suitable for vertically aligned structures (i.e., high-rise timber buildings), whereas compartmentalisation may be more adequate for horizontally aligned structures (i.e., bridges, hall buildings, and stadiums). However, as discussed by Voulpiotis et al. (2021), for tall timber buildings, a mixed design strategy can be used by considering a building as being broken down into compartments of several floors. If progressive collapse occurs in one compartment, the damage would be restricted to that compartment. The structure within each compartment would be designed under the ALP approach, while the boundary members of the compartment would be designed as key elements. Starossek (2006) states that the partial collapse of the Charles de Gaulle airport terminal in 2004 could have been avoided if a compartmentalised design were used, which would have limited ALPs.

## 8.3 SHEAR WALL SYSTEMS

### 8.3.1 General

Mass timber shear wall systems refer to buildings assembled from mass timber load-bearing walls and floors. CLT is usually used for the walls, while either CLT or LVL panels can be used for the floors. This structural system is well suited for use in residential buildings as the walls effectively partition the space. There are generally two types of these buildings:

(1) Balloon-type buildings, which have continuous walls extending multiple storeys and intermediate floors attached to them (Chen & Popovski, 2020); and

(2) Platform-type buildings, which have the floors of each storey directly resting on the walls below, creating a platform for the storey above and separating the continuity of the walls (Huber et al., 2020; Mohammad et al., 2019).

Of the two, platform-type buildings are probably the more common construction type due to their ease of erection, simpler connections, and well-defined load paths (Mohammad & Munoz, 2011; Mohammad et al., 2019). This type of building, shown in Figure 7, is the focus of this section.

**Figure 7. CLT shear walls with floors in Murray Grove, London, UK. (Courtesy of Waugh Thistleton Architects)**

Platform-type buildings are generally considered to be the category of mass timber buildings the least vulnerable to progressive collapse as they have a high potential to offer structural redundancy. However, careful design and detailing are required to ensure robustness (Hewson, 2016; Woodard & Jones, 2020). Due to their capability in offering ALPs, they are best designed using the ALP design method. Nevertheless, Mpidi Bita & Tannert (2019b) present a theoretical tie-force procedure.

This section presents two ALP modelling approaches. The first consists of clearly identifying the ALPs and designing the accidental loads to be resisted solely by one of these load paths. Linear static analysis is used in which the critical parts of the structure are modelled and analysed using structural mechanics principles. This simplified analytical method is presented in Section 8.3.2. In the second approach, the entire building, or a representative part of it, is modelled using FE analysis, allowing more complex ALPs to resist the load. Nonlinear geometric and material static analyses are taken into account. This advanced analysis method is presented in Section 8.3.3 and would result in more economical buildings if progressive collapse governs the design. Sections 8.3.2 and 8.3.3 reference CLT as the wall and floor systems; however, other mass timber products can also be used in such applications. The presented design philosophies are still applicable.

## 8.3.2 Simplified Analytical Method (Linear Static ALP)

Two alternate load-resisting mechanisms are mainly accounted for in the design of robust platform-framed CLT buildings, namely, (1) those with two-bay-long CLT floor panels spanning over the missing element, and (2) those with walls acting as deep beams (Hewson, 2016; Huber et al., 2020; Woodard & Jones, 2020). This section presents modelling for these two ALPs.

### *8.3.2.1 ALP 1: Two-Bay-Long CLT Floors*

Using two-bay-long CLT floors is a good design practice for mass timber buildings. In the event of the loss of a load-bearing element, the floors can then provide an ALP either by acting as simply-supported elements, spanning twice the bay length, when the removed wall is located in the middle of the panels (Figure 8), or as simply-supported elements with a one-bay-long overhang, when the removed element is located at one end of the panels (Figure 9 and Figure 10).

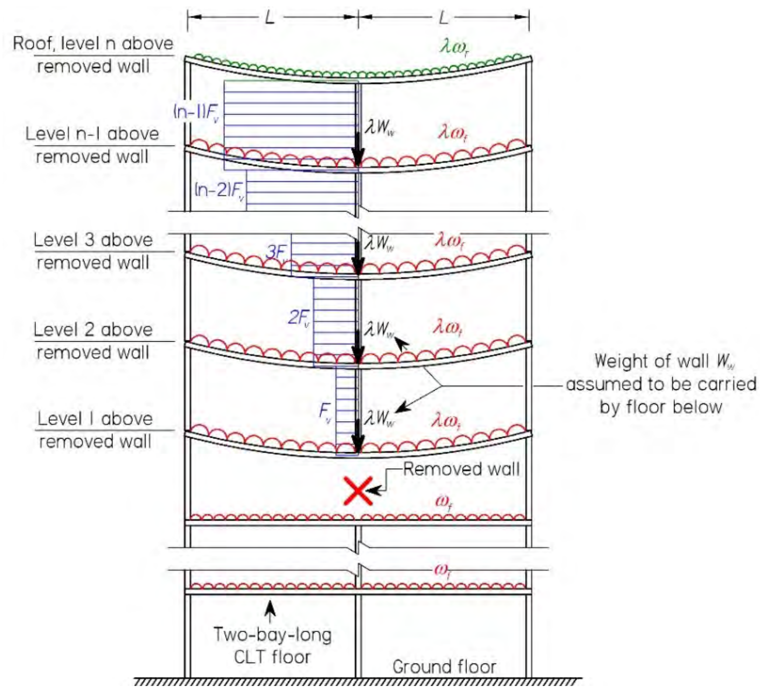


**Figure 8. Accidental load-resisting mechanism using two-bay-long CLT floor panels for platform-framed CLT buildings when an internal wall is removed in the middle of the panels**

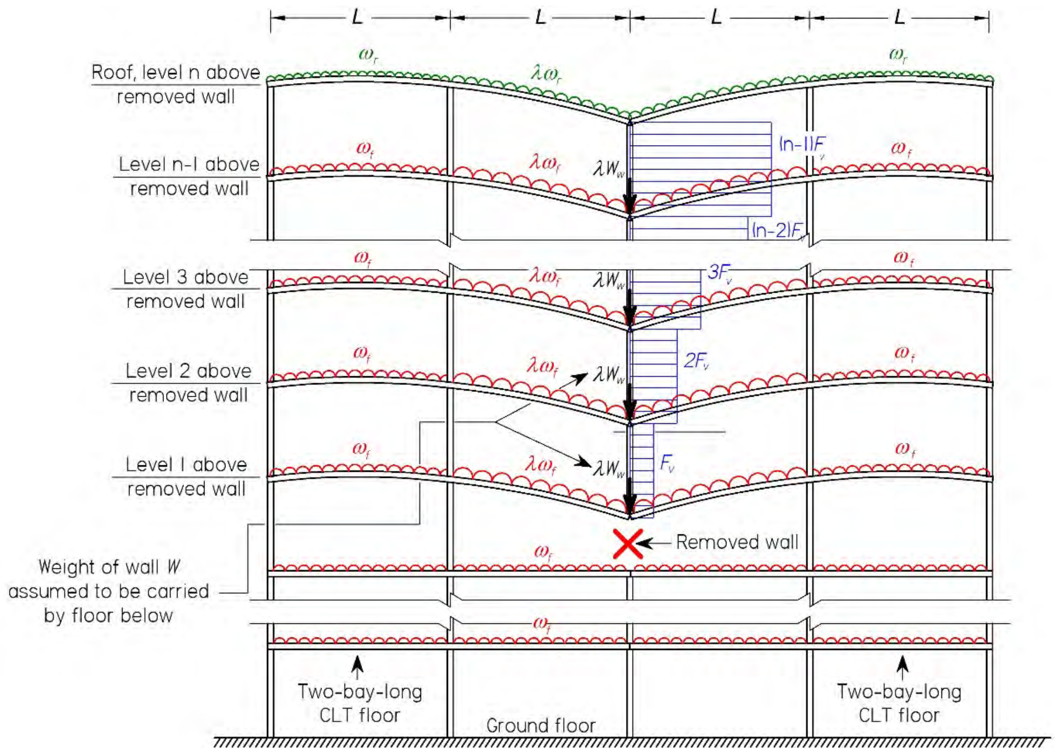


**Figure 9. Accidental load-resisting mechanism using two-bay-long CLT floor panels for platform-framed CLT buildings when an internal wall is removed at the end of the panels**

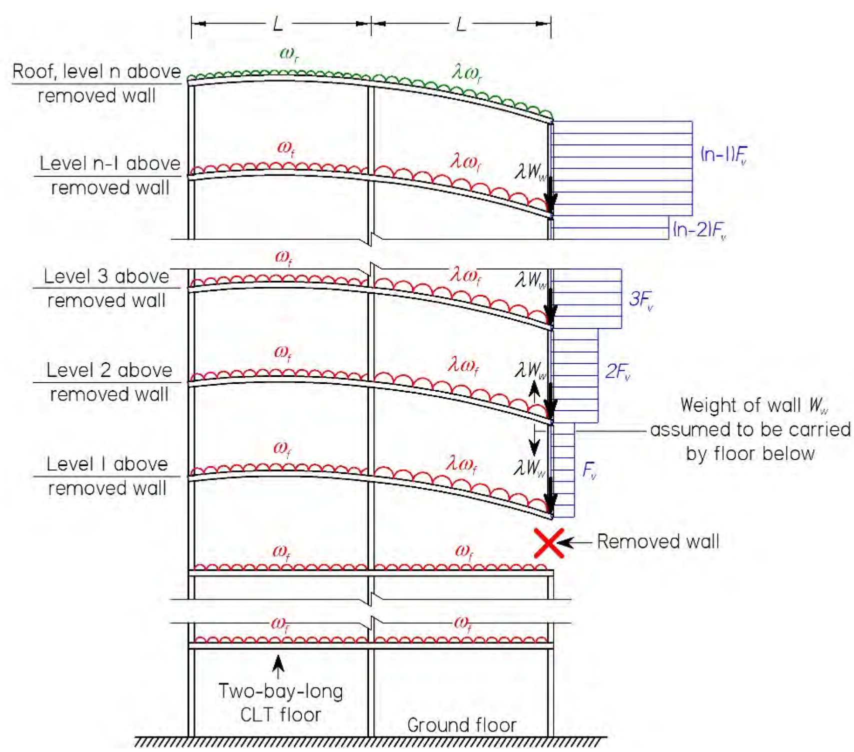


**Figure 10. Accidental load-resisting mechanism using two-bay-long CLT floor panels for platform-framed CLT buildings when an external wall is removed at the end of the panels**

The loads acting on each floor can be analytically calculated by understanding the behaviour of the building under a load-bearing element removal scenario. In a regular building, in which each floor has the same function, all floors have the same design dead and live load values, and therefore the same accidental design load. Hence, after the loss of a load-bearing element, all floors theoretically deform in the same way, and the axial force in the vertical elements directly above the removed one is null (Xue et al., 2018). Using the ALP method, each two-bay-long floor could therefore be designed to resist solely its own accidental design load, not the design loads from the floors above. In reality, the live load on the roof would be lower than the one applied to the floors, and the roof panels would be thinner. If the roof were not linked to the storeys below, it would deform differently than these storeys. But as vertical elements link the storeys together, all storeys deform the same way (assuming stiff wall-to-floor and wall-to-roof connections, as discussed later in this section). This results in axial forces in the vertical walls above the removed one, as shown in Figure 8, Figure 9, and Figure 10, for different load-bearing removal scenarios. In reference to these figures, the axial force $F_v$ is calculated as:

$$\boldsymbol{F_v} = \frac{5\lambda}{4}\boldsymbol{L}\left(\frac{\omega_f(EI)_r - \omega_r(EI)_f}{(EI)_r + (n-1)(EI)_f}\right) + \frac{(EI)_r\lambda W_W}{(EI)_r + (n-1)(EI)_f} \quad \text{for Figure 8} \tag{2}$$

$$\boldsymbol{F_v} = \frac{7\lambda - 1}{8}\boldsymbol{L}\left(\frac{\omega_f(EI)_r - \omega_r(EI)_f}{(EI)_r + (n-1)(EI)_f}\right) + \frac{(EI)_r\lambda W_W}{(EI)_r + (n-1)(EI)_f} \quad \text{for Figure 9} \tag{3}$$

and

$$\boldsymbol{F_v} = \frac{7\lambda - 1}{16}\boldsymbol{L}\left(\frac{\omega_f(EI)_r - \omega_r(EI)_f}{(EI)_r + (n-1)(EI)_f}\right) + \frac{(EI)_r\lambda W_W}{(EI)_r + (n-1)(EI)_f} \quad \text{for Figure 10} \tag{4}$$

where $\omega_f$ and $\omega_r$ are the accidental design uniformly distributed loads (UDLs) applied to the floors and roof, respectively; $W_w$ is the weight of the wall above the removed one, assumed to be carried by the floor below it and acting as a point load; $\lambda$ is the DIF value applied to the elements in the bays adjacent to the removed wall (DoD, 2016); $(EI)_f$ and $(EI)_r$ are the bending stiffness of the CLT floors and roof, respectively, which can be calculated using the methodology given in Gagnon & Popovski (2011) or Blass & Fellmoser (2004); $L$ is the bay span; and $n$ is the number of levels (including the roof) above the removed element. If $F_v$ is positive, then the vertical elements above the removed one are in tension.

In this simplified method, the two-bay-long floors and roof can be modelled as simply-supported beams and designed to resist their accidental floor loads, the weight of the wall above the removed one, plus the axial forces applied to them by the walls above the removed one (Equations 2 to 4). Nevertheless, because Equations 2 to 4 assume axially stiff connections between walls, which cannot always be guaranteed for typical CLT-to-CLT connections (Mohammad & Munoz, 2011), the axial forces calculated from these equations represent the upper bound values of $F_v$. Therefore, unless stiff CLT-to-CLT connections can be guaranteed, if the vertical elements above the removed one are in tension ($F_v$ positive), then $F_v$ should be conservatively ignored in the floor design but applied to the roof design. Inversely, if the vertical elements are in compression ($F_v$ negative), $F_v$ should be conservatively ignored in the roof design but applied to the floor design. The models are summarised in Figure 11 and Figure 12.

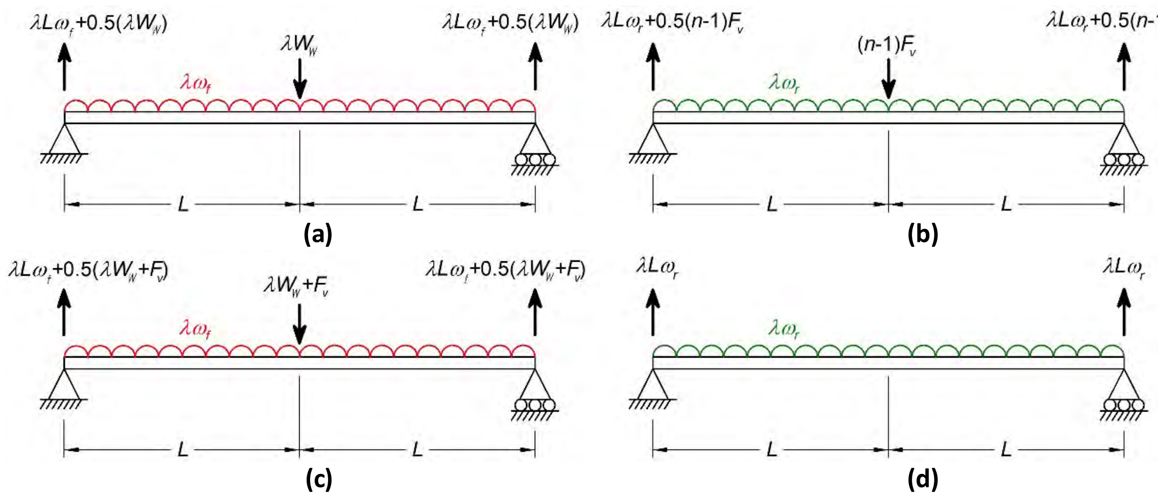


**Figure 11. Simplified model of the two-bay-long CLT panels used as the load-resisting mechanism for platform-framed CLT buildings when an internal wall is removed in the middle of the panels: (a) floor model when $F_v$ is in tension, (b) roof model when $F_v$ is in tension, (c) floor model when $F_v$ is in compression, and (d) roof model when $F_v$ is in compression. The absolute value of $F_v$ was used in these diagrams**

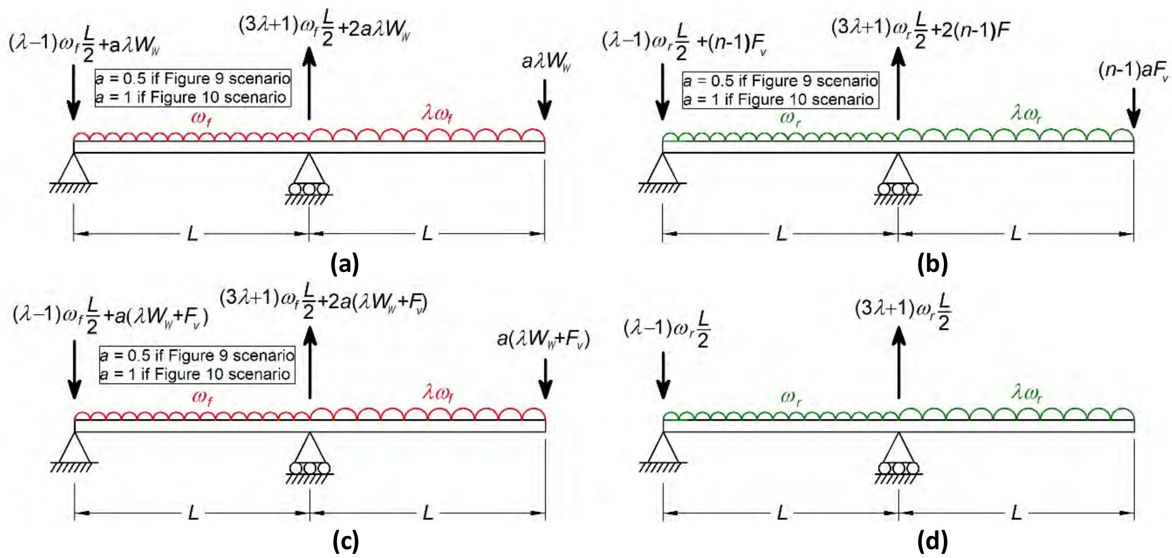


**Figure 12. Simplified model of the two-bay-long CLT panels used as the load-resisting mechanism for platform-framed CLT buildings when an internal or external wall is removed at the end of the panels: (a) floor model when $F_v$ is in tension, (b) roof model when $F_v$ is in tension, (c) floor model when $F_v$ is in compression, and (d) roof model when $F_v$ is in compression. The absolute value of $F_v$ was used in these diagrams**

### *8.3.2.2 ALP 2: Walls as Deep Beams*

If the building layout prevents having two-bay-long CLT floors, or if the two-bay-long floors cannot resist by themselves the loss of a load-bearing element, the walls above the removed element can be designed to act as deep beams (Hewson, 2016; Huber et al., 2020). These walls will then span over the removed one below (Figure 13), and due to their height, will act as efficient beams. However, they must be sufficiently restrained so they do not buckle laterally (Hewson, 2016). This restraint can be achieved by adequately fixing the wall panel to the adjacent perpendicular wall and floor panels. Each wall can be conservatively modelled as simply-supported and designed independently to support and carry the accidental loads from the floor below. Note that the top storey wall would need to carry the accidental loads from both the floor below and the roof above, and it may be the more critical element.

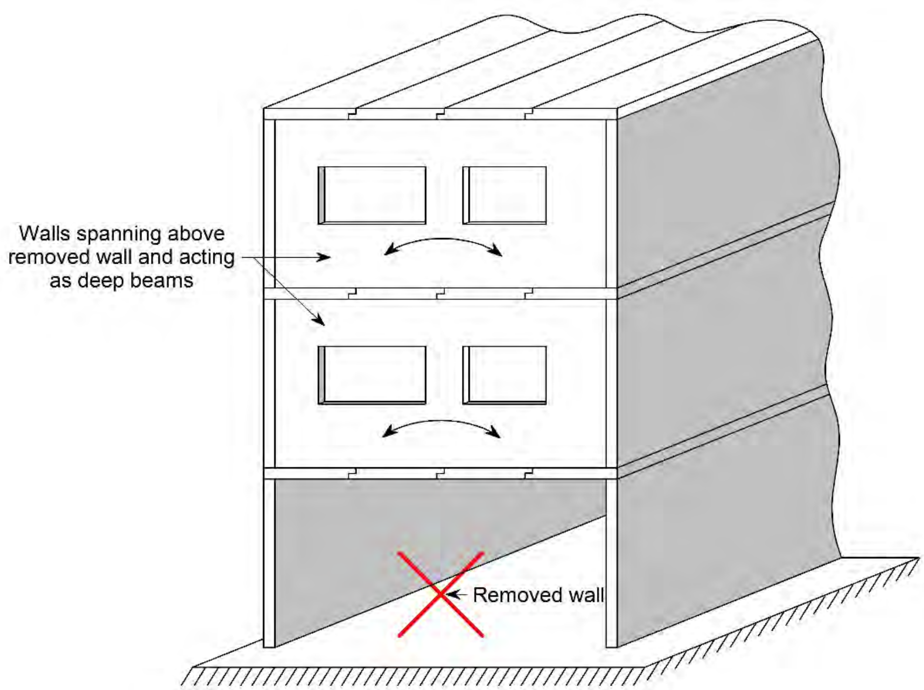


**Figure 13. Accidental load-resisting mechanism using walls as deep beams for platform-framed CLT buildings. (From Hewson, 2016)**

Supports must be provided to the deep beam walls. Huber et al. (2020) numerically showed that the CLT floors at the wall-to-floor interface are efficient in locally providing support to the walls above, as shown in Figure 14. For such mechanisms to develop, the local crushing resistance and shear strength of the CLT floors must not be exceeded. As this localised support may not be straightforward to design for, another approach is to provide enough shear capacity in the wall-to-wall connections, as shown in Figure 14.

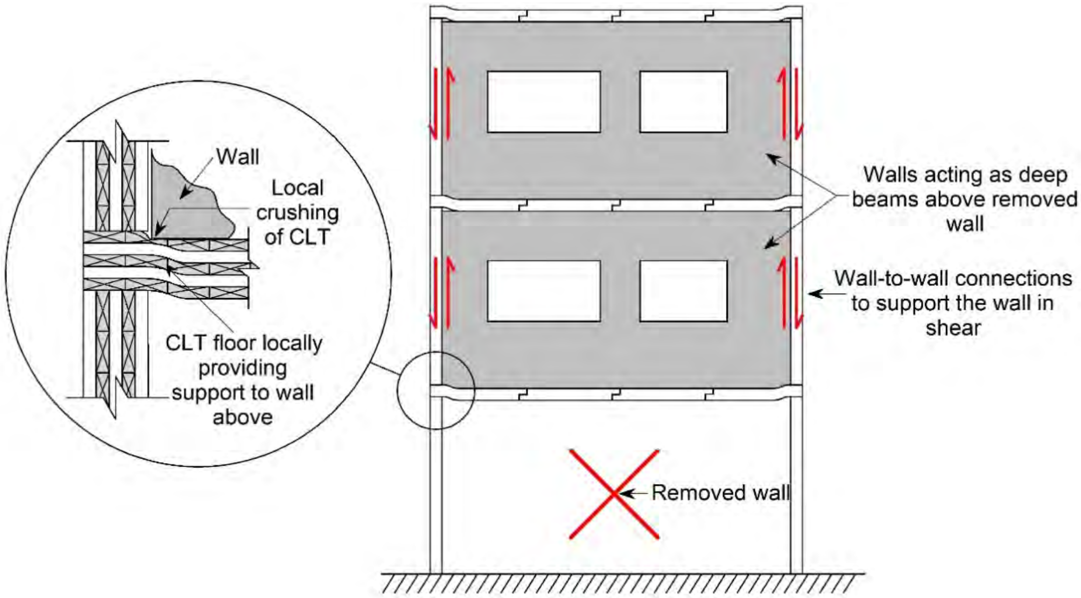


**Figure 14. Supports provided to deep beam walls**

Figures 15(a) and 15(b) show the simplified analytical models for the top-storey wall and remaining walls above the removed element, respectively. The tributary area used to calculate the UDL $\omega_f$ and $\omega_r$ applied to the walls in Figures 15(a) and 15(b) and arising from the one-bay-long floor and roof accidental design loads, respectively, if an external wall is removed, is shown in Figure 15(c). If an internal wall is removed, this tributary area must be multiplied by 2. In the figure, $\lambda$ is the DIF value.

Limit state design checks for the floors, walls, and roof should include:

- In-plane bending strength of the walls;
- Shear strength of the walls;
- Either local crushing of CLT floors or shear strength of the wall-to-wall connections to provide support to the walls and carry the reaction forces in Figures 15(a) and 15(b);
- Axial tensile strength of the floor-to-wall connections so that the floors can be hung from the walls above; and
- Bending and shear strength of the CLT floor and roof panels.

If the walls contain joints, they need to be designed for the walls to act as deep beams.

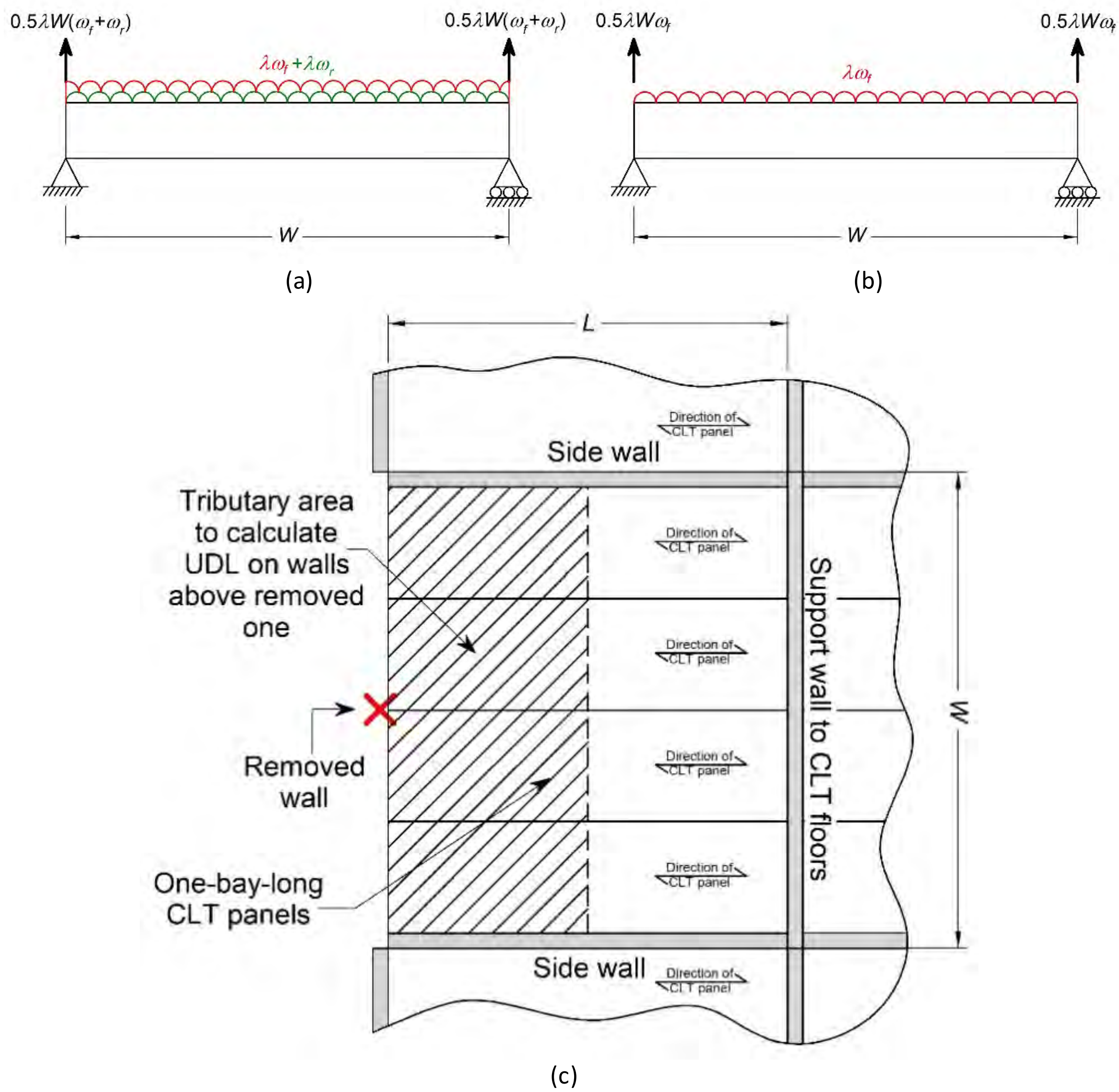


**Figure 15. Simplified model of CLT walls used as the load-resisting mechanism for platform-framed CLT buildings: (a) model using top-storey wall, (b) model using the remaining walls, and (c) the tributary area to be considered when calculating $\omega_f$ and $\omega_r$**

### 8.3.3 Advanced Analysis Method (Nonlinear Static ALP)

As discussed in Section 8.2.2, the aim of the advanced analysis is to model the entire building, or a representative part of it, to capture all ALPs and their contributions in resisting the loss of a load-bearing wall. Huber et al. (2018) and Huber et al. (2020) report a similar approach for platform-framed CLT buildings.

As mentioned in Section 8.2.2.3, nonlinearity principally arises from the connections between elements. For this purpose, the 'component' approach would ideally be used to model these connections. In such FE models, each connection is replaced by a spring (or a series of springs, also referred to as connectors) representing the structural response of the different components (or a group of components) of the connection. The load-deformation curve of the components is assigned to the relevant spring.

Depending on the governing failure mode, brittle or ductile behaviour would be factored in for the connections. Ideally, the computed load-deformation curves for the connections (see Section 8.2.2.3) would result from experimental data (provided by the manufacturer of the fasteners, for instance) to best reproduce the overall structural response of the building and the ALPs. Such curves should be used by a researcher aiming to develop more reliable models. However, as these curves are often not available, the connections can be modelled by (a) calculating the stiffness of dowel-type connections (dowels, bolts, screws, or nails) from relevant design specifications (e.g., Eurocode 5 [CEN, 2004]), and (b) obtaining the capacity either from the design specifications in place or from the manufacturer (preferred). Huber et al. (2018, 2020), and Mpidi Bita & Tannert (2019a) followed this approach. It is also followed in this chapter to illustrate the advanced analysis method and would be appropriate in a design context. However, note that such an approach presents high uncertainty regarding the behaviour of the connections, and such uncertainty should be considered in the design through sensitivity analysis, for instance.

In some cases, such as butt joints, the stiffness and capacity would also depend on whether the connection opens or closes. When the connection closes, the two connected elements are in contact, and the connection would be stiff. Bearing failure of the timber, not failure of the fasteners, would then govern the design. Table 1 provides the model parameters for some typical CLT-to-CLT screwed connections (Mohammad et al., 2019) used in platform-framed CLT buildings; these parameters are based on Eurocode 5 (CEN, 2004) and the design equations in European Technical Assessment (ETA) ETA-12/0063 (Deutsches Institut für Bautechnik [DIBt], 2012) and ETA-12/0373 (DIBt, 2012). In the table, the translational stiffness $k_x$, $k_y$, and $k_z$, and the capacities $R_x$, $R_y$, and $R_z$, are given relative to the local coordinate system of the fastener. For a group of fasteners, the stiffness values can be multiplied by the number of fasteners $n$ in the group, and the capacity by the effective number of fasteners $n_{eff}$, as per Clause 8.1.2 of Eurocode 5. In practice, a spring would be modelled for each fastener or group of closely spaced fasteners. Rotational stiffness would typically be conservatively considered as null (pinned connection) unless data is available.

For more complex connections, such as angle brackets used to connect the floor to the wall above (Figure 16), in the absence of experimental data provided by the manufacturer, a separate, refined FE model of the bracket itself can be built to obtain its stiffness and potentially its capacities. Huber et al. (2020) modelled a bracket with shell elements and used spring elements to model the nails connecting the bracket to the CLT. The nonlinear load-displacement behaviour of the nails was taken from the literature (Izzi et al., 2018). The CLT wall and floor were modelled with solid elements, and surface-to-surface contacts were used between the bracket and the CLT. To obtain the capacities, plasticity was inputted for the bracket material, and to obtain the load-displacement and moment-rotation curves in four degrees of freedom, one CLT element was either translated or rotated relative to the other. These curves were then used as input values for the spring, substituting the brackets in the overall model. Figure 16(b) shows the FE model in Huber et al. (2020).

(a)
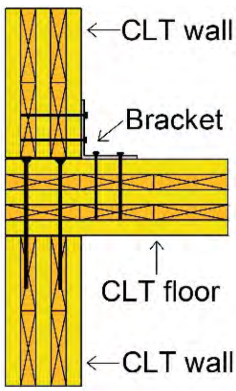


(b)
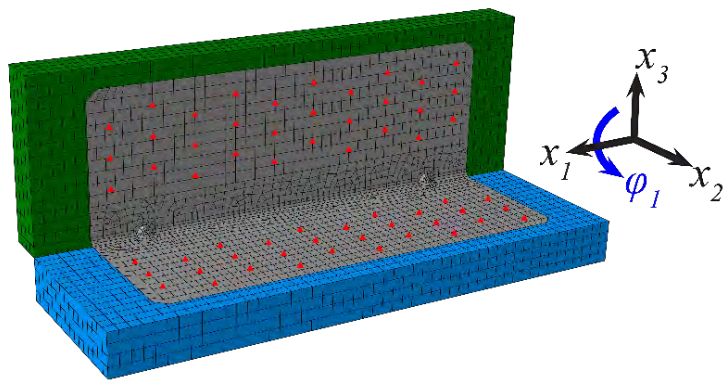


**Figure 16. Angle brackets connecting the floor to the wall above: (a) principle adapted from Mohammad et al. (2019), and (b) FE model of an angle bracket used by Huber et al. (2020)**

Figure 17 illustrates the principles of the FE model using the component approach. As mentioned in Section 8.2.2, nonlinear geometric and material analyses are run. The CLT panels can be modelled as layered shell elements to best reproduce the membrane and bending stiffness. The gravity loads corresponding to the accidental load combination are applied as uniformly distributed loads, and a DIF is factored in for the floors adjacent to the removed element, as discussed in Section 8.2.2.1.

**Table 1. Model parameters for screwed connections for platform-framed CLT buildings based on Eurocode 5 (CEN, 2004) and the ETA-12/0063 (2012) and ETA-0373 (2012) design equations[a]**

| Connection | Stiffness (N/mm) | Failure | | | Model |
|---|---|---|---|---|---|
| | | Governing mode | Type | Capacity | |
| Floor-to-floor<br>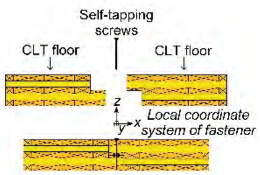 | $k_x = \rho_m^{1.5}d/23$ for connection opening | All failure modes for laterally loaded screws in Clause 8.2.2 of Eurocode 5 | Predominantly ductile | $R_x$ = Calculated as per Clause 8.7.1 of Eurocode 5 | Linear elastic-perfectly plastic |
| | $k_x = \infty$ for connection closing | Timber compression | Ductile | As per timber specification | Rigid |
| | $k_y = \rho_m^{1.5}d/23$ | All failure modes for laterally loaded screws in Clause 8.2.2 of Eurocode 5 | Predominantly ductile | $R_y$ = Calculated as per Clause 8.7.1 of Eurocode 5 | Linear elastic-perfectly plastic |
| | $k_z = 25l_{eff}d$ for connection opening | Withdrawal failure of the threaded part of the screw<br>Tear-off failure of the screw head<br>Tensile failure of the screw | Brittle | $R_z$ = Calculated as per relevant equations in Clause 8.7.2 of Eurocode 5 | Linear |
| | | Pull-through failure of the screw head | Ductile | $R_z$ = Calculated as per relevant equation in Clause 8.7.1 of Eurocode 5 | Linear elastic-perfectly plastic |
| | $k_z = \infty$ for connection closing | Timber compression | Ductile | As per timber specification | Rigid |
| Floor-to-wall below<br>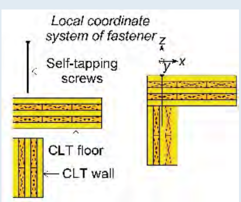<br>Wall-to-wall<br>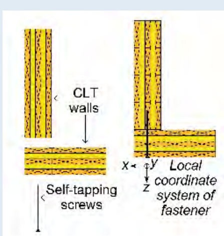<br>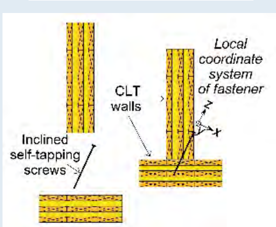 | $k_x = k_y = \rho_m^{1.5}d/23$ | All failure modes for laterally loaded screws in Clause 8.2.2 of Eurocode 5 | Predominantly ductile | $R_x = R_y$ = Calculated as per Clause 8.7.1 of Eurocode 5 | Linear elastic-perfectly plastic |
| | $k_z = 25l_{eff}d$ for connection opening | Withdrawal failure of the threaded part of the screw<br>Tear-off failure of the screw head<br>Tensile failure of the screw | Brittle | $R_z$ = Calculated as per relevant equations in Clause 8.7.2 of Eurocode 5 | Linear |
| | | Pull-through failure of the screw head | Ductile | $R_z$ = Calculated as per relevant equation in Clause 8.7.1 of Eurocode 5 | Linear elastic-perfectly plastic |
| | $k_z = \infty$ for connection closing | Timber compression | Ductile | As per timber specification | Rigid |

[a] Values provided per screw, per shear plane, and relative to the local coordinate system of the fastener.

$d$ = Fastener diameter in mm, $l_{eff}$ = Penetration length of the threaded part of the screw in mm and $\rho_m$ = Mean density of timber in kg/m$^3$

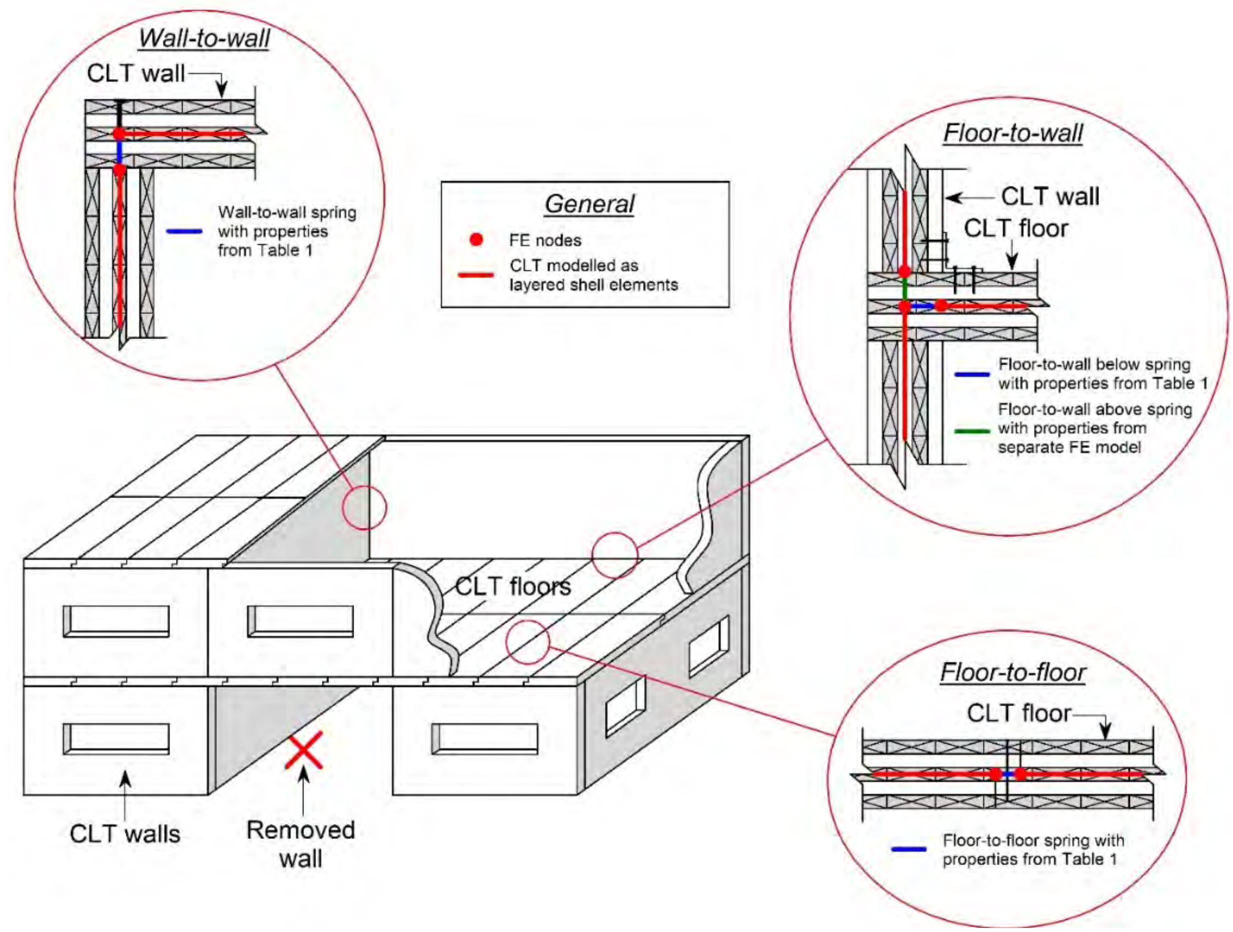


**Figure 17. FE modelling principles for platform-type CLT buildings and advanced analysis**

The design of the CLT panels would be performed similarly to all other load combinations. A brittle connection would pass the design check if the loads in the spring are lower than the design capacities of the connection. A ductile connection would pass the design check if the deformations of the spring do not exceed the design deformation capacities of the connection. As mentioned in Section 8.2.2.3, examples of deformation acceptance criteria for various timber components are provided in the ASCE/SEI 41-13 standard (ASCE, 2013).

## 8.4 POST-AND-BEAM SYSTEMS

### 8.4.1 General

Mass timber post-and-beam systems refer to buildings assembled from mass timber beams, columns, and floors. Glulam or LVL is primarily used for the beams and columns, while either CLT or LVL would be used for the floors. This structural system is well suited to office buildings as it provides open spaces. The beams run in one direction, and the floor panels span in the direction perpendicular to the beams. Additional periphery beams are provided in the direction of the floor panels on the sides of the building. Proprietary connectors are commonly used to connect the beams to the columns. They are typically designed to resist only the shear forces, not the bending moments, meaning that lateral stability must be ensured by other lateral load-resisting systems (e.g., shear walls or bracing systems). They are also rarely designed with robustness in mind (Lyu et al., 2020). The floor panels are screwed to the beams but are not directly connected to the columns. Figure 18 shows a photo of a mass timber post-and-beam building.

**Figure 18. Post-and-beam building with glulam beams and CLT floors in Brisbane, Australia. (Courtesy of Mahyar Masaeli)**

Mass timber post-and-beam buildings are deemed more vulnerable to progressive collapse than platform-type buildings as they have potentially less redundancy and fewer possibilities to redistribute accidental loads. Lyu et al. (2020) experimentally investigated the ability of (a) three types of beam-to-column connectors currently used in mass timber buildings and (b) one novel connector, especially designed with robustness in mind, to generate catenary action under a column removal scenario. The connectors are illustrated in Figure 19. While all the currently used connectors (Figures 19[a] to 19[c]) provided enough rotation for catenary action to potentially develop, they failed before this phenomenon could be taken advantage of and did not enable the beam-and-column system to resist the design accidental loads by itself. On the other hand, the novel connector (Figure 19[d]) allowed catenary action to fully develop and showed that robustness can be improved with the correct design approach. Lyu (2021) also experimentally investigated the structural behaviour of 3D post-and-beam substructures under a column removal scenario. The results showed that two-bay-long CLT panels represent critical elements for redistributing accidental loads through the building after the loss of a column. Various ALPs were found and are discussed in Section 8.4.3.

Mass timber post-and-beam buildings are best designed using either the ALP or the key element design method. This section presents two ALP modelling approaches, similar to the shear wall systems in

Section 8.3. The first consists of clearly identifying the ALPs and designing the accidental loads to be resisted solely by one of these load paths using structural mechanics principles and linear static analyses (see Section 8.4.2). The second approach consists of modelling the entire building, or a representative part of it, using the FE method, and running nonlinear geometric and material static analyses to best capture all ALPs (see Section 8.2.2.3). The key element method is presented in Section 8.4.4 and may result in more economical designs. Sections 8.4.2 to 8.4.4 reference CLT as the floor system; however, the presented design philosophies still apply to other mass timber products.

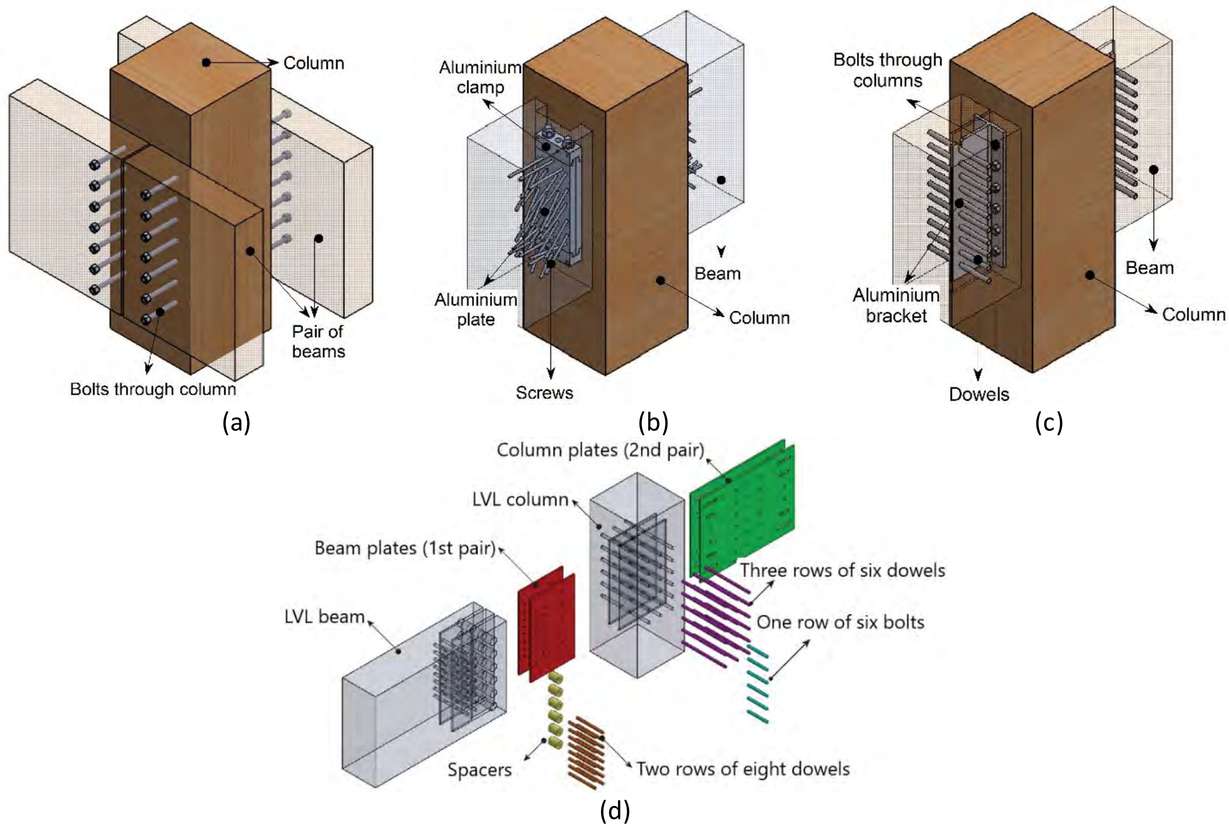


**Figure 19. Beam-to-column connectors investigated in Lyu et al. (2020): (a) double beams bolted through the columns, (b) Megant-type connectors, (c) aluminium bracket bolted through columns and dowelled to beams, and (d) novel connector allowing ductile failure to occur in aluminium plates**

## 8.4.2 Simplified Analytical Method (Linear Static ALP)

Two alternate load-resisting mechanisms are principally considered in the design of robust mass timber post-and-beam buildings, namely, (1) those with two-bay-long CLT floor panels spanning over the missing element, and (2) those with beams spanning more than one bay (Hewson, 2016). This section presents modelling for these two ALPs.

### *8.4.2.1 ALP 1: Two-Bay-Long CLT Floors*

This ALP is the same as the one described in Section 8.3.2.1 for platform-type CLT buildings. The beams connected to the removed column are assumed not to provide any support to the CLT floor and roof panels above. In practice, because the columns above the removed one are not directly connected to all panels, and because all side-by-side panels are assumed to deform independently of each other, the columns are not considered to be applying loads to the floors and roof the way the walls would in platform-type CLT buildings (Equations 2 to 4). The floor and roof panels are designed as simply-supported, with or without an overhang, depending on the location of the removed column.

Therefore, the models for CLT floor panels are the same as those shown in Figure 11(a) and Figure 12(a) when the column is removed in the middle and at the end of the panels, respectively, but with $W_W = 0$. For CLT roof panels, Figure 11(d) and Figure 12(d) apply.

Limit state design checks for the floors and roof should include, but are not restricted to:

- Bending and shear strength of the CLT floor and roof panels;
- When an element is removed at the end of a panel, the axial tensile strength of the floor-to-beam connections at the other end of the panel should be verified to ensure the structural integrity of the building; and
- Under large vertical deformations, CLT panels move horizontally, and the designer must ensure that either there is enough bearing support for the panels to rest on the beams below or that the floor-to-beam connections can be designed to resist the axial load that would eventually develop under large deformation.

Lyu (2021) found that the critical elements were the beams to which the accidental loads were transferred. Observed failure included bending failure of the beams and shear failure of the beam-to-column connections. The beams supporting the two-bay-long floor and roof panels must therefore be structurally checked. The reaction forces from the panels shown in Figures 11(a) and 11(d) and Figures 12(a) and 12(d) are then applied as a UDL to the supporting beams and are considered to be simply-supported. When the column is removed at the edge of the panels, the critical beam is the one located in the middle of the CLT panels. When the column is removed from the middle of the panels, the support beams not only have to support the reaction forces from the CLT panels, resisting the loss of the column, but also the reaction forces of the CLT panels located on the other side of the beams. Figure 20 illustrates the model used to calculate these reaction forces for a building with a minimum of four bays and where $L$ is the bay span. Denoting $W$ the beam span, and assuming that the accidental UDL $\omega_f$ applied to the CLT floor panels in Figure 12(a) and Figure 20 was calculated over beam span $W$, Figure 21 shows the models for checking the critical floor beam when an element is either removed from the middle of the two-bay-long panels or at their edge. The models presented in Figure 21 are also valid for the roof beams by using $\omega_f$ instead of $\omega_r$.

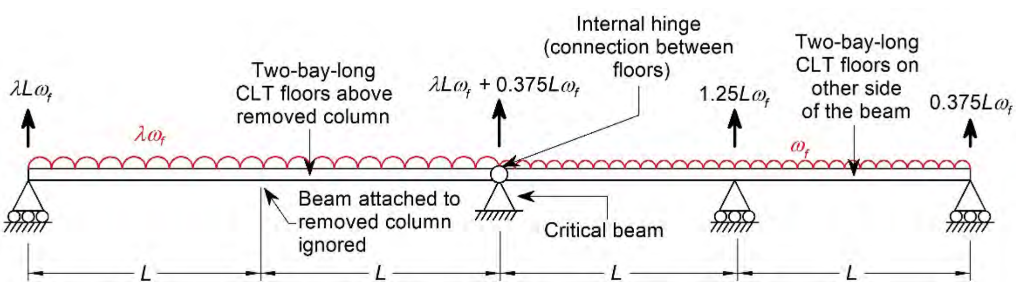


**Figure 20. Model of CLT floor panels for post-and-beam CLT buildings used to calculate reaction forces to be applied to the critical beam when a column is removed from the middle of the two-bay-long CLT floor panels**

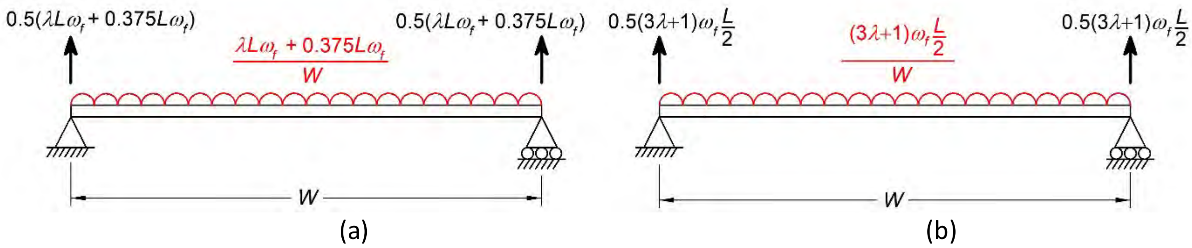


**Figure 21. Simplified model of the critical floor beam supporting the CLT floor panels for post-and-beam CLT buildings when an element is removed (a) from the middle of the two-bay-long panels or (b) at their edge. In the figure, the UDL $\omega_f$ applied to the floor panels is assumed to be calculated over the entire length (*W*) of the beam**

Limit state design checks for the critical beam should include, but are not restricted to:

- Bending strength of the beam; and
- Shear strength of the beam and beam-to-column connections.

Lyu (2021) found that the above design method was conservative and underestimated the experimentally measured failure load by a factor of more than 2.0 as it accounted for only one ALP of all available paths.

#### *8.4.2.2 ALP 2: Beams Longer than One Bay*

The second ALP allows having one-bay-long CLT floor and roof panels by having the beams span either two bays or 1.5 bays, and bridge over the removed column. The latter solution was used at the Library at the Dock in Melbourne, Australia, as discussed in Hewson (2016). In such a case, two 1.5-bay-long beams are splice-connected (only transferring shear) when they join between two columns. In these two solutions, when a column is lost, the continuous beams would still provide support to the floors if correctly designed. Typically, a pair of beams would run on either side of the columns (as in Figure 19[a]). While the beam layout provides continuity through the building, it has the disadvantage of exposing more timber surfaces that could be damaged in cases of fire than if one beam were used.

Figure 22 shows the simplified analytical models for the two-bay-long floor beams above the removed column when a column is removed either from the middle of the beams or at their edge. Similarly, Figure 23 illustrates the simplified analytical models for the 1.5-bay-long floor beams for two possible column removal scenarios (internal or edge support). Note that for the 1.5-bay-long beams in Figure 23, two beams must be modelled. Figure 24 illustrates the tributary area used to calculate the UDL $\omega_b$ applied to the beams and arising from the floor or roof accidental design loads for one-bay-long CLT panels, two-bay-long beams, and when an external column is removed. If an internal column is removed, this tributary area must be multiplied by 2. In the figures, $\lambda$ is the DIF.

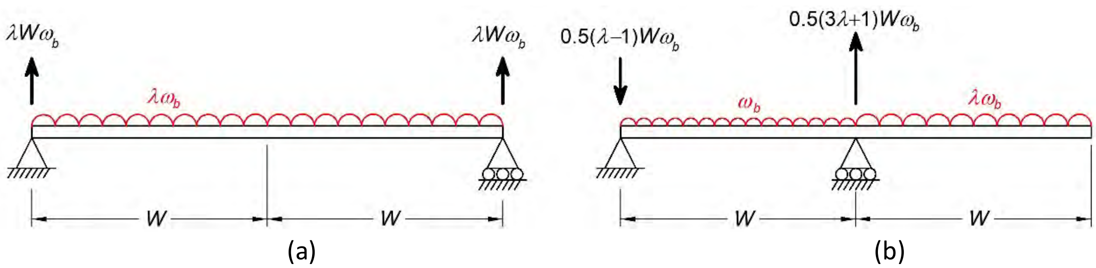


**Figure 22. Simplified model of the two-bay-long beams supporting CLT floor panels and used as the load-resisting mechanism for post-and-beam CLT buildings when an element is removed (a) from the middle of the beams or (b) at their edge**

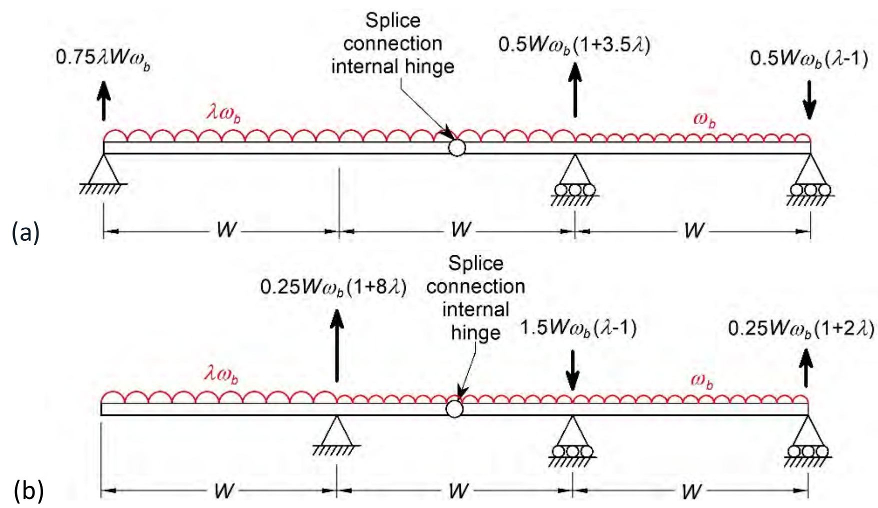


**Figure 23. Simplified model of the 1.5-bay-long beams supporting CLT floor panels and used as the load-resisting mechanism for post-and-beam CLT buildings when an element is removed (a) from the internal support of the beams or (b) at their edge**

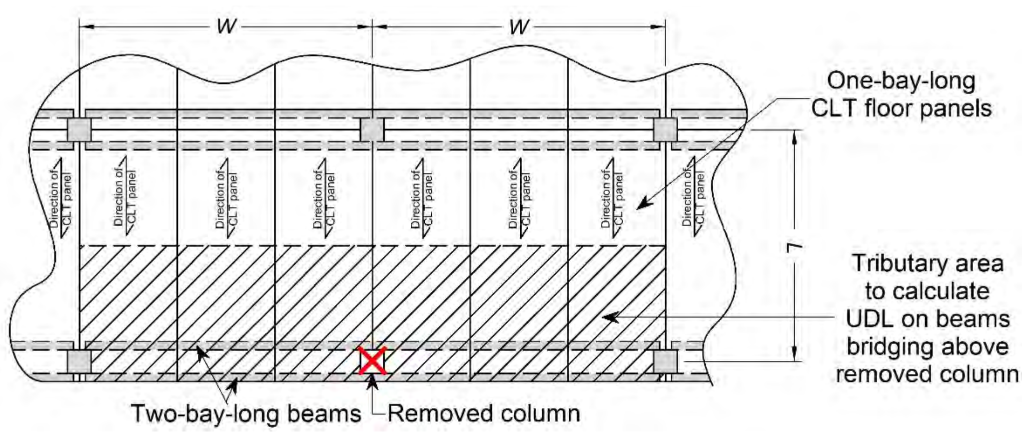


**Figure 24. Tributary area to consider when calculating $\omega_b$ for the beams used as the load-resisting mechanism in ALP 2 for post-and-beam CLT buildings. Illustrated for two-bay-long beams**

Limit state design checks for these ALPs should include, but are not restricted to:

- Bending and shear strength of the beams;
- Shear strength of the splice connection for the 1.5-bay-long beams;
- Shear strength of the beam-to-column connections, including for uplift forces as given in Figure 22(b) and Figure 23; and
- Bending and shear strength of the CLT floor and roof panels.

### 8.4.3 Advanced Analysis Method (Nonlinear Static ALP)

In the advanced analysis method, the modelling principles discussed in Section 8.3.3 for platform-type buildings apply. The methodology would capture the ALPs not modelled in the simplified analytical methods, such as the CLT panels of the bays adjacent to the removed column being supported by the panels of the surrounding bays. The main difference with the platform-type buildings is in the modelling of the beam-to-column connections. Also, although the beam-to-column connections currently used in mass timber buildings and analysed by Lyu et al. (2020) had difficulty generating catenary action and could not resist the accidental loads by themselves, under large deformation, they were found to provide localised support at the columns to the CLT panels above (Lyu, 2021; Lyu et al., 2021). This support was provided despite the connections undergoing large rotation and failing in bending, as illustrated in Figure 25. To accurately model the overall behaviour of the building, it is important to capture this ALP and therefore quantify the residual shear capacity of the beam-to-column connection after it undergoes large deformation. When designing post-and-beam buildings, by proving that the beam-to-column connections can provide such support and transfer the shear forces from the CLT panels to the columns, this ALP can be beneficial. Such demonstrations would require separate numerical or experimental studies, and it is essential that they be performed by a researcher aiming to develop reliable models. However, for commercially available connectors, manufacturers typically only provide the capacities when the connectors deform in either pure shear or tension, and these capacities after the connector undergoes large rotation are unknown. In such cases and in an accidental design situation, the beams on both sides of the columns located above the removed column must therefore be conservatively assumed to be disconnected at both ends. Nevertheless, these beams should still be modelled as they remain connected to the CLT panels and provide reinforcement, under the condition that they are designed to carry the respective forces. The remaining beam-to-column connections (i.e., away from the columns above the removed one) should be modelled as springs, with the shear and tensile capacities provided, for instance, either by the manufacturer, by tests, or by calculations using the relevant design specifications. Because the rotational stiffness of these connections is typically less than the bending stiffness of the beam (Masaeli et al., 2020), connections can realistically be pinned and are commonly assumed to be. If data is not available or if the remaining connection stiffness cannot be calculated, stiff connections could be assumed for all translations and torsion, assuming that the stiffness is shown not to affect the design through sensitivity analyses. As discussed in Section 8.2.2.3, elastic and nonlinear load-deformation curves would be modelled for brittle and ductile failure modes, respectively.

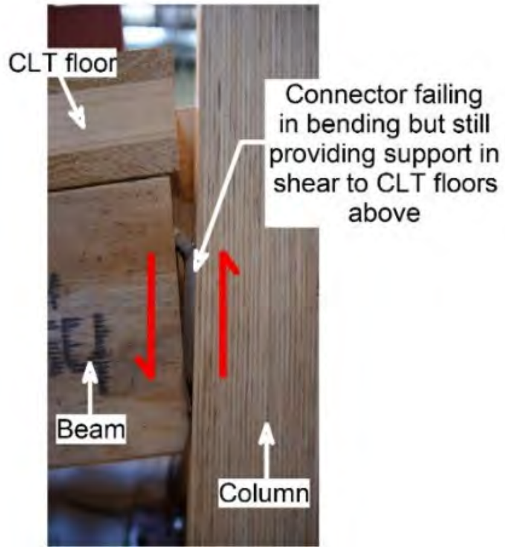


**Figure 25. Example of a beam-to-column connection undergoing large deformation but still providing localised support in shear to CLT floor panels above**

If stability is provided by a bracing system, with the bracing elements connected to the beams and columns using bolted or dowelled metal fin plates, the axial stiffness of the connection with laterally loaded fasteners can be estimated similarly to the screwed connections in Table 1 using Clause 7.1 of Eurocode 5 (CEN, 2004). For steel-to-timber connections, axial stiffness $k_{b,axial}$ of the braced connections is then given per shear plane as:

$$\boldsymbol{k_{b,axial} = 2n\,\frac{{\rho_m}^{1.5}d}{23}} \qquad [5]$$

where $n$ is the number of fasteners, $d$ is the fastener diameter in mm, and $\rho_m$ is the timber density in kg/m$^3$. The axial capacity of these connections with laterally loaded fasteners would be calculated according to the relevant design specifications, such as by following Clause 8.2.3 of Eurocode 5 (CEN, 2004) or by other means. In good design practice, these connections are designed to be ductile, with bending failure developing in the bolts or dowels, and therefore would be generally modelled as elastic-perfectly plastic. Additionally, and similarly to Table 1, Table 2 provides the model parameters for some typical timber-to-timber screwed connections used in post-and-beam CLT buildings; the parameters are based on Eurocode 5 (CEN, 2004) and the ETA-12/0063 (2012) and ETA-12/0373 (2012) design equations.

**Table 2. Model parameters for screwed connections for post-and-beam CLT buildings, based on Eurocode 5 (CEN, 2004) and the ETA-12/0063 (2012) and ETA-12/0373 design equations[a]**

<table>
<tr><th rowspan="2">Connection</th><th rowspan="2">Stiffness (N/mm)</th><th colspan="3">Failure</th><th rowspan="2">Model</th></tr>
<tr><th>Governing mode</th><th>Type</th><th>Capacity</th></tr>
<tr><td rowspan="4">Floor-to-beam<br>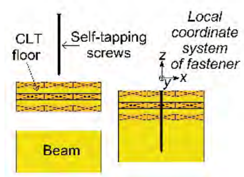</td><td>$k_x = k_y = \rho_m^{1.5} d/23$</td><td>All failure modes for laterally loaded screws in Clause 8.2.2 of Eurocode 5</td><td>Predominantly ductile</td><td>$R_x = R_y$ = Calculated as per Clause 8.7.1 of Eurocode 5</td><td>Linear elastic-perfectly plastic</td></tr>
<tr><td rowspan="2">$k_z = 25 l_{eff} d$ for connection opening</td><td>Withdrawal failure of the threaded part of the screw<br>Tear-off failure of the screw head<br>Tensile failure of the screw</td><td>Brittle</td><td>$R_z$ = Calculated as per relevant equations in Clause 8.7.2 of Eurocode 5</td><td>Linear</td></tr>
<tr><td>Pull-through failure of the screw head</td><td>Ductile</td><td>$R_z$ = Calculated as per relevant equation in Clause 8.7.1 of Eurocode 5</td><td>Linear elastic-perfectly plastic</td></tr>
<tr><td>$k_z = \infty$ for connection closing</td><td>Timber compression</td><td>Ductile</td><td>As per timber specification</td><td>Rigid</td></tr>
<tr><td rowspan="4">Column-to-column<br>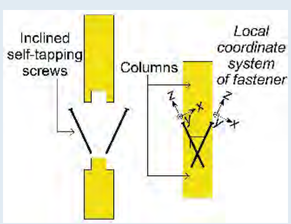<br>*Male-female connection preventing horizontal relative displacement between columns*</td><td>$k_x = k_y = \infty$</td><td>Timber compression</td><td>Ductile</td><td>As per timber specification</td><td>Rigid</td></tr>
<tr><td rowspan="2">$k_z = 25 l_{eff} d$ for connection opening</td><td>Withdrawal failure of the threaded part of the screw<br>Tear-off failure of the screw head<br>Tensile failure of the screw</td><td>Brittle</td><td>$R_z$ = Calculated as per relevant equations in Clause 8.7.2 of Eurocode 5</td><td>Linear</td></tr>
<tr><td>Pull-through failure of the screw head</td><td>Ductile</td><td>$R_z$ = Calculated as per relevant equation in Clause 8.7.1 of Eurocode 5</td><td>Linear elastic-perfectly plastic</td></tr>
<tr><td>$k_z = \infty$ for connection closing</td><td>Timber compression</td><td>Ductile</td><td>As per timber specification</td><td>Rigid</td></tr>
</table>

[a] Values provided per screw, per shear plane, and relative to the local coordinate system of the fastener.

$d$ = Fastener diameter in mm, $l_{eff}$ = Penetration length of the threaded part of the screw in mm and $\rho_m$ = Density of timber in kg/m$^3$

As discussed in Section 8.3.3, the values provided in Table 2 and Equation 3 would be suitable for design purposes, and due to the high uncertainty regarding the behaviour of the connections, a sensitivity analysis, for instance, should be carried out. For more reliable models, the stiffness and capacities of the connections would need to be more accurately determined, either through experimental testing or using a separate FE model, as the one for the floor-to-wall connections presented in Figure 16(b).

Figure 26 illustrates the principles of the FE model that is suitable for design purposes and uses the component approach. Nonlinear geometric and material analyses are run. Loads should be modelled as discussed in Section 8.3.3. As for platform-type buildings, CLT panels are best modelled as layered shell elements to reproduce the membrane and bending stiffness, while beams and columns are best modelled as beam elements. The design of the CLT panels, beams, and columns is performed similarly to all other load combinations and according to the relevant design specifications. As mentioned in Section 8.2.2.3, connections pass the design check if the loads in the spring are lower than the design capacities for brittle connections and if the deformations of the spring do not exceed the design deformation capacities for ductile connections.

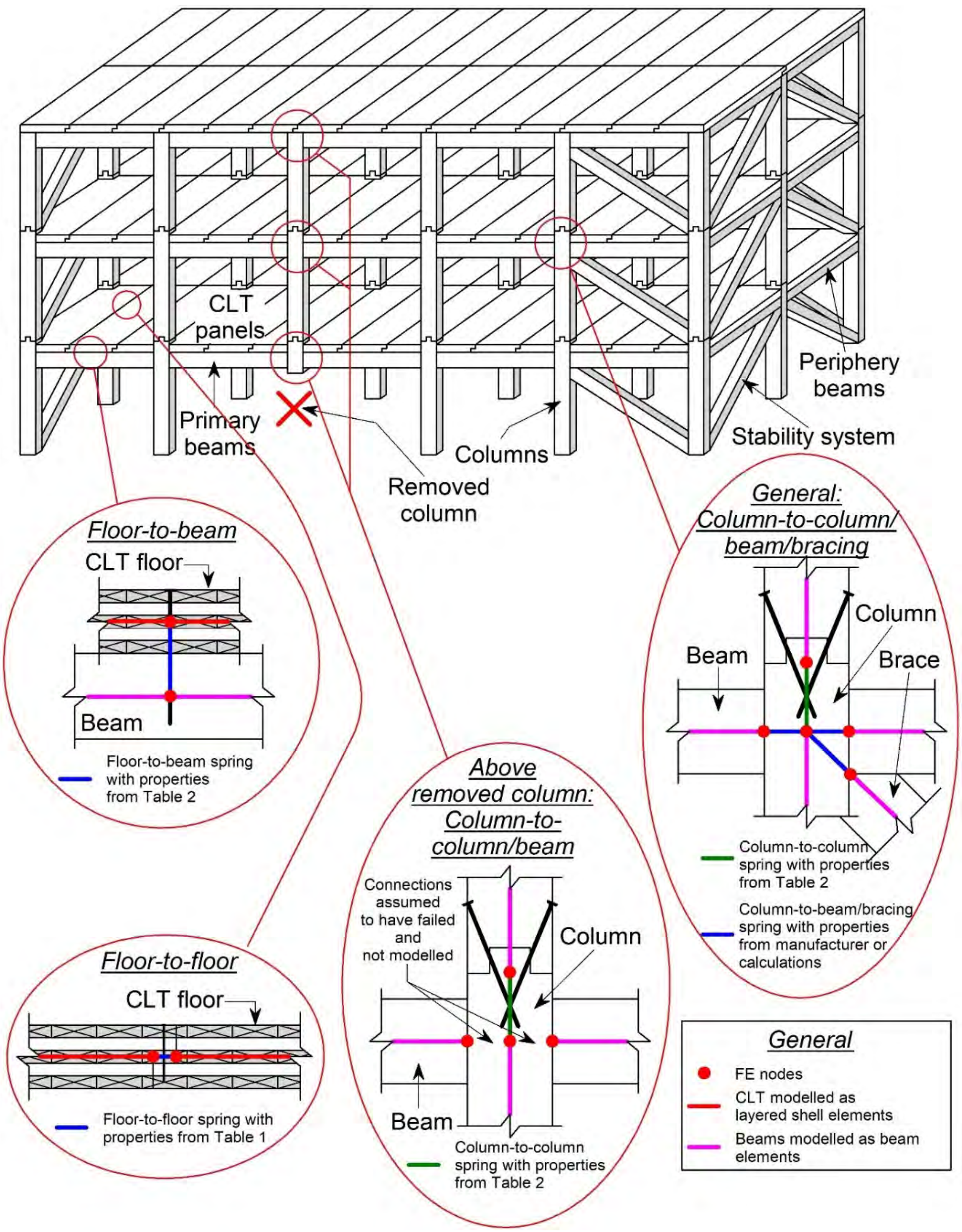


**Figure 26. FE modelling principles for post-and-beam CLT buildings and advanced analysis**

An example of such a model, but one that accounts for damage and that uses the connection behaviours obtained from experimental testing, can be found in Lyu (2021). This model accurately captures the overall structural behaviour, ALPs, and strain development in beams and CLT panels.

### 8.4.4 Key Element Design

When the design does not allow for two-bay-long CLT floor and roof panels or beams spanning more than one bay, then the columns must be designed as key elements.

Key element design can also be suitable for post-and-beam structures in any of the following scenarios:

- Column and beam dimensions are relatively large due to architectural requirements;
- Column and beam dimensions are relatively large due to design requirements for a gravitation load case; or
- Columns can directly transfer loads via bearing into the floor diaphragm.

For post-and-beam structures in one of the above scenarios, if the primary elements and their connection details can resist the key element design loads without further or significant modifications or enhancement, this approach may be more economical than an ALP approach. However, the key element approach can also lead to an onerous connection design due to the high vertical and horizontal loads that the key elements and their associated connections must resist, as is often the case for beams. When designing using the key element approach, the designer must make informed choices on the consequences of the final design.

A key element approach can result in more economical design when connection details can be simplified. ALP methods can often result in complex post-and-beam connection details and dense fixing requirements at floor-to-beam and floor-to-floor connections. These details are not only costly in material, but also in time and labour.

The key element design approaches are discussed in Section 8.2.4.

## 8.5 OTHER SYSTEMS

### 8.5.1 Hybrid Systems

Hybrid structural systems cover buildings that integrate timber elements with other materials, primarily steel, concrete, and/or masonry. The modelling approaches for hybrid systems are generally the same as those for pure timber structures; however, the material properties and the interfaces between the different materials must be carefully considered. While models have been developed for timber-concrete (Dias et al., 2007; Khorsandnia et al., 2014; Oudjene et al., 2013; Oudjene et al., 2018) and steel-timber (Hassanieh et al., 2016; Hassanieh, Valipour, & Bradford, 2017; Hassanieh, Valipour, Bradford, & Sandhaas, 2017) composite floors, no research has yet been performed on timber hybrid systems in terms of progressive collapse. Their behaviour under the loss of a load-bearing element is unknown.

Composite floor systems, such as timber-concrete composite floors, may initially be modelled independently to determine their strength and stiffness properties. These values can then be used in a global model, using an equivalent stiffness for the composite elements, for simplicity. Alternatively, validated analytical design models can be used to determine such properties (Khorsandnia et al., 2012; Yeoh et al., 2011; Zhang et al., 2019). Furthermore, the concrete slabs influence the rotational and translational stiffness at the timber joints. When the concrete slabs are continuous, they should be modelled accordingly.

The stiffness and strength of the connections in various directions must be determined either through experimental testing or analytical models (similar to the approaches mentioned in Sections 8.3.3 and 8.4.3) to best capture system behaviour. Construction tolerances would likely need to be greater for hybrid structures at the interface between different materials. This will likely influence the strength and stiffness of the connections, which needs to be considered in the model used for the analysis.

### 8.5.2 Long-Span Structures

Long-span timber structures usually consist of main frames (i.e., columns and girders), secondary elements, and bracing elements. Thelandersson and Honfi (2009) mention that columns and girders can be seen as key elements and be designed with 'high safety against failure'. The authors also recommend that for high-consequence buildings, the failure of one or more of these key elements should be considered a possibility. Two strategies can be used: For large-span frames, which would result in a large area affected by the collapse of one frame, the failure of the main girders must be avoided, and the secondary system should be designed to provide ALPs via catenary action or bending, therefore supporting the failing girder. For shorter-span frames or if sufficient ALPs cannot be formed, the structure should be designed using a compartmentalisation approach; a weaker secondary system or fuse elements in joints should isolate the failure of the frame. In this way, part of the structure is sacrificed so that a larger part may survive. Dietsch (2011) and Munch-Andersen & Dietsch (2011) present similar considerations for large-span timber structures.

### 8.5.3 Prefabricated Module Structures

Timber buildings may be built with prefabricated modules (Chen et al., 2020). To date, little to no research has been performed on the robustness of timber buildings made in this manner. However, research on light steel modular construction indicates that modules can bridge over removed modules, and that the necessary tying forces after element removal are lower than those required by the tie-force method (Lawson et al., 2008). A a high degree of prefabrication could be advantageous with respect to robustness because automation and industrial quality control may reduce manufacturing tolerances and the probability of human error, at least concerning the finished modules.

## 8.6 SUMMARY

This chapter discusses the progressive collapse resisting mechanisms (i.e., flexural action, compressive arch action, and catenary action) and the magnitude in which they manifest in timber structures. The design and analysis approaches of progressive collapse and their relevance for the design of timber structures are introduced. These approaches include tie forces, redundancy, ALPs for static analysis and dynamic analysis, compartmentalisation, and the key element method. Model development and analysis of shear wall systems and post-and-beam systems are described in detail. A simplified analytical method and an advanced analysis method are provided, along with corresponding recommendations. Key modelling considerations for the progressive collapse analysis of hybrid systems, long-span structures, and prefabricated module structures are also provided. The information presented in this chapter is intended to help practising engineers and researchers become more acquainted with progressive collapse modelling and analysis of timber structures.

## 8.7 REFERENCES

Adam, J. M., Parisi, F., Sagaseta, J., & Lu, X. (2018). Research and practice on progressive collapse and robustness of building structures in the 21st century. *Engineering Structures, 173*, 122-149.

American Society of Civil Engineers. (2005). *Minimum design loads and associated criteria for buildings and other structures* (ASCE/SEI 7-05).

American Society of Civil Engineers. (2013). *Seismic evaluation and retrofit of existing buildings* (ASCE/SEI 41-13).

American Society of Civil Engineers. (2016). *Minimum design loads and associated criteria for buildings and other structures* (ASCE/SEI 7-16).

Arup. (2011). *Review of international research on structural robustness and disproportionate collapse*. https://assets.publishing.service.gov.uk/government/uploads/system/uploads/attachment_data/file/6328/2001594.pdf

Baker, J. W., Schubert, M., & Faber, M. H. (2008). On the assessment of robustness. *Structural Safety, 30*(3), 253-267. https://doi.org/10.1016/j.strusafe.2006.11.004

Blass, H. J., & Fellmoser, P. (2004, August 8–11). *Design of solid wood panels with cross layers* [Conference presentation]. World Conference on Timber Engineering, Lahti, Finland.

Brett, C., & Lu, Y. (2013). Assessment of robustness of structures: Current state of research. *Frontiers of Structural and Civil Engineering, 7*, 356-368.

Byfield, M., Mudalige, W., Morison, C., & Stoddart, E. (2014). A review of progressive collapse research and regulations. *Proceedings of the Institution of Civil Engineers - Structures and Buildings, 167*(8), 447-456. https://doi.org/10.1680/stbu.12.00023

Chen, Z., & Popovski, M. (2020). Mechanics-based analytical models for balloon-type cross-laminated timber (CLT) shear walls under lateral loads. *Engineering Structures, 208*, 109916.

Chen, Z., Popovski, M., & Ni, C. (2020). A novel floor-isolated re-centering system for prefabricated modular mass timber construction – Concept development and preliminary evaluation. *Engineering Structures, 222*, 111168. https://doi.org/10.1016/j.engstruct.2020.111168

Cheng, X., Gilbert, B. P., Guan, H., Underhill, I. D., & Karampour, H. (2021). Experimental dynamic collapse response of post-and-beam mass timber frames under a sudden column removal scenario. *Engineering Structures, 233*, 111918. https://doi.org/10.1016/j.engstruct.2021.111918

Department of Defense. (2016). *Design of buildings to resist progressive collapse* (UFC 4-023-03).

Dias, A. M. P. G., Van de Kuilen, J. W., Lopes, S., & Cruz, H. (2007). A non-linear 3D FEM model to simulate timber-concrete joints. *Advances in Engineering Software, 38*(8), 522-530. https://doi.org/10.1016/j.advengsoft.2006.08.024

Dietsch, P. (2011). Robustness of large-span timber roof structures — Structural aspects. *Engineering Structures, 33*(11), 3106-3112. https://doi.org/10.1016/j.engstruct.2011.01.020

Dietsch, P., & Kreuzinger, H. (2016). *Dynamic effects in reinforced timber beams at time of timber fracture* [Conference presentation]. International Network on Timber Engineering Research, Graz, Austria.

Ellingwood, B. R. (2006). Mitigating risk from abnormal loads and progressive collapse. *Journal of Performance of Constructed Facilities, 20*(4), 315-323. https://doi.org/10.1061/(ASCE)0887-3828(2006)20:4(315)

Ellingwood, B. R., Smilowitz, R., Dusenberry, D. O., Duthinh, D., Lew, H. S., & Carino, N. J. (2007). *Best practices for reducing the potential for progressive collapse in buildings* (NISTIR 7396). https://tsapps.nist.gov/publication/get_pdf.cfm?pub_id=860696

European Committee for Standardization. (2006). *Eurocode 1: Actions on structures - Part 1-7: General actions - Accidental actions* (EN 1991-1-7:2006).

European Committee for Standardization. (2004). *Eurocode 5: Design of timber structures - Part 1-1: General - Common rules and rules for buildings* (EN 1995-1-2:2004).

Gagnon, S., & Popovski, M. (2011). Structural design of cross-laminated elements. In S. Gagnon & C. Pirvu (Eds.), *Canadian CLT handbook*. FPInnovations.

General Services Administration. (2016). *Alternate path analysis & design guidelines for progressive collapse resistance*.

Grantham, R., & Enjily, V. (2004, August 8–11). *UK design guidance for multi-storey timber frame buildings* [Conference presentation]. World Conference on Timber Engineering, Lahti, Finland.

Grantham, R., Enjily, V., Milner, M., Bullock, M., & Pitts, G. (2003). *Multi-storey timber frame buildings: A design guide*. BREPress.

Hassanieh, A., Valipour, H. R., & Bradford, M. A. (2016). Experimental and numerical study of steel-timber composite (STC) beams. *Journal of Constructional Steel Research, 122*, 367-378. https://doi.org/10.1016/j.jcsr.2016.04.005

Hassanieh, A., Valipour, H. R., & Bradford, M. A. (2017). Composite connections between CLT slab and steel beam: Experiments and empirical models. *Journal of Constructional Steel Research, 138*, 823-836. https://doi.org/10.1016/j.jcsr.2017.09.002

Hassanieh, A., Valipour, H. R., Bradford, M. A., & Sandhaas, C. (2017). Modelling of steel-timber composite connections: Validation of finite element model and parametric study. *Engineering Structures, 138*, 35-49. https://doi.org/10.1016/j.engstruct.2017.02.016

Hawkins, N. M., & Mitchell, D. (1979). Progressive collapse of flat plate structures. *Proceedings of the American Concrete Institute, 76*(7), 775-808.

Hewson, N. (2016). *Robustness in structures* (Technical Guide No. 39). https://www.woodsolutions.com.au/articles/mid-rise-timber-buildings-design-guides

Hu, L., Chui, Y. H., & Guerrier-Auclair, S. (2019). Vibration performance of cross-laminated timber floors. In E. Karacabeyli & S. Gagnon (Eds.), *Canadian CLT handbook* (2nd ed.). FPInnovations.

Huber, J. A. J., Ekevad, M., Berg, B., & Girhammar, U. A. (2018). *Assessment of connections in cross-laminated timber buildings regarding structural robustness* [Conference presentation]. World Conference on Timber Engineering, Seoul, South Korea.

Huber, J. A. J., Ekevad, M., Girhammar, U. A., & Berg, S. (2019). Structural robustness and timber buildings – A review. *Wood Material Science & Engineering*, *14*(2), 107-128. https://doi.org/10.1080/17480272.2018.1446052

Huber, J. A. J., Ekevad, M., Girhammar, U. A., & Berg, B. (2020). Finite element analysis of alternative load paths in a platform-framed CLT building. *Proceedings of the Institution of Civil Engineers - Structures and Buildings, 173*(5), 379-390. https://doi.org/10.1680/jstbu.19.00136

Institution of Structural Engineers. (2010). *Practical guide to structural robustness and disproportionate collapse in buildings*.

Izzi, M., Polastri, A., & Fragiacomo, M. (2018). Modelling the mechanical behaviour of typical wall-to-floor connection systems for cross-laminated timber structures. *Engineering Structures, 162*, 270-282. https://doi.org/10.1016/j.engstruct.2018.02.045

Izzuddin, B. A., Vlassis, A. G., Elghazouli, A. Y., & Nethercot, D. A. (2008). Progressive collapse of multi-storey buildings due to sudden column loss — Part I: Simplified assessment framework. *Engineering Structures, 30*(5), 1308-1318. https://doi.org/10.1016/j.engstruct.2007.07.011

Jorissen, A., & Fragiacomo, M. (2011). General notes on ductility in timber structures. *Engineering Structures, 33*(11), 2987-2997.

Karacabeyli, E., & Lum, C. (2022). *Technical guide for the design and construction of tall wood buildings in Canada* (2nd ed.). FPInnovations.

Khorsandnia, N., Valipour, H., & Crews, K. (2014). Structural response of timber-concrete composite beams predicted by finite element models and manual calculations. *Advances in Structural Engineering, 17*(11), 1601-1621. https://doi.org/10.1260/1369-4332.17.11.1601

Khorsandnia, N., Valipour, H. R., & Crews, K. (2012). Experimental and analytical investigation of short-term behaviour of LVL–concrete composite connections and beams. *Construction and Building Materials, 37*, 229-238. https://doi.org/10.1016/j.conbuildmat.2012.07.022

Köhler, J. (2007). *Reliability of timber structures* [Doctoral dissertation, Swiss Federal Institute of Technology].

Lawson, P. M., Byfield, M. P., Popo-Ola, S. O., & Grubb, P. J. (2008). Robustness of light steel frames and modular construction. *Proceedings of the Institution of Civil Engineers - Structures and Buildings, 161*(1), 3-16. https://doi.org/10.1680/stbu.2008.161.1.3

Lyu, C. H. (2021). *Progressive collapse resistance of post-and-beam mass timber buildings: Experimental and numerical investigations on 2D and 3D substructures.* [Doctoral dissertation, Griffith University].

Lyu, C. H., Gilbert, B. P., Guan, H., Underhill, I. D., Gunalan, S., & Karampour, H. (2021). Experimental study on the quasi-static progressive collapse response of post-and-beam mass timber buildings under an edge column removal scenario. *Engineering Structures, 228*, 111425. https://doi.org/10.1016/j.engstruct.2020.111425

Lyu, C. H., Gilbert, B. P., Guan, H., Underhill, I. D., Gunalan, S., Karampour, H., & Masaeli, M. (2020). Experimental collapse response of post-and-beam mass timber frames under a quasi-static column removal scenario. *Engineering Structures, 213*, 110562. https://doi.org/10.1016/j.engstruct.2020.110562

Masaeli, M., Gilbert, B. P., Karampour, H., Underhill, I. D., Lyu, C. H., & Gunalan, S. (2020). Scaling effect on the moment and shear responses of three types of beam-to-column connectors used in mass timber buildings. *Engineering Structures, 208*, 110329. https://doi.org/10.1016/j.engstruct.2020.110329

McKay, A., Marchand, K., & Diaz, M. (2012). Alternate path method in progressive collapse analysis: Variation of dynamic and nonlinear load increase factors. *Practice Periodical on Structural Design and Construction, 17*(4), 152-160. https://doi.org/10.1061/(ASCE)SC.1943-5576.0000126

Mitchell, D., & Cook, W. D. (1984). Preventing progressive collapse of slab structures. *Journal of Structural Engineering, 110*(7), 1513-1532. https://doi.org/10.1061/(ASCE)0733-9445(1984)110:7(1513)

Mohammad, M., & Munoz, W. (2011). Connections in cross-laminated buildings. In S. Gagnon & C. Pirvu (Eds.), *Canadian CLT handbook*. FPInnovations.

Mohammad, M., Ni, C., & Munoz, W. (2019). Connections in cross-laminated buildings. In E. Karacabeyli & S. Gagnon (Eds.), *Canadian CLT handbook* (2nd ed.). FPInnovations.

Mpidi Bita, H., Currie, N., & Tannert, T. (2018). Disproportionate collapse analysis of mid-rise cross-laminated timber buildings. *Structure and Infrastructure Engineering, 14*(11), 1547-1560. https://doi.org/10.1080/15732479.2018.1456553

Mpidi Bita, H., & Tannert, T. (2019a). Disproportionate collapse prevention analysis for a mid-rise flat-plate cross-laminated timber building. *Engineering Structures, 178*, 460-471. https://doi.org/10.1016/j.engstruct.2018.10.048

Mpidi Bita, H., & Tannert, T. (2019b). Tie-force procedure for disproportionate collapse prevention of CLT platform-type construction. *Engineering Structures, 189*, 195-205. https://doi.org/10.1016/j.engstruct.2019.03.074

Munch-Andersen, J., & Dietsch, P. (2011). Robustness of large-span timber roof structures — Two examples. *Engineering Structures, 33*(11), 3113-3117. https://doi.org/10.1016/j.engstruct.2011.03.015

Oudjene, M., Meghlat, E. M., Ait-Aider, H., & Batoz, J. L. (2013). Non-linear finite element modelling of the structural behaviour of screwed timber-to-concrete composite connections. *Composite Structures, 102*, 20-28. https://doi.org/10.1016/j.compstruct.2013.02.007

Oudjene, M., Meghlat, E. M., Ait-Aider, H., Lardeur, P., Khelifa, M., & Batoz, J. L. (2018). Finite element modelling of the nonlinear load-slip behaviour of full-scale timber-to-concrete composite T-shaped beams. *Composite Structures, 196*, 117-126. https://doi.org/10.1016/j.compstruct.2018.04.079

Palma, P., Steiger, R., & Jockwer, R. (2019). *Addressing design for robustness in the 2nd-generation EN 1995 Eurocode 5* [Conference presentation]. International Network on Timber Engineering Research, Tacoma, U.S.A.

Popovski, M., Tung, D., & Chen, Z. (2022). Structural Analysis and Design. In E. Karacabeyli & C. Lum (Eds.), *Technical guide for the design and construction of tall wood buildings in Canada* (2nd ed.). FPInnovations.

Rezai, M., Popovski, M., Hu, L., & Sherstobitoff, J. (2014). Advanced analysis and testing of systems for design. In E. Karacabeyli & C. Lum (Eds.), *Technical guide for the design and construction of tall wood buildings in Canada* (1st ed.). FPInnovations.

Ruth, P., Marchand, K. A., & Williamson, E. B. (2006). Static equivalency in progressive collapse alternate path analysis: Reducing conservatism while retaining structural integrity. *Journal of Performance of Constructed Facilities, 20*(4), 349-364. https://doi.org/10.1061/(ASCE)0887-3828(2006)20:4(349)

Starossek, U. (2006). Progressive collapse of structures: Nomenclature and procedures. *Structural Engineering International, 16*(2), 113-117. https://doi.org/10.2749/101686606777962477

Starossek, U., & Haberland, M. (2010). Disproportionate collapse: Terminology and procedures. *Journal of Performance of Constructed Facilities, 24*(6), 519-528. https://doi.org/10.1061/(ASCE)CF.1943-5509.0000138

Stevens, D., Crowder, B., Sunshine, D., Marchand, K., Smilowitz, R., Williamson, E., & Waggoner, M. (2011). DoD research and criteria for the design of buildings to resist progressive collapse. *Journal of Structural Engineering, 137*(9), 870-880. https://doi.org/10.1061/(ASCE)ST.1943-541X.0000432

Stevens, D., Martin, E., Williamson, E., McKay, A., & Marchand, K. (2012). *Recent developments in progressive collapse design* [Conference presentation]. 4th International Conference on Design and Analysis of Protective Structures, Jeju, South Korea.

Standards New Zealand. (2002). *Structural design actions - Part 0: General principles* (AS/NZS 1170.0:2002).

Stylianidis, P. M., Nethercot, D. A., Izzuddin, B. A., & Elghazouli, A. Y. (2016). Study of the mechanics of progressive collapse with simplified beam models. *Engineering Structures, 117*, 287-304. https://doi.org/10.1016/j.engstruct.2016.02.056

Thelandersson, S., & Honfi, D. (2009). Behaviour and modelling of timber structures with reference to robustness. In C. Sandhaas, J. Munch-Andersen, & P. Dietsch (Eds.), *Proceedings of the Joint Workshop of COST Actions TU0601 and E55* (pp. 125-138). Ljubljana, Slovenia.

Tsai, M.-H. (2010). An analytical methodology for the dynamic amplification factor in progressive collapse evaluation of building structures. *Mechanics Research Communications, 37*(1), 61-66. https://doi.org/10.1016/j.mechrescom.2009.11.001

UK Timber Frame Association. (2008). *Structural guidance for platform timber frame*.

Voulpiotis, K., Köhler, J., Jockwer, R., & Frangi, A. (2021). A holistic framework for designing for structural robustness in tall timber buildings. *Engineering Structures, 227*, 111432. https://doi.org/10.1016/j.engstruct.2020.111432

Woodard, A., & Jones, A. (2020). *Mid-rise timber building structural engineering* (Technical Guide No. 50). https://www.woodsolutions.com.au/publications/mid-rise-timber-building-structural-engineering

Xue, H., Gilbert, B. P., Guan, H., Lu, X., Li, Y., Ma, F., & Tian, Y. (2018). Load transfer and collapse resistance of RC flat plates under interior column removal scenario. *Journal of Structural Engineering, 144*(7), 04018087. https://doi.org/10.1061/(ASCE)ST.1943-541X.0002090

Yeoh, D., Fragiacomo, M., De Franceschi, M., & Heng Boon, K. (2011). State of the art on timber-concrete composite structures: Literature review. *Journal of Structural Engineering, 137*(10), 1085-1095. https://doi.org/10.1061/(ASCE)ST.1943-541X.0000353

Zhang, Y., Raftery, G. M., & Quenneville, P. (2019). Experimental and analytical investigations of a timber-concrete composite beam using a hardwood interface layer. *Journal of Structural Engineering, 145*(7), 04019052. https://doi.org/10.1061/(ASCE)ST.1943-541X.0002336

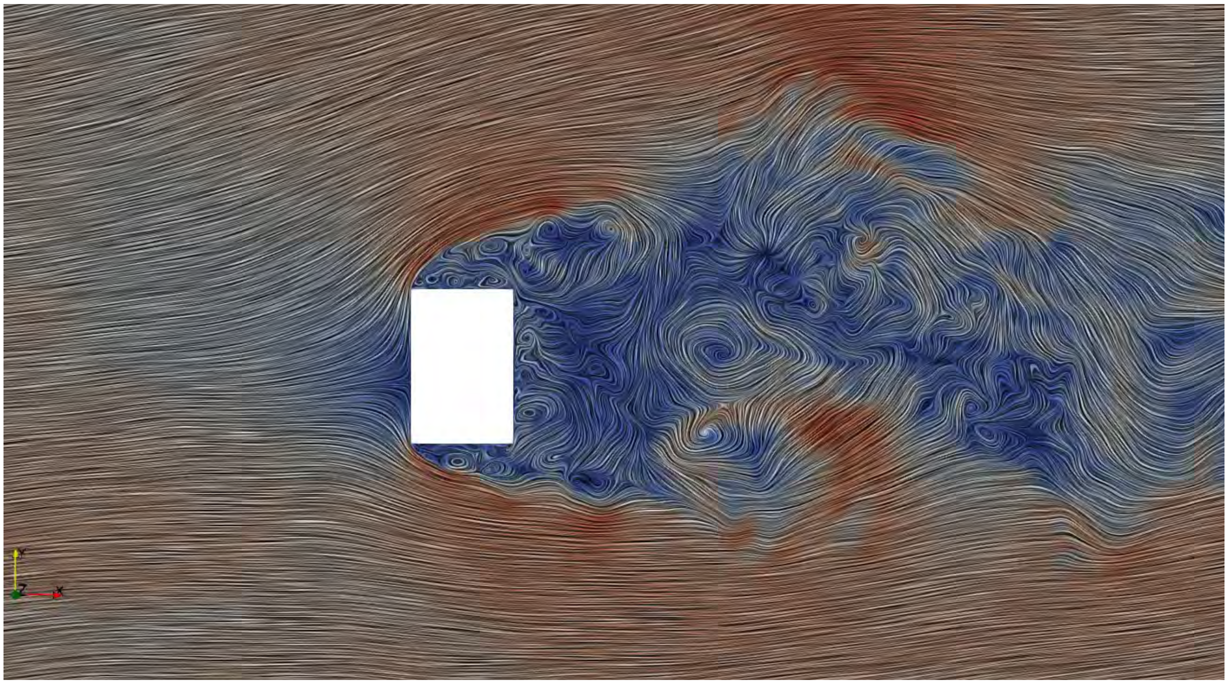

# CHAPTER 9

## Wind-induced response analysis


**Authors**
Girma Bitsuamlak
Matiyas Bezabeh
Samuel Cuerrier Auclair

**Reviewers**
Seifu Bekele
Magne Bjertnæs

# TABLE OF CONTENTS

## 9.1 INTRODUCTION

In recent years, engineered wood products, such as cross-laminated timber (CLT), nail-laminated timber, dowel-laminated timber, and glued laminated timber (glulam), have routinely been used to construct the gravity and lateral load-resisting systems within tall timber buildings. Using timber load-resisting systems in tall buildings results in structures that are more lightweight and flexible compared to traditional systems, and as a result these buildings can be prone to excessive wind vibrations. Within wind engineering literature and practice, it is generally recognised that wind forces govern the structural design of unusually lightweight and flexible buildings for both safety and serviceability limit states. In general, the action of wind on tall buildings depends on wind hazard, nearby buildings, terrain conditions, building shape, and dynamic structural properties. The structural engineer's goal in designing buildings for wind is to correctly estimate wind actions and achieve economic and serviceable buildings. The intent of this chapter is to (a) outline a framework for the wind design of timber buildings, (b) introduce methodologies to estimate the critical responses of tall buildings for satisfactory wind performance, (c) highlight the challenges in designing tall timber buildings for wind actions, and (d) introduce performance-based wind engineering approaches.

## 9.2 INTRODUCTION TO DAVENPORT'S WIND LOADING CHAIN

The formation of wind, its motion near the earth's surface, and its interaction with the built environment is a complex and multiscale phenomenon. Estimating wind actions on buildings requires integrating concepts from meteorology, micrometeorology, climatology, probabilistic mechanics, aerodynamics, and structural dynamics. In 1961, Alan G. Davenport proposed the idea of developing a homogenous framework to estimate the action of wind on structures. This unified framework is called the Alan G. Davenport Wind Loading Chain, or in short, the Wind Loading Chain. The Wind Loading Chain appears in an elaborated graphical format in Davenport (1964) (Figure 1) and a concise format in Davenport (1977) (Figure 2). Figures 1 and 2 present the wind loading process analogous to a chain with several links (i.e., wind climate, terrain, aerodynamics, structural response, and criteria). Each link is subjected to uncertainty, in which the wind climate link is usually the most uncertain. The nature of the chain allows using a statistical approach to model and propagate uncertainties. The weakest link in the chain ultimately governs the chain's reliability and the design of structures. The Wind Loading Chain has been adopted by many building codes and standards around the world (Isyumov, 2012).

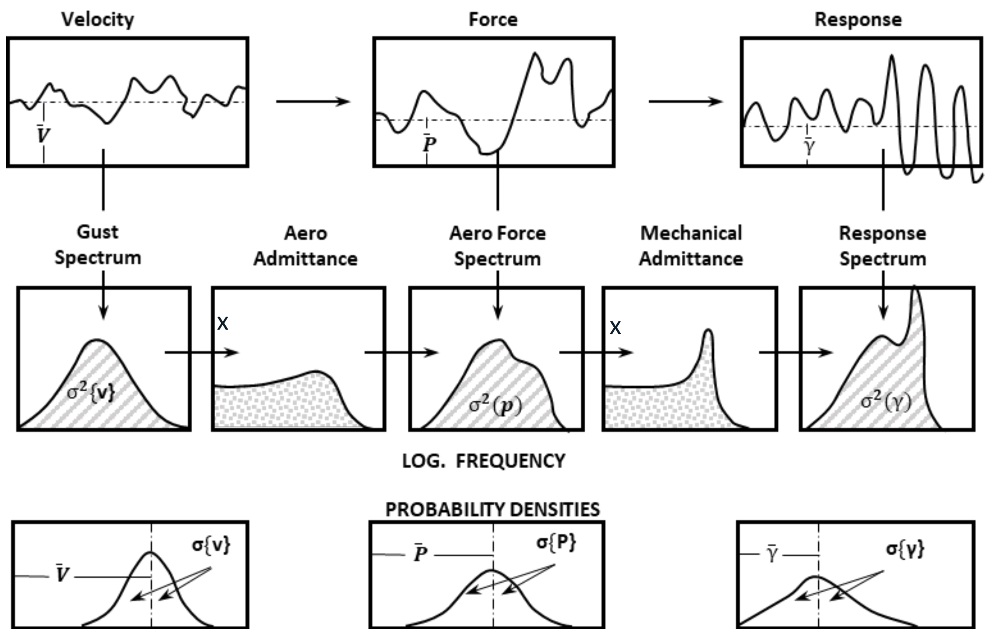


**Figure 1. Elements of the statistical approach to gust loading (Davenport, 1964)**

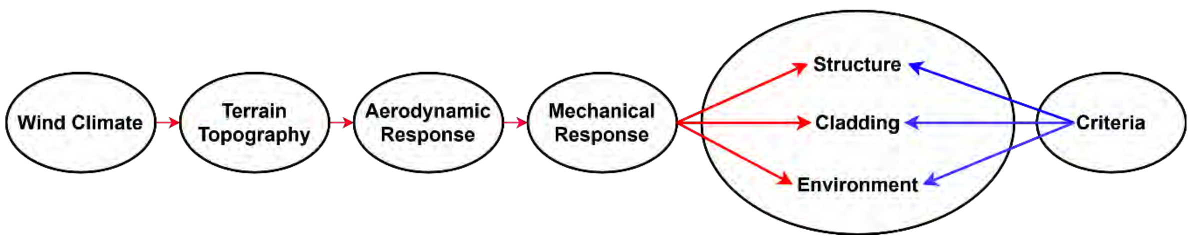


**Figure 2. The Alan G. Davenport Wind Loading Chain (Davenport, 1977)**

The Wind Loading Chain (Figures 1 and 2) starts by studying the wind climate of the region of interest, which entails the wind speed statistics and directionality. Wind climate studies are usually carried out at gradient height using data collected from nearby airport meteorological stations. The main results of wind climate studies are the joint probability distribution of mean wind speed and direction, and the predicted extreme mean wind speeds (Davenport, 1971). Design wind speeds can be derived from extreme value analysis or parent probability distributions using various techniques listed in the study by Bezabeh, Bitsuamlak, and Tesfamariam (2020). The predicted wind speed at the gradient height should be adjusted to account for the terrain roughness and local topography, which is the second element in the Wind Loading Chain (Figure 2). Near the ground, the air motion is gradually slowed due to surface friction. As a result, the mean wind velocity increases with height while the turbulence level decreases with height. The third and fourth elements of the chain are the aerodynamic and dynamic response of structures. The final link in the Wind Loading Chain compares the statistics of engineering demand parameters with the criteria from codes and standards.

## 9.3 AERODYNAMICS OF TALL BUILDINGS

The following sections briefly review the nature of wind flow around bluff bodies and the associated response of tall buildings to atmospheric turbulence, which are the third and fourth elements in the Wind Loading Chain (Figure 2). In quantifying the action of wind on structures, it is paramount to understand the mechanisms by which a flow field induces surface pressure on a bluff body. In the wind engineering context, the term 'bluff body' refers to an obstacle with a large frontal dimension that can cause wakes due to the flow separation from its edges (Holmes, 2015). When the wind interacts with a bluff body, as Figure 3 shows, three regions of the flow determine the overall loading: (1) oncoming flow, (2) wake past the body, and (3) boundary layers on the surface of the bluff body with shear layers. As the figure shows, the main features of flow around a bluff body are flow separation and reattachment, the shear layers, and formation of strong vortices in the wake regions. The magnitude of the fluctuating surface pressure on a bluff body depends on the size of gusts and the bluff body. High-frequency gusts are poorly correlated and have a small effect on buffeting wind load, but they largely influence the flow around the bluff body and consequently the aerodynamic load coefficients. Conversely, low-frequency gusts are well correlated and affect the whole wind load over the building. In general, aerodynamic surface pressure on a bluff body depends on the flow field (level of oncoming and body-generated turbulence), the geometry, and the orientation of the bluff body with respect to the mean wind direction (Bezabeh, Bitsuamlak, & Tesfamariam, 2020).

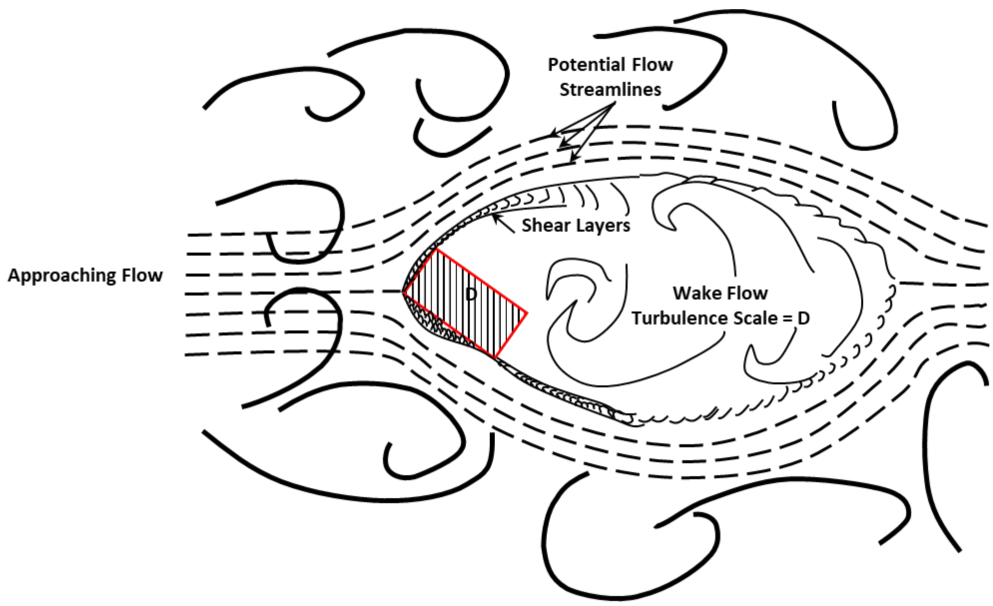


**Figure 3. Turbulent flow around a bluff body (reproduced from Davenport, 1977)**

## 9.4 RESPONSE OF WIND-EXCITED TALL BUILDINGS

The structure of synoptic wind in the atmosphere can be considered the result of two processes. The first entails the movement of large-scale pressure systems at heights greater than approximately 300 m, in which the wind attains a so-called gradient velocity (Bezabeh, Bitsuamlak, & Tesfamariam, 2020). In the second process, closer to the ground, the airflow is affected by the on-ground obstacles, giving rise to a chaotic flow, formally known as turbulent flow. The most characteristic feature of turbulent flow is its randomness in time and space (Bezabeh, Bitsuamlak, & Tesfamariam, 2020). A typical turbulent flow has a mean in the longitudinal direction and three orthogonal fluctuating components. The instantaneous wind speed fluctuation can be treated as a locally stationary random process due to the presence of a spectral gap. On this basis, the wind speed can be considered the sum of the slowly varying mean (averaged over 10 minutes to 1 hour) and turbulent components. Figure 4 shows the mean and longitudinal fluctuating velocity profile approaching a typical building. When wind interacts with a building, due to oncoming turbulence and the building's signature turbulence, wind pressure over the exterior building envelope fluctuates randomly in time and space. As with wind speed, it is customary to average the mean wind loads over a 1-hour duration. The fluctuating component of the wind load is usually described using second-moment statistics (variance) and the associated mean of the peaks within a 1-hour duration. Overall, the wind-induced loads are composed of time-averaged mean and time-varying fluctuating loads.

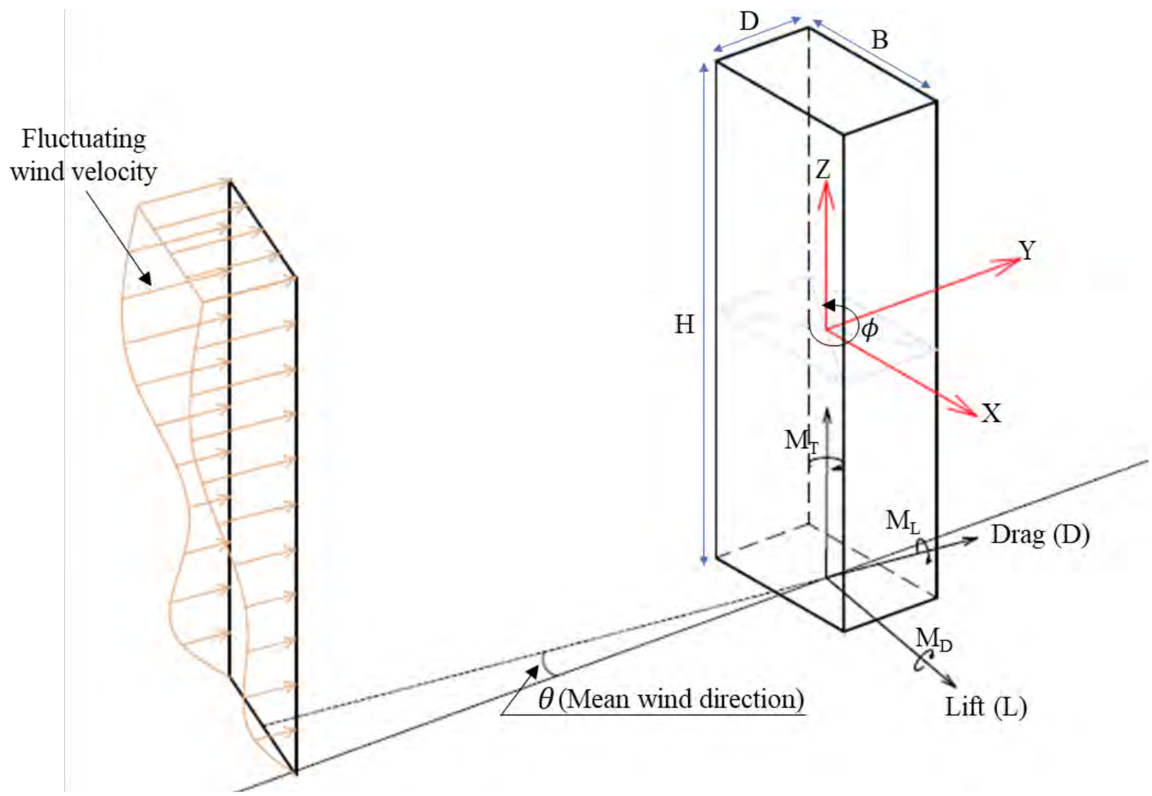


**Figure 4. Three-dimensional schematic view of a generic rectangular tall building with the definition of principal axes, mean wind direction, and directions of drag, lift, and torsional moment**

### 9.4.1 Background and Resonant Responses

As mentioned in Section 9.3, wind effects on buildings are the result of buffeting by oncoming turbulence, turbulence in the shear layers, vortex shedding, wake turbulence, buffeting induced by the wake of upwind structures, and aeroelastic effects. Figure 5(a) presents the typical response of structures under time-varying wind loads. The three main response components are (1) the time-averaged mean, which is a static response, (2) background, which is a slowly varying quasi-static response at frequencies other than the fundamental frequency of the structure, and (3) resonance, which is an amplitude-varying oscillating response at the first few vibration frequencies of the structure (r1, r2, and r3 in Figure 5[b]). Background wind loads are due to random wind pressure fluctuations over the exterior of the building. Usually, background wind loads are less correlated over the height of the building, and their sustained action could excite structures at their natural frequency, resulting in a resonant-type response. The resonant part of the wind loads is caused by inertial forces and depends on the natural frequency of the building, distribution of mass over the height of the building, variation of modal displacements over the height of the building (mode shapes), and structural and aerodynamic damping. The nature of the background and resonance loads is best described using the power spectrum base loads, as shown in Figure 5(b). As the figure shows, background excitation is a wide-band process, while the resonance responses are narrow-band and centred on the first few frequencies of the building. Resonant responses are well correlated over the height of the building and could dominate the response of tall and slender structures with a fundamental frequency of less than 1 Hz. Note that resonant responses of structures depend not only on the instantaneous wind forces but also on the past time history of forces (Holmes, 2015).

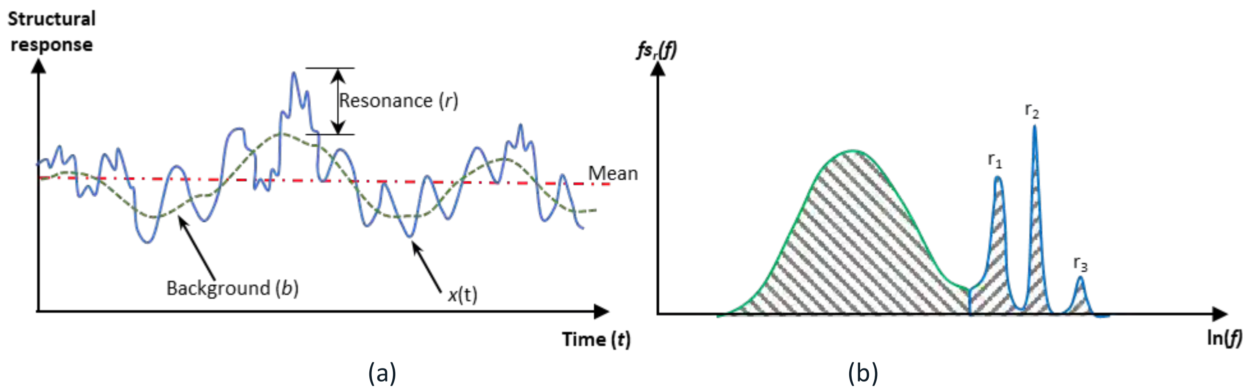


**Figure 5. Typical response of structures under wind load: (a) time history, and (b) power spectrum (Davenport, 1999)**

## 9.4.2 Along-Wind, Across-Wind, and Torsional Loads

Wind actions on tall buildings can be resolved into three components: along-wind, across-wind, and torsional (Figure 4). The along-wind forces occur in the direction of the mean wind speed, and the associated dynamic excitation is mainly caused by the approaching turbulence. Across-wind loads are the result of pressure fluctuation in the flow-separated region (e.g., vortex shedding) and are orthogonal to the mean wind speed direction (Figure 3). Mean and fluctuating across-wind loads are generally related to asymmetries in the flow (disturbance of the flow due to turbulence and immediate surroundings) and building aerodynamics. Note that the effect of oncoming turbulence on the magnitude of the across-wind loads largely depends on the longitudinal wind velocity, turbulence intensity, and wind angle of attack (AOA). For slender and flexible tall buildings, the across-wind loads usually exceed along-wind loads. Asymmetries in pressure fluctuations in the wake regions could also result in dynamic torsional wind loads. Further, torsional building vibrations could be induced due to eccentricities between the resultant wind force and the elastic centre of the buildings. For the design of tall buildings, buffeting in the drag direction and vortex shedding are the critical wind actions for satisfactory performance.

### 9.4.3 Vortex Excitation

The main source of across-wind forces on tall buildings is vortex excitation, a phenomenon related to vortex shedding, in which vortices shed alternately with a frequency ($f_s$) that can be defined by the shape-dependent Strouhal number ($S_t$):

$$\boldsymbol{f_s = S_t U/d} \qquad [1]$$

where *U* is the mean wind velocity and *d* is the width of the building. Figure 6 depicts shedding vortices passing a building with a rectangular in-plan shape. The figure also shows the Kármán vortex street, in which vortices roll down in the wake of the building.

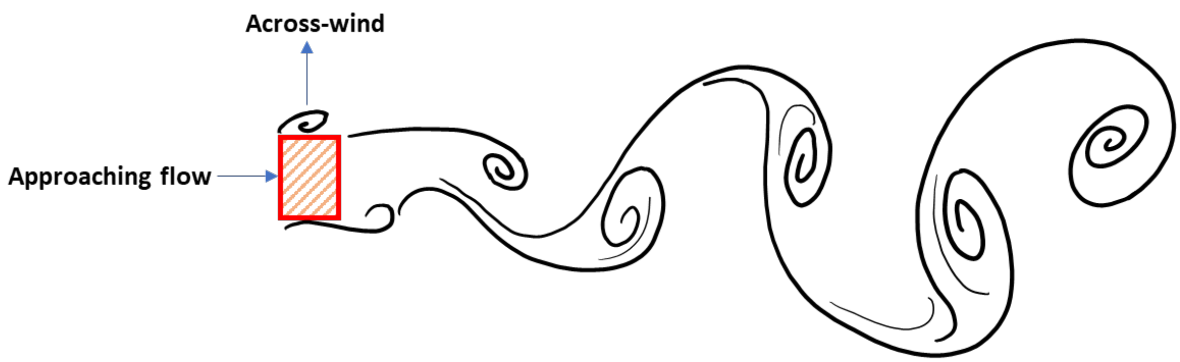


**Figure 6. Vortex shedding flow patterns**

The Strouhal number is shape-dependent and its value varies from 0.1 to 0.4. For a typical square building, $S_t$ is between 0.1 and 0.17. For buildings with a height-to-width ratio less than 6, the spectrum of the across-wind forces is relatively broad, vortex shedding is less organised, and thus, the response is directly proportional to wind speed (Vickery et al., 1983). For very slender buildings, the spectrum of across-wind forces is narrow and roughly centred on $f_s$; hence, the across-wind forces are strongly dependent on the strength and frequency of vortex shedding and weakly dependent on the oncoming turbulence. The effect of oncoming turbulence on the across-wind loads can be twofold: (1) oncoming turbulence could increase the across-wind responses at reduced velocities ($U/fd$) lower than the vortex peak, and (2) oncoming turbulence could significantly reduce the across-wind responses at reduced velocities ($U/fd$) around the vortex peak. While studying a 40-storey tall mass-timber building, Bezabeh, Bitsuamlak, Popovski, and Tesfamariam (2020) reported a reduction of the peak and a slight widening of the across-wind generalised wind force spectra when the upstream terrain exposure changed from open country to urban. Figure 7 depicts the variation of the across-wind actions with and without the presence of vortex shedding. As the figure shows, the effect of vortex excitation is that across-wind loads at wind speeds close to the critical wind speed ($U_{crit}$) are amplified. For lightly damped and low-frequency buildings, once vortex excitation is initiated, a resonance phenomenon could lock vortex shedding to the natural frequency of the building, causing the amplification by the vortex excitation to persist for a range of wind speeds.

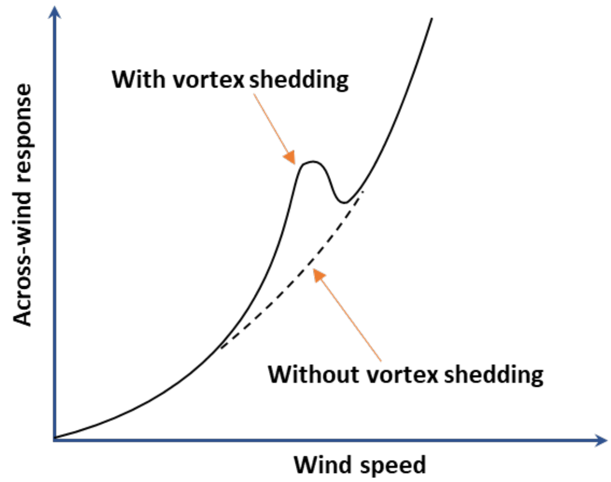


**Figure 7. Across-wind response with and without the presence of vortex shedding**

In general, buffeting-type excitation does not involve instability and can be addressed using quasi-steady theory, which assumes a similarity between the variations in upstream longitudinal wind velocity and the fluctuating wind load on the structure. Lightly damped and low-stiffness buildings operating near the peak of the across-wind spectrum and whose natural frequency is close to the vortex shedding frequency could experience large-amplitude across-wind motions that could persist for a range of wind speeds. Large-amplitude persistent across-wind excitation could lead to aeroelastic feedback, which is an interaction between the building's motion and the aerodynamic forces. In general, for very tall mass-timber buildings, the dynamic across-wind forces can be critical for the structural design.

### 9.4.4 Building Acceleration Under Wind Load

The wind-induced acceleration of a building is the result of the resonant component of the total response. Excessive wind-induced motions can be perceived by building occupants. For the many reasons stated in the literature, acceleration response can be considered the primary indicator of motion perception for occupants in a building. Occupants in buildings undergoing large-amplitude torsional rotation are often subjected to visual distortions and an amplified sense of motion. It is customary to limit the torsional velocity of a building to avoid potential issues with visual perception. The criteria for the serviceability design of tall buildings are presented in Section 9.5.

### 9.4.5 Effects of Dynamic Structural Properties on the Wind Response of Tall Buildings

To assess the wind response of tall buildings, the design engineer must determine the structural dynamic properties. The primary structural properties submitted to the wind engineer include, but are not limited to, mass and modal displacements for each storey of the building, natural frequencies, and structural damping. If the design team does not provide a structural damping ratio, the wind engineer estimates based on standards, building codes, literature review, and experience. Typically, design engineers use finite element software such as ETABS or other similar finite element packages to evaluate the dynamic structural properties. For a typical tall building project, wind engineers evaluate (a) generalised aerodynamic forces and moments from wind tunnel tests, (b) design equivalent static wind loads with companion load combination factors, and (c) building acceleration and drift. The details of a typical wind response prediction using a wind tunnel test procedure are discussed in Section 9.8. In general, increasing the mass and damping usually reduce wind-induced motions. The effect of natural frequency on wind-induced acceleration depends on the shape of the generalised force spectrum. For buildings dominated by vortex excitation, if the reduced frequency lies to the right of the peak of the across-wind load spectrum, increasing the natural frequency of the building reduces the acceleration response. If the reduced frequency lies close to the peak of the across-wind load spectrum, increasing the natural frequency of the building may not result in a reduced acceleration response. However, if the reduced frequency is less than the peak of the across-wind load spectrum, increasing the natural frequency of the building could worsen the acceleration response.

## 9.5 BUILDING DESIGN CRITERIA

Performance levels (limit states) for tall building design can be categorised into two major groups: (1) ultimate limit state (lateral instability, yielding with excessive deformation, fatigue, extensive damage of cladding elements by shear racking), and (2) serviceability limit states (excessive deflection, excessive sway acceleration causing occupant discomfort) (Bezabeh, Bitsuamlak, & Tesfamariam, 2020). The serviceability limit states could govern the design of lightweight, tall, slender, and very flexible buildings. The serviceability limit states of particular interest for the design of tall buildings are excessive deformation (deflection and drift), motion perception and occupant comfort (excessive acceleration), and visual perception. According to the National Building Code of Canada (NBCC) (National Research Council of Canada [NRCC], 2017), under service level wind, the total storey level drift shall not exceed $h/500$, where $h$ is the storey height. In addition, the code states that 'limitation of 1/500 drift per storey may be exceeded if it can be established that the drift as calculated will not result in damage to non-structural elements. Clause 72 of Commentary I of the 2015 NBCC (NRCC, 2017) states that 'unless precautions are taken to permit the movement of interior partitions without damage, a maximum lateral deflection limitation of 1/250 to 1/1000 of the building height should be observed'. In line with the commentary, as an additional general rule, a global drift limit of $H/500$, where $H$ is the total building height, can also be used. Further, in the case of a 1-in-10-year wind event, Clause 77 of Commentary I of the NBCC (NRCC, 2017) limits horizontal peak floor acceleration (PFA) to 15 milli-g and 25 milli-g for residential and office buildings, respectively. In recent years, for buildings whose natural frequency is less than 1 Hz, it became common to use shorter return periods (0.1-year to 1-year) and frequency-dependent criteria for the serviceability design of tall buildings. For this purpose, Clause 77 of Commentary I of the 2015 NBCC (NRCC, 2017) refers to the *Bases for design of structures - Serviceability of buildings and walkways against vibrations* standard (ISO 10137:2007).

## 9.6 DYNAMIC PROPERTIES OF TALL MASS-TIMBER BUILDINGS

Structural and wind engineers are expected to estimate damping ratios, a very important but uncertain parameter that depends on several factors. Especially for mass-timber buildings, there is a lack of information on damping ratios (Bezabeh et al., 2018b). A group of researchers from FPInnovations have been monitoring two mass-timber buildings. Since the monitoring program is still ongoing, the results and discussion presented in this section are preliminary, but they still give valuable insight into damping of mass-timber structures. Figure 8 shows the probability density curve for the measured damping ratio of the 40.9 m tall

Origine building located in Quebec City, Canada. A maximum likelihood damping ratio of 2.6% was obtained from the monitored data after it was fit with a lognormal distribution.

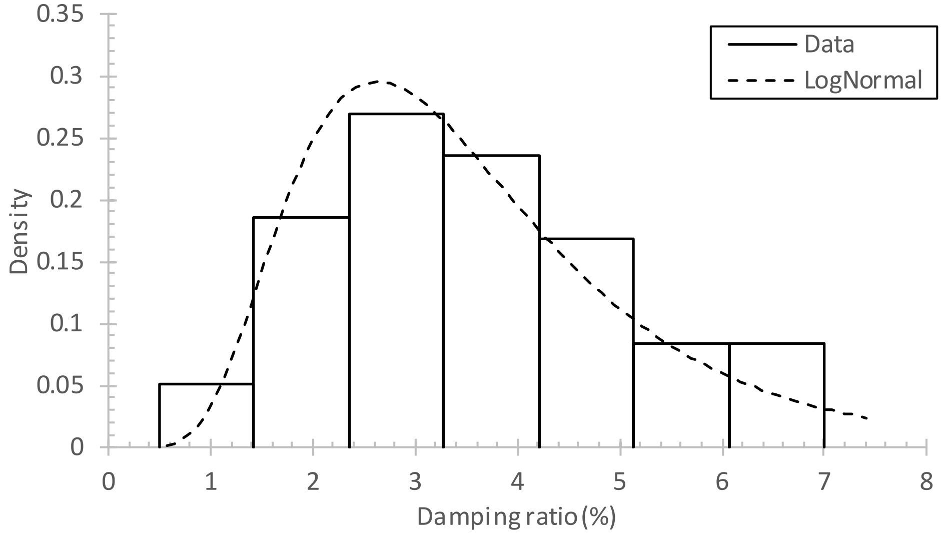


**Figure 8. Density probability curve of the modal damping ratio for the Origine building, Quebec City, Canada**

## 9.7 PREDICTION OF WIND LOAD EFFECTS USING THE NBCC

The NBCC (NRCC, 2017) permits three approaches to determine a design wind load. The procedures are static, dynamic, and wind tunnel testing, and they are differentiated by their level of complexity and range of applicability. According to the NBCC (NRCC, 2017), the specified wind pressure acting on the surface of a building is:

$$\boldsymbol{p = I_w q C_e C_t C_g C_p} \qquad [2]$$

where $I_w$ is the importance factor, $q$ is the mean hourly reference velocity pressure, $C_e$ is the exposure factor, $C_t$ is the topographic factor, $C_g$ is the gust effect factor, and $C_p$ is the external pressure coefficient. The specified wind pressure, $p$, can have a positive or negative sign when directed towards and away from the external surface of the building, respectively. Importance factors are provided in the 2015 NBCC (NRCC, 2017), depending on the building use and its occupancy. The code also tabulates 1-in-10- and 1-in-50-year reference wind velocity pressures for Canadian cities. The variation of mean wind speed (wind pressure) with height is represented by $C_e$. The gust effect factor, $C_g$, accounts for the effect of buffeting due to oncoming turbulence, turbulence in the shear layers, additional inertial forces due to wind excitation, and aeroelastic effects. The external pressure coefficient, $C_p$, accounts for building aerodynamics, the effect of building orientation, and wind speed profile.

The NBCC (NRCC, 2017) permits the use of the static wind analysis procedure to design the lateral load-resisting system (LLRS) of rigid buildings and building envelopes, such as cladding. In the context of wind engineering, buildings with a frequency of vibration greater than 1 Hz are considered rigid. Hence, rigid mass-timber buildings can be designed using this approach. When calculating the design wind loads using the

NBCC, three points to consider are that: (1) partial wind loading could be more critical than full loading, and hence shall be considered in the estimation of a specified wind pressure, (2) in addition to designing taller buildings for full wind loading, a check for additional torsion due to partial loading shall be carried out, and (3) to account for diagonal wind loading and sway in the across-wind direction, taller structures shall also be designed for 75% of the maximum wind pressure simultaneously applied in the two principal directions. The details of the static procedure are provided in Commentary I of the NBCC (NRCC, 2017).

The NBCC (NRCC, 2017) requires more elaborate dynamic or wind tunnel procedures to design buildings whose height is more than four times their minimum effective width, or taller than 60 m, or other buildings whose properties make them susceptible to wind-induced vibrations (if the lowest natural frequency is between 0.25 Hz and 1 Hz). The choice of static or dynamic procedures in the design of mass-timber buildings shall be based on the dynamic properties of the buildings (vibration frequencies, generalised mass, and generalised stiffness) rather than height. This is because the NBCC recommendations based on height comply very well with buildings made from conventional construction materials. Recent studies by Bezabeh et al. (2018a, 2018b) and Bezabeh, Bitsuamlak, Popovski, and Tesfamariam (2020) show that mass-timber buildings shorter than 60 m could be excited by the wind, resulting in excessive dynamic oscillations. In the dynamic analysis procedure, which is recommended for lightweight, low frequency, and low-damped buildings, the background excitation and the amplified resonant response arising from excitation by the wind at the vibration frequency of the building are accounted for through $C_g$. The overall analysis format of both procedures is the same except for the determination of $C_e$ and $C_g$. To calculate the $C_g$, the NBCC (NRCC, 2017) presents a series of charts for the exposure factor, background turbulence factor, size reduction factor, and gust energy ratio at the vibration frequency of the structure.

As described in Section 9.5, the design of mass-timber buildings for wind shall consider excessive drift and occupant comfort (excessive acceleration) limit states. In the design of mass-timber buildings, after proportioning for strength limit state, designs shall be iterated until they satisfy the drift limit. Buildings that satisfy the drift limits may not necessarily satisfy the occupant comfort criteria, as the former limit state is related to stiffness, and the latter depends on stiffness, mass, and damping (Bezabeh, Bitsuamlak, Popovski, & Tesfamariam, 2020). Usually, wind-induced deflection is higher in the along-wind directions, while PFA is critical in the across-wind directions. The gust effect factor can also be used to estimate the along-wind PFA demands of tall buildings. The NBCC (NRCC, 2017) provides equations to estimate the mean peak along-wind and across-wind accelerations of buildings. Equation 3 can be used to estimate the along-wind PFA ($a_D$, in m/s$^2$) and includes $C_g$, $C_{eH}$ exposure factor at the top of the building, the peak factor $g_p$, the peak lateral deflection $\Delta$, the fundamental frequency in the along-wind direction $f_{nD}$, the damping ratio as a percentage of critical damping in the along-wind direction $\beta_D$, the surface roughness coefficient $K$, the size reduction factor $s$, and the gust energy ratio at the vibration frequency of the structure $F$.

$$a_D = 4\pi^2 f_{nD}^2 g_p \left(\sqrt{\frac{KsF}{C_{eH}\beta_D}}\frac{\Delta}{C_g}\right) \quad [3]$$

The across-wind acceleration ($a_W$, m/s$^2$) can be estimated using Equation 4 as a function of the fundamental frequency in the across-wind direction $f_{nW}$, the across-wind effective width in metres $w$, the along-wind effective depth in metres $d$, acceleration due to gravity $g$, average building density $\rho_B$, the damping ratio as a percentage of critical damping in the across-wind direction $\beta_w$, and the wind speed at the top of the building $V_H$. Note that Equations 3 and 4 are empirical in nature. These equations were developed based on the results of wind tunnel tests conducted on steel and concrete buildings and exhibited significant scatter. Hence, in the design of tall mass-timber buildings, it is therefore important to interpret the estimated peak across-wind acceleration using Equations 4 and 5 with proper context.

$$a_w = f_{nW}^2 g_p \sqrt{wd}\left(\frac{a_r}{\rho_B g \sqrt{\beta_w}}\right) \quad [4]$$

where:

$$a_r = 0.0785\left(\frac{V_H}{f_{nW}\sqrt{wd}}\right)^{3.3} \quad [5]$$

Many building codes and standards worldwide have adopted the Wind Loading Chain and the format of the NBCC (Equation 2). The most notable building codes and standards with provisions for the estimation of wind-induced responses include:

- *Eurocode 1: Actions on Structures − Part 1–4: General Actions – Wind Actions* (Annex B–D) (EN 1991-1-4.6:2005)
- Australian/New Zealand Standard. *Structural design actions. Part 2: Wind actions* (AS/NZS1170.2:2011)
- *Wind actions on structures* (ISO 4354:2009)
- *AIJ Recommendations for Loads on Buildings* (2015)
- *Minimum Design Loads for Buildings and Other Structures* (ASCE/SEI 7-16)

## 9.8 WIND TUNNEL METHOD

Design wind loads and dynamic wind responses of buildings can be assessed reliably through wind tunnel techniques (Irwin et al., 2013; Bezabeh, Bitsuamlak, Popovski, & Tesfamariam 2020). The NBCC (NRCC 2015) recommends conducting wind tunnel tests for buildings whose natural frequency is lower than 0.25 Hz or whose height-to-minimum-effective-width ratio is greater than 6. Moreover, the code recommends wind tunnel testing in the case of buildings subjected to wake-buffeting from upwind buildings or channelling effects. In the design of tall mass-timber buildings, the resonant response could be caused by higher modes of vibrations such as torsion and coupled translation-torsion. For example, in the study by Bezabeh, Bitsuamlak, Popovski, and Tesfamariam (2020), the first five modes of a 40-storey tall mass-timber building have frequencies less than 1 Hz, and higher modes exhibit significant nonlinearity and coupling. Note that the provisions of the NBCC reasonably estimate the PFA of buildings dominated by the first uncoupled sway modes of vibrations. Consequently, wind tunnel testing is recommended for the design of tall mass-timber buildings with significant higher mode contributions. In addition, including directional effects of wind when synthesising wind tunnel test results with the local wind speed data of the construction site is important, which usually results in significant cost savings (Warsido & Bitsuamlak, 2015).

A wind tunnel facility for structural engineering applications was developed in the 1960s at Western University (also known as University of Western Ontario), Canada. Since then, similar facilities varying in size were built in different parts of the world, and wind tunnel tests have been used routinely to estimate design wind loads. In general, atmospheric boundary layer wind tunnels have a long testing chamber, floor roughness elements, spires, and end barriers, to allow the development of a boundary layer having similar characteristics to natural wind flow over the terrain. The commonly used test methods to predict the design wind loads and responses of tall buildings are the high-frequency-base-balance (HFBB) procedure, the high-frequency-pressure-integration (HFPI) procedure, and the aeroelastic model procedure.

Figure 9 depicts a typical process of wind tunnel study for tall buildings. As the figure shows, for a typical tall building test in the wind tunnel, the most important inputs are architectural drawings of the study building, site location, dynamic structural properties, and full-scale meteorological wind speed data of the site. The quality of the input information from the design team dictates the accuracy of model-scale testing. The main results of the wind climate studies are the probability distributions of mean wind speed and direction, and the directional extreme mean wind speeds corresponding to various return periods. To avoid issues related to local topography, wind climate studies are usually carried out at the gradient height. Extreme wind speeds can be derived from extreme value analysis or fitted parent probability distributions. Adjustment factors can be used to relate the gradient wind speed in the full scale to the reference wind speed in the wind tunnel. For a site with complex topography, it is necessary to conduct a topography model study. The following sections summarise the main types of wind tunnel studies.

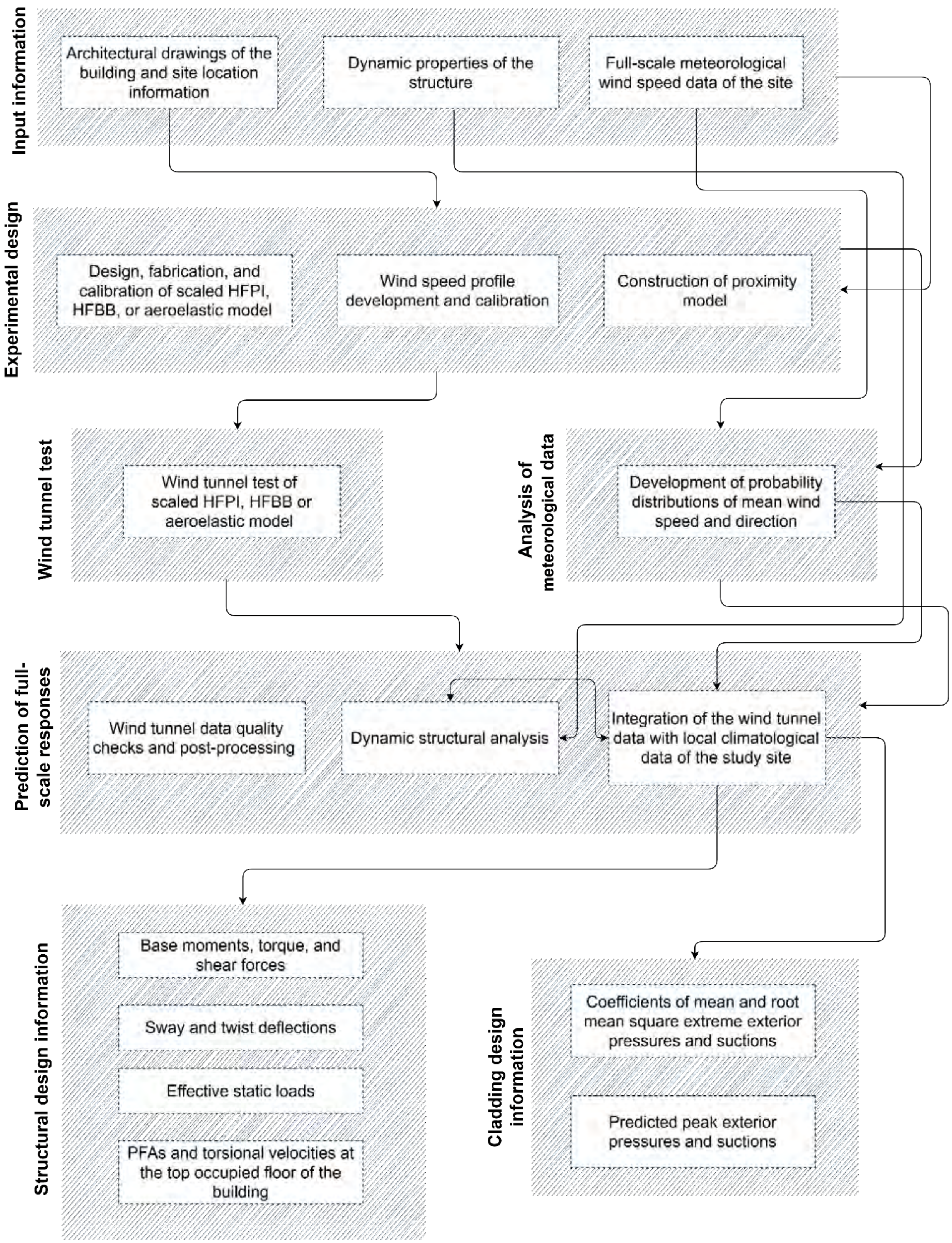


**Figure 9. Flowchart of a typical wind tunnel study for tall buildings**

### 9.8.1 Aerodynamic (Rigid Model) Studies

The most commonly used aerodynamic (rigid model) studies are the HFBB and HFPI procedures. In the HFBB test, a lightweight and stiff replica of the prototype building is mounted on a very sensitive force-balance device to measure the time histories (spectral densities) of the aerodynamic base shears and moments. The typical test set-up is shown in Figure 10(a), which is a photograph taken during the HFBB wind tunnel test of a 40-storey tall mass-timber building at the Boundary Layer Wind Tunnel Laboratory (BLWTL) of Western University. The main assumptions in the HFBB test are that (1) the response of the prototype building is mainly caused by the fundamental sway modes of vibration, (2) the fundamental sway modes of vibration vary linearly over the height of the building (linear sway mode shapes), and (3) the excitation of the building by the wind involves negligible aerodynamic damping. The amplification by the resonance is accounted for analytically in posttest analysis using random vibration theory or time-domain analysis. This testing technique is more widely used than the aeroelastic procedure due to its simplicity to build and test the models. Moreover, as long as the building aerodynamics are the same, the test results can be reused if the structural properties are revised after the test.

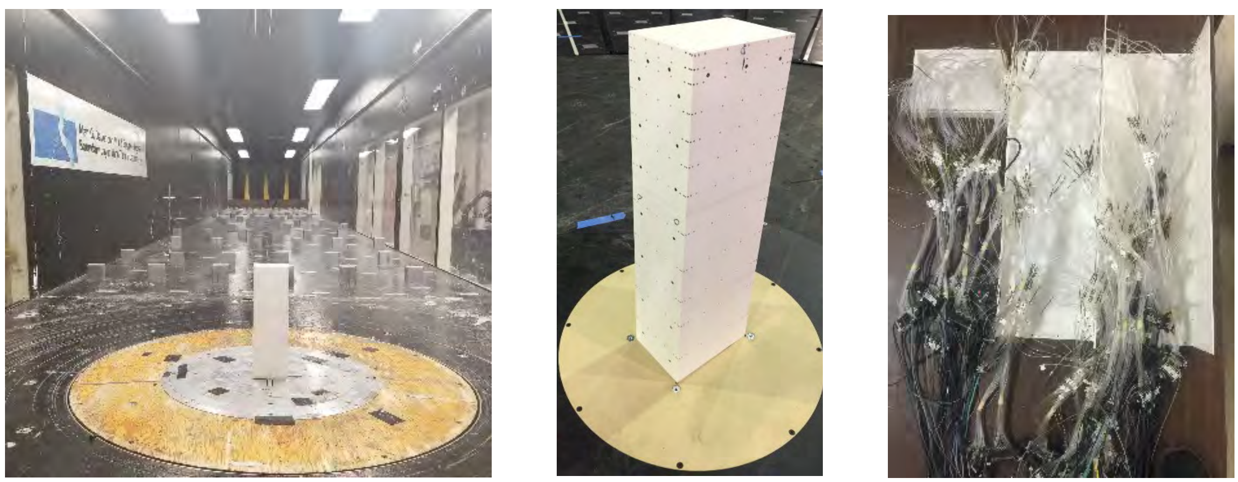

(a) (b) (c)

**Figure 10. Wind tunnel tests of a 40-storey tall mass-timber building model at BLWTL: a) HFBB test, b) HFPI test, and c) instrumentations of the HFPI model with pressure scanners**

The HFPI test utilises hundreds of pressure taps installed on the surface of a rigid model to simultaneously measure the time histories of local aerodynamic forces (Figures 10[b] and 10[c]). Synthesising the measured local pressure requires assigning tributary areas for each tap. The storey-level and the overall aerodynamic base forces can be computed by numerically integrating the time histories of measured pressures. The amplification by the resonance is included analytically in posttest analysis, either using random vibration theory or time-domain analysis. The main advantages of the HFPI test include: (1) the test results from HFPI can be used to design the LLRS and the cladding of the building, (2) the height-wise variation of aerodynamic loads, including torque, are relatively more accurate than in HFBB test results (hence, using HFPI test data, statistical and mechanical coupling of vibration modes can be accurately incorporated in estimating the wind response of a building), and (3) as long as the building aerodynamics are the same, the HFBB and HFPI tests allow structural design changes without needing to repeat the test. The main limitation of this test is the difficulty of installing pressure taps to capture the pressure variations over porous cladding elements, irregular cladding details, structures with very small architectural features (such as lattice members), and buildings with very small cross-sectional area.

### 9.8.2 Aeroelastic (Flexible Model) Studies

Dynamic response evaluation of tall buildings based on the HFBB and HFPI wind tunnel tests involves several simplifying assumptions during the experimental phase and the posttest dynamic analysis. Inherently, the HFBB and HFPI models are both rigid and do not include motion-dependent effects such as aerodynamic damping, which is related to the velocity of the wind-excited building. Aerodynamic damping is usually positive in the along-wind direction. In the across-wind direction, aerodynamic damping can be positive or negative. Negative aerodynamic damping could significantly amplify the dynamic across-wind responses. Aeroelastic tests include aerodynamic damping and do not involve most of the assumptions of HFBB and HFPI tests. Compared to the HFBB and HFPI tests, aeroelastic procedures are more reliable and relatively accurate. Dynamic responses of study buildings, such as lateral drift, acceleration, and base bending moments, can be directly measured from aeroelastic model tests. In aeroelastic tests, models sway and twist similarly to the prototype building under wind excitation; therefore, the dynamic properties of the building, such as mass, damping, and stiffness, shall be modelled. In general, aeroelastic model studies can be split into two categories: (1) base-pivoted two-degrees-of-freedom aeroelastic model and (2) multi-degree-of-freedom aeroelastic model. The choice of model depends on the complexity of the structural system (such as higher mode effect, modal coupling, or the nonlinearity of mode shapes), the shape of the building, and the degree of accuracy sought.

In the base-pivoted two-degrees-of-freedom aeroelastic model, the building model rotates as a rigid body about a pivot point. Figure 11(a) depicts a schematic of the two-degrees-of-freedom aeroelastic model pivoted on a gimbal joint in its base. The active part of the model (above the pivot point) is usually built from high-density lightweight foam. To retain rigid-body motion about the pivot point, a stiffener rod is usually inserted inside the model. The active part of the model is attached to an aluminium rod, which is extended below the floor of the wind tunnel. The aluminium rod is connected to two springs in two orthogonal axes, and these springs provide stiffness to the model. Figure 11(b) shows the test set-up in the wind tunnel during an aeroelastic wind tunnel test of a 40-storey mass-timber building model. An eddy current electromagnetic device is usually used to provide inherent structural damping. The main limitations of this approach are that (a) the response of the prototype building is mainly caused by the fundamental sway modes of vibration, (b) fundamental sway modes are uncoupled, and (c) the prototype building is very stiff in torsion. The main advantage of this method over HFPI and HFBB is its ability to account for aerodynamic damping. Multi-degree-of-freedom aeroelastic models are suitable for buildings with 3D complex mode shapes, including torsion and coupled translation-torsion modes. In this procedure, it is customary to use a lightweight shell (such as balsa wood or 3D printed parts) to model the building geometry and an aluminium spine to model the stiffness (Figures 12[a] and 12[b]). Structural damping is usually provided via strips of foam tape at segments of the exterior shell. During the test, the aeroelastic model is instrumented with accelerometers at the top occupied floor of the building model and a base balance to measure time histories of the overall moments and torsion.

(a) 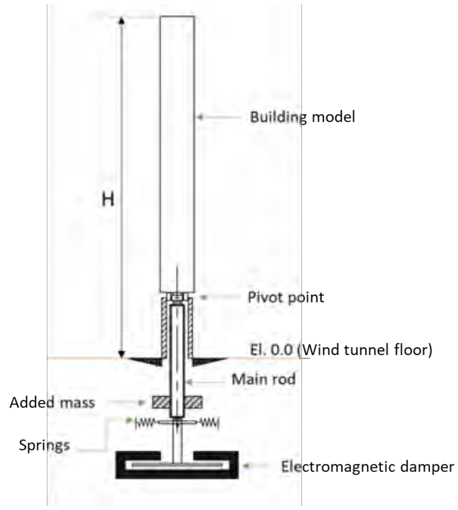


(b) 

**Figure 11. (a) Schematic of the two-degrees-of-freedom aeroelastic model. (b) An aeroelastic wind tunnel set-up of a 40-storey mass-timber building at BLWTL**

(a) 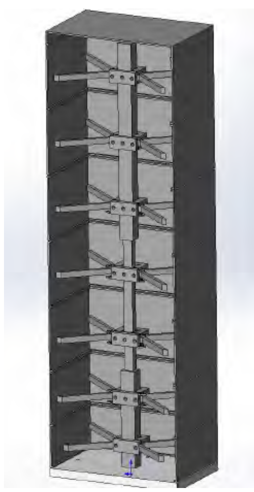

(b) 

**Figure 12. (a) Schematic of a multi-degree-of-freedom aeroelastic model. (b) Multi-degree-of freedom aeroelastic model of a 40-storey mass-timber building opened from the top to show the central aluminium spine**

The most important parts of a typical wind tunnel study are predicting the load information for the strength design of the LLRS and the cladding, and conducting serviceability performance checks (Figure 9). In tall building design, the ultimate limit state usually corresponds to load effects with 500-years to 3000-years of return period, while serviceability limit state requires shorter return periods (i.e., 0.1-year to 50-year). Prediction of full-scale responses and load effects for various return periods require synthesising the wind tunnel data with the full-scale wind speed information. Wind climate synthesis techniques, such as the nondirectional method, traditional sector-by-sector (Simiu & Filliben, 2005), sector-by-sector with copula functions (Warsido & Bitsuamlak, 2015), upcrossing method (Davenport, 1977; Lepage & Irwin, 1985), multivariate extreme wind speed models (Zhang & Chen, 2015), multisector method (Bekele & Holmes, 2014), and storm passage method (Irwin et al., 2005) are usually used. The final product of a typical wind tunnel study is a summary of the relationship between full-scale wind load effects and the return period

(Figure 9). More information about the wind tunnel test of tall buildings can be found in Irwin et al. (2013) and the *Wind Tunnel Testing for Buildings and Other Structures* standard (American Society of Civil Engineers, 2012).

## 9.9 DESIGN AND DYNAMIC RESPONSE OF 30- AND 40-STOREY TALL MASS-TIMBER BUILDINGS FOR WIND

In 2016, the authors of this chapter launched a coordinated research program between the University of British Columbia, Western University, and FPInnovations. The research program includes several aerodynamic and aeroelastic wind tunnel tests at the BLWTL. In total, 11 tall mass-timber buildings were tested in the wind tunnel. Some of the findings have been reported in Bezabeh et al. (2018a, 2018b), Bezabeh et al. (2018), and Bezabeh, Bitsuamlak, Popovski, and Tesfamariam (2020). In Bezabeh et al. (2018a), using pressure model wind tunnel tests, the performance of a 30-storey mass-timber building was assessed deterministically. Subsequently, Bezabeh et al. (2018b) developed a new probabilistic performance-based wind engineering framework to study the implication of uncertainties on the structural reliability of wind-excited mass-timber buildings. In Bezabeh et al. (2018), the structural performance of a 10-storey mass-timber building was evaluated under experimentally simulated stationary and translating tornadoes. In Bezabeh, Bitsuamlak, Popovski, and Tesfamariam (2020), the dynamic response and serviceability performance of five tall mass-timber buildings varying in height (10-, 15-, 20-, 30-, and 40-storey) were examined using aerodynamic and aeroelastic testing. For brevity, the following sections present the dynamic response of 30- and 40-storey tall mass-timber buildings estimated using the wind tunnel testing approach discussed in the previous sections.

Figures 13 and 14 show the structural system of the 30- and 40-storey mass-timber buildings that were studied. As part of the Timber Tower Research Project, the structural system of the studied buildings was first developed in 2013 by Skidmore, Owings, and Merrill (2013). The mass-timber structural system consists of CLT floors, perimeter glulam columns, edge and link reinforced concrete (RC) spandrel beams, and CLT shear and core walls. As Figure 14 shows, the CLT floor system is supported at the mid-span by CLT walls and at the edge by the RC spandrel beams and perimeter glulam columns. In this structural system, the main elements of the LLRS are the CLT core and shear walls, which resist the gravity and lateral wind loads. To increase the net uplift resistance when the wind blows orthogonal to the broader face of the building, four supplemental shear walls are extended from the core walls to the perimeter spandrel beams. These shear walls are coupled using the RC link beams so that the whole LLRS works as a unit. In addition to enhancing the lateral stiffness, these link beams also increase the dead weight of the building. The elements of the LLRS are discontinued at each floor, similar to a platform-type CLT construction. The elements of the LLRS and gravity systems are connected using concrete joints at the interface of the CLT walls and CLT floor. The Holz-Stahl-Komposit (HSK) connection modified by Zhang et al. (2018) is used.

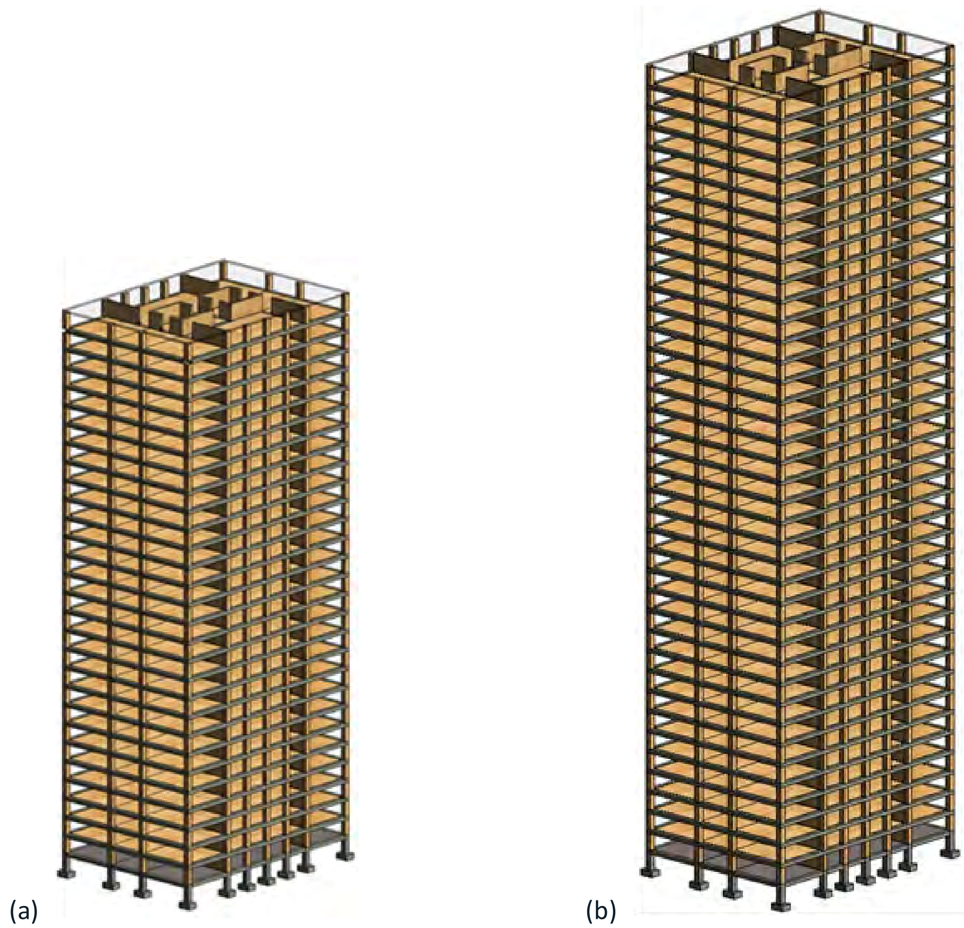


**Figure 13. Three-dimensional views of the (a) 30- and (b) 40-storey mass-timber buildings studied**

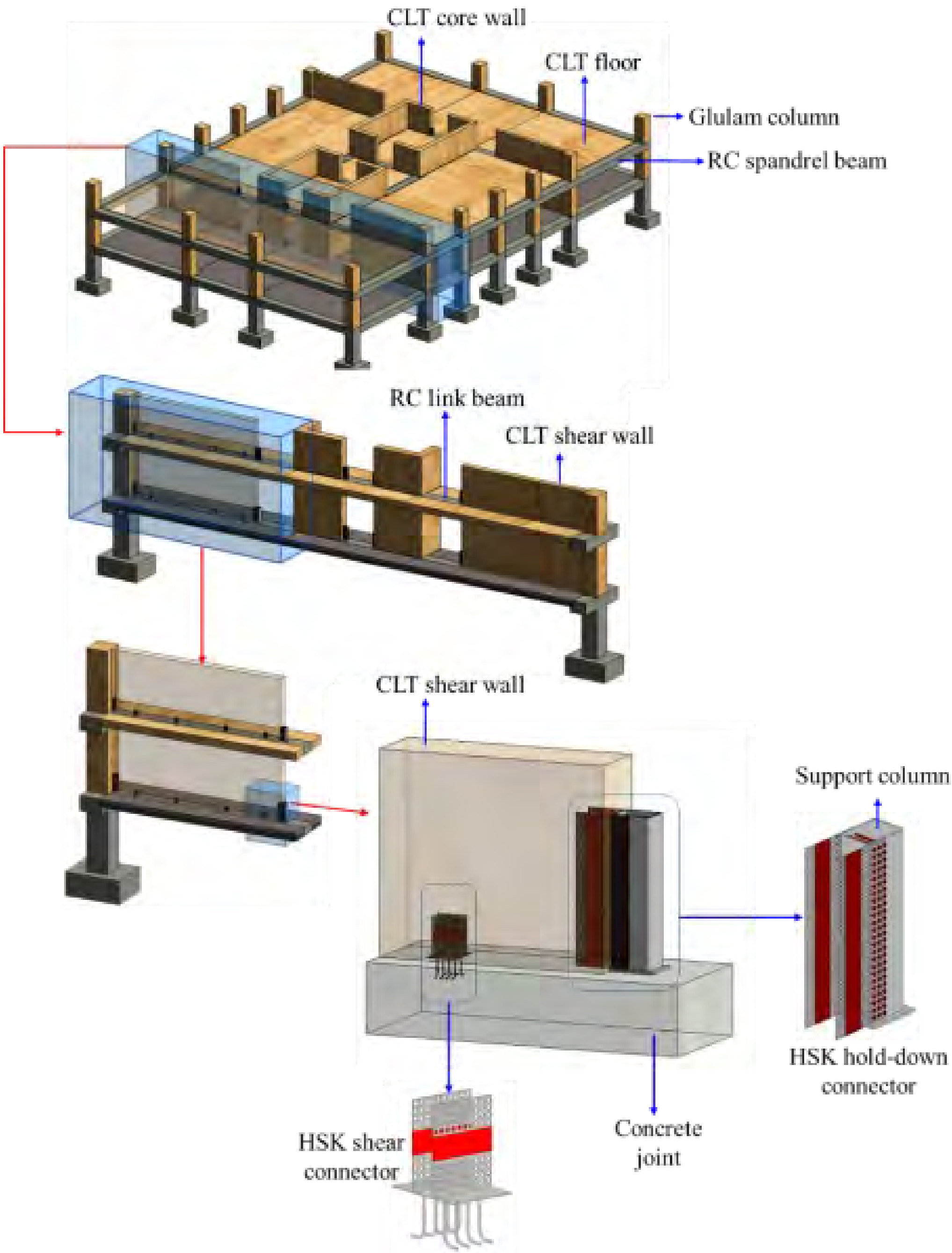


**Figure 14. The structural system of the studied tall mass-timber building**

The floor-to-floor height and the plan dimensions of the studied buildings (the high-end condominium scheme in Skidmore, Owings & Merrill, 2013) are 3.4 m and 42 m x 30 m, respectively. The design of tall-mass timber buildings is not quite conventional. This is partly due to the limited design experience in the structural/timber engineering community, the scarcity of connection systems, and the lack of experimental tests and full-scale measurements (Bezabeh et al., 2018a; Bezabeh, Bitsuamlak, Popovski, & Tesfamariam, 2020). Bezabeh et al. (2018a) developed a step-by-step structural design process for the 30-storey mass-timber building. Figure 15 depicts a flowchart of the design procedure followed for the mass-timber buildings according to the requirements and specifications of the NBCC (NRCC, 2017) and the *Engineering Design in Wood* standard (CSA Group, 2014). In general, the design process involves conceptual design, design of the gravity load-resisting system, design of the LLRS, capacity checks (including second-order effects), design of the connections system, and drift (serviceability) checks.

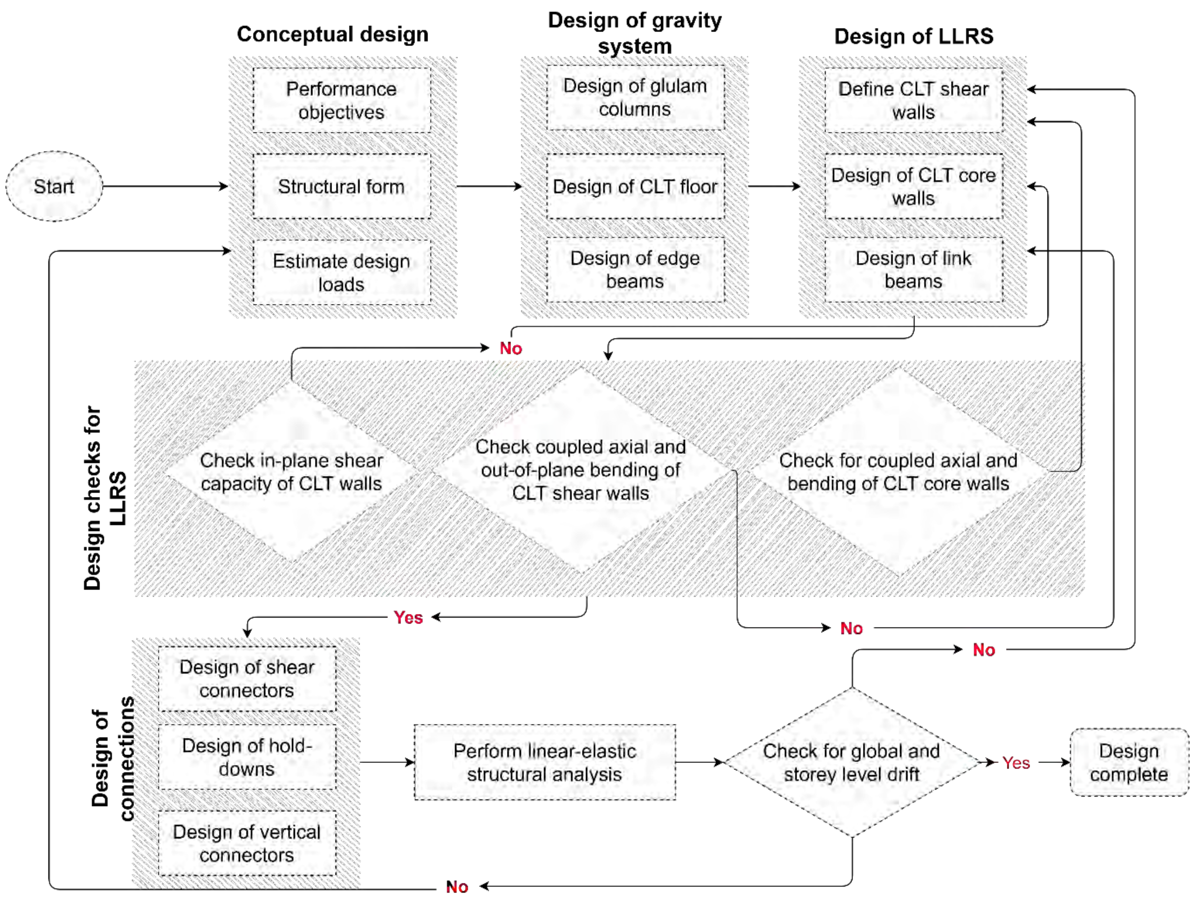


**Figure 15. Structural design flowchart for tall mass-timber buildings for wind loads**

Eigenvalue analysis identified the fundamental frequencies of the studied 40- and 30-storey buildings as 0.22 Hz and 0.33 Hz, respectively. Figures 16 and 17 depict the mode shapes of the buildings. As the figures show, the first two vibration modes of the mass-timber buildings are in translation, while the third mode is in torsion. Higher modes of these buildings (fourth and fifth) show significant nonlinearity and coupling. The vibration frequencies of the first five modes of the 40-storey mass-timber building are less than 1 Hz. Buildings with a frequency of vibration less than 1 Hz are dynamically active under wind loads; hence, it is recommended that they be included in the dynamic response analysis.

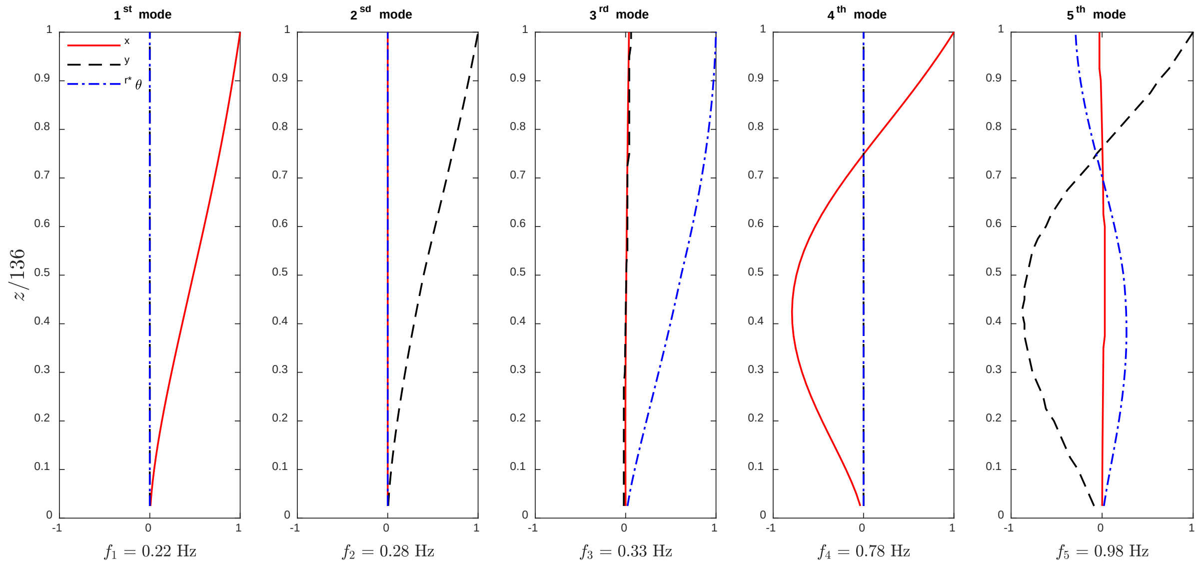


**Figure 16. The first five mode shapes and natural frequencies of the studied 40-storey mass-timber building**

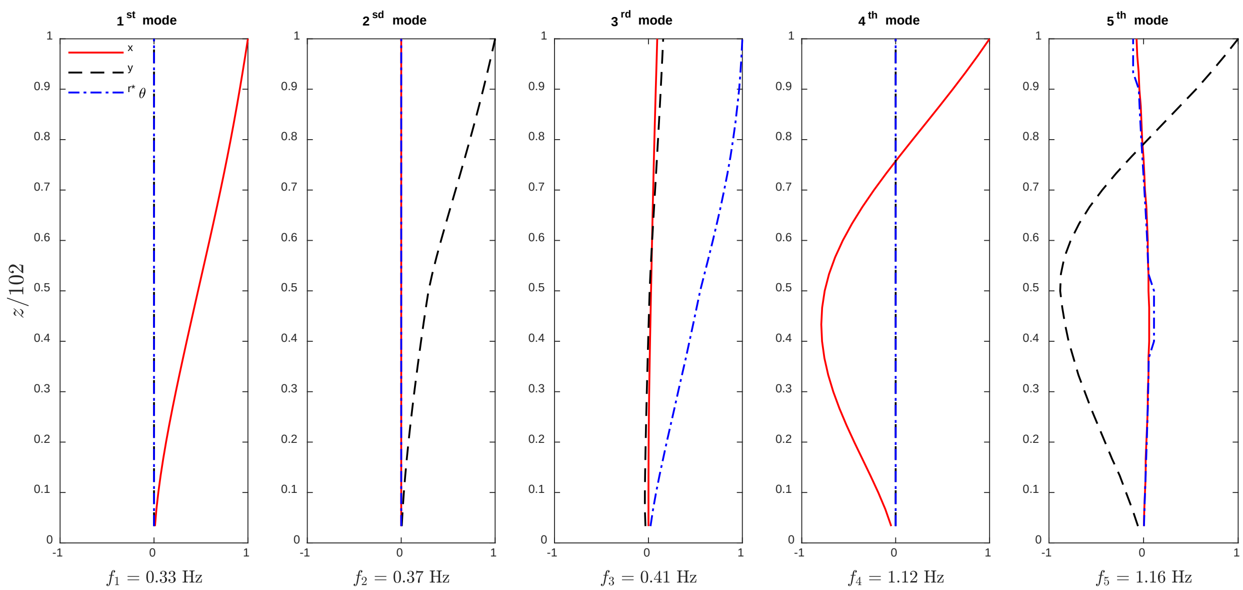


**Figure 17. The first five mode shapes and natural frequencies of the studied 30-storey mass-timber building**

HFPI wind tunnel tests were conducted to obtain floor-by-floor aerodynamic wind load time histories (Figure 18). To study the effect of longitudinal intensity of turbulence, three boundary layers representing open country, suburban, and urban exposures were simulated. Dynamic structural analyses in the frequency domain were performed to calculate the PFA for various levels of critical damping ratio, wind direction, and exposure conditions.

(a)  (b) 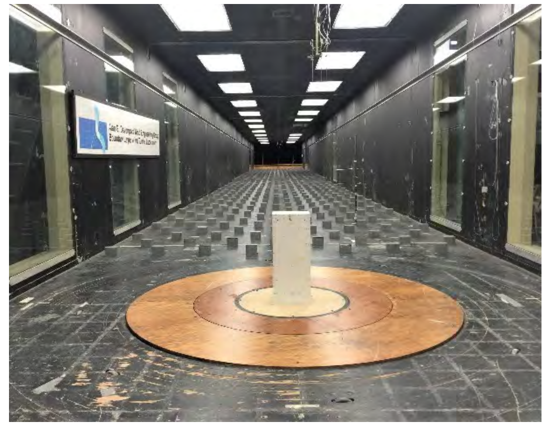

**Figure 18. Wind tunnel test set-ups of the studied (a) 40- and (b) 30-storey mass-timber building models**

The characteristics of the fluctuating aerodynamic wind loads can be described adequately using the spectral densities of the generalised forces. The spectral densities of the generalised along-, across-, and torsional-wind loads corresponding to the first three modal vibrations of the 40- and 30-storey mass-timber buildings are presented in Figures 19 and 20, respectively. In the plots, the vertical axis is the normalised spectral density of the generalised forces, and the horizontal axis is the reduced frequency ($fD/V_h$), where $f$, $D$, $V_h$, $S_{FF}(f)$, and $\sigma_f$ are the frequency, characteristic dimensions of the building, wind speed at the building height, spectral density of the generalised force, and root mean square value of generalised wind force, respectively. Figures 19 and 20 present results for the three exposure conditions defined earlier and a zero-wind AOA.

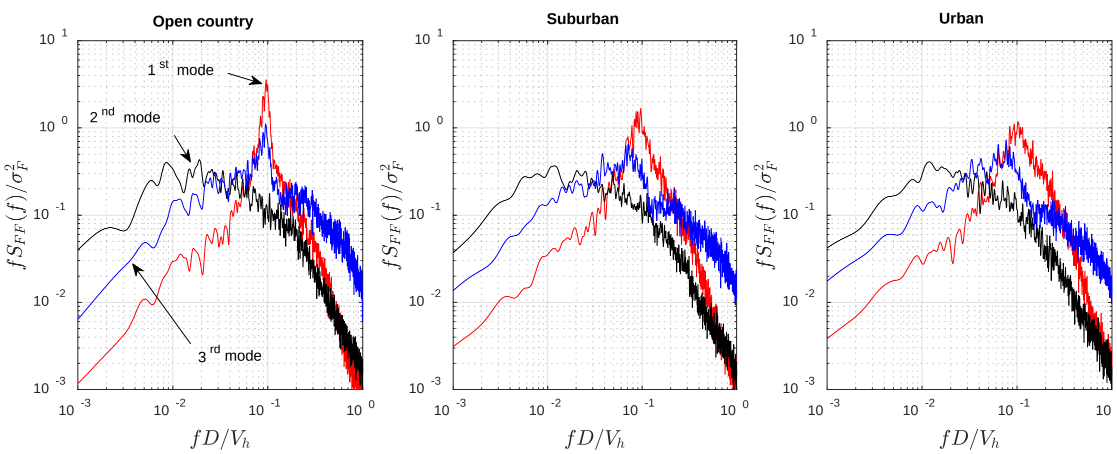


**Figure 19. Spectra of the generalised force of the 40-storey mass-timber building**

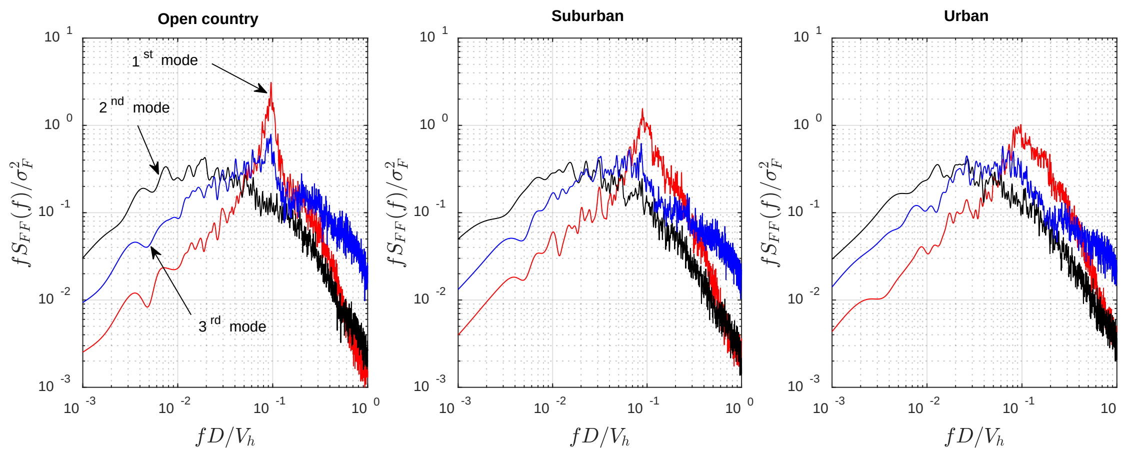


**Figure 20. Spectra of the generalised force of the 30-storey mass-timber building**

As Figures 19 and 20 show, for all exposure conditions, the dynamic excitation of the buildings in the first mode is due to across-wind forces, which is characterised by a peak at the reduced frequency close to the Strouhal number of a rectangular prism. The effect of increasing the turbulence intensity (e.g., from open country to urban exposure) is a reduced peak and slightly broadened spectra. The generalised force spectra in the second mode follow the along-wind speed spectra. Hence, referring to the quasi-steady theory, wind excitation in the second mode is due to along-wind forces. Excitation in the third mode is the result of torsional moments. In all exposure conditions, the torsional moment spectrum has two peaks. The first spectral peak is due to the asymmetry in the vortex shedding forces, and in an open country exposure it occurs at $fD/V_h$ ~ 0.1. The second peak in the torsional spectrum is the result of flow reattachment in the wake region.

A parametric study was conducted for critical damping ratio, exposure condition, and wind AOA on the acceleration response of the studied buildings. Figure 21 presents the results of the dynamic analysis in the form of resultant PFAs as polar plots. To maintain generality, the influence of immediate surroundings was ignored, and directionality effects were included using the upper bound method. The resultant PFAs were calculated at the corner of the building floors, where the contribution from torsional acceleration was accounted for after transforming into translational components. To assess the habitability of the buildings, the recommended comfort criteria of the NBCC (NRCC, 2017) for residential (15 milli-g) and office (25 milli-g) buildings were included in the figures. As Figure 22 shows, for the 30- and 40-storey mass-timber buildings, regardless of the critical damping ratio, the PFAs are reduced when the longitudinal intensity of turbulence increases (e.g., from open country to urban exposure). This is mainly due to the increase in local turbulence that deteriorates the periodicity vortex shedding in the wake regions. In addition, PFAs are the highest for the open country upstream exposure. Wind AOA = 0° and 90° are the most unfavourable wind directions. The acceleration response of buildings is inversely proportional to the square root of the critical damping ratio ($\xi$). Therefore, a small increase in damping could significantly reduce structural loads and acceleration. In all cases, doubling the damping reduces the PFA by almost 30%.

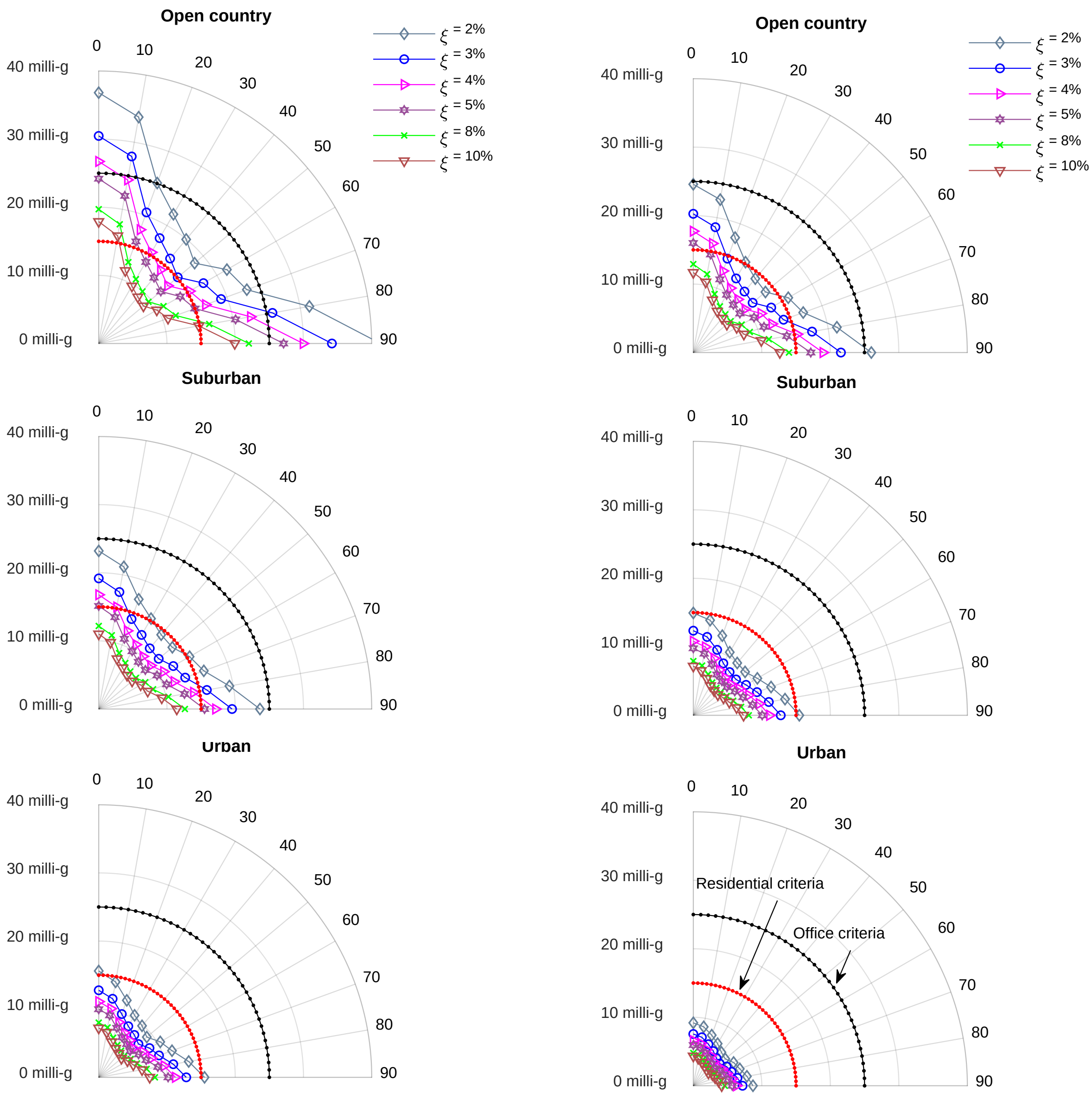


(a) (b)

**Figure 21. Effect of longitudinal turbulence intensity on the dynamic response of mass-timber buildings: a) 40-storey building, and b) 30-storey building**

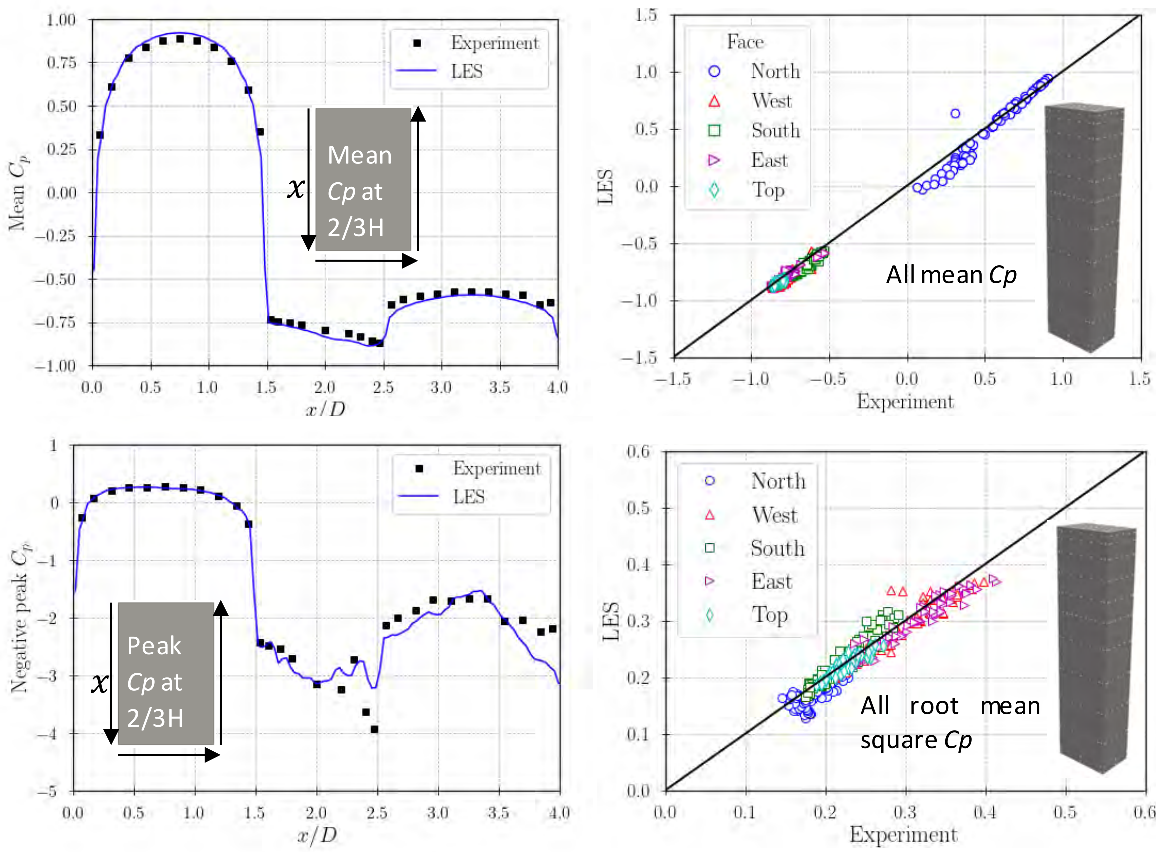


**Figure 22. Large-eddy simulation (LES) and experiment *Cp* value comparisons**

## 9.10 WIND LOAD ESTIMATION BASED ON COMPUTATIONAL FLUID DYNAMICS FOR PRELIMINARY DESIGN

Significant progress has been made in using approaches for wind load evaluation based on computational fluid dynamics (CFD), driven by current advances in computational power and algorithm development. Evaluating peak wind loads requires modelling wind turbulence accurately. The need to resolve the wide range of spatial and temporal turbulence scales in the lower atmospheric boundary layer flows makes the computational process for such applications demanding. As a result, most computational modelling tasks are completed in a high-performance computing environment, such as those provided by Compute Canada, or in commercial environments offered by many companies. Regarding the numerical solvers, either open-source CFD solvers, such as OpenFOAM, or commercial solvers, such as Siemens' STAR-CCM, can be used. Boundary-layer wind tunnel–based studies, which have seen industry-wide acceptance, are often used to validate CFD, a necessity for turbulent flow interactions with bluff bodies at high Reynolds numbers.

As with wind tunnel studies, when modelling wind effects using CFD, care must be taken at each step of the Wind Loading Chain (Figure 2). Dagnew and Bitsuamlak (2013, 2014), Melaku and Bitsuamlak (2020), and Aboshosha et al. (2015) discuss the determination of wind loads using CFD. Table 1 summarises the steps followed in evaluating wind load in boundary layer wind tunnels and the corresponding computational steps that need to be followed to produce comparable numerical results.

**Table 1. Wind load evaluation procedure**

| Wind tunnel procedure | CFD procedure |
|---|---|
| Determine test profile through upwind terrain roughness assessment using standard methods such as ground roughness and spires | Model detailed upwind roughness and topography in large-size computational domain or generate proper inflow turbulence using synthetic methods (Melaku & Bitsuamlak, 2021) |
| Construct physical aerodynamic study building model | Prepare accurate 3D aerodynamic computer model of the study (Dagnew & Bitsuamlak, 2013) |
| Trace inner disc and immediately construct surrounding buildings within a 500 m radius from the study site | Prepare 3D computer model for the immediate surrounding buildings and topographic elements within a 1 km radius |
| Adjust upwind tunnel floor roughness and spires based on test profile requirement | Apply proper inlet boundary conditions based on the result of large-size computational domain numerical simulation or synthetic inflow turbulence generation |
| Conduct wind tunnel for different test configurations (e.g., unsheltered, present, future configurations). Typically, 36 wind directions are tested in 10° increments by rotating the turntable | Perform numerical simulation for different configurations (e.g., unsheltered, present, future configurations). Typically, 36 wind directions are simulated by creating a computational domain and generating appropriate grids for each wind direction |
| Analyse wind tunnel data to obtain overall wind loads for main wind-force resisting system design, detailed pressure coefficient (*Cp*) distributions on the faces of the buildings being studied or on any required portion of the building for component and cladding design | Analyse numerical output data to extract overall wind loads for main wind-force resisting system design, detailed pressure coefficient (*Cp*) distributions on the faces of the buildings being studied or on any required portion of the building for component and cladding design |
| Integrate wind tunnel data with local meteorological information at the study site to account for directional effects (Warsido & Bitsuamlak, 2015) | Integrate numerical output data with local meteorological information at the study site to account for directional effects (Warsido & Bitsuamlak, 2015) |
| Obtain design wind loads and other wind-induced responses as required | Obtain design wind loads and other wind-induced responses as required |

A CFD wind load evaluation based on LES was carried out on a typical tall building that has been used as a test building by several wind tunnel laboratories and CFD researchers. Figure 22 shows that CFD-generated pressure coefficients match quite well with experiment data. Note that these CFD simulations are computationally demanding, and the associated engineering time is intensive. Nevertheless, CFD-based wind load evaluations can be useful for preliminary design as they can be executed by designers and can be easily integrated with optimisation tools for aerodynamic optimisation applications (see Sections 9.11.1 and 9.11.2).

## 9.11 MITIGATION STRATEGIES FOR EXCESSIVE WIND-INDUCED MOTIONS IN TALL MASS-TIMBER BUILDINGS

The results presented in Section 9.9 indicate that under certain circumstances, the resultant PFAs of the studied tall mass-timber buildings could exceed the recommended habitability criteria of the NBCC (NRCC, 2017). If the vibration frequency of a mass-timber building lies within the low-frequency tail of the wind spectrum (the energy-containing region), the resonance component of the wind response contributes significantly to the overall excessive wind-induced vibrations. In general, building motions can be reduced to some extent by changing the exterior geometry of a building. For a given shape, structural engineering solutions involve changing stiffness, mass, and structural damping. The following sections present mitigation strategies for excessive wind-induced motions in tall mass-timber buildings.

### 9.11.1 Dynamic Wind Response Optimisation

In many instances, changing the exterior geometry of a building to reduce wind-induced response involves the architect rather than the structural engineer. Hence, structural engineers usually prefer altering the dynamic properties of the buildings, such as stiffness, mass, and damping (Warsido et al., 2009). This section examines the effectiveness of these parameters on reducing excessive wind-induced vibrations. The results of response optimisation are parametric maps that can guide structural engineers to alter a building's dynamic properties for optimal wind performance. For this purpose, the 40-storey tall mass-timber building designed and analysed in Section 9.9 is considered a benchmark. The generalised mass and stiffness of the benchmark building varied from 50% to 300%, at 10% increments. Four levels of critical damping ratio ($\xi$) were considered, including a very high $\xi = 5\%$ that can only be achieved through external damping systems. To vary the generalised mass and stiffness, two multipliers were used (i.e., generalised stiffness multiplier $\psi_K$ and generalised mass multiplier $\psi_M$). The parametric analysis was conducted for the most unfavourable aerodynamic direction, when the wind blows orthogonal to the broader face of the building (AOA = 0º).

Figure 23 presents the obtained parametric maps for the critical damping ratios of 1.5%, 2%, 3%, and 5%, together with the habitability criteria of the NBCC (NRCC, 2017) for office buildings (25 milli-g). As anticipated, increasing damping, stiffness, and mass of the building always reduces the PFA. The rate at which the mass and stiffness decrease the PFA is similar. For a given damping value, the parametric maps consistently show that excessive wind-induced vibrations can be controlled by (a) increasing the generalised mass while keeping the generalised stiffness at the benchmark value or vice versa, and (b) simultaneously increasing both the generalised mass and stiffness.

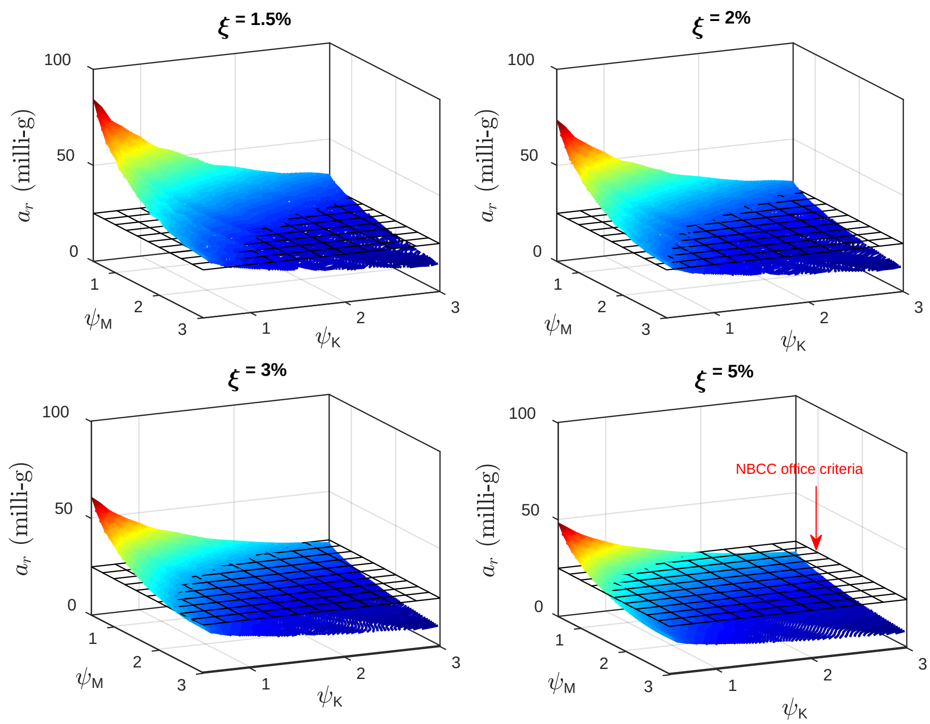


**Figure 23. Parametric maps of the PFA of the 40-storey mass-timber building studied**

A significant change in generalised stiffness might require changing the LLRS of the mass-timber building. In this regard, hybridising the timber building with either steel or concrete would be a practical solution. Recently, efficient hybrid mass-timber structures have been reported in the literature, namely, steel moment frames with CLT infill walls (Tesfamariam et al., 2015; Bezabeh et al. 2017), timber-steel core walls (Goertz et al., 2018), a mass-timber structure with concrete core walls (Tannert & Moudgil, 2017), and steel-timber hybrid tall buildings (Green & Karsh, 2012; Chen & Chui, 2017), timber-concrete hybrid buildings (Tesfamariam et al., 2019). Outrigger structures connecting the CLT core walls and the exterior columns can be used to reduce wind-induced vibrations of tall mass-timber buildings. Overall, increasing the damping capacity is usually more efficient than increasing the stiffness and mass. Moreover, increasing the damping also reduces the susceptibility of the mass-timber buildings to vortex excitation. Enhancing damping capacity can be achieved through passive and active supplemental damping systems. Details of damping enhancement in tall buildings can be found in the literature (e.g., Vickery et al., 1983; Irwin, 2008; Kareem et al., 2013).

### 9.11.2 Aerodynamic Modifications

The results presented in the preceding sections and in the study by Bezabeh, Bitsuamlak, Popovski, and Tesfamariam (2020) show that across-wind motions dominate the wind response of mass-timber buildings taller than 10 storeys. It is generally recognised that vortex shedding in shorter buildings is less organised, with broadened spectra, in which the across-wind responses are relatively small. Figure 23 shows, vortex excitation in taller mass-timber buildings can be suppressed by increasing the stiffness, mass, and damping. At times, altering the dynamic properties of buildings could be a cost-prohibitive approach. On the other hand, aerodynamic measures have been applied routinely to reduce the vortex excitation in tall buildings, such as in Taipei 101, Burj Khalifa, and the Petronas Towers (Irwin, 2008). Studies (Merrick & Bitsuamlak, 2009; Elshaer et al., 2017) have illustrated the effect of shape and the benefits of considering aerodynamic measures at the early design stage of tall buildings. Typical aerodynamic measures include softening of sharp corners by chamfering and rounding, tapering and setbacks over the building height, and using spoilers and through-building openings. For square and rectangular buildings, chamfering of corners up to 10% of the building width has been found to be beneficial in reducing vortex excitation (Kwok, 2013). Chamfering of corners alters the shear layer turbulence and the magnitude of wake energy around the shedding frequency. To illustrate this effect, using a CFD approach with LES, the aerodynamic characteristics of tall mass-timber buildings with sharp and chamfered corners were examined.

Figure 24 compares the pressure gradient of the flow field around the studied buildings. As expected, the chamfering of the corners affected the flow structure in the wake region and the reattachment points of the separated shear layers. The results indicate the possibility of reducing the overall along- and across-wind responses of taller mass-timber buildings. Varying the shape of the cross-section over the height of the building through setbacks and tapering can also be efficient in reducing wind vibrations. This kind of aerodynamic mitigation reduces the coherence of the aerodynamic excitation. With the growth of computational capability, recently, CFD has been used to perform aerodynamic optimisation of tall buildings. For example, Elshaer and Bitsuamlak (2018) developed CFD-based automated shape optimisation algorithms. Moreover, performance-based topology optimisation algorithms, as reported in Spence (2018), can be explored to perform aerodynamic and structural optimisation of tall mass-timber buildings.

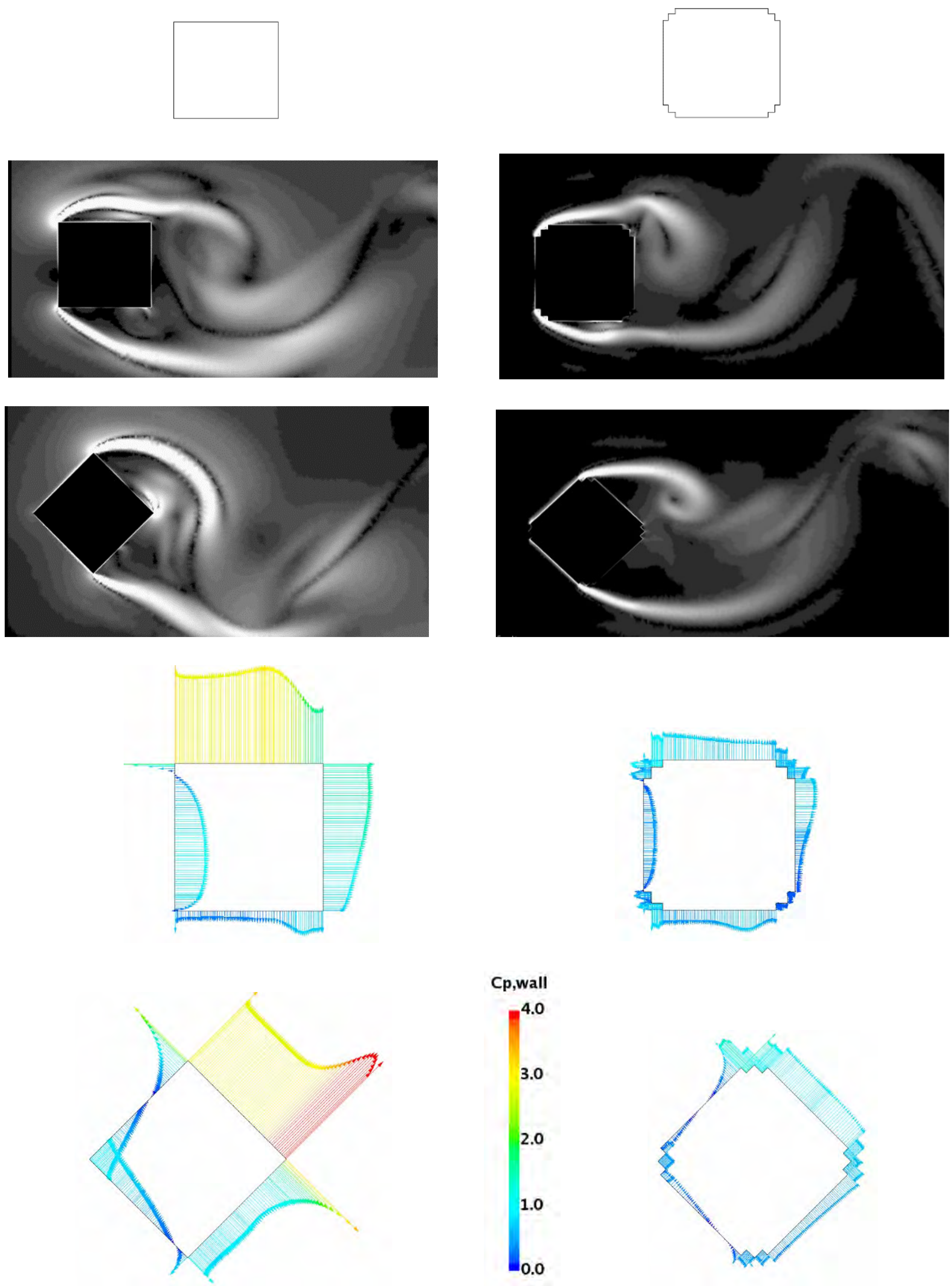


**Figure 24. Comparison of aerodynamic characteristics of tall mass-timber buildings with sharp *(left column)* and chamfered corners *(right column)***

## 9.12 INTRODUCTION TO PERFORMANCE-BASED WIND DESIGN OF TALL MASS-TIMBER BUILDINGS

As discussed in Section 9.2, via Davenport's Wind Loading Chain (Figures 1 and 2), the design of tall mass-timber buildings for wind loads integrates the wind hazard, its turbulence, building aerodynamics, and structural properties to arrive at engineering demand parameters that shall be compared with the criteria. However, each link in the Wind Loading Chain has its uncertainties, and the weakest link always dictates the design outcome. Consequently, the overall reliability of the process is dominated by the link with the largest uncertainty. In the current design approaches used in building codes, uncertainties are accounted for in the design process through safety coefficients (i.e., partial load and resistance factors). The underlying assumption behind this approach is the automatic propagation of uncertainties through the design process. The calibrated load factors in building codes may not account for additional uncertainties due to new construction materials, such as mass timber (Bezabeh et al., 2018b). In general, the issue of damping uncertainty is significant in the design of tall mass-timber buildings. As Figure 21 shows, the dynamic response of tall mass-timber buildings highly depends on the assumed critical damping ratio. The understanding and studies about the source and mechanism of structural damping in mass-timber structures are not as mature compared to concrete or steel buildings. Currently, available full-scale data of damping in mass-timber structures in the literature is very limited and scattered, with a high coefficient of variation. Hence, for wind design and performance assessment of tall mass-timber buildings, the most rational approach is to explicitly model and propagate uncertainties through Davenport's Wind Loading Chain. Furthermore, the current wind design practice for tall buildings considers the first significant yielding point as the ultimate limit state, making tall buildings costly due to an excessive design safety margin (Bezabeh, Bitsuamlak, & Tesfamariam, 2020). Hence, to overcome these limitations, Bezabeh, Bitsuamlak, and Tesfamariam (2020) and Bezabeh (2020) developed new performance-based wind design (PBWD) frameworks for tall buildings by extending Davenport's Wind Loading Chain. Figures 25 and 26 present the developed two-generation frameworks.

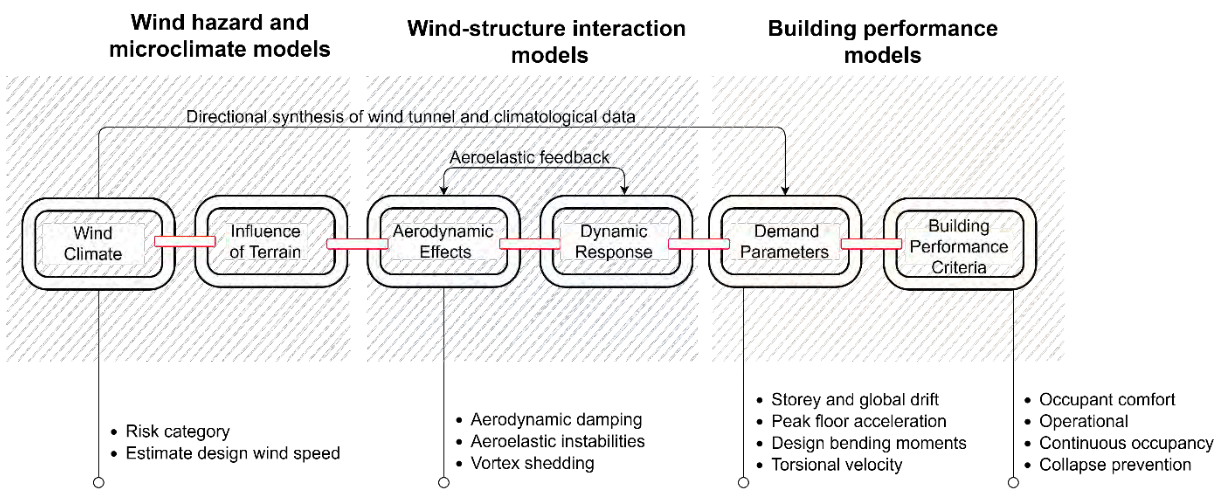


**Figure 25. First-generation PBWD framework**

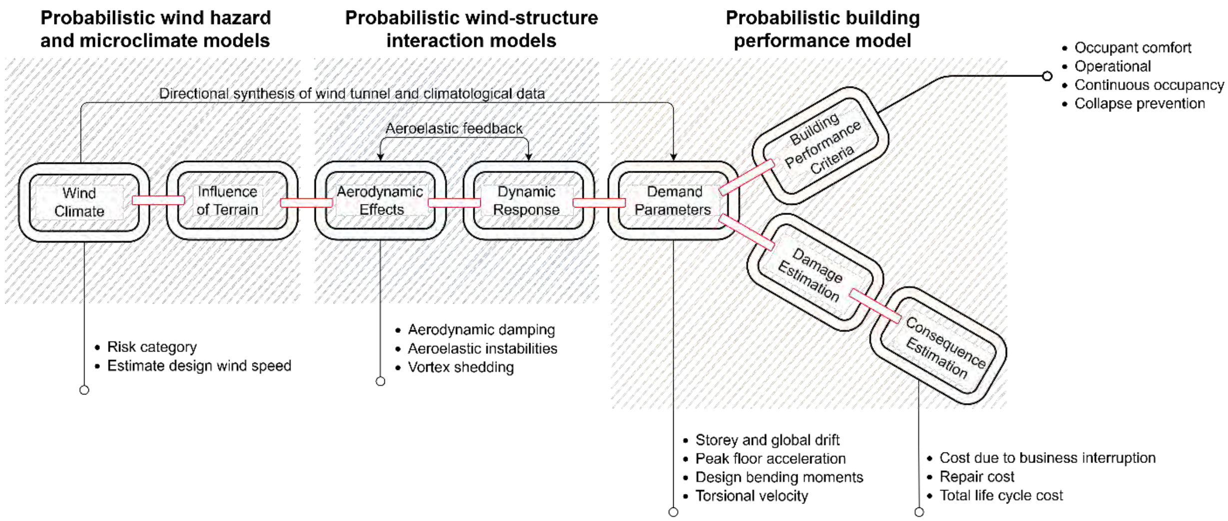


**Figure 26. Second-generation PBWD framework**

The first-generation unified PBWD framework, shown in Figure 25, introduces controlled inelasticity limit states to the Wind Loading Chain. The format of the framework is similar to the PBWD approach presented in the *Prestandard for Performance-Based Wind Design* (American Society of Civil Engineers, 2019) and to the first-generation performance-based earthquake engineering (PBEE) method. The framework follows the current format of the tall building design process but is flexible enough to incorporate multiple performance objectives. The nature of this framework tends to be deterministic, and uncertainties can be accounted for through safety coefficients, such as the limit state design approach. The first step in the PBWD of tall buildings is to develop performance objectives (PO). Tentatively, the authors of this chapter recommend four levels of performance objectives: PO-1 occupant comfort (for 1-in-10-year wind hazard), PO-2 operational (for 1-in-10-year or 1-in-50-year wind hazard), PO-3 continuous occupancy (for 1-in-700-year wind hazard), and PO-4 collapse prevention (1-in-1000-year to 1-in-3000-year wind hazard).

The next-generation unified PBWD framework, shown in Figure 26, allows explicit consideration of uncertainties at each step of the Wind Loading Chain. The performance measures of this framework are the cost of exceeding serviceability limit states, repair cost, and the aggregated life cycle cost of tall buildings. Uncertainties due to the stochastic nature of the wind field, errors during the wind tunnel tests, variability in the structural properties, damping, and the consequences can be represented using probability models. Bezabeh et al. (2018b) used the framework presented in Figure 26 to quantify the habitability risk of a wind-excited 30-storey mass-timber building. Hence, more information about uncertainty modelling and propagation through the Wind Loading Chain can be found in Bezabeh et al. (2018b). Note that the first-generation framework is a subset of the design process shown in Figure 26, in which the primary extension is the probabilistic evaluation of failure consequences. A reader familiar with PBEE methodology developed at the Pacific Earthquake Engineering Research Center (PEER) might notice the similarity between the format of the framework in Figure 26 and the PEER triple integral. The difference, if any, is that the PEER PBEE usually looks for the annual exceedance of decision variables, while the current framework evaluates the annual probabilities of exceeding damage states and passes this information to estimate the total life cycle cost (Bezabeh, Bitsuamlak, & Tesfamariam, 2020). In the presented framework, consequences, including the downtime due to occupant discomfort, damage to the building envelope, damage to the main LLRS, and collapse of the building, can be estimated.

## 9.13 REFERENCES


Aboshosha, H., Elshaer, A., Bitsuamlak, G. T., & El Damatty, A. (2015). Consistent inflow turbulence generator for LES evaluation of wind-induced responses for tall buildings. *Journal of Wind Engineering and Industrial Aerodynamics, 142,* 198-216.

American Society of Civil Engineers. (2012). *Wind tunnel testing for buildings and other structures* (ASCE 49-12).

American Society of Civil Engineers. (2019). *Prestandard for performance-based wind design*. https://doi.org/10.1061/9780784482186

Bekele, S., & Holmes, J. (24–28 August, 2014). *Effects of directionality on wind load and response predictions* [Conference presentation]. The 2014 World Congress on Advances in Civil, Environmental, and Materials Research, Busan, Korea.

Bezabeh, M. (2020). *Performance-based wind design of tall buildings: Concepts, frameworks, and applications* [Doctoral dissertation, University of British Columbia]. https://doi.org/10.14288/1.0395393

Bezabeh, M. A., Bitsuamlak, G. T., Popovski, M., & Tesfamariam, S. (2018a). Probabilistic serviceability-performance assessment of tall mass-timber buildings subjected to stochastic wind loads: Part I – Structural design and wind tunnel testing. *Journal of Wind Engineering and Industrial Aerodynamics, 181,* 85-103. https://doi.org/10.1016/j.jweia.2018.08.012

Bezabeh, M. A., Bitsuamlak, G. T., Popovski, M., & Tesfamariam, S. (2018b). Probabilistic serviceability-performance assessment of tall mass-timber buildings subjected to stochastic wind loads: Part II – Structural reliability analysis. *Journal of Wind Engineering and Industrial Aerodynamics, 181,* 112-125. https://doi.org/10.1016/j.jweia.2018.08.013

Bezabeh, M. A., Bitsuamlak, G. T., Popovski, M., & Tesfamariam, S. (2020). Dynamic response of tall mass-timber buildings to wind excitation. *Journal of Structural Engineering*, *146*(10), 4020199. https://doi.org/10.1061/(ASCE)ST.1943-541X.0002746

Bezabeh, M. A., Bitsuamlak, G. T., & Tesfamariam, S. (2020). Performance-based wind design of tall buildings: Concepts, frameworks, and opportunities. *Wind and Structures, 31*(2), 103-142. https://doi.org/10.12989/was.2020.31.2.103

Bezabeh, M. A., Gairola, A., Bitsuamlak, G. T., Popovski, M., & Tesfamariam, S. (2018). Structural performance of multi-story mass-timber buildings under tornado-like wind field. *Engineering Structures, 177,* 519-539.

Bezabeh, M. A., Tesfamariam, S., Popovski, M., Goda, K., & Stiemer, S. F. (2017). Seismic base shear modification factors for timber-steel hybrid structure: Collapse risk assessment approach. *Journal of Structural Engineering*, *143*(10), 4017136. https://doi.org/10.1061/(ASCE)ST.1943-541X.0001869

Chen, Z., & Chui, Y. H. (2017). Lateral load-resisting system using mass timber panel for high-rise buildings. *Frontiers in Built Environment, 3,* Article 40. https://doi.org/10.3389/fbuil.2017.00040

CSA Group. (2014). *Engineering design in wood* (CSA O86:14).

Dagnew, A., & Bitsuamlak, G. T. (2013). Computational evaluation of wind loads on buildings: A review. *Wind and Structures, 16*(6), 629-660. https://doi.org/10.12989/was.2013.16.6.629

Dagnew, A. K., & Bitsuamlak, G. T. (2014). Computational evaluation of wind loads on a standard tall building using LES. *Wind and Structures, 18*(5), 567-598. https://doi.org/10.12989/was.2014.18.5.567

Davenport, A. G. (1961). The application of statistical concepts to the wind loading of structures. *Proceedings of the Institution of Civil Engineers, 19*(4), 449-472. https://doi.org/10.1680/iicep.1961.11304

Davenport, A. G. (1964). The buffeting of large superficial structures by atmospheric turbulence. *Annals of the New York Academy of Sciences, 116*(1), 135-160. https://doi.org/10.1111/j.1749-6632.1964.tb33943.x

Davenport, A. G. (19–21 September, 1977). *The prediction of risk under wind loading* [Conference presentation]. 2nd International Conference on Structural Safety and Reliability, Munich, Germany.

Davenport, A. G. (1971). *On the statistical prediction of structural performance in the wind environment* [Paper presentation]. Meeting Preprint 1420, ASCE National Structural Engineering Meeting, Baltimore, USA (Vol. 1420, p. 30).

Davenport, A. G. (1999). *The missing links*. Proceedings of the 10th International Conference on Wind Engineering (pp. 3-15). Balkema.

Elshaer, A., & Bitsuamlak, G. T. (2018). Multiobjective aerodynamic optimization of tall building for wind-induced load reduction. *Journal of Structural Engineering, 140*(10). https://doi.org/10.1061/(ASCE)ST.1943-541X.0002199

Elshaer, A., Bitsuamlak, G., & El Damatty, A. (2017). Enhancing wind performance of tall buildings using corner aerodynamic optimization. *Engineering Structures*, *136,* 133-148. https://doi.org/10.1016/j.engstruct.2017.01.019

Goertz, C., Mollaioli, F., & Tesfamariam, S. (2018). Energy based design of a novel timber-steel building. *Earthquakes and Structures*, *15*(4), 351-360. https://doi.org/10.12989/eas.2018.15.4.351

Green, M., & Karsh, E. (2012). *The case for tall wood buildings*. Canadian Wood Council on behalf of the Wood Enterprise Coalition.

Holmes, J. D. (2015). *Wind loading of structures* (3rd ed.). CRC Press.

Irwin, P. A. (2008). Bluff body aerodynamics in wind engineering. *Journal of Wind Engineering and Industrial Aerodynamics, 96*(6-7), 701-712.

Irwin, P., Denoon, R., & Scott, D. (2013). *Wind tunnel testing of high-rise buildings: An output of the CTBUH Wind Engineering Working Group*. Routledge.

Isyumov, N. (2012). Alan G. Davenport's mark on wind engineering. *Journal of Wind Engineering and Industrial Aerodynamics, 104,* 12-24. https://doi.org/10.1016/j.jweia.2012.02.007

Kareem, A., Bernardini, E., & Spence, S. M. J. (2013). Control of the wind induced response of structures. In Y. Tamura & A. Kareem (Eds.), *Advanced structural wind engineering* (pp. 377-410). Springer. https://doi.org/10.1007/978-4-431-54337-4_14

Kwok, K. C. (2013). Wind-induced vibrations of structures: With special reference to tall building aerodynamics. In Y. Tamura & A. Kareem (Eds.), *Advanced structural wind engineering* (pp. 121-155). Springer. https://doi.org/10.1007/978-4-431-54337-4_5

Lepage, M. F., & Irwin, P. A. (1985). A technique for combining historical wind data with wind tunnel tests to predict extreme loads. In K. C. Mehta & R. A. Dillingham (Eds.), *Proceedings of the 5th National Conference on Wind Engineering*.

Melaku, A. F., & Bitsuamlak, G. T. (2021). A divergence-free inflow turbulence generator using spectral representation method for large-eddy simulation of ABL flows. *Journal of Wind Engineering and Industrial Aerodynamics*, *212,* 104580. https://doi.org/10.1016/j.jweia.2021.104580

Merrick, R., & Bitsuamlak, G. (2009). Shape effects on the wind-induced response of high-rise buildings. *Journal of Wind Engineering, 6*(2), 1-18.

National Research Council of Canada. (2017). *Structural commentaries (user's guide – NBC 2015: Part 4 of Division B).*

Simiu, E., & Filliben, J. J. (2005). Wind tunnel testing and the sector-by-sector approach to wind directionality effects. *Journal of Structural Engineering, 131*(7), 1143-1145. https://doi.org/10.1061/(ASCE)0733-9445(2005)131:7(1143)

Skidmore, Owings, & Merrill. (2013). *Timber tower research project*. https://www.som.com/wp-content/uploads/2021/08/timber-tower-final-report-and-sketches-1633640951.pdf

Spence, S. M. J. (2018). Optimization of uncertain and dynamic high-rise structures for occupant comfort: An adaptive kriging approach. *Structural Safety, 75,* 57-66. https://doi.org/10.1016/j.strusafe.2018.05.008

Tannert, T., & Moudgil, M. (2017). Structural design, approval, and monitoring of a UBC tall wood building. In *Structures Congress 2017* (pp. 541-547). American Society of Civil Engineers. https://doi.org/10.1061/9780784480410.045

Tesfamariam, S., Bezabeh, M., Skandalos, K., Martinez, E., Dires, S., Bitsuamlak, G., & Goda, K. (2019). Wind and earthquake design framework for tall wood-concrete hybrid system. University of British Columbia. https://doi.org/10.14288/1.0380777

Tesfamariam, S., Stiemer, S. F., Bezabeh, M., Goertz, C., Popovski, M., & Goda, K. (2015). Force based design guideline for timber-steel hybrid structures: Steel moment resisting frames with CLT infill walls. University of British Columbia. https://doi.org/10.14288/1.0223405

Vickery, B. J., Isyumov, N., & Davenport, A. G. (1983). The role of damping, mass and stiffness in the reduction of wind effects on structures. *Journal of Wind Engineering and Industrial Aerodynamics*, *11*(1-3), 285-294. https://doi.org/ 10.1016/0167-6105(83)90107-1

Warsido, W. & Bitsuamlak, G. T. (2015). Synthesis of wind tunnel and climatological data: A copula based approach. *Structural Safety*, *57,* 8-17. https://doi.org/10.1016/j.strusafe.2015.07.004

Warsido, W., Merrick, M., & Bitsuamlak, G. T. (22–26 June, 2009). *Dynamic optimization for the wind-induced response of a tall building* [Conference presentation]. 11th Americas Conference on Wind Engineering, San Juan, USA.

Zhang, X., & Chen, X. (2015). Assessing probabilistic wind load effects via a multivariate extreme wind speed model: A unified framework to consider directionality and uncertainty. *Journal of Wind Engineering and Industrial Aerodynamics, 147*, 30-42. https://doi.org/10.1016/j.jweia.2015.09.002

Zhang, X., Popovski, M., & Tannert, T. (2018). High-capacity hold-down for mass-timber buildings. *Construction and Building Materials*, *164*, 688-703. https://doi.org/10.1016/j.conbuildmat.2018.01.019

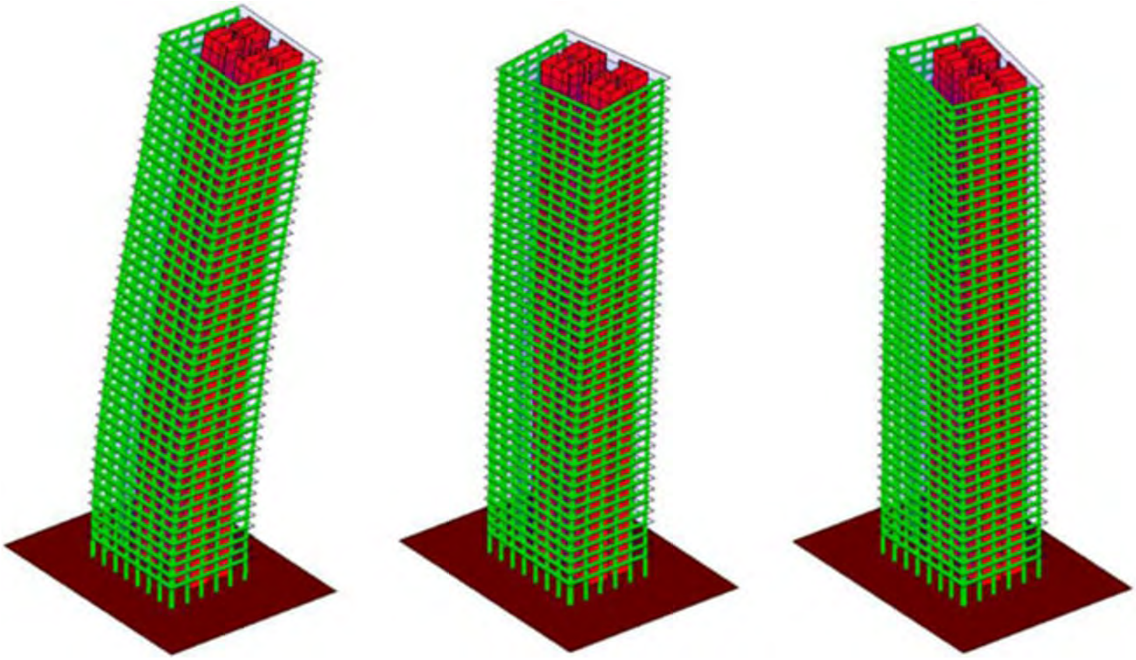

Image courtesy of Nitti et al. (2019)

# CHAPTER 10

## Seismic response analysis


**Authors**
Marjan Popovski
Zhiyong Chen
Ashkan Hashemi
Ali Mikael

**Reviewers**
John van de Lindt
Jasmine McFadden
Luca Pozza
Reid Zimmerman

# TABLE OF CONTENTS

## 10.1 INTRODUCTION

Currently, more than half of the world's population lives in densely populated urban areas, many of which are in high seismic regions. This exposes people to potentially damaging earthquakes. During an earthquake, the ground acceleration, velocity, and displacement (referred to as a ground motion) are transmitted through the structures and generate inertial forces and lateral (and vertical) displacements which a building must be able to sustain without collapse. For that reason, quantifying the seismic response of a building is one of the most important aspects of analysis and design of buildings in active seismic regions.

Past earthquakes have shown that wood-frame construction, when properly designed, has an adequate seismic response (Rainer & Karacabeyli, 2000). This was mostly due to the light weight of wood structures and the inherent use of repetitive members that can redistribute the load in case of a failure of a single member. Lately, mass timber buildings that utilise glued laminated timber (glulam), cross-laminated timber (CLT), laminated veneer lumber, parallel strand lumber, laminated strand lumber, mass plywood panels, and other engineered wood products have become very popular for residential and nonresidential applications. Although mass timber buildings around the world have not yet been subjected to very strong earthquake motions, analyses using numerical models of various mass timber buildings show that they can display adequate seismic performance when properly designed. The seismic response of timber structures is a complex process, involving many interacting factors, which need to be understood and quantified. The main structural aspects include, but are not limited to: (a) properties of the wood or the engineered wood products used as a structural material, (b) building configuration and structural irregularities, (c) dynamic characteristics of the building (stiffness and mass), (d) stiffness and deformational characteristics of the building, (e) damping and energy-dissipating mechanisms, (f) strength and failure modes of the connections, (g) influence of nonstructural components, and (h) redundancy. Numerical modelling plays a critical role in evaluating the seismic response of timber structures.

This chapter provides information related to different types and methods of static and dynamic analyses used to quantify the seismic response of timber structures, along with their advantages and drawbacks. The chapter also highlights the specific modelling requirements and considerations for different types of seismic response analyses, along with their suitability for timber structures. In addition, important aspects of the seismic design approach are discussed from the modelling perspective.

## 10.2 STATIC ANALYSIS

Seismic force–resisting systems (SFRSs) resist seismic loads on buildings. The performance of an SFRS can be determined through a static or dynamic analysis. The key difference between the two is that in dynamic analyses, the inertial loads on a building generated due to accelerations from the ground motion are accounted for during the analysis. Mathematically, the difference between static and dynamic analyses is that in a static analysis, only the stiffness matrix of the finite element (FE) model is solved. In a dynamic analysis, the mass matrix and the damping matrix are included in addition to the stiffness matrix. This is one of the reasons why dynamic analysis requires more computational time than static analysis for the same structure. The designer should choose the appropriate analysis method that can be used effectively to verify the performance of the SFRS based on the defined performance objectives (Popovski et al., 2022).

### 10.2.1 Types of Static Analyses and Applications

There are two main types of static analysis: linear and nonlinear. Linear analysis assumes that the structural system and all main components analysed remain linear elastic throughout the system response. Since it is a known fact that in timber structures most of the nonlinear deformation occurs in the connections while engineered wood members remain linear elastic, linear analyses are suitable in cases where connections are not expected to undergo significant deformations. Examples of such structural systems include various types of trusses, floor systems, arches, and certain types of low-ductility braced or moment-resisting frames.

Nonlinear static analysis is used where a structural system is expected to experience changes in its strength and stiffness properties with varying loads over time. The nonlinear phenomena affecting the strength of a member or a system can be subdivided into two groups: geometric nonlinearity and material nonlinearity. For geometrically nonlinear problems, two sources of nonlinearity can be considered: the P-Δ effect and P-δ effect. The P-Δ effect is related to the overall geometric change of the structure due to its deformation under external loading, while the P-δ effect is the result of a change in the member stiffness due to the combined presence of axial forces and transverse deflection. On the other hand, material nonlinearity comes from the material itself. This is very straightforward in the case of steel structures, where the only source of this type of nonlinearity is the steel material itself. Because most mass timber products behave in a linear elastic fashion, material nonlinearity in the case of timber structures comes mostly from the connections. Suitable nonlinear models should be chosen to represent the nonlinearity of the connections. If it is not the case where timber components behave linearly, a suitable constitutive model, such as Wood$^{S}$ (Chen et al., 2011) or Wood$^{ST}$ (Chen et al., 2020), should be adopted for wood-based components, as described in Chapter 4.1.

Analysis based on undeformed geometry is known as first-order elastic analysis. This implies a linear relationship between forces and displacements if there is also a linear stress-stain relationship in the material. As the load increases and becomes close to the capacity of the structure, the linearity assumption may no longer hold. In this case, second-order analysis, which factors in geometric and material nonlinearity, should be conducted.

Besides the equivalent static procedure that is implemented in many building codes, most commonly conducted static analyses to quantify the seismic response of an SFRS are linear and nonlinear pushover analyses.

### 10.2.2 Linear Pushover Analyses

Generally, pushover analysis is used to assess the performance of structural systems by evaluating their strength, stiffness, and deformation capacity and comparing them with the seismic demand calculated based on the performance objectives considered for the structure. For timber structures, the key parameters are the force-deformation properties of the connections that usually define the global performance of the structure.

In some cases, especially in low-seismicity areas, a structure is designed to remain linear elastic under earthquake loads. For these cases, a static pushover analysis may be carried out to determine the lateral stiffness of the building and eventually calculate the lateral deformation of the structure. This could be critical for high-importance and post-disaster timber structures or structures that are sensitive to lateral deflection. Linear pushover analysis has limited applications other than the cases mentioned.

Given that the system is linear elastic, the pushover curve can be simply constructed by calculating the lateral deflection of the structure subjected to the design-level earthquakes. This means analytical models and methods can be used efficiently. Detailed numerical models or FE models are generally not required to perform these types of analyses except in rare cases where the structure is complex and it is not possible to accurately evaluate its lateral deflection capacity. For example, for a CLT structure in which the arrangement of layers and their individual thickness have an effect on the lateral stiffness, more complex FE models may be required.

### 10.2.3 Nonlinear Pushover Analysis

The nonlinear static analysis procedures, also referred to as nonlinear pushover analyses, are becoming a common engineering practice in seismic performance assessment and design of buildings. Although seismic demands are best estimated using nonlinear time-history analysis, which accounts for mass inertial and damping forces, pushover analyses are frequently used to avoid the intrinsic complexity and computational effort needed by nonlinear dynamic analyses. In the nonlinear static procedures, the SFRS FE model is subjected to an incremental lateral load whose distribution represents the inertial forces expected during ground shaking. The lateral load is applied until the imposed displacement on the building reaches the so-called target displacement, which represents the displacement demand that the earthquake ground motions would impose on the structure. Once loaded to the target displacement, the demand parameters for the structural components are compared with the respective acceptance criteria for the desired performance state. System-level demand parameters, such as storey drifts and base shears, may also be checked.

Although nonlinear static analysis is limited in its ability to capture transient dynamic behaviour with cyclic loading and degradation, it provides a convenient and reliable method for structures whose dynamic response is governed by the first mode of vibration. Consequently, the nonlinear pushover procedures work well for regular, low- and mid-rise timber buildings with symmetrical regular configurations. They are less suitable for taller, slender, or irregular buildings, where multiple vibration modes affect the system behaviour. To overcome some of these drawbacks, several enhanced procedures considering different loading patterns, derived from mode shapes, have been proposed (Kalkan & Kunnath, 2006). These procedures attempt to account for higher mode effects and use elastic modal combination rules. Several sources, including *Improvement of Nonlinear Static Seismic Analysis Procedures* (FEMA 440) (Applied Technology Council [ATC], 2005), *Effects of Strength and Stiffness Degradation on Seismic Response* (FEMA P440A) (ATC, 2009a), and *Applicability of Nonlinear Multiple-Degree-of-Freedom Modelling for Design* (Valley et al., 2010) provide further details on simplifying assumptions and limitations on nonlinear static analysis. However, even when the nonlinear static procedure is not appropriate for evaluating the complete performance of the system, it can be an effective tool to investigate the aspects of the nonlinear response that are difficult to obtain through a nonlinear dynamic analysis. For example, nonlinear static analysis can be useful to (a) check and debug the nonlinear analysis model, (b) augment the understanding of the yielding mechanisms and deformation demands, (c) investigate alternative design parameters, and (d) investigate how variations in the component properties may affect the system response.

The nonlinear stiffness and strength of components in nonlinear pushover analyses of timber structures should be modelled based on the cyclic envelope curve, which implicitly accounts for the strength degradation due to cyclic loading under the earthquake motion (see Section 7.1.4.2.4). The loads are applied at nodes where dynamic inertial forces would develop, and they are monotonically increased without load reversals. A control point is defined for the target displacement that is usually at the top (roof level) of the structure. The plot of the resulting base shear force as a function of the control point (roof) displacement is often recognised as the pushover curve of the structure. The pushover curve can be further simplified by idealised sloping branches of elastic, and post-yield hardening and softening (degrading) behaviour, as shown in Figure 1, and used to examine overall building performance. FEMA 440 (ATC, 2005) and P440A (ATC, 2009a) describe how the idealised pushover curve has been used in simplified nonlinear dynamic analyses to establish minimum strength criteria for lateral dynamic instability. FEMA P440A also provides guidance on how to conduct simplified nonlinear dynamic analyses on a structure-specific basis to reduce the uncertainty in the calculated target displacement relative to the default method given in the *Seismic Evaluation and Retrofit of Existing Buildings* (ASCE/SEI 41-17) standard (American Society of Civil Engineers [ASCE], 2017).

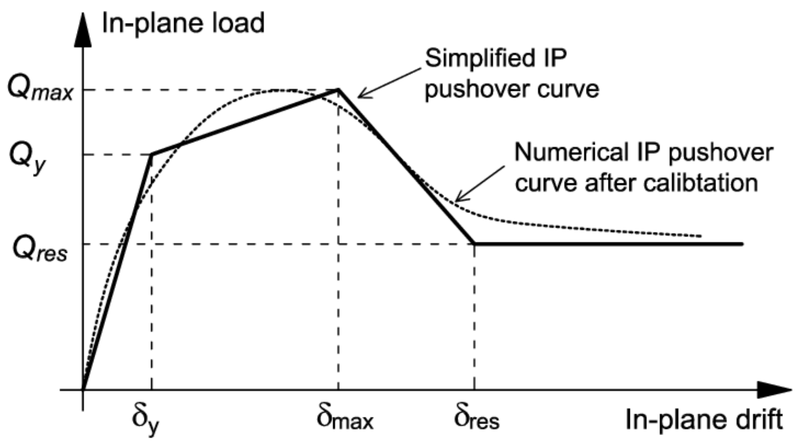


**Figure 1. Idealised static pushover backbone curve for pushover analysis (ATC, 2005).** ***IP, in-plane***

The total gravity load should be applied first, before the incremental lateral load, to capture the effects of gravity-induced forces and P-Δ effects on component yielding and the post-peak response. The lateral load distribution should reflect the expected inertial forces at the storey levels, usually proportional to the floor masses and the shape of the fundamental mode. Other lateral force distributions may be used to further predict the response. Some studies have shown, however, that those do little to improve the accuracy of the nonlinear static procedure (ASCE, 2017; ATC, 2005).

Ductile timber structures are designed in a way that the system demonstrates an inelastic behaviour when subjected to design-level earthquakes. Given the brittle nature of timber, ductility is provided (and localised) in the connections. Nevertheless, controlled crushing of timber fibres may accompany yielding of the fasteners to provide the required ductility. The common practice in designing ductile timber structures is to design so that the timber members remain elastic and the inelastic behaviour is limited to the connections (also known as fuses). Accordingly, the type and behaviour of these connectors would determine the pushover performance of the system. Generally, numerical modelling is required to determine and verify the pushover performance of timber structural systems. The level of complexity should be assessed by the engineer, especially for the permanence of the connections, as they significantly contribute to the performance of the system. Less complex modelling can be used for timber members in some cases, as long as the modelled component can represent the lateral stiffness of the actual member. For example, CLT walls can be modelled by layered shell elements with a stiffness equivalent to the CLT properties. Additionally, timber members are usually capacity designed to remain elastic using an appropriate overstrength factor.

There are different approaches for performing nonlinear static pushover analyses and calculating the target displacement. While selecting the appropriate method is an engineering decision, not all approaches are equally suitable for a timber structure. The two most prevalent in North America are the so-called coefficient method and the capacity spectrum method (ATC, 2005), while in Europe the N2 method (Fajfar & Fischinger, 1988) is widely used. The following sections provide some general aspects of these procedures, along with important specific details for each.

#### *10.2.3.1 Capacity Spectrum Method*

The capacity spectrum method is an analysis procedure that was introduced in the 1970s and further developed in 1980s for seismic assessment of existing buildings. This method graphically illustrates and compares the capacity curve of a given structural system (i.e., pushover curve) with the demand applicable to the structure (Figure 2). The demand curve is presented in a response spectrum scaled down to account for the nonlinearity and/or energy dissipation of the structure. The graphical intersection between the pushover curve and the demand curve represents the performance point of the structure. If there is no intersection between the two, it means that the current design cannot meet the seismic demand and the structure could fail when subjected to a design-level earthquake. To remedy the situation, either the structure needs to be strengthened (raise up the capacity curve) or additional damping should be introduced to the structure to scale down the demand curve. In some cases, both actions must be taken at the same time. The capacity spectrum method is also called acceleration-displacement response spectrum (ADRS) method, referring more directly to the procedure conducted in the method.

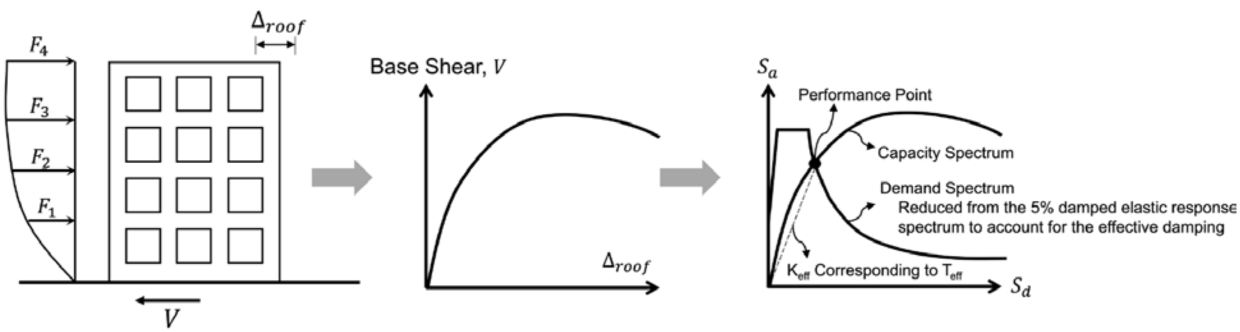


**Figure 2. Capacity spectrum method: Pushover analysis using monotonically increasing loading vector (*left*), pushover capacity curve (*middle*), and capacity spectrum and demand spectrum in ADRS format (*right*) (Najam, 2018)**

To validate the performance of the structure for a design-level earthquake, the nonlinear pushover curve (capacity curve) of the structure should be plotted against the ADRS. The acceleration spectrum should be site-specific, based on the details given for a particular location in the building codes such as the *National Building Code of Canada* (NBCC) (National Research Council of Canada [NRC], 2022) in Canada, the *Minimum Design Loads and Associated Criteria for Buildings and Other Structures* (ASCE/SEI 7-22) standard (ASCE, 2022) in the US, or Eurocode 8 in Europe (European Committee for Standardization [CEN], 2004). Both the acceleration and displacement curves should be scaled down by a reduction factor $K_\xi$ for the calculated system damping $\xi_s$ (Loo et al., 2016). For example, the reduction factor used from Eurocode 8 (CEN, 2004; Priestley et al., 2007a; Priestley et al., 2007b) in relevance to the *Seismic Evaluation and Retrofit of Concrete Buildings* (ATC-40) standard (Comartin et al., 1996) is given in Equation 1.

$$\boldsymbol{K_{\xi}} = \left[\frac{7}{2+\xi_s}\right]^{0.5} \qquad [1]$$

where $\xi_s$ = equivalent damping of the system, also referred to in literature as $\beta_{eq}$. The pushover curve generated from each load case is converted to a capacity spectrum using the following equations:

$$\boldsymbol{S_a(g)} = \frac{V_b}{g\, m_{eff}} \qquad [2]$$

$$\boldsymbol{S_d} = \Delta_{cap} \qquad [3]$$

where $V_b$ is the base shear from the pushover curve, $\Delta_{cap}$ is the design drift capacity of the structure, and $m_{eff}$ is the effective mass of the single-degree-of-freedom (SDOF) structure.

The capacity spectra and the site-specific demand spectra are plotted to obtain the performance point of the building (Figure 2). The effective stiffness and time period of the SDOF can be calculated using the formulas in Equations 4 and 5:

$$\boldsymbol{K_{eff}} = \frac{V_b}{\Delta_{cap}} \qquad [4]$$

$$\boldsymbol{T_{eff}} = 2\pi\sqrt{\frac{m_{eff}}{g \cdot k_{eff}}} \qquad [5]$$

Figure 3 shows a flow chart of the procedure that must be followed to develop using the capacity spectrum method (ADRS curves). As shown in the figure, design of the structure may require some iterations to achieve the optimised design. This is because any adjustments made on the structure would alter the model, the pushover curve, and the system damping, which would result in a different scaling factor.

One potential issue with pushover analysis is that the representation and the distribution of the seismic forces acting on the structure are static. The distribution of lateral inertial forces determines the relative magnitude of the shear forces, bending moments, and deformations within the structure. The actual distribution of these forces is expected to vary continuously during an earthquake response as portions of the structure yield and stiffness characteristics change. The extremes of this distribution depend on the severity of the earthquake shaking, the degree of nonlinear response of the structure, and the influence of the higher modes on the structural response. For this reason, more than one seismic force pattern has been used in the past to bound the range of actions that may occur during actual dynamic response (Figure 4).

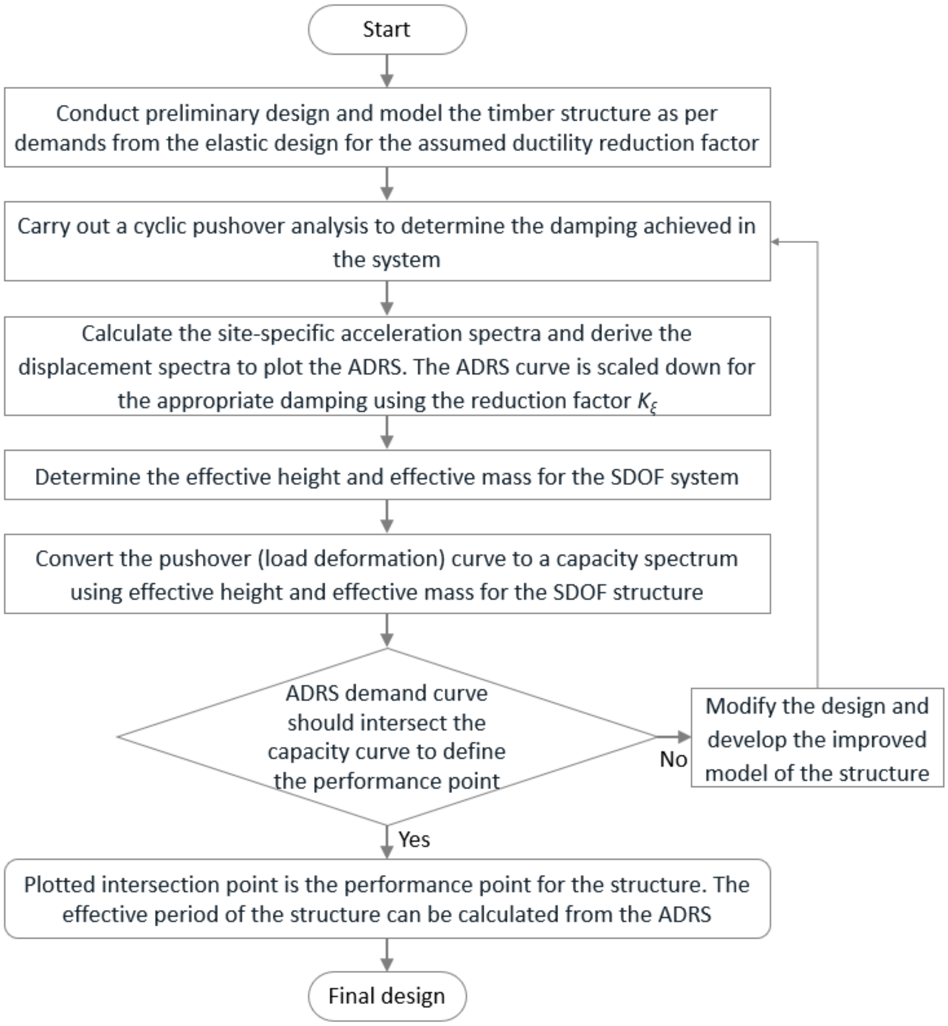


**Figure 3. Example of the procedure for the capacity spectrum method**

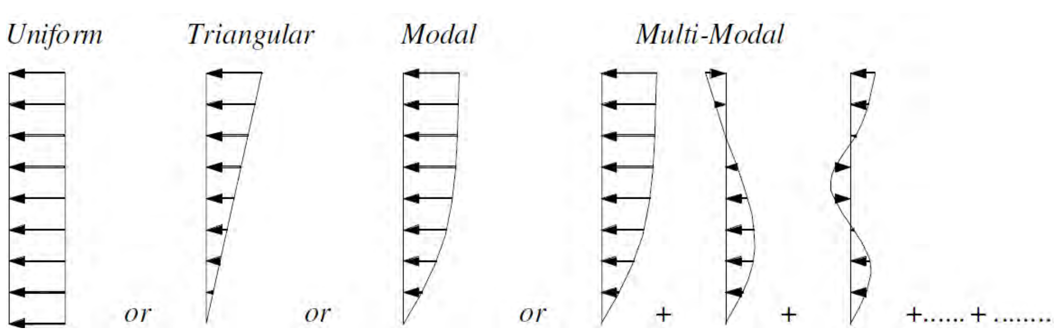


**Figure 4. Different load patterns considered for pushover analysis historically**

The *Prestandard and Commentary for the Seismic Rehabilitation of Buildings* (FEMA 356) (ASCE, 2000) and the *Structural Design Actions – Part 5: Earthquake Actions - New Zealand* (NZS 1170.5:2004) standard (Standards New Zealand, 2004) suggest using two different load patterns for the lateral loads along the height of a building: (a) a triangular distribution and (b) a pattern where the distribution is proportional to the total mass at each level. Research in FEMA 440 (ATC, 2005) has shown, however, that multiple force patterns do little to improve the accuracy of nonlinear static procedures and recommends a single pattern based on the first-mode shape.

Figure 5 illustrates a graphical procedure for estimating inelastic displacements by the capacity spectrum method (Freeman, 2004). By matching ductility ratio markings on the capacity spectrum with the closest effective damped spectrum, a ductility demand of 2.5 and a displacement of 16 cm can be estimated.

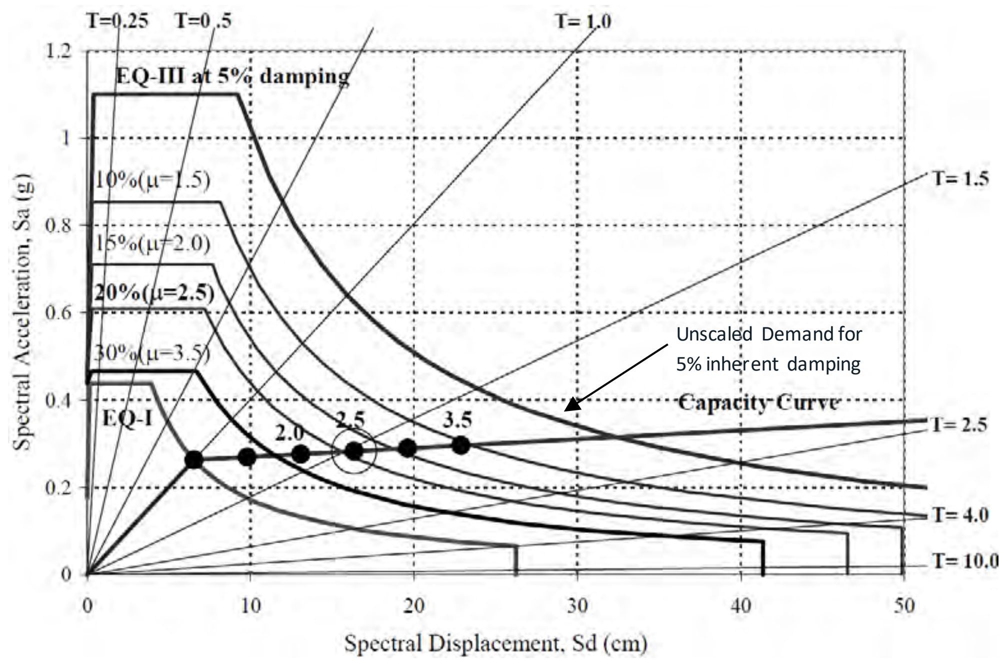


**Figure 5. Example of a conceptual output for applying the capacity spectrum method (Freeman, 2004)**

Another approach to conducting nonlinear pushover analysis using the capacity spectrum method is the one outlined in the ATC-40 guidelines for seismic evaluation of concrete buildings (Comartin et al., 1996). The concept of the pushover curve intersecting with ADRS curves remains the same. There is, however, a slight difference in the process of constructing the pushover load pattern. The pushover curve of the structure is converted into a capacity spectrum using transformation factors that depend on the first-mode shape of the structure based on Equations 6 to 9. As Figure 6 shows, the ATC-40 load pattern is close to the triangular one or the first-mode load pattern in many cases.

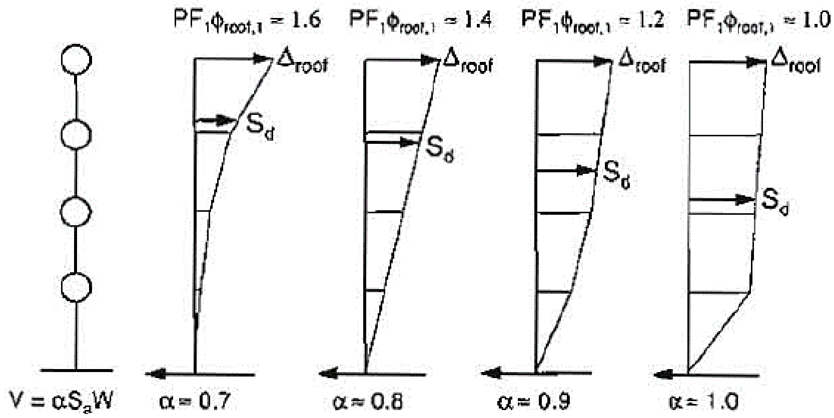


**Figure 6. Capacity spectrum method using the ATC-40 approach**

$$\boldsymbol{PF_1} = \frac{\sum_{i=1}^{N}(w_i\phi_{i1})/g}{\sum_{i=1}^{N}(w_i\phi_{i1}^2)/g} \quad [6]$$

$$\boldsymbol{\alpha_1} = \frac{\left(\sum_{i=1}^{N}(w_i\phi_{i1})/g\right)^2}{\left(\sum_{i=1}^{N}w_i/g\right)\left(\sum_{i=1}^{N}(w_i\phi_{i1}^2)/g\right)} \quad [7]$$

$$\boldsymbol{S_a} = \frac{V/W}{\alpha_1} \quad [8]$$

$$\boldsymbol{S_d} = \frac{\Delta_{roof}}{PF_1\phi_{roof,1}} \quad [9]$$

Improvements and evaluation of the FEMA 356 and ATC-40 methods can be found in the FEMA 440 document (ATC, 2005).

### *10.2.3.2 Coefficient Method*

ASCE/SEI 41-17 (ASCE, 2017) provides guidance on performing a nonlinear static procedure for new and retrofitted buildings. As in any other nonlinear static analysis, a mathematical model directly incorporating the nonlinear load-deformation characteristics of individual components of a building should be subjected to monotonically increasing lateral loads representing inertial forces in an earthquake until a target displacement $\delta_t$ is exceeded (Chen & Popovski, 2021a). The elastic spectral displacement is expressed as a function of the elastic spectral acceleration and the effective period. The target displacement $\delta_t$ is determined using the coefficient method as the product of the elastic spectral displacement and the three modification factors as shown in Equation 10, which account for the characteristics of the system and its damping capabilities:

$$\boldsymbol{\delta_t = C_0 C_1 C_2 S_a \frac{T_e^2}{4\pi^2} g} \quad [10]$$

where $S_a$ is the spectral demand curve scaled based on the damping provided by the system, as shown in Figure 7, and $T_e$ is the effective fundamental period of the building in the direction under consideration.

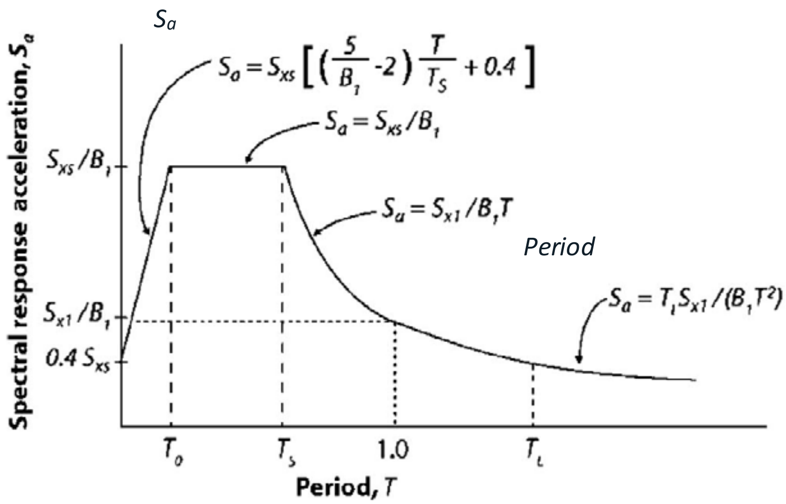


**Figure 7. Spectral scaled demand curve (ASCE, 2017)**

$C_0$ is the modification factor that relates the spectral displacement of an equivalent SDOF system to the roof displacement of the building of a multiple-degree-of-freedom (MDOF) system calculated using one of the following procedures:

- Multiplying the first-mode mass participation factor by the ordinate of the first-mode shape at the control node;
- Multiplying the mass participation factor calculated using a shape vector corresponding to the deflected shape of the building at the target displacement by the ordinate of the shape vector at the control node; or
- Using a value from Table 1.

**Table 1. Values for modification factor $C_0$ as per ASCE/SEI 41-17 (ASCE, 2017)[a]**

| Number of storeys | Shear buildings[b] | | Other buildings |
|---|---|---|---|
| | Triangular load pattern | Uniform load pattern | Any load pattern |
| 1 | 1.0 | 1.0 | 1.0 |
| 2 | 1.2 | 1.15 | 1.2 |
| 3 | 1.2 | 1.2 | 1.3 |
| 5 | 1.3 | 1.2 | 1.4 |
| 10+ | 1.3 | 1.2 | 1.5 |

[a] Linear interpolation shall be used to calculate intermediate values.

[b] Buildings in which, for all storeys, storey drift decreases with increasing height.

$C_1$ is the modification factor that relates the expected maximum inelastic displacements to displacements calculated for linear elastic response calculated per Equation 11. For periods less than 0.2 s, $C_1$ need not be taken as greater than the value at $T$ = 0.2 s. For periods greater than 1.0 s, $C_1$ equals 1.0.

$$C_1 = 1 + \frac{\mu_{strength} - 1}{a\,T_e^2} \qquad [11]$$

where $a$ is the site class factor, which can be 130 for site class A or B and 90 for site class C. The strength ratio $\mu_{strength}$, is a ratio of the elastic strength demand to the yield strength coefficient. The effective period of the system, $T_e$, can be computed using the following equation:

$$T_e = T_i \left(\frac{K_i}{K_e}\right)^{0.5} \qquad [12]$$

where $T_i$ is the fundamental period of the structure in the direction under consideration calculated from elastic dynamic analysis, $K_i$ is the elastic lateral stiffness of the building in the direction under consideration as per ASCE/SEI 41-17 guidelines for various types of structures, and $K_e$ is the effective lateral stiffness of the building in the direction under consideration. Figure 8 displays the parameters discussed and the conceptual pushover curve of the structure.

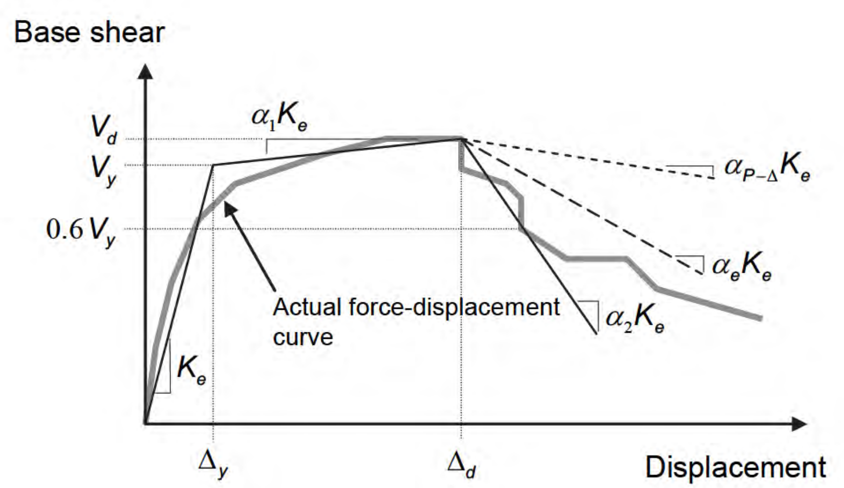


**Figure 8. Idealised pushover curve of the structure (ASCE, 2017)**

$C_2$ is the modification factor that represents the effect of pinching in the hysteretic performance of the system, cyclic stiffness degradation, and strength deterioration on maximum displacement response that is calculated using Equation 13. For fundamental periods greater than 0.7 s, $C_2$ equals 1.0.

$$C_2 = 1 + \frac{1}{800}\left(\frac{\mu_{strength} - 1}{T_e}\right)^2 \qquad [13]$$

The scaling factor $B_1$ shown in Figure 7 can be calculated using the following equation:

$$B_1 = \frac{4}{(5.6 - \ln(100\beta))} \qquad [14]$$

where $\beta$ is the overall damping of the system comprising the hysteretic damping and the inherent damping. Generally, a 3% to 5% inherent damping should be used for most timber buildings. If the building does not contain internal partitions and external cladding, this value should be reduced to 2%.

Note that given the relationship between the target displacement and the effective period, iterations may be required to achieve acceptable convergence (Figure 9).

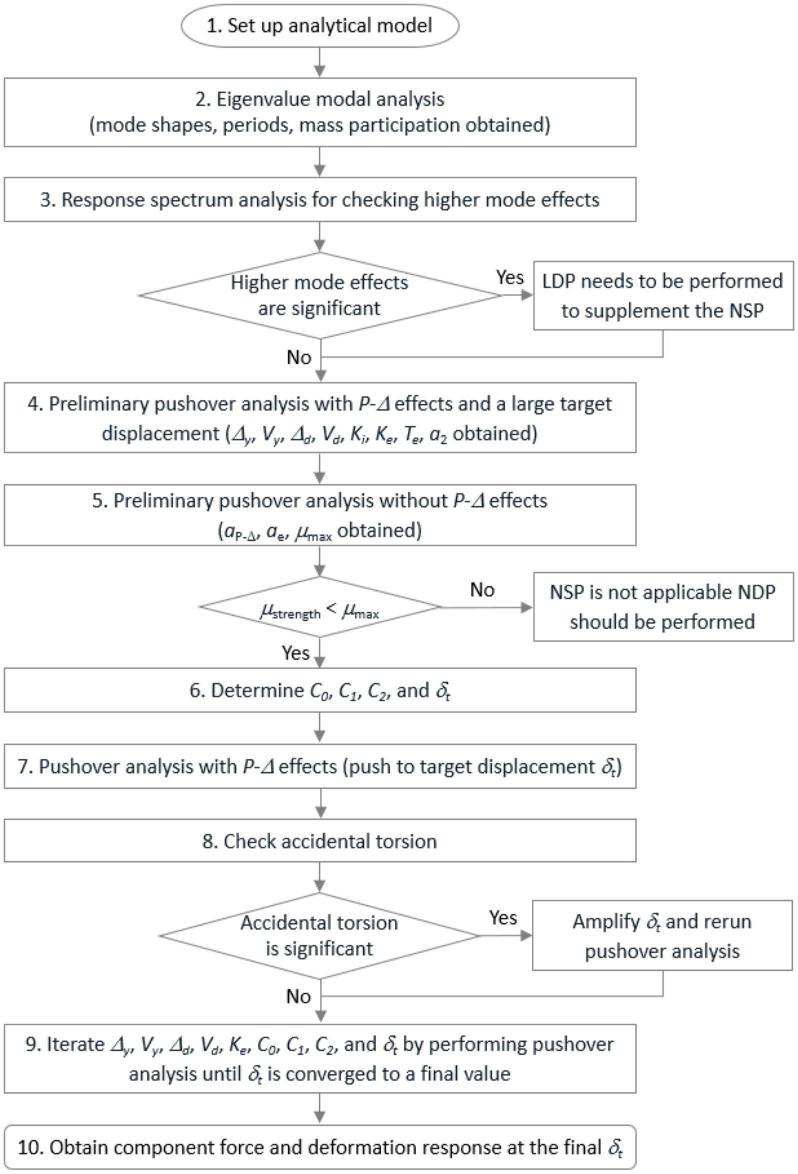


**Figure 9. Key steps of performing the nonlinear static procedure provided in ASCE/SEI 41-17.** ***LDP, linear dynamic procedure; NDP, nonlinear dynamic procedure; NSP, nonlinear static procedure***

This type of nonlinear static procedure is recommended for structures that can satisfy the following conditions:

1. The strength ratio $\mu_{strength}$ is less than $\mu_{max}$ (Equations 7 to 32 of ASCE 41-17). If $\mu_{strength}$ exceeds $\mu_{max}$, nonlinear dynamic analysis must be performed instead.
2. Higher mode effects are not significant. This can be quantified by performing two response spectrum analyses (RSA) (see Section 10.3):
   - RSA with sufficient modes to produce 90% mass participation; and
   - RSA with the first mode only.

   Higher mode effects are considered significant if storey shear (in any storey) in the RSA with 90% mass participation is greater than 130% of the corresponding storey shear in the first mode.

This nonlinear static procedure requires setting up a numerical model, essentially a linear RSA, to determine its applicability, then computing $\mu_{strength}$ and $\mu_{max}$ and determining the target displacement to achieve the desired convergence and obtain the final force and deformation response. The structure should be able to meet the target displacement at the desired performance level.

ASCE/SEI 41-17 (2017) defines two acceptability criteria: one dealing with local component checks for force-controlled or deformation-controlled components, and the second a check for overall stability. The local checks are defined by comparing the calculated demands to the component acceptance criteria. Chapters 4 and 8 of ASCE/SEI 41-17 specify component modelling parameters and acceptance criteria for foundations, frames, walls, diaphragms, and other structural components made of wood. The strength criteria in ASCE/SEI 41-17 often refer to the underlying industry design standards for detailed information on material properties and calculating component strengths. The global dynamic instability check limits the magnitude of the inelastic strength reduction factor, reflecting the influence of P-Δ effects and post-peak negative stiffness in the structural components (Figure 1). The dynamic instability criterion of ASCE/SEI 41-17 is the same as the one developed in FEMA 440. More recently, a revised dynamic instability criterion has been proposed in FEMA P440A, which is more accurate and less conservative than the limit in ASCE/SEI 41-17 and FEMA 440.

#### *10.2.3.3 N2 Method*

The N2 method was originally introduced by Fajfar and Fischinger (1988) and Fajfar and Gašperšič (1996) for seismic damage analysis of reinforced concrete buildings. Fajfar (1999) later extended the approach to a capacity spectrum method (ADRS curves), and in 2004, it was included in Eurocode 8 (CEN, 2004). This method is similar to the other pushover analysis methods discussed in this chapter, but instead of scaling down the demand curve based on the level of damping, it uses a reduction factor based on the ductility $\mu$ and period $T^*$. This method involves the following steps:

(1) Perform a pushover analysis to derive the capacity curve of the structure, which is essentially base shear versus displacement at the roof.

(2) Convert the pushover curve of the structure to that of the equivalent SDOF system. Then, idealise the pushover curve as an elastic-perfectly plastic curve.

(3) Calculate the seismic demand curve based on the considered standard, location, and site conditions.

(4) Evaluate the performance by assessing the intersection between the demand curve and the capacity curve as the performance point of the structure (Figure 10).

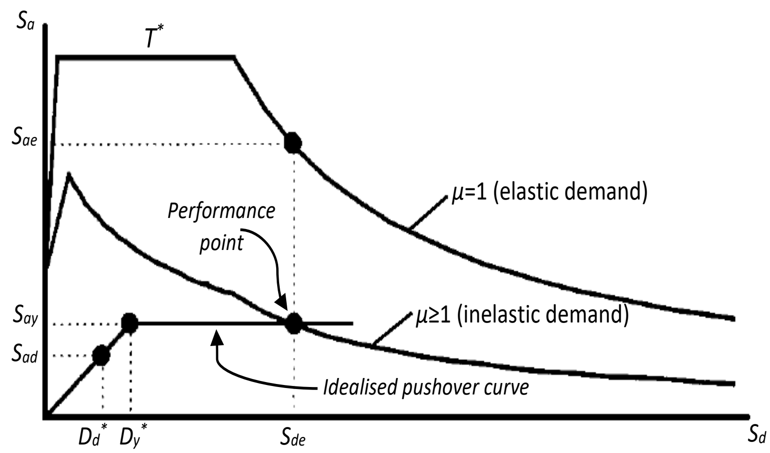


**Figure 10. Obtaining the performance point using the N2 method**

The elastic period of the structure (*T**) can be determined using Equation 15, below:

$$T^{*} = 2\pi\sqrt{\frac{m^{*}D_{y}^{*}}{F_{y}^{*}}} \qquad [15]$$

where $m^*$ is the equivalent mass of the SDOF system, $F^*_y$ is the yield strength, and $D^*_y$ is the yield displacement of the structural system. The capacity curve can be obtained by dividing the force and deformation demands by the effective mass:

$$S_a = \frac{F^{*}}{m^{*}} \qquad [16]$$

The scaling factor $R_\mu$ can be calculated as $R_\mu = \mu$ for $T^* \geq T_c$ or $R_\mu = (\mu - 1)\frac{T^*}{T^c} + 1$ for $T^* < T_c$, where $T_c$ is the corner period at the upper limit of the constant acceleration region of the elastic spectrum, as per the definition provided by Eurocode 8.

According to Lagaros and Fragidakis (2011), the variability between the designs performed using the N2 method and those performed using the ASCE/SEI 41-17 and ATC-40 methods is about 4% to 5%. This means that different pushover analysis methods normally yield reasonably similar results providing the models are well calibrated.

## 10.3 RESPONSE SPECTRUM ANALYSIS

RSA is a linear dynamic analysis method which determines the contribution from each natural mode of vibration on structural performance. It provides insight into dynamic behaviour by measuring pseudospectral acceleration, velocity, or displacement as a function of structural period for a given level of damping. RSA is useful for design decision-making because it relates the selected structural system to its dynamic performance. This method is accepted as a standard (default) analysis method in different standards, such as the Canadian (NRC, 2022) and US (ASCE, 2022) building codes. In this analysis, the nonlinear behaviour of the SFRS is accounted for through force modification factors, for example, $R_d$ and $R_o$ in the NBCC (NRC, 2022), similar to the equivalent static force procedure (ESFP) (Popovski et al., 2022). Other nonlinearity such as P-delta effects can be included in the post-processing phase as part of the iterative design procedure. The theory behind modal analysis and RSA is available in literature (Chopra, 2012; Filiatrault et al., 2013). The following sections provide general guidance and key considerations. Engineering judgment is crucial throughout the entire procedure, from constructing the model to its calibration and results validation.

### 10.3.1 RSA Procedure

The most important steps of the RSA procedure are similar among different standards. Recommendations by the NRC's *Structural Commentaries* (2015) are described below as an example. Section 10.3.1.6 provides particularities related to timber structures. Almost all commercial FE software includes this method of analysis; however, by knowing the procedure, the designer can better control and optimise the analysis options.

(1) Construct the FE model representing the building SFRS (see Sections 10.3.1.1 to 10.3.1.6). If nonstructural components are expected to have significant influence on the seismic response, they should be included in the model as well.

(2) Calculate the period of the building (model) in two orthogonal directions that are considered the main earthquake directions. Note that torsion around the vertical axis is restrained in this step and only translations are allowed per direction. The smallest period is the fundamental period of the $T_a$ and the elastic base shear force is $V_e$ (i.e., not divided by $R_dR_o$).

(3) If the spectral acceleration $S(T_a)$ is higher than 2/3 of $S(0.2)$ or $S(0.5)$, obtain the design elastic force, $V_{ed}$, by multiplying $V_e$ by the larger of the values of either 2/3 $S(0.2)/S(T_a)$ or $S(0.5)/S(T_a)$.

(4) Compare the design elastic force with the empirical design force, $V$, calculated using the empirical code formula $T_c$. Note that for wood-based SFRSs, $V$ calculated using the model's period $T_a$ is amplified by a factor of 1.2, with an upper limit on $T_a$ of $2T_c$ for strength calculations and 2 s for deflection calculations. This means the period $T_a$ can be used in deflection calculations even if it is higher than $2T_c$, but not larger than 2 s, and the ratio of $V_{ed}/V$ is used to calculate the model's deflections.

(5) Determine the design force $V_d$ by multiplying $V_{ed}$ by $I_E$ and dividing by $R_dR_o$. In wood-based SFRSs, this design force is not allowed to be smaller than 100% of the amplified empirical force $V$ determined in step 4. In other regular SFRSs, $V_d$ is permitted to be 80% of $V$. A scale factor of $V_d/V_e$ is applied at results once the torsion effect is properly included.

(6) Determine forces and deflections using a model with unrestrained rotation after adding accidental torsion by applying base shear per level $F_x$ at a centre of mass shifted by ± 0.010 of the dimension perpendicular to the earthquake direction. $F_x$ could be determined from the ESFP multiplied by $R_dR_o/I_E$ or from the elastic dynamic analysis as the difference between shear of the level below and that of the

level above. If the structure is not torsionally sensitive, apply $F_x$ at ± 0.05 of the dimension perpendicular to the earthquake direction.

(7) Apply the scale factor from step 5 at resulting forces to ensure the structure resists a seismic force equivalent to the empirical static force. Multiply deflections by an additional factor $R_dR_o/I_E$, (or $V_{ed}/V$ from step 4, if applicable) to account for the inelastic deformation of the structure.

#### 10.3.1.1 Building Mass

Building codes prescribe the minimum mass to be considered in seismic analysis, based on the applied loads. Building mass in the NBCC, for example, does not include live loads, while in some codes, such as Eurocode 8, a portion of live load is considered. RSA allows the designer to account for the mass distribution throughout the height of the building. Mass distribution influences the building's response mainly through the mode shapes and torsion effects. Local modes may result from the way mass and rigidity are accounted for in the model, especially when mass is calculated directly by software. For example, when the mass of all walls is included automatically in the software while the designer assigns it to the floor level, not only could double counting occur, undesired mode shapes and local stresses might also appear. On the other hand, when the effect of a concentrated mass is studied, the designer ensures that its vibration mode is included in the combined modes (see Section 10.3.2). This control is possible in RSA through the values of participating masses and the corresponding mode shapes. An example of an inefficient model would be using shape modes for columns while the intent is to neglect their mass (because it is included in the floor mass) and account only for their stiffness contribution to the global stiffness of the structure.

#### 10.3.1.2 Stiffness

The advantage of RSA lies in the fact that designers can account for the stiffness of the entire structural system, not only the SFRS, as is the case in the ESFP. This is done through the geometry of structural elements and their connectivity. The first major factor in modelled stiffness properties is the orthotropic characteristics of the wood-based products. These are better accounted for in RSA and commercial software that allows designers to include directional stiffness, especially for products such as CLT panels, in which even edge-gluing might affect the stiffness definition.

Another major contributor to the stiffness of the modelled structure is the connections that connect the elements. The building codes require sources of additional stiffness to be included in the model unless they are connected to the SFRS in a way that allows for their independent movement. This is also critical in mass timber platform-type systems, where stiffer wall segments with an aspect ratio lower than required for the designated $R_dR_o$ are present along with the more slender segments. If those more slender segments are not adequately disconnected from the diaphragms, they will attract lateral loads and penalise the designers to account for a lower value of $R_dR_o$ for the entire system.

Connections of columns to the diaphragm are more straightforward and are often simulated as pinned at their ends in RSA models. This modelling choice could be checked against a control model where the ends of columns have lateral and axial spring elastic stiffness. Pinned ends are also used to model connections in braced-frame systems, but recent research recommends designed and constructed continuous columns to avoid developing the soft-storey mechanism in the lower storeys (Chen & Popovski, 2020, 2021a).

In light-frame construction, the dynamic behaviour of shear walls and diaphragms is more complex since they are made of multiple wood elements: sheathing, studs, joist end chords, and drag struts acting together with steel fasteners and steel hold-down connections. Modelling light-frame diaphragms is challenging especially when it comes to flexible diaphragm assumption. The tributary approach traditionally used in the ESFP is not achievable in a numerical model. Alternatively, an equivalent stiffness based on the expected deflection of the diaphragm could be used to simulate a semirigid diaphragm action (Chen, Chui, Mohammad et al., 2014; Chen, Chui, Ni et al., 2014). An equivalent linear elastic model could be calibrated using a conservation linearisation of diaphragm deflection equation. Such linearisation is already an option in the American wood design standard (American Wood Council, 2021) for the shear walls deflection equation. The most common model for light-frame shear walls (and diaphragms) is the deep beam assumption, which is consistent with linear components of the deflection equation in the *Engineering design in wood* standard (CSA Group, 2019). The stiffness of this model is calibrated mainly to conservatively account for the nonlinear nail slippage component of the equation.

Finally, RSA allows the designer to include gypsum wallboard contribution (Chen et al., 2016; Lafontaine et al., 2017) to the lateral stiffness of the modelled structure. Although this contribution might be neglected along with its resistance when the lateral interstorey drift is more than 1%, it could be beneficial when performing a serviceability check under low- to moderate-level earthquakes, which is required by the NBCC (NRC, 2022).

#### *10.3.1.3 Damping*

Damping can be accounted for in RSA in different ways, most commonly as Rayleigh damping and modal damping. Rayleigh damping is a mathematical way to solve the differential equation of motion that includes a damping component. The background for this theoretical approach to damping can be found in textbooks (Chopra, 2012). This damping is a function of mass and stiffness; therefore, a function of the natural frequencies of the system and commercial software help the designer calibrate this damping for the model. Nevertheless, it requires engineering judgment to ensure that higher modes are not excessively damped as a result of this calibration, as higher damping is associated with higher frequencies.

On the other hand, modal damping allows the designer to assign specific damping ratios for specific vibration frequencies. Conservatively, the conventional 5% of critical damping could be applied for all vibration modes. It is also the ratio assumed in the horizontal spectral accelerations provided in standards, such as the NBCC.

Note that RSA is a linear elastic analysis procedure, and damping included in the procedure should not be confused with the force modification factors that account for the energy dissipated through nonlinear deformation. At 5% of critical damping, the structural behaviour is still assumed to be linear elastic. This ratio is higher than what is measured under ambient vibrations in timber structures (Popovski et al., 2022), but damping measurements on buildings with other material showed a higher damping ratio at higher levels of ground motion.

#### *10.3.1.4 Boundary Conditions*

The most common boundary conditions for platform wood-frame structures are a fixed base and a lower, less ductile, stiff one- or two-storey podium structure, if present. The foundation structure (podium) has its own response to ground motion that affects the shaking at the base of the wood-frame building. When the podium is stiff, with limited ductility, the horizontal spectral acceleration could be used as if the upper structure were sitting at the ground level (ASCE, 2022; NRC, 2022).

NRC's *Structural Commentaries* (2015) recommend nonlinear dynamic analysis where there is discontinuity along the height of a building but provide guidance for a special case where a timber structure is regular and sits on a low concrete podium having limited ductility and stiffness greater than three times the stiffness of each storey in the upper timber structure. In such a case:

- Use RSA for the entire structure. Design the upper structure by analysis using the larger $R_dR_o$ and the lower structure using the smaller $R_dR_o$.
- If the ESFP is permitted, design the upper structure on a fixed base using the larger $R_dR_o$ and the podium separately using the smaller $R_dR_o$ in addition to lateral loads transferred from the upper structure. The transferred loads are equivalent to the lateral capacity of the upper structure.

ASCE/SEI 7-22 (ASCE, 2022) recommends a two-stage static approach, where both upper and lower structures are regular and the average stiffness of the lower structure is required to be greater than 10 times the average stiffness of the upper structure. In addition, the period of the entire structure is less than 1.1 that of the upper timber structure. Similar to NBCC's static approach, the upper and lower structures are designed separately on a fixed base using their respective $R_dR_o$ values, and loads transferred from the upper structure to the top of the lower structure are scaled by the ratio of $(R_dR_o)_{\text{upper}}/(R_dR_o)_{\text{lower}}$.

Nonlinear time-history dynamic analysis results show that podium buildings designed with the two-step analysis procedure may not meet the intended seismic performance. Chen and Ni (2020) have developed a new criterion for using a two-step analysis procedure. When the normalised stiffness ratio is at least 10 times greater than the normalised mass ratio, the buildings designed using the two-step analysis procedure can meet the performance requirement.

#### *10.3.1.5 Modal Superposition*

The modal analysis is performed as a part of the RSA procedure with contribution of all mode shapes of the structure. Every mode shape mobilises a portion of the building mass, called participating mass, or effective modal mass. In each direction, the first mode typically has the highest participating mass and is referred to as the fundamental, or dominant, mode and has the smallest period of natural vibration, called the fundamental period $T_a$. RSA can be described as a decomposition of the complex response of a structure into a combination of multiple SDOF systems that is equal to the number of mode shapes. Once the response of every SDOF system is determined using the design spectrum, a modal superposition is performed to obtain the actual response of the designed structure. Note that displacements and forces are first determined in the modal domain and then combined.

Once the individual modal responses are calculated, their influence on the structure is combined using different modal rules. The most common modal superposition rules are the square root of the sum of the squares and the complete quadratic combination. They are both used as an alternatives to a simple addition of the modal responses that is unlikely to occur at any given time and is extremely conservative. The complete quadratic combination has some advantages over the square root of the sum of the squares as it accounts for the correlation between mode shapes and the damping effects on modal responses while allowing a more realistic summation using the signs of the modal deformation. Commercial software packages offer signing of modal deformation using a reference mode shape, typically the fundamental mode, to further reduce the conservatism resulting from quadratic summation.

#### *10.3.1.6 Model Validation*

Validation of the model is an important step and assures that the model successfully accounts for all intended loads and provides valid results. While Chapter 3 provides a general comprehensive discussion, some important considerations of validation of the models related to seismic response analyses are given below.

To check the weight of the structure, performing static analysis under gravity loads is recommended. This is not time-consuming and allows the designer to check the results of the reactions against a rough or accurate manual estimation of the building weight. To check the lateral stiffness of the structure, a static analysis under horizontal loads applied in the direction of the earthquake allows the designer to spot misconnected elements and deal with unexpected deformation before starting the modal analysis. This is also very helpful later when checking the resulting free vibration periods and the associated mode shapes. The impact of irregularities can be observed in the way they affect the dynamic behaviour of the structure. Mass and stiffness irregularities are carefully checked to ensure that the affected mode shapes are included in the combination. The number of modes included in the analysis depends on the computing capacity, the size of the model, and the number of the degrees of freedom. Including all modes is impractical in models having a high number of degrees of freedom. Typically, modes are included when the sum of the corresponding participating masses reaches at least 90% of the total modelled mass (Saatcioglu & Humar, 2003). This ratio could be increased if needed, especially if irregularities affect modes beyond those captured by this ratio. Some types of software compensate for the ignored modes through a residual mass representing all modes that have very short periods, and ASCE/SEI 7-22 recommends this approach.

RSA is a linear analysis in which all elements and their connections are assumed to resist elastically the forces resulting from a seismic force reduced by $R_dR_o$. If forces in the dissipative elements and connections of the SFRS are above the factored resistance in the design standard, the design is not satisfactory.

### 10.3.2 Use of RSA for Timber Structural Systems

In most standards, such as the NBCC, RSA is the default procedure for seismic analysis while the ESFP is permitted under certain conditions. The development of calculation software and computer capacities has made RSA accessible and cost-effective even in cases where the ESFP is permitted for some SFRSs. Nonlinear dynamic analyses, supported by testing data, are used to design alternative SFRSs that are not included in the code as acceptable solutions. The choice between methods of analysis is also governed by the complexity of a building and its height limit. The ESFP is still a preferred choice for designers. RSA and more sophisticated nonlinear pushover and time-history dynamic analyses are mainly used for more complex structures, taller buildings, and research purposes.

CLT buildings with shear walls in platform-type construction are an example of where using RSA can be particularly helpful even if the ESFP is allowed. The amount of conservatism resulting from using the ESFP might not allow the system to fully benefit from its advantages. In-plane stiffness of CLT wall panels and out-of-plane stiffness of CLT floor panels are more realistically included in FE models than conservative assumptions used in

ESFP analytical solutions. For example, modelling of CLT floor panels as 3D elements better accounts for gravity load contribution. Note, though, that stiffness properties of all connections in a building are needed for proper modelling of the system and that information may not be readily available to the designer. Capacity-based principles in the standard (for example, CSA O86:19) require connections between shear walls and the floors above to be capacity protected, which might result in stiffer connections than those between shear walls and floors below and the ones between the rotating wall segments of the CLT walls. RSA allows the designer to account for that difference in the stiffness in the building model.

In addition to irregular and torsionally sensitive structures where RSA is required, it could also be used in earthquake design of regular light-wood frame structures to reduce the conservatism built in the ESFP, especially thanks to the way RSA accounts for the torsion. The more realistic and optimised the force-distribution and deflection prediction are, the more useful they are when dealing with higher seismic hazards.

With few analytical solutions available for analysis and design of braced timber frames, RSA is very helpful for designing those systems as well. For example, hand calculations of deflection in these systems are challenging especially when it comes to determining the adequate gap between the diagonal member and the frame members. This gap allows for the dissipative connections of the diagonal to deform and reach their ductility (Popovski & Karacabeyli, 2008; Chen & Popovski, 2021b).

Depending on the energy-dissipative mechanisms in the proprietary SFRSs, manufacturers may be able to provide guidance on how to model and use RSA for their systems with regard to $R_dR_o$ values and stiffness considerations in the model. From the code perspective, assigning force modification factors and height limitations for a new system must be approved by the Standing Committee on Earthquake Design. If a proprietary system falls under one of the code's acceptable solutions, the code and the standard require the manufacturer and designer to comply with its height limits and demonstrate equivalent force modification factors.

## 10.4 DYNAMIC TIME-HISTORY ANALYSIS

As mentioned in Section 10.3, RSA is a linear dynamic statistical analysis method which measures the contribution from each natural mode of vibration to indicate the likely maximum seismic response of an elastic structure. It provides insight into dynamic behaviour by measuring pseudospectral acceleration, velocity, or displacement as a function of a structural period for a given earthquake spectrum and level of damping. In RSA the time evolution of the building response (response of the structure at any instant of time) cannot be computed. To do that, dynamic time-history analyses are needed. The time-history analysis provides an evaluation of the dynamic response of the structure subjected to a specified time function for the duration of that function $t$ at each chosen increment of time $\Delta t$. If the time function chosen is an accelerogram of an earthquake motion, then the analysis will yield the response of the system subjected to that earthquake motion at each chosen interval $\Delta t$.

Generally, two types of time-history analyses can be performed: linear and nonlinear. Both approaches require a numerical model with its characteristics tuned well to represent the lateral resistance mechanism of a real structure. If a linear analysis is performed for a structure that is expected to behave in a nonlinear way, the input parameters (such as equivalent viscous damping) should be carefully calibrated to represent the actual structure. This section provides insight about performing time-history analyses of timber structures. Generally, all texts on performing dynamic analyses are equally applicable to timber structures (Chopra, 2017; Clough & Penzien, 1993; Paz & Kim, 2019). Pay special attention, however, to proper and accurate modelling of the connections and load-resisting systems, as they can heavily influence the dynamic performance of the structure.

### 10.4.1 Linear Dynamic Time-History Analyses

There are two types of linear dynamic time-history analyses, which are briefly described in this section. For more detailed information refer to the above-referenced textbooks, by Chopra (2017), Clough and Penzien (1993), and Paz and Kim (2019), on structural dynamics.

#### *10.4.1.1 Modal Response History Analysis*

The response of MDOF structural systems subject to ground motions (accelerations) can be expressed using the well-known equations of motion shown in Equation 17:

$$[\boldsymbol{M}]\{\ddot{\boldsymbol{u}}\}+[\boldsymbol{C}]\{\dot{\boldsymbol{u}}\}+[\boldsymbol{K}]\{\boldsymbol{u}\}=-[\boldsymbol{M}]\{\boldsymbol{i}\}\ddot{\boldsymbol{u}}_{\boldsymbol{g}} \quad [17]$$

where $[M]$ is the mass matrix; $\{\ddot{u}\}$ is the acceleration vector for every degree of freedom; $[C]$ is the damping matrix; $[K]$ is the stiffness matrix of the system; $\{u\}$, $\{\dot{u}\}$, and $\{\ddot{u}\}$ are the displacement, velocity, and acceleration vector for every degree of freedom, respectively; $\{i\}$ is the influence vector that represents the displacements of the masses resulting from the static application of a unit ground displacement; and $\ddot{u}_g$ is the ground acceleration.

The natural frequencies $\omega_n$ and mode shapes $\phi_n$ of the structure are derived by solving the MDOF undamped free vibration equation (the eigenvalue problem), as shown in Equation 18.

$$([\boldsymbol{K}]-\boldsymbol{\omega}_{\boldsymbol{n}}^{2}[\boldsymbol{M}])[\boldsymbol{\Phi}]=\boldsymbol{0} \quad [18]$$

Considering the displacement response of the MDOF system as the superposition of $N$ modal responses:

$$\{\boldsymbol{u}(\boldsymbol{t})\}=[\boldsymbol{\phi}]\{\boldsymbol{q}(\boldsymbol{t})\}=[\{\boldsymbol{\phi}_{\boldsymbol{1}}\},\{\boldsymbol{\phi}_{\boldsymbol{2}}\},\{\boldsymbol{\phi}_{\boldsymbol{3}}\},\dots,\{\boldsymbol{\phi}_{\boldsymbol{N}}\}]\{\boldsymbol{q}_{\boldsymbol{1}}(\boldsymbol{t}),\boldsymbol{q}_{\boldsymbol{2}}(\boldsymbol{t}),\boldsymbol{q}_{\boldsymbol{3}}(\boldsymbol{t}),\dots,\boldsymbol{q}_{\boldsymbol{N}}(\boldsymbol{t})\}^{\boldsymbol{T}} \quad [19]$$

where $\{\phi\}$ is a vector containing $j$ elements that describes a mode shape, with one displacement for each of the $j$ mass degrees of freedom, and $q(t)$ is the time-dependent modal coordinate (scalar) for the mode shape $\{\phi\}$. The system of equations of motion can be transformed into modal coordinates by the substituting $\{u\}=[\phi]\{q\}$. In modal coordinates, the modal equations can be decoupled by pre-multiplying by $[\phi]^T$.

$$\underbrace{[\boldsymbol{\phi}]^{\boldsymbol{T}}[\boldsymbol{M}][\boldsymbol{\phi}]}_{[\boldsymbol{M}^*]}\{\ddot{\boldsymbol{q}}\}+\underbrace{[\boldsymbol{\phi}]^{\boldsymbol{T}}[\boldsymbol{C}][\boldsymbol{\phi}]}_{[\boldsymbol{C}^*]}\{\dot{\boldsymbol{q}}\}+\underbrace{[\boldsymbol{\phi}]^{\boldsymbol{T}}[\boldsymbol{K}][\boldsymbol{\phi}]}_{[\boldsymbol{K}^*]}\{\boldsymbol{q}\}=-[\boldsymbol{\phi}]^{\boldsymbol{T}}[\boldsymbol{M}]\{\boldsymbol{i}\}\ddot{\boldsymbol{u}}_{\boldsymbol{g}} \quad [20]$$

Note that the generalised matrices $[M^*]$, $[C^*]$, and $[K^*]$ are diagonal matrices, in which there are $N$ diagonal entries for each of the $N$ decoupled modes. These are effectively $N$ equations of motion with the same form as in an SDOF equation, as shown in Equation 21 for a certain mode $n$.

$$\boldsymbol{M}_{\boldsymbol{n}}^{*}\ddot{\boldsymbol{q}}_{\boldsymbol{n}}+\boldsymbol{C}_{\boldsymbol{n}}^{*}\dot{\boldsymbol{q}}_{\boldsymbol{n}}+\boldsymbol{K}_{\boldsymbol{n}}^{*}\boldsymbol{q}_{\boldsymbol{n}}=-\{\boldsymbol{\phi}_{\boldsymbol{n}}\}^{\boldsymbol{T}}[\boldsymbol{M}]\{\boldsymbol{i}\}\ddot{\boldsymbol{u}}_{\boldsymbol{g}} \quad [21]$$

As in an SDOF equation of motion, $C_n^* = 2\xi_n M_n^* \omega_n$ and $K_n^* = \omega_n^2 M_n^*$, where $\xi_n$ is the damping for that mode. Making these substitutions in Equation 22 and dividing the equation by $M_n^*$ gives an equation similar to that for an SDOF system, but in modal coordinates $q$:

$$\ddot{\boldsymbol{q}}_{\boldsymbol{n}} + 2\boldsymbol{\xi}_{\boldsymbol{n}}\boldsymbol{\omega}_{\boldsymbol{n}}\dot{\boldsymbol{q}}_{\boldsymbol{n}} + \boldsymbol{\omega}_{\boldsymbol{n}}^2\boldsymbol{q}_{\boldsymbol{n}} = -\frac{\{\boldsymbol{\phi}_{\boldsymbol{n}}\}^{\boldsymbol{T}}[\boldsymbol{M}]\{\boldsymbol{i}\}}{\{\boldsymbol{\phi}_{\boldsymbol{n}}\}^{\boldsymbol{T}}[\boldsymbol{M}]\{\boldsymbol{\phi}_{\boldsymbol{n}}\}}\ddot{\boldsymbol{u}}_{\boldsymbol{g}} = -\boldsymbol{\Gamma}_{\boldsymbol{n}}\ddot{\boldsymbol{u}}_{\boldsymbol{g}} \qquad [22]$$

The response histories can be obtained by solving for the modal coordinates $q_n(t)$ numerically and substituting/transforming them back into $\{u(t)\} = [\phi]\{q(t)\}$ to get the superposition of all the modal displacements at any instant of time $t$. The time-step $\Delta t$ for the analysis can be used based on experience. For example, the SAP2000 manual (https://docs.csiamerica.com/manuals/sap2000/CSiRefer.pdf) recommends using 1/10 of the period of the highest mode.

#### *10.4.1.2 Direct-Integration Response History Analysis*

The direct-integration method is the most common approach used in the practice as it provides a time-history of the response of a system when subjected to earthquake excitation. The term 'direct' implies that the method directly solves the set of (equilibrium) equations of motion simultaneously. In other words, this is a solution that ensures force equilibrium across all degrees of freedom at any point in time. The term 'integration' indicates that the response or state of the vectors $(u(t), \dot{u}(t), \ddot{u}(t))$ at any point in time depends on the previous or past-history state(s) of the structure, beginning from an initial value/state $(u_0, \dot{u}_0, \ddot{u}_0)$ and is solved incrementally one time-step $\Delta t$ at a time until the end of time $t$.

To solve for the state of $N$ degrees of freedom, which comprise $3N$ unknowns $(u(t), \dot{u}(t), \ddot{u}(t))$, the set of equilibrium equations provide $N$ equations. The relationships between accelerations, velocities, and displacements are used to provide the remaining equations. An analytical solution for the equation of motion is not possible if the excitation (force of ground acceleration) varies arbitrarily over time. Such problems are tackled by numerical time-step methods for integration of the equations. There are many different methods used for this purpose, such as the central difference method, Newmark's method, Newton-Raphson method, and others. The most often used method is the Newmark's $\beta$ method.

A family of numerical integration schemes known as Newmark's $\beta$ methods allow for different types of these relationships. The method introduces two factors, $\beta$ and $\gamma$. These parameters define the variation of the acceleration over a time-step and determine the stability and accuracy of the method. If the acceleration between two time-steps is assumed as the average of the two accelerations (average acceleration method), then the values of $\gamma = 1/2$ and $\beta = 1/4$ can be used. If the acceleration is assumed to vary linearly between two time-steps (linear acceleration method), then $\gamma = 1/2$ and $\beta = 1/6$ are more suitable. Using Newmark's method, the equations of motion can be described as shown in Equations 23 and 24.

$$\ddot{\boldsymbol{u}}_{\boldsymbol{n+1}} = \frac{\boldsymbol{1}}{\boldsymbol{\beta\Delta t^2}}(\boldsymbol{u}_{\boldsymbol{n+1}} - \boldsymbol{u}_{\boldsymbol{n}}) - \frac{\boldsymbol{1}}{\boldsymbol{\beta\Delta t}}\dot{\boldsymbol{u}}_{\boldsymbol{n}} - \left(\frac{\boldsymbol{1}}{\boldsymbol{2\beta}} - \boldsymbol{1}\right)\ddot{\boldsymbol{u}}_{\boldsymbol{n}} \qquad [23]$$

$$\dot{\boldsymbol{u}}_{\boldsymbol{n+1}} = \frac{\boldsymbol{\gamma}}{\boldsymbol{\beta\Delta t}}(\boldsymbol{u}_{\boldsymbol{n+1}} - \boldsymbol{u}_{\boldsymbol{n}}) + \left(\boldsymbol{1} - \frac{\boldsymbol{\gamma}}{\boldsymbol{\beta}}\right)\dot{\boldsymbol{u}}_{\boldsymbol{n}} + \boldsymbol{\Delta t}\left(\boldsymbol{1} - \frac{\boldsymbol{\gamma}}{\boldsymbol{2\beta}}\right)\ddot{\boldsymbol{u}}_{\boldsymbol{n}} \qquad [24]$$

Substituting these equations into the equilibrium equation:

$$\boldsymbol{M\ddot{u}_{n+1} + C\dot{u}_{n+1} + Ku_{n+1} = p_{n+1}} \qquad [25]$$

and rearranging gives a general expression for the displacements at the next time-step $u_{n+1}$:

$$\underbrace{\boldsymbol{(a_1 + K)}}_{\hat{K}} \boldsymbol{u_{n+1}} = \underbrace{\boldsymbol{p_{n+1} + a_1 u_n + a_2 \dot{u}_n + a_3 \ddot{u}_n}}_{\hat{p}_{n+1}} \qquad [27]$$

where:

$$\boldsymbol{a_1 = \frac{1}{\beta \Delta t^2} M + \frac{\gamma}{\beta \Delta t} C} \qquad [26]$$

$$\boldsymbol{a_2 = \frac{1}{\beta \Delta t} M + \left(\frac{\gamma}{\beta} - 1\right) C} \qquad [27]$$

$$\boldsymbol{a_3 = \left(\frac{1}{2\beta} - 1\right) M + \Delta t \left(\frac{\gamma}{2\beta} - 1\right) C} \qquad [28]$$

Therefore, the displacements at the subsequent time-step are:

$$\boldsymbol{u_{n+1} = \hat{K}^{-1} \hat{p}_{n+1}} \qquad [29]$$

and the velocities $\dot{u}_{n+1}$ and accelerations $\ddot{u}_{n+1}$ can be calculated from the equations above.

Unlike modal response analyses, the direct-integration method allows for using a full damping matrix that couples the modes (nonclassical damping). The three key considerations for using these numerical methods are:

- Convergence: The results of direct-integration methods are more sensitive to the time-step used compared to the modal response history method. It is recommended that progressively smaller time-steps are used until the results converge and are no longer affected by the time-step size.
- Stability: An unstable numerical solution can increase exponentially with time due to numerical round-off errors. The average acceleration method is unconditionally stable, but the linear acceleration method remains stable only when the time-step is sufficiently small $\frac{\Delta t}{T} < 0.55$.
- Accuracy: The linear acceleration method, in which the acceleration between two points is assumed to vary linearly, is more accurate compared to the average acceleration method.

#### *10.4.1.3 Important Modelling Parameters*

This section discusses some important modelling parameters.

##### 10.4.1.3.1 Inertial mass and gravity loads

The inertial mass considered in the model should be the expected mass, including self-weight of the building plus some allowance for contents, generally following the recommendations to determine seismic masses given in building codes such as ASCE/SEI 7-22, NBCC, and others. It is usually adequate to lump the masses at the floor levels and to include inertial effects in the two horizontal directions, including rotation about the vertical building axis. Vertical inertial effects (i.e., vertical mass and ground motion components) should be modelled for buildings with long-span framing, such as arena roofs or long-span floor systems, where the vertical period of vibration is in the range that may be excited by the vertical component of earthquake ground motions (periods of about 0.1 s or more). Otherwise, where members are sensitive to vertical loads, the influence of the code-specified vertical earthquake load (e.g., the $E_v$ factor in ASCE/SEI 7-22), should be accounted for in the calculated force demands. Gravity loads (defined and factored) should be included in the dynamic analyses to account for their effects on (a) force and deformation demands in structural components and (b) large displacement P-Δ effects. Generally, including gravity loads requires a two-step (nonproportional loading) analysis, whereby the gravity loads are applied first and then held constant while the earthquake ground motions are applied.

##### 10.4.1.3.2 Damping effects

In the context of the nonlinear dynamic procedure, equivalent viscous damping is associated with the reduction in vibrations through energy dissipation other than that which is calculated directly by the nonlinear hysteresis in the modelled elements. This so-called inherent damping occurs principally in (a) structural components that are treated as elastic but where small inelastic cracking or yielding occurs, (b) the architectural cladding, partitions, and finishes, and (c) the foundation and the soil if they are not modelled otherwise. Special energy-dissipative components (e.g., viscous, friction, or hysteretic devices) should be modelled explicitly in the analysis, rather than as inherent damping.

The amount of inherent viscous damping requires careful consideration of the available sources of energy dissipation and whether these are otherwise captured in the analysis. For example, fibre-type component models, which capture the initiation and spread of yielding through the cross-section and along the member lengths, will tend to capture hysteretic energy dissipation at lower deformations than lumped plasticity (hinge) models, in which the inelastic hysteresis is not initiated until the demand exceeds the modelled yield strength of the member. Damping may also occur in the gravity system components that undergo local inelastic deformations but are not modelled directly in the structural analysis.

The equivalent viscous damping is included through the $[C]$ matrix in the equations of motion, and a decision should be made to determine the appropriate value for the inherent damping and how the terms of the damping matrix can be formulated to achieve that value. In commonly used Rayleigh damping formulation, the damping matrix $[C]$ is calculated as a linear combination of the mass and stiffness matrix ($[C]=\alpha[M]+\beta[K]$), where the proportionality factors $\alpha$ and $\beta$ can be chosen to provide a defined percentage of critical damping at two specific periods of vibration. Reasonable periods to specify these damping values are $0.2T_a$ and $1.5T_a$, where $T_a$ is the fundamental period of vibration of the structure. In modal damping formulations, the damping matrix is formulated by specifying values of critical damping for one or more vibration modes, using information about the mode shapes and vibration periods. Alternatively, the damping effects of specific components, such as partition walls, could be modelled with explicitly defined viscous damping terms in the [*C*] matrix or the hysteretic springs in the stiffness [*K*] matrix.

The common Rayleigh and modal damping formulations were originally developed in the context of linear elastic dynamic analysis, where the stiffness matrix [*K*] is constant and the vibration modes can be uniquely calculated. However, for nonlinear analysis, in which member stiffness changes and unique vibration modes do not exist, the application of each method has implementation issues, which are discussed by Hall (2006), Charney (2008), ATC (2010), and others. For example, it is generally accepted that the stiffness proportional term of the damping matrix $\beta[K]$ should exclude or minimise contributions from components in which stiffness changes dramatically during the analysis or for components, such as rigid links, that are assigned artificially high stiffness. Some contend that this concern can be minimised by using the tangent rather than the initial elastic stiffness matrix in the stiffness proportional damping term, while another suggested approach is to eliminate the stiffness proportional damping term and to specify a value only for the mass proportional damping term $\alpha[M]$. Currently, there is no consensus as to how to resolve these issues; moreover, some of the proposed solutions must be implemented within the software formulation and cannot otherwise be controlled by software users. Therefore, software documentation should be consulted for details on the damping implementation and guidance on specifying damping parameters.

The inherent damping depends on many factors specific to a given building, such as structural materials, type and detailing of partition and façade walls, height of building, foundation type, and the analysis model (e.g., lumped plasticity versus fibre-type models). Therefore, it is difficult to generalise the appropriate amount of additional damping to use in a nonlinear analysis. As summarised by ATC (2010), measurements of total damping, expressed in terms of percent critical damping in the first translational mode, range from low values of 0.5% to 1% in buildings under wind and ambient vibrations to 10% in buildings subjected to earthquakes. However, in the latter case, the measured damping of 10% is likely to reflect energy dissipation due to both nonlinear hysteretic and inherent damping. Thus, reported measurements of damping require careful interpretation.

Based on these observations and guidance in various documents, it is suggested that equivalent viscous damping of 1% to 5% of critical damping is specified over the range of elastic periods from $0.2T_a$ to $1.5T_a$. Critical damping values should be specified in the lower end of this range for (a) tall buildings and other structures where there is less participation by partition walls, cladding, and foundations, and (b) service-level earthquake analyses where storey drift ratios are limited to about 0.005. For tall buildings, the Pacific Earthquake Engineering Research Center (PEER) guidelines (2010; 2017) recommend that viscous damping be less than 2.5% over the range of predominant modes, and the Council on Tall Buildings and Urban Habitat (Willford et al., 2008) recommends damping values of 1% to 2%. Beyond limiting the specified damping to values within these ranges, it is further recommended that the sensitivity of the calculated demand parameters to the damping model formulation (e.g., Rayleigh versus modal) and the assumed critical damping values be assessed.

## 10.4.2 Nonlinear Time-History Dynamic Analysis

The nonlinear dynamic procedure, when properly implemented, provides a more accurate assessment of the structural response to strong ground shaking than the nonlinear static procedure. Since the nonlinear dynamic analysis model incorporates inelastic member behaviour under revered earthquake ground motions, the nonlinear dynamic procedure explicitly simulates hysteretic energy dissipation in the nonlinear range. Damping only in the linear range and other non-modelled energy dissipation must be added as viscous damping. The dynamic response is calculated for input earthquake ground motions, resulting in response history data on the pertinent demand parameters. Due to the inherent variability in earthquake ground motions, dynamic analyses for multiple ground motions are necessary to calculate statistically robust values of the demand parameters for a given ground motion intensity or earthquake scenario. As nonlinear dynamic analysis involves fewer assumptions than the nonlinear static procedure, it is subject to fewer limitations than the nonlinear static procedure. However, the accuracy of the results depends on the details of the analysis model and how faithfully it captures the significant behavioural effects. Acceptance criteria typically limit the maximum structural component deformations to values where degradation is controlled, and the nonlinear dynamic analysis models are reliable.

The selected analysis approach has a critically important impact on the appropriateness of any choice made in modelling. For example, nonlinear static (pushover) analyses are affected only by the backbone curve of the response. A nonlinear response history analysis, however, requires a complete hysteretic characterisation of the response of the components that undergo nonlinear behaviour.

### *10.4.2.1 Nonlinear Direct-Integration Response History Analysis*

The numerical integration procedure for nonlinear systems follows the same process for linear systems, with one exception to make an allowance for the nonlinear load-deformation relationships.

For instance, while Equation 27 shows Newmark's equation for linear analysis (Chopra, 2012), for nonlinear analysis, an adjustment is needed to the left side to represent the nonlinearity:

$$\boldsymbol{a_1 u_{n+1} + f_{n+1} = \underbrace{p_{n+1} + a_1 u_n + a_2 \dot{u}_n + a_3 \ddot{u}_n}_{\hat{p}_{n+1}}} \qquad [30]$$

where $\mathrm{f}_{n+1}$ includes the nonlinear restoring forces associated with $\mathrm{u}_{n+1}$ from the load-deformation relationships. An iterative procedure such as the Newton-Raphson algorithm can solve both variables to solve the force equilibrium.

### *10.4.2.2 Incremental Dynamic Analysis*

The incremental dynamic analysis (IDA) procedure uses nonlinear response history analysis to assess the response of a structure to various increasing intensities of ground motions (Vamvatsikos & Cornell, 2002).

IDA involves performing multiple nonlinear dynamic analyses of a structural nonlinear model under a suite of ground motion records, each scaled to several increasing levels of intensity. The scaling levels are appropriately selected to force the structure through the entire range of behaviour, from elastic to inelastic and finally to global dynamic instability, where the structure essentially experiences collapse. Appropriate post-processing can present the results in terms of IDA curves, one for each ground motion record, of the seismic intensity, typically represented by a scalar intensity measure, versus the structural response, as measured by an engineering demand parameter. Possible choices for the intensity measure are scalar (or, rarely, vector) quantities that relate to the severity of the recorded ground motion and scale linearly or nonlinearly with its amplitude. The intensity measure is chosen so that appropriate hazard maps (hazard curves) can be produced for them by probabilistic seismic hazard analysis. In addition, the intensity measure should be correlated with the structural response of interest to decrease the number of required response history analyses. Possible choices are the peak ground acceleration, peak ground velocity, or Arias intensity, but the most widely used is the 5%-damped spectral acceleration at the first-mode period of the structure. The engineering demand parameter can be any structural response quantity that relates to structural, nonstructural, or content damage. Typical choices are the maximum (over all storeys and time) interstorey drifts, the individual peak storey drifts, and the peak floor accelerations.

IDA can be conducted on a single building at a specific location to evaluate the seismic performance of that building in detail under increased input motions until it reaches collapse. IDA can also be used in a more complex process of determining the seismic response factors that can be used for a certain type of SFRS using the equivalent static design procedure in most building codes. One such application of the IDA procedure is detailed in FEMA P695 (ATC, 2009b) to characterise the seismic performance of a structural system with its seismic design coefficients in the US ($R, C_d, \Omega_0$). To quantify the 'safe' collapse margin, IDA is used to incrementally scale the ground motions to seek the median collapse intensity, at which 50% of the ground motions result in collapse. The ratio of this intensity to the maximum considered earthquake (MCE) intensity defines the margin from collapse (collapse margin ratio), and it is adjusted further to account for various sources of uncertainties. Figure 11 shows the results from such IDA analyses in terms of spectral acceleration versus maximum interstorey drift on a six-storey CLT building.

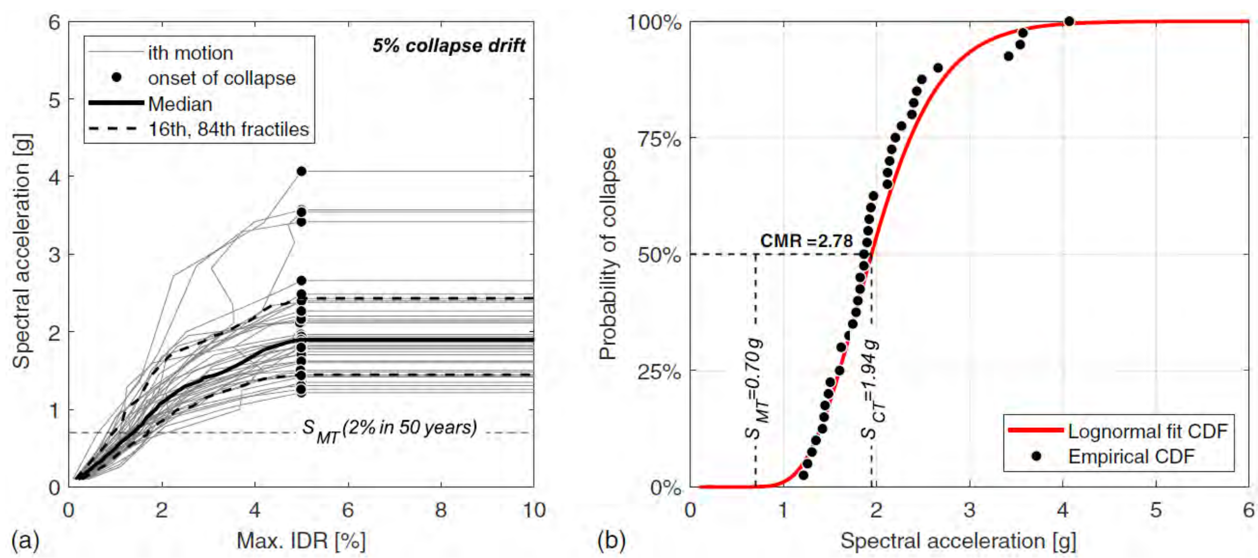


**Figure 11. (a) IDA used to generate relative intensity curves for a six-storey CLT building, and (b) the cumulative distribution function with the collapse margin ratio (Shahnewaz et al., 2020).** ***CDF, cumulative distribution function; IDR, interstorey drift ratio***

A simplified procedure is given in the Canadian Construction Materials Centre's *Technical Guide for Evaluation of Seismic Force Resisting Systems and Their Force Modification Factors ($R_d$ and $R_o$ factors) for Use in the National Building Code of Canada* (DeVall et al., 2021). The procedure requires a two-level analysis; that is, a nonlinear time history analysis at 100% and 200% uniform hazard spectrum (UHS) intensity. This guide has some sections that are particular for cantilevered mass timber balloon-type shear walls as a type of SFRS that is not yet included as an SFRS in the NBCC.

#### *10.4.2.3 The Role and Use of Nonlinear Analysis in Seismic Design*

While buildings are usually designed for seismic resistance using elastic analysis, most will experience significant inelastic deformation during large earthquakes. Modern performance-based design methods require ways to determine the realistic behaviour of structures under such conditions. Enabled by advancements in computing technologies and available test data, nonlinear analyses provide the means for calculating structural response beyond the elastic range, including strength and stiffness deterioration associated with inelastic material behaviour and large displacement. As such, nonlinear analysis can play an important role in the design of new and existing buildings (ASCE, 2017; Popovski et al., 2022).

Once the goals of the nonlinear analysis and design basis are defined, the next step is to identify specific demand parameters and appropriate acceptance criteria to quantitatively evaluate the performance levels. The demand parameters typically include peak forces and deformations in structural and nonstructural components, storey drifts, and floor accelerations. Other demand parameters, such as cumulative deformation or dissipated energy, may be checked to help confirm the accuracy of the analysis and/or to assess cumulative damage effects.

Nonlinear analyses also help designers implement the capacity-based design that is fundamental in the seismic design of buildings. According to this design approach, the designer establishes which elements need to be ductile and yield during the earthquake motions and others that should not yield and be designed with sufficient overstrength to force the yield in the designated elements. This design strategy provides protection from sudden failures in elements that cannot be proportioned or detailed for ductile response. It also limits the locations in the structure where expensive ductile detailing is required, providing greater certainty in how the building will perform during strong earthquakes. Finally, capacity-based design provides reliable energy dissipation in a building by enforcing deformation modes (plastic mechanisms) that are defined by the selection and placement of the ductile components.

#### *10.4.2.4 Choice of Hysteretic Models*

Nonlinear dynamic analysis requires appropriate and complete definition of the hysteretic behaviour of all structural elements and connections, including their loading, unloading, and cyclic behaviours. The choice of hysteretic model used can significantly affect the predicted response of a structure. Several general types of hysteretic models (Figure 12) are available for modelling the nonlinear cyclic behaviour in structural analysis.

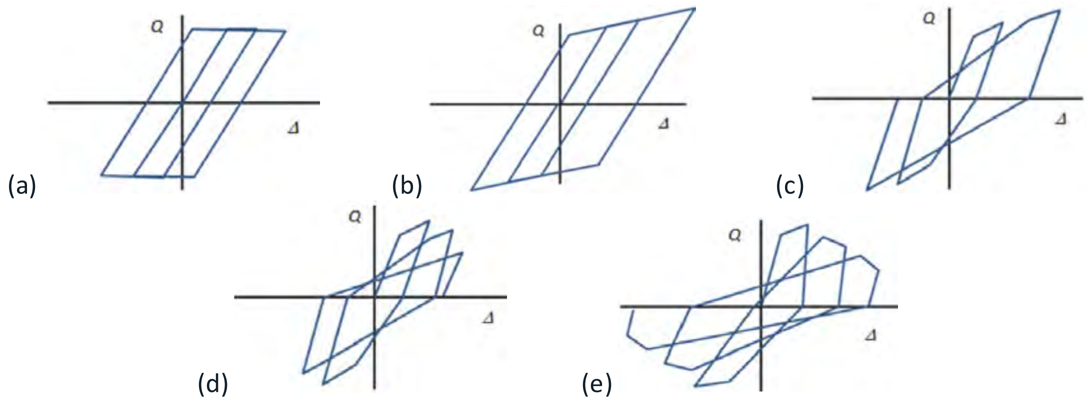


**Figure 12. Different types of nonlinear models (ATC, 2017): (a) elastic-perfectly plastic, (b) strain hardening, (c) stiffness degrading, (d) strength degrading, and (e) cyclic degrading**

The elastic-perfectly plastic model (Figure 12[a]) represents an idealised behaviour in which initial loading produces deformation at a constant stiffness rate until the applied force equals the element's yield strength, at which point the element continues to deform plastically under this constant force at zero stiffness. When the applied force is reduced, the element recovers deformation at the same stiffness rate experienced in the initial loading until the force reverses and again reaches the yield level, when reversed plastic deformation under constant force occurs. The elastic loading stiffness and yield strength remain constant. These models can be used for slip joints, friction dampers, and other similar energy-dissipative devices when used in timber buildings. Models that account for strain hardening (Figure 12[b]) are similar to elastic-perfectly plastic except that the yielding point initiates further deformation at positive nonzero stiffness. Under successive cycles of loading, the yielding does not reinitiate until the applied force exceeds the prior peak applied force in a given direction. This form of hysteresis is representative of the behaviour of some steel elements before the onset of buckling or fracture (ATC, 2017). Stiffness degrading models (Figure 12[c]) capture a behaviour similar to that of strain hardening except that on reloading the deformation occurs at a reduced stiffness. The reduced stiffness is a result of damage that has occurred, such as cracking in concrete or masonry walls, or withdrawal of fasteners between sheathing and studs in a light-frame wall. Strength degrading models (Figure 12[d]) depict a behaviour like that of stiffness degrading ones except that each successive cycle of motion initiates yielding at a lower force level. The reduced yield strength can be attributed to the occurrence of some damage, such as spalling of concrete or masonry in walls. Cyclic degrading models (Figure 12[e]) capture a behaviour similar to that of strength degrading except that in successive cycles of yielding, an increasingly negative post-yield stiffness occurs. This type of behaviour is commonly associated with timber connections and shear walls (Koliou et al., 2018), buckling of steel elements, or reinforcing.

These and other types of nonlinear behaviour can be modelled in several ways, including discrete hinges, distributed plasticity models, and phenomenological methods. As almost all nonlinear deformation in timber structures occurs in the connections, spring elements (discrete hinges) are a convenient means of representing nonlinear behaviour of connections, or forming of plastic hinges in beams in general. In this approach, the element stiffness formulation includes direct mathematical coding of the hysteretic relationship in the form of a macro moment-rotation or a similar relationship.

Figure 13 shows some of the main aspects of the cyclic behaviour of timber connections and components. The hysteretic curves are slightly asymmetrical, with indistinct yield points. There is stiffness degradation for increased load cycles and strength degradation after the maximum load has been reached. There is also strength degradation for subsequent loading cycles at the same deformation level. The initial hysteresis loops at a certain displacement level are relatively thicker, implying larger amounts of energy dissipated. The loops, however, become narrower (pinched) for successive load cycles at same deformation level or for higher deformation levels. The pinching effect is due to the formation of a cavity around the fasteners as a result of the irrecoverable crushing of wood after the first loading cycle. This implies a reduced stiffness as the connection stiffness in this phase solely depends on the contribution of the steel fasteners. As soon as contact with the surrounding wood is re-established at increased deformation levels, the stiffness rapidly increases, which leads to the typical pinched shape of the curves.

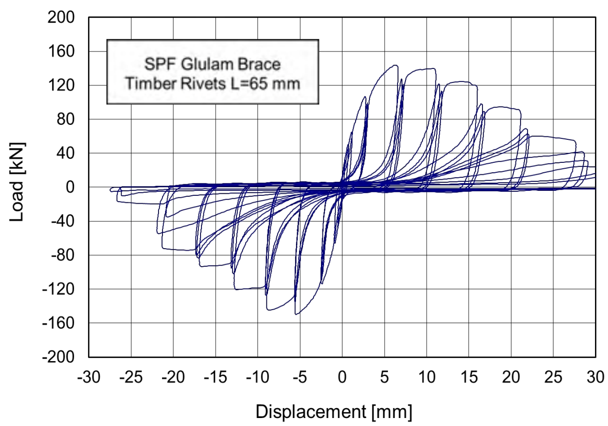


(a)

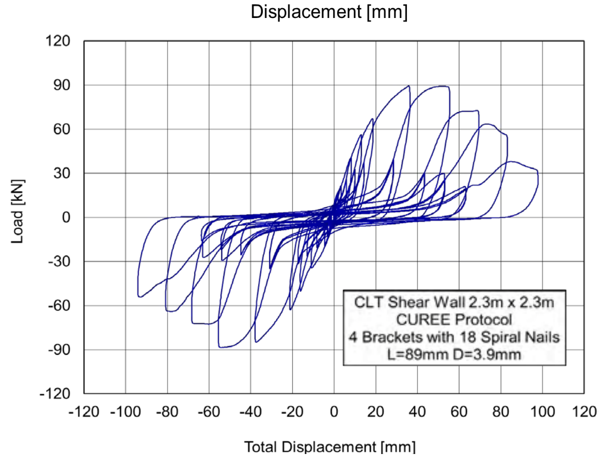


(b)

**Figure 13. Typical hysteresis loops as obtained from experimental tests on (a) glulam brace with riveted connections on both sides tested using the International Standards Organization protocol, and (b) CLT shear walls tested using the Consortium of Universities for Research in Earthquake Engineering (CUREE) protocol. *SPF, spruce-pine-fir***

As can be seen from the hysteretic curves, the performance of wood connections and assemblies is relatively complicated. The response depends on the fastener type, material and manufacturing, embedment properties of the wood or engineered wood products, grain or strand direction, type of loading, rate of loading, potential friction, presence of material imperfections, etc. During the past several decades, many researchers have tried to find a way to develop hysteretic models that can accurately describe and predict the behaviour of timber connections and assemblies. Generally, these hysteretic models can be categorised as three major types: mechanics-based models, piecewise linear functions models, and mathematical models, at different complexity levels and assumptions considering the trade-offs between the model complexity, accuracy, computational efficiency, and physical interpretation. Chapter 7.1 discusses the model types in more detail. Regardless of the types of models, the behaviour of the elements and connections should be modelled using the appropriate envelope and backbone curves.

## 10.4.3 Selection and Scaling of Ground Motions

### *10.4.3.1 General*

The results of time-history analyses highly depend on the input parameters of the analyses. One of the largest sources of uncertainty many analysts face is the choice of ground motions to be used to excite the structure being designed. Appropriate input ground motions are important to obtain meaningful response quantities that have accuracy and variation that represent the perceived earthquake threat.

Input ground motions should be adequately selected and scaled to accurately represent the specific hazard of interest at the building site. Selection of ground motions is usually covered in selected national building codes and design standards such as ASCE/SEI 7-22, NBCC, Eurocode 8, and others. The ground motions should reflect the characteristics of the dominant earthquake source at the building site, such as fault mechanism, distance to the fault, site conditions, and characteristic earthquake magnitude. Recent studies have further shown that the shape of the ground motion response spectra is an important factor in choosing and scaling ground motions, particularly for higher-intensity motions (Baker & Cornell, 2006).

A comprehensive discussion on selecting and scaling of ground motion records is beyond the scope of this text. Designers are encouraged to work with ground motion specialists in the process of selecting and scaling of ground motions. Some of the basics related to ground motion spectra selection and scaling are given below, along with some of the issues to be considered.

- <u>Target hazard spectra or scenario</u>: While the earthquake hazard is a continuum, building codes typically define specific ground motion hazard levels for specific performance checks. Generally, the hazard is defined in terms of response spectral accelerations with a specified mean annual frequency of exceedance, although other definitions are possible, including scenario earthquakes (e.g., an earthquake with a specified magnitude and distance from the site) or deterministic bounds on ground motion intensities.

- <u>Source of ground motions</u>: For building assessment and design, the input earthquake ground motions can either be (a) actual recorded ground motions from past earthquakes, (b) spectrally matched ground motions that are created by manipulating the frequency content and intensity of recorded ground motions to match a specific hazard spectrum, or (c) artificially simulated motions. Opinions differ as to which types are most appropriate. Recorded ground motions are generally scaled to match the hazard spectrum at one or more periods. For example, ASCE/SEI 7-22specifies rules for scaling the ground motions based on their spectral acceleration values for periods between $0.2T_a$ and $1.5T_a$, where $T_a$ is the fundamental period of vibration of the structure. When structures are expected to respond in multiple modes, such as in tall buildings, spectral matching may be more appropriate, since scaling of actual recorded motions to a UHS may bias the analysis results to either overestimate the response at short periods or underestimate it at longer periods.

- Number of ground motions: Given the inherent variability in earthquake ground motions, design standards typically require analyses for multiple ground motions to provide statistically robust measures of the demands. For example, ASCE 7-22 requires analyses for at least seven ground motions (or ground motion pairs for 3D analyses) to determine the mean values of demand parameters for design. In concept, it is possible to obtain reliable mean values with fewer records, such as by using spectrally matched records, but there is currently no consensus on the methods to do so. Moreover, while one could calculate additional statistics besides the mean (e.g., the standard deviation of the demand parameters), the reliability of such statistics is questionable when based on only seven ground motions. This is especially true when spectrally matched records are used, where the natural variability in the ground motions is suppressed.

#### *10.4.3.2 Uniform Hazard Spectrum*

Throughout its design life, a structure is potentially exposed to all possibilities of occurrence of ground motion intensities. A probabilistic seismic hazard analysis can evaluate the hazard of seismic ground motion at a site by considering all possible earthquakes in the area, estimating the associated shaking at the site, and calculating the probability of occurrences as required in performance-based seismic design. The probabilistic seismic hazard analysis is recognised as the most rational means to quantify the seismic hazard at a specific site. In the context of probabilistic seismic hazard analysis, the UHS can provide the very essential probabilistic information required for an advanced seismic design philosophy. A UHS can be very simply described as a ground hazard spectrum in which every ordinate (spectral acceleration value) has an equal probability of exceedance (Figure 14). A UHS can adopt elastic and inelastic response parameters, and thus it can suitably be integrated in a design methodology that accounts for inelastic damage parameters.

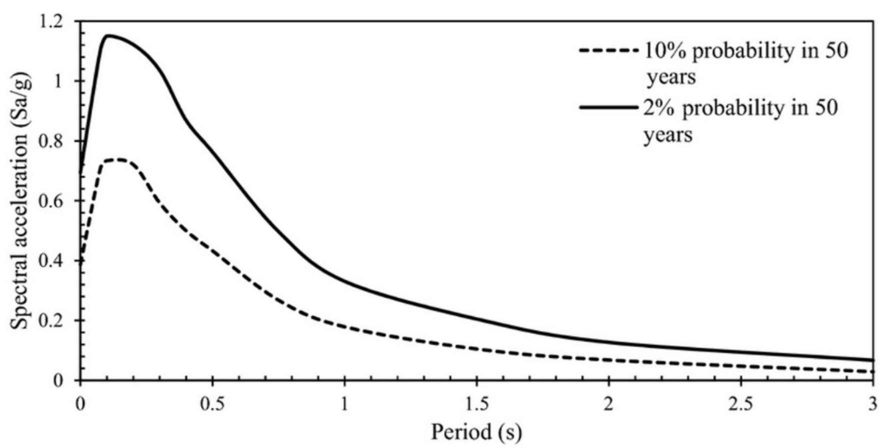


**Figure 14. UHS for a rocky soil location with different probabilities of exceedance**

#### *10.4.3.3 Conditional Mean Spectrum*

The UHS assumes that there is an equal probability of exceeding the earthquake motion every period across the spectrum, as shown in Figure 15. In other words, UHS represents an expected ground motion spectrum that envelopes spectral amplitudes at all periods. Thus, conceptually the earthquake scenario represented by

UHS may be inconsistent with the nature of real earthquake events, as any single ground motion may dominate (cause severe pseduospectral accelerations) only at a singular period (Haselton et al., 2012). This conservatism of the UHS is addressed by the conditional mean spectrum (CMS). The CMS is a spectrum that is more likely to be encountered in any one event. CMSs are generally defined as expected pseudospectral accelerations conditioned on UHS at a selected period. To develop them, the ground motion prediction equation is needed to obtain the mean and standard deviation of the logarithmic intensity measure at the site, for all periods on the spectrum (i.e., the mean spectrum). The mean spectrum defines the average intensity of shaking expected at the site and is the basis of the development of the CMS. The next step requires defining the target pseudospectral acceleration at a conditioning period of interest (e.g., the fundamental period of the structure) (Roy et al., 2014).

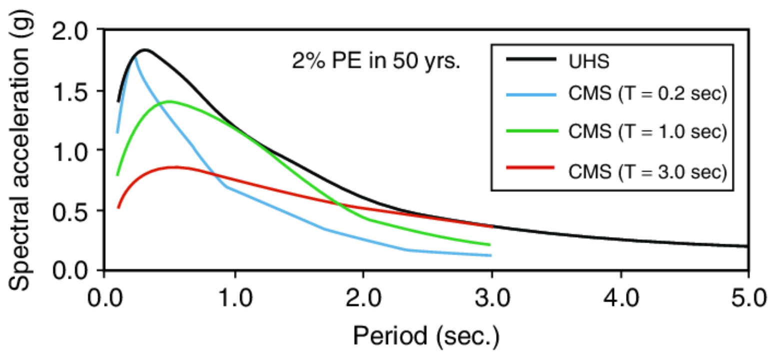


**Figure 15. UHS and CMS for 3 periods for 2% in 50 years motions for a site in LA (lat 34.0890 N, long 118.4350 W) for soil class D (Roy et al., 2014).** ***PE, probability exceedance***

Figure 15 presents UHS for 2% probability of exceedance collected from the website of the United States Geological Survey (http://earthquake.usgs.gov/research/hazmaps/). This spectrum corresponds to a location in Los Angeles, US (lat 34.0890 N, long 118.4350 W), typically representative of site class D, which are stiff soils with shear wave velocity between 182 m/s to 366 m/s. The CMS of this region was obtained from the Geologic Hazards Science Center (https://earthquake.usgs.gov/ws/) for different conditioning periods (ranging from short to long periods). Characteristic conditioning periods were selected as 0.2 s, 1.0 s, and 3.0 s for the CMS. It is evident from Figure 15 that the ordinates of UHS are greater than CMS at all periods other than the period at which CMS is conditioned.

#### *10.4.3.4 Screening and Selection*

Some considerations from ASCE/SEI 7-22 (ASCE, 2022) are listed here to assist with selecting appropriate ground motion records from the available databases:

Step 1: Choose the ground motions that are suitable for the selection based on the aspects listed below.

- Source mechanism: Readings from similar tectonic regimes (subduction, crustal, etc.) should be used where possible due to differences in spectral shapes and durations.
- Magnitude: Similar magnitudes should be selected to ensure appropriate durations.

- Site soil conditions: While reasonable limits on the soil conditions are encouraged, they should not be too restrictive at the detriment of the number of candidate ground motions.
- Usable frequency: Ground motions are processed to remove noise, and the range of usable frequencies must accommodate the range of frequencies critical for the building response.
- Frequency sampling: Ground motion records should be sampled at discrete time intervals, and this needs to be sufficiently fine (1/100 of the lowest period of interest) to capture the essential characteristics of the excitation.
- Site-to-source distance

Step 2: Select the ground motions after the scaling procedure.

- Spectral shape: This is the primary consideration when selecting ground motions as it significantly affects the dynamic response of the building.
- Scale factor: Range limits should be set on scale factors between 0.25 and 4.0 to minimise bias in displacement responses.
- The number of records from a single event: Sometimes should be limited to not more than three or four from a single event to avoid estimates being dominated by a single seismic event.

#### *10.4.3.5 Scaling a Single Horizontal Component for 2D Plane Analyses*

Because of the scarcity of recorded ground motions from large and rare events, it is common to use records from smaller events, which are then scaled upward to the intensity of the design-level earthquake. A common measure of intensity used to decide on a suitable scale factor is pseudospectral acceleration with 5% viscous damping. For any single record, the desired scale factor is one that produces the best fit between the scaled record's spectrum and the target spectrum. For lognormal distributions, the maximum likelihood estimation procedure estimates the sample variance as the sum of squared residuals (SSE) divided by the number of samples.

When selecting records, it is important to match the spectral shapes to account for period elongation and higher modes. Hence, the SSE is usually calculated over a range of periods (giving equal weights to $N$ discrete periods) rather than fitting $S_a$ at a single period only (e.g., matching $S_a$ or $\ln S_a$ at $T_1$ only). Examples of scaling $S_a$ in linear and logarithmic ordinates can be found in Zhang et al. (2020).

Some research findings (Jayaram et al., 2011; Wang, 2011) propose that instead of scaling records individually or independently of one another, the designer should consider the 'average' spectrum of the whole set of records and find the best fit between this average spectrum and the target spectrum. An additional criterion can also be included to match a desired variance in the scaled $S_a$ values at each period, and this will be important if the designer is interested in predicting the distribution of responses (e.g., to estimate collapse probability or for intensity-based assessments).

Since designers are often interested only in the mean or median structural response across a number of ground motions, it may be more effective to select and scale ground motions as a set so that their mean or median intensity matches the target intensity. The ground motion selection process becomes a combinatorial problem to identify an optimal combination of $n$ ground motions, whose mean spectrum produces the lowest SSE. This is one optimisation technique suggested by Jayaram et al. (2011).

Figure 16 compares the scaling and selection of 10 accelerograms (individually versus as a set) from a pool of approximately 8 500 records (considering two component accelerograms for each record) acquired from the PEER NGA-West2 ground motion database (https://ngawest2.berkeley.edu) (record sequence numbers 1 to 10 000). Figure 16(a) and (b) show, for different period ranges, the 10 best-fitting accelerograms in terms of the lowest arithmetic $SSE_{S_a}$ in the pool of records. However, the mean spectrum shown in red appears to exhibit obvious peaks and troughs. On the other hand, accelerograms in Figure 16(c) and (d) better match the target spectra. In these cases, all records were individually scaled by minimising the logarithmic $SSE_{\ln S_a}$ before 10 accelerograms were selected by minimising the mean spectrum's $SSE_{S_a}$. Note that no prescreening or scale factor constraints were used.

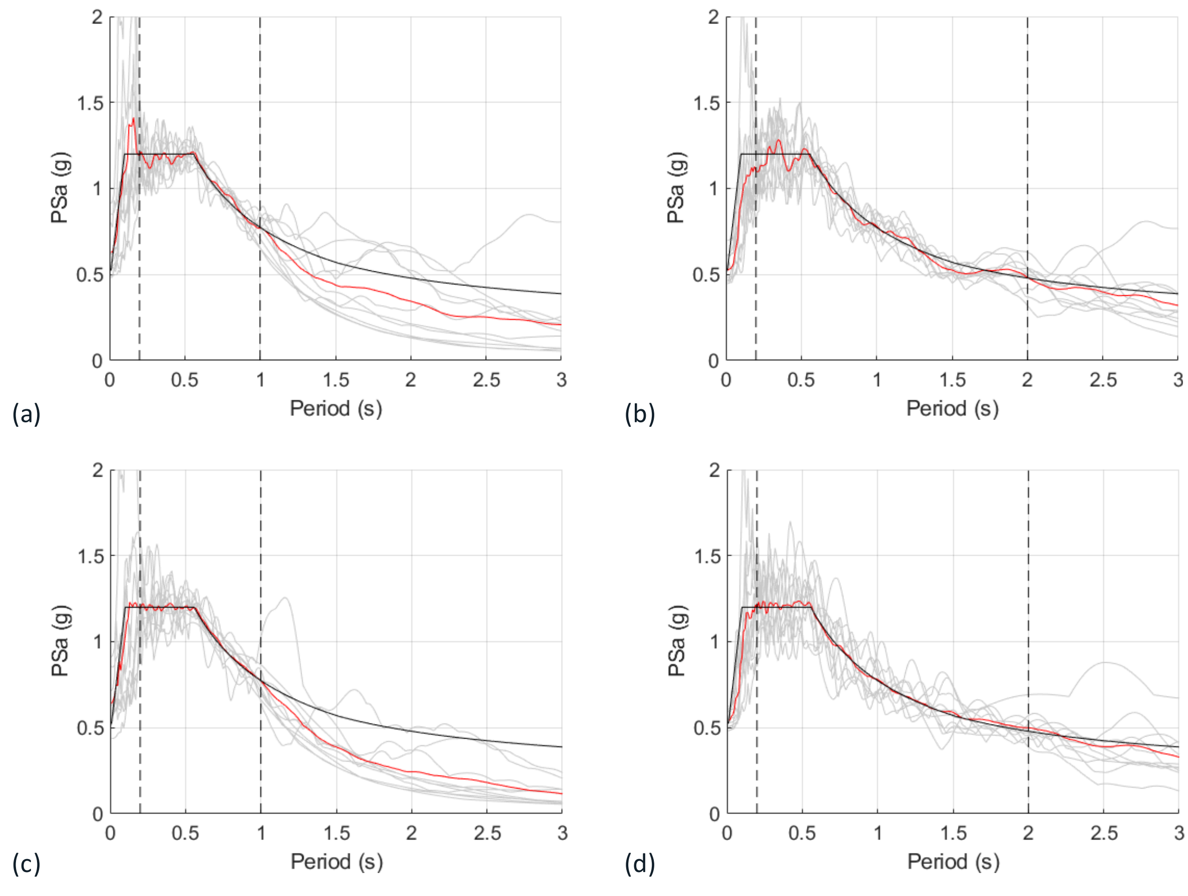


**Figure 15. (a, b) Selecting and scaling ground motions individually, and (c, d) as a set. Scaling range of periods are ([a] and [c]) $T_n$ = 0.2–1.0 s, and ([b] and [d]) $T_n$ = 0.2–2.0 s**

### *10.4.3.6 Scaling Two Horizontal Components for Bidirectional Analyses*

Generally, international standards prescribe a single target spectrum for both record components. This is justified because the average spectrum in both directions (average *H1* and average *H2*) tend to become similar for a set of records selected at random orientations, even if a single record has a considerably different component spectrum. This is acceptable when the structure is symmetric and has relatively similar periods in both directions. However, if the periods are considerably different (e.g., $T_{1x}/T_{1y} > 2$), matching the entire UHS over an extensive range of periods can be conservative. On the other hand, using a single CMS conditioned on the average period ($T_{avg} = T_{1x}/2 + T_{1y}/2$) can lead to unconservative responses at the individual periods $T_{1x}$ and $T_{1y}$. This is shown in Figure 17 (Kwong & Chopra, 2018). One alternative is to use two different CMSs, where each CMS is conditioned on the governing period of each direction. The second alternative is to use a CMS-UHS composite spectrum. The responses obtained from the composite spectrum are generally more conservative than those from two CMSs, but not as conservative as those from the UHS.

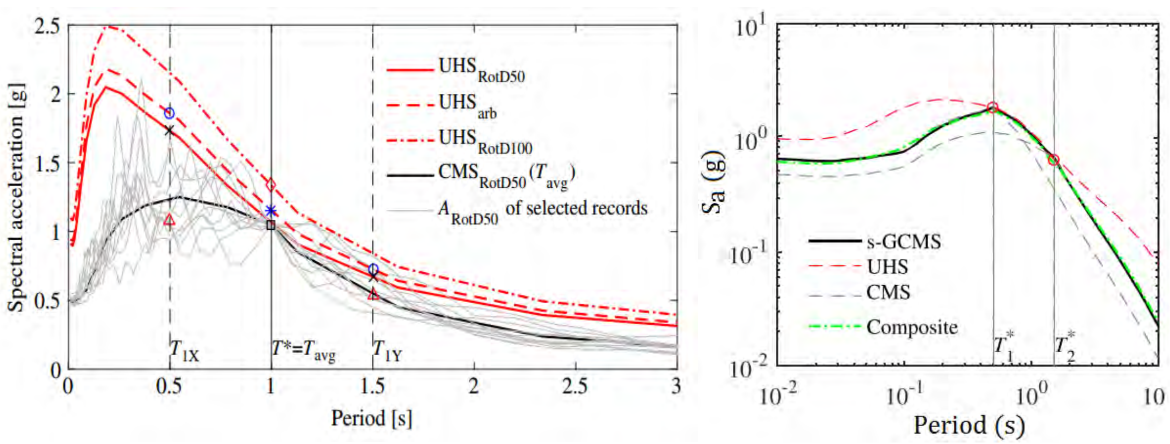


**Figure 16. Target spectra for bidirectional analyses (Kwong & Chopra, 2018).** ***s-GCMS, simplified generalised conditional mean spectrum***

Huang et al. (2009) explained that the orientation of peak responses is basically random for far-field sites. On the other hand, Kalkan and Reyes (2015) ascertained the fact that fault-normal/fault-parallel orientations and maximum-direction orientations were often greater than as-recorded orientations. However, considering that only a finite number of nonlinear dynamic analyses were available, Giannopoulos and Vamvatsikos (2018) suggested that it is more important to use as many different records as possible instead of reducing the number of records to employ different orientations of each. This is because of the larger record-to-record variability compared to orientation-to-orientation variability.

The variability due to orientation can be worsened by the scaling process for bidirectional ground motions. Scaling a pair of components to a single target spectrum based on the pair's jointly defined intensity measure (e.g., RotD50 or GeoMean) means that neither one of the components accurately matches the target $S_a$. This leads to a more excellent dispersion in the responses and necessitates a larger number of analyses. Even if the record undergoes some rotation or different scale factors are applied in each direction (which is not allowed by codes to preserve relative intensity), the component spectra will still remain dissimilar at most periods.

Despite that, it has been proposed that the amount of variability can be reduced by rotating the record components to an optimal azimuth. This is defined as the orientation that leads to the lowest SSE where the deviation from the target spectrum is minimised for both components as a whole (Kwong & Chopra, 2018). This ensures that the selected ground motions match the target spectrum in an 'average' sense regardless of their as-recorded orientation.

Note that this technique was applied in combination with metrics that measure central tendency, such as RotD50 or GeoMean. For these metrics, the component spectra might coincide with the target spectrum on an 'average' sense if component spectra were selected at random orientations. With the RotD100 metric, it is not immediately clear whether the act of rotating components to minimise the SSE would lead to the desired outcome of reducing variability.

Two different procedures used for scaling, depending on whether the pair of component spectra are summarised by a single spectrum (e.g., RotDxx or GeoMean). If the code-defined target spectrum uses a summarising metric like the RotDxx or a GeoMean-based spectrum to quantify seismic demand, then the scaling procedure must use the same type of spectrum for each ground motion to be consistent and to avoid underestimating or overestimating the mean response. In this case, the scaling process is identical to that in Section 10.4.3.5, which involves scaling a single spectrum per record only.

The selection and scaling process is slightly more complicated if the target spectrum is derived based on arbitrary values of $S_a$. Now, each record contains two-component spectra to be fitted to a single target spectrum. However, the two-component spectra often differ significantly in terms of shape and scale, yet the same scale factor must be applied to both components to preserve their relative intensity. Kwong and Chopra (2018) discuss such cases.

#### *10.4.3.7 Scaling Horizontal and Vertical Components for Full 3D Analyses*

Kwong and Chopra (2020) used a multicomponent scaling approach to fit all three components together and at the same time. The two horizontal components were represented by a single geometric mean spectrum. The measure of fit is provided in Equation 31. Here, $w_H$ is a weighting factor to determine the relative importance of the fit between horizontal and vertical spectra. When $w_H = 1$, the procedure fits only the horizontal spectrum and does not consider the fit for the vertical component. The converse happens when $w_H = 0$. The authors suggested using equal weighting $w_H = 0.5$ because preliminary results did not show any specific weighting of significantly better fit.

$$\boldsymbol{SSE_{combined} = w_H SSE_H + (1 - w_H) SSE_V} \qquad [31]$$

The SSE (Equation 31) for both the horizontal spectrum $SSE_H$ and the vertical spectrum $SSE_V$ can be calculated using the same scale factor to preserve the relative intensity between horizontal and vertical components. This scale factor is obtained from fitting either the horizontal spectrum or the vertical spectrum, depending on the direction of interest.

Kwong and Chopra (2020) also considered using different scale factors for the vertical component but did not find a significantly better fit. However, this was because they used a composite spectrum that accounts for the correlation between horizontal and vertical components. Unlike a UHS, this spectrum is more consistent with the relative intensity of natural ground motion record components. In this case, using different scale factors for the vertical components may not result in substantial improvement to the fit. They have also constrained the scale factors between 0.25 and 4.0 as per ASCE/SEI 7-22 (ASCE, 2022), although this would reduce the pool of ground motions with spectral shapes that match the target spectrum well.

#### *10.4.3.8 ASCE/SEI 7-22 Provisions*

In the US, provisions for bidirectional analyses (e.g., ASCE/SEI 7-22 and FEMA P-1050-1) currently utilise the maximum-direction $S_{a,RotD100}$ spectrum (Haselton et al., 2017) to define the seismic hazard. The change from a geometric mean spectrum to the maximum-direction spectrum was first introduced in ASCE/SEI 7-10 to be consistent with how the $MCE_R$ spectrum is constructed (ATC, 2012). ASCE/SEI 7-22 requires the average of all maximum-direction spectra in a suite to match a target spectrum by scaling each pair of components with the same scale factor. The goodness of fit is assessed across a range of periods encompassing the periods dominating both principal directions of the structure. This ranges from the lowest period of both directions (to achieve 90% mass participation), or $0.2T_1$, to the highest period of both translational directions (after developing nonlinear/ductile/period-lengthening behaviour), the fundamental torsional period, or $2T_1$.

For near-fault sites, components need to be rotated to fault-normal/fault-parallel orientations before they are applied to a building. For site conditions, the ground motion components should be applied at arbitrary (random) orientation for an unbiased response prediction, as it has been observed that the direction of maximum spectral acceleration is essentially random for distances more than 5 km and does not depend on the period or the principal direction of the building (Huang, Whittaker, & Luco, 2009). For distances less than 5 km, the fault-normal orientation appears to coincide with the direction of maximum shaking only for periods above 1 s.

Simulation of vertical response is required when it is expected to affect structural response significantly. This includes buildings with long spans, cantilevers, prestressed construction, and discontinuous gravity load paths. Vertical ground motion components can be scaled by different scale factors from the horizontal components. The average of the vertical spectra of the set of records has to exceed the vertical target spectrum within the period range. The lower-bound period for the vertical spectrum does not need to be any lower than either 0.1 s or the highest vertical mode.

#### *10.4.3.9 NBCC Provisions*

A nonlinear dynamic analysis is an acceptable alternative to a linear analysis in NBCC. Since such analyses are still done primarily in a research environment or in cases of special studies, it is essential that the study be conducted and peer-reviewed by individuals who are competent and experienced in making the necessary judgments and decisions. In addition, the resulting design should be reviewed by a qualified independent engineering team. Particular attention should be given to the requirements for stiff elements, the effect of site classification on ground motion values, the use of an appropriate earthquake importance factor, and the restrictions on structural configuration. The following considerations are of particular importance in the special study:

- Independent design review is required when nonlinear time-history analysis is used. The review must be performed by a panel of at least three peer reviewers, including at least one reviewer who has recognised expertise in each of the following areas: nonlinear time-history analysis, earthquake-resistant design, and seismic hazard; and

- The ground motion time-histories used as input should be representative of the seismotectonic environment and the geotechnical conditions at the location of the building, and should be selected and scaled according to the NBCC guidelines.

These guidelines are based on the provisions proposed for ASCE/SEI 7-22 but include several differences that reflect the provisions of the NBCC.

The ground motion records selected must cover the range of periods that contribute significantly to the seismic response of the building in the period range of interest. Typically, suites of ground motion records are selected to cover two or more segments of the period range of interest by considering earthquakes associated with different dominant magnitude–distance scenarios or earthquakes from different sources or tectonic environments. For example, in southwestern British Columbia (Greater Vancouver and Vancouver Island), Canada, contribution from the shallow crustal, subduction interface, and subduction intraslab earthquakes should be considered. The ground motion records selected for each suite must be representative of the magnitude–distance scenario and the tectonic environment. NBCC recommends that a minimum of 11 ground motion records be used for each suite (NRC, 2015). Using fewer than 11 records for a suite is allowed in cases when no fewer than five records are used for each suite, the number of records is approved by the review panel, and the total number of records in all the suites is not less than 11. For example, where earthquakes from only one tectonic environment contribute to the seismic hazard at a site, the number of records per suite can be reduced to five, but the total number of records in all the suites must be at least 11. The response spectra of the ground motion records selected for each suite should match the target spectrum for the scenario-specific period range $T_{RS}$. This is called method A.

For the purposes of ground motion selection and scaling, a period range, $T_R$, should be defined that covers the periods of the vibration modes that significantly contribute to the building's dynamic response, either in the translational direction and/or in torsion. The upper-bound period, $T_{max}$, must be greater than or equal to twice the first-mode period, but not less than 1.5 s; the lower-bound period, $T_{min}$, should be established such that the range of periods from lowest to highest includes at least the periods of the modes that are necessary to achieve 90% mass participation, but not more than 0.15 times the first-mode period (see Figure 18). The dynamic properties of the building should be obtained from the structural model used for the time-history analysis.

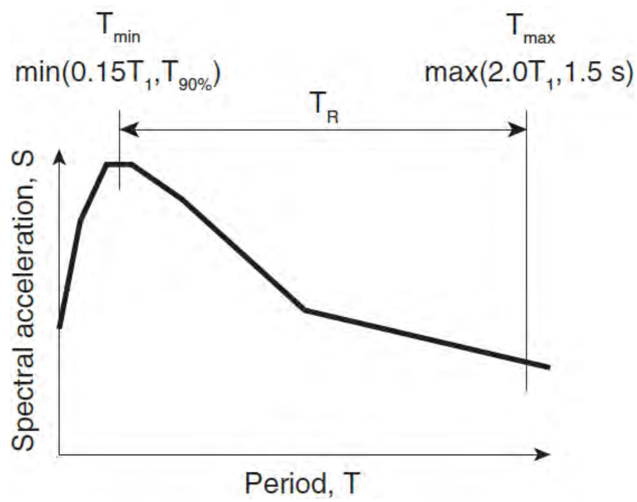


**Figure 17. Period range $T_R$ according to NBCC (NRC, 2022)**

When the analysis is performed on a 2D structural model, the upper- and lower-bound periods should be determined using the periods obtained in the direction considered. When the analysis is performed on a 3D structural model, either with ground motion components in only one horizontal direction or with pairs of orthogonal horizontal ground motion components, the upper-bound period should be based on the longest first-mode period in the two orthogonal directions and the lower-bound period should be established to include the periods of the modes necessary to achieve 90% mass participation in each orthogonal direction, without exceeding 0.15 times the shortest first-mode period in the two orthogonal directions. When vertical ground motions are used in the analysis, the lower-bound period should be established to also include the periods of the modes required to achieve 90% mass participation in the vertical direction.

Appropriate ground motions should be selected based on the tectonic regime, the magnitudes and distances that control the seismic hazard, and the local geotechnical conditions at the site. Recorded ground motions are generally preferred; however, ground motions simulated using a seismological model may be used as an alternative if appropriate records are not available. If sufficient data exists, the ground motions for each suite should be selected from at least two distinct seismic events; where possible, no more than two ground motion records from the same earthquake event should be selected.

The response spectra of the selected motions should have spectral shapes that are similar to those of the target response spectrum (or spectra) defined according to methods A, B1, or B2, as explained below (Figure 19).

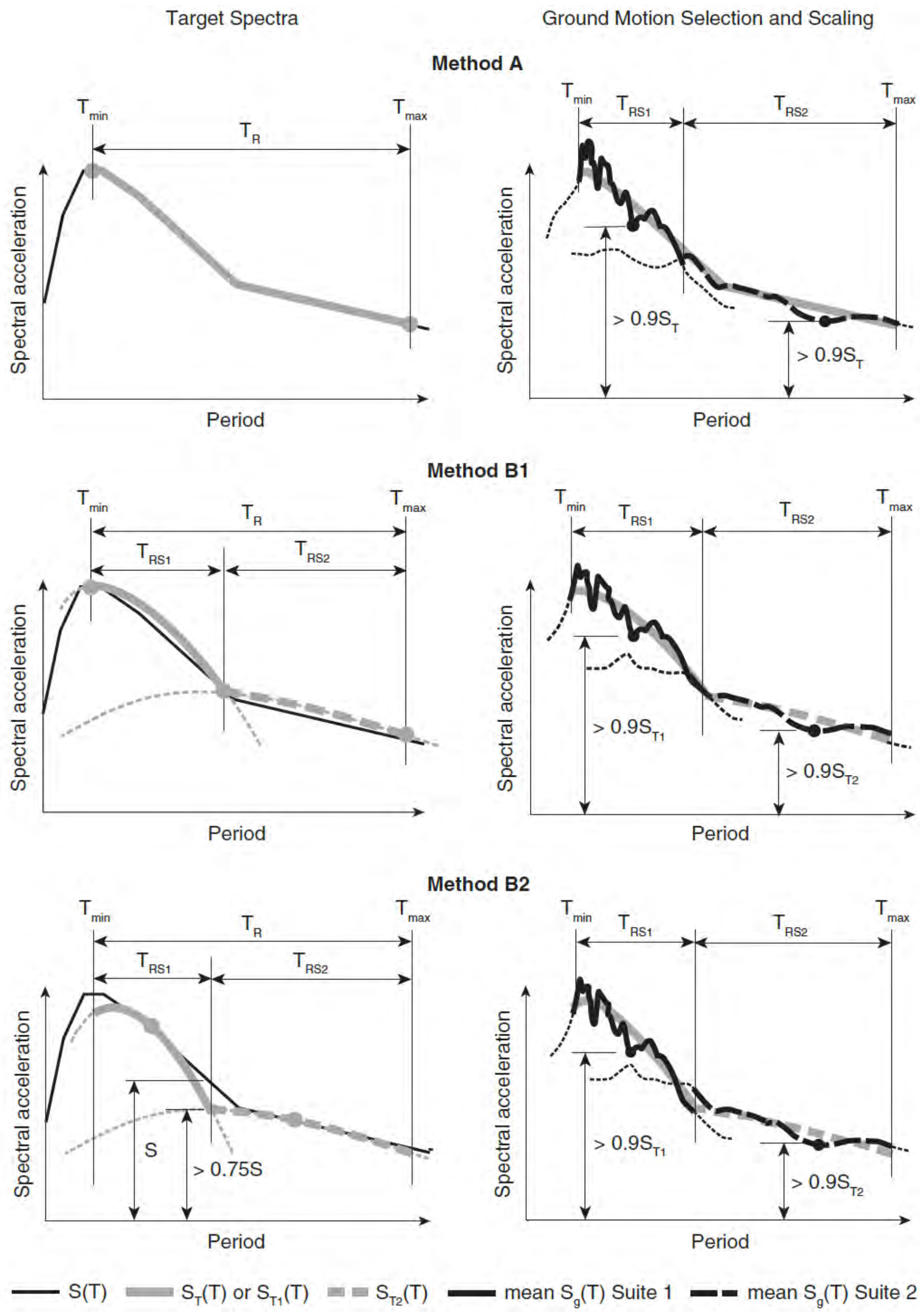


**Figure 18. Definition of target spectrum (or spectra), $S_T(T)$, and scaling of suites of ground motion records over scenario-specific period ranges, $T_{RS}$, using methods A, B1, and B2 according to NBCC (NRC, 2022)**

Method A: A single target response spectrum, $S_T(T)$, may be specified based on the design spectrum for the location for the period range, $T_R$. Suites of ground motion records should be selected to cover appropriate segments of the period range, $T_R$, considering the dominant earthquake magnitude–distance combinations revealed by the site-specific seismic hazard disaggregation. Each period segment constitutes a scenario-specific period range, $T_{RS}$. For locations where earthquakes from different tectonic environments (or sources) contribute to the hazard—as is the case in southwestern British Columbia where shallow crustal, subduction intraslab, and subduction interface earthquakes are expected—a minimum of one scenario-specific period range, $T_{RS}$, should be defined for each tectonic environment (or source) contributing to the hazard. The scenario-specific period ranges, $T_{RS}$, may overlap each other, but together they should cover the period range, $T_R$.

Method B: Two or more site-specific scenario target response spectra, $S_T(T)$, may be specified to cover the period range $T_R$. Each target spectrum is used to select and scale the ground motion records in lieu of the design spectrum, $S(T)$. Suites of ground motion records should be selected for each site-specific scenario target spectrum, $S_T(T)$, considering earthquake magnitude–distance combinations and tectonic sources used to define the scenario target spectra. Each scenario target spectrum should cover a segment of the period range $T_R$, and each period segment constitutes a scenario-specific period range $T_{RS}$. The $T_{RS}$ ranges may overlap each other, but together they should cover the period range, $T_R$. The target spectra may be obtained from two different approaches, B1 or B2, as described below.

*Method B1:* Site-specific scenario target spectra, $S_T(T)$, are created for each dominant earthquake magnitude–distance combination and/or for each tectonic source that contributes to the hazard in the period range, $T_R$, as revealed by site-specific seismic hazard disaggregation. For locations where earthquakes from different tectonic sources contribute to the hazard—as is the case in southwestern British Columbia—a minimum of one scenario target spectrum is required for each source contributing to the hazard. The envelope of the scenario target spectra should be no less than the design spectrum, $S(T)$, over the period range $T_R$.

*Method B2:* The site-specific scenario target spectra, $S_T(T)$, are created for periods that correspond to those periods of the vibration modes that significantly contribute to the dynamic response of the building in the period range, $T_R$. Lengthening of the elastic periods due to anticipated inelastic response is accounted for when selecting the periods. For each period selected, a scenario target spectrum, $S_T(T)$, is created that matches or exceeds the design spectrum value at that period. When developing the scenario target spectrum, site-specific disaggregation should be performed to identify earthquake magnitude–distance combinations that dominate the hazard at each period considered. The scenario target spectra should be representative of one or more spectral shapes for the dominant earthquake magnitude–distance combinations revealed by the disaggregation. Ground motion prediction equations may be used to define the spectral shapes for specific scenarios; conditional mean spectra may be used as scenario target spectra. The envelope of the scenario target spectra should be no less than 75% of the design spectrum, $S(T)$, over the defined period range $T_R$.

Examples of the selection and scaling of ground motion time-histories according to the NBCC guidelines can be found in Tremblay et al. (2015). Additional information on the selection and scaling of ground motion time-histories can be found in Haselton et al. (2012), ATC and CUREE (2011), Baker (2011), and Daneshvar et al. (2015). Information on seismicity in Canada and the assessment of seismic hazard can be found in Atkinson and Adams (2013); Halchuk et al. 2014; Halchuk, Adams, and Allen, 2015; Halchuk, Allen, Rogers, and Adams, 2015; and Rogers et al. (2015). Ground motion time-histories are available in several databases. The Engineering Seismology Toolbox (www.seismotoolbox.ca) contains simulated ground motion records for site classes A, C, D, and E for both western and eastern seismic regions of Canada, as well as predicted ground motions for large subduction earthquakes anticipated in the Cascadia subduction zone (Atkinson, 2009). The PEER NGA-West2 ground motion database (https://ngawest2.berkeley.edu) contains a large number of ground motions recorded during shallow crustal earthquakes in active tectonic regimes (Ancheta et al., 2013). The PEER NGA-East ground motion database (https://ngawest2.berkeley.edu) contains ground motion records for central and eastern North America (Goulet et al., 2014; PEER, 2015).

### 10.4.4 Acceptance Criteria

Given the inherent variability in the response of structures to earthquake ground motions and the many simplifying assumptions made in analysis, the results of any linear or nonlinear analysis for earthquake performance should be interpreted with care. While nonlinear dynamic analyses do, in theory, provide more realistic measures of response than other methods, the results of the nonlinear dynamic analyses can be sensitive to modelling assumptions and parameters. Therefore, the first step before any interpretation of results should be to establish confidence in the reliability of the model through strategies such as those described in Chapters 3 to 7. Moreover, nonlinear static analyses can be used to augment the nonlinear dynamic analysis to interrogate structural behaviour and the effect of design changes on the demands.

According to ASCE/SEI 7-22 and as commonly applied in practice, when seven or more ground motions are run, the calculated mean demand parameter values should be compared to the acceptance criteria for the specified performance levels. Assuming a lognormal distribution of demand parameters with a dispersion (standard deviation of the natural log of the data and similar to a coefficient of variation) of 0.5, the checks based on mean values imply that the acceptance criteria would be exceeded about 40% of the time. This large probability of exceedance is an accepted standard of practice, provided that the likelihood (e.g., mean annual frequency of exceedance) of the specified earthquake intensity is sufficiently low for the performance level being checked. However, where overload of non–ductile force-controlled components may lead to sudden failures that could significantly affect the overall building safety, it is generally recognised that more stringent criteria should be applied.

The PEER *Seismic Design Guidelines for Tall Buildings* (2010) specify required strengths for force-controlled elements equal to 1.3 to 1.5 times the mean demand parameter, where the lower multiplier (1.3) is permitted for systems in which capacity design is used to shield force-controlled members. Assuming dispersion of 0.5 in the displacement demands, there is a 15% to 20% probability that the actual strength demands will exceed the specified required strengths (i.e., 1.3 to 1.5 times the calculated mean demands). Whether these increased deformation demands will translate into increased component force demands depends on the structural configuration and the interaction of yielding and nonyielding components. While relatively straightforward to apply, the simple demand multipliers assume a fixed relationship between ground motion intensities, drifts, and component deformation and force demands. This assumption is very approximate for nonlinear systems. An alternative method to evaluate the increased demands is to (1) repeat the nonlinear dynamic analyses for ground motions whose intensities are factored up by an appropriate factor (e.g., a factor of 1.5 based on the PEER guidelines), and (2) calculate the mean demands for critical force-controlled components under the amplified input motions. This alternative procedure has the benefit of accounting directly for inelastic force redistributions and possible shielding of force-controlled components. While both approaches account for variability in earthquake ground motions, neither directly addresses structural model uncertainties, where the variation in response of specific structural components may change the inelastic mechanisms and distribution of internal forces and deformations. Therefore, where the uncertainty in analysis model parameters is large and has the potential to significantly alter the structural response, it may be appropriate to interrogate the model for such effects. This could be done by systematically varying the model properties for the critical components and conducting dynamic and/or static nonlinear analyses to characterise the change in the calculated demand parameters.

Despite the large inherent uncertainties in earthquake ground motions and their effects on structures, nonlinear dynamic analysis is considered the most reliable method available to evaluate the earthquake performance of buildings. Primarily, the nonlinear dynamic procedure enables the evaluation of design decisions on a more consistent and rational basis compared to other simplified analysis methods. The potential impact of uncertainties in the structural response can, to some extent, be mitigated through capacity-design approaches in new buildings and to some extent in devising structural retrofits for existing buildings. Otherwise, the uncertainties can be addressed using the methods suggested previously. Ultimately, the engineer must understand the capabilities and limitations of any method of analysis and make appropriate use of the analysis to characterise the structural behaviour with sufficient accuracy and confidence for design.

Some of the main acceptance criteria in various codes and standards are also given below:

ASCE/SEI 7-22 (ASCE, 2022)

- At the global level, the allowable limit of the mean storey drift should range from 1% to 3% (at $MCE_R$), depending on $C_d$ and $R$ values, structural typology, and risk category.
- At the element level, the mean force or deformation must not exceed a limit that is dictated by some or all of the following: the element's force or deformation capacity, how critical the element is in terms of consequence of element failure, and the importance level of the structure.
- Gravity-resisting systems must support gravity loads when subjected to the mean building displacements.

NBCC (NRC, 2022)

- The allowable limit of the mean interstorey drift should be a maximum of 2.5% at design ground motion level, which is 2% in 50 years exceedance or a return period of 2476 years.
- NBCC 2022 introduces additional performance requirements for post-disaster and high-importance category buildings in higher seismic categories. The buildings must remain elastic and must meet reduced drift limits when subjected to lower-intensity ground motions that occur more frequently than the design ground motion level. Post-disaster buildings in seismic categories SC2, SC3, and SC4 must have a maximum interstorey drift of 0.5% for 5% in 50 years ground motions (975-year return period earthquakes). Also, buildings, including SFRSs and structural elements not considered part of SFRSs, must remain linear elastic. Connections of elements and components designed with $R_p > 1.5$ must also remain linear elastic. $R_p$ is the component response modification factor, which recognises the energy-dissipative capability of the component and its connection to the structure; it serves the same function as the product of reduction factors, $R_dR_o$.

- High-importance buildings in seismic categories SC3 and SC4 must have a maximum interstorey drift of 0.5% for 10% in 50 years ground motions (476-year return period earthquakes). Also, buildings, including SFRSs and structural elements not considered part of SFRSs, must remain linear elastic. Connections of elements and components designed with $R_p$ > 1.3 must also remain linear elastic.
- In normal-importance buildings higher than 30 m in seismic category SC4, structural elements not considered part of SFRSs must remain linear elastic for 10% probability of exceedance in 50 years ground motions.
- At the element level, the mean force or deformation must not exceed a limit that is dictated by some or all of the following: the element's force or deformation capacity, how critical the element is in terms of consequence of element failure, and the importance level of the structure.
- Gravity-resisting systems must support gravity loads when subjected to the mean building displacements.

<u>NZS 1170.5:2004 (Standards New Zealand, 2004)</u>

- An interstorey drift limit of 2.5% should be satisfied, but a higher limit of 3.75% is allowed if the record includes forward directivity effects.

<u>Eurocode 8 – Part 1 (CEN, 2004)</u>

- The interstorey drift limit should range from 1% to 2.5% depending on (a) whether nonstructural elements are brittle/ductile, (b) the importance class of the structure, and (c) the local seismic hazard conditions.
- Demand-capacity check in terms of forces for brittle elements and in terms of deformations for ductile elements.

<u>Technical guide for evaluating seismic factors in NBCC (DeVall et al., 2021)</u>

- Unacceptable responses are dynamic instability, nonconvergent analysis, and force or deformation demand on an element that exceeds the force or deformation capacity of that element.
- For all responses of motions that are scaled to 100% of UHS, the interstorey drift limits per the NBCC are to be respected. For responses of ground motions that are scaled to 200% of design UHS, the absolute value of the maximum interstorey drift from the suite of analyses should not exceed 4.5%. Nonlinear time-history analysis beyond this drift limit is considered unreliable using current available analysis tools.
- For motions that are scaled to 100% of UHS, in accordance with NBCC, unacceptable responses are not allowed, except under the following conditions where one outlier response is permitted:
    - The suite includes a minimum of 11 ground motions;
    - Additional evaluations indicate that the predicted response is not indicative of unacceptable structural performance; and

  - Spectral matching techniques are not used.

- For motions that are scaled to 200% of UHS, if more than 50% of the ground motions in each suite result in an unacceptable response (basically collapse), the system is considered to have failed.

### 10.4.5 Uncertainties and Accuracy of Modelling

The total variability in earthquake-induced demands is large and difficult to quantify. Considering all major sources of uncertainties, the coefficients of variation in demand parameters are from 0.5 to 0.8 and generally increase with an increase in ground motion intensity. The variability is usually highest for structural deformations and accelerations and lower in force-controlled components of capacity-designed structures where the forces are limited by the strength of yielding members. The variability is generally attributed to three main sources: (a) hazard uncertainty in the ground motion intensity, such as the spectral acceleration intensity calculated for a specified earthquake scenario or return period, (b) ground motion uncertainty arising from frequency content and duration of a ground motion with a given intensity, and (c) structural behaviour and modelling uncertainties.

The modelling uncertainties arise from variability in (a) physical attributes of the structure, such as material properties, geometry, structural details, etc., (b) nonlinear behaviour of the structural components and system, and (c) mathematical model representation of the actual behaviour. Realistic modelling of the underlying mechanics helps reduce uncertainty in demand predictions in nonlinear dynamic analyses compared to nonlinear or linear static analyses, where the underlying uncertainties are masked by simplified analysis assumptions. However, even in nonlinear dynamic analyses it is practically impossible to accurately calculate the variability in demand parameters. Conceptually, it is possible to quantify the corresponding variability in the calculated demands using techniques such as Monte Carlo simulation; however, complete characterisation of modelling uncertainty is a formidable problem for real buildings. Apart from the lack of necessary data to characterise fully the variability of the model parameters (standard deviations and correlations between multiple parameters), the number of analyses required to determine the resulting variability is prohibitive for practical assessment of real structures. Therefore, nonlinear analysis procedures are generally aimed at calculating the median (or mean) demands. The statistical variability in material parameters and model components generally follows a lognormal distribution, which implies that the median and mean (expected) values are not the same. However, as this difference is small for most material and other model parameters, combined with the fact that in practice there is rarely enough data to accurately characterise the difference, then it is reasonable to use either median or mean values to establish the parameters of the analysis model. This includes using median values of material properties and component test data (such as the nonlinear hysteretic response data of a flexural hinge) to calibrate the analysis models. ASCE 41-17 and other standards provide guidance to relate minimum specified material properties to expected values; for example, the *Seismic Provisions for Structural Steel Buildings* standard (American Institute of Steel Construction, 2016) specifies $R_y$ values that relate to expected minimum specified material strengths. By using median or mean values for a given earthquake intensity, the calculated values of demand parameters are median (50th percentile) estimates.

Uncertainties in the evaluation are then accounted for by choosing the specified hazard level (return period) at which the analysis is run and/or the specified acceptance criteria to which the demands are compared.

Separate factors or procedures are sometimes applied to check acceptance criteria for force-controlled or other capacity-designed components.

Nonlinear analysis software is highly sophisticated, requiring training and experience to obtain reliable results. While the software technical user manual is usually the best resource on the features and use of any software, it may not provide a complete description of the outcome of various combinations of choices of input parameters, or the theoretical and practical limitations of different features. Therefore, analysts should build up experience of the software capabilities by performing analysis studies on problems with increasing scope and complexity, beginning with element tests of simple cantilever models and building up to models that encompass features relevant to the types of structures being analysed. Basic checks should be made to confirm that the strength and stiffness of the model are correct under lateral load. Next, cyclic tests should be run to confirm the nature of the hysteretic behaviour of the connection or component. Sensitivity tests with alternative input parameters and evaluation of cyclic versus in-cycle degradation should also be conducted. Further validation using published experimental tests can help build understanding and confidence in the nonlinear analysis software and alternative modelling decisions (e.g., effects of element mesh refinement and section discretisation).

Beyond having confidence in the software capabilities and the appropriate modelling techniques, it is essential to check the accuracy of models developed for a specific project. Checks begin with basic items necessary for any analysis. Additional checks are necessary for nonlinear analyses to help ensure that the calculated responses are realistic. Beyond becoming familiar with the capabilities of a specific software package, the designer should perform the following suggested checks to help ensure the accuracy of nonlinear analysis models for calculating earthquake demand parameters:

- Check the mode shapes of the model. Ensure that the first-mode periods for the translational axes and rotation are consistent with what is expected (e.g., hand calculation or preliminary structural models) and that the sequence of modes is logical. Check for spurious local modes that may be due to incorrect element properties, inadequate restraints, or incorrect mass definitions.
- Check the total mass of the model and that the effective masses of the first few modes in each direction are realistic and account for most of the total mass.
- Generate the elastic (displacement) response spectra of the input ground motions. Check that they are consistent and note the variability. Determine the median spectrum of the records and the variability about the median.
- Perform elastic RSA using the median spectrum of the record set and dynamic response history analysis of the model and calculate the displacements at key points, along with the elastic base shear and overturning moment. Compare the response spectrum results to the median of the dynamic analysis results.
- Perform nonlinear static analyses to the target displacements for the median spectrum of the ground motion record set. Calculate the displacements at key locations, along with the base shear and overturning moment and compare to the elastic analysis results. Vary selected input or control parameters (e.g., with and without P-Δ, different loading patterns, variations in component strength or deformation capacities) and confirm observed trends in the response.

- Perform nonlinear dynamic analyses and calculate the median values of displacements, base shear, and overturning moment and compare to the results of elastic and nonlinear static analyses. Vary selected input or control parameters similar to the variations applied in the static nonlinear analyses and compare to each other and to the static pushover and elastic analyses. Plot hysteresis responses of selected components to confirm that they look realistic, and look for patterns in the demand parameters, including the distribution of deformations and spot checks of equilibrium.

## 10.5 SUMMARY

Seismic response analysis is a crucial evaluation of timber structures in earthquake-prone areas. This chapter provides information related to different types and methods of static and dynamic analyses used to quantify the seismic response of timber structures, along with their advantages and drawbacks. It also highlights the specific modelling requirements and considerations for different types of seismic response analyses, along with their suitability for timber structures. In addition, this chapter discusses important aspects of the seismic design approach from the modelling perspective. The information presented in this chapter is intended to help practising engineers and researchers become more acquainted with seismic response modelling and analysis of timber structures.

## 10.6 ACKNOWLEDGEMENTS

The authors would like to acknowledge Mr. Nicholas Chan for his contributions to Section 10.4.

## 10.7 REFERENCES

American Institute of Steel Construction. (2016). *Seismic provisions for structural steel buildings* (ANSI/AISC 341-16).

American Society of Civil Engineers. (2000). *Prestandard and commentary for the seismic rehabilitation of buildings* (FEMA 356). Federal Emergency Management Agency.

American Society of Civil Engineers. (2007). *Minimum design loads for buildings and other structures* (ASCE/SEI 7-10).

American Society of Civil Engineers. (2022). *Minimum design loads and associated criteria for buildings and other structures* (ASCE/SEI 7-22).

American Society of Civil Engineers. (2017). *Seismic evaluation and retrofit of existing buildings* (ASCE/SEI 41-17).

American Wood Council. (2021). *Special design provisions for wind and seismic, with commentary*. https://awc.org/publications/2021-sdpws/

Ancheta, T. D., Darragh, R. B., Stewart, J. P., Seyhan, E., Silva, W. J., Chiou, B. S. J., Wooddell, K. E., Graves, R. W., Kottke, A. R., Boore, D. M., Kishida, T., & Donahue, J. L. (2013). *PEER NGA-West2 database* (Report 2013/03). Pacific Earthquake Engineering Research Center.

Applied Technology Council. (2005). *Improvement of nonlinear static seismic analysis procedures* (FEMA 440). Federal Emergency Management Agency.

Applied Technology Council. (2009a). *Effects of strength and stiffness degradation on seismic response* (FEMA P440A). Federal Emergency Management Agency.

Applied Technology Council. (2009b). *Quantification of building seismic performance factors* (FEMA P695). Federal Emergency Management Agency.

Applied Technology Council. (2010). *Modeling and acceptance criteria for seismic design and analysis of tall buildings* (PEER/ATC-72-1). Pacific Earthquake Engineering Research Center.

Applied Technology Council. (2017). *Recommended modeling parameters and acceptance criteria for nonlinear analysis in support of seismic evaluation, retrofit, and design* (NIST GCR 17-917-45). National Institute of Standards and Technology.

Applied Technology Council & Consortium of Universities for Research in Earthquake Engineering. (2011). *Selecting and scaling earthquake ground motions for performing response history analysis* (NIST GCR 11-917-15). National Institute of Standards and Technology.

Atkinson, G. M. (2009). Earthquake time histories compatible with the 2005 National Building Code of Canada uniform hazard spectrum. *Canadian Journal of Civil Engineering, 36*(6), 991-1000. https://doi.org/10.1139/L09-044

Atkinson, G. M., & Adams, J. (2013). Ground motion prediction equations for application to the 2015 Canadian national seismic hazard maps. *Canadian Journal of Civil Engineering, 40*(10), 988-998. https://doi.org/10.1139/cjce-2012-0544

Baker, J. W, & Cornell, C. A. (2006). Which spectral acceleration are you using? *Earthquake Spectra*, 22(2), 293-312.

Baker, J. W. (2011). Conditional mean spectrum: Tool for ground-motion selection. *Journal of Structural Engineering, 137*(3), 322-331. https://doi.org/10.1061/(ASCE)ST.1943-541X.0000215

Charney, F. A. (2008). Unintended consequences of modeling damping in structures. *Journal of Structural Engineering, 134*(4), 581-592. https://doi.org/10.1061/(ASCE)0733-9445(2008)134:4(581)

Chen, Z., Chui, Y.-H., Doudak, G., & Nott, A. (2016). Contribution of type-X gypsum wall board to the racking performance of light-frame wood shear walls. *Journal of Structural Engineering, 142*(5), 4016008. https://doi.org/10.1061/(ASCE)ST.1943-541X.0001468

Chen, Z., Chui, Y. H., Mohammad, M., Doudak, G., & Ni, C. (2014, August 10–14). *Load distribution in lateral load resisting elements of timber structures* [Conference presentation]. World Conference on Timber Engineering, Quebec City, Canada.

Chen, Z., Chui, Y. H., Ni, C., Doudak, G., & Mohammad, M. (2014). Load distribution in timber structures consisting of multiple lateral load resisting elements with different stiffnesses. *Journal of Performance of Constructed Facilities, 28*(6), A4014011. https://doi.org/10.1061/(ASCE)CF.1943-5509.0000587

Chen, Z., & Ni, C. (2020). Criterion for applying two-step analysis procedure to seismic design of wood-frame buildings on concrete podium. *Journal of Structural Engineering, 146*(1), 4019178. https://doi.org/10.1061/(ASCE)ST.1943-541X.0002405

Chen, Z., Ni, C., Dagenais, C., & Kuan, S. (2020). Wood$^{ST}$: A temperature-dependent plastic-damage constitutive model used for numerical simulation of wood-based materials and connections. *Journal of Structural Engineering, 146*(3), 4019225. https://doi.org/10.1061/(ASCE)ST.1943-541X.0002524

Chen, Z., & Popovski, M. (2020). Connection and system ductility relationship for braced timber frames. *Journal of Structural Engineering, 146*(12), 4020257. https://doi.org/10.1061/(ASCE)ST.1943-541X.0002839

Chen, Z., & Popovski, M. (2021a). Seismic response of braced heavy timber frames with riveted connections. *Journal of Performance of Constructed Facilities, 35*(5), 4021051. https://doi.org/10.1061/(ASCE)CF.1943-5509.0001618

Chen, Z., & Popovski, M. (2021b). *Expanding wood use towards 2025: Performance and draft design guidelines for braced timber frames under lateral loads*. FPInnovations.

Chen, Z., Zhu, E., & Pan, J. (2011). Numerical simulation of wood mechanical properties under complex state of stress. *Chinese Journal of Computational Mechanics, 28*(4), 629-634, 640.

Chopra, A. K. (2012). *Dynamics of structures: Theory and applications to earthquake engineering* (4th ed.). Prentice Hall.

Chopra, A. K. (2017). *Dynamics of structures: Theory and applications to earthquake engineering* (5th ed.). Prentice Hall.

Clough, R. W., & Penzien, J. (1993). *Dynamics of structures* (2nd ed.). McGraw-Hill.

Comartin, C. D., Niewiarowski, R. W., & Rojahn, C. (1996). *ATC-40. Seismic evaluation and retrofit of concrete buildings* (SSC 96-1). Applied Technology Council.

CSA Group. (2019). *Engineering design in wood* (CSA O86:19).

Daneshvar, P., Bouaanani, N., & Godia, A. (2015). On computation of conditional mean spectrum in eastern Canada. *Journal of Seismology, 19*(2), 443-467. https://doi.org/10.1007/s10950-014-9476-6

DeVall, R., Popovski, M., & McFadden, J. B. W. (2021). *Technical guide for evaluation of seismic force resisting systems and their force modification factors for use in the National Building Code of Canada with concepts illustrated using a cantilevered wood CLT shear wall example* (NRCC-CONST-56478E). Canadian Construction Materials Centre. https://doi.org/10.4224/40002658

European Committee for Standardization. (2004). *Eurocode 8: Design of structures for earthquake resistance - Part 1: General rules, seismic actions and rules for buildings* (EN 1998-1:2004).

Fajfar, P. (1999). Capacity spectrum method based on inelastic demand spectra. *Earthquake Engineering and Structural Dynamics, 28*(9), 979-993. https://doi.org/10.1002/(SICI)1096-9845(199909)28:9<979::AID-EQE850>3.0.CO;2-1

Fajfar, P., & Fischinger, M. (1988). N2 – A method for non-linear seismic analysis of regular buildings. *Proceedings of the Ninth World Conference on Earthquake Engineering, 5*, 111-116.

Fajfar, P., & Gašperšič, P. (1996). The N2 method for the seismic damage analysis of RC buildings. *Earthquake Engineering and Structural Dynamics, 25*(1), 31-46. https://doi.org/10.1002/(SICI)1096-9845(199601)25:1<31::AID-EQE534>3.0.CO;2-V

Filiatrault, A. Tremblay, R., Christopoulos, C., Folz, B., & Pettinga, D. (2013). *Elements of earthquake engineering and structural dynamics* (3rd ed.). Presses internationales Polytechnique.

Freeman, S. A. (2004). Review of the development of the capacity spectrum method. *ISET Journal of Earthquake Technology, 41*(1), 1-13.

Giannopoulos, D., & Vamvatsikos, D. (2018). Ground motion records for seismic performance assessment: To rotate or not to rotate? *Earthquake Engineering and Structural Dynamics, 47*(12), 2410-2425. https://doi.org/10.1002/eqe.3090

Goulet, C. A., Kishida, T., Ancheta, T. D., Cramer, C. H., Darragh, R. B., Silva, W. J., Hashash, Y. M. A., Harmon, J., Stewart, J. P., Wooddell, K. E., & Young, R. R. (2014). *PEER NGA-East database* (Report 2014/17). Pacific Earthquake Engineering Research Center.

Halchuk, S., Adams, J., & Allen, T. I. (2015). *Fifth generation seismic hazard model for Canada: Grid values of mean hazard to be used with the 2015 National Building Code of Canada* (Geological Survey of Canada, Open File 7893). https://doi.org/10.4095/297378

Halchuk, S., Allen, T. I., Adams, J., & Rogers, G. C. (2014). *Fifth generation seismic hazard model input files as proposed to produce values for the 2015 National Building Code of Canada* (Geological Survey of Canada, Open File 7576). https://doi.org/10.4095/293907

Halchuk, S., Allen, T. I., Rogers, G., & Adams, J. (2015). *Seismic hazard earthquake epicentre file (SHEEF2010) used in the fifth generation seismic hazard maps of Canada* (Geological Survey of Canada, Open File 7724). https://doi.org/10.4095/296908

Hall, J. F. (2006). Problems encountered from the use (or misuse) of Rayleigh damping. *Earthquake Engineering and Structural Dynamics, 35*(5), 525-545. https://doi.org/10.1002/eqe.541

Haselton, C. B., Baker, J. W., Stewart, J. P., Whittaker, A. S., Luco, N., Fry, A., Hamburger, R. O., Zimmerman, R. B., Hooper, J. D., Charney, F. A., & Pekelnicky, R. G. (2017). Response history analysis for the design of new buildings in the NEHRP provisions and ASCE/SEI 7 standard: Part I - Overview and specification of ground motions. *Earthquake Spectra, 33*(2), 373-395. https://doi.org/10.1193/032114EQS039M

Haselton, C. B., Whittaker, A. S., Hortacsu, A., Baker, J. W., Bray, J., & Grant, D. N. (2012). Selecting and scaling earthquake ground motions for performing response-history analyses. *Proceedings 15th World Conference on Earthquake Engineering*, *31,* 4207-4217.

Huang, Y.-N., Whittaker, A. S., & Luco, N. (2009). Orientation of maximum spectral demand in the near-fault region. *Earthquake Spectra, 25*(3), 707-717. https://doi.org/10.1193/1.3158997

Jayaram, N., Lin, T., & Baker, J. W. (2011). A computationally efficient ground-motion selection algorithm for matching a target response spectrum mean and variance. *Earthquake Spectra, 27*(3), 797-815. https://doi.org/10.1193/1.3608002

Kalkan, E., & Kunnath, S. K. (2006). Effects of fling step and forward directivity on seismic response of buildings. *Earthquake Spectra*, *22*(2), 367-390. https://doi.org/10.1193/1.2192560

Kalkan, E., & Reyes, J. C. (2015). Significance of rotating ground motions on behavior of symmetric- and asymmetric-plan structures: Part II. Multi-story structures. *Earthquake Spectra, 31*(3), 1613-1628. https://doi.org/10.1193/072012EQS242M

Koliou, M., van de Lindt, J.W., & Hamburger, R.O. (2018). Nonlinear modeling of wood-frame shear wall systems for performance-based earthquake engineering: Recommendations for the ASCE 41 standard. *Journal of Structural Engineering*, *144*(8), 04018905. http://doi.org/10.1061/(ASCE)ST.1943-541X.0002083

Kwong, N. S., & Chopra, A. K. (2018). Determining bidirectional ground motions for nonlinear response history analysis of buildings at far-field sites. *Earthquake Spectra, 34*(4), 1931-1954. https://doi.org/10.1193/052217EQS093M

Kwong, N. S., & Chopra, A. K. (2020). Selecting, scaling, and orienting three components of ground motions for intensity-based assessments at far-field sites. *Earthquake Spectra, 36*(3), 1013-1037. https://doi.org/10.1177/8755293019899954

Lafontaine, A., Chen, Z., Doudak, G., & Chui, Y. H. (2017). Lateral behavior of light wood-frame shear walls with gypsum wall board. *Journal of Structural Engineering, 143*(8), 4017069. https://doi.org/10.1061/(ASCE)ST.1943-541X.0001798

Lagaros, N. D., & Fragiadakis, M. (2011). Evaluation of ASCE-41, ATC-40 and N2 static pushover methods based on optimally designed buildings. *Soil Dynamics and Earthquake Engineering, 31*(1), 77-90. https://doi.org/10.1016/j.soildyn.2010.08.007

Loo, W. Y., Quenneville, P., & Chouw, N. (2016). Rocking timber structure with slip-friction connectors conceptualized as a plastically deformable hinge within a multistory shear wall. *Journal of Structural Engineering, 142*(4), E4015010. https://doi.org/10.1061/(ASCE)ST.1943-541X.0001387

Najam, F. A. (2018). Nonlinear static analysis procedures for seismic performance evaluation of existing buildings – Evolution and issues. In H. Rodrigues, A. Elnashai, & G. M. Calvi (Eds.), *Facing the challenges in structural engineering. Proceedings of the 1st GeoMEast International Congress and Exhibition* (pp. 180-198). Springer. https://doi.org/10.1007/978-3-319-61914-9_15

National Research Council of Canada. (2015). *Structural commentaries* (User's guide – NBC 2015: Part 4 division B).

National Research Council of Canada. (2022). *National Building Code of Canada*.

Nitti, G., Lacidogna, G., & Carpinteri, A. (2019). Structural Analysis of High-rise Buildings under Horizontal Loads: A Study on the Piedmont Region Headquarters Tower in Turin. *The Open Construction & Building Technology Journal*. 13, 81-96. https://doi.org/10.2174/1874836801913010081

Pacific Earthquake Engineering Research Center. (2010). *Seismic design guidelines for tall buildings* (Report 2010/05). University of California.

Pacific Earthquake Engineering Research Center. (2015). *NGA-East: Median ground-motion models for the central and eastern North America region* (Report 2015/04). University of California.

Pacific Earthquake Engineering Research Center. (2017). *Guidelines for performance-based seismic design of tall buildings* (Report 2017/06). University of California.

Paz, M., & Kim Y. H. (2019). *Structural dynamics: Theory and computation* (6th ed.). Springer.

Popovski, M., & Karacabeyli, E. (2008, October 12–17). *Force modification factors and capacity design procedures for braced timber frames* [Conference presentation]. 14th World Conference on Earthquake Engineering, Beijing, China.

Popovski, M., Tung, D., & Chen, Z. (2022). Structural analysis and design. In E. Karacabeyli & C. Lum (Eds.), *Technical guide for the design and construction of tall wood buildings in Canada* (2nd ed.). FPInnovations.

Priestley, M. J. N., Calvi, G. M., & Kowalsky, M. J. (2007b, March 30–April 1). *Direct displacement-based seismic design of structures* [Conference presentation]. New Zealand Society for Earthquake Engineering Conference, Palmerston North, New Zealand.

Rainer, J. H., & Karacabeyli, E. (2000, July 31–August 3). *Wood-frame construction in past earthquakes* [Conference presentation]. World Conference on Timber Engineering, Whistler, BC, Canada.

Rogers, G., Halchuk, S., Adams, J., & Allen, T. (2015). *5th generation (2015) seismic hazard model for southwest British Columbia* [Conference presentation]. 11th Canadian Conference on Earthquake Engineering, Victoria, BC Canada.

Roy, R., Thakur, P., & Chakroborty, S. (2014). Spectral matching of real ground motions: Applications to horizontally irregular systems in elastic range. *Advances in Structural Engineering, 17*(11), 1623-1638. https://doi.org/10.1260/1369-4332.17.11.1623

Saatcioglu, M., & Humar, J. (2003). Dynamic analysis of buildings for earthquake-resistant design. *Canadian Journal of Civil Engineering, 30*(2), 338-359.

Shahnewaz, M., Yuxin, P., Alam, M. S., & Tannert, T. (2020). Seismic fragility estimates for cross-laminated timber platform building. *Journal of Structural Engineering, 146*(12), 4020256. https://doi.org/10.1061/(ASCE)ST.1943-541X.0002834

Standards New Zealand. (2004). *Structural design actions - Part 5: Earthquake actions - New Zealand* (NZS 1170.5:2004).

Tremblay, R., Atkinson, G. M., Bouaanani, N., Daneshvar, P., Léger, P., & Koboevic, S. (2015). *Selection and scaling of ground motion time histories for seismic analysis using NBCC 2015* [Conference presentation]. 11th Canadian Conference on Earthquake Engineering, Victoria, BC, Canada.

Valley, M., Aschheim, M., Comartin, C., Holmes, W. T., Krawinkler, H., & Sinclair, M. (2010). *Applicability of nonlinear multiple-degree-of-freedom modeling for design* (NIST GCR 10-917-9). National Institute of Standards and Technology.

Vamvatsikos, D., & Cornell, C. A. (2002). Incremental dynamic analysis. *Earthquake Engineering and Structural Dynamics, 31*(3), 491-514. https://doi.org/10.1002/eqe.141

Willford, M., Whittaker, A., & Klemencic, R. (2008). *Recommendations for the seismic design of high-rise buildings*. Council on Tall Buildings and Urban Habitat.

Wang, G. (2011). A ground motion selection and modification method capturing response spectrum characteristics and variability of scenario earthquakes. *Soil Dynamics and Earthquake Engineering, 31*(4), 611-625. https://doi.org/10.1016/j.soildyn.2010.11.007

Zhang, R., Wang, D.-S., Chen, X.-Y., & Li, H.-N. (2020). Comparison of scaling ground motions using arithmetic with logarithm values for spectral matching procedure. *Shock and Vibration, 2020*, 8180612. https://doi.org/10.1155/2020/8180612

FPInnovations

Global contributors

Natural Resources Canada | Ressources naturelles Canada

Canada

Canadian Wood Council | Conseil canadien du bois

American Wood Council

Québec